ISSN 2148-7847

Journal of Thermal Engineering

Volume 12
Number 2
Year 2026

YTU PRESS

www.jten.yildiz.edu.tr

ISSN 2148-7847

Journal of Thermal Engineering

Volume 12 Number 2 Year 2026

EDITOR-IN-CHIEF
Ahmet Selim Dalkilic, *Yildiz Technical University, İstanbul, Türkiye*

ASSOCIATE EDITORS
Ali Celen, *Erzincan Binali Yıldırım University, Erzincan, Türkiye*
Baha Zafer, *İstanbul University, İstanbul, Türkiye*
Bekir Şener, *Yildiz Technical University, İstanbul, Türkiye*
Erdal Çetkin, *İzmir Institute of Technology, İzmir, Türkiye*
Emre Alpman, *Marmara University, İstanbul, Türkiye*
Erman Aslan, *İstanbul University, İstanbul, Türkiye*
Hasan Köten, *İstanbul Medeniyet University, İstanbul, Türkiye*
Hatice Mercan, *Yildiz Technical University, İstanbul, Türkiye*
Müslüm Arıcı, *Kocaeli University, Kocaeli, Türkiye*
Mustafa Kılıç, *Adana Science and Technology University, Adana, Türkiye*
Nader Javani, *Yildiz Technical University, İstanbul, Türkiye*
Naime Filiz Özdil, *Adana Science and Technology University, Adana, Türkiye*
Şevket Özgür Atayılmaz, *Yildiz Technical University, Adana, Türkiye*
Özgen Açıkgöz, *Yildiz Technical University, İstanbul, Türkiye*
Yaşar İslamoğlu, *Sakarya University, Sakarya, Türkiye*
Yasin Karagoz, *İstanbul Medeniyet University, İstanbul, Türkiye*
Zerrin Sert, *Eskişehir Osmangazi University, Eskisehir, Türkiye*

EDITORIAL BOARD
Adrian Bejan, *Duke University, United States*
Afshin J. Ghajar, *Oklahoma State University, United States*
Ali Chamkha, *Prince Mohammad Bin Fahd University, Saudi Arabia*
Bekir Sami Yilbas, *King Fahd University of Petroleum and Minerals, Dhahran, Saudi Arabia*
Chi-Chuan Wang, *National Chiao Tung University, Taiwan*
Gopal Nath Tiwari, *Indian Institute of Technology, India*
Hakan F. Oztop, *Fırat University, Türkiye*
Hari Mohan Srivastava, *University of Victoria, Canada*
Hamadiche Mahmoud, *Université de Lyon 1, France*
Hamid Niazmand, *Ferdowsi University Of Mashhad, Iran*

ISSN 2148-7847

Journal of Thermal Engineering

Volume 12 Number 2 Year 2026

Josua P. Meyer, *University of Pretoria, South Africa*
Kambiz Vafai, *University of California, United States*
Karan Surana, *The University of Texsas, United States*
Mehmet Kanoğlu, *University of Gaziantep, Türkiye*
Mohammad Mehdi Rashidi, *Bu-Ali Sina University, Iran*
Mohammad Hassan Saidi, *Sharif University of Technology, Iran*
Muhammad Ali Rob Sharif, *The University of Alabama, United States*
Moh'd A. Al-Nimr, *Jordan University of Science and Technology, Jordan*
Mohsen Sheikholeslami, *Babol Noshirvani University of Technology, Iran*
Mustafa Turkyilmazoglu, *Hacettepe University, Türkiye*
N.K. Anand, *Texas A&M University, United States*
Omid Mahian, *Xi'an Jiaotong University, Xi'an, China*
Sergio Nardini, *Seconda Università degli Studi di Napoli, Italy*
Wei-Mon Yan, *National Chiao Tung University, Taiwan*

Abstracting and Indexing: Directory of Open Access Journals (DOAJ), EBSCO Host Online Research Databases, Web of Science, Emerging Sources Citation Index (ESCI), Scopus, TRDizin, MIAR, Scilit, OUCI, Research4Life, Ideal Online, Sherpa Romeo, ASCI

Journal Description: The journal is supported by Yildiz Technical University officially, and is a blind peer-reviewed free open-access journal, published bimontly (January-March-May-July-September-November).

Publisher: Yildiz Technical University

Editor-in-Chief: Prof.Dr. Ahmet Selim Dalkılıç, dalkilic@yildiz.edu.tr

Language of Publication: English

Frequency: Bimontly (6 issues per year)

Regular Issues: January (1) - March (2) - May (3) - July (4) - September (5) - November (6)

Publication Type: Online e-version

Journal of Thermal Engineering is supported by Yildiz Technical University officially, and is a blind peer-reviewed free open-access journal, published bimontly. • Journal of Thermal Engineering is a peer reviewed open access journal established as an origin for research in Heat Transfer and Thermodynamics mainly. • Journal of Thermal Engineering make every effort to ensure the accuracy of all the information (the "Content") contained in our publications. However, Journal of Thermal Engineering, our agents, and our licensors make no representations or warranties whatsoever as to the accuracy, completeness, or suitability for any purpose of the Content. Any opinions and views expressed in this publication are the opinions and views of the authors, and are not the views of or endorsed by Journal of Thermal Engineering. The accuracy of the Content should not be relied upon and should be independently verified with primary sources of information. Journal of Thermal Engineering shall not be liable for any losses, actions, claims, proceedings, demands, costs, expenses, damages, and other liabilities whatsoever or howsoever caused arising directly or indirectly in connection with, in relation to, or arising out of the use of the Content.

ISSN 2148-7847

Journal of Thermal Engineering

Volume 12 Number 2 Year 2026

CONTENTS

Research Articles

427 **Improving insulation and energy efficiency in arid climate buildings with palm fiber-reinforced adobe: Impact on thermal and mechanical properties**
Abdelkader BASSOUD, Abdelmalek BADA, Hamid KHELAFI, Abderahemane Mejedoub MOKHTARI, Abderrahmane MOULAY-ALI, Abdelghani IDDER

441 **Numerical and Experimental Study on the Impact of Insulation in Centrifugal Casting**
R Allwin YESUVADIAN, K S KEERTHIPRASAD

453 **Experimental study of the Heat Transfer Coefficient of an Automobile Radiator Using Alumina & Titania based Nanofluids as Coolants**
Salman Basha SHEIK, Praveena Devi NAGIREDDY, Kiran Kumar KUPIREDDI

466 **Performance analysis of solar still with separate evaporatively cooled condenser**
Niladri SARKAR, Aneesh SOMWANSHI, Anil Kr. TIWARI

484 **Thermal regulation of an EV battery pack using mineral oil: Jordan case study**
Heba ALZABEN, Tayseer FADDAH, Amir Al SAWAIR

498 **Thermal performance evaluation of an underground U-bend tube heat exchanger integrated with phase change material**
Md. Nur ALAM, Dipayan MONDAL, Mohammad Rafat ISLAM

519 **Experimental investigation of a low-cost evacuated tube in a parabolic trough collector with and without porous insert**
Pooja RAVAL, Bharat RAMANI, Karan MOTWANI, Nikhilkumar CHOTAI

532 **Techno-economic analysis of a residential solar thermal-biodiesel heating and cooling system under the mediterranean climate**
Nyasha Netsai BEMA, Kemal MASERA

550 **Experimental analysis and optimization of the air-cooled solar panel**
Vineet SINGH, Vinod Singh YADAV, Niraj KUMAR, Anurag MAHESWARI, Javed Khan BHUTTO, Sultan ALSHEHERY, Mohammed Azam ALI, Manoj KUMAR

579 **Thermal and nanoscale relations of particles in mineral oil: An analysis of metallic and non-metallic particles**
A.T. AKINSHILO, M.G. SOBAMOWO, L. KOLSI

ISSN 2148-7847

Journal of Thermal Engineering

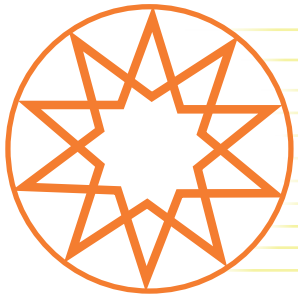

Volume 12 Number 2 Year 2026

595 **Investigation of thermal and hydrodynamic performance of a plate compact heat exchanger with Levenberg-Marquardt artificial neural network method**
Aykut BACAK

610 **Water heater employing granular coal photothermal absorber and solar thermal collector combination**
Alfan SARIFUDIN, Indri YANINGSIH, Budi KRISTIAWAN, Aditya WIBAWA, Ahmad FUDHOLI, Muhammad AZIZ

635 **Performance evaluation of solar nozzle plant useful for electricity generation: A numerical analysis**
Anand GONDCHAWAR, Bhavesh KANABAR, Ramesh BHORANIYA

656 **Influence of viscous dissipation, chemical reaction, thermophoresis and heat absorption on the flow via an exponentially stretching sheet**
Sunmoni MUDOI, Dipak SARMA

665 **Thermodynamic performance analysis of an air conditioning system integrated with a solid desiccant dehumidifier wheel using solar reactivation**
Shriramshastri CHAVALI, Ravikant NANWATKAR, Sachin MUTALIKDESAI, Tarang SHINDE, Aparna BAGDE, Pravin NITNAWARE, Shruti DIKSHIT, Sourabh KULKARNI

684 **3D mathematical investigation of MHD flow imposed with bioconvective conditions over casson nanofluid induced by permeable surface utilizing lie symmetry transformation**
Saloni GUPTA, Chinta Mani TIWARI

702 **Enhancement of exhaust manifolds using hybrid Graphene-TiO_2 nano fluids in multi-cylinder diesel engines: A CFD study on TiO_2 advantages**
Ramesh Kumar R, Channa Keshava Naik N, Ali B. M. ALI, Bharath L, Ahmed Kateb Jumaah AL-NUSSAIRI, Vijaykumar B P, Amir KHAN, Aseel SMERAT, Anwar KHAN

723 **Numerical investigation of radiative hybrid nanofluid flow containing sodium alginate and aluminium alloys over a power-law stretching/shrinking sheet with suction**
Pawan Kumar JANGIR, Ruchika MEHTA, Anurika MEHTA, Tripti MEHTA

ISSN 2148-7847

Journal of Thermal Engineering

Volume 12 Number 2 Year 2026

739 **Thermal gradients and ferrite formation in weld joints: A detailed study of temperature effects on microstructure and mechanical properties**
Loay M. MUBARAK, Hussein M, Ahmed Hashim KAREEM, Bassam Ali AHMED, Hasan Shakir MAJDI

756 **Insights of physico-chemical and thermal conductivity enhancement of polyvinylidene fluoride (PVDF) mixed znonanoparticles for heat transfer applications**
Mohammed MUQTASID, S. SRINIVASAN, R. PADMANABAN, M. SIVAKUMAR, A.P. LINGASWAMY

767 **Energy and financial efficiency of a single family house in Algeria, the best way to get rid of state subsidies**
Rabea KAOULAL, Sifia BELGHERRAS, Sidi Mohammed El Amine BEKKOUCHE

784 **Numerical analysis of two-phase flow in u-bend pipes: effects of curvature, and pipe orientation on pressure drop and liquid hold-up**
Md. Zahid HASAN, Dipayan MONDAL, Mihir Ranjan HALDER

802 **The development and evaluation of a solar Stirling engine integrated with an annular Fresnel lens concentrator system**
Yasir MEHMOOD, Asnaf AZIZ, Abid HUSSAIN, Fasih Ur RAHMAN, Afzal KHAN, Muhammad ABUBAKKAR, Imad RASOOL

Review Articles

815 **Simulation of the thermal marangoni effect in a free surface cavity: Heatline and entropy visualizations**
Nagham Yass KHUDAIR, Qusay Rasheed AL-AMIR, Hayder K. RASHID

830 **A comprhensive review on aircooled battery thermal mangement system of electric vehicles**
Prem Kumar S, Krishnappa GB, Madhu DEVEGOWDA

J Ther Eng, Vol. 12, No. 2, pp. 427−440, March, 2026

Journal of Thermal Engineering
Web page info: https://jten.yildiz.edu.tr
DOI: 10.14744/thermal.0001034

Research Article

Improving insulation and energy efficiency in arid climate buildings with palm fiber-reinforced adobe: Impact on thermal and mechanical properties

Abdelkader BASSOUD[1,*], Abdelmalek BADA[1], Hamid KHELAFI[1], Abderahemane Mejedoub MOKHTARI[2], Abderrahmane MOULAY-ALI[1], Abdelghani IDDER[1]

[1]Department of Civil Engineering, Laboratory LaGCEMS, at Ahmed Draia University, Adrar, 01000, Algeria
[2]Laboratory of Materials, Soils and Thermic, University of Science and Technology Mohamed Boudiaf, Oran, 31000, Algeria

ARTICLE INFO

Article history
Received: 08 May 2025
Revised: 03 September 2025
Accepted: 04 September 2025

Keywords:
Adobe; Arid zone; Clay; Flexural Strength; Palm Fiber; Sand; Thermal Insulation

ABSTRACT

Improving the thermal insulation of contemporary cement buildings is a significant challenge, particularly in desert environments subject to high temperatures. Adobe, a raw earth-based material, represents a practical solution due to its natural thermal properties. However, its low mechanical strength, particularly in bending, limits its integration into modern construction. This study demonstrates that a 13 cm layer of adobe reinforced with palm fibers, used as ceiling insulation, improves the thermal insulation of the building by approximately 133%, while reducing annual energy consumption by up to 53%. Furthermore, the impact of the length and dosage of palm fibers on the mechanical and thermal properties of adobe was examined through a series of tests. Four dosages (0.25%, 0.50%, 0.75% and 1% by weight) and four fiber lengths (25 mm, 50 mm, 75 mm and 100 mm) were tested. The results reveal that concentrations between 0.5% and 1% offer the best performance. In particular, the 50 mm fibers at 0.5% increased the compressive strength by about 20%, while the 75 mm fibers at 1% improved the flexural strength by up to 45%, reaching 1.70 MPa.

Cite this article as: Bassoud A, Bada A, Khelafi H, Mokhtari AM, Moulay-Ali A, Idder A. Improving insulation and energy efficiency in arid climate buildings with palm fiber-reinforced adobe: Impact on thermal and mechanical properties. J Ther Eng 2026;12(2):427−440.

INTRODUCTION

Climate change is now one of the most pressing threats of our time, leading to a significant increase in global energy consumption, with alarming forecasts for 2050. In this context, the building sector plays a significant role, accounting for nearly 36% of total energy consumption, according to the International Energy Agency (IEA). This trend is particularly pronounced in arid regions, such as southern Algeria, where the energy consumption of buildings can reach up to 45% [1]. Urban expansion and the transformation of Saharan building practices, driven by the growing demand for housing [2], exacerbate this issue, mainly since heat transfer through building walls directly affects indoor

***Corresponding author.**
*E-mail address: bas_aek@univ-adrar.edu.dz

This paper was recommended for publication in revised form by Editorin-Chief Ahmet Selim Dalkılıç

Published by Yıldız Technical University Press, İstanbul, Turkey
Yıldız Technical University. This is an open access article under the CC BY-NC license (http://creativecommons.org/licenses/by-nc/4.0/).

thermal comfort, leading to increased use of air conditioning and, consequently, higher energy consumption [3].

In response to this challenge, thermal insulation of exterior walls has become essential to limit heat loss and energy consumption [4]. While natural materials insulate better thermally than synthetic ones [5, 6], the optimal thickness of insulation varies depending on climatic conditions and economic factors [7]. Furthermore, the production of many commonly used insulators, whether petrochemical or natural, remains energy-intensive [7, 8].

In this context, earth construction emerges as a sustainable and ancient solution. Present for over 9,000 years [9], earth architecture remains a cornerstone of traditional building practices in many regions, particularly in arid and temperate climates [9, 10]. It is estimated that over 40% of the world's population currently lives in earth-based housing [3], highlighting its resilience, adaptability, and relevance in contemporary sustainable construction. Adobe, a sun-dried raw earth brick, perfectly illustrates the multiple benefits of earth materials [11]. It offers a low environmental impact [12, 13], excellent thermal insulation, affordability, fire resistance, and the ability to absorb indoor pollutants. Adobe also promotes self-construction [9, 11, 14, 15], is fully recyclable [16], and requires minimal energy for production [17].

However, despite its numerous advantages, Adobe has notable drawbacks, primarily its low mechanical strength and vulnerability to seismic activity [18]. Its flexural strength, typically ranging from 0.2 to 0.83 MPa [19, 20], demonstrates its fragility. These structural limitations have led to the increasing adoption of cement-based alternatives [21]. However, these modern materials are associated with significant energy consumption during production [8] and high costs, which can be a barrier in economically disadvantaged regions [22, 23].

Recent studies have explored the enhancement of adobe bricks through the integration of various types of fibers [9, 10, 24, 25]. This process aims to strengthen the tensile strength and durability of Adobe while preserving its ecological and economic benefits. Fibers (mineral, synthetic, and natural) act as reinforcements, effectively inhibiting or reducing crack propagation [26]. An increasing number of studies have demonstrated promising results with various fibers: the incorporation of 1.75% Shibuya fiber increased compressive strength by 40% and flexural strength by 12% [27] palm fibers improved tensile strength and ductility [27]. Significant improvements in flexural strength have been reported with the use of red millet fibers (0.17 MPa) [22], barley straw (0.28 MPa) [28], eucalyptus pulp (0.45 MPa) [29], and hibiscus fibers (up to 1.13 MPa) [30]. Natural fibers such as straw, rice husk, and kenaf can improve not only the mechanical strength but also the thermal performance of earth materials [31-33].

Incorporating fibers has also been associated with a reduction in drying shrinkage, thus minimizing the risk of cracking during the hardening process [34-35]. including plant-based materials like hemp, jute [36], Grewia optiva [37], Pinus roxburghii, alfa [38], banana [39], Synthetic fibers such as glass-reinforced polymer fibers and polyethylene have also been explored [40].

This diversity of reinforcement materials reflects the growing interest in improving the mechanical performance, thermal behavior, and overall durability of Adobe as a sustainable building material [41-42].

This study aims to improve thermal insulation performance and reduce energy consumption in modern cement buildings in the Sahara by incorporating a layer of palm fiber-reinforced adobe as a thermal sealant at the ceiling level. It also examines the specific role of palm fibers by analyzing the effects of their incorporation, dosage, and length on the mechanical and thermal properties of adobe bricks. The overall goal is to promote the sustainable use of natural resources and encourage the reassessment of local materials, especially in arid and hot regions where clay is readily available.

MATERIALS AND METHODS

Description of the Study Region

The arid zone in Algeria encompasses a vast portion of the Sahara, covering approximately 80% of the country's total surface area. For this study, we selected the province of Adrar, located in the southern region of Algeria. This region is characterized by a desert climate, marked by extremely hot summers and cold winters [43]. *Figure 1* presents our recorded temperature and relative humidity data in Adrar over one year.

In the Adrar region, construction materials are predominantly cement-based, while load-bearing structures are made of reinforced concrete, as illustrated in Figure 2.

Materials

a) Clay & sand

For the production of adobe bricks, clay and sand were sourced from the Adrar region, located south of Algeria. Laboratory tests conducted at the University of Adrar on these local soils yielded the following results:

According to analysis results, clay is classified as highly plastic. It is made up of fine particles; more than 51% of its elements have a diameter of less than 0.080 mm. the sand is very clean, with an almost total absence of fine clay particles and a low SO4 sulfate salt content.

b) Fiber

Palm fibers, which are natural fibers, are characterized by their strength. It is extracted from the palm tree, which is generally found in warm climates, and is used to make rope, fabric and other products. The figure.2. b shows palm fibers. The table.2 shows the physical and mechanical properties.

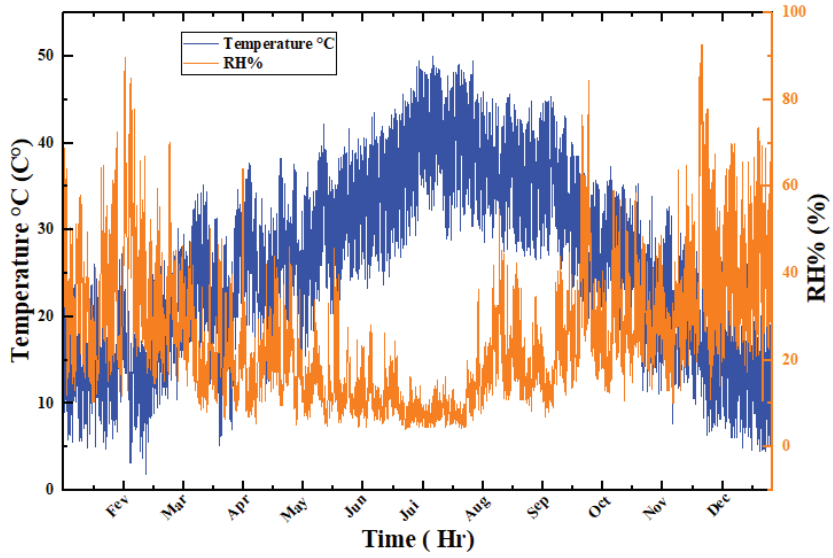

Figure 1. Temperature and humidity in Adrar.

Figure 2. Building materials in Adrar.

Table 1. Physical characteristics of materials

	density	Grain size distribution	Fineness modulus	PH [44]	Mica	$CaCO_3$	SiO_2	Salinity		
Sand	2.78 t/m³	89% of the grains are of fine to medium size (0.1 mm - 2 mm)	89%	7.1	1.9%	2.1%	96%	0.03%		
					Plasticity Index (PI) [45]	**Kaolinite**	**Illite**	**Quartz**	**Others**	**Water absorption capacity**
Clay	2.59 g/cm³	51%<0.08		8	55.10%	63%	18%	12%	7%	40%

Table 2. Physical properties of palm fiber

Length (mm)	Dimensions(mm)	Specific weight g/cm³	Tensile strength (kg/cm²)
50- 200	0.045	0.632	1832.23

Table 3. Samples composition (Source: authors)

Sample	Fiber%	Fiber length (mm)
A1	0	0
A0.25-25	0.25	25
A0.25-50	0.25	50
A0.25-75	0.25	75
A0.25-100	0.25	100
A0.5-25	0.5	25
A0.5-50	0.5	50
A0.5-75	0.5	75
A0.5-100	0.5	100
A0.75-25	0.75	25
A0.75-50	0.75	50
A0.75-75	0.75	75
A0.75-100	0.75	100
A1-25	1%	25
A1-50	1%	50
A1-75	1%	75
A1-100	1%	100

Adobe Mixing Ratios

To evaluate different sample mixtures, we carefully mixed the clay soil by hand with various parts of drinking water until we obtained a homogeneous adobe mixture. The percentage of water in the mixture varied between 23% and 25%, corresponding to a quantity of water ranging from 160 g to 1850 g.

Seventeen different adobe mixes were prepared for this study; we compared an ordinary adobe brick mix without any additives (0%) to sixteen mixes containing four rates of natural fiber (0.25%, 0.50%, 0.75%, and 1% by weight of dry fiber) and four different fiber lengths (25 mm, 50 mm, 75 mm, and 100 mm). All data are shown in Table.3. The name of the sample includes two numbers, the first indicating the percentage by weight of fibers in the adobe and the second indicating the length of the fibers used in the preparation of the mixture. For each mix, three identical samples were prepared in order to repeat the tests three times. In total, 51 samples were made for each type of test, both thermal and mechanical Figure 3.

Figure 4 shows two scanning electron microscopy (SEM) micrographs of fiber-reinforced adobe. The first image (a) reveals the composition of adobe made from dune sand and fibers. Sand particles, which have retained their

Figure 3. sample preparation a: adobe, b: palm fiber, c: samples [photo by author].

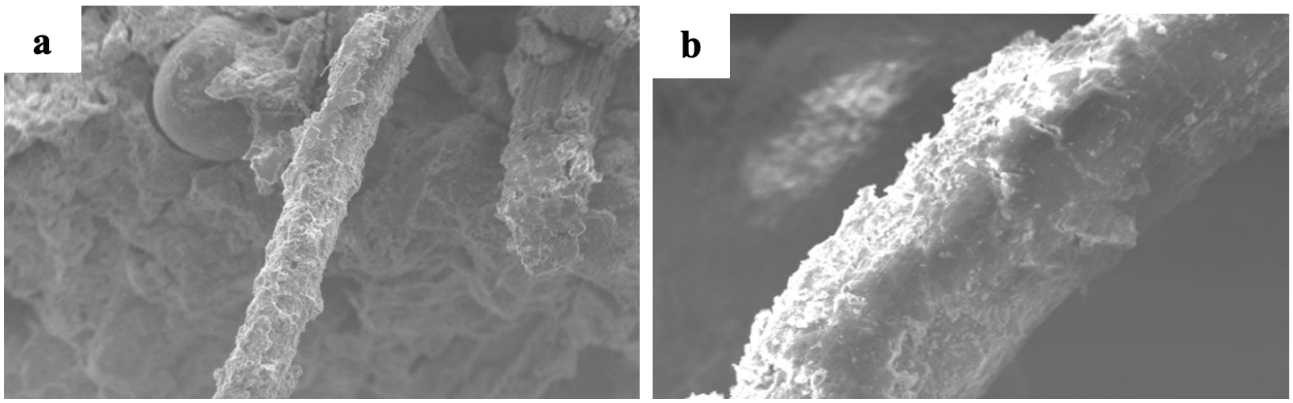

Figure 4. Image according to SEM. a: adobe fiber-reinforced. b: Fiber, x200 μm.

characteristic granular morphology, are predominantly larger than the fibers. This granulometric distribution influences the density, porosity and mechanical properties of the composite material. The second micrograph focuses on the fiber-matrix interface, showing significant roughening of the fiber surface. This morphological feature is crucial to the mechanical properties of the composite. As indicated in [46], increased roughness promotes better mechanical anchorage with the surrounding soil particles. This microscopic interlocking phenomenon improves fiber-matrix adhesion, increases resistance to raveling, enables better stress distribution and contributes to an increase in the material's toughness. These microscopic observations provide valuable insights into the reinforcement mechanisms at work in fiber-reinforced adobe.

Experimental Tests

Mechanical test

Uniaxial compression testing was carried out on the prepared samples to determine their compressive strength. Tests of mechanical compressive strength were conducted according to EN:101511 [47], a loading speed of 0.01 MPa/s was selected. each specimen was subjected to an increasing load at constant speed until it failed, as illustrated in Figure 5.b.

The flexural strength of the samples was determined in accordance with European standard EN1015-11 [48].

The test protocol involves applying a concentrated load to the center of a prismatic specimen, supported at both ends, as shown in Figure 4a. This configuration, known as a three-point bending test, creates a maximum bending moment at the center of the specimen. For our study, we used specimens of standard dimensions 40x40x160 mm^3.

Thermal properties

We determined the thermal characteristics of the samples by conducting tests at the University of Adrar using an HM150 apparatus figure 6. Employs the thermal flow meter technique by the following standards: ASTM C518, ISO 8301, and DIN EN 12667 [49, 50]. We subjected the samples, measuring 400 × 400 × 40 mm^3, to controlled measurements. (Fig. 8)

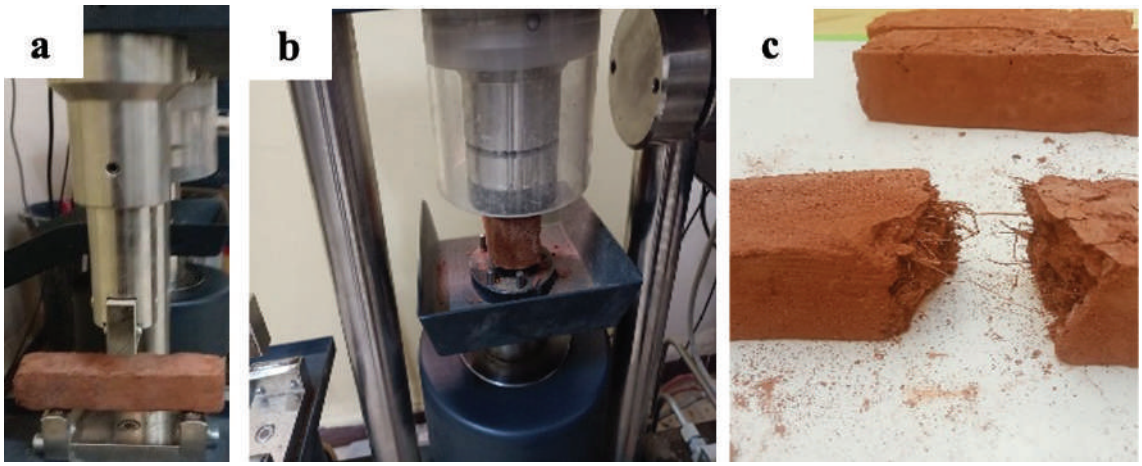

Figure 5. Experimental tests: (a) Bending test, (b) Compression test, and (c) Specimen failure after testing.

Figure 6. Thermal test.

Building simulation

To evaluate the impact of fiber-reinforced adobe on thermal insulation by selecting a typical building model from the Saharan region (Fig. 7). We incorporated fiber-reinforced adobe as an insulating layer on the ceiling and modeled the building's thermal performance using TRNSYS 18 (Tab.4). The simulation allowed us to assess how fiber-reinforced adobe helps maintain stable indoor temperatures in the extreme climate of the Saharan region.

Two floor variants were investigated in this study. The first represents the standard waterproofing system commonly used in the Saharan region, while the second variant incorporates a fiber-reinforced adobe layer, as detailed in the table 5.

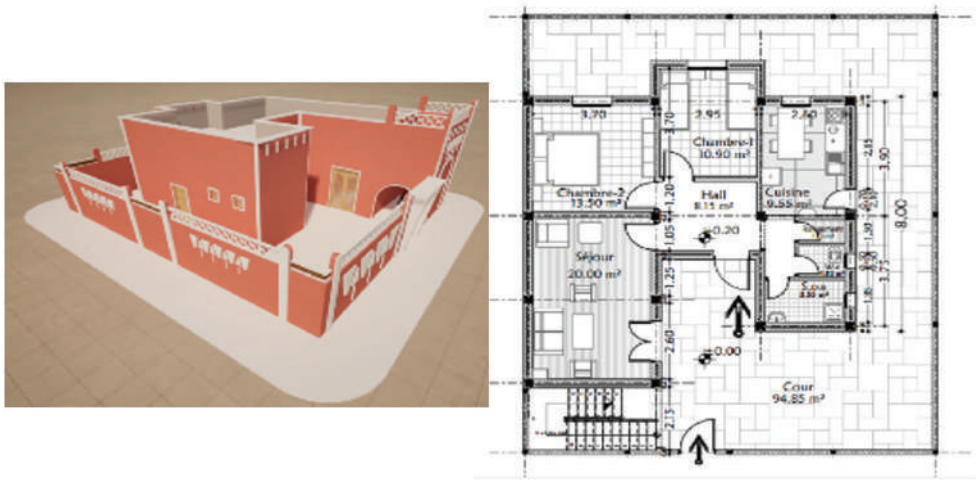

Figure 7. Saharan building.

Table 4. TRNsys Types

	Building Modeling	Building Data	Climatic Data	Ground Temperature	Result
TRNSYS18					

Table 5. Constituents of variants of floor

Element	Wall	Floor	
		Variant 1	Variant 2 With Fiber-Reinforced Adobe
Constituents	1.5 cm External Plaster 15 cm Brick 5 cm Air Gap 10 cm Brick 2 cm Internal Plaster	2 cm Tiles 2.5 cm Mortar Bed 10 cm Sand 3 cm Mortar 5 cm Reinforced Concrete 16 cm Concrete Slab 2 cm Plaster	2 cm Tiles 2.5 cm Mortar Bed 13 cm Fiber-Reinforced Adobe 5 cm Reinforced Concrete 16 cm Concrete Slab 2 cm Plaster
Total thickness	33.5	40	40
U W/m²k	0.653	1,855	0.604

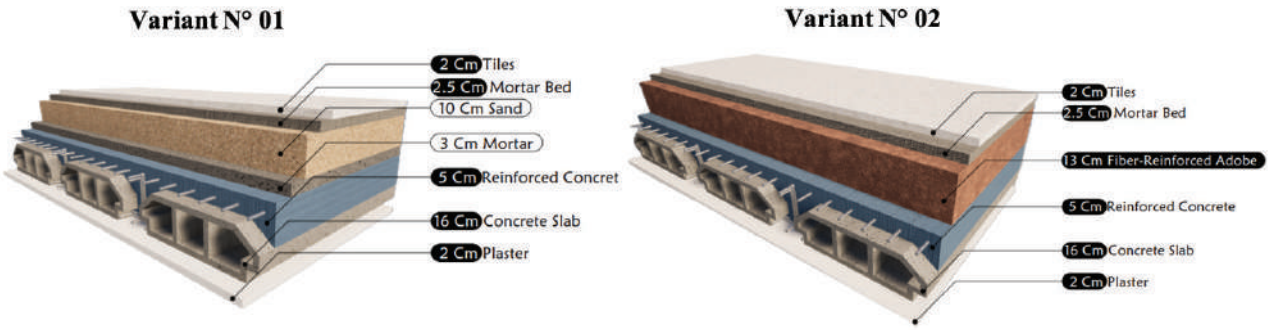

Figure 8. Components of thermal seals. V1: Saharan seal. V2: Sealing with fibered adobe.

Table 6. Equipment Intensity

Equipement	Zone	Occupancy time	Power W	Power W (KJ/h)
Computer	Bedroom	Occupation	230	828
Television	Living room	Occupation	150	540
Cooking appliances	Kitchen	occupation	700	2520
Refrigerator 200 L	Kitchen	24/7	87.5	315

Table 11. Lighting gains [51]

Local	Recommended light intensity lux	Power output of lamps or tubes w/m²	
		Incandescent lamps	Fluorescent lamps
Rooms	120	25	8

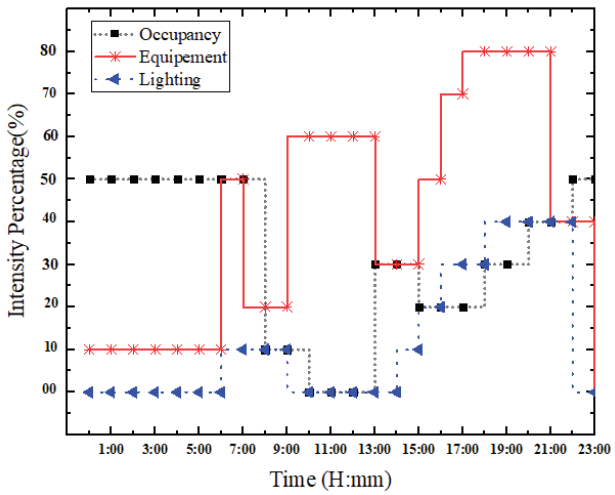

Figure 9. Occupancy intensity.

Internal Gains

The sensible power dissipated per person is estimated at 100 W/person according to the current standards (DTR3-4) [51]

Lighting gains based on lamp type are presented as follows:

The figure 9 illustrates the percentage of occupancy intensity, equipment use, and lighting in a Saharan building during a typical day, from 1 a.m. to midnight. Occupancy levels fluctuate, peaking during daylight hours and decreasing at night. Equipment use increases with occupancy. Lighting use follows a similar trend, increasing as daylight diminishes and peaking in the evening.

Energy Needs

We assessed the cooling energy demand during summer to maintain indoor conditions at 27 °C and 50% relative humidity, and the heating energy demand in winter to maintain 20 °C. These comfort conditions are defined by the Algerian thermal regulation standard DTR C3.4. [51]

Research Uncertainty and Limitations

This study presents certain limitations and uncertainties. The hypothesis of a uniform distribution of palm fibers simplifies reality. However, ensures a replicated experimental framework. We conducted our tests with three replicates per mixture, thereby reducing the influence of random errors, although total variability may not be fully accounted

for. Modeling has taken into account only floor variation, which highlights its specific role but does not reflect all actual conditions. Finally, the energy assessment is based on DTR regulatory comfort temperatures (25°C in summer, 20°C in winter), although occupant preferences may differ. These limitations serve to delineate the scope of the present study while simultaneously highlighting directions for future research.

RESULTS AND DISCUSSION

Compressive Strength

Figure 10 shows the evolution of the compressive strength of adobe samples as a function of the percentage (0%, 0.25%, 0.5%, 0.75%, 1%) and length (25, 50, 75, 100 mm) of palm fibers incorporated, compared with the control sample without fibers (0%). For fibers of 25 mm length, a reduction in compressive strength was observed, reaching 6%, 10%, and 20% depending on the dosage. The 0.5% dosage yielded the most promising results, with a 20% increase in strength for 50 mm fibers, followed by 10% and 2% increases for 75 mm and 100 mm lengths, respectively. In contrast, the 0.25% and 1% dosages showed a slight reduction of 2% and 4% at 100 mm, but more significant decreases of 10% and 25% for shorter fiber lengths. These results suggest that fiber length can have a positive effect on compressive strength at lower dosages. However, the 0.75% dosage consistently produced adverse effects on compressive strength across all fiber lengths. The optimal configuration identified was 0.5% fiber content with a length of 50 mm. Additionally, the uniformity of fiber dispersion within the matrix plays a critical role in maintaining mechanical integrity. These findings align with those of Gao et al. [52, 53], who reported a non-linear relationship between fiber length and mechanical strength, as well as the existence of an optimal fiber length that maximizes load transfer within the material.

When compared with other natural fibers reported in the literature, palm fiber reinforced adobe exhibits competitive performance. For example, wheat long straw at a 1% dosage achieved a compressive strength of 4.98 MPa [54], while wheat crushed straw at the exact dosage reached 19.11 MPa [54], and doum fiber achieved 19.91 MPa at 1% [55]. Lavender straws, used at a higher dosage of 6%, yielded 3.9 MPa [56]. Sawdust fibers at 1% reached 8.11 MPa [57], and neem straw at 2% attained 6.35 MPa [58]. These comparisons highlight that while palm fibers may not attain the very high compressive strengths of specific agricultural residues like crushed wheat straw or doum fiber, they still offer a viable and sustainable reinforcement, especially when dosage and fiber length are carefully optimised.

Flexural Strength

Figure 11 shows the flexural strength of adobe samples as a function of the dosage (0%, 0.25%, 0.5%, 0.75%, 1%) and length (25, 50, 75, 100 mm) of incorporated palm fibers, compared to a control sample without fibers.0%

The results reveal a substantial improvement in flexural strength for all fiber dosages. The 1% dosage showed the most pronounced increase, ranging from 20% to 45%. The 0.75% dosage follows closely with an improvement ranging from 13% to 43%. The 0.5% dosage shows a moderate increase from 12% to 20%. Even the lowest dosage of 0.25% shows a positive increase, albeit more modest, from 4% to 20%.

These data highlight the significant influence of palm fiber dosage on the flexural strength of adobe. Fiber length has an important role to play, particularly for the 1% dosage, where the effect is most noticeable.

The addition of palm fibers considerably improves the bending strength of adobe. This improvement depends on both the dosage and the length of the fibers used. This

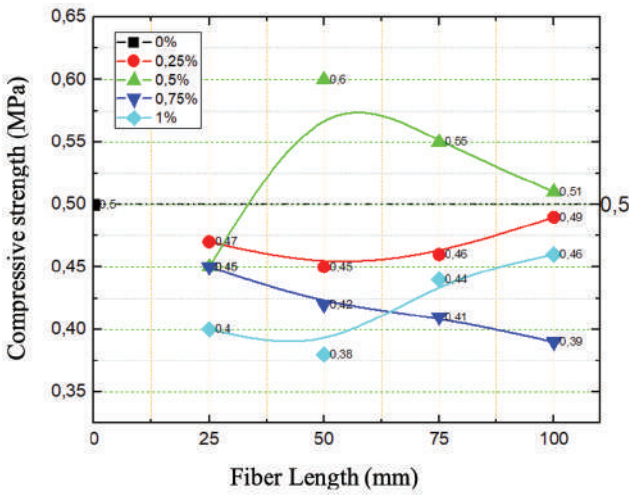

Figure 10. Compressive strength.

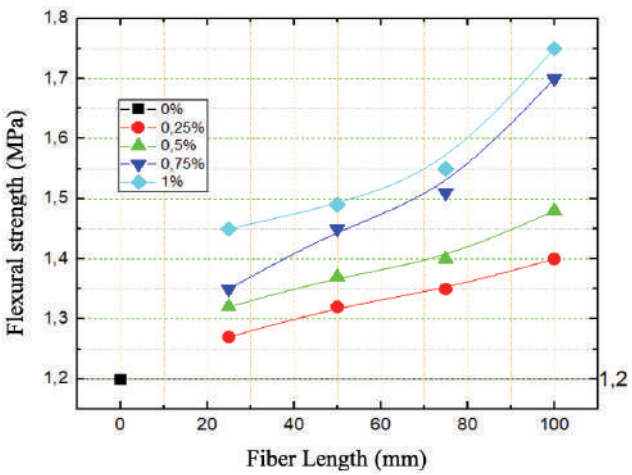

Figure 11. Flexural strenght.

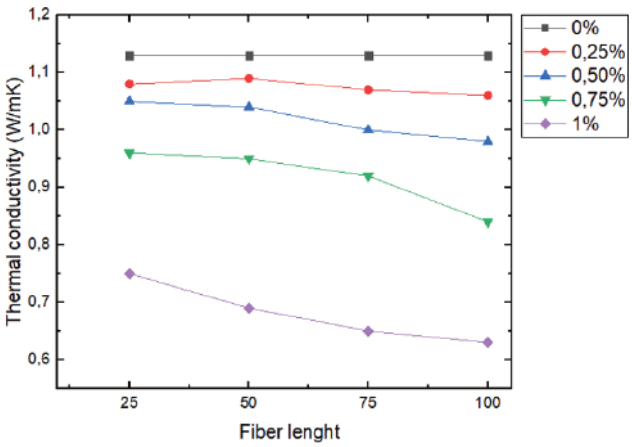

Figure 12. Thermal conductivity.

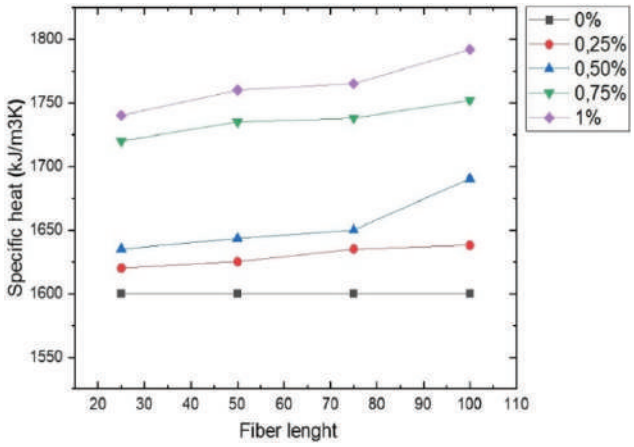

Figure 13. specific heat.

reinforcement not only increases mechanical strength, but also delays the appearance and propagation of cracks in the material.

It is essential to stress that the homogeneity and uniform distribution of the fibers guarantees a consistent improvement in mechanical properties throughout the material.

In our study, palm fiber–reinforced adobe achieved a flexural strength of up to 1.7 MPa, positioning it favorably among both natural and synthetic fiber reinforcements reported in the literature. For comparison, lower strengths have been reported for red millet fiber (0.17 MPa) [22], barley straw (0.28 MPa) [28], waste tire textile fiber (0.285 MPa) [59],, wool fiber (0.139 MPa) [60], eucalyptus pulp (0.45 MPa) [29], alfa fiber (0.488 MPa) [29], polypropylene fiber (0.83 MPa) [61], banana fiber (0.95 MPa) [61], sawdust fibers (0.4 MPa) [57], lavender straws (0.28 MPa) [56], neem straw at 2% (0.65 MPa) [58], doum fiber (0.412 MPa) [55], and crushed wheat straw (0.78 MPa) [54]. Palm fibers also compare closely with wheat long straw (1.42 MPa) [54], although they fall below alfa fiber in some cases (2.01 MPa) [38] and hemp fiber (3.11 MPa) [62]. These findings highlight palm fibers as a highly promising natural reinforcement for adobe, particularly in hot and arid regions, offering an effective and sustainable means of improving mechanical properties while supporting local resource use.

Thermal Properties

Figure 12 presents the results of the thermal conductivity tests conducted on adobe samples reinforced with varying percentages and lengths of palm fibers. An apparent decrease in thermal conductivity was observed, demonstrating the positive effect of palm fiber addition in enhancing the thermal insulation performance of adobe. The thermal conductivity dropped from 1.15 W/m·K (reference sample without fibers) to 0.65 W/m·K in the best-performing mix, which included 1% palm fiber with a length of 100 mm. Specifically, a reduction of 0.07 W/m·K was recorded for a fiber content of 0.25%, 0.15 W/m·K for 0.5%, and the reduction further increased to 0.2 W/m·K and 0.45 W/m·K for fiber contents of 0.75% and 1%, respectively.

Compared to values reported in the literature for other natural fiber reinforcements, palm fibers show competitive thermal performance. For example, wheat long straw at a 2% dosage yielded a thermal conductivity of 0.411 W/m·K [54], and hemp shiv at a 6% dosage reached a much lower value of 0.2 W/m·K [63]. While hemp-based materials exhibit superior insulation, the use of palm fibers remains a sustainable and effective solution, especially in arid regions where such resources are abundant and locally available.

These results clearly demonstrate that reinforcing adobe with palm fibers significantly enhances its thermal characteristics by effectively reducing its thermal conductivity.

Figure 13 shows the variation in the specific heat capacity of the samples as a function of fiber content and length. Improvements of 1.56%, 5%, 7.81%, and 12.5% were recorded for fiber dosages of 0.25%, 0.50%, 0.75%, and 1%, respectively.

These results demonstrate the positive effect of palm fibers on improving the specific heat capacity of adobe, a key parameter that plays an important role in thermal insulation and heat storage.

Adobe with a higher specific heat can absorb more heat during the day without significantly raising their temperature. As a result, the indoor temperature increases more gradually during peak heat periods, effectively delaying or reducing the intensity of heat reaching the interior. This delay in temperature changes, known as thermal lag, leads to a more stable indoor temperature throughout the day.

Thermal Insulation of The Building

The variation in the internal temperature of the building for the two variants, compared to the external temperature

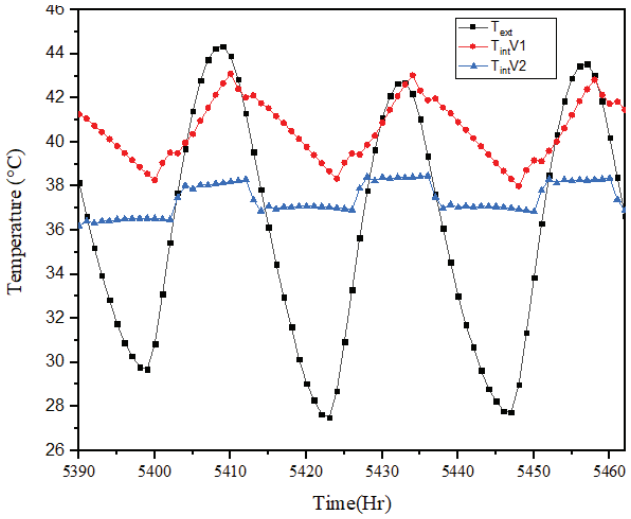

Figure 14. internal temperature of the building.

during a summer period, is illustrated in **Figure 14**. A significant daily temperature difference between day and night was observed, reaching up to 17°C, with a maximum temperature of 45°C, highlighting the severity of the climate. For Variant 1, with the Saharan sand-based waterproofing, the temperature difference between the exterior and interior does not exceed 3°C. In contrast, for Variant 2, with a floor waterproofing system incorporating fiber-reinforced adobe, the temperature difference reaches 7°C, representing an improvement of 133%.

Figure 15 shows the variation in temperature on both sides of the floor, external and internal, for the two variants. In Figure 15.a, we observed a difference between the temperatures on the two sides, with a notable daily variation. However, in Figure.15b, we recorded that the temperature on the internal side remains relatively independent of the temperature on the external side.

The variation in the internal and external surface temperatures of the floor for the two variants during the period starting in August is presented in Figure 16. It was observed that the temperature on the internal side for Variant N°2(with adobe) figure 16a remains nearly stable, while for Variant N°1(Fig. 16.b), it fluctuates between 47°C and 38°C. In contrast, the temperature on the external side reaches up to 62°C, with a significant daily temperature difference of 33°C. This highlights the highly aggressive effect of the climate in arid and hot regions on construction materials, particularly cement-based products. Therefore, adobe presents an ideal solution for floor insulation in buildings, protecting against the effects of external temperatures.

Energy Balance

Figure 17 presents the energy needs for cooling (Fig. 17.a) and heating (Fig. 17.b) for two construction variants: V1, which uses sand, and V2, which incorporates fiber-reinforced adobe as the terrace sealing material.

Regarding cooling needs, Figure 14. a shows that the summer period extends approximately six months, from May to October. However, the winter lasts around five months, from November to March. It shows the significant

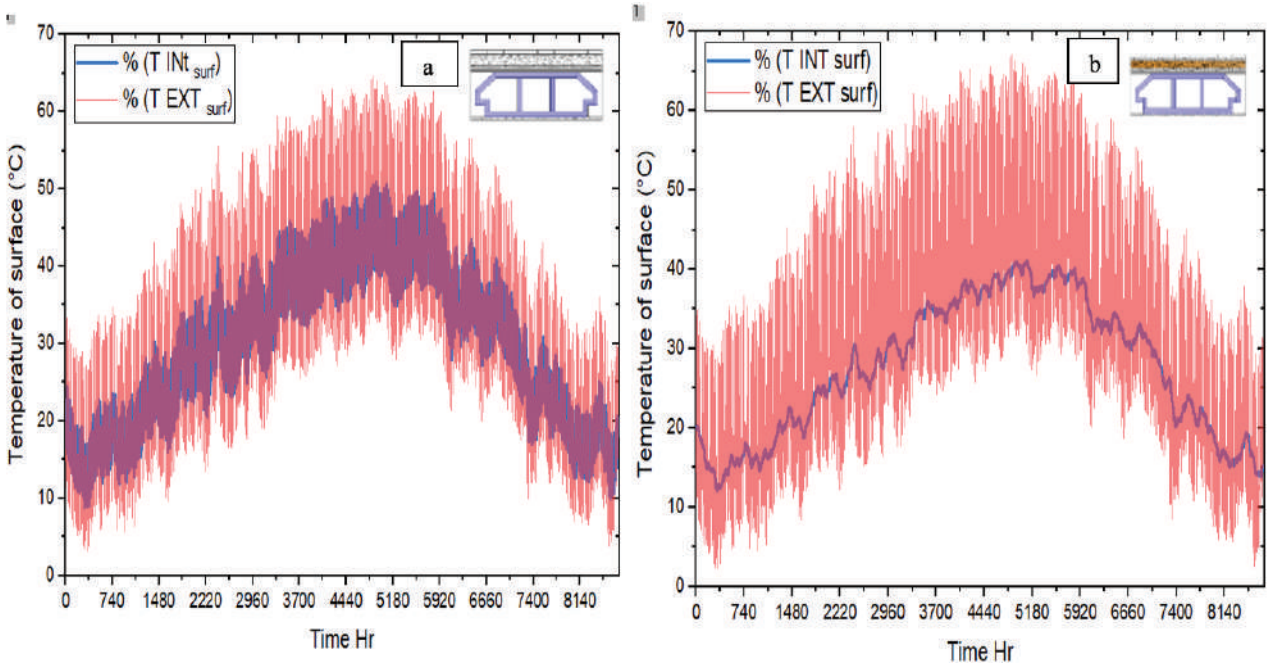

Figure 15. variation in temperature on both sides of the floor.

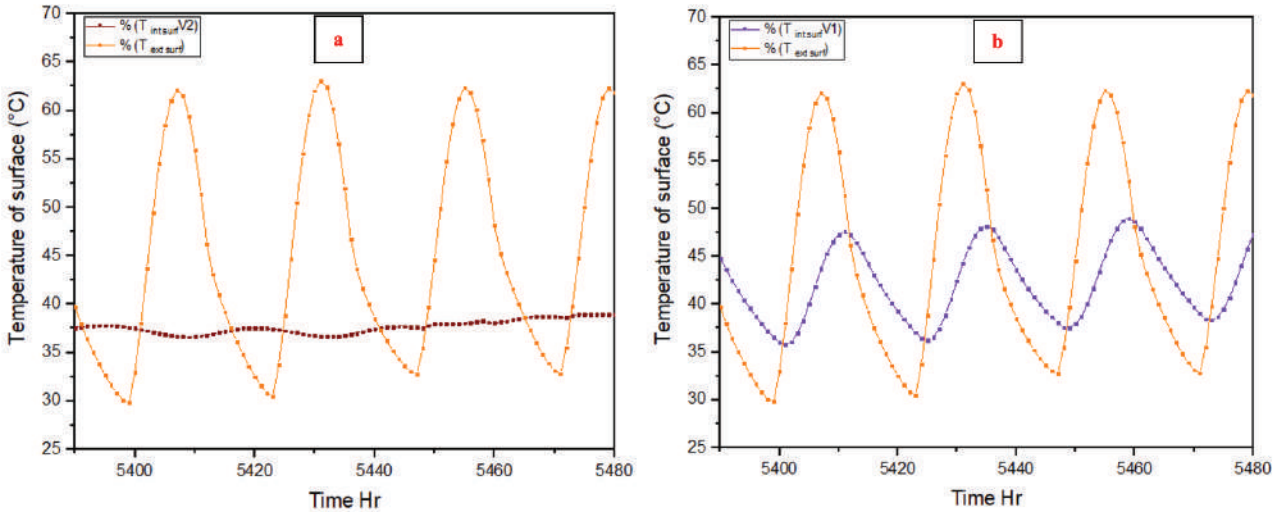

Figure 16. variation in temperature on both sides of the floor in summer period.

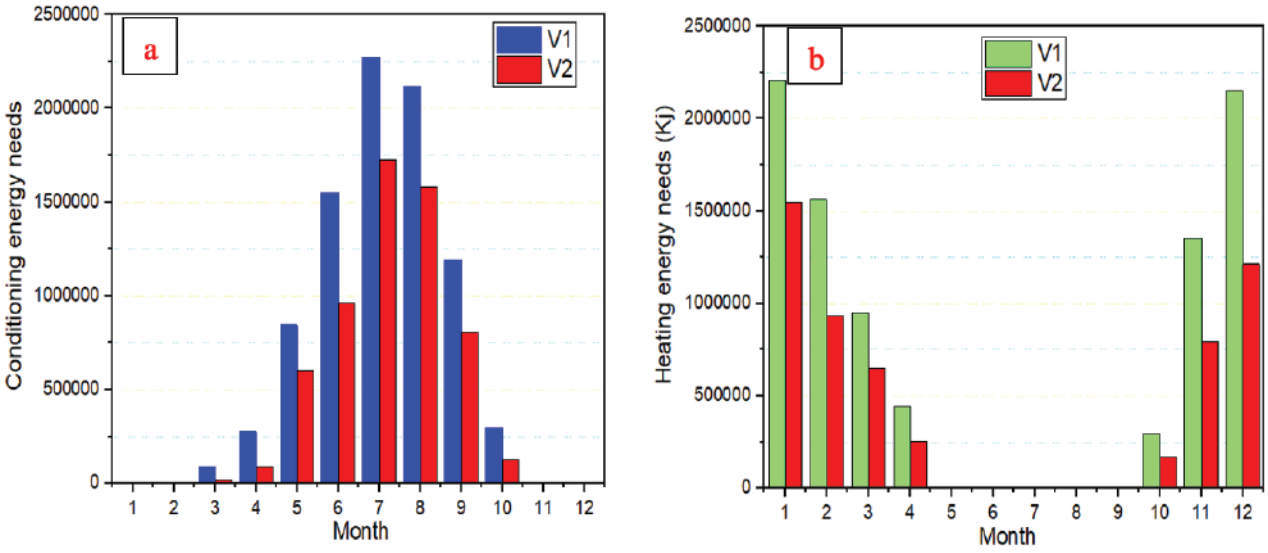

Figure 17. Energy needs. (a) Cooling, (b). Heating.

thermal demand of the examined location, defined by an extended hot season, emphasizing the necessity for efficient building insulation.

CONCLUSION

This study on the incorporation of palm fibers into Adobe reveals significant and promising results for improving the mechanical properties of this traditional building material.

The addition of palm fibers showed different effects on the compressive and flexural strength of Adobe. For compressive strength, the results were mixed, with a notable improvement for some combinations of fiber dosage and length, notably 0.5% of 50 mm fibers, while other combinations showed a decrease in strength. On the other hand, flexural strength was considerably improved for all dosages and fiber lengths tested, with increases of up to 45% for the highest dosages.

These results underline the importance of fiber dosage and length in optimizing the mechanical properties of reinforced Adobe. The optimum dosage appears to be around 0.5% to 1%, while the most effective fiber lengths vary between 50 and 75 mm, depending on the mechanical property under consideration.

The improvement in flexural strength is particularly significant, as it indicates a better ability of the material to

resist tensile stresses and delay the onset and propagation of cracks.

The homogeneity of fiber distribution in the adobe matrix plays a role in achieving optimal and uniform mechanical properties.

Integrating palm fiber-reinforced adobe as a thermal insulation layer offers substantial benefits, notably reducing annual energy consumption by up to 53%. This underscores the material's strong potential as a sustainable and efficient solution for modern construction in hot and arid climates. Furthermore, the results highlight the vulnerability of conventional cement-based materials to harsh climatic conditions, reinforcing the suitability of Adobe for thermal insulation, particularly in thermal sealing on the roof. The improvement in Adobe's specific heat capacity due to palm fiber incorporation further enhances its ability to store and regulate heat, making it a promising material for energy-efficient and climate-resilient building design

This study shows the considerable potential of using palm fibers as a natural additive and reinforcement in Adobe. It opens up new prospects for the improvement and modernization of this traditional building material, offering a sustainable and environmentally-friendly solution to meet current performance requirements in the construction sector. However, further research may be required to optimize formulations further and explore other aspects such as long-term durability and behavior in the face of varied environmental conditions.

Perspectives

This study serves as an introduction to the exploration of new methods for construction in arid zones, focusing on improving the durability of adobe bricks. Additionally, future work may involve the development of insulating sheets made from earth-based materials, contributing to more sustainable and energy-efficient building solutions.

ACKNOWLEDGMENTS

The authors are pleased to express their sincere thanks and appreciation for the assistance provided by the members of the LSTGP USTOran Laboratory, to all the engineers of the LTPO Laboratory in Oran, to Engineer Soulimani Yacine and to all the engineers of the Civil Engineering Laboratory of the University of Adrar.

AUTHORSHIP CONTRIBUTIONS

Authors equally contributed to this work.

DATA AVAILABILITY STATEMENT

The authors confirm that the data that supports the findings of this study are available within the article. Raw data that support the finding of this study are available from the corresponding author, upon reasonable request.

CONFLICT OF INTEREST

The author declared no potential conflicts of interest with respect to the research, authorship, and/or publication of this article.

ETHICS

There are no ethical issues with the publication of this manuscript.

STATEMENT ON THE USE OF ARTIFICIAL INTELLIGENCE

Artificial intelligence was not used in the preparation of the article.

REFERENCES

[1] Bassoud A, Khelafi H, Mokthari AM, Bada A. Evaluation of summer thermal comfort in arid desert areas. Case study: Old adobe building in Adrar (South of Algeria). 2021;205:108140. [Crossref]

[2] Khaoula A, Djamel A. Evaluation of summer thermal comfort using in situ measurement and dynamic simulation, hot and arid climate in Algerian Saharan region as a case study. J Therm Eng 2023;9:218-232. [Crossref]

[3] Aljawad RH. Thermal performance analysis of local building materials for energy efficiency in Iraq. J Therm Eng 2024;1011-1020. [Crossref]

[4] Aktemur C, Bilgin F, Tunckol S. Optimisation on the thermal insulation layer thickness in buildings with environmental analysis: an updated comprehensive study for Turkey's all provinces. J Therm Eng 2021;7:1239-1256. [Crossref]

[5] Zıad S, Benoudjafer I, Benoudjafer I. Towards the use of natural thermal insulation on the exterior of vertical building walls in desert regions: A case study in the city of Bechar, Algeria. J Therm Eng 2024;10:308-320. [Crossref]

[6] Durmaz S, Çolak AB, Mercan H, Dalkılıç AS. Determination of optimum insulation thickness in submarines. J Therm Eng 2023;9:1655-1666. [Crossref]

[7] Shahid M, Optimum insulation thickness for external building walls for different climate zone in India. J Therm Eng 2024;1198-1211. [Crossref]

[8] Rima B, Nadir B. Thermal and physiochemical characterization of bricks incorporating date palm fiber for use as insulation materials in buildings. J Eng Fibers Fabr 2024;19. [Crossref]

[9] Minke G. Building with Earth : design and technology of a sustainable architecture. Birkhäuser 2021. [Crossref]

[10] Houben H, Guillaud H, CRATerre: Traité de Construction en Terre. Éditions Parenthèses 2006.

[11] Maini S. Earthen architecture for sustainable habitat and compressed stabilised earth block technology. The Auroville Earth Institute 2005.
[12] Obafemi APO, Sevinç K. Environmental impacts of adobe as a building material: The north cyprus traditional building case. Case Stud Constr Mater 2016;4:32-41. [Crossref]
[13] Zami MS, Angela L. Economic benefits of contemporary earth construction in low-cost urban housing – State-of-the-art review. J Build Apprais 2010;5:259-271. [Crossref]
[14] Adam EA, Agib ARA. Compressed stabilised earth block manufacture in Sudan. UNESCO 2001.
[15] Hadjri K, Osmani M, Baiche B, Chifunda CC. Attitudes towards earth building for Zambian housing provision. Proc Inst Civil Eng-Eng Sustain 2007. [Crossref]
[16] Calatan G, Dico C, Hegyi A, Calin M. Experimental Research on the Recyclability of the Clay Material Used in the Fabrication of Adobe Bricks Type Masonry Units. Procedia Engineering 2017;181:363-369. [Crossref]
[17] Shukla A, GN Tiwari, MS Sodha. Embodied energy analysis of adobe house. Renew Energy 2009;34:755-761. [Crossref]
[18] Islam M. Present status and problems of earthen architecture in Bangladesh: role of education. Proceedings of the Seminar TERRA Education, France. 2010.
[19] Fratini F, Pecchioni E, Rovero L, Tonietti U. The earth in the architecture of the historical centre of Lamezia Terme (Italy): Characterization for restoration. Appl Clay Sci 2011;53:509-516. [Crossref]
[20] Silveira D, Varum H, Costa A, Martins T, Pereira H, Almeida J. Mechanical properties of adobe bricks in ancient constructions. Constr Build Mater 2012;28:36-44. [Crossref]
[21] Khiem TQ, Satomi T, Takahashi H. Improvement of mechanical behavior of cemented soil reinforced with waste cornsilk fibers. Constr Build Mater 2018;178:204-210. [Crossref]
[22] Babé C, Kidmo DK, Tom A, Mvondo RRN, Boum RBE, Djongyang N. Thermomechanical characterization and durability of adobes reinforced with millet waste fibers (sorghum bicolor). Case Stud Constr Mater 2020;13:e00422. [Crossref]
[23] Thanushan K, Yogananth Y, Sangeeth P, Coonghe GJ, Sathiparan N. Strength and durability characteristics of coconut fiber reinforced earth cement blocks. J Nat Fibers 2021;18:773-788. [Crossref]
[24] Alam MJ, Biswas M, Mia MB, Alam S, Hossain M. Influence of rice husk and cabuya fiber on the physical and mechanical properties of adobe. Eng Appl Sci Res 2025;52:112-124
[25] Pérez SPM, Guevara JR, Perales JFR, Chumacero JMG, Diaz ES, Llatas FDH, et al. Influence of prickly pear gum on the physical and mechanical properties of adobe reinforced with palm fiber. Eng Appl Sci Res 2024;51:495-504.
[26] Yao W, Li J, Wu K. Mechanical properties of hybrid fiber-reinforced concrete at low fiber volume fraction. Cement and concrete research 2003;33:27-30. [Crossref]
[27] López X, Torbisco D, Rodrigue J, Eyzaguirre C. Benefits of cabuya fiber in the mechanical properties of compacted adobe. 7th International Engineering, Sciences and Technology Conference 2019. [Crossref]
[28] Bouhicha M, Aouissi F, Kenai S. Performance of composite soil reinforced with barley straw. Cement and concrete composites 2005;27:617-621. [Crossref]
[29] Ojo EB, Bella OK, Mustapha K, Teixeria RS, Santos SF, JR SH. Effects of fiber reinforcements on properties of extruded alkali activated earthen building materials. Constr Build Mater 2019;227:116778. [Crossref]
[30] Millogo Y, Aubert JE, Hamard E, Morel JC. How properties of kenaf fibers from Burkina Faso contribute to the reinforcement of earth blocks. Mater 2015;8:2332-2345. [Crossref]
[31] Piani TL, Weerhim J, Perani M, Krabbenborg D, Koene L, Solomous G, et al. Dynamic behaviour of adobe bricks in compression: the tole of fibers and water content at various loading rates. Constr Build Mater 2020;230:117038. [Crossref]
[32] Millogo Y, Aubert JE, Hamard E, Morel JC,. How properties of kenaf fibers from Burkina Faso contribute to the reinforcement of earth blocks. Mater 2015;8:2332-2345. [Crossref]
[33] Ceballos NA, Zuleta FO, Quşsberth A, Predencio MG, Jimenez LI. Mechanical characterization of adobe with natural fiber in the Andean Zone of Bolivia. Matec Web of Conferences 2024;403:02011. [Crossref]
[34] Sadouri R, Kébir H, Benyoucef M, Enhancing mechanical properties and crack resistance of earth-sand building materials through alfa fiber reinforcement: an experimental investigation. Gradjevinski Materijali I Konstrukcije 2024;67:17-27. [Crossref]
[35] Ouédraogo M, Dao K, Millago Y, Aubert JE, Messan A, Seynou M, Z et al. Physical, thermal and mechanical properties of adobes stabilized with fonio (Digitaria Exilis) straw. J Build Eng 2019;23:250-258. [Crossref]
[36] Islam MS, Iwashita K. Earthquake resistance of adobe reinforced by low cost traditional materials. J NatDisaster Sci 2010;32:1-21. [Crossref]
[37] Sharma V, Marwaha B, Vinayak H. Enhancing durability of adobe by natural reinforcement for propagating sustainable mud housing. Int J Sustain Built Environ 2016;5:141-155. [Crossref]
[38] Elhamdouni Y, Khabbazi A, Benayad C, Mounier S. Thermophysical and mechanical characterization of

clay bricks reinforced by alfa or straw fibers. Mater Sci Eng 2017. [Crossref]
[39] Rajalakshmy A, Vishnudas S, Lekshmi MS, Nair PA. Feasibility Study of Natural Fiber Reinforced Mud Blocks as a Building Material. EasyChair 2020.
[40] Pekrioglu Balkis A. The effects of waste marble dust and polypropylene fiber contents on mechanical properties of gypsum stabilized earthen. Constr Build Mater 2017;134:556-562. [Crossref]
[41] Mha BZ, Kaoutoing D, Doko V, Ntamack GE. Thermal characterization of adobes stabilized with natural fibers, hyperrhénia hirta and stipa offneri. Using the Asymmetric Hot Plate Method Coupled With the Quadripolar Formalism 2025. [Crossref]
[42] Charai M, Salhi M, Horma O, Mezrhab A, Karkri M, Amraqui S. Thermal and mechanical characterization of adobes bio-sourced with pennisetum setaceum fibers and an application for modern buildings. Constr Build Mater 2022;326:126809. [Crossref]
[43] Benzid MC. Enhancing heat efficiency in arid environments using a PVT collector for revealed facade shelter. J Therm Eng 2025;390-406. [Crossref]
[44] EN N. 933-9+ A1. Essais pour déterminer les caractéristiques géométriques des granulats-Partie 2013.
[45] AFNOR N. P94-051. Reconnaissance et essais-Détermination des limites d'Atterberg-Limite de liquidité à la coupelle-Limite de plasticité au rouleau 1993.
[46] Mohamed AEMK. Improvement of swelling clay properties using hay fibers. Constr Build Mater 2013;38: 242-247. [Crossref]
[47] Methods of Test for Mortar for Masonry—Part 11: Determination of Flexural and Compressive Strength of Hardened Mortar. European Committee for Standardization: Brussels, Belgium.2020.
[48] Methods of test for mortar for masonry–Part 11: Determination of flexural and compressive strength of hardened mortar. European Committee for Standardization Brussels, Belgium.1993.
[49] C518 Standard Test Method for Steady-State Thermal Transmission Properties by Means of the Heat Flow Meter Apparatus. ASTM International.
[50] Thermal performance of building materials and products: Determination of thermal resistance by means of guarded hot plate and heat flow meter methods - Products of high and medium thermal resistance; English version of DIN EN 12667. GlobalSpec 2023.
[51] Document Technique reglementaire Algerien Climatisation, Règles de Calcul des Apports Calorifiques des Bâtiments. CNERIB 1998;2.
[52] Gao L, Hu G, Xu N, Fu J, Xiang C, Yang C. Experimental study on unconfined compressive strength of basalt fiber reinforced clay soil. Adv Mater Sci Eng 2015;561293. [Crossref]
[53] Tabakouei AR, Narani SS, Abbaspour M, Aflaki E, Siddiqua S. Coupled specimen and fiber dimensions influence measurement on the properties of fiber-reinforced soil. Measurement 2022;188. [Crossref]
[54] Alioui A, Kaitouni SI, Azalam Y, Armouzi NA, Bendada EM, Mabrouki M. Effect of straw fibers addition on hygrothermal and mechanical properties of carbon-free adobe bricks: From material to building scale in a semi-arid climate. Build Environ 2024;255. [Crossref]
[55] El-yahyaoui A, Manssouri I, Lehleh Y, Sahbi H, Limami H. Enhancing the mechanical and thermal insulation properties of clay-based construction materials with neutral carbon footprint through the use of Doum fibers. Mater Chem Phys 2024;314. [Crossref]
[56] Giroudon M, Preneron AL, Aubert JE, Mogniont C. Comparison of barley and lavender straws as bioaggregates in earth bricks. Constr Build Mater 2019;202:254-265. [Crossref]
[57] Limami H, Manssouri I, Noureddine O, Erba S, Sahbi H, Khaldoun A. Effect of reinforced recycled sawdust-fibers additive on the performance of ecological compressed earth bricks. J Build Eng 2023;68. [Crossref]
[58] Babé C, Kidmo DK, Tom A, Mvando RRN, Kola B, Djongyang N. Effect of neem (Azadirachta Indica) fibers on mechanical, thermal and durability properties of adobe bricks. Energy Reports, 2021;7:686-698. [Crossref]
[59] Gao L, Hu G, Xu N, Fu J, Xiang C, Yang C. Experimental investigation of non-stabilized and cement-stabilized rammed earth reinforcement by Waste Tire Textile Fibers (WTTFs). Constr Build Mater 2020;260:120432. [Crossref]
[60] Aymerich F, Fenu L, Meloni P, Effect of reinforcing wool fibers on fracture and energy absorption properties of an earthen material. Constr Build Mater 2012;27:66-72. [Crossref]
[61] Donkor P, Obonyo E. Earthen construction materials: Assessing the feasibility of improving strength and deformability of compressed earth blocks using polypropylene fibers. Materials & Design 2015;83:813-819. [Crossref]
[62] Calatan G, Hegyi A, Dico C, Mircea C. Determining the optimum addition of vegetable materials in adobe bricks. Procedia technology 2016;22:259-265. [Crossref]
[63] Laborel-Préneron A, Magniont C, Aubert JE, Hygrothermal properties of unfired earth bricks: Effect of barley straw, hemp shiv and corn cob addition. Energy Build 2018;178:265-278. [Crossref]

J Ther Eng, Vol. 12, No. 2, pp. 441−452, March, 2026

Journal of Thermal Engineering
Web page info: https://jten.yildiz.edu.tr
DOI: 10.14744/thermal.0001071

Research Article

Numerical and Experimental Study on the Impact of Insulation in Centrifugal Casting

R Allwin YESUVADIAN[1,*], K S KEERTHIPRASAD[2]

[1]*Department of Mechanical Engineering, VVIET, Karanataka, 570028, India*
[2]*Department of Mechanical Engineering, MIT, Thandavapura, Karanataka, 571302, India*

ARTICLE INFO

Article history
Received: 13 March 2025
Accepted: 12 May 2025

Keywords:
ANSYS; Horizontal Centrifugal Casting; Mould Insulation; Numerical Heat Transfer Analysis; Solidification rate

ABSTRACT

There is significant increase in use of metals across various engineering, household and industrial applications along with continuous evolving process of manufacturing to produce precise shape and finish of components. Previous studies have mainly focused on mould pre heating to manage thermal gradients while the present work examines an alternate approach by the use of thermal insulation to reduce the heat loss during casting. Transient thermal investigation of the centrifugal casting mold was done in this work. In order to assess the heat transmission properties for both insulated and non-insulated mold surfaces and comprehend how different solidification rates affect the end quality of castings produced, ANSYS simulation software was utilized for analysis. Different insulation conditions were tested mechanically, and scanning electron microscopy (SEM) was used to look into microstructural differences. According to the findings, applying mold insulation along with preheating and rotating at an optimal speed improved heat retention and decreased heat loss by 27%. This results in better solidification, fewer casting flaws, and higher-quality cast products, accompanied by a 12.67% decrease in the outer mold surface temperature.

Cite this article as: Allwin Yesuvadian R, Keerthiprasad KS. Numerical and Experimental Study on the Impact of Insulation in Centrifugal Casting. J Ther Eng 2026;12(2):441−452.

INTRODUCTION

With ongoing developments in the extraction of raw materials and their conversion into completed products for engineering purposes, materials have been used for centuries. For forming metals into intricate shapes, one of the most ancient and popular production processes is still in use today. Typically, the procedure is melting raw materials, putting them into a mold of the appropriate size and shape, and then letting them harden into the desired shape. When traditional gravity casting is compared with centrifugal casting, the efficiency of centrifugal casting has become more significant in producing cylindrical components, since the cast is produced by the centrifugal forces developed during the rotation of the mould with less defects. Its inherent dynamic operation characterized by rapid phase transitions, high temperature gradients, and complex solidification behaviour. These kind of factors often lead to casting defects such as porosity, inclusions or non-uniform grain structures, which can influence the end application

***Corresponding author.**
*E-mail address: allwinphd@gmail.com

This paper was recommended for publication in revised form by Editor-in Chief Ahmet Selim Dalkilic

Published by Yıldız Technical University Press, İstanbul, Turkey
Yıldız Technical University. This is an open access article under the CC BY-NC license (http://creativecommons.org/licenses/by-nc/4.0/).

performance of the product. The grain structures formed during solidification is especially crucial as it directly affects the strength and durability of the component. For both metallic and non-metallic materials, such as glass and concrete, centrifugal casting is widely employed because it provides better control over crystal development and solidification, improving the quality and dependability of the casting.

It is very much important to understand the process, metal flow behaviour and influence of process parameters in production of casts with good quality. Though there are several studies addressing various aspects of cylindrical casting, a significant scope still exists to optimize and refine the process for better overall performance. All of which are closely linked to casting process parameters [1,2]. Researchers have investigated various parameters to study their effects on microstructure and interfacial bonding in bimetal castings. Some of the key process parameters include mould's rotational speed [3-5], the preheating temperature [6], the temperature of the first solidified layer [7], melt pouring rate [8], temperature of superheat of the melt, and the rate of cooling of the mould during casting.

A critical aspect in the production of castings through centrifugal casting lies in understanding the heat dissipation within the rotating mould, since the manner in which molten metals lose heat during this process profoundly influences their solidification rates [9,10], subsequently impacting the final properties of the castings. Thus, the present study focuses on performing numerical heat transfer analysis of the mould. By exploring the rate of heat transfer and controlling its mechanisms with and without insulation of rotating mould, we can explore the process well so as to optimize the casting process to achieve superior quality and performance of the resulting metal components.

In addition to heat transfer mechanisms, the study also goes through the evaluation of mechanical properties of the cast specimens. Various parameters such as mould length, the use of thermal insulation are examined in order to understand how they affect the final quality of the castings produced. Along with this, Scanning Electron Microscopy (SEM) is used to analyze the surface finish and microstructure and structural characteristics. The approach of combining all these not only improves our understanding of the casting process but also offers a comprehensive evaluation of casting quality developing the way for advancements in engineering applications that demand strong and reliable materials.

MATERIAL AND METHODS

ANSYS Simulation

The fluidity of the melt has a very vital part in the production of high quality, defect free castings [11], since it determines how effectively the molten metal can fill the mould cavity before solidification begins [12]. Adequate fluidity ensures smooth flow of the molten metal throughout the surfaces of the mould, reducing the defects such as porosity, cold shuts, and incomplete filling. However, maintaining sufficient fluidity is often challenging due to the rapid heat transfer that occurs from the molten metal to its surroundings due to high temperature differences, which

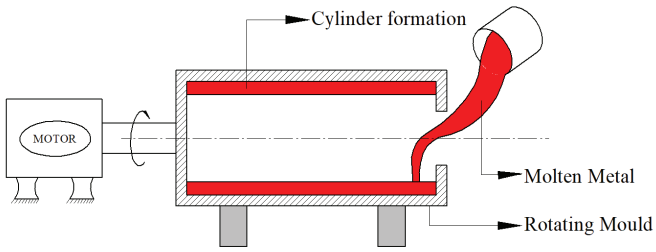

Figure 1. Schematic diagram of principle of Horizontal centrifugal casting process.

Table 1. Material Properties of Mould & Insulating layer

Particulars	Mould	Insulating Layer
Material	Mild steel	Asbestos
Thermal conductivity (W/ mK)	55	0.08
Specific Heat (J/kgK)	500	810
Thickness (mm)	10	25
Heat Transfer Coefficient (W/m^2K)	111.08	111.08
Coefficient of thermal expansion ($/^0C$)	10.8 to 12.5 x 10^{-6}	5 x 10^{-6}

can lead to premature solidification [13]. In order to overcome this issue, one of the widely used approach is reducing the temperature difference by preheating the mould [1,6,7] before the molten metal, which delays the solidification, due to retaining of heat in molten metal for a longer duration than usual and hence flow of the melt will be better. As a result, the metal flows more uniformly, improving the mould filling and improving the overall casts quality.

In this study, an additional strategy along with mould pre heating has been explored by incorporating an insulation layer around the rotating mould. This strategy is designed to further minimize the loss of heat from mould's inner surface to the surrounding air, effectively slowing down the rate of heat transfer, and hence there is more time for the molten metal to flow smoothly promoting better filling and improved casting quality. The rationale behind this modification is that by insulating the mould, the heat loss to the external environment is minimized, and the melt has additional time to settle and solidify into the required shape.

The below Figure 2 (a) to Figure 2 (h) shows the results of simulation for a mould of length 45mm, with and without insulation.

The insulation layer serves as a barrier [14], slowing down the cooling rate and enabling more controlled solidification, which is mainly useful when involved with high-viscosity [11] or high-melting-point metals that require extended fluidity [15].

To investigate the effects of this insulation on the fluidity and cooling behavior of the molten metal, transient heat transfer analysis was conducted with ANSYS v19.1 workbench software. There were two different mould dimensions considered with/without insulation for the simulation. The rate of heat transfers between the melt,

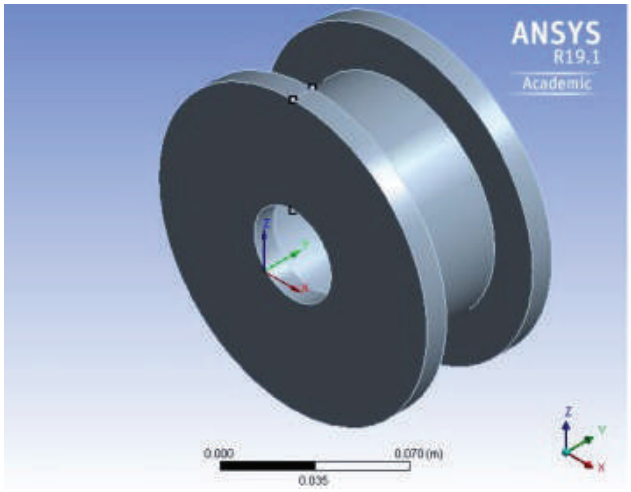

Figure 2. (a) CAD model of Mould without insulation.

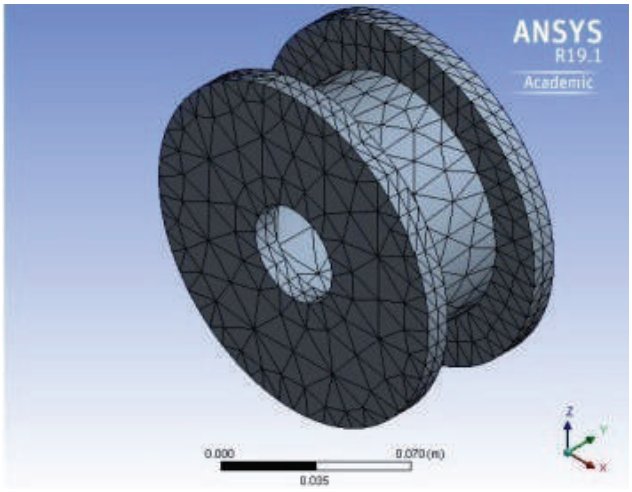

Figure 2. (b) FE Model of Mould without insulation.

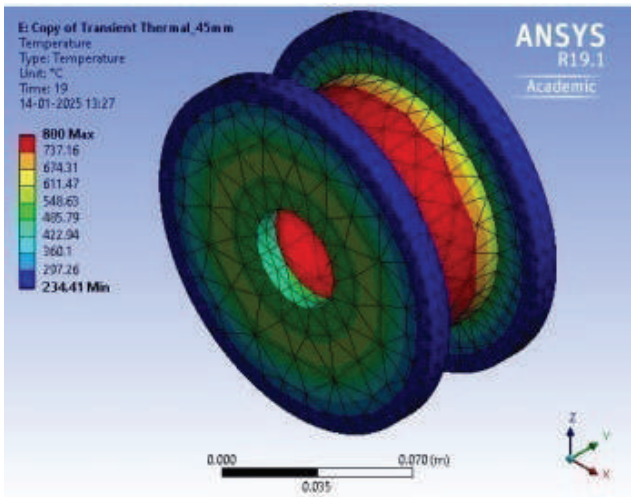

Figure 2. (c) Temperature of Mould without insulation.

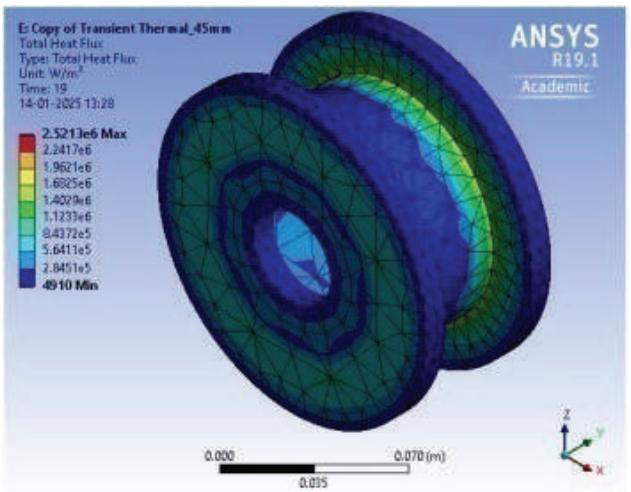

Figure 2. (d) Heat Flux in Mould without insulation.

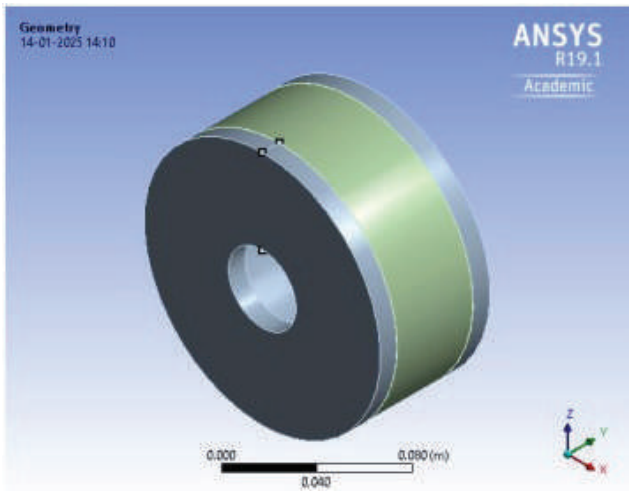

Figure 2. (e) CAD model of Mould without insulation imported into ANSYS.

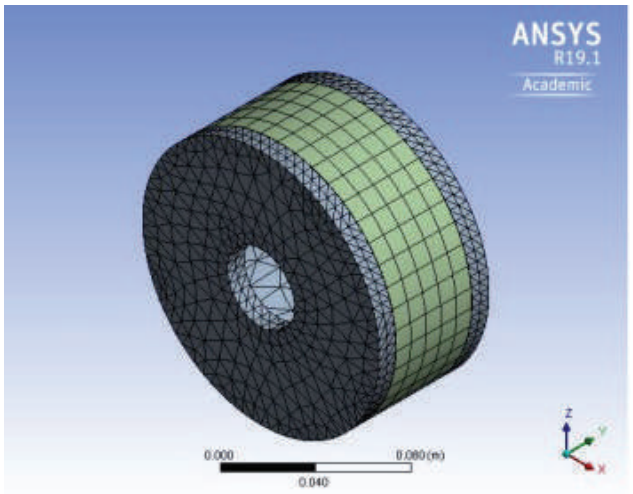

Figure 2. (f) FE Model of Mould without insulation in ANSYS.

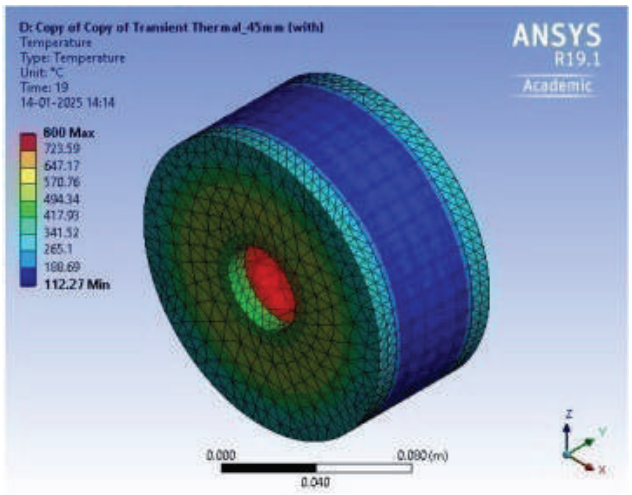

Figure 2. (g) Temperature of Mould with insulation.

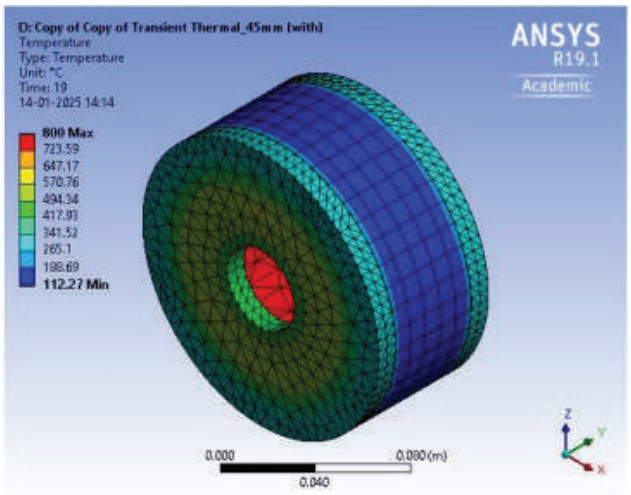

Figure 2. (h) Heat Flux in Mould with insulation.

mould and surroundings were analyzed with particular focus on the temperature distribution [16] and the cooling rates over time. The properties of the mould material and molten metal as shown in the Table 1 above were the inputs the simulation model.

Theoretical Comparison

The results from simulation were validated along with the theoretical calculations to validate the analytical and theoretical results of transient thermal behaviour of the rotating mould. The theoretical validation carried out using MATLAB, a largely used tool known for its numerical and analytical capabilities. Heat transfer equations were employed in MATLAB, along with material properties, geometry, and boundary conditions that was used in simulation. This method enabled to get accurate estimation of heat flux and temperature distribution, which was validated with ANSYS results. The main inputs included thermal conductivity, density, specific heat capacity and mould dimensions along with thickness of insulation. Boundary conditions used were constant inner surface temperature and surrounding convective heat transfer coefficient. The heat transfer equations were solved using finite difference method.

Governing equation

The two cases of the mould with and without insulation of the rotating mould are presented in the Figure 3 (a) and Figure 3 (b). The transient heat transfer for a cylindrical body is given by;

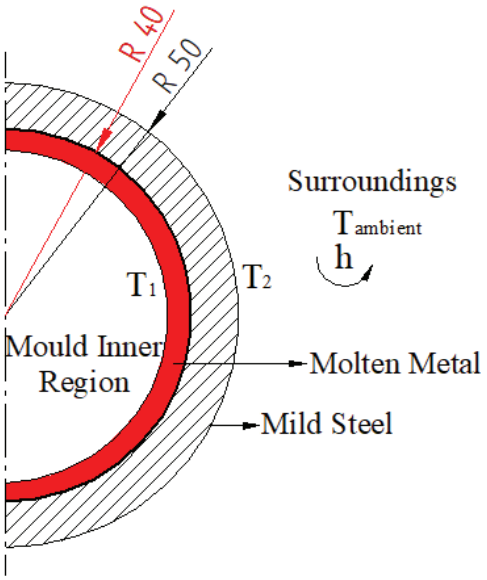

Figure 3 (a) Mould Without insulation.

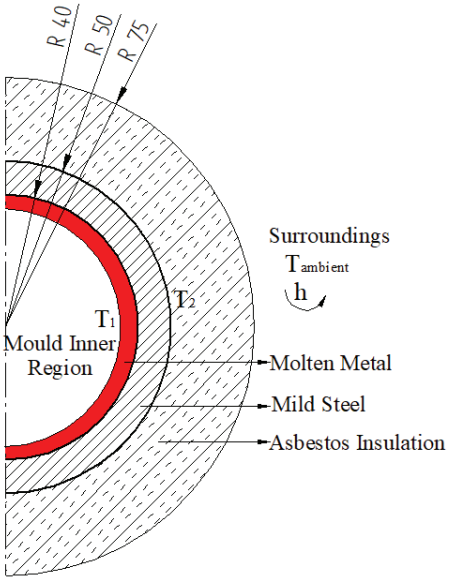

Figure 3 (b) Mould With insulation.

$$\frac{\partial T}{\partial t} = \frac{\alpha}{r}\frac{\partial}{\partial r}\left(r\frac{\partial T}{\partial r}\right) \quad (1)$$

Where, temperature is represented as T in °C, time t in s, radius r of cylinder, thermal diffusivity α in m^2/s. The initial temperature is set to $T_{ambient}$ = 30°C and boundary conditions like T(r, 0) = $T_{ambient}$= 30°C, inner surface at r = r_i , $T(r_i, t)$ = 800°C and at outer surface r = r_0 , heat loss due to convection; $-k\left(\frac{\partial T}{\partial r}\right)_{r=r_0} = h(T(r_0, t) - T_{ambient})$ are applied during time step. Heat flux at the outer surface is calculated as $q_{outer} = -k\left(\frac{\partial T}{\partial r}\right)_{r=r_0}$, while the average outer surface temperature is calculated using $T_{avg.outer}$= $T(r_0, t)$.

The above case is for transient thermal analysis of the mould without insulation. If the insulation layer needs to be considered then the heat conduction now spans into two regions as follows;

Region 1: Mild Steel ($r_{inner} \le r \le r_{cylinder}$)

$$\frac{\partial T_1}{\partial t} = \frac{\alpha_1}{r}\frac{\partial}{\partial r}\left(r\frac{\partial T_1}{\partial r}\right) \quad (2)$$

Region 2: Asbestos ($r_{cylinder} \le r \le r_{outer}$)

$$\frac{\partial T_2}{\partial t} = \frac{\alpha_2}{r}\frac{\partial}{\partial r}\left(r\frac{\partial T_2}{\partial r}\right) \quad (3)$$

Where, α_1 and α_2 are the thermal diffusivity of mild steel and asbestos respectively. T_1 temperature of the mould at the inner surface and is considered as same as the molten aluminum temperature assuming that there is negligible heat loss from the melt poured from furnace. T_2 is the temperature at outer surface of the mould in both with and without insulation cases. In first case for mould without insulation the thermal conductivity k in boundary condition equation is considered as $k_{mildsteel}$ and for second case where the mould is insulated the value of thermal conductivity k in above boundary condition equation is considered as $k_{asbestos}$. The heat transfer coefficient is considered as h in both the cases. The heat transfer from the mould outer surface to surrounding is considered as forced convection since the mould in rotating at 1000 rpm the air particles around the mould will be in motion.

Finding value of heat transfer coefficient

In this present study, the system functions under dynamic conditions because of the mould's high rotational speed. This makes it challenging to accurately determine the heat transfer coefficient (h), a key factor that strongly affect the overall thermal behaviour [17]. Under these conditions, the heat transfer is primarily dominated by forced convection which results from continuous relative motion between rotating mould surface and the surrounding air.

Factors Influencing the Heat Transfer Coefficient (h);

1. Mould Geometry & Dimensions
2. Material Properties
3. Insulation Considerations
4. Rotational Speed and Turbulence Effects
5. Ambient and Surface Temperature Conditions

We know that outer radius of the mould (r_{outer}) = 0.05m, Rotational Speed (N) = 1000 rpm, then Angular Velocity (ω) = $\frac{2\pi N}{60}$. Therefore the outer Surface Velocity (v) can be found as ω * r_{outer}.

Now noting down the Air properties at the film temperature (T_f) = $\frac{T_{outer} + T_\infty}{2}$ and finding the Reynold's no (Re) using the formula $\frac{v\, D_{outer}}{\nu}$. We have for forced convection around a cylinder, the empirical correlations for R_e in the range of 40,000 – 400,000, we have; Nu = C. Re^m. $Pr^{0.333}$, where C = 0.0266 and m = 0.805.

Now using $Nu = \frac{h D_{outer}}{k}$
we can find the value of h using
$h = \frac{Nu*k}{D_{outer}}$.

Though practically there exist dynamic conditions, forced heat transfer coefficient could be considered because of mould rotation as mentioned above. Finite difference method (FDM) is used for discretizing the heat equation in radial direction and time and the results from solving the above partial differential equation are obtained from MATLAB.

Experimentation

With wide variety of process parameters already studied in precious researches, the presence of insulation on to the mould which is rotating is done in this present study. The experimental set up consisted of a Horizontal centrifugal casting machine, which is capable of rotating upto 2000 rpm. To compare the type of casts produced with the parameter of insulating the thickness, Aluminum metal was chosen, due to its abundance availability and one of the easy to cast metals. The properties of Aluminum metal are as shown in Table 2 below.

Table 2. Material Properties of Aluminum

Particulars	Value
Density (kg/m^3)	2,660
Thermal Conductivity (W/mK)	237
Specific Heat (J/kgK)	900
Elastic Modulus (MPa)	70,300
Melting Point (^{0}C)	660
Poisons ratio	0.3

Production of Casts

The Aluminum was melted in and electric furnace with a super heat temperature of 150°C so as to melt the metals for casting. Hence the molten metal temperature is considered as 800°C at the inner surface of the mould in case of simulation and MATLAB.

The mould with constant rotational speed of 1000 rpm was considered in order to understand the type of casts we obtain with and without insulating the mould. The superheated molten aluminum at 800°C is taken from the furnace and poured into the rotating mould. The heat losses from the melt from furnace to centrifugal casting machine are ignored in this study. Also the rotation of the mould at high speeds to produce the cast is a dynamic condition which will lead to consideration of forced convection between the surrounding and outer surface of the rotating mould, leading the greater heat transfer coefficient values. This dynamic condition is also not considered in the study; instead it is assumed that the mould is in static condition in case of ANSYS simulation as well as MATLAB calculations.

Figure 4 (a) and Figure4 (b) shows the two cylinders casted from horizontal centrifugal casting machine with and without insulation respectively. In both cases, the mould was rotated at 1000 rpm while molten pure aluminum metal at 800°C was poured into the rotating mould. The mould was not pre heated while it was at ambient temperature before pouring the molten metal. It can be observed from Figure 5 (a) that the inner surface finish of the finished cast is rough when compared to the one in Figure 5 (b) This is because of the smooth flow of melt

Figure 4. (a) Mould without Insulation.

Figure 4. (b) Mould with Asbestos Insulation.

Figure 5. (a) Cast cylinder without Insulation.

Figure 5. (b) Cast cylinder with Asbestos Insulation.

inside the rotating mould [12], since an added insulation with asbestos around the rotating mould reduces the heat loss as discussed in previous chapters, and allows fractionally more time for solidification.

SEM Analysis

The SEM images presented in Figure 6 (a), Figure 6(b), Figure 7 (a) and Figure 7 (b) illustrate the microstructure of aluminum castings produced by centrifugal cas.ting at identical rotational speeds, both with and without mould insulation. The images presented aforesaid were captured along the circular direction of the inner surface of the castings. From literatures it can be noticed that mould rotational speed significantly influences microstructure formation, when the speed of rotation of mould is increased which directly affects the rate of solidification of the melt. When the melt is poured into the rotating mould, the centrifugal force drives the molten metal outward, which leads to rapid conduction of heat through the ould and already solidified layers (if any) resulting in faster cooling rates.

By adding the layer of insulation around the mould, the heat loss is reduced, allowing more time for the molten metal to flow over the inner surface of the mould with uniform solidification [11]. Microstructures produced show rougher grain finished as shown in Figure 6 (without insulation) while finer grains can be seen due to smoother flow of molten metal as shown in Figure 7 (with insulation). It is evident that both rotation speed and insulation has an impact on the grain formation. Quick cooling rates without insulation leads to coarser grains whereas slower more controlled cooling with the help of insulation leads to finer grains comparatively due to more gradual solidification.

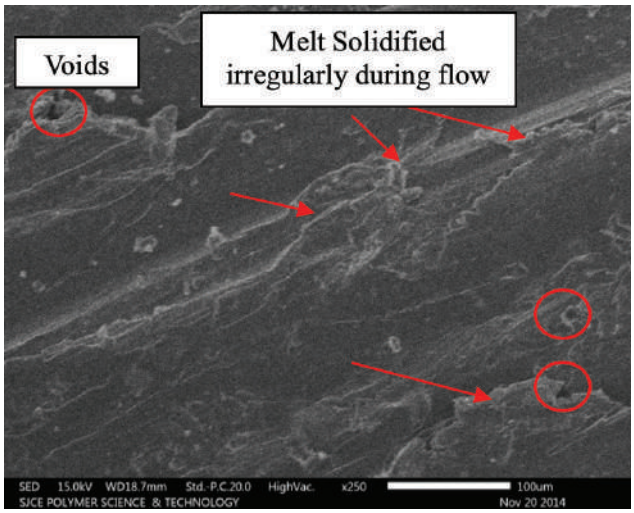

Figure 6. (b) SEM image-2 of Al cast without insulation.

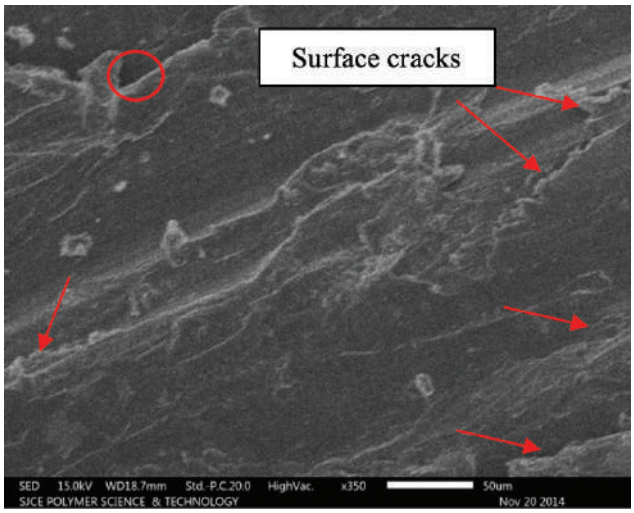

Figure 6. (a) SEM image-1 of Al cast without insulation.

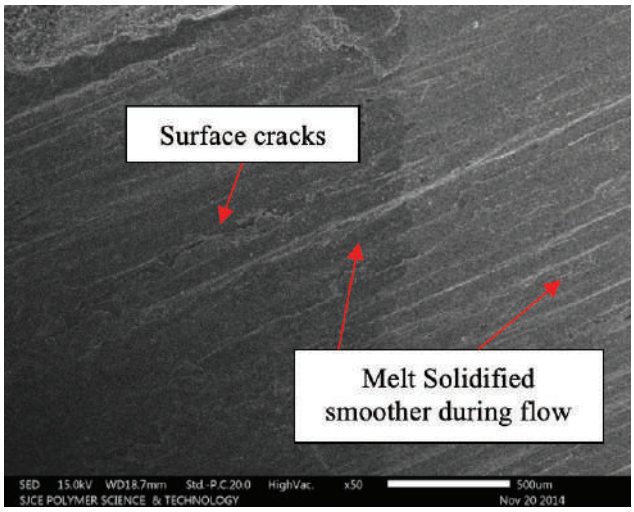

Figure 7. (a) SEM image-1 of Al cast with insulation.

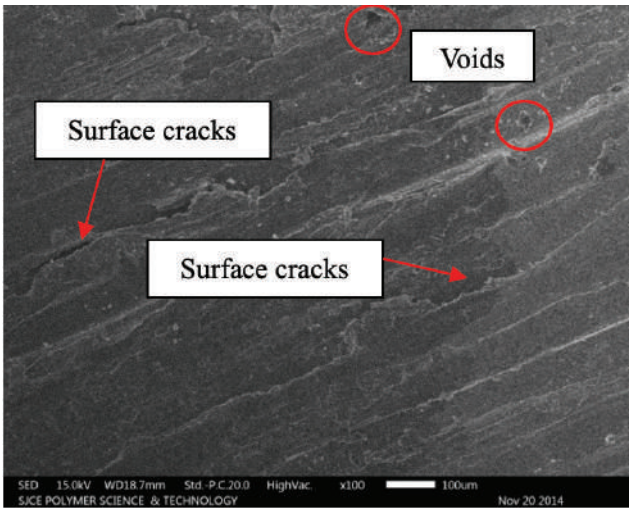

Figure 7. (b) SEM image-2 of Al cast with insulation.

RESULTS AND DISCUSSION

The mould in the centrifugal casing machine was first analyzed in ANSYS workbench software, for studying the rate of heat transfer behaviour. The simulation was done for two cases which are (i) with and (ii) without insulation for two different mould lengths of 70 mm and 45 mm. The results obtained from ANSYS simulation were compared with that obtained from MATLAB where the governing partial differential equation of the heat transfer was solved using finite difference method to compare the results from ANSYS. The results of both are presented in Table 3 below;

Figures 8 (a) and 8 (b) illustrate that the simulated and theoretical results for heat flux, both with and without insulation, show strong agreement. Similarly, Figures 9 (a) and 9 (b) compare the theoretical and simulated results for the average temperature distribution at the outer surface of the mould under insulated and non-insulated conditions, also demonstrating excellent correlation.

The results obtained from MATLAB programming as well as ANSYS simulation shows considerable similarity there by validating that the results are accurate.

The Figure 10 (a) shows the comparison of results of average heat flux over the mould for with insulation and without insulation. As depicted in the above Figure 10 (a), it can be observed that the insulation of the mould plays a significant role in reduction in heat loss which substantially allows more heat to stay inside the mould as we can see in the average temperature distribution is reduced at the outer surface of the mould as shown in Figure 10 (a).

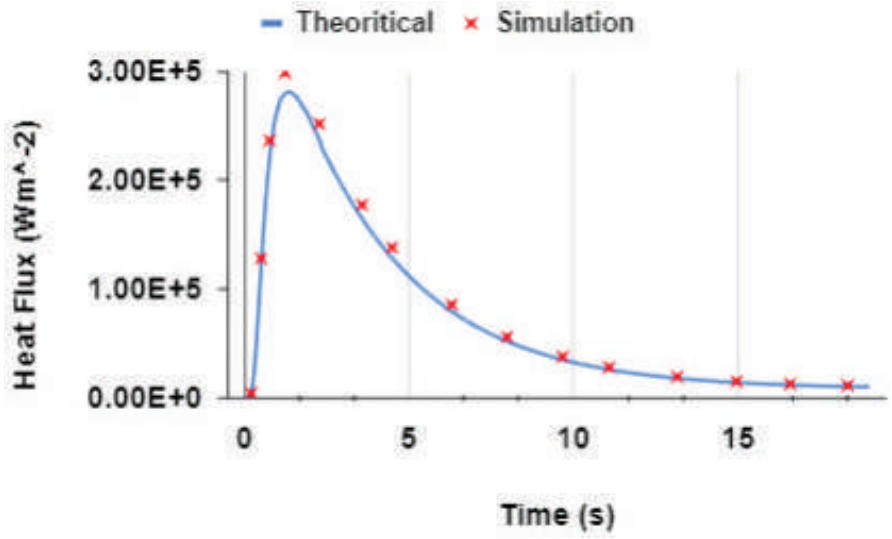

Figure 8. (a) Comparison of Theoretical and Simulation Heat Flux without Insulation.

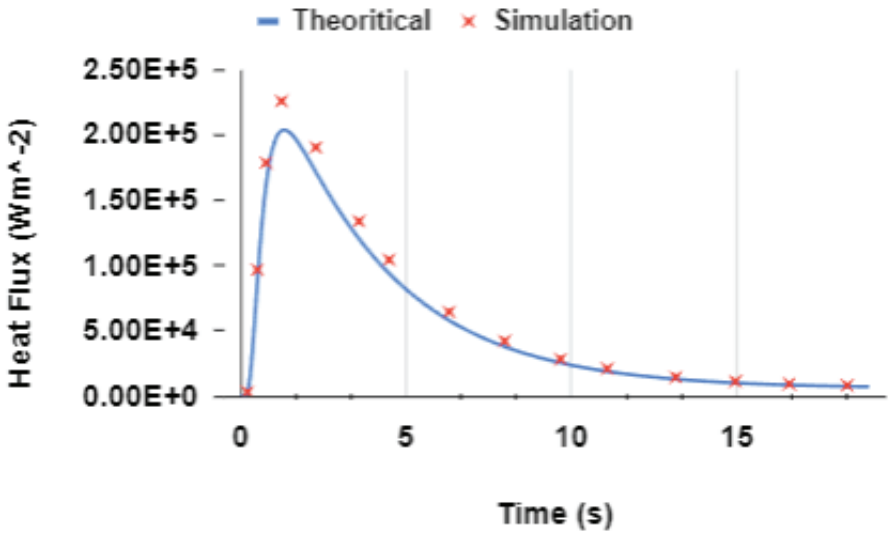

Figure 8. (b) Comparison of Theoretical and Simulation Heat Flux with Insulation.

Table 3. Results from ANSYS and MATLAB

Parameter	Insulation	MATLAB	ANSYS
Max Heat Flux (x 10^5 W/m^2)	With	2.265	2.039
	Without	2.997	2.809
Average Temperature at outer surface of mould at 19s (^{0}C)	With	689.27	668.59
	Without	792.26	765.58

Figure 10 (a) presents a comparison of heat flux results obtained from ANSYS Workbench simulations and MATLAB computations. For the insulated mould, the simulation predicts a peak heat flux of 2.039×10^5 W/m^2, while for without insulation of mould, it is 2.809×10^5 W/m^2. The MATLAB results exhibit good correlation, with error margins of 11% and 6.69%, respectively.

Figure 10 (b) presents the average temperature distribution at mould's outer surface. It can be observed from the above results that, average maximum temperature at

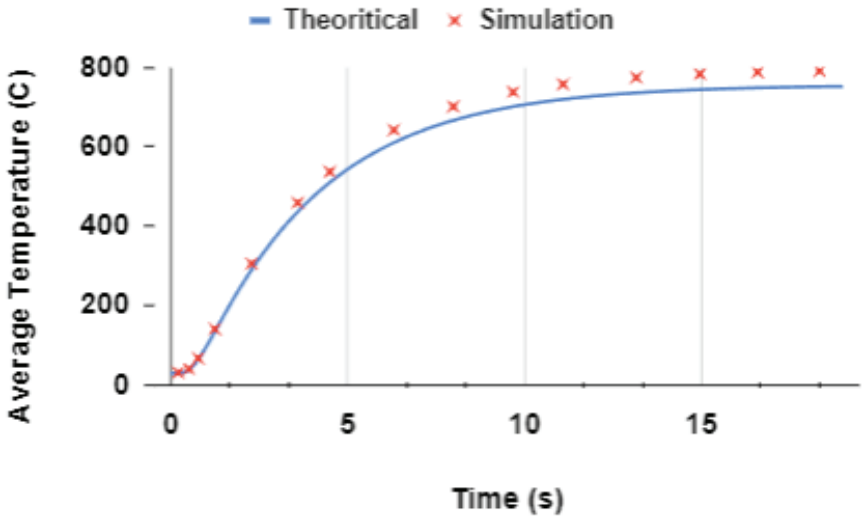

Figure 9. (a) Comparison of Theoretical and Simulation Average Outer Surface of Mould Temperature without Insulation.

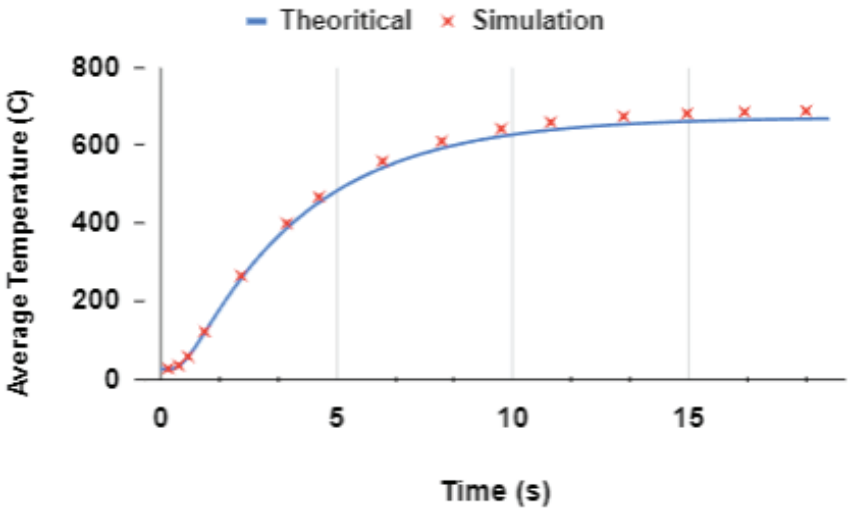

Figure 9. (b) Comparison of Theoretical and Simulation Average Outer Surface of Mould Temperature with Insulation.

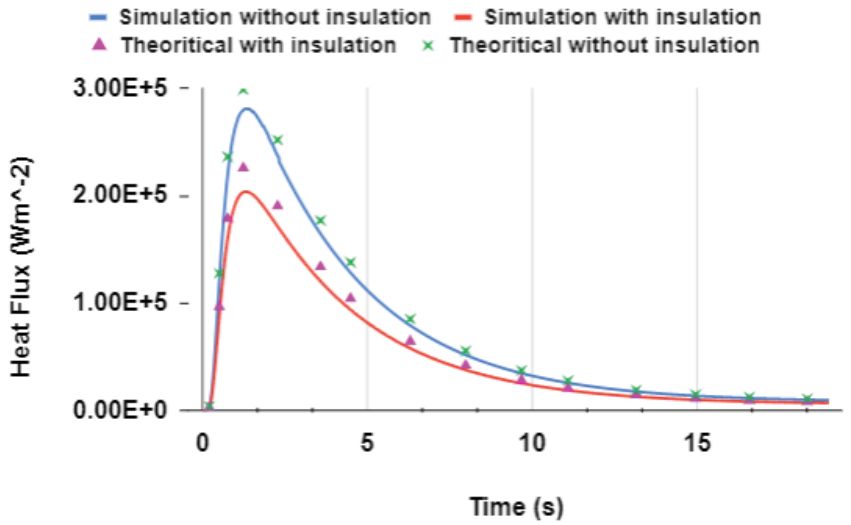

Figure 10. (a) Comparison of Average Heat flux of the Mould with and without Insulation.

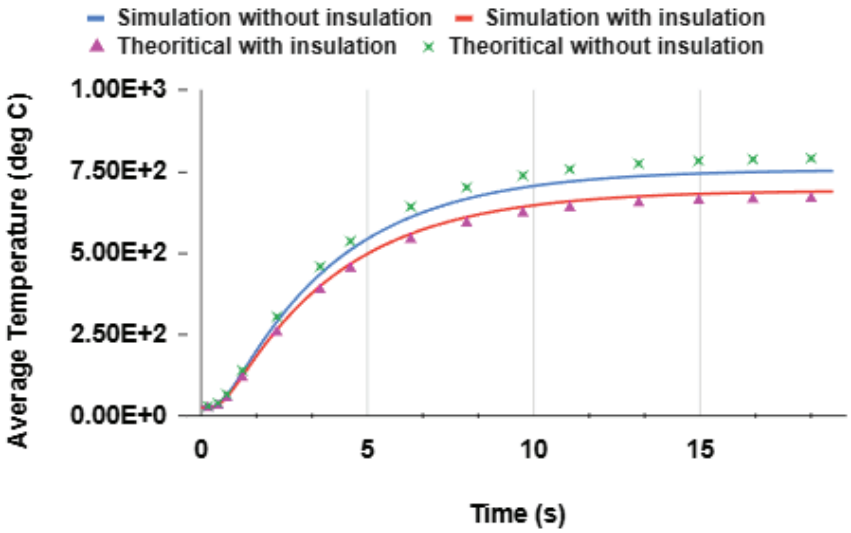

Figure 10. (b) Comparison of Average Temperature of the Mould outer surface with and without Insulation.

the outer surface reached 668.59°C for mould with insulation and 765.59°C for mould without insulation. The theoretical calculations are in good agreement with simulation results, with a few deviation of 3.09% and 3.49% respectively.

The presence of additional heat inside the mould aids the solidification rate, by increasing the time for the molten metal to solidify [14]. This reduction in solidification rate allows the molten metal to flow better [11] inside the mould as it rotates at certain speeds, hence better grain structure can be obtained comparatively which can be witnessed in the sample specimens fabricated with horizontal centrifugal casting machine with a rotational speed of 1000 rpm and without preheating the mould as shown in Figure 5 (a) and Figure 5 (b).

CONCLUSION

In this present study the effectiveness of adding an insulation layer around the rotating mould in order to improve the quality of casts produced from centrifugal casting machine and also obtain defect free castings are demonstrated The combination of transient thermal analysis using ANSYS software and theroritical validation using MATLAB and experimental observations, the study shows that the mould insulation substantially reduces the heat loss and provides lesser temperature gradients during the casting process. The key findings of the present study are shown below;

- Heat Loss reduction by 27.41% due to thermal insulation, enhancing the thermal efficiency.
- Average outer surface temperature of the mould was decreased nu 12.67% with insulation reducing the thermal gradients.
- Presence of insulation, reduced heat loss and smoother flow of molten metal leading to more uniform solidification minimizing the defects.
- The overall quality of the castings are improved with better surface finish without post processing of casts, with fewer defects.
- The results obtained from ANSYS simulation and MATLAB calculations are in good agreement.
- Finer and better microstructure grains observed in casts produced with insulated mould.

In comparison to process parameters studied in previous literatures such as rotational speed of mould and preheating, addition of insulated layer is proved to be a highly effective method for improving the cast quality with minimum defects. Future work can be focused on optimizing the insulation materials, thickness and extending the analysis to 3D thermal fluid simulations for better understanding of solidification process. Advance microstructural analysis and real time thermal monitoring can also be considered to enhance the quality of casting process.

NOMENCLATURE

$T_{ambient}$	Surrounding Temperature (°C)
$T_{average\ outer}$	Average Temperature at outer surface of the mould (°C)
T_f	Film Temperature (°C)
r_i	Inner radius of the rotating mould (m)
r_0	Outer radius of the rotating mould (m)
k	Thermal Conductivity (W/mK)
$k_{mildsteel}$	Thermal Conductivity of mild steel(W/mK)
$k_{asbestos}$	Thermal Conductivity of asbestos (W/mK)
h	Heat Transfer Coefficient (W/m^{2}K)
t	Time (s)
v	Kinematic Viscosity (m^2/s)
q_{outer}	Average Heat flux at outer surface of the mould (W/m^2)
ω	Angular Velocity (rad/s)
N	Speed of rotation of mould (rpm)
v	Outer Surface Velocity (m/s)
Re	Reynold's no
Nu	Nusselt no
Pr	Prandtl no
SEM	Scanning Electron Microscope
CAD	Computer Aided Drafting
FE	Finite Element
FEM	Finite Element Method
FDM	Finite Difference Method

AUTHORSHIP CONTRIBUTIONS

R Allwin Yesuvadian: Conceptualization, Methods, Experimentaiton, Writing – Original Draft and Editing of Manuscript. K S Keerthiprasad: Supervision, Validation and Review.

DATA AVAILABILITY STATEMENT

The authors attest that the information in the article supports the study's conclusions. Upon reasonable request, the corresponding author will provide the raw data supporting the study's findings.

CONFLICT OF INTEREST

The authors declared no potential conflicts of interest with respect to the research, authorship, and/or publication of this article.

FUNDING

The authors declare that no funds, grants, or other support were received during the preparation of this manuscript.

ETHICS

There are no ethical issues with the publication of this manuscript.

REFERENCES

[1] Wang X, et al. Influence of casting temperature and mould preheating temperature on centrifugal casting by numerical simulation. J Mater Eng Perform 2023;32(15):6786–6809. [CrossRef]

[2] Keerthi Prasad KS, Murali MS, Mukunda PG. Analysis of fluid flow in centrifugal casting. Front Mater Sci China 2010;4:103–110. [CrossRef]

[3] El-Sayed MA. Effect of the mould rotational speed on the quality of centrifugal castings. Int J Appl Eng Res 2014;9(21):11575–11582.

[4] Santoso N, Suharnadi B, Tulung Prayoga B, Dwi Setyana L. Characteristic of interface bimetal aluminum-copper for bimetal bushing produced by centrifugal casting. Acta Metall Slovaca 2021;27(1):28–31. [CrossRef]

[5] Bohacek J, Kharicha A, Ludwig A, et al. Heat transfer coefficient at cast-mould interface during centrifugal casting: Calculation of air gap. Metall Mater Trans B 2018;49:1421–1433. [CrossRef]

[6] Pandey S, Parhi S, Jha SK. Effect of the mould rotational speed on the quality of bimetallic pipe fabricated by centrifugal casting process. Int J Emerg Res Manag Technol;6. [CrossRef]

[7] Wang X, et al. Influence of casting temperature and mould preheating temperature on centrifugal casting by numerical simulation. J Mater Eng Perform 2023;32(15):6786–6809. [CrossRef]

[8] Sarvari M, Divandari M. Effects of melt/solid volume ratio and rotational speed on the interface of Al/Mg bimetal in centrifugal casting. J Adv Mater Eng 2016;35(2):83–94. [CrossRef]

[9] Lu S, Xiao F, Zhang S, Mao Y, Liao B. Simulation study on the centrifugal casting wet-type cylinder liner based on ProCAST. Appl Therm Eng 2014;73(1):512–521. [CrossRef]

[10] Deng C, Wang X, Du X. Numerical simulation of mould filling and solidification process of out layer of muitiple tube during centrifugal casting. Foundry Technol 2016;37(6):1197–1201.

[11] Erhunmwun İ. Numerical determination of the rate of solidification in centrifugal casting. IJESA 2020;4(3):135–138.

[12] Erhunmwun İ, Akpobi J, Osunde T. Numerical analysis of the temperature distribution in centrifugal casting. Int J Eng Sci Appl 2019;3(1):1–7.

[13] Xu D, Yu Q, Li X, An G. Mould filling behavior of melts with different viscosity under centrifugal force field. J Mater Sci Technol 2002;18(2):149.

[14] Kim JH, Kim CH. Filling and solidification analysis for the casting process of cylinder liner. J Korea Foundry Soc 2004;24(4):225–230.

[15] Bentoumi L, Touba B, Bessaïh R, Bouttout A. Impact of thermal insulation on energy consumption in buildings. J Therm Eng 2024. [CrossRef]

[16] Kürekci NA, Özcan M. A practical method for determination of economic insulation thickness of steel, plastic and copper hot water pipes. J Therm Eng 2020;6(1):72–86. [CrossRef]

[17] Saleh B, Jiang J, Ma A, Song D, Yang D. Effect of main parameters on the mechanical and wear behaviour of functionally graded materials by centrifugal casting: A review. Met Mater Int 2019;25(6):1395–1409. [CrossRef]

[18] Setyana L, Santoso N, Suharnadi B, Tulung Prayoga B, Wiyadi W. Bonding of interface bimetal aluminum-bronze for bimetal bushing produced by solid liquid method. Acta Metall Slovaca 2022;28(2):80–84. [CrossRef]

J Ther Eng, Vol. 12, No. 2, pp. 453−465, March, 2026

Journal of Thermal Engineering
Web page info: https://jten.yildiz.edu.tr
DOI: 10.14744/thermal.0001090

Research Article

Experimental study of the Heat Transfer Coefficient of an Automobile Radiator Using Alumina & Titania based Nanofluids as Coolants

Salman Basha SHEIK[1,2,*], Praveena Devi NAGIREDDY[1], Kiran Kumar KUPIREDDI[3]

[1]*Department of Mechanical Engineering, SR University, Warangal, 506371, India*
[2]*Department of Mechanical Engineering, Sasi Institute of Technology & Engineering, Tadepalligudem, 534101, India*
[3]*Department of Mechanical Engineering, National Institute of Technology Warangal, 506371, India*

ARTICLE INFO

Article history
Received: 28 August 2025
Revised: 06 November 2025
Accepted: 09 November 2025

Keywords:
Alumina; Ethylene Glycol; Heat Transfer; Nanofluids; Titania

ABSTRACT

Better engine cooling capability remains a desperate challenge in automotive heat management, as traditional water–ethylene glycol coolants regularly manifest limited heat transfer potential. This work investigates the improvement of radiator operation using alumina and titania-based nanofluids as a progressive heat-transfer approach. Nanofluids were produced by ultrasonic dispersion of nanoparticles (0.02–0.08 vol%) in water–ethylene glycol mixtures, followed by experimental testing in a customized automobile radiator test rig at an inlet temperature of 65°C and flow rates of 7–14 L min^{-1}. The specific-heat equation was employed to determine the rate of heat transfer, and differential surface-fluid temperature analyses were used to obtain convective heat-transfer coefficients. The results show that adding alumina and titania nanoparticles notably enhances heat transfer. The hybrid nanofluid (0.06 vol% alumina + 0.02 vol% titania) achieved a highest heat transfer coefficient of nearly 6400 W m^{-2} K^{-1}, depicting a 155.6% increase over distilled water and about 60% advancement compared to the base water–ethylene glycol mixture. Radiator efficacy improved by 25–47%, while specific heat capacity was reduced by up to 73%, specifying a faster heating–cooling reaction. The results proposed that nanoparticle-induced micro-convection and improved thermal conduction govern the observed enhancements. The novelty of this work lies in experimentally quantifying the integrated thermal impact of alumina–titania nanofluids under practical automotive conditions, extending existing literature focused primarily on single nanoparticles. These results provide design insights for developing high-efficiency cooling systems in electronic thermal management, automobiles, and renewable-energy heat exchangers.

Cite this article as: Sheik SB, Nagireddy PD, Kupireddi KK. Experimental study of the Heat Transfer Coefficient of an Automobile Radiator Using Alumina & Titania based Nanofluids as Coolants. J Ther Eng 2026;12(2):453−465.

***Corresponding author.**
*E-mail address: sheiksalmanbasha@gmail.com

This paper was recommended for publication in revised form by Editor-in Chief Ahmet Selim Dalkilic

Published by Yıldız Technical University Press, İstanbul, Turkey
Yıldız Technical University. This is an open access article under the CC BY-NC license (http://creativecommons.org/licenses/by-nc/4.0/).

INTRODUCTION

A cooling system is an essential part of performance because it allows the necessary temperature ranges for operation in the engine. The management of temperature in a thermal management system helps to improve engine efficiency and to reduce engine wear and overheating, which will directly affect performance in the vehicle. Therefore, since radiators are compact heat exchangers and important parts of the cooling system, they stand to benefit a lot from the use of modern automotive coolants. Choi introduced the term "nanofluids" in 1995, and they are fluids engineered with nanometer-sized solid particles, which are suspended in a base fluid and form a solid-liquid composite material. Over the past 2-3 decades, nanofluids have received a tremendous amount of research. A primary use of nanofluids is to argue their applicability in automotive, industrial, and other technology sectors, and often as coolants and friction-reducing agents. The present experimental comparison focuses on the performance of nanofluids in comparison to traditional coolants, i.e., pure water.

Shriram Sonawane et al. [1] studied the capacity of nanofluids in increasing the functioning of automotive cooling bodies and contributed to the development of automotive thermal management. Since designing these nanofluids for practical applications would be beneficial, including some potential advantages when implementing them in automotive cooling systems. Kundan Kumar et al. [2] expressed that improving heat transfer performance through nanofluids provides great advancements in the application of nanofluids as potential replacements in the automobile cooling system. The study cites nanofluids as a key component for radiator innovation that enhances automotive performance while also being environmentally friendly. The engine heat transfer ability is improved when utilizing nanofluids, since colloidal suspensions of nanoparticles have favorable thermal properties when properly formulated in traditional engine coolants. Chandan Kumar, et al. [3] investigated that paraffin wax in sustained-centigrade nanofluids works with phase change materials to improve thermal management by efficiently regulating temperatures and actively absorbing heat during high-load situations in a vehicle, which improves the sustainability of radiator performance in internal combustion engines.

Atul Bhattad et al. [4] investigated the preparation and use of nanofluids in IC engines. Amr M Hassaan et al. [5] investigated the application of hybrid nanofluids, specifically MWCNTs-Al, to an automobile radiator. The results indicate that hybrid nanofluids can provide better performance of radiators and improve thermal management in vehicles. Najmul Hidayat et al. [6] investigated the heat transfer capability of hybrid Al_2O_3-TiO_2 nanofluid in an automobile radiator. Chandan Kumar et al. [3] examined the thermal efficiency of pure coolant and hybrid nanofluid with various concentrations for cooling fluids (0.25%, 0.30%, and 0.35% wt. of nanoparticles) and fluid flow rates (20, 24, and 28 L min^{-1}) at inlet temperatures of 70, 80, and 90 °C respectively.

Kundan Kumar et al. [7] investigation explores the orientations and use of nanofluids with Al_2O_3 and TiO_2-based suspensions to improve heat transfer coefficient air performance related to automotive/alternator radiators. The addition of nanoparticles to any coolant, including traditional engine coolants, will improve heat capacity and thermal conductivity characteristics. Experimental results confirmed that radiator systems that included nanofluids increased their heat transfer performance effectiveness, which supported sustainability and operational performance improvements. Budi Kristiawan et al. [8] studied the thermal properties of hybrid nanofluids in a cooling system, which implements a helically twisted tube inside a brushless direct electric motor. The data collected were for Nusselt number and dropped stator temperatures; however, an assessment of the automobile radiator heat transfer coefficient was not present in the data. The hybrid nanofluids tested were noted to have significant heat transfer capability over water-based fluids according to the research, although there was no research focused on automotive applications. The experimental data of the Al_2O_3-water showed superior performance, and then the TiO_2-water, with hybrid nanofluids showing better thermal performance especially at the higher concentration and best ratios of the nanoparticles, which gave better overall and convective heat transfer coefficients [9].

The CFD investigation was completed using inlet temperatures at 60, 70, and 80 °C. Overall, and while CuO nanofluid represented the best-performing nanofluid in terms of temperature reductions and pressure drops, the performance parameters calculated for Al_2O_3 and TiO_2 show their potential use as coolants in radiator applications [10]. The authors address hybrid nanofluid thermal performance in a car radiator. They show that AlTi (Al_2O_3+TiO_2) leads to the greatest increase in the overall performance while CuTi (CuO+TiO_2) showed decreased performance. The papers support the use of THNF(Al_2O_3+CuO+TiO_2) hybrid coolant as it leads to lower entropy generation and offers moderate thermal performance improvements that demonstrate its potential for improving the heat transfer characteristics for an automobile radiator [11]. Research on Al_2O_3 and TiO_2-nanofluids utilization in automotive radiators showed significant improvement in radiator cooling performance. Research reports that Al_2O_3-nanofluid with a 0.3% vol. fraction showed the highest radiator effectiveness improvement of 24.21%. The use of TiO_2-water nanofluid indicated a radiator effectiveness improvement of 47% when operating with its best volume concentration. The heat transfer rates for both nanofluids were improved under a specific volume concentration at a specific Reynolds number, resulting in better operation of the vehicle cooling system [12].

A.T. Akinshilo et al. (2020) [13] investigated heat transfer and fluid flow of an electrically conducting magnetohydrodynamic (MHD) nanofluid in diverging or converging channels made from a porous medium of internally generated heat. The governing equations in this problem are high order and nonlinear, the homotopy perturbation approach

was considered an appropriate tool of analysis for obtaining approximate solutions. Researchers then studied the nonlinear influence of heat radiation in Casson nanofluid, which is entrapped between a porous medium and the flow over a narrow needle, including the internal heat generation [14]. The homotopy perturbation method (HPM) has also been employed to examine the fluctuating flow and heat transfer of a nanofluid being injected by an expanding or retracting porous channel, with the system being exposed to a constant magnetic flux [15]. The study investigates the flow and thermal transfer of magneto-hydrodynamic nanofluid inside a rotating system, using more complex, non-linear ordinary differentials and the homotopy perturbation method (HPM) to obtain analytical solutions [16].

Recently, mutiple studies have been focusing on the development of nanofluids as useful alternatives for traditional heat-transfer fluids due to their better thermal conductivity and energy efficiency. Kiaei et al. (2023) [17] evaluated the performance of an Al_2O_3 and CuO nanofluid compared with mono-disperse nanoparticles and pure water-based fluids, showing that radiator thermal performance was increased with higher Reynolds numbers and nanoparticle volume fractions. Ukueje et al. (2022) [18] aligns with the conventional opinion that hybrid nanofluid takes advantage of the synergistic effect of the disparate nanoparticles, thus making it a more effective heat-transfer medium. Dai et al. (2024) [19] proved that optimization of mixing ratios can significantly increase the thermal conductivity of Cu-Al hybrid suspensions, which in turn allowed increasing the overall heat-transfer performance. Nanoparticle agglomeration, viscosity modulation, and flow turbulence are the phenomena that have been significantly sensitive to the performance of radiators, which is supported by recent numerical simulations. Such studies emphasize how essential nanofluids are in improving the heat-transfer capacity of radiator systems [20]. The results demonstrated that there is a notable enhancement in heat transfer rate in the existence of a typical inserted perverted tape [21].

Table 1 presents the notable enhancement of heat transfer properties, such as the Nusselt number, convective heat transfer coefficient, heat transfer rate, overall U, etc., of

Table 1. Details of percentage improvement of heat transfer properties of hybrid nanofluids

Hybrid composition	Metric reported	Concentration reported	Key experimental conditions	Reference
MWCNT–CuO hybrid (aqueous)	Convective heat transfer coefficient enhanced by 295%	Reported concentrations varied 0.05–0.15 wt% (highest effects at ~0.1 wt%)	Coolant flow 7 L min^{-1}, inlet 80 °C (automotive radiator test rig)	[22]
CNC (cellulose nanocrystal) + CuO hybrid (CNC/CuO)	Heat transfer efficiency improved by 92.43%	Fixed volume fraction 0.01 vol% (hybrid)	Scaled-down and commercial radiator tests; flowrates 0.75–1.25 L min^{-1}, radiator inlet 80 °C	[23]
Graphene nanoplatelets (GnP) + cellulose nanocrystals (CNC)	Convective heat transfer coefficient +51.91%	Reported test used 0.01% hybrid in optimized tube (base fluid DW:EG 40:60)	Counterflow radiator test rig (laboratory)	[24]
GnP + CNC hybrid	Overall heat transfer coefficient +46.72%	Same as above (reported optimized concentration 0.01% in tube study)	Counterflow radiator test rig	
CuO–MgO–TiO_2 ternary hybrid	Coolant-side heat transfer coefficient +46%	0.5 vol% (hybrid)	Flat-tube car radiator tests (varied flow rate, frontal air velocity)	[25]
Al_2O_3–TiO_2–SiO_2 tri-hybrid	Coolant-side heat transfer coefficient +39.7%	0.3 vol% (maximum reported)	Coolant flow 2–12 LPM, working temperature 70 °C, air velocity ~4 m/s	[26]
MWCNT + Al_2O_3 hybrid (EG + DW base 1:1)	Heat transfer increase +35%	Volume concentrations tested 0.03–0.12%	Inlet temperatures 40–75 °C; flow rate 0.6–0.96 m^3/h (as reported)	[27]
SiC + MWCNT hybrid	Reported heat-transfer boost (approx.)	Concentrations discussed in paper (see source)	Automotive radiator system experiments (paper reports thermophysical tests and radiator performance)	[28]
Glycerin/Al_2O_3	Enhanced heat transfer coefficient is 62%	0.05, 0.1 and 0.15% volume fractions of nanofluids	Engine model and a car radiator test rig	[29]
CuO/Water	Improved heat transfer characteristics from 16% - 31%	Cu based water nanofluid of 0.025, 0.05 and 0.075% volume concentration	Tractor engine radiator test rig	[30]

hybrid nanofluids in radiator or radiator-like tests, together with the composition, concentration, and experimental circumstances specified by the authors.

The difficulties involving stability, erosion, and corrosion came when the volume fraction of nanoparticles increased in nanofluid. Hence, the optimum concentration of nanofluids plays an important role [31].

Despite these advances, limited experimental studies have examined the condensed thermal and hydrodynamic performance of hybrid nanofluids under actual automobile radiator operating conditions. Addressing this gap, the present study provides an experimental evaluation of alumina–titania nanofluids to establish reliable heat-transfer correlations for automotive and energy-system cooling applications.

The research aims to provide comprehensive experimental details on the heat transfer and flow properties of specific alumina and titania nanofluids in automotive radiators, with a novel focus on confirming stable dispersions to specifically assess the effect of nanoparticle type and volume fraction on cooling system efficiency. The originality of the current research work lies in the experimental investigation of the hybrid nanofluids between alumina and titania under the real-life conditions of an automotive radiator. Contrary to the antecedent studies, which have mainly focused on individual formulations of nanofluid solely dependent upon numerical modeling. The present research work provides experimental support for the synergistic effect of combined nanoparticle effect on important thermophysical parameters, including specific heat, thermal conductivity, and convective heat-transfer coefficient. The results demonstrate a direct relation between nanoparticle composition and efficiency of radiator, thereby contributing new experimental evidence to guide future automotive and energy-system cooling design.

CHARECTERIZATION AND SYNTHESIS

This section presents the characterization of Al_2O_3 (CAS: 1344-28-1) and TiO_2 (CAS: 13463–67–7) fine metal oxides purchased from Nano Research Lab (NRL), Jharkhand, and also the synthesis of nanofluids.

Analysis of Al_2O_3 Nanoparticles

Nanoparticles of aluminum oxide (Al_2O_3) are well known for their excellent thermal properties, which makes them an optimal addition to nanofluids for heat transfer applications. The aluminum oxide nanoparticles in this study are high purity (99.9%), therefore consistent with a low level of impurities. The X-ray diffraction (XRD) patterns in Figure 1 suggest an average particle size of 30-50 nm, which creates a large surface area to volume ratio and enhances thermal conductivity and stability of the nanofluid. Al_2O_3 nanoparticles with a specific surface area of 130-140 m^2/g are efficient in the dispersion rate of the base fluid while avoiding aggregation to create uniform suspensions.

Figure 2 shows the spherical shape in co-occurrence with the crystallographic structure evaluated using TEM characterization, represents that the Al_2O_3 nanoparticles reveal isotropic electrical and thermal properties under a steady dispersion state. However, in experimental nanofluid systems, particle accumulation and settling may affect the reliability of electrical conductivity.

The nanoparticles have a bulk density of 1.5 g/cm^3 and a true density of 3.97 g/cm^3, demonstrating the highly compact and dense nature of the material used. The density values of Al_2O_3 nanoparticles (CAS: 1344-28-1) were opted from supplier specifications (Nano Research Lab, Jharkhand, India), which are established on standardized measurements (ASTM D1895B and helium pycnometry methods). The XRD and TEM analysis was conducted in this research to validate the consistency of particle size and structural morphology with the collected data.

The substrate is prevalent in automotive radiators, as it is highly stable to 2055°C melting, ensuring system dependability in hot systems. The atomic weight of the

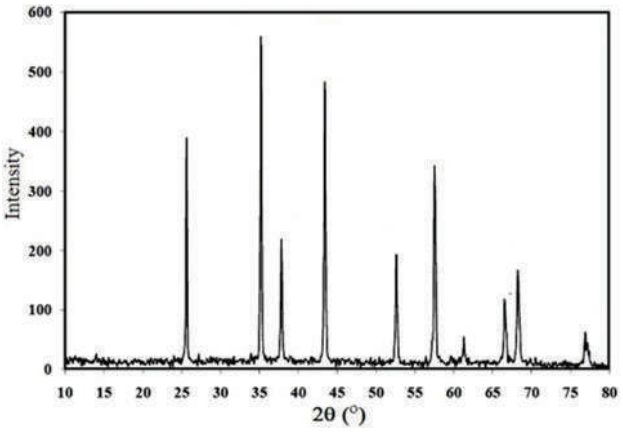

Figure 1. XRD data for Alumina nanoparticles.

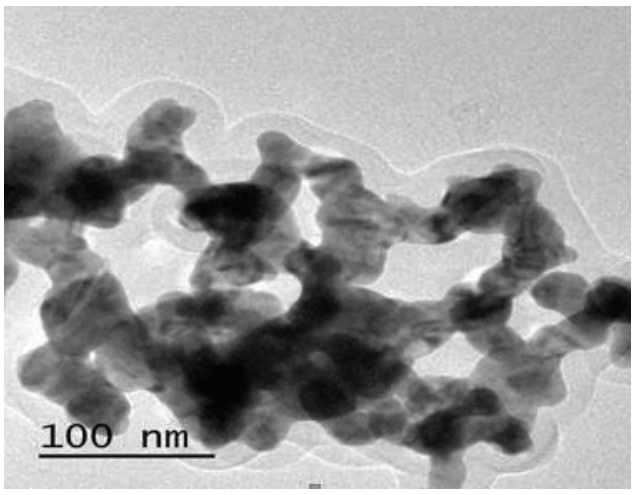

Figure 2. TEM analysis of Al_2O_3 nanoparticles.

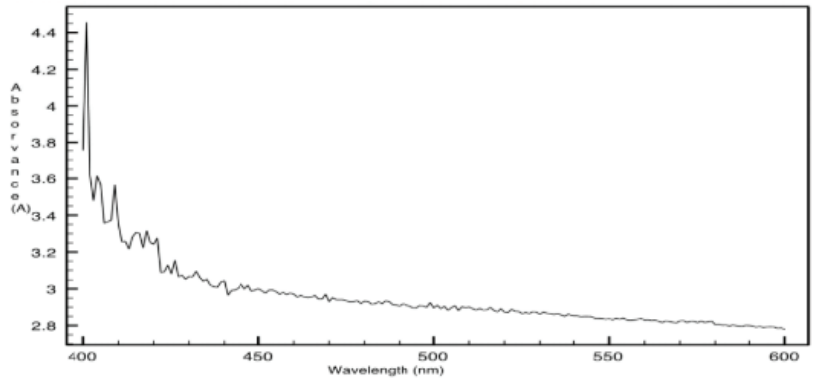

Figure 3. UV-Vis spectrometer reading of Al_2O_3 nanoparticles.

Al_2O_3 nanoparticles is 101.95 g/mol, which indicates the fast interactions within the fluid matrix. There is significant absorption below 400 nanometers; this is used with Figure 3, and the UV-Vis absorption spectra of the Al_2O_3 nanoparticles demonstrate the wide band gap for Al_2O_3 nanoparticles. The atomic and nanoscale properties of Al_2O_3 establish a unique optical behavior suitable for optical and electronic applications.

Combining these properties makes Al_2O_3 nanoparticles an attractive medium for enhancing the thermal behavior of nanofluids. Specifically, incorporating these nanoparticles in the coolant fluid blend with water can enhance the thermal efficiencies of the overall automotive cooling system. This phenomenon was examined in this study.

Analysis of TiO_2 Nanoparticles

The titanium oxide (TiO_2) nanoparticles (CAS: 13463–67–7) have a purity of 99.9% with a spherical morphology. XRD analysis, shown in Figure 4, shows that the TiO_2 nanoparticles do have a crystalline structure, and indicating the peak position at 25.3° (101), indicating to the anatase phase (2θ = 25.3°, 37.8°, 48.0°, and 54.0°), is clearly noticeable and aligns with standard JCPDS card no. 21-1272.

The size of the crystallites calculated using the Scherrer equation indicates that the approximated size of the nanoparticles is ~10 nm. The SEM image shown in Figure 5 confirmed that the average crystalline sizes of TiO_2 nanoparticles are in the range of ~10-20 nm. They also have a very high specific surface area (SSA) of between 200 and 220 m^2/g, suggesting that they have a large reactive surface area. They are white in colour with a bulk density of between 0.15 and 0.25 g/cm^3 and a true density of 4.23 g/cm^3, indicating they are compact and light weight when in bulk, and are in accordance with a spherical morphology with its crystallographic structure.

The bulk and true density values of TiO_2 nanoparticles were taken from the supplier's technical specifications sheet (Nano Research Lab, Jharkhand, India) and measured using standard laboratory procedures. An identical structural morphology has been observed in the literature

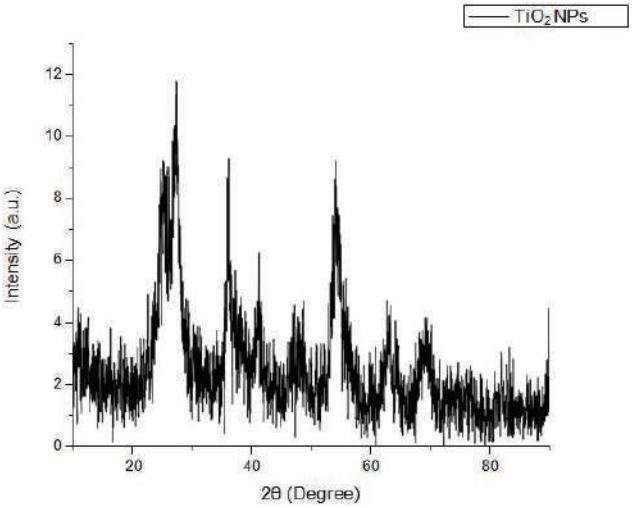

Figure 4. XRD analysis of TiO_2 nanoparticles.

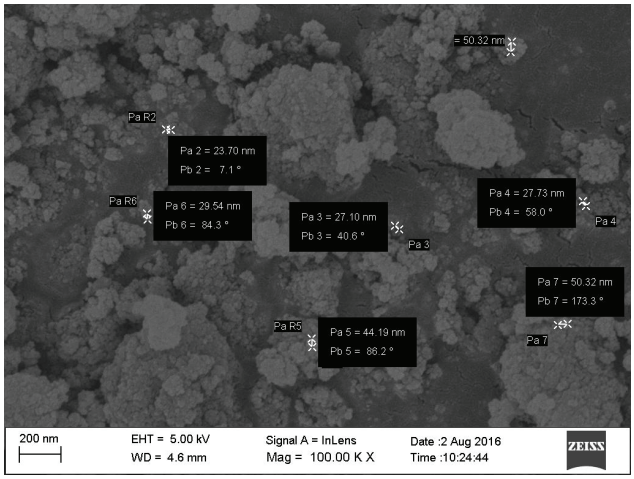

Figure 5. SEM image of TiO_2 nanoparticles (analysis report provided by Nano Research Lab, Jharkhand).

[32]. The stability of particle size and structural morphology with these data was validated through the XRD and SEM analyses provided by the supplier in the present study. Furthermore, the atomic weight of TiO_2 is 79.8658 g/mol, which corroborates their expected chemical composition. With these properties, TiO_2 nanoparticles are suitable for various applications such as photocatalysis, coatings, and biomedical applications.

Synthesis of Alumina & Titania-based nanofluids

Al_2O_3 and TiO_2-based nanofluids were produced using the ultrasonic processor shown in Figure 6 to achieve stable dispersion and retention of the nanoparticles within the base fluids. The production process of the nanofluids was via the ultrasonication technique, where the duration was 12 hours of ultrasonication at varying volume concentrations. Six formulations were created, including distilled water, distilled water along with ethylene glycol (EG), 0.02 vol% TiO_2, 0.06 vol% TiO_2, 0.08 vol% Al_2O_3, and 0.06 vol% Al_2O_3 and 0.02 vol% TiO_2 in both distilled water and ethylene glycol. The extended duration of ultrasonication produced stable nanofluids due to the particles not yielding any large clusters. This allows for clearer systematic investigation of the thermal and physical behaviour of nanofluids when finding the effects of types of nanoparticles and concentrations of the nanoparticles.

EXPERIMENTATION

A test setup for a vehicle radiator was experimentally tested to evaluate the potential of applying Alumina (Al_2O_3) and Titania (TiO_2)-based nanofluids as cooling fluids during the performance evaluation. The experimental testing setup was shown in Figure 7, while the working of the radiator was represented in Figure 8. The detailed features of the test rig used in this research are represented in Table 2.

The experimental testing involved filling the tank with coolant until it reached the specified measurement mark before turning on the power supply and heater. The temperature control was established at 75°C prior to starting the process. The flow rate was then adjusted based on the flow meter measurement before the fan and the pumps were turned on to initiate circulation. It was the aim of the process to measure outlet coolant flow rate and temperature differential across the inlet, outlet, and surface at varying pump discharge rates. Thus, this process was an effective method for accurately measuring data to characterize the thermal behavior and flow characteristics of nanofluids under specified operating conditions.

The radiator system consisted of a half-horsepower pump that circulated Al_2O_3 and TiO_2 nanofluids through the radiator system managed by a flow control valve. The heating coil used with thermostat controls maintains the nanofluids in a range from 50 to 75°C, as indicated by the Cengel et al. study [33]. There were a number of

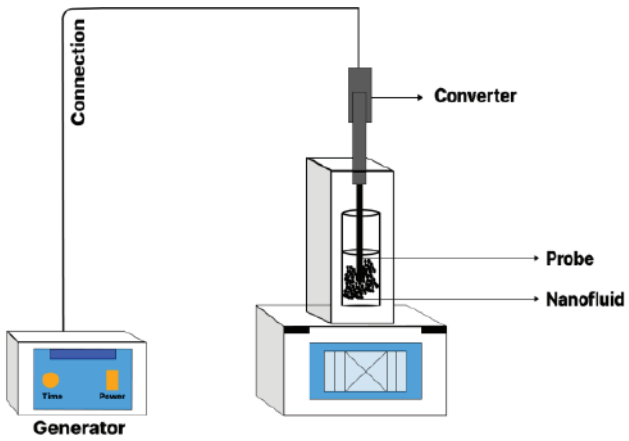

Figure 6. Probe sonication of Nanofluids.

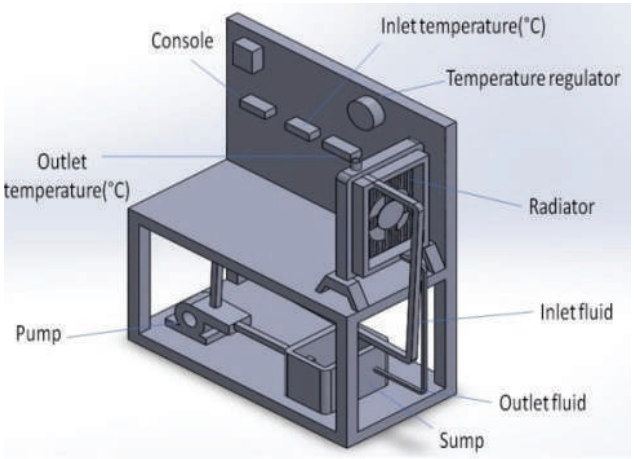

(a)

(b)

Figure 7. (a) 3D Model of an Automobile Radiator Test Setup. (b) Experimental setup of an Automobile radiator Test Setup.

Table 2. Specifications of the Automobile Radiator Test Rig

Component / Parameter	Specification / Description
Type of Apparatus	Automobile Radiator Testing Setup (Heat Transfer Laboratory Setup)
Radiator Fan Speed	1500 RPM
Water Pump Capacity	0.25 HP centrifugal pump
Pump Head Range	4 m – 15 m
Heater Capacity	2000 W (Electrical immersion heater)
Working Fluid	Water / Water–Ethylene Glycol / Nanofluids (Alumina, Titania, Hybrid)
Flow Measurement	Rotameter calibrated for 0 – 20 L min^{-1}
Temperature Measurement	K-type thermocouples (±0.5 °C) connected to NI-9213 DAQ
Cooling Air Flow	Axial fan coupled with variable-speed motor
Power Source	230 V AC, 50 Hz
Make	SASI Institute of Technology & Engineering
Test Performed	Determination of Rate of Heat Transfer and Convective Heat Transfer Coefficient
Safety & Monitoring	Thermostat control with over-temperature cutoff and cooling-system inspection provision

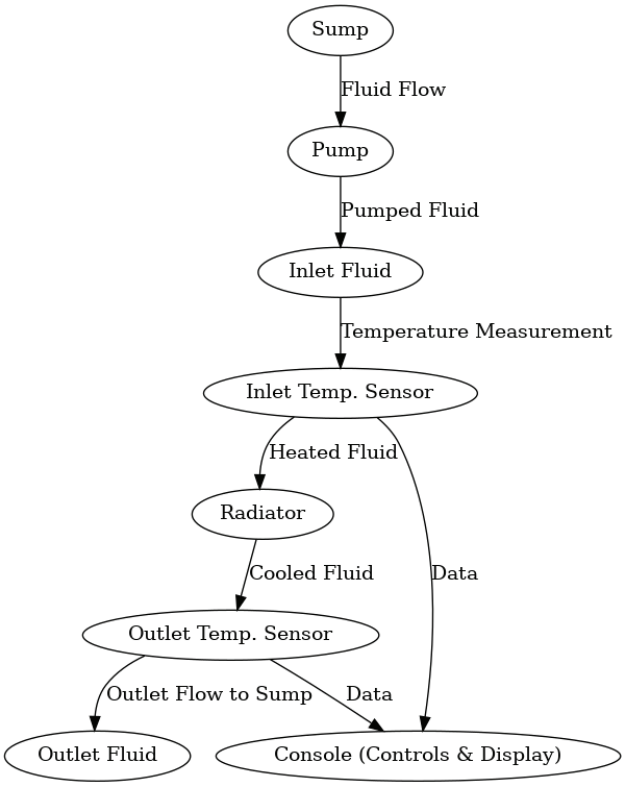

Figure 8. Flowchart of working of automobile radiator test rig.

thermocouple instruments to ensure the system was measured accurately along many points in the system. For the radiator performance measurements, there were two thermocouples used to log inlet temperature and outlet temperature from the flow line, and four other thermocouples monitored the radiator wall temperatures. There was a fan system mounted next to the radiator to enhance the cooling system. Researchers used the conceived system to provide further heat transfer and flow investigations on nanofluids at different operational conditions. The nanofluid formulation was employed to obtain the specific heat capacity (C_p) values while the team obtained flow rate (m°) and temperature measurement. The formula would then be used to calculate radiator heat dissipation, which made it possible to assess Al_2O_3 and TiO_2-based nanofluids' thermal performance.

$$Q = m^{\circ}_{nf}\, Cp_{nf} \Delta T \tag{1}$$

Heat Transfer Measurement

The rate of heat transfer (Q) of the nanofluid was calculated using the measured mass flow rate of nanofluid (m°_{nf}), specific heat of nanofluid (Cp_{nf}), and temperature difference between the inlet and outlet of the radiator using the relation

$$Q = m^{\circ}_{nf}\, Cp_{nf} (T_{in} - T_{out}) \tag{2}$$

The inlet, outlet, and surface temperatures were reported using K-type thermocouples attached to a data acquisition system.

The heat transfer coefficient (h) of the nanofluid was then acquired from the calculated heat transfer rate (Q) and the measured radiator surface temperature difference using:

$$h = \frac{Q}{A_s(T_s - T_m)} \tag{3}$$

where A_s is the effective heat transfer area of the radiator, T_s is the average surface temperature (measured by wall-mounted thermocouples), and T_m is the average fluid temperature.

All temperature values were steadily monitored using K-type thermocouples (accuracy ± 0.5°C) connected to a calibrated data acquisition system. They are positioned at the radiator inlet, outlet, and four wall locations to track coolant and surface temperatures. The method ensures accuracy and repeatability consistent with standards for radiator performance testing.

All thermocouples were attached to a digital data acquisition system with automatic cold-junction compensation for specific temperature recording. Prior to testing, all thermocouples were calibrated using a certified laboratory mercury thermometer in a constant-temperature bath to minimize systematic error. These temperature readings were subsequently used to find the mean fluid and surface temperatures need to compute the convective heat-transfer coefficient.

Density Measurement

The density of the nanofluid was measured by using the correlation established by Das et al. [34]. The correlation is empirical, meaning that it relies on the volume concentration of the nanoparticle and the base fluid to predict the effective density of the nanofluid. The equation is as follows:

$$\rho_{nf} = (1 - \emptyset)\rho_f + \emptyset\rho_p \quad (4)$$

The correlation from Xuan et al. [35] is utilized to define the specific heat of the nanofluid. This correlation classifies a mathematical formulation for nanofluid effective specific heat to include the characteristics of the base fluid and nanoparticle volume fraction. The relationship is as follows:

$$Cp_{nf} = \frac{(1-\emptyset)(\rho Cp)_f + \emptyset(\rho Cp)_p}{\rho_{nf}} \quad (5)$$

Where $\emptyset$ represents the nanoparticle volume fraction, ρ and C_p represent the density and specific heat capacity of the base fluid (f) and nanoparticles (p). The equation takes into consideration nanoparticle dispersion, which strongly affects heat transfer performance during cooling system operations and electronic cooler and industrial heat transfer applications.

RESULTS AND DISCUSSION

Thermal efficiency testing for an automotive radiator was carried out at a constant inlet temperature of 65°C and volumetric flow rates of 7, 10, and 14 L min^{-1}. The outcome of nanoparticle addition on thermo-physical and thermal-hydraulic functioning was investigated in terms of both engineering trends and the fundamental physical phenomena governing energy transport in nanofluids.

The improvement in thermal conductivity and convective performance can be explained through several nanoparticle-scale mechanisms as reported in contemporary literature [14], [15]. When nanoparticles are suspended in the base fluid, rapid Brownian motion of particles generates localized micro-convection currents, promoting better energy exchange between the fluid molecules and solid particles. In addition, the formation of ordered liquid layers at the solid–liquid interface provides an interfacial thermal bridge, which enhances the effective thermal conductivity beyond simple mixture models.

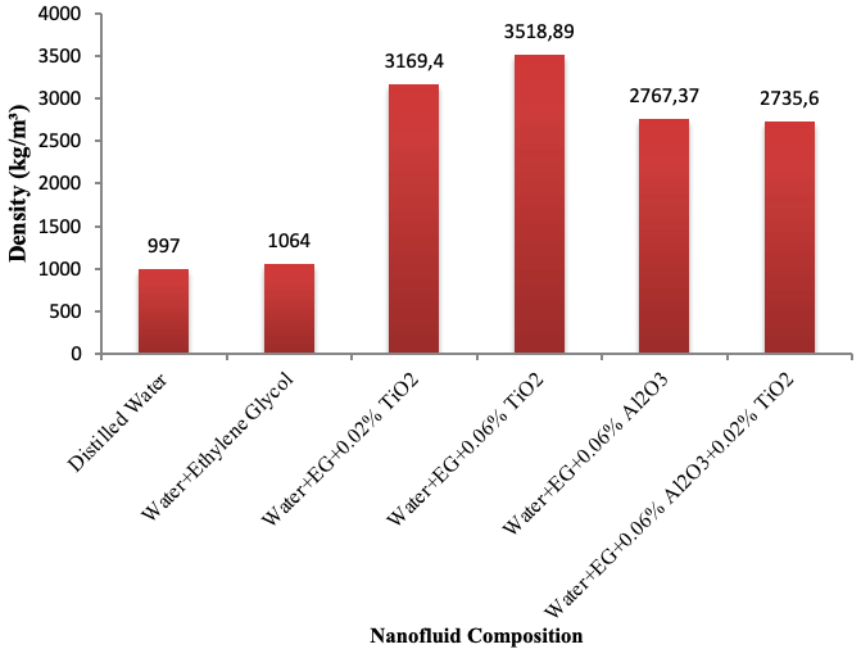

Figure 9. Density of nanofluids.

The properties of the nanofluids changed slightly from the properties of the base fluid. Density increased, thermal conductivity increased, but the specific heat value decreased slowly compared to the base fluid. Viscosity increased in the volumetric fraction more than heat transfer efficiency would possibly want. Additional evidence showed the heat transfer coefficient was probably biased to increase exponentially as the volumetric fractions of Al_2O_3 and TiO_2 nanoparticle-based fluids were increased.

Density

The broad effects of the increase in density were seen in Figure 9, wherein the densities of all of the prepared nanofluids were greatly opposed to distilled water (997 kg/m^3). While that of the Water and Ethylene Glycol mixture is increased by 6.72%, 1064 kg/m^3. This was reflected by the 217.89% and 252.95% respectively, when 0.02% and 0.06% TiO_2 were added, with a total air content of 3518.89 kg/m^3. For the 0.08% Al_2O_3 nanofluid this enhancement was 177.57%, and for the 0.06% Al_2O_3 + 0.02% TiO_2 mixture this was relatively similar at 174.38%. The increase in density at these higher concentrations and its effect on flow behavior indicate that optimization will be required when incorporating these nanofluids in automotive cooling applications.

Specific Heat

The specific heat capacity of various nanofluid compositions was considered to determine the potential for application in automobile cooling applications. The specific heat of conventional nanofluid compositions was decreased compared to that of distilled water (4180 J/kg-K). For example, the water + ethylene glycol treatment was 19.38% less, the 0.02% TiO_2 treatment was 73.03% less, and the 0.06% TiO_2 treatment was 71.81% less. The 0.08% Al_2O_3 treatment decreased specific heat by 68.98%, and the Al_2O_3 + TiO_2 decreased 68.74%; both would decrease thermal performances.

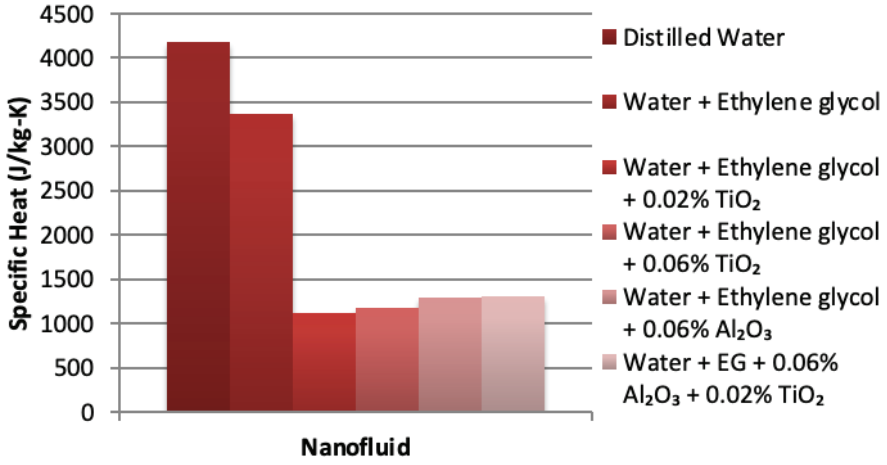

Figure 10. Specific heat of nanofluids.

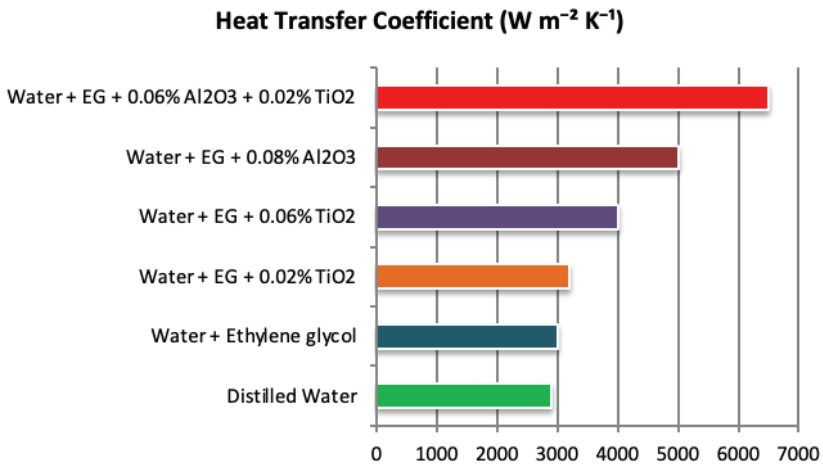

Figure 11. Heat transfer coefficients of nanofluids.

As presented in Figure 10, the addition of TiO_2 and Al_2O_3 nanoparticles noticeably lowers the specific heat capacity when compared to distilled water and water-ethylene glycol mixtures. Specific heat capacity is important because a lower specific heat capacity means that the nanofluid will heat quicker and release heat quicker, which would lead to heating at a greater rate. This reduction of specific heat capacity should also be paired with other thermal properties like thermal conductivity and convective heat transfer coefficient to ensure that nanofluids could be used for cooling without changing temperatures too quickly or too often. The results also indicated that Al_2O_3 nanofluids have a greater potential for heat transfer, meaning they would be good candidates for further research on enhanced automotive radiators.

Heat Transfer Coefficient

An automobile radiator test rig was used to compare the heat-transfer coefficients of the mixtures. The coefficient for distilled water was ≈ 2645 W m^{-2} K^{-1}; all nanofluids exhibited higher values, as shown in Figure 11. The increment on the heat transfer coefficient ranged from 2.83% for the water and ethylene Glycol mixture to 155.64% for the combination of water, ethylene glycol, 0.06% Al_2O_3, and 0.02% TiO_2.

The increase is attributed to the combination of (i) enhanced thermal conductivity from solid inclusions, (ii) Brownian-motion-induced micro-convection within the boundary layer, and (iii) thinning of the thermal boundary layer due to disturbance of the near-wall region by nanoparticles. These mechanisms collectively accelerate heat diffusion from the wall to the fluid.

An empirical equation has been used to generalize the effect of working parameters on the convective heat transfer coefficient (h) through the experimental data. The correlation amongst the Nusselt number (*Nu*), Reynolds number (*Re*), and nanoparticle concentration (φ) proposed by Hussein et al. (2014) [36] and Said et al. (2015) [37] can be expressed as:

$$Nu = 0.328 \times Re^{0.62} \times \varphi^{0.18} \quad (6)$$

This generalized correlation suggests that the convective heat transfer coefficient improves depending on nanoparticle concentration and flow velocity. The trend corresponds to previous research studies, confirming the robustness of the current results and indicating that nanofluid concentration and volumetric flow rate are important in improving heat transmission.

This improvement offers better heat transfer from the surface to the fluid, thus demonstrating the promise of nanofluids for high-end heat transfer applications, including automotive radiators. At concentrations over 0.08 vol % Al_2O_3 or 0.06 vol % TiO_2, viscous drag and particle agglomeration begin to offset these benefits, producing a saturation or slight decline in heat transfer coefficient.

Flow Rate

Heat transfer coefficients of the various fluid combinations for the three different flow rates (7, 10, and 14 L min^{-1}) are displayed in Figure 12. The study demonstrates that water offers the highest heat transfer coefficient at all the study's flow rates and that water managed to offer a coefficient of approximately 7200 W/m^2-K at a 14 L min^{-1} flow rate. However, for systems that need to do better, notably (i.e., carrying a full level transition at near 0–14 L min^{-1}), the water + EG + 0.08 vol% Al_2O_3 improved to approximately 6400 W/m^2-K.

Moreover, the mixture of additives with both TiO_2 and Al_2O_3 has benefits over water and ethylene glycol as well, and they can cater to better usage. In Addition of ethylene glycol (EG) results in reducing the heat transfer coefficient,

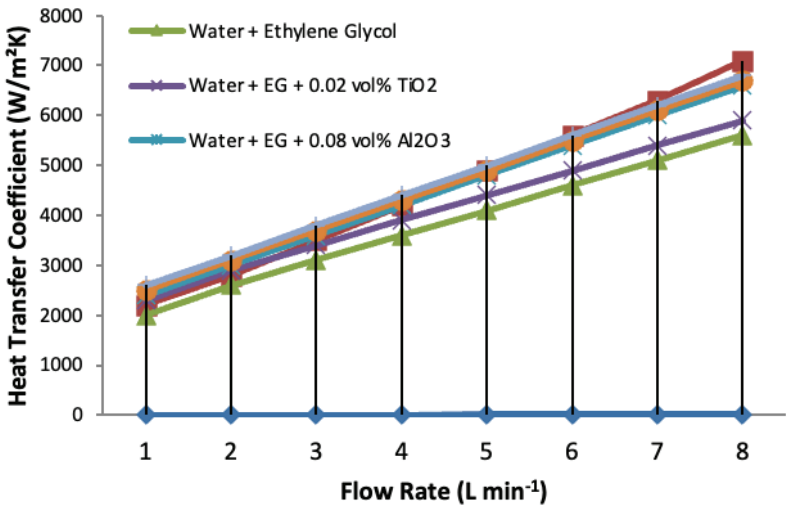

Figure 12. Heat transfer coefficient vs flow rate of nanofluids.

and among the mixtures tested, the lowest coefficients are provided by the water + EG mixture. On the other hand, the addition of nanoparticles like TiO_2 and Al_2O_3 enhances heat transfer ability.

The present study demonstrated an enhancement in the convective heat-transfer coefficient corresponds to previous studies. Shankara R. P., et al. (2020) [22] reported a 295% enhancement in convective heat transfer coefficient was observed for aqueous MWCNT–CuO hybrid (at 0.05–0.15 wt%, with peak effects near 0.1 wt%) at 7 L min^{-1} coolant flow and 80°C inlet in the radiator experiments. The 92.43% improvement in heat transfer efficiency was reported for a CNC+CuO hybrid at 0.01 vol% in scaled-down and commercial radiator tests using an 80°C inlet and flow rates of 0.75–1.25 L min^{-1}. Ganesan T. et al. (2018) [25] and Kumar A. et al. (2023) [26] reported hybrid fluids (CuO–MgO–TiO_2, Al_2O_3–TiO_2–SiO_2) coolant-side HTC gains in the ~40% range at concentrations of 0.3–0.5 vol% under the test conditions described in those studies. Similarly, K. G. Sundari et al. (2020) [29] reported nanofluids with 0.05, 0.1, and 0.15 vol. % of TiO_2 nanomaterial in glycerine and the increase in the heat transfer coefficient is 62% at 0.15 vol. %. Ravi Sankar R. et al. (2018) [30]. The Reported experimental and numerical study for the enhanced heat transfer properties of a radiator with Cu/water nanofluid of 0.025, 0.05, and 0.075 vol. % concentration is finished with an inlet temperature of 50 - 60°C under the unstable flow system.

The current research finds up to 155% enhancement of the total heat-transfer coefficient and 25-47% enhancement of the radiator effectiveness, which is within the bounds of published data [22-30]. Such similarities prove the fact that the thermal enhancement is due to the nanoparticle-induced micro-convection and interfacial energy transportation processes, which are always highlighted in the literature.

It is noted that the final thermal performance of an automobile radiator can be controlled by the combined heat transfer coefficients on both the coolant and air sides. The effective heat transfer coefficient of the radiator is restricted by the lower of the two values, commonly the air-side coefficient. Therefore, the present research demonstrates substantial improvement in liquid-side heat transfer using Al_2O_3 and TiO_2 nanofluids; the overall system performance must also account for air-side resistance. Further performance enhancement can be achieved through concurrent optimization of airflow conditions and fin geometry.

CONCLUSION

Combining alumina and titania nanoparticles with the water–ethylene glycol (EG) solution resulted in a notable improvement in thermal transfer efficiency of the automobile radiator. The hybrid nanofluid (0.06 vol% Al_2O_3 + 0.02 vol% TiO_2) achieved a maximum heat transfer coefficient of nearly 6,400 W/m^2·K, representing a 155.6% enhancement compared to distilled water and about a 60% improvement over the base water and ethylene glycol mixture. The radiator effectiveness also increased by nearly 25–47%, consistent with previously reported studies.

At nanoscale particle concentrations of 0.06 vol% Al_2O_3 and 0.02 vol% TiO_2, the hybrid nanofluid demonstrated an overall heat transfer improvement of nearly 60% in comparison with deionized water. Additionally, the specific heat capacity of the nanofluids decreased by up to 73% relative to water, indicating faster heat absorption and dissipation, which is beneficial for dynamic thermal management applications.

The rate of heat transfer improved substantially by 27% when the volume fraction of TiO_2 changed from 0.02% to 0.06%. The heat transfer rates of the 0.08 vol% Al_2O_3 nanofluid were greater than those of the TiO_2 nanofluids at volume fractions of 0.02% and 0.06% by 27% and 49.6%, respectively. If the flow rate was enhanced to 14 L min^{-1}, there are considerable increases in the heat transfer coefficients related to both the water-ethylene glycol solutions and the nanofluids. This substantial increase in performance is beyond what would be expected from changes in both a change in physical properties and a change in thermal conductivity separately. The improvement in heat transfer is most likely due to the Brownian motion of the nanoparticles. The experimental and analytical results were comparable, and the heat transfer coefficients were similar for both Al_2O_3 and TiO_2-based nanofluids. The rate of heat transfer in the case of hybrid nanofluids is greater when compared with mono nanofluids.

These improvements can be applied to reduce the required radiator surface area, increase cooling system compactness, and improve fuel economy through better thermal efficiency and reduced vehicle weight. The present results not only demonstrate the technical feasibility of using alumina–titania nanofluids in automobile radiators but also indicate potential applications in broader heat-exchange and energy systems. These include waste-heat recovery, electronic cooling, and renewable-energy devices where enhanced convective performance can lead to reduced energy consumption and improved operational reliability. Thus, the study offers practical relevance to both academic researchers and practicing heat engineers working on sustainable thermal management technologies.

This study presents an experimental evaluation of alumina–titania nanofluids in a real automobile radiator system, providing quantitative insights into hybrid nanoparticle interactions that enhance convective heat transfer and efficiency of the radiator in addition to the levels reported for conventional or mono nanofluids.

NOMENCLATURE

A_s	Effective surface area of the radiator, m^2
C_p	Specific heat capacity of fluid, $J \cdot kg^{-1} \cdot K^{-1}$
d_p	Average nanoparticle diameter, nm

h	Convective heat transfer coefficient, $W \cdot m^{-2} \cdot K^{-1}$
k	Thermal conductivity, $W \cdot m^{-2} \cdot K^{-1}$
$\dot{m}$	Mass flow rate of coolant, $kg \cdot s^{-1}$
Q	Rate of heat transfer, W
Re	Reynolds number
Pr	Prandtl number
Nu	Nusselt number
T_s	Average surface temperature of radiator, °C or K
T_m	Mean fluid temperature, °C or K
T_{in}	Inlet fluid temperature, °C or K
T_{out}	Outlet fluid temperature, °C or K
ΔT	Temperature difference between inlet and outlet, °C or K
ρ	Density of fluid, $kg \cdot m^{-3}$
μ	Dynamic viscosity, Pa·s
φ	Volume fraction of nanoparticles
η	Thermal efficiency of radiator, %
ε	Radiator effectiveness
θ	Temperature difference ratio

Abbreviations

EG	Ethylene Glycol
Al_2O_3	Alumina
TiO_2	Titania
CAS	Chemical Abstracts Service
THNF	Ternary Hybrid Nanofluid
CFD	Computational Fluid Dynamics
DAQ	Data Acquisition System
XRD	X-ray Diffraction
TEM	Transmission Electron Microscopy
SEM	Scanning Electron Microscopy
UV–Vis	Ultraviolet–Visible Spectroscopy

Subscripts

f	Refers to fluid
m	Refers to medium
p	Refers to nanoparticle
nf	Refers to nanofluid

AUTHORSHIP CONTRIBUTIONS

Authors equally contributed to this work.

DATA AVAILABILITY STATEMENT

Authors confirm that the data that supports the findings of this study are available within the article. The raw data that supports the findings of this study are available from the corresponding author, upon reasonable request.

CONFLICT OF INTEREST

The authors declare no potential conflicts of interest with respect to the research, authorship, and/or publication of this article.

ETHICS

There are no ethical issues with the publication of this manuscript.

REFERENCES

[1] Shriram S, Sonawane P, Thakur P. Nanofluids. 2024. [CrossRef]

[2] Kumar K, Agrawal A. Optimizing heat transfer efficiency with nanofluids in automotive radiator applications for enhanced performance: A comprehensive review article of research findings. Int J Res Appl Sci Eng Technol 2023. [CrossRef]

[3] Kumar C, Agrawal A. Improving automotive radiator performance through nanofluid-based heat transfer enhancement coupled with pipeline incorporation of phase change materials. Int J Res Appl Sci Eng Technol 2023. [CrossRef]

[4] Bhattad A, Atgur V, Banapurmath NR, Khan TMY, Vadlamudi C, Krishnappa S, et al. Review on mono and hybrid nanofluids: Preparation, properties, investigation, and applications in IC engines and heat transfer. Energies 2023;16. [CrossRef]

[5] Hassaan AM. An experimental investigation examining the usage of a hybrid nanofluid in an automobile radiator. Sci Rep 2024. [CrossRef]

[6] Hidayat N, Sudarmadji S. Studi numerik kinerja pendingin coolant hybrid-nanofluid Al2O3-TiO2 pada radiator. Rekayasa Mesin 2024;15(1). [CrossRef]

[7] Kumar K, Agrawal A. Enhancing automotive radiator performance through optimal heat transfer with nanofluids. Int J Res Appl Sci Eng Technol 2023. [CrossRef]

[8] Kristiawan B, Hibatullah MA, Santoso B, Musabbikhah, Enoki K, Wijayanta AT. Thermal performance of Al_2O_3/water hybrid nanofluids for cooling system using a helically coiled tube in a brushless direct current motor. Numer Heat Transf A Appl 2024. [CrossRef]

[9] Kiaei MB, Adibi P, Abedini E. Heat transfer evaluation of single and hybrid nanofluids as cooling media in car radiators: A 3D-CFD approach in flat tubes. Proc Inst Mech Eng Part E J Process Mech Eng 2023. [CrossRef]

[10] Dante S. CFD analysis of heat transfer characteristics of automobile radiator using various nanofluids. 2023. [CrossRef]

[11] Daly C. Comparative energy and exergy analysis of a car radiator using alumina and CuO doped TiO2 hybrid nanocoolants. 2023. [CrossRef]

[12] AbdulGhafor IA. Enhancing the effectiveness of the cooling system for automotive engine by employing different nanofluids: Literature review. Anbar J Eng Sci 2022. [CrossRef]

[13] Akinshilo AT, Ilegbusi A, Ali HM, Surajo A. Heat transfer analysis of nanofluid flow with porous medium through Jeffery Hamel diverging/converging channel. J Appl Comput Mech 2020;6(3):433–444.

[14] Akinshilo AT, Mabood F, Ilegbusi AO. Heat generation and nonlinear radiation effects on MHD Casson nanofluids over a thin needle embedded in porous medium. Int Commun Heat Mass Transf 2021;127:105547. [CrossRef]
[15] Akinshilo AT. Flow and heat transfer of nanofluid with injection through an expanding or contracting porous channel under magnetic force field. Eng Sci Technol Int J 2018;21(3):486–494. [CrossRef]
[16] Akinshilo AT. Thermal performance evaluation of MHD nanofluid transport through a rotating system undergoing uniform injection/suction with heat generation. BioNanoScience 2019;9:740–748. [CrossRef]
[17] Kiaei MB, Adibi P, Abedini E. Heat transfer evaluation of single and hybrid nanofluids as cooling media in car radiators: A 3D-CFD approach in flat tubes. Proc Inst Mech Eng Part E J Process Mech Eng 2023. [CrossRef]
[18] Ukueje WE, Abam FI, Obi AI. A perspective review on thermal conductivity of hybrid nanofluids and their application in automobile radiator cooling. J Nanotechnol 2022;2022:1–51. [CrossRef]
[19] Dai J, Zhai Y, Li ZH, Wang H. Mechanism of enhanced thermal conductivity of hybrid nanofluids by adjusting mixing ratio of nanoparticles. J Mol Liq 2024. [CrossRef]
[20] Alqahtani AM, Rafique K, Mahmood Z, Al-Sinan BR, Khan U, Hassan AM. MHD rotating flow over a stretching surface: The role of viscosity and aggregation of nanoparticles. Heliyon 2023. [CrossRef]
[21] Hamza N, Aljabair S. Numerical and experimental investigation of heat transfer enhancement by hybrid nanofluid and twisted tape. Eng Technol J 2023;41(1):69–85. [CrossRef]
[22] Shankara RP, Banapurmath NR, Souza AD, Dhaded SS. Experimental investigation of enhanced cooling performance with the use of hybrid nanofluid for automotive application. IOP Conf Ser Mater Sci Eng 2020;872(1):012074. [CrossRef]
[23] Xian HW, Sidik NAC, Saidur R. Hybrid nanocoolant for enhanced heat transfer performance in vehicle cooling system. Int Commun Heat Mass Transf 2022;133:105922. [CrossRef]
[24] Praveenkumara BM, Murthy HMS, Gowda BS, et al. Effect of low-concentration CuO and RGO hybrid nanofluids on thermal performance of automotive radiator: An experimental study and correlations development. J Therm Anal Calorim 2025;150:5775–5793. [CrossRef]
[25] Ganesan T, Kannan PS. Heat-transfer enhancement of nanofluids in a car radiator. Mater Tehnol 2018;52(4):507–512. [CrossRef]
[26] Kumar A, Hassan MA. Heat transfer in flat tube car radiator with CuO-MgO-TiO2 ternary hybrid nanofluid. Powder Technol 2023. [CrossRef]
[27] Efemwenkiekie KU, Oyedepo SO, Giwa SO, Sharifpur M, Owoeye TF, Akinlabu KD, et al. Experimental investigation of heat transfer performance of novel bio-extract doped mono and hybrid nanofluids in a radiator. Case Stud Therm Eng 2021;28:101494. [CrossRef]
[28] Ramalingam S, Dhairiyasamy R, Govindasamy M. Assessment of heat transfer characteristics and system physiognomies using hybrid nanofluids in an automotive radiator. Chem Eng Process 2020;150:107886. [CrossRef]
[29] Sundari KG, Asirvatham LG, S JJM, Ninolin E, B S. Feasibility of glycerin/Al2O3 nanofluid for automotive cooling applications. J Therm Eng 2020;6(4):619–632. [CrossRef]
[30] Ravi Sankar R. Application of nanotechnology to improve the performance of tractor radiator using Cu-water nanofluid. J Therm Eng 2018;4(4):2188–2200. [CrossRef]
[31] Barai R, Kumar D, Wankhade A. Heat transfer performance of nanofluids in heat exchanger: A review. J Therm Eng 2023;9(1):86–106. [CrossRef]
[32] Raja S, Koperundevi G. Titania-based transformer nanofluid: A study on the synthesis for enhanced breakdown strength and its humidity ageing. IET Nanodielectr 2020. [CrossRef]
[33] Cengel YA, Ghajar AJ. Heat and Mass Transfer: Fundamentals and Applications. 5th ed. McGraw-Hill Education; 2015.
[34] Das SK, Choi SUS, Patel HE. Heat transfer in nanofluids. Heat Transf Eng 2006;27(10):3–19. [CrossRef]
[35] Xuan Y, Li Q. Heat transfer enhancement of nanofluids. Int J Heat Fluid Flow 2000;21(1):58–64. [CrossRef]
[36] Hussein AM, Bakar R, Kadirgama K, Sharma K. Heat transfer enhancement using nanofluids in an automotive cooling system. Int Commun Heat Mass Transf 2014;53:195–202. [CrossRef]
[37] Said Z, Sundar LS, Sharma KV, et al. Experimental and CFD study of heat transfer augmentation in automobile radiators using hybrid nanofluids. Int J Heat Mass Transf 2015;89:134–146.

J Ther Eng, Vol. 12, No. 2, pp. 466−483, March, 2026

Journal of Thermal Engineering
Web page info: https://jten.yildiz.edu.tr
DOI: 10.14744/thermal.0001092

Research Article

Performance analysis of solar still with separate evaporatively cooled condenser

Niladri SARKAR[1], Aneesh SOMWANSHI[2], Anil Kr. TIWARI[1,*]

[1]*Department of Mechanical Engineering, National Institute of Technology, Raipur, 490042, India*
[2]*Department of Mechanical Engineering, MATS University Raipur, 490042, India*

ARTICLE INFO

Article history
Received: 13 May 2025
Revised: 07 October 2025
Accepted: 26 October 2025

Keywords:
Air Cooler; Distillate Output; Economic Analysis; Separate Condenser; Solar Still

ABSTRACT

Potable water scarcity is a serious global issue, and solar stills provide an eco-friendly way to produce clean water using sunlight. Their efficiency mainly depends on the temperature difference between the basin water and the glass cover. Adding an external condenser helps to boost this difference by keeping the condensation surface cooler, leading to more water output. Actively cooling the condenser can enhance this effect even further, significantly improving the distillate yield. In this study, the performance of a single-slope solar still with a separate condenser integrated into an air cooler system was investigated. A low-power exhaust fan directs the moist air towards the condenser. The condenser plate is cooled by water from the air cooler's tank, which flows over it. This evaporatively cooled condenser enhances the condensation process, leading to increased overall productivity of the solar still. Mathematical model of the design was created and validated through experiments. Effect of parameters like water depth, mass flow rate of water over condenser, relative humidity and wind velocity of air on stills performance has been investigated. The depth of water in the solar still's basin has very little impact on the distillate produced. When the depth of water in basin increased from 1cm to 5cm the total daily distillate output is decreased only by 4.9%. The mass flow rate of water flowing over condenser has very negligible effect on still's performance. Unlike conventional still with increase in wind velocity from 1m/s to 4m/s the hourly distillate output decreases by 2.7%. With increase in humidity of air the output decreases. In Raipur, Chhattisgarh (India) for months of May (summer), January (winter), and October (autumn) the system produced 7.83 kg, 3.45 kg and 5.30 kg of distilled water daily. The water is produced at a reasonable cost of Rs. 1.30/kg (US$ 0.0151/kg). Due to continuous cooling of condenser, the system is able to generate some amount of water even in night time.

Cite this article as: Sarkar N, Somwanshi A, Tiwari AK. Performance analysis of solar still with separate evaporatively cooled condenser. J Ther Eng 2026;12(2):466−483.

***Corresponding author.**
*E-mail address: aktiwari.mech@nitrr.ac.in

This paper was recommended for publication in revised form by Editorin-Chief Ahmet Selim Dalkılıç

Published by Yıldız Technical University Press, İstanbul, Turkey
Yıldız Technical University. This is an open access article under the CC BY-NC license (http://creativecommons.org/licenses/by-nc/4.0/).

INTRODUCTION

Freshwater scarcity is an escalating challenge as population growth, urbanization, and industrial activity strain conventional sources. In many regions, declining rainfall, over-drawn aquifers, and rising salinity now limit supplies for both drinking and agriculture. Salinity in particular reduces soil fertility and crop yields, while pollutants from industry, sewage, and agricultural runoff further degrade surface and groundwater quality. These factors collectively heighten public-health risks and sustain the burden of water-borne disease. Numerous high and medium-tech techniques for purifying water that rely on conventional energy sources have been developed as a result of scientific and technological advancements. But "solar distillation" stands out as an easy, economical, and ecologically acceptable method for generating drinkable water that is dependent on renewable energy sources rather than traditional energy sources. A device that uses solar energy to clean water is called solar still (SS). Its principle is basically vaporization and condensation. Several designs for passive solar stills have been extensively investigated and examined by researchers in an effort to increase their efficiency. The designs include inverted absorber solar still, floating solar still, and hybrid membrane solar stills powered by fossil fuel [1-8].

Recent studies have shown growing interest in improving the efficiency of solar stills, particularly through design modifications like adding external condensers, using nanomaterials, using PCM, or coupling with other renewable systems. These advancements aim to boost water output and address limitations like low productivity [9-17]

In a SS, solar energy heats impure or salty water, causing it to evaporate. The water vapour then condenses on a cool surface and is collected as pure water, leaving behind impurities and salts. The temperature difference between the water (T_w) in basin and condenser surface (T_c) is the driving factor responsible for getting pure water (condensate). Studies [18–22] have demonstrated that the difference in temperature between the water (where evaporation takes place) and condenser (T_w-T_c) is decreased when water vapour condenses inside a solar still.

It has been suggested that the condenser and the SS chamber be separated in order to increase this temperature differential. In this configuration, water vapour passes from the main chamber of the solar still into a condensation chamber that is separated from the main chamber (SS chamber). As a result, the still's glass surface experiences relatively little condensation. The (T_w-T_c) between the evaporative and condenser rises as a result of the majority of condensation occurring in the condensing chamber, which accelerates evaporation and increases distillate output [23–32]. This design of SS was called as SS with separate condenser (SSSC).

The impact of integrating a connected passive condenser on a passive solar still's efficiency was investigated by Fath and Elsherbiny [23]. They used both theoretical analysis and experimental in their approach to this subject. Diffusion, purging, and spontaneous circulation are the three mass transfer modes in a solar still-condenser system that the researchers examined. The diffusion and purging modes were the focus of their studies, and they discovered that the outcomes closely matched the theoretical expectations. They claimed that employing the separate condenser increased production by almost 70% in purging mode. A SS with an integrated passive condenser and a natural circulation method for humidification and dehumidification was studied by Fath and colleagues [33]. The system produced 5.1L/m^2 each day, according to their research.

Madhlopa and Johnstone's [34] analytical studied on the performance of a passive SS with a separate condenser. They proposed the design consists of three basins: Basin 1 is located in the evaporation chamber and is covered with a glass cover, while Basins 2 and 3 are situated in the condenser chamber. Basin 3 is covered with an opaque condensing cover. Basin 1 produces the first effect, Basin 2 the second effect, and Basin 3 the third effect. When compared to a conventional SS, they found a 62% increase in productivity. Three major components contribute to the total distillate output: the first effect, which has one evaporator basin, makes up 60% of the output; the second effect, which has an additional condenser basin, makes up 22%; and the third effect, which has two additional evaporator basins, makes up 18%.

Monowe et al. [35] proposed, a new design for a portable thermal-electrical solar still with an external condenser and reflecting booster. The system is engineered to reduce the loss of latent heat from condensation by capturing and storing it in the condenser. This stored heat can subsequently be used to operate the still at night or to preheat saline water for household usage. According to preliminary results, the still can operate as efficiently as 77% when the preheated water is used for household use and as efficiently as 85% when the stored heat is used for both nocturnal operation and system recharging with fresh preheated saline water.

A modified SS with an external condenser and an Al_2O_3-water nanofluid was studied by Kabeel et al. [36]. They discovered that when the external condenser was the only one used, the productivity of the solar still improved by 53.2%. When the nanofluid was incorporated along with the external condenser, the productivity enhancement rose to approximately 116%. Rabhi et al. [37] examined the effectiveness of a modified single-basin, (SSSS) with a condenser and pin fins for heat absorption. Their findings showed that using absorber fins on the basin liner was not as effective as incorporating an external condenser. Interestingly, they discovered that, in comparison to a traditional SS, the external condenser increased water productivity by 32.18%. On the other hand, the SS with basic pin fins only had a 14.53% rise.

The thermal performance of an inflatable plastic SS with a passive condenser was investigated by Bhardwaj et al. [38]. According to their findings, the device produced about

0.75 litres of drinkable water every hour. Furthermore, they observed that the water output was increased to more than 0.95 litres per hour by employing airflow over the passive condenser.

Rahmani and Boutriaa [39], performed transient simulation of a basin-type solar still with an external condenser is proposed. The performance of the still is analyzed under the combined influence of wind conditions and varying condenser areas during both winter and summer seasons. The study includes an optimization of the condenser design aimed at maximizing distillate yield. Results indicate that the non-conventional solar still (NCL) achieves a maximum daily yield of 2.71 kg/m² in winter and 4.73 kg/m² in summer. Later, Kabeel et al. [40] provided a thorough analysis of various solar stills that were connected to separate condensers. They come to the conclusion that increasing the area available for condensation raises the rate at which condensation occurs, which in turn raises the rate at which evaporation occurs in the basin. Ultimately, the (T_w-T_c) between the evaporating and condensing zones determines how efficient is the condensation process.

Saini et al. [41] investigated the performance of SSSS integrated with SPV module and passive condenser. The impact of different packing factors β_c=0, 0.25, 0.45, 0.65 and 0.85 β_c=0, 0.25, 0.45, 0.65 on the performance of solar cells using various PV technologies has been studied. For the c-Si SPV module, the maximum overall energy efficiency was found to be 57.5%, 55.2%, 53.4%, 53.1%, and 41.4% for packing factors of 0.85, 0.65, 0.45, 0.25, and 0, respectively. Additionally, the system's productivity was measured and found to be 1.78 kg, 2.83 kg, 3.66 kg, 4.12 kg, and 4.92 kg, 1.78 kg per day for packing factors of 0.85, 0.65, 0.45, 0.25 and 0, respectively

In previous investigations researchers investigated different configurations of SS having separate condenser unit. This unit helps to collect water vapour from SS and condenses it separately beneath condensing plate this helps to enhance overall productivity of SS. With separate condensing unit the rate of water condensation will increase due to lower condenser temperature. Water cooled condenser will further helps to reduce temperature more in comparison to condenser without cooling. This is found to be a notable research gap identified by reviewing different works on solar still having separate condenser. To decrease the temperature of condenser even more here in this work we presented a new design of SS with separate evaporatively cooled condenser. The condenser cover is evaporatively cooled by flowing cool tank water from air coolers tank contributes to decreasing the temperature of condensing cover furthermore and allows more water vapour to condense beneath condensing plate. SS having separate condenser is connected with the tank of an air cooler. The proposed design is an extension of the design proposed by Somwanshi & Tiwari [42]. In their previous design they proposed to connect an air cooler tank by a passive solar still. The cooled tank water from tank of cooler utilized to cool glass cover. Cooling the glass cover of a solar still can greatly increase its efficiency. This raises the temperature differential between the glass cover and the water in the basin, which significantly boosts the still's output. The use of air cooler is very common during summers for space cooling. The water in cooler tank is cooled due to continuous evaporation process. The coolness in tank water remains unutilized. Authors proposed to use this cooled tank water to cool the cover of SS their proposed design helps to get the annual distillate output by 56.5%.

Tiwari and Somwanshi [43] subsequently presented another concept of a small size solar still plant integrated to garden fountain. The concept worked reasonably well to produce reasonable amount of potable water to meet the demand of drinking water in small communities.

In this work we proposed to cool the cover of SS having separate condenser. The condenser unit has been separated and connected with air cooler's tank. The proposed design is shown in Figure 1. The water from condenser cover is collected and recirculated back to air coolers tank.

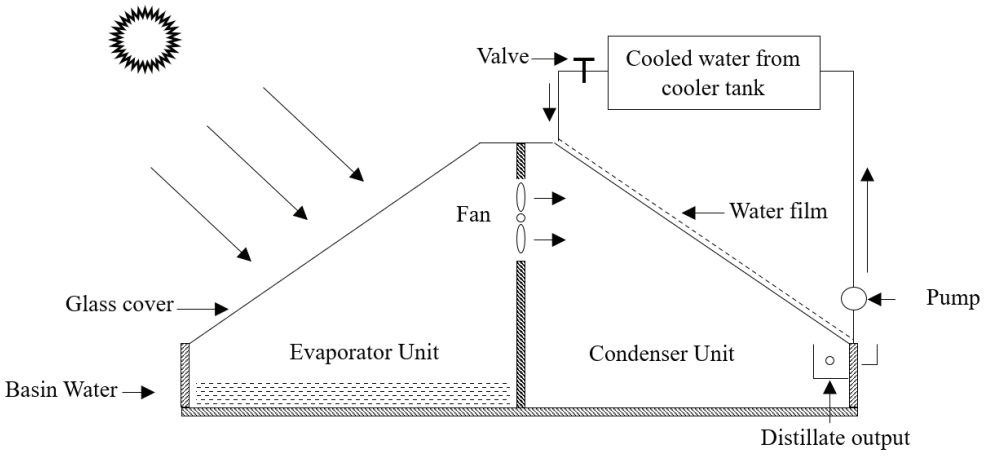

Figure 1. Schematic of the proposed design.

The mathematical model of the proposed system has been created and experimentally validated experiments were carried out at Raipur, Chhattisgarh, India (21.2787° N, 81.8661° E). The effect of parameters like MFR of water flowing over cover, depth of water in the basin, relative humidity of air and wind velocity on the performance of proposed has been investigated. The performance of the proposed system has been investigated for a day in summer (May), winter (Jan) and autumn (October). Economic analysis has been performed to determine the cost of distillate output produced.

MATHEMATICAL ANALYSIS

Thermal network of the proposed system (Fig. 2). and Figure 3 shows different internal and external heat transfer of the proposed still.

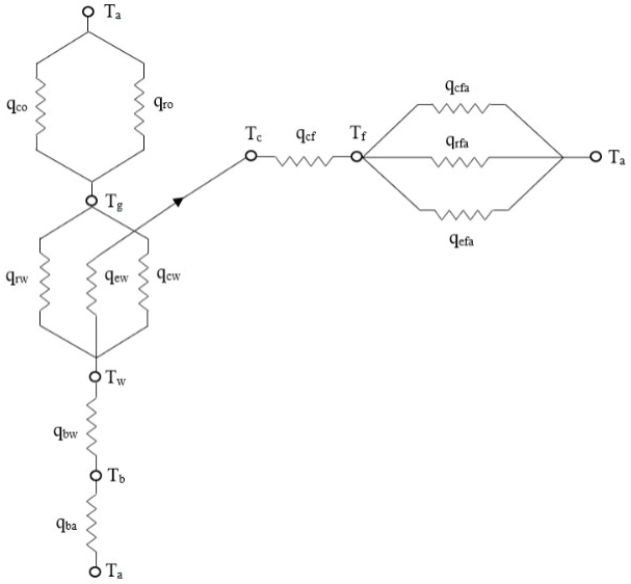

Figure 2. Thermal network of proposed design.

Referring Figure 3 Energy balance equation of proposed system considering unit area are as follows

i. The solar distillation unit is vapour-tight.
ii. The heat capacity of glass, aluminum and condenser is neglected.
iii. The thickness of water film considered very small.

Glass Cover

$$\tau_1 I + q_{rw} + q_{cw} + q_{ew}(1-\phi) = q_{ca} + q_{ra} \quad (1)$$

In Eq.1, ϕ is the fraction of water vapour incident to external condenser, the value of ϕ is considered 1 when all vapours are forced by internal fan towards external condenser.

Eq. 1 can be written as,

$$\tau_1 I + h_{rw}(T_w - T_g) + h_{cw}(T_w - T_g) = h_{ca}(T_g - T_a) + h_{ra}(T_g - T_a) \quad (2)$$

Or,

$$\tau_1 I + h_i(T_w - T_g) = h_o(T_g - T_a) \quad (3)$$

$$h_i = h_{rw} + h_{cw} \quad (4)$$

$$h_o = h_{ca} + h_{ra} \quad (5)$$

Basin Water

$$M_w c_w \frac{dT_w}{dt} = \tau_2 I + q_{bw} - q_{cw} - q_{rw} - q_{ew} \quad (6)$$

Or,

$$M_w c_w \frac{dT_w}{dt} = \tau_2 I + h_b(T_b - T_w) - h_{cw}(T_w - T_g) - h_{rw}(T_w - T_g) - h_{ew}(T_w - T_c) \quad (7)$$

Basin Liner

$$\tau_3 I = q_{bw} + q_{ba} \quad (8)$$

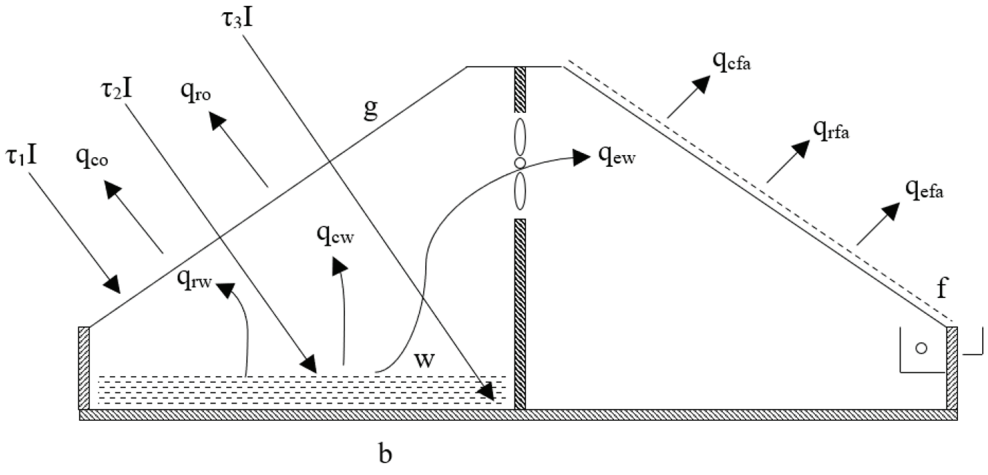

Figure 3. Internal & external heat transfer rate of the proposed still.

Or,

$$\tau_3 I = h_b(T_b - T_w) + U_b(T_b - T_a) \quad (9)$$

Separate Consender

$$q_{ew} = q_{cf} \quad (10)$$

$$h_{ew}(T_w - T_c) = h_f(T_c - T_f) \quad (11)$$

Water Film

Considering the thickness of water film very small the energy balance of strip of thickness (dx) Figure 4, will be

$$\dot{m}_f c_w \frac{dT_f}{dx} dx = \dot{q}_{cf} b dx - \dot{q}_{cfa} b dx - \dot{q}_{rfa} b dx - \dot{q}_{efa} b dx \quad (12)$$

$$m_f c_w \frac{dT_f}{dx} dx = h_f(T_c - T_f) b dx - h_2(T_f - T_a) b dx - 0.013 h_{ca}(P_f - \gamma P_a) \quad (13)$$

From Eq. (3) and Eq. (9) the glass temperature and temperature of basin liner will be given by,

$$T_g = \frac{\tau_1 I + h_i T_w + h_o T_a}{h_i + h_o},\ T_b = \frac{\tau_3 I + h_b T_w + U_b T_a}{h_b + U_b} \quad (14)$$

From Eq. (14) and Eq. (7) we have,

$$\frac{dT_w}{dt} + K_1 T_w = K_2 + K_3 T_c \quad (15)$$

In Eq. 15 the expressions for constants K_1, K_2 and K_3 are given in Appendix-I

Solving Eq. (15) considering the water temperature at time t=0 as T_{c0}

$$T_w = K_4 + K_5 T_c \quad (16)$$

From Eq. (11) and Eq. (16) the value of T_c will be given by,

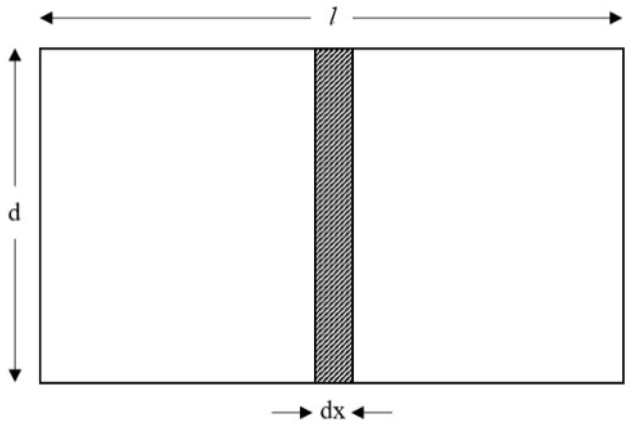

Figure 4. Considering strip of width 'dx'.

$$T_c = K_6 + K_7 T_f \quad (17)$$

Substituting the value of T_c in Eq. 13, we have

$$\frac{dT_f}{dx} = -A T_f^{\,2} + B T_f + C \quad (18)$$

The saturated vapour pressure can be written as,

$$P = R_1 T^2 + R_2 T + R_3$$

The values of R_1, R_2 and R_3 are determined by the fitting (polynomial degree 2) from the saturation vapour pressure table in the temperature range of 7° C to 55° C.

Integrating Eq. 18 we have

$$\frac{T_f - (B/2A) - C_1}{T_f - (B/2A) + C_1} = \beta \exp(-2AC_1 x) \quad (19)$$

In Eq. 19 the value of β and C_1 will be given by,

$$\beta = \frac{T_{f0} - (B/2A) - C_1}{T_{f0} - (B/2A) + C_1}$$

In above equation T_{f0} is the initial film temperature flowing over cover at x=0

The exit film temperature at x=d will be,

$$T_{fe} = (B/2A) + C_1\left[\frac{1 + \beta \exp(-2AC_1 d)}{1 - \beta \exp(-2AC_1 d)}\right] \quad (20)$$

The average film temperature will be given by,

$$T_{fa} = (B/2A) + \frac{1}{Ad} \ln\left[\frac{\exp(2AC_1 d) - \beta}{(1 - \beta)}\right] - C_1$$

By substituting the value of T_{fa} into Equation (17), we can determine the average glass temperature ($\bar{T}_g$), and then obtain the water temperature using Equation (16).

Hourly yield is given by,

$$\dot{m}_{ew} = \frac{h_{ew}(T_w - \bar{T}_c)}{L} \times 3600 \quad (21)$$

The value of various constants and the correlation for determining different heat transfer coefficients used in mathematical model are given in Appendix-II

Expressions for Determine τ_1, τ_2 and τ_3 [18]

$$\tau_1 = (1 - R_g)\alpha_g \quad (22)$$

$$\tau_2 = (1 - R_g)(1 - \alpha_g)(1 - R_w)\alpha_w \quad (23)$$

$$\tau_3 = (1 - R_g)(1 - \alpha_g)(1 - \alpha_w)(1 - R_w)\alpha_b \quad (24)$$

Description of Proposed Design

Figure 1 shows a schematic and a picture of the proposed design. Various dimensions of the design have been

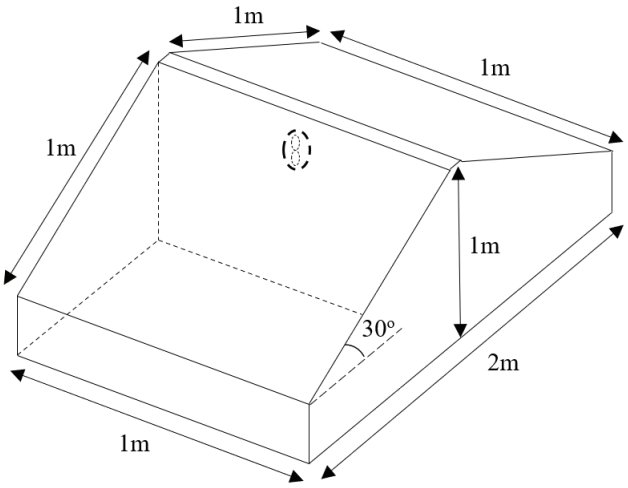

Figure 5. Dimensions of the proposed still.

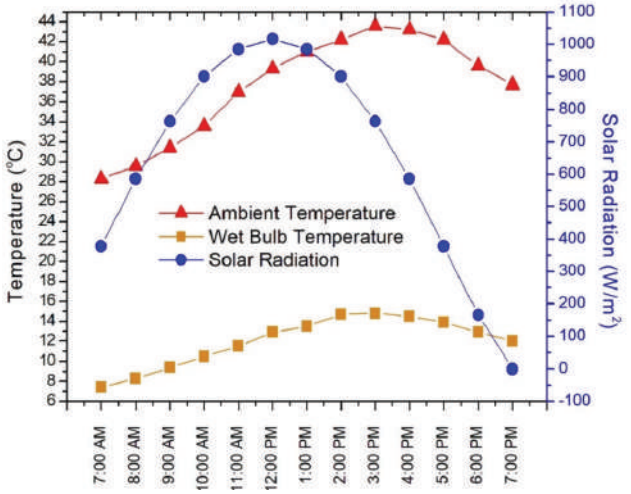

Figure 6. Solar radiation and ambient temperature during the experiment.

shown in Figure 5. The whole setup consists of two different parts separated by an insulated partition. The part at left side is evaporator unit and side towards right is called as condenser unit. A low-power (5W) solar exhaust fan is used to drive the vapours produced by the water in the evaporative chamber absorbing solar energy into the condenser unit. The condenser plate is made of aluminum sheet and it is continuously cooled by cooled tank water pumped from the cooler tank connected with condenser unit. With flow of cooled water (inlet temperature equal to WBT of ambient air) the condenser helps to carry the heat generated by vapours condensed in the bottom of the condenser plate. As a result, the condenser cover and basin water have a greater temperature differential. Both the condenser unit and the glass cover (evaporator unit) have a surface area of one metre square.

The water flowing over condenser is collected and recirculated back to cooler tank. To maintain the mass flow rate of water flowing over condenser a valve has been provided with inlet pipe (Fig.1) The hot water recirculated back to cooler tank is not going to affect the performance of air cooler [44].

Validation of Model

To validate the proposed mathematical model, an experiment was carried out on May 22, 2023, at Raipur, Chhattisgarh, India (21°14′40″N, 81°37′50″E). The hourly solar radiation and ambient temperature and relative humidity during experiment is recorded and shown in Figure 6. An image of the experimental setup is shown in Figure 7, and Table 1 lists the specifics of the instruments used in the experiment. The uncertainty of various

Figure 7. Photograph of the experimental setup.

Table 1. Various instrument used during experiment

Range	Instrument
0°C to 150°C	Temperature sensor K type- constantan
-50°C to 199.9°C	RTD- Platinum temperature sensor
0.0m/s to 45.0m/s	Digital anemometer
0W/m² to 1500W/m²	Pyranometer (Kipps and Zenon)

instruments utilized in experiment is shown in Table 2. The initial temperatures of the water, glass cover, and condensing cover were noted before the experiment started. The mass flow rate (MFR) of the cooled water passing over the condensing cover was measured at 0.065 kg/s, while the water depth in the solar still's (SS) basin was kept at 2 cm.

From 7:00 AM to 7:00 PM, hourly readings of the basin water, glass cover, and condensing cover temperatures were taken. A mathematical model was used to determine the corresponding theoretical values for the temperature of the condensing cover, glass cover, and basin water. The experimental results nearly match the theoretical values, as seen in Figure 8, 9, 10 and 11. Root mean square of percentage deviation e represents the closeness of the theoretical and experimental values. 'e' is given by [13],

$$e = \sqrt{\frac{\sum (e_x)^2}{n}}$$

$$e_x = [\frac{X_{pre(x)} - X_{\exp t(x)}}{X_{pre(x)}}] \times 100$$

The correlation between the predicted values and experimental values is given by coefficient of correlation (r). The correlation coefficient is given by the following equation

$$r = \frac{N\sum X_{pr}X_{\text{ex}} - (\sum X_{pr})(\sum X_{\text{ex}})}{\sqrt{N\sum X_{\text{ex}}{}^2 - (\sum X_{\exp})^2}\sqrt{N\sum X_{pr}{}^2 - (\sum X_{pr})^2}}$$

The experimentally measured water temperatures closely match the computed values. The standard error ("e") ranges from 6.79 to 8.55, while the correlation coefficient ("r") lies between 0.998 and 0.999, indicating an excellent fit between the theoretical and experimental results (see Figs. 8–10). This confirms that the model predicts water temperature with high accuracy. However, the deviation between theoretical and experimental distillate yield is higher, at about 14.6 %. For solar distillation systems, such a difference is generally considered acceptable while calculate the distillate output. Moreover, as shown Table 2, the combined total uncertainty of all measurement instruments is 2.661 %. This low level of uncertainty indicates that the reported trends and the solar still's performance remain reliable, and the small variations do not significantly affect the conclusions drawn from the study.

Table 2. Uncertainty analysis

Uncertainty Parameters	Uncertainty
Temperature (U_T) K thermocouple [Sensor accuracy (sa), calibration (c), Resolution (R), Repeatability (Re)]	$U_T = [U_{sa}^2 + U_c^2 + U_R^2 + U_{\text{Re}}^2]^{1/2}$ $U_T = [1.27^2 + 0.29^2 + 0.058^2 + 0.3^2]^{1/2} = 1.338$
Temperature (U_{T1}) RTD [Sensor accuracy (sa), calibration (c), Resolution (R), Repeatability (Re)]	$U_{T1} = [U_{sa}^2 + U_c^2 + U_R^2 + U_{\text{Re}}^2]^{1/2}$ $U_{T1} = [0.202^2 + 0.115^2 + 0.029^2 + 0.1^2]^{1/2} = 0.255$
Air velocity Measurement U_A [Accuracy(a), Calibration (c), Resolution (R), *Reeability* (Re)	$U_A = [U_a^2 + U_c^2 + U_R^2 + U_{\text{Re}}^2]^{1/2}$ $U_A = [0.087^2 + 0.043^2 + 0.029^2 + 0.1^2]^{1/2} = 0.142$
Mass flow rate (U_m)	$U_m = [(\frac{\Delta V}{V})^2 + (\frac{\Delta t}{t})^2]^{1/2}$ $U_m = [(\frac{0.0001}{0.010})^2 + (\frac{1}{154})^2]^{1/2} = 0.0119$
Solar Radiation (U_s) [Calibration (c), Cosine error (co), Repeatability (Re)]	$U_s = [U_c^2 + U_{co}^2 + U_{\text{Re}}^2]^{1/2}$ $U_s = [1^2 + 2^2 + 0.5^2]^{1/2} = 2.291$
Total Uncertainty U_o	$U_o = [U_T^2 + U_{T1}^2 + U_A^2 + U_m^2 + U_s^2]^{1/2}$ $U_o = [1.338^2 + 0.255^2 + 0.142^2 + 0.019^2 + 2.291^2]^{1/2}$ $U_o = \pm 2.661\%$

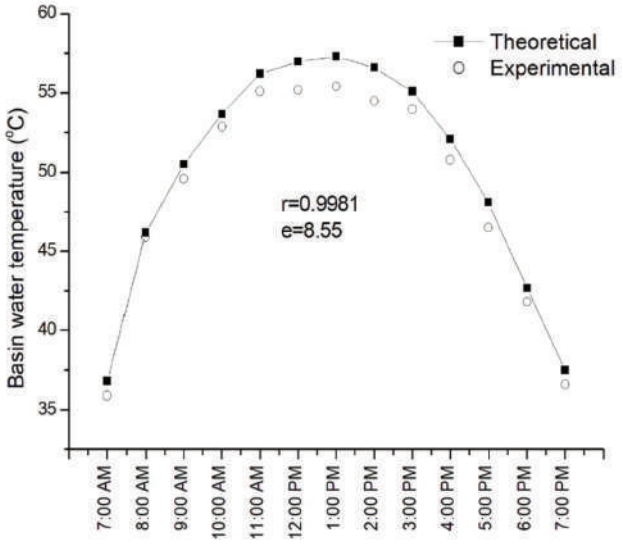

Figure 8. Theoretical and experimental water temperature.

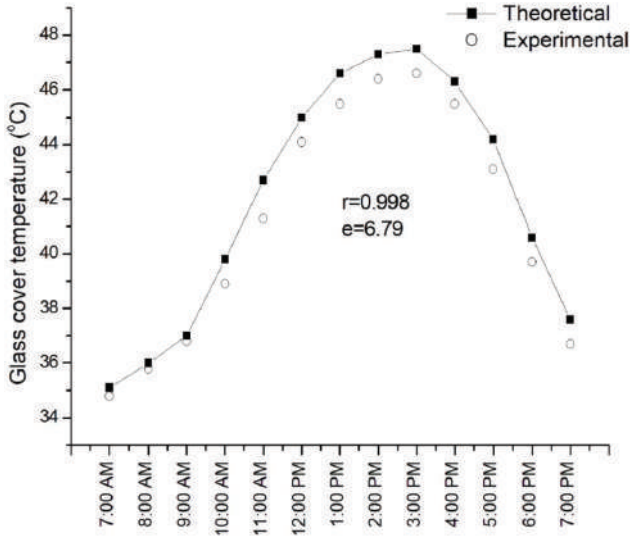

Figure 9. Theoretical and experimental glass temperature.

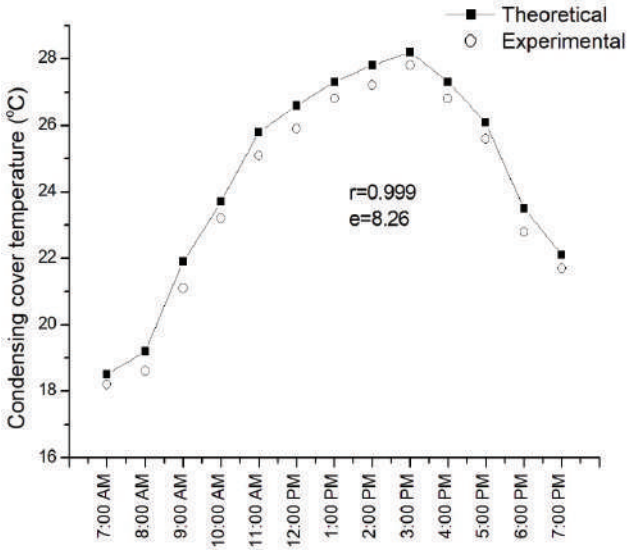

Figure 10. Theoretical and experimental condensing cover temperature.

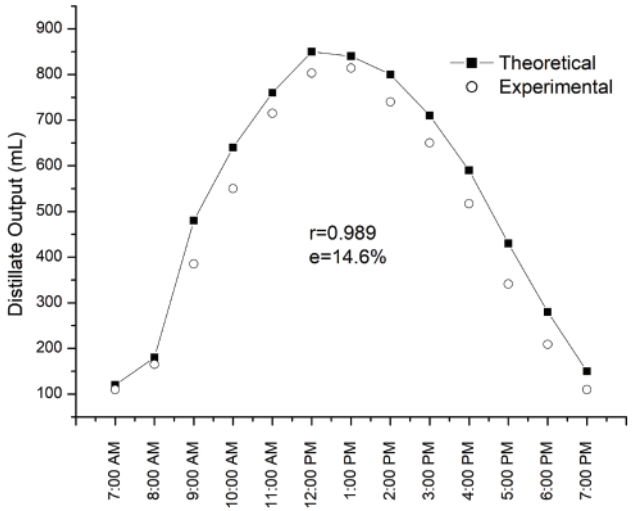

Figure 11. Theoretical and experimental hourly distillate output.

NUMERICAL COMPUTATIONS

Effect of MFR and Depth of Water in Basin

Numerical analysis has been done on the impacts of the water depth in the basin and the mass flow rate (MFR) of water passing over the condensing cover of a solar still (SS). The solar still's total daily distillate output during a summer day was computed. In this analysis, the beginning glass temperature was set at 1°C below the water temperature, and the initial condensing cover temperature was set to the surrounding air's wet bulb temperature (WBT). Furthermore, it was thought that the water's initial temperature was taken same as the surrounding air temperature. These computations were performed for a day (24h) in summer for climate of Raipur, Chhattisgarh, India. Hourly ambient temperature solar radiation and wet bulb temperature for a day in summer is shown in Figure 12.

To analyse the effect of water depth on stills performance MFR is kept constant. The water depth in the basin was varied at 1 cm, 2 cm, 3 cm, 4 cm, 5cm and the MFR of water flowing over the cover was set at 0.065 kg/s. Raipur's average wind speed was considered as 2 m/s (monthly average for May)

As the basin's water depth increased, the daily distillate output slightly decreased (Fig. 13). In particular, the daily

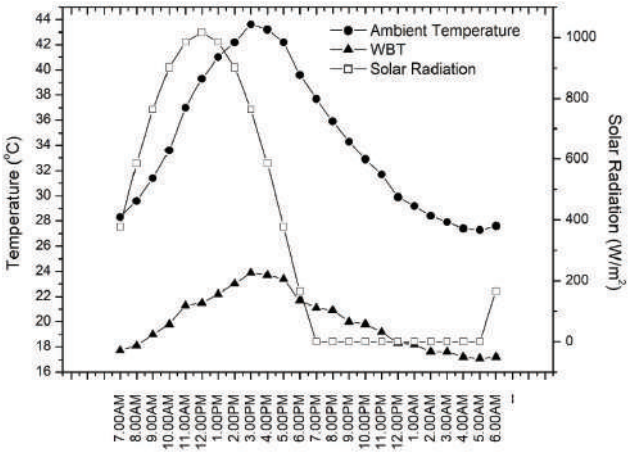

Figure 12. Hourly solar radiation, ambient temperature and WBT of summer (May).

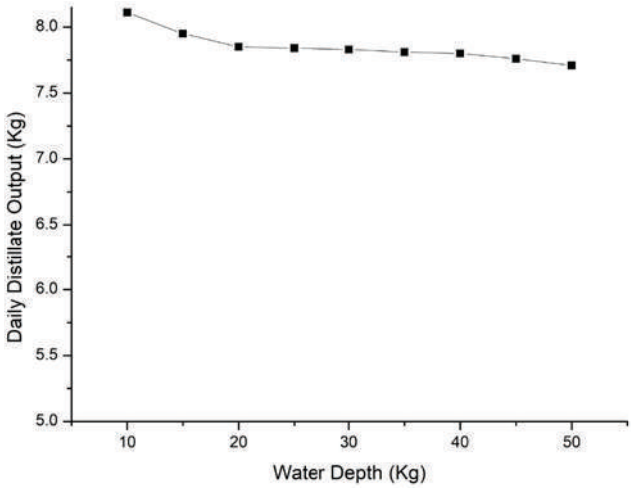

Figure 13. Effect of increasing the depth of water in basin.

distillate output decreased by just 4.9% when the water depth increased from 1 cm to 5 cm. On the other hand, the distillate yield of traditional solar stills (SS) usually decreases more noticeably as the water depth increases. In this design as evaporation and condensation zones are separated and condensation rate is now actively enhanced by flowing cooled water over condenser. The cooled condenser continuously maintains the temperature difference between water and condenser and hence the depth of water does not affect significantly.

Additional numerical calculations were carried out to evaluate the daily distillate output of the proposed design by altering the MFR of water running over the condensing cover in order to examine the impact of the MFR of water flowing over the cover. The basin's water depth was 2 cm, meteorological data considered are same as given above (Fig 14). The effect of changing the MFR of water flowing over the condensing cover was found to be nearly insignificant, as seen in Figure 14. While flowing evaporatively cooled water over cover due to thermal saturation the surface cover temperature of condenser remains low even at lower MFR with increase MFR further does not significantly lower condenser temperature hence distillate output does not increase noticeably.

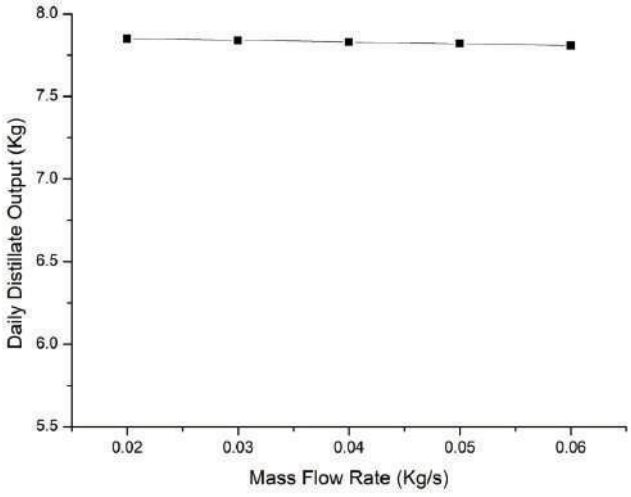

Figure 14. Effect of varying MFR of water flowing over condensing cover.

Effect of Relative Humidity and Wind Velocity

To analyze the effect of relative humidity of ambient air and wind velocity we considered a typical set of parameters to compute hourly yield from the proposed device. For analyzing the effect of relative humidity, we considered ambient temperature as T_a=35°C, I=800W/m² and wind velocity was taken as v_a=2m/s. Numerical computation was performed to determine hourly yield by varying relative humidity from 0.2 to 0.9. The hourly yield with varying relative humidity for typical data set was computed and shown in Figure 15. The result is as expected like other evaporative cooling devices the system works less effectively when the humidity is high. The hourly output decreases with increase in relative humidity of air. The inlet temperature of water flowing through condenser is considered equal to WBT. An increase in ambient humidity raises the wet-bulb temperature of air, thereby reducing the cooling potential and effectiveness of the condenser. For a typical set of parameters when the relative humidity increases from 0.2 to 0.9 the decrease in hourly output is 5.7%.

To study the effect of wind velocity we considered T_a=35°C, I=800W/m² and γ=0.2 Numerical computation was performed to determine hourly yield by varying wind velocity as 1m/s, 2m/s, 3m/s and 4m/s. The hourly yield has been computed at different wind velocity and shown in Figure 16. Unlike conventional solar distillation system were the distillate output increases with increase in wind velocity. Here in this design, we found the slight decrease

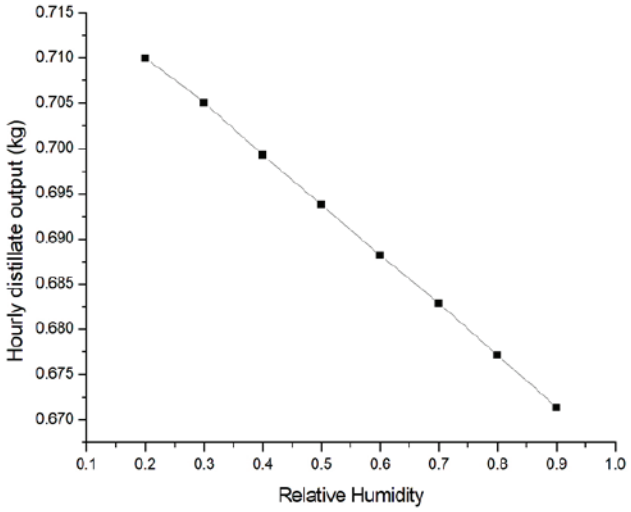

Figure 15. Effect of relative humidity of air on distillate output (T_a=35°C, I=800W/m^2).

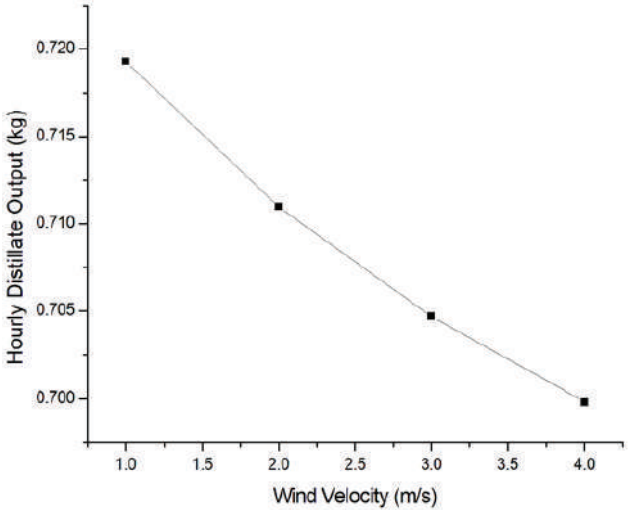

Figure 16. Effect of relative humidity of air on distillate output (T_a=35°C, I=800W/m^2, Relative Humidity=0.2).

in hourly distillate output with the increase in wind velocity. Since the proposed design has a separate condensing unit which is evaporatively cooled by cooled water flowing over it. The condenser is already very effective so the evaporation is more dominating factor. Glass cover gets cooled due to increase in convective coefficient between glass and ambient air. The air inside gets cooled this reduces the greenhouse effect. The rate of evaporation gets reduced at high wind velocity thereby decreases the distillate output produced by system. When the wind velocity increases from 1m/s to 4m/s the decrease in the hourly distillate output is 2.7%.

Performence of the Proposed Design

Numerical computation has been performed to determine the performance of the proposes SS for a summer (May) winter (Jan.) and autumn (Oct.) day in the climate of Raipur Chattisgarh. The climate data for Jan. and Oct. is shown in Figure 17. Slight improvement in output was observed with a lower basin water depth due to enhanced thermal response. Despite this, maintaining an intermediate water depth is recommended to reduce the need for frequent replenishment. Additionally, operating with a reduced MFR of cooling water is advisable, as it minimizes pumping power requirements without significantly compromising productivity. For further computations authors considered depth of water in basin as 2cm and MFR as 0.020kg/s.

The performance of the propose design in May, January and October has been computed. Climate data for (May) is shown in Figure 12. Climate data for January and October

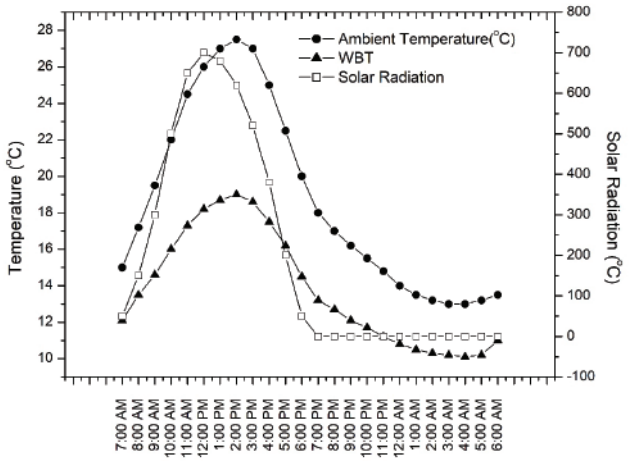

(a)

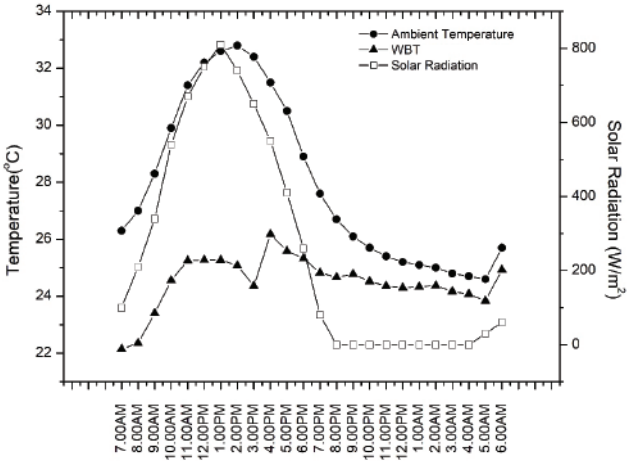

(b)

Figure 17. Climatic data for (a) Winter (Jan.), (b) Autumn (Oct.).

is shown in Figure 16. the total solar radiation received in a day for May, January, and October is 740.3 MJ/m^2, 441.7 MJ/m^2 and 535.7 MJ/m^2. The maximum ambient temperature reached in day for May, January and October is 43.6°C, 27.1°C and 33.4 °C, respectively. Hourly water temperature, temperature of glass cover and condenser cover has been computed and shown in Figure 18,19, and 20.

During the summer month of May, the highest temperature difference between the basin water and the condenser was seen as 29°C around 12:00 PM, resulting in the peak distillate yield of approximately 0.93 kg for that hour. In contrast, during January (winter), the maximum temperature difference reached 26.6°C at 1:00 PM, producing a corresponding maximum hourly distillate output of 0.55 kg. For the month of October, the peak temperature difference of 28.4°C occurred at 2:00 PM, with the associated maximum distillate generation being 0.67 kg per hour.

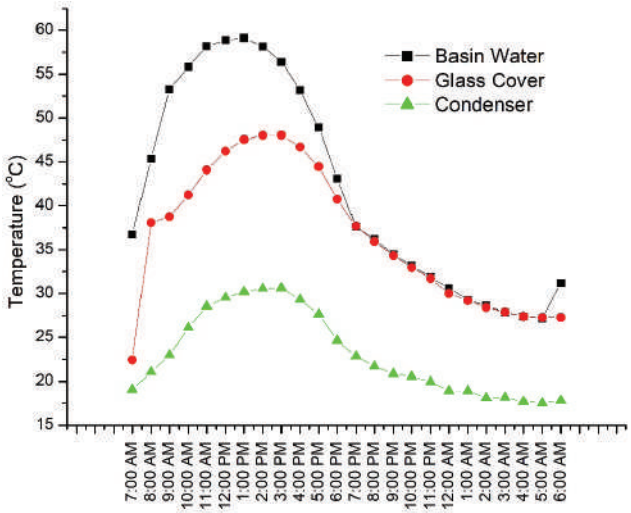

Figure 18. Computed temperature of basin water, glass cover & condenser during summer (May).

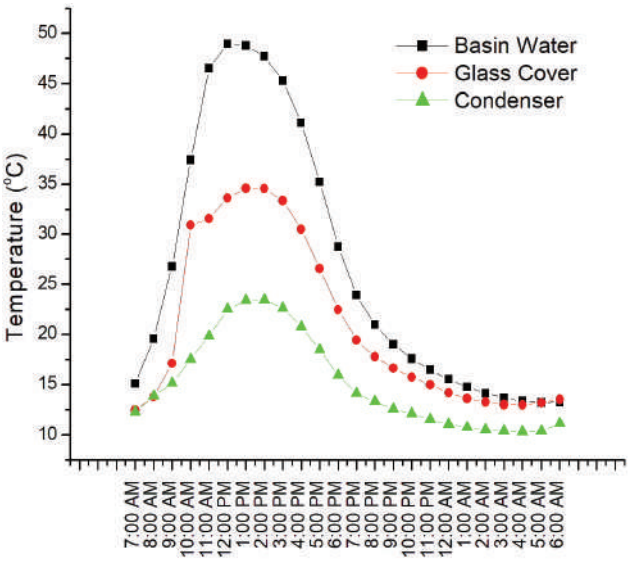

Figure 19. Computed temperature of basin water, glass cover & condenser during winter (January).

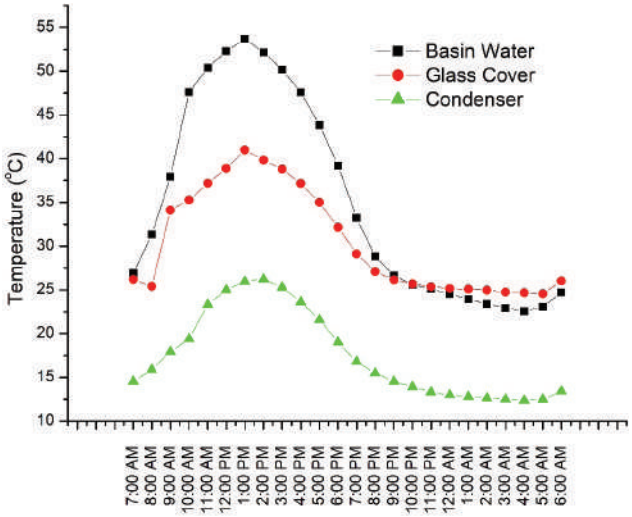

Figure 20. Computed temperature of basin water, glass cover & condenser during autumn (October).

The continuous cooling of condenser by cooled water helps to maintain the temperature difference between water and condensing cover during day time (6.00AM-6.00PM) as well as in night (6.00PM-6.00AM). This helps to produce distilled water during day as well as during night.

The hourly distillate output produced by the proposed system during different months have been computed and shown in Figures 21, 22 and 23. The total distillate output produced in May, Jan. and Oct.is 7.83kg/day, 3.45kg/day and 5.30kg/day, respectively. The system helps to produce

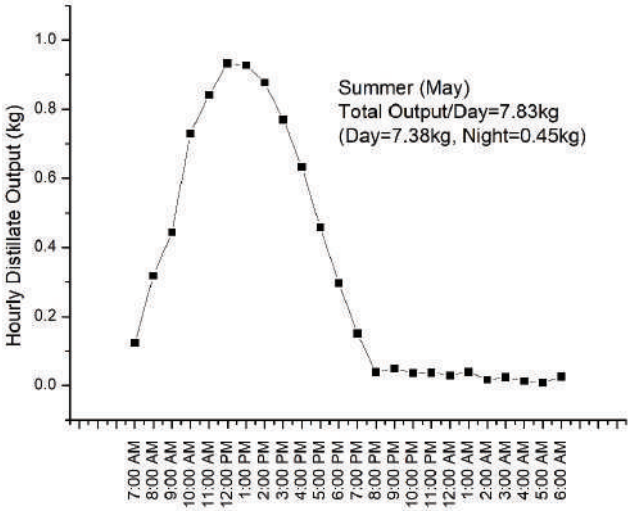

Figure 21. Hourly distillate output produced in a day for May.

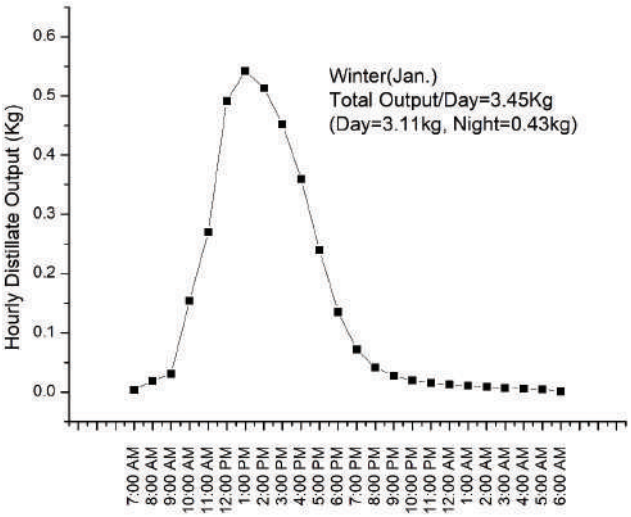

Figure 22. Hourly distillate output produced in a day for January.

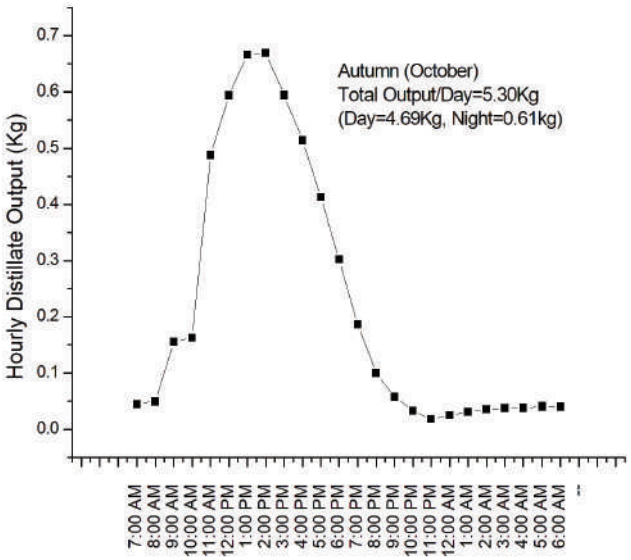

Figure 23. Hourly distillate output produced in a day for October.

some amount of distillate during night time also. The distillate output produced during night for May, Jan. and Oct. are 0.45kg, 0.43kg and 0.61kg, respectively.

Economic Analysis

An economic analysis was conducted to determine the cost per liter of water produced by the proposed solar still (SS). The following assumptions were made for the analysis:

1. The rate of interest (i) is assumed to be 10%, with a total plant life of 20 years.
2. The annual maintenance cost (AMC) is estimated at 12% of the initial annual cost.
3. The salvage value of the plant is considered to be 50% of the total cost of usable items.
4. The cost of items is based on current market prices (as shown in Table-3).
5. The cost of the desert cooler is excluded from the calculation. (Since desert cooler generally used in household for room cooling)
6. The daily water yield is calculated as the average between the yields in summer and winter.
7. The number of clear days in Raipur is taken as 309 days per year
8. The system uses a 5 W PV-powered exhaust fan, and its cost has been accounted for, while its auxiliary energy demand is considered negligible

The *TAC* of the plant will be given by
$TAC = CC \times CRF + AMC - SV \times SFF$
TAC = 2269.9
CRF and *SFF* is given by,

$$CRF = \frac{i(1+i)^n}{(1+i)^n - 1},$$

CRF = 0.117

$$SFF = \frac{i}{(1+i)^n - 1}$$

SFF = 0.017
Cost/L of water produced will be given by,
Cost/Litre = TAC/ TAD = Rs.1.30/L(US$0.015)

Sensitivity Analysis Energy Equivalence and Water Quality

To assess the robustness of the proposed system, a sensitivity analysis was performed considering variations in solar availability and pump reliability. The results (Table 4) show the effect of reduced or enhanced solar radiation (±25%) and pump failure scenarios (10% and 20% downtime) on annual water output, cost of water, and payback period. We considered sensitivity scenario based on seasonal bands:

Table 3. Details of items

S. No	Material	Cost
1	M.S. Sheet (1.5mm)	Rs. 6265.35 (72.62 US$)
2	Glass (4 mm) 1m^2	Rs. 320 (3.71 US$)
3	Condenser plate (Aluminum 1m^2)	Rs. 220 (2.55 US$)
4	Solar fan (5W)	Rs. 250 (2.90 US$)
5	Solar pump	Rs. 550 (6.37 US$)
6	Putty	Rs. 60 (0.70 US$)
7	Pipes fittings (valve, etc.)	Rs. 400 (4.64 US$)
8	Mics.	Rs. 500 (5.79 US$)
	Total	**Rs. 8565.35 (99.27 US$)**

(i) Winter (low) representative winter solar availability and ambient conditions (ii) Annual-average (base); and (iii) Summer(high) representative summer conditions. Outputs are computed with the same model using seasonal inputs. While higher insolation generally increases yield, productivity does not scale strictly linearly due to seasonal changes in (Tw–Tc) and convective losses. The payback period (PBP) will be given by

PBP=CC/Annual Net Saving

Annual Net Saving = (Annual Distillate Output) x (Selling Price)

In pump failure scenario the system still run as conventional solar distillation system having separate condenser without cooling. The daily distillate output considered with pump failure as 3kg/day

The analysis indicates that although the total annual cost remains constant, lower output under adverse conditions increases the unit cost of water and extends the payback period, whereas favourable conditions shorten it. For different scenario discussed in table the cost/kg of water produced is between Rs 0.94/kg to Rs 1.43/kg and the payback period between 0.236-0.535year.

`In addition, an energy equivalence analysis was carried out (Table 5) to quantify the environmental benefit of the system under the same scenarios. The annual distillate output was converted into equivalent energy savings, coal displaced, and associated CO_2 emissions avoided. This parallel evaluation highlights both the economic feasibility and sustainability advantage of the system, demonstrating its potential for potable water generation even under variable operating conditions. Energy equivalence (Q_E) and the mass of coal burned (M_c) will be given by,

$$Q_E(kWh) = \frac{(Anualloutput)L}{3600}$$

$$M_c = \frac{Q_E \times 3600}{(CV)_{coal} \times \eta_{plant}}$$

In above Equation $(CV)_{coal}$ calorific value of coal is taken as 20,000KJ/kg and plant efficiency η_{plant} is considered 0.35. The energy equivalence analysis shows that the system can significantly offset coal consumption and associated CO_2 emissions. Depending on the operating scenario, the

Table 4. Sensitivity Analysis (Selling Price /kg=Rs15)

Case	Solar availability	Pump availability	Annual water output	Cost/kg	Payback (year)
Base (Average)	100%	100%	1742.8 kg	Rs1.30/kg	0.327
Higher (Summer)	125%	100%	2419.5 kg	Rs0.94/kg	0.236
Lower (Winter)	75%	100%	1066.0 kg	Rs2.12/kg	0.535
Pump Failure (30 days/Year)	100%	90%	1663.6 kg	Rs1.36/kg	0.343
Pump Failure (60 days/Year)	100%	80%	1584.4 kg	Rs1.43/kg	0.360

Table 5. Energy equivalence of distillate output

Case	Annual distillate output	Energy equivalence	Equivalent coal burned (kg)	Co_2 emission avoided (kg) 0.65 kg Co_2/(kWh)
Base	1742.8 kg	1094 kWh	563 kg	711 kg
Higher	2419.5 kg	1519 kWh	781 kg	987 kg
Lower	1066.0 kg	669 kWh	344 kg	435 kg
Pump failure (30days)	1663.6 kg	1045 kWh	538 kg	350 kg
Pump failure (60days)	1584.4 kg	995 kWh	512 kg	647 kg

Table 6. Chemical analysis of distillate water compared with WHO standards

Parameters	Distillate	WHO limits	Remarks
pH	7.1	6.5-8.5	Safe
TDS (mg/L)	12	<500	Very Low
Hardness (mg/L as $CaCO_3$)	6	<200	Very Soft
Bacteria	Nil	0	Safe

annual freshwater yield corresponds to an energy saving of about 669–1519 kWh, which is equivalent to avoiding the burning of 344–781 kg of coal and reducing 435–987 kg of CO_2 emissions

To check the quality of water produced by the system a chemical analysis has been performed and shown in Table 6. It is seen that the water produced is fit for drinking fulfilling all recommendations limits as prescribed by WHO.

CONCLUSION

The proposed design of SS contains two different sections separated by a common plate the section towards left is called evaporative section and two the right is called as condenser section. The water vapours produced in the evaporator section is forced towards condensing section by a low power exhaust fan in between. The condenser plate is evaporatively cooled by flowing cooled tank water from an air cooler. The cooled condenser behaves as a heat sink

Table 7. Summary of solar still modifications integrated with passive condensers

Reference	Modification	Operating Condition	Key Result	Unique Feature / Novelty
Fath et al. [23]	Single-slope still with passive condenser; studied diffusion, purging, and circulation.	Hot/arid climate; ~800 W/m²	70% increase in yield	Passive condenser integration
Fath et al. [33]	Natural convection-based humidification system with built-in condenser.	Laboratory; ~700–800 W/m²	5.1 kg/m²·day output	Humidification–dehumidification system
Madhlopa & Johnstone [34]	External condenser with added basin areas.	Malawi; ~850 W/m²	Up to 60% gain	Multi-basin + external condenser
Monowe et al. [35]	Portable still with external condenser and reflector.	Field test; ~850–900 W/m²	5–8 L/m²·day output	Portable + reflector-assisted
Kabeel et al. [45]	Used external condenser with Al_2O_3 nanofluid.	Egypt; ~850 W/m²	Up to 116% enhancement	Nanofluid-based heat transfer
Al-Nimr & Al-Ammari [46]	PV/T-integrated still with external finned condenser.	700 W/m² solar input	7.9 kg/m²·day	PV/T integration with finned condenser
Rabhi et al. [47]	Still with pin-finned absorber and condenser.	Tunisia; ~850 W/m²	43.7% efficiency	Pin-finned absorber plate
Belhadi et al. [48]	Double-slope still with capillary film condenser.	Mediterranean climate	7.15 kg/m²·day	Capillary film condenser
Kumar et al. [49]	Single-slope still with external condenser.	Semi-arid climate	39.4% higher yield	Conventional SS + external condenser
Bhardwaj et al. [38]	Inflatable still with household-type passive condenser.	Lab conditions	~0.75 L/h output	Inflatable structure
Hassanaa & Abo-Elfadl [50]	Tested various condensers and saline water types.	Lab & seasonal tests	Max 52% gain with heat sink + steel fibers	Different condenser materials tested
Rahmani & Boutriaa [39]	NCL-driven condenser under seasonal changes.	Algeria; summer & winter	4.73 (summer), 2.71 (winter) kg/m²·day	Natural circulation loop condenser
Saini et al. [51]	PV-powered still with passive condenser and fan.	India; ~800 W/m²	Enhanced yield and efficiency	PV-driven fan for improved cooling
Rashid et al. [6]	Review of floating solar stills and floating solar-driven membranes.	Global review	Yields often exceed land-based SS; modular & scalable	Floating platforms reduce heat loss, allow hybridization
Hussein et al. [7]	Comprehensive review of inverted solar still designs and models.	Global review	Yields up to 11 kg/m²·day in modified inverted systems	Inverted geometry improves absorptivity & reduces losses
Al-Obaidi et al. [8]	Review of hybrid membrane + thermal desalination powered by fossil fuels.	Global review	Higher recovery & efficiency, but high energy/GHG cost	Future focus: renewables + hybridization
Present Work	Solar still with evaporatively cooled condenser (SS + air cooler).	India; May (Summer), ~850–900 W/m²	7.83 kg/day; cost US $0.015/kg	Evaporatively cooled condenser with low-cost operation

and thus helps to condense more quantity of vapours this enhances the overall distillate output of the system. The present work proposes the overall thermal performance analysis of this system. During the study the conclusions drawn are as follows: -

1. The mathematical model of the design has been developed and validated by experiment in Raipur, Chhattisgarh, India (21°14′40″N and 81°37′50″E)
2. As the basin water depth increased, a slight reduction in daily distillate output was observed. Specifically, when the water depth increased from 1 cm to 5 cm, the daily distillate yield decreased by only 4.9%
3. The mass flow rate of water flowing over the condenser plate has negligible affect on the distillate output produced.
4. For a typical set of parameters, it is seen that the hourly distillate output decreases by 5.7% when the relative humidity of air increased from 0.2 to 0.9
5. With increases in wind velocity from 1m/s to 4m/s the hourly distillate output decreases by 2.7 %.
6. Considering 2cm depth of water in basin and at mass flow rate of 0.020kg/s the system generates 7.83kg/day, 3.44kg/day and 5.30 kg/day total distillate for a day in May, Jan. and Oct. The total radiation received for a day in May, Jan and Oct. is 740.3MJ/m^2, 441.7MJ/m^2 and 535.7MJ/m^2, respectively.
7. The system is capable of generating distilled water even during nighttime due to the effective cooling provided by the separate condenser. The distillate output produced during night (6.00PM-6.00AM) is 0.45kg/m^2, 0.43kg/m^2 and 0.61kg/m^2 for a day in months of May, Jan. and Oct. This output represents an additional benefit, as it utilizes the stored heat without requiring significant extra energy input apart from minimal auxiliary power. While this quantity is modest, it can still contribute to daily freshwater availability, particularly in water-scarce areas
8. The cost of water produced is Rs 1.30/L (US$ 0.015/L)

Applicability of the Proposed Design

- Rural Households: The system's low maintenance, passive solar powered, and simple construction make it suitable for decentralized water purification in rural areas lacking reliable potable water access.
- Off-grid Communities: Since the system operates without electrical power (except minimal pumping for condenser cooling, which can be solar-powered), it is highly suitable for off-grid or remote communities where grid access is limited.
- Disaster Relief: The compact design, ability to produce clean water using only solar energy and minimal infrastructure, makes it a promising option for rapid deployment during natural disasters or emergency relief operations.

Additionally, we have estimated daily water output under typical rural solar insolation conditions, indicating that the unit can provide 3–8 liters/day, which is sufficient for basic drinking water needs of a small family. A comparison table (Table-7) has been given to compare the present work with some past works on solar distillation system having separate condenser. When compared we found that the proposed system works reasonably well to fulfill the pure water requirements of small communities in rural areas.

Limitation of the present work

1. Economic analysis did not include the cost of the air cooler, as it was assumed to be a pre-existing household appliance. In communities without coolers, the overall cost and payback period would be higher.
2. Scale formation effects were not studied. In hard-water areas, scaling can reduce heat transfer efficiency. Practical adoption will require mitigation strategies such as cleaning, water softening, or anti-sealant coatings.
3. Implementation aspects such as user training, large-scale deployment, and socio-economic challenges were beyond the scope of this work. These will be addressed through field trials and user studies in future work.

NOMENCLATURES

A_b	Area of basin, m^2
A_g	Area of glass cover, m^2
A_c	Area of condensing plate, m^2
c_w	Specific heat of water, $Jkg^{-1}K^{-1}$
h_i	Total internal heat transfer coefficient, W / m^2K
h_0	Total external heat transfer coefficient, W / m^2K
h_2	Sum of convective & radiative heat transfer coefficient between water and water film, W / m^2K
h_{rw}	Radiative heat transfer coefficient between water and glass cover, W / m^2K
h_{cw}	Convective heat transfer coefficient between water and glass cover, W / m^2K
h_{ew}	Evaporative heat transfer coefficient between water and glass cover, W / m^2K
h_{ca}	Convective heat transfer coefficient between glass and air, W / m^2K
h_{ra}	Radiative heat transfer coefficient between glass and air, W / m^2K
h_b	Heat transfer coefficient between basin liner and water, W / m^2K
h_f	Convective heat transfer coefficient between condensing plate and water film, W / m^2
i	Annual rate of interest
Lv	Latent heat of vapourization of water, J / kg
$\dot{m}_f$	Mass flow rate of water flowing over condensing plate (film flow rate), kg / s
$\dot{m}_{ew}$	Distillate output produced per hour, kg / h
M_w	Mass of water in basin of solar still, kg
P_w	Saturated vapour pressure at water temperature, N / m^2
P_g	Saturated vapour pressure at glass temperature, N / m^2
$\dot{Q}_u$	Rate of heat added by solar still into tank, W

$\dot{Q}_m$ Rate of heat taken by make-up water, W
$\dot{Q}_T$ Rate of heat loss from top of storage tank, W
$\dot{Q}_s$ Rate of heat loss from sides of storage tank, W
$\dot{Q}_b$ Rate of heat loss from bottom of storage tank, W
q_{rw} Rate of radiative heat transfer from water to glass, W
q_{cw} Rate of convective heat transfer from water to glass, W
q_{ew} Rate of evaporative heat transfer from water to glass, W
q_{ca} Rate of convective heat transfer from glass to air, W
q_{ra} Rate of radiative heat transfer from glass to air, W
$\dot{q}_{cf}$ Rate of convective heat transfer from condensing plate to film, W
$\dot{q}_{cfa}$ Rate of convective heat transfer from film to air, W
$\dot{q}_{rfa}$ Rate of radiative heat transfer from film to air, W
I Solar radiation, W / m^2
T_g Temperature of glass cover, °C
T_w Temperature of water in basin, °C
T_a Ambient temperature, °C
T_b Temperature of basin liner, °C
T_{w0} Initial water temperature, °C
T_{wt} Tank (reservoir) water temperature, °C
T_{wl_n} Exit water temperature from nth row of plant, °C
U_s Side loss coefficient of the storage tank, $Wm^{-2}K^{-1}$
U_t Top loss coefficient of the storage tank, $Wm^{-2}K^{-1}$
U_b Bottom loss coefficient of the storage tank, $Wm^{-2}K^{-1}$
v_a Velocity of air, m/s
α_g Absorptivity of glass cover
σ Stefans-Boltzmann constant, W / m^2K^4
ρ_w Density of water, kg / m^3

Abbreviations

SS Solar still
MFR Mass flow rate
TAC Total annual cost
TAD Total annual distillate produced
CC Capital cost
CRF Capital recovery factor
AMC Annual maintenance cost
SV Salvage value
SFF Sinking fund factor
CF Cash flow
U Uncertainty
WBT Wet bulb temperature

REFERENCES

[1] Awasthi A, Kumari K, Panchal H, Sathyamurthy R. Passive solar still: Recent advancements in design and related performance. Environ Technol Rev 2018;7(1):235-261. [CrossRef]

[2] Durkaieswaran P, Murugavel KK. Various special designs of single basin passive solar still - A review. Renew Sustain Energy Rev 2015;49:1048-1060. [CrossRef]

[3] Murugavel KK, Chockalingam KKSK, Srithar K. Progresses in improving the effectiveness of the single basin passive solar still. Desalination 2008;220(1-3):677-686. [CrossRef]

[4] Ansari O, Asbik M, Bah A, Arbaoui A, Khmou A. Desalination of the brackish water using a passive solar still with a heat energy storage system. Desalination 2013;324:10-20. [CrossRef]

[5] Sarkar Md NI, Sifat AS, Reza SMS, et al. A review of optimum parameter values of a passive solar still and a design for southern Bangladesh. Renew Wind Water Solar 2017;1:1-13. [CrossRef]

[6] Rashid FL, Al-Obaidi MA, Hussein AK, Akkurt N, Ali B, Younis O. Floating solar stills and floating solar-driven membranes: Recent advances and overview of designs, performance and modern combinations. Sol Energy 2022;247:355-372. [CrossRef]

[7] Hussein AK, Rashid FL, Abed AM, Al-Khaleel M, Togun H, Ali B, et al. Inverted solar stills: A comprehensive review of designs, mathematical models, performance, and modern combinations. Sustainability 2022;14:13766. [CrossRef]

[8] Al-Obaidi MA, Alsarayreh AA, Rashid FL, Sowgath MT. Hybrid membrane and thermal seawater desalination processes powered by fossil fuels: A comprehensive review, future challenges and prospects. Desalination 2024;583:117694. [CrossRef]

[9] Al-Obaidi MA, Alsarayreh AA, Rashid FL, Sowgath MT, Alsadaie S, Ruiz-García A, et al. Hybrid membrane and thermal seawater desalination processes powered by fossil fuels: A comprehensive review, future challenges and prospects. Desalination 2024;583:117694. [CrossRef]

[10] Rashid FL, Shareef AS, Alwan HF. Enhancement of fresh water production in solar still using new phase change materials. J Adv Res Fluid Mech Therm Sci 2019;61:63-72.

[11] Chaichan MT, Kazem HA. Water solar distiller productivity enhancement using concentrating solar water heater and phase change material (PCM). Case Stud Therm Eng 2015;2:24-31. [CrossRef]

[12] Rashid FL, Al-Obaidi MA, Hussein AK, Akkurt N, Ali B, Younis O. Floating solar stills and floating solar-driven membranes: Recent advances and overview of designs, performance and modern combinations. Sol Energy 2022;247:355-372. [CrossRef]

[13] Hussein AK, Rashid FL, Rasul MK, Basem A, Younis O, Homod RZ, et al. A review of the application of hybrid nanofluids in solar still energy systems and guidelines for future prospects. Sol Energy 2024;272:112485. [CrossRef]

[14] Rashid FL, Al-Obaidi MA, Mohammed HI, Togun H, Ahmad S, Ameen A. A review of the current situation and prospects for nanofluids to improve solar still performance. J Therm Anal Calorim 2024;149(23):13511-13531. [CrossRef]

[15] Hidouri K, Togun H, Rashid FL, Abed AM, Hussein AK, Ali B, et al. Environmental studies for various simple and hybrid solar still configurations: A comprehensive review. J Therm Eng 2024;10(6):1698-1714. [CrossRef]

[16] Ajit A, Pandey H, Gupta NK. Analysis of solar water desalination using hybrid nanofluids: An experimental study. J Therm Eng 2023;9(6):1502-1515. [CrossRef]
[17] Chauhan MK, Chauhan AK, Khan Y, Singh AP. Experimental and theoretical investigation of thermal efficiency and productivity of single slope basin type solar distillation system using honey-comb. J Therm Eng 2021;9(6):1559-1571. [CrossRef]
[18] Tiwari GN. Solar Energy: Fundamentals, Design, Modelling and Applications. Alpha Science Int'l Ltd; 2002.
[19] Gaur MK, Norton B, Tiwari GN, editors. Solar Thermal Systems: Thermal Analysis and Its Application. Bentham Science Publishers; 2022. [CrossRef]
[20] Tiwari A, Tiwari GN. Solar Distillation Practice for Water Desalination Systems. Anshan; 2008.
[21] Tiwari GN, Sahota L. Advanced Solar-Distillation Systems: Basic Principles, Thermal Modeling, and Its Application. Autumner; 2017. [CrossRef]
[22] Tiwari GN, Tiwari A. Handbook of Solar Energy. Vol. 498. Singapore: Autumner; 2016. [CrossRef]
[23] Fath HES, Elsherbiny SM. Effect of adding a passive condenser on solar still performance. Energy Convers Manag 1993;34:63-72. [CrossRef]
[24] Fath HES, Hosny HM. Thermal performance of a single-sloped basin still with an inherent built-in additional condenser. Desalination 2002;142:19-27. [CrossRef]
[25] ElSherbini A, Maheshwari GP. Effectiveness of shading air-cooled condensers of air-conditioning systems. 2010. [CrossRef]
[26] Mugisidi D, Fajar B, Syaiful S, Utomo T. Solar still with an integrated conical condenser. CFD Lett 2023;15(8):122-134. [CrossRef]
[27] Bhardwaj R, ten Kortenaar MV, Mudde RF. Maximized production of water by increasing area of condensation surface for solar distillation. Appl Energy 2015;154:480-490. [CrossRef]
[28] Mohaisen HS, Esfahani JA, Ayani MB. Improvement in the performance and cost of passive solar stills using a finned-wall/built-in condenser: An experimental study. Renew Energy 2021;168:170-180. [CrossRef]
[29] Mevada D, Panchal H, Nayyar A, Sharma K, Manokar AM, El-Sebaey MS, et al. Experimental performance evaluation of solar still with zig-zag shape air cooled condenser: An energy-exergy analysis approach. Energy Rep 2023;10:1198-1210. [CrossRef]
[30] E1-Bahi A, Inan D. A solar still with minimum inclination, coupled to an outside condenser. Desalination 1999;123:79-83. [CrossRef]
[31] Toosi SSA, Goshayeshi HR, Heris SZ. Experimental investigation of stepped solar still with phase change material and external condenser. J Energy Storage 2021;40:102681. [CrossRef]
[32] Tuly SS, Rahman MS, Sarker MRI, Beg RA. Combined influence of fin, phase change material, wick, and external condenser on the thermal performance of a double slope solar still. J Clean Prod 2021;287:125458. [CrossRef]
[33] Fath HES, Elsherbiny S, Ghazy A. A naturally circulated humidifying/dehumidifying solar still with a built-in passive condenser. Desalination 2004;169(2):129-149. [CrossRef]
[34] Madhlopa A, Johnstone C. Numerical study of a passive solar still with separate condenser. Renew Energy 2009;34(7):1668-1677. [CrossRef]
[35] Monowe P, Masale M, Nijegorodov N, Vasilenko V. A portable single-basin solar still with an external reflecting booster and an outside condenser. Desalination 2011;280(1-3):332-338. [CrossRef]
[36] Kabeel AE, Omara ZM, Essa FA. Numerical investigation of modified solar still using nanofluids and external condenser. J Taiwan Inst Chem Eng 2017;75:77-86. [CrossRef]
[37] Rabhi K, Nciri R, Nasri F, Ali C, Bacha HB. Experimental performance analysis of a modified single-basin (SSSS) with pin fins absorber and condenser. Desalination 2017;416:86-93. [CrossRef]
[38] Bhardwaj R, ten Kortenaar MV, Mudde RF. Inflatable plastic solar still with passive condenser for single family use. Desalination 2016;398:151-156. [CrossRef]
[39] Rahmani A, Boutriaa A. Numerical and experimental study of a passive solar still integrated with an external condenser. Int J Hydrog Energy 2017;42(48):29047-29055. [CrossRef]
[40] Kabeel AE, Harby K, Abdelgaied M, Eisa A. A comprehensive review of tubular solar still designs, performance, and economic analysis. J Clean Prod 2020;246:119030. [CrossRef]
[41] Saini V, Sahota L, Jain VK, Tiwari GN. Performance and cost analysis of a modified built-in-passive condenser and semitransparent photovoltaic module integrated passive solar distillation system. J Energy Storage 2019;24:100809. [CrossRef]
[42] Somwanshi A, Tiwari AK. Performance enhancement of a single basin solar still with flow of water from an air cooler on the cover. Desalination 2014;352:92-102. [CrossRef]
[43] Tiwari AK, Somwanshi A. Techno-economic analysis of mini solar distillation plants integrated with reservoir of garden fountain for hot and dry climate of Jodhpur (India). Sol Energy 2018;160:216-224. [CrossRef]
[44] Sodha MS, Somwanshi A. Variation of water temperature along the direction of flow: Effect on performance of an evaporative cooler. J Fundam Renewable Energy Appl 2012;2:1-6. [CrossRef]
[45] Kabeel AE, Omara ZM, Essa FA. Enhancement of modified solar still integrated with external condenser using nanofluids: An experimental approach. Energy Convers Manag 2014;78:493-498. [CrossRef]

[46] Al-Nimr MA, Al-Ammari W. A novel hybrid PV-distillation system. Sol Energy 2016;135:874-883. [CrossRef]
[47] Rabhi K, Nciri R, Nasri F, Ali C, Bacha HB. Experimental performance analysis of a modified single-basin single-slope solar still with pin fins absorber and condenser. Desalination 2017;416:86-93. [CrossRef]
[48] Belhadj MM, Bouguettaia H, Marif Y, Zerrouki M. Numerical study of a double slope solar still coupled with capillary film condenser in south Algeria. Energy Convers Manag 2015;94:245-252. [CrossRef]
[49] Kumar RA, Esakkimuthu G, Murugavel KK. Performance enhancement of a single basin single slope solar still using agitation effect and external condenser. Desalination 2016;399:198-202. [CrossRef]
[50] Hassan H, Abo-Elfadb S. Effect of the condenser type and the medium of the saline water on the performance of the solar still in hot climate conditions. Desalination 2017;417:60-68. [CrossRef]
[51] Saini V, Sahota L, Jain VK, Tiwari GN. Performance and cost analysis of a modified built-in-passive condenser and semitransparent photovoltaic module integrated passive solar distillation system. J Energy Storage 2019;24:100809. [CrossRef]

APPENDIX I

$$K_1=\frac{H_1U_b+H_2h_o+h_{ew}}{M_wc_w} \qquad K_2=\frac{\tau_1H_2I+\tau_2I+\tau_3H_1I+H_1U_bT_a+H_2h_oT_a}{M_wc_w} \qquad K_3=\frac{h_{ew}}{M_wc_w}$$

$$K_4=\frac{K_2}{K_1}(1-e^{-K_1t})+T_{w0}e^{-K_1t} \qquad K_5=\frac{K_3}{K_1}(1-e^{-K_1t}) \qquad K_6=\frac{h_{ew}K_4}{h_f+h_{ew}-h_{ew}K_5} \qquad K_7=\frac{h_f}{h_f+h_{ew}-h_{ew}K_5}$$

$$A=\frac{0.013h_{cfa}.R_1b}{\dot{m}_fc_w} \qquad B=\frac{b}{\dot{m}_fc_w}(h_fK_7-h_f-h_2-0.013h_{cfa}R_2) \qquad H_1=\frac{h_b}{h_b+U_b}$$

$$H_2=\frac{h_i}{h_i+h_o} \qquad C=\frac{b}{\dot{m}_fc_w}(h_fK_6+h_2T_a-0.013h_{cfa}R_3+0.013h_{cfa}\gamma R_1T_a^{\,2}+0.013h_{cfa}\gamma R_2T_a+0.013\gamma h_{cfa}R_3)$$

APPENDIX II [18]

$$h_{ra}=\varepsilon_g\sigma\left[\frac{(T_g+273)^4-(T_a+261)^4}{T_g-T_a}\right] \qquad h_{ca}=2.8+3v_a \qquad P_w=\exp\left[25.317-\left(\frac{5144}{273+T_w}\right)\right]$$

$$h_{rw}=\varepsilon_{eff}\sigma[(T_w+273)^2+(T_g+273)^2](T_w+T_g+546) \qquad P_g=\exp\left[25.317-\left(\frac{5144}{273+T_g}\right)\right]$$

$$h_{cw}=0.884\left[(T_w-T_{g/c})+\frac{(P_w-P_{g/c})(T_w+273)}{(268.9\times10^3-P_w)}\right]^{1/3} \qquad \frac{1}{\varepsilon_{eff}}=\frac{1}{\varepsilon_w}+\frac{1}{\varepsilon_g}-1$$

$$h_{ew}=16.273\times10^3h_{cw}\frac{(P_w-P_c)}{(T_w-T_c)} \qquad h_b=135 \qquad h_f=135$$

J Ther Eng, Vol. 12, No. 2, pp. 484−497, March, 2026

Journal of Thermal Engineering
Web page info: https://jten.yildiz.edu.tr
DOI: 10.14744/thermal.0001097

Research Article

Thermal regulation of an EV battery pack using mineral oil: Jordan case study

Heba ALZABEN[1,*], Tayseer FADDAH[1], Amir Al SAWAIR[2]

[1]*Department of Mechanical Engineering, Al Hussein Technical University, Amman, Jordan*
[2]*Department of Electrical Engineering, Al Hussein Technical University, Amman, Jordan*

ARTICLE INFO

Article history
Received: 30 October 2024
Revised: 05 May 2025
Accepted: 12 May 2025

Keywords:
Electrical Vehicle Battery; Immersion Cooling; Mineral Oil Cooling; Thermal Management

ABSTRACT

Thermal management is vital for optimizing the performance, lifespan, and safety of electric vehicle (EV) battery packs. This paper experimentally explores the use of mineral oil as a thermal regulation medium for EV batteries under Jordanian climate conditions. The study includes analyses of the electrical and thermal behavior of battery cells at different temperatures, the compatibility and impact of mineral oil on battery materials, and the practical feasibility of integrating such a system within an EV module. Battery testing was conducted under three cooling conditions: no cooling, air cooling, and mineral oil cooling. The electrical behavior of the battery was studied across these three cooling cases under 0.5C and 1C discharge rates, as well as under a 0.5C charge rate. The results indicate that mineral oil significantly moderates the battery temperature, keeping it within optimal operational ranges compared to other cooling methods. Specifically, the temperature delta is reduced by 50% at a discharge rate of 0.5C, while temperature uniformity is maintained within 2°C. This study designs and utilizes a mineral oil cooling system to investigate the thermal behavior of an existing battery module from the HTU student Racing Formula Team under Jordanian climatic conditions. The ambient temperatures during the testing period ranged between 28°C and 34°C. The findings suggest that mineral oil cooling is a feasible solution for improving the thermal management of EV batteries under variable conditions.

Cite this article as: Alzaben H, Faddah T, Al Sawair A. Thermal regulation of an EV battery pack using mineral oil: Jordan case study. J Ther Eng 2026;12(2):484−497.

INTRODUCTION

Electrical Vehicles (EV) are widely regarded as the future of the automotive industry [1, 2]. The battery, component of EVs, is responsible for storing energy and discharging it to the powertrain, making it a critical factor in the industry's advancement [3]. Proper thermal management of EV batteries is essential, as extreme heat can damage their chemistry [4], while harsh cold weather can degrade their performance and limit their capacity [5]. Most EV manufacturers recommend storing vehicles in environments protected from cold weather to safeguard battery performance [6, 7]. Consequently, a thermal management system for

*Corresponding author.
*E-mail address: heba.alzaben@htu.edu.jo

This paper was recommended for publication in revised form by Editor-in Chief Ahmet Selim Dalkilic

Published by Yıldız Technical University Press, İstanbul, Turkey
Yıldız Technical University. This is an open access article under the CC BY-NC license (http://creativecommons.org/licenses/by-nc/4.0/).

batteries is essential for maintaining battery temperature within an optimal range, minimizing thermal safety risks, and extending battery lifespan [8]. Rapid and efficient heat dissipation methods play a crucial role in ensuring longer battery life and safe operation [9]. To achieve optimal performance, lithium-ion batteries should within a temperature range of 15–35°C. Furthermore, the ideal operating temperature may vary depending on the geographical location of the country [9]. Nagasubramanian [10] investigated the impact of extremely cold temperatures on Li-ion battery cells, examining their electrical performance characteristics. Different tests were conducted to measure performance parameters across a temperature range of -40°C to 35°C. The study analyzed several parameters, including internal resistance (both ohmic and interfacial resistance between cathode and anode), specific energy, delivered power, energy density, and voltage drops across these temperature conditions. Similarly, a study conducted in the UK by Koncar et al. [5] assessed and quantified the impact of extreme cold temperatures on EV batteries. This study focused on vehicles utilizing Li-ion battery cells in their battery packs, where probabilistic analysis of power consumption was performed under different winter temperatures. The findings revealed that during the coldest ambient temperatures, an additional 630 MW of peak power was observed on the grid compared to optimal temperature conditions.

Different cooling methods are currently employed, including air cooling, liquid cooling, and phase change material (PCM) cooling. Among these methods, air cooling is the most commonly used because it is simple in design, lightweight, environmentally friendly, and cost-efficient. It is particularly suitable for mild temperature control compared to other cooling methods [9, 11]. In air cooling system, heat generated by the battery dissipates into the surrounding air, resulting in cooling based on the natural principles of heat transfer [12]. This method is generally preferred for small battery packs due to their lower power demands [12]. However, air cooling method has many limitations, including a low heat transfer coefficient, which restricts its ability to meet the cooling requirements in extreme temperatures. Additionally, temperature non-uniformity can lead to safety risks, including fire hazards [13]. Phase change material (PCM) cooling offers higher efficiency due to its high latent heat capacity. However, it is not suitable for EV batteries due to their low thermal conductivity and significant volume expansion during the melting process [11]. Also, materials used in PCM cooling typically exhibit high flammability [13], and when used directly, they pose risks such as toxicity and leakage [14]. These limitations are particularly challenging in the EV industry, especially in regions with extreme ambient temperatures. For example, in Jordan, summer temperatures can reach up to 45°C [15], directly affecting battery performance [8,9]. Furthermore, when battery temperatures rise to 60-70°C, the battery management system (BMS) may disconnect, negatively impacting battery health and overall performance [16]. Therefore, it is essential to explore various cooling methods capable of maintaining consistent thermal performance under extreme ambient conditions. Liquid cooling is considered a highly effective approach for EV battery thermal management due to its high thermal conductivity and heat capacity. It delivers up to 3,500 times the efficiency of air cooling, enabling energy savings of up to 40% [17]. Immersion cooling is an emerging technology for battery thermal management [13], classified into single phase cooling (utilizing sensible heat) and two-phase cooling (utilizing latent heat), both enhance cooling performance by dissipating heat from battery cells. Immersion cooling also holds significant potential for preventing thermal runaway and its subsequent propagation [13]. Several studies have investigated the use of liquid cooling methods, particularly mineral oil for lithium-ion batteries cooling. Trimbake et al. [11] were the first to experimentally examine mineral oil-based cooling for lithium-ion batteries, analyzing charging and discharging characteristics in terms of temperature uniformity both among cells and within individual cells. Their findings indicated that mineral oil maintained uniform temperatures (within 1°C) and suggested that modular jet oil cooling is a viable cooling option for lithium-ion battery packs. Liu et al., [18] compared mineral oil and natural ester oil for lithium-ion battery immersion cooling. Their study found that both oils effectively reduced battery temperature and restricted temperature variation among cells to within 2°C. The researchers suggested that natural ester oil could be a promising candidate for immersion cooling of lithium-ion batteries. Satyanarayana et al. [19] conducted experimental immersion cooling studies using mineral oil and therminol oil on a 20-cell, 10A lithium-ion battery stack at different discharge rates. Their findings revealed that, at a 3C discharge rate, the maximum battery module temperature was reduced by 43.83% with forced air cooling, 49.17% with therminol oil cooling, and 51.54% with mineral oil cooling compared to natural air-cooling method [19]. However, this study utilized partial immersion cooling. The results demonstrated that immersion cooling provides superior temperature control across different discharge rates. Among the tested methods, mineral oil cooling proved to be more effective than therminol oil cooling due to its lower viscosity, leading to better heat dissipation. Overall, mineral oil cooling systems enhance battery safety by minimizing the risk of thermal runway [11, 12], preventing direct oxygen contact with battery cells in the case of punctures, and demonstrating superior heat dissipation efficiency compared to air cooling [11].

Lecuna et al. [20] compared mineral oil to other synthetic and natural liquids used in power transformers cooling. Their study highlighted that mineral oil not only performs effectively in narrow channels but also exhibits a superior convection heat transfer coefficient, making it a viable cooling solution for compact battery systems. Mineral oil is widely recognized for its high thermal conductivity, high

heat capacity, good electrical insulation, low cost, low toxicity, non-combustibility, low corrosion properties, and it is available in large quantities [18]. However, oil-immersed cooling systems also present certain limitations [18]. Studies have shown that beyond a certain flow rate, further increases in coolant circulation might reduce temperatures but at the cost of higher pumping power requirements [18]. To the best of our knowledge, no previous study has investigated the thermal management of lithium-ion batteries using mineral oil cooling systems under Jordanian climate conditions, where heat dissipation rates are significantly affected by ambient conditions such as temperature and pressure [21-23]. This study investigates the thermal and electrical behavior of lithium-ion batteries and evaluates long-term material compatibility under Jordanian climatic conditions. The findings provide novel insights into the practical feasibility and effectiveness of mineral oil-based cooling for EV batteries. Thus, it provides a novel insight into its practical feasibility and effectiveness.

MATERIALS AND METHODS

Project Description

The proposed method of using mineral oil for cooling EV batteries offers a dual advantage: it not only effectively cools the batteries but also insulates them from external extreme temperatures that could impact their performance, safety, and service life. Mineral oil is intended to thermally regulate the battery cells, ensuring they remain within an optimal temperature range, as specified in datasheets and studies on battery chemistry and performance [11-19]. Additionally, its insulative properties can help mitigate performance limitations caused by extreme temperatures [10]. Regarding safety requirements for lithium-ion batteries, one of the primary concerns is excessive temperature rise, which may lead to an increased risk of cell explosions [24]. Another major risk is punctures in any of the battery cells. If the inner battery material comes into contact with oxygen molecules, a chemical reaction could trigger ignition and cause a chain reaction within the cells [25, 26]. Therefore, by using mineral oil for battery cooling, the risk of oxygen to battery cells is significantly reduced. Additionally, integrated control systems can be explored to detect punctures in the cells, providing early alerts and allowing sufficient time for professional intervention, ultimately preventing fire or explosion hazards. Mineral oil is known for its excellent thermal properties and insulation capabilities, as presented in Table 1 below. It is cost effective, widely available, biodegradable and environmentally friendly, non-toxic, and non-combustible material [11]. In addition, mineral oil has the potential to stabilize battery temperature under both high heat and severe cold conditions, ensuring optimal battery performance and longevity.

As presented in Table 1, mineral oil is suitable for most applications due to its high flash and ignition temperatures, allowing it to withstand extreme thermal conditions [27]. In general, maintaining a stable battery temperature is crucial for optimal performance, with the peak efficiency range typically between 15°C and 35°C [9]. However, keeping batteries within this range can be challenging, especially when external environmental factors significantly impact temperature. This research aims to mitigate the effects of external temperature fluctuations, whether high heat during the summer or extreme cold in winter, where many EVs lose approximately 30% of their expected driving range [3]. During cooling, the batteries are fully submerged in mineral oil, which is continuously circulated using a pump connected to a small reservoir. A heat exchanger is incorporated into the system to cool the oil before it is recirculated back to the battery pack, effectively maintaining optimal operating temperatures. For heating in cold winters conditions, heating coils will be integrated into the oil transfer tubes, allowing the oil to be warmed before circulating through the battery system. This regulated heating process is crucial for maintaining battery efficiency and longevity, preventing performance loss due to low temperatures.

In this study, an accumulator prototype, designed by the HTU Racing Formula Team was used as presented in Figure. 1. This prototype is set to compete in the 2024 Formula Student competition, where the intense racing

Table 1. Mineral oil thermal and electrical properties

Properties	Specifications
Boiling temperatures	Greater than 280°C and an auto ignition temperature > 320°C [27].
Freezing temperature	-40°C [27]
Density (ρ)	924 kg/m^3 [12]
Viscosity (μ)	0.05 Pa.s [12]
Thermal conductivity (k)	0.1296 W/m·K [29,30]
Heat capacity (C_p)	1.9 KJ/kg K [28]
Electrical conductivity (σ)	10^{-12} to 10^{-15} (S/m) [31]

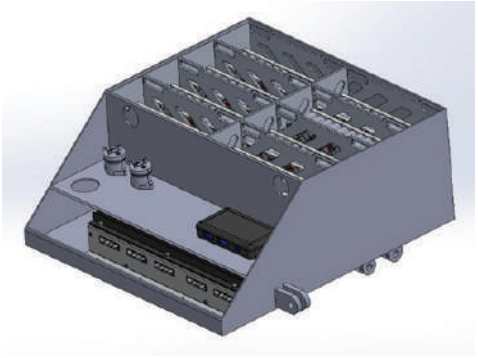

Figure 1. Battery accumulator prototype (Obtained from the HTU Racing Formula Team).

conditions are expected to exhaust and overheat the batteries. Testing the proposed thermal management system under these conditions will provide valuable insights into its effectiveness and performance.

Experimental Setup

The experiment was conducted between April and June 2024 under hot Jordanian conditions, with ambient temperatures ranging from 28°C to 34°C. The experimental setup is summarized in the flow chart presented (Fig. 2).

The set up for testing the electrical and thermal characteristics of the batteries utilized a 12S/8P Panasonic (Tesla) 18650 Li-ion Battery Pack. This battery pack was designed, manufactured, and provided by the HTU Racing Formula Team. It consists of 96 Li-ion cells, capable of delivering a maximum voltage of 50.4V at full charge, as illustrated in Figure 2. The battery data presented in Table 2 was obtained through extensive and repeated testing of a single cell by the HTU Racing Formula Team. (Fig. 3) A total of 28 thermistors (10k NTC type) were used in the experiment. Their placement included 24 thermistors placed on the negative tabs of the cells (2 per tab), one thermistor at the container inlet, one thermistor at the container outlet, one thermistor for ambient temperature, and one thermistor to monitor the load temperature for safety purposes. A microcontroller-based circuit was implemented, comprising 4 microcontroller units (MCUs) connected via serial communication with a PC. The system recorded data at a sampling rate of 30 seconds, ensuring precise monitoring of thermal and electrical parameters.

The second component used in the research is battery Management System (BMS), provided by the HTU Racing Formula Team (Supower *Battery, China). It is* a 12S pack, and the expected voltage gap between the cells is 2.5-4.2 Volt. The selected BMS is rated as operating on a 44.4 V pack, which is just above the nominal voltage of the used module allowing safe operation of the cells. The cut-off limit of the BMS was hard-wired to stop discharge at 38.5 V.

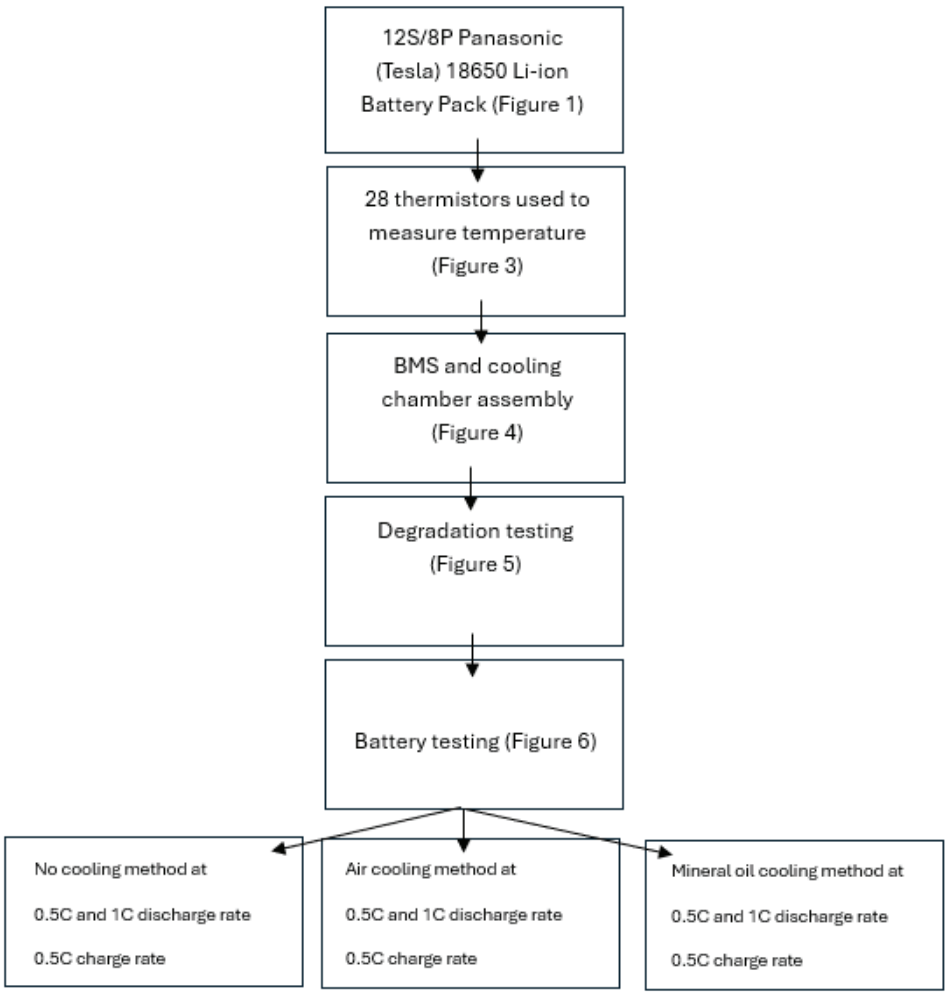

Figure 2. Experimental set up flow chart.

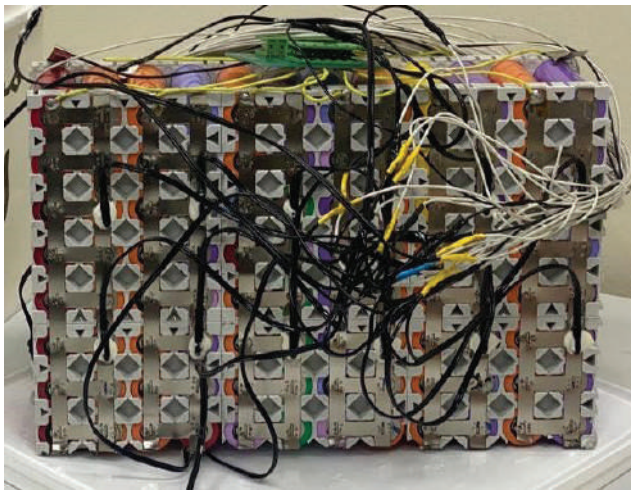

Figure 3. Battery module used for testing (Obtained from the HTU Racing Formula Team).

Table 2. Battery module testing characteristics (obtained from the battery data sheet)

Properties	Specifications
Battery capacity	24 Ah
Nominal voltage	43.2 V
Cutoff voltage	30 V
Charging voltage	50.4 V
Weight	4.6 kg
Size	7cm×24cm×17cm

Table 3. Pierburg Pump Specifications (Pierburg CWA 150 Tecomotive, Germany obtained from [32])

Properties	Specifications
Operating Voltage	9 - 16 V
Current Consumption	15 A maximum
Nominal diff. Pressure	Greater than 1.4 bar
Max Speed	6700 rpm
Weight	1 kg

This poses a limit on the discharge and charge cycles, utilizing only 60% of the pack capacity. The third component used in the experimental setup is Coolant Pump (Pierburg CWA 150 Tecomotive, Germany). The pump specifications are summarized in Table 3 below. This pump was also provided by the HTU Racing Formula Team. It is considered a standard automotive pump, which is suitable for different types of fluids.

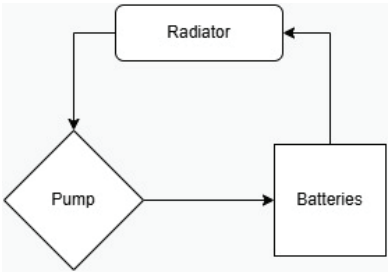

Figure 4. Schematic diagram for the cooling system used in the testing.

The fourth component used in the experimental setup is a cooling chamber. A metal container with one inlet and one outlet was designed and manufactured to place the battery module with proper spacing for oil to flow around (as presented in Fig. 4) to allow for effective heat transfer in the chamber while achieving the desired immersion cooling with mineral oil. Furthermore, a household fan was used to imitate the dispersed and turbulent flow observed in vehicles with active air cooling. Air cooling was achieved after directing the natural flow of air caused by a vehicle moving towards the battery pack. The fan will direct a high-speed turbulent flow of air towards the battery cells.

Material Degradation Testing

Material degradation testing is important due to lengthy battery exposure to mineral oil; therefore, it was conducted to evaluate the long-term effects of mineral oil on different components of an EV battery module (Fig. 5). This type of testing is very important, as the integrity of materials with direct contact with the cooling medium has an impact on safety, efficiency, and durability of the battery system.

The experiment involved submerging a complete battery module, including all its associated wiring and printed circuit boards (PCBs) for one month in mineral oil (100% Paraffin). This setup is designed to simulate the actual

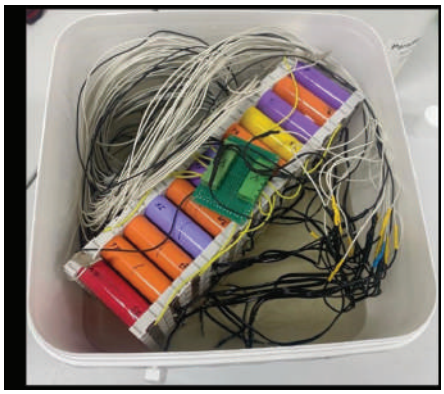

Figure 5. Degradation testing for the battery pack immersed in mineral oil.

conditions under which the battery would operate under a mineral oil environment. Two lithium-ion cells were tested; one covered with a heat shrink and another uncovered cell, to assess the impact of mineral oil on the cell casings. Over one month period, observations and measurements were recorded to detect any signs of material degradation, chemical reactions, or physical alterations to battery cells. It is observed that there are no significant changes in the structure or functionality of the battery module, wiring, PCBs, or the lithium-ion cells, which confirm the compatibility of mineral oil as a cooling medium with the materials being used in the EV battery systems. However, it was observed that the thermal paste used to mount the thermistors to the batteries had loosened when immersed in mineral oil, in which it was suggested that the thermal paste is not suitable to be used with mineral oil, which is likely due to the oil's properties affecting the adhesive quality of the thermal paste. Additionally, mineral oil affects certain types of plastics, specifically polycarbonate (PC) and acrylonitrile butadiene styrene (ABS), which are known for their brittle nature and are not used in battery packs [33]. Furthermore, mineral oil also demonstrated properties that act as a protective insulator for metals while reducing the risk of corrosion. This characteristic adds another layer of benefit for using mineral oil in battery systems, as it could potentially enhance the longevity and reliability of metallic components [34]. In future experimental trials, different placement strategies for the thermistors will be adopted along with the use of an alternative type of thermal glue specifically compatible with mineral oil and its superior adhesive properties under test conditions, which will consequently improve the reliability of temperature measurements.

Battery Testing

The testing methodology was designed to evaluate the efficiency of different cooling methods for an EV battery, using an existing battery module from the HTU Racing Formula Team. This study focused on three cooling cases: no cooling, air cooling, and mineral oil cooling. First, the battery module was placed in a custom-designed container,

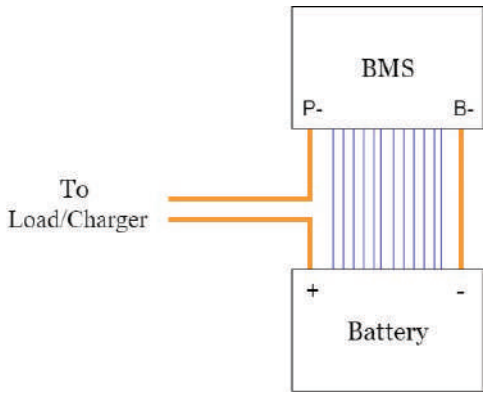

Figure 6. Testing power connection.

Table 4. Charge and Discharge Cycles

Cooling cases	Discharge rate	Charge rate
No cooling	0.5C	0.5C
	1C	
Air cooling	0.5C	0.5C
	1C	
Mineral oil cooling	0.5C	0.5C
	1C	

linked to a BMS (Fig. 6) and interfaced with four Arduino microcontrollers. These controllers were connected to thermistors positioned around the battery module to record temperature data every 30 seconds. Arduino boards were used to facilitate real-time temperature monitoring, which enabled continuous measurement of thermal metrics to assess the performance of the cooling system.

Data logging was programmed in Python, which not only collected the data from the thermistors but also processed it into a structured format. Then, it was exported to an Excel spreadsheet for further analysis. The testing was structured among three parameters: a discharge rate of 1C (equivalent to 24 Amps), a discharge rate of 0.5C (equivalent to 12 Amps) alongside a charging protocol set at 0.5C (equivalent to 12 Amps). The selected discharge and charge rates were limited to the existing battery load and a more spacious area compared to the lab, where the experiments were conducted, to utilize higher rates of charge. In addition, battery module testing under different thermal loads was conducted. Battery testing cases are presented in table 4 below while focusing on the overall capacity to maintain optimal battery temperatures, enhance battery efficiency, and potentially extend the battery's operational lifespan. In this research the 1C charge rate was not investigated as it is utilized in more intensive EV battery studies, however, it will be considered for future work studies.

Review of Literature Related to Mineral Oil Cooling Used for Lithium-Ion Batteries

A comparison with similar studies involving the use of mineral oil cooling for lithium-ion batteries is presented in this section. Table 5 provides a direct comparison among different studies while considering the temperature delta, type of cells number of cells, and nature of the work. In this study the temperature delta was within 2°C where 18650 Panasonic cell types were used with 96 cells in total. The findings of this study align closely with those of Trimbake et al. [11], Lui et al, [18], and Satyanarayana et al. [19], in which mineral oil demonstrated significant temperature reduction (~18°C in this study, ~15–20°C in their studies).

The temperature uniformity observed in this study was within 2°C that matches findings from the literature. This study tested mineral oil cooling with an operational

Table 5. Summary of research work related to mineral oil cooling for e-vehicle battery pack

Literature	Temperature Delta (ΔT, °C)	Type of cells	Number of Cells
Trimbake et al. [11]	< 1	18650	4 cells
Ya-Chi Ho [35]	>3	18650	1 cell
Satyanarayana et al. [19]	< 2	18650	20 cells
Celen [36]	>5	LiFePO4 Pouch	60 cells
Ya-Chi Ho [37]	>2	18650	1 cell
Lui et al. [18]	>2	18650	4 cells

EV battery module under Jordan climate (28°C–34°C) with full immersion cooling for the battery pack, filling a gap in practical implementation studies. The results also indicate that mineral oil cooling systems not only ensure effective thermal regulation but also maintain material integrity and safety, aligning with the goals of previous literature while expanding its scope. Its consistent performance across both mean temperature and low maximum temperature delta offers promising implications for its utilization in improving battery efficiency, lifespan and safety. Nevertheless, the limited availability of published data and long-term documentation regarding the performance of mineral oil immersion cooling for lithium-ion batteries leads that most battery producers hesitating to adopt these methods in their industry. Furthermore, the scarcity of available data highlights a significant knowledge gap within the industry concerning the environmental requirements for operating an oil immersion cooling method for different applications [38]. Therefore, it is important to investigate further the mineral oil cooling under different environmental conditions and verify that it is a suitable method for thermal management of lithium-ion batteries.

Uncertainty Analysis

There are many variables that have a significant impact on the accuracy of the measurements, such variables include environmental conditions and inadequate calibration [39]. To enhance the accuracy and reliability of the collected data, an uncertainty analysis is conducted using the specifications provided in the manufacturers' datasheets. The stated accuracies for the experimental devices were as follows: ±1°C for the thermistor, and ±3% for the pump. The uncertainty analysis accounted for the experimental equipment used, as well as potential sources of error such as probe positioning, calibration quality, and inherent measurement variability. The uncertainties associated with the main experimental parameters were calculated using Equation (1) [39].

$$U_R = \left[\left(\frac{\partial R}{\partial X_1}U_1\right)^2 + \left(\frac{\partial R}{\partial X_2}U_2\right)^2 + \left(\frac{\partial R}{\partial X_3}U_3\right)^2 + \ldots\ldots + \left(\frac{\partial R}{\partial X_n}U_n\right)^2\right]^{\frac{1}{2}} \quad (1)$$

R denotes to the dependent experimental parameter, and U_R represent its associated uncertainty. The independent experimental parameters are denoted as X_1, X_2, X_3,…, X_n, with their respective uncertainties given by U_1, U_2, U_3,…, U_n. Therefore, it is very important to ensure that all devices and sensors are well calibrated prior to experimental work in order to minimize systematic errors.

RESULTS AND DISCUSSION

Electrical Study Results: Discharge Behavior

Depth of discharge (DOD) was investigated as part of an electrical study at two discharge rates (e.g., 0.5C and 1C) among three cooling cases as presented in Figure 7 below, which will help to study the effect of different cooling methods towards battery discharge capacity. DOD is defined as a percentage of the discharge capacity relative to the maximum available capacity of the battery cell [40], in which a higher DoD means a larger amount of capacity being discharged. For EV vehicles a higher capacity is desirable, as it means a larger range for the vehicle driven.

It is observed that the BMS cutoff voltage (ca. 39V) allows the battery to discharge at a capacity of around 65 % (Fig.7), though this capacity varies depending on thermal and electrical control. The initial voltage was found to drop significantly at higher discharge rates. The air-cooling method reduces the voltage drop for the two discharge rates (i.e., 0.5C and 1C). At a 0.5C discharge rate, mineral oil cooling maintains a consistent slope throughout the discharge process, achieving a higher depth of discharge (DoD) compared to the no-cooling case. At a 1C discharge rate, the cells cut off with a slightly higher DoD, indicating that the internal resistance of the cells (likely due to increased heat generation) is deviating more. This is expected, as all cells experience an increase in internal resistance under high-power discharge conditions. Table 6 below summarizes the depth of discharge (DoD) for the two discharge rates, in which the DoD varies slightly with C-rate and thermal mitigation. This comparison helps to study the effect of different cooling methods along with discharge rates on the capacity consumption of the cells. These results are best interpreted with the temperature

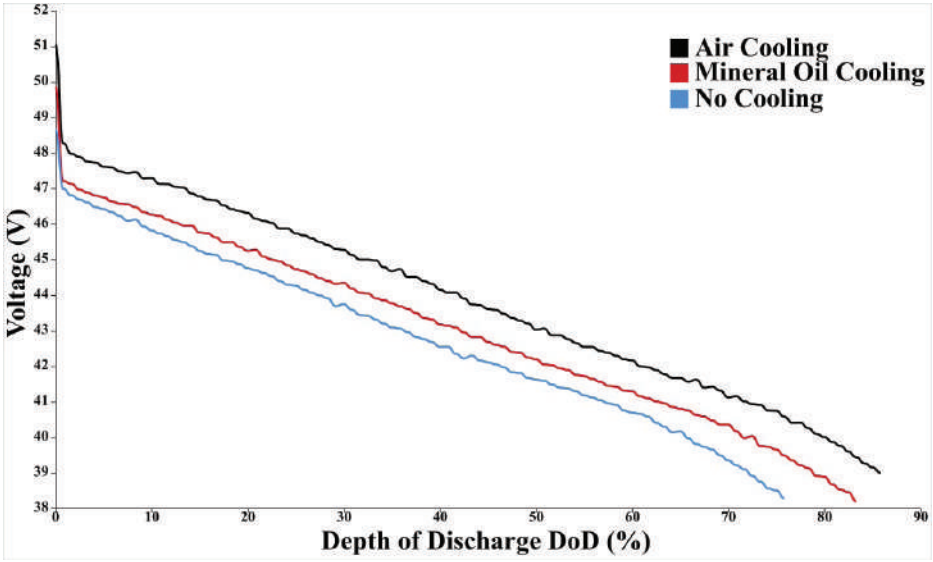

(a)

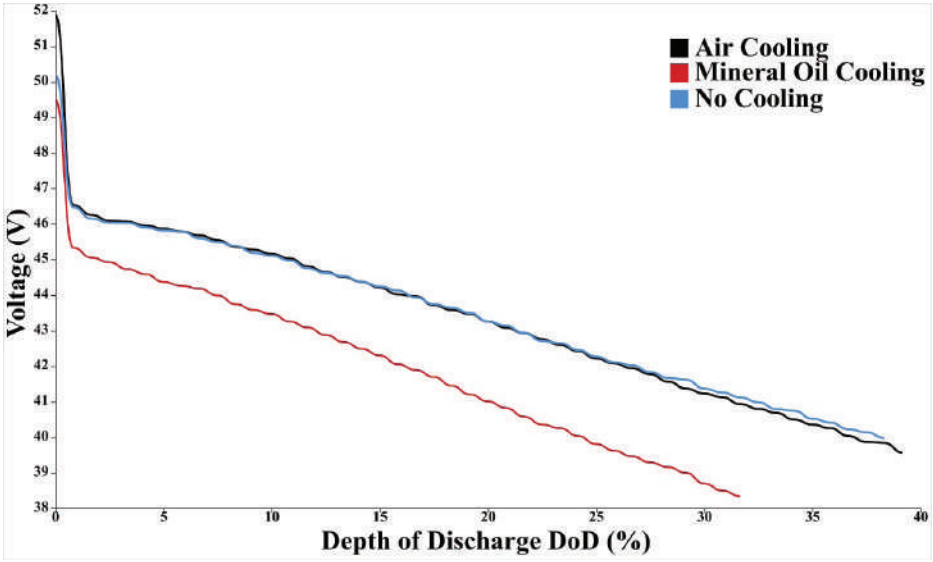

(b)

Figure 7. Depth of Discharge (DoD) of the battery pack among different cooling methods, with discharge rates of (a) 0.5C, and (b)1C.

Table 6. Depth of discharge (DOD) for discharge cycles

Depth of discharge by cooling method (100%)			
Discharge current	**No cooling**	**Air cooling**	**Mineral oil cooling**
0.5C	63.6%	73.3%	69.8%
1C	65.3%	67.6%	53.6*%

delta graphs (please check Figures. 9,10, and 11) in the thermal study section below, as they show the effect of heating which changes the battery electrical behavior. As an example, of mineral oil cooling, battery cells achieve a high DoD at 0.5C discharge rate compared to 1C. Therefore, in order to effectively interpret the noted value of 53.6 %, further investigations with a programmable cut-off BMS are required. The BMS used for this study had a relatively high cut-off voltage. Future work will include a suitable cut-off value in the 32-34 V range.

Electrical Study Results: Charge Behavior

The charging method selected in this study is the constant current-constant voltage (CC-CV) method because it allows maximum capacity utilization and ends charging with a stable terminal voltage for the battery pack. This method is divided into two stages as follows:

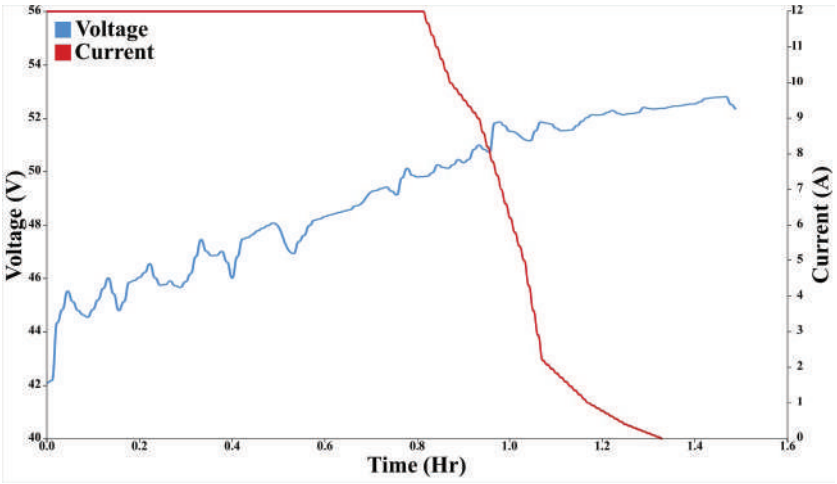

(a)

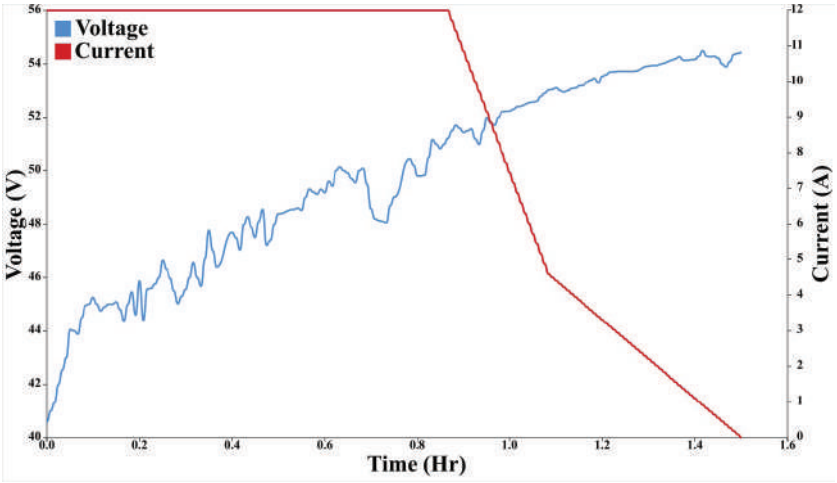

(b)

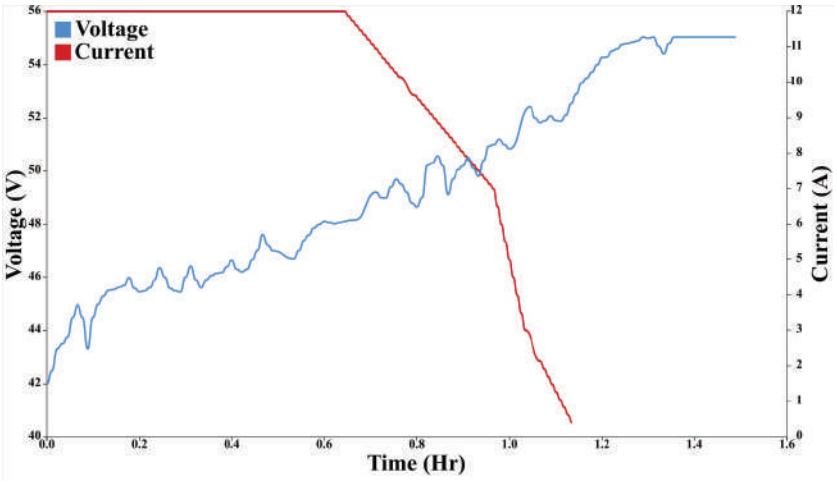

(c)

Figure 8. The electrical behavior of the battery pack during charge at 0.5C, showing CV and CC phases among different cooling cases (a) No cooling (b) Air cooling (c) Oil cooling.

Stage 1: Bulk Charging (Constant Current CC). The current is kept constant at a level usually equal or lower than 1C, while the voltage level rises to the float voltage.

Stage 2: Float Charging (Constant Voltage CV). Once the voltage reaches the pack's maximum voltage, the charger stabilizes at a slightly higher voltage called the float voltage. In this phase, the current organically decreases as the state of charge (SoC) of the cells reaches 100%.

Figure 8 presents different charge cycles among the three cooling cases, with cycle duration varying for each case. This variation is likely due to thermal regulation, which enhances the cells' ability to discharge and charge. Charging for both the no cooling and oil cooling cases was completed in less than 1 hour, with the oil-cooling case reaching a higher float voltage. This indicates that more capacity was charged within the same timeframe. The air-cooling case took 1.2 hours to complete, demonstrating superior performance compared to the no cooling case in terms of charge and discharge capacity. It was observed that stage 1 ended at around 70% SoC, while Stage 2 continued until the end of the charging process. The pulsing in voltage levels is attributed to the charger's properties, which cause oscillations until the desired float voltage is reached, after which the voltage stabilizes.

Thermal Study Results: 0.5C Discharge

The data obtained from the thermal investigation of electric vehicle (EV) battery cooling methods during a 0.5C discharge cycle illustrates distinct temperature management capabilities of no cooling, air cooling, and mineral oil cooling systems. While analyzing the mean temperature and the maximum temperature delta graphs, a notable difference in performance was observed among different cooling methods under constrained testing conditions. As an example, in Figure 9, the mean temperature reveals distinct trajectories for the three cooling cases. With no cooling, the temperature steadily rises, highlighting a lack of heat mitigation. For air cooling it does not stabilize effectively compared to mineral oil cooling. Despite starting at a higher initial temperature due to elevated ambient conditions, overall mineral oil cooling consistently maintains the lowest and had the most stable mean temperature throughout the testing, which suggests its superior capability in heat absorption and dissipation. The main reason why the experimental runs have different initial temperatures is due to the test area being affected by the ambient temperature because experiments were conducted on different times of the day, which will be eliminated in future experimental runs.

For the maximum temperature delta presented in Figure 10, different variations in the peak temperatures relative to initial values were observed. For no cooling case, a sharp rise was observed that causes a potential risk for thermal runaway. On the other hand, air cooling showed an improved behavior but allows for a considerable temperature increase. Mineral oil cooling demonstrated the smallest increase in the maximum temperature delta while starting from a higher baseline due to the surrounding ambient conditions. This confirms its effectiveness in managing heat under less-than-ideal initial conditions, further proving its robustness as a thermal regulation mechanism.

Thermal Study Results: 1C Discharge

For the 1C discharge rate, it is observed that the temperature rises sharply for the no cooling scenario as presented in Figure 11, emphasizing the inadequacy of passive thermal management under intense discharge conditions. The rapid temperature increase from the initial state could potentially lead to thermal runway. In contrast, the air-cooling

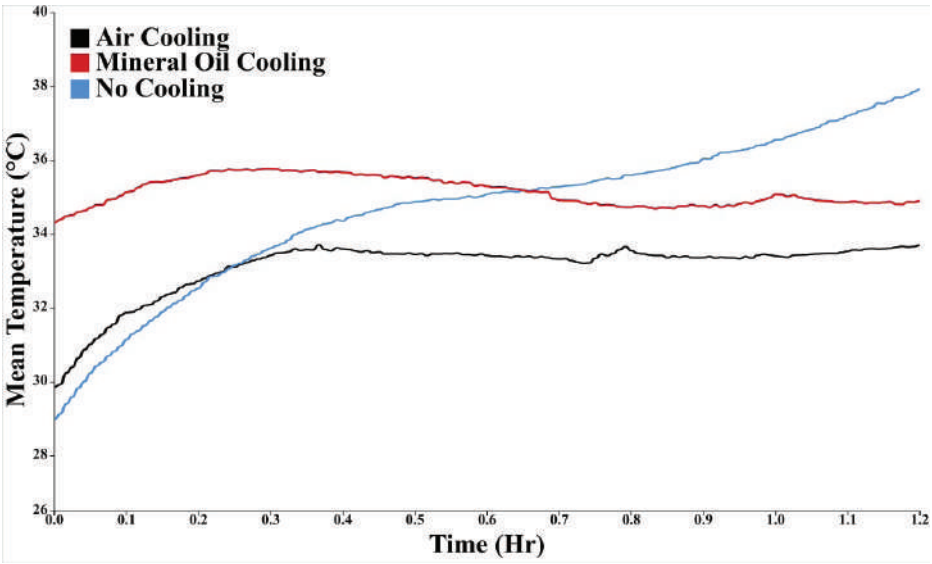

Figure 9. The mean temperature across the cells at 0.5C discharge rate for three cooling cases.

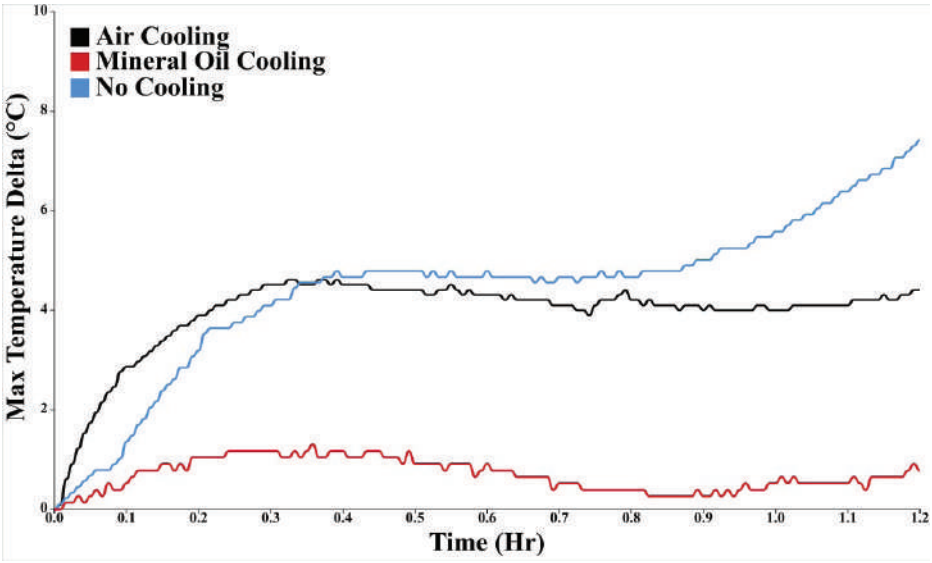

Figure 10. The maximum temperature delta at 0.5C discharge rate among three cooling cases.

case moderates the temperature rise but fails to stabilize after the initial period, indicating that while it can dissipate heat, it is insufficient to manage the sustained thermal output under 1C discharge rate. For mineral oil cooling, the temperature remains stable and low throughout the cycle compared to no cooling case. Maintaining thermal stability is crucial for the battery, as it helps to prevent excessive thermal stress that could degrade battery components and reduce performance.

These experiments were conducted using a suboptimal heat exchanger in a confined space, which may have hindered heat dissipation and led to higher ambient temperatures. Furthermore, the proximity of resistor loads to the pump contributed to localized heat generation, potentially worsening ambient conditions within the cooling system operation. Despite these limitations, the performance of mineral oil cooling compared to other methods highlights its potential effectiveness in real-world applications.

Thermal Study Results: 0.5C Charge

The thermal performance of different cooling methods at 0.5C charge rate for EV battery packs is presented in Figure 12 for the maximum temperature delta, such data is important to select the proper cooling method that can impact battery efficiency and lifespan during the charging cycle.

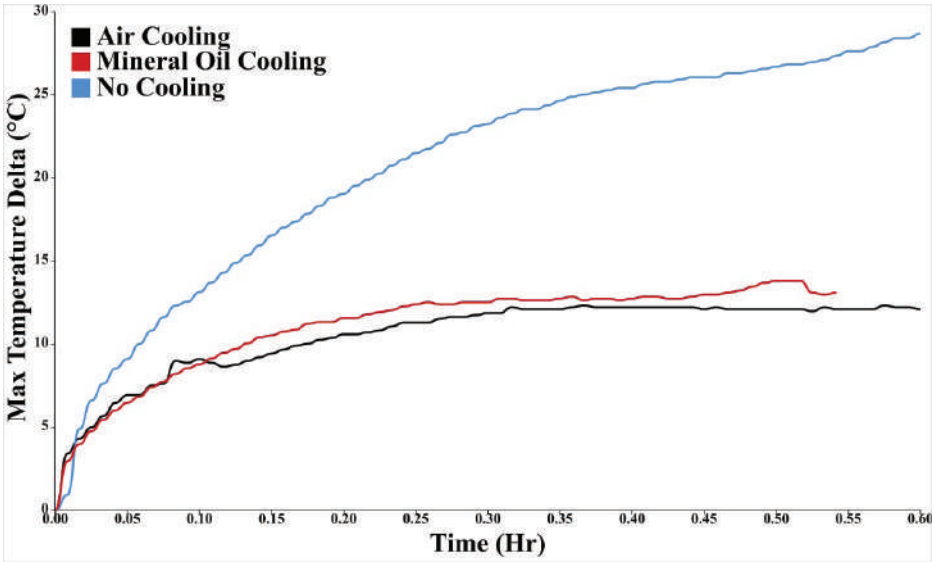

Figure 11. The maximum temperature delta at 1C discharge rate among three cooling cases.

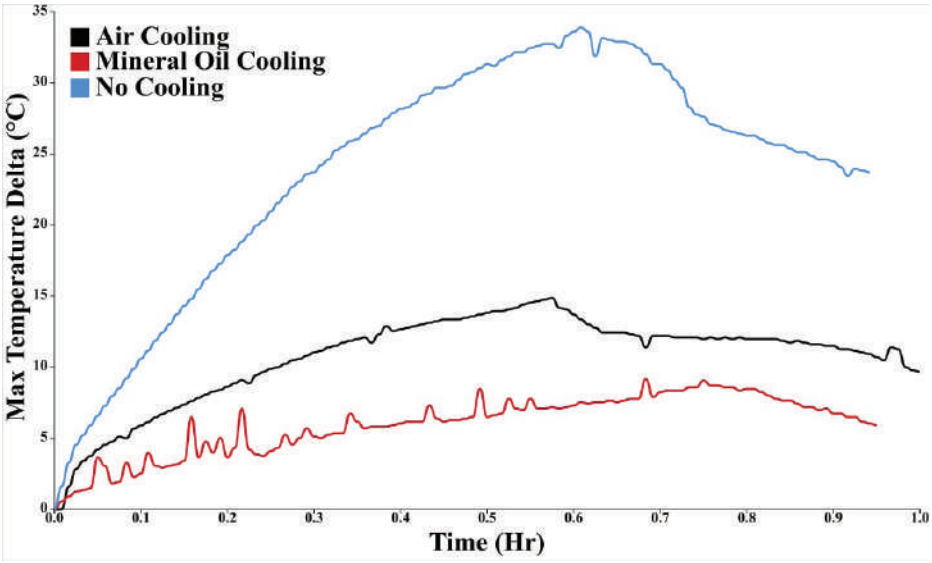

Figure 12. The max temperature delta at 0.5C charge rate among three cooling cases.

From Figure 12, the no cooling case shows a drastic increase in the maximum temperature delta, highlighting the high thermal risk associated with unmanaged charging. On the other hand, air cooling cases show a lower temperature rise, yet it plateaus at a moderate level, which indicates some heat accumulation. For mineral oil cooling, it maintains the lowest and most consistent maximum temperature delta, affirming its effectiveness in minimizing temperature fluctuations that can accelerate battery degradation.

CONCLUSION

This study integrated mineral oil cooling system into an operational EV battery module under real-world climatic conditions, demonstrating its feasibility in addressing thermal challenges. Unlike prior studies that focused on partial immersion cooling experiments or controlled laboratory environments, this research provides practical insights on the performance and material compatibility of full immersion cooling systems. The use of mineral oil for lithium-ion batteries has attracted significant interest among many researchers globally; however, most investigations remain exploratory, involving experimental approaches. Mineral oil has high thermal capacity and effective heat transfer characteristics, which make it an exceptionally viable solution for thermal management in EV batteries. Its ability to maintain battery efficiency and safety across varying environmental conditions, particularly under high discharge rates, offers a notable advantage. In this study the temperature delta for mineral oil cooling method was within 2°C, which is consistent with previous observations found in the literature. Notably, at a 1C discharge rate, the mineral oil cooling method achieved a lower depth of discharge (DoD) (53.6%) compared to air cooling (67.6%). This suggests that mineral oil cooling helps to conserve battery capacity and mitigates the buildup of internal resistance.

For future work, it is recommended to conduct lithium-ion battery testing under Jordanian winter conditions and under telemetry monitoring to further investigate the impact of ambient temperature on mineral oil characteristics and to optimize cooling solutions for diverse environmental conditions. A comprehensive thermal analysis comparing air and mineral oil cooling will be performed, incorporating heat dissipation and energy consumption calculations to theoretically validate the experimental results. Additionally, expanding the study to include a wider range of C-rates, which would require the use of industrial resistors capable of handling the specified high discharge rates.

ACKNOWLEDGMENT

Authors would like to express their appreciation to the HTU Student's Racing Formula Team for their continuous support and collaboration throughout this project. The authors also extend special thanks to Eng. Yousef Okour, Manager of the HTU Workshops, for his ongoing support and valuable guidance..

AUTHORSHIP CONTRIBUTIONS

Conceptualization, Methodology, Supervision, Writing – Original and review draft Preparation: [Alzaben.H], Formal Analysis and Investigation, Writing – Review and Editing, Experimentation, Resources: [Faddah, T, AlSawair, A].

DATA AVAILABILITY STATEMENT

The authors confirm that the data that supports the findings of this study are available within the article. Raw data that supports the finding of this study are available from the corresponding author, upon request.

CONFLICT OF INTEREST

Authors declare no conflicts of interest in this article.

ETHICS

There are no ethical issues with the publication of this article.

FUNDING

This Project was Funded By Al Hussein Technical University (HTU), Amman, Jordan.

STATEMENT ON THE USE OF ARTIFICIAL INTELLIGENCE

Artificial intelligence was not used in the preparation of the article.

REFERENCES

[1] Skouras TA, Gkonis PK, Ilias CN, Trakadas PT, Tsampasis EG, Zahariadis TV. Electrical vehicles: Current state of the art, future challenges, and perspectives. Clean Technol 2020;2:1–16. [CrossRef]

[2] Khaleel M, Nassar Y, El-Khozondar HJ, Elmnifi M, Rajab Z, Yaghoubi E, et al. Electric vehicles in China, Europe, and the United States: Current trend and market comparison. Int J Electr Eng Sustain 2024;1–20.

[3] Faraz A, Ambikapathy A, Thangavel S, Logavani K, Prasad GA. Battery electric vehicles (BEVs). Springer 2021;137–160. [CrossRef]

[4] Zhang J, Zhang L, Sun F, Wang Z. An overview on thermal safety issues of lithium-ion batteries for electric vehicle application. IEEE Xplore 2018;6:23848–23863. [CrossRef]

[5] Koncar I, Bayram IS. A probabilistic methodology to quantify the impacts of cold weather on electric vehicle demand: A case study in the UK. IEEE Xplore 2021;9:88205–88216. [CrossRef]

[6] Jaguemont J, Boulon L, Dubé Y. A comprehensive review of lithium-ion batteries used in hybrid and electric vehicles at cold temperatures. Appl Energy 2016;164:99–114. [CrossRef]

[7] Senol M, Bayram IS, Naderi Y, Galloway S. Electric vehi-cles under low temperatures: A review on battery performance, charging needs, and power grid impacts. IEEE Xplore 2023;11:39879–39912. [CrossRef]

[8] Gungor S, Gocmen S, Cetkın E. A review on battery thermal management strategies in lithium-ion and post-lithium batteries for electric vehicles. J Therm Eng 2023;9:1078–1099. [CrossRef]

[9] Debbarma A. Thermal management system of e-vehicle Li-ion battery modules: A comprehensive review. J Therm Eng 2021;10:1679–1697. [CrossRef]

[10] Nagasubramanian G. Electrical Characteristics of 18650 Li-ion Cells at Low Temperatures. Springer 2001;31:99–104. [CrossRef]

[11] Trimbake A, Singh CP, Krishnan S. Mineral oil immersion cooling of lithium-ion batteries: an experimental investigation. J Electrochem Energy Convers Storage 2022;19:021007. [CrossRef]

[12] Adhikari N, Bhandari R, Joshi P. Thermal analysis of lithium-ion battery of electric vehicle using different cooling medium. Appl Energy 2024;360:122781. [CrossRef]

[13] Liu Y, Aldan G, Huang X, Hao M. Single-phase static im-mersion cooling for cylindrical lithium-ion battery module. Appl Therm Eng 2023;233:121184. [CrossRef]

[14] Xu L, Wang S, Xi L, Li Y, Gao J. A Review of Thermal Management and Heat Transfer of Lithium-Ion Batt eries. Energies 2024;17:3873. [CrossRef]

[15] WorldData.info. The climate in Jordan. Available at: https://www.worlddata.info/asia/jordan/climate.php. Accessed on Dec 20, 2024.

[16] Andrea D. Battery management systems for large lithium-ion battery packs. Massachusetts;Artech house; 2010.

[17] Wu C, Sun Y, Tang H, Zhang S, Yuan W, Zhu L, and Tang Y. A review on the liquid cooling thermal management system of lithium-ion batteries. Applied Energy, 375, 124173; 2024. [CrossRef]

[18] Liu J, Chen H, Yang M, Huang S, Wang K. Comparative study of natural ester oil and mineral oil on the applicability of the immersion cooling for a battery module. Renew Energy 2024;224:120187. [CrossRef]

[19] Satyanarayana G, Sudhakar DR, Goud VM, Ramesh J, Pathanjali GA. Experimental investigation and comparative analysis of immersion cooling of lithium-ion batteries using mineral and therminol oil. Appl Therm Eng 2023;225:120187. [CrossRef]

[20] Lecuna R, Delgado F, Ortiz A, Castro PB, Fernandez I, Renedo CJ. Thermal-fluid characterization of alternative liquids of power trans-formers: A numerical approach. IEEE Xplore 2015;22:2522–2529. [CrossRef]

[21] Zhang X, Li Z, Luo L, Fan Y, Du Z. A review on thermal management of lithium-ion batteries for electric vehicles. Energy 2022;238:121652. [CrossRef]

[22] Shahjalal M, Shams T, Islam ME, Alam W, Modak M, Hossain SB, Iqbal A. A review of thermal management for Li-ion batteries: Prospects, challenges, and issues. J Energy Storage 2021;39:102518. [CrossRef]

[23] Ma S, Jiang M, Tao P, Song C, Wu J, Wang J, et al. Temperature effect and thermal impact in lithium-ion batteries: A review. Prog Nat Sci: Mater Int 2018;28:653–666. [CrossRef]
[24] Chen Y, Kang Y, Zhao Y, Wang L, Liu J, Li Y, et al. A review of lithium-ion battery safety concerns: The issues, strategies, and testing standards. J Energy Chem 2021;59:83–99. [CrossRef]
[25] Martins LS, Guimarães LF, Junior ABB, Tenório JAS, Espinosa DCR. Electric car battery: An overview on global demand, recy-cling and future approaches towards sustainability. J Environ Manag 2021;295:113091. [CrossRef]
[26] Lisbona D, Snee T. A review of hazards associated with pri-mary lithium and lithium-ion batteries. Process Saf Environ Prot 2021;89:434–442. [CrossRef]
[27] Gakhar L, Wiencek JM. A possible additional role of mineral oil in successful flash cooling. J Appl Crystallogr 2005;38:945–950. [CrossRef]
[28] Mao C, Tang X, Zou H, Zhou Z, Yin W. Experimental investigation of surface quality for minimum quantity oil–water lubrication grinding. Int J Adv Manuf Technol 2012;59:93–100. [CrossRef]
[29] Huang Q, Song H, Chen Y, Huang H, Wang Y. Effect of Vegetable oil instead of Mineral oil on the Performance of Panel-type Radiator. IEEE 2023;1–6. [CrossRef]
[30] Xiang D, Shen L, Wang H. Investigation on the thermal conductivity of mineral oil-based alumina/aluminum nitride nanofluids. Mater 2019;12:4217. [CrossRef]
[31] Judendorfer T, Pirker A, Muhr M. Conductivity measurements of electrical insulating oils. IEEE 2011;1–4. [CrossRef]
[32] Tecomotive. Pierburg CWA150. Available at: https://www.tecomotive.com/en/products/CWA150.html . Accessed on March 15, 2024.
[33] Raddadi N, Fava F. Biodegradation of oil-based plastics in the environment: Existing knowledge and needs of research and innovation. Sci Total Environ 2019;679:148–158. [CrossRef]
[34] Ramli NM, Mahmud MS, Zuhan MKNM, Musa M, Razali MN. Evaluation of Oxidative and Thermal Stability of Base Oil for Automotive Application. Springer 2022;553–562. [CrossRef]
[35] Ho YC, Chen PC, Cheng YJ, Hsu CT, Yao DJ, Sharon NML, et al. Visualization of Graphene Mineral Oil Immersion Cooling for Electric Vehicle Battery Temperature Analysis. Aspen 2022;15–18. [CrossRef]
[36] Celen A. Experimental investigation on single-phase immersion cooling of a lithium-ion pouch-type battery under various operating conditions. Appl Sci 2023;13:2775. [CrossRef]
[37] Ho YC, Chen PC, Hu EL, Wu TL, Lin CH, Yao DJ. Visualization Experiment of Immersion Cooling of the Battery Thermal Management System using Mineral Oil and Aluminum Nitride Nanofluids. Aspen 2023.
[38] Eiland R, Fernandes JE, Vallejo M, Siddarth A, Agonafer D, Mulay V. Thermal performance and efficiency of a mineral oil immersed server over varied environmental operating conditions. J Electron Packag 2017;139:041005. [CrossRef]
[39] Tai LD, Garud KS, Lee MY. Experimental Study on Thermal Management of 5S7P Battery Module with Immersion Cooling Under High Charging/Discharging C-Rates. Batteries 2025;11:59. [CrossRef]
[40] Dayani S, Markotter H, Nidda JK, Schmidt A, Bruno G. Quantification of the Deep Discharge Induced Asymmetric Copper Deposition in Lithium-Ion Cells by Operando Synchrotron X-Ray Tomography. Adv Mater Technol 2024;9:2301246. [CrossRef]

J Ther Eng, Vol. 12, No. 2, pp. 498−518, March, 2026

Journal of Thermal Engineering
Web page info: https://jten.yildiz.edu.tr
DOI: 10.14744/thermal.0001098

Research Article

Thermal performance evaluation of an underground U-bend tube heat exchanger integrated with phase change material

Md. Nur ALAM[1], Dipayan MONDAL[1,*], Mohammad Rafat ISLAM[1]

[1]*Department of Mechanical Engineering, Khulna University of Engineering & Technology, Khulna, 9203, Bangladesh*

ARTICLE INFO

Article history
Received: 19 December 2024
Revised: 07 April 2025
Accepted: 10 April 2025

Keywords:
Double U-shape Pipe; Ground Heat Exchanger; Numerical Simulation; Phase Change Material; Thermal Performance

ABSTRACT

This study presents a numerical investigation of the thermal performance of a U-bend tube ground heat exchanger (GHE) with paraffin wax as the phase change material (PCM) using ANSYS Fluent R1 2020. Using a U-tube instead of the straight tube results in the same or increased surface area at the reduced pipe length which further lowers the initial cost associated with GHE construction. Though there is a handful of studies regarding the performance enhancement of GHE, studies related to GHE with PCM, particularly fitted with a U-tube are inadequate, The GHE was constructed with a double U-shaped pipe, buried 45 meters underground, and the borehole was filled with paraffin wax as PCM due to its availability, steadiness, corrosion resistance, non-toxicity, and high latent heat capacity. The governing equations in this study are solved by the Realizable k-ε turbulence model. Air was circulated at velocities ranging from 0.5 ms^{-1} to 5 ms^{-1} in increments of 0.5 ms^{-1} for 12 hours to explore the system's performance, with an inlet temperature of 309 K in all cases. Upon increasing the velocity from 0.5 ms^{-1} to 5 ms^{-1}, it was found that at 12 hours of operation, the mean rate of heat transfer per meter increased from 76.27 Wm^{-1} to 116.45 Wm^{-1}, thus the highest velocity exhibiting a 65.5% increase over the lowest, while the temperature drop decreased as velocity increased, ranging from 9.09 °C at 0.5 ms^{-1} to 7.2 °C at 5 ms^{-1}. When it comes to effectiveness, initially for all air velocities the system's maximum effectiveness was found to be between 64% and 61%. After 12 hours, effectiveness dropped to 47% at 0.5 ms^{-1} and to 37% at 5 ms^{-1} demonstrating that effectiveness reduces over time and at lower velocities the system is more effective. Moreover, it was also found that after 40 meters of GHE, there was a minimal temperature change, thus using GHE beyond this length gives insignificant thermal benefits. This necessitates future research on finding the optimal length for GHE, focus should also be given to improving performance under various environmental conditions, design optimization, and thermal performance improvement, using phase change materials to reduce initial costs.

Cite this article as: Alam MN, Mondal D, Islam MR. Thermal performance evaluation of an underground U-bend tube heat exchanger integrated with phase change material. J Ther Eng 2026;12(2):498−518.

***Corresponding author.**
*E-mail address: dipkuet@me.kuet.ac.bd, dip.kuet@gmail.com

This paper was recommended for publication in revised form by Editr-in-Chief Prof. Dr. Ahmet Selim Dalkılıç

Published by Yıldız Technical University Press, İstanbul, Turkey
Yıldız Technical University. This is an open access article under the CC BY-NC license (http://creativecommons.org/licenses/by-nc/4.0/).

INTRODUCTION

Energy usage is increasing rapidly worldwide due to population growth and improved living conditions, leading to a rise in greenhouse gas emissions. Around 40% of the world's energy consumption is utilized in heating and cooling spaces [1]. Traditional HVAC systems are not sustainable and contribute to environmental pollution. Geothermal energy, found beneath our feet, can be harnessed for cooling and heating buildings [2], [3]. Soil temperature below the ground surface is consistent year-round, but comparatively higher in the cold season and lower in the hot season relative to ambient temperatures [4]. Ground heat exchangers (GHE) facilitate heat transfer with underground soil, by receiving heat during winter and by releasing the same during summer. These systems can be placed horizontally or vertically, and the conditioned air is to be used for cooling or heating the buildings [5], [6]. The longer pipelines and excavation costs increase initial investment. Also, increase soil wetness or use a backfilling material with higher heat conductivity than native soil to reduce pipe length. Kong et al. [7] studied the thermal behavior of the GSHP with various U-tube variant buried pipes experimentally and numerically, their findings reveal that smooth U-tubes performed better than petals. Pu et al. [8] explored a numerical study on vertical U-tube type heat exchangers for GSHP systems revealing that increasing U-tube diameter and Reynolds number enhances integrated performance. Jalaluddin et al. [9] compared the performance of various GHEs on a steel pile foundation, revealing that double-tube GHEs had the maximum heat transfer rate, while factors like soil type, operation duration, inlet temperature, and material also influenced performance. Liu et al. [10] used a transient 3D model in ANSYS FLUENT to explore the behavior of the EAHE system integrated with the PCM. Gao et al. [11] studied to evaluate pile-foundation heat exchanger efficiency for geothermal energy utilization in Shanghai, analyzing single, double, and triple U-shaped and W-shaped high-density Polyethylene-based ground-coupled heat exchangers (GCHE). Their study revealed that with a modest medium flow rate, the W-shaped configuration seems to be the most effective. Chen et al. [12], [13] examined how PCM grout affects ground source heat pump (GSHP) efficiency. The system efficiency improves with PCM grouts with equivalent thermal conductivity, especially in buildings with low thermal demand. Qi et al. [14] investigated to explore PCM usage as backfill in ground source heat pumps, emphasizing its benefits stemming from their minimal thermal impact radius and stable temperature. Ahmed et al. [15] explored the optimal performance of a HEPC system using the CFD simulation by considering the velocity of air at 1.5 ms^{-1} through the buried pipe of 60 m length, 0.062 m dia., 0.003 m thickness, and 8 m depth. Yang et al. [16] found that borehole ground heat exchangers with PCM backfill boost heat exchange rate, delay soil temperature variation, improve energy storage, and reduce soil thermal interference radius. Bottarelli et al. [17] conducted a test on shallow horizontal GHEs using PCMs to improve heat pump performance and prevent winter thermal depletion. Yusof et al [18] examined an EAHE technique using a laboratory simulator and found that a certain flow rate and ground temperature reduce temperature and transfer heat best. Li et al [19] developed a numerical representation of a horizontal spiral-coil GSHP system and examined performance aspects such as soil thermal conductivity and pipe spacing. Misra et al. [20] introduced EAHE to evaluate the thermal performance under unstable situations and found that transient conditions considerably affected the performance. Florides et al. [21] examined the efficiency of vertical and horizontal ground heat exchanger modeling. Their study revealed that, while working in identical conditions, vertical heat exchangers perform better than horizontal heat exchangers. Cui et al. [22] in their study, recommended a vertical over horizontal ground heat exchanger when it comes to both thermal performance and cost-effectiveness.

Ghosal et al. [23] introduced a MATLAB model to estimate the behavior of EAHE systems and analyze the impact of factors on greenhouse air temperatures which reveals that EAHE systems significantly increase winter temperatures by 7-8°C and lower summer temperatures by 5-6°C compared to a similar greenhouse without it. Morshed et al. [24] examined two EAHE setups in Basra Province (Iraq): dry soil and moist soil made artificially and found that wet systems had a higher average COP (6.41) than dry systems (5.07). Hsu et al. [25] studied an integrated system for earth-air heat exchangers in high-density housing, using water-filled raft foundations. Tested in Yilan, Taiwan, it showed similar cooling potential and lower construction costs than conventional EAHEs. Aditya et al. [26] compared GSHP and hybrid GSHP (HGSHP) systems' costs to conventional ones in various climatic conditions, revealing that the performance is influenced by factors such as ground conditions, meteorological conditions, drilling costs, power pricing, and gas pricing. Gao et al. [27] evaluated the operational capability of 26 GSHP systems in Sichuan, Chongqing, and Shaanxi, analyzing heat pump performance, water transfer factor, and energy efficiency ratio, and providing recommendations for improvement in system design, construction, and operation. Zhuo et al. [28] experimentally explored the effects of SSPCM used as backfill on borehole GHE systems. Their findings reveal that there is a considerable reduction in temperature variation by up to 10°C because of using SSPCM as backfill material, especially around the heat source. Zhang et al. [29] examined the thermal behavior of PCM-integrated LTHS through fin incorporation. They observed that, upon increasing the PCM's thermal conductivity by 0.2 $Wm^{-2} \cdot K$, there is a significant reduction in melting and solidification time of the PCM by 43% and 35 %. Moreover, it was also found that HTF velocity has a significant effect on heat exchanger efficiency compared to the fluid's temperature

and thermal conductivity of PCM. Emmi and Bottarelli [30] numerically studied the thermal capability of HGHE directly coupled with PCM. Results found show that coupling PCM directly with HGHEs performs better compared to using PCM added to the backfill material. Hadjadj et al. [31] experimentally investigated the effect of air speed on HWAHE performance. The authors discovered that as air velocity increased, efficiency trended downward. Han et al. [32] examined the thermal performance of a solar-coupled GSHP system in a large building, finding high efficiency but decreasing efficiency with increasing heat exchanger spacing. Zhou et al [33] developed a PCM-filled EAHE to minimize HVAC energy usage, increasing cooling capacity by 20.24% and lowering output temperature by 0.83°C. In addition, Mondal et al. [34], [35] conducted the parallel, counter, and cross-flow water-to-air u-bend heat exchanger and also a cooling system adopted by the vapor absorption system, while Mondal and Islam [36] reported another study for intermittent system adopted by ammonia absorption refrigeration system. To fit the refrigerants in HVAC&R systems, Mondal et al. and Islam et al. [37]–[41] measured the transport properties as well as the heat transfer characteristics of several refrigerants that will take in the future revolution of industries. Moreover, Das et al. [42] and Arefin et al. [43] assessed the thermodynamic analysis of the dual and single cascading vapor compression cycle, respectively, for the low-temperature application. Moreover, Bari et al. [44] presented the analysis of heat transmission in a refrigerant compartment, while Shahariar et al. [45] represented the performance of LiCl desiccant dehumidifier. Rifert et al. [46] studied several approaches for estimating heat transfer in horizontal and smooth pipes during condensation when vapor velocity is present. The authors suggested a semiempirical dependence $Nu = 0.0144Fr^{36}Pr^{0.43}$ to calculate condensation heat transfer when $Re > 800$ and β (A parameter responsible for governing vapor velocity) > 10. Rifert et al. [47] reviewed over 40 semi-empirical and empirical techniques to predict heat transfer coefficients in condensation processes within plain tubes. The authors concluded that during the condensation of various refrigerants, the correlations suggested by Thome et al. [48], Cavallini et al. [49], Shah [50], and Rifert et al. [51], [52] can be used to predict the heat transfer coefficients. Camaraza-Medina et al. [53] after comparing 22 different published experimental data of condensable fluid inside horizontal, vertical tubes, and inclined tubes, suggested a new model for heat transfer calculation during film condensation within pipes, good enough to be considered satisfactory for practical design.

From the above discussion, the thermal efficiency and pipe length of a ground heat exchanger are critical considerations in calculating excavation costs and soil volume requirements. Adding phase change material (PCM) may greatly increase thermal performance. PCM-filled GHEs improve summer cooling capacity by enhancing heat transfer and delaying the transition from heating to cooling mode, resulting in excellent cooling performance. PCM-air is more energy-efficient than PCM-water, making it a good choice for energy storage systems. Hence, by introducing PCM into the conventional ground heat exchanger system, a significant improvement may be obtained in thermal performance. Moreover, by utilizing a U-bent tube design instead of a traditional straight tube, the overall surface area of the GHE can either be maintained or even increased while simultaneously reducing the required length of the pipe. The reduction in pipe length contributes to a friendly and space-efficient system without compromising performance. Additionally, the pressure drop at the U-bent tube section is minimized compared to straight tubes, resulting in improved fluid flow dynamics, lower pumping power requirements, and further optimization of the system's energy efficiency. There are few studies on phase change material double U-shaped tube heat exchangers, which reduce pipe depth and improve GHE thermal performance. This simulation study examines the thermal performance of a U-tube ground heat exchanger with PCM as the backfill material buried under soil by varying air velocity ranging from 0.5 ms^{-1} to 5 ms^{-1}. A transient three-dimensional simulation model has been developed and analyzed numerically via FLUENT 2020 R1 to find the system's best design and operation characteristics.

MATERIALS AND METHODS

Assumption

A 3D domain has been introduced in the numerical model by encompassing a complex dynamic process of heat transfer that includes convective heat transfer, heat conduction, and PCM melting as well as solidification for the inside pipe, soil, and borehole, respectively. The specific assumptions are considered as follows:

- Thermophysical properties of air are assumed to be constant and incompressible.
- The soil around the borehole is homogeneous and isotropic with constant thermo-physical properties.
- PCM are assumed to have temperature-independent thermophysical properties.
- The physical contact of material layers is assured, and the thermal resistance of the pipe thickness and borehole is neglected.
- Air is assumed to mix uniformly inside the Ground Air Heat Exchanger (GAHE) pipe ensuring uniform temperature with no stratification.
- The heat transfer is modeled as transient and occurs in three dimensions through the surrounding soil.
- Apart from air velocity, all other parameters are assumed to be constant

Material

PCM is filled inside the borehole as backfill material around the pipe buried in the ground as part of the model.

Table 1. Thermophysical properties of air, soil, and paraffin wax [10] (The properties are taken at a reference temperature of 293.15 K)

Parameters	Value		
	Air	Soil	Paraffin wax
Density, kg/m^3	1.165	1700	800
Latent heat, J/kg	-	-	250×10^3
Melting Temperature, °C	-	-	25
Specific heat capacity, J/(kg.K)	1006	1300	3220
Thermal conductivity, W/(m.K)	0.0262	1.1	0.35
Viscosity, kg/(m.s)	1.8×10^{-5}	-	0.094

As a fluid for heat transmission, the surrounding air moves along the borehole's axis through the pipe. Paraffin was used as PCM to fill the gap between the borehole walls and the pipe. The properties of air, soil, and paraffin wax as PCM are listed below in Table 1. All the properties are taken at a reference temperature of 293.15 K.

Physical Model As Proposed Geometry

Figure 1 represents the schematic diagram of an underground heat transfer model with a vertical double U-tube ground heat exchanger (GHE) with inlet and outlet, phase change material (PCM), and ambient soil. The following displays both the orientation and the physical dimension.

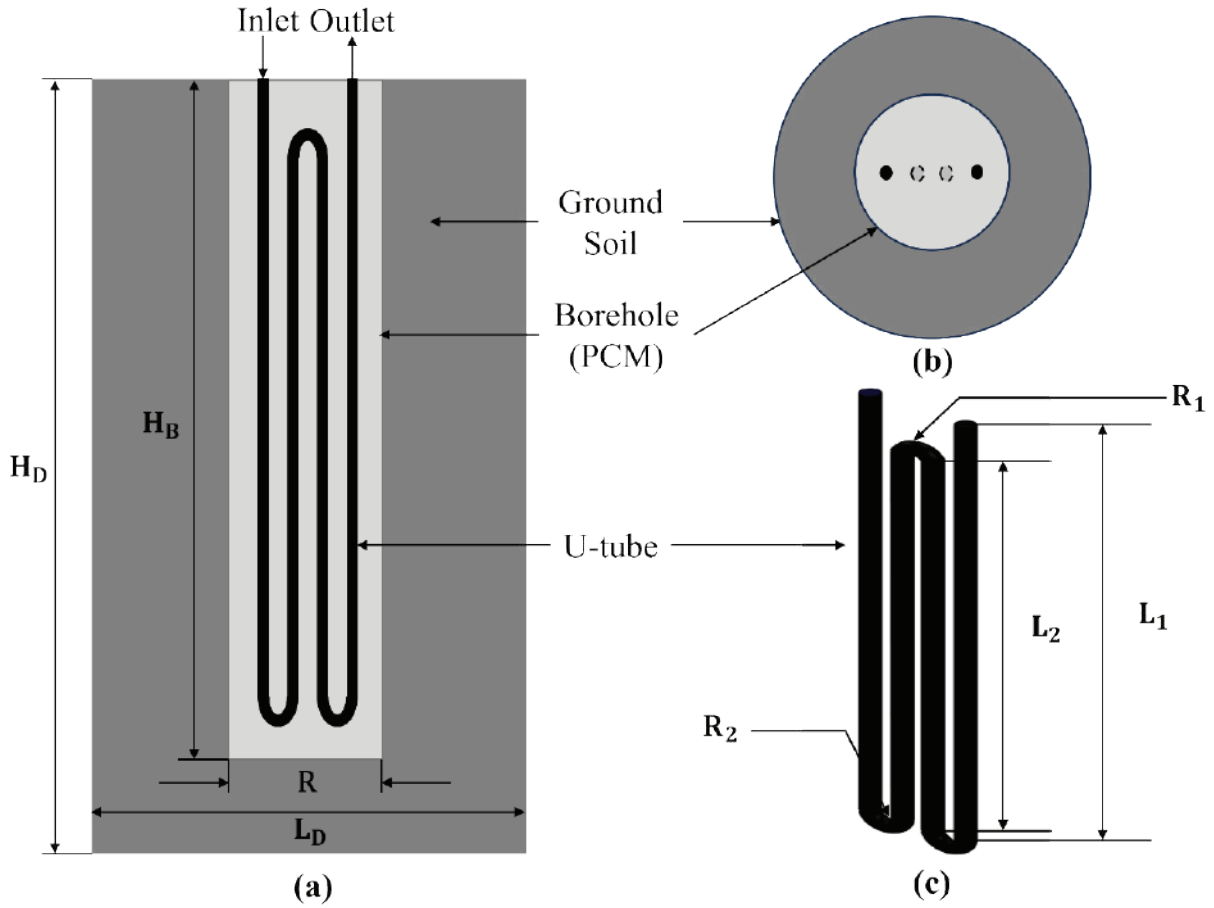

Figure 1. Schematic diagram of ground heat exchanger: (a) front view, (b) top view, and (c) tube geometry.

Table 2. The specifications of the proposed geometry

Parameters	Value	Parameters	Value
Domain length, L_D (m)	10	Tube radius, mm	16
Domain width, W (m)	5	Tube length, L_1 (m)	40
Domain height, H_D (m)	45	Tube length, L_2 (m)	39.65
Borehole height, H_B (m)	42	Tube bend radius, R_1 (mm)	57
Borehole radius, R (mm)	300	Tube bend radius, R_2 (mm)	25

Meanwhile, the specifications of the physical model are listed in Table 2.

Formation of the Problem

To simulate the study using ANSYS FLUENT, some governing equations were used that characterized the GHE's heat transfer and fluid movement. However, the governing equations [54] used for this study are described as:

The continuity equation is defined as,

$$\frac{\partial \rho_a}{\partial t} + \frac{\partial}{\partial x_i}(\rho_a u_i) = 0 \tag{1}$$

The momentum equation is defined as,

$$\frac{\partial}{\partial t}(\rho_a u_i) + u_j \frac{\partial}{\partial x_j}(\rho_a u_i) = -\frac{\partial p_a}{\partial x_i} + \eta_a \frac{\partial^2 u_i}{\partial x_j \partial y_j} \tag{2}$$

The energy equation is defined as,

$$\rho_a C_a \left(\frac{\partial T}{\partial t} + u_j \frac{\partial T}{\partial x_j}\right) = \frac{\partial}{\partial x_j}[(\lambda_a + C_a . \frac{\eta_t}{\sigma_T}) \frac{\partial T}{\partial x_j}] \tag{3}$$

Where, ρ_a, P_a, η_a, and λ_a denote density, pressure, dynamic viscosity, and thermal conductivity of air, respectively. Again, x_i & x_j, and u_i & u_j represent the length and velocity components, respectively.

Turbulence model:

The 'Realizable k-ε turbulence model' is widely used to simulate GSHE systems due to its ability to produce reliable outcomes for confined wall internal flows with modest mean pressure gradients [55]. Hence this model is to be employed at transport equations as follows:

Transport equation for 'k';

$$\frac{\partial}{\partial t}(\rho k) + \frac{\partial}{\partial x_j}(\rho k u_j) = \frac{\partial}{\partial x_j}\left[\left(\mu \frac{\mu_t}{\sigma_k}\right)\frac{\partial k}{\partial x_j}\right] + G_k + G_b - \rho\varepsilon - Y_M + S_k \tag{4}$$

Transport equation for 'epsilon (ε)';

$$\frac{\partial}{\partial t}(\rho\varepsilon) + \frac{\partial}{\partial x_i}(\rho\varepsilon u_j) = \frac{\partial}{\partial x_j}\left[\left(\mu \frac{\mu_t}{\sigma_\varepsilon}\right)\frac{\partial \varepsilon}{\partial x_j}\right] + \rho C_1 S_\varepsilon - \rho C_2 \left(\frac{\varepsilon^2}{k + \sqrt{\nu\varepsilon}}\right) + \frac{\varepsilon}{k} C_1 C_{3\varepsilon} G_b + S_\varepsilon \tag{5}$$

Where,

$$C_1 = \max\left[0.43, \frac{\eta}{\eta+5}\right]$$

$$\eta = S\frac{k}{\varepsilon}; S = \sqrt{2S_{ij}S_{ij}}$$

$$\mu_t = \rho C_\mu \frac{k^2}{\varepsilon}$$

Where α_k and α_ε represent the Prandtl numbers for k and ε; μ_a and μ_t denote the dynamic viscosity and turbulent (or eddy) viscosity of air; G_k and G_b represent the turbulence-generated kinetic energy for the velocity gradients and buoyancy, respectively. Again, Y_M represents the dilatation dissipation rate, while S_ε & S_k denote the user-defined source terms. Also, the constants for the k-ε realizable model are listed as, $c_{1\varepsilon}$=1.44, c_2=1.90, σ_k=1.00, σ_ε=1.20.

Phase change model:

For modelling the solidification and melting of PCM grout, the enthalpy porosity approach was used. [56], [57]. The melt interface is not well traced by this method, which regards the liquid-solid mushy zone as a porous zone with the same porosity as the liquid fraction. This model uses the enthalpy balance to determine the liquid fraction at each iteration. The summation of sensible enthalpy (h) and the latent heat (ΔH) gives the total enthalpy [54]:

$$H = h + \Delta H \tag{6}$$

$$h = h_{ref} + \int_{T_{ref}}^{T} c_p . dT \tag{7}$$

$$\Delta H = \beta L \tag{8}$$

Where T_{ref} and h_{ref} represents the reference temperature and enthalpy respectively, and L denotes the PCM's latent heat. If PCM's melting and solidification temperatures are considered of T_{liquid} and T_{solid}, respectively, then the liquid fraction (β) is defined as:

$$\beta = \begin{cases} 0, & T < T_{solid} \\ \frac{T - T_{solid}}{T_{liquid} - T_{solid}}, & T_{solid} < T < T_{liquid} \\ 1, & T > T_{liquid} \end{cases} \tag{9}$$

The usual momentum equation should include a sink term to account for solid phase pressure drop:

$$S_{hj} = \frac{(1-\beta)^2}{\beta^3+\theta} A_{mush}\, u_j \quad (10)$$

Where θ denotes a small number (0.001) to avoid zero division; A_{mush} represents the mushy zone which measures the damping amplitude, varying from 10^4 to 10^7 which is considered as 10^5 for this study [58], [59].

Effectiveness:

The ratio of the actual drop in air temperature to the maximum possible drop in air temperature in in ground heat exchanger system is termed as effectiveness [18]. The equation below is applied to determine the effectiveness [60]:

$$\varepsilon = \frac{Actual\ Temperature\ Drop\ at\ Any\ Point\ of\ Time}{Maximum\ Possible\ Temperature\ Drop} = \frac{T_{ai}-T_{ao}}{T_{ai}-T_{w,initial}} \quad (11)$$

where, T_{ai} and T_{ao} are the inlet and outlet air temperature, and $T_{w,\ initial}$ is the initial temperature of the pipe wall.

Boundary conditions and solver setup

For the top surface, the energy balance of the soil surface is as follows [10]:

$$-\lambda_s\left(\frac{\partial T}{\partial y}\right)_{y=0} = CE - LR + SR \quad (12)$$

Here, CE refers to the heat transfer between the soil surface and surrounding air.

$$CE = h_{sur}(T_{amb} - T_{ss}) \quad (13)$$

Where, T_{amb} and T_{ss} represent the temperature of ambient air and soil surface, respectively; h_{sur} denotes the convective heat transfer coefficient of the soil surface which is estimated as follows [61]:

$$h_{sur} = \begin{cases} 5.678[0.775 + 0.35(\frac{v_{wind}}{0.304})], v_{wind} < 4.88 \\ 5.678[0.775 + 0.35(\frac{v_{wind}}{0.304})^{0.78}], v_{wind} \geq 4.88 \end{cases} \quad (14)$$

Where v_{wind} represents the velocity of air at the soil surface; LR denotes the soil surface emitted long-wave radiation which is expressed as:

$$LR = \epsilon \Delta R \quad (15)$$

Where $\epsilon(=1)$ is the ground surface emittance and ΔR is a quantity that is dependent on the soil radiative characteristics, the effective sky temperature, and the relative humidity of the ground and air above the ground surface. Here, ΔR= 63 W/m^2 [62]; may be used as the first approximation.

Again, the SR is the amount of solar radiation that the soil surface absorbs as:

$$SR = (1-\alpha)G \quad (16)$$

Where G and α represent the incident solar global irradiance and soil surface albedo. However, the following equations provide a good description of the radiation and convection heat transfer processes based on the explanation above [63]:

$$-\lambda_s\left(\frac{\partial T}{\partial y}\right)_{y=0} = h_{sur}(T_{sol-air} - T_{ss}) \quad (17)$$

$$T_{sol-air} = T_{amb} + \frac{(1-\alpha)G}{h_{sur}} - \frac{\epsilon \Delta R}{h_{sur}} \quad (18)$$

Where $T_{sol\text{-}air}$ defines the solar-air temperature. Beyond the boundary, the temperature of the soil at the bottom surface stays constant at the same level as the soil surface's mean yearly temperature. Therefore, it is seen as:

$$T(bottom, t) = 20℃ \quad (19)$$

For faraway surfaces, adiabatic conditions are used. The surrounding soil and pipe walls were coupled to facilitate heat transfer. However, a brief description of the boundary conditions is listed in Table 3.

The coupled technique was used to solve the pressure-velocity coupling in the solver configuration. Second-order and least square cell-based (LSCB) techniques were chosen for the solution of pressure and velocity gradients, respectively. For turbulent kinetic energy and momentum, the second-order upwind approach was used. When the residuals were less than those for energy and other variables, convergence was attained. A brief description of the solver setup is listed in Table 4.

Mesh Independence and Model Validation

ANSYS software 2020 R1 was used to generate the required mesh and a 3D non-uniform mesh was applied to the study. After the creation of geometry, the following mesh has been generated in ANSYS meshing of tetrahedrons type. Figure 2 illustrates the grid layout and provides an in-depth look at the borehole cross-section. The mesh independence test determines if the output is mesh-dependent for validation. An independence test is performed using three different grid sizes to ensure the precision of the proposed work's simulated outcomes. The temperatures

Table 3. Brief description of the boundary conditions

Items		Description
Top surface		Wall (Convection)
Bottom surface		Wall (Temperature)
		Temperature specified at 288 K
Faraway surface		No-slip wall (Heat flux)
Inlet	: Inlet	Velocity-inlet
	: Temperature (T)	309 K
	: Velocity (v)	0.5 ~ 5 m/s
Outlet		Pressure-outlet
Other walls		No-slip, coupled wall
Initial temperature for all zones (T)		288 K

Table 4. Brief description of the solver setup

Item	Description	
Solver type	Pressure Based Solver	
Condition	Transient	
Gravity	On	
Turbulence model	k-ε (K-Epsilon),	
Near wall treatment	Standard wall functions	
Solver method	Pressure-velocity coupling: Coupled	
Initialization	Standard initialization	
Spatial Discretization	Gradient	Least square cell based
	Pressure	Second order
	Momentum	Second-order upwind
	Turbulent kinetic energy and dissipation rate	First order upwind

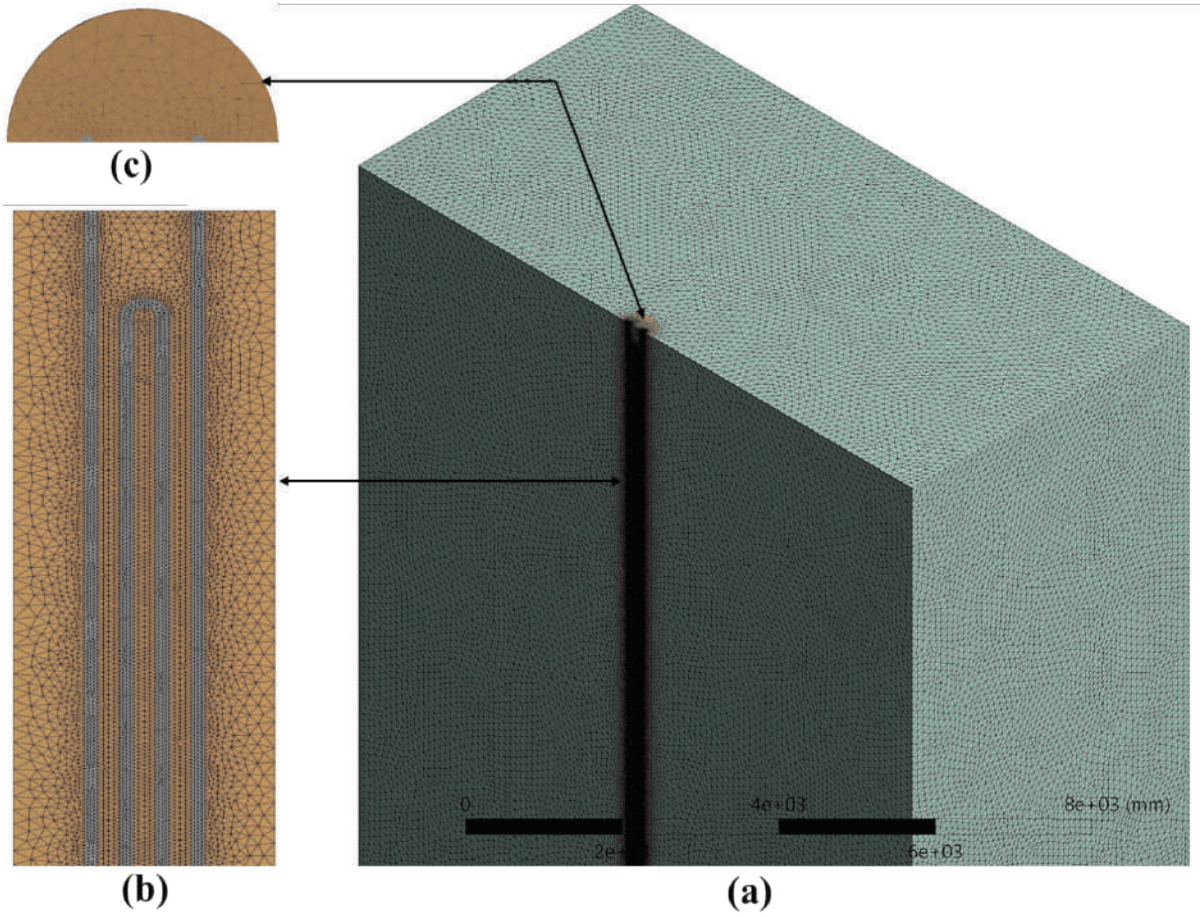

Figure 2. Illustration of mesh generation.

of the air at the outflow, which correspond to the various grid sizes, are depicted in Figure 3(a). This is being done to confirm the reliability of the results. In the figure, in element no. 23620924, the outlet air temperature came to 27.1 °C. This is selected for further calculation. Keeping all the dimensions the same and the flow inlet and boundary conditions, the model is validated, as shown in Figure 3(b). To assess the workflow, the model was validated & compared with Chen et al. [12] with an error of 1.48%. In contrast, the information about the mesh generation is listed in Table 5.

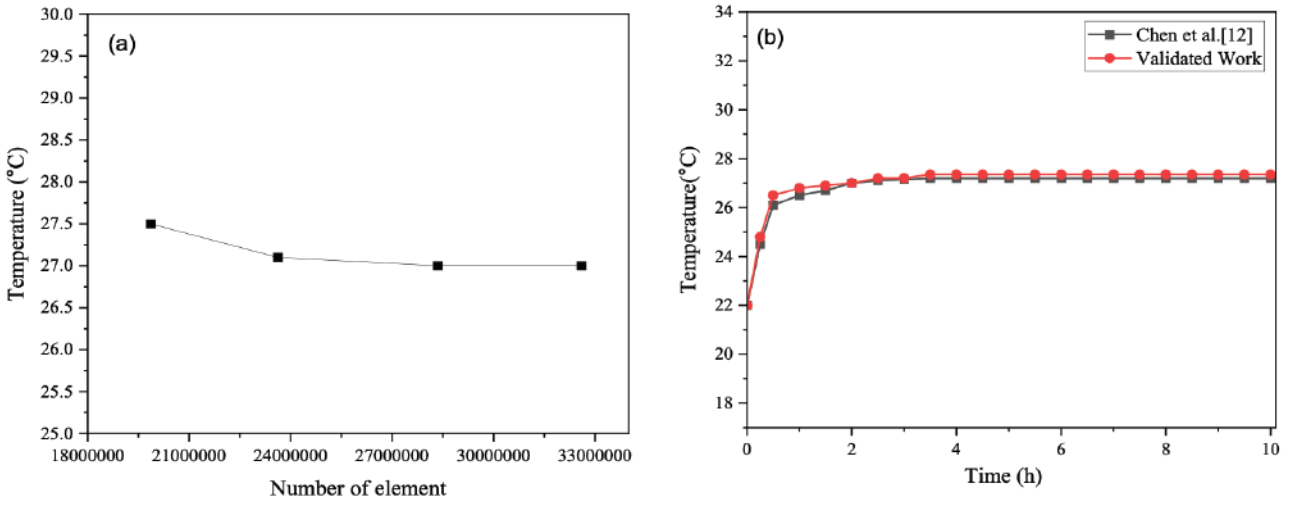

Figure 3. Illustration of (a) Mesh independency test, and (b) Model validation.

Table 5. Information about the mesh generation with mesh quality

Parameters	Value & description	Parameters	Value
Type of mesh	Tetrahedrons	Mesh quality (in avg.)	
Mesh method	Patch conforming	Aspect Ratio	1.78800
Element size	1000 mm	Skewness	0.20527
No. of elements	23620924	Orthogonal Quality	0.79354
No. of nodes	4100399	-	-

RESULTS AND DISCUSSION

In this study, numerical investigations were carried out for air velocities between 0.5 ms^{-1} and 5 ms^{-1} over 12 hours. Temperature, pressure, and velocity contours were used to improve understanding of fluid dynamics and heat transfer. Important insights are provided by these contours: Velocity contours display flow patterns, pressure contours draw attention to variations, and temperature contours display thermal gradients. To avoid repetition, only the contours for 3 ms^{-1} and 5 ms^{-1} are presented. Figures 4, 5, and 6 show the temperature, pressure, and velocity contours for these velocities. Figure 4 shows the difference in temperature between the inlet and outlet at velocity levels 3 ms^{-1} and 5 ms^{-1} respectively. Figure 4(a) shows a 9°C difference in temperature at 3 ms^{-1}, while Figure 4(b) shows a temperature difference of 7°C at 5 ms^{-1}. This signifies a decreasing temperature gradient between the inlet and outlet with increasing velocity. Figure 5 shows the pressure contour at velocity levels 3 ms^{-1} and 5 ms^{-1}. From Figures 5(a) and 5(b), it is observed that the pressure drop between the inlet and outlet at 3 ms^{-1} is around 6.26 MPa whereas at 5 ms^{-1} the pressure drop was found to be 8.91 MPa. Thus, by increasing the velocity from 3 ms^{-1} to 5 ms^{-1}, the pressure fall between the inlet and outlet increases. Finally, Figure 6 shows the velocity contour at 3 ms^{-1} and 5 ms^{-1}. The velocity of air remains constant throughout the tube.

Figure 7(a) illustrates the change in temperature at the GHE outlet with time. The simulation was conducted with different air velocities, from 0.5 ms^{-1} to 5 ms^{-1}, over a period of 12 hours of operation. For all air velocities, initially, the temperature at the outlet was low, but after some time, it gradually increased and eventually stabilized. The inlet air temperature was 309 K for all air velocities. As seen in the figure, the outlet temperature was recorded to be 299.91 K 300.03 K, 300.12 K, 300.21K, 300.38 K, 300.62 K, K, 300.9 K, 301.24 K, 301.53 K, 301.8 K for 0.5 ms^{-1} to 5 ms^{-1} correspondingly the temperature difference or drop in air temperature, shown in Fig. 7(b), was 9.09 °C, 8.97 °C, 8.88 °C, 8.79 °C, 8.62 °C, 8.38 °C, 8.1 °C, 7.76 °C, 7.47 °C, and 7.2 °C for 0.5 ms^{-1} to 5 ms^{-1} respectively. When air velocity is 5 ms^{-1}, the difference in temperature between inlet and output is lower than that of when air velocity is 0.5 ms^{-1}. Thus, upon increasing the air speed, the outlet temperature rises. Due to relatively lower velocity, the air comes in contact relatively more time through the tube with the PCM and therefore, the temperature drop may occur more than the higher velocity over time. A greater temperature drop is the result of improved cooling caused by increased air-PCM

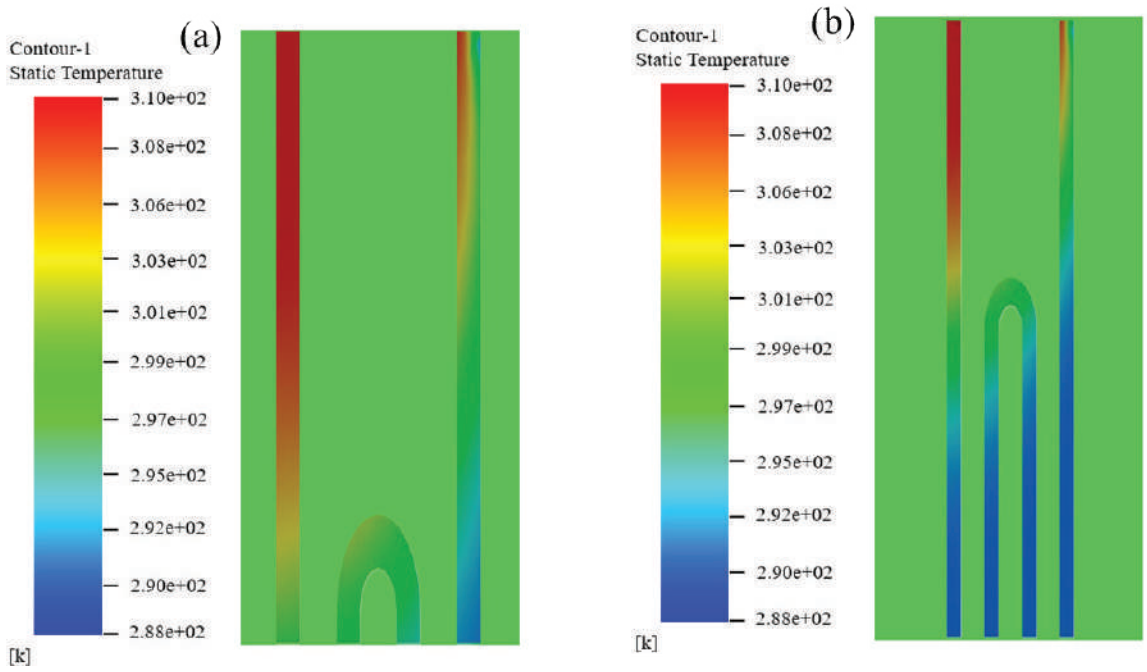

Figure 4. Temperature contour of the tube with PCM at an air velocity of (a) 3 ms^{-1} and (b) 5 ms^{-1}.

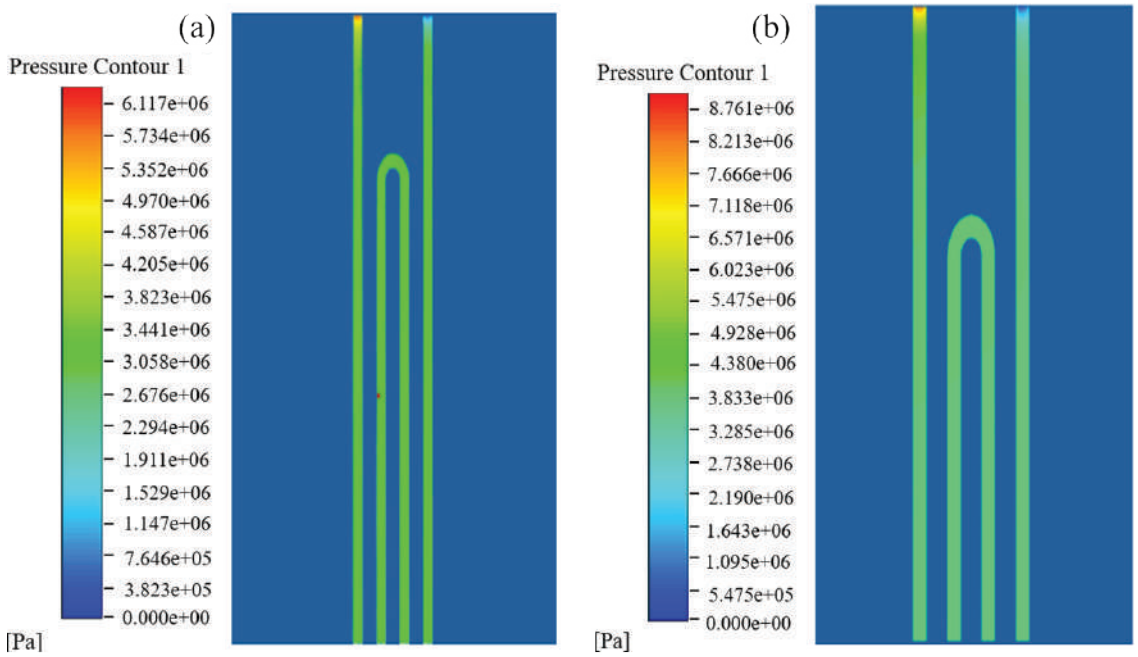

Figure 5. Pressure contour of the tube with PCM at an air velocity of (a) 3 ms^{-1} and (b) 5 ms^{-1}.

interaction. Therefore, the air velocity should be decreased from the standpoint of exit temperature.

Figure 8 depicts the heat transfer rate over time for different air velocities. Initially, a higher heat transfer rate was found for all cases; over time it decreases and eventually becomes almost constant and remains horizontal for all air velocities. First, there exists a significant difference in temperature between the soil and air before the system begins to function. When the system begins to work, the soil around the buried pipes progressively gets heated up, reducing this difference between the two as heat is being dissipated to the surrounding soil. Thus, this also reduces the reducing heat

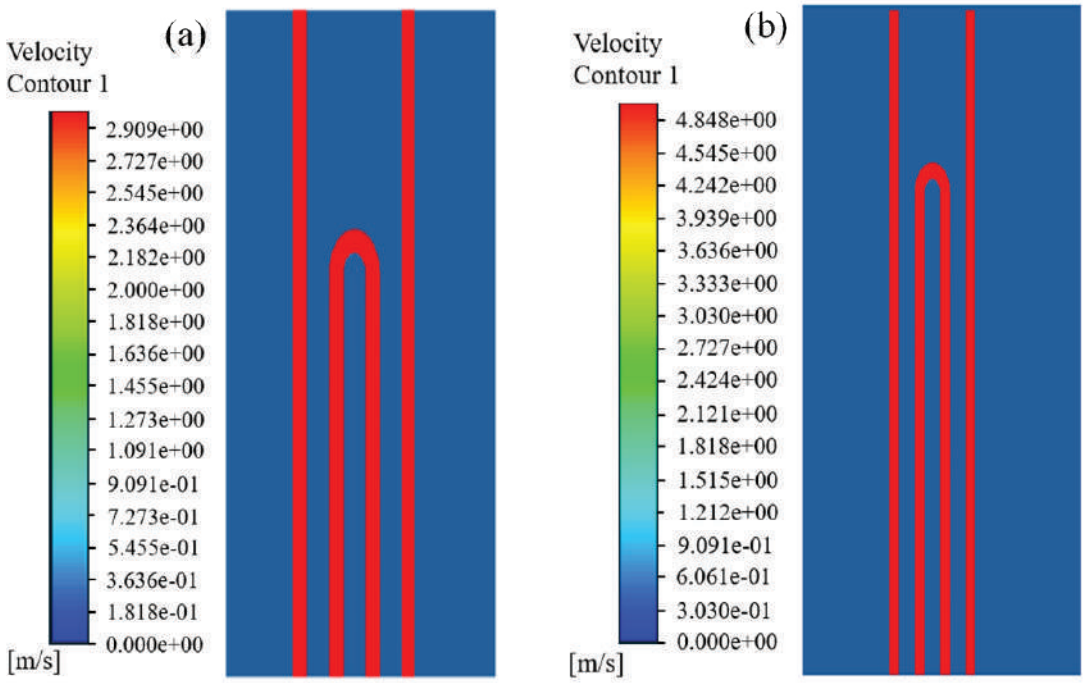

Figure 6. Velocity contour of the tube with PCM at an air velocity of (a) 3 ms^{-1} and (b) 5 ms^{-1}.

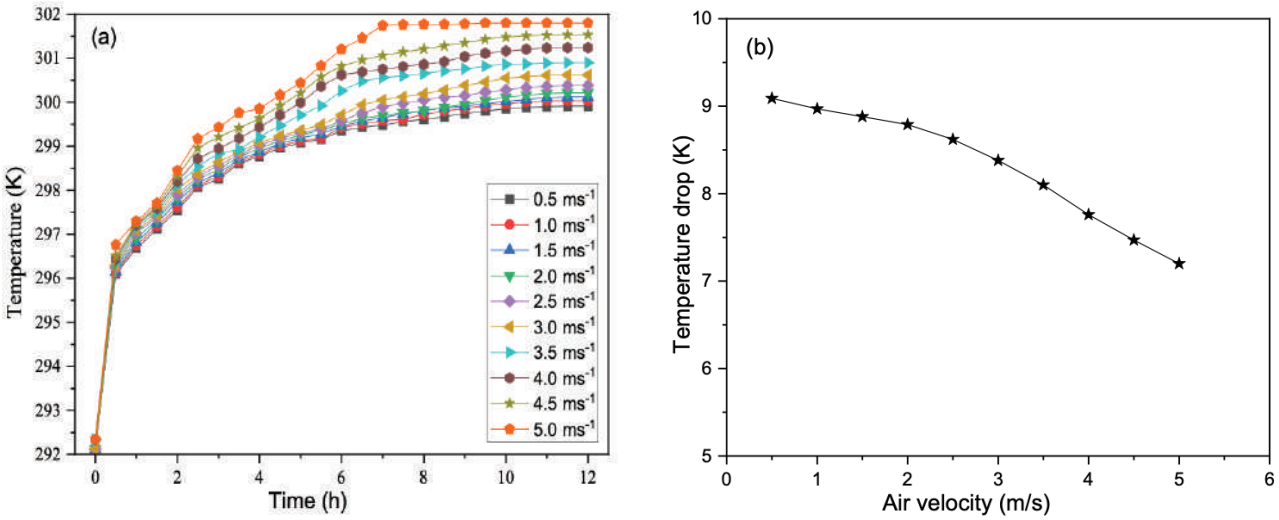

Figure 7. Illustration for the GHE: (a) temperature changes at the outlet over time and (b) variation of temperature drop with air velocities 0.5 ms^{-1} to 5 ms^{-1}.

transfer. After 12 hours of operation, the mean heat transfer rate per meter was 76.27 Wm^{-1}, 80.08 Wm^{-1}, 83.98 Wm^{-1}, 88.7 Wm^{-1}, 93.05 Wm^{-1}, 97.97 Wm^{-1}, 102.66 Wm^{-1}, 107.35 Wm^{-1}, 111.61 Wm^{-1} and 116.45 $Wm^{-1}$for air velocities from 0.5 ms^{-1} to 5 ms^{-1} respectively. It is also noticed from the figure that despite having a larger temperature drop at a lower velocity, the heat transfer rate of the system increases as air velocity increases. The rate of heat transfer per meter at 0.5 ms^{-1} is lower than that of 5 ms^{-1}. Compared to 0.5 ms^{-1} the heat transmission rate per meter for 5 ms^{-1} is roughly 65.5% higher. This is because, at higher air velocity, the boundary layer is comparatively thinner, which results in the convective heat transfer coefficient increasing, which ultimately contributes to the increased heat transfer. Secondly, a higher velocity of air means higher turbulence, which results in better air mixing, this also accelerates the heat transfer rate. A higher air velocity is therefore preferred in terms of when a better heat transfer rate per meter is desired.

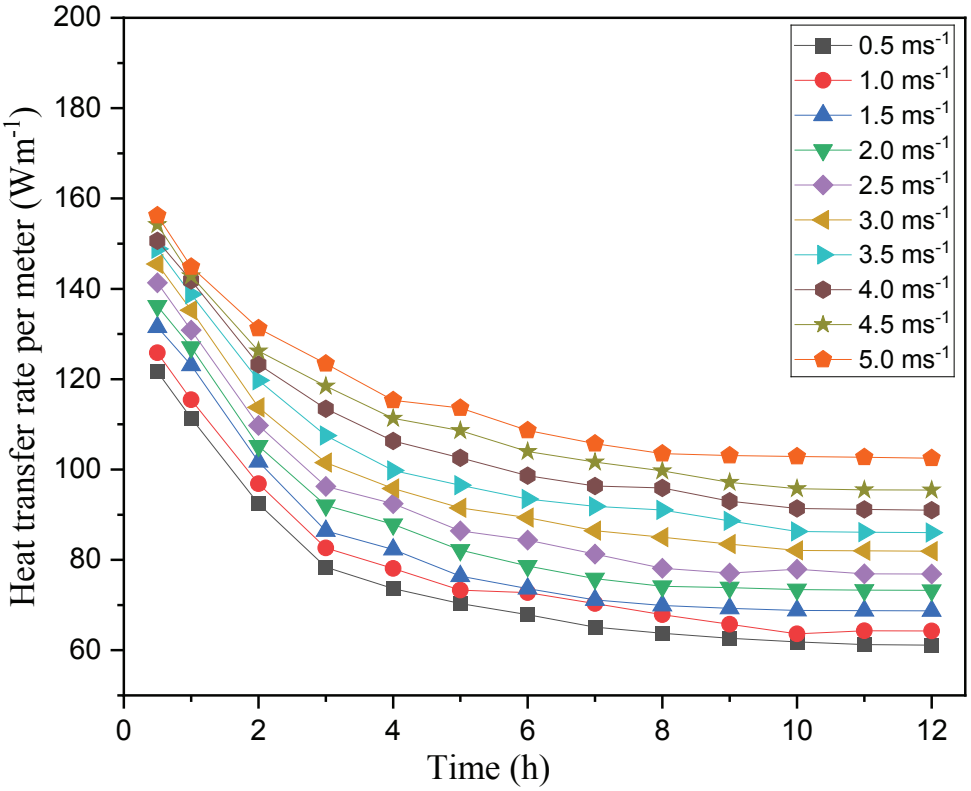

Figure 8. Heat transfer rates per meter over time for different air velocities.

Figure 9 depicts variation in cooling capacity with time at different air velocities. Initially, a large temperature gradient between hot air and the ground is responsible for the heat transfer, and as the warm air circulates through the system, it gradually cools down. During the first half of the system's operation, cooling capacity increases because air gives up its heat to the ground, with higher air velocities resulting in faster circulation and more heat transfer. The cooling capacity continues to rise further and reaches its maximum point around 6 hours in all velocity levels, with the maximum values being: 1,297.01 W at 5.0 ms^{-1}, 1,243.28 W at 4.5 ms^{-1}, 1,180.6 W at 4.0 ms^{-1}, 1,120.15 W at 3.5 ms^{-1}, 1,064.18 W at 3.0 ms^{-1}, 1,017.16 W at 2.5 ms^{-1}, 999.254 W at 2.0 ms^{-1}, 976.866 W at 1.5 ms^{-1}, 941.045 W at 1.0 ms^{-1}, and 925.373 W at 0.5 ms^{-1}. Upon reaching the maximum point in each case, the temperature differential between air and ground is at its most efficient for heat transfer as the air has cooled as much as it can. However, there is a decline in cooling capacity afterward. This is due to the temperature differential responsible for heat transfer decreases as air temperature gradually approaches the ground temperature.

Figure 10 illustrates the effectiveness of the GHE system over the period of operation time. The effectiveness of the GHE system during each hour of a 12-hour operation has been calculated from Eq. (11). After an hour of continuous operation, the system's maximum effectiveness was found to be between 64% and 61% for all air velocities. The effectiveness decreases in a similar trend for all velocities over the period of system functioning. Consequently, the effectiveness was determined to be 47%, 44%, 46.5%, 46%, 45%, 44%, 42%, 40%, 39%, and 37% for 0.5 ms^{-1} to 5 ms^{-1}, respectively, at 12 hours of continuous operation. According to the results, the ground heat exchanger (GHE) system's effectiveness steadily declines during operation. After 12 hours of continuous operation, effectiveness drops by about 26.56% for 0.5 ms^{-1} and 39.34% for 5 ms^{-1} than that after 1 hour of operation. Hence, the GAHE system is found to be more effective at 0.5 ms^{-1} than at 5 ms^{-1}. Effectiveness reduces over time primarily because of the diminishing temperature gradient between the ground and the incoming air. As the air passes through the GHE, it gradually warms up, reducing the driving force for heat transfer. Higher air velocities, although they increase the heat transfer rate, result in a smaller temperature gradient between air and ground, leading to lower effectiveness. Conversely, lower velocities maintain a higher temperature difference for a longer period, which helps sustain the system's effectiveness over time.

Figure 11 illustrates the air temperature variation along the length of the pipe in the ground heat exchanger after 12 hours of uninterrupted operation, which is essential for accurately ascertaining the required pipe length. The length of the pipe is one of the prime factors that control the cost associated with the construction of GHE. Consequently,

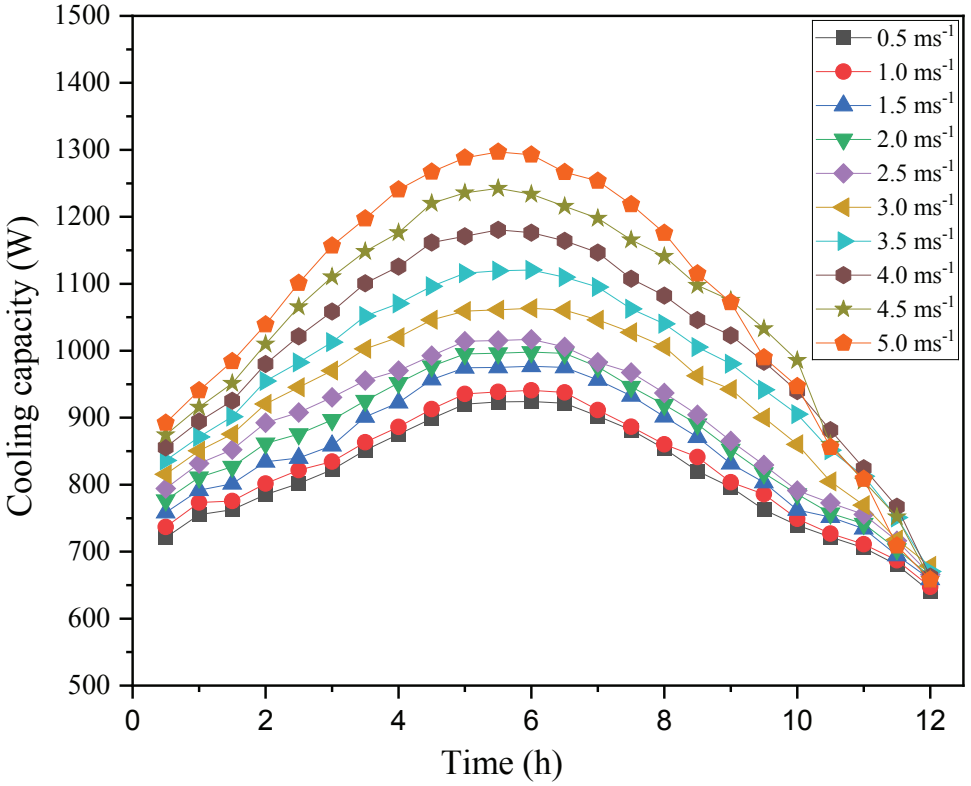

Figure 9. Cooling capacity variation with time as a function of air speed.

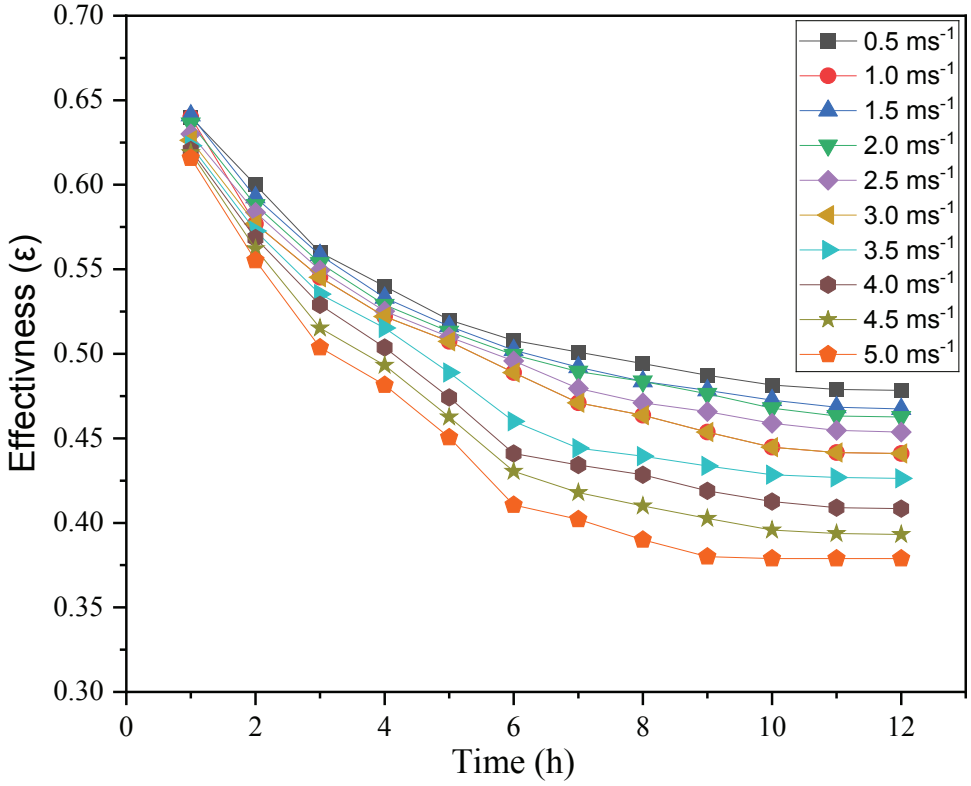

Figure 10. Effectiveness of ground heat exchanger (GHE) system.

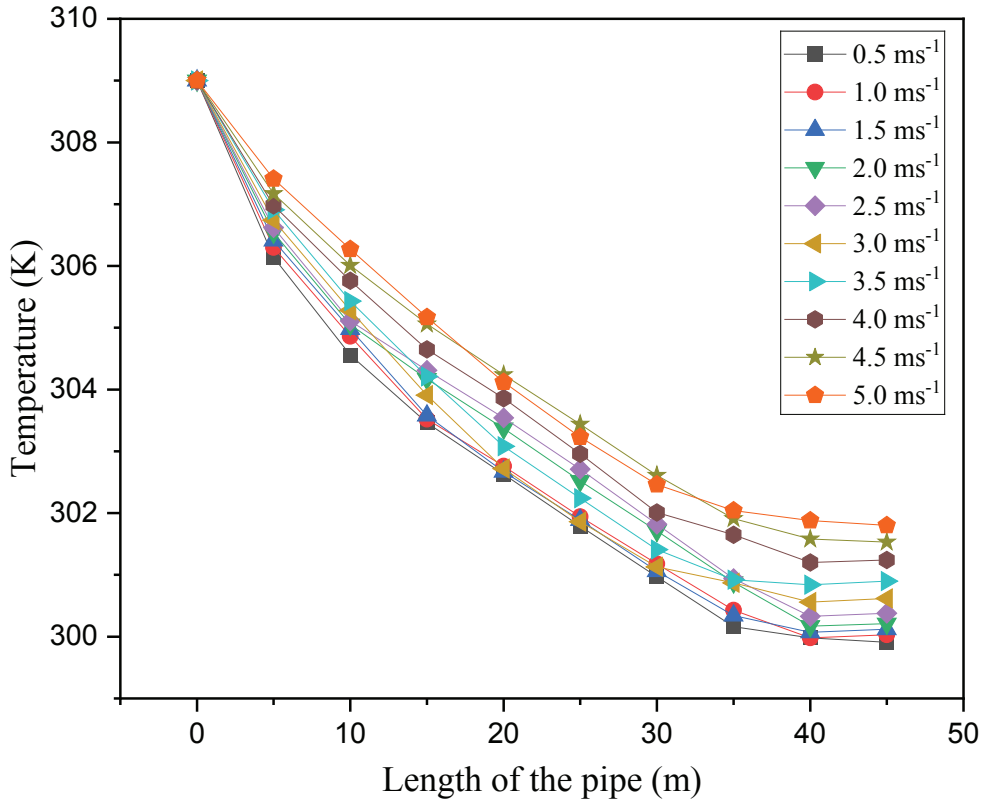

Figure 11. Variation of air temperature along the pipe length after 12 h of continuous operation.

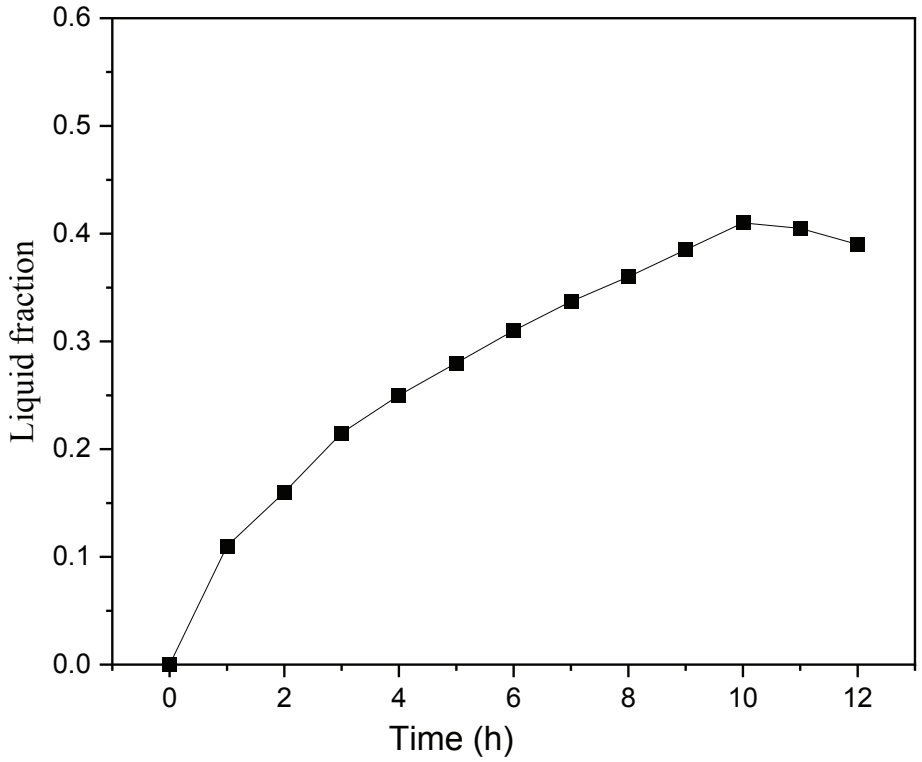

Figure 12. Variation of the liquid fraction of PCM with time.

while designing the system, it is essential to compute the necessary length for a specific reduction in air temperature. The length of the pipe is dictated by the thermophysical properties of the adjacent soil. At 12 hours of uninterrupted operation, a decrease in temperature of 9.09 °C is observed at the outlet of the ground heat exchanger with a flow rate of 0.5 ms^{-1}. After 40 meters, the graph became steady, and beyond that distance, the temperature decrease was minimal.

Figure 12 illustrates the progression of the liquid fraction of the phase change material (PCM) with time of operation. The liquid percentage of PCM initially increases over time, then declines after attaining its maximum value. The solid PCM process begins with the 0% liquid fraction. Upon receiving heat, the temperature of the PCM starts to increase, eventually reaching the melting point, and then the liquid fraction starts to rise. At the melting point, the temperature remains constant, and solids and liquids coexist. The liquid fraction approaches 100%, indicating the conclusion of the melting phase. When heat is withdrawn, the liquid fraction declines, but initially remains at 100% until solidification. The explanation is that the ambient air temperature exceeds and falls below the phase change temperature (PCT) during the charging and discharging phases, respectively.

In Figures 13 and 14, the heat transfer characteristics (Nusselt number and heat transfer coefficient) were plotted against Reynolds number, and all the data showed an increasing trend with the increase in Reynolds number. The heat transfer characteristics, including the average Nusselt number and average heat transfer coefficient, increased with the rise in the Reynolds number, which indicated more turbulent flow. Turbulence enhanced fluid mixing and thinner the thermal boundary layer around the pipe, which causes more effective convective heat transfer. It is noted that higher air velocity has a higher heat transfer coefficient.

Figure 15 illustrates the disparity in output temperature between the GHE utilizing phase change material and a conventional GHE. The GHE utilizing phase change material exhibits a lower exit temperature compared to the alternative. Phase change material absorbs heat from the surroundings with its large latent heat. So, the heat exchanger's performance is improved by using phase change material. Conventional GHEs are reliable and effective for heating and cooling, but their performance can be affected by seasonal variations and thermal depletion. GHEs with PCMs allow the system to store excess thermal energy when temperatures are high, for later use, ensuring better thermal regulation. It offers improved efficiency by stabilizing temperatures within the system. The PCM's ability to absorb and release heat helps mitigate temperature fluctuations, leading to better performance in peak load situations.

Figure 16 depicts the comparison between the results of the study conducted by Mathur et al. [55], Zhou et al. [33], Yusof et al. [18], Yang et al. [16], Agrawal et al. [60] and

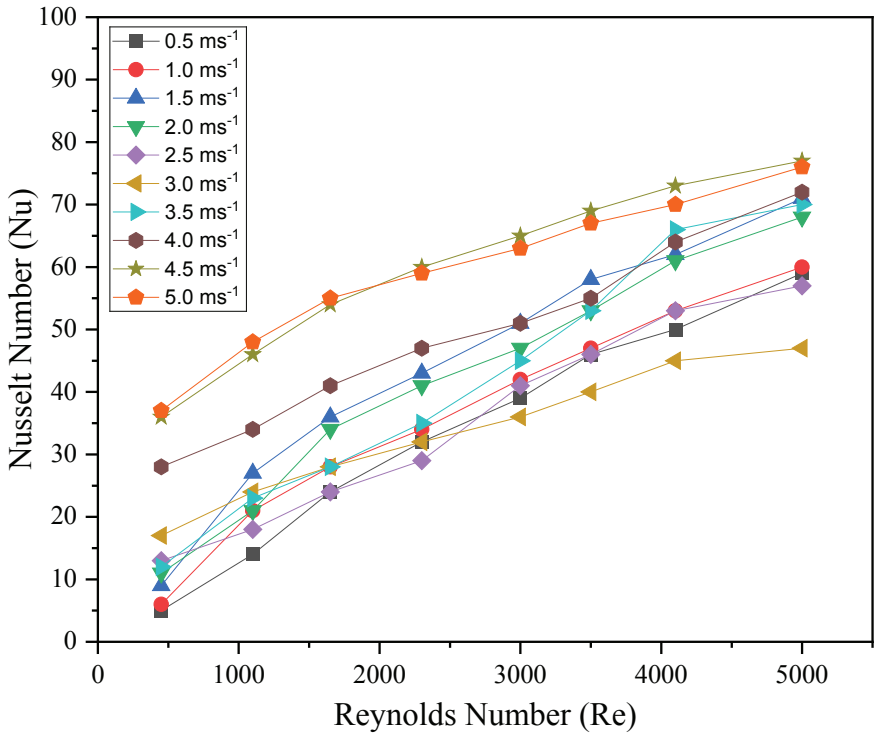

Figure 13. Nusselt number variation with Reynolds number at different air velocity.

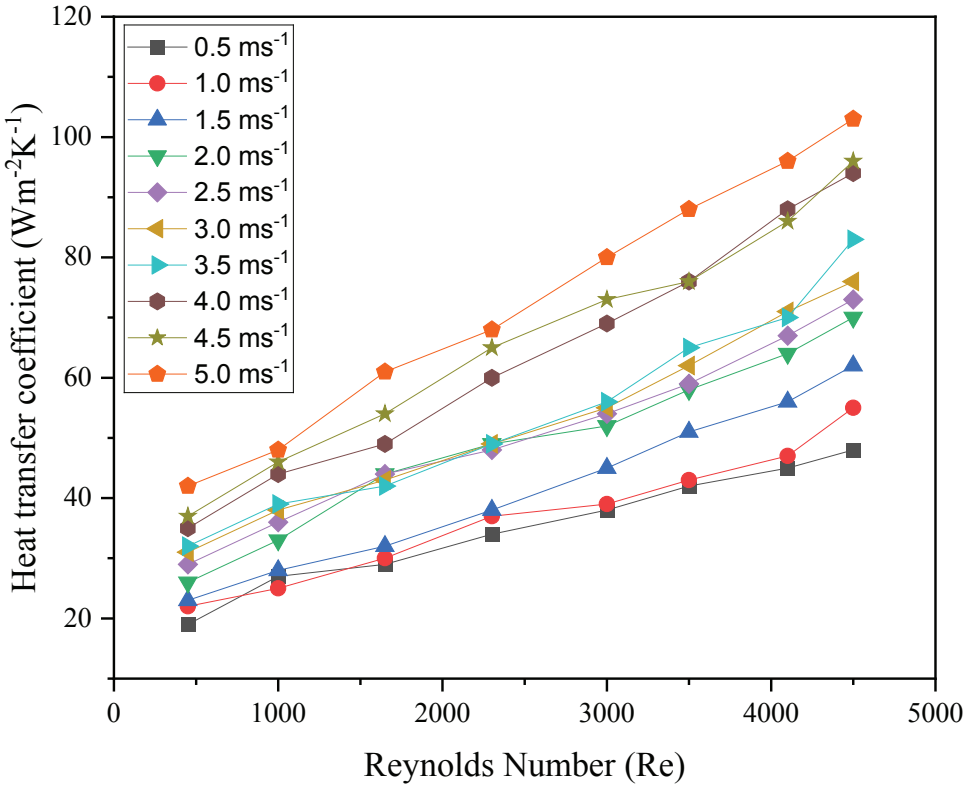

Figure 14. Various heat transfer coefficients with Reynolds number for different air velocities.

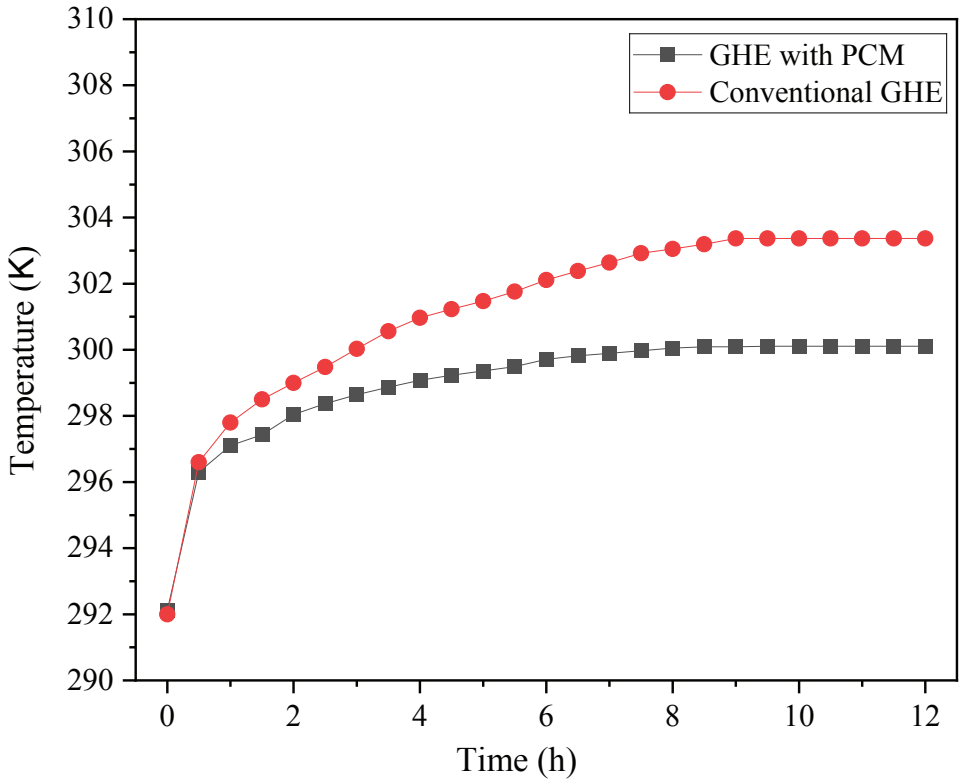

Figure 15. Comparison of GHE with PCM against conventional GHE at a velocity of 5 ms^{-1}.

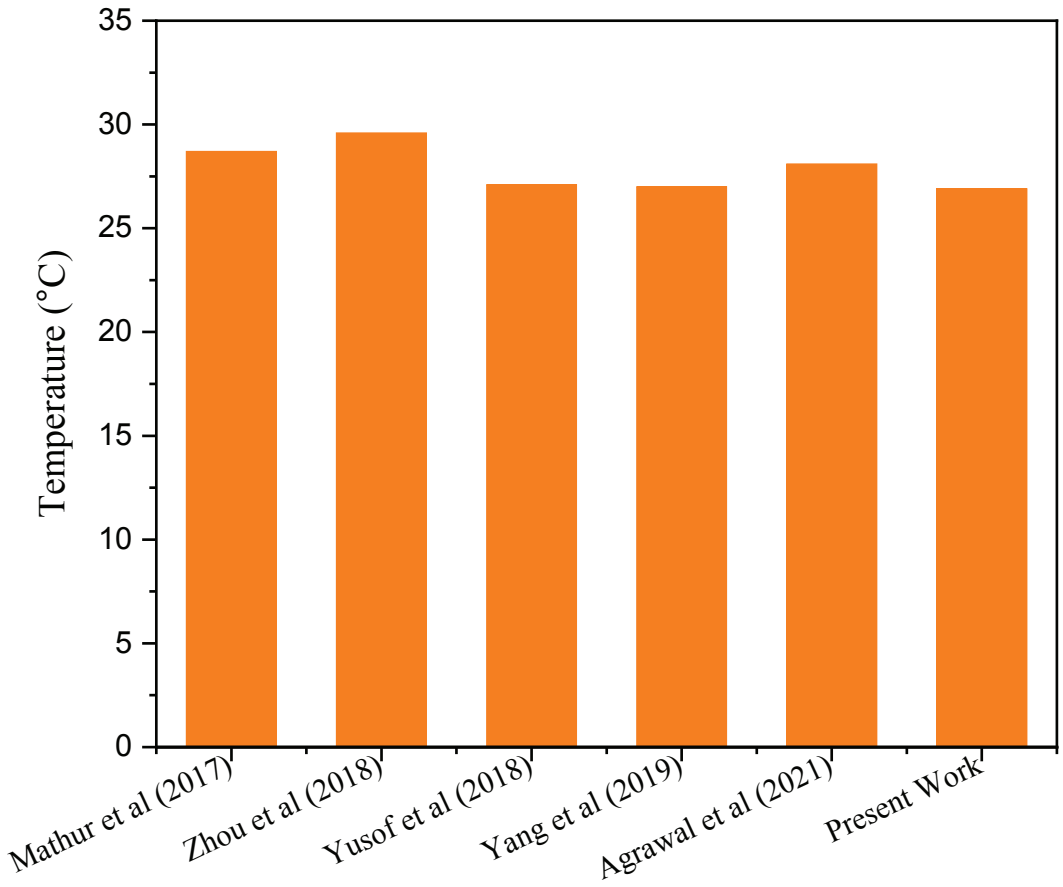

Figure 16. Comparison of the temperature variation of this work over previous studies on GSHE.

the present study. In these studies, the outlet temperature of GHE is found to be 28.7 °C, 29.6 °C, 27.1 °C, 27 °C, 28.1 °C, and 26.9 °C. Thus, compared to previous studies, the lowest ground temperature of the heat pump was observed in the present study. Where Figure 17 compares the effectiveness of the GHE across studies conducted by Zhang et al. [64], Hu et al. [65], Chen et al. [13], and the present study. After 10 hours of operation, the effectiveness values were 0.07821, 0.2475, 0.179191, and 0.48158, 0.46789, 0.37895, respectively, depending on the conditions used. Zhang et al. used a horizontal tube setup at 2 ms^{-1}, while the present study used a vertical arrangement, showing a much higher effectiveness of 0.46789—about six times greater than Zhang et al.'s result. Hu et al.'s effectiveness, measured at a lower velocity of 0.419 ms^{-1}, was still lower than even the minimum value of effectiveness from the present study at 5 ms^{-1}. As for Chen et al., who also used paraffin wax as the PCM, their results were 0.472 times lower than the lowest effectiveness observed in the present study, even at a velocity of 0.3 ms^{-1}. These differences can be explained by variations in the dimensional parameters and operating conditions between the studies.

Meanwhile, Figure 18 shows the heat transfer rate per meter across studies conducted by Jalaluddin and Miyara [66], who used water as the working fluid at a flow rate of 4 l/min and silica sand as the backfill material, Kim et al. [67], using the same working fluid at a speed of 0.3 ms^{-1} with cement-based grouts, Yang et al. [16], also used water at 0.6 ms^{-1} with oleic acid as the backfill material and the present study where PCM was used as the backfill material with air as the working fluid and in this case, at a velocity of 0.5 ms^{-1}. Although the operational parameters such as velocity, soil temperature, and U-Tube dimensions differ in each case, due to the variation in these parameters, the thermal performance of the GHE may vary and differ from one study to another. The comparison aims to showcase how the Ground Source Heat Exchanger (GHE) responds to various backfill materials. After 12 hours of operation, the PCM-coupled GHE of the present study achieves a heat transfer rate of 61.12 W/m, which is 2.27 times higher than the result obtained by Jalaluddin and Miyara [66] and 1.05 times greater than that of Kim et al. [67]. The present study also shows a heat transfer rate 2.5 times greater than that of Yang et al. [16] after 10 hours of operation. Thus, the GHE with PCM as the backfill material and air as the working fluid demonstrates a better heat transfer rate per meter than the other three studies.

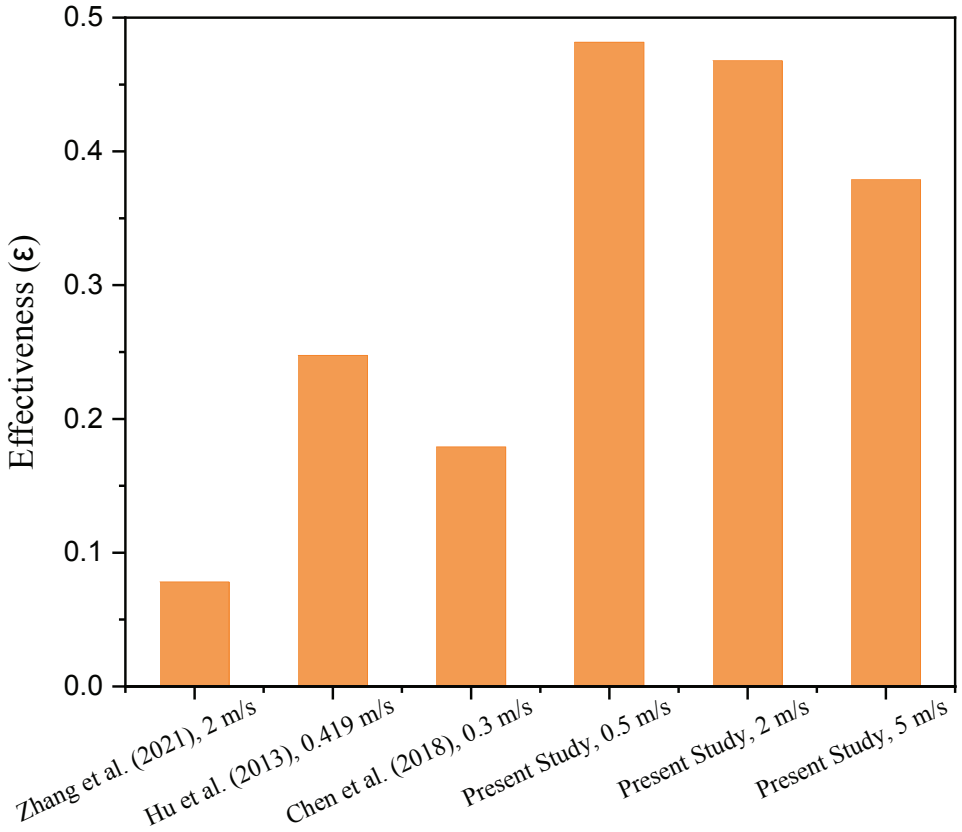

Figure 17. Effectiveness variation of the work compared to the previous studies on GSHE.

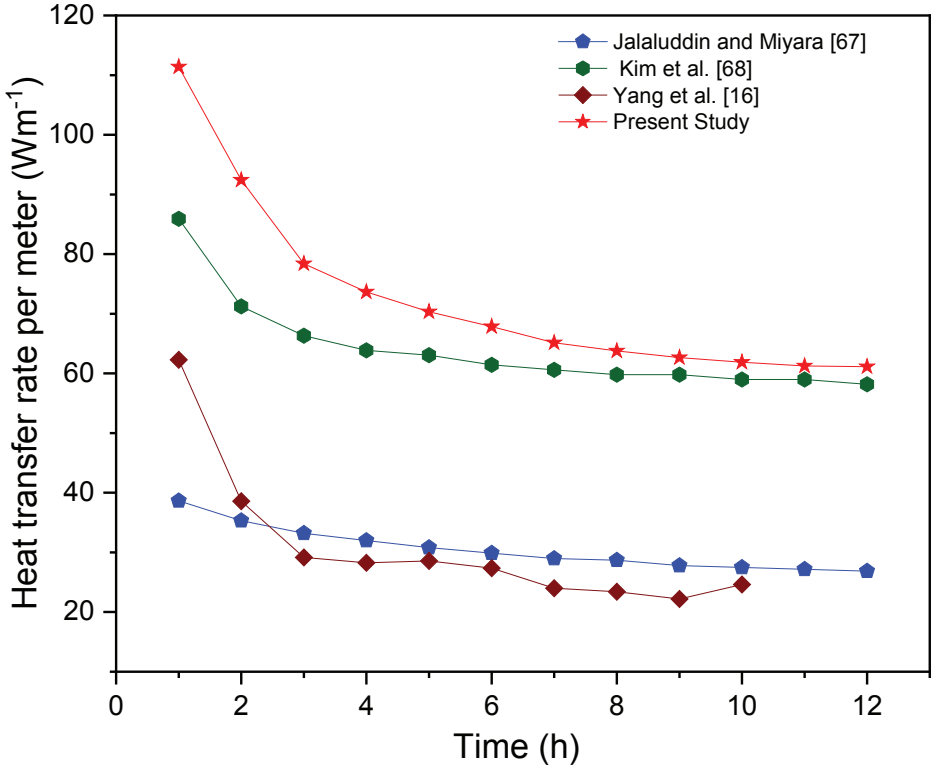

Figure 18. Variation of the heat transfer rate per meter of the present study compared with previous studies on GSHE.

CONCLUSION

In this study, the main concentration was on the thermal performance of an underground u-bend type heat exchanger with phase change material. A double U-shape tube was designed and numerically simulated under certain conditions. In this work, paraffin wax was used as PCM in the backfilling of the borehole around the pipe. Outlet temperature, rate of heat transfer, cooling capacity, and effectiveness of the system were measured and plotted in the graph and compared for air velocity ranging from 0.5 ms^{-1} to 5 ms^{-1}. In summary, the subsequent findings have been discovered.

- A reduced air velocity should result in a lower heat exchanger exit temperature. The temperature drop at the exit was 9.09°C and 7.2°C respectively for air velocity 0.5 ms^{-1} and 5 ms^{-1} after 12 hours of continuous operation. Therefore, the finding recommends a lower velocity flow for a better temperature drop at the outlet
- At higher speeds, the heat transfer rate increases. The heat transfer rate per meter is 76.27 Wm^{-1} for 0.5 ms^{-1} and 116.45 Wm^{-1} for 5 ms^{-1} air velocity after 12 hours of operation. Therefore, to obtain a high heat transfer rate per meter, high air velocity is preferred. This is true for the overall cooling capacity as well.
- The system's effectiveness declines with time. The parameter decreases by 26.56% and 39.34% for 0.5 ms^{-1} and 5 ms^{-1}, respectively, after 12 hours of uninterrupted operation in comparison to the outcomes after 1 hour of operation. Additionally, the system's effectiveness during any given operating hour was shown to decline as air velocity increased.
- After 40 m length of the GHE, the change in temperature is minimal.
- Thus, high air velocity is preferable for higher heat transfer rate and cooling capacity, but higher velocity increases the outlet temperature and results in reduced temperature drop between inlet and outlet and decreased effectiveness.

The study reveals that using PCM as the backfill with good thermal qualities near ground heat exchanger pipes enhances the overall performance of the system. Additionally, the ground heat exchanger's length may be significantly reduced by using U-tubes. Ground heat exchangers are energy-efficient, adaptable heating and cooling systems used in both commercial and residential establishments. They work in every climatic condition and can cut carbon emissions. Future studies should concentrate on enhancing system performance under a variety of environmental circumstances, design optimization which also includes finding the optimal length of the GHE, and thermal performance enhancement with phase change materials.

NOMENCLATURE

A_{Mush}	Mushy zone constant
CE	Convective heat flow between the soil surface and ambient air, (W/m^2)
$EAHE$	Earth air heat exchanger
GHE	Ground heat exchanger
$GSHP$	Ground source heat pump
G	Incident solar global irradiance, (W/m^2)
$HVAC$	Heating, ventilation, and air conditioning
HTF	Heat transfer fluid
$HEPC$	Horizontal earth pipe cooling
$HWAHE$	Helical water air heat exchanger
ΔH	Latent enthalpy, (J/kg)
LR	Soil surface emitted long-wave radiation, (W/m^2)
$SSPCM$	Shape stabilized phase change material
T_{soil}	Soil natural temperature field, (°C)
$T_{sol\text{-}air}$	Solar-air temperature, (°C)
T_{ss}	Source term energy, W/m^3
T_{amb}	Ambient air temperature, (°C)
$T_{amb,m}$	Mean of monthly ambient air temperature, (°C)

AUTHORSHIP CONTRIBUTIONS

Md. Nur Alam (M. N. Alam): Conceptualization, methodology, investigation, data acquisition, analysis, writing original draft, and editing manuscript.

Dipayan Mondal (D. Mondal): Conceptualization, methodology, investigation, analyzing and interpreting the data, writing, review and editing, writing of reviewer response, discussion, and supervising.

Mohammad Rafat Islam (M. R. Islam): Analyzing and interpreting the data, reviewing and editing, and writing reviewer response.

DATA AVAILABILITY STATEMENT

The corresponding author will make the data available upon reasonable request.

CONFLICT OF INTEREST

There were no conflicts of interest disclosed by the authors, nor was there any major financial contribution that could have impacted on the outcome of this study

ETHICS

The publication of this manuscript raises no ethical issues.

STATEMENT ON THE USE OF ARTIFICIAL INTELLIGENCE

Artificial intelligence was not used in the preparation of the article.

REFERENCES

[1] Omer AM. Energy, environment and sustainable development. Renew Sustain Energy Rev 2008;12:2265– 2300. [CrossRef]

[2] Sawhney RL, Buddhi D, Thanu NM. An experimental study of summer performance of a recirculation type underground airpipe air conditioning system. Build Environ 1998;34:189–196. [CrossRef]
[3] Esen M, Yuksel T. Experimental evaluation of using various renewable energy sources for heating a greenhouse. Energy Build 2013;65:340–351. [CrossRef]
[4] Naili N, Hazami M, Kooli S, Farhat A. Energy and exergy analysis of horizontal ground heat exchanger for hot climatic condition of northern Tunisia. Geothermics 2015;53:270–280. [CrossRef]
[5] Santamouris M, Mihalakakou G, Balaras CA, Lewis JO, Vallindras M, Argiriou A. Energy conservation in greenhouses with buried pipes. Energy 1996;21:353–360. [CrossRef]
[6] Mihalakakou G, Lewis JO, Santamouris M. On the heating potential of buried pipes techniques — application in Ireland. Energy Build 1996;24:19–25. [CrossRef]
[7] Kong XR, Deng Y, Li L, Gong WS, Cao SJ. Experimental and numerical study on the thermal performance of ground source heat pump with a set of designed buried pipes. Appl Therm Eng 2017;114:110–117. [CrossRef]
[8] Pu L, Qi D, Li K, Tan H, Li Y. Simulation study on the thermal performance of vertical U-tube heat exchangers for ground source heat pump system. Appl Therm Eng 2015;79:202–213. [CrossRef]
[9] Jalaluddin, Miyara A, Tsubaki K, Inoue S, Yoshida K. Experimental study of several types of ground heat exchanger using a steel pile foundation. Renew Energy 2011;36:764–771. [CrossRef]
[10] Liu Q, Huang Y, Ma Y, Peng Y, Wang Y. Parametric study on the thermal performance of phase change material-assisted earth-to-air heat exchanger. Energy Build 2021;238. [CrossRef]
[11] Gao J, Zhang X, Liu J, Li KS, Yang J. Thermal performance and ground temperature of vertical pile-foundation heat exchangers: A case study. Appl Therm Eng 2008;28;2295–2304. [CrossRef]
[12] Chen F, Mao J, Li C, Hou P, Li Y, Xing Z, et al. Restoration performance and operation characteristics of a vertical U-tube ground source heat pump system with phase change grouts under different running modes. Appl Therm Eng 2018;141:467–482. [CrossRef]
[13] Chen F, Mao J, Chen S, Li C, Hou P, Liao L. Efficiency analysis of utilizing phase change materials as grout for a vertical U-tube heat exchanger coupled ground source heat pump system. Appl Therm Eng 2018;130:698–709. [CrossRef]
[14] Qi D, Pu L, Sun F, Li Y. Numerical investigation on thermal performance of ground heat exchangers using phase change materials as grout for ground source heat pump system. Appl Therm Eng 2016;106:1023–1032. [CrossRef]
[15] Ahmed SF, Amanullah MTO, Khan MMK, Rasul MG, Hassan NMS. Parametric study on thermal performance of horizontal earth pipe cooling system in summer. Energy Convers Manag 2016;114:324–337. [CrossRef]
[16] Yang W, Xu R, Yang B, Yang J. Experimental and numerical investigations on the thermal performance of a borehole ground heat exchanger with PCM backfill. Energy 2019;174:216–235. [CrossRef]
[17] Bottarelli M, Bortoloni M, Su Y, Yousif C, Aydin AA, Georgiev A. Numerical analysis of a novel ground heat exchanger coupled with phase change materials. Appl Therm Eng 2015;88:369–375. [CrossRef]
[18] Yusof TM, Ibrahim H, Azmi WH, Rejab MRM. Thermal analysis of earth-to-air heat exchanger using laboratory simulator. Appl Therm Eng 2018;134:130–140. [CrossRef]
[19] Li C, Mao J, Zhang H, Xing Z, Li Y, Zhou J. Numerical simulation of horizontal spiral-coil ground source heat pump system : Sensitivity analysis and operation characteristics. Appl Therm Eng 2017;110:424–435. [CrossRef]
[20] Misra R, Bansal V, Agrawal GD, Mathur J, Aseri TK. CFD analysis based parametric study of derating factor for Earth Air Tunnel Heat Exchanger. Appl Energy 2013;103:266–277. [CrossRef]
[21] Florides G, Theofanous E, Joseph-Stylianou J, Tassou S, Christodoulides P, Zomeni Z, et al. Vertical and Horizontal Ground Heat Exchanger Modeling. In Proceedings of the Conference: World Renewable Energy Congress, 2013, KTISIS Institutional Repository, Cyprus University of Technology, Cyprus.
[22] Cui Q, Shi Y, Zhang Y, Wu R, Jiao Y. Comparative study on the thermal performance and economic efficiency of vertical and horizontal ground heat exchangers. Adv Geo-Energy Res 2023;7:7–19. [CrossRef]
[23] Ghosal MK, Tiwari GN. Modeling and parametric studies for thermal performance of an earth to air heat exchanger integrated with a greenhouse. Energy Convers Manag 2006;47:1779–1798. [CrossRef]
[24] Morshed W, Leso L, Conti L, Rossi G, Simonini S, Barbari M. Cooling performance of earth-to-air heat exchangers applied to a poultry barn in semi-desert areas of south Iraq. Int J Agric Biol Eng 2018;11:47–53. [CrossRef]
[25] Hsu CY, Chiang YC, Chien ZJ, Chen SL. Investigation on performance of building-integrated earth-air heat exchanger. Energy Build 2018;169:444–452. [CrossRef]
[26] Aditya GR, Mikhaylova O, Narsilio GA, Johnston IW. Comparative costs of ground source heat pump systems against other forms of heating and cooling for different climatic conditions. Sustain Energy Technol Assessments 2020;42:100824. [CrossRef]

[27] Gao B, Zhu X, Yang X, Yuan Y, Yu N, Ni J. Operation performance test and energy efficiency analysis of ground-source heat pump systems. J Build Eng 2021;41:102446. [CrossRef]
[28] Zhou Z, Liu Q, Tao Y, Peng Y, Zhou T, Wang Y. Analysis of a borehole ground heat exchanger with shape-stabilized phase change material backfill. Appl Therm Eng 2022;222. [CrossRef]
[29] Zhang XY, Ge YT, Burra, Lang PY. Experimental investigation and CFD modelling analysis of finned-tube PCM heat exchanger for space heating. Appl Therm Eng 2024;244. [CrossRef]
[30] Emmi G, Bottarelli M. Enhancement of shallow ground heat exchanger with phase change material. Renew Energy 2022;206. [CrossRef]
[31] Hadjadj A, Benhaoua B, Atia A, Khechekhouche A, Lebbihiat N, Rouag A. Air velocity effect on the performance of geothermal helicoidally water-air heat exchanger under El Oued climate, Algeria. Therm Sci Eng Prog 2019;20. [CrossRef]
[32] Han J, Cui M, Chen J, Lv W. Analysis of thermal performance and economy of ground source heat pump system: a case study of the large building. Geothermics 2021;89:101929. [CrossRef]
[33] Zhou T, Xiao Y, Liu Y, Lin J, Huang H. Research on cooling performance of phase change material-filled earth-air heat exchanger. Energy Convers Manag 2018;177:210–223. [CrossRef]
[34] Mondal D, Ikram MO, Rabbi MF, Moral MNA. Experimental Investigation and Comparison of Bend Tube Parallel & Counter Flow and Cross Flow Water to Air Heat Exchanger. Int J Sci Eng Res 2014;5:686–695.
[35] Mondal D, Alam A, Islam MA. Experimental Observation of a Small Capacity Vapor Absorption Cooling System 2014;5:456–467.
[36] Mondal D, Islam MA. Experimental Investigation on an Intermittent Ammonia Absorption Refrigeration. Mech Eng Res J 2018;11:59–65.
[37] Mondal D, Hori Y, Kariya K, Miyara A, Alam MJ. Measurement of Viscosity of a Binary Mixture of R1123 + R32 Refrigerant by Tandem Capillary Tube Method. Int J Thermophys 2020;41:1–20. [CrossRef]
[38] Mondal D, Kariya K, Tuhin AR, Amakusa N, Miyara A. Viscosity measurement for trans-1,1,1,4,4,4-hexafluoro-2-butene(R1336mzz(E)) in liquid and vapor phases. Int J Refrig 2021;133:267–275. [CrossRef]
[39] Mondal D, Kariya K, Tuhin AR, Miyoshi K, Miyara A. Thermal conductivity measurement and correlation at saturation condition of HFO refrigerant trans-1,1,1,4,4,4-hexafluoro-2-butene (R1336mzz(E)). Int J Refrig 2021;129:109–117. [CrossRef]
[40] Mondal D, Tuhin AR, Kariya K, Miyara A. Measurement of Kinematic Viscosity and Thermal Conductivity of 3,3,4,4,5,5-HFCPE in Liquid and Vapor Phases. Int J Refrig 2022;140:150–165. [CrossRef]
[41] Islam L, Mondal D, Islam A, Das P. Effects of Heat Transfer Characteristics of R32 and R1234yf with Al2O3 Nanoparticle through U-Bend Tube Evaporator. J Eng 2024:24. [CrossRef]
[42] Das P, Mondal D, Islam A, Afroj M. Thermodynamic performance evaluation of a solar powered Organic Rankine cycle (ORC) and dual cascading vapor compression cycle (DCVCC): Power generation and cooling effect. Energy Convers Manag X 2024;23:100662. [CrossRef]
[43] Arefin MM, Mondal D, Islam MA. Optimizing cascade refrigeration systems with low GWP refrigerants for Low-Temperature Applications: A thermodynamic analysis. Energy Convers Manag X 2024;24:100722. [CrossRef]
[44] Bari MA, Mondal D, Hasib MA. Impact of air flow, temperature distribution, and heat transmission in a refrigerator compartment with and without shelves: A numerical approach. J Therm Eng 2024;10:1590–1606. [CrossRef]
[45] Shaharier MT, Mondal D, Hasib MA, Islam MA. Effects of gas-liquid flow and dehumidification performance of a liquid desiccant dehumidifier: A numerical approach for vertical smooth & rough, and inclined rough plates. J Therm Eng 2024;10:1559–1576. [CrossRef]
[46] Rifert VG, Gorin VV, Sereda VV, Treputnev VV. Improving Methods to Calculate Heat Transfer During the Condensation Inside Tubes. J Eng Phys Thermophys 2019;92:797–804. [CrossRef]
[47] Rifert V, Sereda V, Gorin V, Barabash P, Solomakha A. Heat transfer during film condensation inside plain tubes. Review of experimental research. Heat Mass Transf 2020;56:691–713. [CrossRef]
[48] Thome JR, Hajal J, Cavallini A. Condensation in horizontal tubes, part 2: New heat transfer model based on flow regimes. Int J Heat Mass Transf 2003;46:3365–3387. [CrossRef]
[49] Cavallini A, Col DD, Doretti L, Matkovic M, Rossetto L, Zilio C, et al. Condensation in horizontal smooth tubes: A new heat transfer model for heat exchanger design. Heat Transf Eng 2006;27:31–38. [CrossRef]
[50] Shah MM. A new flow pattern based general correlation for heat transfer during condensation in horizontal tubes. IHTC 2014;1–15. [CrossRef]
[51] Rifert VG, Sereda VV, Barabash PO, Gorin VV. Condensation inside smooth horizontal tubes: Part 2. improvement of heat exchange prediction. Therm Sci 2017;21:1479–1489. [CrossRef]
[52] Rifert V, Sereda V, Gorin V, Barabash P, Solomakha A. Substantiation and the range of application of a new method for heat transfer prediction in condensing inside plain tubes. Energetika 2018;64:146–154. [CrossRef]

[53] Camaraza-Medina Y, Hernandez-Guerrero A, Luviano-Ortiz JL, Mortensen-Carlson K, Cruz-Fonticiella OM, García-Morales OF. New model for heat transfer calculation during film condensation inside pipes. Int J Heat Mass Transf 2019;128:344–353. [CrossRef]

[54] ANSYS. ANSYS Fluent Theory Guide. Available at: https://dl.cfdexperts.net/cfd_resources/Ansys_Documentation/Fluent/Ansys_Fluent_Theory_Guide.pdf. Accessed on 28 Feb 2026.

[55] Mathur A, Priyam, Mathur S, Agrawal GD, Mathur J. Comparative study of straight and spiral earth air tunnel heat exchanger system operated in cooling and heating modes. Renew Energy 2017;108:474–487. [CrossRef]

[56] Tay NHS, Belusko M, Liu M, Bruno F. Investigation of the effect of dynamic melting in a tube-in-tank PCM system using a CFD model. Appl Energy 2015;137:738–747. [CrossRef]

[57] Fornarelli F, Camporeale SM, Fortunato B, Torresi M, Oresta P, Magliocchetti L, et al. CFD analysis of melting process in a shell-and-tube latent heat storage for concentrated solar power plants. Appl Energy 2016;164:711–722. [CrossRef]

[58] Archibold AR, Gonzalez-Aguilar J, Rahman MM, Goswami DY, Romero M, Stefanakos EK. The melting process of storage materials with relatively high phase change temperatures in partially filled spherical shells. Appl Energy 2014;116:243–252. [CrossRef]

[59] Li WQ, Qu ZG, He YL, Tao WQ. Experimental and numerical studies on melting phase change heat transfer in open-cell metallic foams filled with paraffin. Appl Therm Eng 2012;37:1–9. [CrossRef]

[60] Agrawal KK, Misra R, Agrawal GD. CFD simulation study to evaluate the economic feasibility of backfilling materials for ground-air heat exchanger system. Geothermics 2021;90:102002. [CrossRef]

[61] Mihalakakou G, Santamouris M, Lewis JO, Asimakopoulos DN. On the application of the energy balance equation to predict ground temperature profiles. Sol Energy 1997;60:181–190. [CrossRef]

[62] Badescu V. Simple and accurate model for the ground heat exchanger of a passive house. Renew Energy 2007;32:845–855. [CrossRef]

[63] Khatry AK, Sodha MS, Malik MAS. Periodic variation of ground temperature with depth. Sol Energy 1978;20:425–427. [CrossRef]

[64] Zhang X, Xu M, Liu L, Yang Q, Song KI. Study on thermal performance of casing-type mine heat recovery device with phase change materials filling in annular space. Int J Energy Res 2021;45:1–20. [CrossRef]

[65] Hu P, Yu Z, Zhu N, Lei F, Yuan X. Performance study of a ground heat exchanger based on the multipole theory heat transfer model. Energy Build 2013;65:231–241. [CrossRef]

[66] Jalaluddin, Miyara A. Thermal performance investigation of several types of vertical ground heat exchangers with different operation mode. Appl Therm Eng 2012;33–34:167–174. [CrossRef]

[67] Kim D, Kim G, Kim D, Baek H. Experimental and numerical investigation of thermal properties of cement-based grouts used for vertical ground heat exchanger. Renew Energy 2017;112:260–267. [CrossRef]

J Ther Eng, Vol. 12, No. 2, pp. 519−531, March, 2026

Journal of Thermal Engineering
Web page info: https://jten.yildiz.edu.tr
DOI: 10.14744/thermal.0001099

Research Article

Experimental investigation of a low-cost evacuated tube in a parabolic trough collector with and without porous insert

Pooja RAVAL[1,*], Bharat RAMANI[2], Karan MOTWANI[3], Nikhilkumar CHOTAI[3]

[1]*Gujarat Technological University, Gujarat, 380001, India*
[2]*Principal, LTIET, Gujarat, 360001, India*
[3]*Department of Mechanical Engineering, Marwadi University, Gujarat, 380001, India*

ARTICLE INFO

Article history
Received: 13 February 2025
Revised: 16 April 2025
Accepted: 12 May 2025

Keywords:
Circular Ring Wire Mesh Insert; Evacuated Tube; Nusselt Number; Parabolic Trough Collector; Thermal Efficiency

ABSTRACT

This research paper addresses the challenges of high upfront cost, maintaining vacuum, limited configurations and manufacturers, and fluid thermal retention in the evacuated receiver tube used in parabolic trough collector. These challenges affect the collectors cost and efficiency, which lowers its acceptance for the industrial market. Two attempts have been made to overcome this issue: developing an in-house evacuated tube of the specific configuration with locally available materials to reduce the cost. Furthermore, a novel porous insert is designed and examined inside the tube to improve fluid thermal retention, which will enhance the overall efficiency of the collector. An in-house developed evacuated tube with a notched circular ring porous insert is examined experimentally. The experimental tests were conducted using a manually tracked mechanism with a 2.36 m^2 aperture area and a 0.50 m focal length, utilizing water as the heat transfer fluid. Performance was evaluated with and without inserts at varying mass discharge rates (0.04, 0.06, and 0.08 kg/s), considering parameters such as Nusselt number, outlet fluid temperature, heat gain and thermal efficiency. The results demonstrate that the receiver tube with inserts significantly outperforms the plain tube (without insert). At higher mass flow rates, the insert-enhanced thermal efficiency is 31.2% and 20.46% in the Nusselt number. Also, a higher outlet fluid temperature is obtained in a tube with an insert, indicating improved thermal retention. This study establishes that incorporating novel inserts and developing in-house evacuated tube can be a viable solution for optimizing the cost and performance of the collector.

Cite this article as: Raval P, Ramani B, Motwani K, Chotai N. Experimental investigation of a low-cost evacuated tube in a parabolic trough collector with and without porous insert. J Ther Eng 2026;12(2):519−531.

INTRODUCTION

In parabolic trough collector (PTC), the receiver tube is considered to be the crucial component of the system. In general, the sun rays from the sun are concentrated on the receiver tube with the help of the reflector, which is placed at the focal distance from it [1]. The working heat

***Corresponding author.**
*E-mail address: pmghodasara@gmail.com

This paper was recommended for publication in revised form by Editor-in-Chief Ahmet Selim Dalkılıç

Published by Yıldız Technical University Press, İstanbul, Turkey
Yıldız Technical University. This is an open access article under the CC BY-NC license (http://creativecommons.org/licenses/by-nc/4.0/).

transfer fluid (HTF) is passed from the heating element or tube, which collects the thermal energy from the peripheral surface of the tube [2]. The thermal energy collected by the working fluid can be helpful for industrial and commercial applications. The importance of the receiver tube in PTC becomes significant due to its cost and efficiency. The cost of the receiver tube can be nearly 30 to 40% as compared to the overall cost of the system [3]. This cost consists of metal and glass tubes, coating, vacuum insulation, sealing, manufacturing and assembly. Out of this, vacuum insulation, sealing and coating are major components that make the receiver tube more expensive. On the other hand, including these three components on the receiver tube is a very vital part from the efficiency point of view.

Selective coating on the receiver tube, which has high absorptivity and low emittance, is selected [4]. Absorptivity helps to absorb more concentrated radiation from the sun, which ultimately maximizes the heat gain of the receiver tube and causes a rise in the temperature of the receiver surface and HTF. The low emittance property of the coating helps to decrease the heat losses due to an increase in the temperature of the tube [5]. This coating includes complex chemical depositions, which require advanced technologies, which makes this coating expensive [6-7].

Furthermore, vacuum insulation and sealing between metal and glass tubes reduce the conduction and convection losses from the receiver tube at higher temperatures. Sustaining a vacuum for a long time and managing the thermal stress of the receiver tube with heating and cooling requires precise manufacturing, which adds complexity and high cost [8].

Evacuated receiver tube with double side opens are very expensive compared to the evacuated tube used in the non-concentrating collector. The reason for this is the lower demand in the market, less production, and very limited manufacturers available globally. Evacuated tube used in non-concentrating collectors is designed for low-temperature applications up to 150°C. In contrast, the evacuated tube used in PTC is designed for high-temperature applications up to 400°C [9]. It has been noticed that due to the limited manufacture of such evacuated tube in the world, the additional cost of importing the receiver tube of specific configurations from different parts of the country will make it more expensive. Further, there is also the possibility of breaking glass tube due to fragile material and the loss of vacuum of the evacuated tube during adverse working industrial conditions. Figure 1 indicates the evacuated tube used in PTC.

Therefore, the authors have attempted to develop an in-house double-end open evacuated receiver tube for small PTC in the present experimental work. The evacuated tube is described in detail in the next section.

The above discussion states the importance of an evacuated tube for improving the efficiency of the PTC by restricting heat losses from the external part of the tube. The next focus of the authors was to emphasize the

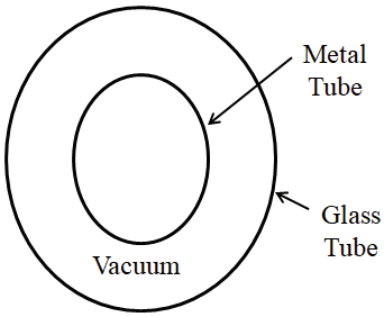

Figure 1. Indicates evacuated tube used in PTC.

performance by internal means of the receiver tube. The authors have recognized two types of methods from various literature reviews, such as the use of nanofluid [10] and inserts [11]. The use of nanofluid can enhance the working fluid conductivity, which can boost the thermal gain and overall efficiency of the solar collector. Hussein et al. [12] evaluated the thermal performance of the flat plate collector with nanofluid as CuO/H_2O over three months in Iraq. Results indicate that 1% CuO/H_2O nanofluid improves the collector efficiency by 32%, and 11.3% performance surpasses was observed while using pure H_2O. Ajbar et al. [13] carried out a simulation analysis on PTC with eight hybrid nanofluids. The thermal efficiency of PTC in all hybrid nanofluids was found to be better compared to the base fluid as Syltherm 800. Challenges such as nanofluid stability, chances of corrosion and erosion of inside tube material, and thermal instability at high temperatures may affect the performance of the PTC for a long time [14].

Next, a literature review was focused and conducted on inserting an insert in the receiver tube to improve the internal heat transfer coefficient of the fluid, which can lead to internal heat gain of the fluid and the overall performance of the PTC. Generally, two types of inserts are categorized: active and passive [15]. From the literature, authors have come across that active types of inserts are not more favorable due to their complexity and high cost [16]. Meanwhile, passive types of insert enhance thermal energy transfer and improve the system performance without requiring any external energy.

Various researchers have proven that inserts inside the receiver significantly improve the heat transfer enhancement in solar thermal systems compared to the plain tube. Twisted tapes [17], [18], wire coils [19], fins [20], [21], wire mesh [22], [23], perforated plates [24], and porous inserts [25] are found to be passive inserts, which various authors have researched. Most of the inserts have been researched in the field of heat exchangers and solar thermal systems. Several experimental and numerical studies have been conducted on PTC using inserts such as twisted tapes and fins; however, most investigations have been limited to numerical analysis. Farhad et al. [26] carried out a numerical study involving

dual twisted tape inserts within a Reynolds number range of 10000 to 20000. The Nusselt number was found to be 19.58% higher compared to a plain tube, demonstrating enhanced heat transfer performance [26]. Piyush et al. [27] performed an experimental study on a solar-based air heater utilizing dual-arc artificial roughness, which revealed a significant enhancement in heat transfer performance. The Nusselt number was found to increase by a factor of 2.27 compared to a conventional solar air heater. However, this improvement was accompanied by a substantial rise in pressure drop, which was 3.10 times higher than the plain solar air heater. Karunaraja et al. [28] carried out an experimental investigation on solar drying using a solar tunnel dryer under the meteorological conditions of Negamam. The solar tunnel dryer using thermal storage materials exhibited 2–3% higher thermal efficiency than no storage material. Sand as a thermal storage material was found to be the most effective in this study. Prem et al. [29] conducted a review study, presenting various techniques for enhancing the efficiency of solar stills. Among these, passive augmentation techniques were highlighted as an effective approach for converting polluted water into potable water.

Furthermore, these inserts perform differently, whether they are solid or porous. Twisted tapes, conical displacers, and fins are considered to be part of the solid inserts. Such types of inserts have high durability and low-pressure drop, but they can cause high fouling resistance and are heavier in weight. Meanwhile, porous inserts have their own advantages, such as being light in weight and generating turbulence with moderate pressure drop with chances of low to moderate fouling resistance.

Pooja et al. [23] experimentally studied the behaviour of the wire mesh inside the receiver tube and compared its results with that of the plain tube. Two types of inserts were studied under the laboratory setup: wire mesh twisted tape (WMTT) and circular ring wire mesh (CRWM). Parameters such as friction factor, Nusselt number, and performance evaluation criteria (PEC) were determined to compare the various inserts. Figure 2 (a) and (b) illustrate WMTT and CRWM inserts. Experimental results show that wire mesh performs better as compared to plain tube. Meanwhile, the efficacy of CRWM inserts has been found to be more promising than that of WMTT. Although CRWM demonstrates a higher Nusselt number, it also results in a greater pressure drop. In contrast, WMTT shows a slightly improved Nusselt number, while maintaining a relatively lower pressure drop. The PEC for both inserts was evaluated to assess overall performance, revealing that CRWM exhibits a superior PEC compared to WMTT. Therefore, in the current research paper, the authors have attempted to investigate the other configuration of CRWM for optimizing the thermal performance of the PTC.

This research paper consists of two broader aims: first, develop a notch-based CRWM inserts for improving the thermal retention of the fluid and second, fabricate low-cost in-house evacuated receiver tube for optimizing the cost of the PTC. An experimental investigation of in-house developed tube with and without insert is carried out to evaluate the performance of the PTC. The following subsections of this paper discuss the development of an in-house evacuated tube, CRWM insert, design and experimental part of PTC, data analysis and validation, and results and discussions.

DEVELOPMENT OF IN-HOUSE EVACUATED TUBE FOR PTC

Evacuated tube consists of four major parts, i.e. metal tube, glass tube, coating and vacuuming between metal and glass tube. Metal tube must be selected based on higher thermal conductivity, corrosion resistance, temperature

(a) WMTT

(b) CRWM

Figure 2. (a) and (b) Illustrates WMTT and CRWM inserts.

Figure 3. Illustration of in-house developed evacuated receiver tube.

range and mechanical strength. The most common materials used in solar thermal collectors are copper and stainless steel [30]. It has been observed that stainless steel as a material is more suitable for higher temperature applications above 250°C due to its strong mechanical properties. At the same time, copper is the best option for low to medium-temperature applications [31]. Secondly, a glass tube made of borosilicate is generally used to cover the metal tube, which has high transmittance and is capable enough to withstand high temperatures. The vacuum is created in this concentric metal and glass tube, which maintains thermal insulation to prevent energy losses at high temperatures. It also protects the metal tube and its coating from the surrounding environment.

Next, coating with thickness in a range of 0.2 to 2 microns is used on the external peripheral surface of the receiver tube, which helps to enhance absorption of the sun radiation and simultaneously reduces thermal energy emission losses with an increase in temperature. Black chrome and matte black paint coating can be used on the external peripherals surface of the tube, which is locally available, less expensive, and easy to apply [5]. Coatings, such as ceramic-metal composites, carbon or graphene-based, titanium nitride oxide, etc., are also examined in PTC [32]. Lastly, an enclosure of metal and glass tubes with coating is vacuumed and sealed for thermal insulation. Different types of sealing, such as glass to metal, metal bellows, elastomer, epoxy resin, brazed sealing, and compression sealing options, are available to make a perfect vacuum sealing. Selection of sealing is based on temperature range, thermal stability and vacuum retention [33]. From the literature review, it was noted that sealing such as epoxy resin, compression sealing, and elastomer can withstand up to a temperature range of 150 - 200°C. While glass-to-metal, brazed sealing and metal bellows are more suitable for higher temperature ranges up to 500°C.

In the present study, a metal tube made of copper material was selected, with inner and outer diameters of 22 mm and 25 mm and an effective tube length of 1000 mm. Illustration of an in-house developed evacuated receiver tube is shown in Figure 3. A locally available matt black coating was applied on the external surface of the copper tube. Borosilicate glass tube having inner and outer diameter of 47 mm and 50 mm were selected to form an enclosure on the metal tube. Finally, the rubber seal was cut and fitted according to the space between the copper and glass tube. A heat-resistant adhesive was applied to enhance the bonding between the contact surface of the seal and copper. The Glass tube was slid and rotated over the copper tube to maintain a proper gap, disturbing the adhesive uniformly and preventing air pockets from forming. A vacuum pump was used to evacuate air and obtain the desired pressure level between the copper and glass tube to integrate the vacuum seal. The vacuum pressure of -25 cm of Hg, equivalent to -0.3333 bars, was kept between enclosures. Pressure monitoring was done for two continuous days to ensure the vacuum and seal between glass and metal were tightened, ensuring leak detection. Figure 4 highlights the vacuum process conducted in the laboratory.

Circular Ring Wire Mesh Insert

Wire mesh is a porous type of insert used in the present study to examine its impact on the heat transfer performance of the PTC. Wire mesh of stainless steel with 18 pores per inch (PPI) (70% porosity) was selected due to being readily available in the local market. It was cut into a circular ring with the help of tin spins and fitted into the circular rod of 3 mm diameter and 1000 mm length. Twenty numbers of CRWM were located on the circular rod with a

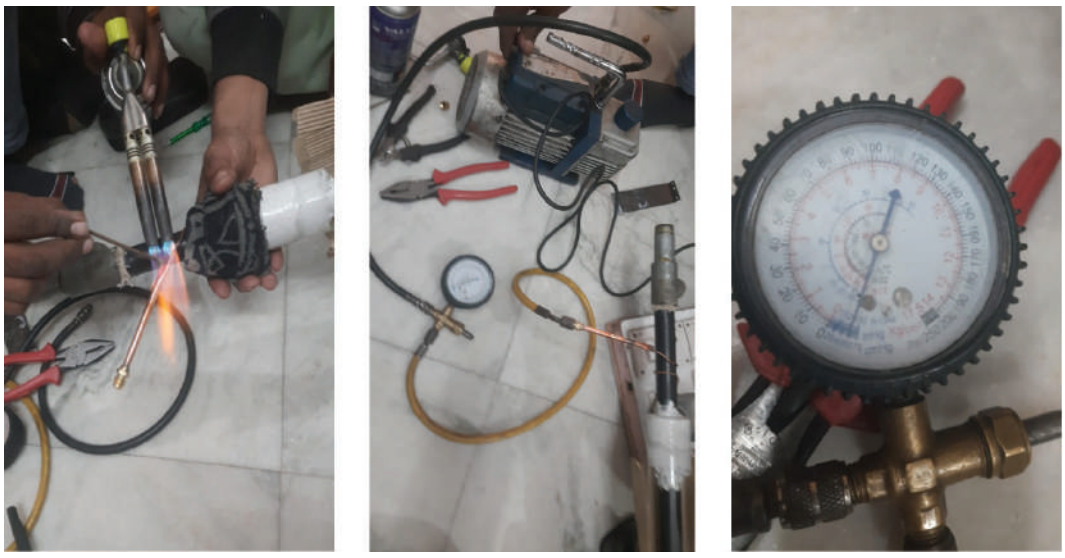

Figure 4. Highlights the vacuum process conducted in the laboratory.

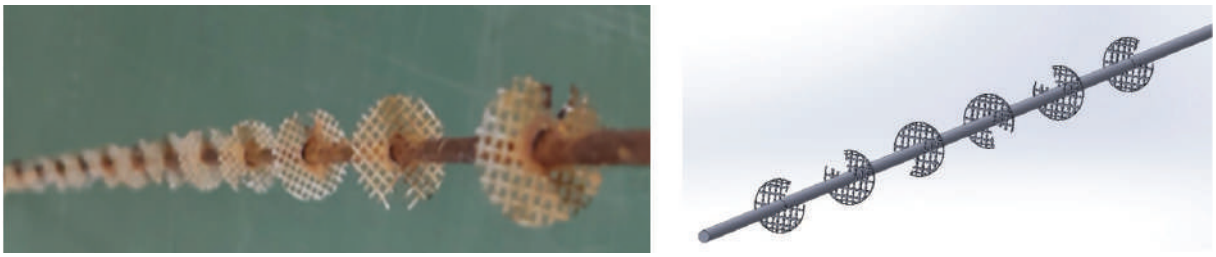

Figure 5. (a) and (b) Represents real and CAD model of circular ring wire mesh-18 PPI.

pitch distance of 50 mm. Furthermore, a V-notch cut was made in the circular ring, generating more turbulence and a larger surface area to increase heat transfer and help minimize the pressure drop. Real and CAD models of circular ring wire mesh-18 PPI are shown in Figure 5 (a) and (b).

Design of Parabolic Trough Collector

The concept design of the parabola is demonstrated in Figure 6. The PTC contains of a parabolic reflector with an eccentricity equal to one, designed to concentrate all sun radiation on the focal point. The receiver tube is located on the focal point, which absorbs the concentrated radiation. Generally, glass or aluminum sheets with high reflectivity are selected for a parabolic reflector. Parameters such as focal length, aperture size, rim angle, receiver tube diameter, and concentration ratio can be analyzed while designing PTC. The following equations (1 to 4) were used to design PTC [34]. The specifications for the design PTC are shown in Table 1.

Aperture area of the collector can be calculated using equation (1),

$$Aperture\ Area = Length\ of\ collector(W) * Width\ of\ parabola(l) \quad (1)$$

Surface area of receiver tube can be determined using equation (2),

$$Receiver\ area = \Pi * d_{go} * L \quad (2)$$

Where, d_{go} = diameter of the glass tube and L = glass tube length

Concentration ratio can be calculated using equation (3) [33],

$$CR = \frac{Aperture\ area}{Receiver\ area} = \frac{(W - d_{go})\ * l}{\Pi * d_{go} * L} \quad (3)$$

Focal point of the parabola can be calculated as mentioned in below equation (4),

$$F = \frac{W}{4 * tan\Phi/2} \quad (4)$$

Where, Φ = rim angle

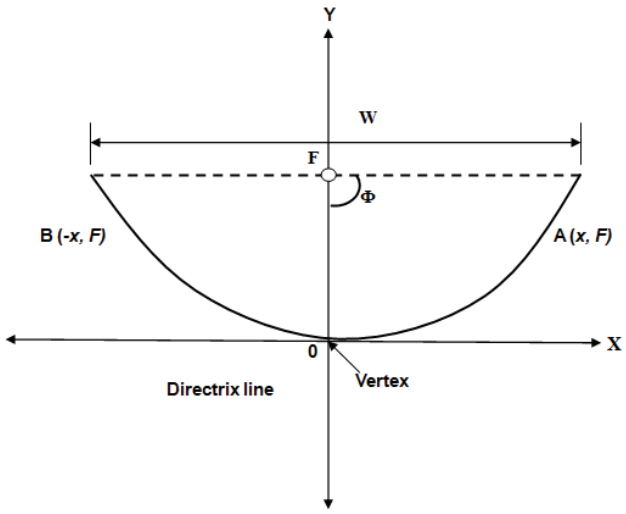

Figure 6. Demonstrates concept design of the parabola.

Table 1. Specification of PTC

Parameter	Value
Aperture width	1.865 m
Aperture area	2.36 m^2
Parabola length	1.3 m
Focal length	0.50 m
Rim angle	90°
Concentration ratio	15.03

Experimental Setup and Procedure

The experimental setup was fabricated and installed at Marwadi University, Rajkot, which is at 22°18'N latitude and 70°47'E longitude. The setup consists of a parabolic-shaped mirror reflector, evacuated receiver tube, inlet and outlet fluid thermocouple, pyranometer, anemometer, temperature gun, data logger, and miscellaneous accessories for fitting.

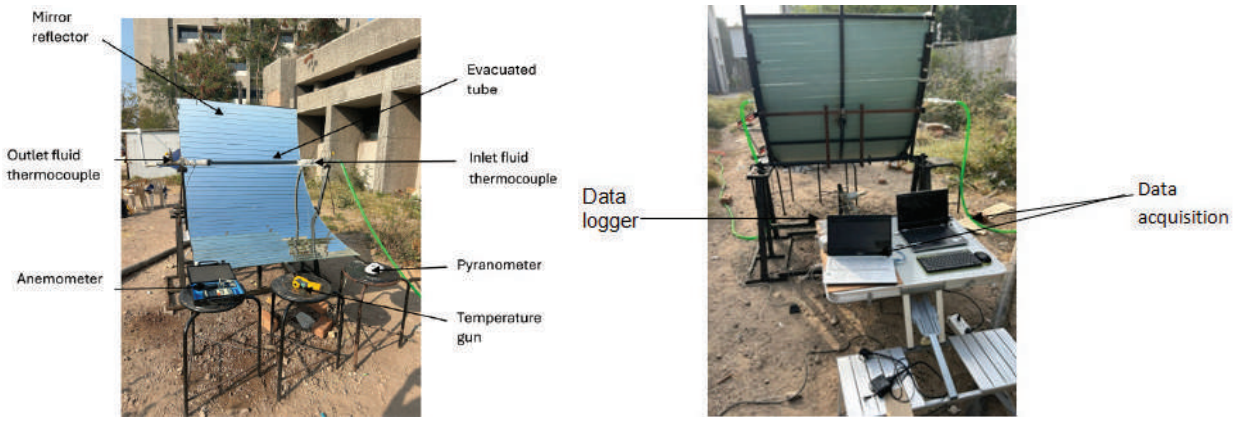

Figure 7. Experimental setup of PTC.

The PTC was installed on the ground and oriented southward with manual tracking (east to west) to ensure uninterrupted solar radiation. The copper receiver tube, with a diameter of 25 mm, was coated with matte black and mounted coaxially within a glass envelope that was evacuated to minimize heat loss, as depicted in Figure 3. Ro water was used as the HTF and properties are calculated at the bulk mean temperature. K-type thermocouples were connected at both ends of the tube to measure the fluid inlet and outlet temperature. The ends of the receiver tube were insulated with fiber wool to avoid thermal losses. A pyranometer (Class C) was employed to monitor solar radiation throughout the experiment. To measure the wind velocity and ambient temperature of the surrounding atmosphere, an anemometer was used. The average surface of the receiver tube was measured with the help of an infrared thermometer, which is also known as a temperature gun. Lastly, a data logger was used to record the fluid temperature reading and solar radiation for an interval of every 1 minute. The experimental setup of PTC is shown in Figure 7.

Experiments were performed on the PTC in January 2025 from 9.30 am to 4.30 pm. Two types of cases are examined in PTC: plain tube (without insert) and tube having notched CRWM insert. Data were collected under consistent ambient conditions and solar flux to facilitate a fair performance assessment of both cases. The study was conducted under three different discharge rates to judge the performance of the evacuated receiver tube with and without the insert. The discharge rate was measured using a calibrated beaker, and a flow control valve was used to adjust the flow rate. The experiment begins by allowing an inlet of water from one side with a known mass discharge rate to pass through the other end of the evacuated receiver

Table 2. Parameters and equations for data reduction

Parameters	Equation	Unit	Equation number
Useful heat gain (Q_u)	$Q_u = \dot{m} * c_p * (T_{fo} - T_{fi})$	W	(5) [35]
Heat transfer coefficient (h)	$h = \frac{Q_u}{A_r(T_{sur} - T_m)}$	W/m²K	(6)
Bulk fluid temperature (T_m)	$T_m = (T_{fo} + T_{fi})/2$	K	(7)
Nusselt number (Nu)	$Nu = \frac{hd_i}{k}$	-	(8) [35]
Dittus-Boelter correlation for turbulent flow	$Nu = 0.023(Re)^{0.8}(Pr)^{0.4}$	-	(9)
Reynolds number	$Re = \frac{\rho * v * d_i}{\mu}$	-	(10)
Prandtl number	$Pr = \frac{\mu * Cp}{k}$	-	(11)
Thermal efficiency	$\eta = \frac{Q_u}{I * A_p}$	-	(12)

tube. Manual tracking of PTC in the east-to-west direction was continuously carried out to concentrate radiation on the receiver tube. The performance parameters, such as the Nusselt number, outlet fluid temperature, heat gain and thermal efficiency, were assessed to identify the significance of the insert in PTC.

Data Analysis and Validation

For the calculation and analysis of the data, reading from all instruments was considered on hourly basis. The equations and parameters applied during data processing are presented in Table 2.

Figure 8 represents a comparison of the experimental and theoretical calculated Nusselt number. The Dittus-Boelter correlation for the Nusselt number mentioned in equation (9) was used to validate the turbulent flow behavior within the tube. These equations are relevant for fully developed turbulent flow conditions. The data used for the experimental Nusselt number was obtained across two mass discharge rates (0.06 and 0.08 kg/s) under nearly identical solar heat flux conditions (760 W/m^2). The mass discharge rate of 0.04 kg/s is not considered here in the validation due to the Reynolds number coming to less than 4000, which does not apply to the Dittus-Boelter equation. The data presented in Fig. 8 exhibits a strong correlation with the theoretical models, with deviations of ±2.6%. Furthermore, the results also indicate with an increase in Reynolds number, the Nusselt number shows a corresponding amplifies, suggesting an enhancement in convective heat transfer. These observations validate the accuracy and reliability of the experimental setup, confirming its suitability for the study.

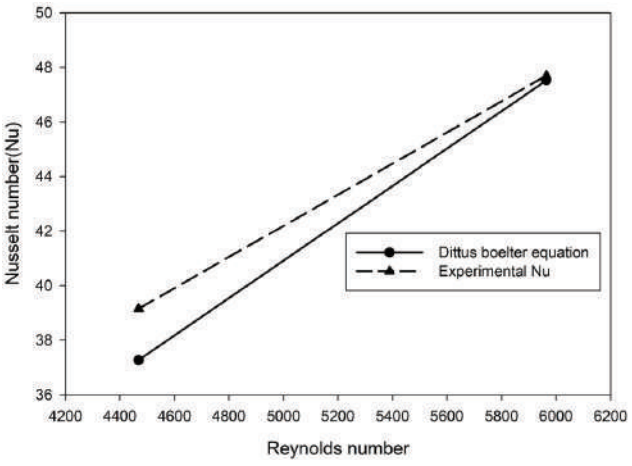

Figure 8. Comparison of experimental and theoretical Nusselt number.

Measurement of Uncertainty

This section outlines the inherent uncertainties associated with the experiment. Various instruments, including the thermocouples, solar pyranometer, flow meter, and data logger are employed to gather data during the test. The statistical uncertainty X (z) of the variables used in the data analysis can be calculated from the equation (13), where Y (z) represents the accuracy of the components. Additionally, the uncertainty for F (b) can be determined using equation (14) [36]. Table 3 provides the accuracy and uncertainty of devices. The cumulative uncertainty of the experiment is 1.34%.

$$X(z) = \frac{Y(z)}{\sqrt{3}} \tag{13}$$

$$F(b) = \sqrt{(A)^2 + (B)^2 + (C)^2 + (D)^2} \tag{14}$$

Where *A, B, C* and *D* are uncertainty in solar pyranometer, thermocouple, flow rate and data logger acquisition respectively.

RESULTS AND DISCUSSION

Solar Flux with Time

The data presented in Figure 9 demonstrates the variation in solar flux over several days, measured between 9:30 am and 4:30 pm under no cloud conditions at Marwadi University, Rajkot (22°18'N latitude and 70°47'E longitude) in January 2025. The data selected for processing corresponds to the six different days with the least cloud cover. It is important to note that, on all selected days, the overall solar energy received by the collector was nearly identical. The maximum solar flux was available between 12.30 to 1.30 pm and began to fall till 4.30 pm. The average solar fluxes received during the peak solar noon (12.30 to 1.30 pm) were 863 W/m^2.

Table 3. Accuracy and uncertainty of measuring devices

Instrument	Unit	Accuracy	Uncertainty (%)
Solar pyranometer	W/m^2	± 2	1.154
K type thermocouple	°C	± 0.25°C	0.144
Flow rate	LPM	± 0.06	0.034
Data logger acquisition	°C	<0.02	0.0115

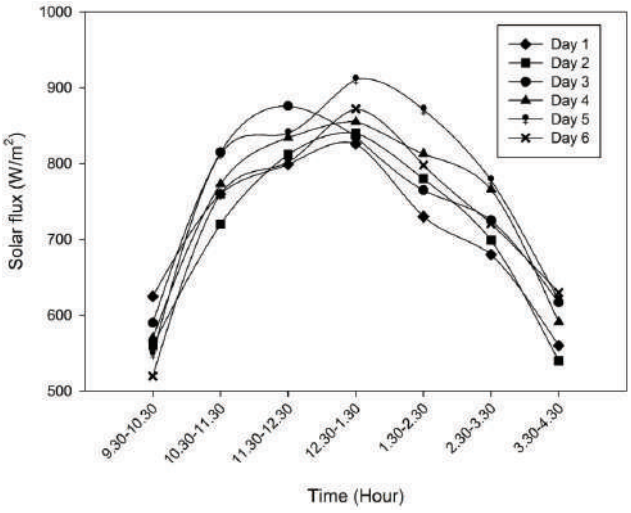

Figure 9. Solar flux variation with time at different days.

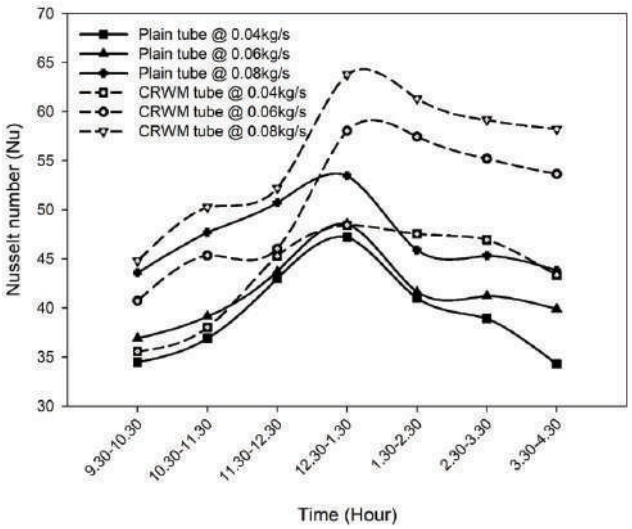

Figure 10. Comparison of Nusselt number with time at different mass discharge rates between plain and CRWM inserted tubes.

Impact of Mass Discharge Rates on Nusselt Number in the Case of Plain and CRWM Inserted Tubes

Figure 10 shows the comparison of the Nusselt number between a plain and CRWM inserted tube at three different mass discharge rates. It can be analyzed from the figure that as the mass discharge rate rises, the Nusselt number increases for both the plain and CRWM tubes. This trend is due to the rise in Reynolds number with the increasing mass discharge rate, which in turn enhances the Nusselt number. The highest Nusselt number is observed between 12:30 to 1:30 pm when the solar flux is at its peak. It can also be noted that tube with insert have a higher Nusselt number compared to plain tube in all mass discharge rates.

Table 4 presents the percentage gain in the average Nusselt number between plain and CRWM inserted tubes across all mass discharge rates. The percentage gain in the average Nusselt number is 20.46%, 17.64%, and 10.6%, with respective mass discharge rates of 0.08, 0.06, and 0.04 kg/s. These values clearly signify two key trends: first, a higher mass discharge rate will approach a higher Nusselt number, and second, the use of inserts in the tube has a higher Nusselt number as compared to the plain tube.

Impact of Mass Discharge Rates on Outlet Fluid Temperature in the Case of Plain and CRWM Inserted Tubes

Figure 11 presents the variation of outlet fluid temperature for various mass discharge rates considered in the present study for both the plain and porous insert. It can be observed that fluid outlet temperature increases with the rise in time. Solar radiation attains the highest value around 2 pm and then slowly decreases. It is further noted that the outlet fluid temperature varies from 23°C to 32°C for the tube with insert, and the same is from 21°C to 29°C for a tube with no inserts. It can be noted that tube with inserts gives higher outlet fluid temperature with respect to the plain tube. This is due to the turbulence effect and volumetric heat transfer phenomenon happening with the presence of insert in the tube. Furthermore, additional resistance to fluid flow offered by the insert inside the receiver tube, which results in the fluid being retained for a longer period within the tube. This extended residence time allows for superior heat absorption, causing to a higher temperature rise in the fluid relative to the plain tube, where the fluid flows more quickly.

The figure also illustrates that the outlet temperature of the fluid decreases with rise in the mass discharge rate and the same trend is found for both cases i.e. plain and CRWM tubes. This may be due to the reason that at lesser mass discharge rates, the fluid remains in contact with the

Table 4. Percentage gain in the average Nusselt number at all mass discharge rates

Mass discharge rate (kg/s)	Average Nu Plain tube	Average Nu CRWM tube	% Rise in Nu
0.04	39.41	43.59	10.6%
0.06	41.59	48.93	17.64%
0.08	46.22	55.68	20.46%

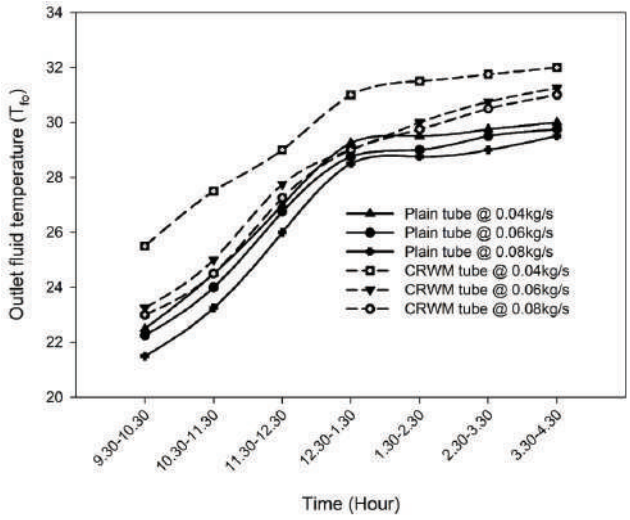

Figure 11. Variation of outlet fluid temperature with time at different discharge rates for plain and CRWM inserted tubes.

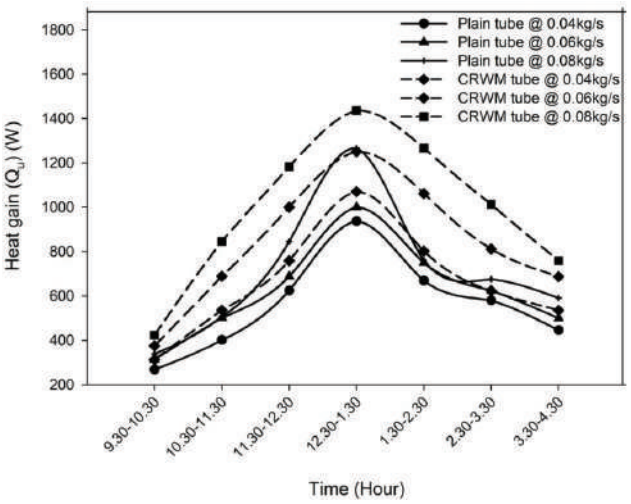

Figure 12. Comparison of heat gain with time at different mass discharge rates for plain and CRWM inserted tubes.

heated surface for a longer duration, allowing more time for heat transfer and leading in a higher outlet temperature. In contrast, at higher mass discharge rates, the fluid moves through the tube more rapidly, reducing the time available for heat absorption, which leads to a lower outlet temperature. However, despite a decrease in solar heat flux after the peak period, the increase in outlet temperature is not as pronounced.

Table 5 presents the percentage increase in the average outlet fluid temperature for both plain and CRWM tubes across different mass discharge rates. The percentage rise in the outlet fluid temperature is 8.1%, 4.42%, and 3.41% at respective mass discharge rates of 0.04, 0.06, and 0.08 kg/s. The output of the experiment signifies that using inserts at lesser mass discharge rates tends to elevated outlet fluid temperature. Varun et al. [37] investigated a similar type of study in PTC having 1500 mm absorber tube length using water as the HTF at mass flow rates of 0.5 to 4 liter per minute. It compared the thermal performance of finned and plain tubes based on outlet fluid temperature, temperature difference, heat transfer, and efficiency. Results showed that the finned tube increased the outlet temperature by 1.23% to 4.75%, with a greater rise at lower flow rates. A similar trend is observed in the present study which supports the effectiveness of inserts in the PTC.

Impact of Mass Discharge Rates on Heat Gain in the Case of Plain and CRWM Inserted Tubes

Figure 12 presents a comparison of heat gain between the plain and CRWM tubes at three different mass discharge rates. The data shows that as the mass discharge rate increases, the useful heat gain also increases, resulting in enhanced thermal efficiency of the PTC. It is observed that the maximum heat gain occurs around solar noon, between 12:30 to 1:30 pm, for both tube configurations, after which the heat gain decreases due to the reduction in solar flux intensity. Additionally, the figure demonstrates that the CRWM tube consistently achieves higher heat gain than the plain tube. This improvement is attributed to the CRWM structure, which better retains the fluid within the tube, allowing for increased fluid retention time and, consequently, more significant heat gain compared to the plain tube.

Table 6 presents the percentage increase in the average heat gain for both plain and CRWM tubes across all mass discharge rates. The heat gain in the tube with inserts shows an 18.1%, 34.2%, and 38.9% increase compared to the plain tube at mass discharge rates of 0.04 kg/s, 0.06 kg/s, and 0.08 kg/s, respectively. These results indicate that higher mass

Table 5. Percentage rise in outlet fluid temperature at different mass discharge rates

Mass discharge rate (kg/s)	Average T_{fo} Plain tube (°C)	Average T_{fo} CRWM tube (°C)	% Rise in T_{fo}
0.04	27.50	29.75	8.1%
0.06	27.14	28.34	4.42%
0.08	26.64	27.55	3.41%

Table 6. Percentage rise in heat gain at different mass discharge rates

Mass discharge rate (kg/s)	Average Q_u Plain tube (W)	Average Q_u CRWM tube(W)	% Rise in Q_u
0.04	561	663	18.1%
0.06	625	839	34.2%
0.08	712	989	38.9%

discharge rates, combined with the use of inserts, lead to improved heat gain compared to the plain tube.

Impact of Mass Discharge Rates on Thermal Efficiency in the Case of Plain and CRWM Inserted Tubes

Figure 13 illustrates a comparison of thermal efficiency between plain and CRWM tube at all three mass discharge rates. The figure indicates that as the mass discharge rate increases, the useful thermal gain also increases, which, in turn, enhances the thermal efficiency of the PTC. It can be noted that the thermal efficiency is maximum at solar noon between 12.30 to 1.30 pm for both tube configurations and then decreases due to a reduction in solar flux intensity, which leads to a drop in the thermal gain and efficiency. The figure also demonstrates that the CRWM tube consistently outperforms the plain tube in terms of thermal efficiency. This improvement can be recognized by the improved heat transfer characteristics of the CRWM tube, which is likely a result of increased turbulence and better fluid mixing due to its corrugated surface design. The corrugations promote more effective interaction between the fluid and the tube surface, causing a reduction in the thermal boundary layer and increasing convective heat transfer.

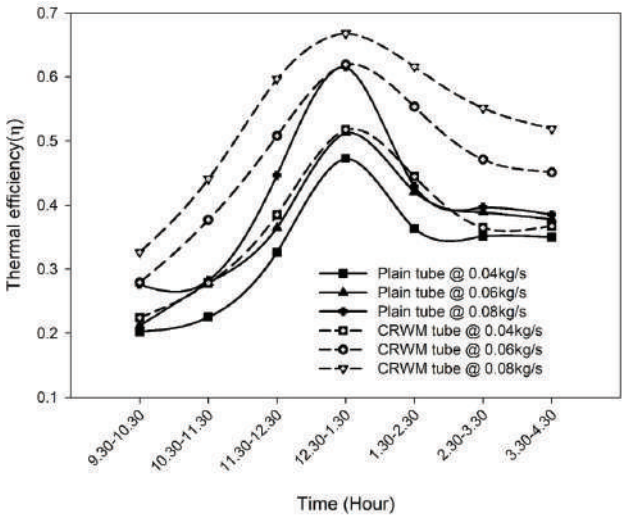

Figure 13. Comparison of thermal efficiency with time at different mass discharge rates for plain and CRWM inserted tubes.

Table 7 presents the percentage increase in the average thermal efficiency for both plain and CRWM tubes across all mass discharge rates. The percentage rise in thermal efficiency is 31.2%, 27.4%, and 12.6% of the tube with insert compared to the plain tube at respective mass discharge rates of 0.08, 0.06, and 0.04 kg/s. This result indicates that a high mass discharge rate and tube with an insert have better thermal efficiency than the plain tube.

Cost Analysis of Evacuated Tube And PTC

For this study, the receiver tube material was chosen as a copper, with an inner and outer diameter of 22 mm and 25 mm with a length of 1300 mm is selected. A borosilicate glass tube, measuring 1000 mm in length, was used to envelop the copper tube with an inner and outer diameter of 47 mm and 50 mm. A vacuum pump was then employed to create a vacuum inside the tube, which was subsequently sealed with a heat-resistant sealing material. The estimated cost of the evacuated receiver tube is found to be Rs. 5300. Table 8 demonstrates the estimated cost of the evacuated tube.

Table 8. Estimated cost of evacuated tube

Material	Cost (Rs)
Copper tube	1800
Glass Cover	500
Sealing material	1500
Vacuum Process	1500
Total Cost	5300

Table 7. Percentage rise in thermal efficiency at different mass discharge rates

Mass discharge rate (kg/s)	Average eff. Plain tube	Average eff. CRWM tube	% Rise in eff.
0.04	0.328	0.369	12.6%
0.06	0.365	0.466	27.4%
0.08	0.405	0.531	31.2%

Table 9. Estimated cost of PTC

Item	Material	Cost (Rs.)
Framework and support	Galvanized iron	17000
Reflector	Mirror	3000
Evacuated tube	Copper and Glass tube	5300
Pyranometer	Class C	46500
Manometer	Inverted acrylic	1500
Thermocouple	K type	5000
Data logger	Modules and PCB	5000
Wire mesh insert	Stainless steel	1000
Miscellaneous	Valves, insulation, fittings	20000
Total Estimated Cost		104300

According to the literature by Chafie et al. [38] the total cost of an evacuated tube mentioned for 4 m length is shown as $ 2127, which is approx Rs. 1,40,000 (considering 1$ = Rs. 66). If the cost of one meter is calculated then it comes to approx. Rs. 35,000. Assuming 15% additional import duties and extra charges on the cost of the evacuated tube will make the tube cost approx. Rs. 40,000 per meter. This comparison shows enormous potential for further examination of the evacuated receiver tube for the small-size PTC, which can be implemented for industrial applications.

In this research, the experimental setup of the PTC was fabricated in the workshop using materials sourced from the local market. Table 9 provides a list of the parts used, along with the associated costs.

CONCLUSION

This paper focuses on optimizing the cost and performance of the evacuated tube used in parabolic solar trough collector. In-house development of the tube with locally available materials in the market approach was used to fabricate the low-cost evacuated receiver tube. A novel notch-based porous insert was fabricated and experimentally examined to improve the thermal retention of the fluid inside the tube. An experimental setup with an aperture area of 2.36 m^2 with a focal length of 0.50 m was designed and constructed to examine the in-house developed tube and porous insert. Water is used as the working fluid, and three mass discharge rates (0.04, 0.06 and 0.08 kg/s) were selected for this study. In six days with different mass discharge rates, experimental readings from the time duration of 9.30 am to 4.30 pm were conducted in the month of January (2025). Parameters such as Nusselt number, outlet fluid temperature, heat gain and thermal efficiency were evaluated to compare performance with and without porous inserts in the tube. The key outcomes of this experimental study are as follows:

1. The solar radiation reading for six different days in the month of January (2025) for the 22°18'N latitude and 70°47'E longitude was measured with the help of a pyranometer. The average solar flux of 863 W/m^2 was noted during the peak solar noon between 12.30 to 1.30 pm.
2. Nusselt number was examined at different mass discharge rates between a plain tube and a tube with an insert. The result reveals that the tube with an insert has a higher Nusselt number than the plain tube at all three mass discharge rates. The rise in Nusselt numbers is 10.6%, 17.64%, and 20.46% for mass discharge rates of 0.04, 0.06, and 0.08 kg/s, respectively.
3. In a similar way, the outlet fluid temperature of the water was studied with and without an insert in the tube at three different mass discharge rates. The experimental results indicate that the tube with the insert has a higher outlet temperature rise of 8.1%, 4.42% and 3.41% for mass discharge rates of 0.04, 0.06 and 0.08 kg/s, respectively.
4. Finally, heat gain and thermal efficiency of the collector were determined for both cases at different mass discharge rates. It was noted that tube with inserts show a superior performance and thermal efficiency rise compared to the plain tube. Additionally, both parameters in tube with inserts show excellent results at higher mass discharge rates. This study also signifies that the tube with an insert improves the thermal retention of the fluid, which ultimately enhances heat gain and thermal efficiency.
5. The cost of the in-house developed evacuated receiver tube was evaluated and compared with existing literature, which shows a positive impact. This type of evacuated tube is more suitable for the small size of parabolic trough collectors, which has high potential for low and medium-temperature industrial applications.

The findings of this study demonstrate a significant enhancement in the efficiency of the collector. This improved efficiency makes the collector highly suitable for a wide range of industrial applications. Its enhanced

performance ensures reliable and cost-effective thermal energy solutions for diverse sectors.

In the future scope, the developed evacuated receiver tube can be further examined for higher temperatures using oil as the working fluid along with the notched circular ring wire mesh insert.

NOMENCLATURE

A_p	Aperture area (m^2)
A_r	Receiver area (m^2)
C_p	Fluid Specific heat (KJ/kg.K)
d_i	Tube internal diameter (m)
d_{go}	Glass outer diameter (m)
F	Focal length (m)
h	Heat transfer coefficient ($W/m^2.K$)
k	Thermal conductivity (W/m.K)
$\dot{m}$	Mass discharge rate (Kg/s)
Pr	Prandtl number
Q_u	Useful heat gain (W)
Re	Reynolds numbers
T_m	Bulk fluid temperature (K)
T_{fi} & T_{fo}	Inlet and outlet fluid temperature (K)
T_{sur}	Receiver surface temperature (K)

Abbreviations

CR	Concentration Ratio
CRWM	Circular ring wire mesh
HTF	Heat transfer fluid
LPM	Liter per minute
PEC	Performance evaluation criteria
PPI	Pores per inch
PTC	Parabolic trough collector
WMTT	Wire mesh twisted tape

Greek symbols

μ	Fluid dynamic viscosity (kg/m.s)
ρ	Fluid density (kg/m^3)
v	Velocity of fluid (m/s)
Φ	Rim angle (°)

ACKNOWLEDGMENT

The authors sincerely thank Marwadi University, Rajkot, for the financial support (Grant No. MU/R&D/21-22/MRP/FT05) to conduct this research project under the Minor Research Project scheme.

AUTHORSHIP CONTRIBUTIONS

Authors equally contributed to this work.

DATA AVAILABILITY STATEMENT

The authors confirm that the data that supports the findings of this study are available within the article. Raw data that support the finding of this study are available from the corresponding author, upon reasonable request.

CONFLICT OF INTEREST

The author declared no potential conflicts of interest with respect to the research, authorship, and/or publication of this article.

ETHICS

There are no ethical issues with the publication of this manuscript.

STATEMENT ON THE USE OF ARTIFICIAL INTELLIGENCE

Artificial intelligence was not used in the preparation of the article.

REFERENCES

[1] Smith J, Brown R. Energy efficiency and urbanization. J Sustain Energy 2022;12(3):45–58.

[2] Lippke F. Parabolic trough technology for solar power plants. Energy Environ Sci 2012;5(2):89–94.

[3] Motwani K, Chotai N, Patel J, Hadiya R. Design and experimental investigation on cut tube absorber for solar parabolic trough collector. Energy Sources Part A 2024;46(1):9173–9192. [CrossRef]

[4] Kennedy CE. Review of Mid- to High-Temperature Solar Selective Absorber Materials. Golden, CO; 2002. [CrossRef]

[5] Motwani K, Patel J. Cost analysis of solar parabolic trough collector for cooking in Indian hostel – a case study. Int J Ambient Energy 2022;43(1):561–567. [CrossRef]

[6] Kasaeian A, Daviran S. Optical and thermal investigation of selective coatings for solar absorber tube. Int J Renew Energy Res 2016;6(1).

[7] Cheng J, et al. Improvement of thermal stability in the solar selective absorbing Mo–Al2O3 coating. Sol Energy Mater Sol Cells 2013;109:204–208. [CrossRef]

[8] Liu J, Lei D, Li Q. Vacuum lifetime and residual gas analysis of parabolic trough receiver. Renew Energy 2016;86:949–954. [CrossRef]

[9] Mahmoud MS, Abbas AS. Solar parabolic trough collector tube heat transfer analysis with internal conical pin fins. J Green Eng 2020;10(10).

[10] Waghole DR, Warkhedkar RM, Kulkarni VS, Shrivastva RK. Experimental investigations on heat transfer and friction factor of silver nanofliud in absorber/receiver of parabolic trough collector with twisted tape inserts. Energy Procedia 2014;45:558–567. [CrossRef]

[11] Raval P. Heat transfer enhancement techniques using different inserts in absorber tube of parabolic trough solar collector: A review. J Therm Eng 2024:1068–1091. [CrossRef]

[12] Hussein AM, Awad AT, Ali HHM. Evaluation of the thermal efficiency of nanofluid flows in flat plate solar collector. J Therm Eng 2024;10(2):299–307. [CrossRef]

[13] Ajbar W, Hernández JA, Parrales A, Torres L. Thermal efficiency improvement of parabolic trough solar collector using different kinds of hybrid nanofluids. Case Stud Therm Eng 2023;42:102759. [CrossRef]
[14] Jaiswal P, et al. Nanofluids guided energy-efficient solar water heaters: Recent advancements and challenges ahead. Mater Today Commun 2023;37:107059. [CrossRef]
[15] Anbarsooz M, Amiri M, Rashidi I, Javadi M. Heat transfer augmentation in solar collectors using nanofluids: A review. Curr Biochem Eng 2020;6(2):72–81. [CrossRef]
[16] Shank K, Tiari S. A review on active heat transfer enhancement techniques within latent heat thermal energy storage systems. Energies 2023;16(10):4165. [CrossRef]
[17] Muter DM, Al-Hadithi MB. Numerical investigation of heat transfer enhancement in parabolic trough solar collector with twisted tape insert. Glob Sci J 2020.
[18] Rawani A. Enhancement in thermal performance of parabolic trough collector with serrated twisted tape inserts. Int J Thermodyn 2017;20(2):111–111. [CrossRef]
[19] Keklikcioglu O, Ozceyhan V. Experimental investigation on heat transfer enhancement in a circular tube with equilateral triangle cross sectioned coiled-wire inserts. Appl Therm Eng 2018;131:686–695. [CrossRef]
[20] Al-Aloosi W, Alaiwi Y, Hamzah H. Thermal performance analysis in a parabolic trough solar collector with a novel design of inserted fins. Case Stud Therm Eng 2023;49:103378. [CrossRef]
[21] Zaboli M, Ajarostaghi SSM, Saedodin S, Pour MS. Thermal performance enhancement using absorber tube with inner helical axial fins in a parabolic trough solar collector. Appl Sci 2021;11(16):7423. [CrossRef]
[22] Waramit P, Chanmak P, Peamsuwan R, Krittacom B. Forced convection enhancement of air flowing inside circular pipe with varying the pitch (P) of wire-mesh porous media. Energy Rep 2021;7:70–82. [CrossRef]
[23] Raval P, Ramani B, Chotai NJ, Motwani K. Wire mesh-based heat transfer enhancement in absorber tube of solar collector-An experimental study. Int J Thermofluids 2024;24:100878. [CrossRef]
[24] Thapa S, Samir S, Kumar K. Performance evaluation of solar parabolic trough receiver using multiple twisted tapes with circular perforation and delta winglet. Proc Inst Mech Eng Part E J Process Mech Eng 2022;236(4):1296–1307. [CrossRef]
[25] Ioannides MG, Cammi A, Savoldi L. Improving the overall thermal performance of parabolic trough solar collectors using porous media. Renew Energy Power Qual J 2024;19(5). [CrossRef]
[26] Afsharpanah F, Sheshpoli AZ, Pakzad K, Ajarostaghi SSM. Numerical investigation of non-uniform heat transfer enhancement in parabolic trough solar collectors using dual modified twisted-tape inserts. J Therm Eng 2020:133–147. [CrossRef]
[27] Jain PK, Chaurasiya PK, Verma TN, Tiwari D. Investigation of the heat discharge from a solar-powered air heater with distinctive dual arc artificial roughness. Sustain Energy Technol Assess 2023;60:103543. [CrossRef]
[28] Natarajan K, Thokchom SS, Verma TN, Nashine P. Convective solar drying of Vitis vinifera & Momordica charantia using thermal storage materials. Renew Energy 2017;113:1193–1200. [CrossRef]
[29] Chaurasiya PK, et al. A review of techniques for increasing the productivity of passive solar stills. Sustain Energy Technol Assess 2022;52:102033. [CrossRef]
[30] Khashaei A, Ameri M, Azizifar S. Heat transfer enhancement and pressure drop performance of Al2O3 nanofluid in a laminar flow tube with deep dimples under constant heat flux: An experimental approach. Int J Thermofluids 2024;24:100827. [CrossRef]
[31] Morka JC, Molua OC, Egheneji A, Edobor M, Ighrakpata FC. Experimental study corrosion parameters of copper as an eco-friendly heat collector for solar water heaters. J Geogr Environ Earth Sci Int 2023;27(5):49–55. [CrossRef]
[32] Gao XH, Guo ZM, Geng QF, Ma PJ, Liu G. Structure, optical properties and thermal stability of TiC-based tandem spectrally selective solar absorber coating. Sol Energy Mater Sol Cells 2016;157:543–549. [CrossRef]
[33] Selvakumar N, Rajaguru K, Gouda GM, Barshilia HC. AlMoN based spectrally selective coating with improved thermal stability for high temperature solar thermal applications. Sol Energy 2015;119:114–121. [CrossRef]
[34] Kalogirou SA. Solar thermal collectors and applications. Prog Energy Combust Sci 2004;30(3):231–295. [CrossRef]
[35] Cengel YA, Ghajar AJ. Heat and Mass Transfer. McGraw-Hill; 2014.
[36] Limboonruang T, Oyinlola M, Harmanto D, Bunyawanichakul P, Phunapai N. Optimizing solar parabolic trough receivers with external fins: An experimental study on enhancing heat transfer and thermal efficiency. Energies 2023;16(18):6520. [CrossRef]
[37] Varun K, Arunachala UC, Elton DN. Trade-off between wire matrix and twisted tape: SOLTRACE® based indoor study of parabolic trough collector. Renew Energy 2020;156:478–492. [CrossRef]
[38] Chafie M, Aissa MFB, Bouadila S, Balghouthi M, Farhat A, Guizani A. Experimental investigation of parabolic trough collector system under Tunisian climate: Design, manufacturing and performance assessment. Appl Therm Eng 2016;101:273–283. [CrossRef]

J Ther Eng, Vol. 12, No. 2, pp. 532−549, March, 2026

Journal of Thermal Engineering
Web page info: https://jten.yildiz.edu.tr
DOI: 10.14744/thermal.0001100

Research Article

Techno-economic analysis of a residential solar thermal-biodiesel heating and cooling system under the mediterranean climate

Nyasha Netsai BEMA[1], Kemal MASERA[1,*]

[1]*Department of Mechanical Engineering, Faculty of Engineering, Middle East Technical University Northen Cyprus Campus, Mersin, 99738, Turkiye*

ARTICLE INFO

Article history
Received: 17 February 2025
Revised: 15 September 2025
Accepted: 16 September 2025

Keywords:
Biodiesel as an Auxiliary Fuel; Biodiesel for Space Conditioning; Energy Demand in Residential Buildings; Solar Thermal Cooling; Solar-Biodiesel Hybrid

ABSTRACT

This case study focused on the design of an economic and sustainable solar-biodiesel thermal system to meet the growing heating and cooling energy demand in Cypriot residential buildings. While the application of solar thermal systems in the residential sector has been one of the most efficient solutions to energy shortage issues experienced globally, auxiliary systems are often neglected. Therefore, this study addresses intermittency issues of solar and wind energy by exploring biodiesel as an auxiliary energy source. Biodiesel as an auxiliary fuel eliminates the use of expensive energy storage systems such as solar PV batteries and PCMs in solar thermal applications The proposed system which integrates evacuated tube solar collectors, thermal energy storage tank, Lithium-Bromide absorption chiller and a biodiesel boiler is modelled using TRNSYS. Different from most studies this study implements a user-centered method in determining residential space conditioning energy demand through a survey. TMY data is used to represent the available solar energy resources in Cyprus. The 10.5kW proposed system demonstrated a performance capability by satisfying 37800kJ/h of space conditioning energy demand. Thermal energy from solar managed to meet 100% and 87.7% of the cooling and heating energy demand respectively. The cost analysis reflected a payback period of 7.3 years and total savings of $37,200 over 20 years, highlighting the energy and cost effectiveness of renewable energy thermal systems in residential buildings.

Cite this article as: Bema NN, Masera K. Techno-economic analysis of a residential solar thermal-biodiesel heating and cooling system under the mediterranean climate. J Ther Eng 2026;12(2):532−549.

INTRODUCTION

The motivation of this research is founded upon the growing energy demand for space heating and cooling systems in Cyprus. Electricity prices have been on the rise since natural gas prices are constantly fluctuating [1]. High energy demand has resulted in power outages, which inconveniences residents as their thermal comfort is disturbed especially during summer seasons. Considerable number of residents in Cyprus have resorted to using solar Photovoltaics, however, the limitation of solar PV grid integration is the unpredictability of solar energy. Integrating

***Corresponding author.**
*E-mail address: nyashabema@gmail.com

This paper was recommended for publication in revised form by Editor-in-Chief Ahmet Selim Dalkılıç

Published by Yıldız Technical University Press, İstanbul, Turkey
Yıldız Technical University. This is an open access article under the CC BY-NC license (http://creativecommons.org/licenses/by-nc/4.0/).

solar PVs into the grid is a complicated process as balancing available solar energy to instantaneously match energy demand is still a challenge faced by system operators [2]. Therefore, there is a need for practical sustainable solutions to meet the growing energy demand while maintaining thermal comfort within residential buildings. According to the IEA, energy consumption in residential buildings increased by 1% in 2022 and is expected to increase as the world population is increasing [3]. Space heating and cooling contributes a substantial amount of energy consumed in residential buildings. As of 2022, about 2 billion air conditioning units were in operation for space cooling, accelerating electricity demand in residential buildings. The addition in generational capacity has been noted during peak hours and is expected to rise over the coming years [3]. Additionally, there is limited research in the implementation of solar thermal systems in domestic homes [4]. For these reasons, alternative energy solutions and improved designs, such as the solar-biodiesel thermal system proposed in this study, are necessary in complying with Net Zero Emissions goals.

Use of biofuels is advantageous due to minimal environmental effects and economic benefits. Biofuels can be a better option for parameters such as thermal efficiency and fuel consumption [5]. Unlike wind and solar energy, biofuels are not intermittent. Biodiesel is biodegradable and non-toxic [6]. The contribution of biodiesel to atmospheric CO2 emissions is non-existent, reducing the GHG emission profile of biodiesel [6]. Biodiesel is the first generation of biofuel and a renewable clean-burning mono-alky ester fuel that is made from natural renewable feedstock such as soybean, cottonseed oil, canola oil, corn oil, jatropha and waste animal fats [7, 8] . Used cooking oil can also be recycled to produce biodiesel and new feed-stocks are emerging from further research and on the market [9]. Several factors and biodiesel properties such as anti-foaming, oxygen content, corrosion, chemical structure, conductivity, cetane number, and cold flow properties must be considered when using pure biodiesel instead of convectional diesel. These factors mainly depend on feedstock type [8]. Feedstock is the most expensive material in biodiesel manufacturing processes and contributes to 80% of the operating costs [8, 9]. The selection of cheaper feedstock such as waste fats and oils is advantageous because production cost is still a major challenge in biodiesel production. Apart from the feedstock, total production costs include cost of other reactants, nature of purification and the storage type [8]. Compared to natural gas, biodiesel can be a better alternative for auxiliary thermal energy systems in residential buildings. Shanableh et al. [10] studied the production of biodiesel from waste cooking oil and canola oil in North Cyprus. The results supported biodiesel production using waste cooking oil as an alternative fuel. Furthermore, Lopestro et al. [9] investigated the incorporation of biodiesel in a small community nanogrid to promote the production of biodiesel from waste oils. The results showed a 19% reduction in fossil fuel use. National Sustainable Agriculture Information Services encourages the formation of local biodiesel clubs to educate residents on safe homebrewing techniques [11].

Although many studies have investigated the application of thermal systems in residential buildings for space heating and cooling, the originality and novelty of this study is primarily based on the hybrid solar-biodiesel thermal system. Noro et al. [12] explored the potential of evacuated tube solar collectors (ETSC) to drive an absorption chiller during summer seasons. A gas boiler was integrated as an auxiliary system to drive the chiller and meet the cooling load in case of solar energy insufficiency. A similar study conducted by Sibilio et al, incorporated a gas boiler in the design of a solar thermal system for space heating and cooling in Italy. Although the system's performance surpassed that of a convectional system, and offered more economic and environmental benefits, the use of natural gas as a backup fuel decelerates green energy transition in residential buildings [13]. The same approach of adding an auxiliary boiler was taken by Hussein et al. [14] while modelling an absorption cooling system for residential purposes under Iraq weather conditions. Sarmouk et al. [15] developed and experimentally validated a TRNSYS model for space heating in Algeria. Although the experiment set up included a gas boiler for auxiliary purposes, only the solar mode was considered for the study. The exemption of the gas boiler from the numerical model conceals environmental effects of the system. Likewise, Marcos et al. conducted a solar powered air conditioning experiment in Spain to validate the efficiency of a highly efficient flat plate vacuum solar collector. The study incorporated an absorption chiller and storage tank. However, the solar system provided 65.3% of the heating energy demand, with fossil fuel covering the remaining [16].

Studies focusing on renewable energy systems often neglect the significancy of auxiliary systems energy sources. Careful consideration on the design of auxiliary systems is important to accelerate energy transition by minimizing dependency on fossil fuels. For instance, Redpath et al. [17] modelled a concentrated solar driven small scale absorption chiller which met 100% and 94% of heating and cooling energy demand respectively. Although the system contributed to CO2 savings of 3,966,247 tons per year, the remaining 6% supplied by the grid emphasizes the need for sustainable energy back-up solutions. Lebedeva et al. [18] analyzed the influence of PCMs in energy storage tanks and the results indicated a CO2 emission reduction of 5-7% and 21% decrease in the use of an auxiliary heater. However, CO2 emissions could further be reduced by opting for cleaner auxiliary energy sources. An economic analysis is of major importance when designing renewable energy systems. According to Pedro et al., the operation of a solar driven absorption chiller in Spain yielded less economic benefits when compared to an electric vapor compression chiller. However, this study focused solely on the cooling season, resulting in high investment costs and minimum

savings per year [19]. In contrast, Salameh at al. [20] investigated the techno-economic performance of a solar driven Li-Br absorption chiller with an auxiliary electric heater and achieved better economic results. Despite high initial costs, the solar cooling system costs only 43.2% of what a convectional vapor compression system costs due to annual savings. However, the solar-driven absorption cooling system still consumed a considerable amount of electricity, which could be further reduced by the system proposed in the current study. Similarly, Düzcan et al. [21] compared thermal performances of flat plate and ETSCs in assisting an absorption chiller connected to an auxiliary electric heater.

In contrast to existing literature studies, which incorporates convectional fuels to power auxiliary energy systems, the proposed novel hybrid solar-biodiesel thermal system is distinguished by its dependency on 100% renewable and clean energy. This distinction represents a notable research gap due to its unique approach and ability of utilizing sustainable energy resources in line with the Net Zero Energy goals. This study aims to model and simulate a hybrid solar-biodiesel thermal energy system, which includes ETSC, an absorption chiller and a thermal energy storage tank (TES) to meet heating and cooling energy demand for a typical residential building in Cyprus. TMY (2022) weather data is used to calculate solar irradiance and determine the best tilt and azimuth angles using Ms Excel. The proposed system is modelled using TRNSYS 16. Heating and cooling loads were estimated by conducting a survey where 16 house owners residing in Cyprus were interviewed regarding their heating and cooling energy consumption. The authenticity of their answers was supported by local authority statistics [22]. Furthermore, the methodology approach taken in this study differs from existing literature in that, instead of estimating energy demand using ASHRAE standards, the study employed a survey approach to estimate energy consumption data from the users' (participants) perspective. The survey was conducted specifically for existing buildings, offering valuable insights into air conditioning use preferences of residents, thus reflecting real-world usage patterns. The scope of this study considers the unavailability of solar energy at nighttime and recommends use of biodiesel to supplement and meet the energy deficiency.

MATERIALS AND METHODS

The goal to design a novel hybrid solar-biodiesel thermal system to meet space heating and cooling energy demand is achieved by determining the space heating and cooling energy demand and estimating the solar energy available in Cyprus. An in-person survey was conducted to determine energy requirements while TMY (2022) data was used to develop a model in M.s Excel and estimate solar irradiance. System optimization and sizing were performed by selecting the necessary parameters and varying parameters such as the number of collectors and size of the TES tank. Simulations were performed using TRNSYS 16. The size of the absorption chiller was selected relative to the cooling energy requirements, to avoid oversizing the system. The results were analyzed based on the cost and thermal performance of the proposed system.

Case Study Location

Cyprus is in the Eastern part of the Mediterranean and, therefore, experiences hot summers above 40°C. According to Cyprus Met Department, the highest temperature recorded in Nicosia was 46°C in July 2023 and a total of 48 days (about 1 and a half months) had temperatures which exceeded 40°C [23]. Consequently, the electricity demand spiked due to the dependency on air conditioners.

Research Instrument

A structured interview was employed using questions in Table 1. Permission to conduct the survey was granted by the Middle East Technical University Northern Cyprus Campus Ethical Board (Bayek), after careful analysis of the interview questions and considerations of human safety. Cypriot house owners were asked questions regarding their heating and cooling energy consumption. In addition, electric bills were requested to verify participants' answers by matching their electricity usage to their electric bills. This control strategy was only useful in determining whether the participant overestimated or underestimated the actual usage, not in determining the actual air condition usage. The survey mainly focused on family houses and non-English-speaking participants were considered by using the local Turkish language to reduce communication barrier issues. A total of 16 households were interviewed and the data was collected and processed.

Data Normalization

Since the sample size of the survey (n) was 16, which is less than 30 and the standard deviation is unknown, t scores were used to estimate the mean and to construct the confidence interval for the population mean. Equation (1) shows the margin of error formula where T_c is the t score, S is the standard deviation of the sample population and n is the sample size. Margin of error represents the expected range for the true population parameter, the mean. The wider the range, the higher the uncertainty and the opposite is true for a narrow range or interval.

$$E = T_c \times \frac{S}{\sqrt{n}} \tag{1}$$

The confidence interval is constructed using equation (2) where x is the sample mean and μ is the population mean. The t score was found to be 2.31 from a 0.95 confidence level and degree of freedom of 15, (n-1).

$$\overline{x} - E < S\mu < \overline{x} + E \tag{2}$$

Table 1. Space conditioning interview questions

1. Do you have any solar system installed in your house for electricity production? YES NO
2. Do you depend on electrical energy from the National grid? YES NO
3. Do you use an air conditioning system? YES NO
4. How many air-conditioned rooms do you have in your house? Number: _____
5. Can you please tick the boxes for the hours you use the air conditioner during winter (mid- December to end-February)

1	2	3	4	5	6	7	8	9	10	11	12	13	14	15	16	17	18	19	20	21	22	23	24

Total number of boxes ticked :_____

6. Can you please tick the boxes for the hours you use the air conditioner during spring (March to mid-May)

1	2	3	4	5	6	7	8	9	10	11	12	13	14	15	16	17	18	19	20	21	22	23	24

Total number of boxes ticked :_____

7. Can you please tick the boxes for the hours you use the air conditioner during spring (mid-May-end-August)

1	2	3	4	5	6	7	8	9	10	11	12	13	14	15	16	17	18	19	20	21	22	23	24

Total number of boxes ticked :_____

8. Can you please tick the boxes for the hours you use the air conditioner during spring (September to end-November)

1	2	3	4	5	6	7	8	9	10	11	12	13	14	15	16	17	18	19	20	21	22	23	24

Total number of boxes ticked :_____

9. If known, please write the capacity of your air conditioning system ___Btu ____kWh
10. Are you willing to provide a receipt of your yearly/monthly electric bill YES NO

The data presented in **Figure 1** highlights a greater need for cooling energy during the summer period, (end of May-end of August). This is due to high temperatures reaching 45°C during mid-summer. The normalized average hourly energy consumption was calculated as 10.5kW which is equal to 3 air conditioning units of capacity 12000BTUs/12660kJ each. Energy demand is also high during summer months because of the summer school holidays which increases the population of people staying at home, using their air conditioners to cool their spaces. This highlights, to an extent, the effect of lifestyle and culture on energy consumption. It should be noted that this study does not represent the entire population of Cyprus, as it relied on voluntary participants, therefore, different air conditioner usage patterns may differ to non-participants. Despite normalizing the data and accounting for errors as presented in **Figure 1**, air conditioner usage is subjective [24]. Therefore, there is potential for overestimating or underestimating actual air conditioning usage, which possibly increase the inaccuracy of results.

Furthermore, the average hours of air conditioning use were determined, and it was realized that on a daily average, Cypriot residents use their air conditioners 12 hours during summer, 7 hours during winter, 4 hours during fall and 3 hours during the spring season. **Figure 2** shows the average air conditioner usage hours per seasons. The proposed system was modelled in order to meet daily space heating and cooling demand at these specific hours.

Solar Collector Optimization

The tilt and azimuth angles are important parameters which require accurate and careful analysis before installing

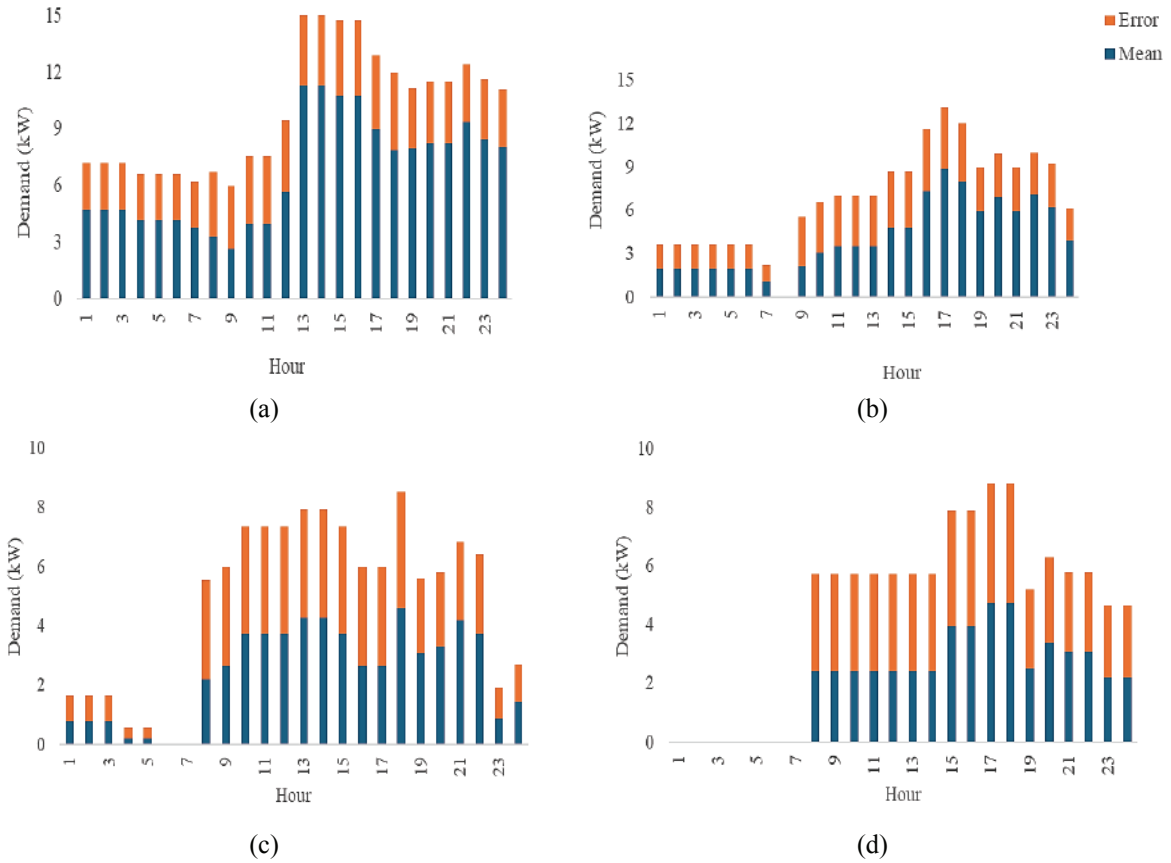

Figure 1. Estimated average heating and cooling energy consumption in a typical Cypriot family house for the 4 seasons. (a) summer season, (b) winter season, (c) fall season and (d) spring season.

solar collectors. The tilted surface enhances irradiation absorption by optimizing light exposure and allows for an extended collector lifetime by avoiding early degradation caused by ground or dust pollution and other surface environmental effects. The best tilt and azimuth angles were optimized in Ms. Excel by using the solver add-in feature. The best tilt and azimuth angles for maximum irradiation absorption for each separate month are different. For this reason, the overall yearly best tilt and azimuth angles were selected as 30 °C and 0 °C respectively.

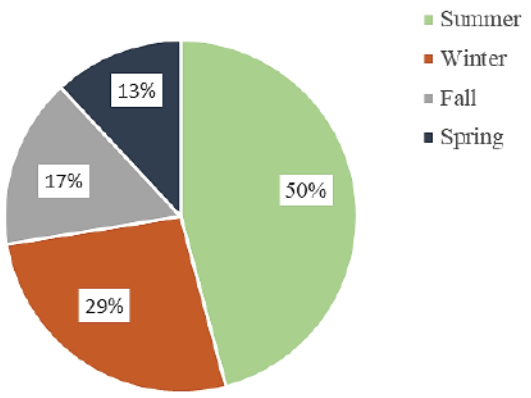

Figure 2. Estimated average and seasonal hours of air conditioner usage in a Cypriot family house.

System Description

The schematic of the proposed hybrid solar-biodiesel thermal system is shown in **Figure 3**. The solar energy harvested by the ETSC and absorbed by the HTF is transferred to the working fluid, (water) and stored inside the thermal energy storage tank. During winter seasons, this working fluid circulates through the indoor heat exchangers, to warm the cold space. After the working fluid warms the space by releasing its thermal energy, it returns to the thermal energy storage tank to collect energy and the cycle continues. During summer seasons, the working fluid from the TES tank is pumped into the absorption chiller, which produces chilled water for space cooling. The chilled water cools the space and returns to the absorption chiller. A biodiesel boiler is used as a back-up system, to heat the water in the storage tank when solar energy is unavailable.

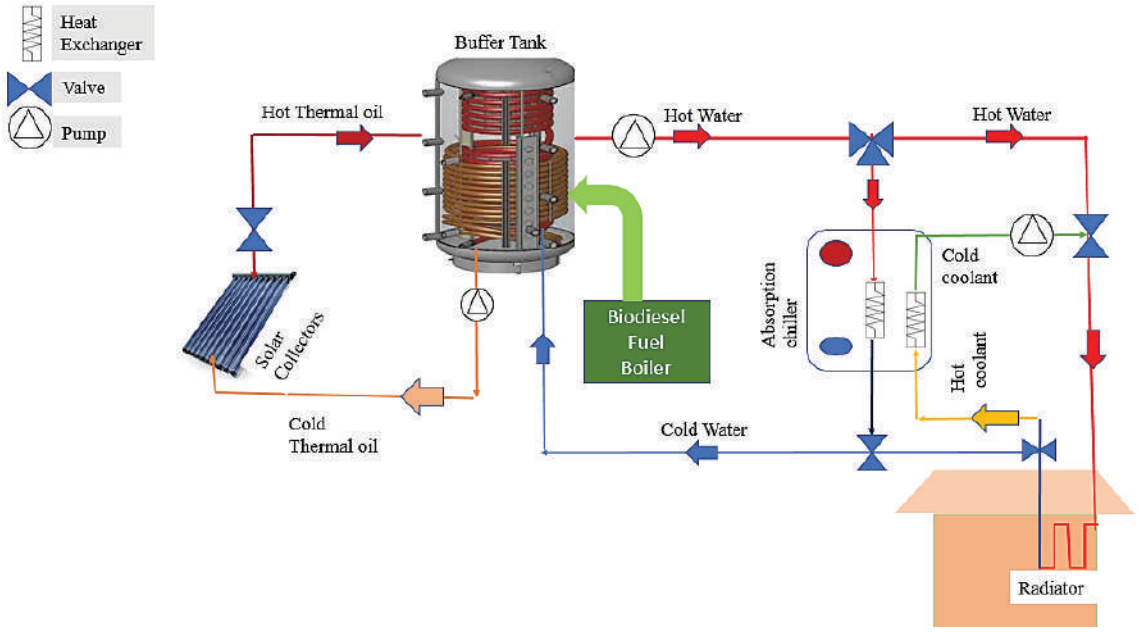

Figure 3. Schematic of the proposed thermal energy system for space heating and cooling. The system incorporates evacuated tube solar collectors, thermal energy storage tank, absorption chiller, biodiesel boiler and indoor radiators.

System's Design Specifications

The TRNSYS models are represented in **Figure 4** and **Figure 5** for space heating and cooling respectively. The TES tank was included in the TRNSYS 16 model as type 60c. **Table 2** shows the parameters and inputs used to design the system. Water was chosen as the working fluid and a heat exchanger (immersed coil) was also selected to transfer heat energy from the ETSC and promote uniform

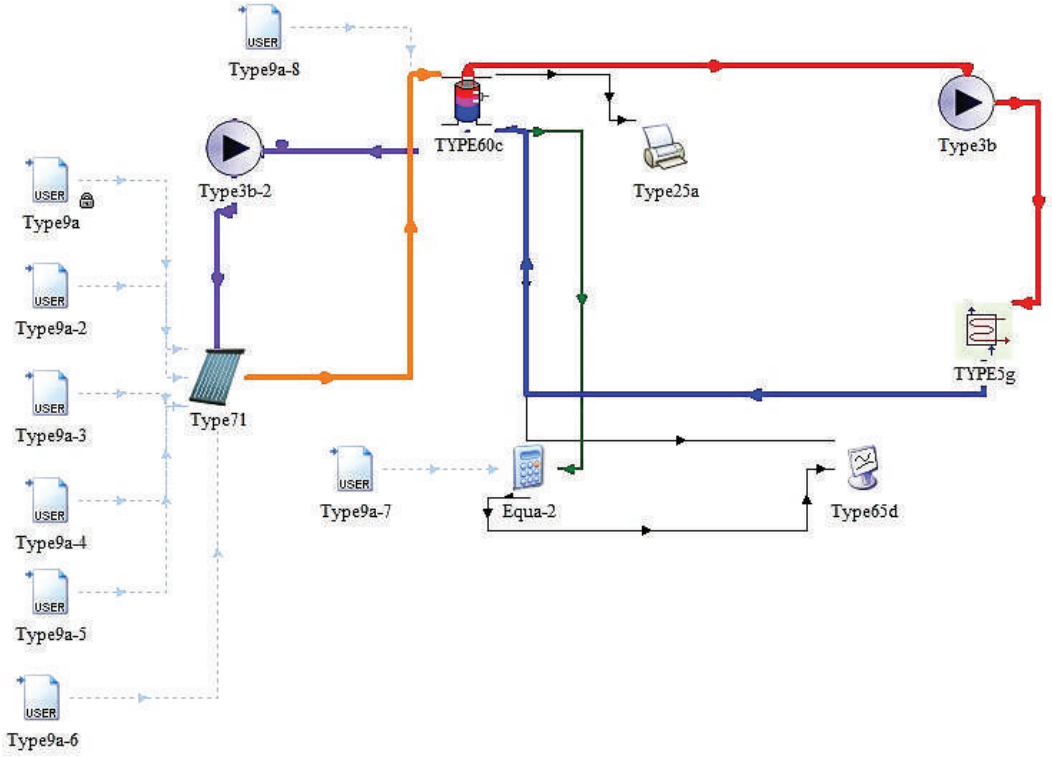

Figure 4. TRSNYS model of the proposed thermal system design for space heating.

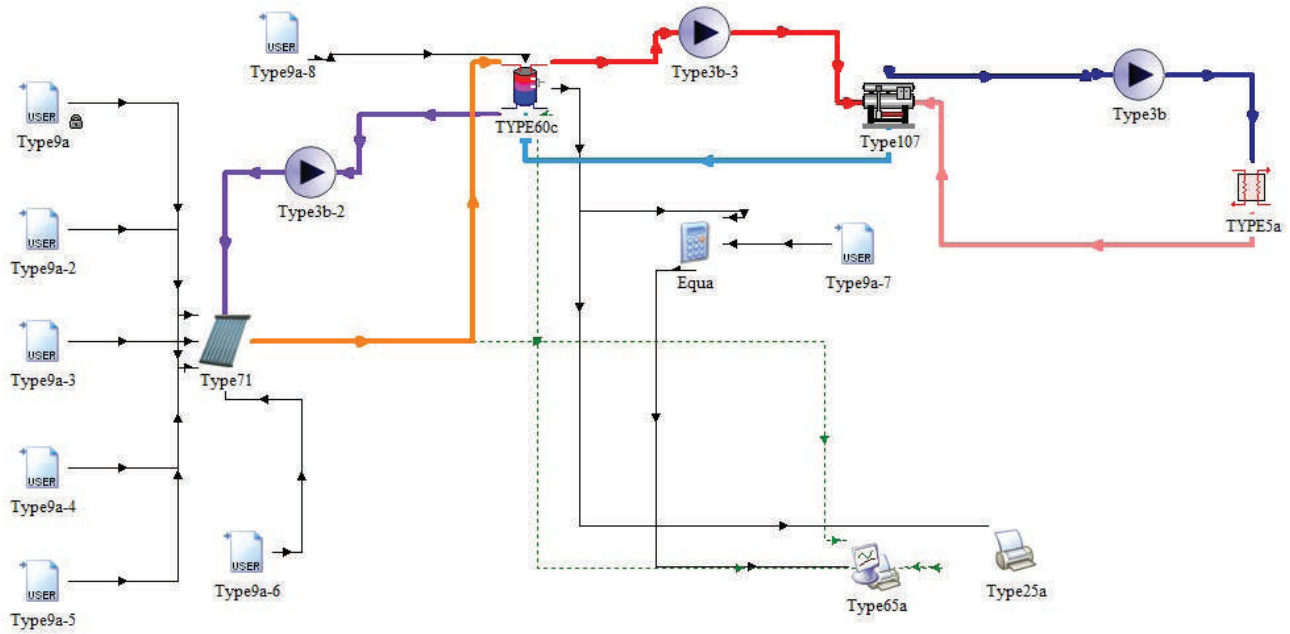

Figure 5. TRSNYS model of the proposed thermal system design for space cooling.

Table 2. Proposed system design parameters

Parameter		Units
ETSC gross area	3.476	m^2
Number of ETSC collectors	4	-
ETSC fluid specific heat	3.5	KJ/kg. K
ETSC efficiency mode	2	-
ETSC fluid flowrate at test conditions	0.02	kg/ms^2
ETSC intercept efficiency (a0)	0.744	0.744
ETSC a1	3.72	W/m. K
ETSC a2	0.013	W/m^2K
Collector tilt angle	30	°C
Collector azimuth angle	0	°C
Storage tank fluid density	1000	Kg/m^3
Storage tank loss coefficient	0.833	W/m^2 k
Storage tank fluid thermal conductivity	0.388	W/m K
Storage tank fluid auxiliary heater mode	2	-
Storage tank Gas heater	0	-
Storage tank fluid gas flue temperature	0	-
Pump 1 maximum fluid flowrate	30	Kg/h
Pump 1 fluid specific heat	2.12	kJ/kg K
Pump 2 maximum fluid flowrate	30	Kg/h
Pump 2 fluid flowrate	4.190	kJ/kg K
Heat exchanger specific heat of water	4.190	kJ/kg K
Specific heat of air	1.003	kJ/kg K
Absorption chiller rated capacity	10.5	kW
Absorption chiller COP	0.8	-

Table 3. Feedstock caloric values

Ref	Biodiesel type	Calorific Value kJ/kg	Ref	Biodiesel type	Calorific value kJ/kg
[26]	Algal	40,666	[27]	Rapeseed	39,458
[27]	ethyl palmitate	41,011	[27]	Crambe	40,564
[27]	ethyl oleate	40,450	[28]	Cottonseed oil	42,100
[27]	ethyl stearate	41,548	[29]	Castor oil	38,600
[27]	Soybean	39,480	[27]	Jatropha	39,455

temperature distribution within the tank. Type 107 in **Figure 5** models a single-effect hot-water fired absorption chiller and a capacity of 10.5kW was chosen for this chiller after considering the cooling requirements of a typical residential building in Cyprus. An indoor set point of 26°C was considered in accordance with Kim et al. [25], whose study reported that 75% of occupants preferred indoor set points between 26 and 26.3 for heating seasons.Thermal energy to drive the chiller was supplied by the TES tank. Type 9a, is a data reading component, selected to read weather data files such as ambient temperature and direct normal irradiation. This component was also used to read the demand data obtained from the survey.

Equation (3) was added to the equation box shown in **Figure 4** and **Figure 5** to calculate the energy deficiency.

$$\text{Energy Deficiency} = \text{Energy Demand} - \text{Energy Supplied} \quad (3)$$

Equation (4) calculates the amount of biodiesel required to supplement the energy deficiency using biodiesel caloric values in **Table 3**. Type 9a containing the hourly energy demand values was connected to the equation.

$$Biodiesel\ amount\ (kg) = \frac{Energy\ Deficiency(kJ)}{Biodiesel\ Calorific\ Value\ (\frac{kJ}{kg})} \quad (4)$$

Cost Assessment

The cost analysis assessed the financial viability of the proposed thermal system and compared it against a conventional air conditioner. The parameters, costs and price sources of the components are presented in **Table 4**. The cost of biodiesel varies depending on various factors such as the location, policies on biofuels and feedstock type. Due to lack of information on the price of biodiesel in Cyprus and outdated biodiesel price data in Turkey, the European highest price of 2 $/kg was used to perform the cost analysis of the proposed system in Cyprus. The estimated total cost of the system amounted to $19,000. The following assumptions were made in the Life Cycle Cost Assessment (LCCA):

- Electricity price (2024) was estimated at 0.15$/kWh according to TRNC KibTech tariffs. Fluctuations in electricity prices are often affected by a change in minimum wage [22].
- Due to unavailability of price data in TRNC, biodiesel prices were estimated using the highest biodiesel price of $2/kg in United State of America.

Table 4. Proposed system's cost parameters

Parameter	Units	Proposed system	Electric AC	Source
Estimated useful life	years	20	20	-
O and M	$	190	40	York
Inflation rate	%	3.1	3.1	Congressional Budget Office
Discount Rate	%	3.3	3.1	(CB-TRNC)
Cost of biodiesel	$/kg	2	0	IEA
Biodiesel demand	kg	123.3	-	-
Cost of electricity	$/kWh	0.15	0.15	Local Authority (KIBTECH)
Cost of 10.5kW AC unit	$	-	4000	Makro Cyprus, LG Cyprus
ETSC with Pumps	$	1500	-	Unihot, Solartwin,
TES tank	$	6,000	-	Storathem, Heatex
Indoor HE (radiators)	$	2,000	-	Heatmiser, Stelrad, Vailant
Boiler	$	2,500	-	CleanBurn, Bioheat,
Absorption chiller	$	7,000	-	Trotec, Cryo-Abco
Electricity consumption	kWh	2275	22570	

- Inflation and discount rates were estimated using average rates for 2024.
- A yearly inflation rate of 3.10% was assumed on electricity and O&M costs [30].
- A nominal discount rate of 3.33% was applied on all cash flows [30].

The methodology for assessing the financial feasibility of installing, maintaining and operating the proposed thermal system over a period of 20 years follows 3 common criteria, Pay Back Period (PBP), Return on Investment (ROI) and a Life-Cycle Cost Analysis (LCCA) The LCCA compares the system's costs of providing energy against the costs of installing and operating an electric air conditioner to provide the same amount of energy. Equation (5) calculates energy savings and Equation (6) calculates the payback period where O and M represents the operation and maintenance costs [31].

$$Savings\ (\$) = (\text{Total AC costs at PV}) - (\text{Total proposed system costs at PV}) \quad (5)$$

$$Simple\ Payback\ Period = \frac{Investment\ Costs - Incentives}{Average\ Savings\ per\ year} \quad (6)$$

Return on Investment (ROI) is determined by dividing the annual energy savings by the total investment costs. This metric measures the cost performance of the proposed system. A positive ROI means the investment is profitable. However, this cost evaluation method does consider the time value of money. Return on Investment per year, expressed as a percentage is calculated using Equation (7) [32].

$$Return\ on\ Investment = \frac{Savings - Investment\ Cost}{Investment\ Cost} \times 100 \quad (7)$$

The cost of installing and operating an electric air conditioner is considered and compared to the cost of the proposed system. LCCA considers the capital expenditure, inflation rate, discount rate, biodiesel costs, operation and maintenance costs and lifetime of the system.

Uncertainty Analysis

Uncertainty analysis is necessary to determine the accuracy of the model and acknowledge the limitations of the study. The main sources of uncertainty associated with this study stems from model simplification, cost assumptions, and data recording errors (**Table 5**). The overall uncertainty was calculated using Equation (8) [33].

$$Uncertainty = \sqrt{\sum (Specific\ Uncertainity)^2} = \pm 5.1\% \quad (8)$$

Table 5. Uncertainty of the study

Parameter	Uncertainty (%)
Data	3.0
Simulation	2.2
Biodiesel calorific Value	3.5
Cost	0.1
Emission	0.1
Uncertainty	5.1

RESULTS AND DISCUSSION

A hybrid solar-biodiesel thermal system was proposed to meet space heating and cooling energy demand for a typical family residential building in Cyprus. Although there is very limited research and data on Cyprus' heating and cooling energy demand, similar research has been performed from various locations under the Mediterranean climate. While a cooling energy consumption of 60,480MJ, and heating energy consumption of 38,700MJ with hourly load of 37.8MJ was obtained from this study, a similar study conducted by Florides et al. [34], modelled a typical Cyprus family house that requires 78,235MJ of cooling energy with a maximum hourly load of 40 MJ and 12,582MJ of heating energy with a maximum hourly load of 51.6 MJ in a year. The load was calculated from type 19 TRNSYS component.

Most researchers have modelled the heating and cooling energy demand from observing the internal gains of the modelled building component in TRNSYS which uses the ASHRAE standards, however, this study considered the freedom that occupants have over their air conditioning system. Occupants use air conditioning systems according to their preferences, freedom and ability to afford electrical energy, even if their thermal comfort levels might deviate from ASHRAE's standards [35, 36]. The findings highlight the willingness of participants to sacrifice their thermal comfort for less electric payments. Regardless, some participants still use their air conditioning systems to cater for their thermal comfort needs. Participants' freedom of choice in using their air conditioners might result in higher energy usage and increased carbon footprint, compared to adhering to ASHRAE's thermal comfort standards. However, the aim of this study is to design a system that effectively meets the space heating and cooling energy demand in residential buildings according to occupants' preferences while considering their actual energy consumption patterns. The scope is to develop a sustainable, responsive and energy efficient solution that not only focuses on improving occupants' thermal comfort, but also caters for the real-world energy needs of residential buildings with similar energy consumption conditions, thereby encouraging a sustainable, user-oriented approach to space conditioning.

Evacuated Tube Solar Collector

The results show that the ETSC had the lowest useful energy gain in December and the highest useful energy gain was achieved in September. **Figure 6** (a) shows the monthly maximum useful energy gained by the solar collector fluid in kJ/hr and **Figure 6** (b) shows the useful energy gain

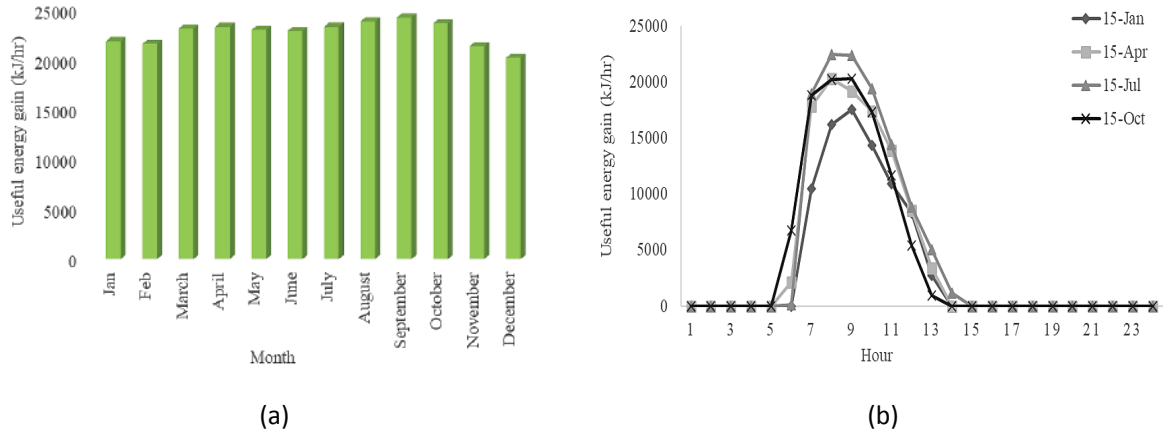

Figure 6. Collector useful energy gain. (a) monthly maximum useful energy gain and (b) hourly useful energy gained on 15 January, 15 April, 15 July and 15 October.

of the collector on the 15th day of January, April, July and October. The results for December, January and February are expected because of the winter season which has low ambient temperatures, high wind speeds and cloudy days. This lowers the temperatures within the tubes, reducing the thermal performance of the collector.

Although July is the peak summer month, September achieved the maximum useful energy gain, reaching 24,200kJ/hr as shown in **Figure 6** (a). This is due to very high ambient temperatures reaching 38°C in July. Very high ambient conditions are not optimal for ETSC efficiency and factors such as overheating, and increased system degradation are for concern. Factors including solar irradiation, inlet and outlet temperatures significantly influence the useful energy gain. A higher temperature difference between the collector outlet and inlet increases the useful energy gain. The unavailability of thermal energy during night times affects the overall thermal efficiency during winter seasons due to longer nights and shorter days.

The outlet temperatures of the working fluid were highest during the summer-fall seasons as illustrated in **Figure 7**. As expected, the highest collector outlet temperatures were attained with maximum monthly temperatures of 204°C, 206°C and 206°C in July, August and September, respectively. According to Kate et al. [37], ETSC can achieve temperatures above 200°C. The highest collector outlet temperatures for the winter season (December and January) achieved were 158°C and 156°C respectively. Winter season has shorter days, reducing the efficiency of ETSC. However, the ETSC temperatures are substantially high for space heating purposes during winter seasons.

In this case, the ETSC is highly efficient and suitable for the Mediterranean climate. The results are consistent with Hayek et al. [38], who experimentally analysed the performance of ETSCs in Lebanon. However, there is a contrast

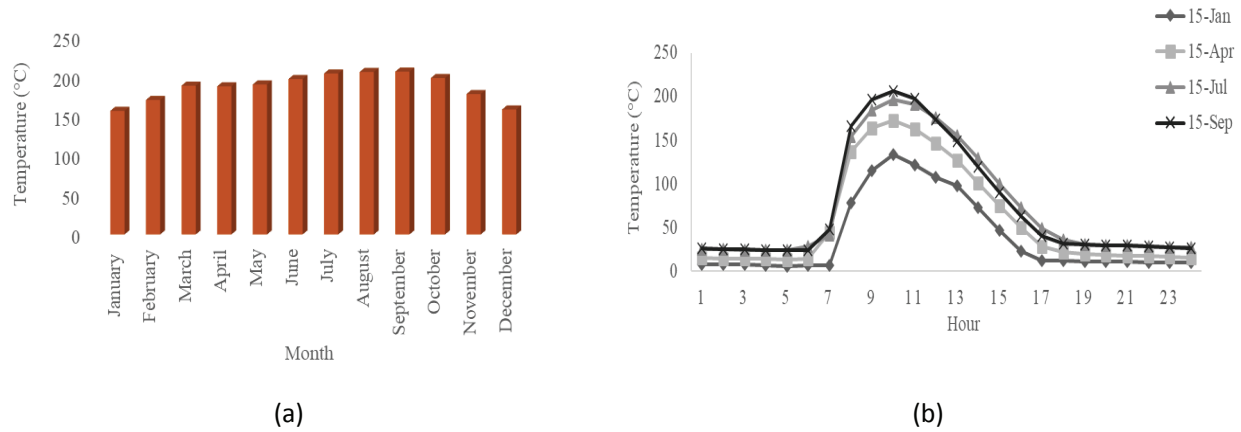

Figure 7. Collector outlet temperatures. (a) highest reached monthly temperatures and (b) hourly temperatures on the 15th day of January, April, July and September

with Adriana et al. [39], whose results suggested that ETSC can only perform well under cold weather conditions. The choice of HTF plays a significant role in improving thermal performance of ETSCs. The lowest fluid outlet temperature obtained was 2°C in January. To maintain the HTF from freezing, glycol oil is recommended due to its thermal properties. According to MEGlobal, thermal oil has lower freezing temperatures of below –10°C and high boiling temperatures above 120°C [40]. Most importantly, the position and orientation of ETSC matter for maximum radiation absorption and to avoid shading of the collectors with buildings or even self-shedding within the collector array.

Thermal Energy Storage Tank

Maximum tank temperatures reaching 100°C were achieved during the summer seasons as illustrated in **Figure 8** (a). July and August had maximum storage temperatures of 100°C while January and December had maximum storage temperatures of 68°C and 71°C respectively. It is evident from **Figure 8** (b) that minimum storage temperatures for the summer seasons are higher compared to those for winter season. This is due to the flow of energy from a higher temperature source (storage tank) to a lower temperature source (surroundings). The winter ambient temperatures are lower compared to the summer ambient temperatures.

The temperatures drop drastically during predawn hours as shown by the daily temperature patterns in **Figure 9**. There is a uniform trend which shows that the energy storage tank stores the lowest energy during the early morning hours of the day (4th - 6th hour). This is due to the absence of solar energy to supply thermal energy to the

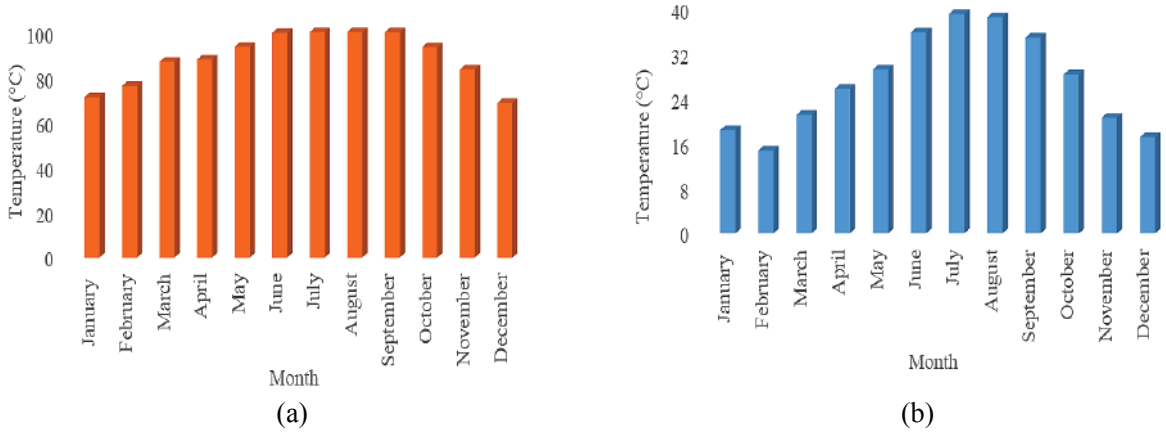

Figure 8. Monthly temperatures of the water in the thermal energy storage tank. (a) highest reached temperatures and (b) lowest temperatures reached.

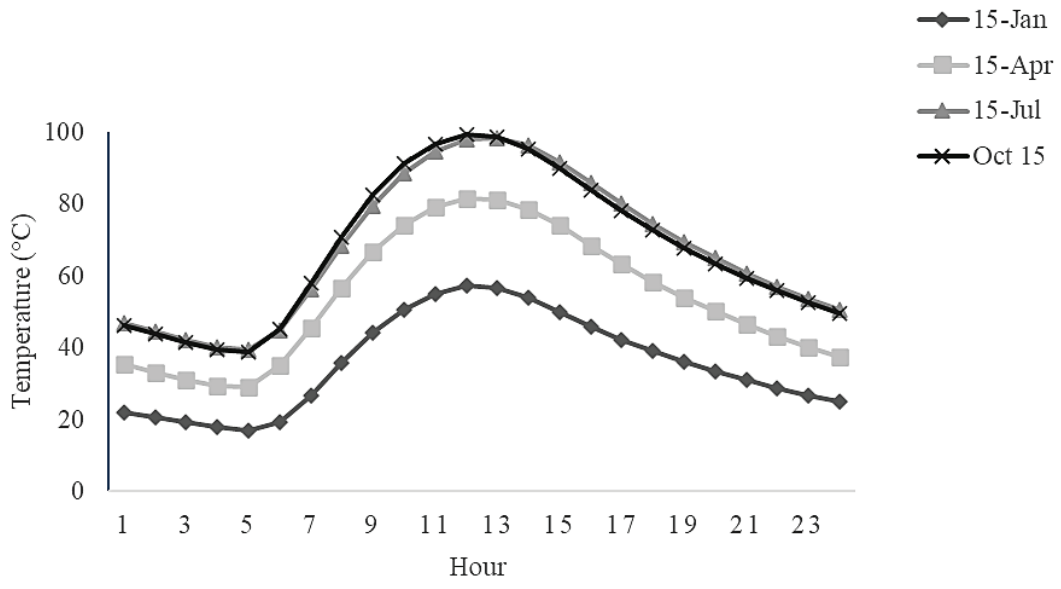

Figure 9. Hourly thermal energy storage temperature on the 15th of January, April, July and October.

storage tank, while the tank continuously discharges energy to the surroundings. The maximum amount of energy is stored during peak hours, 12 pm to 3 pm. The trend shows a decline in the energy stored as the sun sets. The winter season has the lowest energy stored due to less energy input from the ETSC. Considering the estimated demand these results show that the energy stored is sufficient to meet three quarters of the energy demand.

This study judges the thermal performance of the proposed system to meet the estimated demand. **Figure 10** (b) shows an energy deficiency, concluding that the total demand cannot be entirely satisfied using solar energy. The heating hours are during sunrise time and evening hours, after sunset, where solar energy is unavailable. The energy stored in the energy storage tank is insufficient to meet the total demand. Since the spring season requires less heating energy, the solar thermal system almost met all of the demand as illustrated in **Figure 10** (d). However, there is a small deficiency caused by lack of solar energy at nighttime. Although the winter and spring seasons suffered a deficiency, there were periods with excess energy during these seasons. **Figure 10** (b) and (c) illustrates the ability of the solar thermal system with energy storage to meet the entire cooling demand required for the summer and fall seasons. This is facilitated by the availability of abundant solar energy during the summer period. According to Kaushik et al. [41], cooling demand peaks at times of abundant solar radiation, making it possible to meet the entire cooling demand during the day. Temperatures often dip during nighttime, reducing the need for cooling energy when solar energy is unavailable. The cooling demand is higher than the heating demand, therefore, the system's ability to meet all of the cooling energy demand is of major importance. In addition, **Figure 10** indicates a substantial amount of excess energy that can be used for other domestic purposes requiring hot water or can be shared with neighboring households.

Although temperatures of the working fluid in the storage tank reached 100°C during the summer season, the highest thermal losses also occurred during the summer season, with the highest losses reaching 5,326kJ/hr as shown in **Table 6**. There is a substantial amount of thermal losses incurred for the summer seasons (July and August) when the water temperature reaches close to and beyond 100 °C. This means that some vapor starts to evaporate, thereby causing a mass loss from the buffer tank. TRNSYS 16 allows the use of a pressure relief valve to account for the boiling effects of the water when the user-specified fluid boiling temperature is reached. The pressure valve opens to release sufficient energy and maintain the tank at boiling temperature. Various boiler mountings and certain accessories including safety valves, stop valves, pressure gauges,

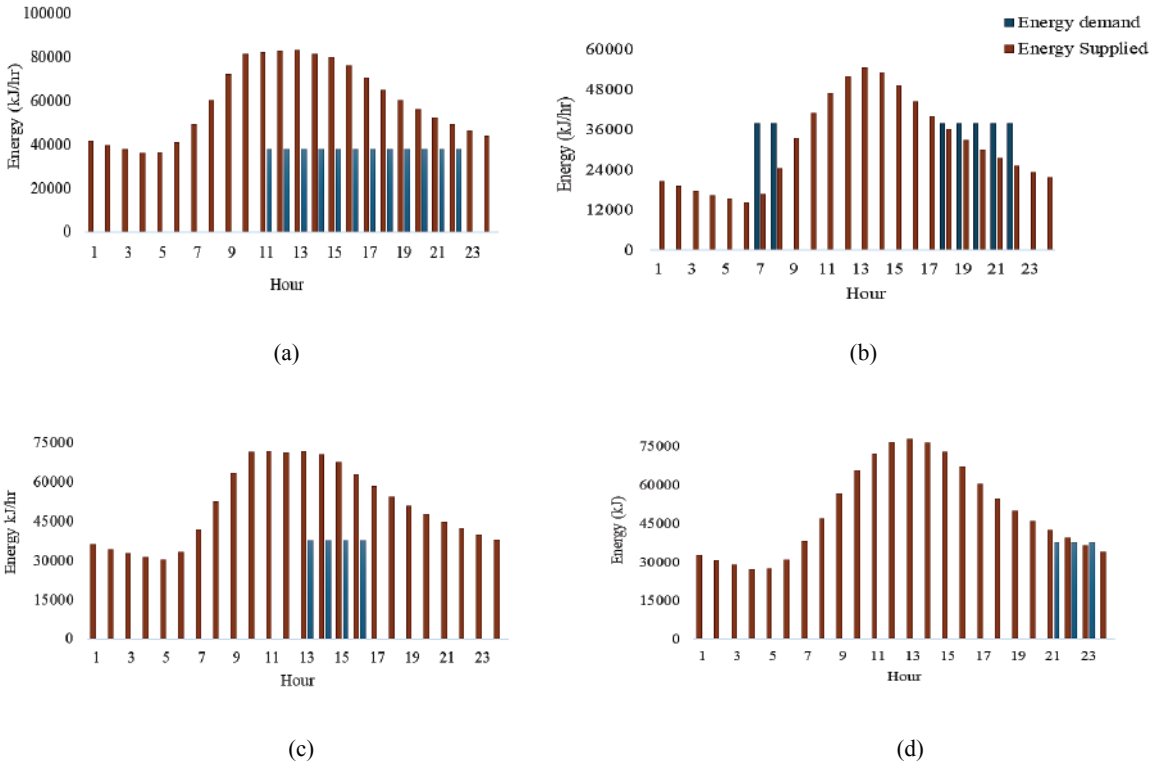

Figure 10. Energy demand and energy supplied by the proposed thermal system on (a) 15 July, (b) 15 January, (c) 15 October and (d) 15 April.

Table 6. Effect of storage temperature difference on thermal energy (21 July)

Hour	Tank temperature (°C)	Ambient Temperature (°C)	Delta T (°C)	Thermal Energy (kJ)	Thermal Losses (kJ)
1	51.9	27.5	24.4	32,636.65	178.15
2	49.2	26.9	22.3	30,944.52	162.00
3	46.8	26.6	20.2	29,416.67	146.65
4	44.6	26.3	18.3	28,040.27	132.67
5	42.7	26.1	16.6	26,857.29	119.11
6	42.0	26.3	15.7	26,377.34	107.84
7	47.7	27.7	20.0	29,968.50	138.92
8	59.7	29.1	30.6	37,500.35	214.81
9	72.4	30.6	41.8	45,533.50	296.81
10	83.9	31.9	52.0	52,749.75	370.53
11	92.9	33.1	59.8	58,413.42	427.89
12	98.8	34	64.8	62,104.74	3544.53
13	100.0	34.7	65.3	62,850.00	5326.55
14	99.8	35.1	64.7	62,729.39	465.83
15	97.9	35.2	62.7	61,520.28	452.69
16	93.4	34.9	58.5	58,678.91	423.36
17	87.5	34.3	53.2	55,018.21	386.80
18	81.6	33.4	48.2	51,316.97	351.58
19	76.2	32.3	43.9	47,880.56	319.03
20	71.2	31.5	39.7	44,773.11	288.82
21	66.8	30.8	36.0	41,964.93	262.03
22	62.7	30	32.7	39,421.55	238.64
23	59.1	29.2	29.9	37,113.71	217.59
24	55.7	28.5	27.2	35,021.45	197.93

flame loss detectors and water level indicators are important to maintain safety and reduce failure from high pressure issues [42]. According to Agarwal et al. [42], safety valves can be mounted on boilers to allow the escape of excess steam from the boiler and ensure normal pressure within the boiler. In addition, location of valves must be optimized and all mountings should be properly arranged. Safety valves protect the energy storage tank by opening and allowing the flow of steam, relieving the tank from build-up pressure [43]. High temperatures achieved during the summer causes the HTF to evaporate, therefore, fluid refilling is necessary during maintenance

However, thermal losses are relatively less as shown in **Figure 11**, except for summertime which is due to increased temperature difference between the tank and the ambient temperature. These results are consistent with Martyna et al. [44], who recorded the highest thermal energy losses during the summer months, August and July for a study conducted in Poland. A storage tank at high temperature loses more energy than a storage tank closer to ambient temperature [45]. This is because of a larger temperature difference between the tank temperature and the temperature of the surroundings/ambient temperatures. As the second law of thermodynamics states, heat energy flows from a high energy source to a low energy source, increasing thermal energy losses. In addition, factors such as radiation play a role to a lesser extent. The tank radiates more energy during the summer season compared to winter seasons.

System's Thermal Performance

The results demonstrated the ability of the solar thermal system with an integrated TES tank to meet 100% of the cooling load and 87.7% of the heating load. Out of 425,750MJ stored by the storage tank, 268,700MJ was in excess and could be used for other purposes such as heating water for domestic use. The results align with Salameh et al, who optimized a 10kW solar assisted cooling system for a house under the Mediterranean climate. Their results showed the ability of an ETSC to meet the cooling demand at worst cooling days. In contrast, Figaj et al. [46] modelled a solar thermal driven absorption chiller which satisfied only 18% of the space cooling demand for a single floor residential building in Poland. Cyprus benefits from the sunny mediterranean climate compared to Poland with low solar radiation. Moreover, the system offered less economic benefits compared to a convectional system due to cheaper gas

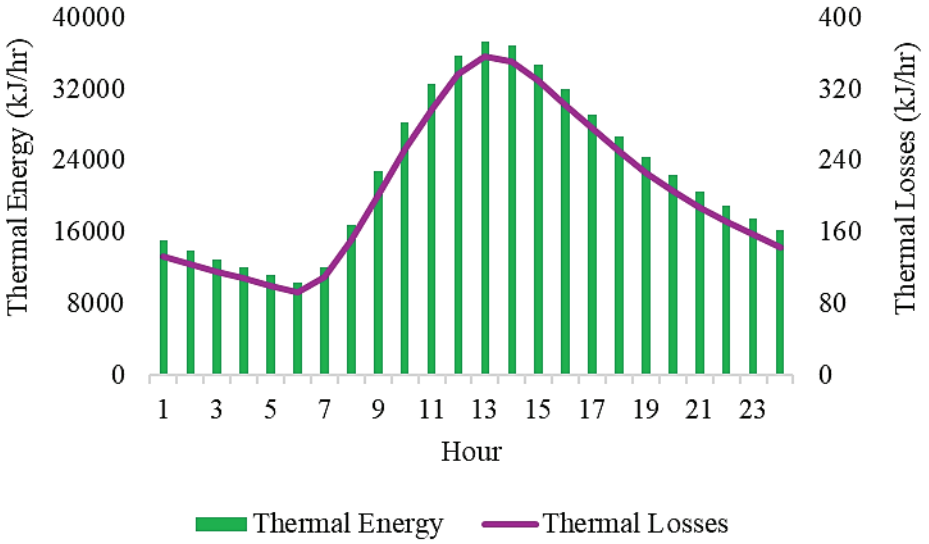

Figure 11. Hourly thermal energy and corresponding thermal losses on January 15.

and electricity prices in Poland. Therefore, the proposed system is well suited for Mediterranean climates.

The prospect of distributing this excess energy to adjacent residential buildings is an additional option to mitigate energy wastage. With the exception of space as a limiting factor, the system is scalable for larger buildings when designed properly [47]. The heating season suffered an energy deficiency of 4,758MJ, which is supplemented by a biodiesel boiler, using pure biodiesel (B100). The amount of biodiesel required was calculated according to the feedstock in **Table 3** and the resulting **Table 7** shows the amount of biodiesel required in kgs. In addition, the amount of natural gas required to meet the yearly energy deficiency is 95.2kg, which is the least amount of fuel required among the other biodiesel fuels. Castor oil has the highest mass required to meet the energy deficiency and this translates to higher fuel costs. Jatropha and rapeseeds have the second highest amount required while cotton seed oil has the least mass among the biodiesel feedstock types mentioned.

Cost Analysis

According to the LCCA performed, the Present value (PV) of the proposed hybrid solar-biodiesel thermal system amounting to $34,000 is significantly lower than $71,200 of the convectional air conditioner. The Payback period reflected that it takes 7.3 years to recover the initial money invested in installing the proposed system. The ROI had a value of 9% while the total savings amounted to $ 37,200. The cost of meeting the total energy demand for the first whole year while using an electric air conditioner and buying electricity from the grid amounted to $3,400. The proposed system consumes biodiesel worth $309 and an additional $341 for running the absorption chiller per year. During the first 10 years of operation, the proposed thermal system has higher costs compared to an electric air conditioner, however, the electric air conditioner becomes expensive from the 11th year.

Domestic solar systems require minimal maintenance compared to large scale solar system. Regular maintenance includes periodic cleaning to remove accumulated dust and dirt particles and replacement of malfunctioning components [47]. The absorption chiller requires maintenance over a period of time due to the corrosive nature of lithium bromide [46]. Boiler tubes can benefit from regular maintenance since they are susceptible to prolonged overheating [41]. Periodic Maintenance of pumps, fuel tanks and boiler

Table 7. Supplementary biodiesel required according to feedstock type

Biodiesel-Feedstock Type	Mass of Biodiesel kg	Biodiesel-Feedstock Type	Mass of Biodiesel kg
Algal	117.0	Rapeseed	120.6
Ethyl palmitate	116.0	Crambe	117.3
Ethyl oleate	117.6	Cotton seed oil	113.0
Ethyl stearate	114.5	Castor oil	123.3
Soybean	120.5	Jatropha	120.6
Natural gas	95.2		

water treatment is necessary to improve system's performance. The thermal energy storage tank must be checked for leakages during maintenance [42].

The suitability of a space conditioning thermal system investment is affected by 2 factors, time and risk [31]. Weather conditions and deflation/inflation in electricity prices are the main risk factors associated with this investment. Weather conditions influence the demand patterns while the inflation of electricity prices benefits the investor as he is exempted from paying electric bills. However, the inflation of electricity prices might affect the cost of biodiesel, posing as a risk to the investor. An electric air conditioner is associated with monthly electricity bills throughout the life of the air conditioner while the proposed system has high investment costs and considerable operating and maintenance costs.

Biodiesel Environmental Analysis

The proposed system prevents the use of fossil fuel based auxiliary energy systems. The results show that using biodiesel as an auxiliary fuel eliminates the emission of 5.3 tons of CO_2 per household over 20 years. This study conclusively demonstrates the environmental benefits of using biofuels instead of burning natural gas. Biodiesel is considered as renewable biodiesel due to its carbon neutrality [6]. However, biodiesel is still considered a niche energy source rather than main source and cannot compete with other fossil fuels on the market. Land competition is a possible challenge as land for energy crops is limited, hence it is difficult to secure continuous supply for biodiesel. If poorly controlled, the use of land for energy can lead to deforestation, increased water demand and other environmental issues. In that case, natural gas becomes more advantageous than biodiesel. However, the environmental issues can be mitigated by sustainable agricultural practices including but not limited to soil conservation, waste management, waste recycling and environmental impact assessments. The overall benefits of GHG reduction should not come at the detriment of environmental damage due to deforestation. According to Bart and Cavallaro, the topic of biofuel is a dilemma between energy and climate [48]. The EU approved certain biofuel feedstocks to promote the sustainability of biofuels by encouraging advanced biofuels which are processed from lignocellulosic materials such as forest waste and agricultural residues. This control strategy eliminates first generation biofuels and prioritizes food security [49].

CONCLUSION

This work presents a techno-economic analysis of a proposed hybrid solar-biodiesel thermal system to meet space heating and cooling energy demand for a typical family residential building in North Cyprus. Auxiliary systems of small-scale renewable energy systems are often overlooked. Therefore, the study addressed the use of biodiesel in fueling an auxiliary heating and cooling thermal energy system. The results indicated that evacuated tube solar collectors have a high thermal performance with outlet temperatures reaching 200°C during summer seasons and are pertinent for regions under the Mediterranean climate. The cooling and heating energy demand was estimated from the survey to be 60,480MJ and 38,700MJ respectively, with an hourly load of 37.8MJ. Although high thermal losses occurred during summer seasons, the thermal energy storage tank was efficient enough to supply 100% of the cooling demand and 87% of the heating demand. Heating energy deficiency of 4,757MJ was met using 123.3 kg of biodiesel instead of 95.2kg of natural gas. A lifecycle cost analysis revealed that despite the high cost of biodiesel, the proposed system is cost efficient compared to a convectional air conditioner starting from year 16. The proposed system had a Return On Investment of 9%, Payback Period of 7.3 years and total savings of $ 37,200 for a lifetime of 20 years. These findings support energy transition in residential buildings. However, biodiesel is still considered a niche energy source rather than main source and cannot compete with other fuels on the market. Further research could explore the potential of biodiesel homebrewing in Cyprus, to promote sustainable utilization of resources and minimize dependency on fossil fuels. In conclusion, this research aligns with the goals of sustainable energy practices and transition, and significantly contributes to the 2050 climate goals.

NOMENCLATURE

Abbreviations

ASHRAE	American Society of Heating, Refrigeration and Air Conditioning Engineers
B100	Pure biodiesel
CO_2	Carbon Dioxide
COP	Coefficient of Performance
ETSC	Evacuated Tube Solar Collector
GHG	Green House Gas
HTF	Heat Transfer Fluid
IEA	International Energy Agency
LCCA	Life Cycle Cost Assessment
Li-Br	Lithium Bromide
O&M	Operation and Maintenance
PBP	Pay Back Period
PCM	Phase Change Material
PV	Photovoltaic
ROI	Return On Investment
TES	Thermal Energy Storage
TMY	Typical Meteorological Year

Special Characters

E	Error margin
S	Standard deviation
T	Temperature, °C
T_c	Critical Value
n	Sample size

n-1 Degree of freedom
$\bar{x}$ Sample mean

Greek Letters
μ population mean

Subscripts
c Score, t score

AUTHORSHIP CONTRIBUTIONS

Nyasha Netsai Bema: Methodology, Software, Data curation, Writing (Original draft)

Kemal Masera: Conceptualization, Supervision, Writing (review and editing)

DATA AVAILABILITY

[dataset] National Renewable Energy Laboratory (NREL). (2022). Typical Meteorological Year (TMY) Data. NREL Data Repository. https://data.nrel.gov/submissions/69. Accessed on: March, 2023.

CONFLICT OF INTEREST

The author declared no potential conflicts of interest with respect to the research, authorship, and/or publication of this article.

ETHICS

There are no ethical issues with the publication of this manuscript.

STATEMENT ON THE USE OF ARTIFICIAL INTELLIGENCE

Artificial intelligence was not used in the preparation of the article.

REFERENCES

[1] International Renewable Energy Agency. Renewable Energy Roadmap for the Republic of Cyprus. Available at: www.irena.org/publications. Accessed on July 18, 2025.

[2] Khalid M. Smart grids and renewable energy systems: Perspectives and grid integration challenges. Energy Strateg Rev 2024;51:101299. [CrossRef]

[3] International Energy Agency. The Future of Cooling Opportunities for energy-efficient air conditioning Together Secure Sustainable. Available at: www.iea.org/t&c/. Accessed on July 18, 2025.

[4] Kumar AR, Ramakrishnan M. A scoping review on recent advancements in domestic applications of solar thermal systems. J Therm Eng 2022;8(3):425–443. [CrossRef]

[5] Pathak B, Patel N. Effect of modifying bowl geometry for IC engine fueled with diesel and biofuels - Review. J Therm Eng 2024;10(1):244–261. [CrossRef]

[6] Wan Osman WNA, Rosli MH, Mazli WNA, Samsuri S. Comparative review of biodiesel production and purification. Carbon Capture Sci Technol 2024;13:100264. [CrossRef]

[7] Rodionova MV, Poudyal RS, Tiwari I, Voloshin RA, Zharmukhamedov SK, Nam HG, et al. Biofuel production: Challenges and opportunities. Int J Hydrog Energy 2017;42(12):8450–8461. [CrossRef]

[8] Abbaszaadeh A, Ghobadian B, Omidkhah MR, Najafi G. Current biodiesel production technologies: A comparative review. Energy Convers Manag 2012;63:138–148. [CrossRef]

[9] Lopresto CG. Sustainable biodiesel production from waste cooking oils for energetically independent small communities: An overview. Int J Environ Sci Technol 2025;22:1–16. [CrossRef]

[10] Al Shanableh F. Characterization of Cold Flow Properties of Biodiesel Transesterified from Waste Frying Oil [PhD thesis]. Nicosia: Near East University; 2017.

[11] National Center for Appropriate Technology. The National Sustainable Agriculture Information Service. Available at: www.attra.ncat.org. Accessed on July 18, 2025.

[12] Noro M. Heating and cooling feasibility of absorption heat pumps driven by evacuated tube solar collectors: An energy and economic analysis. Sustainability 2022;14(10):6137. [CrossRef]

[13] Sibilio S, Ciampi G, Rosato A, Entchev E, Yaici W. Parametric analysis of a solar heating and cooling system for an Italian multi-family house. Int J Heat Technol 2016;34(S2):S458–S464. [CrossRef]

[14] Hussein HA. Modeling and simulation of an absorption solar cooling system under Iraqi weather conditions. Eng Technol J 2017;35(4):356–364. [CrossRef]

[15] Sarmouk MD, Smaili A, Fellouah H, Merabtine A. Experimental and numerical investigations of a solar space heating system based on design of experiments method. Sol Energy 2021;216:396–410. [CrossRef]

[16] Marcos JD, Izquierdo M, Parra D. Solar space heating and cooling for Spanish housing: Potential energy savings and emissions reduction. Sol Energy 2011;85(11):2622–2641. [CrossRef]

[17] Redpath D, Paneri A, Singh H, Ghitas A, Sabry M. Design of a building-scale space solar cooling system using TRNSYS. Sustainability 2022;14(18):11549. [CrossRef]

[18] Lebedeva K, Migla L. Latent thermal energy storage for solar driven cooling systems. In: Proceedings of the 19th International Scientific Conference Engineering for Rural Development. Jelgava, Latvia: Latvia University of Life Sciences and Technologies; 2020. p. 1134–1139. [CrossRef]

[19] Martínez PJ, Martínez P, Soto VM, Bujedo LA, Rodriguez J. Design of a 35 kW solar cooling demonstration facility for a hotel in Spain. Appl Sci 2020;10(2):496. [CrossRef]
[20] Salameh T, Tawalbeh M, Juaidi A, Abdallah R, Hamid AK, Assad MEH. Optimization and life cycle analysis of solar-powered absorption chiller designed for a small house in the United Arab Emirates using evacuated tube technology. Renew Energy 2022;198:200–212. [CrossRef]
[21] Düzcan A, Kara YA. Investigation of the usage potential of the evacuated tube and the flat plate collectors to assist an absorption chiller. Sustain Energy Technol Assess 2021;47:101437. [CrossRef]
[22] TRNC Electricity Corporation (KIB-TEK). KKTC Elektrik Kurumu. 2024. Available at: https://www.kibtek.com/. Accessed on July 18, 2025.
[23] Department of Meteorology, Republic of Cyprus. Cyprus Met Department. Available at: https://www.dom.org.cy/. Accessed on June 18, 2024.
[24] Peng P, Gong G, Chun L, Fang X, Li W. Investigation of physiological and subjective responses under composite air carrying energy radiant air-conditioning system. J Build Eng 2021;43:103146. [CrossRef]
[25] Kim J, Song D, Kim S, Park S, Choi Y, Lim H. Energy-saving potential of extending temperature set-points in a VRF air-conditioned building. Energies 2020;13(9):2160. [CrossRef]
[26] Karmakar R, Kundu K, Rajor A. Fuel properties and emission characteristics of biodiesel produced from unused algae grown in India. Pet Sci 2018;15(2):385–395. [CrossRef]
[27] Oliveira LE, Da Silva MLCP. Comparative study of calorific value of rapeseed, soybean, jatropha curcas and crambe biodiesel. Renew Energy Power Qual J 2013;1(11):679–682.
[28] Aydin H, Bayindir H. Performance and emission analysis of cottonseed oil methyl ester in a diesel engine. Renew Energy 2010;35(3):588–592. [CrossRef]
[29] Gokdogan O, Eryilmaz T, Yesilyurt MK. Thermophysical properties of castor oil (Ricinus communis L.) biodiesel and its blends. CT&F Cienc Tecnol Futuro 2015;6(1):95–128. [CrossRef]
[30] Statista. Average inflation rate in Cyprus from 1980 to 2030. Available at: https://www.statista.com/statistics/382109/inflation-rate-in-cyprus/. Accessed on July 15, 2025.
[31] Rout A, Sahoo SS, Singh S, Pattnaik S, Barik AK, Awad MM. Benefit-cost analysis and parametric optimization using Taguchi method for a solar water heater. In: Design and Performance Optimization of Renewable Energy Systems. Elsevier; 2021. p. 101–116. [CrossRef]
[32] Association of College and Research Libraries. Metrics for decisions. Available at: www.ala.org/acrl/standards/. Accessed on July 18, 2024.
[33] Radheshyam, Santhosh K, Kumar GN. Effect of 1-pentanol addition and EGR on the combustion, performance and emission characteristic of a CRDI diesel engine. Renew Energy 2020;145:925–936. [CrossRef]
[34] Florides GA, Kalogirou SA, Tassou SA, Wrobel LC. Modelling and simulation of an absorption solar cooling system for Cyprus. Sol Energy 2002;72(1):43–51. [CrossRef]
[35] Yi CY, Childs C, Peng C, Robinson D. Thermal comfort modelling of older people living in care homes: An evaluation of heat balance, adaptive comfort, and thermographic methods. Build Environ 2022;207:108550. [CrossRef]
[36] Mishra AK, Loomans MGLC, Hensen JLM. Thermal comfort of heterogeneous and dynamic indoor conditions — An overview. Build Environ 2016;109:82–100. [CrossRef]
[37] Hudon K. Future Energy. Elsevier; 2014.
[38] Hayek M, Assaf J, Lteif W. Experimental investigation of the performance of evacuated-tube solar collectors under eastern Mediterranean climatic conditions. Energy Procedia 2011;6:618–626. [CrossRef]
[39] Greco A, Gundabattini E, Gnanaraj DS, Masselli C. A comparative study on the performances of flat plate and evacuated tube collectors deployable in domestic solar water heating systems in different climate areas. Climate 2020;8(6):78. [CrossRef]
[40] MEGlobal. Ethylene Glycol Product Guide INTRODUCTION 2 Precautions 2. Available at: www.equate.com. Accessed on July 13, 2024.
[41] Kaushik SC, Verma A, Tyagi SK. Advances in solar absorption cooling systems: An overview. J Therm Eng 2024;10(4):1044–1067. [CrossRef]
[42] Agarwal S, Suhane A. Study of boiler maintenance for enhanced reliability of system a review. Mater Today Proc 2017;4(2):1542–1549. [CrossRef]
[43] Nobel International. Technical Manual on Installation, maintenance & use instructions of Buffer Water Tanks. 2022. Available at: https://nobel.bg/download/technical-manual-buffer-water-tank/. Accessed on July 14, 2025.
[44] Bocian M, Siuta-Olcha A, Cholewa T. On the circulation heat losses in domestic hot water systems in residential buildings. Energy Sustain Dev 2022;71:406–418. [CrossRef]
[45] NPRO Energy. Heat Loss in Heat Storages. Available at: https://www.npro.energy/main/en/5gdhc-networks/heat-losses-gains. Accessed on June 18, 2024.
[46] Figaj R, Żołądek M. Experimental and numerical analysis of hybrid solar heating and cooling system for a residential user. Renew Energy 2021;172:955–967. [CrossRef]
[47] Shehadi M. Optimizing solar cooling systems. Case Stud Therm Eng 2020;21:100663. [CrossRef]

[48] Bart JCJ, Palmeri N, Cavallaro S. Biodiesel Science and Technology. Woodhead Publishing Limited; 2010. [CrossRef]
[49] Panoutsou C, Chiaramonti D, Sandford C, et al. Advanced biofuels to decarbonise European transport by 2030: Markets, challenges, and policies that impact their successful market uptake. Energy Strateg Rev 2021;34:100633. [CrossRef]

J Ther Eng, Vol. 12, No. 2, pp. 550−578, March, 2026

Journal of Thermal Engineering
Web page info: https://jten.yildiz.edu.tr
DOI: 10.14744/thermal.0001101

Research Article

Experimental analysis and optimization of the air-cooled solar panel

Vineet SINGH[1,*], Vinod Singh YADAV[2], Niraj KUMAR[3], Anurag MAHESWARI[4], Javed Khan BHUTTO[5], Sultan ALSHEHERY[6], Mohammed Azam ALI[6], Manoj KUMAR[1]

[1]Department of Mechanical Engineering, School of Engineering & Technology, IFTM University, Moradabad, 244102, India
[2]Department of Mechanical Engineering, NIT, Srinagar Pauri Garhwal, Uttarakhand, 246174, India
[3]Department of Mechanical Engineering and Design Institute, Jaypee Institute of Information Technology, Noida, 201309, India
[4]Department of Mechanical Engineering, Government Polytechnic Mawana Khurd, Meerut, Uttar Pradesh, 250401, India
[5]Department of Electrical Engineering, College of Engineering, King Khalid University, Abha, 61421, Saudi Arabia
[6]Department of Mechanical Engineering, King Khalid University, Abha, 61421, Saudi Arabia

ARTICLE INFO

Article history
Received: 21 December 2024
Revised: 07 March 2025
Accepted: 13 March 2025

Keywords:
Exergy; Fins; MINITAB; Optimization; RSM; Solar Panel

ABSTRACT

The efficiency and sustainability of solar panels throughout the day remain significant challenges, primarily due to the temperature rise in solar cell materials during peak sunlight hours, which reduces their efficiency. This study aims to enhance the efficiency of solar panels using an air-cooling mechanism. Based on prior insights, an indoor experimental setup was developed, featuring a cooling system with 196 circular pin fins, each with a diameter of 3 mm and a length of 16 mm, mounted on the rear surface of the solar panel. An aluminum heat sink of 3 mm thickness was integrated to support the fins, while a variable-speed fan supplied airflow across the fins. The solar flux and airflow rate were identified as critical parameters influencing solar panel efficiency. These parameters were optimized using Response Surface Methodology, with ranges of 400–800 W/m² for solar flux and 0.01–0.02 m³/s for airflow rate. Optimization was performed using MINITAB 17 and Design Expert 18 software. The optimized input conditions, solar flux of 403.33 W/m² and airflow rate of 0.0221 m³/s, yielded the following outcomes: exergy efficiency of 15.79%, power output of 4.12 Wp, module temperature of 22.43°C, and solar panel efficiency of 14.48%, with a composite desirability score of 0.5737. This work is novel and new in its simple and light weight arrangement as compared to heavy vibrating pumps required in liquid and nano-fluid cooling. Additionally, the optimization approach and economic analysis of the solar panel cooling system are relatively new and have received little attention in previous literature. Perturbation plots revealed that solar flux had a more pronounced effect on panel performance compared to airflow rate. This study highlights the potential of air-cooling systems to mitigate midday efficiency losses and improve the operational sustainability of solar panels. The findings contribute to advancing cooling technologies for solar energy systems, promoting greater energy efficiency and reliability.

Cite this article as: Singh V, Yadav VS, Kumar N, Maheswari A, Khan Bhutto J, Alshehery S, et al. Experimental analysis and optimization of the air-cooled solar panel. J Ther Eng 2026;12(2):550−578.

***Corresponding author.**
*E-mail address: vineetpsh@gmail.com

This paper was recommended for publication in revised form by Editor-in Chief Ahmet Selim Dalkilic

Published by Yıldız Technical University Press, İstanbul, Turkey
Yıldız Technical University. This is an open access article under the CC BY-NC license (http://creativecommons.org/licenses/by-nc/4.0/).

INTRODUCTION

Environmental problems and economic crises of fossil fuels search the alternative methods for energy production. Solar energy is one of the best ways to convert it into electrical energy. The solar panels show its importance by directly converting solar energy into useful electrical energy. The solar panel is formed by the parallel and series combination of the solar cells. The solar cell is formed by the P-N junction in which holes and electrons cross the depletion layer by absorbing the solar energy. However, the number of factors affect the performance of the solar panel of which some factors are external and internal. The external factors are uncontrollable by the human being but the internal factors can be controlled and modified to hike the solar panel's performance [1]. The higher surface temperature of the solar cell enhanced the thermal resistance of the depletion layer and slowed down the speed of the electrons, so the performance of the PV module was lacking. However, a number of design have been investigated to cool the solar panel, the purpose is to avoid over heating and sustain the performance. A number of cooling methods like active [2, 3, 4], passive [5, 6, 7], nanoparticles [8, 9, 10] and PCM combined with other cooling [11, 12, 13] fluids have been used.

Active cooling requires an external energy source to pump the water and air. The active cooling enhances the heat transfer coefficient and turbulence due to that it has large ability to cool the solar cell. It included the forced air, forced water, and PV/T system. In the active cooling method, the net power produced by the photovoltaic module is obtained by deducting the pump or blower power from the solar panel output power. The passive cooling method requires no additional prime mover; it's based on fully natural circulation. The heat pipe, natural air, and water circulations are considered to be passive cooling approaches in which heat transfer is lower leading to poor performance at higher temperatures. The main advantage of passive cooling is its lower cost due to negligible variable cost. It improved the productivity of solar panel very little due to natural circulation. The Phase Change Material (PCM) works well for performance enhancement of the solar panel by absorbing maximum heat trapped inside it. In the primary heating process, PCM material starts to heat with melting and absorbs a part of sensible heat. In secondary heating, the phase change of PCM material starts which absorbs the latent heat. Due to the heat absorption from the PV cell during day time, the PV cells cooled and produced more power. The cycle is reversed at night time, at the time of the absence of the Sun, which cools down the solar panel, and PCM material reaches in initial state.

PCM cooling gets popularity due to its large absorption capacity, low cost, and chemical stability. The selection of the PCM material depends on the maximum, and minimum temperature of the solar panel and atmospheric temperature. Based on these temperature ranges, the PCM material properties selected, the main PCM material properties are namely thermal, physical, kinetic, chemical, economic, and environmental listed in [14]. Rok et al. [15] performed an experimental and numerical simulation on the performance improvement of the 250 W solar panel using PCM cooling. The RT28HC is used as a PCM material for the cooling of solar panel. The experimental results depicted that PCM material reduced the surface temperature of solar panel by 35.6°C as compared to without cooled solar panel. Rajvikram et al. [16] enhanced the thermal conductance of PCM by using the aluminum sheet as a thermal conductivity enhancer. The test has been conducted for three months. The outcomes of the study indicated that if PCM material with an aluminium sheet attached at the back of the solar panel, the average efficiency enhanced to be 24.4% with an ordinary decline in the temperature of the 10.35°C. Yahya et al. [11] investigated the multi-layered PCM material in solar panel temperature reduction. The approach involves integrating PCM with metallic PCM attached at the back end of the solar panel. The ANSYS FLUENT software has been used for determining the solidification and melting phase. This cooling system enhanced the PV module performance by 35.8% compared to the panel without cooling at the ambient temperature of 40°C and solar flux of 1000 W/m^2.

Fatih et al. (2020) studied the performance of the phase change material, thermoelectric, and aluminium fins on the solar panel cooling. The outcomes of the study saw that the aluminium fins produced the maximum power and the PCM and TEM generated the lowest power. The PCM material worked as the insulator due to the lesser thermal conductivity of the PCM material. Mais et al. [17] experimented to determine the cooling effect of the RT 35 (PCM) on solar panel. The outcomes of the study show that the 16°C temperature has been reduced by using PCM but If the rectangular fins have been used as the thermal conductivity enhancer then further 2°C temperature drop was again achieved. Rajvikram et al. [18] investigated the PCM, fins, and water for the cooling of the solar panel. The outcomes of the study depicted that in two consecutive days reading, the power output enhanced to 8.12% and 9.39% higher than without cooled solar panel. The temperature measurement of the cooled and without cooled solar panel were lower than the 50°C and 70°C.

The thermoelectric cooling, worked on the principle of the Peltier Effect requires no cooling fluids, only electric energy is required to cool the solar panel. In this cooling, a cold and hot heat source has been generated in which heat flow occurs from lower to higher temperatures. The amount of cooling provided by this technique is lower than the active cooling but more than the passive cooling.

The active cooling technique with forced air cooling, required little design change and feasible to fit fan and blower with the solar panel. A number of researchers published the work on active air cooling. In the below section active air cooling on solar panels is given concisely.

Teo et al. [2] explored the effect of air cooling on the power output of the solar panel, and results were compared with those without a cooled solar panel. The results indicated that

the overall temperature reduced by this approach was 30°C, and efficiency improvement recorded to be 4%. Golzari et al. [19] experimentally investigated, the effect of air cooling channel on the performance of the solar panel. The results showed, that solar panel temperature was reduced by 5°C and efficiency improvement of the solar panel was recorded to be 2.6%. Elminshawy et al. [20] performed the experimentation on solar panel cooling by geothermal air cooling. It reduced the solar panel temperature by 9.75°C and improved the solar panel efficiency by 22.98%. Arifin et al. [21] investigated the effect of the aluminum rectangular fin on the heat transfer rate and performance improvement of the solar panel, due to this cooling, the maximum temperature of the solar panel decreased from 85.3°C to 72.8°C. Lebbi et al. [22] investigated the effect of water and air cooling on the back and the front side of the solar panel, for water cooling drip irrigation system was used, and the fan was used for air flow. This cooling effect condensed, the module temperature by 15°C and raised the panel efficiency by 5.7%.

Saleri et al. [23] used thermoelectric cooling on the rear side of the solar panel to lower the solar panel temperature and enhance efficiency. This design has been proven to reduce the solar panel temperature by 15°C and heighten the efficiency by 5.7%. Li et al. [24] investigated the influence of compressed air on the cleaning and cooling of the solar panel. The results reveal that, the efficiency improvement of the solar panel was recorded to be 33.42% by using this technique. Almuwailhi and Zeitoun [25] conducted experiments on solar panel cooling in natural convection, forced convection, and evaporative cooling, and compared the results with those without cooled solar panel. They identified, the temperature of the solar panel lessened by 6°C in forced air cooling with efficiency improvement recorded to be 4% by use of this cooling technique. Abdullah et al. [26] conducted, a study on the air cooling on the efficiency of the solar panel. They identified, the efficiency improvement of the solar panel recorded to be 0.8% as compared to without air-cooled solar panel. Abdullah et al. (2024) [27] investigated experimentally a photovoltaic solar panel on Trombe wall for heating the room in the winter season. This system operates with the help of solar energy without supplying electricity. The experimental models have been prepared, one with DC fan and other without DC fan. The outcomes of the study revealed that the system having the DC fan has higher electrical and thermic efficiency as compared to another system. Abhijeet et al. (2024) [28] performed the energy and exergy analyses of the 380 kW power roof top photovoltaic grid-connected system. They concluded that the system generated the 732.4 kWh/year through this plant. Furthermore, results have been validated with the responses' neural network linear, non-linear, and exponential behaviour. Amjad et al. (2025) [29] used a porous medium to cool the solar panel. They concluded that the solar panel efficiency enhanced to the level of 19% and 5.1% efficiency increased as compared to without cooled solar panel. The cooling fluids properties are responsible for desirable heat transfer and solar panel performance. On the other hand, the various researchers used the number of designs at the rear side of the solar panel. Table 1 presents the various designs of solar panel cooling, used previously so far.

Table 1. Various design of the heat sink with air cooling in solar panel

S. No.	Author,s Description	Design Description	Design Picture	Outcomes of the study
1	Choi et al. [3] (2022)	Dimples were provided on the rear side of the solar panel.	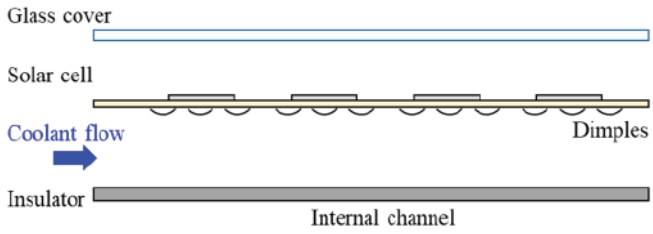	At St =1.1 Heat to mass transfer enhanced by 68%.
2	Hussein et al. (2023)[30]	A cooling air duct was provided at the rear side of the solar panel.		Enhanced the efficiency 2.1% and save, the energy around 7.9%

3	Nabil et al. (2022) [31]	Front side cooling was providing by open air cooling.	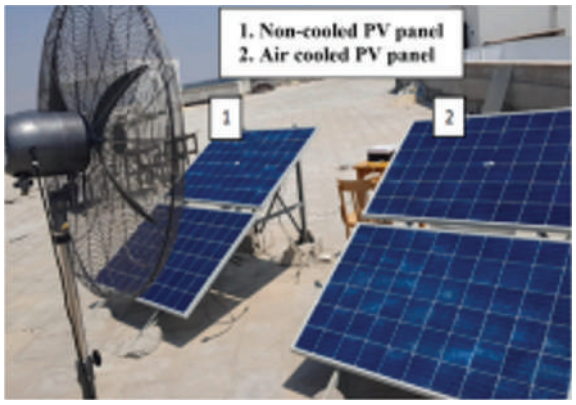	increase the efficiency of solar panel by 2.9%.
4	Amelia R. A. et al. [32]	Used dc fans to blow the dry air.	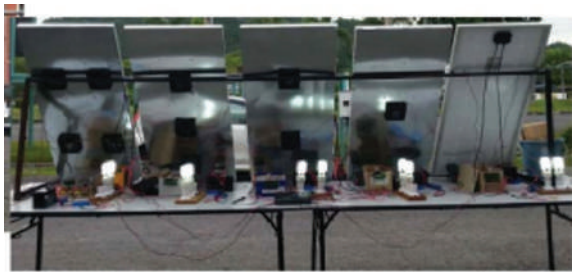	The increasing the number of fans enhanced the power output. If the one fan used then power output increased 12.93%, if the dc fan increased 2, 3 and 4, the power output increased 37.17%, 41.28% and 44.34% respectively.
5	Hernandez et al. (2013) [33]	Create the air channel path at the back of solar panel and used the forced air to cooled.		7.5% power output can be enhanced by use of this technology.
6	Hernandez-Parez et al. (2019) [34]	A heat sink fixed at the back of the solar panel.	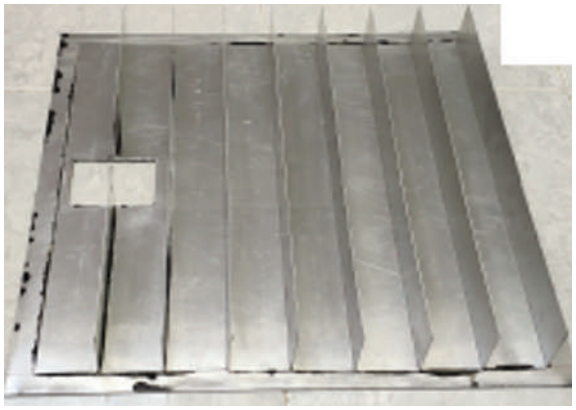	Reduced, the solar panel temperature around 10°C at peak sunny hours.

7	Feng et al. (2018)[35]	Cross fins heat sink fixed at the back side of the solar panel.	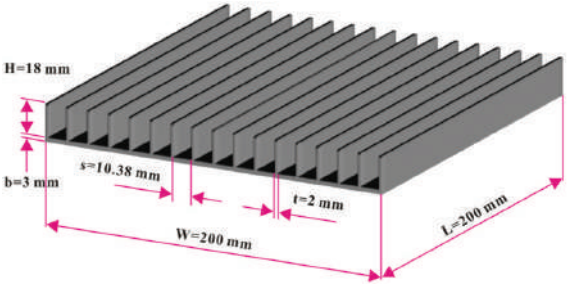	Enhanced, the heat transfer coefficient by 15%.
8	Huang et al. (2014) [36]	A heat sink of long rectangular fin fixed at the bottom side of the solar panel.	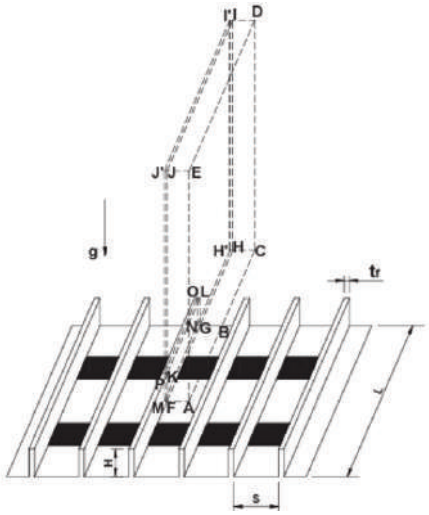	Enhanced performance at due to increased mass flow rate of air.
9	Shaeri et al. (2017) [37]	Long rectangular fins have been attached at the back end of the solar panel.	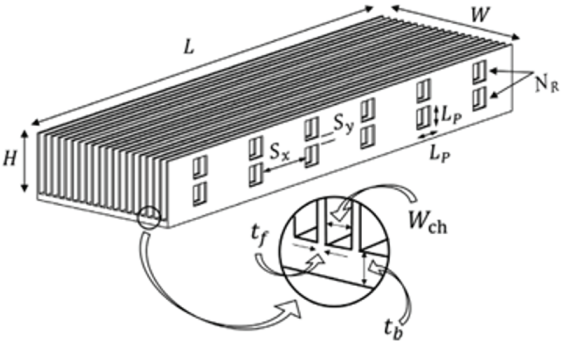	Mass based thermal resistance have been reduced by 49%.
10	Chu et al. (2019) [38]	A heat sink of triangular fins having alternative layout fitted at the back side of the solar panel	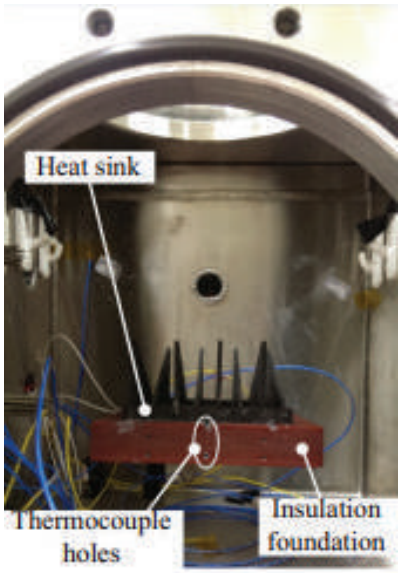	The heat transfer coefficient enhanced by 16%.

Research Gap, Novelty and Application of the Work

Table 1 displays, the several designs of heat sink produced at the rear side of the solar panel in air cooling. The air cooling is feasible requires little change in design at the rear side of the solar panel. Fins are produced on the cooling surface to enhance; the heat transfer by increasing the surface area of the cooling surface. In previous research, rectangular fins were mostly used in the study and very few researchers focused on the high-density pin fins [37]. Although, cylindrical high density pin fins can be produced in large numbers as compared to rectangular fins for making the heat sink compact. Therefore, in this study, high-density pin fins were integrated into the rear surface of a solar panel, and an optimization technique was employed to determine the optimal heat flux and air flow rate for maximizing the panel's performance. The use of high-density pin fins significantly improves the efficiency and operational lifespan of the solar panel. Enhanced efficiency leads to increased power production and a reduction in the panel's size, allowing for the same power output to be achieved at a lower investment cost. This work is novel and new in its simple and light weight arrangement as compared to heavy vibrating pumps required in liquid and nano-fluid cooling. Additionally, the approach of optimization and economic analysis of the solar panel cooling system is also new very little focused in the previous literature with high density pin fins.

The reduced investment cost makes solar panels more accessible and appealing, particularly to farmers and economically disadvantaged communities, encouraging wider adoption to meet energy demands. Furthermore, the lower cost of solar-powered irrigation reduces farming expenses, thereby increasing farmers' profitability. This approach addresses a critical societal challenge by promoting sustainable and cost-effective energy solutions for agriculture and beyond.

EXPERIMENTAL SETUP

Figure 1(a) illustrates the experimental arrangement of the solar panel air-cooling system. The setup consists of two 10 Wp solar panels as presented in Table 2 in which first solar panel is without fins and the second is with fins. The second number of solar panel consists of 196 cylindrical fins, each with an external diameter of 3 mm and fin length of 16 mm. The fins are arranged in horizontal and vertical rows with a spacing of 10 mm and 23 mm, as depicted in Figures 1(b) and 1(c). The solar panel size measures to be 323 mm in length and 217 mm in width. The experimental investigation was conducted to measure various parameters, including solar flux intensity, ambient temperature, photovoltaic (PV) module temperature, air velocity, current, and voltage generated by solar panels. The total experimental observations collected was 13 as per the requirement of Design Expert software for optimization purposes, with the corresponding data summarized in Table 3. These runs provided a comprehensive dataset for analyzing and optimizing the performance of the solar panel cooling system.

Table 2. Specification of solar panels

Parameters	Nominal Value
Nominal Maximum Power (P_m)	10 W
Max voltage (V_m)	18.00 V
Max current (I_m)	0.6 A
Open circuit voltage (V_{OC})	22.00 V
Short circuit current (I_{SC})	0.71 A
Module Efficiency (η_P)	15.4%
Cell Material	Polycrystalline Si
Size	323 mm*217 mm*30 mm
Operating Temperature Range	-40 °C to +80 °C
Temperature Coefficient	-0.2726 %/°C
NOCT	48 °C

Instruments played a critical role in capturing measured data during the experiments. A pyranometer was used to measure solar flux intensity, thermocouples were employed to record surface and air temperatures, an anemometer determined air velocity, and a multimeter was utilized to measure current and voltage outputs from the solar panel. The experiments were conducted at varying discharges of the air (0.01 m^3/s to 0.02 m^3/s) on three consecutive dates in the months 14, 15, and 16 which gives the average reading of the months. The experimental data have been collected from the (01/01/2023 to 21/12/2023). The schematic representation of the experimental setup with instruments is given in Figure 2. Details regarding the accuracy and measurement ranges of the instruments are provided in Table 4.

MODELLING OF THE SOLAR PANEL WITH FINS

Figure 3(a) illustrates the different layers of the solar panel along with the pin fins attached to its rear side. The material properties of each layer are detailed in Figure 3(a) and summarized in Table 5. The solar cell layer exhibits an absorptivity of 1, ensuring no heat flux passes through it; instead, heat transfer occurs from the solar cell to the lower layers of the panel due to the temperature gradient. When solar flux is incident on the panel, the solar cell reaches the highest temperature among all layers, causing heat transfer both to the upper and lower surfaces of the panel.

Figure 3(b) presents the thermal resistance circuit diagram for the solar panel cooling system. Heat transfer from the solar cell occurs primarily through conduction in the top and bottom layers, with the conduction resistances of each layer represented in the diagram. At the top, heat dissipates through a combination of convection and radiation. On the bottom side, heat transfer is improved by the addition of circular pin fins and fan-forced convection. Consequently,

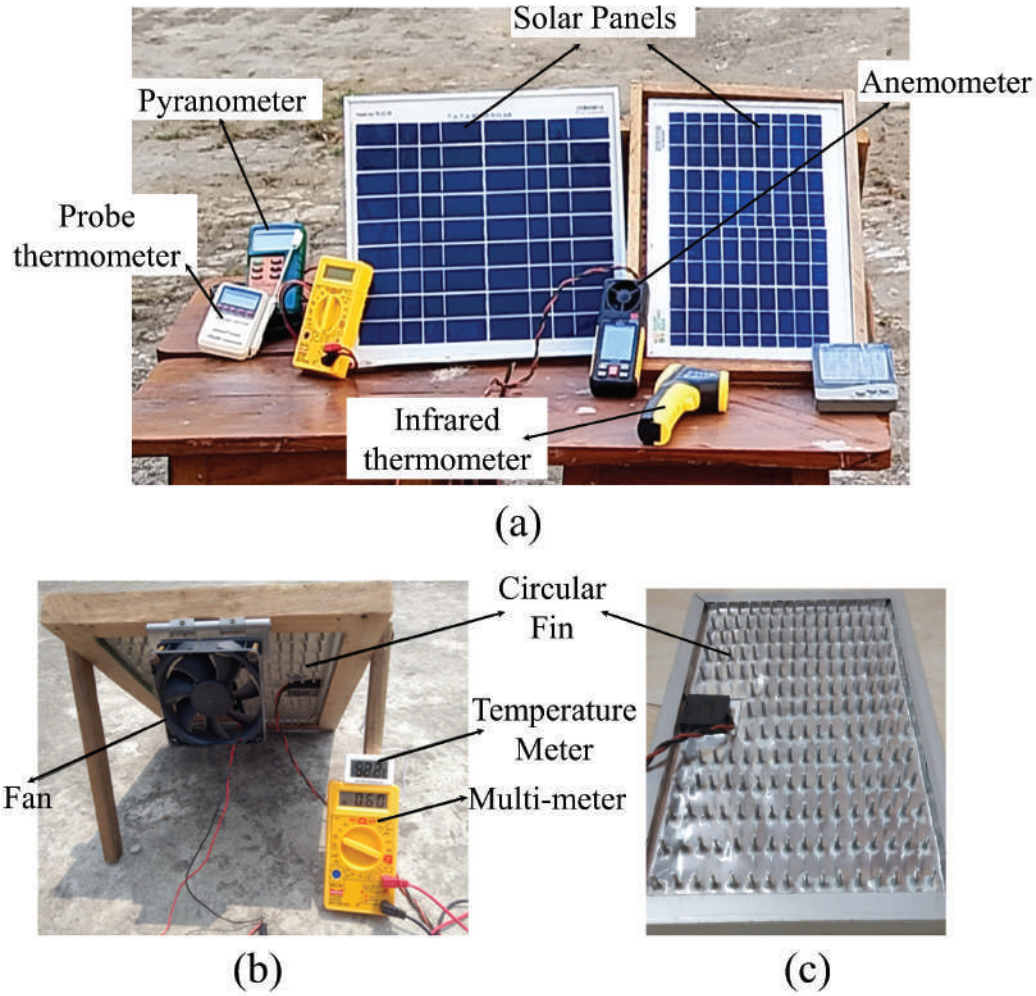

Figure 1. Solar panel air cooling system (a) Experimental setup (b) Rear side of experimental setup (c) Rear side of the solar panel with circular fins.

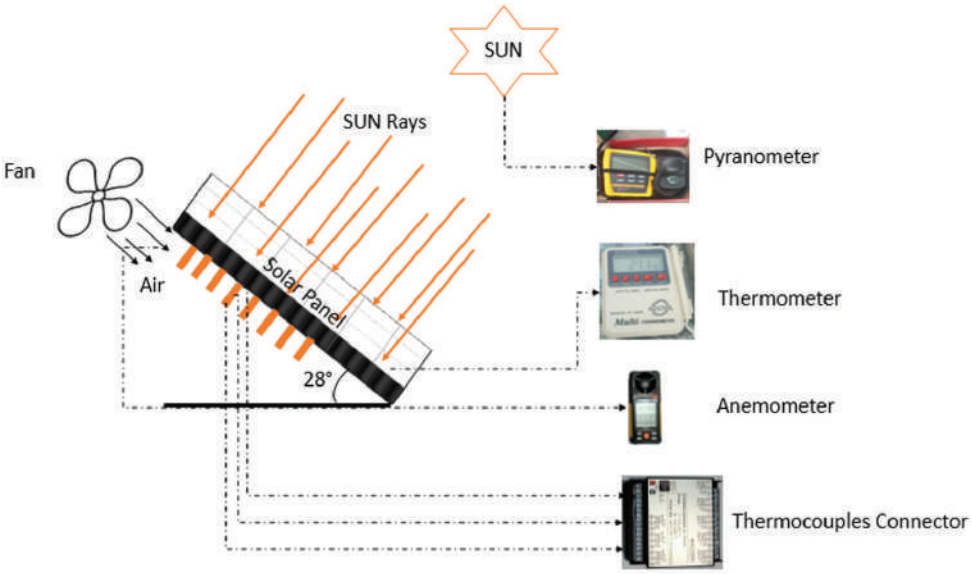

Figure 2. Schematic representation of the Experimental setup.

Table 3. Experimental data of 13 runs of the experimental observations

Run	Solar Flux (W/m^2)	Air Flow Rate (m^3/s)	Module Temperature (°C)	Power Output (W)	Solar Panel Efficiency (%)	Exergy Efficiency (%)
1	400	0.02	23.7432	4.07912	14.3631	15.658
2	600	0.015	49.9903	5.11237	12.0009	13.0828
3	600	0.015	49.9903	5.11237	12.0009	13.0828
4	600	0.015	49.9903	5.11237	12.0009	13.0828
5	600	0.015	49.9903	5.11237	12.0009	13.0828
6	600	0.0220711	47.0408	5.22545	12.2663	13.3722
7	600	0.015	49.9903	5.11237	12.0009	13.0828
8	800	0.02	62.8051	6.1614	10.8475	11.8255
9	400	0.01	28.6053	3.95485	13.9255	15.181
10	800	0.01	66.4771	5.97369	10.5171	11.4652
11	317.157	0.015	10.7076	3.49849	15.5363	16.937
12	600	0.00792893	52.8758	5.00174	11.7412	12.7997
13	882.843	0.015	69.2981	6.43314	10.2632	11.1885

Table 4. Performance parameters of the measuring instruments

Instrument	Model	Range	Accuracy
Temperature measurement	J K PT-100, 8 channel scanner	J: 0-600°C K:0-1200°C	4.25%
Velocity measurement	AVM-03 Digital Anemometer	0-30 m/s	4%
Solar Flux Intensity	LX -107 Solar Power Meter	Lux: 2000 W/m^2	5%
Surface contact temperature measurement	ST-92838 Multi Thermometer	-50 to 300°C	3.5%

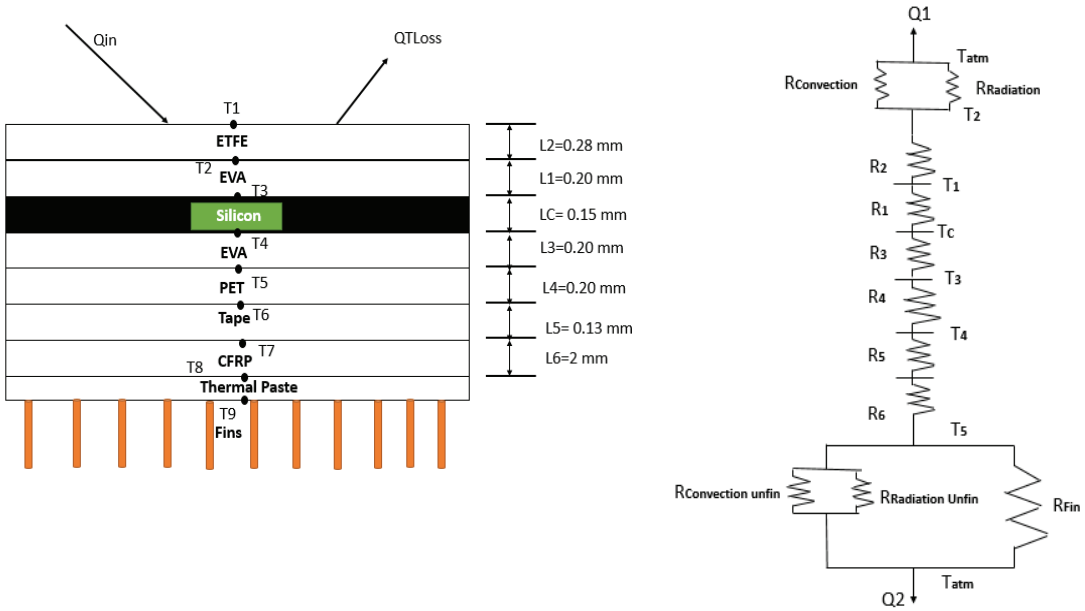

(a) Layers of the solar panel and the fins

(b) Resistance diagram of the heat transfer in solar panel

Figure 3. Heat transfer layers and resistance network.

the bottom layer dissipates heat to the atmosphere through the fins and the un-finned areas of the panel›s rear surface.

The total amount of heat transfers from solar cells to the atmosphere.

$$Q_{Cell} = Q_1 + Q_2 \quad (1)$$

Q_{Cell} is the heat flow through the solar cell, Q_1 is the heat flow through the top surface of the solar panel, Q_2 is the heat flow through the bottom surface of the solar panel.

$$Q_{cell} = \frac{T_C - T_{atm}}{R_1 + R_2 + \frac{R_{Convection} R_{Radiation}}{(R_{Radiation} + R_{Convection})}} + \frac{T_C - T_{atm}}{R_3 + R_4 + R_5 + R_6 + \frac{R_{Unfin} R_{Fin}}{R_{unfin} + R_{Fin}}} \quad (2)$$

Where T_C is the cell temperature, T_{atm} is the atmospheric temperature, R_1, R_2, R_3, R_4, R_5 and R_6 are the thermal resistance of the conduction of various layers of the solar panel, $R_{Convection}$ is the convection resistance from top surface, $R_{Radiation}$ is the radiation resistance from the top surface, R_{Fin} is the thermal resistance due to fins, R_{Unfin} is the thermal resistance due to unfin surface area.

The unfin rear side surface of the solar panel contributes the heat transfer by convection and radiation.

So the thermal resistance of the unfin surface of the PV modules is assumed by the following relation.

$$R_{unfin} = \frac{R_{Convection\ unfin} R_{Radiation\ Unfin}}{R_{Convection\ Unfin} + R_{Radiation\ Unfin}} \quad (3)$$

Where $R_{Convection\ unfin}$ is the unfin surface convection resistance and $R_{Radiation\ Unfin}$ is the unfin surface radiation thermal resistance.

The R_1, R_2, R_3, R_4, R_5 and R_6 are thermal resistance of the conduction of various layers of the solar panel. The values of these thermal are given below.

$$R_1 = \frac{L_1}{K_1 A},\ R_2 = \frac{L_2}{K_2 A},\ R_3 = \frac{L_3}{K_3 A},\ R_4 = \frac{L_4}{K_4 A},$$
$$R_5 = \frac{L_5}{K_5 A},\ R_6 = \frac{L_6}{K_6 A}$$

Where L_1, L_2, L_3, L_4, L_5, and L_6 are the thickness of the several covers of the solar panel presented in Figure 3 (a). K_1, K_2, K_3, K_4, K_5 and K_6 are the thermal conductivity of the EVA, ATFE, EVA, PET, TAPE, and CFRP layers of the solar panel, A is the surface area of the solar panel.

The convection and radiation thermal resistance of the top surface of the solar panel of material ETFE is given by the following equations.

$$R_{Convection} = \frac{1}{h_C A} \quad (4)$$

Where h_C is the solar panel top surface convection heat transfer coefficient.

$$R_{Radiation} = \frac{1}{\sigma \varepsilon A (T_C + T_{atm})(T_C^2 + T_{atm}^2)} \quad (5)$$

Where σ is the Stefan Boltzmann Constant and ε is the emissivity of the upper layer of the solar panel.

The unfin surface convection and radiation thermal resistance also represented by following equations [39].

$$R_{Convection} = \frac{1}{h_{Cb} A_{Unfin}} \quad (6)$$

Where h_{Cb} is the convection heat transfer coefficient from unfin surface and A_{Unfin} is the unfin surface area of the solar panel.

$$R_{Radiation} = \frac{1}{\sigma \varepsilon A_{Unfin} (T_{Cb} + T_{atm})(T_{Cb}^2 + T_{atm}^2)} \quad (7)$$

Where T_{Cb} is the temperature of the base of the solar panel.

The fin thermal resistance for the convection boundary is represented by the following equation.

$$R_{Fin} = \frac{TC_b - T_{atm}}{q_{Fin}} \quad (8)$$

Where q_{Fin} is the heat flow through the fins.

$$R_{Fin} = \left[1 + \frac{mL\emptyset}{Bi_C}\right]\left[\sqrt{hpkA}\emptyset\right]^{-1} \quad (9)$$

Where m is the constant depending on the fin length and diameter and L is the length of the fins.

Where φ is the function represented by the following equation [40].

$$\emptyset = \frac{mLtanhmL + Bi_e}{mL + Bi_e tanhmL} \quad (10)$$

Where B_{ie} is the fin tip Biot Number, B_{ic} is the fin base Biot Number and B_i is the fin Biot Number.

$$B_{ic} = \frac{h_c L}{k}, B_{ie} = \frac{h_e L}{k}, B_i = \frac{h t_e}{k} \quad (11)$$

Where L is the length of the fin, k is the thermal conductivity of the fin material represented in Table 4, t_e is the fin tip thickness, A is the crossectional area of the fin base and p is the perimeter of the fin tip.

The h_c is the fin base contact conductance for aluminium it is taken as 1000 W/m^2. k, h is the fin convection coefficient and h_e is the fin tip convection coefficient.

The h and h_e is found by the following formula of the Nusselt Number [41].

$$Nu = \left[\frac{1}{\frac{(RePr)^3}{8}} + \frac{1}{\left[0.664\left(\sqrt{Re}\right)(Pr^{0.33})\left(\sqrt{(1} + \frac{3.65}{\sqrt{Re}}\right)\right]^3}\right] \quad (12)$$

Where R_e and P_r is the Reynold Number and Prandlt Number of the air.

The Pr is the Prandlt Number calculated by following the formula [42].

$$Pr = \frac{\mu C_P}{k}, Re = \frac{\rho V D_h}{\mu} \quad (13)$$

Now heat transfer coefficient has been determined by the subsequent equation [43].

$$h = h_e = \frac{Nuk}{D_h} \quad (14)$$

where ρ, μ, and k are the density, dynamic viscosity, and thermal conductivity of the air. The D_h represents the hydraulic diameter of the pin fin.

Efficiency and Exergy of the Solar Panel

Figure 4 represents the various energy interactions in the control volume of the solar panel. The W_p represents the pump work, W_e is the solar panel electrical work, Q_{in} is the solar energy reached on the solar panel, Q_{out} is the energy lost in the atmosphere, and CV is the control volume. The system is considered to be a steady state with kinetic and potential energy terms of the air at the inlet and outlet are neglected. To apply the first law of thermodynamics for the Figure 4 control volume [44].

$$\frac{dU_{CV}}{dt} = (Q_{in} - Q_{out}) - (W_e - W_p) + m_{air}(h_1 - h_2) \quad (15)$$

Where h_1 and h_2 are the enthalpy of the air at the inlet and outlet section of the solar panel. m_{air} is the mass flow rate of the air.

$$\text{At steady state, } \frac{dU_{CV}}{dt} = 0 \quad (16)$$

$$0 = Q_{in} - Q_{out} - W_e + W_p + m_{air}C_p(T_1 - T_2) \quad (17)$$

$$Q_{in} + W_p = W_e + m_{air}C_p(T_2 - T_1) + Q_{out} \quad (18)$$

In equation (18), the left-hand part represents the input energy, and right-hand side first part represents the electric work output, the second part represents the heat carried by air and the third part represents the energy loss in the atmosphere.

The electrical efficiency of the solar plate is given by the following relation

$$\eta_e = \frac{W_e}{Q_{in} + W_p} \quad (19)$$

η_e is the effective efficiency of the solar panel.

Now apply the exergy balance for the solar panel control volume [45]

$$\frac{dE_{XCV}}{dt} = E_{Xin} - E_{Xout} - E_d \quad (20)$$

Where E_{Xin} is the exergy entering the PV module, E_{Xout} called the exergy leaving the system, E_d is the exergy destruction inside the system.

$$\text{For steady state } \frac{dE_{XCV}}{dt} = 0 \quad (21)$$

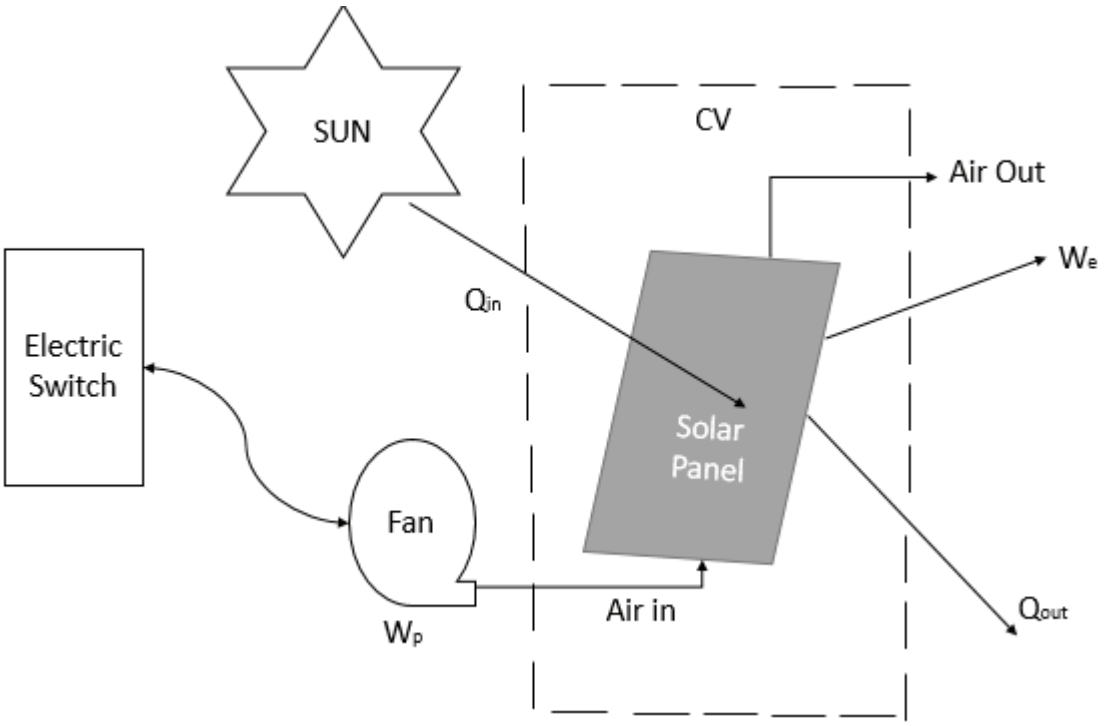

Figure 4. Heat and Work Interactions within the Solar Panel's Control Volume.

$$E_{Xin} = E_{Xout} + E_d \quad (22)$$

$$E_{SUN}+W_p+m_{air}\varphi_1=\left(1-\frac{T_{atm}}{T_b}\right)Q_{out}+W_e+m_{air}\varphi_2+E_d \quad (23)$$

Where E_{SUN} is the exergy received from the Sun and φ1 and φ2 are the inlet and outlet flow exergy.

$$E_{SUN}+W_p=W_e+m_{air}(\varphi_2-\varphi_1)+\left(1-\frac{T_{atm}}{T_b}\right)Q_{out} \quad (24)$$

Equation (22) left hand term represents the exergy supplied to the solar panel, right hand side first term represents the exergy recovered, second term shows the exergy recovered by air and third term represents the exergy loss in the atmosphere.

Now exergetic efficiency of the air

$$\varphi = \frac{W_e}{E_{SUN}+W_p} \quad (25)$$

The exergy reached on the solar panel [46].

$$E_{SUN} = A_P I_t[1 - \frac{4}{3}\left(\frac{T_a}{T_{SUN}}\right) + \frac{1}{3}\left(\frac{T_a}{T_{SUN}}\right)^4] \quad (26)$$

Cost Estimation of the Solar Panel

The cost estimation of the modified solar panel justifies the suggested cooling techniques. The best way to compare the Levelized Cost of Energy (LCOE) of the simple solar panel and the modified solar panel. The LCOE is the ratio of the total investment in the life cycle of the solar panel to the total power production by the solar panel in its life cycle. The total investment of the project is the sum of the cost of the solar panel, material cost, manufacturing cost, maintenance, operational cost, and fixed cost. The total power production is counted in kWh with every year depreciation will be counted. So following equation has been used for the calculation of the LCOE of the system.

$$LCOE = \frac{\sum_0^n \frac{(I+M+F)}{(1+r)^n}}{\sum_0^n (\frac{E}{(1+r)^n}} \quad (27)$$

Where I is the investment, M is the maintenance cost, F is fixed cost and E is energy produced throughout the life cycle, r is the discount rate and n is the number of years.

The initial investment is the sum of the cost of the solar panel, material, and manufacturing. It is assumed by the following relation.

$$I = xp + \rho vy + m \quad (28)$$

Where x is the cost of the solar panel ($/Wp), p is the power of the solar panel, ρ is the density of fin materials, v is the volume of the fins material, y is the cost of the material ($/kg), m is the manufacturing cost. The volume of the fins is given by the following equation.

$$v = \frac{\pi}{4} d^2 L \quad (29)$$

Where d is the diameter and L is the length of the fins.

Optimization Technique

The optimization has been performed to know the optimum values of the input variables on which, the system of the solar panel cooling gives the maximum power output and efficiency. For which Response Surface Methodology (RSM) has been used. In year 1951 [47], RSM was used in chemical industries for improving production but recent times due to development of the various Design of Experiment (DoE) models, the RSM is used each and every field to maximize the output. The best thing with the RSM is that it easily converts the responses in terms of the explanatory variables by 2nd order model. The model accuracy has been determined based on the various error factors and validated with the actual experimental setup.

In this analysis, a Central Composite Design (CCD) has been used for defining the input variables and total number of the run. The CCD based on two input variables (Solar Flux, Discharge) [48], code and coded values of the input variables are given in Table 6, the total number of the runs is 13 in which, cube points are 4, center points in the cube are 5 and axial points in the cube are 4 as shown in Figure 5. Table 3 represents the total number of experimental runs and corresponding responses. The variable α represents the rotatibility of the matrix and it is determined by the following equation.

Table 5. Properties of the several layers of the solar panel

Materials	Density (Kg/m^3)	Thermal Conductivity (W/m. k)	Specific Heat Capacity (J/kg. K)
ETFE	1730	0.24	1172
EVA	945	0.35	2090
Silicon	2330	148	700
PET	1350	0.275	1275
CFRP	1490	6.83	1130
Tape	1012	0.19	2000

$$\alpha = \left(2^k\right)^{\frac{1}{4}} \quad (30)$$

Where k represents the number of factors. In the two factors design k = 2, then α = 1.414. In CCD design, based on the total number of the runs, the responses have been calculated and with the help of the ANOVA analysis 2nd order polynomial has been generated. The 2nd order polynomial of response variables have been represented by following equation [49].

$$Y = A_\circ + \sum_{i=1}^{k} A_i x_i + \sum_{i=1}^{k} A_{ii} x_i^2 + \sum_{j\geq 1}^{k} A_{ij} x_i x_j + B \quad (31)$$

The x_i and x_j are the input variables and Y is the dependent variable. A_0, A_i, A_{ii} and A_{ij} are the constant of the linear and square terms. The B represents the error or the noise in the model equation. Based on the data of the Table 3, the following model equations have been developed for the responses namely module temperature (Tm), power output (W), solar panel efficiency (η_P) and exergy efficiency (η_{eX}).

$$T_m = -44.12 + 0.2420S - 707Q - 0.000122S^2 + 3633Q^2 + 0.298SQ \quad (32)$$

$$W = 1.2827 + 0.007098S + 4.69Q - 0.000002S^2 + 50Q^2 + 0.01586SQ \quad (33)$$

$$\eta_P = 20.471 - 0.02178S + 63.6Q + 0.000011S^2 - 327Q^2 - 0.0268SQ \quad (34)$$

$$\eta_{eX} = 22.317 - 0.02375S + 69.4Q + 0.000012S^2 - 356Q^2 - 0.0292SQ \quad (35)$$

Based on these model equations error of all the responses has been calculated and the model has been validated with experimental data. Table 7, Table 8, and Table 9 represents the error analysis of the responses. In Table 7 and Table 8, the P values of all responses are less than 0.01 showing the model is significant. Table 9 shows the values of the R^2, adjusted R^2 and predicted R^2 values which are larger than 0.75 shows the model is best fitted with this data.

Figure 6 represents the residual plots for all data sets of

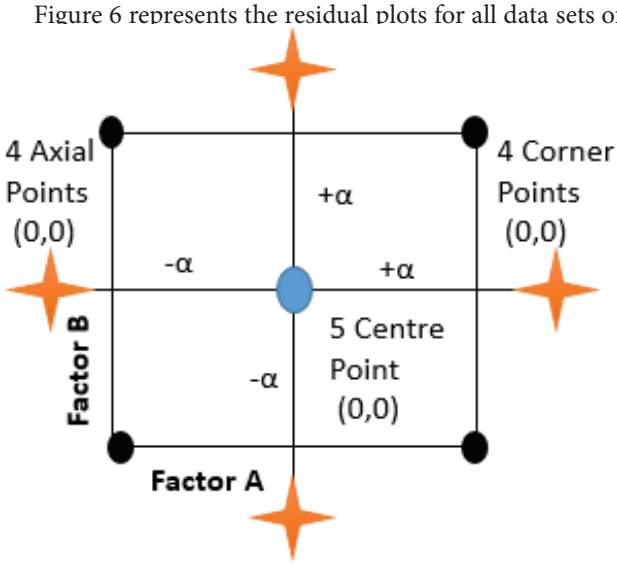

Figure 5. Location of the points in CCD design for two factors [49].

Table 6. Numerical values of the input variables

Input Variables	Coded Level		
	-1	0	1
Solar Flux (W/m²)	400	600	800
Air Discharge (m³/s)	0.01	0.015	0.02

the responses. Residual is the difference between the actual value and the predicted average value obtained by ANOVA analysis. If the value of the particular data point is greater than the average value of the response, the residual is positive [50, 51]. If the value of particular point value is less

Table 7. P-values and F-values for ANOVA analysis on module temperature (Tm) and power output of solar panel (P)

		Silicon Cell Temperature (TC)					Power Output (P)				
Sources	**DF**	**Adj. SS**	**Adj. MS**	**F-value**	**P-value**	**Significant**	**Adj. SS**	**Adj. MS**	**F-value**	**P-value**	**Significant**
Model	5	3397.2	679.44	998.26	<0.0001		8.60	1.72	37987.13	< 0.0001	
S	1	3191.74	3191.74	4689.43	< 0.0001		8.51	8.51	1.880E+05	< 0.0001	
m	1	35.22	35.22	51.75	0.0002		0.0494	0.0494	1090.25	< 0.0001	
S*S	1	166.1	166.14	244.09	< 0.0001		0.0367	0.0367	810.79	< 0.0001	
m*m	1	0.057	0.0574	0.0843	0.7800		0.0000	0.0000	0.2407	0.6387	
S*m	1	0.354	0.3541	0.5202	0.4941		0.0010	0.0010	22.23	0.0022	
Error	4.76	1.80	0.6806	-	-		0.0003	0.0000	-	-	
Lack of Fit	4.76	1.80	1.59	17982.92	0.000		0.0003	0.0001	30784.03	0.000	
Pure Error	0.00	0.00	0.000	-	-		0.0000	0.0000	-	-	
Total	12	3401.96	-	-	-		8.60	-	-	-	

Table 8. P-values and F-values for ANOVA analysis on solar panel efficiency (η_P) and exergy efficiency (η_{eX})

		Solar panel Efficiency (η_P)					Exergy Efficiency (η_{eX})				
Sources	**DF**	**Adj. SS**	**Adj. MS**	**F-value**	**P-value**	**Significant**	**Adj. SS**	**Adj. MS**	**F-value**	**P-value**	**Significant**
Model	5	27.52	5.50	998.26	<0.0001		32.70	6.54	998.26	< 0.0001	
S	1	25.85	25.85	4689.43	< 0.0001		30.72	8.51	4689.43	< 0.0001	
m	1	0.2853	0.2853	51.75	0.0002		0.3391	0.0494	51.75	0.0002	
S*S	1	1.35	1.35	244.09	< 0.0001		1.60	1.60	244.09	< 0.0001	
m*m	1	0.000	0.0005	0.0843	0.7800		0.0006	0.0006	0.0843	0.7800	
S*m	1	0.002	0.0029	0.5202	0.4941		0.0034	0.0034	0.5202	0.4941	
Error	7	0.038	0.0055	-	-		0.0459	0.0066	-	-	
Lack of Fit	3	0.038	0.0129	17982.92	0.000		0.0459	0.0153	-	0.000	
Pure Error	4	0.00	0.000	-	-		0.0000	0.0000	-	-	
Total	12	27.56	-	-	-		32.75	-	-	-	

Table 9. Error Analysis of the responses

Error	**Module Temperature**	**Power Output**	**Solar Panel Efficiency**	**Solar Panel Exergy Efficiency**
Std. Dev.	0.8250	0.0067	0.0742	0.0809
Mean	47.04	5.07	12.27	13.37
C.V. %	1.75	0.1327	0.6053	0.6053
R^2	0.9986	1.0000	0.9986	0.9986
Adjusted R^2	0.9976	0.9999	0.9976	0.9976
Predicted R^2	0.9900	0.9997	0.9900	0.9900
Adeq Precision	100.7990	638.2172	100.7990	100.7990

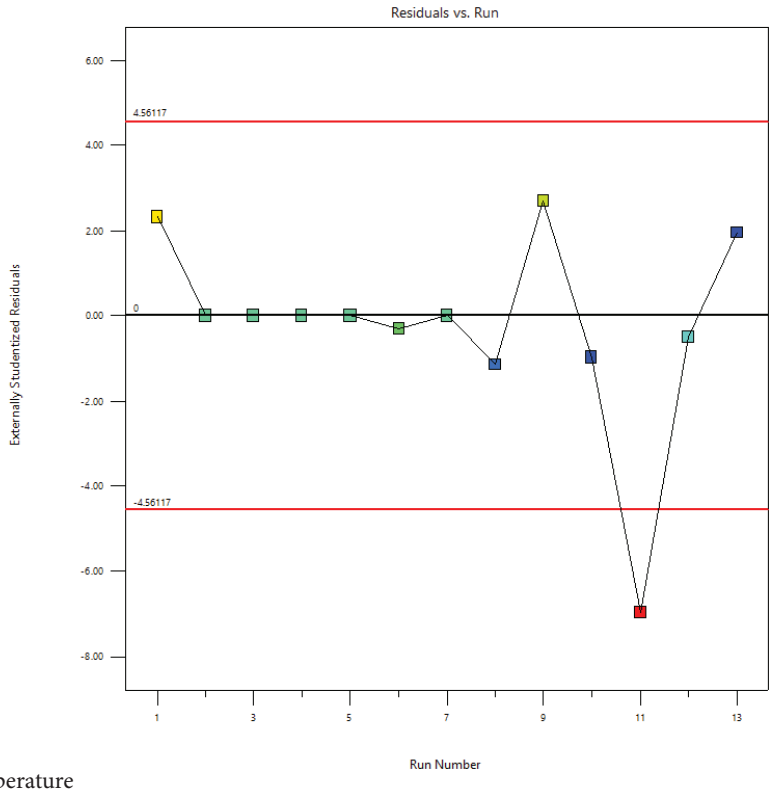

(a) Residual plot of module temperature

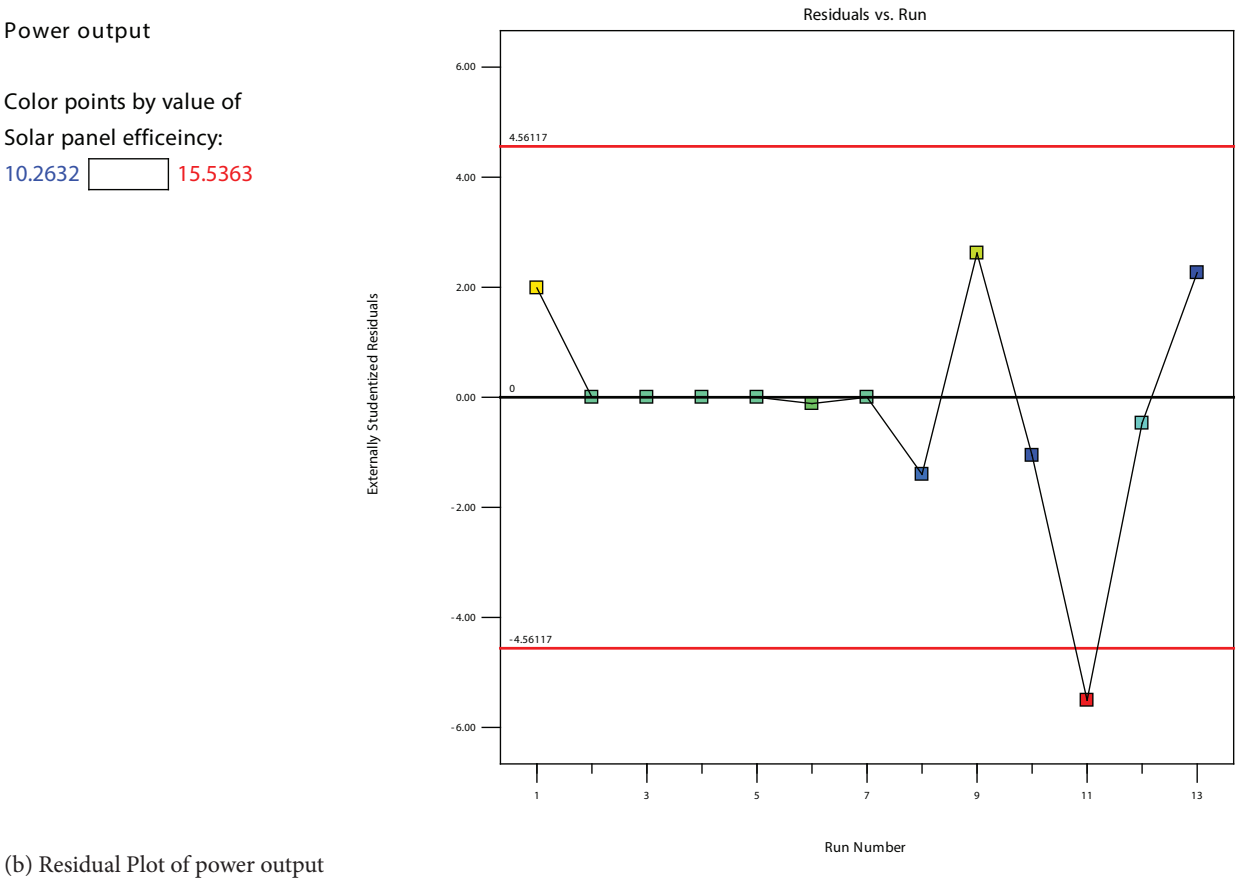

(b) Residual Plot of power output

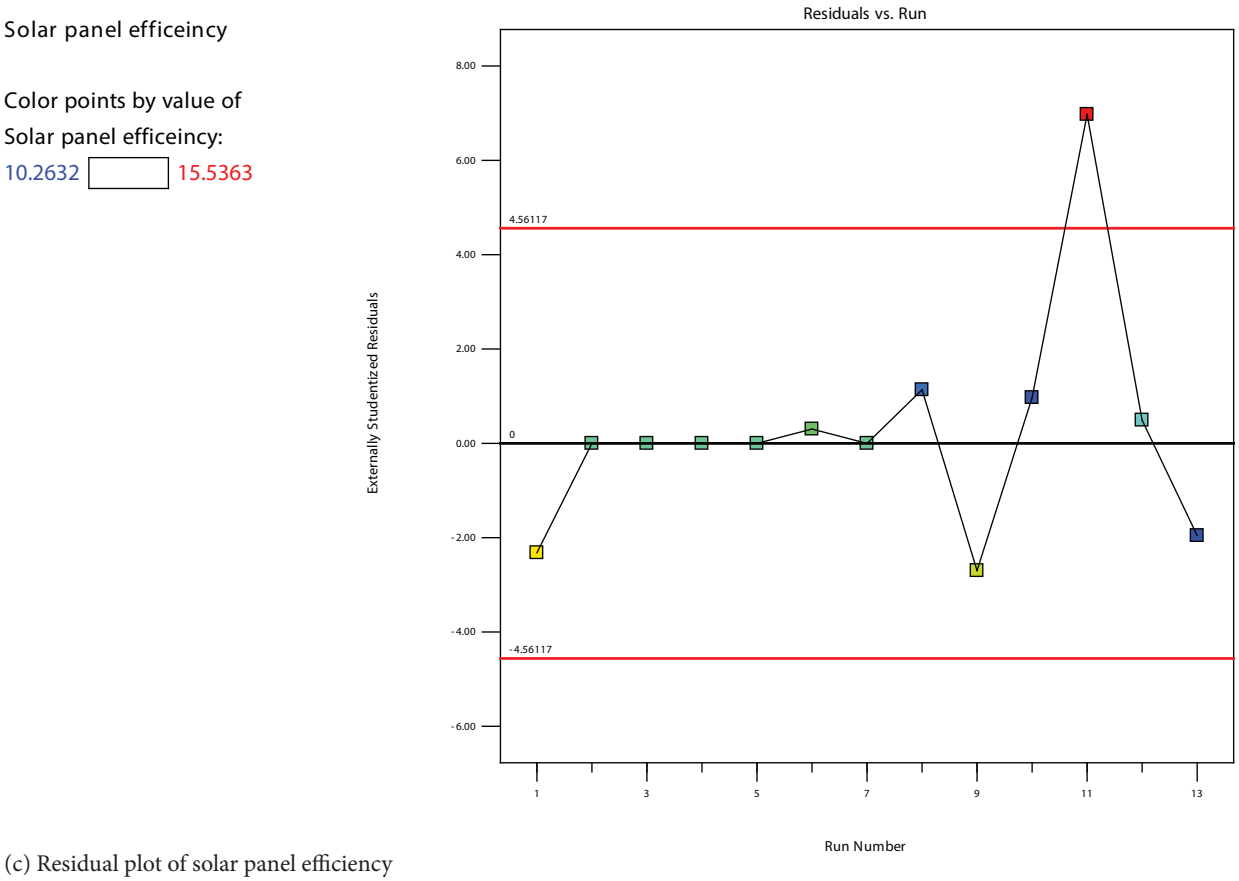

(c) Residual plot of solar panel efficiency

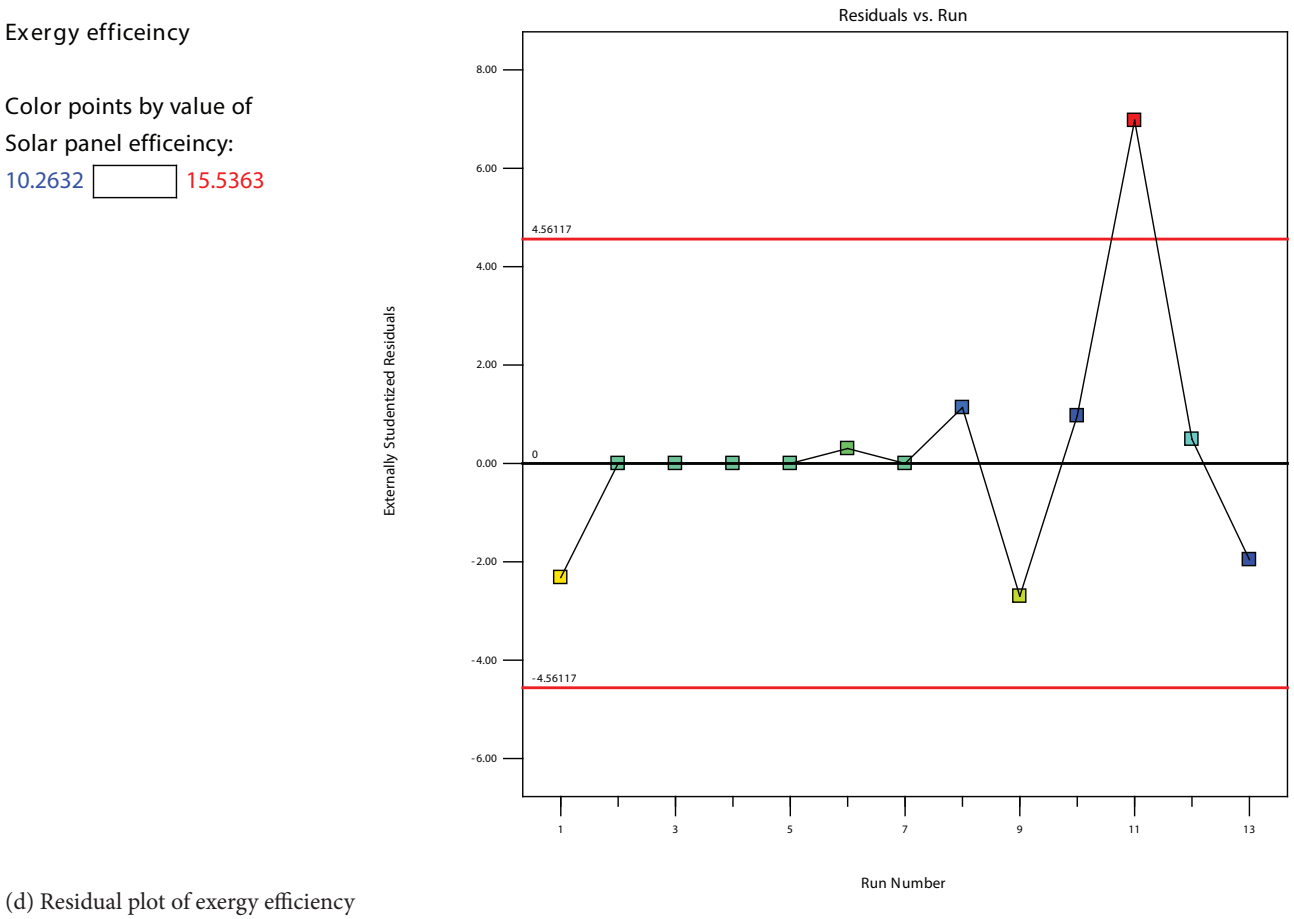

(d) Residual plot of exergy efficiency

Figure 6. Residual plot of the response parameters.

than the average value of the response, the residual is negative. So, for all runs, the sum of the residuals is zero. Figure 6 (a), Figure 6(b), Figure 6 (c), and Figure 6 (d) show that the residual of all responses is maximum at 11 run or data set since the solar flux at 11 run is very less only 317 W/m^2 beyond the range of the solar flux 400 W/m^2 to 800 W/m^2. It is clearly indicated from Figure 6 (a), Figure 6 (b), Figure 6 (c), and Figure 6 (d), the all data sets are well organised about the average line which shows the accuracy of the responses.

Figure 7 shows the perturbation plots of the responses concerning the input variables. The perturbation plots depicted, the behaviour of the response variable by treating the input variables at constant variables. Figure 7 (a) shows the value of the reference point to be (0.00, 49.85°C). In Figure 7 (a), if a point on the curve moves far from the reference point, a steep change in the graph of solar flux is to be noted at the constant value of the air discharge which shows, the sensitivity of module temperature with solar flux. The lower and constant slope of line B represents the lower sensitivity with air flow rate. Figure 7 (b) reference point is (0.00, 4.95 Wp) and the slope of the solar flux curve and air flow rate curve have constant values since both lines are straight in nature [52].

It indicates that solar flux and air flow rate both constantly affect the power production of solar panel. Figure 7 (c) shows, the intersection coordinate of both curves A and B is (0.00, 12%) gives the optimum value of the solar panel efficiency [53]. The solar flux steep change of the graph at constant discharge shows the solar flux is further likely to affect the solar panel efficiency as compared to the air flow rate. On other hand, the discharge line B slope remains constant give the indication that, the solar panel efficiency constantly changes with the discharge of air. Figure 7 (d) shows the perturbation plots of exergy efficiency of solar panel. Figure 7 (d) reference point is (0.00, 13.01%). Curve A (solar flux) higher steep changes in slope shows, the sensitivity of solar flux with the exergy efficiency at a constant value of the air flow rate, and the lower and constant variation in line B slope (Air flow rate) shows lower sensitivity with the exergy efficiency [54].

RESULTS AND DISCUSSION

Module Temperature Variation with Input Variables

Figure 8 shows the 3D plots of the module temperature with solar flux and air flow rate in which if the solar

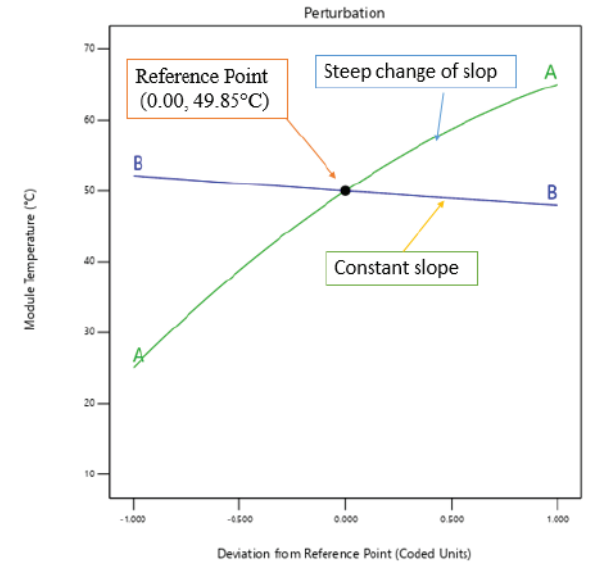

(a) Perturbation plot of the module temperature

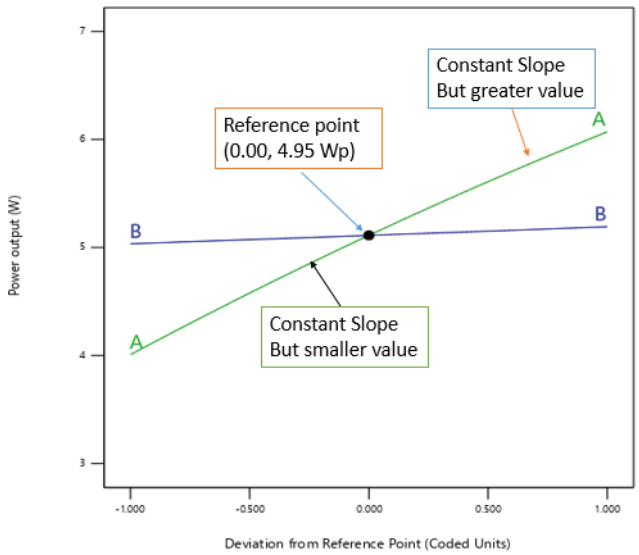

(b) Perturbation plot of the power output

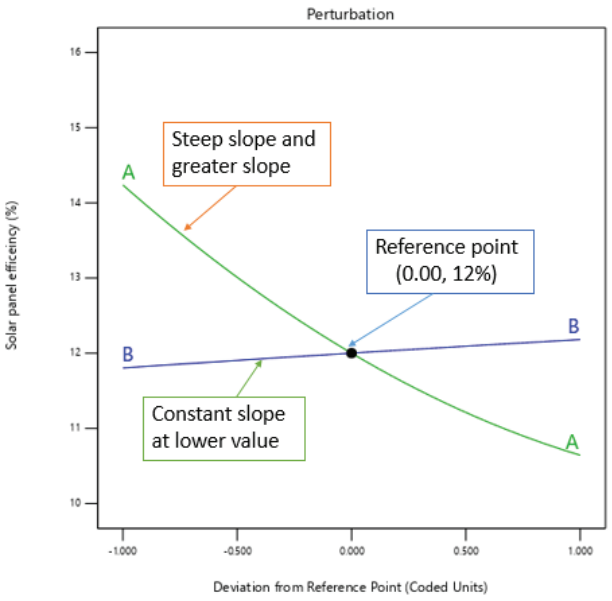

(c) Perturbation plot of the solar panel efficiency

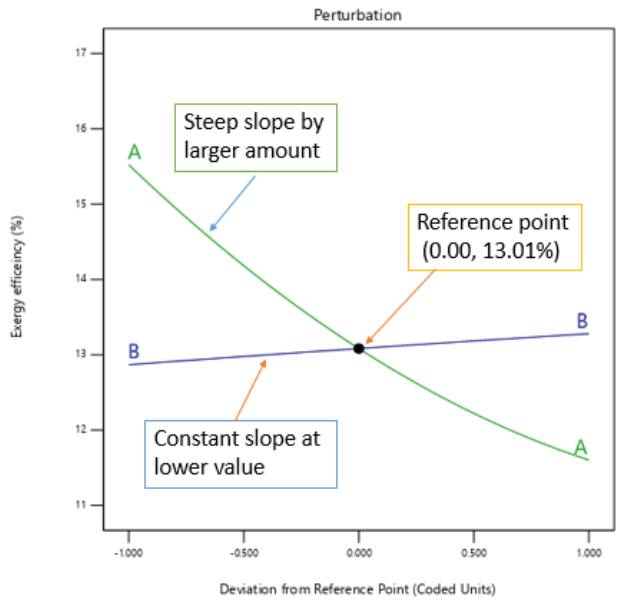

(d) Perturbation plot of the exergy efficiency

Figure 7. Perturbation plot of the responses with respect to input variables.

flux increases then the module temperature increases sharply due to the supply of higher solar energy on the surface of the solar panel. The higher energy content enhanced the trapped heat inside the solar panel which will increase the solar panel temperature. On the another hand with air flow rate, the module temperature is reduced due to an increase of mass flow rate since at higher mass flow rate more heat is carried by the air which lowers the module temperature [55]. Figure 8 indicates that the module temperature is 27.6°C at the solar flux of 400 W/m^2 and it increased to 67.1°C at the solar flux of 800 W/m^2. The 58.9% hike in module temperature occur due to two times increasing the solar flux. Figure 8 also shows that if the solar flux is more than 720 W/m^2, the module temperature is higher than 60°C. So, at higher solar flux air flow rate should be more than 0.02 m^3/sec [56] which enumerated that at high solar flux systems cooling is very much required to sustain the efficiency of the solar panel.

Power Output of Solar Panel with Input Variables

Figure 9 shows the trend of the power output with solar flux and air discharge. It is seen from the figure that if the solar flux is enhanced, the solar panel's power output is enhanced due to the supply of the higher solar energy [51], [57]. The solar panel's power output is increasing as

the air flow rate increases, due to a reduction in the module temperature leading to an increase in the efficiency of the solar panel. As the airflow rate increases, the mass flow rate increases which carries a higher amount of heat to cool down the solar panel. The cooling of solar panel enhances the output power. The increased air discharge also increases energy consumption so it is not always advantageous to increase the air discharge. It is true up to the optimum values of the discharge, after crossing the optimum condition, the power consumption by the fan is greater than the power production of the solar panel which reduces the net efficiency of the solar panel.

Solar Panel Efficiency Variation With Input Variables

Figure 10 denotes the solar panel efficiency with respect to the solar flux and the airflow rate. Figure 10 clearly shows that as the solar flux increases, the solar panel efficiency is enhanced due to an growth in power output with the solar flux [58]. As the solar flux increases,

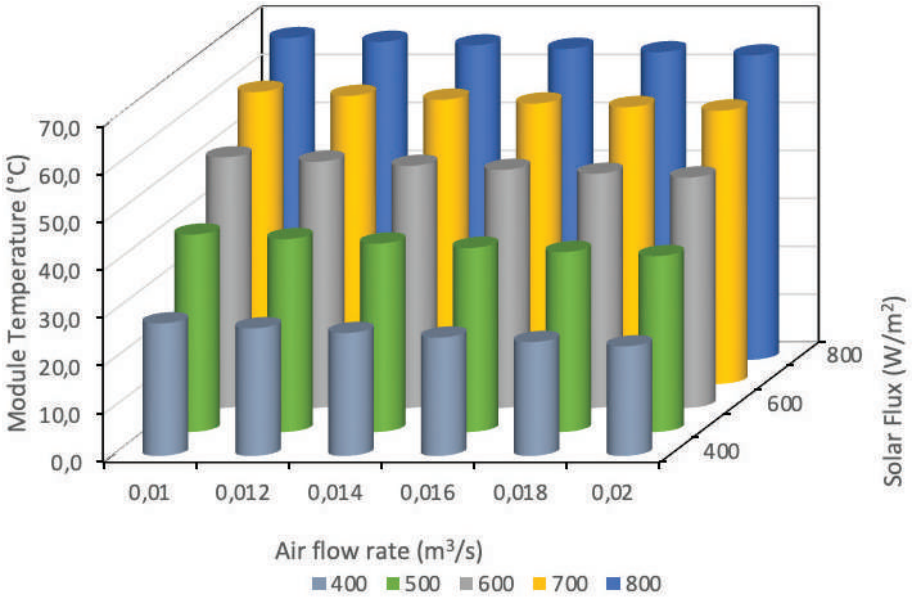

Figure 8. Temperature variation of solar panel with input variables.

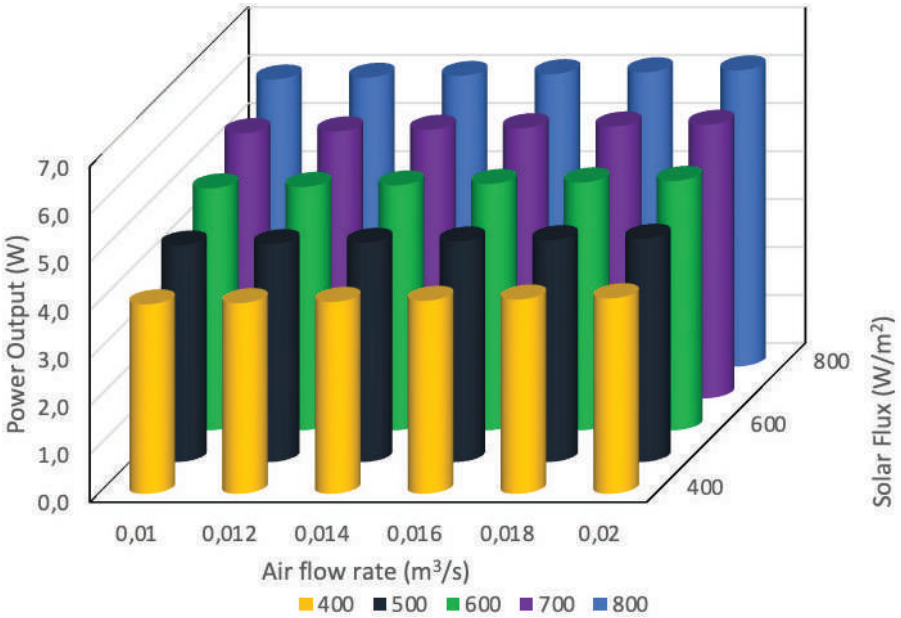

Figure 9. Power output variation of solar panel with input variables.

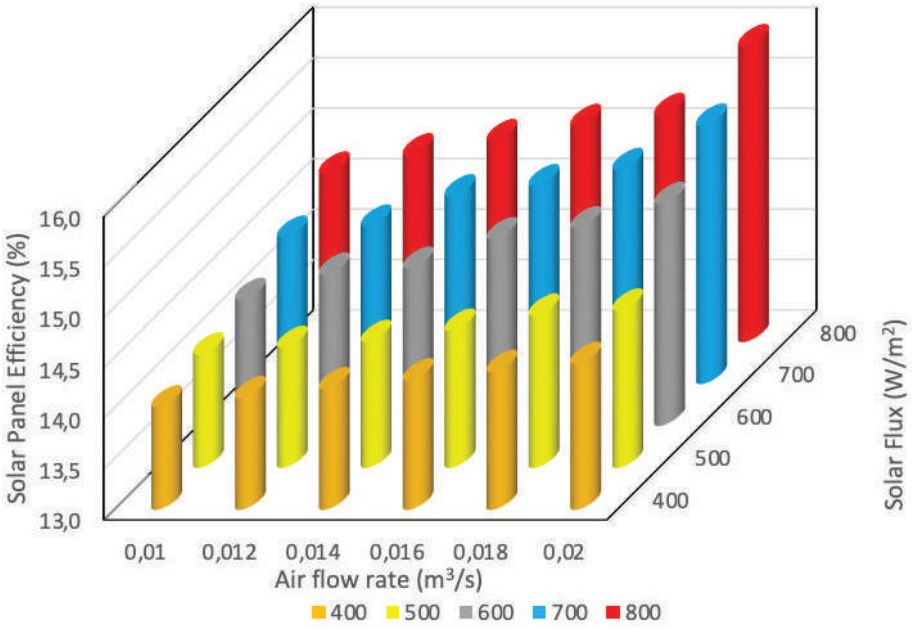

Figure 10. Solar panel efficiency variation with input variables.

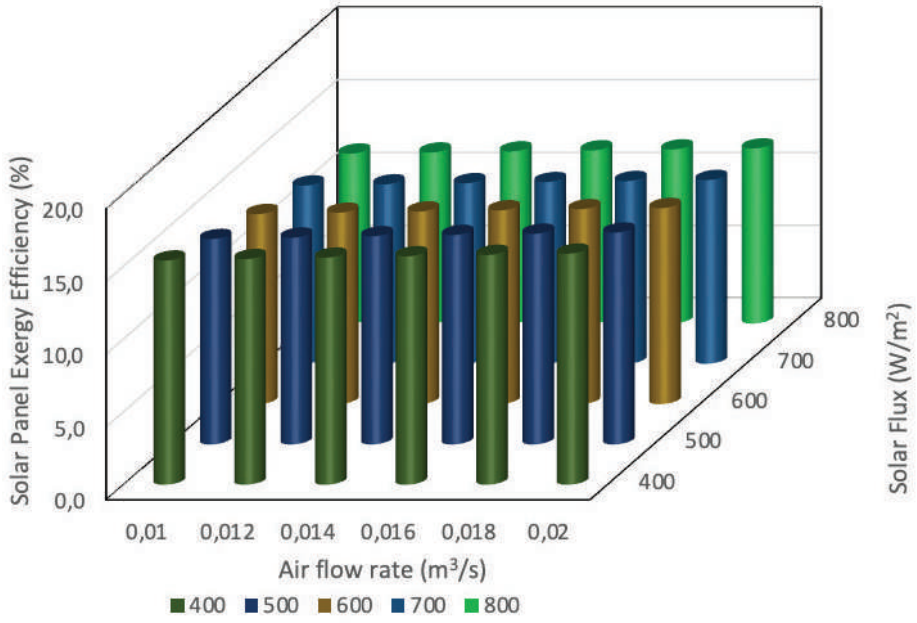

Figure 11. Solar panel exergy efficiency variation with input variables.

the module temperature too increases but enhancement of power output due to the intensity of solar flux is more dominating as compared to reduction of the power output of solar panel due to enhancement of the module temperature. So, the overall outcome is an increase in the efficiency of solar panels due to an increase in solar flux intensity. The solar panel efficiency variation with air discharge is an increasing trend due to the reduction in solar panel temperature. As the air discharge increases more heat is carried by the air which enhances the heat-carrying capacity of air. The cooled solar panel gives higher solar panel efficiency as compared to without cooled solar panels. Increasing the air discharge also increases the fan input power so net efficiency starts to reduce after reaching the optimum values. So, it is not always advantageous to enhance the air discharge.

Solar panel exergy efficiency variation with input variables

Figure 11 represents, the exergy efficiency of the solar panel with respect to the solar flux and discharge of air. Figure 11 trends of the exergy efficiency show that if the solar flux rises then the exergy efficiency declines [59] since an increase in solar flux increases the module temperature of the solar panel. The exergy efficiency is represented by equation number (25), so from this equation, it can be observed that if the solar flux increases, the input exergy increases which reduces the exergy efficiency. The input exergy is the sun of the solar exergy and fan input electric work. Figure 11 exergy efficiency variation with air discharge shows that if the air discharge increases then the exergy efficiency of the solar panel increases. The exergy efficiency of the solar panel increases with air discharge since at a higher air mass flow rate, the cooling effect of the solar panel is enhanced and the module temperature of the solar panel is reduced [60]. However, increasing the air discharge also enhances the fan input exergy so always increasing the air discharge do not enhance the exergy efficiency.

LCOE of the solar panel

Figure 12 depicts the LCOE of the finned solar panel and without the finned solar panel. it is seen from Figure 12, the LCOE of the without-finned solar panel is 2.4033 INR/kWh, and with finned solar panel is 2.21 INR/kWh. The 8.75 % reduction in LCOE has been noted due to the chilling of solar panels by air. The LCOE is measured to compare the cost required to produce the 1 unit of the electricity. Moreover, figure clearly show that the cost of production of the electricity is only 2.21 INR/kWh in the finned solar air heater. This data is for the 10 Wp solar panel, if the size of the solar panel enhanced then the LCOE is reduced due to production of the more power by the solar panel.

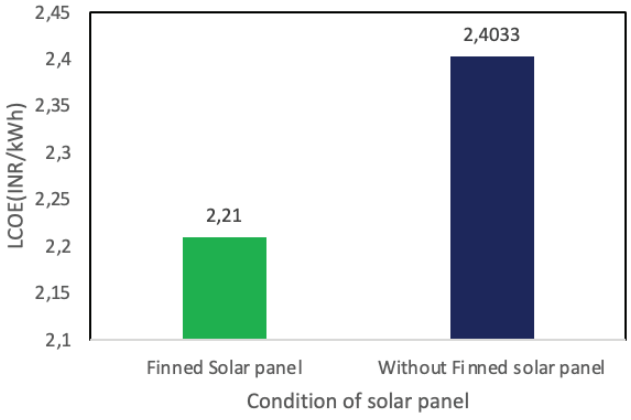

Figure 12. LCOE of the solar panel with and without fins.

Optimum Values of The Responses with Input Variables

Figure 13 illustrates, the optimization plots of the responses with respect to the input variables, this figure shows the ranges of input variables, optimum values of input variables, optimum value of response variables, and composite desirability of the optimization. Figure 13 depicts, the optimum values of the input variables namely solar flux and air discharge is 403.3586 W/m^2 and 0.0221 m^3/sec on which responses exergy efficiency 15.781%, the power production of the solar panel 4.1196 Wp, module temperature 22.4279°C and solar panel efficiency 14.4815%. The red colour numbers indicate, the optimum values of the input variables and blue colour words represents the optimum values of the output variables.

The desirability represents, the correlation among input and output variables. The individual desirability and the composite desirability of the input and response variables are given in Figure 12. The composite desirability of the optimization plots is given as 0.5737 and the individual desirability of responses exergy efficiency, power output, module temperature, and the solar panel efficiency is namely 0.79996, 0.2164, 0.79996, and 0.79996.

Validation of the model

The optimum condition obtained by the optimization process has been validated by running the experimental setup. Three consecutive test has been conducted and the average value of the responses corresponding optimum values of the solar flux (403.3586 W/m^2) and air flow rate (0.02 m^3/s). Table 10 represents the predicted values through the models, experimental average values of responses and percentage error.

Percentage Change in Performance of Air Cooled Solar Panel with Respect to Simple Solar Panel

Figure 14 shows the percentage change in module temperature, power output, solar panel efficiency, and exergy

Table 10. The verification test of output response

	Predicted value	Experimental value	Error (%)
Module Temperature (°C)	22.42	21.63	3.5%
Fan power output (W)	4.1196	3.963	3.8%
Solar Panel Efficiency (%)	14.48	13.94	3.67%
Solar panel Exergy Efficiency (%)	15.7871	15.2997	3.1%

Solar Flux (403.3586 W/m^2) and Discharge (0.0221 m^3/s)

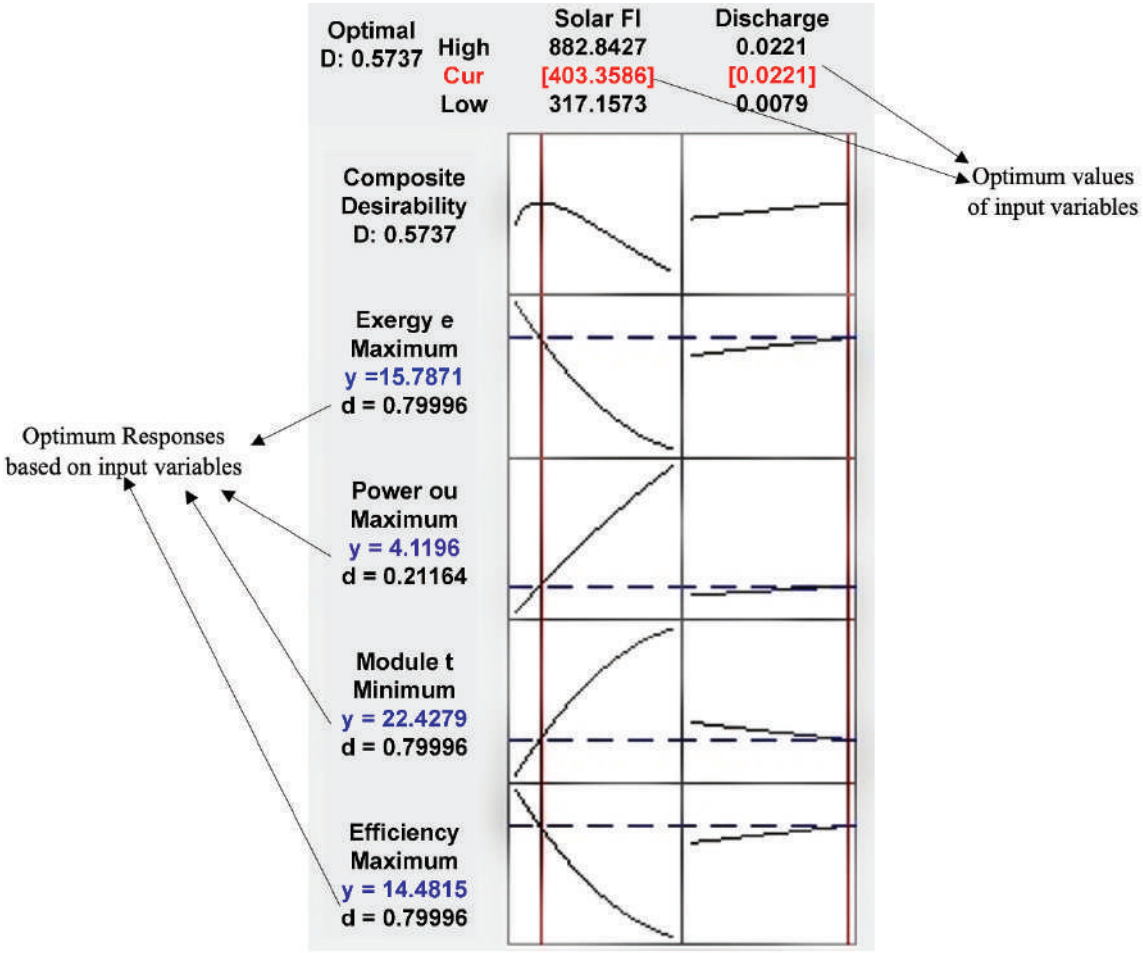

Figure 13. Desirability, optimum values of the inputs and responses.

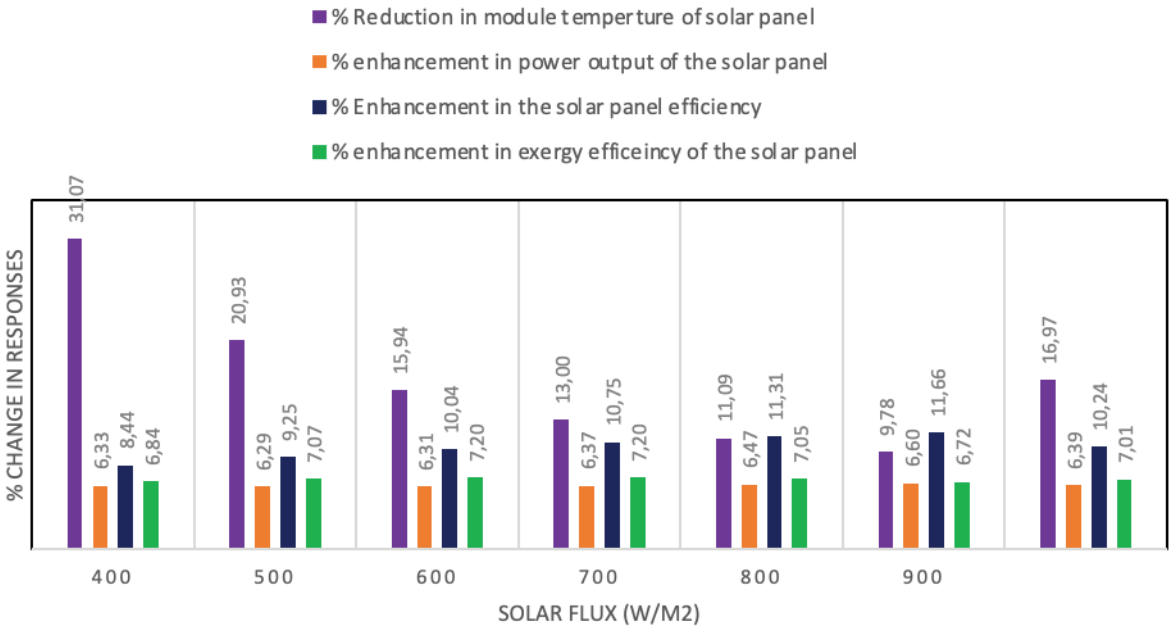

Figure 14. Solar panel performance enhancement due to air cooling as compared to without cooled system.

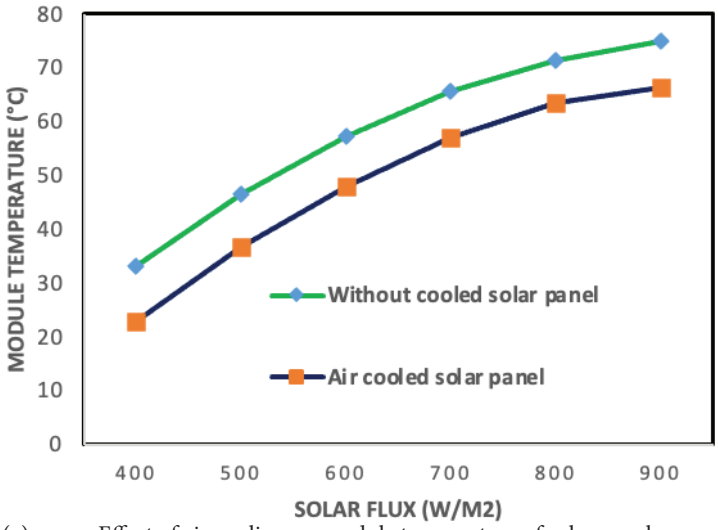

(a) Effect of air cooling on module temperature of solar panel

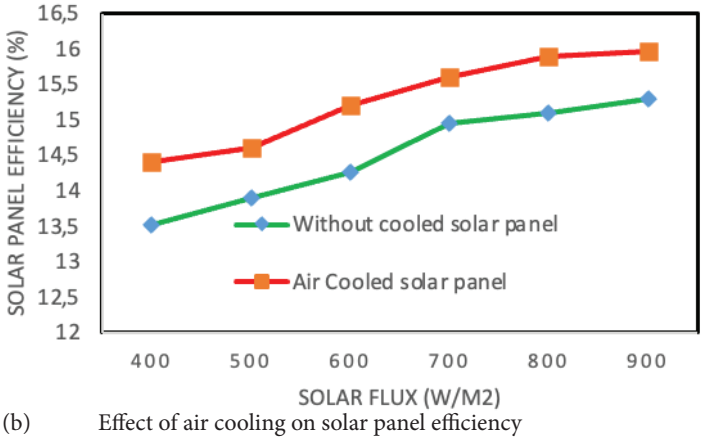

(b) Effect of air cooling on solar panel efficiency

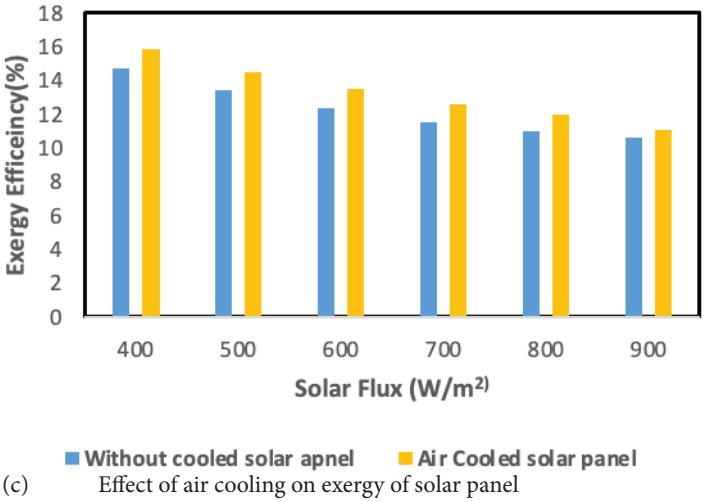

(c) Effect of air cooling on exergy of solar panel

Figure 15. Comparison of module temperature, solar panel efficiency and solar panel exergy with air or without air cooled solar panel.

efficiency of air-cooled solar panel at an air discharge of 0.02 m^3/s. The percentage reduction of the module temperature of the solar panel depicts that as the solar flux increases then the reduction in module is less since at the higher solar flux air cooling is not sufficient to lower down the module temperature. Figure 14 clearly shows that as the solar flux increases then the percentage change in the power production of the solar panel increased since at the higher solar flux the input energy supplies increased which will further enhance the power output of the solar panel.

The solar panel efficiency also enhanced as the solar flux increased at the air discharge 0.02 m^3/s, the percentage change of the solar panel efficiency is higher at the higher solar flux. The exergy efficiency percentage growth with solar flux increases initially but after reaching to optimum solar flux, the exergy efficiency starts to reduce since augmentation in the solar flux raises the module temperature which reduces the exergy efficiency of the solar panel.

Figure 15 illustrates the comparison between the air cooled and without cooled solar panel performance. Figure 15 (a) depicts that if the soar flux increasing, the module temperature of the soar panel always increasing trends. The maximum module temperature of without cooled and with air cooled solar panel are noted to be 74.86°C and 66.25°C at air flow rate of the 0.02 m^3/s and solar flux 900 W/m^2. Figure 15 (b) display the percentage variation of the solar panel efficiency with the solar flux. As the solar flux increasing, the power production through the solar panel enhanced which increase the solar panel efficiency. Figure 15 (c) shows the exergy efficiency variation with the solar flux. As the solar flux increasing, the exergy efficiency reduces due to increase in the solar panel temperature at higher solar flux. The maximum exergy efficiency obtained to be 15.9% and 14.73% at the solar flux of 400 W/m^2 and 0.02 m^3/s discharge.

Validation of the Results

The results of the current study are validated with the Anurag et al. (2022) [61]. Anurag et al. (2022) performed the experimental and numerical of the air-cooled solar panel by various configurations of the fins produced below the surface of the solar panel. Table 11 shows the variation of the solar flux, solar panel temperature, and solar panel efficiency variation for the longitudinal fins in tabular form. Figure 16 illustrates the validation of the results of the current study with the Anurag et al. (2022) [61]. Figure 16 (a) depicts reasonable agreement between the surface temperature variation of current research with Anurag et al. (2022). Both studies agreed that as the solar flux growths, the solar panel surface temperature increases. The current study showed that at the solar flux of 1100 W/m^2, the maximum temperature reached to 68.32°C which is very near to the 67.32°C solar panel surface temperature of Anurag et al. (2022). Figure 16 (b) also displays that the solar panel efficiency increases as the solar flux increases. The maximum efficiency of the solar panel is reached to 16.52% and 16.1% in the Anurag et al. (2022) and current study. The cooling of the solar panel is very much required as the solar flux is very high in the summer time in between the 11 AM to 3 PM, in this duration the solar panel performance is drastically reduced but air cooling made this drastic reduction

Table 11. Anurag et al. (2022), solar flux, solar panel surface temperature and solar panel efficiency variation for the longitudinal fins

Time	9 AM	10 AM	11 AM	12 PM	1 PM	2 PM	3 PM	4 PM
Solar Flux (W/m^2)	700	850	1000	1100	1080	910	720	390
Solar Panel Surface Temperature (°C)	55	63.8	69	67.89	66.89	66	56.65	42
Solar Panel Efficiency (%)	15.3	16.1	16.4	16.52	15.1	13.29	13.2	13.12

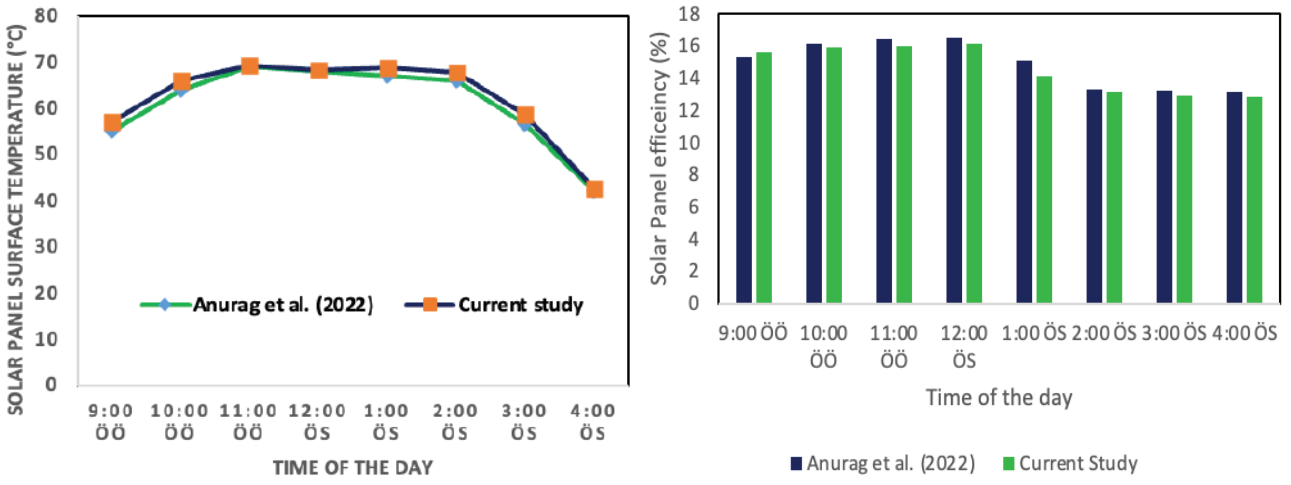

(a) Validation of the surface temperature of the solar panel

(b) Validation of the solar panel efficiency

Figure 16. Validation of the current study with Anurag et al. (2022)

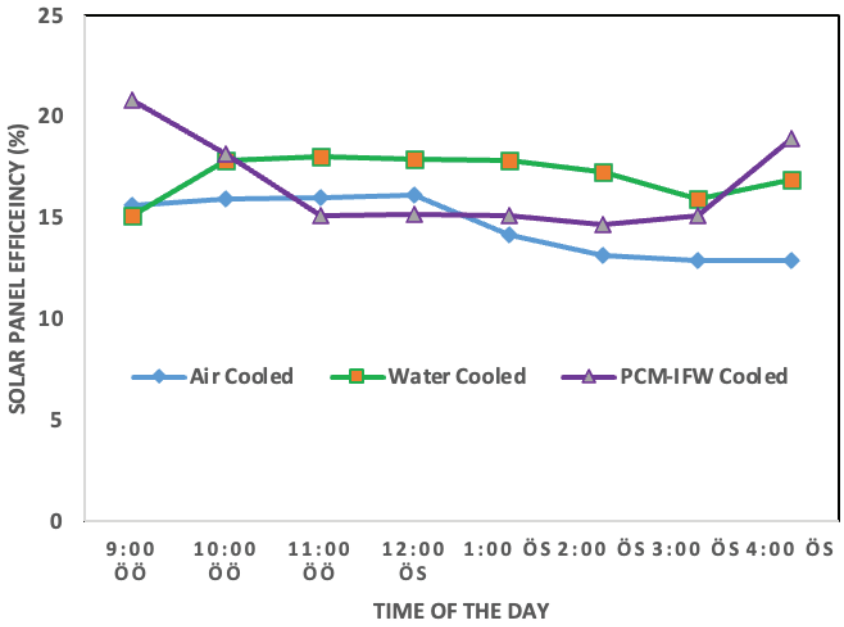

Figure 17. Comparison of the solar panel efficiency with air, water and PCM cooling in summer season.

curve to flatten and maintain the performance of the solar panel within the permissible limit.

Comparison of Air Cooling with the Water and Paraffin Wax with Iron Filling Waste

This section discusses and compares the performance enhancement of solar panel due to the air, water, and PCM-IFW (Iron Filling Waste) cooling. The current research compares with the liquid water cooling [62] and PCM-IFW cooling [63]. Figure 17 depicts that in the morning from 9 AM to 10 AM, the PCM material with IFW gives the maximum efficiency, but after 10 AM to 3 PM, the water cooling at a mass flow rate of 1.5 LPM gives the maximum efficiency. In the morning between 9 AM to 10 AM, the PCM material started to melt and changes the phase, this process absorbs the latent heat and cools down the module at a desirable limit but when all PCM material melted, then it absorbs the sensible heat and lower down the cooling rate and reduce the efficiency. Although, in water cooling, always fresh water at optimum mass flow rate is supplied to the solar panel surface, which maintains the solar panel efficient at a constant level throughout the day. On the other hand, the air has low heat absorbing capacity since air cooling has lower cooling efficiency as compared to the PCM and water cooling.

CONCLUSION

Fossil fuels are exhaustible in nature and not economical due to hikes in price, creating the requirement of alternative fuels that are renewable and eco-friendly to the environment. Solar panel are best fitted to fill this gap since they convert solar energy into electrical energy without creating any harmful effect in the atmosphere. The main drawback of the solar panel is the low performance at high temperatures. So, at the time of the solar panel's working, solar cooling must be required for the sustainability of the efficiency. High solar panel efficiency reduces the initial investment so that it can be afforded by the farmers and the poor people located in rural and remote areas. This research focused on the performance improvement of the solar panel by the use of air cooling. The air cooling is chosen for the study due to its simple arrangement and noncorrosive nature. The main limitation of the study is the lower cooling effect due to the lower thermal diffusivity of the air. However, it is the most used method as a cooling medium in all fields of engineering like automobiles, electronic equipment, and the aerospace industry due to cost-effective and easy of implement. For the thermal analysis of the cooling arrangement, the system has been designed and optimized by the Response Surface Methodology, and the optimum setting of the input and output variables has been determined based on the constraints of the optimization. The percentage enhancement in the responses due to air cooling compared with the without cooled solar panel. The following are the main concluding points of this study.

1. The solar flux and the air mass flow rate are two important input variables that affect the performance of the solar panel. As the solar flux enhanced from 400 W/m^2 to 800 W/m^2, the module temperature augmented from 22.9°C to 63.5°C which hamper the thermal performance from 14.4% to 10.8%.
2. Enhancing the solar flux increases the module temperature of the solar panel due to that the performance

of the solar panel decays throughout the day. The exergy analysis shows that from 400 W/m^2 to 800 W/m^2 increase in solar flux reduces the exergy efficiency from 15.9% to 12.0%.

3. In the optimization process, the optimal solar flux and air discharge were found to be 403.3586 W/m^2 and 0.0221 m^3/s on which responses are module temperature 22.4279°C, power output 4.1196 Wp, PV module efficiency 14.41% and exergy efficiency 15.78%.
4. At higher solar flux and high air discharge is feasible to drop down the temperature of the solar panel since increasing discharge continuously reduces the air temperature. However, at very high temperature of the solar panel, the air cooling will be ineffective in dropping the temperature of the solar panel at the optimum limit, this situation can be handled by using liquid cooling and phase change material. At 800 W/m^2 solar flux if the air discharge increases from 0.01 m^3/s to 0.02 m^3/s, the solar panel efficiency increases from 14.7% to 15.9%.
5. At the discharge of 0.01 m^3/s, the 9.16% reduction in temperature and 3% enhancement in the power output has been recorded and if the discharge is increased to 0.02 m^3/s, the temperature drop is 16.96% and enhancement in power output is 6.39%.
6. The composite desirability of the output and input variables is 0.5737.
7. The R^2, adjusted R^2 and predicted R^2 values are 0.9986, 0.9976, and 0.99 showing the good accuracy of the model generated by analyses of variance.

Role and Significance of the Study

The world›s energy demand is growing day by day. In the current scenario, most of the energy demand has been fulfilled by the use of fossil fuels. The government is focusing on green energy technology which is renewable and free from pollution. Solar panels are the best way of the production of electricity by Sun energy. This study has been performed to enhance the solar panel efficiency to fill the energy demand of the world. The study focused to use the high-density pin fin which can be fixed with the outer plate of the solar panel and air can be blown by the use of the fan. The air cooling is feasible and easily handled.

Limitations of the study and future work

The main limitation of the study is the lower cooling effect due to the lower thermal diffusivity of the air. However, it is the most used method as a cooling medium in all fields of engineering like automobiles, electronic equipment, and the aerospace industry due to cost-effective and easy of implement. This can be overcome by the use of supplying the already-cooled air or supplying the liquid water in dry air at varying concentrations to enhance the heat-carrying capacity of air. The second limitation of air cooling is the noise produced at the time of the flow of the air over the fined surface by the fan or blower. This effect can be mitigated by the use of a partial vacuum in the air duct, using passive techniques, and using the phase change material for cooling the solar panel.

In the future, the research will be focused to know the effect of the humidity in the moist air on solar panel cooling. The system will be optimized to know the effect of the humidity and air dry bulb temperature on the performance of the solar panel. Furthermore, the research will also include cooling the different types of solar panels with PCM, Nano-fluids, and liquid water.

ACKNOWLEDGMENT

The authors thank IFTM University›s management and vice chancellor for permitting them to conduct the study and providing the facilities they needed.

CONFLICT OF INTEREST

The Author’s declare that they have not any conflict of interest.

REFERENCES

[1] Sharaf M, Yousef MS, Huzayyin AS. Review of cooling techniques used to enhance the efficiency of photovoltaic power systems. Environ Sci Pollut Res 2022;29:26131–26159. [Crossref]

[2] Teo HG, Lee PS, Hawlader MNA. An active cooling system for photovoltaic modules. Appl. Energy 2012;90:309–315. [Crossref]

[3] Choi SM, Kwon HG, Kim T, Moon HK,Cho HH. Active cooling of photovoltaic (PV) cell by acoustic excitation in single-dimpled internal channel. Appl Energy 2021;309:118466. [Crossref]

[4] Deivakumaran S, Chua YL, Koh YY. Active cooling system for solar panels with silver nanofluid and water. IOP Conf Ser Earth Environ Sci 2023;1205. [Crossref]

[5] Tonui JK, Tripanagnostopoulos Y. Performance improvement of PV / T solar collectors with natural air flow operation. 2008;82:1–12. [Crossref]

[6] Yun GY, Mcevoy M, Steemers K. Design and overall energy performance of a ventilated photovoltaic façade. 2007;81:383–394. [Crossref]

[7] Nuwayhid RY. Thermal analysis of photovoltaic-thermoelectric hybrids. J Therm Eng 2024; 10:1149–1163. [Crossref]

[8] Gelis K, Al-Khatib OA, Ozbek K. Development of partitioned rectangular-shaped heat sink for photovoltaic thermal systems and performance evaluation using TiO2/Water-based nanofluids. Appl Therm Eng 2024;248:123220. [Crossref]

[9] Gelis K, Celik AN, Ozbek K, Ozyurt O.Experimental investigation into efficiency of SiO2/water-based nanofluids in photovoltaic thermal systems using response surface methodology. Sol Energy 2022;235229–241. [Crossref]

[10] Vithanage V, Hosan S, Perera H, Galpaya C, Induranga A. Impact of water based nanofluids in heat exchanger type active solar PV cooling systems : A comparative CFD analysis. 2025.
[11] Sheikh Y, Jasim M, Qasim M, Qaisieh A, Hamdan MO, Abed F. Enhancing PV solar panel efficiency through integration with a passive Multi-layered PCMs cooling system: A numerical study. Int J Thermofluids. 2024;23:100748. [Crossref]
[12] Sudhakar P, Santosh R, Asthalakshmi B, Kumaresan G, Velraj R. Performance augmentation of solar photovoltaic panel through PCM integrated natural water circulation cooling technique. Renew Energy 2021;172:1433–1448. [Crossref]
[13] Akkoyunlu MT, Abdallatif Y. A comprehensive investigation of solar panel cleaning technologies: A review study. J Therm Eng 2024;10:1715–1741. [Crossref]
[14] Hasan A, McCormack SJM, Huang J, Norton B. Characterization of phase change materials for thermal control of photovoltaics using Differential Scanning Calorimetry and Temperature History Method. Energy Convers Manag 2014;8:322–329. [Crossref]
[15] Stropnik R, Stritih U. Increasing the efficiency of PV panel with the use of PCM. Renew Energy 2016;97:671–679. [Crossref]
[16] RM, LS, RS, AH, DA. "Experimental investigation on the abasement of operating temperature in solar photovoltaic panel using PCM and aluminium. Sol Energy 2019;188 327–338:2019. [Crossref]
[17] Alzgool M.Performance Enhancement by Cooling the PV Panels Using Phase Change Material (RT35): ANSYS Simulation and Experimental Investigation. Int J Energy Prod Manag 2024;9:73–81. [Crossref]
[18] Madurai Elavarasan R, Nadarajah M, Pugazhendhi R, Gangatharan S. An experimental investigation on coalescing the potentiality of PCM, fins and water to achieve sturdy cooling effect on PV panels. Appl Energy 2023;356:122371. [Crossref]
[19] Golzari S, Kasaeian A, Amidpour M, Vatan SN, Mousavi S. Experimental Investigation of the Effects of Corona Wind on the Performance of an Air-Cooled PV/T. Renew Energy 2018. [Crossref]
[20] Alrobaian AA. Performance of PV panel coupled with geothermal air cooling system subjected to hot climatic. 2017;148:1–9. [Crossref]
[21] Arifin Z, Danardono D, Prija D, Hadi S. Numerical and Experimental Investigation of Air Cooling for Photovoltaic Panels Using Aluminum Heat Sinks 2020;2020. [Crossref]
[22] Lebbi M, Baissi MT, Hassani S. Energy performance improvement of a new hybrid PV / T Bi-fluid system using active cooling and self-cleaning : Experimental study. Appl Therm Eng 2020;116033. [Crossref]
[23] Salehi R, Jahanbakhshi A. Reza Golzarian M, Khojastehpour M. Evaluation of solar panel cooling systems using anodized heat sink equipped with thermoelectric module through the parameters of temperature, power and efficiency. Energy Convers Manag 2021;11. [Crossref]
[24] Li D, King M, Dooner M, Guo S, Wang J. Study on the cleaning and cooling of solar photovoltaic panels using compressed airflow. Sol Energy 2021;221:433–444. [Crossref]
[25] Almuwailhi A, Zeitoun O. Investigating the cooling of solar photovoltaic modules under the conditions of Riyadh. J King Saud Univ Eng Sci 2023;35:123–136. [Crossref]
[26] Abdullah AA, Attulla FS,. Ahmed OK, Algburi S. Effect of cooling method on the performance of PV/Trombe wall: Experimental assessment. Therm Sci Eng Prog 2021;30: 101273. [Crossref]
[27] Abdullah AA. The effect of operating conditions and climate change on the performance of the photopholtaic Trombe wall: An empirical estimate. J Therm Eng 2024;10:1241–1252. [Crossref]
[28] Rathore A. Energy, exergy and performance analysis of a 380 kWP roof-top PV plant assisted with data-driven models for energy generation. J Therm Eng 2024;10:1164–1183. [Crossref]
[29] Hamzawy AH, Abed QA, "An experimental study on the impact of porous media in improving the heat transfer performance characteristics of photovoltaic-thermal system. J Therm Eng 2025;11:181–195. [Crossref]
[30] Wang G, Yang Y, Yu W, Wang T, Zhu T. Performance of an air-cooled photovoltaic/thermal system using micro heat pipe array. Appl Therm Eng 2022;217:119184. [Crossref]
[31] Nabil T, Mansour TM.Augmenting the performance of photovoltaic panel by decreasing its temperature using various cooling techniques. Results Eng 2022;15:100564 [Crossref]
[32] Tian MW, Khetib Y, Yan SR, Rawa M. Energy, exergy and economics study of a solar/thermal panel cooled by nanofluid. Case Stud Therm Eng 2021;28:101481. [Crossref]
[33] Mazón-Hernández R, García-Cascales JR, Vera-García F, Káiser AS, Zamora B. Improving the electrical parameters of a photovoltaic panel by means of an induced or forced air stream. Int J Photoenergy 2013;2013. [Crossref]
[34] Hernandez-Perez JG, Carrillo JG, Bassam A, Flota-Banuelos M, Patino-Lopez LD. A new passive PV heatsink design to reduce efficiency losses: A computational and experimental evaluation. Renew Energy 2020;147:1209–1220. [Crossref]
[35] Feng S, Shi M, Yan H. Sun S, Li F, Lu TJ. Natural convection in a cross-fin heat sink. Appl Therm Eng 2018; 132; 30–37. [Crossref]
[36] Huang GJ, Wong SC, Lin CP. Enhancement of natural convection heat transfer from horizontal rectangular fin arrays with perforations in fin base. Int J Therm Sci 2014;84:164–174. [Crossref]

[37] Shaeri MR, Bonner R.Laminar forced convection heat transfer from laterally perforated-finned heat sinks. Appl Therm Eng 2017;116:406–418. [Crossref]
[38] Chu WX, Lin YC, Chen CY, Wang CC. Experimental and numerical study on the performance of passive heat sink having alternating layout. Int J Heat Mass Transf 2019;135:822–836. [Crossref]
[39] Kanargi B, Lee PS, Yap C.International Journal of Heat and Mass Transfer A numerical and experimental investigation of heat transfer and fluid flow characteristics of an air-cooled oblique-finned heat sink. 2018;116:393–416. [Crossref]
[40] Çengel YA, Ghajar AJ, Kanoğlu M.Heat and mass transfer : fundamentals & applications.
[41] Hadipour A, Rajabi Zargarabadi M, Rashidi S. An efficient pulsed- spray water cooling system for photovoltaic panels: Experimental study and cost analysis *Renew Energy* 2021;164:867–875. [Crossref]
[42] Peng Z, Herfatmanesh MR, Liu Y. Cooled solar PV panels for output energy efficiency optimisation. Energy Convers Manag 2017;150: 949–955. [Crossref]
[43] Subasi A, Sahin B, Kaymaz I. Multi-objective optimization of a honeycomb heat sink using Response Surface Method. Int J Heat Mass Transf 2016;101:295–302. [Crossref]
[44] Singh V, Yadav VS. Optimizing the performance of solar panel cooling apparatus by application of response surface methodology. 2022;236. [Crossref]
[45] Singh V, Yadav VS. Application of RSM to Optimize Solar Pump LCOE and Power Output. 2022;69:1–12. [Crossref]
[46] Singh V, Yadav VS, Saxena V, Kumar N, Maheswari A. Theoretical Analysis of 1st Law and 2nd Law Efficiency of a Solar Pump for Geographical Location 28.10'N, 78.23'E. Lect Notes Mech Eng 2022;411–417. [Crossref]
[47] Waila VC, Sharma A, Singh V, Gupta NK. Solar photovoltaic water pump performance optimization by using response surface methodology. Environ Prog Sustain Energy 2023. [Crossref]
[48] Choudhary S, Sharma A, Gupta S, Purohit H, Sachan S. Use of RSM technology for the optimization of received signal strength for LTE signals under the influence of varying atmospheric conditions. Evergr Jt J Nov Carbon Resour Sci Green Asia Strateg 2020;07:500–509. [Crossref]
[49] LMA Campos, Moura HOMA, Cruz AJG, Assumpção SMN, de Carvalho LS, Pontes LAM. Response surface methodology (RSM) for assessing the effects of pretreatment, feedstock, and enzyme complex association on cellulose hydrolysis. Biomass Convers Biorefinery 2020:12;1–12. [Crossref]
[50] Response Surface Methodology (RSM) flowchart. https://www.researchgate.net/figure/Response-Surface-Methodology-RSM-flowchart_fig1_316577916 Accessed on Sep 27, 2022.
[51] Le HS, Galal A, Alhamrouni I, Aly AA. Heat transfer efficiency optimization of a multi-nozzle micro-channel heat sink utilizing response surface methodology. Case Stud Therm Eng 2022;37:102266. [Crossref]
[52] Chiang KT, Chang FP. Application of response surface methodology in the parametric optimization of a pin-fin type heat sink. Int Commun Heat Mass Transf 2006;33:836–845. [Crossref]
[53] Onokwai AO, Owamah HI, Ibiwoye MO, Ayuba GC, Olayemi OA. Application of Response Surface Methodology (RSM) for the optimization of energy generation from Jebba hydro-power plant, Nigeria. ISH (J Hydraul Eng) 2020;28:1–9.
[54] Qader BS, Supeni EE, Ariffin MKA, Talib ARA. RSM approach for modeling and optimization of designing parameters for inclined fins of solar air heater. Renew Energy 2019; 136:48–68. [Crossref]
[55] Rout A, Singh S, Mohapatra T, Sahoo SS, Solanki CS. Energy, exergy, and economic analysis of an off-grid solar polygeneration system. Energy Convers Manag 2021;238:114177. [Crossref]
[56] Karami N, Rahimi M. Heat transfer enhancement in a PV cell using Boehmite nanofluid. 2014;86:275–285. [Crossref]
[57] Trivedi V, Saxena A, Javed M, Kumar P, Singh V. Design of Six Seater Electrical Vehicle (Golf Cart). Evergreen 2023;10:953–961. [Crossref]
[58] Chandel SS, Agarwal T. Review of cooling techniques using phase change materials for enhancing efficiency of photovoltaic power systems. Renew Sustain Energy Rev 2017;73:1342–1351. [Crossref]
[59] Kumar M, Ansari NA, Sharma A, Singh VK, Gautam R, Singh Y. Prediction of an optimum engine response based on various input parameters on common rail direct injection diesel engine-a response surface methodology. Available at: https://scholar.archive.org/work/7wxig7vx2naklk3futcbp36jmi/access/wayback/http://scientiairanica.sharif.edu/article_22272_8d700f88d1a63567d2e8ea087bbbacb0.pdf. Accessed: Jul. 30, 2022.
[60] Singh V, Trivedi V, Mishra VR. Use of response surface methodology and CFD for analysing and optimization of simple-air cooled solar panel. Int J Energy Water Resour 2024:0123456789. [Crossref]
[61] Shrivastava A, Jose JP, Borole YD, Saravanakumar R, Sharifpur M, Harasi H, et al. A study on the effects of forced air-cooling enhancements on a 150 W solar photovoltaic thermal collector for green cities. Sust Ener Tech Assessments 2022;49:101782. [Crossref]
[62] Sainthiya H, Beniwal NS. Comparative analysis of electrical performance parameters under combined water cooling technique of photovoltaic module: An experimental investigation," Energy Sources Part A Recover. Util Environ Eff 2020:42:1902–1913. [Crossref]
[63] Ali AA, Lafta DA, Noori SW, Abdulamir F, Rashid FL. Innovative materials integrated with PCM for enhancing photovoltaic panel efficiency: An experimental investigation. J Energy Storage 2024:102. [Crossref]

APPENDIX

Calculation of cell Temperature

The cell temperature was calculated using the energy balance of the solar panel and the Nominal Operating Cell Temperature (NOCT) conditions.

$$T_{Cell} = \frac{T_a + (T_{CNOCT} - T_{aNOCT})\left(\frac{G_T}{G_{TNOCT}}\right)\left(1 - \left(\frac{\eta_{mpSTC}(1 - \alpha_p T_{cSTC})}{\tau\alpha}\right)\right)}{1 + (T_{CNOCT} - T_{aNOCT})\left(\frac{G_T}{G_{TNOCT}}\right)\left(\frac{\alpha_p \eta_{mpSTC}}{\tau\alpha}\right)}$$

From the solar panel manufacturer data

$$T_{CNOCT} = 48°C, T_{aNOCT} = 20°C, G_{TNOCT} = 800\frac{W}{m^2}, \qquad T_{CSTC} = 25°C, \eta_{mp} = 0.154,$$
$$\tau\alpha = 0.9, \alpha_p = -\frac{0.002726}{°C}$$

Put these values in the above equation, the cell temperature equation in terms of the atmospheric temperature and the solar flux.

$$T_{Cell} = \frac{T_a + 0.022946 G_T}{1 - 0.0000181279 G_T}$$

So when Ta = 45°C and G_T = 1000 W/m^2

T_{Cell} = 69.20°C

The top surface heat transfer coefficient at airflow velocity of V = 3 m/s

$$h_T = 2.8 + 3V = 2.8 + 3 * 3 = 11.8\, W/m^2 k$$

The radiation heat transfer coefficient

$$h_r = \varepsilon\sigma(T_C + T_a)(T_C^2 + T_a^2)$$
$$\varepsilon = 0.83, T_C = T_{average} = 57.21°C, T_a = 45°C$$
$$h_r = 6.41\, W/m^2 k$$

So total heat transfer coefficient from the top surface of the solar panel

$$h_e = h_c + h_r = 11.8 + 6.41 = 18.21\, W/m^2.k$$

Total heat transfer

$$Q_{Top} = (T_{Cell} - T_a)/(\frac{L_{EVA}}{K_{EVA}} + \frac{L_{ETFE}}{K_{ETFE}} + \frac{1}{h_e})$$

L_{EVA}= 0.20 mm, K_{EVA}=0.35 W/mk, LETFE= 0.28 mm, K_{ETFE} = 0.24 W/mk

$$Q_{Top} = 427.1965\frac{W}{m^2}$$

Now EVA plate temperature

$$T_{EVA} = T_{Cell} - \left(\frac{L_{EVA}}{K_{EVA}}\right) Q = 68.12°C$$

Now ETFE plate temperature

$$T_{ETFE} = T_{EVA} - \left(\frac{L_{ETFE}}{K_{ETFE}}\right) Q = 67.4°C$$

Now efficiency of solar panel

$$\eta = \eta_{mp}(1 + \alpha_{STC}(T_C - T_{CSTC})$$

$$\eta = 0.154(1 - 0.002726(69.42 - 25) = 0.1353$$

Percentage reduction in solar panel efficiency

$$\%\Delta\eta = \frac{0.154 - 0.1353}{0.154} = 12.28\%$$

The power output from solar panel

$$P = P_m(1 - \alpha_P(T_{cell} - T_{CSTC}) = 10(1 - 0.002726(69.42 - 25) = 8.78\ W$$

Bottom layer of solar panel temperature

Heat transfer from bottom of solar panel

$$\mathrm{Q_{Bottom}} = \mathrm{A_P} * \mathrm{I_t} * \alpha - \mathrm{P} - \mathrm{Q_{Top}}$$

$$\mathrm{Q_{Bottom}} = 0.071 * 1000 * 0.97 - 8.78 - 427.19 * 0.071$$

$$\mathrm{Q_{bottom}} = 29.75\ \mathrm{W} = \frac{29.75}{0.071} = 419.14\frac{\mathrm{W}}{\mathrm{m^2}}$$

Temperature of bottom layer

$$\mathrm{T_{Bottom}} = \mathrm{T_{cell}} - \left(\frac{\mathrm{L_{EVA}}}{\mathrm{K_{EVA}}} + \frac{\mathrm{L_{PET}}}{\mathrm{K_{PET}}} + \frac{\mathrm{L_{CFRP}}}{\mathrm{K_{CFRP}}} + \frac{\mathrm{L_{Tape}}}{\mathrm{K_{Tape}}}\right) * \mathrm{Q_{Bottom}}$$

$$T_{Bottom} = 68.24°C$$

Exergy Analysis

Exergy reached on the surface of solar panel

$$E_{SUN} = A_P I_t[1 - \tfrac{4}{3}\left(\tfrac{T_a}{T_{SUN}}\right) + \tfrac{1}{3}\left(\tfrac{T_a}{T_{SUN}}\right)^4]$$

Put I_t =1000 W/m^2, Ta = 318 K, T_{Sun} =5770 K, Ap =0.071 m^2

$$E_{SUN} = 64.85\ W$$

Exergy efficiency

$$\varphi = \frac{W_e}{E_{SUN}}$$

$$\varphi = 13.44\ \%$$

Uncertainty Calculations

Uncertainty in the power output of solar panel

The power of the solar panel›s maximum voltage and current

$$P = f(I, V)$$

So uncertainty in the power production of solar panel

$$y_P = \sqrt{\left(\frac{\partial P}{\partial I}\right)^2 y_I^2 + \left(\frac{\partial P}{\partial V}\right)^2 y_V^2}$$

The uncertainty in the current $y_I = 3\%\ and\ in\ Voltage\ y_V = 3.5\%$. The measurement of the current at some time is the 0.8 amp and V = 10 V.

Now uncertainty in the current $y_I = 0.8 * \frac{3}{100} = 0.024$

Uncertainty in the voltage $y_V = 10 * \frac{3.5}{100} = 0.35$

$$P = VI \quad so\ that \frac{\partial p}{\partial I} = V\ and \frac{\partial P}{\partial V} = I$$

So uncertainty in power measurement

$$y_P = \sqrt{(V)^2 y_I^2 + (I)^2 y_V^2}$$

$$y_P = \sqrt{(10)^2 (0.35)^2 + (0.8)^2 (0.024)^2}$$

$$y_P = 3.5\%$$

J Ther Eng, Vol. 12, No. 2, pp. 579−594, March, 2026

Journal of Thermal Engineering
Web page info: https://jten.yildiz.edu.tr
DOI: 10.14744/thermal.0001102

Research Article

Thermal and nanoscale relations of particles in mineral oil: An analysis of metallic and non-metallic particles

A.T. AKINSHILO[1,*], M.G. SOBAMOWO[1], L. KOLSI[2]

[1]Department of Mechanical Engineering, University of Lagos, Lagos, 100213, Nigeria
[2]Department of Mechanical Engineering, University of Ha'il, Ha'il, 55212, KSA

ARTICLE INFO

Article history
Received: 04 March 2025
Accepted: 15 July 2025

Keywords:
Heat Transfer; MHD; Micro Channel; Nanolayer; Particle Size

ABSTRACT

The mineral oil, a viscous liquid which is a derivative product from petroleum processing, having wide range of engineering applications, is studied in this paper. Thermal analysis of mineral oil in a microchannel incorporating nanoscale relations of metallic and non-metallic nanoparticles is investigated. The thermal effect on the nano layer is considered, which shows the relationship between the base fluid and nanoparticle. Also, the effect of nanoparticle size on the thermal layer is examined to understand the fluid performance under thermal load. The mechanics of the heat transfer and fluid transport are developed using coupled nonlinear system of higher partial differentials. They are analyzed using the Homotopy perturbation method upon transformation from partial to ordinary equations utilizing suitable similarity transforms. Results obtained from analysis show that optimum nanolayer thickness increases the surface layer of the nanoparticle, consequently increasing fluid temperature. Also, it is observed that the volume of the nanoparticle concentration from 1 to 8 % improves heat transfer and enhances shear stress at the wall boundary. The heat transfer rate using the graphite particles is higher compared to the copper particles, about 23 times more. Nanolayer thickness of 1nm and particle radius size within 5 to 20 nm studied shows good agreement with literature. Study may provide useful insight to tribologist and scientist interested in lubricant designs and process cooling.

Cite this article as: Akinshilo AT, Sobamowo MG, Kolsi L. Thermal and nanoscale relations of particles in mineral oil: an analysis of metallic and non-metallic particles. J Ther Eng 2026;12(2):579−594.

INTRODUCTION

The mineral oil, which is a viscous liquid obtained from the processing of petroleum products, is a colorless and odorless liquid. Mineral oil can be paraffinic, aromatic or naphthenic type. Having wide usage in refrigeration compressors, electric transformer cooling, amongst many other practical applications. Due to its thermal and viscous properties, researchers have studied this fluid in the bid to enhance its performance. Heat transfer cell was designed and developed by Eli [1] to accurately calculate the heat transport coefficient and thermal conductivity of the mineral oil

*Corresponding author.
*E-mail address: ta.akinshilo@gmail.com

This paper was recommended for publication in revised form by Editor-in Chief Ahmet Selim Dalkilic

Published by Yıldız Technical University Press, İstanbul, Turkey
Yıldız Technical University. This is an open access article under the CC BY-NC license (http://creativecommons.org/licenses/by-nc/4.0/).

at room temperature. The study reported shows that 40 nm copper oxide nanoparticles are not suitable with mineral oil as a base fluid for transformer cooling due to heat convection. The effect of chemically reactive species in steadily flowing mineral oil with aluminum oxide nanoparticles was analyzed numerically by Nazir et al. [2], where they observed that magnetic dipole and particle shape impact thermal conductivity. The concentration of nanoparticles on heat transfer and thermophysical properties of alumina nanosuspension for refrigeration application was studied by Jashi et al. [3]. They compared the experimentally observed results against model results for thermal conductivity and viscosity, which shows nanoparticle concentration has a direct effect on conductivity. Khoirudin et al. [4] analyzed mineral oil data to analyze the effect of breakdown voltage and thermal conductivity. Findings suggested that nanoparticles increase breakdown voltage and thermal conductivity. The impact of temperature reduction and loading capacity on distribution transformers using mineral oil was investigated by Taheri et al. [5], where they discovered addition of nanofluids increases loading capacity. Karaman et al. [6] presented their study on the influence of nanoparticles on temperature distribution in mineral oils. Study reveals that high thermal conductive fluids reduce thermal stress in oils. The rheological behavior of hybrid nanofluid (TiO_2 - Al_2O_3) in mineral oil was experimentally investigated by Shelton et al. [7]. It was reported that the ratio of nanoparticle mixture, concentration, and composition impacts the mineral oil rheological characteristics. Saman et al. [8] treated nanoparticles with plasmas to study their effects on breakdown strength, discharge resistance and thermo-physical properties of the mineral oil-based fluid. It is noted that the treatment of nanoparticles with plasma improved particle dispersion and stability, providing enhanced interaction between the base fluid and nanoparticles.

To conserve energy, reducing heat loss during fluid transfer becomes pertinent. The need to raise fluid thermal conductivity arises. This results in the inclusion of nanosized particles in pure fluid, which increases fluid thermal capacity as fluid is travelling through channels [9-10]. The nanofluid mixture finds relevant application in energy conservation, lubrication, fuel cells and micro-electronic processes [11-14]. Kiran et al. [15] used graphite in their study as an additive in lubricants, with results indicating inclusion of graphite led to a reduction of friction coefficient and deformation, preventing wear in steel. Also, copper nanoparticles were used by Guo et al. [16] in their study on tribological performance, with results showing copper reduces wear, friction coefficient and improves performance in engine oils. Dogonchi and Ganji studied the effect of nanofluid flow between stretchable and shrinkable plane walls, considering Brownian motion and thermal radiation [17-18]. It was presented that heat transfer rate is enhanced by stretching and radiation. Kumar et al. [19] studied the nanofluid flow over a bidirectional stretching surface, they showed that the boundary layer thickness of Cu-water is higher than methanol-Cu. The stability of nanoparticles and heat transfer of fluid over a moving and stationary thin needle was studied by Mabood and Akinshilo [20], where it was shown that increasing the volume concentration of nanoparticles decreases with fluid motion. Hdhiri et al. [21] studied nanofluid flow and convective heat transfer in the heated cavity, where it is shown that heat transfer is strongly dependent on Prandtls number.

Nanoscale relations between nanoparticles and base fluid have been receiving attention in recent times, owing to the inadequacy of established nanofluid models to justify the rise of the nanofluid thermal conductivity. Established conductivity models, including the Maxwell model [22] and the Hamilton and Crosser model [23], did not capture the effect of the nanolayer; consequently, could not justify the improvement in conductivity of nanofluid even at low volume concentration. The nanolayer effectively shows the connection between the base fluid and the nanoparticle as described by Acharya et al. [24]. The nanolayer shows the relationship between the base liquid and nanoparticle, showing a higher thermal conductivity than the nanoparticle and lower conductivity than the base fluid. The nanolayer and particle diameter were studied by Rana and Beg [25] using water-alumina nanofluid on inclined flow, where they concluded that nanoparticle diameter impacts thermal profile. The inter-particle spacing relations between particles were formulated by Graham [26] using a cell theory to derive the relation dependence of zero shear rate viscosity on volume concentration of uniformly dispersed solid spherical particles. Further, Gosunkanda et al [27] investigated the particle spacing effect in convective heat transfer through a cylindrical annulus.

The mineral oil has rigid but spherical particles that rotate during flow. Thermal fluidic mechanics comprises of macroscopic velocity field and a rotational motion component described in governing relations for micropolar fluids formulated by Eringen [28]. These governing relations are nonlinear, partial and higher-order systems of coupled equations. Simplified using similarity transforms into ordinary, higher-order differentials which can be analyzed using numerical or analytical techniques. Numerical methods such as Runge-Kutta, finite volume and finite elements methods have been used in the past. Analytical methods, including the Homotopy perturbation, Adomian decomposition, differential transformation, variation iteration, methods of weighted residuals, have been equally used to provide approximate analytical solutions to higher-order boundary value problems [29-31]. These methods suffer from their various limitations and rounding errors. However, the Homotopy perturbation method, an analytical method which provides ease of changing parameters, high procedural stability, yet has high convergence and accuracy, is used in this paper to study the thermal and fluid relation in the micro channel.

Nanoparticles' effect on fluids has been studied widely over the years, ranging from their use in heat transfer to fluid transport in various media, including channel flows, heat exchangers, solar collectors, and medical applications,

among others. The impact of improved thermal conduction leads to efficient heat transfer, energy conservation, improved thermal loading and less stress are significant and interesting observations. [32-39]. Studies presented in the literature do not capture both experimentally/ theoretically the relationship between the nanolayer and the particles for the mineral oil transport. It is not clear if this impact thermal distribution. Also, to what extent does this particle layer affect thermal conductivity, as it may explain the atypical rise in thermal conductivity.

In light of the above, this paper focus on theoretical study of the nanoscale relationship between the hydrodynamic nano layer, nanoparticle size, and inter-particle spacing of particles under thermal heating using metallic and non-metallic particles in mineral oil. To understand the anomalous increase in base fluid thermal conductivity upon nanoparticles inclusion and fluid performance under thermal load. Utilizing mineral oil (ISO grade 32), a mineral-based hydraulic fluid which serves as sealant, lubricant or coolant due to its inherent properties such as resistance to thermal breakdown, low temperature fluidity, amongst others. ISO grade 32 was selected over other grades including 46 and 68 due to its low viscosity of 30.4 cSt at 40 °C [40], which makes it a thin oil, flowing easily and suitable for static and high-powered rotating machinery. Copper and graphite as metallic and non-metallic nanoparticles respectively, aiding its stability and performance. The mechanics of the heat transfer and fluid transport are described with nonlinear, coupled models analyzed using the Homotopy perturbation method. Thereafter, the impact of rheological parameters are presented and discussed. Understanding derived from study may provide good insights into thermal transport designs of oil additives applications.

MODEL DEVELOPMENT

The mineral oil is characterized as a micropolar fluid, composed of arbitrary, rigid, and spherical oriented particles exhibiting micro rotations and flowing under steady-state conditions [41-42]. The magnetic field is applied perpendicularly to the microchannel, the flow maintains a constant speed through the channel. The nanofluid considered is a Newtonian fluid, with the temperature of the top and bottom wall taken as T_2 and T_1 respectively. As seen in Figure 1, the plate surface is perpendicular to the y-axis and normal to the x-axis. With the following dimension: length 50 mm, depth 40 mm, width 35 mm and depth between the plates 100 μm.

Considered Assumptions

The nanofluid mix is assumed to be incompressible and in non - thermal equilibrium (due to localized heating effect or thermal gradient in the channel). With respect to the above conditions, the continuity, momentum, micro-rotation and energy equations, which depict the concept of mass, momentum of flow, fluid particle rotation and energy conservation in and out of the channel, are reformulated as follows [43-44]:

Continuity equation

$$\frac{\partial u}{\partial x}+\frac{\partial v}{\partial y}=0, \tag{1}$$

Momentum equation

$$\rho_{nf}\left(u\frac{\partial u}{\partial x}+v\frac{\partial u}{\partial y}\right)=-\frac{\partial p}{\partial x}+(\mu_{nf}+\kappa)\left(\frac{\partial^2 u}{\partial x^2}+\frac{\partial^2 u}{\partial y^2}\right)+\kappa\frac{\partial N}{\partial y}-\sigma_f B_0^2 u, \tag{2}$$

$$\rho_{nf}\left(u\frac{\partial v}{\partial x}+v\frac{\partial v}{\partial y}\right)=-\frac{\partial p}{\partial x}+(\mu_{nf}+\kappa)\left(\frac{\partial^2 v}{\partial x^2}+\frac{\partial^2 v}{\partial y^2}\right)-\kappa\frac{\partial N}{\partial x}, \tag{3}$$

Micro-rotation equation

$$\rho_{nf} j\left(u\frac{\partial N}{\partial x}+v\frac{\partial N}{\partial y}\right)=-\kappa\left(2N+\frac{\partial u}{\partial y}-\frac{\partial v}{\partial x}\right)+\gamma_{nf}\left(\frac{\partial^2 N}{\partial x^2}+\frac{\partial^2 N}{\partial y^2}\right), \tag{4}$$

Energy equation

$$u\frac{\partial T}{\partial x}+v\frac{\partial T}{\partial y}=\frac{k_{nf}}{(\rho c_p)_{nf}}\left(\frac{\partial^2 T}{\partial x^2}+\frac{\partial^2 T}{\partial y^2}\right)-\frac{1}{(\rho c_p)_{nf}}\frac{\partial q_{rad}}{\partial y}+Q(T-T_\infty), \tag{5}$$

Where the magnetic field, pressure, velocity in the x and y directions, electric conductivity, temperature, viscosity vortex, micro-rotation velocity, radiative heat flux, spin gradient viscosity, and micro-inertia density respectively

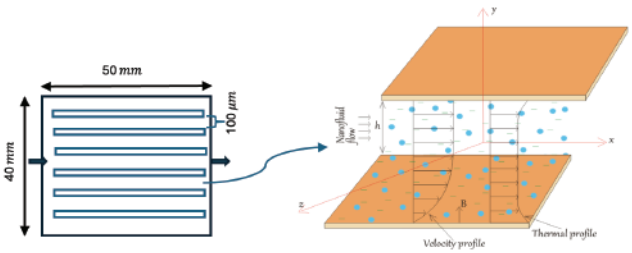

Figure 1a. Physical model and schematics of the problem.

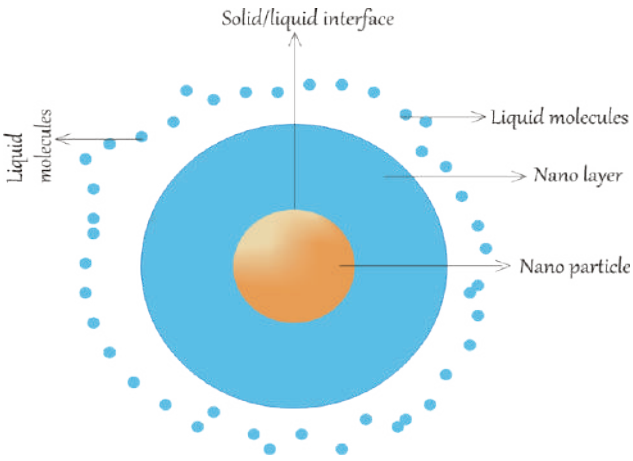

Figure 1b. Nanoparticle interfacial layer.

are represented as B_0, P, u, v, σ_f, T, κ, N, q_{rad}, j *and* γ_{nf}. Where $\gamma_{nf} = \left(\mu_{nf} + \frac{\kappa}{2}\right) j$.

Rooseland approximation is used to quantify the radiation heat transfer [45]. This approximation technique is confirmed to be valid for short radiation travel distances before scattering. Radiative heat transfer leaves the micropolar fluid before it is scattered within the thick optical fluid. The Rooseland approximation is formed to account for this effect. Radiative heat flux is presented as:

$$q_{rad.} = -\left(4\sigma^*/3k^*_{nf}\right)\frac{\partial T^4}{\partial y}. \quad (6)$$

The coefficient of absorption of the nanofluid is given as k^*_{nf} and the Stefan Boltzmann constant is represented as σ^*.More so, temperature of flow varies with distance. Therefore, the Taylor series is utilized in expanding temperature, T^4. T^4 is expanded about T_∞ by neglecting higher order terms.

$$T^4 \cong 4T_\infty^3 T - 3T_\infty^4. \quad (7)$$

Eq. (5) is rewritten:

$$u\frac{\partial T}{\partial x} + v\frac{\partial T}{\partial y} = \frac{k_{nf}}{(\rho c_p)_{nf}}\left(\frac{\partial^2 T}{\partial x^2} + \frac{\partial^2 T}{\partial y^2}\right) - \frac{16\sigma^* T_\infty^3}{3k^*_{nf}(\rho c_p)_{nf}}\frac{\partial^2 T}{\partial y^2} + Q(T - T_\infty), \quad (8)$$

The effective density and dynamic viscosity are given as ρ_{nf} and μ_{nf}, while $(\rho Cp)_{nf}$ and k_{nf} are the specific capacitance of heat and thermal conductivity of the nanofluid, respectively. The Eqs. (9) show the nanofluid parameters where the d is the diameter of the nanoparticle, Γ is the interfacial thickness layer, β is the nanolayer ratio, γ is the ratio of the interfacial layer thickness and particle size, ϕ is the nanoparticle volume and electrical conductivity σ_{nf}; these are introduced as [24]. The liquid-solid interfacial layer and nanoparticle diameter play a crucial role in the amplified thermal conductivity. The classical thermal conductivity relations proposed by Maxwell [22] and Hamilton and Crosser [23] were not utilized in this paper since the relations do not consider the interfacial layer and nanoparticle diameter in their thermal conductivity relations. Consequently, their model did not sufficiently capture the anomalous increased nanofluid thermal conductivity. Also, the relationship between the nanofluid viscosity and the pure fluid viscosity is examined using the dynamic viscosity model formulated by Graham [26] and Gasukonda et al. [27], where ψ the inter-particle spacing between the particles is considered. This gives better insight into the rheological properties of the nanoparticles and the base fluid. The thermophysical properties of the fluid and nanoparticles are expressed in Table 1.

$$\begin{aligned}
&\rho_{nf} = (1-\phi)\rho_f + \phi\rho_s,\\
&\left(\rho C_p\right)_{nf} = (1-\phi)\left(\rho C_p\right)_f + \phi\left(\rho C_p\right)_s,\\
&\frac{\mu_{nf}}{\mu_f} = \left(1 + 2.5\phi + 4.5\left(\frac{1}{2\psi/d(2+2\psi/d)(1+2\psi/d)^2}\right)\right),\\
&\frac{k_{nf}}{k_f} = \frac{(k_s-\beta k_f)\phi\beta(2\gamma_1^3-\gamma_2^3+1)+(k_s-2\beta k_f)\gamma_1^3[\phi\gamma_2^3(\beta-1)+1]}{\gamma_1^3(2\gamma_1^3-\gamma_2^3+k_s)+(\beta k_f-k_s)\phi(\gamma_1^3+\gamma_2^3-1)}.\\
&\text{Where } \gamma_1 = 1+\frac{\Gamma}{2d},\ \gamma_2 = 1+\frac{\Gamma}{d}
\end{aligned} \quad (9)$$

Given the microelements rotational factor close to the wall as s. Hence, s = 0, denotes there is no microelements close to the wall and particle flow concentration as occurred. Turbulent and weak concentration occurs at s = 1 and s = 0.5, respectively. Fluid suction and injection occur at $v_0 > 0$ and $v_0 < 0$.

The principle of energy conservation is satisfied at the nanoscale with the no-slip and no thermal jump condition, due to velocity and temperature of the fluid layer in contact with the channel are similar i.e. no discontinuity in the channel. This is presented in Eq. (10) below:

$$\begin{aligned}
&u = 0,\ v = -v_0 \quad N = -s\left.\frac{\partial u}{\partial y}\right|_{y=-h} \quad T = T_1,\ At\ \ y = -h,\\
&u = 0,\ v = v_0, \quad N = -s\left.\frac{\partial u}{\partial y}\right|_{y=+h} \quad T = T_2,\ At\ \ y = +h.
\end{aligned} \quad (10)$$

With similarity variables given as:

$$\begin{aligned}
&\eta = \frac{y}{h}, u = -\frac{v_0 x}{h}f'(\eta), N = \frac{v_0 x}{h^2}g(\eta), v = v_0 f(\eta),\\
&\theta = (T-T_1)/(T_2-T_1), T_2 = T_1 + Ax.
\end{aligned} \quad (11)$$

The similarity variables in Eq. (11) is substituted into the governing relations Eq. (1-4,8) and boundary conditions Eq. (10). Neglecting the pressure gradient in the governing relations, the equations are transformed into an ordinary differentials. To further simplify the problem, it is non-dimensionalized into physical parameters and simply expressed as Eq.(12-15) below, with the physical parameters given as Eq. (16):

Table 1. Thermal physical properties of nanofluid. [13, 46, 47]

	$\rho(Kg/m^3)$	Cp (J/KgK)	$k(W/mK)$
Copper (Cu)	8933	385	401
Graphite	2210	709	1950
Mineral oil (ISO grade 32)	861.55	1867.31	0.1345

$$\left(1+\left(1+2.5\phi+4.5\left(\frac{1}{2\psi/d(2+2\psi)(1+2\psi/d)^2}\right)\right)\chi\right)f^{iv} - \left(1+2.5\phi+4.5\left(\frac{1}{2\psi/d(2+2\psi)(1+2\psi/d)^2}\right)\right)\chi g'' - \left(1-\phi+\frac{\rho_s}{\rho_f}\phi\right)\left(1+2.5\phi + 4.5\left(\frac{1}{2\psi/d(2+2\psi)(1+2\psi/d)^2}\right)\right)Re(ff''' - f'f'') - \left(1+2.5\phi+4.5\left(\frac{1}{2\psi/d(2+2\psi)(1+2\psi/d)^2}\right)\right)Mf'' = 0, \quad (12)$$

$$\left(1+\left(\frac{1+2.5\phi+4.5}{2}\left(\frac{1}{2\psi/d(2+2\psi)(1+2\psi/d)^2}\right)\right)\chi\right)g'' + \left(1+2.5\phi+4.5\left(\frac{1}{2\psi/d(2+2\psi)(1+2\psi/d)^2}\right)\right)\chi(f''-2g) - \left(1-\phi+\frac{\rho_s}{\rho_f}\phi\right)\left(1+2.5\phi + 4.5\left(\frac{1}{2\psi/d(2+2\psi)(1+2\psi/d)^2}\right)\right)Re(fg'-gf') = 0, \quad (13)$$

$$\theta''+\left((1-\phi)+\frac{(\rho c_p)_s}{(\rho c_p)_f}\phi\right)\left(\frac{3}{3+4Nr}\right)\frac{k_f}{k_{nf}}PrRe(f'\theta-f\theta')+\xi\theta=0. \quad (14)$$

The boundary conditions are presented as:

$$f(-1)=-1,\ f'(-1)=0,\ f(+1)=1,\ f'(+1)=0,\quad g(-1)=0,\ g(+1)=0,\quad \theta(-1)=0,\ \theta(+1)=1. \quad (15)$$

Where Reynold number is defined as Re, magnetic parameter is denoted as M. Prandtl number is shown as Pr, radiation parameter is Nr and heat generation is given as ξ, micropolar parameter as χ accounts for the particle micro-rotation throughout the fluid. Justifying the colloidal stability of fluid elements to remain dispersed. The non-dimensional parameters are presented as follows:

$$\chi=\kappa/\mu_f,\ P_r=\mu_f C_{p,f}/k_f,\ \mathrm{Nr}=k_{nf}k^*_{nf}/4\sigma^*T_\infty^3,\quad Re=\rho_f v_0 h/\mu_f,\ M=\sigma_f B_0^2 h^2/\mu_f,\ \xi=\frac{Q(\rho C_P)_{nf}}{(T-T_\infty)}. \quad (16)$$

Fluid undergoes suction when Re > *0*; similarly, injection flow is seen when Re < *0*. Important engineering parameters of physical impact are the skin friction and Nusselt number, which are presented as:

$$C_f^*=-\left(\frac{2}{\rho_f u^2}\right)(\mu_{nf}+\kappa)\left.\frac{\partial u}{\partial y}\right|_{y=-h},\quad Nu^*=-\left(\frac{h}{k_f(T_2-T_1)}\right)\left(k_{nf}+\frac{16\sigma^*T_\infty^3}{3k^*_{nf}}\right)\left.\frac{\partial T}{\partial y}\right|_{y=-h}. \quad (17)$$

With the aid of similarity variables in Eq. (11), we can write Eq (17) as:

$$C_f=\left|\left(\frac{\mu_{nf}}{\mu_f}+\chi\right)f''(-1)\right|,\quad Nu=\left|\frac{k_{nf}}{k_f}\left(\frac{3+4Nr}{3}\right)\theta'(-1)\right|. \quad (18)$$

The concentration ratio of pure fluid to solid particles is considered low. Therefore, the nanoparticle concentration volume range of 1-8% of the total volume is selected, which is within reasonable range of nanoparticle concentration for microfluidics [48]. The flow condition is for steady/laminar flow. Therefore, Reynolds number were selected over a reasonable range $5 \le Re \le 20$ for entry region length with no surface roughness [49], the micro polar parameter is selected over a low range $1 \le \chi \le 8$ for low micro-rotation of fluid particles. The nanolayer range is selected over a range $0.45 \le h \le 1$ for spherical-shaped particles. This is based on molecular dynamics simulation verified with experiment by Yu et al [50] and consistent with analysis reported by Yu and Choi [51]. The diameter range varies between 10 nm ≤ d ≤ 40nm for the nanoparticles. The nanoparticles induce depletion in the nanolayer region if it is ten times larger than the molecular diameter of water. This is valid for mineral oil (ISO grade 32) having a density lower than water [39,52-54]. Other parameters used are selected over a reasonable range from the values expressed in [24].

Analytical Solution

The fluid transport and heat transfer through the channel, considering the interfacial hydrodynamic layer, diameter of the nano-sized particle and thermal radiation, is studied using the Homotopy perturbation method (HPM). The fundamentals and principles of HPM, an analytical method, have been extensively described in [55-56] by J.H. He. HPM, a method of approximate analytical solution with fast convergence and procedural stability is the method selected to obtain the solutions to the system of coupled nonlinear boundary value problem. Applying the HPM procedure as discussed above to the governing equations, the Homotopy of the Eqs. (12-14) can be constructed as follows

$$(p,\eta)=(1-p)\left[\frac{d^4f}{d\eta^4}\right] + p\left[\begin{array}{l}\frac{d^4f}{d\eta^4}-\left(1+2.5\phi+4.5\left(\frac{1}{\frac{2\psi}{d(2+2\psi)\left(1+\frac{2\psi}{d}\right)^2}}\right)\right)\chi\frac{d^2g}{d\eta^2} \\ -\left(1-\phi+\frac{\rho s}{\rho f}\phi\right)\left(1+2.5\phi+4.5\left(\frac{1}{\frac{2\psi}{d(2+2\psi)\left(1+\frac{2\psi}{d}\right)^2}}\right)\right) \\ Re\left(f\frac{d^3f}{d\eta^3}-f\frac{d^2f}{d\eta^2}\right)- \\ \left(1+2.5\phi+4.5\left(\frac{1}{\frac{2\psi}{d(2+2\psi)\left(1+\frac{2\psi}{d}\right)^2}}\right)\right)M^2\frac{d^2f}{d\eta^2}\end{array}\right] \Big/\left(1+\left(1+2.5\phi+4.5\left(\frac{1}{2\psi/d(2+2\psi)(1+2\psi/d)^2}\right)\right)\chi\right)=0 \quad (19)$$

$$H_2(p,\eta)=(1-p)\left[\frac{d^2g}{d\eta^2}\right]+p\left[\frac{d^2g}{d\eta^2}-\left(1+2.5\phi+4.5\left(\frac{\frac{1}{2\psi}}{d(2+2\psi)\left(1+\frac{2\psi}{d}\right)^2}\right)\right)\chi\left(\frac{d^2f}{d\eta^2}-2g\right)-\left(1-\phi+\frac{\rho s}{\rho f}\phi\right)(1-\phi)^{2.5}Re\left(f\frac{dg}{d\eta}-g\frac{df}{d\eta}\right)\right]/\left(1+\left(\frac{1+2.5\phi+4.5}{2}\left(\frac{1}{2\psi/d(2+2\psi)(1+2\psi/d)^2}\right)\right)\chi\right)=0, \quad (20)$$

$$H_3(p,\eta)=(1-p)\left[\frac{d^2\theta}{d\eta^2}\right]+p\left[\frac{d^2\theta}{d\eta^2}+\left((1-\phi)+\frac{(\rho C_p)_s}{(\rho C_p)_f}\phi\right)\left(\frac{3N}{3N+4}\right)\frac{k_f}{k_{nf}}PrRe\left(\frac{df}{d\eta}\theta-f\frac{d\theta}{d\eta}\right)+\xi\theta\right]=0. \quad (21)$$

Substituting the homotopy of the governing Eq. (19-21) in the power series (P) for velocity, rotation and temperature presented in Eq. (22) below:

$$f=P^0f_0+P^1f_1+P^2f_2+\ldots \quad (22a)$$

$$g=P^0g_0+P^1g_1+P^2g_2+\ldots \quad (22b)$$

$$\theta=P^0\theta_0+P^1\theta_1+P^2\theta_2+\ldots \quad (22c)$$

These are expanded from the zeroth to the second order for accuracy and convergence of the analytical solutions. Eq. (22a) is substituted into (19) for the velocity profile and selected at the various order (zeroth to second) yields

$$p^0:\frac{d^4f_0}{d\eta^4} \quad (23a)$$

$$p^1:\frac{\left[\begin{array}{l}\frac{d^4f_1}{d\eta^4}-\left(1+2.5\phi+4.5\left(\frac{\frac{1}{2\psi}}{d(2+2\psi)\left(1+\frac{2\psi}{d}\right)^2}\right)\right)\chi\frac{d^2g_0}{d\eta^2}-\left(1-\phi+\frac{\rho s}{\rho f}\phi\right)\\ \left(1+2.5\phi+4.5\left(\frac{\frac{1}{2\psi}}{d(2+2\psi)\left(1+\frac{2\psi}{d}\right)^2}\right)\right)Re\left(f_0\frac{d^3f_0}{d\eta^3}-f_0\frac{d^2f_0}{d\eta^2}\right)-\\ \left(1+2.5\phi+4.5\left(\frac{\frac{1}{2\psi}}{d(2+2\psi)\left(1+\frac{2\psi}{d}\right)^2}\right)\right)M^2\frac{d^2f_0}{d\eta^2}\end{array}\right]}{\left(1+\left(1+2.5\phi+4.5\left(\frac{1}{2\psi/d(2+2\psi)(1+2\psi/d)^2}\right)\right)\chi\right)} \quad (23b)$$

$$p^2:\frac{\left[\begin{array}{l}\frac{d^4f_2}{d\eta^4}-\left(1+2.5\phi+4.5\left(\frac{1}{2\psi/d(2+2\psi)(1+2\psi/d)^2}\right)\right)\chi\frac{d^2g_1}{d\eta^2}-\left(1-\phi+\frac{\rho s}{\rho f}\phi\right)\\ \left(1+2.5\phi+4.5\left(\frac{1}{2\psi/d(2+2\psi)(1+2\psi/d)^2}\right)\right)Re\,f_0\frac{d^3f_1}{d\eta^3}\\ +\left(1-\phi+\frac{\rho s}{\rho f}\phi\right)(1-\phi)^{2.5}Re\,f_0\frac{d^2f_1}{d\eta^2}-\\ \left(1+2.5\phi+4.5\left(\frac{1}{2\psi/d(2+2\psi)(1+2\psi/d)^2}\right)\right)M\frac{d^2f_1}{d\eta^2}\end{array}\right]}{/\left(1+\left(1+2.5\phi+4.5\left(\frac{1}{2\psi/d(2+2\psi)(1+2\psi/d)^2}\right)\right)\chi\right)} \quad (23c)$$

Eq. (22b) is substituted into (20) for the rotation profile and selected at the various order (zeroth to second) yields

$$p^0:\frac{d^2g_0}{d\eta^2} \quad (24a)$$

$$p^1:\frac{\left[\begin{array}{l}\frac{d^2g_1}{d\eta^2}-\left(1+2.5\phi+4.5\left(\frac{1}{2\psi/d(2+2\psi)(1+2\psi/d)^2}\right)\right)\chi\left(\frac{d^2f_0}{d\eta^2}-2g_0\right)-\left(1-\phi+\frac{\rho s}{\rho f}\phi\right)\\ \left(1+2.5\phi+4.5\left(\frac{1}{2\psi/d(2+2\psi)(1+2\psi/d)^2}\right)\right)Re\left(f_0\frac{dg_0}{d\eta}-g_0\frac{df_0}{d\eta}\right)\end{array}\right]}{/\left(1+\frac{\left(1+2.5\phi+4.5\left(\frac{1}{2\psi/d(2+2\psi)(1+2\psi/d)^2}\right)\right)}{2}\chi\right)} \quad (24b)$$

$$p^2:\frac{\left[\begin{array}{l}\frac{d^2g_2}{d\eta^2}+\left(1+2.5\phi+4.5\left(\frac{1}{2\psi/d(2+2\psi)(1+2\psi/d)^2}\right)\right)\chi\frac{d^2f_1}{d\eta^2}-2g_1-\left(1-\phi+\frac{\rho s}{\rho f}\phi\right)\\ \left(1+2.5\phi+4.5\left(\frac{1}{2\psi/d(2+2\psi)(1+2\psi/d)^2}\right)\right)Re\,f_0\frac{dg_1}{d\eta}+\left(1-\phi+\frac{\rho s}{\rho f}\phi\right)\\ \left(1+2.5\phi+4.5\left(\frac{1}{2\psi/d(2+2\psi)(1+2\psi/d)^2}\right)\right)Reg_0\frac{df_1}{d\eta}\end{array}\right]}{/\left(1+\frac{\left(1+2.5\phi+4.5\left(\frac{1}{2\psi/d(2+2\psi)(1+2\psi/d)^2}\right)\right)}{2}K\right)} \quad (24c)$$

Eq. (22c) is substituted into (21) for the temperature profile and selected at the various order (zeroth to second) yields

$$p^0:\frac{d^2\theta_0}{d\eta^2} \quad (25a)$$

$$p^1:\frac{d^2\theta_1}{d\eta^2}+\left((1-\phi)+\frac{(\rho C_p)_s}{(\rho C_p)_f}\phi\right)\left(\frac{3Nr}{3Nr+4}\right)\frac{k_f}{k_{nf}}PrRe\left(\frac{df_0}{d\eta}\theta_0-f_0\frac{d\theta_0}{d\eta}\right)+\xi\theta_0 \quad (25b)$$

$$p^2:\frac{d^2\theta_2}{d\eta^2}+\left((1-\phi)+\frac{(\rho C_p)_s}{(\rho C_p)_f}\phi\right)\left(\frac{3Nr}{3Nr+4}\right)\frac{k_f}{k_{nf}}PrRe\left(\frac{df_0}{d\eta}\theta_1-f_0\frac{d\theta_1}{d\eta}\right)+\xi\theta_1 \quad (25c)$$

The Eq. (23-25) is analyzed using the boundary condition Eq. (15) at the various orders of the homotopic series. The final solution for the velocity, rotation and temperature profile at the various order (zero to second) are summed up and reported as follow in Eq. (26)-(28).

$$\begin{aligned}f=&\frac{3\eta}{2}-\frac{\eta^3}{2}+\left(-(Re/140-Re\,\phi/140)/8\chi\left(1+2.5\phi+4.5\left(\frac{1}{2\psi/d(2+2\psi/d)(1+2\psi/d)^2}\right)\right)+8\right)-\\&(Re\,\phi\,\rho s)/\left(1120\rho f\left(\chi\left(1+2.5\phi+4.5\left(\frac{1}{2\psi/d(2+2\psi/d)(1+2\psi/d)^2}\right)\right)+7\right)\right.\\&\left.+(Re\,\phi\,\rho s)/\left(560\rho f\left(\chi\left(1+2.5\phi+4.5\left(\frac{1}{2\psi/d(2+2\psi/d)(1+2\psi/d)^2}\right)\right)+1\right)\right)\eta^7\right.\\&\left.+\left(\begin{array}{l}((3\,Re)/40-\\(3\,Re\,\phi)/40\end{array}\right)\right.\\&\left./\left(6\chi\left(1+2.5\phi+4.5\left(\frac{1}{2\psi/d(2+2\psi/d)(1+2\psi/d)^2}\right)\right)+6\right)\right.\\&\left.+(Re\,\phi\,\rho s)/\left(80\rho f(\chi\left(1+2.5\phi+4.5\left(\frac{1}{2\psi/d(2+2\psi/d)(1+2\psi/d)^2}\right)\right)+1)\right)\eta^6\right.\\&\left.+(-((3\,Re)/16-(3\,Re\,\phi)\right.\\&/16+\left(M\left(1+2.5\phi+4.5\left(\frac{1}{2\psi/d(2+2\psi/d)(1+2\psi/d)^2}\right)\right)\right.\\&\left./8\right)\left(5\chi\left(\begin{array}{l}1+2.5\phi\\+4.5\left(\frac{1}{2\psi/d(2+2\psi/d)}\right.\\(1+2\psi/d)^2\end{array}\right)\right)+5\right)\\&+\ldots..\end{aligned} \quad (26)$$

$$
\begin{aligned}
g = {} & \frac{\eta}{2} + \frac{1}{2}\eta^4\Bigg[\Bigg(\Bigg(Re\left(1 + 2.5\phi + 4.5\left(\frac{1}{2\psi/d(2+2\psi/d)(1+2\psi/d)^2}\right)\right) \\
& /2\left(Re\,\phi\left(4.5\left(\frac{1}{2\psi/d(2+2\psi/d)}{(1+2\psi/d)^2}\right)\right)\right)\Bigg)/2\Bigg) \\
& /\left(4(\chi\left(1 + 2.5\phi + 4.5\left(\frac{1}{2\psi/d(2+2\psi/d)(1+2\psi/d)^2}\right)\right) + 2)\right) \\
& + \left(Re\,\phi\,ps\left(4.5\left(\frac{1}{\frac{2\psi/d}{(2+2\psi/d)(1+2\psi/d)^2}}\right)\right)\right) \\
& /\left(8\rho f\left(\chi\left(1 + 2.5\phi + 4.5\left(\frac{1}{2\psi/d(2+2\psi/d)(1+2\psi/d)^2}\right)\right) + 2\right)\right) + \\
& \eta^5\Bigg(\Bigg(\Bigg(\Bigg(Re\left(\frac{1 + 2.5\phi + 4.5}{2\psi/d(2+2\psi/d)(1+2\psi/d)^2}\right)\Bigg)/4 - \Bigg(Re\,\phi\left(1 + 2.5\phi + 4.5\left(\frac{1}{2\psi/d(2+2\psi/d)(1+2\psi/d}\right.\right. \\
& /4 \\
& /\left(5\left(\chi\left(1 + 2.5\phi + 4.5\left(\frac{1}{2\psi/d(2+2\psi/d)(1+2\psi/d)^2}\right)\right) + 2\right)\right) \\
& + \left(Re\,\phi\,\rho s\left(1 + 2.5\phi + 4.5\left(\frac{1}{2\psi/d(2+2\psi/d)}{(1+2\psi/d)^2}\right)\right)\right) \\
& /\left(20\rho f\left(\chi\left(1 + 2.5\phi + 4.5\left(\frac{1}{2\psi/d(2+2\psi/d)(1+2\psi/d)^2}\right)\right) + 2\right)\right) \\
& + \eta^2((2\chi\left(1 + 2.5\phi + 4.5\left(\frac{1}{2\psi/d(2+2\psi/d)}{(1+2\psi/d)^2}\right)\right) \\
& - \left(3\,Re\left(1 + 2.5\phi + 4.5\left(\frac{1}{2\psi/d(2+2\psi/d)(1+2\psi/d)^2}\right)\right)\right))/2 \\
& + \left(3\,Re\,\phi\,ps\left(1 + 2.5\phi + 4.5\left(\frac{1}{2\psi/d(2+2\psi/d)}{(1+2\psi/d)^2}\right)\right)\right)/ \\
& (4\rho f(\chi\left(1 + 2.5\phi + 4.5\left(\frac{1}{2\psi/d(2+2\psi/d)(1+2\psi/d)^2}\right)\right) + 2))) \\
& - (\left(Re\left(1 + 2.5\phi + 4.5\left(\frac{1}{2\psi/d(2+2\psi/d)}{(1+2\psi/d)^2}\right)\right)\right)/2 \\
& +\ldots.
\end{aligned}
\tag{27}
$$

$$
\begin{aligned}
\theta = {} & \begin{pmatrix}
(\eta+1)320k_{nf}\rho\,C_f + 240Nrk_{nf}\rho\,C_f + 71Nr\,PrRe\,\xi\,k_f\rho\,C_f(1-\phi) \\
+ 71Nr\,PrRe\,\xi\,k_f\rho\,C_s\,\phi - 34Nr\,PrR \\
4N\,PrRe\,\xi\,\eta^3k_f\rho\,C_f + 11Nr\,PrRe\,\xi\,\eta^4k_f\rho\,C_f \\
+ 4N\square\square\,PrRe\,\xi\,\eta^5k_f\rho\,C_f - 56Nr\,PrRe\,\xi\,\eta k_f\rho\,C_f(1-\phi) \\
- 56Nr\,PrRe\,\xi\,\eta k_f\rho\,C_s(1-\phi) + 34Nr\,PrRe\,\xi\,\eta^2k_f\rho\,C_f\,\phi \\
- 4Nr\,PrRe\,\xi\,k_f\rho\,C_f\,\eta^3\,\phi - 11Nr\,PrRe\,\xi\,\eta^4k_f \\
-4Nr\,PrRe\,\xi\,\eta^5k_f\rho\,C_f\,\phi - 34Nr\,PrRe\,\xi\,\eta^2k_f\rho\,C_s\,\phi \\
+ 4Nr\,Pr\,\xi\,\eta^3k_f\rho\,C_s\,\phi + 11Nr\,PrRe\,\xi\,\eta^4k_f\rho\,C_s\,\phi \\
+4Nr\,PrRe\,\xi\,\eta^5k_f\rho\,C_f\,\phi
\end{pmatrix} \\
& /(160k_{nf}\rho\,C_f(3N+4)) + \frac{\eta}{2} + 0.5 + \ldots..
\end{aligned}
\tag{28}
$$

As the second-order coefficient for velocity, rotation and temperature in Eqs. (26 - 28) are too voluminous to be written. They are expressed in tables and graphically in the results. The analytical solution obtained from this study was further solved numerically using the Runge-Kutta Fehlberg method to validate the obtained analytical solution through HPM. As observed from Table 2, close-range solutions are observed. This proves the accuracy of the current study with the flow process of the analysis as described in Figure 2.

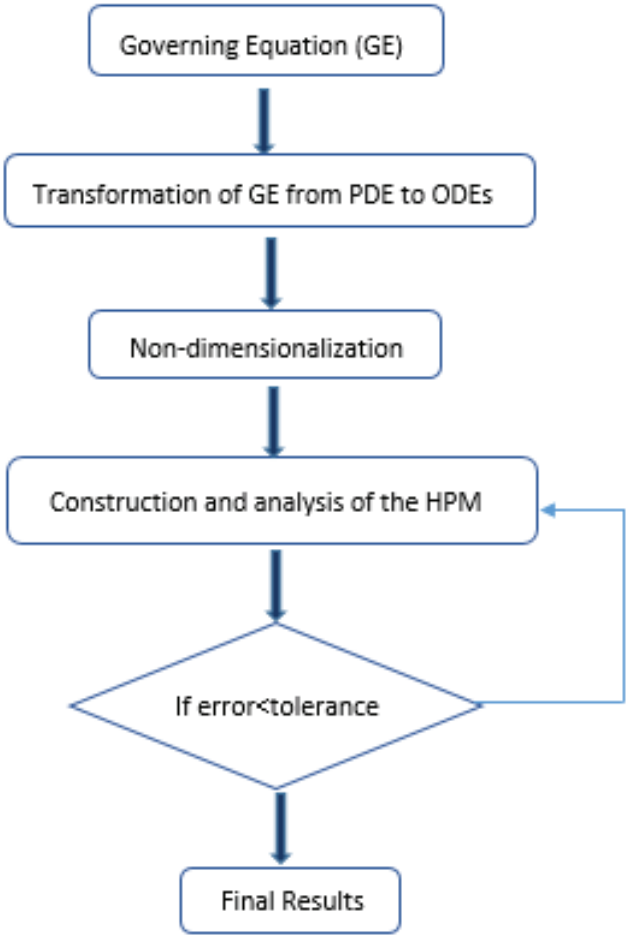

Figure 2. Flow chart of the analysis.

RESULTS AND DISCUSSION

Based on the analytical solutions reported in the previous section, with reference to underlying assumptions and

Table 2. Comparison of values for temperature profile with numerical method

η	$\theta(\eta)$ RKF-45	$\theta(\eta)$ Present study	Error	RMSD
0	0.0000	0.000000000	0.00000000	0
0.2	0.2000	0.200001085	0.00001085	5.42×10^{-7}
0.4	0.4000	0.400001653	0.00001653	8.26×10^{-7}
0.6	0.6000	0.600001598	0.00001598	7.98×10^{-7}
0.8	0.8000	0.800009426	0.00009426	4.71×10^{-6}
1.0	1.0000	1.000000000	0.00000000	0

Table 3. Impact of the Nusselt number on varying parameters of χ=M=1, Re=5, Nr=10 and Pr=10.

Γ	ϕ	ξ	d	ψ	Nusselt1 10^6	Nusselt2 10^6
0.5	0	2	10	1	**1.3162**	**31.0648**
0.75	0.02				**1.3212**	**31.1911**
1	0.04				**1.3262**	**31.3174**
	0.06				**1.3313**	**31.4436**
		4	30	1	**1.3320**	**31.4444**
		6	40	1.5	**1.3328**	**31.4452**

accuracy of the method utilized. These are used to generate and discuss plots here. These show graphically the heat transfer and flow through the microchannel. Reported plots are obtained at a constant value Re = 5, M = 1, Γ = 1, d = 10, β = 1.2, χ = ξ = 1, Nr = 10, Pr = 10, ϕ = 0.01, ψ = 1.5 unless stated otherwise. The validity of the analytical solution obtained in this work, is compared with the Runge Kutta Fehlberg (RKF-45) numerical solution for the simple case. As observed in Table 2, good agreements are established between the methods of solution. Also, the root mean square deviation (RMSD), as a method of quantifying uniformity, shows the temperature distribution pattern is uniform/similar having low values. The impact of the nanolayer between the nanoparticle and fluid, as well as particle size, heat generation, particle volume, and inter-particle spacing, is shown in Table 3. Nusselt[1] refers to heat transfer using copper nanoparticles, and Nusselt[2] using graphite particles. As seen, the rheological parameters have large effects on heat transfer. The effect of large nanoparticle volume and nanolayer on heat transfer, setting constant other rheological parameters, shows increasing heat transfer, which can be physically explained due to higher particle concentration enhancing fluid thermal conductivity and contact area, consequently, heat exchange increases. With larger inter-particle spacing, which decreases particle agglomeration, this impacts thermal conductivity, decreasing fluid heat transfer. Also, a large particle size decreases fluid transfer as it absorbs more heat. The heat transfer rate using graphite particles is very high compared to copper particles, this agrees with the results given by Gosunkanda et al. [27]. However, increasing thermal heat generation ($4 \leq \xi \leq 6$) minimizes the rate of heat transfer. From analysis heat transfer rate of the graphite is about 23 times more compared to copper. This rate is obtained on the basis of constant thermal conductivity of copper i.e. oxidation does not occur. Actually, exposure of copper particles to mineral oil will form a thin oxide layer on the particle surface. This will further reduce conductive properties of copper to < 8.3 % [57]. Increasing the rate derived. Similarly, graphite as it flows through the channel, due to the effect of weak bonds by Van der Waals forces shows inter layer sliding. This impacts the thermal conductivity, hindering heat flow [58]. Consequently, reducing heat transfer rate. Therefore, the derived rate expressed will decrease. The impact of the magnetic field is shown in Figure 3, as seen fluid velocity distribution rises from the bottom plate. The fluid approaches the center of the plate $\eta = 0$, a reverse trend is observed showing velocity drop. This is due to the interaction between the Lorentz force field (which increases due to magnetic intensity) with the micro polarity of the fluid. The rising field intensity along the region of flow resists the flow with rotating particles, reducing fluid streamline patterns. This force is perpendicular to the flow direction and acts as a barrier, altering the flow pattern. The volume concentration effect on fluid transport is shown in Figure 4. This shows an increasing volume concentration of nanoparticles from 1 – 8 %, velocity distribution decreases, which is because of abating thickness in the momentum boundary layer during flow transport. It is observed in Figure 5 that flow declines with rising micro-rotation of fluid particles during flow, as colliding rotating particles lower the kinematic viscosity.

The effect of the magnetic parameter on the fluid micro rotation is reported in Figure 6. This shows rotation of micro particles reduces at the lower plate. Towards the mid – plate rotation of fluid particles rises to the upper plate. This is because of the applied magnetic field known as the Lorentz force through the porous wall, which resists fluid

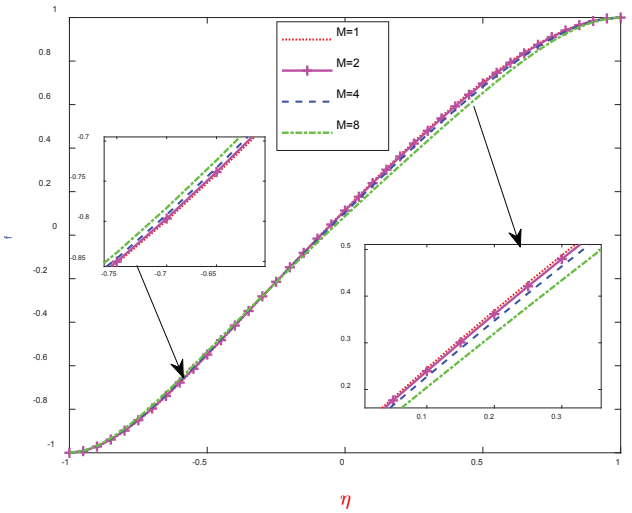

Figure 3. Effect of magnetic parameter on velocity profile.

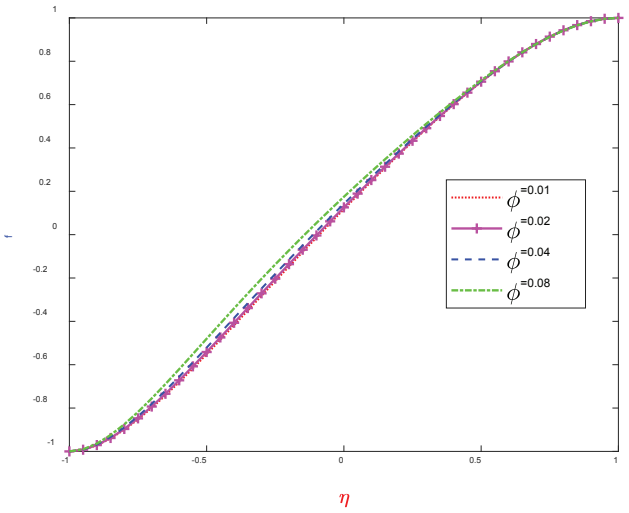

Figure 4. Effect of volume concentration on velocity profile.

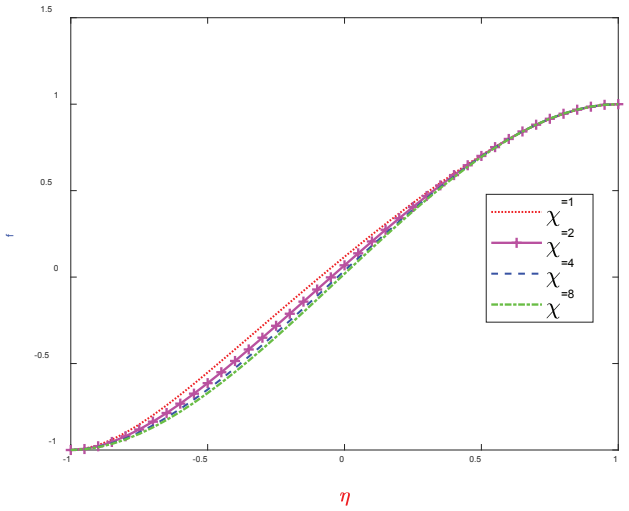

Figure 5. Effect of micropolar parameter on velocity profile.

flow towards the boundary. Enhancement of the nanoparticle volume reduces rotation of fluid particles as seen in Figure 7. This causes high energy exchange between molecules, decreasing the thickness of the boundary layer, consequently reducing micro rotation of fluid particles, towards the upper plate around $0.4 \geq \eta \geq 0.8$ a slight rise in particle rotation is noticed. The effect of increasing micropolar parameter on rotation is shown in Figure 8. As seen in the graphical plot, there is a sharp rise in fluid rotation due to a rise in vortex viscosity. The rotation rises significantly towards the bottom plate, then declines towards the upper plate. The Reynolds parameter impact on the rotation profile is seen in Figure 9, which shows a rise in rotation of fluid particles till about $-1 \geq \eta \geq -0.4$, and thereafter a sharp decline in rotation is noticed up to the wall of the upper plate, which is due to the dominance of inertia fluid forces in this region.

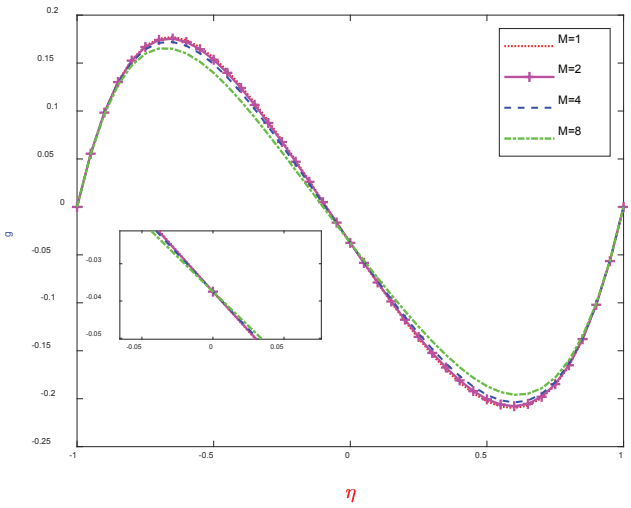

Figure 6. Effect of magnetic parameter on rotation profile.

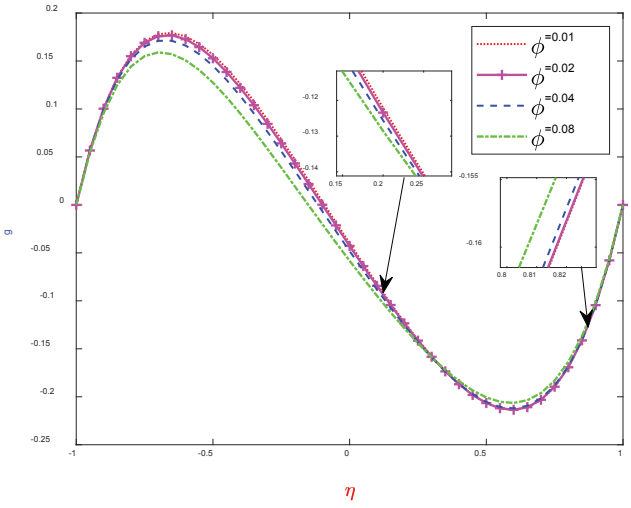

Figure 7. Effect of volume concentration on rotation profile.

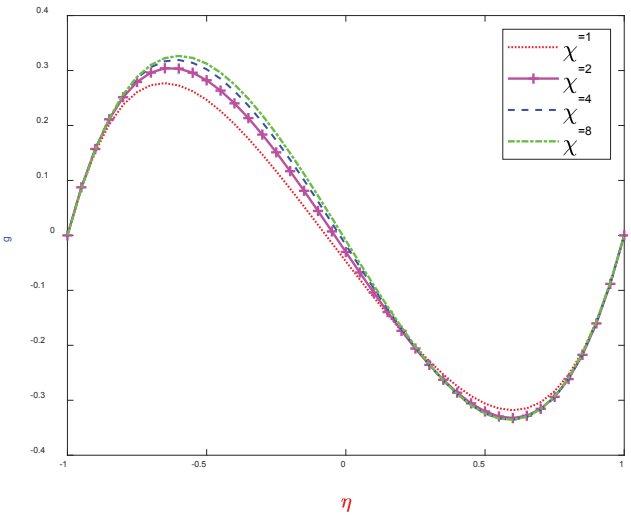

Figure 8. Effect of micropolar parameter on rotation profile.

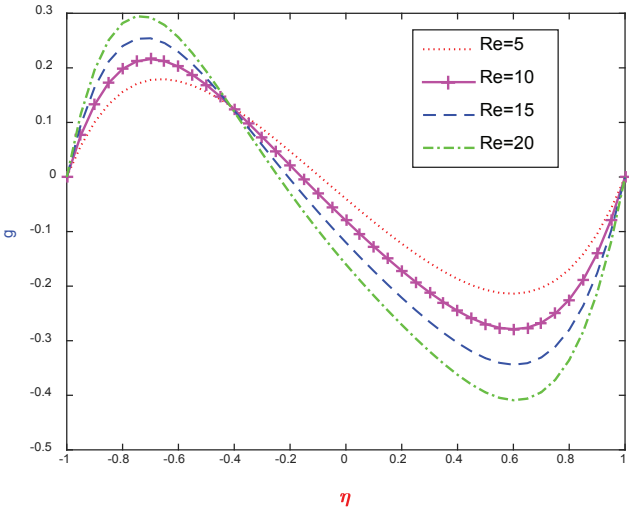

Figure 9. Effect of Reynolds number on rotation profile.

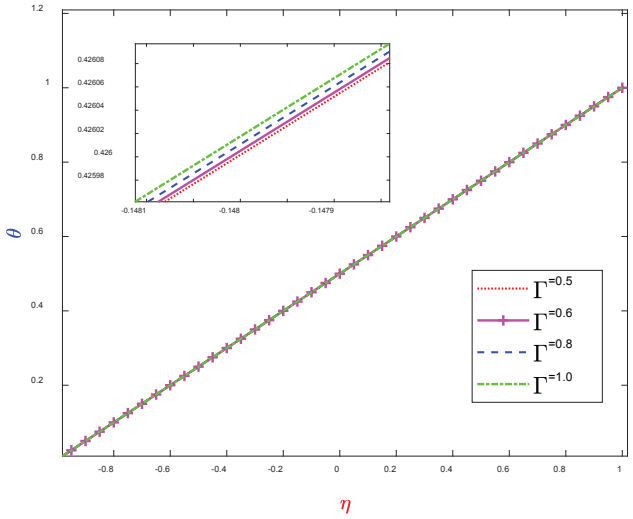

Figure 10. Effect of the nano layer on the temperature profile.

Nanolayer influence on thermal distribution is reported in Figure 10. This shows that increasing the surface layer of the nanoparticle increases fluid temperature. Fluid conductivity increases through improved heat transfer between nanoparticles and fluid, as observed from the graph. Enhanced Nanolayer improves temperature distribution, which is in line with the result reported by Gosunkanda et al. [27]. This conclusion that nanolayer thickness is crucial to thermal conductivity is also supported and experimentally validated by Yu and Choi [51]. The impact of large nano particle size on the nanofluid is observed in Figure 11, which shows that increasing the size of the nano particle from 10nm to 40 nm lowers the thermal profile. This is due to the large surface area of nanoparticles. As separation distance between particle decreases with larger volume concentration, which increases the heat transfer rate, consequently reducing the thermal boundary layer, thus temperature. This agrees with the conclusion by Yu and Choi [51] using experiment, that nanolayer thickness is crucial to thermal enhancement. Volumetric increase of nanoparticles from 1 to 8 % is reported in Figure 12, shows that nanoparticles have a significant influence on thermal distribution. As observed, temperature rise is due to enhanced thermal conductivity from nanoparticle to the base fluid. With higher particle concentration increase, the Van der Waals attractive potential may dominate electro-static repulsive potential, which may cause fluid particles to agglomerate [62]. Heat generation parameter influence on thermal distribution is shown in Figure 13. Heat generation internally is a cumulative effect of thermal energy sources including viscous dissipation and chemical reaction within the fluid. As observed from the graph, increased heat source improves fluid temperature, this is expected as heat generation reduces the thermal layer thickness, thus temperature is higher.

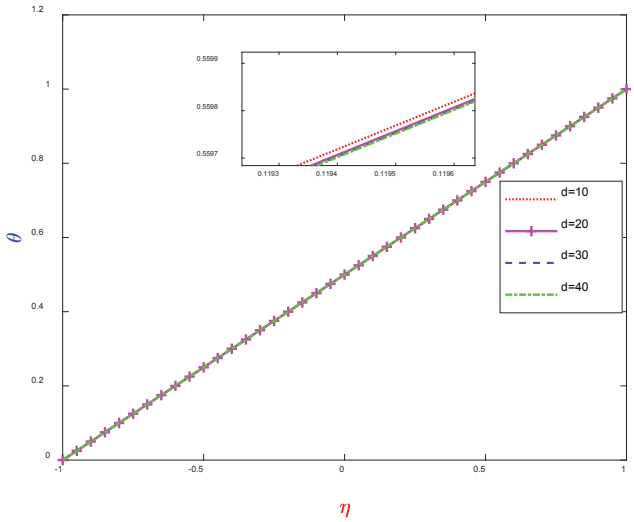

Figure 11. Effect of nanoparticle size on temperature profile.

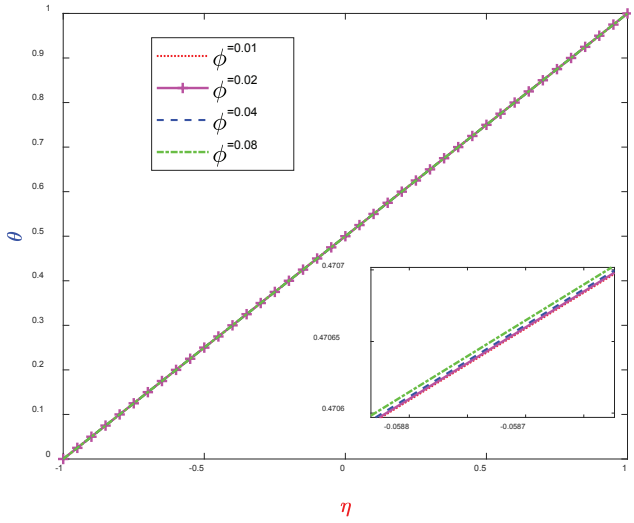

Figure 12. Effect of nanoparticle volume on temperature profile.

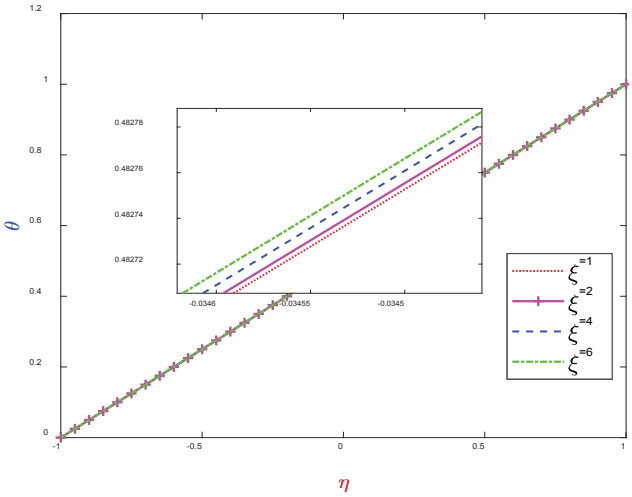

Figure 13. Effect of heat generation on temperature profile.

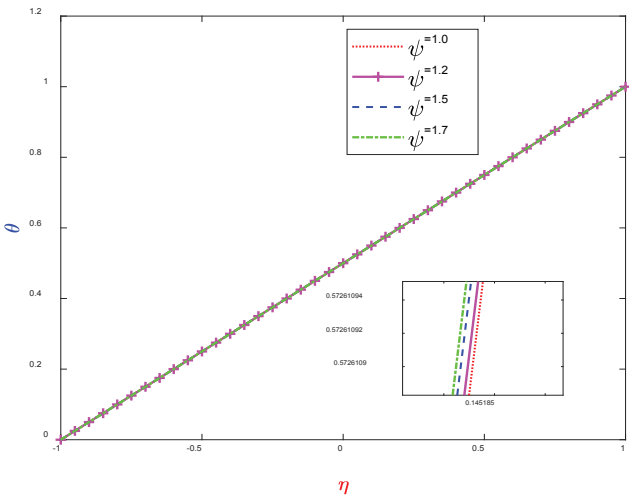

Figure 14. Effect of interparticle spacing on temperature profile.

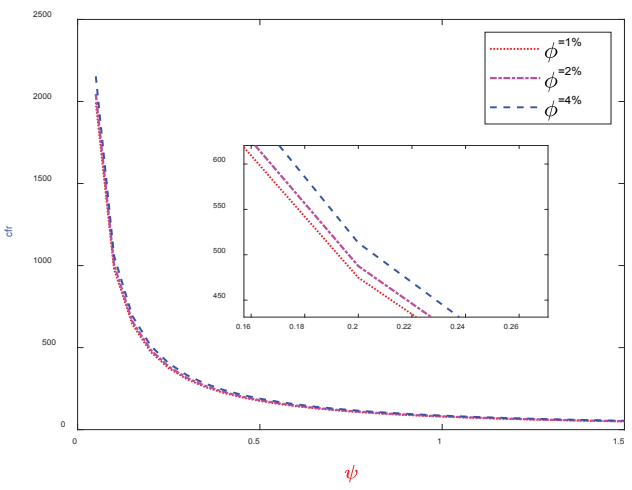

Figure 15a. Effect of copper nanoparticle volume and interparticle spacing on Skin friction.

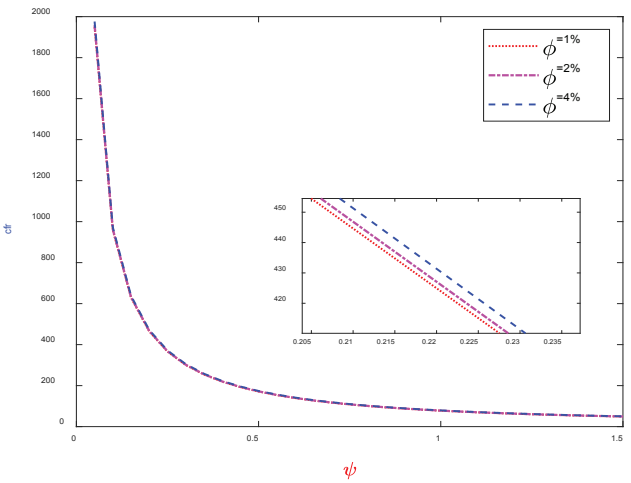

Figure 15b. Effect of graphite nanoparticle volume and interparticle spacing on Skin friction.

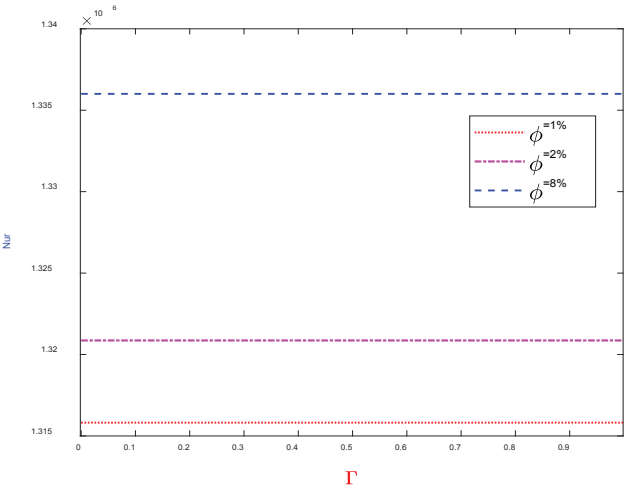

Figure16a. Effect of copper nanoparticle volume and size on Nusselt number.

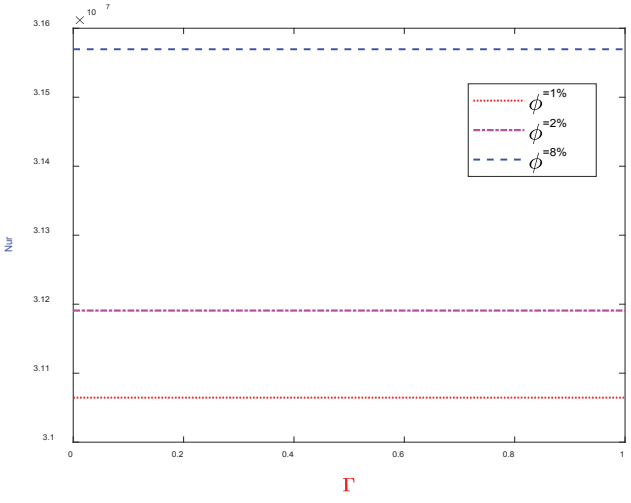

Figure 16b. Effect of graphite nanoparticle volume and size on Nusselt number.

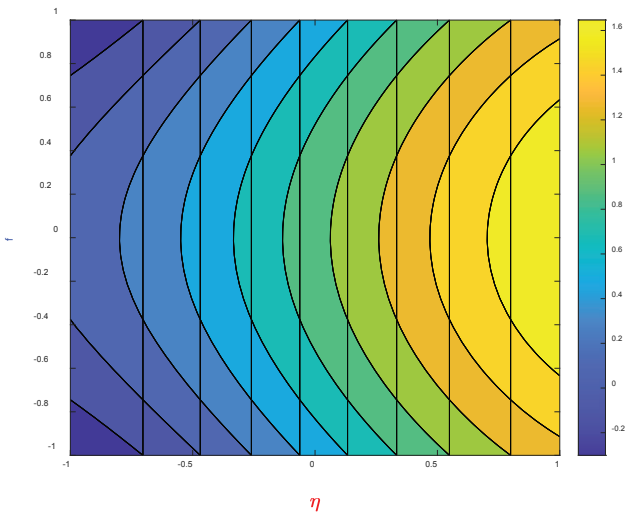

Figure 17. Contour plot of the velocity profile.

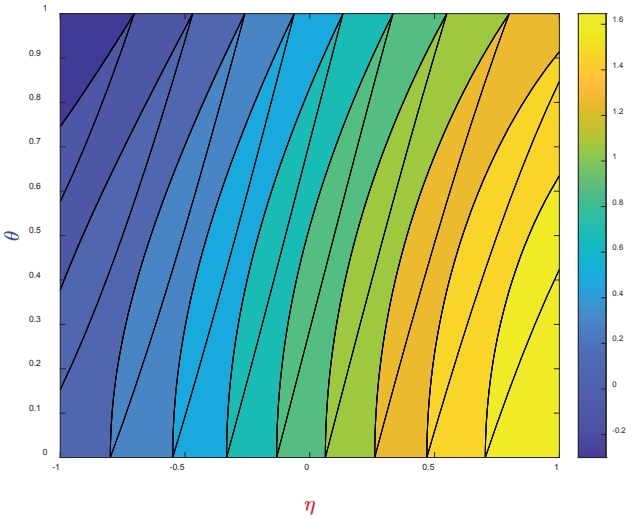

Figure 18. Contour plot of the temperature profile.

The effect of inter-particle spacing on thermal distribution is shown in Figure 14. This shows thermal distribution increases, as heat exchange between fluid molecules become more efficient. Further, the increase in particle separation distance implies lower Van der Waals attractive potential. If this potential is unable to dominate electrostatic repulsive potential the fluid is more stable [62]. Figure 15 shows the effect of nanoparticle volume and inter-particle spacing on skin friction, both on copper and graphite particles, as observed from the graphical representation larger volume of nanoparticles (1 – 8 %) increases skin friction which is highest at particle spacing of approximately 0.1 nm. This can be physically explained due to the larger particle volume increases shear stress between fluid layers, which causes dissipation of energy between the fluid and the boundary walls of the channel. Also, inter-particle spacing, which describes the gap between particles, shows that graphite has lower skin friction compared to copper particles as the gap widens between particles. The Nusselt number effect is shown in Figure 16 for both copper and graphite nanoparticles. As observed from the plot, nanoparticle volume concentration ranging from 1 – 8 % increases the heat transfer across the fluid channel, which can be explained due to the solid particle increase of fluid thermal conductivity. Consequently, heat transfer improves, with graphite having higher thermal characteristics compared to copper particles. However, a limitation which is not considered is particle agglomeration/ sedimentation. High thermal conductivity has been discussed as the focal point for high rate of heat transfer noticed. This might be impacted by nanoparticle agglomeration/sedimentation which increases heat potential energy, therefore heat conduction. This limitation can be addressed through the use of mechanical or chemical stability enhancement techniques to ensure uniform nanoparticle dispersion, which has been described thoroughly in [59]. The contour plot of the flow profile is shown in Figure 17; This is a graphical expression of the magnetic field intensity on the nano-mix flows through the microchannel. Shear stress equally plays a key role, as momentum is highest at the inner walls of the plate. The temperature profile contour plot is seen in Figure 18, as shown; the thermal distribution is higher at the upper plate. This is due to the influence of increased flow in this region.

PRACTICABILITY OF STUDY

The practicability of nanofluid flow in microchannel is an essential requirement, which should be discussed as it pertains to the system performance. Based on the aforementioned flow/operating conditions the impact of thermal variation, magnetic field and shearing as it may impact this study will be discussed.

The effect of thermal variation on the nanofluid is significant as it may cause nanoparticles to agglomerate, which is undesired. High temperature distribution leads to rapid movement of suspended particles, this is accounted for by the Brownian motion. Since high fluid temperature which increases the Brownian motion is also directly proportional to coefficient of diffusion, which causes particles to agglomerate. Addition of surfactant and polymers to nanoparticles have been reported [60-61] to mitigate agglomeration, however treating nanoparticle using plasma and mechanical techniques can help stabilize particles and prevent degradation at high temperature [62].

Several studies have reported nanoparticles agglomerate due to the application of magnetic field [63-64]; this may be due to decreasing particle repulsive potential which leads to particle aggregation. Study [65] suggest the use of oleic acid as dispersant, to help maintain particle stability under magnetic force field.

The effect of shear may be pronounced on nanofluid flow through micron sized channel, as it impact fluid viscosity.

High shearing leads to nanoparticle cluster breakdown. Long shear period may cause cluster to rebuild causing drag. Surfactant and polymer may be used as drag reducing agents or stabilizers. Due to its ability to alters the rheological and chemical nature of the fluid at boundary walls [62].

CONCLUSION

This paper examines the impact of nanoscale relations and heat generation on the thermal fluid transport of mineral oil in a microchannel. The mineral oil base fluid contains metallic and non-metallic particles of copper and graphite, respectively, considering the interfacial layer, which explains the anomalous increase in thermal conductivity of the nanofluid. The effect of fluid rheological parameters such as nano layer, particle size, interparticle spacing, thermal generated heat, and concentration volume of nanoparticles is evaluated on heat transfer and fluid transport. These are developed using nonlinear, higher-order differential models analyzed using the homotopy perturbation method, an analytical method. Results obtained from the study show:

i. A larger nano layer increases the surface layer contact between fluid and particles, consequently improving thermal distribution in the fluid.
ii. High volume of the nanoparticle concentration enhances heat transfer, as particles become more thermally conductive, with graphite having a higher heat transfer rate to copper.
iii. A higher particle concentration increases shear stress at the boundary, with copper having higher stress than graphite.
iv. High heat generation depletes the thermal boundary layer, raising the thermal transfer between the fluid and the channel surface.

This study may provide useful insight into mineral oil applications, including transformer cooling and lubrication in compressors amongst others. Further, since particle interaction, size and density are considered factors affecting nanofluid stability [59]. An interesting future outlook worthy of investigation will be the nanoscale relations effect on nanofluid stability.

AUTHORSHIP CONTRIBUTIONS

A.T. Akinshilo: Conceptualization, methodology/ Analysis, Investigation, Writing.
M.G. Sobamowo :Analysis
L. Kolsi: Validation

DATA AVAILABILITY STATEMENT

The authors confirm that the data that supports the findings of this study are available within the article. Raw data that support the finding of this study are available from the corresponding author, upon reasonable request.

CONFLICT OF INTEREST

The author declared no potential conflicts of interest with respect to the research, authorship, and/or publication of this article.

ETHICS

There are no ethical issues with the publication of this manuscript.

STATEMENT ON THE USE OF ARTIFICIAL INTELLIGENCE

Artificial intelligence was not used in the preparation of the article.

NOMENCLATURE

Re	Reynolds number
M	Magnetic Parameter
Γ	Interfacial layer (nm)
d	Diameter of the nanoparticle (nm)
Pr	Prandtl number
ϕ	Nanoparticle concentration
Nr	Radiation parameter
χ	Micropolar parameter
ξ	Heat generation parameter
β	Nanolayer ratio
γ	Ratio of interfacial layer thickness to particle size
ψ	Interparticle spacing (nm)
Nu	Nusselt number
(u,v)	Velocity components (m/s)
T	Nanofluid Temperature (K)
T_∞	Temperature away from the surface (K)
B_0	Magnetic field $(\Omega^{1/2})\ m^{-1}\ s^{1/2}\ kg^{1/2}$)
q_r	Radiative heat flux Kg/s^3
$\sigma^\star$	Stefan Boltzmann constant $Wm^{-2}\ k^{-4}$
k*	Mean absorption coefficient m^{-1}
ρ	Density kg/m^3
μ	Dynamic viscosity $kgm^{-1}\ s^{-1}$
ν	Kinematic viscosity $m^2\ s^{-1}$
k	Thermal conductivity $Wm^{-1}\ k^{-1}$
(ρC_p)	Heat capacitance $Jm^{-3}\ k^{-1}$
σ	Electrical conductivity Sm^{-1}
v_0	Suction/injection velocity m/s

REFERENCES

[1] Eli W. Nanofluid enhancement of mineral oil and thermal properties instrument design [Master's thesis]. University of Louisville; 2014.
[2] Nazir U, Sohail M, Naz S, Mukdasai K, Singh M, Singh A, et al. Effective role of mineral oil and biological nanometer on thermal energy influenced by magnetic dipole and nanoparticle. Front Mater 2023;10:22-33. [CrossRef]

[3] Jashi Y, Zanwar D, Gupta V. Influence of nanoparticle concentration on thermophysical properties and heat transfer performance of Al2O3 nanosuspension for refrigeration system. Mater Today Proc 2022;56(2):995-1000. [CrossRef]
[4] Khoirudin, Sukarman A, Abdulah B, Kristiawan AT, Wijayanta K, Enoki. The influence of nanofluids on thermal and electrical properties in mineral oil. In: The 5th Asean UEC Workshop 3; 2023; Bangkok, Thailand.
[5] Taheri AA, Abdali A, Taghilou M, Alhelou HH, Mazlumi K. Investigation of mineral oil based nanofluids effect on oil temperature reduction and loading capacity increment of distribution transformers. Energy Rep 2021;7:4325-4334. [CrossRef]
[6] Karaman HS, El-Dein AZ, Mansour DA, Lehtonen M, Darwish MMF. Influence of mineral oil based nanofluid oil based nanofluids on temperature distribution and generated heat energy inside minimum oil circuit breaker in making process. Nanomaterials 2023;13:1-19. [CrossRef]
[7] Shelton J, Saini NK, Hasan SM. Experimental study of rheological behavior of TiO2-Al2O3/mineral oil hybrid nanofluid. J Mol Liq 2023;380(15):121688. [CrossRef]
[8] Saman NM, Zakaria IH, Ahmad MH, Abdul-Malek Z. Effects of plasma treated alumina nanoparticles on breakdown strength, particle discharge resistance and thermophysical properties of mineral oil-based nanofluids. Materials 2021;14:1-27. [CrossRef]
[9] Khan H, Haneef M, Shah Z, Muhammad S, Islam S, Khan W. The combined magneto hydrodynamic and electric field effect on unsteady Maxwell nanofluid flow over a stretching surface under the influence of variable heat and thermal radiation. Appl Sci 2018;8(2):160. [CrossRef]
[10] Mahanthesh B, Gireesha BJ, Animasaun IL. Exploration of non-linear thermal radiation and suspended nanoparticles effects on mixed convection boundary layer flow on nano liquids on a melting vertical surface. J Nanofluids 2018;7(5):833-843. [CrossRef]
[11] Mahian O, Bellos E, Markides CN, Taylor RA, Alagumalai A, Yang L, et al. Recent advances in using nanofluids in renewable energy systems and the environmental implications of their uptake. Nano Energy 2021;86:106069. [CrossRef]
[12] Azwadi N, Sidik C, Samion S, Ghaderian J, Muhammad Yazid MNAW. Recent progress on the application of nanofluids in minimum quantity lubrication machining: A review. Int J Heat Mass Transf 2017;108(Part A):79-89. [CrossRef]
[13] Akinshilo AT. Thermal performance evaluation of MHD nanofluid transport through a rotating system undergoing uniform injection/suction with heat generation. BioNanoScience 2019;9(3):740-748. [CrossRef]
[14] Akinshilo AT. Mixed convective heat transfer analysis of MHD fluid flowing through an electrically conducting and non-conducting walls of a vertical micro-channel considering radiation effect. Appl Therm Eng 2019;156:506-513. [CrossRef]
[15] Venkat Kiran KU, Azenkeng A, Roy S. Exploring the potential of coal derived graphite as next generation lubricant additive for multifunctional applications. Manuf Lett 2024;14(Supplement):296-303. [CrossRef]
[16] Guo Z, Zhang Y, Wang J, Gao C, Zhang S, Zhang P, et al. Interactions of Cu nanoparticles with conventional lubricant additives on tribological performance and some physicochemical properties of an ester base oil. Tribol Int 2020;141:105941. [CrossRef]
[17] Dogonchi AS, Ganji DD. Study of nanofluid flow and heat transfer between non-parallel stretching walls considering Brownian motion. J Taiwan Inst Chem Eng 2016;69:1-13. [CrossRef]
[18] Dogonchi AS, Ganji DD. Investigation of MHD nanofluid flow and heat transfer in a stretching/shrinking convergent/divergent channel considering thermal radiation. J Mol Liq 2016;220:592-603. [CrossRef]
[19] Sathish Kumar M, Sandeep N, Rushi Kumar B, Viljayaragavan R. Effect of nonlinear thermal radiation on MHD Siko nanofluid flow over a bidirectional stretching surface. IOP Conf Ser Mater Sci Eng 2017;263:062023. [CrossRef]
[20] Mabood F, Akinshilo AT. Stability analysis and heat transfer of hybrid Cu-Al2O3 nanofluids transport over a stretching surface. Int Commun Heat Mass Transf 2021;123:105215. [CrossRef]
[21] Hdiri N, Souayeh B, Alfannakh H, Beya BB. Natural convection study with internal heat generation on heat transfer and fluid flow within a differentially heated square cavity filled with different working fluids and porous media. BioNanoScience 2019;9:702-722. [CrossRef]
[22] Maxwell JC. A Treatise on Electricity and Magnetism. Vol. 1. Oxford: Clarendon Press; 1873.
[23] Hamilton RL, Crosser OK. Thermal conductivity of heterogeneous two-component systems. Ind Eng Chem Fundam 1962;1(3):187-191. [CrossRef]
[24] Acharya N, Mabood F, Shahzad SA, Badruddin IA. Hydrothermal variations of radiative nanofluid flow by the influence of nanoparticles diameter and Nanolayer. Int Commun Heat Mass Transf 2022;130:105781. [CrossRef]
[25] Rana P, Beg OA. Mixed convection flow along an inclined permeable plate: Effect of magnetic field, Nanolayer, conductivity and nanoparticle diameter. Appl Nanosci 2015;5:569-581. [CrossRef]
[26] Graham AL. On the viscosity of suspensions of solid spheres. Appl Sci Res 1981:275-286. [CrossRef]
[27] Gosunkonda S, Gorti VPNS, Baluguri SB, Sakam SR. Particle spacing and chemical reaction effects on convective heat transfer through a nanofluid in cylindrical annulus. Procedia Eng 2015;127:263-270. [CrossRef]

[28] Eringen AC. Theory of micropolar fluids. J Math Mech 1966;16(1):1-18. [CrossRef]
[29] Afiridi MI, Qasim M. Entropy generation and heat transfer in boundary layer flow over a thin needle moving in a parallel stream in the presence of nonlinear Rosseland radiation. Int J Therm Sci 2018;123:117-128. [CrossRef]
[30] Sathish Kumar M, Sandeep N, Rushi Kumar B, Viljayaragavan R. Effect of nonlinear thermal radiation on MHD Siko nanofluid flow over a bidirectional stretching surface. IOP Conf Ser Mater Sci Eng 2017;263(06):60-65. [CrossRef]
[31] Nadeem S, Akram S. Peristaltic transport of a hyperbolic tangent fluid model in an asymmetric channel. Z Naturforsch A 2009;64:559-567. [CrossRef]
[32] Khedher NB, Mohammed HI, Abed AM, Biswas N, Togun H, Hammoodi KA, et al. Maximizing charging/discharging capabilities of horizontal shell-and-tube latent heat storage systems with innovative curved fin inserts. Int J Heat Mass Transf 2025;236(1):126289. [CrossRef]
[33] Sohrabi N, Hammoodi KA, Hammoud A, Jasim DJ, Karouei SHH, Kheyri J, et al. Using different geometries on the amount of heat transfer in a shell and tube heat exchanger using the finite volume method. Case Stud Therm Eng 2024;55:104037. [CrossRef]
[34] Rashid FL, Dhaidan NS, Mahdi AJ, Kadhim SA, Hammoodi KA, Al-Obaidi MA, et al. Heat transfer enhancement of phase change materials using tree shaped fins: A comprehensive review. Int Commun Heat Mass Transf 2025;162:108573. [CrossRef]
[35] Ali AJ, Eddin BE, Al-Musawi STM, Majdi HS, Chaichan MT. Fe3O4 Au nanoparticles influence on bio-nanofluid thermal conductivity. J Therm Eng 2025;11(1):159-169. [CrossRef]
[36] Matthews J, Tella H. Unsteady magnetohydrodynamic free convection flow of Al2O3-Cu/water nanofluid over a permeable linear stretching sheet through a porous medium with viscous dissipation and heat source/sink. J Therm Eng 2025;11(2):344-356. [CrossRef]
[37] Khrishna Varma KPV, Venkateswarlu K, Kalyai T, Hemalatha S, Kumar PV. Numerical analysis of spiral tube heat exchanger circulated with zinc oxide nanofluids. J Therm Eng 2025;11(2):377-389. [CrossRef]
[38] Eriksen AB, Kosinski P, Balakin BV, Kosinska A. Experimental study of a direct absorption solar collector with stationary nanofluids. Energy Convers Manag 2024;23:100683. [CrossRef]
[39] Akinshilo AT, Folaranmi A, Ilegbusi AO. Theoretical study of the MWCNT particle layer and size impact on sodium alginate heat transfer. Phys Scr 2024;99(9):095238. [CrossRef]
[40] Phillips 66 Lubricants. Synthetic PAO-Based, Rust and Oxidation-Inhibited Air Compressor Oil. Available at: https://www.phillips66lubricants.com/product/syncon-r-o-oil-iso-vg-32-68/. Accessed on June 3, 2025.
[41] Bhattacharjee B, Chakraborti P, Choudhuri K. Theoretical analysis of single-layered porous short journal bearing under the lubrication of micropolar fluid. J Braz Soc Mech Sci Eng 2019;41:365. [CrossRef]
[42] Ramzan M, Javed M, Rehman S, Saeed A, Kumam P, Galal AM. Irreversibility analysis of melting rheology in micropolar Al2O3 - mineral oil nanofluid with homogeneous and heterogeneous reaction. Numer Heat Transf A Appl 2024;85(3):444-466. [CrossRef]
[43] Akinshilo AT, Sobamowo MG, Adingwupu A. Evaluation of micropolar fluid transport through penetrable medium: Effect of flow and thermal slip. AUT J Mech Eng 2022;6(3):427-442.
[44] Alizadeh M, Dogonchi AS, Ganji DD. Micropolar nanofluid flow and heat transfer between penetrable walls by the presence of thermal radiation and magnetic field. Case Stud Therm Eng 2018;12:319-322. [CrossRef]
[45] Akinshilo AT, Ilegbusi AO, Ali HM, Sanusi M, Sobamowo MG. Impact of melting and radiation on MHD mixed convective heat transfer slip flow through vertical porous embedded micro channel. J Cent South Univ 2023;30:3670-3681. [CrossRef]
[46] Phillips 66 Lubricants. Heat Transfer Oil. Available at: https://www.phillips66lubricants.com/product/heat-transfer-oils/. Accessed on August 8, 2024.
[47] Kazaz O, Karimi N, Paul MC. Reduction and nanoparticle interaction for enhanced light absorption and heat conversion. J Mol Liq 2024;411:125702. [CrossRef]
[48] Wan J, Benson B, Bruzek MJ, Anthony JE, Sinko PJ, Prudhomme RK, et al. Microfluidic generation of droplet with high loading of nanoparticles. Langmuir 2012;18(37):13143-13148. [CrossRef]
[49] Li H, Li Y, Huang B, Xu T. Flow characteristics of the entrance region with roughness effect within rectangular microchannels. Micromachines 2020;11(1):30. [CrossRef]
[50] Yu CJ, Richter AG, Datta A. Molecular layering, a liquid on a solid substrate on X-ray reflectivity study. Physica B 2000;281(1-3):27-31. [CrossRef]
[51] Yu W, Choi SUS. The role of interfacial layer in the enhanced thermal conductivity of nanofluids: A renovated Maxwells model. J Nanopart Res 2003;5:167-171. [CrossRef]
[52] Karim KE, Kim B. First law of thermodynamics on the boundary flow through a carbon nanotube. Phys Rev E 2021;103:053115. [CrossRef]
[53] Babu JS, Sathian SP. The role of activation energy and reduced viscosity on the enhancement of water flow through carbon nanotubes. J Chem Phys 2011;134:194509. [CrossRef]
[54] Faramani AB, Aluru NR. Existence of multiple phases of water at nanotube interfaces. J Phys Chem 2016;120:23763-23771. [CrossRef]

[55] He JH. Homotopy perturbation method for solving boundary value problems. Phys Lett A 2006;350:87-88. [CrossRef]

[56] He JH. Homotopy perturbation method: A new nonlinear analytical technique. Appl Math Comput 2003;135:73-79. [CrossRef]

[57] Park J, Kim D, Kim H, Lee J, Chung W. Thermal radiative copper oxide layer for enhancing heat dissipation of metal surface. Nanomaterials 2021;11(11):2819. [CrossRef]

[58] Ouyang W, Qin H, Urbakh M, Hod O. Controllable thermal conductivity on twisted homogeneous interfaces of graphene and hexagonal boron nitride. Nano Lett 2020;20(10):7513-7518. [CrossRef]

[59] Khoirudin, Kristiawan B, Sukarman, Abdulah A, Santoso B, Wijayanta AT, et al. Flash point improvement of mineral oil utilizing nanoparticles to reduce fire risk in power transformers: A review. Fire 2024;7(305):1-25. [CrossRef]

[60] LotfizadehDehkordi B, Kazi S, Hamdi M, Ghadimi A, Sadeghinezhad E, Metselaar H. Investigation of viscosity and thermal conductivity of alumina nanofluids with addition of SDBS. Heat Mass Transf 2013;49:1109-1115. [CrossRef]

[61] Shanbedi M, Zeinali Heris S, Maskooki A. Experimental investigation of stability and thermophysical properties of carbon nanotubes suspension in the presence of different surfactants. J Therm Anal Calorim 2015;120:1193-1201. [CrossRef]

[62] Chakraborty S, Panigrati PK. Stability of nanofluid: A review. Appl Therm Eng 2020;174:115259. [CrossRef]

[63] Andreu JS, Camacho J, Faraudo J. Aggregation of superparamagnetic colloids in magnetic fields: The quest for the equilibrium state. Soft Matter 2011;7:2336-2339. [CrossRef]

[64] Ezzaier H, Marins JA, Claudet C, Hemery G, Sandre O, Kuzhir P. Kinetics of aggregation and magnetic separation of multicore iron oxide nanoparticles: Effect of the grafted layer thickness. Nanomaterials 2018;8:623. [CrossRef]

[65] Teng X, Yang H. Effects of surfactants and synthetic conditions on the sizes and self-assembly of monodisperse iron oxide nanoparticles. J Mater Chem 2004;14:774. [CrossRef]

J Ther Eng, Vol. 12, No. 2, pp. 595−609, March, 2026

Journal of Thermal Engineering
Web page info: https://jten.yildiz.edu.tr
DOI: 10.14744/thermal.0001103

Research Article

Investigation of thermal and hydrodynamic performance of a plate compact heat exchanger with Levenberg-Marquardt artificial neural network method

Aykut BACAK[1]

[1]*ASELSAN INC., Golbasi Yerleskesi, Ankara, 06830, Turkiye*

ARTICLE INFO

Article history
Received: 06 March 2024
Revised: 20 April 2024
Accepted: 26 April 2024

Keywords:
Artificial Neural Network; Compact Heat Exchanger; Heat Transfer Coefficient; Levenberg-Marquardt; Pressure Drop

ABSTRACT

Compact heat exchangers are an essential device for efficiently transferring thermal energy between fluids. In contrast to larger objects of the same kind, they do this by optimizing the surface area for heat transmission inside a more compact space. This study theoretically calculates the heat transfer coefficient and pressure drop of a plate compact heat exchanger using design parameters such as air flow rate (1-4 kg/s), inlet air temperature (300-350 K), outlet air temperature (400-450 K), passage width (0.003-0.05 m), divider width (0.001-0.005 m), and heat exchanger length (0.15-1 m) at atmospheric pressure (101325 Pa). The study uses the Levenberg-Marquardt artificial neural network method to investigate heat transfer coefficients in compact heat exchangers. Results demonstration that the coefficient increases with mass flow rate doubling and 93% tripling. The maximum coefficient increases by 7.9% with a divider width of 0.001 m, while it decreases with shorter route lengths. The investigation revealed that pressure decreases exhibit a more pronounced rise in relation to the width of the divider. The factors increased by 1.04, 1.08, 1.13, 1.17, and 1.22 for divider widths of 0.001 m and 0.005 m, respectively, at varying temperatures. The change in the width of the divider had little effect on the pressure decrease at constant average temperatures. The Mean Squared Error (MSE) for heat transfer was -0.1787, whereas the MSE for pressure drop was 3.988. The training phase of the ANN was flawless, achieving projected values over 200 W/m^{2}K and a pressure decrease surpassing 5000 Pa.

Cite this article as: Bacak A. Investigation of thermal and hydrodynamic performance of a plate compact heat exchanger with Levenberg-Marquardt artificial neural network method. J Ther Eng 2026;12(2):595−609.

INTRODUCTION

Plate-fin heat exchangers (PFHE) are utilized widely and frequently in the heating, cooling, air conditioning, power generation, and heat recovery industries. In these fields, heat exchangers (HEX) are complicated systems that depend on design factors like the width of the divider, the passage, the air temperature, the atmospheric pressure, and the mass flow rate. It is difficult to predict the movement

***Corresponding author.**
*E-mail address: bacakaykut@gmail.com

This paper was recommended for publication in revised form by Editor-in Chief Ahmet Selim Dalkilic

Published by Yıldız Technical University Press, İstanbul, Turkey
Yıldız Technical University. This is an open access article under the CC BY-NC license (http://creativecommons.org/licenses/by-nc/4.0/).

of heat and the reduction of pressure in various fin types utilized in PFHEs, including plain, wavy, serrated, perforated, and louvered fins. Because there are so many geometric parameters, there isn't a lot of experimental data in the literature. Because of this, some experimental correlations were used to make an educated guess about how well the fin would work in PFHEs. Most people think that mistakes in estimating caused by correlations are much worse than mistakes in measuring, mostly because they involve compressing data. Currently, artificial neural networks (ANN) are utilized to address the challenge of forecasting the thermal characteristics of various HEXs.

The literature review undertaken in this article is examined in three segments: investigations into thermal performance utilizing ANN methodologies, research aimed at enhancing thermal and hydrodynamic efficiency, and thermo-economic analyses. The studies in the literature on thermal effects are summarized in the following paragraph. Ermis [1] uses ANN to look at how heat moves through small HEXs. The ANN uses experimental data to guess the heat transfer coefficient (HTC), the pressure drops (ΔP), and the Nusselt number. The network uses a feed-forward back-propagation algorithm and various hidden numbers to predict heat transfer values. The trained ANN outperforms experimental results, with an absolute mean relative error of less than 6%. Demir [2] uses an ANN model to pretend the thermal performance of a chevron-type plate HEX using water as the operating fluid. The model estimates outer temperatures based on cold water mass flow rate, inlet hot water temperature, and inlet cold water temperature, employing partial data. The experimental and predicted results are very close to each other. The network predicts outlet temperatures of 2.58% for hot water and 1.80% for cold water. Shi et al. [3] examine the equivalent thermal conduction resistance of printed circuit heat exchangers (PCHE) and their impact on thermal convection resistance. The consequences show that PCHEs with unequal numbers of hot and cold plates have a sensitive equivalent thermal conduction resistance, with a maximum value of 1.7–2.4 times the smallest value. The proposed correlations have acceptable accuracy for overall engineering claims. The ANN model is better at making predictions, so it is recommended for important needs. Dossumbekov et al. [4] aims to develop models for calculating the Nusselt number in a micro-HEX utilizing hybrid nanofluids through advanced methodologies. This research utilizes experimental data from a different study to suggest models based on multilayer perceptron (MLP) and Group Method of Data Handling (GMDH) neural networks (NN). The models are very accurate, with R2 values of 0.9948 and 0.9972, correspondingly. The overall Absolute Relative Deviation (AARD) of the studies is 2.43% and 1.56%, respectively. Li et al. [5] emphasize optimizing the thermal hydraulic performance of a PCHE for the supercritical carbon dioxide (S-CO_2) Brayton cycle. The four parameters that were chosen were the airfoil fin's maximum thickness, maximum thickness location, transverse pitch, and staggered pitch. The study used computational fluid dynamics (CFD) simulations, machine learning, and optimization algorithms. Results presented that growing the extreme thickness location value improved the PCHE's performance by about 6.2% associated with the basic structure. The study also used the sequential quadratic programming (SQP) algorithm and non-dominated sorting genetic algorithm II (NSGA-II) for optimization. Zhu et al. [6] propose experimental systems for two-phase flow heat transfer in mini channels utilizing ANN models. The models forecast heat transfer performance acceptably with a Mean Absolute Relative Deviation (MARD) of 11.41% and 6.06%, respectively. The ANN study can be transferred across various datasets but demonstrations unacceptable performance for various situations. This study can benefit advanced thermal management systems. Zarea et al. [7] utilize the Bees Algorithm (BA) in the model of a cross-flow plate-fin HEX with an offset strip fin. The algorithm is optimized using the second law of thermodynamics and minimizes entropy generation units. The study compares BA's effectiveness and accuracy with other algorithms like GA, Particle Swarm Optimization (PSO), Imperialist Competitive Algorithm (ICA), and initial project. The results display BA offers higher accuracy in finding the optimum configuration. Hernández-Gil et al. [8] employ an ANN and mathematical approaches to compute the heat transfer area, considering the nonlinear fluctuations of the global HTC due to fluid properties and surface geometry. The method was tested in two different situations, and the results showed that it could predict the heat transfer area with an error rate of less than 2.8%. Zeng et al. [9] investigate the ΔP and heat transfer characteristics of a high-efficiency plate-fin structure in an air preheater, focusing on the critical Reynolds number for turbulent flow conversion and separating HTCs using the Genetic Algorithm method. The findings will aid in the in the future design of high-efficiency heat preheaters. Gupta et al. [10] developed an ANN model to predict the performance parameters of perforated micro-pin fin heat sinks under different geometric parameters and inflow circumstances. A 3-D CFD simulation system was used to produce dataset examples. The model forecasts the Nusselt number and friction factor with a mean absolute percentage error (MAPE) of 4.45% and 1.80%, correspondingly. A multi-objective non-dominated sorting genetic algorithm (NSGA-II) was employed for optimization, resulting in an increase in thermal performance between 11.5% and 39.77%.

The studies in the literature where thermal and hydrodynamic effects are examined together are summarized in the following paragraph. Peng and Lin [11] dynamically optimized the Support Vector Regression (SVR) model to the research method, and k-fold cross-validation was projected to forecast the thermal-hydraulic performance of compact heat exchangers (CHEs). The model's performance was evaluated with 48 experimental data points and

associated with the ANN method. The SVR model showed better estimate performance with mean squared errors (MSE) of 2.645×10^{-4} for testing the j factor and 1.231×10^{-3} for testing the f factor. Peng and Lin [12] present an application of ANNs to forecast ΔP and heat transfer characteristics in PFHEs. The research assesses the thermal efficiencies of five PFHEs and constructs a feed-forward neural network utilizing a backpropagation algorithm. The ANN is trained on experimental data to predict the j and f factors in PFHEs. It gets MSEs of less than 1.5% for the j factor and 1% for the f factor. Nascimento et al. [13] employ an optimization technique and a Random Vector Functional Link (RVFL) network to develop a counter-flow PFHE featuring offset-strip fins. CFD simulations created a dataset for training and testing, thereby reducing processing time and ensuring the accuracy of PFHE. The Non-Dominated Sorting Genetic Algorithm III (NSGA-III) was computed to accomplish optimal effectiveness, minimal volume, and ΔP at both the hot and cold sides. Experimental endorsement employing the Shear Stress Transport (SST) k-ω turbulence model indicated 4.36% and 3.27% discrepancies in ΔP and convective HTC measurements, respectively. Singh et al. [14] suggest employing Response Surface Methodology (RSM) and ANN to optimize the design of fin-tube heat exchangers (FTHEs) equipped with vortex generators. The ANN was better at forecasting the Nusselt number and friction factor than the RSM, with R-squared values of 0.990 and 0.954. The best design configurations were recommended based on how well they exchanged heat or lowered ΔP, making sure that both goals were met in a balanced way.

The studies in the literature where thermo-economic analysis is examined in conjunction with the ANN method are summarized in the following paragraph. Xie et al. [15] concentrate on enhancing a plate-fin type CHE through the application of a GA. The GA searches, combines, and optimizes structure sizes, with the minimum total volume and yearly price as objective functions. The fin geometries are fixed, and three shape parameters are varied with or without ΔP constraints. The improved CHE offers 30% lesser volume or 15% lower yearly price with ΔP constraints and 49% lower volume or 16% lower annual cost without ΔP constraints. Jilak et al. [16] optimize a plate HEX design employing a multi-objective evolutionary algorithm/decomposition, considering thermal efficiency and manufacturing cost as objective functions. The ε-NTU method was utilized to look at the chances of ΔP and efficiency. A ceramics factory in Kerman Province did an experiment and found that the expected design led to a 19.962% increase in efficacy rate and a 9.533% decrease in price. We used Pareto front analysis to show how the best points for design variables are spread out. Peng and Lin [17] demonstrate the efficacy of GA and Backpropagation Neural Networks (BP) in enhancing PFHE. The main objectives are minimizing total weight and annual cost, ensuring the smallest size with minimal capital cost, and maximizing ΔPs. The GA combined with the BP method optimizes variables such as core length, number of hot side layers, fin height, and pitch, making this method universally applicable for various PFHEs.

The literature research indicated that ANNs are more effective for thermal analysis in engineering applications, particularly in HEXs. The Levenberg-Marquardt ANN method has not yet been utilized or evaluated for thermal properties in PFHE. This paper's investigation focuses on examining the effectiveness of ANN with the Levenberg-Marquardt method in analyzing thermal features (such as ΔP and heat transfer) in a PFHE. A theoretical calculation was established to study the thermal performance of PFHE. The theoretical data was analyzed using the ANN approach to demonstrate its effectiveness in representing design parameters. A methodology utilizing cross-validation was created to evaluate the anticipated inaccuracy of the ANN method built from insufficient data in predicting PFHEs behavior under various operating situations and design parameters. With this study, it has been determined that compact heat exchangers produce solutions within a very low deviation range of ±10, and solutions are provided in a short time with ANN management without requiring additional experimental work and thermal analysis. As can be seen from the literature studies, the Levenberg-Marquardt ANN method has almost never been used in compact heat exchanger studies, and this study takes its place in the literature as a guide for compact heat exchanger designers, manufacturers, and researchers.

THERMAL CALCULATION

The thermal and hydrodynamic performance of the Compact HEX as shown in Figure 1 was analyzed by calculating the HTC and pressure loss using EES V9.944 software. The e-NTU method was utilized to determine the heat transfer capability of the compact HEX. The thermal and hydrodynamic calculations of the compact heat exchanger are calculated as shown in equations (1) to (14) [18].

The effectiveness of a cross-flow HEX with distinct fluids as proposed:

$$\varepsilon = \frac{q}{q_{\max}} = \frac{C_h\left(T_{h,in} - T_{h,out}\right)}{C_{\min}\left(T_{h,in} - T_{h,out}\right)} = \frac{C_c\left(T_{c,out} - T_{c,in}\right)}{C_{\min}\left(T_{h,in} - T_{h,out}\right)} \quad (1)$$

where C_{min} is the lesser of the C_h and C_c magnitudes. NTU is calculated as follows:

$$NTU = \frac{AU_{Ave}}{C_{\min}} = \frac{1}{C_{\min}} \int_0^A UdA \quad (2)$$

where A is the heat transfer area as used in the description of U. In design work U can commonly be preserved as constant.

$$C^* = \frac{C_{\min}}{C_{\max}} \quad (3)$$

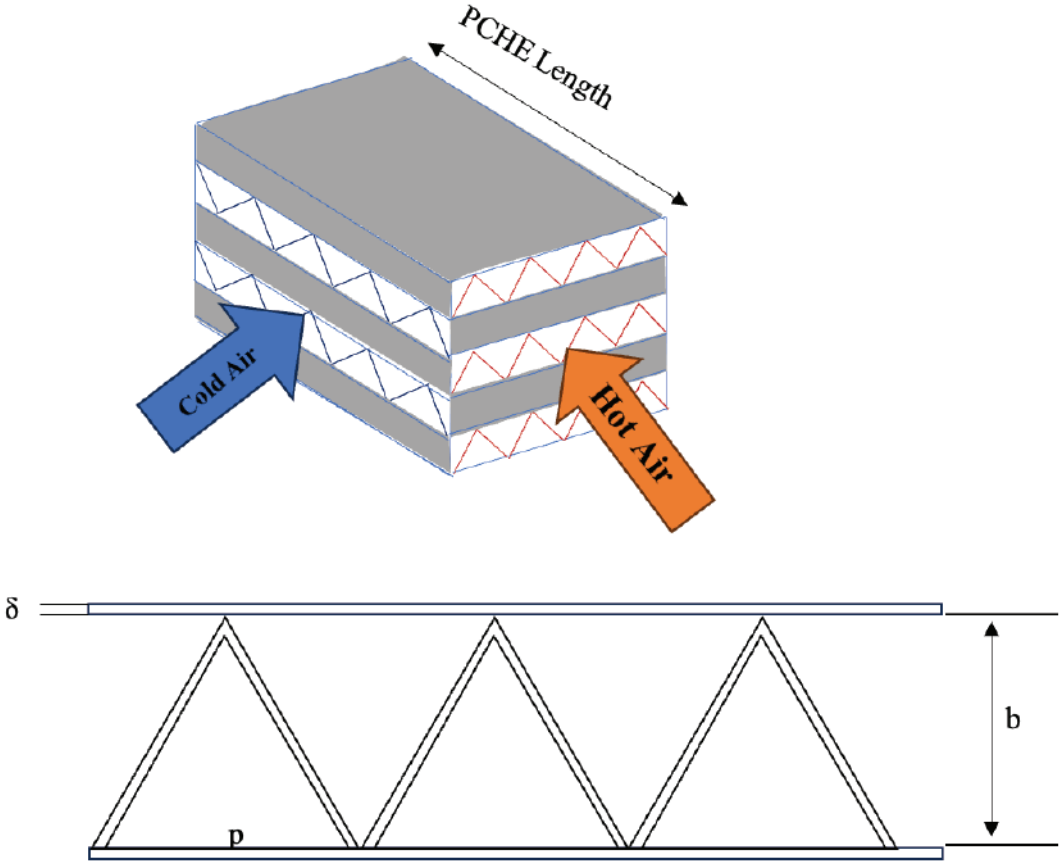

Figure 1. Geometry and design parameters.

where C_{min} and C_{max} are correspondingly, the lesser and the greater of the two magnitudes C_h and C_c.

U is the average HTC and A_{tot} is total heat transfer surface area calculated from:

$$\frac{1}{U_h}=\frac{1}{\eta_{o,h}h_h}+\frac{\alpha}{(A_w/A_h)k}+\frac{1}{(A_c/A_h)\eta_{o,c}h_c} \tag{4}$$

$$\frac{1}{U_c}=\frac{1}{\eta_{o,c}h_c}+\frac{\delta}{(A_w/A_c)k}+\frac{1}{(A_h/A_c)\eta_{o,h}h_h} \tag{5}$$

Where U_h is based on a unit of hot-side total area and Uc is based on a unit of cold-side total area. A_w signifies the overall wall area; $\eta_{c,h}$ and $\eta_{o,h}$ represent temperature effectiveness of the total area A_h and A_c, correspondingly.

$$\eta_o=1-\frac{A_{fr}}{A_{tot}}(1-\eta_f) \tag{6}$$

where A_f is the frontal area, A is the total area, η_f is number of fins and η_o is the weighted average of the 100% effectiveness of the prime surface. Gardner [19] gives relations for η_f for a number of fin geometries.

$$\eta_f=\frac{\tanh(ml)}{ml} \tag{7}$$

$$m=\sqrt{\frac{2h}{k\delta_f}} \tag{8}$$

where h is the HTC, k is the thermal conductivity, and δ is the fin thickness.

Mass flux, G, can be expressed as:

$$G=\frac{\dot{m}}{\sigma A_{fr}} \tag{9}$$

The variables are defined as follows: $\dot{m}$ represents the mass flow rate, σ is the ratio of the free flow area to the frontal area, and A_{fr} denotes the frontal area. Calculate the Reynold's number using the following formula:

$$\mathrm{Re}=\frac{GD_h}{\mu} \tag{10}$$

D_h represents the hydraulic diameter, μ stands for dynamic viscosity, and G is the result of multiplying

the maximum mass velocity by the density of the fluid. Hydraulic diameter is estimated as follows:

$$D_h = \frac{2a\left(b-\delta_f\right)}{a+2\left(l_f-\delta_f\right)} \tag{11}$$

The Colburn j_H factor which is a function of the Stanton the Prandtl number and is calculated as follows:

$$j_H = St\,\mathrm{Pr}^{2/3} \tag{12}$$

$$St = \frac{Nu}{\mathrm{Re\,Pr}} = \frac{h}{Gc_p} = \frac{q_w}{c_p G(T_m - T_w)} \tag{13}$$

Pressure Drop Calculation

Pressure drop in compact HEX is calculated as follows:

$$\frac{\Delta P}{P_{in}} = \frac{G^2}{2g_c}\frac{v_{in}}{P_{in}}\left[\left(1+\sigma^2\right)\left(\frac{v_{out}}{v_{in}}-1\right)+f\frac{A}{A_c}\frac{v_{ave}}{v_{in}}\right] \tag{14}$$

where σ is the ratio of minimum free flow area to frontal area and *f* is the Fanning friction factor.

ANN Model Development

An MLP-based ANN method has been established to estimate the HTC and ΔP of the compact HEX. MLP networks, which consist of interconnected layers, are one of the ANN models that can make predictions with high accuracy due to their strong systematic structure. Structurally, an MLP network contains an input layer, a hidden layer, and an output layer. Air flow rate, air temperature, passage width, and HEX length are described as shown in Table 1 as input parameters in the input layer of the developed MLP network. In the network model, the layer afterward the input layer is the hidden layer, and every MLP network has at least one hidden layer. The lack of a set way to calculate the neuron, which is an important part of the hidden layer, makes it hard for MLP networks to grow. To compute the number of neurons in the hidden layer, the most commonly used technique is to evaluate the performance of network models created with dissimilar neuron numbers. In the developed network model, performance analyses of MLP networks with numerous neuron numbers are made, and the model with 10 neurons in the hidden layer is selected. In the output layer, which is the next layer from the hidden layer, two different parameters are estimated, namely HTC and ΔP. Figure 2 presents the symbolic configuration scheme and basic architecture of the created MLP network. The machine-learning model has three stages: training, prediction, and validation. A specific part of the data in the study should be reserved for training. Training is the stage of teaching the available data to the machine. Prediction, on the other hand, is the stage of creating the machine's outputs that performs the learning from the data at hand. On the other hand, validation is the validation phase of the results obtained in the prediction phase with theoretical calculations. The ANN develops a total of 13860 data points, reserving 9702 for model training, 2079 for validation, and another 2079 for testing. As the training algorithm, the LM-type ANN training algorithm, which is frequently used in ANN models and has high learning ability, is preferred. Transfer functions are utilized in the hidden and output layers of the MLP network to estimate the HTC and ΔP, respectively. Table 2 contains info on how data is examined for ANN approaches.

To evaluate the approximation performance of the designed ANN method, coefficient of determination (R) and MSE parameters, which are extensively used in the previous studies, are selected. In addition to these performance parameters, the values of HTC and ΔP attained from the ANN method and the margin of deviation (MoD) values, which represent the relational deviation among the target ones, are also calculated. The statistical equations working in the computation of the performance factors are as indicate:

$$MSE = \frac{1}{N}\sum_{i=1}^{N}\left(X_{Calc(i)} - X_{ANN(i)}\right)^2 \tag{15}$$

Table 1. Input parameters for thermal and ANN calculation

	Symbol	Values	Unit
Mass Flow Rate	m	1-4	kg/s
Inlet Temperature	T_i	300-350	K
Outlet Temperature	T_o	400-450	K
Width of Passages for Second Fluid	b_2	0.003-0.05	m
Width of Divider	a	0.001-0.005	m
Atmospheric Pressure	P_{Atm}	101325	Pa
Length of Heat Exchanger	L	0.15-1	m

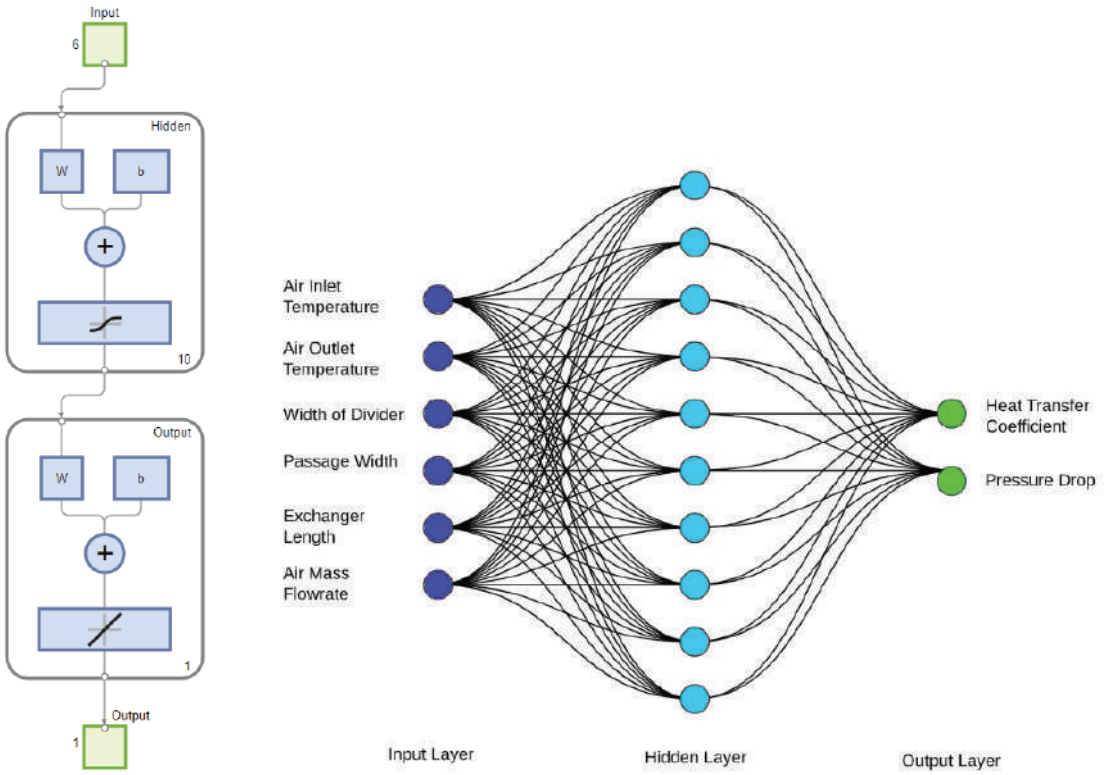

a) b)

Figure 2. The effectiveness of the training process of ANN architectures (a), and basic structural topology of an MLP network.

Table 2. Details of the estimated data for both ANN models

	Data Number				Number of Neuron
	Training	Validation	Test	Total	
for Heat Transfer Coefficient	9702	2079	2079	13860	10
for Pressure Drop	9702	2079	2079	13860	10

$$R = \sqrt{1 - \frac{\sum_{i=1}^{N}\left(X_{Calc(i)} - X_{ANN(i)}\right)^2}{\sum_{i=1}^{N}\left(X_{Calc(i)}\right)^2}} \quad (16)$$

The MoD values, which show how far off the predicted values are from the target values using the ANN, are also calculated and looked at with the performance parameters. These numbers show how far off the predicted values are from the target values. The accurate method utilized to find the MoD is shown below:

$$MoD(\%) = \left[\frac{X_{Calc} - X_{ANN}}{X_{Calc}}\right] x100 \quad (17)$$

RESULTS AND DISCUSSION

This study employs theoretical calculations to determine the heat transfer coefficient and pressure drop of a plate-compact heat exchanger. The design parameters considered include the air flow rate (ranging from 1 to 4 kg/s), inlet air temperature (ranging from 300 to 350 K), outlet air temperature (ranging from 400 to 450 K), passage width (ranging from 0.003 to 0.05 m), divider width (ranging from 0.001 to 0.005 m), and heat exchanger length (ranging from 0.15 to 1 m). The calculations are done at normal atmospheric pressure (101325 Pa). To research used the Levenberg-Marquardt artificial neural network technique to examine heat transfer coefficients in compact heat exchangers. Neither the theoretical nor the ANN study includes further experimental studies since the calculated

values are derived from a curve that accurately represents the experimental data of Kays and London [18].

Figure 3 shows how the total HTC changes based on different design parameters of small HEXs. Figure 3(a) displays the variation in HTC based on various HEX lengths ranging from 0.003 to 0.04 m and the width of the divider. The input and output air temperatures in the diagram are 300 K and 400 K, correspondingly, when figuring out the HTC. The air flow rate is 1 kg/s, and the length of the HEX is 1 m. Figure 3(a) shows that when the divider width grows, the HTC increases for all channel widths. The HTC increases by around 27.9% when the width of passages triples and by about 57.7% when the width of passages increases tenfold, as seen in the figure. A rise in the width of channels consequences in a growth in the heat transfer surface area, although this rise is not proportionate.

Figure 3(b) displays the change in the HTC value of the plate compact HEX based on the divider width and air mass flow rate parameters. The figure illustrates that the HTC value increases as the width of the divider value grows for all air mass flow rate values. For an air mass flow rate of 1 kg/s, the HTC value increases by 4.8%, 11.9%, 18.9%, and 26.1% when the width of the divider value increases by 2, 3, 4, and 5 times, respectively, as shown in the figure. When analyzing this perspective with an airflow rate of 3 kg/s, the rise rates are 7.2%, 14.3%, 21.7%, and 28.4%, respectively. At high mass flow rates, the HTC value grows more rapidly with the increase in the divider width. As the air flow rate increases, the HTC value rises. The figure shows that the HTC increases by an average of 51.3% with a doubling of the mass flow rate and by about 93% with a tripling of the mass flow rate. In compact HEXs, there is no direct relationship between mass flow rate and HTC. Figure 3(c) shows the change in HTC value for a plate compact HEX based on the divider width and average air temperature. The figure displays that the HTC value rises as the divider's breadth increases. At an average air temperature of 350 K, the HTC value increases by 4.8%, 11.9%, 19.2%, and 26.1% when the width of the divider value increases by 2, 3, 4, and 5 times. For an average temperature of 400 K, these values are 4.3%, 9.1%, 15.9%, and 22.7%, respectively. Higher temperatures result in slightly greater increases in the HTC compared to lower temperatures. As the average air temperature increases, the HTC value naturally increases. With a divider width of 0.001 m, the maximum HTC increases by 7.9%, compared to an increase of roughly 5% with a divider

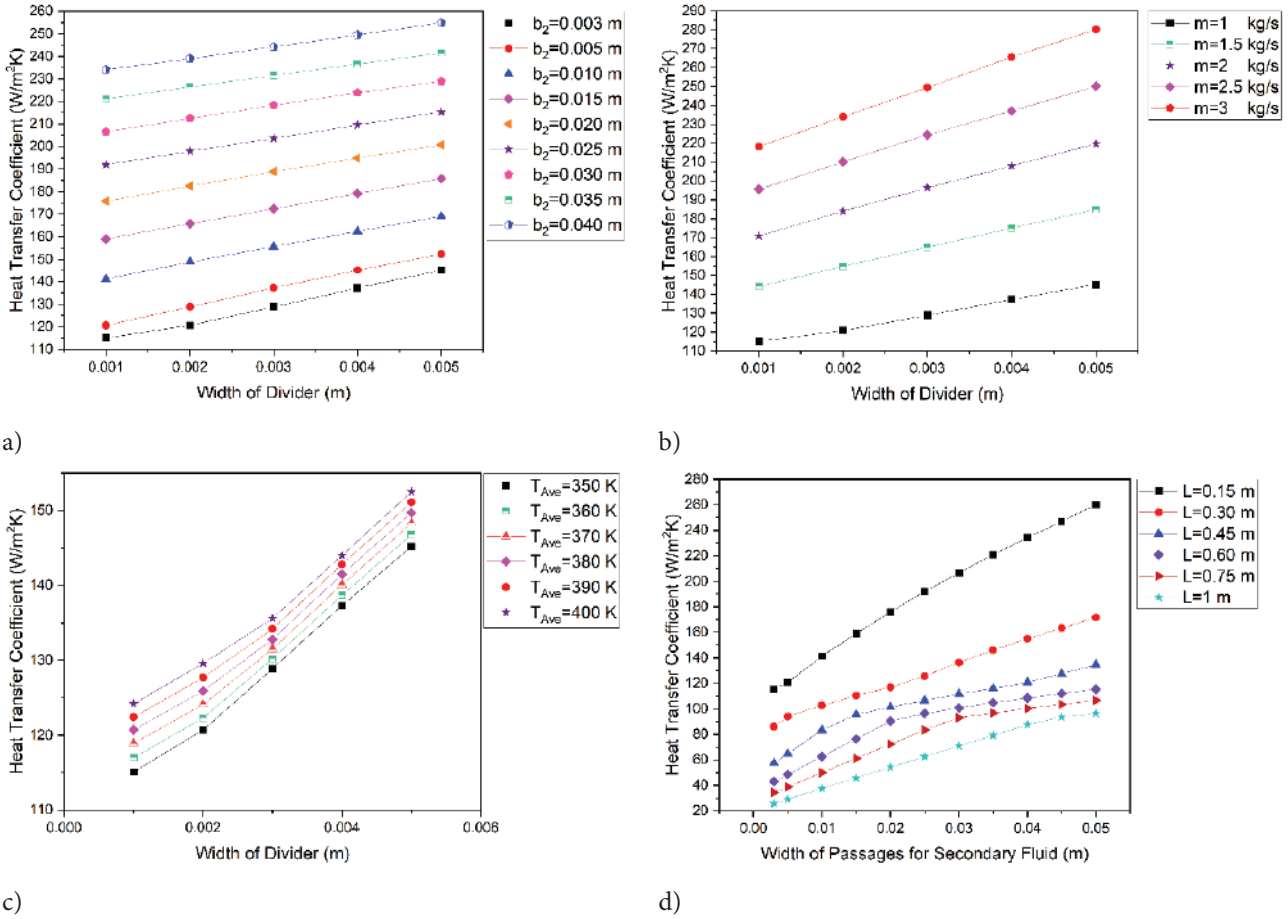

Figure 3. Heat transfer coefficient variation with respect to a) length of heat exchanger, b) mass flow rate, c) average temperature, and, d) width of passages for secondary fluid.

width of 0.005 m. An increase in the average temperature of compact HEXs with larger heat transfer areas leads to a gradual rise in the HTC at a slower rate.

Figure 3(d) shows how the HTC value of the plate compact HEX changes when the passageways are wider or the HEX is longer. When creating the figure, the divider width is 0.001 m, the air input temperature is 300K, the air exit temperature is 400K, and the air flow rate is 1 kg/s. The graphic illustrates that as the length of the compact HEX rises, the HTC value falls. With a passage width of 0.003 m, the HTC decreases by 80.2% when the exchanger length is raised from 0.15 m to 1 m. For a passage width of 0.05 m, this decline reduces to 53.8%. Increasing the length of the exchanger in wider channels results in a less significant decrease in the HTC value. The figure indicates that increasing the channel width while keeping the exchanger length constant leads to a higher HTC value. For a 1 m exchanger length, the HTC increases by factors of 2.7, 6.8, and 12.9 with a 3, 6, and 9-fold increase in passage length. For a 0.15 m exchanger length, these values are 1.9, 3.77, and 6.33 times, respectively. It has been discovered that the HTC diminishes as the route lengthens in exchangers with shorter dimensions.

Figure 4 shows how the divider width, mass flow rate, average temperature, passageway width, and exchanger length all affect the pressure loss in a compact HEX. Figure 4(a) illustrates the relationship between pressure loss in a compact HEX and the dimensions of the divider and passageways. The diagram is determined using the following parameters: input air temperature of 300K, output air temperature of 400K, exchanger length of 0.15m, and air flow rate of 1 kg/s. The figure illustrates that pressure loss rises as the width of the divider and channels grows. For a passage width of 0.003 m, the pressure loss increases by 1.18, 1.38, 1.59, and 1.80 times when the divider thickness increases by 2, 3, 4, and 5 times. For a divider width of 0.04 m, these ratios are 1.06, 1.14, 1.21, and 1.28, respectively. It was noted that the rate of rise diminished as the passage width expanded.

Figure 4(b) illustrates the relationship between pressure loss in the compact HEX and the width of the divider, as well as the air mass flow rate values. The divider width was set at a constant value of 0.001 m, while the passage width was maintained at a constant value of 0.003 m during the figure construction. The graphic illustrates that the pressure loss of the compact HEX rises as the width of the divider value grows. For an air flow rate of 1 kg/s, the pressure loss

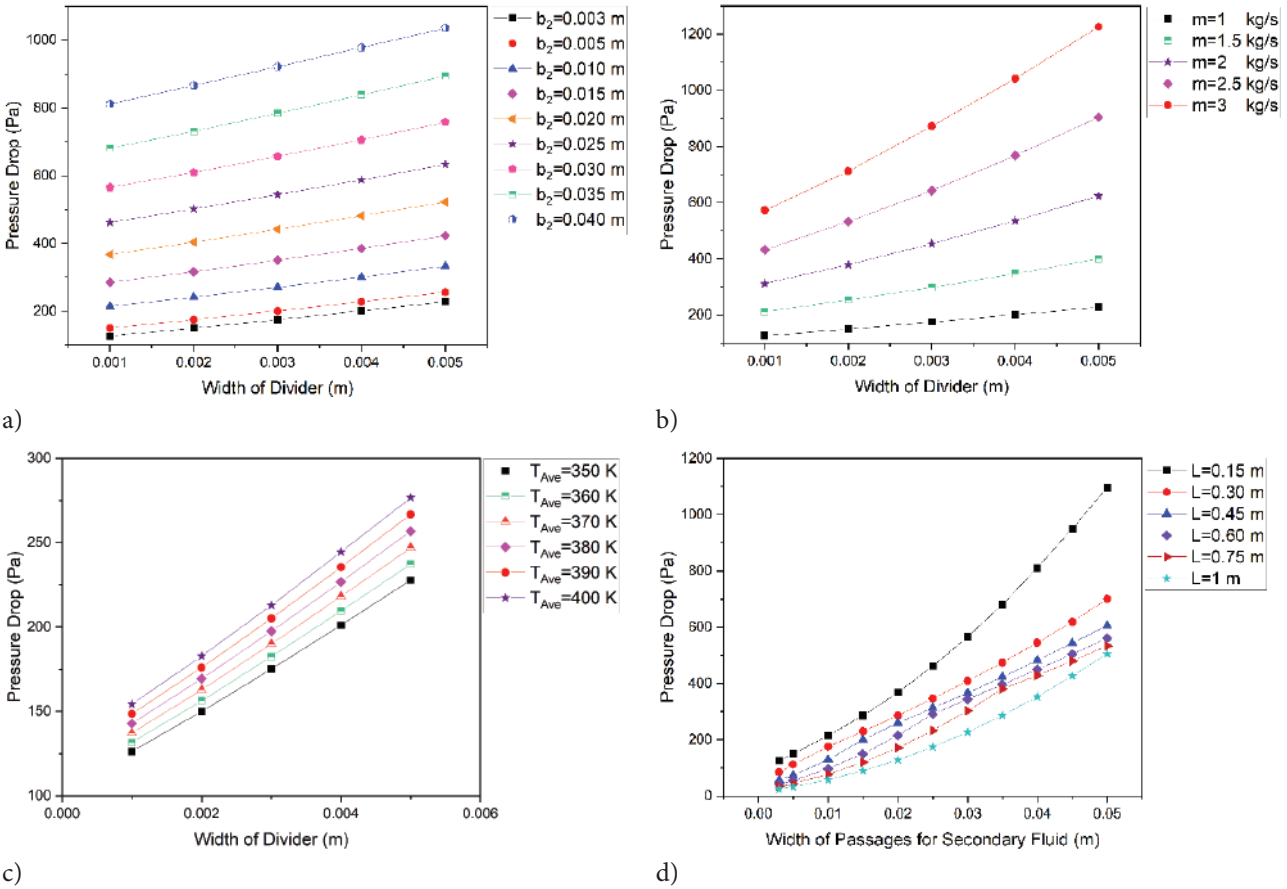

Figure 4. pressure drop variation with respect to a) length of heat exchanger, b) mass flow rate, c) average temperature, and, d) width of passages for secondary fluid.

increases by factors of 1.05, 1.12, 1.19, and 1.26 as the width of the divider is increased by 2, 3, 4, and 5 times, respectively. When the air flow rate is 3 kg/s, the pressure loss factors are 1.07, 1.14, 1.22, and 1.28 for the same increases in divider width. It is found that growth rates rise proportionally with an increase in air flow rate. The pressure loss change due to mass flow rate was computed as 1.25, 1.48, 1.70, and 1.89 times for a 0.001 m divider width and as 1.27, 1.51, 1.72, and 1.93 times for a 0.005 m divider width. It has been found that the pressure loss increases more significantly with larger dimensions of the divider width.

Figure 4(c) depicts the relationship between pressure loss in the compact HEX and the average air temperature across the divider's breadth. The figure was created with a constant air mass flow rate of 1 kg/s, an exchanger length of 1 m, and a passage width of 0.003 m. The figure illustrates that pressure loss rises as the width of the divider and the average temperature value increase. At an average air temperature of 350 K, the pressure loss value increases by factors of 1.18, 1.39, 1.59, and 1.80 as the width of the divider value increases by 2, 3, 4, and 5 times. When the average temperature is 400 K, these values change to 1.18, 1.38, 1.58, and 1.79 times, respectively. Changes in the average air temperature cause the pressure loss values for average air temperatures of 350 K and 400 K to go up by the same amount. For a divider width of 0.001 m, the pressure loss goes up by 1.04, 1.08, 1.13, 1.17, and 1.22 at different temperatures. For a divider width of 0.005 m, the pressure loss goes up by 1.04, 1.08, 1.12, 1.17, and 1.21 at different temperatures. The consequences display that changing the

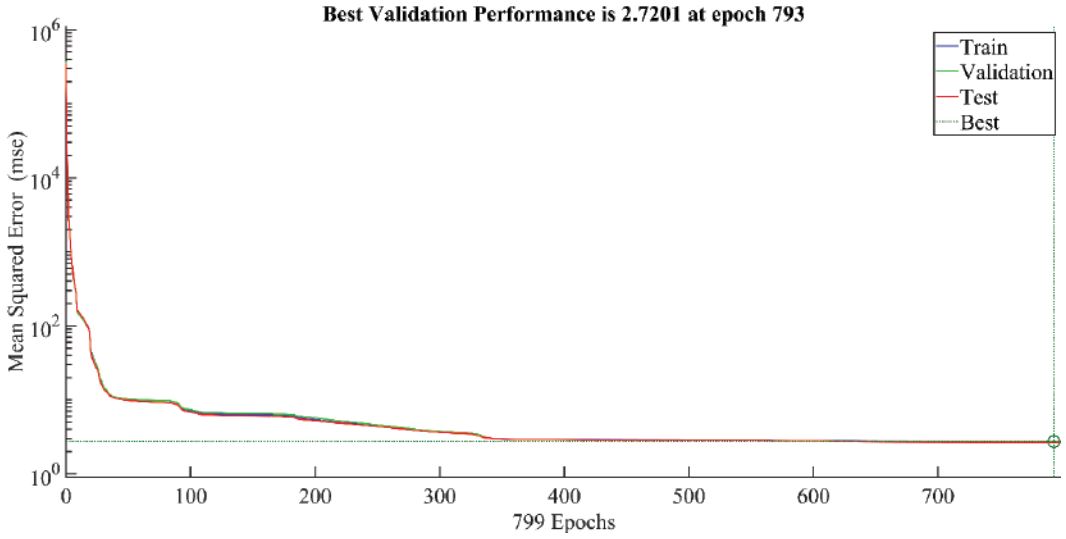

(a)

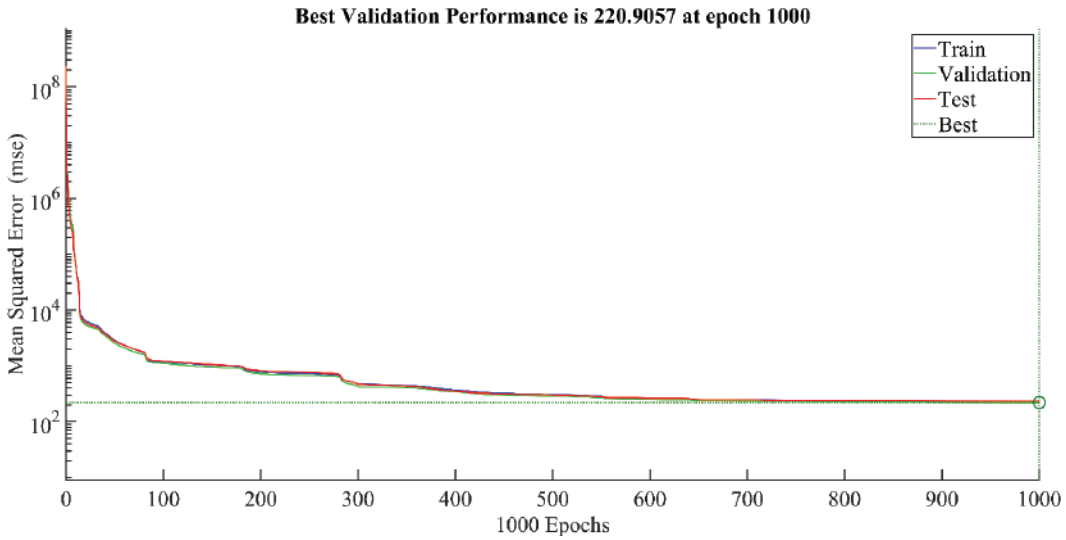

(b)

Figure 5. The training performance of the ANN model in model for (a) heat transfer coefficient, (b) pressure drop.

width of the divider has slight outcome on the ΔP when the average temperature stays the same.

Figure 4(d) displays the pressure loss value variation in the compact HEX based on the width of the channel and the exchanger length. When designing this figure, the divider width was maintained at a constant value of 0.001 m, with an air input temperature of 300 K, an air output temperature of 400 K, and an air flow rate of 1 kg/s. The figure demonstrates that the pressure loss goes up as the channel gets wider and the exchanger length value goes down. The pressure loss values for passage widths of 0.015, 0.03, and 0.045 m increased by 1.98 and 3.32 times when the exchanger length was 0.15 mm. When the exchanger length was 1 m, they increased by 2.53 and 4.75 times. The results show that the pressure loss increases as the length of the exchanger increases, especially when the width of the passage changes.

It was determined whether the training stage of the ANN structure was carried out appropriately by analyzing the training performance. The outcomes of the ANN training are illustrated in Figure 5(a) for HTC and in Figure 5(b) for ΔP, respectively. In spite of initially large MSEs throughout training the ANN architecture, they shrank with time. An epoch in MLP networks is a cycle in which data is directed after the output layer to the input layer to lower the number of errors. The MLP method that use this study are named feed-forward backpropagation (FF-BP) NN methods. The HTC model finished training afterward epoch 793, and the ΔP model finished later epoch 1000. The MSE values went down with each stage of training, validation, and testing. Figure 5 shows that the NN has finished its training. When training an ANN, it is important to look at the error histograms, which show the differences among the modeled and real results, to figure out where the training errors are coming from.

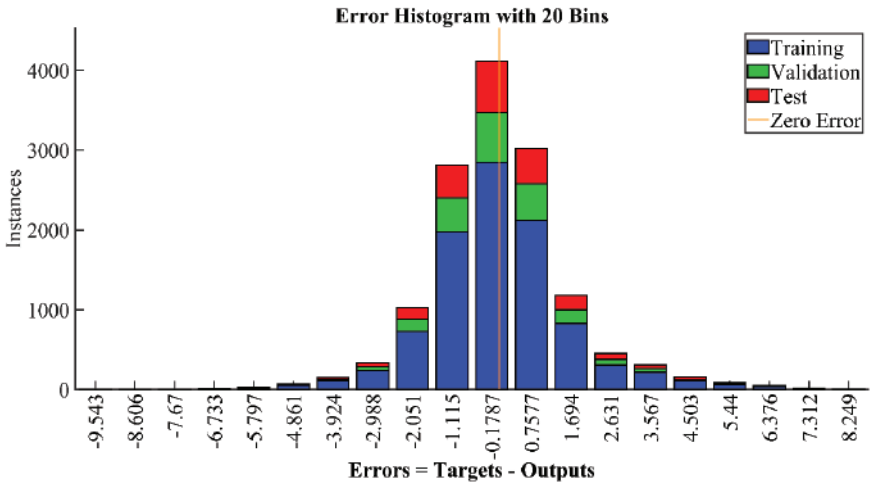

(a)

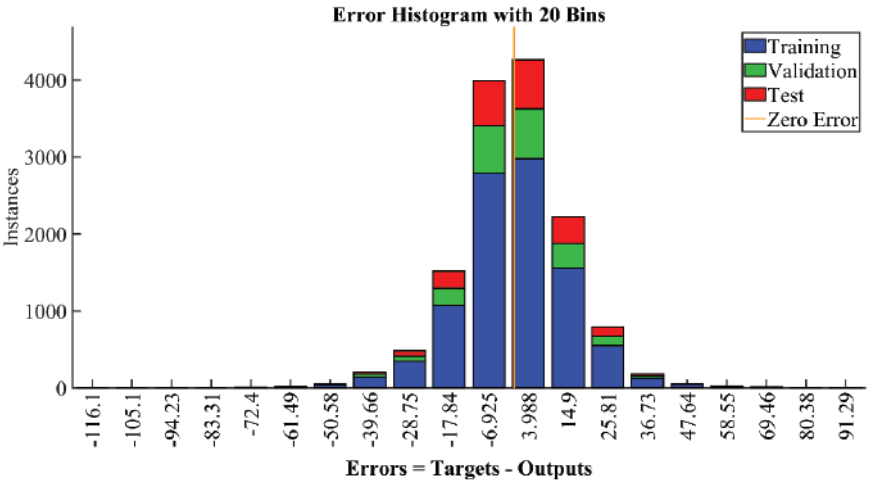

(b)

Figure 6. Error histogram for ANN model for a) heat transfer coefficient, and b) pressure drop.

The error histogram of the ANN model is shown in Figure 6. When we looked at the error histogram, we saw that the estimated error data for all three values were very near to the yellow line, which meant that there was no inaccuracy. Also, there are very few mistakes in the abscissa. The error histogram for the ANN model shows that the NN study's training stage was done correctly, with only a few mistakes. The MSE for heat transfer and ΔP was -0.1787 and 3.988, respectively. The results show that the ANN's training stage, which was meant to predict the heat transfer and ΔP values, went perfectly.

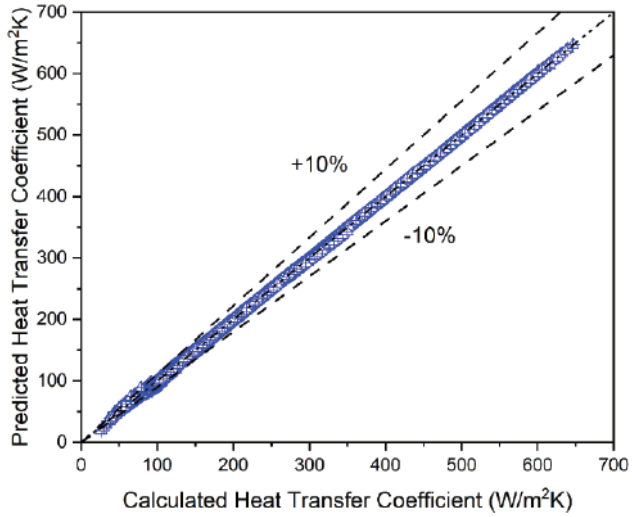

(a)

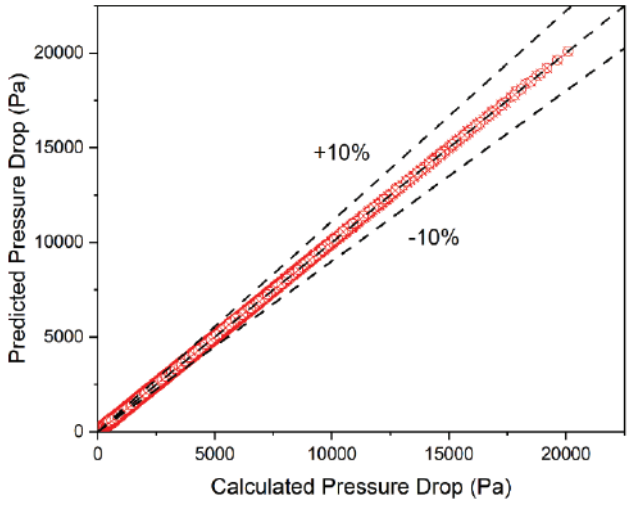

(b)

Figure 7. Target and prediction values in ANN model for (a) heat transfer coefficient, and (b) pressure drop

Figure 7(a)-(b) displays target and estimated measurements for two scenarios involving HTC and ΔP. The goals are on the x-axis, and the ANN predictions are on the y-axis. The data points for the two ANN models are either very close to zero or on a straight line. The consequences show that the data points have a margin of error of plus or minus 10 percentage points. The figures show that predicted values for HTC exceeding 200 W/m²K and ΔP surpassing 5000 Pa are within ±10 margins, whereas values below these thresholds are within ±15 margins. Table 3 details the consequences of two separate ANN representations created to forecast NN values in numerous situations. The MoD values calculated for ANN methods were found to be very low.

Figure 8 shows the MoD values, which show how different the ANN model-generated output values are from the theoretical calculations. An examination of the 13860 generated data points indicates that the majority are situated along the error line, in proximity to zero. This has become clear as we've looked at the data. Because the MoD values are so close to the line, which means 0% error, it means that the differences between the values of HTC and ΔP that the ANN and the theoretical data give are very small. It has been found that the average MoD values for heat transfer and ΔP are -0.003% and 0.0582%, respectively. The lowest values for the given parameters are -0.13% and -0.189%, and the highest values are 0.249% and 3.394%. The MoD value analysis shows that the MLP NN that is used can make very accurate predictions about the outputs of the compact plate HEX. These results are obtained by analyzing the MoD values.

A thorough error analysis of the ANN methods was performed by calculating the variances among the method results and the target data for each data point, as illustrated in Figures 9a–b. Figure 9a illustrates the differences among ANN outputs and the necessary HTC, while Figure 9b presents the ΔP. The deviations in HTC and ΔP productions after the anticipated values are given in Figure 9. The figures show the minimum, maximum, and average values of the target-prediction parameter for HTC are -10.01, 8.717, and 0.00078, respectively. These numbers are -121.50, 96.74, and 0.0978 for ΔP. The outputs generated by four

Table 3. MoD values for both ANN models in heat transfer coefficient and pressure drop

	MoD (%)			MSE	MAPE	R
	Min	Max	Ave			
for Heat Transfer Coefficient	-0.13	0.249	-0.003	2.046	0.00746	0.999
for Pressure Drop	-0.189	3.394	0.0582	173.85	0.02045	1

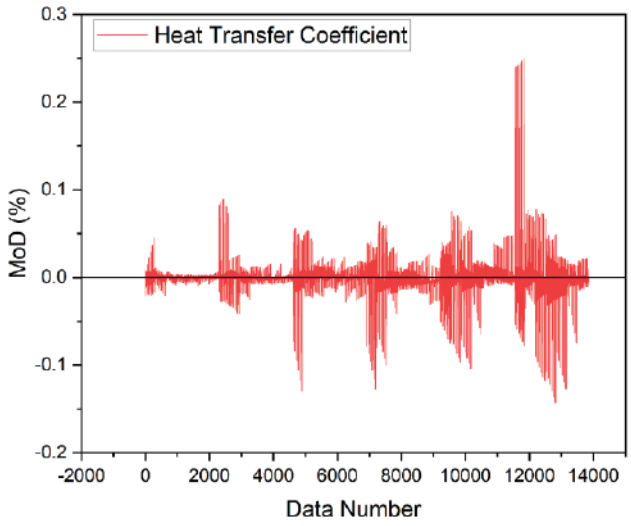

(a)

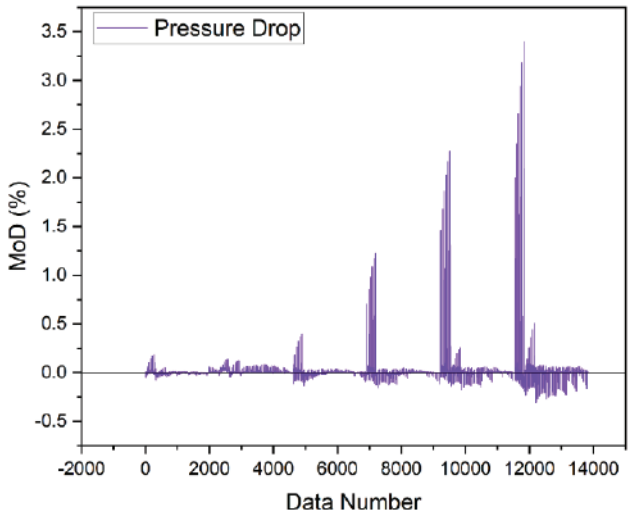

(b)

Figure 8. The calculated MoD values for each data point in ANN model for (a) heat transfer coefficient, and (b) pressure drop.

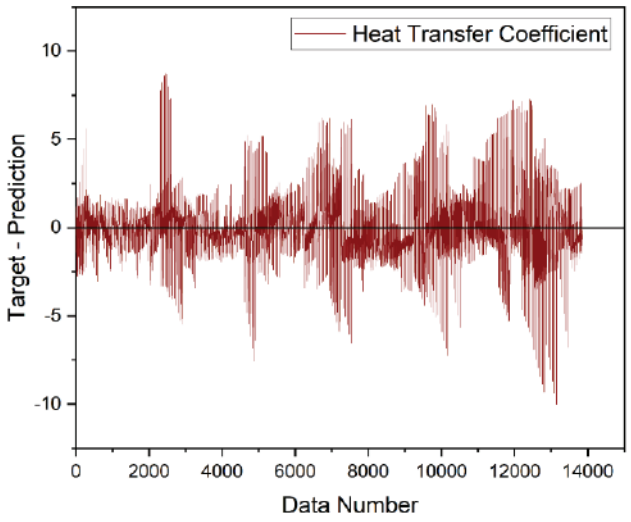

(a)

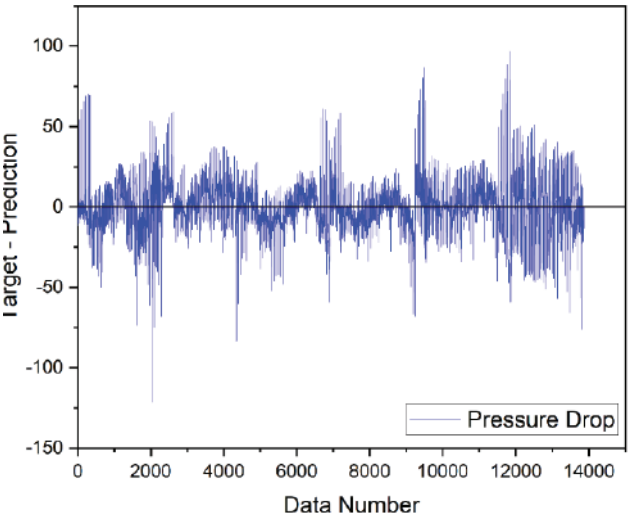

(b)

Figure 9. The differences between target values and ANN outputs in ANN model for (a) heat transfer coefficient, and (b) pressure drop.

distinct ANN models exhibit considerable similarity. The Ministry of Defense and the deviation results show that the two artificial neural network models can give neural network values with moderate standard deviations.

The MAPE values for HTC and P are shown in Figure 10. The minimum, maximum, and average MAPE values for the HTC parameter are 4.082E-07, 0.2495, and 0.00967, respectively. For ΔP, the corresponding values are determined as 1.733E-06, 3.394, and 0.02535.

CONCLUSION

This study examines the efficiency of a plate-type compact HEX in heat transfer and the pressure loss relative to its design specifications. It then looks at how those results compare to those found using the Levenberg-Marquardt artificial neural network method. To get the air inlet and output temperatures to change while keeping the atmospheric pressure and fin thickness the same, the designers had to think about a lot of different things, like the air flow rate, the width of the divider, the width of the route, and the length of the compact heat exchanger. The study produced the following results:

1. The study shows that the heat transfer coefficient in heat exchangers goes up as the channel width and air mass flow rate go up. On average, they go up by 51.3% and 93%, respectively. The coefficient also increases naturally with increasing air temperature, with a divider

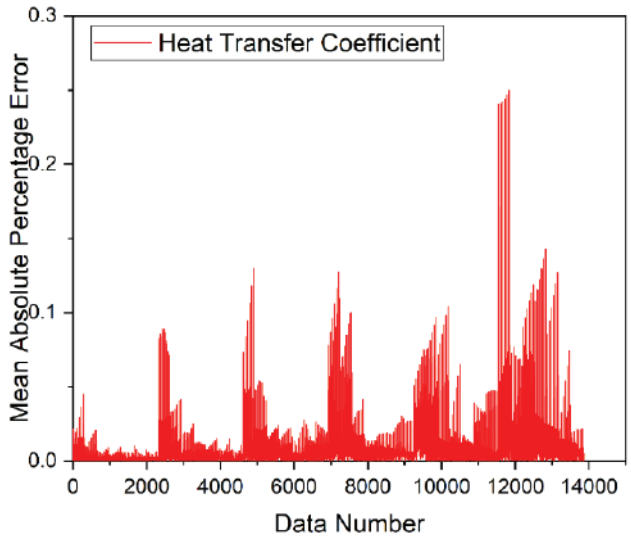

(a)

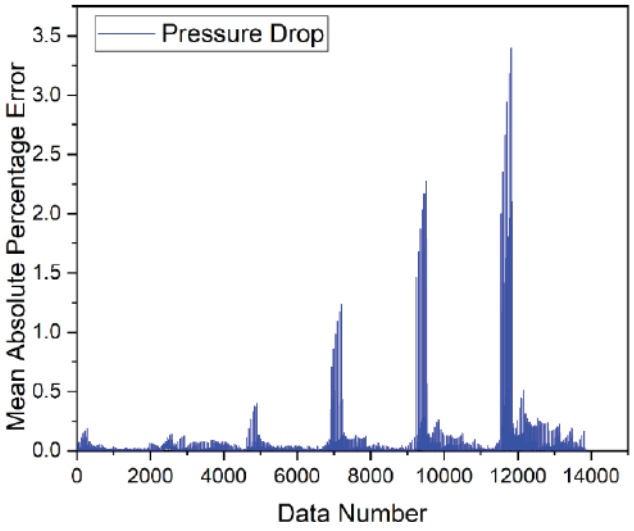

(b)

Figure 10. Mean absolute percentage error in ANN model for (a) heat transfer coefficient, and (b) pressure drop.

width of 0.001 m resulting in a 7.9% increase. Increasing channel width while maintaining exchanger length leads to higher heat transfer coefficient values.

2. The study reveals that increasing divider thickness leads to higher pressure loss, but the rate of rise decreases with passage width. Pressure drops factors increase proportionally with air flow rate, with growth rates rising proportionally with divider width. Larger divider width sizes make pressure loss worse. As the average air temperature changes, the pressure drops more, and the divider widths of 0.001 m and 0.005 m show similar increases. But the width of the divider has little effect on the drop in pressure.
3. The training phase of the ANN successfully estimated heat transfer and pressure drop values, with MSE values of -0.1787 and 3.988, respectively.
4. The study found that the predicted values for heat transfer coefficient and pressure drop are within a ±10 margin, while values below these thresholds are within a ±15 margin.
5. The MoD value analysis reveals that the MLP NN, which is implemented, accurately predicts the outputs of the compact plate heat exchanger, with average values of -0.003% and 0.0582%.
6. The heat transfer coefficient parameter has MAPE values of 4.082E-07, 0.2495, and 0.00967, while the pressure drop has MAPE values of 1.733E-06, 3.394, and 0.02535.

NOMENCLATURE

A	*Area [m²]*
b	*Width of passages [m]*
cp	*Specific heat [J/kg.K]*
D	*Diameter [m]*
DP	*Pressure drop [Pa]*
f	*Fanning friction factor*
G	*Mass flux [kg/m²]*
g	*Proportionality factor in Newton's second law*
h	*Heat transfer coefficient [W/m²K]*
j_H	*Colburn factor*
l	*Fin length [m]*
m	*Fin effectiveness parameter*
$\dot{m}$	*Mass flow rate [kg/s]*
n	*Efficiency*
Nu	*Nusselt number*
p	*Fin pitch [m]*
Pr	*Prandtl number*
q	*Heat transfer capacity [W]*
Re	*Reynolds number*
St	*Stanton number*
T	*Temperature [K]*
U	*Total heat transfer coefficient [W/m²K]*
v	*Velocity [m/s]*
X	*Data*
δ	*Width of divider [m]*
δ_f	*Fin thickness [m]*
ε	*Effectiveness*
σ	*Ratio of the free flow area to the frontal area indices*
Ave	*Average*
c	*cold*
$Calc$	*Calculated*
f	*Front*
f	*Fin*
fr	*Frontal*
h	*hot*
h	*Hydraulic*
in	*Inlet*
max	*Maximum*

min *Minimum*
o *Overall*
out *Outlet*
p *Constant pressure*
tot *Total*
w *Wall*

Abbreviations

ANN	Artificial neural network
CFD	Computational fluid dynamics
CHE	Compact heat exchanger
GA	Genetic algorithm
HEX	Heat exchanger
HTC	Heat transfer coefficient
MAPE	Mean absolute percentage error
MLP	Multilayer perceptron
MoD	Margin of deviation
NN	Neural network
MSE	Mean squared error
PCHE	Printed circuit heat exchanger
PFHE	Plate fin heat exchanger

DATA AVAILABILITY STATEMENT

The authors confirm that the data that supports the findings of this study are available within the article. Raw data that support the finding of this study are available from the corresponding author, upon reasonable request.

CONFLICT OF INTEREST

The author declared no potential conflicts of interest with respect to the research, authorship, and/or publication of this article.

ETHICS

There are no ethical issues with the publication of this manuscript.

STATEMENT ON THE USE OF ARTIFICIAL INTELLIGENCE

Artificial intelligence was not used in the preparation of the article.

REFERENCES

[1] Ermis K. ANN modeling of compact heat exchangers. Int J Energy Res 2008;32:581–594. [CrossRef]
[2] Demir MH. Thermal Modeling and Performance Analysis for a Chevron Type Heat Exchanger by Using Artificial Neural Network with Limited Experimental Data. Eur J Sci Technol 2020;18:779–789.
[3] Shi H, Chang H, Ma T, Wang Q. Prediction of Equivalent Thermal Conduction Resistance of Printed Circuit Heat Exchangers. J Therm Sci 2022;31:2281–2292. [CrossRef]
[4] Dossumbekov YK, Zhakiyev N, Nazari M A, Salem M, Abdikadyr B. Sensitivity Analysis and Performance Prediction of a Micro Plate Heat Exchanger by Use of Intelligent Approaches. Int J Thermofluids 2024;100601. [CrossRef]
[5] Jiang T, Li MJ, Yang JQ. Research on optimization of structural parameters for airfoil fin PCHE based on machine learning. Appl Therm Eng 2023;229:120498. [CrossRef]
[6] Zhu G, Wen T, Zhang D. Machine learning based approach for the prediction of flow boiling/condensation heat transfer performance in mini channels with serrated fins. Int J Heat Mass Transf 2021;166:120783. [CrossRef]
[7] Zarea H, Kashkooli FM, Mehryan AM, Saffarian MR, Beherghani EN. Optimal design of plate-fin heat exchangers by a Bees Algorithm. Appl Therm Eng 2014;69:267–277. [CrossRef]
[8] Hernández-Gil JA, Colorado-Garrido D, Alaffita-Hernández FA, Escobedo-Trujillo BA. Heat exchanger design considering variable overall heat transfer coefficient: An artificial neural network approach. Heat Transfer 2022;51:2488–2509. [CrossRef]
[9] Zeng M, Du LX, Liao D, Chu WX, Wang QW, Luo Y, et al. Investigation on pressure drop and heat transfer performances of plate-fin iron air preheater unit with experimental and Genetic Algorithm methods. Appl Energy 2012;92:725–732. [CrossRef]
[10] Gupta D, Saha P, Roy S. Multi-Objective Optimization of Air-Cooled Perforated Micro-Pin Fin Heat Sink Via an Artificial Neural Network Surrogate Model Coupled With NSGA-II. J Therm Sci Eng Appl 2024;16:011004. [CrossRef]
[11] Peng H, Ling X. Predicting thermal–hydraulic performances in compact heat exchangers by support vector regression. Int J Heat Mass Transf 2015;84:203–213. [CrossRef]
[12] Peng H, Ling X. Neural networks analysis of thermal characteristics on plate-fin heat exchangers with limited experimental data. Appl Therm Eng 2009;29:2251–2256. [CrossRef]
[13] Nascimento CAR, Mariani VC, Coelho LS. Integrative numerical modeling and thermodynamic optimal design of counter-flow plate-fin heat exchanger applying neural networks. Int J Heat Mass Transf 2020;159:120097. [CrossRef]
[14] Xie C, Yan G, Ma Q, Elmasry Y, Singh PK, Algelany AM, et al. Flow and heat transfer optimization of a fin-tube heat exchanger with vortex generators using Response Surface Methodology and Artificial Neural Network. Case Stud Therm Eng 2022;39:102445. [CrossRef]
[15] Xie GN, Sundén B, Wang QW. Optimization of compact heat exchangers by a genetic algorithm. Appl Therm Eng 2008;28:895–906. [CrossRef]

[16] Jilak A, Assareh E, Nedaei M. Application of a novel multi-objective optimisation method integrated with the artificial neural networks for optimum design of a plate heat exchanger. Australian J Mech Eng 2017;1–15. [CrossRef]

[17] Peng H, Ling X. Optimal design approach for the plate-fin heat exchangers using neural networks cooperated with genetic algorithms. Appl Therm Eng 2008;28:642–650. [CrossRef]

[18] Kays WM, London AL. Compact heat exchangers. Florida; Krieger Publishing Company; 1984.

[19] Gardner KA. Efficiency of extended surface. Trans American Soc Mech Eng 1945;67:621–628. [CrossRef]

J Ther Eng, Vol. 12, No. 2, pp. 610−634, March, 2026

Journal of Thermal Engineering
Web page info: https://jten.yildiz.edu.tr
DOI: 10.14744/thermal.0001104

Research Article

Water heater employing granular coal photothermal absorber and solar thermal collector combination

Alfan SARIFUDIN[1,2,*], Indri YANINGSIH[3], Budi KRISTIAWAN[3], Aditya WIBAWA[4], Ahmad FUDHOLI[5,6], Muhammad AZIZ[7,8]

[1]*Department of Computer Engineering, Automotive and Robotics Program, BINUS ASO School of Engineering, Bina Nusantara University, Jakarta, 15143, Indonesia*
[2]*Department of Industrial Engineering, Automotive and Robotics Program, , BINUS ASO School of Engineering, Bina Nusantara University, Jakarta, 15143, Indonesia*
[3]*Department of Mechanical Engineering, Universitas Sebelas Maret, Indonesia*
[4]*Research Center for Geological Resources, National Research and Innovation Agency (Badan Riset dan Inovasi Nasional / BRIN), 57126, Indonesia*
[5]*Solar Energy Research Institute, Universiti Kebangsaan Malaysia, Selangor, 43600, Malaysia*
[6]*Center for Energy Conversion and Conservation, National Research and Innovation Agency (Badan Riset dan Inovasi Nasional / BRIN), 15310, Indonesia*
[7]*Department of Mechanical Engineering, The University of Tokyo, Tokyo, 113-8656, Japan*
[8]*Institute of Industrial Science, The University of Tokyo, Tokyo, 113-8656, Japan*

ARTICLE INFO

Article history
Received: 07 January 2025
Revised: 30 April 2025
Accepted: 06 May 2025

Keywords:
Differential Scanning Calorimetry (DSC); Renewable Energy; Solar Energy; Spectrophotometry; Thermogravimetric Analysis (TGA); Thermodynamic

ABSTRACT

Coal's conventional use causes environmental problems and threatens future energy security. This research presents a photothermal method for coal use, integrating a granular coal photothermal absorber into a solar thermal collector for solar water heater. This method offers a novelty in utilizing heat energy from coal, which is usually burned coal, but this photothermal method converts light into heat. Therefore, the photothermal method will not produce emissions and can be used repeatedly. The solar thermal collector combines a Fresnel lens and a parabolic reflector. Scanning electron microscope and energy dispersive spectroscopy analysis shows the granular coal photothermal absorber's light-trapping carbon structure, with optimal sizes of 10-20 mesh generating temperatures of 378.15 K and an absorbance of 1.04. Thermogravimetric analysis and differential scanning calorimetry reveal a working temperature range of 336.31–684.31 K, with an optimal light-to-heat conversion temperature of 399.25 K, achieving 86.64% energy efficiency and 21.29% exergy efficiency. Performance tests show optimal solar water heater storage temperatures of 317.88 K and 316.75 K. The water temperature in the storage corresponds to the application of warm water bathing. The solar thermal collector's maximum energy and exergy efficiencies are 33.06% and 5.51%, respectively, with average efficiencies of 22.90% and 3.44%. The solar water heater system peaks at 27.85% energy and 5.90% exergy efficiency, with average efficiencies of 20% and 3.09%. This approach highlights potential sustainable energy use and reduced environmental impacts of coal utilization.

Cite this article as: Sarifudin A, Yaningsih I, Kristiawan B, WibawaA, Fudholi A, Aziz M. Water heater employing granular coal photothermal absorber and solar thermal collector combination. J Ther Eng 2026;12(2):610−634.

***Corresponding author.**
*E-mail address: alfansarifudin.indonesia@gmail.com, alfan.sarifudin@binus.edu

This paper was recommended for publication in revised form by Editor-in Chief Ahmet Selim Dalkilic

Published by Yıldız Technical University Press, İstanbul, Turkey
Yıldız Technical University. This is an open access article under the CC BY-NC license (http://creativecommons.org/licenses/by-nc/4.0/).

INTRODUCTION

Coal is one of the most abundant natural rocks and is currently the most widely used energy source worldwide. In 2023, the coal supply reached 156,636,851 TJ, which is equivalent to 27% of the world's energy supply, and its dominant supply is only below oil at 29% [1]. Currently, the most popular method for utilizing the energy contained in coal is combustion [2]. However, coal combustion has the negative effect of releasing carbon emissions into the atmosphere, damaging the environment [3]. In addition, coal combustion also faces concerns due to its limited resources and non-renewable (non-renewable). In response to these problems, utilizing coal without burning is considered an appropriate option. It includes the photothermal process, where coal is used as a light absorber to convert solar radiation into heat. This concept is promising because solar energy is renewable with abundant availability, although its utilization is still very low. The potential of solar energy reaching Earth reaches about 440,000 TWh [4]. However, the use of solar energy is still low because, by 2022, it will only be 1,322.62 TWh or less than 1% of the global energy mix and its potential [5], [6].

Coal is a sedimentary rock whose primary composition element is carbon. He et al. [7] have classified various carbon-based materials as photothermal absorbers. Therefore, converting solar radiation energy into heat via a photothermal method is more prospective for sustainability and protecting the environment than just burning it. Moreover, several previous studies have proven that natural rocks with a granular structure are useful as photothermal absorbers in various types of solar thermal collectors and applications. Natural materials with dark colors and pores have the potential to produce reliable photothermal performance for low and medium temperatures such as solar water heaters [8]. The granular structure is a type of light trap structure that can increase light absorbance because it recaptures the reflected light [9]. Table 1 presents the latest research developments regarding solar photothermal absorbers with granular structures from natural rock materials.

Solar thermal performance is also greatly influenced by the type of its collector [21]. Most of the previous research presented in Table 1 used a flat plate type. Therefore, the temperature generation performance was relatively low. Based on the classification carried out by Bie et al. [22], solar thermal collector (STC) temperatures are classified into low (<353.15 K), intermediate (353.15 K to 523.15 K), and high (>523.15K). The low-temperature generation by flat plate is because the concentration ratio is ≤1 times [23]. The experiment conducted by Elmaadawy et al. [18] using a parabolic reflector tracking system (PRTC) could be classified as an intermediate temperature. It is because the PRTF's temperature could reach a temperature of 375.15 K [16]. This happens because the concentration of the parabolic reflector is 15-40 times higher than the flat plate type [24].

As shown in Table 1, it can be understood that there has been no research using coal as a photothermal absorber material for solar thermal collectors. The latest research conducted by Sarifudin et al. [25], who compared natural

Table 1. Development of research on solar photothermal absorbers with granular structures from natural rock materials

Materials	Application	Type of Collectors	Performance			Ref.
			α	T	η	
Pebble	Solar water heater	Flat plate	Na	336.95 K	86.40%	[10]
Granit	Solar water heater	Flat plate	Na	ΔT 7.64 K	64.44%	[11]
Gravel	Solar dryer	Flat plate	Na	332.45 K	50.12%	[12]
Pumice-carbon-silver	Solar steam generation and water treatment	Prismatic	94,9%	<318.15 K	88,80%	[13]
Pumice	Solar desalination	Flat plate	Na	≈343.15 K	28.80%	[14]
Gravel	Solar desalination	Hemispherical	Na	342.15 K	65.68%	[15]
Gravel	Solar desalination	Parabolic concentrator solar tracking system	Na	375.15 K	41.83%	[16]
Gravel - limestone (composite)	Solar air heater	Flat plate	93,5%	333.15 to 343.15 K	10%	[17]
Gravel, wick, and carbon black nanoparticles	Solar desalination	Flat plate	Na	344.15 K	50%	[18]
Fine stone (black basalt)	Solar desalination	Flat plate	Na	335.25 K	32.07%	[19]
Pebbles	Solar desalination	Flat plate	Na	332.15 K	44%	[20]

*Note: α is the light absorbance of the photothermal absorber, η is the efficiency of the solar collector system, and T is the temperature of the absorber or the material heated by the absorber.

rocks with the granular structure of andesite, coal, and pumice using controlled laboratory experimental methods, found that coal material was the best. Furthermore, tests using concentrated xenon light radiation in laboratory scale condition showed better heat generation performance than direct radiation [26]. Therefore, the next urgency is to know coal material as a photothermal absorber which is installed in concentrated solar collectors. Moreover, this research also tested the optimal granular size and operational limits.

The novelty of this research is in the utilizing a different design type of STC. A type of STC with an equivalent concentration level is necessary to obtain a temperature generation comparable to the results of the research findings by Elmaadawy et al. [18]. Fresnel Lens is a type of solar collector with a concentration equivalent to a value of 15-40 times [27].

This research uses a stationary system to consider system simplification. The tracker system is more complicated because it requires an electrification device to control the automation system and drive motor. However, the stationary system has a weakness due to the sun's movement, so the light's focus cannot always be precisely on the absorber. Therefore, the Fresnel lens collector is combined with a compound parabolic reflector to reflect the unfocused light to the absorber. A compound parabolic reflector is a collector with an intermediate performance because its concentration reaches 1-5 times with an operational temperature range of 333.15 to 513.15 K [28]. Moreover, Fresnel lens collectors have the advantages of using little material, cost-effectiveness, and high optical efficiency [29].

Based on the background of the problems above and the solutions offered, this research aims to determine the morphology and element composition of a granular coal photothermal absorber (GCPA). Considering the research findings of Attia et al. [15] and Mohamed et al. [19], granular size influences performance. Therefore, this study also optimizes size for temperature generation and light absorbance. Furthermore, this study also wants to know the operating temperature limit of GCPA without damage and its enthalpies. Finally, this study calculates the efficiency of energy and exergy for the fundamental component of GCPA and the systems of STC and SWH.

MATERIALS AND METHODS

The main objectives of this research lay in the development of GCPA materials and the STC-SWH system. Therefore,

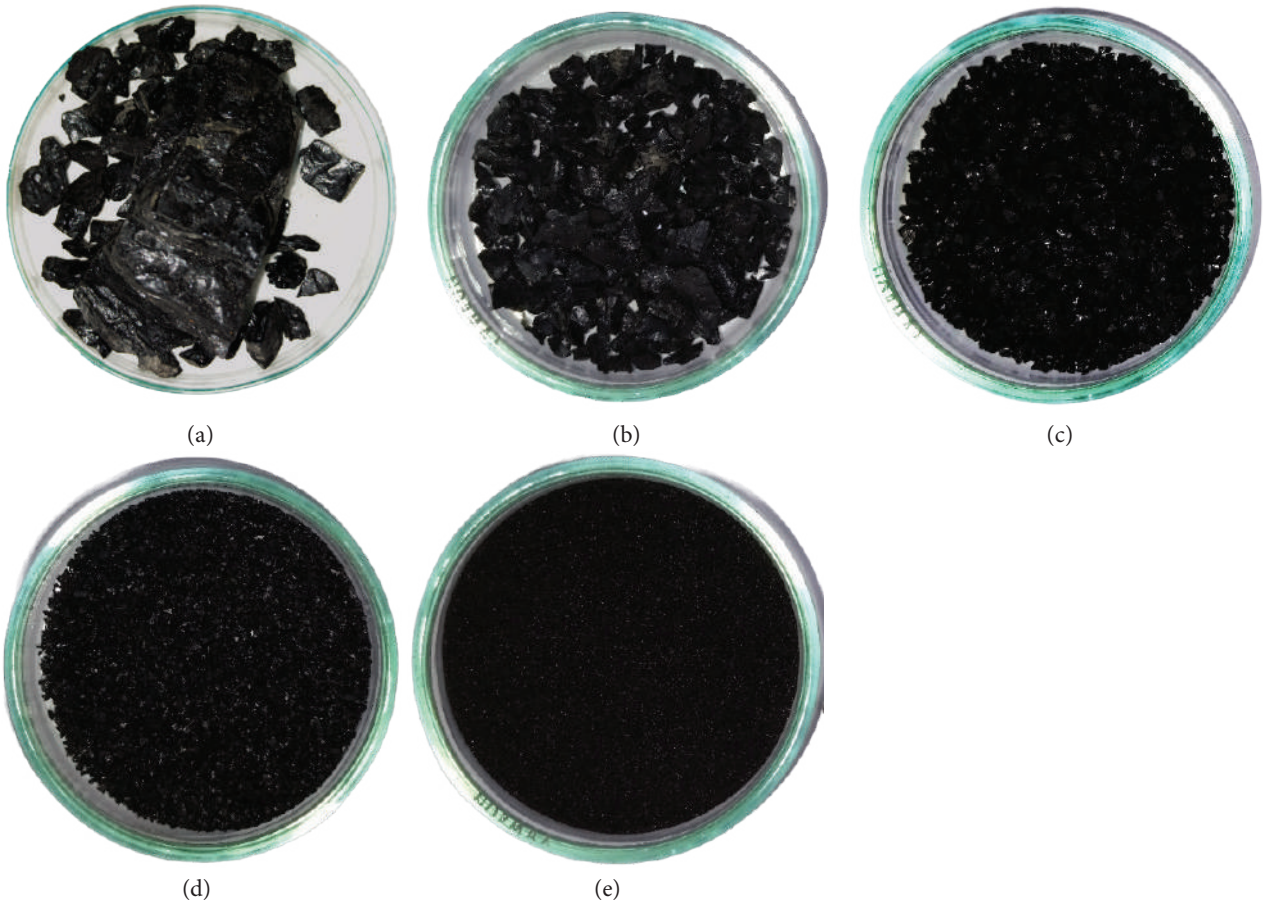

Figure 1. Granular coal in different sizes: (a) chunk, (b) 5−10 mesh, (c) 10−20 mesh, (d) 20−60 mesh, and (e) 60−100 mesh.

below is presented the process of making GCPA and the STC-SWH specifications that were researched and developed.

GCPA Preparation

The raw materials in this research are coal chunks with random sizes and dirty, as shown in Figure 1 (a). GCPA in various sizes that are ready to be tested are presented in Figure 1 (b)–(e). Specimens are prepared from coal chunks, which are then crushed [26]. The crushed materials are then sieved to pass through a big mesh and retained on a small mesh. Next, the sieve material is washed using water to obtain clean natural material. Washing not only removes dirt from the material but also removes fine grains that cover the pores of the material. The material that has been cleaned is then dried in an oven at 423.15 K for 3 h. After baking, the material is left in the open space for 48 h to make the temperature return to room temperature. The material preparation procedure is illustrated in Figure 2.

STC-SWH Specification

The STC-SWH tested in this study is presented in Figure 3(a), and its main components are presented in Figure 3(b). Moreover, the detailed information about each component is listed in Table 2.

Analytical Method

This study was conducted through a tiered experiment with a workflow shown in Figure 4. More detailed information regarding the analytical methods used is explained in each subchapter.

Scanning Electron Microscopy and Energy Dispersive Microscopy (SEM-EDS)

SEM test was carried out to determine the morphological properties of the material. Furthermore, the EDS test was used to determine the composition of the elements contained. Preparation is carried out with gold plating to ensure the GCPA structure does not burn easily during testing.

Temperature Generation in Simulator

The dried material was then tested for its temperature generation performance using a Fresnel lens collector under one solar illumination (1000 W/m^2). The power used by the xenon lamp is 100 W and 12 V DC voltage. The temperature generation test was conducted in a controlled room at a temperature of 298.15±1 K and humidity of 51.6 to 82.2 for 1200 s. The thermometer used has an accuracy of 0.25 K with a maximum error of ±2 K. The hygrometer used has an accuracy of 0.1% with a maximum error of ±3%. The 20 g of GCPA was tested in dry conditions.

Optical Analysis

Optical absorbance testing uses a spectrophotometer with a wavelength of 360–1100 nm (Vis-Infrared). Tests were carried out in dry conditions with all size variations. The purpose is to determine the optical properties of absorbance and transmittance of the material. Transmittance ($\%T$) is defined as the amount of transmitted light (I) at each incident light wavelength (I_o), formulated in Eq. (1) [31], [32].

$$\%T = \frac{I}{I_o} \tag{1}$$

Meanwhile, absorbance (α_s) is defined as a logarithmic function formulated in Eq. (2) [33] or (3).

$$\alpha_s = \log_{10}\left(\frac{1}{\%T}\right) \tag{2}$$

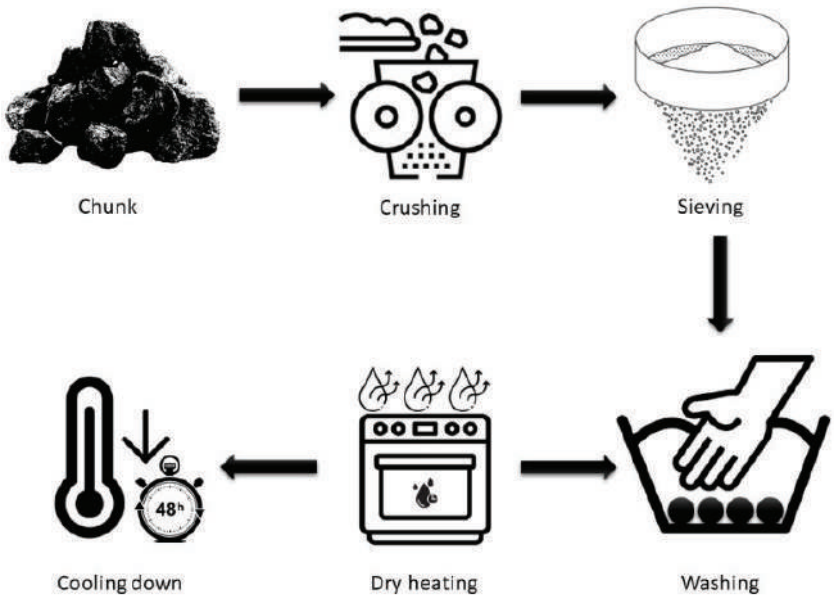

Figure 2. Material preparation process.

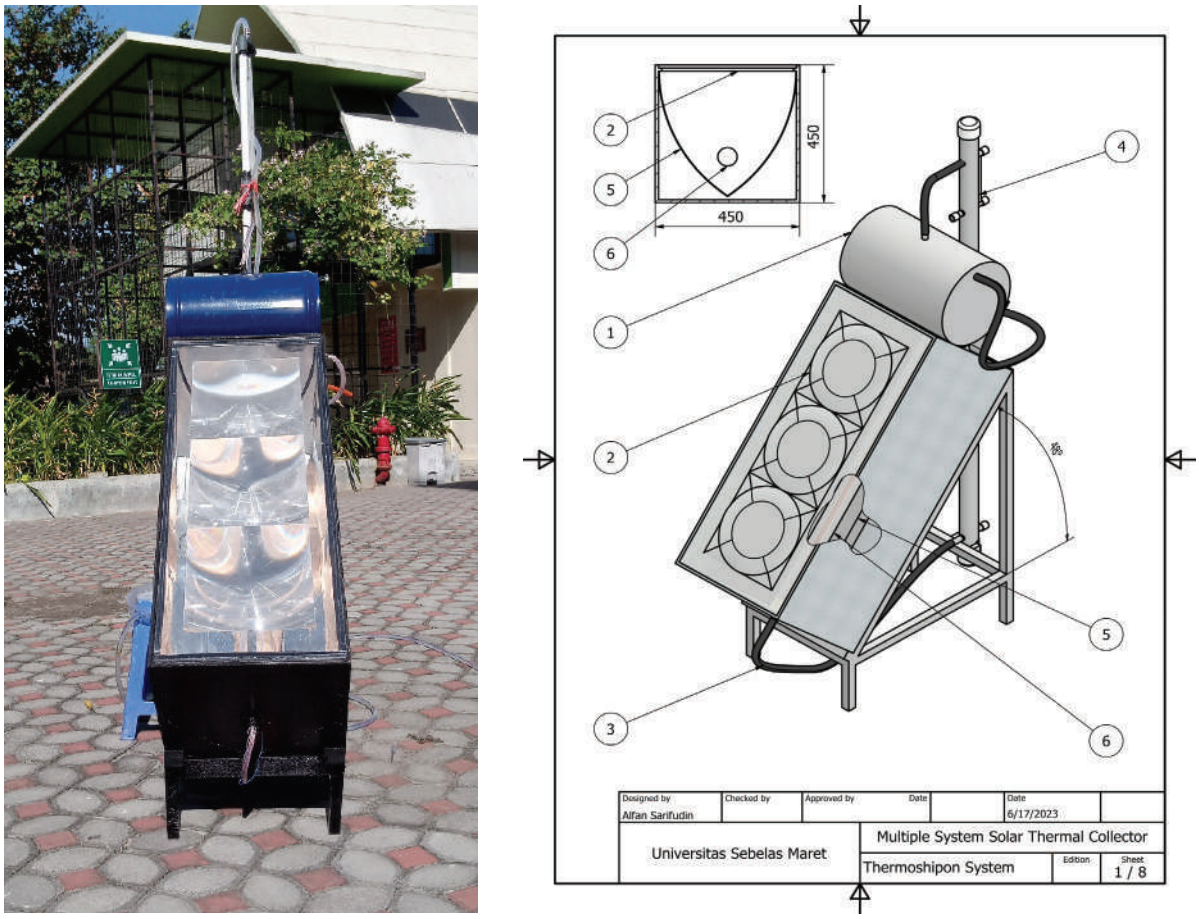

(a) (b)

Figure 3. Developed STC-SWH: (a) real view, and (b) main components illustration.

Table 2. Detail information of Figure 3 (b)

No.	Components	Specification
1.	Water tank	25 L or 23,325 kg of water
2.	Fresnel Lens	0.3 m × 0.3 m
3.	Plumbing	Insulator hose ¾ inch
4.	Water volume meter	1 mL
5.	Compound parabolic reflector	PVC mirror
6.	Tube receiver	48° (optimal angle) [30]. More detailed specifications are shown in Figure 5.

$$\alpha_s = \log_{10}\left(\frac{I_o}{I}\right) \tag{3}$$

To calculate the absorbance for all wavelengths is formulated in Eq. (4) [34].

$$\alpha = \frac{\int_{\lambda_{min}}^{\lambda_{max}} [1 - \%T(\lambda)] I_s(\lambda) d\lambda}{\int_{\lambda_{min}}^{\lambda_{max}} I_s(\lambda) d\lambda} \tag{4}$$

where λ_{max} is the maximum wavelength, and λ_{min} is the minimum wavelength. I_s is the wavelength resulting from the solar irradiation spectrum, and $T(\lambda)$ is the total transmittance at that wavelength (λ).

If the spectrophotometer machine directly displays absorbance and transmittance data at each wavelength, the absorbance and transmittance for all wavelengths are formulated in Eqs. (5) and (6).

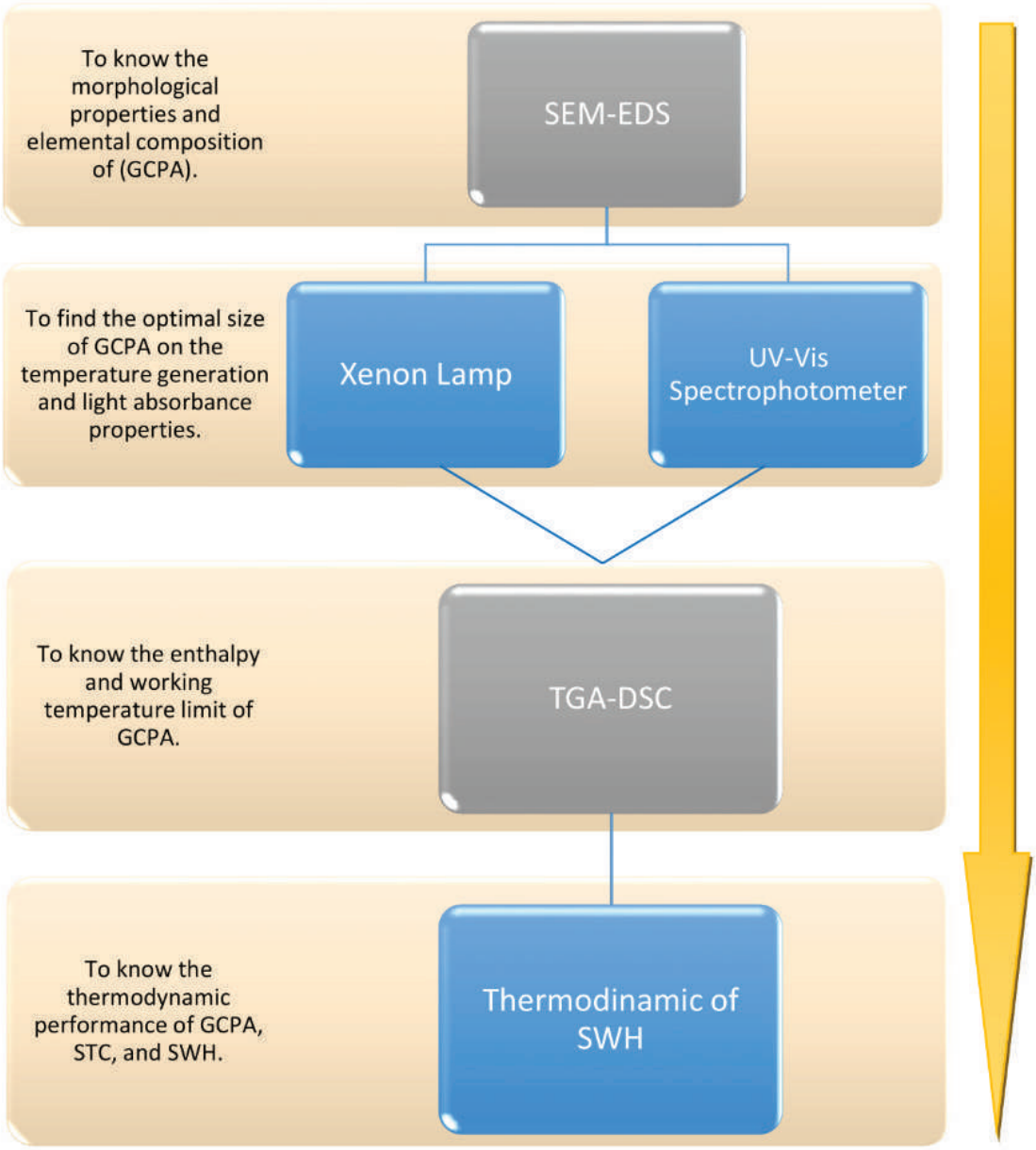

Figure 4. Workflow of the current research.

$$\alpha(\lambda) = \frac{\sum_{\lambda_{min}}^{\lambda_{max}} \alpha_s}{n} \quad (5)$$

$$\%T(\lambda) = \frac{\sum_{\lambda_{min}}^{\lambda_{max}} \%T}{n} \quad (6)$$

where n is the number of wavelength data taken.

TGA-DSC

Thermogravimetric analysis (TGA) testing is carried out to determine mass changes in the material because of thermal transition and degradation in the material. In this way, the working temperature operational limit of the photothermal absorber material will be known without significant damage. Furthermore, a differential scanning calorimetry (DSC) test is carried out to determine changes in material enthalpy due to physical and chemical degradation with changes in temperature at a certain time. These tests used granular coal material with optimal temperature generation and light absorbance performance. Apart from the fact that only material with the optimal size is selected in testing at STC-SWH, it is also because thermal degradation in coal is not influenced by particle size [35, 36]. Testing

was carried out, increasing the temperature by 1 K/min from 290.31 to 1,273.31 K.

Thermodynamics Analysis

The thermodynamic analysis is carried out in two conditions: unloaded and loaded conditions. Each test is carried out to determine the performance of the components (absorber) and main systems (STC and SWH). Unloaded condition testing is used to determine the GCPA performance in converting light to heat by temperature generation, energy efficiency, and exergy efficiency. The test was carried out on August 15-17 without being used to heat water. Meanwhile, the loaded condition test was carried out on August 12-14 to heat the water in the system. The position of each temperature sensor and the specifications of the components on the receiver tube are presented in Figure 5.

The loaded condition instrument was used to analyze the performance of the STC-SWH system. The sensor installation position in the system is presented in Figure 6.

The energy conversion efficiency ($\eta_{ece.abs}$) in the photothermal absorber is formulated by Yan and Li (2023) in Eq. (7).

$$\eta_{ece.abs} = \frac{m \times \Delta H_T}{I \times A_{abs} \times (\Delta t)} \quad (7)$$

where m is the mass of the absorber, ΔH_T is the change in enthalpy of the absorber at (T), I is the light illumination intensity, A_{abs} the surface area of the absorber exposed to radiation, and Δt is the time required to reach (T).

The measurements were carried out by Yan and Li (2023) in direct radiation conditions without being focused, whereas in this experimental case, the light was focused. Therefore, the focus value of the light radiation (F) is required, formulated in Eq. (8).

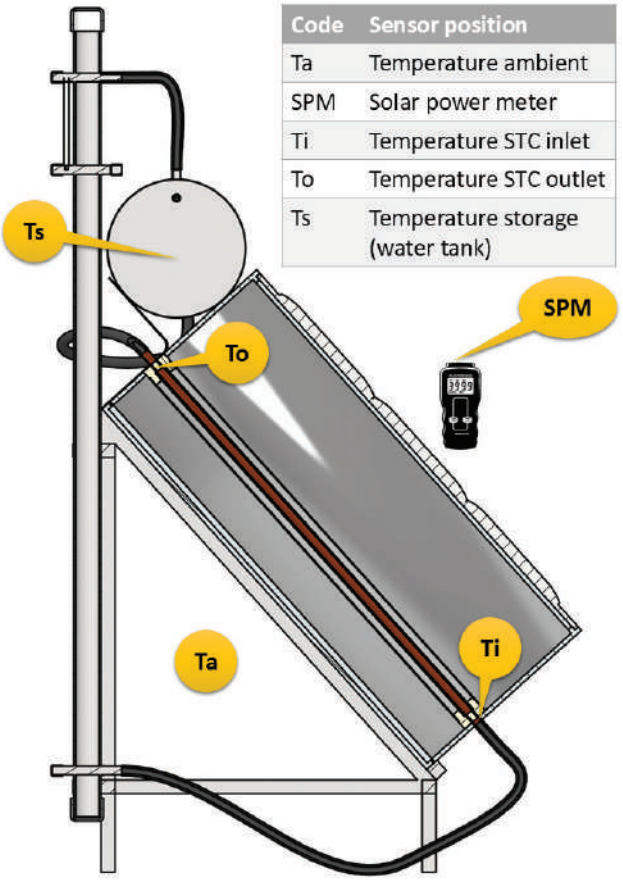

Figure 6. Sensor installation position for loaded condition test.

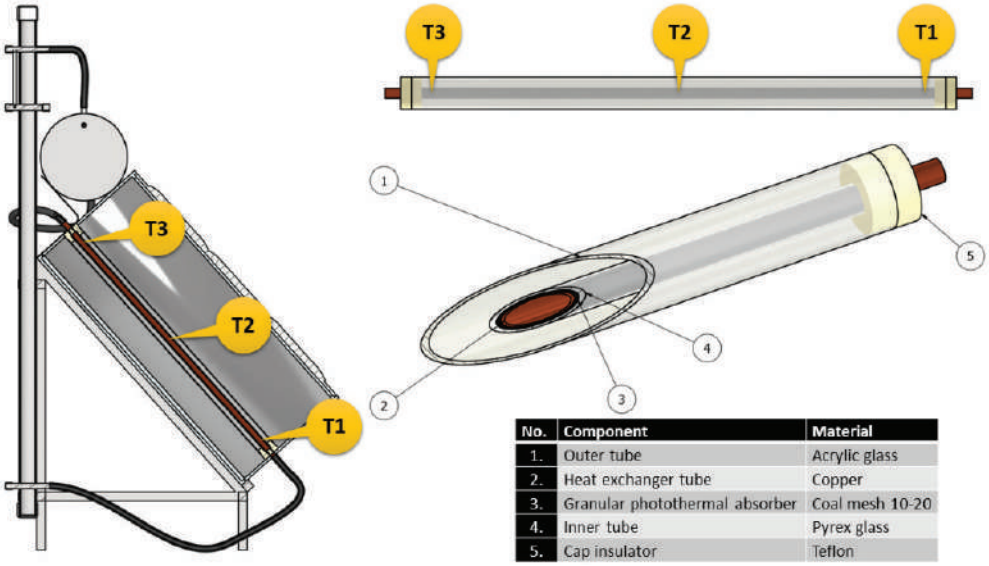

No.	Component	Material
1.	Outer tube	Acrylic glass
2.	Heat exchanger tube	Copper
3.	Granular photothermal absorber	Coal mesh 10-20
4.	Inner tube	Pyrex glass
5.	Cap insulator	Teflon

Figure 5. Installation position of the temperature sensor in the absorber and receiver components.

$$\eta_{abs} = \frac{m \times \Delta H_T}{F \times I \times A_{abs} \times (\Delta t)} \quad (8)$$

The radiation focus value (F) comes from the combined material transmittance (%T) and concentration ratio (C), formulated in Eq. (9).

$$F = \%T_{total} \times C \quad (9)$$

The concentration ratio factor (C) is the ratio of the lens surface area (A_{lens}) to the absorber surface area ($A_{absorber}$), formulated in Eq. (10) [37].

$$C = \frac{A_{lens}}{A_{absorber}} \quad (10)$$

The lens surface area in the simulation is 0.09 m^2 and the lens surface area in the SWH is 0.44 m^2. The absorber surface area in the simulator is 8.10×10^{-3} m^2 and the absorber surface area in SWH is 1.76×10^{-1} m^2.

The light that passes through a lens cannot be completely transmitted. Therefore, the transmittance of the system is the combination of several lenses' transmittance, which through the light passes, as formulated in Eq. (11).

$$\%T_{total} = \%T_1 \times \ldots \times \%T_n \quad (11)$$

The transmittance for the lens in the simulator is 92%, while the combined transmittance in the SWH is 0.73%. The transmittance of SWH is smaller than that of the simulator transmittance because the lens on the SWH is thicker and composed of two layers of sandwich (acrylic lens, Frensnel lens, and glass tube). The lens on the simulator only consists of a Fresnel lens. In addition, the SWH testing conditions are in a real environment, so there is dust that can reduce transmittance, while the simulator is placed in a closed room. The transmittance value is calculated using equation 11 and measured by comparing the intensity of light illumination transmitted by the lens to the intensity of light illumination on the lens surface.

Eqs. (7) to (11) can be simplified and Eq. (12) can be obtained.

$$\eta_{energy.abs} = \frac{m \times \Delta H_{(t,m,T)}}{\%T_{total} \times A_{lens} \times I \times (\Delta t)} \quad (12)$$

The exergy efficiency of the photothermal absorber is the ratio between the heat exergy converted by the photothermal absorber to the maximum potential exergy obtained from the radiation source, formulated in Eq. (13).

$$\eta_{exergy.abs} = \frac{\dot{E}x_{abs.heat}}{\dot{E}x_{sources}} \quad (13)$$

The heat conversion exergy by a photothermal absorber was formulated by Li et al. (2023) and Hu et al. (2023) using the maximum possible limit approach for heat energy that can be utilized in the Carnot formula written in Eq. (14).

$$\dot{E}x_{abs.heat} = \dot{Q}_{abs}\left(1 - \frac{T_a}{T_{abs}}\right) \quad (14)$$

where $\dot{Q}_{abs}$ is the heat flow in the absorber, T_a is the ambient temperature, and T_{abs} is the absorber temperature.

The heat flow rate of the photothermal absorber is formulated in Eq. (15).

$$\dot{Q}_{abs} = \eta_{opt.abs} \times \dot{G}_{sources} \quad (15)$$

where $\eta_{opt.abs}$ is the optimal energy efficiency and $\dot{G}_{sources}$ is the rate of solar radiation energy.

Exergy produced from light radiation sources ($\dot{E}x_{sources}$) is formulated using the Petela equation which is formulated in Eq. (16) [39].

$$\dot{E}x_{sources} = A_{abs} \times I_{sources}\left[1 + \frac{1}{3}\left(\frac{T_a}{T_{sources}}\right)^4 - \frac{4}{3}\left(\frac{T_a}{T_{sources}}\right)\right] \quad (16)$$

where A_{abs} is the surface area of the absorber, $I_{sources}$ is the intensity of the light radiation source, T_a is the ambient temperature, and $T_{sources}$ is the temperature of the light radiation source. The temperature of the arc of light in a xenon lamp is 1280.15 K [40], and the surface temperature of the sun is 6,273.15 to 20,273.15 K [41].

Based on the explanation of Eqs. (13) to (16), the exergy efficiency of the photothermal absorber can be simplified to Eq. (17).

$$\eta_{exergy.abs} = \frac{\eta_{opt.abs}\left(1 - \frac{T_a}{T_{sources}}\right)}{\left[1 + \frac{1}{3}\left(\frac{T_a}{T_{sources}}\right)^4 - \frac{4}{3}\left(\frac{T_a}{T_{sources}}\right)\right]} \quad (17)$$

Solar thermal collector energy efficiency ($\eta_{energy\ STC}$) is the ratio of the energy produced to the energy required to operate the system in Eq. (18) [42]. Where the energy produced is in the form of heat [43] and the energy input is in the form of solar radiation [44].

$$\eta_{energy\ STC} = \frac{\dot{E}_{output}}{\dot{E}_{input}} = \frac{\dot{E}_{useful\ heat}}{\dot{E}_{solar\ radiation}} = \frac{\dot{Q}}{\dot{G}} \quad (18)$$

Useful energy in the heat form ($\dot{E}_{heat}$) [45] or heat flowing in the pipe of STC ($\dot{Q}_{heat\ flow}$) [46] is formulated in Eq. (19).

$$\begin{aligned} \dot{E}_{useful\ heat} &= \dot{Q}_{heat\ flow.STC\ to\ WT} \\ &= Cp \times \dot{m} \times \left(T_{out(col)} - T_{in(col)}\right) \end{aligned} \quad (19)$$

In the thermosiphon mechanism, the mass flow rate of water ($\dot{m}$) is very slow, so it is difficult to measure. However, by the second law of the thermodynamics approach, which states that heat flows from high potential to low potential, the mass flow rate can be calculated. Evidence of mass flow in the system is a change in temperature increase in the storage even though the connecting hose between the STC outlet and storage inlet is an insulator, so the heat flow is convection. Finally, the system will go to the Zeroth law of thermodynamics (energy balance), which is formulated in Eq. (20).

$$\dot{Q}_{heat\ flow.STC\ to\ WT} \approx \dot{Q}_{haet\ change.wt} + \dot{Q}_{haet\ change.stc} + \dot{Q}_{heat\ flow\ loss.wt} + \dot{Q}_{heat\ flow\ loss.STC} \quad (20)$$

The water heat change rate in the tank is formulated in Eqs. (21) and (22) [47].

$$\Delta\dot{Q}_{heat\ change.wt} = \frac{\overline{Cp}_{water} \times m_{water\ in\ tank} \times \Delta T_{water\ in\ tank}}{\Delta t} \quad (21)$$

$$\Delta\dot{Q}_{heat\ change.wt} = \frac{\overline{Cp}_{water} \times m_{water\ in\ tank} \times (T_{tn} - T_{tn-1})}{\Delta t} \quad (22)$$

The water heat change rate in the STC is formulated in Eqs. (23) and (24).

$$\Delta\dot{Q}_{heat\ change.STC} = \frac{\overline{Cp}_{water} \times m_{water\ in\ STC} \times \Delta T_{water\ in\ STC}}{\Delta t} \quad (23)$$

$$\Delta\dot{Q}_{heat\ change.STC} = \frac{\overline{Cp}_{water} \times m_{water\ in\ STC} \times \frac{((T_{outlet} + T_{intlet})_{Tn} - (T_{outlet} + T_{intlet})_{tn-1})}{2}}{\Delta t} \quad (24)$$

where T_{tn} is the temperature in the n^{th} period and T_{tn-1} is the temperature in the previous period.

Considering that the value of Cp_{water} changes for changes in temperature, the average value in the range of temperature changes is used, formulated in Eq. (25).

$$\overline{Cp}_{water} = \left| \frac{Cp_{water.T_{t1}} + Cp_{waterT_{t2}}}{2} \right| \quad (25)$$

The water mass in the full tank and STC is 23.325 and 0.094 kg, respectively. Evaporation and condensation that occur do not change the mass significantly because the installed measuring instrument does not detect any changes in water volume.

Heat flow loss in the water tank ($\dot{Q}_{heat\ flow\ lost.wt}$) is calculated using Newton's law of cooling in Eq. 26, where k is the heat transfer coefficient and T_t is the temperature at the time (t) [48].

$$\frac{dQ}{dt} = k(T_{ambient} - T_t) \quad (26)$$

For application in this case study, Eq. 26 can be written as Eq. (27).

$$\dot{Q}_{heat\ flow\ loss.wt} = k(T_{ambient} - T_t) \quad (27)$$

When solar radiation power has a value of 0, no heat energy from solar radiation conversion enters the water tank, so the heat energy change rate in the tank is the heat loss rate, as formulated in Eq. (28).

$$\frac{\Delta Q_{heat\ flow\ loss.wt}}{\Delta t} = k(T_{ambient} - T_t) \quad (28)$$

The heat loss rate at the collector is also formulated similarly in Eq. (29).

$$\frac{\Delta Q_{heat\ flow\ loss.STC}}{\Delta t} = k(T_{ambient} - T_t) \quad (29)$$

Based on calculations of the temperature data of the system in Figure 13 using Eqs. (28) and (29), the k value in the water tank was found to be -3,844 J/s·K while at the collector, it was -0,086 J/s·K.

The K value validation is carried out using the Zeroth law of thermodynamics (energy balance between systems), which applies Eq. (30).

$$\begin{aligned} \dot{Q}_{heat\ flow.STC\ to\ WT} &\approx \dot{Q}_{haet\ change.wt} + \dot{Q}_{haet\ change.stc} \\ &+ \dot{Q}_{heat\ flow\ loss.wt} + \dot{Q}_{heat\ flow\ loss.STC} \\ &\approx \overline{Cp} \times \dot{m} \times (T_{out(col)} - T_{in(col)}) \end{aligned} \quad (30)$$

The validation test of each calculation in Eq. (30) using the coefficient of variation shows that the error level is 0%. The calculation results are presented in Figure 14.

Energy input ($\dot{E}_{input}$) per unit time is formulated in Eq. (31) [49], where I_s is the solar intensity and A_{STC} is the STC surface area. The conservation of energy in terms of the first law of thermodynamics (energy cannot be created or destroyed but can change form) is formulated in Eq. (31). Where the input energy ($\dot{E}_{input}$) turns into useful energy in the form of heat ($\dot{E}_{useful\ energy\ (heat)}$) and useless energy ($\dot{E}_{useless\ energy}$).

$$\begin{aligned} \dot{E}_{input} &= \dot{E}_{solar\ radiation} = \dot{G} \\ &= I_s \times A_{STC} \rightarrow \dot{E}_{useful\ energy\ (heat)} \\ &+ \dot{E}_{useless\ energy} \end{aligned} \quad (31)$$

Useless energy is formed due to the apparent motion of the sun and errors in collector geometry, which result in the focus of light not being able to fall precisely on the absorber. Furthermore, useless energy occurs because there is light that is reflected and transmitted by the collector and absorber. Useless energy is also caused by absorber conversion inefficiencies. Therefore, the absorber cannot convert all the sunlight obtained as formulated in Eq. (32).

$$\dot{E}_{useless\ energy} = \dot{G}_{unfocused} + \dot{G}_{reflectance} + \dot{G}_{transmittance} + \dot{E}_{inefficiencies.abs} \quad (32)$$

The contribution of useless energy ($\%\dot{E}_{useless\ energy}$) to STC is formulated in Eq. (33).

$$\%\dot{E}_{useless\ energy} = \frac{\dot{E}_{useless\ energy}}{\dot{E}_{input}} = \frac{\dot{E}_{useless\ energy}}{\dot{E}_{solar\ radiation}} \quad (33)$$

Eqs. (32) and (33) are too complicated because it requires measuring many parameters, so $\%\dot{E}_{useless\ energy}$ is calculated using the simpler formula in Eq. (34).

$$\%\dot{E}_{useless\ energy} = 1 - \eta_{energy.STC} \quad (34)$$

The exergy balance at STC is formulated in Eq. 35 [50], [51].

$$\dot{E}x_{inlet} - \dot{E}x_{outlet} = \dot{E}x_{destruction} \quad (35)$$

where $\dot{E}x_{inlet}$ is the exergy rate at the inlet, $\dot{E}x_{destruction}$ is the exergy rate of destruction, and $\dot{E}x_{outlet}$ is the exergy rate at the outlet.

Next, each exergy rate is formulated following Eqs. (36) and (37) [52].

$$\dot{E}x_{inlet} = \dot{m} \times \overline{Cp} \times \left\{(T_{inlet} - T_0) - T_0 \times ln\left(\frac{T_{inlet}}{T_0}\right)\right\} \quad (36)$$

$$\dot{E}x_{outlet} = \dot{m} \times \overline{Cp} \times \left\{(T_{outlet} - T_0) - T_0 \times ln\left(\frac{T_{outlet}}{T_0}\right)\right\} \quad (37)$$

where $\dot{m}$ is water's mass flow rate, Cp is water's specific heat coefficient, T_{inlet} is the temperature at the inlet, T_0 is the ambient temperature, and T_{outlet} is the temperature at the outlet. The mass flow rate of water in the thermosiphon mechanism is difficult to measure because it is very slow. The solution, mass flow rate is calculated using Eqs. (38) and (39).

$$\dot{Q}_{heat\ flow.STC\ to\ WT} = \overline{Cp} \times \dot{m} \times \left(T_{outlet(STC)} - T_{inlet(STC)}\right) \quad (38)$$

$$\dot{m} = \frac{\dot{Q}_{heat\ flow.STC\ to\ WT}}{\overline{Cp} \times \left(T_{outlet(STC)} - T_{inlet(STC)}\right)} \quad (39)$$

Exergy efficiency in STC is formulated as the increase in exergy between the inlet and outlet flow relative to the input exergy [53]. Therefore, exergy efficiency is formulated as useful exergy relative to exergy from solar radiation in Eq. 40 [54].

$$\eta_{exergy\ STC} = \frac{\dot{E}x_{outlet} - \dot{E}x_{inlet}}{\dot{E}x_{input}} = \frac{\dot{E}x_{useful}}{\dot{E}x_{\dot{G}}} \quad (40)$$

Exergy input ($\dot{E}x_{input}$) from solar radiation is formulated in Eq. 41 [54].

$$\dot{E}x_{input} = \dot{E}x_{\dot{G}} = \bar{I}_{solar} \times A_{collector} \times \left[1 + \left\{\frac{1}{3}\left(\frac{T_0}{T_s}\right)^4\right\} - \left\{\frac{4}{3}\left(\frac{T_0}{T_s}\right)\right\}\right] \quad (41)$$

where $\bar{I}_{solar}$ is the solar intensity, $A_{collector}$ is the collector surface area, and T_s is the solar surface temperature.

Next, the sustainability index (SI) is calculated in Eq. (42), which is a crucial exergy-based effectiveness parameter [55].

$$SI_{SWH} = \frac{1}{1 - \eta_{exergy.SWH}} \quad (42)$$

SWH energy efficiency (η_{SWH}) [56] or charging efficiency [57] is defined as the ratio of heat energy stored as hot water in the tank to solar radiation energy formulated in Eq. (43). Therefore, SWH energy efficiency can be interpreted as the efficiency of storing heat energy in the SWH system.

$$\eta_{energy.SWH} = \frac{E_{saved}}{E_{input}} = \frac{E_{heat\ water\ tank}}{E_{solar\ radiation}} = \frac{Q_{water\ in\ tank}}{G_{cumulative}} \quad (43)$$

where the amount of heat in the tank ($Q_{water\ in\ tank}$) is formulated in Eq. (44) [58], [59], [60] and $G_{cumulative}$ is formulated in Eq. (45) [61].

$$Q_{water\ in\ tank} = cp \times m \times (T_{tn} - T_0) \quad (44)$$

$$G_{cumulative} = A_{collector} \int_{t0}^{tn} I_s(t)\, dt \quad (45)$$

where cp is the specific heat coefficient of water, m is the mass of water, T_{tn} is the temperature at time t, and T_0 is the initial temperature. Then, $A_{collector}$ is the collector's surface area, I_s is the solar intensity, and t is the duration of exposure.

As the first law of thermodynamics, energy conservation in SWH satisfies Eq. (46), where the total energy input is converted to the total saved and unsaved energy.

$$\sum E_{input} = \sum E_{saved} + \sum E_{not\ saved} \quad (46)$$

The total energy that cannot be stored is the accumulated useless energy and heat loss, formulated in Eq. (47).

$$\sum E_{not\ saved} = \sum E_{useless} + \sum E_{heat\ loss} \quad (47)$$

Exergy SWH compares exergy outcome to exergy input, formulated in Eq. (48) [62].

$$\eta_{exergy.SWH} = \frac{Exergy\ outcome}{Exergy\ input} \quad (48)$$

The outcome exergy is formulated using the Jeter equation because it comes from the heat source (photothermal absorber), as written in Eq. (49) [63].

$$Exergy\ outcome = Q_{water\ in\ tank} \times \left\{1 - \left(\frac{T_a}{T_s}\right)\right\} \quad (49)$$

where $Q_{water\ in\ tank}$ is the increase in heat stored in the water tank, T_a is the ambient temperature, and $T_{sources}$ is the temperature of the source (absorber).

Furthermore, the exergy input is the accumulated exergy of solar energy received by the STC, formulated using the Petela formula [39], which can be written as Eq. (50).

$$Exergy\ input = G_{cumulative} \times \left\{1 - \left(\frac{4}{3} \times \frac{T_a}{T_s}\right) + \left[\frac{1}{3} \times \left(\frac{T_a}{T_s}\right)^2\right]\right\} \quad (50)$$

Where $G_{cumulative}$ is the accumulated solar energy received by STC, T_a is the ambient temperature, and T_s is the source temperature (the sun's surface).

Uncertainty Analysis

To analyze uncertainty in experimental measurement data using Eq. (51), population deviation (σ), as used by Gitan and Al-Kayiem (2023).

$$\sigma = \sqrt{\frac{\sum(x_i - \bar{\mu})^2}{N}} \quad (51)$$

Meanwhile, the sample deviation (SD) can be calculated by using Eq. (52).

$$SD = \sqrt{\frac{\sum(x_i - \bar{x})^2}{N - 1}} \quad (52)$$

where x_i is the i value, $\bar{x}$ is the population mean, μ is the sample mean, and N is the population number.

Next, the uncertainty during measurement is represented as a coefficient of variation (CV), which is formulated in Eqs. (53) and (54).

$$\%CV_{population} = \frac{\sigma}{\bar{x}} \times 100\% \quad (53)$$

$$\%CV_{sample} = \frac{SD}{\bar{\mu}} \times 100\% \quad (54)$$

Considering that there are many variations in the sample in research, the formulation of the average CoV is for simplification in Eq. (55).

$$\%\overline{CV}_{sample} = \frac{\sum \%CV_{sample}}{n} \quad (55)$$

where n is the number of sample variations.

Uncertainty in performance is calculated using the error propagation equation (δ_l) formulated in Eq. (56) [65], [66], [67].

$$\delta_l = \sqrt{\delta_x^2 + \ldots + \delta_y^2} \quad (56)$$

RESULTS AND DISCUSSION

SEM-EDS

The SEM test with a magnification of 7,800 times in Figure 7 (a) shows that the material has a rough and crack gap structure like porous. The light trapping effect of the photothermal absorber to increase absorbance is caused by the presence of specific structures, including rough [68] and porous [69]. Therefore, the rough and crack gap structure of GCPA has a positive effect on temperature generation. These findings support the statement of Tuncer et al. [70] in his review study on carbon nanomaterial-based photothermal absorbers, that differences in particle size, shape, and concentration directly affect the thermal performance.

The EDS graph at three points is presented in Figure 7 (b), (c) and (d). This GCPA specimen is dominated by non-metal elements of carbon (C) and oxygen (O). The absence of the hydrogen element in the specimen indicates that the structure has changed to char. The release of H element bonds in coal is caused by baking during material preparation. The H element is released from the chemical structure of Carboxylic acid (C(=O)OH) because its decomposition temperature is only around 373.15 to 473.15 K [71]. However, it is also possible that hydrogen element is not found due to the inability of EDX to detect elements that have only one shell of K atoms, such as hydrogen and helium. The metal group elements aluminum (Al), iron (Fe), and niobium (Nb) contribute less than 5% based on mass concentration and less than 1% based on atomic concentration. The concentration contribution of each element in GCPA is presented in Table 3. The different elements composition of each coal do not indicate test inconsistencies, but different geological conditions of coal formation produce different element compositions [72].

Temperature Generation

The temperature generation test bar diagram in Figure 8 shows that a granular size of 10 to 20 mesh is optimal.

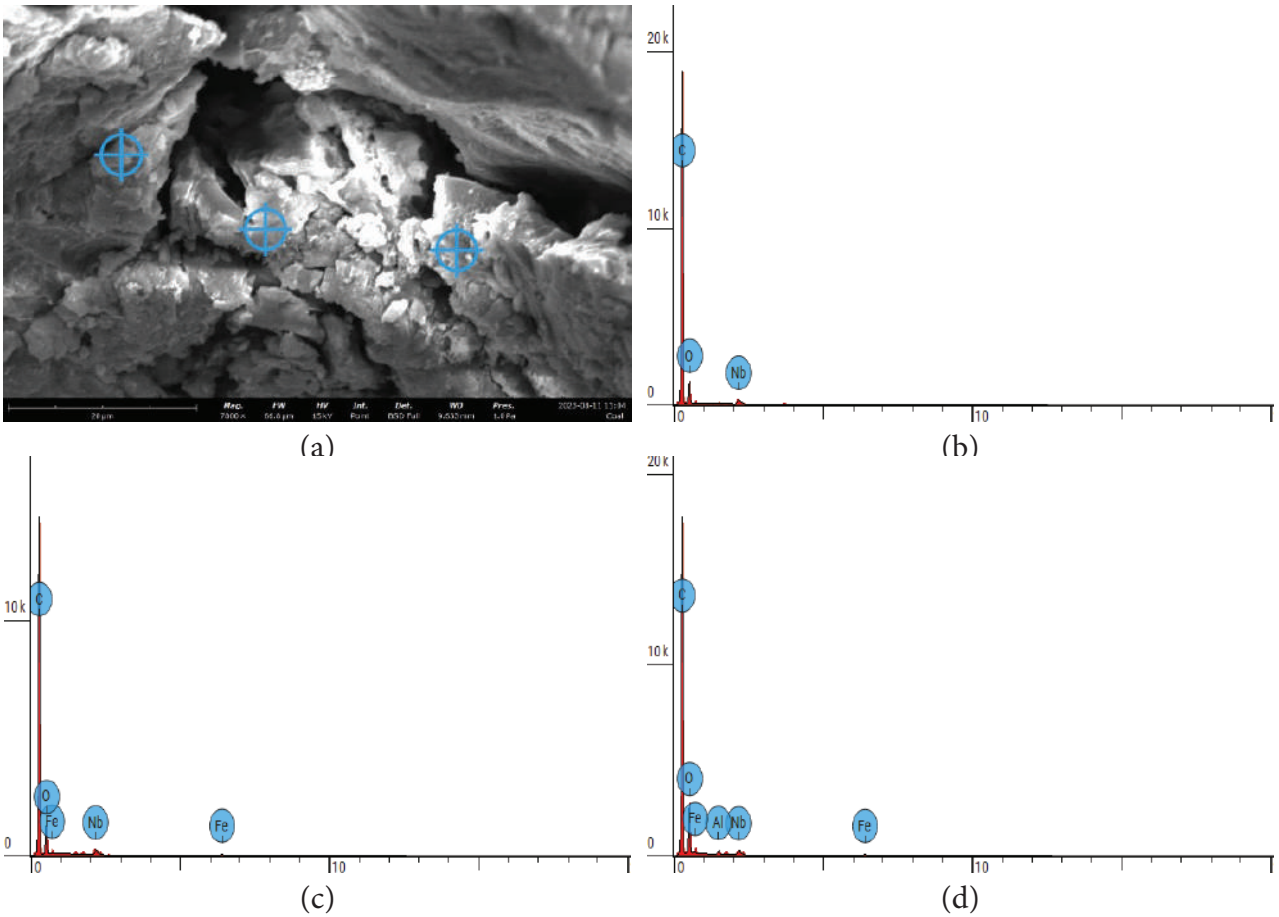

Figure 7. (a) SEM, (b) EDS graph spot 1, (c) EDS graph spot 2, and (d) EDS graph spot 3.

Table 3. Quantification of elements in GCPA

Position	Element			Concentration	
	Number	Symbol	Name	Atomic	Weight
Spot 1	6	C	Carbon	86.290%	80.619%
	8	O	Oxygen	13.323%	16.583%
	41	Nb	Niobium	0.387%	2.797%
Spot 2	6	C	Carbon	83.056%	75.479%
	8	O	Oxygen	16.003%	19.374%
	26	Fe	Iron	0.525%	2.221%
	41	Nb	Niobium	0.416%	2.926%
Spot 3	6	C	Carbon	78.073%	70.110%
	8	O	Oxygen	20.792%	24.875%
	13	Al	Aluminum	0.298%	0.602%
	26	Fe	Iron	0.504%	2.106%
	41	Nb	Niobium	0.332%	2.307%

There is a tendency that materials with higher absorbance will produce higher temperatures. The absorbance value of the material can be seen in Figure 9 (b) and Figure 10. However, other material properties such as thermal resistance, latent and sensible heat, hydrophilic–hydrophobic, and light-trapping capability can affect the temperature performance of photothermal absorbers [9]. The optimal granular photothermal absorber size and scale for each

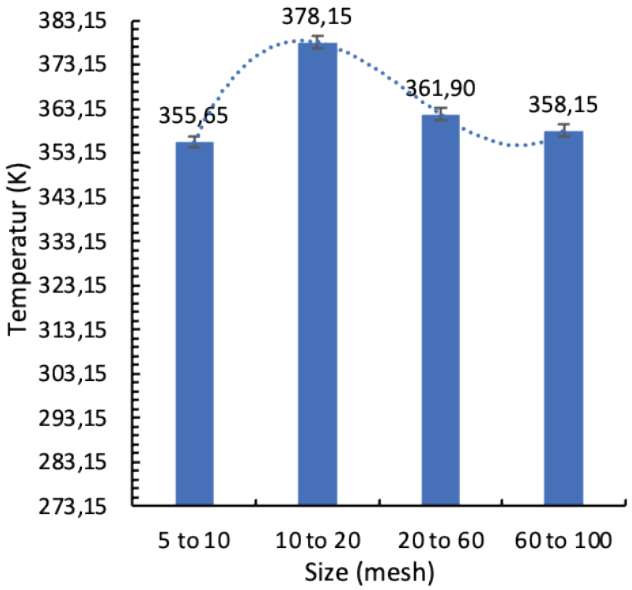

Figure 8. Temperature average of each GCPA size.

material can vary. Attia et al. [73], using granular gravel material from 4 to 16 mm, found the optimal size to be 16 mm. Meanwhile, Mohamed [19] used basalt stone 1 to 2 cm and found the optimal size to be 2 cm. Furthermore, the test used Au nanoparticles of 25 to 40 nm; the optimal size was 25 nm [74].

Optical Analysis

The transmittance and absorbance of each wavelength of light are presented in Figure 9. The light absorbance for all granular sizes tends to increase with an increasing wavelength of up to 910 nm. The optimal absorbance is in the infrared spectrum, with wavelengths from 700 to 910 nm. However, the transmittance increases after a wavelength of 910, and the absorbance decreases.

Figure 10 shows that the transmittance trend is inversely proportional to the temperature generation while the absorbance is directly proportional. Other research comparing different concentrations shows that materials with higher absorbance have higher temperature generation [75]. Anomalies appear in the size ranges of 40–60 and 60–100 but remain insignificant as they fall within overlapping measurement uncertainty limits. Therefore, determining the optimal material for a photothermal absorber is insufficient, as with one of the absorbance spectrophotometry or temperature generation tests using a lamp simulator. Based on the highest temperature generation test and the highest absorbance spectrophotometry test, it is known that the optimal granular size is mesh 10 to 20. The optimal mesh size confirms that the contact gaps between granules can trap light optimally and show a trend of higher absorbance, resulting in higher temperatures. The elemental concentrations in natural materials are generally less uniform than in purified materials, leading to more significant uncertainty in test results. Furthermore, the material's transmittance and absorbance values may be inconsistent due to the random arrangement of its granular structure, which leads to variations in the size of gaps acting as light traps. The SEM-EDS test data results in Figure 7 confirm the condition of non-uniformity of elemental composition and random gap size.

TGA-DSC

TGA-DSC testing on GCPA, which has a mesh size of 5-10, is presented in Figure 11 and is divided into four stages. The first stage is dehydration and desorption, starting from the beginning of the test, characterized by an endothermic reaction at a temperature of 290–336.31 K. In

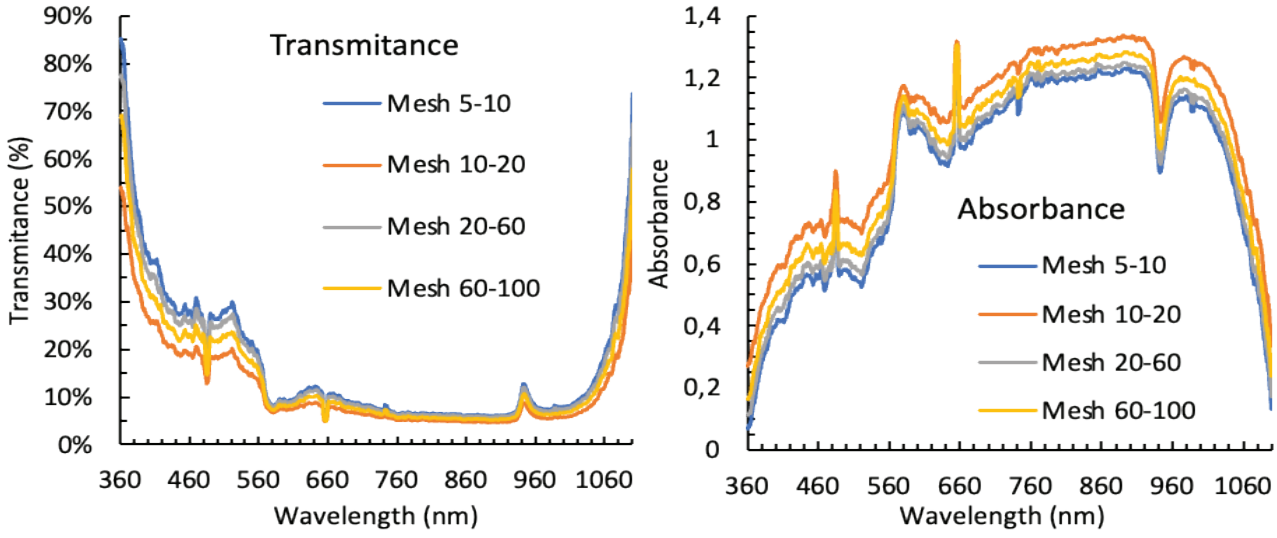

Figure 9. Optical properties (a) transmittance and (b) absorbance.

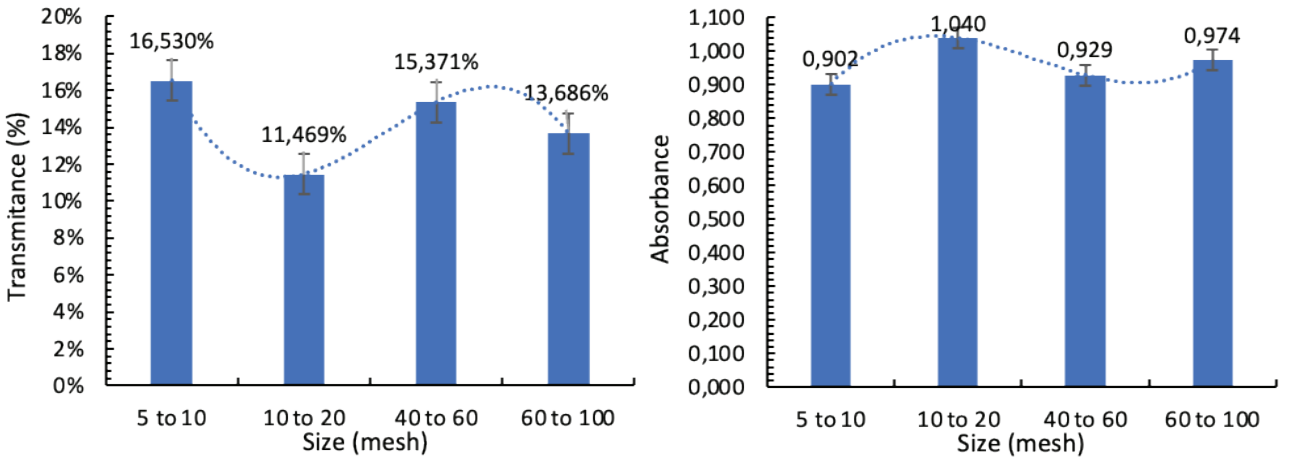

Figure 10. Optical properties throughout the wavelength (a) transmittance and (b) absorbance.

the first stage, an endothermic reaction occurs due to the removal of water vapor and gas desorption [76]. Next, the second stage begins when an exothermic reaction occurs at a temperature of 336.31-684.31 K with a mass change of 11.95%.

In the second stage, this is the ideal working temperature for the photothermal absorber because GCPA releases heat. Furthermore, there was no significant damage to the material in this area, as indicated by the lack of substantial change in mass. In the oxidation phase, the mass can increase or decrease depending on the major functional groups contained in the coal [76]. The increase in mass in coal samples is due to the presence of carboxyl groups (-COOH), which contribute to the increase in CO_2 gas and carbonyl groups (-C==O), which contribute to the increase in *CO* gas. Meanwhile, mass loss is caused by methyl groups ($-CH_3$) and methylene ($-CH_2-$).

The third stage (degradation) begins when the exothermic oxidation reaction ends, characterized by rapid mass changes due to pyrolysis and combustion reactions, depending on the availability of oxygen during the reaction. Mandal et al. [77] reported the degradation of combustion in Indian coal, and Kellali et al. [78] reported that the degradation of pyrolysis in lignite coal occurs exothermically and endothermically. In the degradation stage, the mass release is permanent; therefore, at this stage, the coal is considered

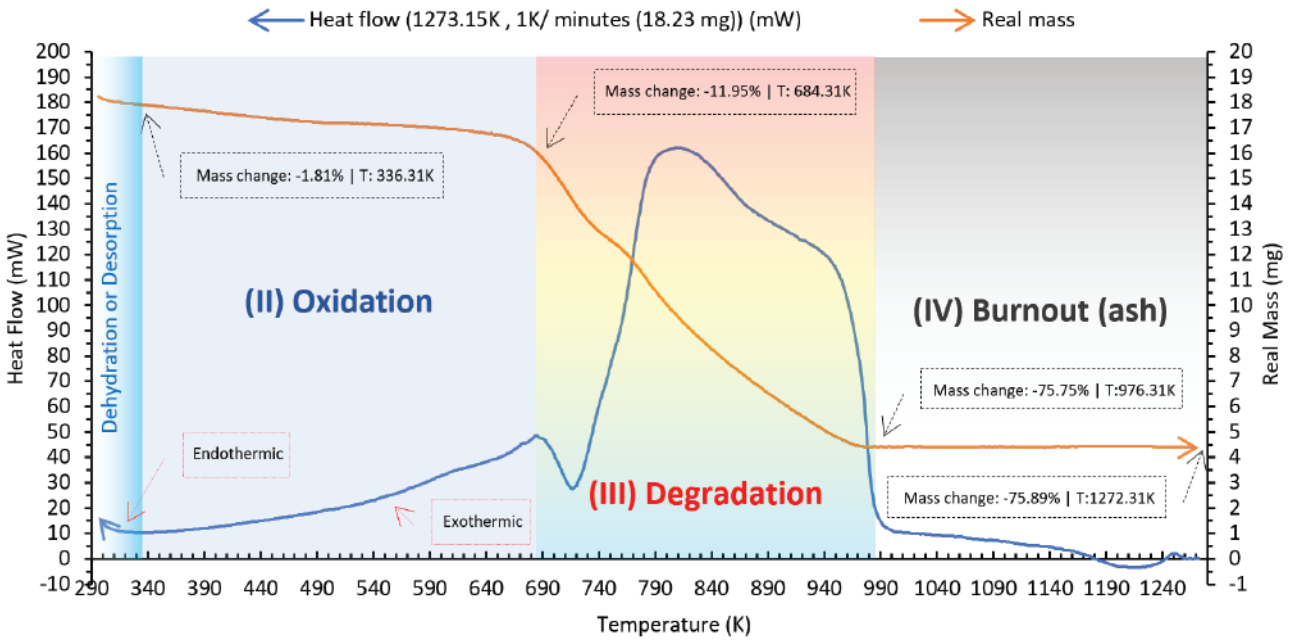

Figure 11. TGA-DSC of granular coal.

to have experienced structural damage as a photothermal absorber. The TGA test shows that the degradation stage starts at a temperature of around 684.31K, in Figure 11, while in the photothermal absorber test in the collector, the highest temperature is 399.25K, in Figure 12. These results show that the collector design is safe and does not cause damage because the generation temperature is still below the degradation temperature.

The degradation stage ends when the change in specimen mass begins to slope and begins to enter the burnout stage. In the burnout stage, the mass change is insignificant compared to the temperature change. The graphic data shows that heating with a temperature change reaching 296 K for 296 min only experienced a mass change of 0.14%, and ash contained in the GCPA is 24.11%. Furthermore, the visual characteristic that can be observed is that the specimen has turned to ash.

Thermodynamics Analysis

Temperature generation of GCPA

The results of testing the temperature generation of GCPA under real sunlight are presented in Figure 12. The highest light intensity during the test occurred at noon. Meanwhile, the highest GCPA temperature is at 1:00 PM for all sensor points. The maximum temperature in real testing was 399.25 K, so the results were higher than using a xenon lamp simulator of 378.15 K. This happens because the wavelength spectrum of sunlight is more diverse, the power intensity is higher, and the test duration is longer. Moreover, the direct test was carried out in a closed system (the absorber was in the receiver tube), while in the simulator, the absorber was tested in an open system (the absorber was on a petri dish). However, there is a possibility that the temperature generation in the simulator is higher than in the real test, depending on the different parameter conditions of each test.

Simulator testing and real testing are not intended to compare directly the two methods. Still, simulator testing is carried out as a guide to selecting the most optimal parameters (granular size) that will be tested in real conditions. This consideration is made because, in real testing, natural conditions cannot be controlled, and it can result in unreliable and biased data. As an alternative, comparative testing in real conditions must be carried out simultaneously using several collectors. However, the simultaneous method would be too expensive and impractical.

Energy and exergy efficiency of GCPA

The results of energy efficiency measurements for all GCPA size specimens and test conditions are presented in Table 4. A photothermal absorber with a higher temperature means a higher energy conversion efficiency.

The calculation results from Eq. (17) presented in

Table 5 show that exergy efficiency is lower than energy efficiency. Exergy can have a higher or lower value than

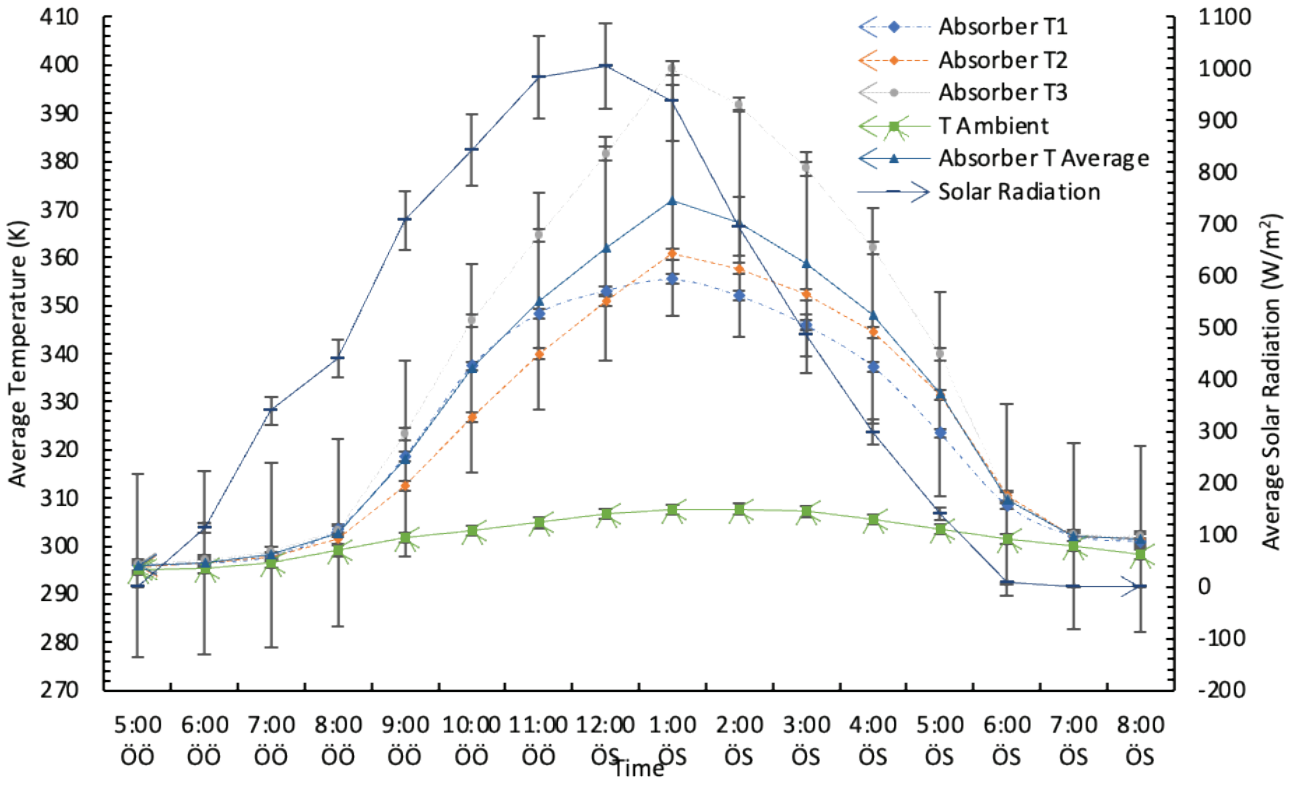

Figure 12. Temperature generation of absorbers in tube collector under unload condition.

Table 4. Energy conversion efficiency at all GPA sizes and test conditions

Radiation Source	Specimen (mesh)	m (Kg)	T_0 (K)	T_1 (K)	A_{lens} (m^2)	$\Delta H_{(t,m,T)}$ (W)	I (W/m^2)	$\%T_{total}$ (%)	Δt (s)	η_{abs} (%)
Xenon Lamp	5 to 10	0.02	298.15	355.65	0.09	1,791,263.38	1000.00	0.92	1800	24.04
	10 to 20	0.02	298.15	378.15	0.09	1,939,533.42	1000.00	0.92	1800	26.03
	20 to 60	0.02	298.15	361.90	0.09	1,820,620.96	1000.00	0.92	1800	24.43
	60 to 100	0.02	298.15	358.15	0.09	1,805,449.12	1000.00	0.92	1800	24.23
	100 to 200	0.02	298.15	344.40	0.09	1,740,111.86	1000.00	0.92	1800	23.35
Sun	10 to 20	0.24	296.12	399.25	0.44	33,574,316.06	1005.40	0.73	28800	86.64

Table 5. Efficiency Exergy Absorber

Radiation Sources	Specimen (mesh)	$\eta_{ece.abs}$ (%)	T_a (K)	T_{abs} (K)	$T_{sources}$ (K)	$\eta_{exergy.abs}$ (%)
Xenon lamp	5 to 10	24.04%	298.15	355.65	1,280.15	5.63%
	10 to 20	26.03%	298.15	378.15	1,280.15	7.97%
	40 to 60	24.43%	298.15	361.90	1,280.15	6.23%
	60 to 100	24.23%	298.15	358.15	1,280.15	5.88%
Sun	10 to 20	86.64%	307.57	399.25	6,273.15	21.29%

energy because exergy analysis reviews energy quality based on reference sources and the environment.

Temperature of system

The loaded condition test, in Figure 13, shows the highest intensity of solar radiation at 12.00. Meanwhile, the optimal temperature in the collector is reached at 2:00 PM, and the water in the storage is reached at 3:00 PM.This finding follows the trend conducted by Yanbolagh et al. [79], where the highest ambient temperature and water temperature in the collector occurred at 2:00 PM.The time shift to reach the optimal temperature in each component is closely related to the flow of energy and exergy in the system. Further discussion regarding this phenomenon is presented in the energy and exergy analysis of each system. Overall, the water storage temperature performance of SWH has met the needs

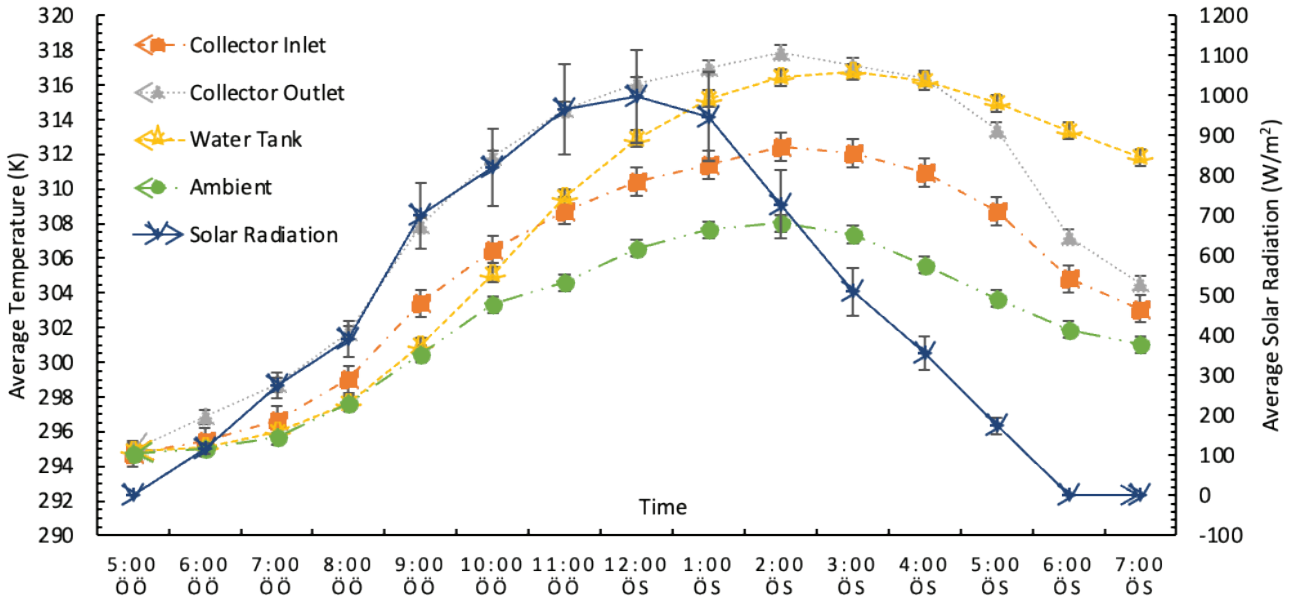

Figure 13. Temperature generation of STC-SWH system in load condition.

for warm water bathing in the range of 309.15 K to 318.15 K and generally ranges in 313.15 K [80].

Energy and exergy efficiency of STC

Figure 14 shows the energy flow rate in the STC and water tank (WT) systems. The positive heat change rate indicates that the system has increased storing heat. Meanwhile, the heat change rate is negative, indicating a decrease in stored heat which occurs starting between 3:00 PM. This condition occurs because the cooling heat rate release is faster than the heat that can be transferred from the photothermal absorber to the water working fluid.

Figure 16 shows that the highest STC energy efficiency occurs at 11:00 AM at 33.27%. After 11:00 AM, the

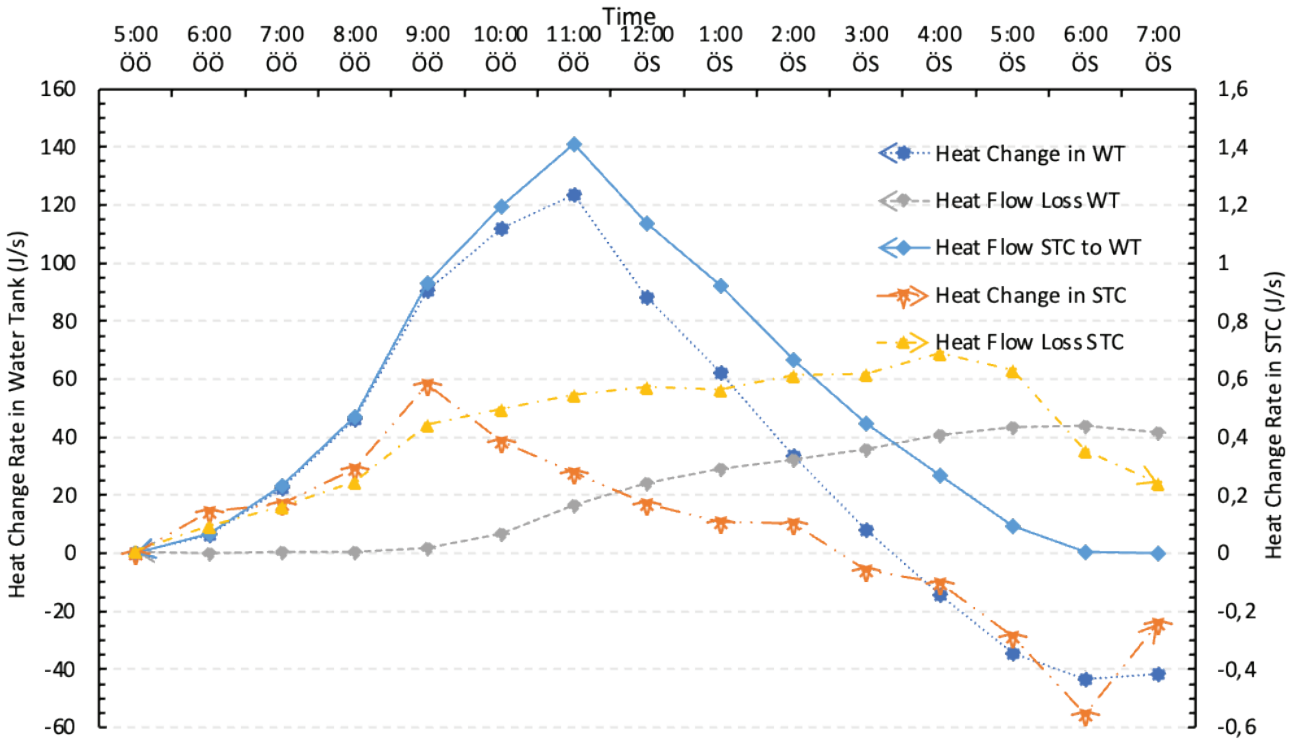

Figure 14. Heat energy flow rate in STC, WT, and STC to WT.

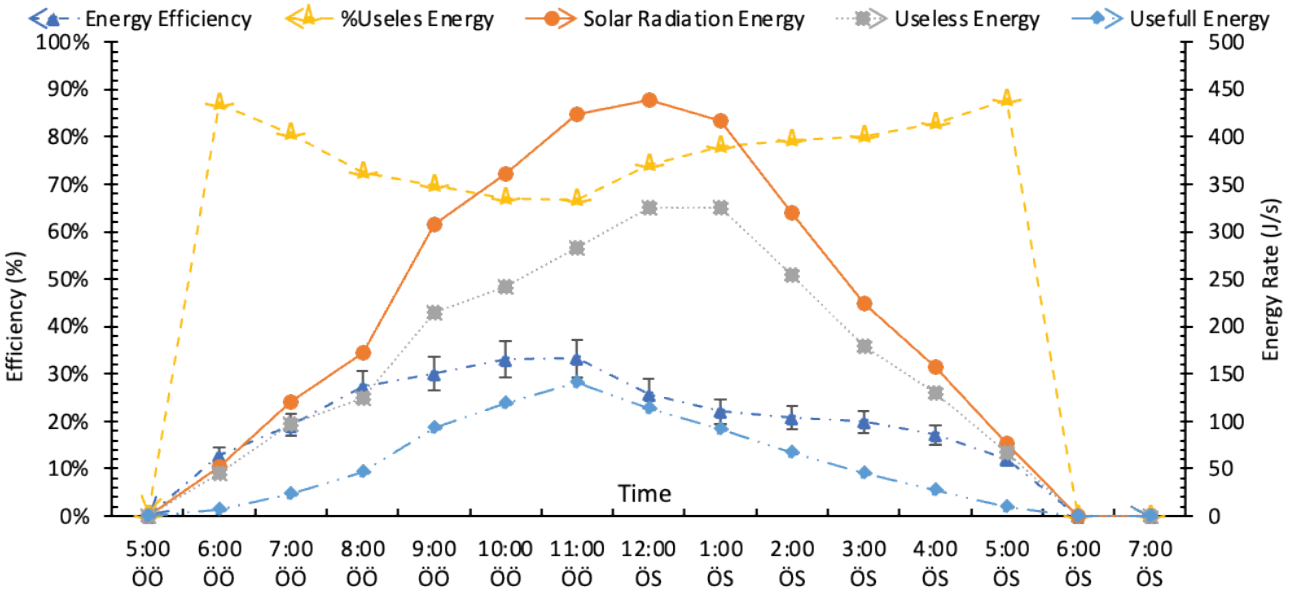

Figure 15. Energy efficiency and energy rate in STC.

efficiency cannot increase anymore because the increase in useless energy continues until 2:00 PM at 87.83%, but the rate of useful energy decreases. The rate of useless energy in percentage increases because the energy conversion efficiency of the photothermal absorber tends to decrease as the light intensity is too low (yellow graph line). However, cumulatively useless energy increases as the intensity of solar radiation entering the system increases (grey graph line). The average STC energy efficiency is 22.84%, and the average useless energy contribution is 77.16%.

Figure 16 and Figure 16 shows that exergy increases drastically as the mass flow rate increases. The mass flow rate will flow faster if the temperature difference is more significant. In the thermosiphon mechanism, the fluid flows faster due to the difference in the density of the water being higher, where a higher temperature will reduce the density and flow upwards. This finding aligns with research conducted by Bhakta and Singh using a parabolic concentrating solar water heater where a drastic increase in mass flow rate resulted in an instant rise in energy efficiency [81, 82].

Figure 17 shows that the highest exergy efficiency was achieved at 11:00 AM at 5.51%, and the average was 3.44%. Furthermore, the highest SI was 1.06, with an average of 1.04. At 5.00 AM and 6.00 PM to 7.00 PM, the SI value is 0, indicating there is no exergy flow to activate the system.

The exergy efficiency of this novel STC shows better performance than that of collector tubes without combination. Ataee and Ameri (2023) reported in their review research that the exergy efficiency of evacuated tubes is limited to 2.3–2.45%. This is because the collector combination increases the focus value of the light, thereby increasing the temperature generation. Higher outlet temperature has a positive impact on STC exergy. Conversely, higher inlet and ambient temperatures have a negative impact on STC exergy.

Energy and exergy efficiency of SWH

Figure 18 shows that the average contribution of unsaved energy dominates at 79.08%, influenced by useless energy at 75.03%. Therefore, the average energy efficiency that can be stored is only 20.92%. In addition, the heat loss contribution increases more rapidly with increasing time compared to the cumulative heat energy in the tank, which

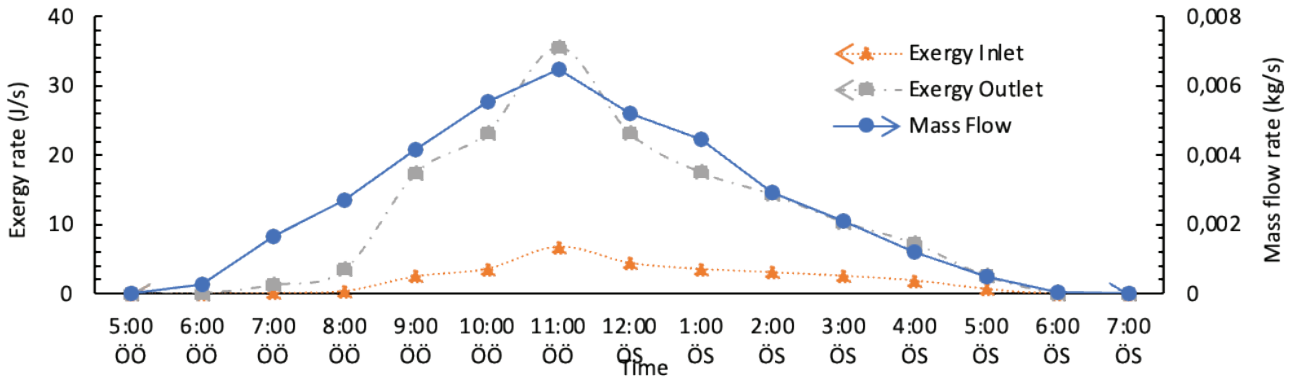

Figure 16. Exergy of STC and mass flow rate.

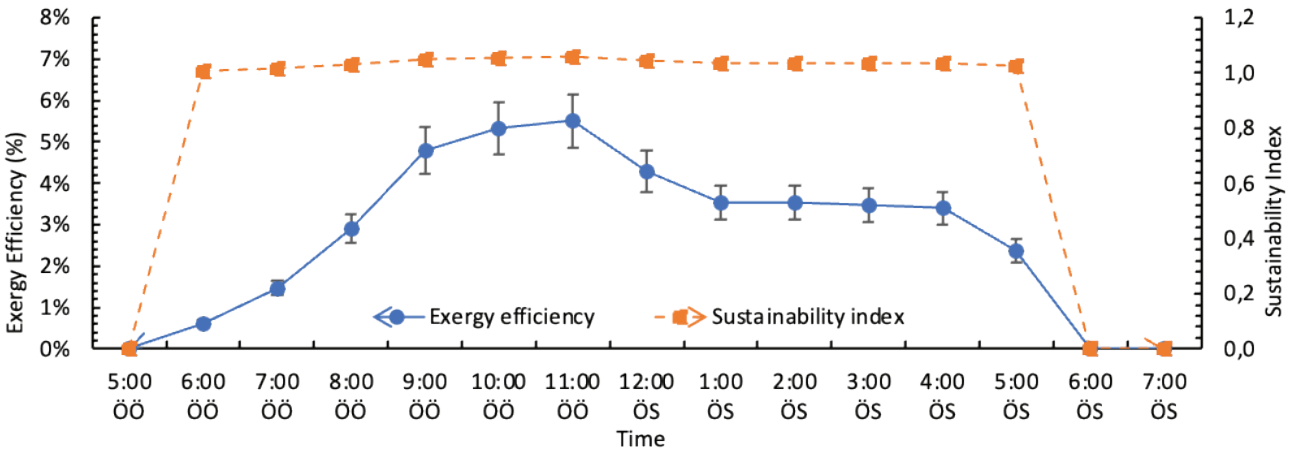

Figure 17. Exergy efficiency and sustainability of STC.

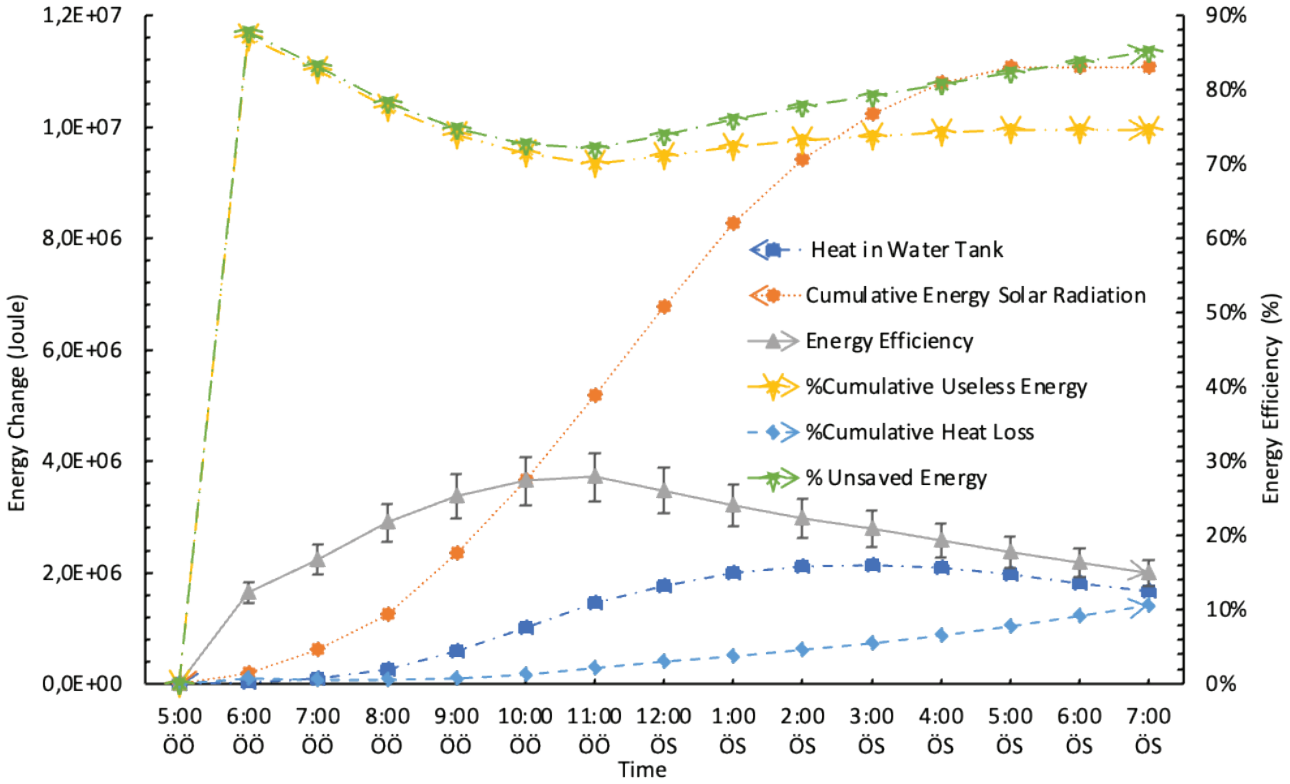

Figure 18. Energy change and energy efficiency of SWH.

decreases SWH efficiency since 3:00 PM. The exergy input in Figure 19 follows the trend of exergy cumulative solar radiation trend input in Figure 18. This indicates that the exergy input is predominantly influenced by the cumulative solar radiation energy.

The exergy input to the SWH increases in the morning along with the increase in solar radiation, peaking in the afternoon before stabilizing, while the exergy outcome peaks early in the afternoon and then decreases even though the exergy input is still high, as shown in Figure 19. The continuous increase in tank temperature causes faster heat dissipation and decreases the energy conversion efficiency, as shown in Figure 18. Meanwhile, the ambient temperature also increases until noon before starting to decrease in the afternoon. This condition contributes to the decrease in exergy outcome because the temperature difference between the working fluid and the environment becomes smaller. Therefore, the potential energy that can be converted decreases. This trend follows the findings of Hasan et al. (2018), which showed that increasing ambient temperature can reduce the exergy in the SWH system. In addition, although the cumulative energy from radiation continues to increase, the decrease in solar radiation in the afternoon further limits the increase in exergy outcome, indicating that the

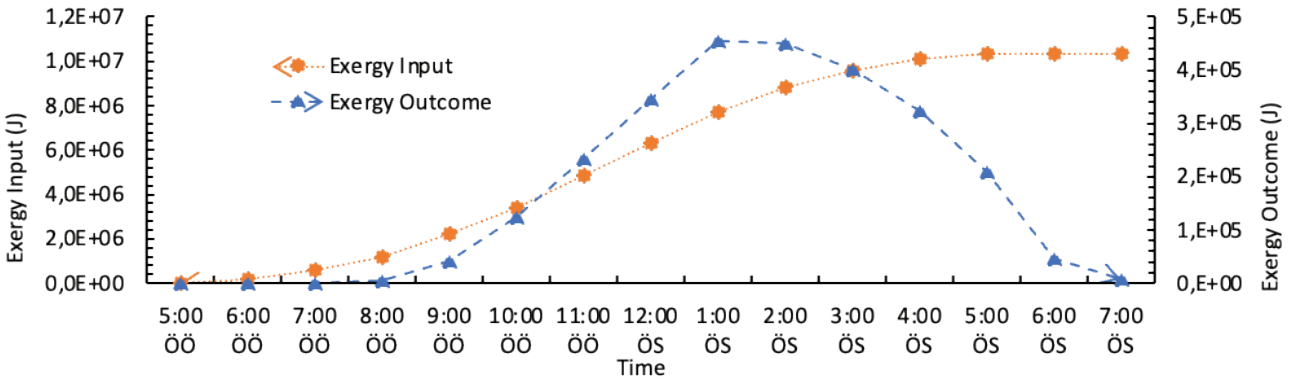

Figure 19. Exergy input and outcome in STC.

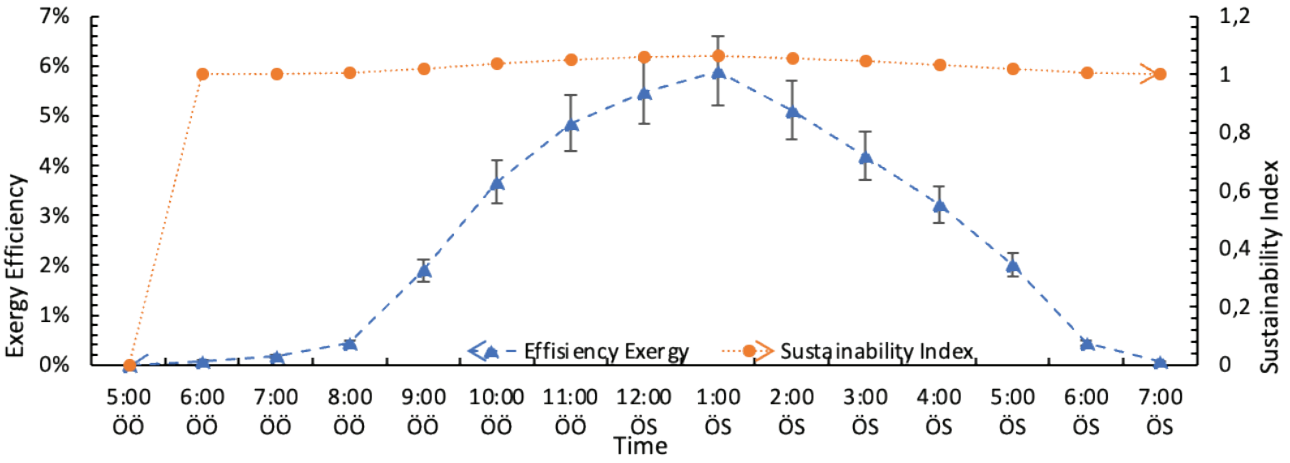

Figure 20. Exergy Efficiency and Sustainability Index SWH.

thermal dynamics and solar radiation greatly influence the system performance throughout the day.

The average and highest exergy efficiency, shown in Figure 20, is 3.09% and 5.90%. Furthermore, the average and highest sustainability index is 1.032 and 1.063. Exergy outcome and SI SWH at 6:00 PM to 7:00 PM are not yet worth 0 because there is still exergy stored. However, it will continue to experience exergy loss due to heat loss. Eventually, the outcome exergy and SI SWH values will become 0 if the water storage temperature is the same as the initial temperature.

Uncertainty of Measurement and Performance

Table 6 shows that the solar and xenon lamp radiation parameters have higher uncertainty conditions of more than 1%. These results are reasonable because the uncertainty in testing under sunlight can reach 15% to 60% on

Table 6. Uncertainty of measurement

Parameter and Performance	Symbol	Unit	$\%\overline{\text{CoV}}$
Xenon radiation	$\bar{G}_{xenon}$	W/m²	7.07%
T ambient control condition	$\bar{T}_{ambient.25\pm1K}$	K	0.35%
Absorber temperature generation under Xenon illumination mesh 5-10	$\bar{T}_{abs.50-10.xenon}$	K	0.11%
Absorber temperature generation under Xenon illumination mesh 10-20	$\bar{T}_{abs.10-20.xenon}$	K	0.09%
Absorber temperature generation under Xenon illumination mesh 20-60	$\bar{T}_{abs.20-60.xenon}$	K	0.09%
Absorber temperature generation under Xenon illumination mesh 60-100	$\bar{T}_{abs.60-100.xenon}$	K	0.08%
Solar radiation unloaded test (15-17 Agustus 2023)	$\bar{G}_{solar.ul}$	W/m²	8.18%
Absorber T1 unloaded test	$\bar{T}_{1.ul}$	K	0.29%
Absorber T2 unloaded test	$\bar{T}_{2.ul}$	K	0.32%
Absorber T3 unloaded test	$\bar{T}_{3.ul}$	K	0.37%
Average Absorber T unloaded test	$\bar{\bar{T}}_{ul}$	K	6.43%
Temperature of ambient	$\bar{T}_{ambient.l}$	K	0.35%
Solar radiation loaded test (12-14 Agustus 2023)	$\bar{G}_{solar.l}$	W/m²	11.67%
Temperature of collector inlet	$\bar{T}_{in.col}$	K	0.26%
Temperature of collector outlet	$\bar{T}_{out.col}$	K	0.13%
Temperature of water tank	$\bar{T}_{wt}$	K	0.15%
Temperature of ambient	$\bar{T}_{ambient.l}$	K	0.16%

Table 7. Calculated performance uncertainty due to error propagation

Key Performance	δ_I
Energy Efficiency of Absorbers	6.586%
Exergy Efficiency of Absorber	6.605%
Energy Efficiency of STC	11.709%
Exergy Efficiency of STC	11.713%
Energy Efficiency of SWH	11.709%
Exergy Efficiency of SWH	11.710%

cloudy days and 2% -40% on sunny days [83]. High measurement uncertainty in solar radiation is caused by changes in natural conditions that cannot be controlled. Meanwhile, sources of uncertainty in xenon lamp radiation are unstable electricity, dust, shocks, measuring instruments, lamp quality, and instrument setup. However, the ambient temperature parameters have low uncertainty conditions. These different parameter conditions can still result in low measurement uncertainty for most performance. Only the average temperature generation performance at three test points without loading produces high measurement uncertainty conditions. This condition occurs because the focus of the lens moves due to changes in the angle of solar radiation, which indicates that the temperature at the absorber is uneven and hot spots are moving. However, no research has examined the maximum limit of parameter uncertainty to consider the reliability data of photothermal absorbers, STC, and SWH technology performance.

The uncertainty value due to error propagation for each calculated performance is classified as high because it is more than 1%, as presented in Table 7. The uncertainty in error propagation in this test is high due to the high uncertainty in the solar radiation intensity. Meanwhile, measurement uncertainty for other performances has a small impact on calculated performance error propagation because the value is less than 1%.

CONCLUSION

This study comprehensively examines the performance of granular coal photothermal absorber in the novel design of a solar thermal collector, a combination of Fresnel lens-compound parabolic reflector, applied to solar water heater. Based on experimental data and comprehensive analysis, it is concluded that:

- Granular coal photothermal absorber has a light trap structure, that is, the gap between granules' contact, fracture porosity, and rough surfaces.
- The main composition of granular coal photothermal absorber is carbon and oxygen , with minority elements niobium , iron , and aluminum.
- The temperature generation test using a xenon lamp and the absorbance test using spectrophotometry found that granular coal photothermal absorber size 10 to 20 was the best.
- The ideal operational limit of granular coal photothermal absorber in the oxidation stage region, at a temperature of 336.31 K to 684.31 K, with a maximum mass change of 11.95%.
- In the unloaded condition test (real environment test using solar thermal collector), the maximum generation absorber temperature was 399.25 K, with an energy conversion efficiency of 86% and an exergy efficiency of 21.29%.
- In loaded condition testing (real environment test using solar water heater), it was found that the optimal temperature of the solar thermal collector outlet and water in the solar water heater storage was 317.88 K and 316.75 K.
- The stored water temperature performance has met the ideal for warm bathing.
- The maximum solar thermal collector energy efficiency is 33.06%, and the average is 22.90%, while the maximum exergy efficiency is 5.51%, and the average is 3.44%.
- The maximum solar water heater energy efficiency is 27.85%, and the average is 20%, while the maximum solar water heater exergy efficiency is 5.90%, and the average is 3.09%.

LIMITATIONS AND FUTURE IMPROVEMENTS

This study shows that granular coal has good potential as a photothermal absorber in thermal solar collectors, especially for low to medium temperature applications. This material can absorb heat well, but some aspects can still be further developed. One of the main challenges is to improve efficiency and exergy. Furthermore, expanding the operational temperature range allows this technology to be applied in various applications. In addition, although material properties such as size, shape, type, and absorbance are known to affect temperature and heat performance, this relationship has not been formulated mathematically with high accuracy. Further studies are also needed to evaluate the material's durability in long-term use and analyze the economic aspects in commercial-scale applications.

In the future, innovation is needed in the development of absorber materials with higher thermal stability and longer durability so that the efficiency and service life of the system can be improved. More innovative collector designs, such as integrating tracking and geometry engineering, can potentially significantly improve energy the efficiency of energy and exergy. In addition, exploring combinations of other photothermal materials can help improve overall system performance. The application of more complex numerical models and computational simulations is also needed to formulate the mathematical relationship between

material properties and performance. This approach can improve the accuracy of predicting collector performance under various environmental conditions. Therefore, this technology can be applied more widely and effectively.

AUTHORSHIP CONTRIBUTIONS

Authors equally contributed to this work.

DATA AVAILABILITY STATEMENT

The authors confirm that the data that supports the findings of this study are available within the article. Raw data that support the finding of this study are available from the corresponding author, upon reasonable request.

CONFLICT OF INTEREST

The author declared no potential conflicts of interest with respect to the research, authorship, and/or publication of this article.

ETHICS

There are no ethical issues with the publication of this manuscript.

STATEMENT ON THE USE OF ARTIFICIAL INTELLIGENCE

Artificial intelligence was not used in the preparation of the article.

REFERENCES

[1] IEA, "Energy Statistics Data Browser," iea.org. Available at: https://www.iea.org/data-and-statistics/data-tools/energy-statistics-data-browser?country=WORLD&fuel=Energy supply&indicator=TESbySource Accessed Dec 25, 2024.

[2] Vojáček O, Brabec J, Macháč J. Costs of achieving emission limits in coal-burning power plants under the recent best available techniques regulation amendment: Evidence from national microeconomic data J Clean Prod 2022;352:131600. [Crossref]

[3] Zhang Z, Zhao Z, Zhang L. Recent progress in the gasification reaction behavior of coal char under unconventional combustion modes. Appl Therm Eng 2023;220:119742. [Crossref]

[4] NASA. The Balance of Power in the Earth-Sun System 2005. Available: https://eospso.nasa.gov/sites/default/files/publications/NASA-Facts-EnergyBalance.pdf. Accesed on March 2, 2026.

[5] Our World in Data, "Power Generation and Cumulative Capacity of Solar Energy," ourworldindata.org. Available: https://ourworldindata.org/grapher/solar-energy-consumption-by-region?tab=table&time=earliest..2023 Accessed on Sept. 02, 2023.

[6] Energy Institute, "Statistical Review of World Energy Data," energyinst.org. Available at: https://www.energyinst.org/statistical-review/resources-and-data-downloads. Accesed on March 02, 2026.

[7] He W, Zhou L, Wang M, Cao Y, Chen X, Hou Xç Structure development of carbon-based solar-driven water evaporation systems. Sci Bull 2021;66:1472–1483. [Crossref]

[8] Sarifudin A, Yaningsih I, Kristiawan B, Ubaidillah. Recent Material Research Advances for Photothermal Absorbers. Evergreen 2024;11:2035–2062. [Crossref]

[9] Sarifudin A. A comprehensive review of granular structures as photothermal absorber materials. Therm Sci Eng Prog 2024;14:102689. [Crossref]

[10] Kanimozhi B, Nitin shinde Y, Paul Bedford S, Swaroop Kanth K, Vikash Kumar S. Experimental Analysis of Solar Water Heater Using Porous Medium with Agitator. Mater Today Proc vol. 2019;16:1204–1211. [Crossref]

[11] Wirawan M, Mirmanto M, Fahrurrozi I. The Influence of the Tilt Angle of a Flat Plate Solar Collector with Granite Stone Absorber on Its Performance. Int J Adv Eng Manag 2023;5:1234–1238.

[12] Ternenge Abur B, Dandakouta H, Ejilah RI, Adisa AB. Modeling and Simulation of an Indirect Natural Convection Solar Dryer with Thermal Storage Bed. Int J Eng Manuf v. 2020;10:24–42. [Crossref]

[13] Li J, Jing Y, Zhou X, Mao J. Multifunctional photothermal materials based on natural pumices for high efficiency <scp>solar-driven</scp> interface evaporator. Int J Energy Res 2021;45:20132–20142. [Crossref]

[14] Bilal A, Jamil B, Haque NU, Ansari MA. Investigating the effect of pumice stones sensible heat storage on the performance of a solar still. Groundw Sustain Dev 2019;9:100228. [Crossref]

[15] Attia MEH, Kabeel AE, Abdelgaied M. Optimal concentration of El Oued sand grains as energy storage materials for enhancement of hemispherical distillers performance. J Energy Storage 2021;36. [Crossref]

[16] Elashmawy M. Improving the performance of a parabolic concentrator solar tracking-tubular solar still (PCST-TSS) using gravel as a sensible heat storage material. Desalination 2020;473: 114182. [Crossref]

[17] López-Sosa LB, Ortíz-Carrión A, Espinosa-Gómez D, Zárate Medina J, González-Avilés M, Solar air heating system with low environmental impact materials: Mathematical model and optothermal characterization. Sustain Energy Technol Assessments 2021;47:101399. [Crossref]

[18] Elmaadawy K, Kandeal AW, Khalil A, Elkadeem MR, Liu B, Sharshir SW. Performance improvement of double slope solar still via combinations of low cost materials integrated with glass cooling. Desalination 2021;500:114856. [Crossref]

[19] Mohamed AF, Hegazi AA, Sultan GI, El-Said EMS. Enhancement of a solar still performance by inclusion the basalt stones as a porous sensible absorber: Experimental study and thermo-economic analysis. Sol Energy Mater Sol Cells 2019;200:109958. [Crossref]

[20] Arunkumar T, Wang J, Dsilva Winfred Rufuss D, Denkenberger D, Kabeel AE. Sensible desalting: Investigation of sensible thermal storage materials in solar stills. J Energy Storage 2020;32:101824. [Crossref]

[21] Sarifudin A, Yaningsih I, Kristiawan B. Solar Thermal Technology First Elec Yogyakarta: Propublikasi Republik Indonesia, 2024. Available at: https://propublikasi.com/buku/pb00001/. Accessed on: March 2, 2026.

[22] Bie Y, Li Z, Lei J, Ma Z, Li M, Krolczyk G, et al. Solar medium-low temperature thermal utilization and effect analysis of boundary condition: A tutorial. Sol Energy 2020;197:238–253. [Crossref]

[23] Barone G, Buonomano A, Forzano C, Palombo A. Solar thermal collectors. Sol Hydrog Prod Process Syst Technol 2019;151–178. [Crossref]

[24] Farjana SH, Huda N, Mahmud MAP, Saidur R. Solar process heat in industrial systems – A global review. Renew Sustain Energy Rev 2018;82:2270–2286. [Crossref]

[25] Sarifudin A, Yaningssih I, Kristiawan B, Wibawa A. Investigation of Granular Natural Stone Materials as Photothermal Absorbers for Sustainable and Environmentally Friendly Energy Harvesting. J Appl Eng Sci 2024;22:1–16. [Crossref]

[26] Sarifudin A, Yaningsih I, Kristiawan B, Miyazaki T, Thu K. Temperature Generation of Granular Photothermal Absorber Natural Materials Using Fresnel Lens Collector. In: Salim MA, Khashi NS, Chew KW, Photong C, editors. Proceedings of the 9th International Conference and Exhibition on Sustainable Energy and Advanced Materials. 2024. 313–317. [Crossref]

[27] Chamsa-ard W, Brundavanam S, Fung C, Fawcett D, Poinern G. Nanofluid Types, Their Synthesis, Properties and Incorporation in Direct Solar Thermal Collectors: A Review. Nanomaterials 2017;7:131.

[28] Kalogirou SA. Solar thermal collectors and applications. Prog Energy Combust Sci 2004;30:231–295. [Crossref]

[29] Jensen AR, Sifnaios I, Caringal GP, Furbo S, Dragsted J. Thermal performance assessment of the world's first solar thermal Fresnel lens collector field. Sol Energy 2022. [Crossref]

[30] Sarafraz MM, Tlili I, Tian Z, Bakouri M, Safaei MR. Smart optimization of a thermosyphon heat pipe for an evacuated tube solar collector using response surface methodology (RSM). Phys A Stat Mech its Appl 2019;534:122146. [Crossref]

[31] Sharma MK, Bhattacharya J. Dependence of spectral factor on angle of incidence for monocrystalline silicon based photovoltaic solar panel. Renew Energy 2022;184:820–829. [Crossref]

[32] Pu J, Shen C, Yang S,. Zhang C,. Chwieduk D, Kalogirou SA. Feasibility investigation on using silver nanorods in energy saving windows for light/heat decoupling. Energy 2022;245: 123289. [Crossref]

[33] Gupta VK, Kumar S, Kukreja R, Chander N. Experimental thermal performance investigation of a direct absorption solar collector using hybrid nanofluid of gold nanoparticles with natural extract of Azadirachta Indica leaves. Renew Energy 2023;202:1021–1031. [Crossref]

[34] Gao M, Zhu L, Peh CK, Ho GW. Solar absorber material and system designs for photothermal water vaporization towards clean water and energy production. Energy Environ Sci 2019;12: 841–864. [Crossref]

[35] Dwivedi KK, Prabhansu MK Karmakar, Chatterjee PK. Thermal degradation, characterization and kinetic modeling of different particle size coal through TGA. Therm Sci Eng Prog 2020; 18:100523. [Crossref]

[36] Yan D, Li M.Stearic acid-modified MOF-based composite phase change materials for solar-thermal energy conversion and storage. Sol Energy 2023;262:111843. [Crossref]

[37] Coccia G, Aquilanti A, Tomassetti S, Ishibashi A, Nicola G Di. Design, manufacture and test of a low-cost solar cooker with high-performance light-concentrating lens. Sol Energy 2021; 224:1028–1039. [Crossref]

[38] Hu T, Kwan TH, Yang H, Wu L. Photothermal conversion potential of full-band solar spectrum based on beam splitting technology in concentrated solar thermal utilization. Energy 2023;268:126763. [Crossref]

[39] Petela R. Exergy of undiluted thermal radiation. Sol Energy 2003;74:469–488. [Crossref]

[40] Milanese M, Colangelo G, de Risi A. Development of a High-Flux Solar Simulator for Experimental Testing of High-Temperature Applications. Energies 2021;14:3124. [Crossref]

[41] A. Interrante. Layers of the Sun, NASA. Available: https://blogs.nasa.gov/sunspot/2023/09/26/layers-of-the-sun/ Accessed on: Oct 08, 2023.

[42] Agrawal A, Kumar A, Parekh AD.Experimental investigation of atmospheric air to water generation based on both end open evacuated tube collector solar air heater. Sol Energy 2023; 263:111953. [Crossref]

[43] Arslan E. Applying regression techniques to determine mathematical equations of exergy, electricity, and energy values of photovoltaic thermal collector. Sol Energy 2023;255:369–380. [Crossref]

[44] Ozbas E, Selimli S, Ozkaymak M, Frej A. Evaluation of internal structure modifications effect of two-phase closed thermosyphon on performance: An experimental study. Sol Energy 2021; 224:1326–1332. [Crossref]
[45] Tuncer AD, Amini A, Khanlari A. Developing an infrared-assisted solar drying system using a vertical solar air heater with perforated baffles and nano-enhanced black paint. *Sol Energy* 2023;263. [Crossref]
[46] Hasan MF, Mahadi MSUR, Miyazaki T, Koyama S, Thu K. Exergy analysis of serpentine thermosyphon solar water heater. Appl Sci 2018;8. [Crossref]
[47] Al-Askaree EH, Al-Muhsen NFO. Experimental investigation on thermal performance of solar water heater equipped with Serpentine fin core heat exchanger. Clean Eng Technol 2023;12: 100593. [Crossref]
[48] Vivas-Cortez M, Fleitas A, Guzmán PM, Nápoles JE, Rosales JJ.Newton's Law of Cooling with Generalized Conformable Derivatives. Symmetry (Basel) 2021;13:1093. [Crossref]
[49] Kabeel AE, Harby K, Abdelgaied M, Eisa A. Performance improvement of a tubular solar still using V-corrugated absorber with wick materials: Numerical and experimental investigations," Sol Energy 2021;217:187–199. [Crossref]
[50] Afshari F, Tuncer AD, Sözen A, Çiftçi E, Khanlari A. Experimental and numerical analysis of a compact indirect solar dehumidification system. 2021. [Crossref]
[51] Ghazouani M, Bouya M, Benaissa M. Thermo-economic and exergy analysis and optimization of small PTC collectors for solar heat integration in industrial processes. Renew Energy 2020;152:984–998. [Crossref]
[52] Mugi VR, Chandramohan VP. Energy and exergy analysis of forced and natural convection indirect solar dryers: Estimation of exergy inflow, outflow, losses, exergy efficiencies and sustainability indicators from drying experiments. J Clean Prod 2021;282:124421. [Crossref]
[53] Yang M, Zhi L, Diao K, Zhu Y, Taylor RA. Optical and thermal performance analysis of a compact solar collector with heat-pipe evacuated tube. Sol Energy 2022; 258:118–129. [Crossref]
[54] Guimarães Barbosa E, Eduardo Viana de Araujo M, Zhang Y, Arêdes Martins M. Exergetic, enviro-economic and exergoeconomic (3E) assessment of a stationary parabolic trough solar collector with thermal storage. Sol Energy 2023;255:487–496. [Crossref]
[55] Selimefendigil F, Şirin C, Ghachem K, Kolsi L. Exergy and environmental analysis of an active greenhouse dryer with Al2O3 nano-embedded latent heat thermal storage system: An experimental study. Appl Therm Eng 2022;217:119167. [Crossref]
[56] Singh OK. Development of a solar cooking system suitable for indoor cooking and its exergy and enviroeconomic analyses. Sol Energy 2021;217:223–234. [Crossref]
[57] Abi Mathew A, Thangavel V. A novel thermal storage integrated evacuated tube heat pipe solar air heater: Energy, exergy, economic and environmental impact analysis. Sol Energy 2021;220:828–842. [Crossref]
[58] Hachchadi O, Tapsoba G, Dery P, Mechaqrane A, Meloche P, Izquierdo R. Experimental optimization of the heating element for a direct-coupled solar photovoltaic water heater. Sol Energy 2023;264:112037. [Crossref]
[59] Jing P, Zhou X, Xu Z, Xu Z. Numerical and Experimental Investigation on Photothermal Performance of Polyimide/High-Electrical-Performance-Coating Composite Films Considering Surface Roughness. J Therm Sci 2022;31:1206–1219. [Crossref]
[60] Çimen M, Colakoglu M, Güngör A. Overheating limitation of thermosiphon solar collectors by controlling heat pipe fluid in all glass evacuated tubes. Sol Energy 2021;230:515–527. [Crossref]
[61] Eltawil MA, Algonaian AA, Amer BMA. Innovative extraction process for date fruits syrup (Dibs) using electro-thermal solar energy. Sol Energy 2020;221:521–535. [Crossref]
[62] Kabeel AE, Diab MR, Elazab MA, El-Said EMS. Solar powered hybrid desalination system using a novel evaporative humidification tower: Experimental investigation Sol Energy Mater Sol Cells 2022;248:112012. [Crossref]
[63] Jeter SM. Maximum conversion efficiency for the utilization of direct solar radiation. Sol Energy 1981;26:231–236. [Crossref]
[64] Gitan AA, Al-Kayiem HH. Assessment of hybrid solar-thermal multi-chamber dryer integrated with desiccant dehumidifier for uniform drying. Sol Energy 2023;262:111880. [Crossref]
[65] Hassan H, Osman OO, Abdelmoez MN, abo-Elfadl S. Experimental assessment of novel designed solar hot water storage collector incorporating an array of partitioned ducts absorber. Sol Energy 2023;262:111838. [Crossref]
[66] Ihoume I, Tadili R, Arboui N, Bazgaou A, Idrissi A, Benchrifa M, Fatnassi H. Performance study of a sustainable solar heating system based on a copper coil water to air heat exchanger for greenhouse heating. 2021;232:128–138. [Crossref]
[67] Schmelzer C, Georgii MJ, Vajen OK. Accuracy of key performance indicators in solar-assisted heating systems due to measurement uncertainties. Sol Energy 2023;249:255–267. [Crossref]
[68] Zhao W, Xiao L, Cui Z, Fang J, Zhang C, Li X et al. Moth-eye-inspired texturing surfaces enabled self-cleaning aluminum to achieve photothermal anti-icing. Opt Laser Technol 2021; 141:107115. [Crossref]

[69] Tang Y, Zhao X, Li D, Zuo X, Tang A, Yang H. Nanoporous carbon-enabled composite phase change materials with high photo-thermal conversion performance for multi-function coating. Sol Energy Mater Sol Cells 2022; 248:112025. [Crossref]

[70] Tuncer AD, Badali Y, Khanlari A. Application of carbon-based nanomaterials in solar-thermal systems: An updated review. Sol Energy 2024; 282:112932. [Crossref]

[71] Zhao S, Zhang Y. DFT study on the chemisorption and reforming of naphthalene over bio-char: The detailed mechanism of carbon deposition and hydrogen production. Fuel 2023; 332: 126144. [Crossref]

[72] Dai S, Finkelman RB, French D, Hower JC, Graham IT, Zhao F. Modes of occurrence of elements in coal: A critical evaluation. Earth-Science Rev 2021;222:103815. [Crossref]

[73] Attia MEH, Kabeel AE, Abdelgaied M, Abdel-Aziz MM, Bellila A, Abdullah A. Optimal size of black gravel as energy storage materials for performance improvement of hemispherical distillers. J Energy Storage 2021; 43:103196. [Crossref]

[74] Chen M, He Y, Zhu J, Kim DR. Enhancement of photo-thermal conversion using gold nanofluids with different particle sizes. Energy Convers Manag 2016;112:21–30. [Crossref]

[75] Zhu W, Zuo X, Ding Y, Yan H, An Y, Yang W. Experimental investigation on the photothermal conversion performance of cuttlefish ink nanofluids for direct absorption solar collectors. Appl Therm Eng 2023; 221:119835. [Crossref]

[76] Kumar Mohalik N, Mandal S, Kumar Ray S, Mobin Khan A, Mishra D, Krishna Pandey J. TGA/DSC study to characterise and classify coal seams conforming to susceptibility towards spontaneous combustion. Int J Min Sci Technol 2022; 32:75–88. [Crossref]

[77] Mandal S, Mohalik NK, Ray SK, Khan AM, Mishra D, Pandey JK. A comparative kinetic study between TGA & DSC techniques using model-free and model-based analyses to assess spontaneous combustion propensity of Indian coals. Process Saf Environ Prot 2022; 159: 1113–1126. [Crossref]

[78] Kellali S, Richard F, Batiot B, Cremona P, Rogaume T. Modelling of lignite pyrolysis using a finite rate chemistry approach: comparison between parallel and competitive chemical schemes. J Anal Appl Pyrolysis 2023;172:105975. [Crossref]

[79] Yanbolagh DJ, Saraei A, Mazaheri H, Mehrabadi SJ. Exergoeconomic, Environmental, Economic, and Energy-Matrices (4E) Analysis of Three Solar Distillation Systems Equipped with Condenser and Different Heaters. J Therm Eng 2021;7:1640–1653. [Crossref]

[80] Sousa V, Meireles I. Dynamic simulation of the energy consumption and carbon emissions for domestic hot water production in a touristic region. J Clean Prod 2022; 355:131828. [Crossref]

[81] Bhakta AK, Singh SN. Thermo-Hydraulic Performance Analysis of Parabolic Concentrating Solar Water Heater. J Therm Eng 2020; 6:802–815. [Crossref]

[82] Ataee S, Ameri M. Energy and exergy parameter analysis of a U-pipe evacuated tubular solar collector with filled and unfilled layer. Appl Therm Eng 2023; 233:121190. [Crossref]

[83] Biencinto M, González L, Valenzuela L. Using time-windowed solar radiation profiles to assess the daily uncertainty of solar thermal electricity production forecasts J Clean Prod 2022; 379:134821. [Crossref]

J Ther Eng, Vol. 12, No. 2, pp. 635−655, March, 2026

Journal of Thermal Engineering
Web page info: https://jten.yildiz.edu.tr
DOI: 10.14744/thermal.0001105

Research Article

Performance evaluation of solar nozzle plant useful for electricity generation: A numerical analysis

Anand GONDCHAWAR[1], Bhavesh KANABAR[1], Ramesh BHORANIYA[1,*]

[1]*Department of Mechanical Engineering, Marwadi University, Rajkot, Gujarat, 360003, India*

ARTICLE INFO

Article history
Received: 13 February 2025
Accept: 18 July 2025

Keywords:
Electricity Generation; Natural Convection; Solar Nozzle Plant; Updraft Tower

ABSTRACT

Passive solar electricity generation relies on natural heat transfer, avoiding the use of fans or pumps. To decrease overall cost, it is essential to discover some new techniques for optimizing the solar chimney plant's overall efficiency and capacity. The smoke jack devised by Leonardo da Vinci (1452-1519) has been quoted by many reviewers as the initial illustration of the principles of the solar chimney. The fundamental reason why it works is that it contains a venturi or nozzle. Thus, it is important to evaluate the performance of solar chimney plant using solar nozzles. Hence, this study numerically investigates the different configurations of solar chimney power plants (SCPP) with and without the use of solar nozzle design. The numerical analysis of the system has been done in ANSYS software with its latest available version (2022 R_1). The three different model configurations of SCPP were studied and found that using solar nozzle design; one can achieve increased air release velocity at the outlet, thus, enhancing overall system performance. This SCPP design offers a sustainable electricity generation solution for both urban and rural environments. The solar nozzle plant is primarily depending on three governing equations i.e. mass, momentum and energy conservation laws. The natural convection heat transfer phenomenon related to SCPP is the useful fundamental law of heat transfer. The solar chimney equation plays a pivotal role in deciding different design parameters such as chimney dimensions, and the air released velocities at various parts. With the help of appropriate formulae; the efficiency of the overall design can be calculated. Results show that with the help of solar nozzle design, one can improve air release velocity at the outlet by a significant amount to the conventional basic design of SCPP with no nozzle. This increase in air updraft velocity will have a considerable impact on the power output of the electricity generation plant when the turbine is fixed at the nozzle outlet region. The solar nozzle model 6 with 3 m of nozzle height shows an optimum increment of nearly 29 % than solar chimney model of 3 m height and with no nozzle used.

Cite this article as: GondchawarA, KanabarB, BhoraniyaR. Performance evaluation of solar nozzleplantusefulforelectricitygeneration:Anumericalanalysis.JTherEng2026;12(2):635−655.

***Corresponding author.**
*E-mail address: rameshkumar.bhoraniya@marwadieducation.edu.in

This paper was recommended for publication in revised form by Editor-in-Chief Ahmet Selim Dalkılıç

Published by Yıldız Technical University Press, İstanbul, Turkey
Yıldız Technical University. This is an open access article under the CC BY-NC license (http://creativecommons.org/licenses/by-nc/4.0/).

INTRODUCTION

A solar tower power generating plant primarily uses solar energy for its operations. It is considered as a 'passive sustainable energy plant' that generates electricity. Passive solar technologies are those that do not use fans or pumps in the collection and usage of solar heat, instead, these technologies use the natural modes of heat transfer to distribute the thermal energy of solar gains among different spaces [1]. A passive, non-mechanical technique of producing energy is a solar chimney principle, often referred to as a thermal chimney [2]. Among the various forms of energy, solar energy is one that one receives from the Sun and is the prime energy source for solar updraft towers (SUT). This SUT uses natural convection heat transfer mechanisms. In this, any fluid motion is developed by the buoyant effect, which suggests the rise of warmer fluid and the fall of the cooler fluid (especially due to density differences) [3].Solar chimney power plants are privileged systems that can provide power output even in cloudy weather and during hours when there is no sun [4]. It can be further divided into two sub-categories i.e. internal or external flow depending upon the type of fluid flow. Use of clean energies such as solar, wind, geothermal, tidal, etc. for the generation of electrical power is helpful to reduce air pollution. Thus, it will surely save the environment on our planet earth**.** Wherever needed, the electricity can be produced by applying cleaner technologies to the power generation units. There is another method namely 'sustainable energy power generation techniques' which insists on the use of solar chimneys as shown in figure 1. It is use of the green energy options for generating electricity. This electricity will be helpful to both urban and rural developments. Figure 1 shows that the solar collector comprises a translucent cover to admit shorter wavelength solar radiation and retain long wavelength radiation that is emitted by the heated ground. Buoyancy-driven flow that is generated in the chimney is used to drive pressure-staged turbines installed at the chimney base for electric power generation [5].

In solar chimney sustainable power generation units, the solar radiations are fallen upon a large greenhouse-like structure available at the bottom. The collected solar radiations at the base region heat the surrounding air nearby collector portion, and thus creating an updraft within a tall chimney. The solar chimney is considered to be the plant's actual thermal engine [6]**.** During the morning time, sun radiations start falling on the absorber section and it slowly heats the absorber base. This will heat the air present within SCPP, thus creating an upward lift. If turbines are positioned in between the airflow; this lift will be beneficial to produce mechanical energy and then electricity by the help of generators. This upward lift drives turbine blades which are fixed nearer to the base of the solar chimney, thus generating electricity. The energy sources can be divided into two main categories i.e. Primary and secondary energy sources. The main energy consumption sources are fossils like coal, natural gases, etc., nuclear, and renewable options such as hydro-power, geothermal, solar, wind, etc. It is better to say electricity as secondary energy consumption source. The enhanced accumulation of CO_2 emission in developing countries poses a significant threat to the environment [7]. The SCPP uses solar energy which

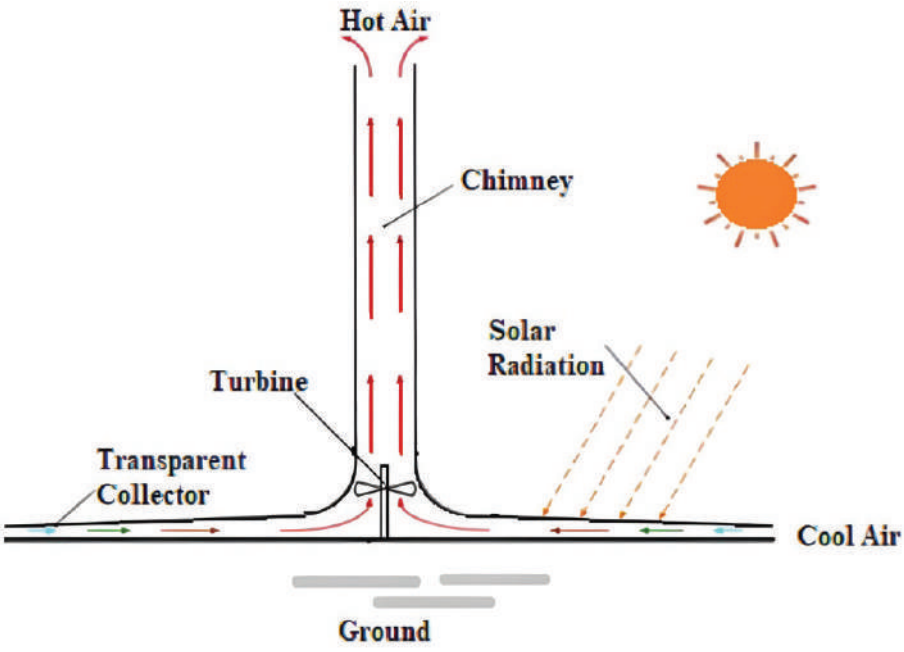

Figure 1. The basic structure of conventional SCPP.

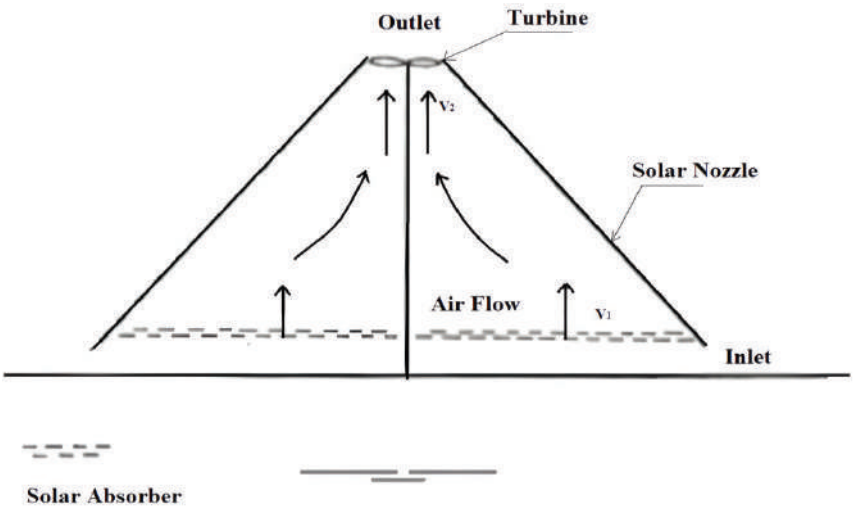

Figure 2. The Open ended conical shaped solar nozzle design. [From Williams [33], with permission from Global Warming Solutions.

is green energy option and has several advantages over conventional energy sources.

- It is available in abundant quantities free of cost in nature, completely pollution-free and thus an environmental friendly source of energy.
- It is known as one of the main renewable energy sources. It uses a clean and simple technology.
- It has a lower operational and maintenance cost, despite having higher construction costs. Fuel is not required in such a design. Here, no need to use fuels like coal, natural oil, etc., thus it's less polluting.

LITERATURE SURVEY

Al-Abadi et al. [8] have numerically investigated the combined solar-waste heat sources tower to increase power production. Here, a simulating software tool ANSYS FLUENT has been used. The main aim was to know the effects of waste energy of flue gases on the performance of solar towers. Hence, seven different models have been numerically tested having various chimney heights and diameters. Amongst these seven models, a circular shaped model with a two-ring burner was found to be the best option and thus recommended to use. The optimum of nearly 121.1 kW of power is produced. It delivered the highest thermal efficiency among other available choices. Cuce et al. [9] have conducted numerical analysis to know the appropriate values of the chimney as well as collector inclination angles for the pilot plant. The convergent and divergent chimneys have angles of -0.25° and + 0.25° respectively and it is found that the system notably performs if it has a slope for the chimney of nearly 0.6 ° and a diverging angle of about 1.5°. Marzouk [10] has used Aladdin artificial intelligence enhanced modeling tool to optimize Manzanares pilot plant design. By analyzing numerical results conducted for nine different locations in the world, results suggest that due to advancements in PV technology in recent years, the commercially built SUTPP that only generates electricity seems to have less chance of being established in the market. Tesfaye et al. [11] have done experimental and numerical analysis to increase the performance of the SCPP plant considering an optimum power output of around 30 kW. It is found that as one increase chimney height, it enhances power output up to a certain optimum height value, beyond which the effect is negligible. The pressure drop will result in significant energy losses along the chimney. It will start to overcome the energy rise because of the stack effect. The maximum chimney height is 45 m for a 0.2 m diameter, after that enhancing height results in negative of total pressure. Mirzamohammad et al. [12] have numerically modeled two different designs i.e. with and without using buried pipes. The impact of solar radiations and pressure variation in the turbine section by changing temperature in the computational domain is determined for both above cases. Due to the creation of obstacles in the airflow path after the rising pressure drop in the turbine, the air velocity in the chimney decreases subsequently. Singh et al. [13] have numerically investigated a high-capacity sustainable power unit that provides a cleaner and economically preferable option to conventional design. It is concluded that the geometrical features have a great impact on the performances of the SUTPP. The amount of solar radiations available and geometrical constraints mainly affect the efficiency and power output of the plant. Cuce et al. [14] have experimentally and numerically investigated the various effects of using solar absorbing materials like gravel or sand in a solar chimney power plant. It is found that using soil material as 'Sand', we can achieve a temperature rise of 67.3 K at a surrounding temperature of 290 K. Considering ambient temperature of

300 K, we can get a temperature rise of 64.8 K. Jiren et. al. [15] have performed a numerical study on an axisymmetric model of the prototype of solar chimney power generating plant using the different chimney heights and shapes which was built in Manzanares, Spain. By enhancing solar radiation intensity, the release velocity of air increases. It also enhances its temperature inside SCPP. By increasing the dimensions of the chimney and collector, one can raise the power output. Das et al. [16] have proposed a numerical investigation of SCPP. The aim was to evaluate the performance of SCPP using different collector roof designs. It is found that overall chimney efficiency increases by raisingits height and it decreases by raising collector roof angles. The different effect of collector roof angles on performance is evaluated. Various angles are: 20°, 25°, 30°, 35° and respective collector efficiencies are 87.2 %, 73.1 %, 60.5 %, and 51.8 %. Hoseini et al. [17] numerically found that an effective method for enhancing power output of SCPP is providing collector angles vs. horizon. The use of divergent collectors is more advisable than horizontal convergent collectors, as it produces higher velocity as well as mass flow rates. Jammei et al. [18] have numerically studied the different effects of varying geometrical parameters of SCPP. Researchers studied different tower convergence or diversion angles, and concave or convex wall forms with respective to the variation of velocity in the chimney. The various forms of chimney walls are simulated and studied with the aid of ANSYS FLUENT software**.** In basic design, the average air release velocity was found to be nearly 15 m/s; while it rises up to 23 m/s for the last model showing an enhancement of 49 %. Aurybi et al. [19] performed a numerical analysis on solar power plant. It was found that a hybrid SCPP design increases air velocity by 24 % and temperature by 9 %. Comparing numerical results of the conventional model with proposed model; the later produced more output power. Mekhail [20] performed numerical as well as experimental studies. Researcher used a small-scale SCPP plant which is installed in Aswan city for analysis purpose. With an increment in chimney's height by 14 m, there is an enhancement in the maximum theoretical power output of 3 W to 2 kW approximately. From the results obtained, it is clear that the bigger scaled model can produce theoretically an output that is 600 times more than a smaller one. Ming et al. [21] have numerically investigated SCPP. In this research work, some equipment is used to spread seawater droplets equally in the form of the surface. This is done when air flow is passed through the base of the chimney inside SCPP. With addition and humidification processes of the warm airflow, resulted in reduced air temperatures. Ayadi et al. [22] performed numerical as well as experimental analysis to check the performances of solar chimneys. Tests have been conducted in warm and tropical situations particularly of Kota, India. The impact of collector roof inclination is studied. Results indicate that using a negative roof angle, the thermodynamic efficiency of solar plants is enhanced. The air release velocity measured inside the solar chimney section is increased by 125 % by varying of angle by 2.5 °. Sundus et. al. [23] have performed experimental as well as numerical analysis. Results show that the selection of the correct ground material in the collector plays a prime role in increasing its performance. By raising the ground absorptivity, the ground temperature in the collector regions will be enhanced. The painted wooden material with a dark green color was the best choice among studied materials. Lal et al. [24] have performed experimental and numerical studies to find out the impact of various parameters like inlet temperature, chimney height, and solar radiation intensity on the system performance. Juo et al. [25] numerically studied the effects of turbine pressure drop, solar radiation, and ambient temperature on solar chimney system performance. Fasel et al. [26] have numerically demonstrated the impacts of using an unsteady RANS for SCPP. Pretorius [27] numerically evaluated the performances of larger-scaled SCPPs. Schlaich et al. [28] theoretically studied the SCPP plant. It was observed that constructing a solar tower of 1000 m height was difficult in previous times, but today, it could be constructed using recent advanced technologies. Caicedo et al. [29] studied radial turbine design for solar chimney power plants. Haaf et al. [30] experimentally (Part I) studied the solar chimney power generating plant installed at the Manzanares. The performances of solar collector and the converter were primarily influenced by local climatic conditions as well as site location. Soil characteristics like absorptive coefficient, coarseness etc. play a vital role in deciding how much amount of Sun's radiation energy could be converted into thermal energy. It was also observed that the upwind air release velocity for this pilot plant was 15 m/s. Haaf [31] experimentally investigated (Part II) the Manzanares pilot plant with a power output ranging to 55 kW. The system includes cost saving collector design along with a properly constructed energy converter unit inside the chimney of SCPP. Polyester film panels along with some soiled PVC panels were used achieving a greater transparency level.

Literature Gap and Motivation

After studying the above literatures on SCPP, we found some gaps and motivations for performing the research work. The current study explores the use of solar nozzles to enhance air release velocity and overall system performance in SCPP designs. The earliest work was done by Haaf et al. [30, 31] to develop a prototype design of solar chimney at Manzanares, Spain. Afterward, many researchers studied solar chimney plants to enhance its performance, but very few studied solar nozzle plant. Mainly Padki [32] studied a simple analytical model of solar nozzle plant and found that using chimney of varying inlet and outlet cross sectional area (i.e. converging or nozzle shaped chimney), could increase the overall system performance. However, no experimental or numerical studies were conducted. Williams [33, 34, 35] theoretically determined the performances of solar nozzle plants (Figure 2) with varying

Table 1. Optimum air velocities for different SCPP designs

Sr. No.	Researchers name, type of study, country, year	SCPP with/without nozzle	Chimney height, Absorber/base specifications etc.	Optimum air velocity (m/s)
1	Haaf W, Experimental Study, Manzanares Spain, 1983-84, [30, 31]	SCPP without nozzle	H= 194.6; $R_{coll.}$ = 122	15
2	Williams A, Theoretical study, UK, 2016 [33]	SCPP with nozzle	H= 5,$A_{Absorber}$= 25	36.80
3	Das et al., Numerical study, India, 2018 [21]	SCPP without nozzle	H= 5; $R_{coll.}$ = 0.3	1.85

dimensions and suggested researchers to further validate/disprove the ideas.

The objective of the current numerical study is to investigate various effects of using solar nozzle design compared to conventional SCPP design. Figure 2 shows the open-ended conical-shaped solar nozzle design with a solar absorber at its base. The smoke jack devised by Leonardo da Vinci (1452-1519) has been quoted in many reviews as the earliest illustration of principles of the solar chimney and if we look carefully at the smoke jack the key reason why it works is that it includes a venturi or nozzle [6]. Hence, it is important to evaluate the performance of SCPP using solar nozzles. Based on the literature review; some of the important designs of SCPP and their optimum air velocities are tabulated in Table 1.

METHODOLOGY

The design of SCPP will be based on various laws and stated as below:

a) Law of conservation of mass,

b) Law of conservation of momentum, and

c) Law of conservation of energy

Now, to calculate dimensions and other different parameters for SCPP, the following equations are used:

Maximum air velocity flowing in the tower (chimney) [28] is given by equation (1),

$$U_{tower,max} = \sqrt{\frac{2\times g\times H_{tower}\times \Delta T}{T_O}} \quad (1)$$

The power output of the solar tower is stated as shown by equation (2),

$$P = Q_{Solar} \times n_{plant} \quad (2)$$

The tower (chimney) converts the heat flow produced by the collector into kinetic energy. The total pressure difference in N/m^2 is represented in equation (3):

$$\Delta P_{tot} = \Delta P_S + \Delta P_d \quad (3)$$

Considering static pressure difference equals zero, $\Delta P_S = 0$, then the total pressure difference will be as shown in equation (4):

$$\Delta P_{tot} = 0 + \Delta P_d = \Delta P_d \quad (4)$$

The total power output in watts is represented by equation (5),

$$P_{tot} = \Delta P_{tot} \times v_{towermax} \times A_{Collector} \quad (5)$$

$$n_{tower} = \frac{P_{tot}}{Q} \quad (6)$$

To calculate the air velocity at the entrance height of the chimney (bottom or inlet of chimney section) inside SCPP, the following equation is used:

$$v_i^2 = \frac{2\,\Delta T_i\, g\, h_o}{T_a} \quad [32](7)$$

Now, using the continuity equation, the air exit velocity (v_e) is given by equation (8):

$$v_e = v_i \times \frac{A_i}{A_e} \quad (8)$$

A_i: (Cross-sectional area at chimney entrance, m^2)

A_e:(Cross-sectional area at chimney exit, m^2)

At the chimney exit, the turbine is fixed and the air exit velocity can be represented as equation (9),

$$v_e^2 = 2 \times C_p \times \Delta T' \quad (9)$$

Solar insolation can be represented by following equation (10),

$$I = \rho \times v_i \times C_p \times \Delta T_i \quad (10)$$

Based on the above equations, we are going to design various components of our hybrid SCPP. The radiation Discrete Ordinates model (DO) is used for numerical analysis. According to this model, when radiation passes from one medium to another, the following equation (11) is used:

$$n_1 \times \lambda_1 = n_2 \times \lambda_2 \quad (11)$$

The solar irradiance method and fair weather conditions are used during the ANSYS-FLUENT analysis (Figure 3). For the fair weather conditions method following equations are applied and taken from the ASHRAE handbook and represented in equation 12:

$$E_{dn} = S_{etrn}\, S_{unprime} \quad (12)$$

The equation (13) for diffused solar irradiations on a vertical surface is stated below:

$$E_d = C\, Y\, E_{dn} \quad (13)$$

Here, 'C' is constant.

The equation (14) for diffuse solar irradiation for surfaces other than vertical surfaces is:

$$E_d = C\, E_{dn} \frac{(1+cos\epsilon)}{2} \quad (14)$$

There will be some ground reflected irradiations. Equation (15) represents such solar irradiations that fall on surface:

$$Er = E_{dn}(C + sin\beta)\rho_g \frac{(1-cos\epsilon)}{2} \quad (15)$$

Assumptions

- The density variation of air-fluid is a function of temperature and follows Boussinesq approximations.
- Fluid is 'air' and flow has a steady state. A turbulent model is used. The thermo-physical properties of air are assumed to be constant.
- The solar heat flux incident and absorbed in the absorber region is constant throughout the day. The sky is assumed to be clear and not cloudy during solar load calculations.

NUMERICAL ANALYSIS

The solar chimney power generating plant and solar nozzle plant are designed with the use of ANSYS-ICEM software (Figures 4, 5, and 6). We have performed numerical analysis with the help of the latest available version of ANSYS software. The following dimensions are considered while designing: dimensions of base = 3 m length and 3 m width, base height (inlet height) = 0.1 m, overall height (h) of the plant is varying based on different models (i.e. from 1 m to 7 m), the material of chimney and nozzle is polycarbonate, top dimensions of the nozzle or chimney = 0.5 m × 0.5 m. The squared cross-section (for chimney and nozzle) is considered with advantages of ease of manufacturing, and handling as well and the availability of workshop facilities. The model is designed in ICEM-ANSYS software (2022-R_1). The mesh is created in ICEM with body type hexagonal cells. The 3-dimensional RNG k-epsilon viscous turbulence model with steady-state conditions is considered for numerical analysis. The discrete ordinate radiation model is used for analysis purposes. The air density is defined by Boussinesq approximations and assumed to be 1.1455 Kg/m^3. The limitation of the study is that a flow of 'air' i.e. the fluid flowing inside the solar chimney; assumed to be incompressible flow, but in real situations, air is a compressible fluid. The various thermo-physical properties of materials are shown in Table 2. Comparing the dimensions mentioned in Table 1; height of chimney varies from 1 m to 7 m, while the base area is 9 m^2. Both SCPPs with and without nozzle designs are considered during numerical study.

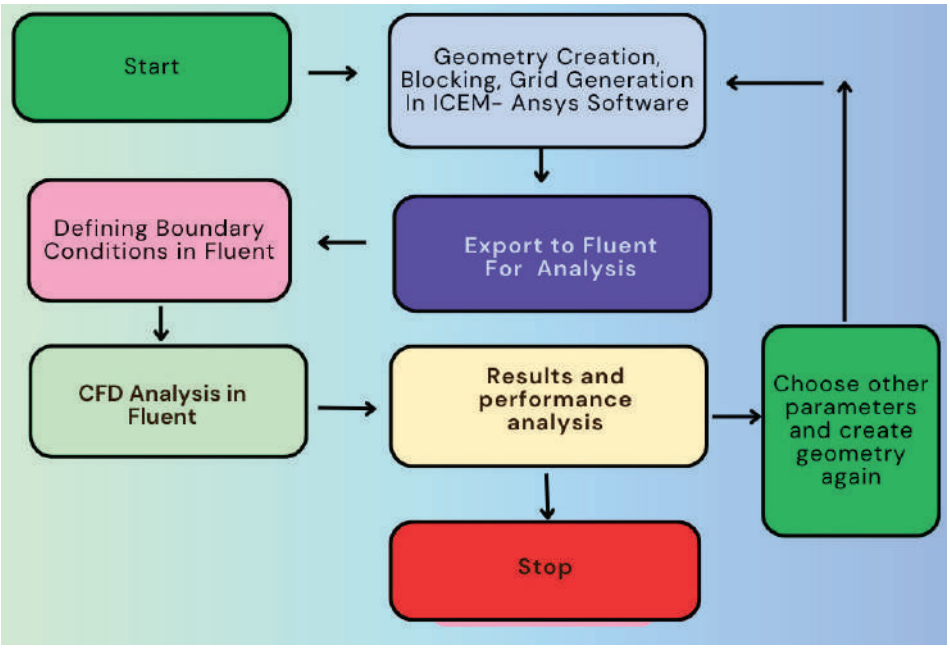

Figure 3. Flowchart of numerical analysis of solar nozzle plant.

The boundary conditions considered during analysis were: inlet conditions: gauge total pressure (Pa) = 0 Pa, total temperature (T) = 308 K, outlet conditions: gauge pressure = 0 Pa, backflow total temperature = 308 K, backflow turbulent intensity = 5%., the static pressure = 0 Pa. The multiphase model kept OFF and the viscous k-epsilon (2 equations) standard model was used. The enhanced wall treatment with a full buoyancy effect was used. The radiation discrete ordinates (DO) model was used considering solar load using a solar ray tracing model with solar calculator load conditions. The Rajkot city (India) location was used for solar loading conditions i.e. longitude 70.9 ° and latitude 22.27° with any summer day conditions. Wall conditions were: base thickness = 0.03 m, material = gravel, thermal boundary type = mixed, wall motion = stationary wall with no-slip conditions, solar nozzle: material= polycarbonate, radiation boundary type= semi- transparent. The following solver setting is used: pressure velocity coupling = SIMPLEC type, discretization scheme = second order and upwind. The location considered is 'Rajkot' (Gujarat, India) with direct solar irradiance = 810 W/m^2. The chimney material is 'polycarbonate'.

The radiation model is used with solar radiation 'ON' and the solar ray tracing model is applied for this location. The complete analysis in ANSYS-FLUENT is done for the above conditions and grid independence test results are shown in Figure 4. The grid independence test is performed and the most suitable grid size is selected for performing numerical analysis. The fine mesh type II (Figure 4) with nodes sized 38800 is selected for analysis.

Figure 5 shows a solar chimney plant designed in ICEM-ANSYS. It indicates a wire-frame view of SCPP, the designing of which is done using ANSYS software.

On the other hand, Figure 6 represents the solar nozzle plant in its three-dimensional view.

RESULTS AND DISCUSSION

Table 3 shows various models that are numerically analyzed to evaluate the performances of SCPP with and without a nozzle. There are a total of 8 models numerically studied. Out of these 8 models, 4 models are with solar chimney power generating plants (i.e. without nozzle) and the remaining 4 models are with solar nozzle power plants. All models were numerically studied with two different conditions i.e. fair weather as well as theoretically maximum solar irradiance conditions. Fair weather conditions have a sunshine factor of 0.9 while the theoretically

Table 2. Thermo-physical properties of materials [16]

	Thermo-physical properties ↓	(Part name) →	Nozzle	Absorber	Solar collector	Fluid
1	**Material name**		Polycarbonate	Gravel	Glass	Air
2	**Density (kg/m^3)**		1200	1840	2700	1.1455
3	**Sp. heat Cp (J/kgK)**		1170	840	840	1005

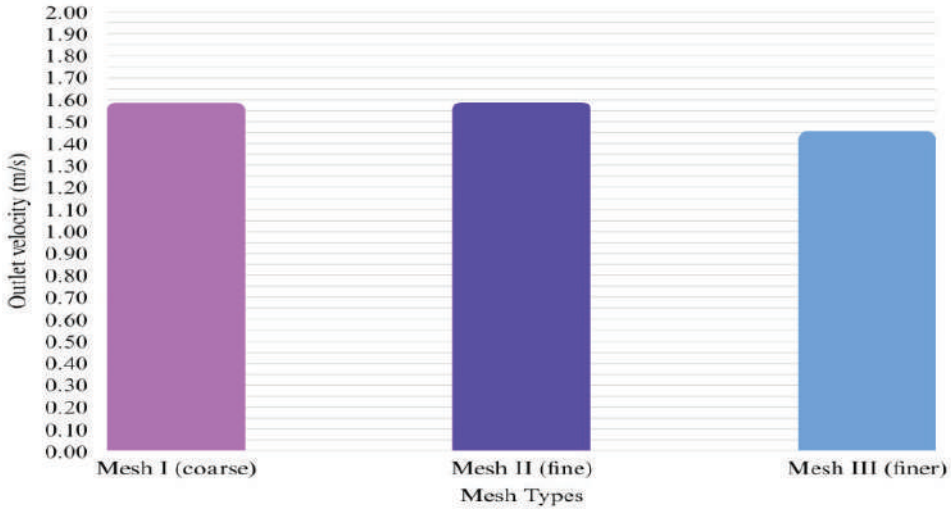

Figure 4. Mesh independence test.

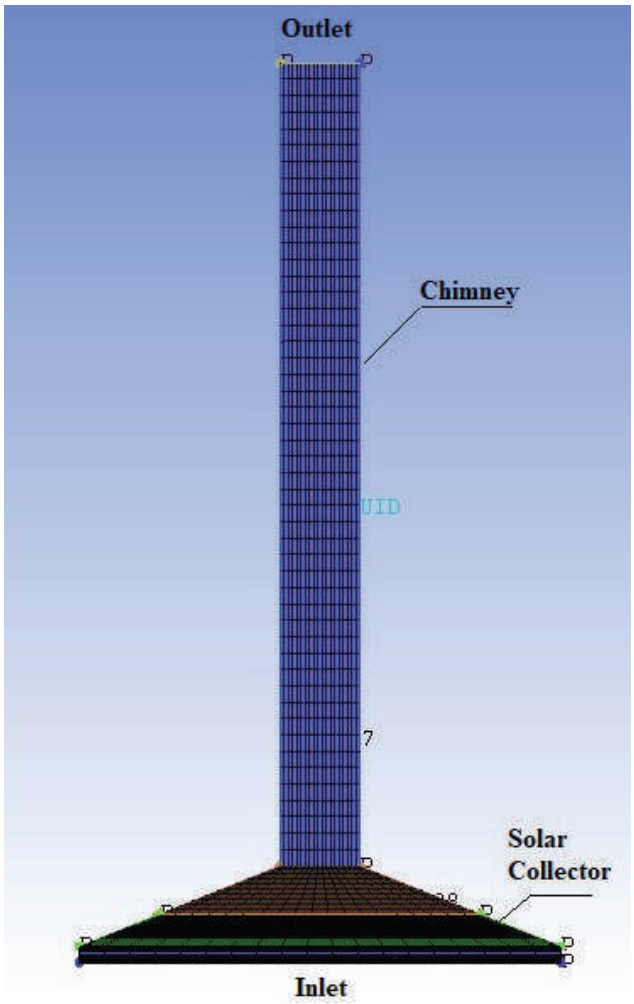

Figure 5. SCPP (designed in ANSYS-ICEM).

maximum method has a sunshine factor of 1. Figures 7 (a) and (b) show velocity contours and pathlines contours for model 1 (SCPP model with chimney height of 7 m) using fair weather conditions while Figure 9 (a) and Figure 9 (b) represent the same contours but using the maximum theoretical method in solar loading model. The numerical findings of all the above SCPP models are compared to the experimental results of Manzanares pilot plant which was located in Spain and studied by Haaf et al. in the year 1983. Figure 7 (a) shows the velocity contours, highlighting the maximum air velocity region near the chimney inlet and is indicated by reddish spots in Figures 7(a) and (b). Figure 8 shows the velocity magnitude and position plots for various sections in SCPP. The solar radiation falls on the absorber regions and is responsible for the rise in air temperature in the vicinity of the absorber. The heat transfer takes place due to the natural convection method. The static pressure of air is taken as zero at both inlet and outlet. At the center of the chimney, we get maximum velocity it reduces as we

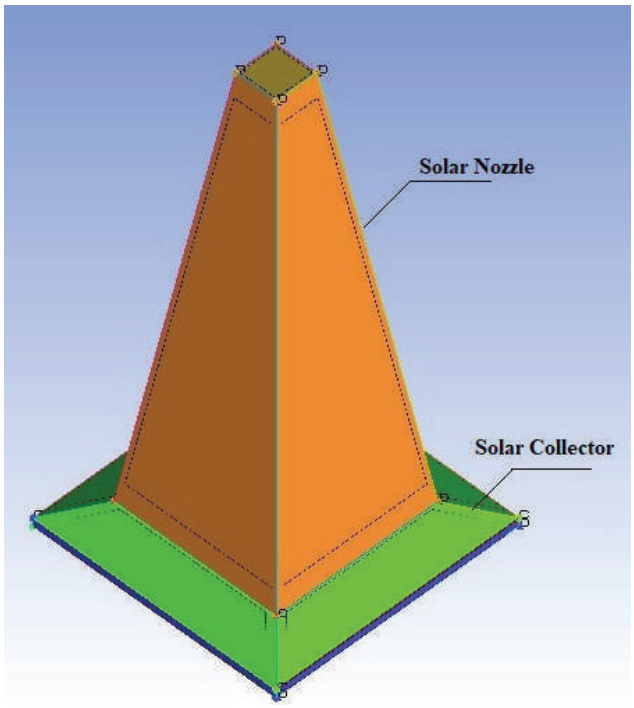

Figure 6. 3-D solar nozzle plant.

proceed towards the walls and is defined by the boundary layer theory.

Figure 9 (a) shows the velocity contours for a solar chimney power generation plant with a chimney height of 7 m. The cross-sectional region of the chimney is squared with a dimension of 0.5 m× 0.5 m. The maximum air velocity inside the chimney is 1.5 m/s using fair weather conditions (FWC). The solar ray tracing model is used with a sunshine factor of 0.9. Figure 9 shows the velocity contours, highlighting the optimum air velocity region near the chimney inlet. It is indicated by the reddish color in the figure. The power is generated by fixing turbines in this region. This can be converted into electricity using an electrical generator. The pathlines contour for the maximum theoretical method is represented in Figure 9 (b). During the numerical study, the gravel is considered as an absorbing material and is useful for maintaining air temperatures all over periods in the day i.e. during night times when solar radiations are minimal; absorbing materials help to gain stored thermal energy and thus continuous power generation is possible with these SCPP units.

Figure 10 (a) indicates the velocity contours, highlighting the maximum air release velocity at the nozzle outlet region and is denoted by reddish regions in Figure 10 (a) and Figure 10 (b). The numerical value for optimum velocity in the solar nozzle plant having a height of 7 m is nearly 1.75 m/s. The average total temperature at the nozzle outlet is 316.18 K. Figure 10 (b) shows pathlines for model 2. This is a design of a solar nozzle power generating plant

Table 3. Various models (model no.1 to 8) of SCPP and solar nozzle plant numerically designed using ANSYS and comparing with Manzanares pilot plant (model 9, Haaf et al. 1983)

Model No.	Absorber base (Material, dimensions etc.)	Chimney or nozzle (Material, dimensions etc.)	Numerical results with Fair Weather Conditions (FWC)	Numerical results with Theoretical Maximum Solar Irradiance Method (TM)	% Increase in air velocity (comparing SCPP with and without nozzle)
1	Material: Gravel Size: 3 m × 3 m (SCPP model with no nozzle)	Chimney material: Polycarbonate Size: Nozzle height = 7 m Top = 0.5 m × 0.5 m	Maximum air velocity inside chimney = 1.50 m/s Average total temp. at chimney outlet = 317.96 K	Maximum air velocity inside chimney = 1.77 m/s Average Total Temp. at Chimney Outlet = 321.54 K	0
2	Material: Gravel Size: 3 m × 3 m (Solar nozzle model)	Nozzle material: Polycarbonate Size: Nozzle height = 7 m Top = 0.5 m × 0.5 m	Maximum air velocity at nozzle outlet =1.75 m/s Average total temp. at outlet = 316.18 K	Maximum air velocity at nozzle outlet= 1.99 m/s Average total temp. at outlet = 318.44 K	16.66 (For FWC) 12.42 (For TM)
3	Material: Gravel Size: 3 m × 3 m (SCPP model with no nozzle used)	Chimney material: Polycarbonate Size: Chimney height = 5 m Squared cross section 0.5 m × 0.5 m size.	Maximum air velocity inside chimney = 1.32 m/s Average Total Temp. at Outlet = 317.63 K	Maximum air velocity inside chimney = 1.52 m/s Average total temp. at outlet = 319.69 K	0
4	Material: Gravel Size: 3 m × 3 m (Solar nozzle model)	Nozzle material: Polycarbonate Size: Nozzle height = 5 m Top = 0.5 m × 0.5 m	Maximum air velocity at nozzle outlet = 1.43 m/s Average total temp. at outlet = 315.20 K	Maximum air velocity at nozzle outlet= 1.61 m/s Average total temp. at outlet = 317.03 K	8.33 (For FWC) 5.92 (For TM)
5	Material: Gravel Size: 3 m × 3 m (SCPP model with no nozzle)	Chimney Material: Polycarbonate Size: Chimney height = 3 m Top = 0.5 m × 0.5 m	Maximum air velocity inside chimney = 0.92 m/s Average total temp. at outlet =314.51 K	Maximum air velocity inside chimney = 1.05 m/s Average total temp. at outlet = 316.67 K	0
6	Material: Gravel Size: 3 m × 3 m (Solar nozzle model)	Nozzle material: Polycarbonate Size: Nozzle height = 3 m Top = 0.5 m × 0.5 m	Maximum air velocity at nozzle outlet = 1.09 m/s Average total temp. at outlet = 314.01K	Maximum air velocity at nozzle outlet= 1.23 m/s Average total temp. at outlet = 315.44K	18.47 (For FWC) 17.14 (For TM)
7	Material: Gravel Size: 3 m × 3 m (SCPP model with no nozzle)	Chimney material: Polycarbonate Size: Chimney height = 1 m Top = 0.5 m × 0.5 m	Maximum air velocity inside chimney = 0.55 m/s Average total temp. at outlet = 311.84 K	Maximum air velocity inside chimney = 0.65 m/s Average total temp. at outlet = 313.29 K	0
8	Material: Gravel Size: 3 m × 3 m (Solar nozzle model)	Nozzle material: Polycarbonate Size: Nozzle height = 1 m Top = 0.5 m × 0.5 m	Maximum air velocity at nozzle outlet = 0.71 m/s, Average total temp. at outlet = 312.54 K	Maximum air velocity at nozzle outlet= 0.76 m/s Average total temp. at outlet = 313.21 K	29.09 (For FWC) 16.92 (For TM)
9	Manzanares pilot plant, Spain (Experimental study, W. Haaf et al 1983)	Tower height = 194.6 m, Tower radius = 5.08 m	The Air upwind velocity on release for pilot plant = 15 m/s	-	-

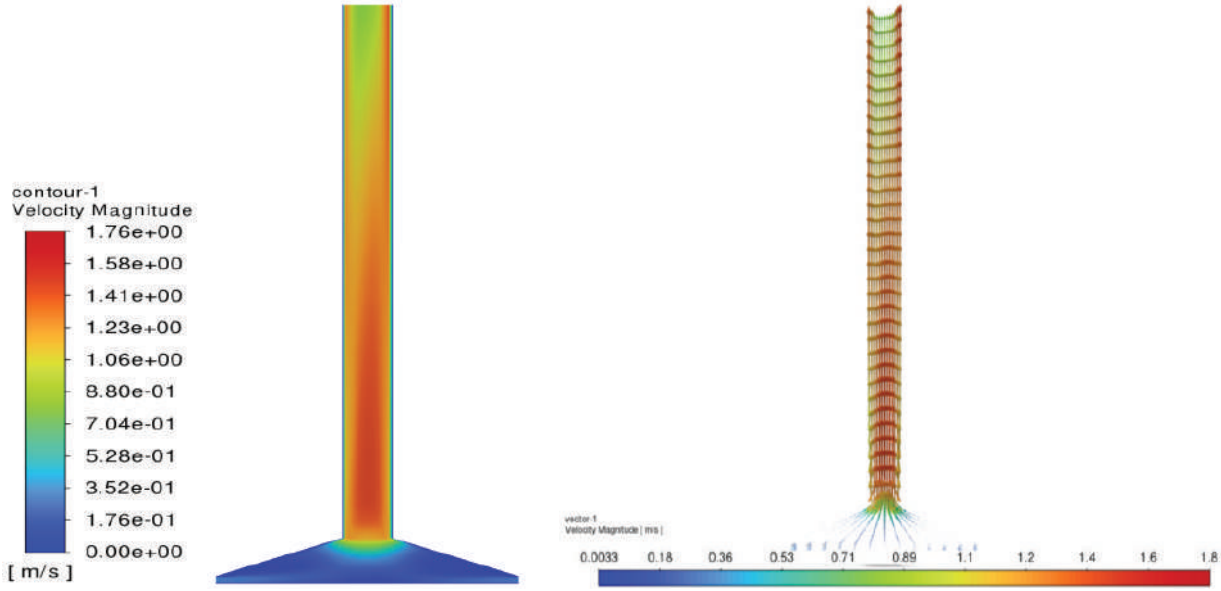

(a) (b)

Figure 7(a). Contours of velocity magnitude for SCPP model 1. **(b)** Pathlines for SCPP model 1.

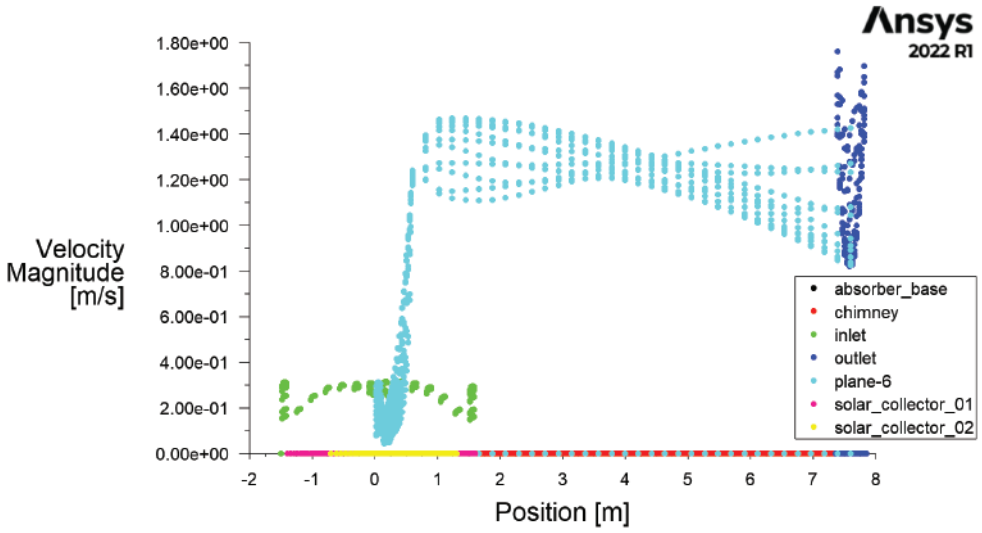

Figure 8. Velocity magnitude vs. position plot for model 1.

with a nozzle height of 7 m. Figure 10 (b) clearly indicates that, in this design, maximum air velocity is obtained at the nozzle outlet region. Above this nozzle outlet, a chimney is fixed to deliver air to the proper height to the surrounding atmosphere. Thus, the turbine is fixed in the regions of the nozzle outlet to gain maximum power output. Using equations (1) to (6) and considering dimensions for the model 3 (table 3) of SCPP with chimney height of 5 m, the various theoretical values for SCPP are: $U_{tower,max}$= 1.749 m/s, ΔP_d = 1.746 N/m^2, ΔP_{tot}= 1.746 N/m^2, P_{tot}= 27.49 W or 0.0274 kW, η (*Efficiency of chimney*)= 0.3665 %. The maximum air velocity inside the chimney (Numerical Value using solar irradiance theoretical maximum method) is 1.52 m/s for model 3 (Table 2). So, Theoretical and numerical values for maximum air velocity inside the chimney are close to each other.

Figure 11 (b) shows the velocity vs. position plot for a plane passing through SCPP's central axis and positioned in the vertical direction. The velocity, total pressure, incident radiation and heat flux contours for solar model 3are shown in Figures 11 (a),12 (a), 12 (b), 13 (a) and (b) respectively. Figure 14 suggests that the

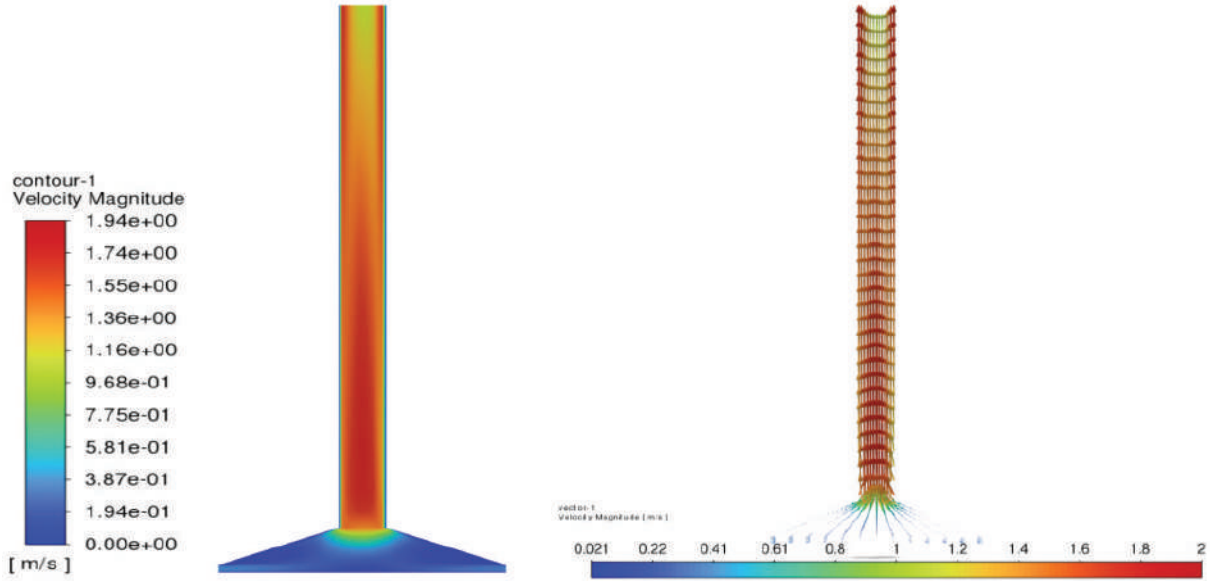

(a) (b)

Figure 9(a). Velocity magnitude contour for SCPP model 1with TM method **(b)** Pathlines contour for model 1.

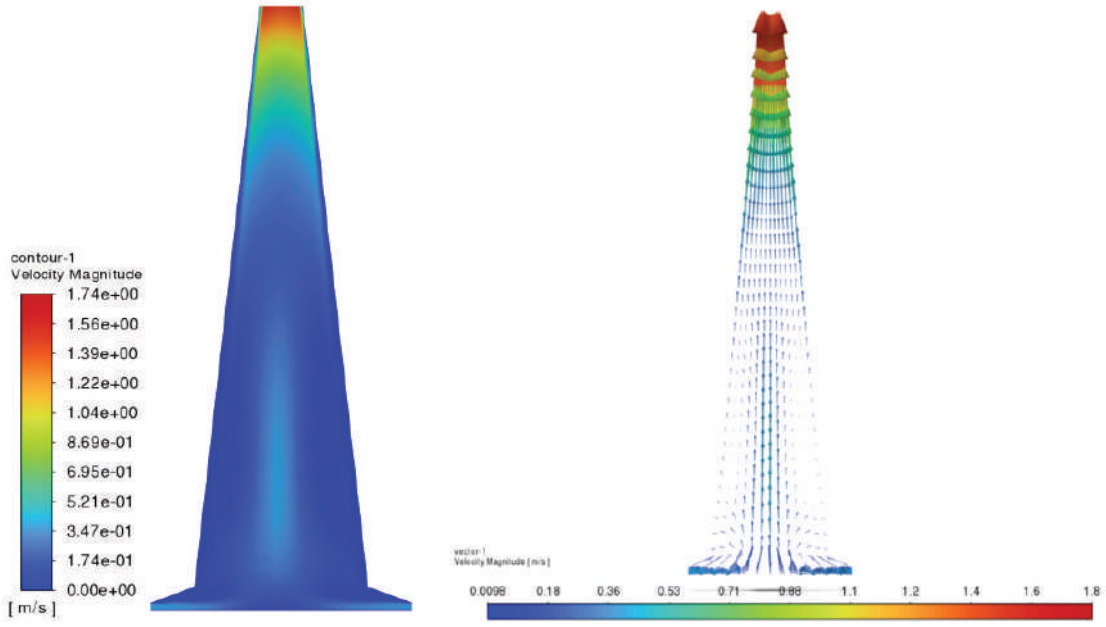

(a) (b)

Figure 10(a). Contours of velocity magnitude for solar nozzle model 2 **(b)** Pathlines contour for model 2.

maximum air release velocity is found at the chimney inlet. The numerical value for optimum velocity inside the solar chimney plant having a height of 5 m is nearly 1.32 m/s. The average total temperature at the chimney outlet is 317.63 K.

Figure 12 (a) shows the total pressure contours for model 3 of a solar chimney power generating plant with a chimney height of 5 m. The total pressure is the sum of static pressure and dynamic pressure. The static pressure is assumed to be zero, so total pressure is nothing but the dynamic pressure of the air-fluid. Figure 12 (b) suggests the incident radiations that fall over SCPP and its effect is especially studied over the collector, chimney and absorber regions. These regions mainly contribute to the solar loading and thus resulting the rise of air temperature. Figure 13 (a) shows the solar heat flux contours for

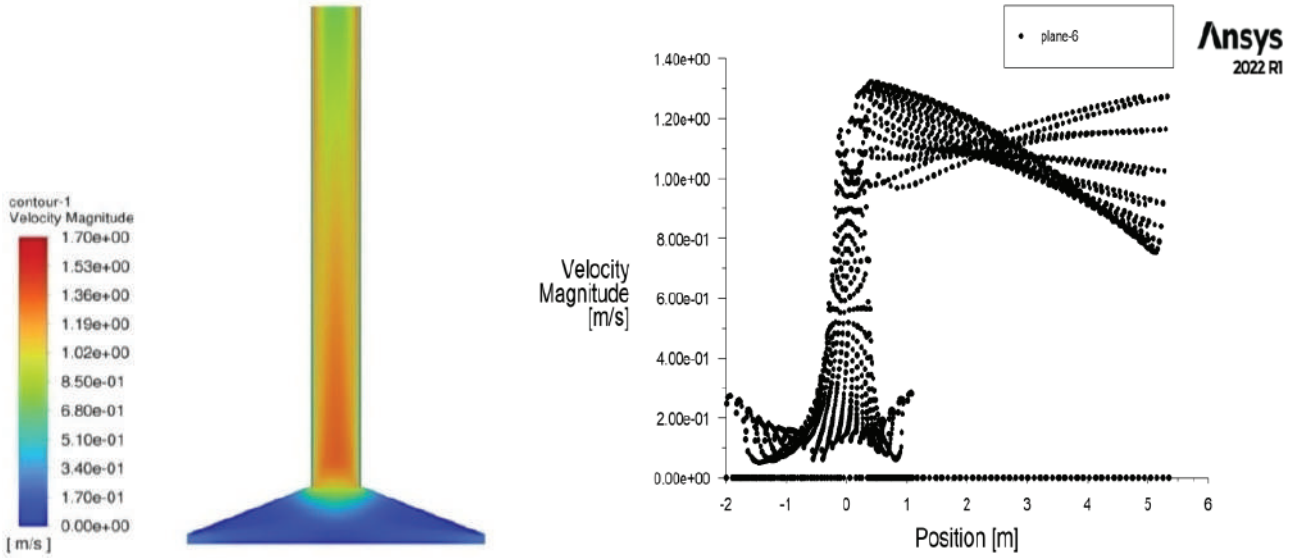

(a) (b)

Figure 11(a). Velocity contours for SCPP- model 3 **(b)** Velocity and position graph for a central plane in model 3.

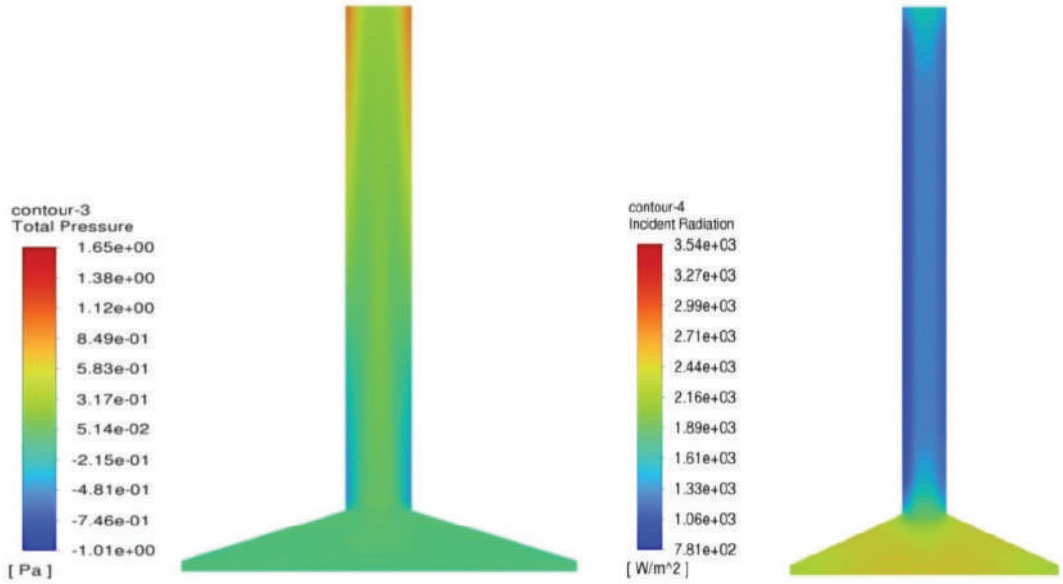

(a) (b)

Figure 12(a). Total pressure contours for SCPP- model 3**(b)** Incident radiations contour for model 3.

solar chimney plant model 3. In this numerical analysis, both collector and chimney regions participate in solar ray tracing and solar loading, to gain maximum of incident radiation energy. The numerical readings are taken considering a day in summer month at Rajkot (India) location and afternoon timings when solar radiations have higher availability and sky is clear. Figure 13 (b) shows pathlines for model 3. The following figures i.e. Figure 14 to Figure 23 show the rest of numerical models (as per Table 2) with different contours of velocity, solar heat flux and pathlines of velocities.

For model 4 with the solar nozzle of height 5 m, theoretical kinetic energy at the chimney outlet is 0.00785 kW and chimney efficiency is 0.25 % and is close to its numerical results (using equations 01 to 06). Figure 15 (b) suggests the solar heat flux for model 04 with a nozzle height of 5 m. The reddish as well as green spots are observed near the walls of an absorber and the chimney regions and they are clearly visible in Figure 15 (a), which indicates

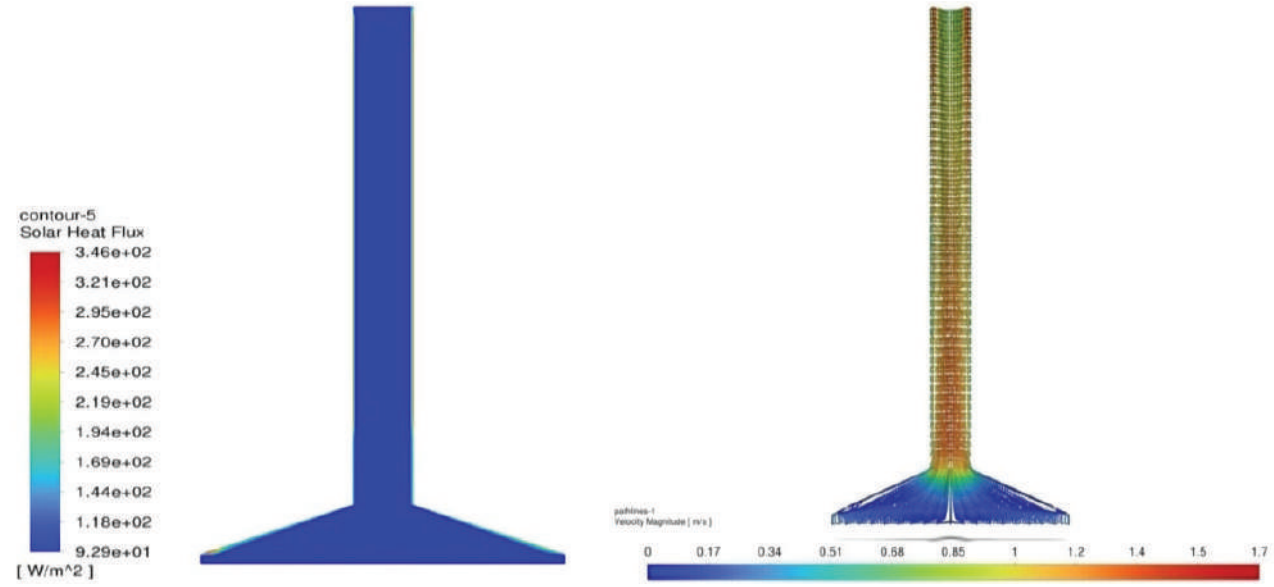

(a) (b)

Figure 13(a). Solar heat flux contours for SCPP- model 3 **(b)** Pathlines contour for model 3.

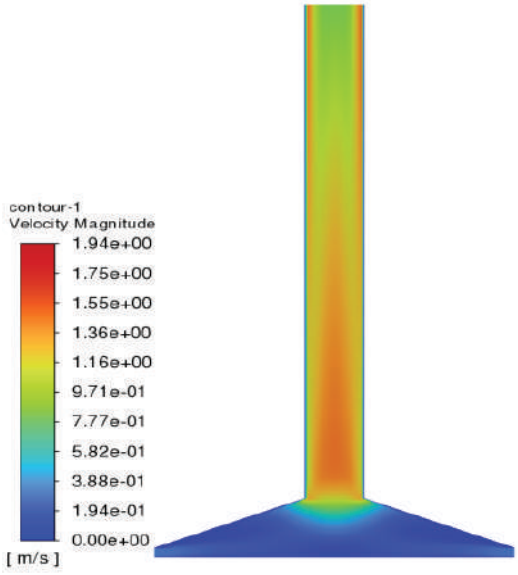

Figure 14. Velocity contours for SCPP- model 3 using theoretical maximum solar irradiance method.

the absorbed solar radiations in those regions. When solar radiations fall on those surfaces, the air in the vicinity of it gains heat and rises up due to buoyancy effects. Thus, this results in maximum temperature at the nozzle outlet as per Figure 15(a).

Figure 16 (b) shows volumetric absorbed radiations in W/m^3 with respective positions in meters for a vertical plane passing through the central axis of SCPP. Figures 17 (a) and 17 (b) show model 5 of a solar chimney power generating plant with an overall height of the chimney is 3 m. The numerical value of maximum air velocity with fair weather conditions is 0.92 m/s. The numerical analysis suggests that with a theoretical maximum method (TM) the value is 1.05 m/s. It is close to its FWC value.

Figures 18 (a) and 18 (b) show velocity contours as well as pathlines contours for solar nozzle model 6 with a nozzle height of 3 m. The maximum air velocity at the nozzle outlet is1.09 m/s and the average total temperature is 314.01 K (calculated by numerical method with fair weather conditions).

Amongst all studied models, model 7 and model 8 are with the least overall heights i.e. of 1 m height and the numerical results of an investigation are indicated in Figures 19 (a), 19 (b), 20 (a) and 20 (b). The maximum numerical value of air release velocity inside the chimney in Figure 18 (a) is nearly 0.55 m/s. The average total temperature at the chimney outlet is nearly 311 K. Figure 18 (b) indicates the pathlines of the air flow inside the SCPP design. The air enters from the bottom regions inside the SCPP (i.e. from the inlet section) and it receives the solar heat at the collector regions (due to incident solar radiations). Because of the increase in its temperature, it rises upward into the chimney, thus creating an upward thrust. This upward thrust is then converted into power output when air falls over the turbine blades. Thus, we can generate electricity from the SCPP.

From Figure 20 (a), it's clear that the maximum velocity of air-fluid is obtained at the nozzle outlet regions for solar nozzle power plant with a height of nozzle equal to one meter. The air movement increases near the nozzle outlet

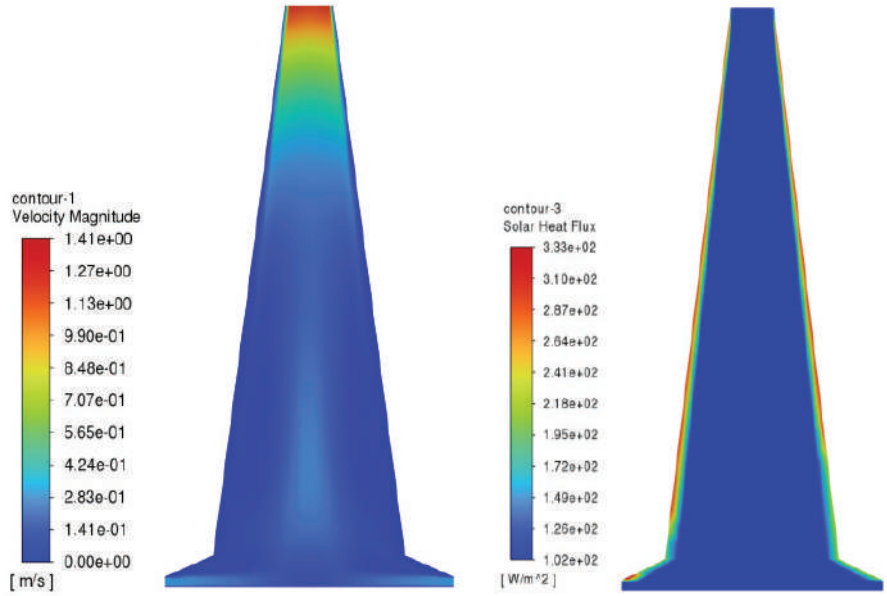

(a) (b)

Figure 15(a). Velocity contour for solar nozzle model 4 **(b)** solar heat flux contours for model 4.

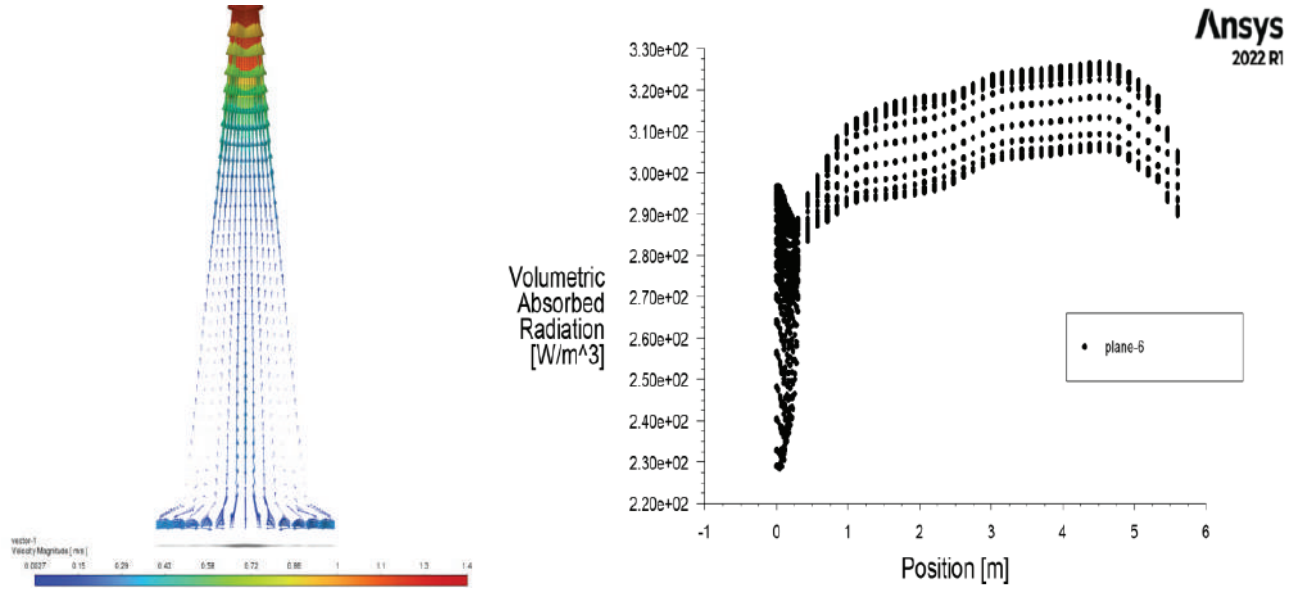

(a) (b)

Figure 16(a). Pathlines contours of velocity magnitude for solar nozzle model 4 **(b)** Volumetric absorbed radiation vs. position contours for model 4.

as indicated in Figure 20 (b), as air is passed through this converging shape i.e. nozzle shape. The turbulent model is used for numerical analysis. Figure 21 shows the velocity and position plot for model 8. Figure 20 and 21 show chimney heights and maximum air velocity comparison for fair weather and theoretical maximum conditions for various mentioned models in Table 2.

Figure 22 and 23 shows that as chimney height increases, the corresponding values of maximum air velocities also increase. For a given overall height of the plant, the maximum value of air velocity in m/s is higher

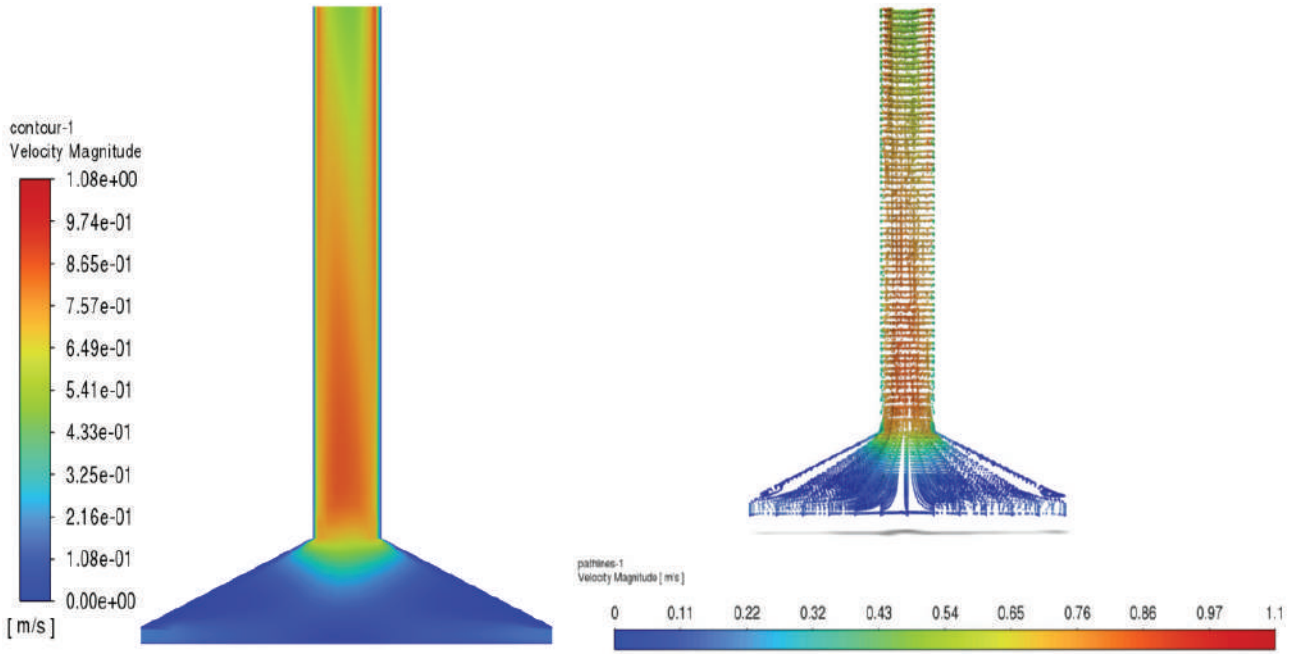

(a) (b)

Figure 17(a). Velocity contours for SCPP- model 5 **(b)** Pathlines contours for SCPP model 5.

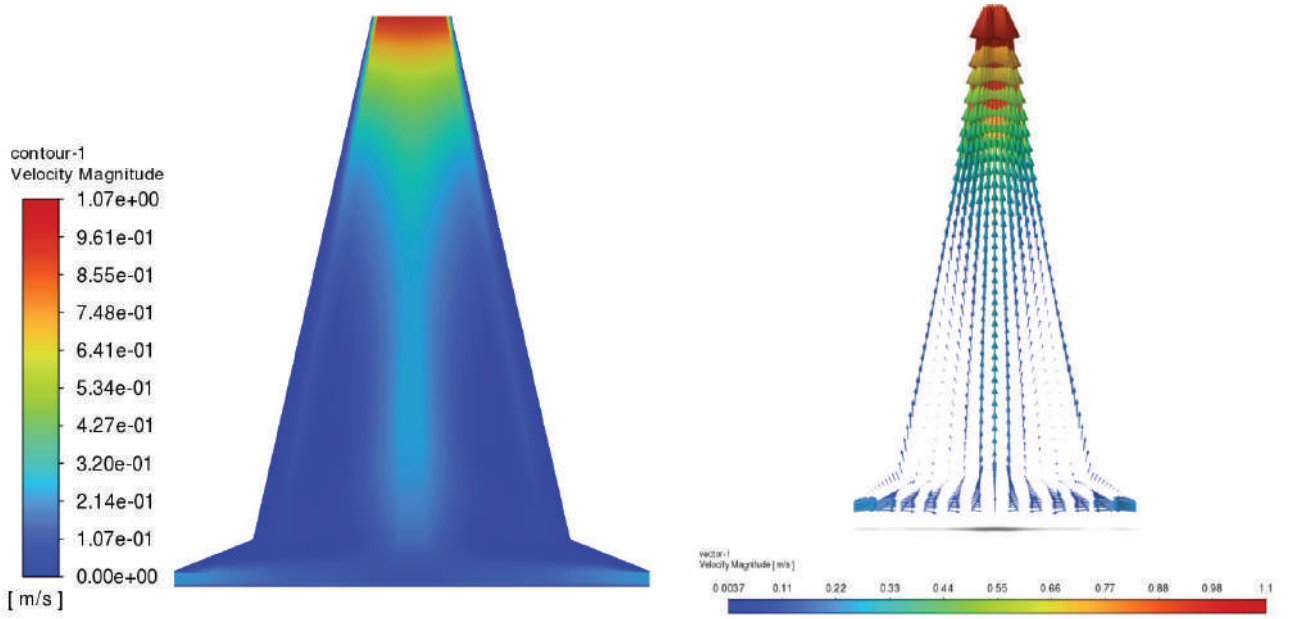

(a) (b)

Figure 18 (a). Velocity contours for solar nozzle- model 6 **(b)** Pathlines contours for SCPP model 6.

for solar nozzle plant than that of SCPP with no nozzle plant.

Figure 23 suggests that as chimney height (in m) increases, the corresponding values of maximum air velocities (in m/s) also rise. For a given overall height, the value of air velocity in m/s is higher for solar nozzle plant with theoretically maximum method (TM) than that of fair weather conditions (FWC). Figures 24 and 25 show that as chimney height increases, the average temperature of air at outlet also rises (for both plants i.e. SCPP with and without nozzle).

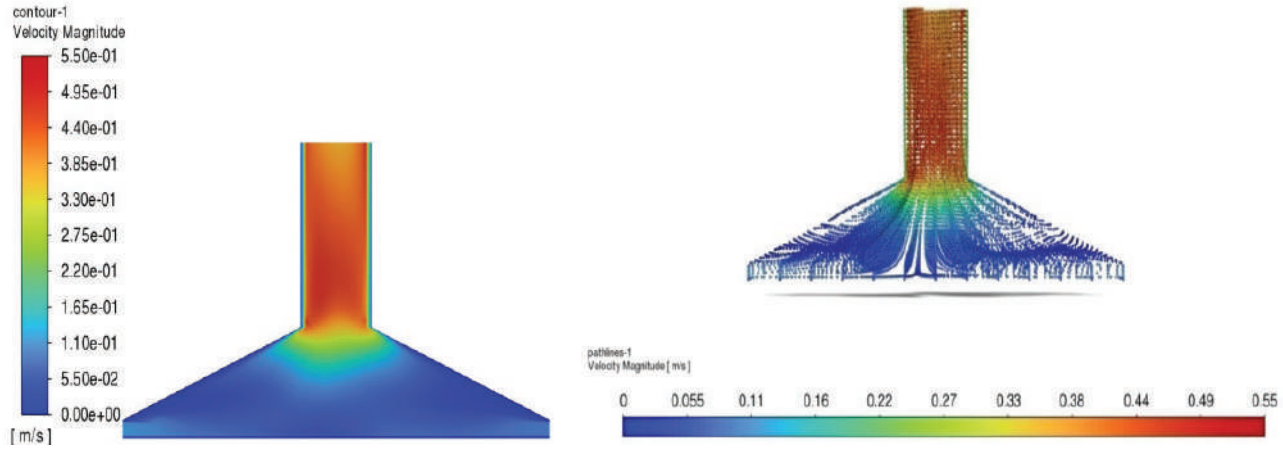

(a) (b)

Figure 19 (a). Contour of velocity magnitude for SCPP model 7**(b)** Pathlines contour of velocity magnitude for SCPP model 7.

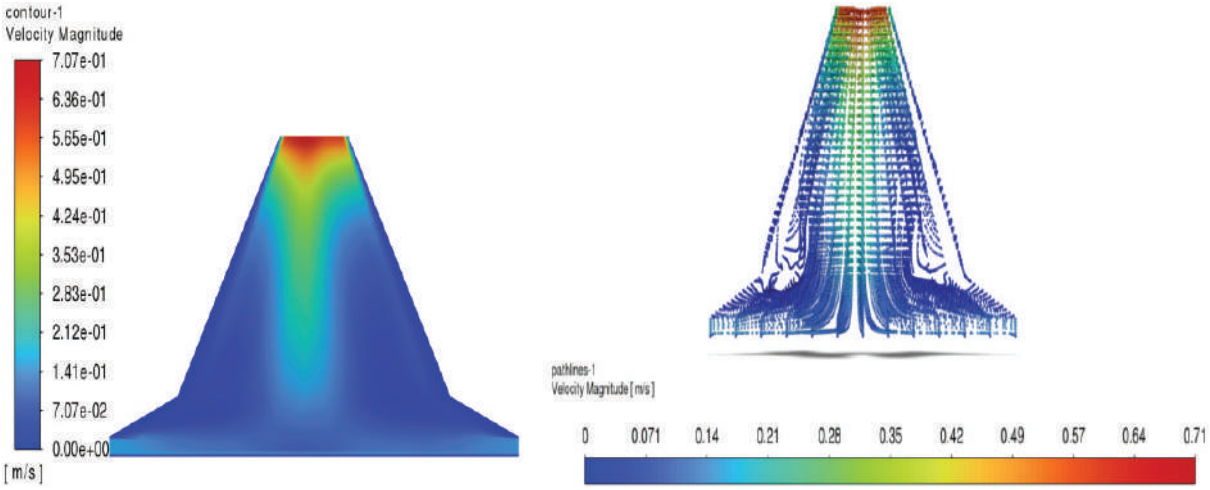

(a) (b)

Figure 20(a). Contour of velocity magnitude for solar nozzle model 8 **(b)** Pathlines contour of velocity magnitude for solar nozzle model 8.

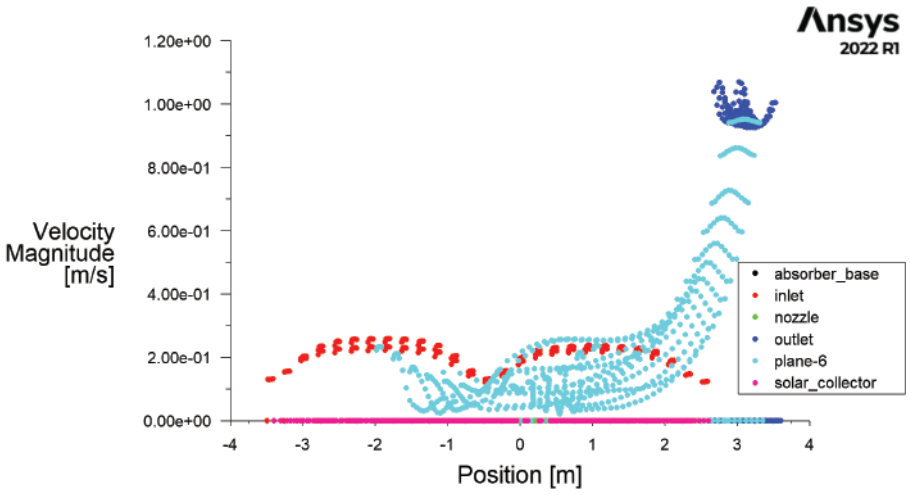

Figure 21. Velocity magnitude vs. position plot for solar nozzle plant - model 8.

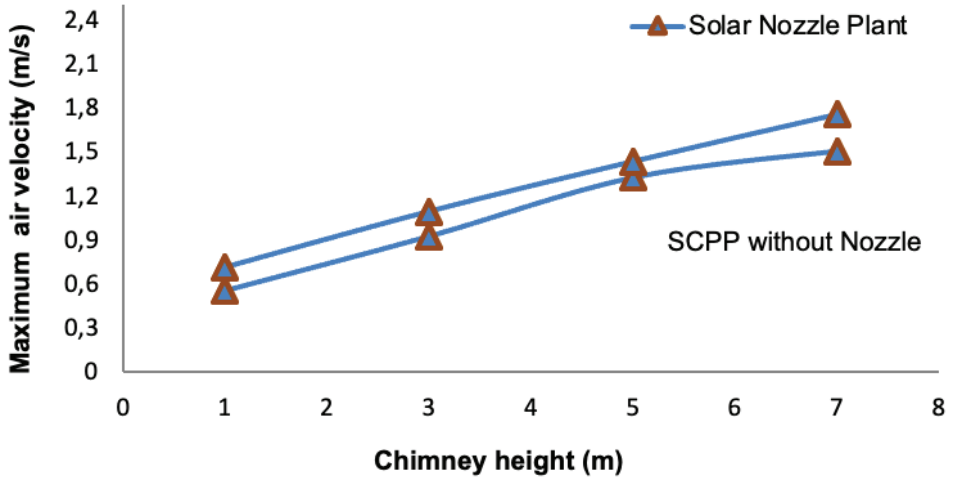

Figure 22. Comparison of chimney height with max. air velocity (FWC) for SCPP with and without nozzle.

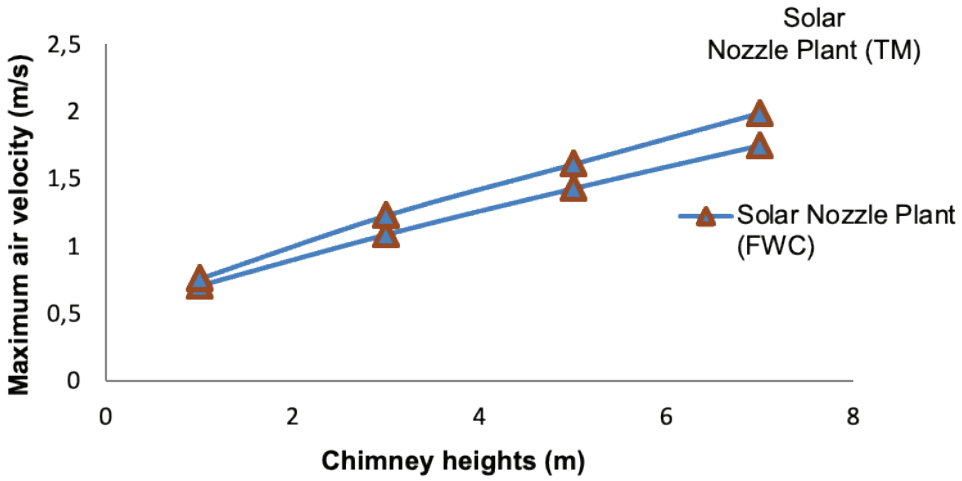

Figure 23. Comparison of chimney height with max. air velocity with FWC and TM for solar plant with nozzle.

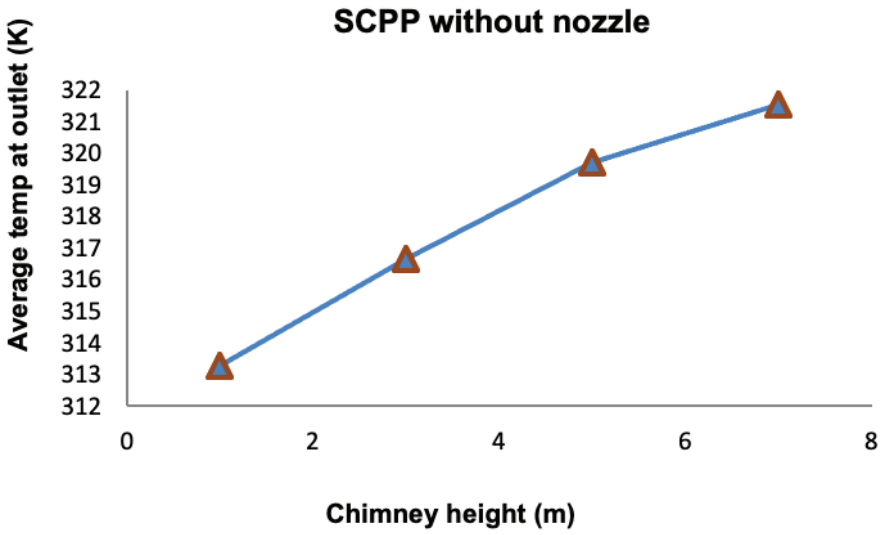

Figure 24. Comparison of Chimney height and average temperature at outlet for SCPP without nozzle (Using TM method).

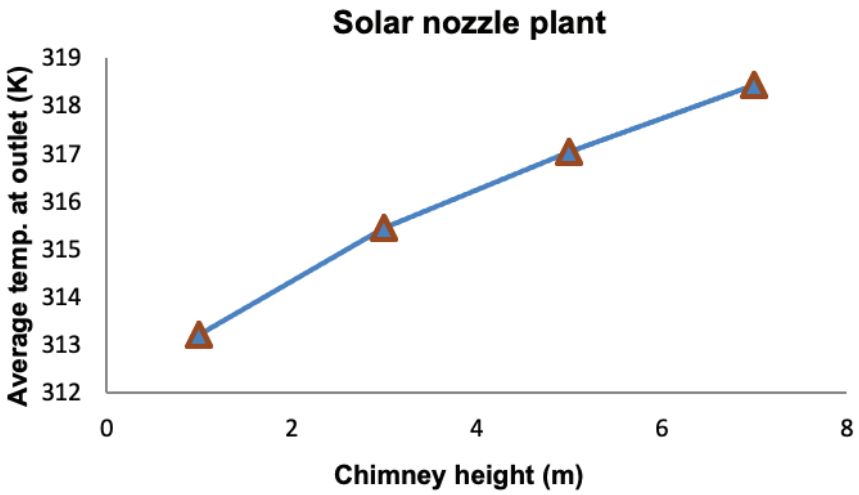

Figure 25. Comparison of Chimney height and average temperature at outlet for solar nozzle plant (Using TM method).

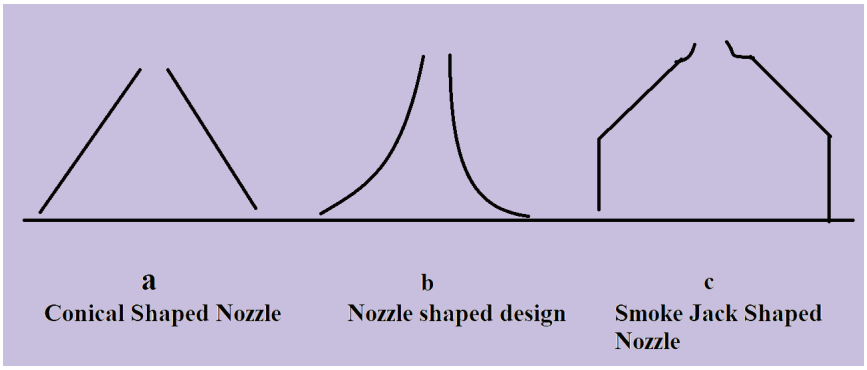

Figure 24. Different Shapes of solar nozzles [33].

CONCLUSION

Numerical analysis of all models show that as chimney height increases corresponding maximum air velocity also increases (Figures 22 and 23). Figure 23 shows that for all solar nozzle models, for both fair weather and theoretical maximum conditions the numerical results are nearer to each other. The base and inlet dimensions are kept constants for all numerical cases i.e. 3 × 3 m and inlet height = 0.1 m, respectively. Considering the 7 m height model (i.e. models 1 and 2), the solar nozzle model (model 2) shows a 16.66 % increment over SCPP model (model 1) having the same height and no nozzle. Model 4 (solar nozzle with nozzle height of 5 m) shows an increment in maximum air velocity compared to model 3 (SCPP model with chimney height of 5 m) by nearly 8.33 %. The solar nozzle model 6 with height of nozzle 3 m shows an optimum increment of nearly 29 % than the SCPP model of 3 m height and with no nozzle used. Another model i.e. solar nozzle model with a height of 1 m of nozzle shows an increment of 8.47 % than model 8.

The percentage (%) change in air release velocity for model 1 (SCPP with chimney height of 7 meters) by using the theoretical maximum solar irradiance method (TM) (Table 2) than fair weather conditions (FWC) is 18 %. Similarly, the percentage (%) change in air outlet velocities for other remaining models i.e. 2, 3, 4, 5, 6, 7, and 8 (SCPP with a chimney as well as solar nozzle designs) by using theoretical maximum solar irradiance method (TM) (Table 2) than fair weather conditions (FWC) are 13.71 %, 15.15 %, 12.58 %, 14.13 %, 12.84 %, 18.18 %, and 7.04 % respectively. The percentages of increase in air outlet temperature (K) for solar nozzle models (2, 4, and 6) compared to model 8 with nozzle height of 1 m, and using theoretical maximum solar irradiance method are: 1.07 %, 2.04 %, and 2.63 %respectively (Figure 25). Also, the percentages of rise in air outlet temperature (K) for SCPP models without nozzle (i.e. models 1, 3, and 5) compared to model 7 with chimney height of 1 m are: 0.71 %, 1.21 %, and 1.66 %respectively (Figure 24).

The main results obtained are summarized as follows:

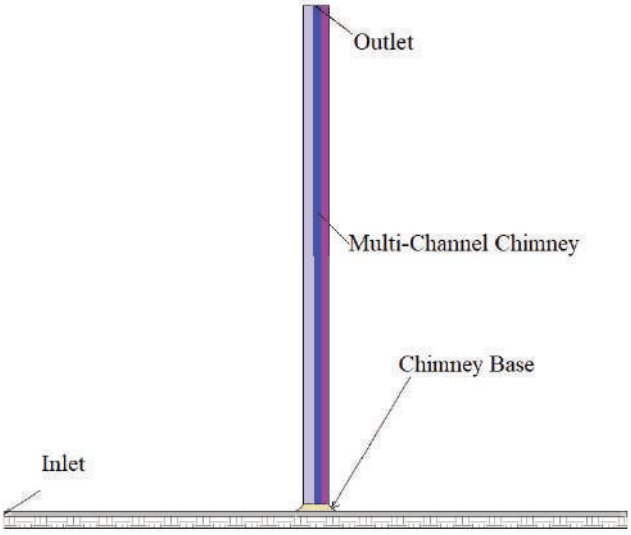

Figure 25. Multi-channel solar chimney.

1. The results demonstrate that incorporating a solar nozzle design significantly increases air release velocity compared to conventional SCPP designs, leading to a potential 16.99 (for FWC) and 12.42 (for TM conditions) % improvement in air release velocity for 7 meters overall heighted system. For 5, 3 and 1 meter heighted system design, the percentages increase in air exit velocity (comparing with and without nozzle designs for both conditions i.e. FWC and TM) changes to 8.33 (FWC), 5.92 (TM), 18.47 (FWC), 17.14 (TM), 29.09 (FWC), 16.92 (TM), respectively (Table 02).
2. This increase in air updraft velocity will have a considerable impact on the power output of the electricity generation plant when the turbine is fixed at the nozzle outlet region.
3. From Table 2, it is quite clear that, for all considered models, the maximum air release velocity is higher with the use of a solar nozzle than with no nozzle. Hence, it is found that the application of solar nozzles in SCPP design enhances air release velocity at nozzle outlet than a conventional design, thus improving power output.
4. The numerical results with theoretical maximum irradiance method show maximum air release velocity compared to fair weather conditions.

FUTURE SCOPE

Already there is an abundant amount of research work done in the field of solar updraft tower power generation plant; still there is a scope available for extending research in this field. A lot of areas like the influence of geometrical constraints on chimney performance, collector dimensions etc., overall sizing of the plant, materials selections, availability of solar radiation intensities that are based on location selections etc. are needed to evaluate further to get optimum results for the SUT. In this study, conical shaped nozzle design is used. The numerical study can further be extended to find out optimum air release velocity using smoke jack shaped and conical shaped nozzle (Figure 24). Research can be extended to evaluate the performance of using multi-channels (For example: number of multi channels = 10, 20 to 100, etc.) inside the chimney in SCPP (Figure 25) [36]. A hybrid system should be tested further to calculate the impact of various mentioned parameters on the overall performance and efficiency of SUT (For example: Integrated design of SUT using Geothermal + solar + wind energy for power generation applications).

NOMENCLATURE

H_{Nozzle}	Height of nozzle i.e. distance from solar absorber to top of the nozzle (m)
H	Height of chimney (m)
R_{Coll}	Radius of collector
R_{Chim}	Radius of chimney
$U_{tower,max}$	Maximum air velocity flowing in the tower (chimney) in m/s
P	Power output in Watts
ΔP_{tot}	Total pressure difference
P_{tot}	The total power output in watts
V_1	Inlet velocity of air flowing through nozzle (m/s)
V_2	Updarft air velocity through nozzle (m/s)
T	Ambient temperature (°C)
g	Acceleration due to gravity (9.81 m/s^2)
I	Solar insolation
ρ	Density of air
S_{etrn}	The top of the atmosphere direct normal solar irradiance
$S_{unprime}$	The correction factor used to account for reduction in solar load through the atmosphere
C	Constant
Y	The ratio of sky diffuse radiation on a vertical surface to that on a horizontal surface
E_d	The direct irradiation at the earth's surface
E_{dn}	The direct normal irradiation at the earth's surface on a clear day
ϵ	The tilt angle of the surface (in degrees) from the horizontal plane
ρ_g	The ground reflectivity
v_i	Velocity of air at chimney entrance in m/s
ΔT_i	Temperature difference at chimney entrance height
g	Acceleration due to gravity, 9.81 m/s^2
T_a	Ambient air temperature in K
h_o	Height of chimney entrance above ground in m
$n_{1,2}$	Refractive indices
$\lambda_{1,2}$	Wavelengths of solar radiations

Abbreviations

SCPP	Solar chimney power plant
FWC	Fair weather conditions

TM Theoretical maximum using solar irradiance method
PV Photovoltaic

ACKNOWLEDGEMENTS

This research work is supported and funded by Dr. Alan Williams (Ammanford, UK) i.e. 'Global Warming Solutions' in the United Kingdom. Thankful to facilities provided by 'Marwadi University Rajkot' Gujarat, India to carry out research and development work in the Mechanical Engineering Department.

AUTHORSHIP CONTRIBUTIONS

All authors contributed to this work.

Anand Gondchawar: Conceptualization, Software, Validation, Writing- Original draft, review and editing. **Bhavesh Kanabar:** Funding activities, and supervision. **Ramesh Bhoraniya:** Writing- review and editing, funding activities, and supervision.

DATA AVAILABILITY

The authors confirm that the data that supports the findings of this study are available within the article. Raw data that support the findings of this study are available from the corresponding authors, upon reasonable request.

CONFLICT OF INTEREST

The authors declared no potential conflicts of interest with respect to the research, authorship, and/or publication of this article.

ETHICAL APPROVAL

There are no ethical issues with the publication of this research article.

REFERENCES

[1] Athienitis A, Kalogirou SA, Candanedo L. Modeling and simulation of passive and active solar thermal systems. In: Comprehensive Renewable Energy. Elsevier; 2012. p. 357-417. [CrossRef]
[2] Al-Abadi N, Ahmed AK, Algburi S, Ahmed OK. Enhancement of the performance of solar chimneys using associated petroleum gas. Int J Sustain Energy 2024;43(1). [CrossRef]
[3] Bahrami M. Forced Convection Heat Transfer. Simon Fraser University; 2015. ENSC 388 (F09).
[4] Cuce PM, Cuce E, Mandal DK, Gayen DK, Asif M, Bouabidi A, et al. ANN and CFD driven research on main performance characteristics of solar chimney power plants: Impact of chimney and collector angle. Case Stud Therm Eng 2024;60:104568. [CrossRef]
[5] Guo P, Wang Y, Meng Q, Li J. Experimental study on an indoor scale solar chimney setup in an artificial environment simulation laboratory. Appl Therm Eng 2016;107:818-826. [CrossRef]
[6] Bergermann S. The Solar Chimney. 2002.
[7] Natarajan R, Suni ACK, Pedasingu LR, Sampath Y. Numerical and experimental study on the collector and chimney modifications of a solar chimney power plant. J Therm Eng 2024;10(6):1539-1558. [CrossRef]
[8] Al-Abadi N, Ahmed AK, Algburi S, Ahmed OK. Enhancement of the performance of solar chimneys using associated petroleum gas. Int J Sustain Energy 2024;43(1). [CrossRef]
[9] Cuce PM, Cuce E, Mandal DK, Gayen DK, Asif M, Bouabidi A, et al. ANN and CFD driven research on main performance characteristics of solar chimney power plants: Impact of chimney and collector angle. Case Stud Therm Eng 2024;60:104568. [CrossRef]
[10] Marzouk OA. Energy generation intensity (EGI) of solar updraft tower (SUT) power plants relative to CSP plants and PV power plants using the new energy simulator "Aladdin". Energies 2024;17(2):405. [CrossRef]
[11] Tesfaye A. Design and Development of Low-Power Output Solar Chimney Power Plant. Research Gate; 2023.
[12] Mirzamohammad A, Yazdi ME, Lavasani A. Improvement of combined solar chimney power plant with gas power plant. Sci Rep 2023;13:11220. [CrossRef]
[13] Singh VP, Dwivedi G. Technical analysis of a large-scale solar updraft tower power plant. Energies 2023;16(1):494. [CrossRef]
[14] Cuce E, Saxena A, Cuce PM, Sen H, Eroglu H, Selvanathan SP, et al. Performance assessment of solar chimney power plants with natural thermal energy storage materials on ground: CFD analysis with experimental validation. Int J Low-Carbon Technol 2022;17:752-759. [CrossRef]
[15] Bhoraniya R, Jiren M, Harichandan A. CFD analysis of solar chimney power plant: Effect of chimney height, shape and collector size. J Sol Energy Res 2019;4(1):61-71.
[16] Das P, Chandramohan VP. CFD analysis on flow and performance parameters estimation of solar updraft tower (SUT) plant varying its geometrical configurations. Energy Sources Part A 2018;40(12):1532-1546. [CrossRef]
[17] Hoseini H, Mehdipour R. Evaluation of solar-chimney power plants with multiple-angle collectors. J Comput Appl Res Mech Eng 2018;8(1):85-96.
[18] Jameei A, Akbarzadeh P, Zolfagharzadeh H, Eghbali S. Numerical study of the influence of geometric form of chimney on the performance of a solar updraft tower power plant. Energy Environ 2018;30(4):685-706. [CrossRef]

[19] Aurybi MA, Al-Kayiem HH, Gilani SI, Ismaeel AA. CFD analysis of hybrid solar chimney power plant. MATEC Web Conf 2018;225:04011. [CrossRef]
[20] Mekhail T, Rekaby A, Fathy M, Bassily M, Harte R. Experimental and theoretical performance of mini solar chimney power plant. J Clean Energy Technol 2017;5(4):294-298. [CrossRef]
[21] Ming T, Gong T, De Richter RK, Cai C, Sherif S. Numerical analysis of seawater desalination based on a solar chimney power plant. Appl Energy 2017;208:1258-1273. [CrossRef]
[22] Ayadi A, Driss Z, Bouabidi A, Abid MS. Experimental and numerical study of the impact of the collector roof inclination on the performance of a solar chimney power plant. Energy Build 2017;139:263-276. [CrossRef]
[23] Al-Azawiey SS, Hassan SB. Heat absorption properties of ground material for solar chimney power plants. Int J Energy Prod Manag 2016;1(4):403-418. [CrossRef]
[24] Lal S, Kaushik S, Hans R. Experimental investigation and CFD simulation studies of a laboratory scale solar chimney for power generation. Sustain Energy Technol Assess 2015;13:13-22. [CrossRef]
[25] Guo P, Li J, Wang Y. Numerical simulations of solar chimney power plant with radiation model. Renew Energy 2013;62:24-30. [CrossRef]
[26] Fasel HF, Meng F, Shams E, Gross A. CFD analysis for solar chimney power plants. Sol Energy 2013;98:12-22. [CrossRef]
[27] Pretorius J, Kroger D. Critical evaluation of solar chimney power plant performance. Sol Energy 2005;80(5):535-544. [CrossRef]
[28] Schlaich J, Bergermann R, Schiel W, Weinrebe G. Design of commercial solar updraft tower systems-Utilization of solar induced convective flows for power generation. J Sol Energy Eng 2005;127(1):117-124. [CrossRef]
[29] Caicedo P, Wood D, Johansen C. Radial turbine design for solar chimney power plants. Energies 2021;14:674. [CrossRef]
[30] Haaf W. Solar chimneys part 1: Principle and construction of pilot plant in Manzanares. Int J Sol Energy 1983;2:3-20. [CrossRef]
[31] Haaf W. Solar chimneys part II: Preliminary test results from the Manzanares pilot plant. Int J Sol Energy 1984;2:141-161. [CrossRef]
[32] Padki MM, Sherif SA. On a simple analytical model for solar chimneys. Int J Energy Res 1999;23:345-349. [CrossRef]
[33] Williams A. The Solar Nozzle- A Research Proposal. Global Warming Solutions UK; 2016.
[34] Williams A. Solar Electricity Using Natural Convection- A Research Proposal. Global Warming Solutions UK; 2023.
[35] Williams A. The Multi-Channel Solar Chimney-Commercial Scale. Global Warming Solutions UK; 2020.
[36] Gondchawar A, Kanabar B, Bhoraniya R. Comprehensive review of hybrid solar updraft tower power generation systems for electricity production in tropical regions. Int J Energy Water Res 2025. [CrossRef]

J Ther Eng, Vol. 12, No. 2, pp. 656−664, March, 2026

Journal of Thermal Engineering
Web page info: https://jten.yildiz.edu.tr
DOI: 10.14744/thermal.0001108

Research Article

Influence of viscous dissipation, chemical reaction, thermophoresis and heat absorption on the flow via an exponentially stretching sheet

Sunmoni MUDOI[1,*], Dipak SARMA[1]

[1]*Department Of Mathematics, Cotton University, Guwahati, 781001, India*

ARTICLE INFO

Article history
Received: 26 November 2024
Accept: 17 January 2025

Keywords:
Heat Absorption, Chemical Reaction, Thermophoresis, Viscous Dissipation, Eckert Number, Schmidt Number

ABSTRACT

The effects of convective boundary conditions on the flow of a viscous fluid through a porous sheet that is expanding exponentially are studied in this study, along with additional factors such as heat absorption, viscous dissipation, thermophoresis, chemical reactions, and others. The numerical solutions to the governing equations are evaluated using the bvp4c technique in conjunction with similarity requirements. The effect of different parameters on different physical variables are depicted using graphs. The fluid›s velocity increases with the increase in thermophoretic parameter. The temperature profile decreases with the rise in Grashof number and Schmidt number. While the concentration profile escalates with the rise in Schmidt number. Many real-world situations involve the co-existence of thermophoresis, viscous dissipation, chemical processes, heat absorption etc.

Cite this article as: Mudoi S, Sarma D. Influence of viscous dissipation, chemical reaction, thermophoresis and heat absorption on the flow via an exponentially stretching Sheet. J Ther Eng 2026;12(2):656−664.

INTRODUCTION

A common issue in fluid dynamics is fluid flow over stretched surfaces, which has substantial importance to several industrial and technical uses. Not only does the dynamic interaction between a fluid and a stretched surface shed light on fundamental fluid mechanics, but it also plays a crucial part in the optimisation of mass and heat transfer processes. When considering how various physical phenomena, such as heat absorption, chemical reactions, viscous dissipation, thermophoresis, etc., interact with one another, the research of this issue becomes more complex.

The impact of heat absorption or generation is crucial in many real-world scenarios. This could be from internal exothermic chemical reactions taking place in the fluid or by heating the system from outside sources. For processes to be optimised in fields ranging from materials processing to renewable energy systems, it is crucial to comprehend how heat is absorbed or created and its subsequent impact on temperature distributions and rates of transfer of heat. Boundary layer above an uninterrupted flat surface, was described by Sakiadis BC [1]. Sakiadis B.C. [2] also describe boundary-layer equations for axisymmetric, two-dimensional flow. Using convective boundary conditions, Hayat and Obaidat [3] studied the boundary layer flow of a nanofluid across an exponentially stretched sheet. Hayat and coauthors [4] investigated the role of convective

***Corresponding author.**
*E-mail address: sunmoni77.mudoi@gmail.com

This paper was recommended for publication in revised form by Editor-in Chief Ahmet Selim Dalkilic

Published by Yıldız Technical University Press, İstanbul, Turkey
Yıldız Technical University. This is an open access article under the CC BY-NC license (http://creativecommons.org/licenses/by-nc/4.0/).

heat and mass transport in the Powell-Eyring fluid flow through an exponentially extending sheet PloS one. Khan et al. [5] performed a numerical analysis of a nanofluid flowing past through a stretched sheet that is being heated convectively in three dimensions. Magnetohydrodynamics unsteady flow of heat transfer through a sheet with stretching capacity for radiating fluid in the presence of the Dufour effect was studied by Sivaiah and Reddy [6]. Nandhini, and co-authors [7] evaluated the impact of chemical reaction as well as that of the radiation absorption about Casson fluid across an exponential sheet under slip conditions with ethanol as that solvent.

The issue is made more difficult by chemical processes occurring within the fluid. Fluid movement frequently coexists with chemical reactions in industrial and environmental applications. These reactions add to the complexity in this type of analysis of heat transfer as well as that of the flow by drastically changing the fluid's properties, such as density and viscosity. Paul and Das [8] studied about a sheet that has been stretched exponentially experiences thermal and mass transfer while undergoing chemical reaction. Goud, Reddy, Wakif [9] analysed about an inclined spinning disc with nanofluid is subjected to a numerical investigation of the heat & mass transport characteristics of the MHD flow with chemical reaction and heat absorption. An unstable MHD heat and mass transfer fluid flow is present, together with radiation and heat absorption, along with that of the Soret effect. This is studied on an infinite vertical plate by Goud and Reddy [10]. Veera Krishna [11] studied about MHD free convective Casson nanofluids passing through an endlessly oscillating vertical porous plate undergo chemical reaction, Newtonian heating and heat absorption. A chemical reaction with Soret effects along with the impact of absorption of heat and is present in the unstable MHD Casson oscillatory flow fluid across a vertical inclined porous plate was analysed by Kodi and Mopuri [12]. Jayarami Reddy [13] investigated a radiating fluid flowing through an accelerated inclined porous plate with hall current in a MHD heat & mass transfer flow. Patil and co-authors [14] investigation on thermal radiation along with that of the chemical reaction-induced MHD Williamson nanofluid flow across a permeable stretching sheet. The impact of radiation and viscous dissipation on MHD heat transfer in Casson nanofluid flows across a nonlinear stretching surface with chemical reactions was investigated by Kumar et al. [15].

Another important issue to take into account is viscous dissipation, a phenomenon where mechanical energy is transformed into that of the thermal energy within a fluid which is viscous in nature. The shearing of the fluid layers as it passes over the stretching surface produces heat. It is essential to properly account for viscous dissipation in order to estimate temperature profiles and with accuracy the rates of transfer of heat. Through a porous material with viscous dissipation, along with that of the thermal radiation and there is unstable flow of heat transfer and MHD through a stretching sheet. This study was done by Anuar Ishak [16]. B. Zigta's [17] investigation into impacts of viscosity dissipation, chemical reaction, along with that of the heat radiation on a MHD flow. Under the influence of suction and injection, the dynamics of thermal radiation and heat production and absorption on a viscous MHD micropolar fluid are investigated by Adeyemi et al. [18]. Rahman et al. [19] examined the impact of variations in the thermophysical parameters of the heat transfer fluid on pumping performance, specifically regarding delivery rate, slip factor coefficient, and volumetric efficiency. Dang et al. [20] investigated the numerical study of non-Newtonian free stream flow in three-dimensional magnetohydrodynamics caused by a permeable stretching surface.

Consideration of suspended particles in the moving fluid requires consideration of thermophoresis, which describes how particles move in response to temperature gradients. In applications ranging from nanoparticle deposition in materials manufacturing to aerosol dynamics in environmental research, this phenomenon can have an impact on concentration profiles and overall mass transfer rates. Shehzad et al. [21] studied the impact of Joule heating and thermophoresis on Jeffrey fluid radiative flow with mixed convection. Effects of thermophoresis, viscous dissipation etc. on MHD flow through a radiatively permeable, sloped surface with changing thermal conductivity was analysed by Reddy [22]. Umme et al. [23] examine the impact of thermophoresis and Brownian diffusion on the convective boundary layer flow of micropolar fluids across a stretched wedge-shaped surface. Makinde and Animasaun [24] investigated the effects of thermophoresis and Brownian motion on the magnetohydrodynamic bioconvection of nanofluid, including nonlinear thermal radiation and quartic chemical reaction, along the upper horizontal surface of a paraboloid of revolution. Ganjikunta et al. [25] investigated the effects of activation energy and diffusion thermodynamics on unsteady magnetohydrodynamic Maxwell fluid flow across a porous, vertically stretched sheet, including thermophoresis and Brownian motion.

Research on flow across a stretching sheet up to this point has mostly concentrated on these components' individual effects or small combinations. However, many real-world situations involve the co-existence of thermophoresis, viscous dissipation, chemical processes, heat absorption etc. Therefore, it's crucial to have a thorough understanding of how they all interact. Natural convection across a wavy surface inclined in a porous, saturated medium: effects of thermal radiation and stratification, was researched by Wu and Lei [26]. Srinivasacharya and coauthors [27] studied about heat convective boundary conditions with slip viscous flow across an increasingly extending porous sheet. Researchers looked at the effects of radiation and chemical reaction on the flow of a nanofluid through a nonlinearly porous stretched sheet with a nonuniform heat source during MHD heat transfer was studied by Reddy, Mangamma [28]. Mahmood et al. [29] researched about tri-hybrid nanofluid

numerical analysis across that given nonlinear sheet in conditions of heat generation, heat absorption, and slip. The current study intends to look into how these variables interact to affect the flow characteristics near an exponentially stretched sheet. The current study's objective is to offer information on the impacts of heat absorption and chemical reaction on a fluid that is unstable, incompressible, viscous, electrically conducting, Newtonian, chemically reactive, and radiating. This research was motivated by Srinivasacharya and Jagadeeshwar [30], who studied about how flow across an exponentially stretched sheet is affected by thermophoresis and viscous dissipation.

MATHEMATICAL FORMULATION

Take into consideration a stretched sheet in flow of a laminar slip, a viscous incompressible fluid with concentration C_∞ and temperature T_∞. By placing the positive $\bar{x}$-axis parallel and that of $\bar{y}$-axis perpendicular to the sheet, the Cartesian framework is determined. A $U_*(\bar{x}) = U_0 e^{\frac{\bar{x}}{L}}$ assumption is made regarding the sheet's stretching velocity, where $\bar{x}$ denotes distance from the slit. Consider that a fluid with a heat transfer coefficient of h_f also a temperature of T_f is used to either convectively cool or heat the sheet, where $h_f = h\sqrt{\frac{U_0}{2L}}$, the velocity vector is ($\bar{u}_x$, $\bar{u}_y$), $\bar{C}$ is the concentration and $\bar{T}$ is the temperature. The flow across the sheet is injected/sucked at a velocity of $V_*(\bar{x}) = V_0 e^{\frac{\bar{x}}{2L}}$; V_0 is strength of suction or injection. On top of that, $N(\bar{x}) = N_0 e^{-\frac{x}{2L}}$ is supposed to be the fluid's slip velocity.

Applying the approximations of boundary layer of that fluid & using Boussinesq approximation; the governing equations of flow of the fluid are given by:

$$\frac{\partial \bar{u}_x}{\partial \bar{x}} + \frac{\partial u_y}{\partial \bar{y}} = 0 \tag{1}$$

$$\bar{u}_x \frac{\partial \bar{u}_x}{\partial \bar{x}} + \bar{u}_y \frac{\partial \bar{u}_x}{\partial \bar{y}} = \nu \frac{\partial^2 \bar{u}_x}{\partial \bar{y}^2} + g\beta(\bar{T} - T_\infty) + g\beta^*(\bar{C} - C_\infty) \tag{2}$$

$$\bar{u}_x \frac{\partial \bar{T}}{\partial \bar{x}} + \bar{u}_y \frac{\partial \bar{T}}{\partial \bar{y}} = \alpha \frac{\partial^2 \bar{T}}{\partial \bar{y}^2} + \frac{\mu}{\rho c_p}\left(\frac{\partial \bar{u}_x}{\partial \bar{y}}\right)^2 + \frac{Q_x}{\rho c_p}(\bar{T} - T_\infty) \tag{3}$$

$$\bar{u}_x \frac{\partial \bar{C}}{\partial \bar{x}} + \bar{u}_y \frac{\partial \bar{C}}{\partial \bar{y}} = D \frac{\partial^2 \bar{C}}{\partial \bar{y}^2} - \frac{\partial}{\partial \bar{y}}[V_T(\bar{C} - C_\infty)] - K_c(\bar{C} - C_\infty) \tag{4}$$

where D mass diffusivity of given medium, α thermal diffusivity, ν kinematic viscosity, V_T thermophoretic velocity, c_p specific heat capacity at constant pressure. V_T can be written as:

$$V_T = -\frac{\nu k_t}{T_r}\frac{\partial \bar{T}}{\partial \bar{y}} \tag{5}$$

where the thermophoretic coefficient k_t and the reference temperature *Tr*. Boundary conditions are

$$\bar{u}_x = U_* + Nu\frac{\partial \bar{u}_x}{\partial \bar{y}},\ \bar{u}_y = -V_*(\bar{x}), -k\frac{\partial \bar{T}}{\partial \bar{y}} = h_f(T_f - \bar{T}),\ \bar{C} = C_w \ \ at\ \bar{y} = 0 \tag{6}$$

$$\bar{u}_x \to 0,\ T \to T_\infty,\ C \to C_\infty\ \ as\ \ \bar{y} \to \infty \tag{7}$$

steam function $\psi(x,y)$ is given as,

$$u' = \frac{\partial \psi}{\partial y'},\ v' = -\frac{\partial \psi}{\partial x'} \tag{8}$$

We use some non-dimensional quantities, those are:

$$x = \frac{\bar{x}}{L}, y = \bar{y}\sqrt{\frac{U_0}{2\nu L}}e^{\frac{\bar{x}}{2L}}, \psi = \sqrt{2\nu L U_0}e^{\frac{\bar{x}}{2L}}F(x,y), Q = \frac{Q_x \nu}{U_0^2},$$
$$Gr = \frac{g\beta\nu(\bar{T}_w - T_\infty)}{U_0^3}, Gm = \frac{g\beta^*\nu(\bar{C}_w - C_\infty)}{U_0^3}, \gamma = \frac{K_c x}{U_0^2},$$
$$\bar{T} = T_\infty + (T_f - T_\infty)T(x,y), \bar{C} = C_\infty + (C_f - C_\infty)C(x,y)$$

These non-dimensional quantities are used to create the governing equations, which have the following form:

$$F''' + FF'' - 2F'^2 - GrT - GmC = 0 \tag{9}$$

$$\frac{1}{Pr}T'' + FT' + Ec\, e^{2x}F'' - QT = 0 \tag{10}$$

$$\frac{1}{Sc}C'' + FC' - \tau(T'C' + CT') + \gamma C = 0 \tag{11}$$

where $S = V_0\sqrt{\frac{2L}{\nu U_0}}$ is suction parameter according to $S > 0$ or $S < 0$ respectively, *Ec* is the Eckert number, *Bi* Biot number, τ is the Thermophoretic parameter, *Q* is the heat absorption parameter, *Sc* Schmidt number, *Pr* Prandtl number The transformed boundary conditions are as follows:

$$F(x,0) + 2\frac{\partial F}{\partial x}(x,0) = S, F'(x,0) = 1 + \lambda F''(x,0)$$
$$T'(x,0) = -Bi\big(1 - T(x,0)\big), C(x,0) = 1$$
$$F'(x,y) \to 0, T(x,y) \to 0, C(x,y) \to 0 \quad as\ \ y \to \infty \tag{12}$$

Dimensionless Sherwood number $Sh_{\bar{x}}$, skin friction C_f, Nusselt number $Nu_{\bar{x}}$ are given by:

$$\sqrt{\frac{L}{2x}}\sqrt{Re_{\bar{x}}}C_f = F''(x.0), \sqrt{\frac{2}{Lx}}\frac{Nu_{\bar{x}}}{\sqrt{Re_{\bar{x}}}} = -T'(x,0),$$
$$\sqrt{\frac{2}{Lx}}\frac{Sh_{\bar{x}}}{\sqrt{Re_{\bar{x}}}} = -C'(x,0) \tag{13}$$

Solution of the Problem

The equations (2)-(4) with boundary conditions (6)-(7) are converted to non-dimensional (9)-(11) equations along with respective boundary conditions (12), by using the dimensionless quantities and then solved those equations by bvp4c method in MATLAB. Values of Sherwood

number, skin friction as well as Nusselt number were found numerically by this method.

To apply finite difference-based solver bvp4c the dimensionless equations (9)-(11) respectively transformed as:

$$F = y1,\ F' = y1' = y2,\ F'' = y2' = y3;$$
$$T = y4, T' = y4' = y5;\ C = y6, C' = y6' = y7$$
$$y3' = -y1y3 + 2y2^2 + Gry4 + Gmy6 + \frac{1}{K}y2$$
$$y5' = Pr(-y1y5 - Ece^{2x}y3 + Qy4)$$
$$y7' = Sc(-y1y7 + \tau(y5y7 + y6y5))$$

Also initial as well as the boundary conditions (12) are transformed as:

$$y1(0) + 2y2(0) = S;\ y2(0) = 1 + \lambda y3(0);$$
$$y5(0) = -Bi(1 - y4(0));\ y6(0) = 1$$
$$y2(\infty) = 0;\ y4(\infty) = 0;\ y6(\infty) = 0$$

These transformed results are used in MATLAB to perform the numerical computation of the solution.

RESULTS AND DISCUSSION

This paper analyses the fluid flow pattern over an exponentially stretching sheet that is influenced by heat absorption, viscous dissipation, thermophoresis, and chemical reactions in a magnetohydrodynamic flow. The governing equations of the flow model are solved using the bvp4c technique. Analyses have been conducted on the influence of physical parameters on the model solution, including the Grashof number, suction parameter, thermophoretic parameter, Schmidt number, Prandtl number, and Eckert number.

The effect of the thermophoretic parameter τ temperature profile is presented in Figure 1. Increase in the value of τ increases the temperature of the fluid as shown in Figure 1. This is because fluid particles start to move away from cold settings when the thermophoretic parameter increases. Figure 2 shows how the velocity profile changes when the suction parameter S is present. By boosting the value of S, velocity is seen to be increasing. According to Figure 3, the temperature of the fluid falls as the suction parameter S value rises. On the other hand, as seen in Figure 4, concentration rises as suction S increases. Suction effects in fluid flow change the fluid's velocity and pressure distribution close to surfaces or inside flow fields. Suction includes the evacuation of fluid from a particular area. By reducing the thickness of the boundary layer close to the surface, it improves heat transfer while reducing drag and delaying separation.

The fluid velocity decreases with increasing *Pr* which is shown in Figure 5. In physical meaning, the result is possible that the fluids with greater *Pr* have high viscosity, this makes the fluid thicker and so it moves slowly. The fluid temperature increases with increasing *Pr,* which is describe in Figure 6. This is possible because, growing *Pr* reduce the boundary layer thickness. When *Pr* increases, the thickness of fluids boundary layer decreases because *Pr* is the reciprocal of momentum to thermal diffusivity. The decrease in the Prandtl number causes a reduction in momentum

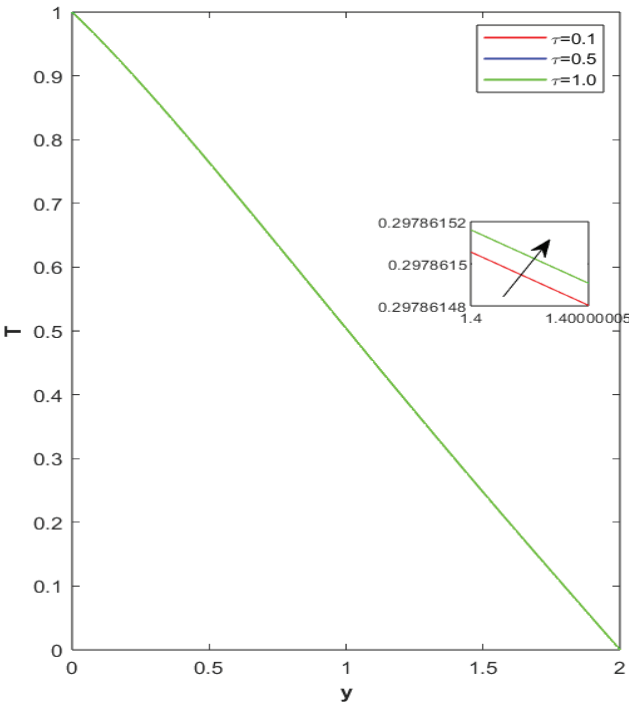

Figure 1. Temperature profile for the values of τ.

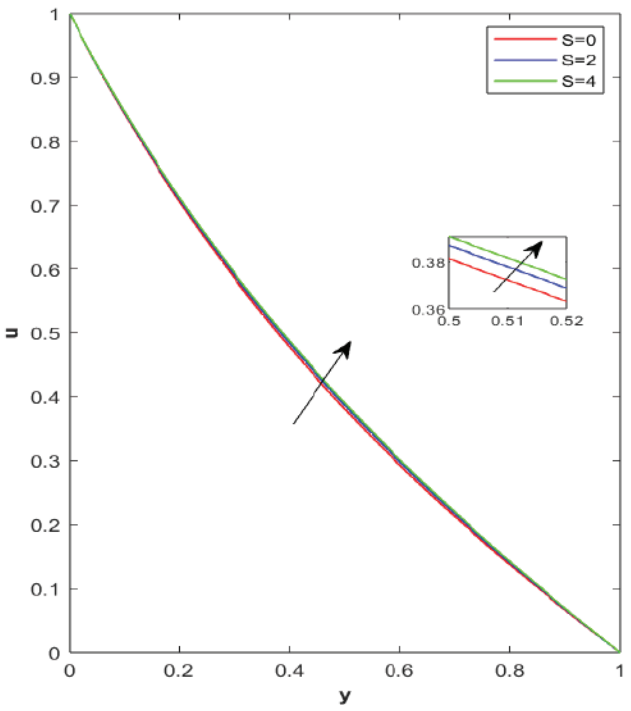

Figure 2. Velocity variation against the values of S.

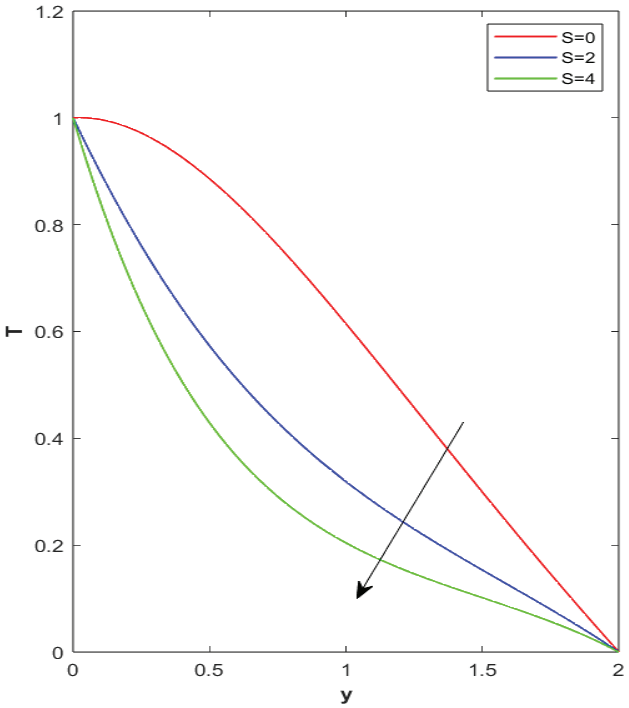

Figure 3. Temperature variation against the values of S.

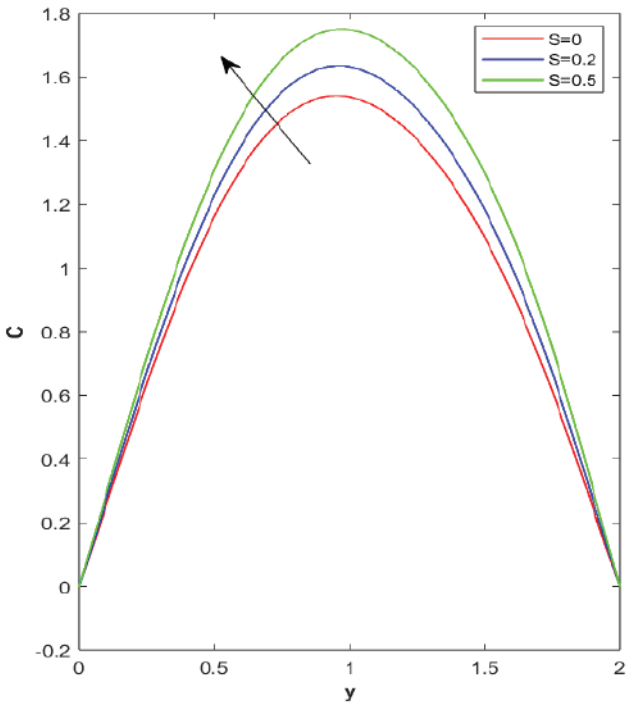

Figure 4. Concentration variation against the values of S.

diffusivity relative to thermal diffusivity. Consequently, the velocity profile becomes steeper as momentum diffuses less effectively compared to heat. Conversely, the increase in thermal diffusivity concerning momentum diffusivity amplifies the rate of thermal diffusion. Thus, the temperature profile becomes smoother and broader due to enhanced heat transfer away from the sheet, resulting in a lower temperature gradient near the surface. The effects of the thermal Grashof number (*Gr*) on u are depicted in Figure 7. In these situations, fluid velocity falls off as *Gr* values rise. The viscous force and thermal buoyancy force are defined by *Gr*. Thus, as *Gr* increases, the forces of heat and concentration get stronger. An increase in the Grashof number amplifies the dominance of buoyancy forces over viscous forces. Consequently, the fluid's momentum near the surface decreases as buoyancy becomes more influential, leading to a reduction in the velocity profile. Figure 8 shows how the value of the fluid's velocity will increase with the value of *Ec*. Figure 9 clearly shows that the temperature rises as the value of *Ec* rises. A decrease in the Eckert number for the velocity profile implies that the kinetic energy per unit mass of the fluid becomes relatively less significant compared to the heat energy per unit mass. This could mean that the influence of heat transfer on the flow dynamics is becoming more pronounced. In the case of temperature, this means that the thermal energy per unit mass becomes more significant, indicating enhanced heat transfer. This might be due to various factors, such as the influence of the magnetic field or the properties of the stretching sheet. With increasing amounts of *Sc*, as shown in Figures 10 and 11, temperature falls as concentration rises. The fact that *Sc* is a ratio of momentum to mass diffusivity enhances the efficiency of mass and momentum transfer in the boundary layer concentration. A decrease in the Schmidt number for the temperature profile suggests that viscous effects become

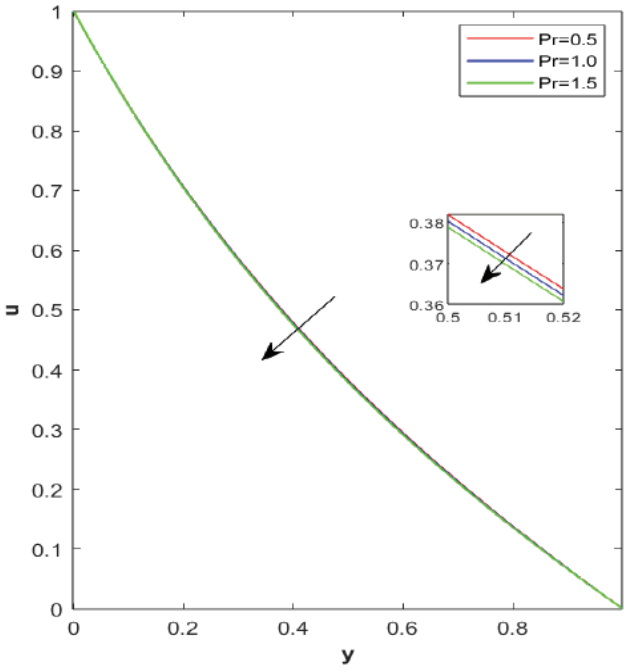

Figure 5. Velocity variation against Pr.

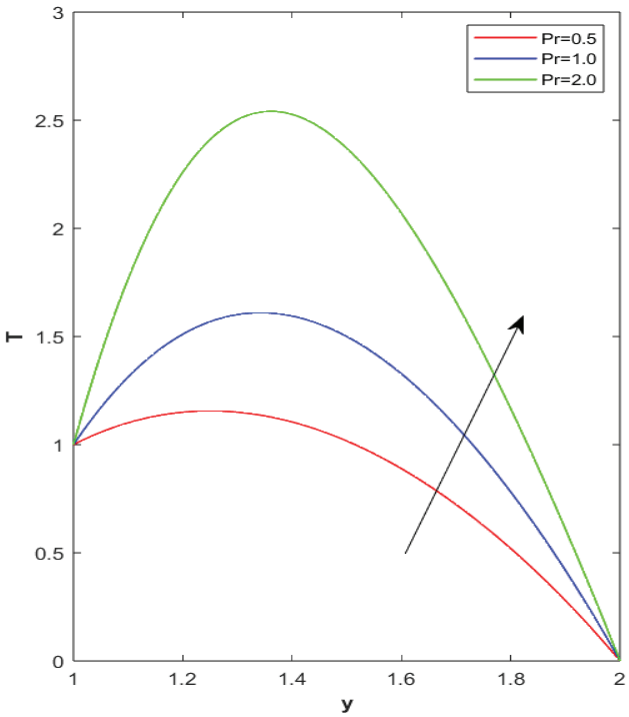

Figure 6. Temperature variation for Pr.

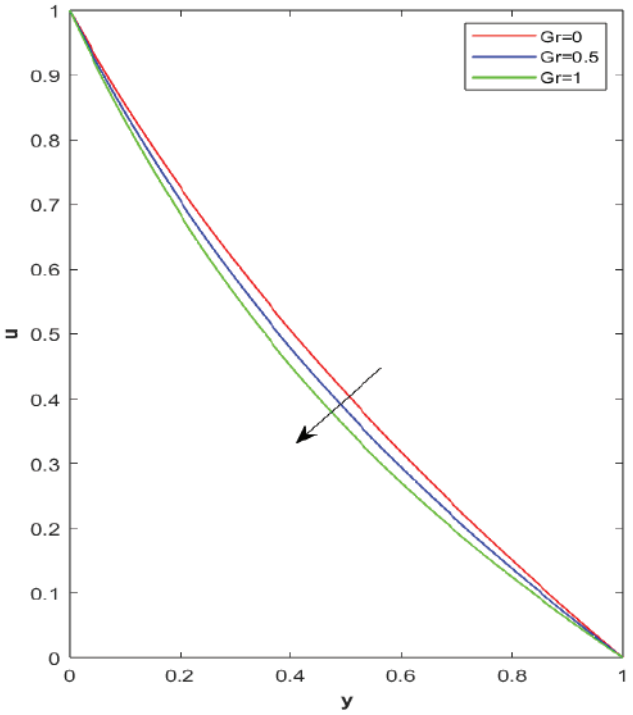

Figure 7. Velocity variation for Gr.

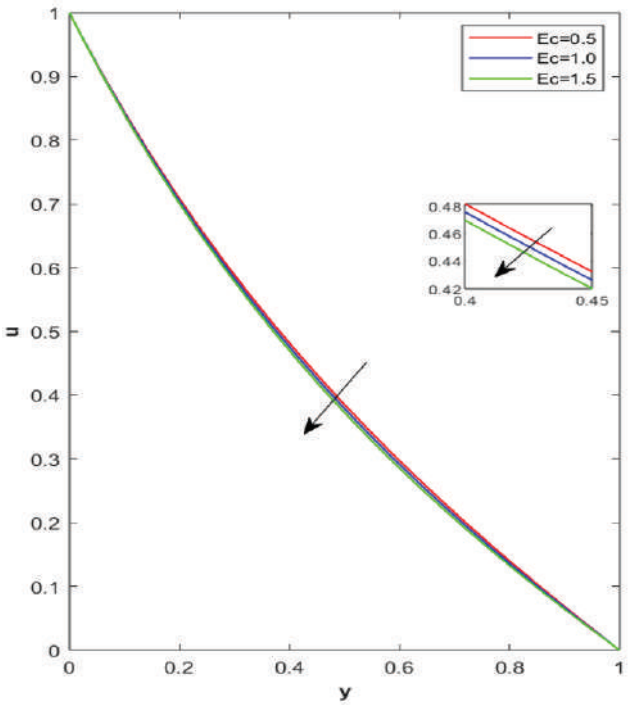

Figure 8. Velocity variation for Ec.

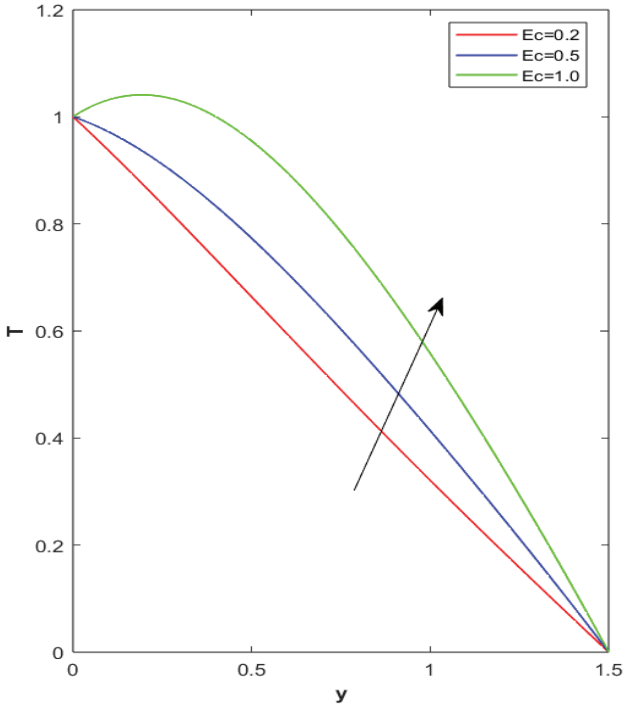

Figure 9. Temperature variation for Ec.

weaker in temperature transport compared to thermal diffusion. An increase in the Schmidt number for the concentration profile means that the relative importance of mass diffusion is increased compared to viscous effects.

Table 1 presents a comparison of our work with previously published research. The values of the Nusselt number are nearly identical to those reported in earlier studies, which validates our findings. This consistency in the results

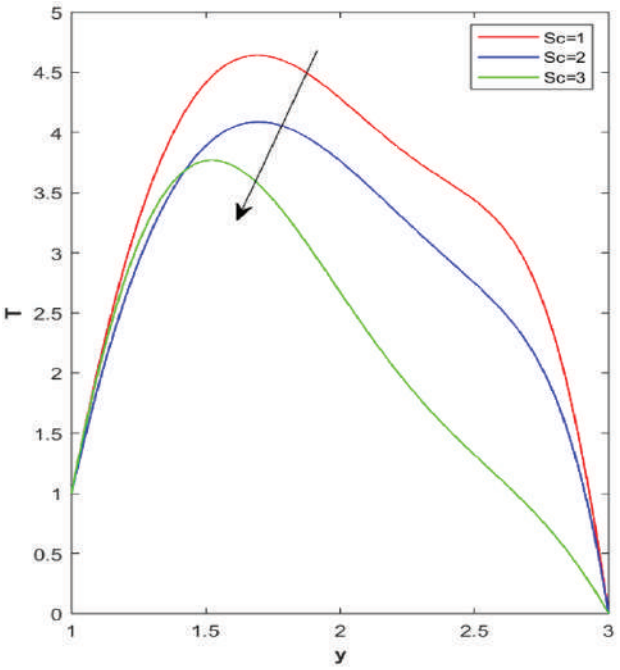

Figure 10. Temperature profile for Sc.

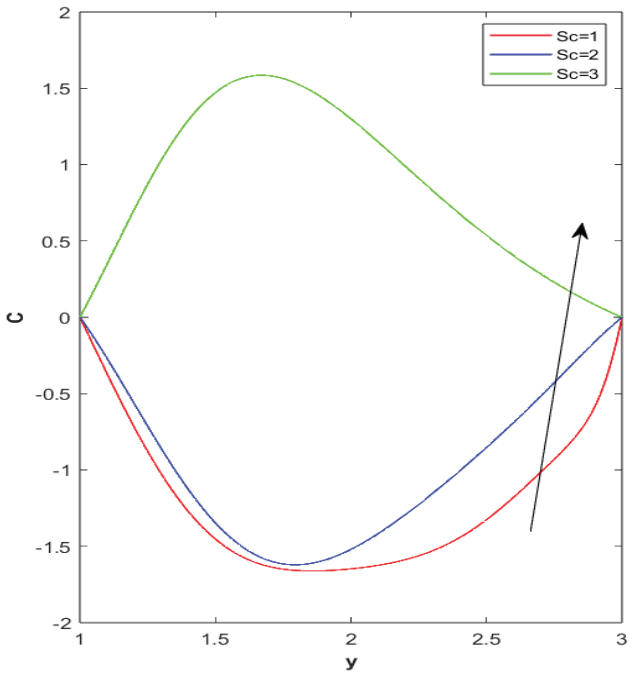

Figure 11. Concentration profile for Sc.

Table 1. Comparison of $-T'(x, 0)$ value with previously published papers

Sc	*τ*	AhmedA [31]	Present work
0.1		1.05131	1.0513
5.0		0.92841	0.9284
10		0.76340	0.7634
	0.1	0.48266	0.4826
	0.5	0.45182	0.4518
	1.0	0.42311	0.4232

Table 2. Changes of $-T'(x, 0)$, $F''(x, 0)$, $-C'(x, 0)$ for various values of *Pr, S, Ec, τ, Sc*

Pr	*S*	*Ec*	*τ*	*Sc*	$F''(x, 0)$	$-T'(x, 0)$	$-C'(x, 0)$
0.2					1.5853	0.6197	1.0116
0.5	2	0.5	0.1	2	1.5824	0.5507	1.6556
1					1.5744	0.4392	3.5145
	0				1.5689	0.2376	1.2004
0.5	2				1.5242	0.8298	1.5315
	4				1.4980	1.2499	1.0188
		0.2			1.5392	0.6107	7.5256
		0.5			1.5549	0.4112	7.5330
		1.0			1.5809	0.0687	7.7634
			0		1.5549	0.4113	6.9305
			0.1		1.5548	0.4112	1.2598
			0.5		1.5546	0.4111	1.0391
				1	1.5549	0.4111	1.8905
				2	1.5549	0.4111	2.3400
				3	1.5548	0.4111	3.2356

indicates that our study, considering all the relevant factors, aligns with previous research and confirms the accuracy of our approach.

The value of Skin Friction, Sherwood number, Nusselt Number for various parameter with different values are displayed in Table 2. The value of $C'(x, 0)$ decreases with the increasing value of *Pr, S, Ec, τ, Sc*. The value of $F''(x, 0)$ deceases with rising *Pr and S*, but increase with *Ec*. $T'(x, 0)$ will increase with *S* but this value will decrease with increasing *Pr and Ec*.

CONCLUSION

The numerical analysis of the flow over an exponentially stretched sheet while accounting for viscous dissipation, chemical reaction, thermophoresis, and heat absorption is performed using suction as well as that of injection, velocity slip, and thermal convective boundary conditions. The bvp4c method is used to solve the dimensionless governing equations. Following is a list of the key findings:

- The fluid›s velocity increased as the value of a thermophoretic parameter increased.
- Suction/injection parameters boost fluid velocity while lowering temperature.
- Prandtl number raises the fluid's temperature while lowering its speed.
- The fluid's temperature and velocity are both reduced by the thermal Grashof number (Gr)
- The fluid's temperature drops while its concentration rises when the Schmidt number (*Sc*) impact is applied.
- *Ec* decreases the fluid's velocity while its temperature increases.

Heat transport and fluid dynamics appear to be connected to the subject you brought up. A future study in this field could look like this: Take a closer look at the impacts of viscosity dissipation, chemical reactions, thermophoresis, and heat absorption by expanding the study to non-Newtonian fluids, which are more like fluids found in real environments; Determine how the stretching sheet›s porosity and permeability affect mass movement, heat transfer, and flow behaviour; Examine the effects of viscous dissipation, chemical reactions, thermophoresis, and heat absorption by expanding the study to multi-phase flows, such as gas-liquid or liquid-liquid flows; Analyse how heat transmission, mass transport, and flow behaviour are affected by nanoparticles in an exponentially extending sheet. Several engineering domains may find use for these prospective research avenues as they contribute to a deeper comprehension of intricate fluid flow and heat transport phenomena.

DATA AVAILABILITY STATEMENT

The authors confirm that the data that supports the findings of this study are available within the article. Raw data that support the finding of this study are available from the corresponding author, upon reasonable request.

CONFLICT OF INTEREST

The author declared no potential conflicts of interest with respect to the research, authorship, and/or publication of this article.

ETHICS

There are no ethical issues with the publication of this manuscript.

STATEMENT ON THE USE OF ARTIFICIAL INTELLIGENCE

Artificial intelligence was not used in the preparation of the article.

REFERENCES

[1] Paul A, Das TK. Thermal and mass transfer aspects of MHD flow across an exponentially stretched sheet with chemical reaction. Int J Ambient Energy 2023;1–27. [CrossRef]

[2] Goud BS, Yanala DR, Wakif A. Numerical analysis on the heat and mass transfer MHD flow characteristics of nanofluid on an inclined spinning disk with heat absorption and chemical reaction. Heat Transf 2023;52:3615–3639. [CrossRef]

[3] Goud BS,Yanala DR. Chemical reaction and Soret effect on an unsteady MHD heat and mass transfer fluid flow along an infinite vertical plate with radiation and heat absorption. J Indian Chem Soc 2022;99:100762–100762. [CrossRef]

[4] Zigta B. Effect of Thermal Radiation, Chemical Reaction and Viscous Dissipation on MHD Flow. Int J Appl Mech Eng 2018;23:787–801. [CrossRef]

[5] Nandhini CA, Jothimani S, Chamkha AJ. Effect of chemical reaction and radiation absorption on MHD Casson fluid over an exponentially stretching sheet with slip conditions: ethanol as solvent. Eur Phys J Plus 2023;138. [CrossRef]

[6] Srinivasacharya D, Jagadeeshwar P. Effect of Viscous Dissipation and Thermoporesis on the Flow Over an Exponentially Stretching Sheet. Int J Appl Mech Eng 2019;24:425–438. [CrossRef]

[7] Hayat T, Saeed Y, Alsaedi A, Asad S. Effects of Convective Heat and Mass Transfer in Flow of Powell-Eyring Fluid Past an Exponentially Stretching Sheet. PLOS One 2015;10:e0133831. [CrossRef]

[8] Khan J, Mustafa M, Hayat T, Alsaedi A. Numerical study on three-dimensional flow of nanofluid past a convectively heated exponentially stretching sheet. Can J Phys 2015;93:1131–1137. [CrossRef]

[9] Krishna MV. Chemical reaction, heat absorption and Newtonian heating on MHD free convective Casson hybrid nanofluids past an infinite oscillating vertical porous plate. Int Commun Heat Mass Transf 2022;138:106327–106327. [CrossRef]

[10] Mustafaa M, Hayat T, Obaidat S. Boundary layer flow of a nanofluid over an exponentially stretching sheet with convective boundary conditions. Int J Numer Method Heat Fluid Flow 2013;23:945–959. [CrossRef]
[11] Ishak AM. Unsteady MHD Flow and Heat Transfer over a Stretching Plate. J Appl Sci 2010;10:2127–2131. [CrossRef]
[12] Kodi R, Mopuri O. Unsteady MHD oscillatory Casson fluid flow past an inclined vertical porous plate in the presence of chemical reaction with heat absorption and Soret effects. Heat Transf 2021;51:733–752. [CrossRef]
[13] Reddy MG. Effects of Thermophoresis, Viscous Dissipation and Joule Heating on Steady MHD Flow over an Inclined Radiative Isothermal Permeable Surface with Variable Thermal Conductivity. J Appl Fluid Mech 2014.
[14] Sakiadis BC. Boundary-layer behavior on continuous solid surfaces: II. The boundary layer on a continuous flat surface. AIChE J 1961;7:221–225. [CrossRef]
[15] Sakiadis BC. Boundary-layer behavior on continuous solid surfaces: I. Boundary-layer equations for two-dimensional and axisymmetric flow. AIChE J 1961;7:26–28. [CrossRef]
[16] Shehzad SA, Alsaedi A, Hayat T. Influence of thermophoresis and joule heating on the radiative flow of jeffrey fluid with mixed convection. Brazilian J Chem Eng 2013;30:897–908. [CrossRef]
[17] Sivaiah G, Reddy KJ. Unsteady mhd heat and mass transfer flow of a radiating fluid past an accelerated inclined porous plate with hall current. Int J Res Granthaalayah 2017;5:42–59. [CrossRef]
[18] Sivaiah G, Reddy KJ. Unsteady mhd heat and mass transfer flow of a radiating fluid past an accelerated inclined porous plate with hall current. Int J Res Granthaalayah 2017;5:42–59. [CrossRef]
[19] Wu T, Lei C. On numerical modelling of conjugate turbulent natural convection and radiation in a differentially heated cavity. Int J Heat Mass Transf 2015;91:454–466. [CrossRef]
[20] Srinivasacharya D, Jagadeeshwar P. Slip Viscous Flow Over an Exponentially Stretching Porous Sheet with Thermal Convective Boundary Conditions. Int J Appl Comput Math 2017;3:3525–3537. [CrossRef]
[21] Patil VS, Humane PP, Patil AB. MHD Williamson nanofluid flow past a permeable stretching sheet with thermal radiation and chemical reaction. Int J Model Simul 2022;43:185–199. [CrossRef]
[22] Reddy YD, Goud BS, Chamkha AJ, Kumar MA. Influence of radiation and viscous dissipation on MHD heat transfer Casson nanofluid flow along a nonlinear stretching surface with chemical reaction. Heat Transf 2022;51:3495–3511. [CrossRef]
[23] Reddy YD, Mangamma I. Significance of radiation and chemical reaction on MHD heat transfer nanofluid flow over a nonlinearly porous stretching sheet with nonuniform heat source. Numer Heat Transf Part A: Appl 2023;1–27. [CrossRef]
[24] Mahmood Z, Eldin SM, Rafique K, Khan U. Numerical analysis of MHD tri-hybrid nanofluid over a nonlinear stretching/shrinking sheet with heat generation/absorption and slip conditions. Alex Eng J 2023;76:799–819. [CrossRef]
[25] Afify AA. MHD free convective flow and mass transfer over a stretching sheet with chemical reaction. Heat Mass Transf 2004;40:6–7. [CrossRef]
[26] Adeyemi CA, Olajuwon BI, Bayo A, Raji M. Dynamics of thermal radiation and heat generation/absorption on a viscous MHD micropolar fluid over a stretching sheet with suction/injection. J Therm Eng 2024;836–846. [CrossRef]
[27] Hanı U, Ali M, Alam MS. MHD boundary layer micropolar fluid flow over a stretching wedge surface: Thermophoresis and brownian motion effect. J Therm Eng 2024;10:330–349. [CrossRef]
[28] Rahman RA, Suwandi A, Nurtanto M. Experimental investigation on the effect of thermophysical properties of a heat transfer fluid on pumping performance for a convective heat transfer system. J Therm Eng 2021;7:1628–1639. [CrossRef]
[29] Makinde OD, Animasaun IL. Thermophoresis and Brownian motion effects on MHD bioconvection of nanofluid with nonlinear thermal radiation and quartic chemical reaction past an upper horizontal surface of a paraboloid of revolution. J Mol Liq 2016;221:733–743. [CrossRef]
[30] Ganjikunta A, Kuntumalla BL, Vaddemani RR. Effects of Activation Energy and Diffusion Thermo an Unsteady MHD Maxwell Fluid Flow over a Porous Vertical Stretched Sheet in the Presence of Thermophoresis and Brownian Motion. CFD Letters 2024;16:18–37. [CrossRef]
[31] Dang K, Makkar V, Sharma N. Numerical analysis of three-dimensional magnetohydrodynamics non-Newtonian free stream flow induced by permeable stretching surface. J Therm Eng 2024;1465–1479. [CrossRef]

J Ther Eng, Vol. 12, No. 2, pp. 665−683, March, 2026

Journal of Thermal Engineering
Web page info: https://jten.yildiz.edu.tr
DOI: 10.14744/thermal.0001109

Research Article

Thermodynamic performance analysis of an air conditioning system integrated with a solid desiccant dehumidifier wheel using solar reactivation

Shriramshastri CHAVALI[1], Ravikant NANWATKAR[2,*], Sachin MUTALIKDESAI[3], Tarang SHINDE[4], Aparna BAGDE[5], Pravin NITNAWARE[6], Shruti DIKSHIT[1], Sourabh KULKARNI[1]

[1]School of Engineering & Technology, D Y Patil University Ambi, Pune 410507, Maharashtra, India
[2]STES's NBN Sinhgad Technical Institutes Campus, Ambegaon, Savitribai Phule Pune University, Pune-41, India
[3]Marathwada Mitra Mandal's Institute of Technology, Lohegaon, Savitribai Phule Pune University, Pune-47, India
[4]Yashoda Shikshan Prasarak Mandal Yashoda Technical Campus, Satara, 415011, India
[5]JSPM Narhe Technical Campus, Savitribai Phule Pune University, Pune, 41, India
[6]D Y Patil College of Engineering Akurdi, Savitribai Phule Pune University, Pune, 411044, India

ARTICLE INFO

Article history
Received: 07 January 2025
Accepted: 31 May 2025

Keywords:
Air-conditioning System, Solid Desiccant Dehumidifier Wheel, Dehumidification Effectiveness, Regeneration Effectiveness, Adsorption Rate, Coefficient of Performance

ABSTRACT

The present study investigates the thermodynamic performance of an air-conditioning system integrated with a solid desiccant dehumidifier wheel (SDDW) using a combined heating mode of electrical and solar heaters. The obtained results were compared with standard results. During the experimentation, the solid desiccant wheel with silica gel as an adsorption material was used along with a conventional vapour compression cycle. The effect of inlet air temperature in the range of 23.6 °C to 37.2 °C and air inlet velocity in the range of 1.5 m/s to 4.1 m/s on the thermodynamic performance of an air-conditioning system integrated with a solid desiccant dehumidifier wheel was experimentally investigated. A combined electrical and solar heater mode was used to supply regeneration air for the solid desiccant dehumidifier at a constant velocity of 4.5 m/s. Experimentation was performed in all three seasons, namely summer, rainy and winter, to find the effect of seasonal variation on the performance of the air-conditioning system. The dehumidification effectiveness and adsorption rate in all three seasons increased with a decrease in the air inlet temperature. A maximum experimental value of dehumidification effectiveness was obtained in the summer season. At 23.6 °C and 1.5 m/s air inlet velocity, the maximum value of dehumidification effectiveness was 0.19. While at the same temperature, the maximum value of the adsorption rate at 4.1 m/s air inlet velocity was 0.4 kg/hr. In all three seasons, regeneration effectiveness increased with an increase in the inlet air temperature. While the regeneration effectiveness was reduced due to an increase in air let velocity. A maximum value of dehumidification effectiveness obtained in the summer season at 37.2 °C inlet air temperature and 1.5 m/s velocity was 0.298. The coefficient of Performance in all three seasons for the vapour compression cycle decreased with an increase in the inlet air temperature and ve-

***Corresponding author.**
*E-mail address: ravikant.nanwatkar@sinhgad.edu

This paper was recommended for publication in revised form by Editor-in Chief Ahmet Selim Dalkilic

Published by Yıldız Technical University Press, İstanbul, Turkey
Yıldız Technical University. This is an open access article under the CC BY-NC license (http://creativecommons.org/licenses/by-nc/4.0/).

locity. A maximum experimentation value of the Coefficient of Performance obtained in the winter season for the vapour compression cycle at 23.6 °C inlet air temperature and 1.5 m/s air inlet velocity was 0.51. The combined use of these heating methods resulted in a 33% increase in effectiveness compared to the use of the electric heater alone.

Cite this article as: Chavali S, Nanwatkar R, Mutalikdesai S, Shinde T, Bagde A, Nitnaware P, Dikshit S, Kulkarni S. Thermodynamic performance analysis of an air conditioning system integrated with a solid desiccant dehumidifier wheel using solar reactivation. J Ther Eng 2026;12(2):665−683.

INTRODUCTION

Air-conditioning plays a pivotal role in human life, serving as a cornerstone for achieving healthy and productive comfort conditions within buildings. The quality of indoor comfort conditions is defined by factors such as temperature, humidity, and the adequate supply of fresh air. Traditional cooling systems contribute significantly to global electricity demand and carbon emissions, especially in regions with high cooling needs. Energy-efficient air conditioning systems play a critical role in mitigating climate change by reducing energy consumption and lowering greenhouse gas emissions. By adopting advanced technologies such as solid desiccant dehumidifiers, variable speed compressors, and renewable energy integration, energy-efficient air conditioning minimises reliance on fossil fuels. These systems not only improve energy performance but also align with global sustainability goals, fostering cleaner energy practices and reducing the environmental footprint of cooling technologies. Jain et al. [1] examined that an air conditioning system with solid desiccant has higher performance due to the use of wet surface heat exchangers in the hot and humid climate conditions. G. W. Scherer [2] found that the modulus and viscosity of silica gel increase due to drying. Dai et al. [3] developed a mathematical model for parameter analysis of desiccant dehumidification for performance improvement. Mazzei et al. [4], through an extensive literature review, found that the use of hybrid systems with desiccant wheels saves the operating costs. Harshe et al. [5] found that the developed rotary desiccant wheels were useful for optimising energy recovery and dehumidification applications. Zhai et al. [6] developed equation equation-based model for desiccant wheels. It can be used to combine the simulation of heat and mass transfer of desiccant wheels. Ge et al. [7] developed a mathematical model that can be used to predict the performance of a compound desiccant wheel. Li. et al. [8] found that an integration of a solar desiccant dehumidification system in a traditional air-conditioning system significantly improves the energy-saving potential for hot, wet weather. A. Christy [9] found that the heating process removes free and hydrogen-bonded silanol groups and alters the ratio between the two. Narayanan et al. [10] developed a numerical model for a non-adiabatic desiccant wheel. A prediction of the numerical model shows good agreement with experimental results. A. Yadav and L. Yadav [11] obtained better results for the effective regeneration sector desiccant wheel as compared with the ordinary regeneration sector desiccant wheel through a developed mathematical model. Angrisani et al. [12] found that a solar desiccant cooling unit consisting of 16 m^2 of evacuated solar collectors was economically feasible. Giannetti et al. [13] perform a general analysis of heat and mass transfer entropy generation rate for desiccant wheels, aiming for design. Chan et al. [14] obtained a developed composite material for an air conditioning system by mixing silica gel, polyacrylic acid and sodium polyacrylate. An optimal composite material was obtained at a mixing ratio of 10:1:1. The absorption capacity of the composite material was 41 % greater than compared of silica gel at 25 °C air temperature and a relative humidity of 70%. Mandegari et al. [15] developed a two-dimensional unsteady-state numerical model for the simulation of heat and mass transfer. The results obtained from the model were validated through experimental data. It was observed that minimum exergy destruction occurs at lower process air velocity and rotational speed of 0.2 m/s and 4 r.p.h. respectively. In the country, higher regeneration air temperature and moderate regeneration air velocity, observed for minimum exergy destruction, are 140 °C and 1.7 m/s, respectively. Zouaoui et al. [16] observed that cool air at satisfactory conditions was generated only when a source of water at low temperature was available. Muthu et al. [17] obtained the regeneration section angle and regeneration air temperature for the optimum performance of the rotary desiccant wheel. Antonellis and Joppolo [18] studied correlations used to calculate desiccant wheel performance and found that these correlations can be easily used in energy simulation programs for comparing desiccant wheel-based air conditioning systems with conventional configurations. Shahzad et al. [19] observed that the CO_2 emission growth rate was higher. The efficiency improvement of water and power is the key to controlling CO_2 emissions. Rjibi et al. [20] found that the best performance of the desiccant evaporative cooling system was for a regeneration temperature of 60 °C. Goyal et al. [21] proposed a ternary simulation model to predict complete adsorption and desorption breakthrough of nitrogen, carbon dioxide and water vapour in an initially clean silica gel bed. Bilal et al. [24] observed that metal-organic frameworks (MOFS) 841 and 801 yielded maximum adsorption of 0.5 g/g and 0.3 g/g, respectively at 25 °C temperature. MOF-801 indicate excellent water production of 0.2-0.3 L/kg/day at 20 - 40 °C temperature and relative humidity 5% - 40%. From the simulation, Dezfouli et al. [25] found that

the solar hybrid desiccant cooling system has 17.3% energy-saving potential for buildings with a high latent load. Tsai and Wu [26] proposed the optimised control strategies to operate the rotary desiccant wheel system in the hotel. Ma et al. [27] observed a higher dehumidification capacity of the desiccant wheel at low inlet process air conditions. Hussain [28] obtained optimum performance parameters such as dehumidification effectiveness, regeneration effectiveness, dehumidification coefficient of performance, regeneration rate in kg/hr, and vapour compression cycle coefficient of performance under certain operating conditions. From the numerical results Zhang et al. [29] found that during the regeneration process, a hump curve of air humidity ratio exits in the channel all the time. For the performance of desiccant wheel, it is proposed to accelerate the hump of air humidity ratio from the duct entrance to exit as soon as possible. Olmuş et al. [30] found that dehumidification efficiency increases from 13.94% to 33.04% with an increase in the regeneration temperature from 50°C to 70°C at 1.3 m/s air frontal velocity. Shaharier et al. [31] observed an enhancement in the performance of the liquid desiccant dehumidifier due to the use of a rough plate.

During the literature survey, it was found that extensive work had been carried out to investigate the performance of the air-conditioning system. In a traditional air-conditioning system, both the latent and sensible loads are handled by the vapour compression refrigeration cycle. But under high latent load conditions, it is necessary to maintain a low Apparatus Dew Point Temperature of the cooling coil to remove the moisture from the process outside air. A dehumidified, cooled air is further reheated to counteract the effect of low Apparatus Dew Point Temperature before being supplied to the conditioned space. Both processes impose a penalty on energy consumption and make the whole process quite energy-intensive. The desiccant cooling can be either a perfective supplement in combination with the traditional vapour compression refrigeration cycle technology to attenuate the effects of its drawbacks, or an alternative to it for assuring more accessible, economical and cleaner air-conditioning. The extensive work has been carried out on the air-conditioning system with a desiccant wheel, but quite limited work has been carried out on the desiccant wheel air-conditioning system with a hybrid mode of regeneration air supply. Hence, present research and development highlight the significant potential of integrating a desiccant dehumidifier air-conditioning system with a hybrid regeneration air supply mode. The hybrid regeneration air supply mode consists of a conventional heater and a flat plate solar collector to heat the regeneration air. The research objectives of this study are to analyse the thermodynamic performance of an air conditioning system integrated with a solid desiccant dehumidifier wheel powered by a conventional heater and solar energy.

METHOD AND MATERIALS

The research objectives of this study are to analyse the thermodynamic performance of an air conditioning system integrated with a solid desiccant dehumidifier wheel powered by a conventional heater and solar energy. Traditional air conditioning systems, relying solely on the vapour compression method, struggle to efficiently handle both sensible

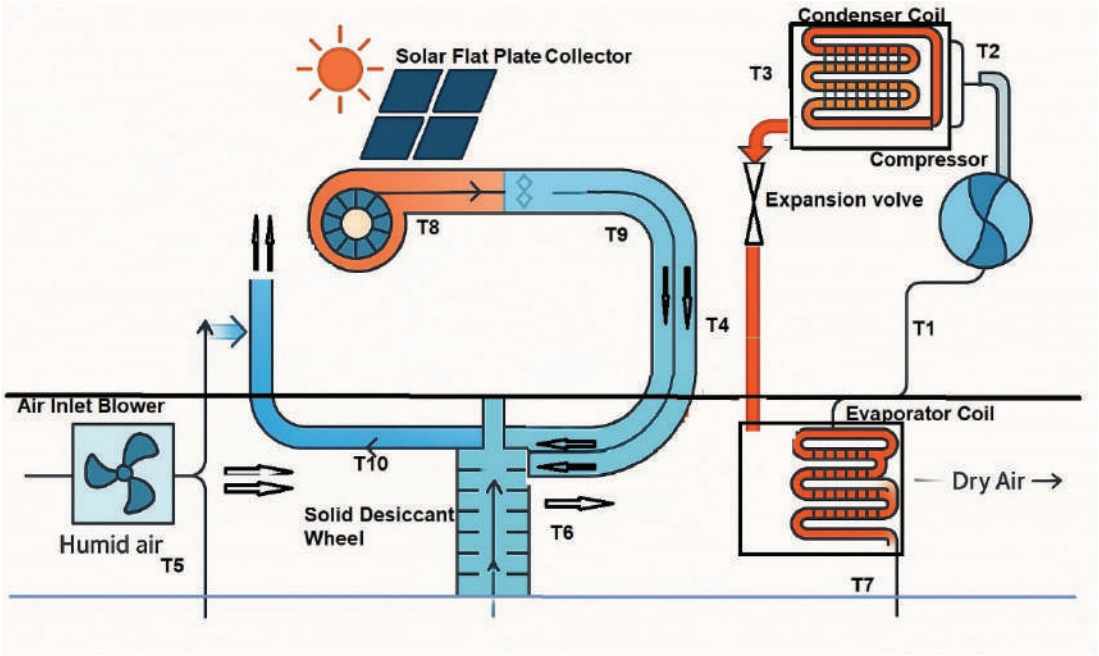

Figure 1. Schematic view of a hybrid rotary desiccant air conditioning system.

and latent heat loads, leading to degradation in their coefficient of performance. In response to this limitation, a rotary desiccant-assisted air conditioning system has been devised to maintain comfort parameters inside conditioned spaces by independently controlling temperature and humidity.

The novelty of this design lies in the regeneration of the rotary desiccant wheel is accomplished using solar energy as a non-conventional energy source, complemented by traditional heating coils. This innovative approach aims to address the limitations of conventional systems and explore the potential of solar reactivation in enhancing the efficiency and sustainability of air conditioning technologies. The innovative approach may result in a reduction in the size of the cooling coil due to the separation of sensible and latent load, contributing to space and energy efficiency. Furthermore, the separation of latent and sensible loads may lead to a decrease in the pressure ratio across the compressor, enhancing its efficiency.

The given diagram 1, represents a solar assisted desiccant based air conditioning system combined with a vapor compression cycle refrigeration (VCR) for high efficiency cooling and dehumidification. The system starts with the Air Inlet Blower that drags in moist surrounding air (T5) and precipitates it to the Solid Desiccant Wheel. This desiccant wheel dries incoming air, thus, doing dehumidification and the air is warm and dry at T6. This fails to provide adequate cooling effect on air since this dry air is passed through the Evaporator Coil of the VCR system where it undergoes further cooling, hence, the output is dry and cool air (T7) which is blown to the conditioned space.

The VCR cycle begins with Compressor which compresses the low-pressure refrigerant that is in vapour state (at T1) to a high pressure and temperature state (at T2). This hot refrigerant is then passed through the Condenser Coil, where it gives the heat up to surroundings and turns to a high- pressure liquid (T3). The temperature and pressure (T4) of the Expansion Valve is then lowered, thus allowing it to absorb heat in the evaporator coil in the process of air cooling.

At the same time, Solar Flat Plate Collector harnesses solar energy and heats ambient air (T8). This hot air is driven through the desiccant wheel in an regeneration path, so that the desiccant can get rid of the absorbed moisture, and as such, regain the drying capability. After regeneration the exhaust air (T9) is discharged or reused as the return air (T10). The combination of solar thermal energy with desiccant dehumidification and conventional VCR cooling makes the system efficient, with a lowering of the electrical load and sustainable air conditioning.

Figure 1 and 2 represents a schematic view and an actual photograph of the hybrid rotary desiccant air conditioning system using solar reactivation and traditional heating coils. It consists of a traditional vapour compression refrigeration system along with the rotary desiccant wheel consisting of silica gel as adsorbent material. The properties of silica gel are given in Table 1.

Figure 2. Actual photograph of a hybrid rotary desiccant air conditioning system.

Table 1. Properties of Silica gel. [22]

Features	Silica gel
Chemical composition	Sio2 Chemically inert
Chemical stability	Highly stable in ph ≤ 7 and mild alkaline media
Mechanical stability	Narrow pore gel is unstable in aqueous media
Thermal conductivity	0.14–0.2 W/m/K and 0.08–1.2 BTU/ft/°F
The heat of adsorption for water	2512 kj/kg H_2O and 1080 BTU/lb H_2O

A flat plate solar collector, along with a conventional heater, is used to heat the atmospheric air known as regeneration air. During the experimentation mixture of normal atmospheric air and regeneration air is supplied to the rotary desiccant wheel, where silica gel absorbs moisture from the air. A blower present at the respective location draws the air. A dehumidified air is further supplied to the conventional vapour compression cycle, where is rejects the heat to the refrigerant present in the evaporator coils. A final conditioned air is then supplied to the control space. The selection and design of system components are contingent upon local meteorological conditions, the load to be managed, and the type of air conditioning cycle to be implemented. The temperature sensor is located at different positions to measure the temperature of the air and refrigerant. A location of temperature sensor and input experimental parameters are summarised in Tables 2 and 3, respectively. During the experimentation, the inlet air temperature is varied in the range of 23.6 °C to 37.2 °C. The air inlet velocity is varied in the range of 1.5 m/s to 4.1 m/s. In the country, the regeneration air velocity is maintained constant, which is 4.5 m/s.

All experimental work is carried out in Pune City, Maharashtra, India. Pune city lies between 18° 32‴ North latitude and 73° 51‴ East longitude. Normal temperature of Pune city in the summer season lies between 22°C - 41°C. While the temperature in the winter season lies between. 8°C - 25°C. The average relative humidity is around 69%, although it varies from around 51% during summer to 92% monsoon season. A general dehumidification process and regeneration process obtained from a hybrid rotary desiccant air conditioning system using solar reactivation and traditional heating coils is shown in Figure 3. Processes A, B, and C represent the dehumidification process using the desiccant wheel and sensible cooling. Process 7-8-D-E represents the regeneration process.

Table 2. Location of Temperature Sensor

Temperature Sensor	Location
T1	Temperature of refrigerant at the exit of the evaporator
T2	Temperature of refrigerant at the exit of the compressor
T3	Temperature of refrigerant at the exit of the condenser
T4	Temperature of refrigerant at the exit of the expansion valve
T5	Atmospheric air temperature
T6	Dehumidified air temperature
T7	Final conditioned air temperature
T8	Atmospheric air temperature for regeneration purposes,
T9	Regenerative (Heated) air inlet temperature
T10	Regenerative (Heated) air outlet temperature.

Table 3. Summary of Experimental Parameters

Season	Summary, Winter, Rainy
Air Inlet Temperature (°C)	23.6, 24.1, 27.6, 28.9, 33.4, 35.6 and 37.2
Air Inlet Velocity (m/s)	1.5, 2.6, 3.3 and 4.1
Regeneration Air Velocity (m/s)	4.5

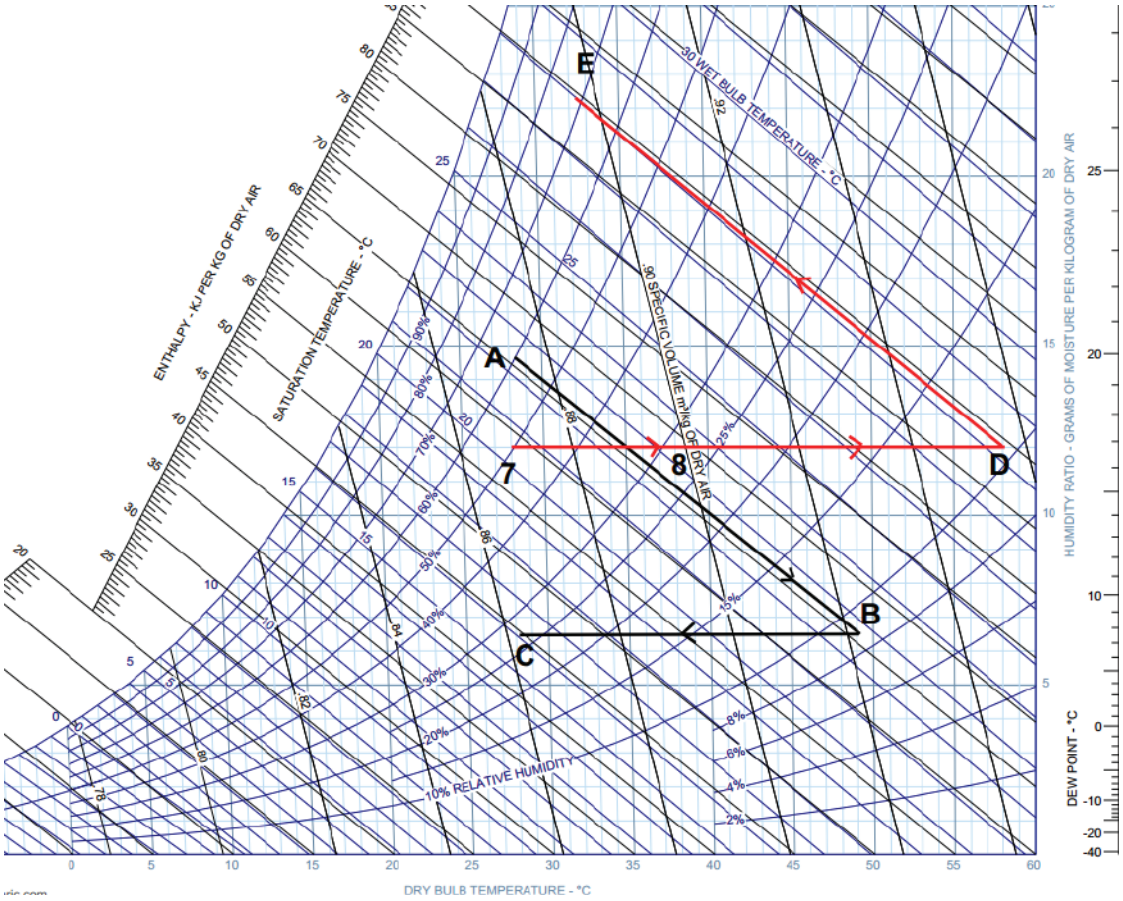

Figure 3. Dehumidification and Regeneration process on the psychrometric chart.

The thermodynamic performance of a hybrid rotary desiccant air conditioning system is found by using following equations. [23]

1) Dehumidification Effectiveness:

$$\eta_{deh} = \frac{\omega_1 - \omega_2}{\omega_1} \tag{1}$$

Where ω_1 = Humidity ratio at process air inlet temperature (kg/kg of dry air).

ω_2 = Humidity ratio at process air outlet temperature (kg/kg of dry air).

2) Regeneration Effectiveness :

$$\eta_{deh} = \frac{\omega_3 - \omega_4}{\omega_4} \tag{2}$$

Where ω_3 = Humidity ratio at regeneration air outlet temperature (kg/kg of dry air).

ω_4 = Humidity ratio at regeneration air inlet temperature (kg/kg of dry air).

3) Adsorption Rate (kg/hr):

$$AR = \rho_a \times V_p \times (\omega_1 - \omega_2) \tag{3}$$

Where ρ_a = Density of air (kg/m³).

V_p = Volumetric flow rate of process air (m³/hr).

4) Regeneration Rate (kg/hr) :

$$AR = \rho_a \times V_R \times (\omega_3 - \omega_4) \tag{4}$$

Where V_p = Volumetric flow rate of regeneration air (m³/hr)

5) Dehumidification Coefficient of Performance (DCOP):

$$DCOP = \frac{\rho_a \times V_p \times \Delta h_{vs} \times (\omega_1 - \omega_2)}{\rho_a \times V_R \times c_p \times (T_9 - T_5)} = \frac{\rho_a \times V_p \times \Delta h_{vs} \times (\omega_1 - \omega_2)}{\rho_a \times V_R \times (h_9 - h_5)} \tag{5}$$

Where Δh_{vs} = Latent heat of vaporisation of the water (kj/kg).

c_p = Specific heat of air at constant pressure (kj/kg K).

h_5 = Specific enthalpy of air at process inlet temperature (kj/kg).

h_9 = Specific enthalpy of air at regeneration inlet temperature (kj/kg).

6) Vapour Compression Cycle Coefficient of Performance:

$$VCCOP = \frac{h_1 - h_4}{h_2 - h_1} \quad (6)$$

Where h_1 = Specific enthalpy of refrigerant at inlet of compressor (kj/kg).

h_2 = Specific enthalpy of refrigerant at outlet of compressor (kj/kg).

h_4 = Specific enthalpy of refrigerant at inlet of evaporator (kj/kg).

RESULTS AND DISCUSSION

The testing conducted on the air conditioning system using solid desiccant provided valuable insights into its performance and efficiency under different conditions. The results indicate that the moisture removal capacity of the system depends on various design and operating parameters. The energy conservation benefits of the desiccant system also studied. The effect of regeneration temperature, process air inlet temperature, regeneration air and process air velocity, mass flow rate of process air, climatic conditions and methods of regeneration on the desiccant wheel are studied with velocity of 4.5m/s.

Variation of Dehumidification Effectiveness in the Summer Season

Figure 4 (a-d) indicates the variation of dehumidification effectiveness vs. inlet air temperature at different air velocities during the summer season with a 4.5 m/s regeneration velocity. Dehumidification effectiveness is a measure of how well a desiccant wheel removes moisture from the air. A considerable reduction in the dehumidification effectiveness is observed due to an increase in the inlet air temperature. At lower inlet air temperature, the relative humidity is higher, resulting

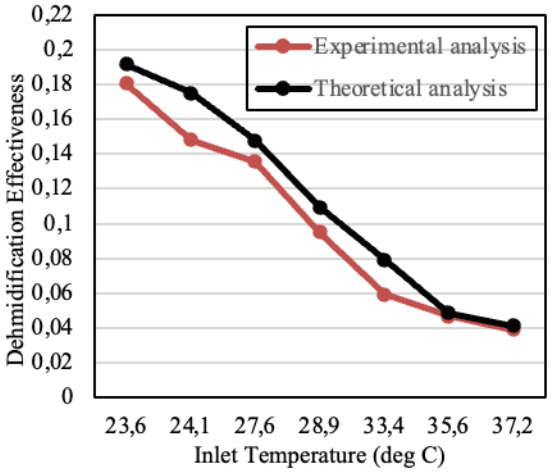

Figure (a)

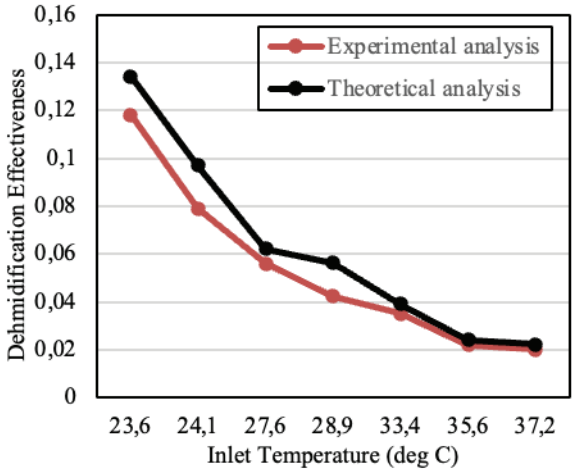

Figure (b)

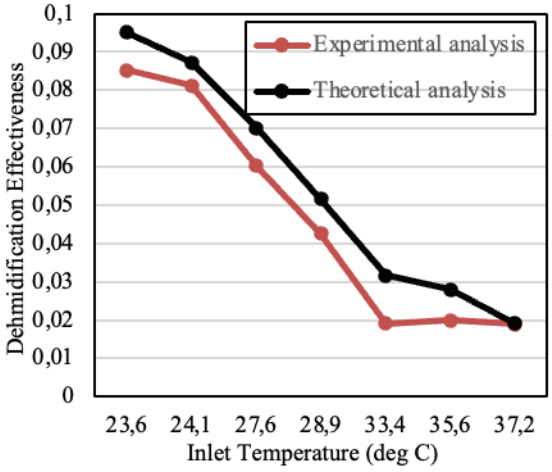

Figure (c)

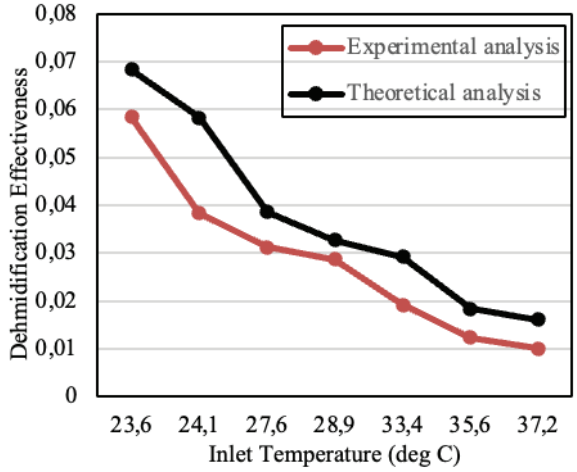

Figure (d)

Figure 4. Variation of dehumidification effectiveness in the summer season for air inlet velocity of a) 1.5m/s, b) 2.6m/s, c) 3.3m/s and d) 4.1m/s.

in the increased specific humidity of the desiccant wheel. Hence, a major difference in vapour partial pressure between the inlet air and the desiccant wheel leads to higher diffusion of the water vapour droplets inlet air to the desiccant material surface. Due to this, higher dehumidification effectiveness is obtained at lower inlet air temperature. Experimental investigation indicates that dehumidification effectiveness decreases from 0.19 to 0.032, with the increase in the inlet air temperature from 23.6 °C to 37.2 °C, at 1.5 m/s air inlet velocity. A similar nature is observed during theoretical and experimental studies. It is also found that dehumidification effectiveness reduces due to increases in the inlet air velocity. It is because the higher air inlet velocity minimises the contact time between the desiccant surface and the inlet air. Thus, the lower amount of water vapour is absorbed by the desiccant material due to the lower contact time, which ultimately decreases the dehumidification effectiveness.

Variation of Dehumidification Effectiveness in the Rainy Season

A variation in the dehumidification effectiveness for the rainy season at different air inlet temperatures is shown in Figure 5 (a-d). Similar to the summer season, the dehumidification effectiveness at 4.5 m/s regeneration velocity decreases with increase in the inlet air temperature at different inlet air velocities. The relative humidity of air at a lower air inlet temperature results in better performance. Due to the higher environmental humidity level during the rainy season, the drop in the effectiveness of the dehumidifier is much lower than that of the summer season. Experimentation investigation indicates that dehumidification effectiveness decreases from 0.130 to 0.067, with the increase in the

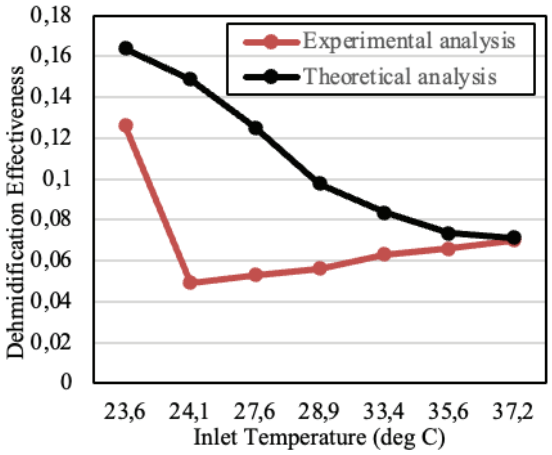

Figure (a)

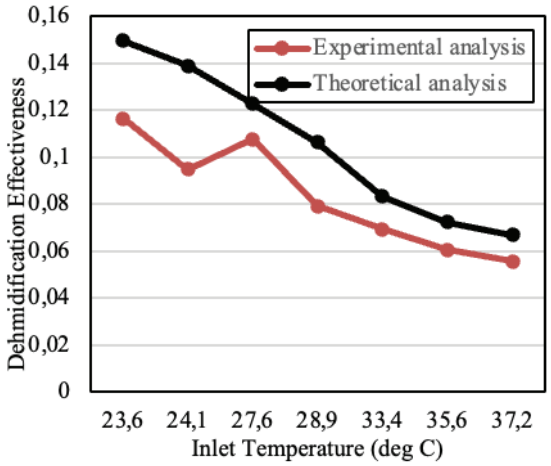

Figure (b)

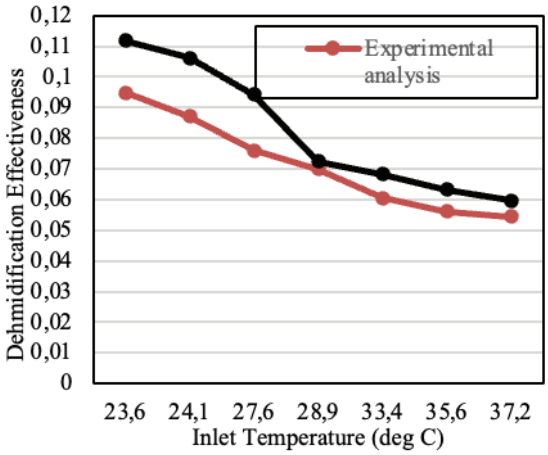

Figure (c)

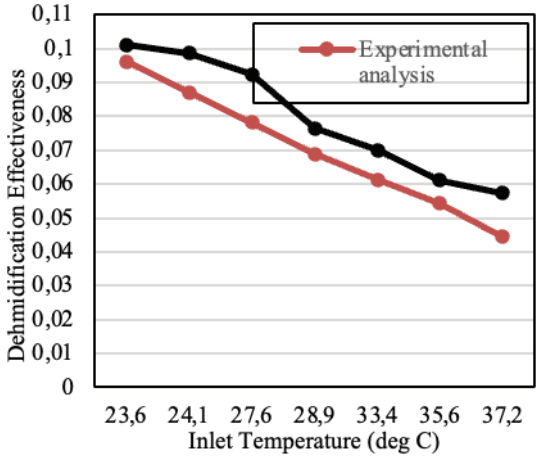

Figure (d)

Figure 5. Variation of dehumidification effectiveness in rainy season for air inlet velocity of a) 1.5m/s, b) 2.6m/s, c) 3.3m/s and d) 4.1m/s.

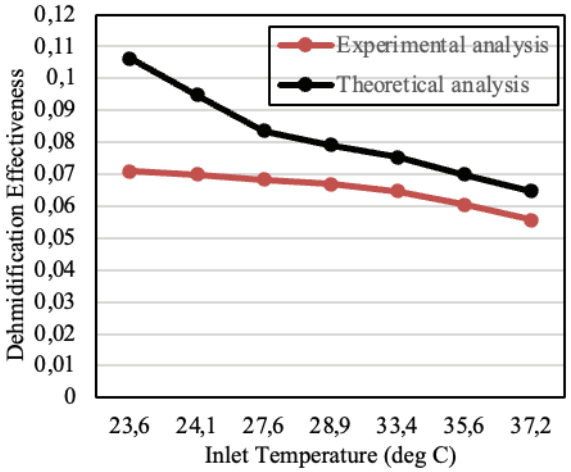

Figure (a)

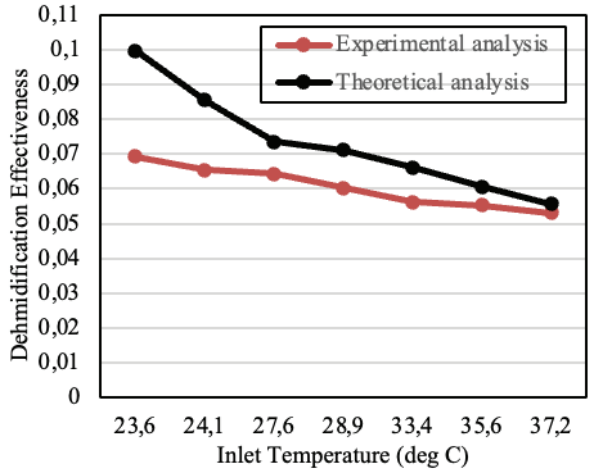

Figure (b)

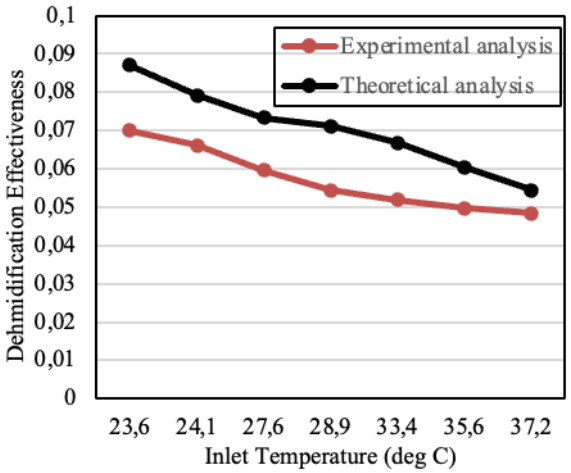

Figure (c)

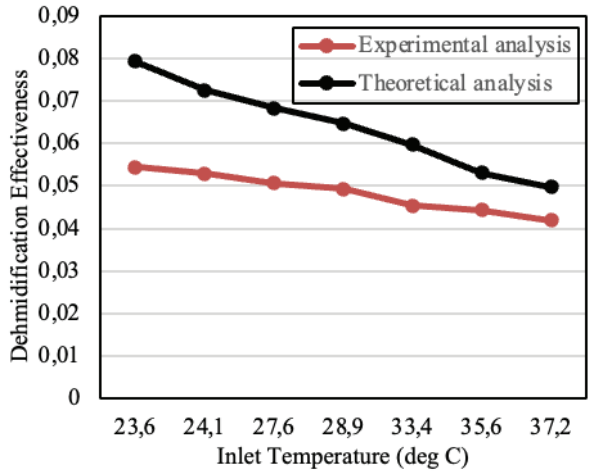

Figure (d)

Figure 6. Variation of dehumidification effectiveness in winter season for air inlet velocity of a) 1.5m/s, b) 2.6m/s, c) 3.3m/s and d) 4.1m/s.

inlet air temperature from 23.6 °C to 37.2 °C, at 1.5 m/s air inlet velocity. Better dehumidification effectiveness is obtained at lower air inlet velocity, because of a higher contact time of the inlet air with the desiccant wheel.

Variation of Dehumidification Effectiveness in the Winter Season

Figure 6 (a-d) represents the variation of dehumidification effectiveness vs. inlet air temperature during the winter session at different air velocities. Alike summer and rainy sessions, dehumidification effectiveness decreases with an increase in the air inlet temperature and velocity. A lower value of dehumidification effectiveness is observed in the winter session when compared with summer and rainy seasons. A specific humidity of atmospheric air in the winter session is lower than compared to summer and rainy seasons, resulting in a lower humidity adsorption rate, which reduces dehumidification effectiveness. The findings reveal that fluctuations of dehumidification effectiveness depend on the air inlet temperature and velocity, since high air inlet temperature and velocity slow down the desiccant's rate of moisture adsorption. Hence low air inlet temperature and velocity is recommended for better dehumidification effectiveness in all seasons.

Variation of Regeneration Effectiveness in the Summer Season

In an air conditioning system, regeneration effectiveness is known as the efficiency of a component called a regenerator in recovering heat from the exhausted air and transferring it to the incoming fresh air. A variation in regeneration effectiveness with inlet air temperature in the summer season at different air velocities, as shown in Figure 7 (a-d). Regeneration effectiveness at

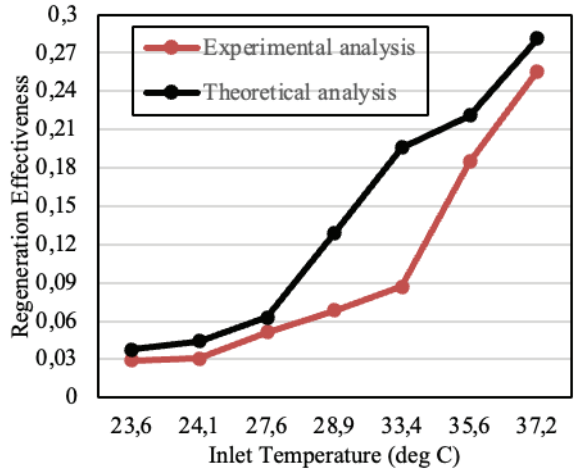

Figure (a)

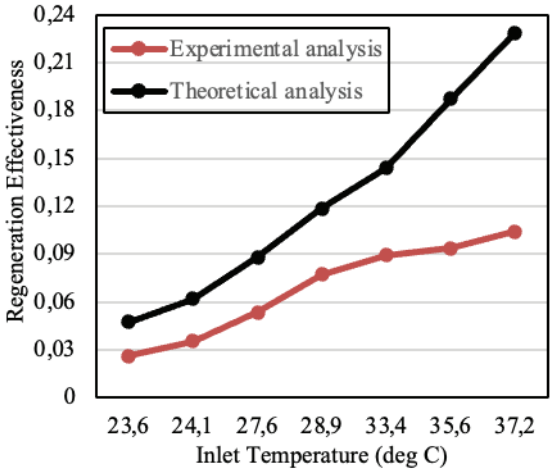

Figure (b)

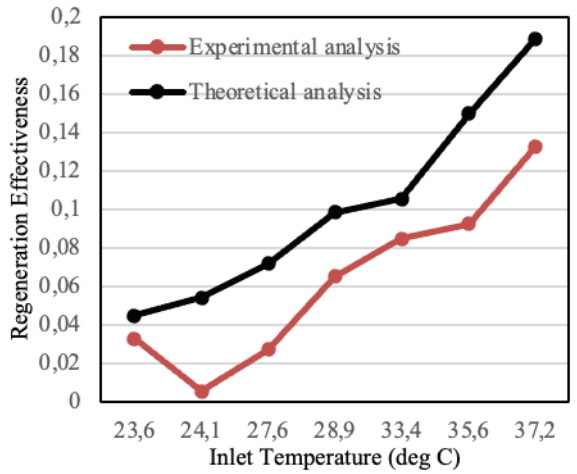

Figure (c)

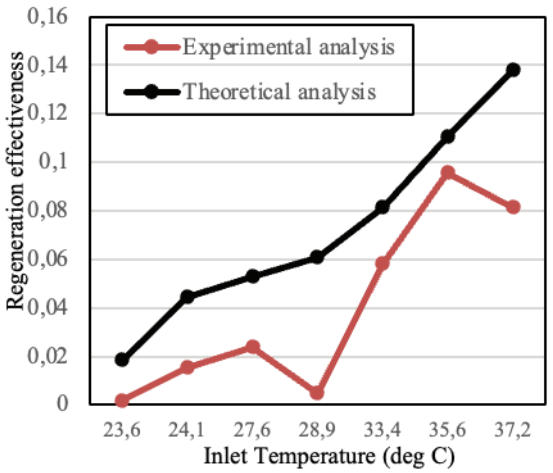

Figure (d)

Figure 7. Variation of regeneration effectiveness in the summer season for air inlet velocity of a) 1.5m/s, b) 2.6m/s, c) 3.3m/s and d) 4.1m/s.

4.5 m/s regeneration air inlet velocity increases with an increase in the air inlet temperature. As the ambient or air inlet temperature increases, the regeneration temperature also increases, which allows the desiccant wheel to regenerate. As the desiccant wheel is regenerated, it releases moisture into the incoming air. This moisture content is then transferred to the adsorption section, allowing the system to absorb more moisture from the incoming air. Thus, the regeneration effectiveness increases with air inlet temperature. A similar nature is observed for theoretical and experimental investigations at different inlet air velocities. For various air inlet temperatures the maximum value of regeneration effectiveness is obtained at 1.5 m/s air inlet velocity as compared with other velocities. As the inlet air velocity increases from 1.5 m/s, the air stays in contact with the desiccant wheel for a shorter duration of time, hence, the regeneration effectiveness is less at the higher velocity. A maximum value of regeneration effectiveness obtained during experimentation at 37.2 °C air inlet temperature and 1.5 m/s air velocity is 0.298. While at the same temperature, at 4.1 m/s air velocity, the value of regeneration effectiveness is 0.08.

Variation of Regeneration Effectiveness in the Rainy Season

Figure 8 (a-d) represents the variation of regenerative effectiveness vs. inlet air temperature at different air velocities during the rainy season with a 4.5 m/s regeneration velocity. A regenerative effectiveness in the rainy session also increases with the increase in air inlet temperature as similar to the summer season. Moreover, reduced velocities of air at its inlet lead to higher effectiveness of regeneration in line with longer contact between the desiccant

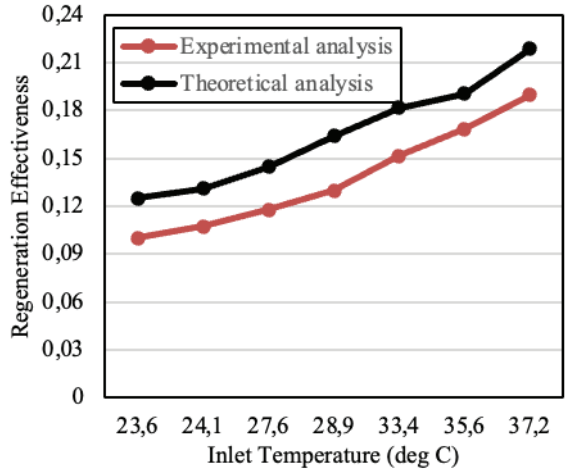

Figure (a)

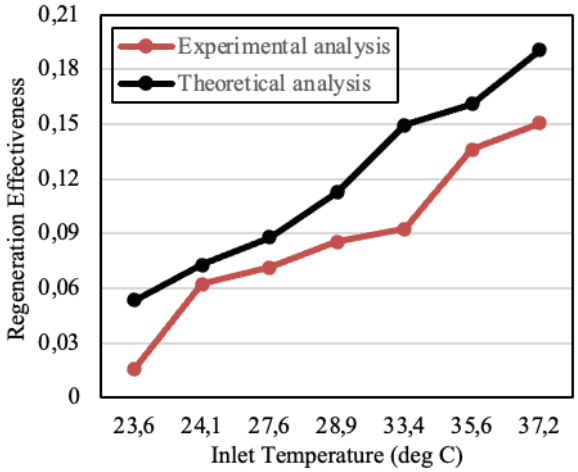

Figure (b)

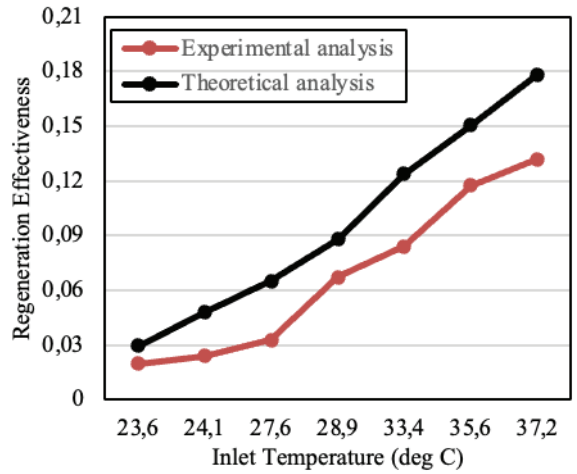

Figure (c)

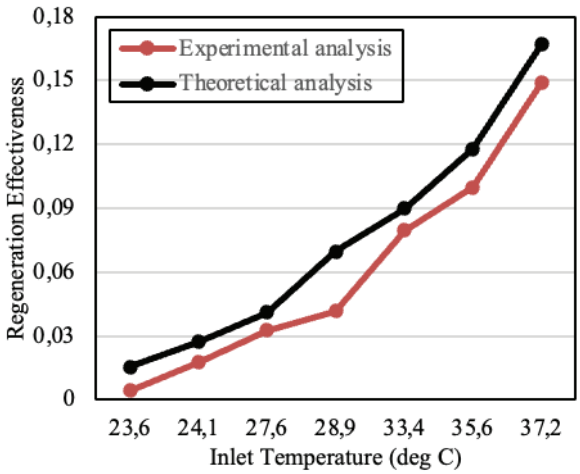

Figure (d)

Figure 8. Variation of regeneration effectiveness in rainy season for air inlet velocity of 1.5 m/s, b) 2.6 m/s, c) 3.3 m/s and d) 4.1 m/s.

surface and the inlet air. An experimental value of regeneration effectiveness at 37.2 °C air inlet temperature and 1.5 m/s inlet air velocity is 0.189. On the other hand, for the same air inlet temperature, at 4.1 m/s, the value of regeneration effectiveness reduced to 0.149. It is due to the lesser contact time between the incoming air and the desiccant wheel.

Variation of Regeneration Effectiveness in the Winter Season

A variation of regeneration effectiveness for different air inlet temperatures in the winter session at air inlet velocities in the range of 1.5 m/s to 4.1 m/s is shown in Figure 9 (a-d). In summer and rainy seasons, the regeneration effectiveness at 4.5 m/s regeneration velocity increases with an increase in the air inlet temperature. An experimental value of regeneration effectiveness in the winter season at 37.2 °C air inlet temperature and 1.5 m/s inlet air velocity is 0.239. While for the same air inlet temperature and velocity, the value of regeneration effectiveness in the summer season is 0.298. It indicates that regeneration effectiveness in the winter session is lower as compared with the summer session. It may be due to the reduction in moisture-absorbing ability of the desiccant wheel, as the specific humidity of atmospheric air is low in the winter season as compared to summer. The regeneration effectiveness in the winter season also decreases with an increase in the air inlet velocities, similar to summer and rainy seasons.

Variation of Adsorption Rate in the Summer Season

Figure 10 (a-d) represents the variation of adsorption rate vs. inlet air temperature at different air velocities during the summer season with a 4.5 m/s regeneration velocity. In

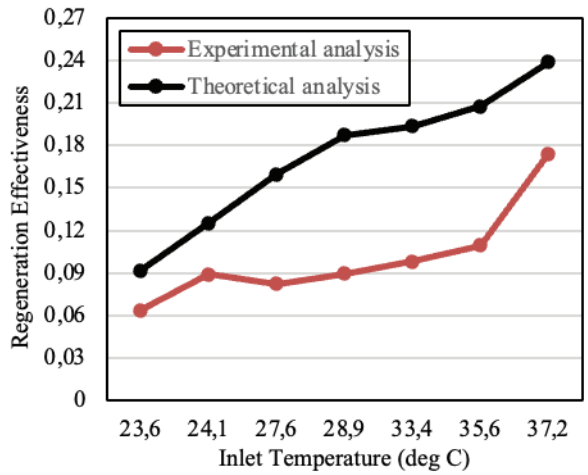

Figure (a)

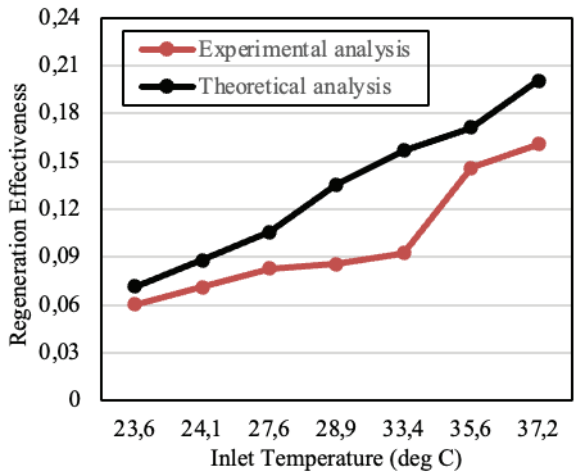

Figure (b)

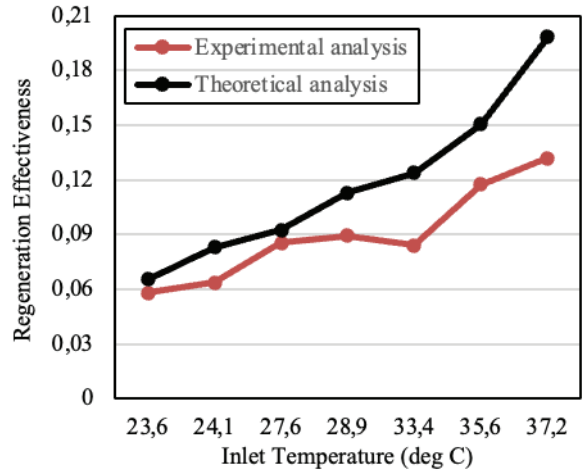

Figure (c)

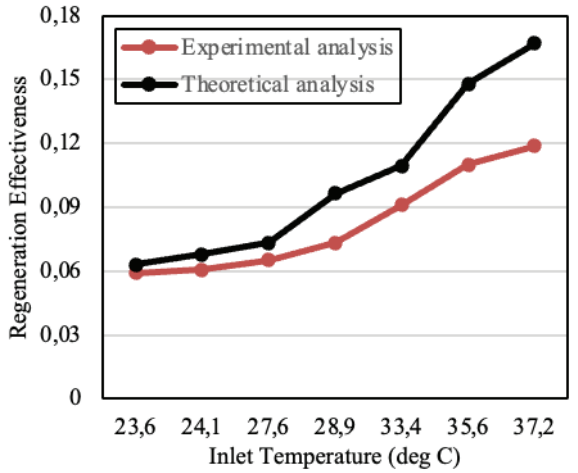

Figure (d)

Figure 9. Variation of regeneration effectiveness in winter season for air inlet velocity of a) 1.5 m/s, b) 2.6 m/s, c) 3.3 m/s and d) 4.1 m/s.

the air conditioner system adsorption rate is defined as the speed at which a solid adsorbent material absorbs water vapour from the air. The adsorption rate reduces due to an increase in the air inlet temperature at all velocities. High ambient temperatures characteristic of the summer season result in higher relative humidity of the air. Lower temperature provides higher presence of water vapour content in the air, hence a major difference of vapour partial pressure obtained between the inlet air and desiccant material surface, and this creates a higher diffusion of the water vapour droplets from the air to the surface. As, adsorption process is exothermic and has a preference for cooler air, a lower adsorption rate is obtained with an increase in the inlet temperature. On the other side, as the velocity of the inlet air increases, the adsorption rate also increases as a result of the increased mass properties flow rate of the humid air through the adsorber vessel. During the experimental maximum adsorption rate obtained at 23.6 °C air inlet temperature and 4.1 m/s air velocity is 0.30 kg/hr, while for the same inlet air temperature adsorption rate obtained at 1.5 m/s air velocity is 0.20 kg/hr.

Variation of Adsorption Rate in the Rainy Season

A variation of adsorption rate for different air inlet temperatures in the rainy session at various air inlet velocities is shown in Figure 11 (a-d). Similar to the summer season, the adsorption rate in the rainy season also decreases due to an increase in the inlet air temperature. The atmospheric air has slightly higher specific humidity in the rainy season as compared with summer season, hence increase in the adsorption rate is observed in the rainy season as compared with summer season. An experimental value of adsorption rate in the summer season at 23.6 °C air inlet temperature and 1.5 m/s air velocity is 0.20 kg/hr. While at the same

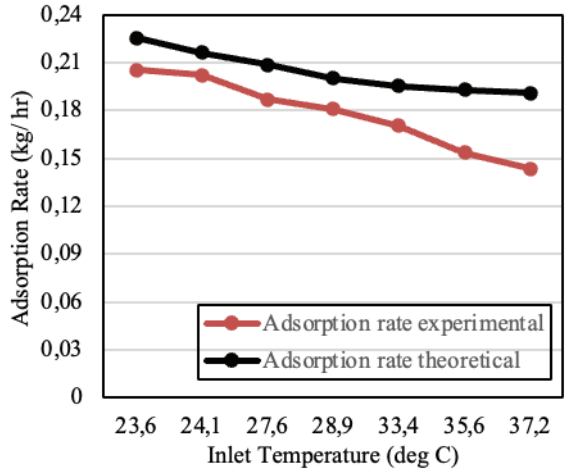

Figure (a)

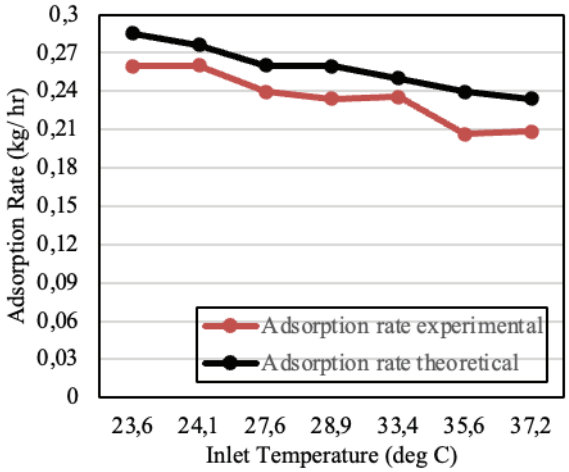

Figure (b)

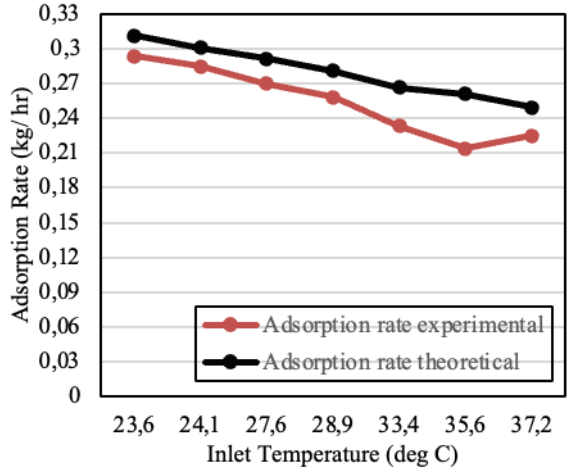

Figure (c)

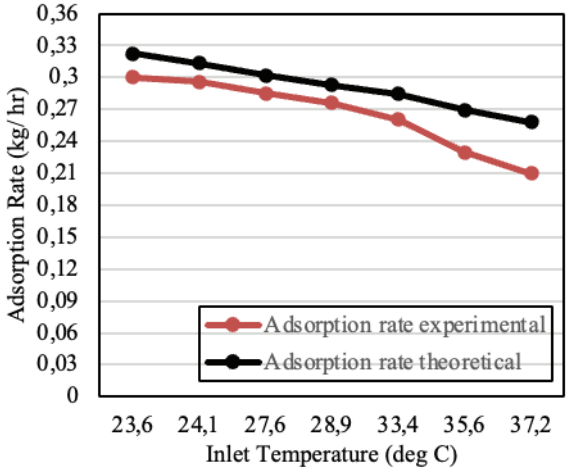

Figure (d)

Figure 10. Variation of adsorption rate in the summer season for air inlet velocity of a) 1.5 m/s, b) 2.6 m/s, c) 3.3 m/s and d) 4.1 m/s.

conditions, a value of adsorption rate in the rainy season is 0.252 kg/hr. Like summer season adsorption rate in the rainy season also increase with increase in the air inlet velocity.

Variation of Adsorption Rate in the Winter Season

Figure 12 (a-d) indicates the variation of adsorption rate with inlet air temperature at different air velocities in the range of 1.5 m/s to 4.1 m/s. In winter season also adsorption rate decreases with increase in the air inlet temperature. An adsorption rate, in the winter season is low as compared with summer and rainy season. In winter season temperature air is low as compared with other seasons. Cold air has a lower capacity to hold water vapour, results in the reduction of adsorption rate. An adsorption rate in the winter season also increases with increase in the air inlet velocity similar to summer and rainy season. A maximum experimentation value of adsorption rate at 23.6 °C air inlet temperature and 4.1 m/s air inlet velocity in the summer, rainy and winter season is 0.30, 0.40, 0.25 kg/hr respectively.

Comparison of Dehumidification Coefficient of Performance for Summer, Rainy and Winter Seasons

A variation of dehumidification coefficient for summer, rainy and winter seasons with inlet air temperature at various air inlet velocities in the range of 1.5 m/s to 4.1 m/s is shown in the figure 13 (a-d). A dehumidification coefficient of performance (DCOP) for all the seasons decreases with increase in the air inlet temperature. A dehumidification coefficient for summer and rainy seasons closely matches with each other. While, in the winter season lower dehumidification coefficient was obtained as compared to summer and rainy seasons. This is because the adsorption process is exothermic, and the temperature

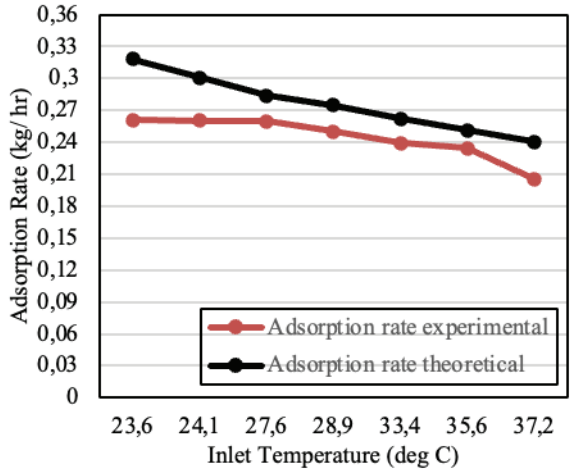

Figure (a)

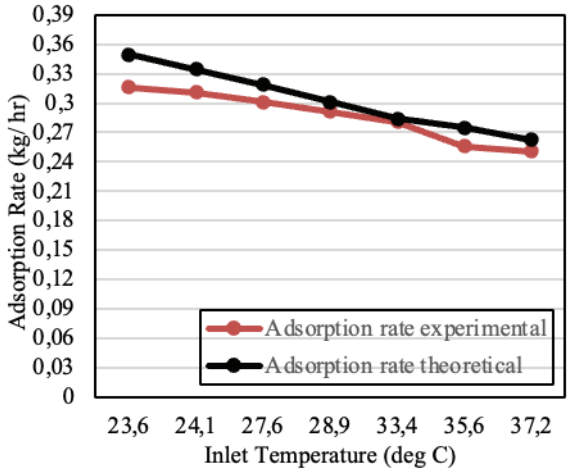

Figure (b)

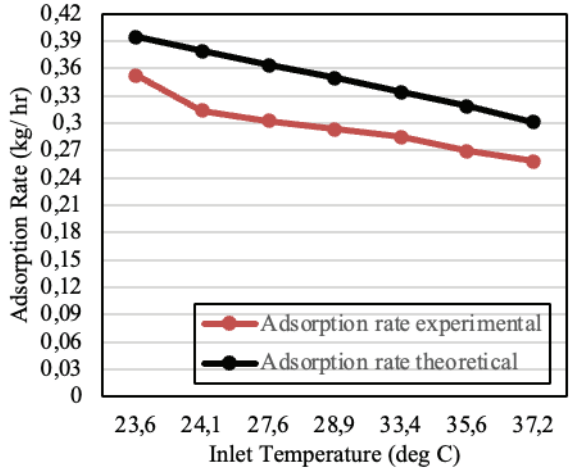

Figure (c)

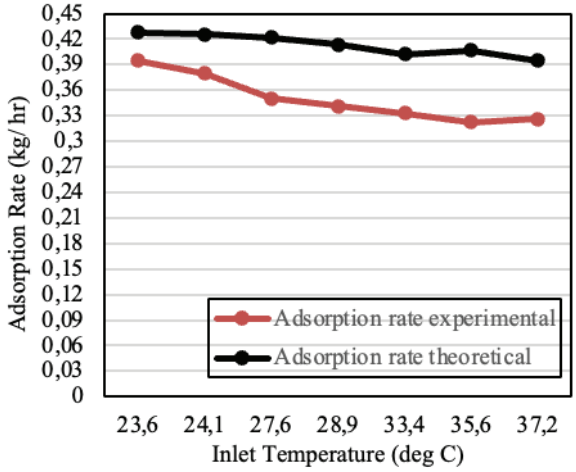

Figure (d)

Figure 11. Variation of adsorption rate in rainy season for air inlet velocity of a) 1.5 m/s, b) 2.6 m/s, c) 3.3 m/s and d) 4.1 m/s.

relationship that gives higher moisture content in the air enhances a higher vapor pressure difference between the inlet air and the desiccant material to promote diffusion of moisture. Also, increased regeneration temperature contributes to desiccant regeneration thereby enabling greater levels of moisture adsorption consequently leading to improved dehumidification coefficient of performance. Similar nature is observed for all the air inlet velocities. It is also clear that for in all the three seasons the value of dehumidification coefficient of performance increases with the increase in the air inlet velocities. As with increase in the inlet velocity there the air mass flow rate of air also increases. It provides desiccant wheel with more humid air of which moisture should be removed and thus ultimately increases Dehumidification Coefficient of Performance.

Comparison of Regeneration Rate for Summer, Rainy and Winter Seasons

Figure 14 (a-d) represents a variation of regeneration rate for various inlet air temperature at different air inlet velocities. A regeneration rate is known as the speed at which a desiccant wheel is able to reabsorb moisture after it has been saturated by absorbing moisture from the air. The value of regeneration rate for all three seasons increases with increase in temperature. For various inlet air temperatures, value of regeneration rate in the summer season is considerably more as compared with rainy and winter seasons. In the summer season the ambient temperature is more. As the ambient temperature increases it also affects the regeneration temperature which also increase leads to increased removal of the moisture from desiccant wheel during regeneration phase. Thus, the regeneration rate also increases with increase in the ambient temperature. For all

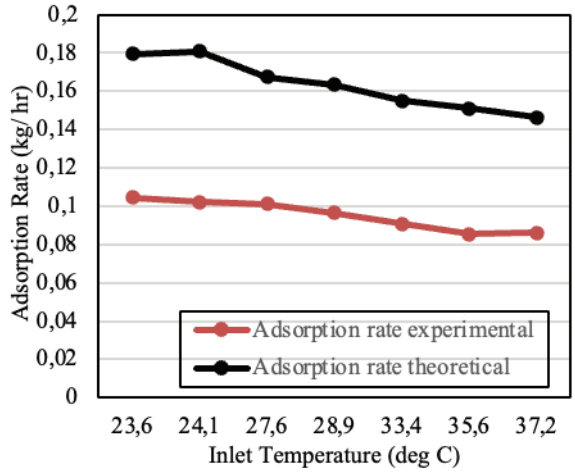

Figure (a)

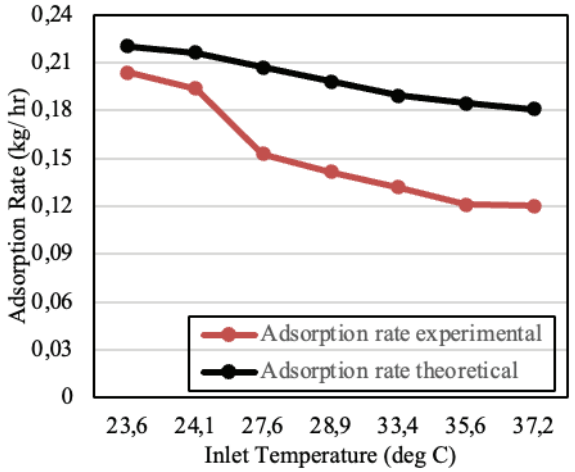

Figure (b)

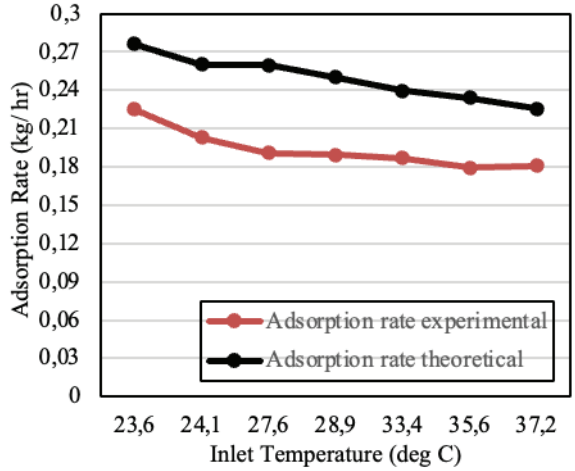

Figure (c)

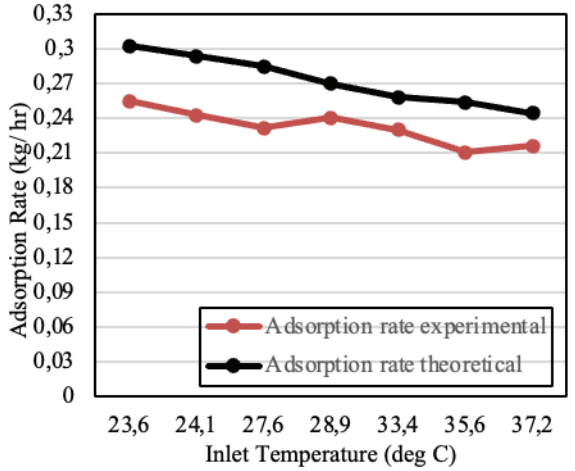

Figure (d)

Figure 12. Variation of adsorption rate in winter season for air inlet velocity of a) 1.5 m/s, b) 2.6 m/s, c) 3.3 m/s and d) 4.1 m/s.

the air inlet velocities similar nature is observed. Figure 14 (a)-(d) also indicate that for all the three seasons the value of regeneration rate increases with the decrease in the process air inlet velocities. It is because the lower process air inlet velocity maximizes the contact time between desiccant surface and incoming process air. Thus, then this rotary desiccant surface moves to regeneration sector where hot regenerated air takes the moisture from desiccant surface and hence regeneration rate increases.

Comparison of Vapour Compression Cycle Coefficient of Performance (VCCOP) for Summer, Rainy and Winter Seasons

A variation of vapour compression cycle coefficient of performance (VCCOP) for summer, rainy and winter seasons with inlet air temperature at various air inlet velocities in the range of 1.5 m/s to 4.1 m/s is shown in the figure 15 (a-d). It shows that for all air inlet velocities, the value of coefficient of performance for vapour compression cycle in summer, rainy and winter season decreases with increase in the inlet air temperatures. It is because as the ambient temperature increases the rate of heat transfer from the condenser decreases. Hence cooling capacity of the air-cooled condenser reduces which increases the load of the vapour compression refrigeration system. Thus, less heat is absorbed by the refrigerant from the air at the evaporator section which ultimately decreases coefficient of performance. It is also observed that, in all three seasons coefficient of performance for vapour compression cycle decreases with the increase in the process air inlet velocities. A less contact time between the inlet air and cooling coil results in the reduced coefficient of performance due to increase in the air inlet velocity. The coefficient of performance for vapour compression cycle

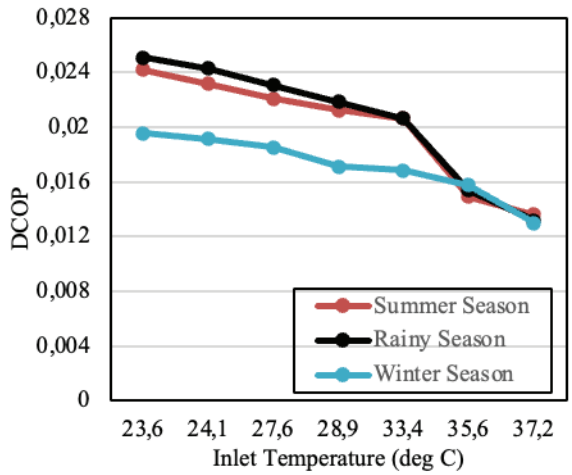

Figure (a)

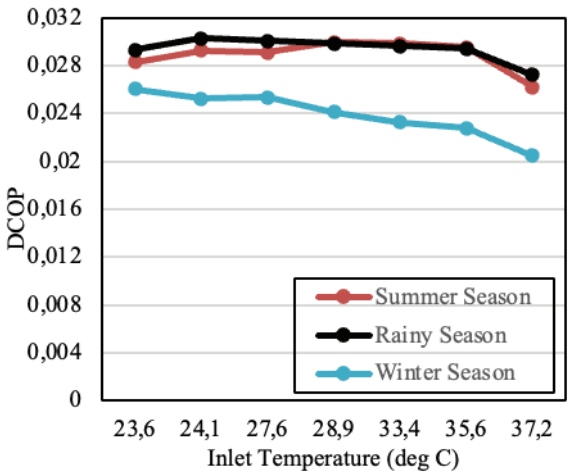

Figure (b)

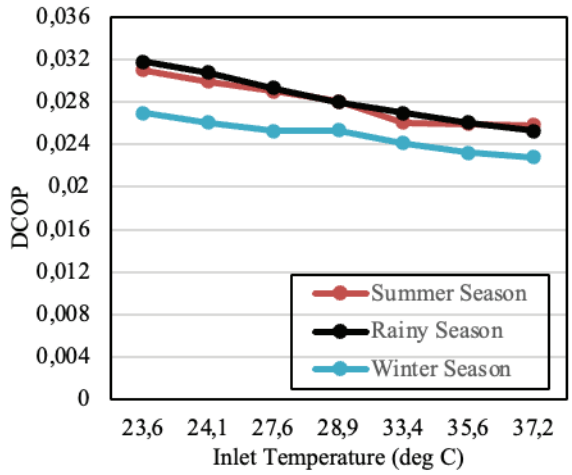

Figure (c)

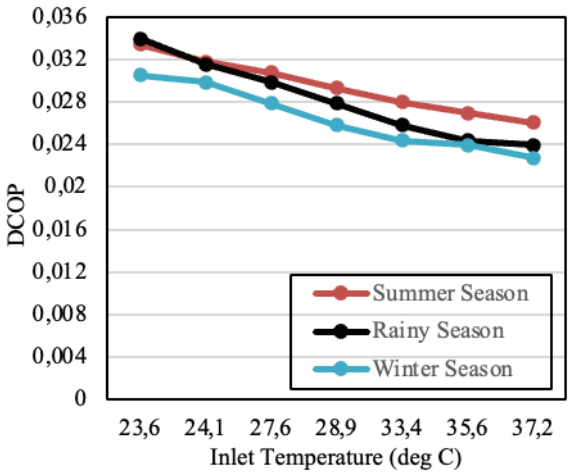

Figure (d)

Figure 13. Variation of dehumidification coefficient in summer, winter and rainy season for air inlet velocity of a) 1.5m/s, b) 2.6m/s, c) 3.3m/s and d) 4.1m/s.

is more in the winter season as compared to summer and rainy. A less power consumption in the winter season may results better coefficient of performance. A similar nature was observed for various parameters such as dehumidification and regeneration effectiveness, adsorption rate, dehumidification coefficient of performance and vapor compression cycle coefficient of performance by Hussain [23] when air conditioning system with solid desiccant dehumidifier wheel is powered by waste heat recovery system.

CONCLUSION

The experimental investigation of the air conditioning system with solid desiccant dehumidifier wheel and combined heating methods results in a 33% increase in effectiveness compared to the use of the electric heater alone. Hence this system may be effectively used in the higher humidity industries such as food processing, pharmaceuticals, and electronics manufacturing. Following are the major conclusion drawn from the experimentation investigation of air conditioning system with solid desiccant dehumidifier wheel at 4.5 m/s constant regeneration air velocity.

1) Dehumidification effectiveness in all three seasons increases with decrease in the air inlet temperatures and velocity. A lower value of dehumidification effectiveness is observed in the winter session when compared with summer and rainy seasons. A maximum experimentation value of dehumidification effectiveness obtained in the summer season at 23.6 °C inlet air temperature and 1.5 m/s air inlet velocity is 0.19.
2) In all the three seasons, regeneration effectiveness increases with increase in the inlet air temperature.

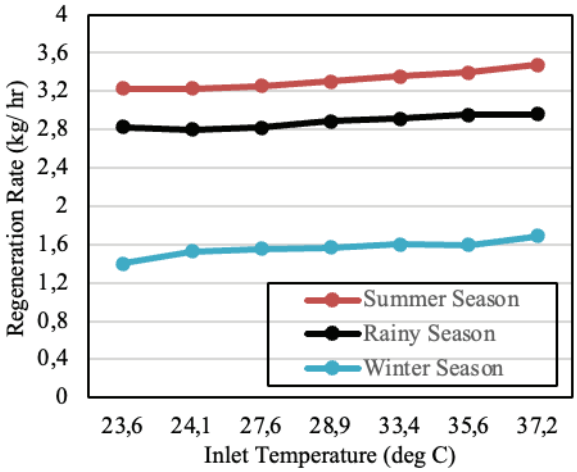

Figure (a)

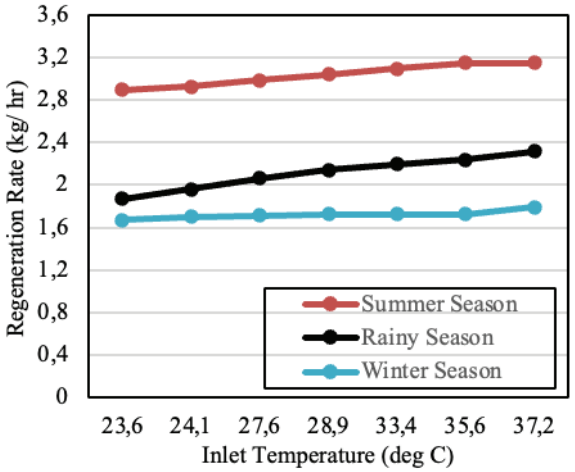

Figure (b)

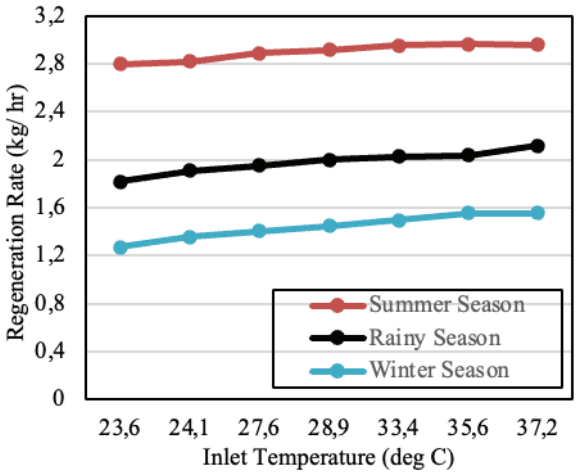

Figure (c)

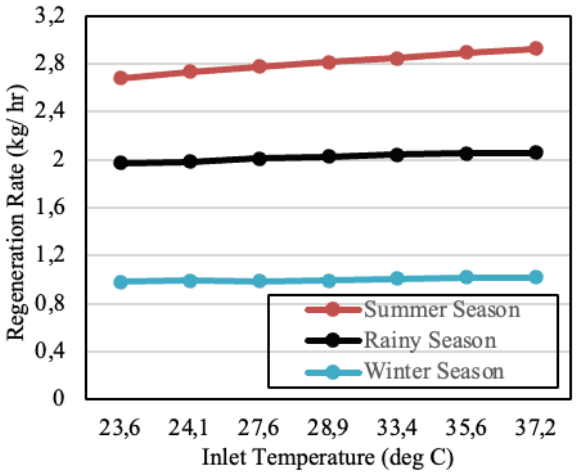

Figure (d)

Figure 14. Variation of regeneration rate in summer, winter and rainy season for air inlet velocity of a) 1.5m/s, b) 2.6m/s, c) 3.3m/s and d) 4.1m/s.

While it reduces due to the increase in air let velocity. A better regeneration effectiveness is obtained in the summer season as compared to rainy and winter season. A maximum experimentation value of dehumidification effectiveness obtained in the summer season at 37.2 °C inlet air temperature and 1.5 m/s air inlet velocity is 0.298.

3) Adsorption rate in the summer, rainy and winter season increases with decrease in the inlet air temperature. On the other side, adsorption rate increases with increase in the air inlet velocity. A rainy season has better adsorption rate as compared to summer and winter season. A maximum experimentation value of adsorption rate obtained in the rainy season at 23.6 °C inlet air temperature and 4.1 m/s air inlet velocity is 0.4 kg/hr.
4) In all the three seasons, dehumidification coefficient of performance increases with decrease in the inlet air temperatures. While it reduces due to the reduction in the air let velocity. A dehumidification coefficient of performance is low in the winter season as compared to summer and rainy season.
5) Coefficient of Performance in all the three seasons for vapour compression cycle decreases with increase in the inlet air temperature and velocity. A higher Coefficient of Performance is obtained in the winter season as compared with summer and rainy season. A maximum experimentation value of the Coefficient of Performance obtained in the winter season for vapour compression cycle at 23.6 °C inlet air temperature and 1.5 m/s air inlet velocity is 0.51.

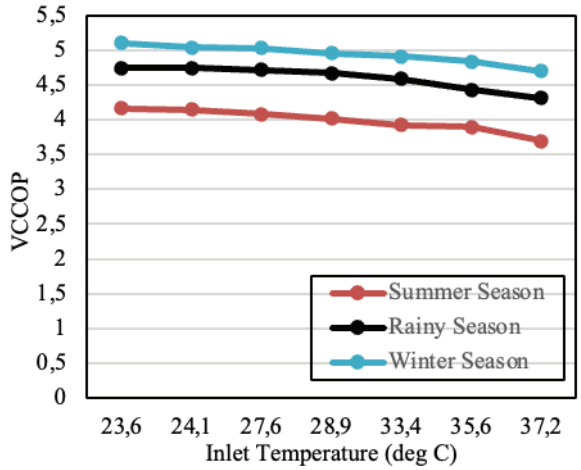

Figure (a)

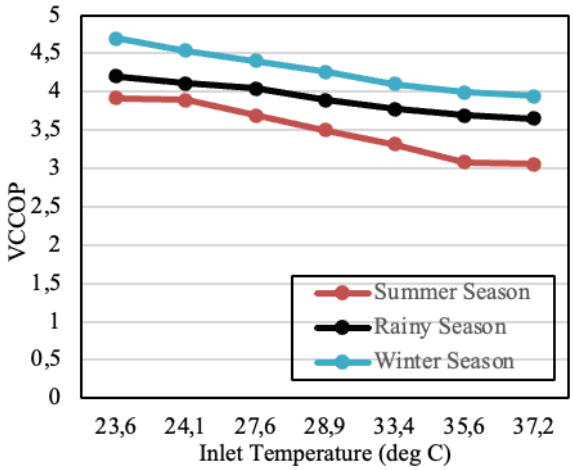

Figure (b)

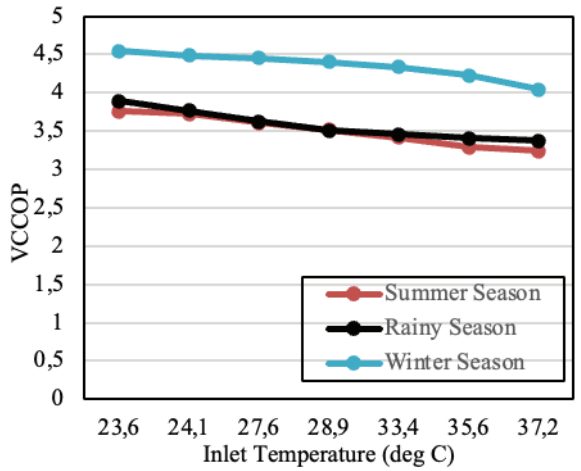

Figure (c)

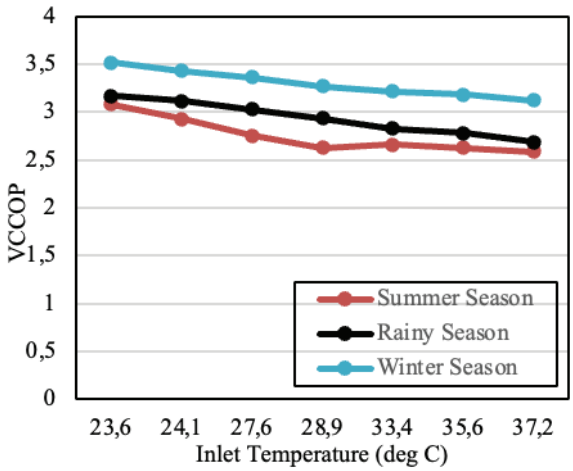

Figure (d)

Figure 15. Vapour compression cycle coefficient of performance in summer, winter and rainy season for air inlet velocity of a) 1.5m/s, b) 2.6m/s, c) 3.3m/s and d) 4.1m

DATA AVAILABILITY STATEMENT

The authors confirm that the data that supports the findings of this study are available within the article. Raw data that support the finding of this study are available from the corresponding author, upon reasonable request.

CONFLICT OF INTEREST

The author declared no potential conflicts of interest with respect to the research, authorship, and/or publication of this article.

ETHICS

There are no ethical issues with the publication of this manuscript.

STATEMENT ON THE USE OF ARTIFICIAL INTELLIGENCE

Artificial intelligence was not used in the preparation of the article.

REFERENCES

[1] Jain S, Dhar PL, Kaushik SC. Evaluation of solid-desiccant-based evaporative cooling cycles for typical hot and humid climates. Int J Refrig 1995;18:287–296. [Crossref]

[2] Scherer GW. Effect of drying on properties of silica gel. J Non-Cryst Solids 1997;215:155-168. [Crossref]

[3] Dai YJ, Wang RZ, Zhang HF. Parameter analysis to improve rotary desiccant dehumidification using a mathematical model. Int J Therm Sci 2001;40:400–408. [Crossref]

[4] Mazzei P, Minichiello F, Palma D. HVAC dehumidification systems for thermal comfort: a critical review. Appl Therm Eng 2005;25:677−707. [Crossref]
[5] Harshe YM, Utikar RP, Ranade VV, Pahwa D. Modeling of rotary desiccant wheels. Chem Eng Technol 2005;28:1473−1479. [Crossref]
[6] Zhai C, Archer DH, Fischer JC. ES2008-54185 Performance Modeling Of Desiccant Wheels (1): Model Development. ASME 2nd International Conference on Energy Sustainability 2008;2. [Crossref]
[7] Ge TS, Ziegler F, Wang RZ. A mathematical model for predicting the performance of a compound desiccant wheel (A model of compound desiccant wheel. Appl Therm Eng 2010;30:1005−1015. [Crossref]
[8] Li Y, Lu L, Yang H. Energy and economic performance analysis of an open cycle solar desiccant dehumidification air-conditioning system for application in Hong Kong. Solar Energy 2010;84:2085−2095. [Crossref]
[9] Christy A. Effect of Heat on the Adsorption Properties of Silica Gel. Int J Eng Technol 2012;4:484−488. [Crossref]
[10] Narayanan R, Saman WY, White SD. A non-adiabatic desiccant wheel: Modeling and experimental validation. Appl Therm Eng 2013;61:178-185. [Crossref]
[11] Yadav A, Yadav L. Comparative performance of desiccant wheel with effective and ordinary regeneration sector using mathematical model. Heat Mass Transfer 2014;50:1465−1478. [Crossref]
[12] Angrisani G, Roselli C, Sasso M, Tariello F. Assessment of energy, environmental and economic performance of a solar desiccant cooling system with different collector types. Energies 2014;7:6741−6764. [Crossref]
[13] Giannetti N, Rocchetti A, Saito K, Yamaguchi S. Entropy parameters for desiccant wheel design. Appl Therm Eng 2015;75:826−838. [Crossref]
[14] Chen CH, Hsu CY, Chen CC, Chen SL. Silica gel polymer composite desiccants for air conditioning systems. Energy and Buildings 2015;101:122−132. [Crossref]
[15] Ali Mandegari M, Farzad S, Pahlavanzadeh H. Exergy Performance Analysis and Optimization of a Desiccant Wheel System. J Therm Sci Eng Appl 2015;7:031013. [Crossref]
[16] Zouaoui A, Zili-Ghedira L, Ben Nasrallah S.Open solid desiccant cooling air systems: A review and comparative study. Renew Sustain Energy Rev 2016;54:889−917. [Crossref]
[17] Muthu S, Talukdar P, Jain S. Effect of regeneration section angle on the performance of a rotary desiccant wheel. J Therm Sci Eng Appl 2016;8. [Crossref]
[18] De Antonellis S, Joppolo CM. Simplified models for the evaluation of desiccant wheels performance. Desiccant Heating Ventilating, and Air- Conditioning Systems 2016;63−85. [Crossref]
[19] Shahzad MW, Burhan M, Ang L, Ng KC. Energy-water-environment nexus underpinning future desalination sustainability. Desalination 2017;413:52−64. [Crossref]
[20] Rjibi A, Kooli S, Guizani A. The effects of regeneration temperature of the desiccant wheel on the performance of desiccant cooling cycles for greenhouse thermally insulated. Heat Mass Transfer 2018;54:3427−3443. [Crossref]
[21] Goyal P, Purdue MJ, Farooq S. Adsorption and diffusion of moisture and wet flue gas on silica gel. Chemical Engineering Science 2020;227: 115890. [Crossref]
[22] Pourhakkak P, Taghizadeh M, Taghizadeh A, Ghaedi M. Chapter 2 – Adsorbent. Interface Science and Technology, Volume 33, 2021, Pages 71-210 [Crossref]
[23] Hussain T. Effects of different air inlet temperatures and regeneration air inlet velocities on the performance of Hybrid Desiccant Air Conditioning System. IOP Conf Ser: Mater Sci Eng 2022;1224;012012. [Crossref]
[24] Bilal M, Sultan M, Morosuk T, Den W, Sajjad U, Aslam MMA, et al. Adsorption-based atmospheric water harvesting: A review of adsorbents and systems. Int Commun Heat Mass Transf 2022;133:105961. [Crossref]
[25] Dezfouli MMS, Sopian K, Kadir K. Energy and performance analysis of solar solid desiccant cooling systems for energy efficient buildings in tropical regions. Energy Convers Manag 2022;14:100186. [Crossref]
[26] Tsai HY, Wu CT. Optimization of a rotary desiccant wheel for enthalpy recovery of air-conditioning in a humid hospitality environment. Heliyon 2022;8. [Crossref]
[27] Ma Z, Liu X, Zhang T. Experimental investigation and effectiveness analysis of a desiccant wheel dehumidification system with low air humidity. Appl Therm Eng 2023;225:120279. [Crossref]
[28] Hussain T. Optimization and comparative performance analysis of conventional and desiccant air conditioning systems regenerated by two different modes for hot and humid climates: Experimental investigation. Energy Built Environ 2023;4;281−296. [Crossref]
[29] Zhang XJ, Dai YJ, Wang RZ. A simulation study of heat and mass transfer in a honeycombed rotary desiccant dehumidifier. Appl Therm Eng 2003;23:989-1003. [Crossref]
[30] Olmuş U, Guzelel YE, Neyfel Cerci K, Buyukalaca O. Effect of operating parameters on the performance of rotary desiccant wheel energized by PV/T collectors. JTEN 2023; 9:988−997. [Crossref]
[31] Shaharier MT, Mondal D, Hasib MA, Islam MA. Effects of gas-liquid flow and dehumidification performance of a liquid desiccant dehumidifier: A numerical approach for vertical smooth & rough, and inclined rough plates. JTEN 2024;10:1559−1576. [Crossref]

J Ther Eng, Vol. 12, No. 2, pp. 684−701, March, 2026

Journal of Thermal Engineering
Web page info: https://jten.yildiz.edu.tr
DOI: 10.14744/thermal.0001110

Research Article

3D mathematical investigation of MHD flow imposed with bioconvective conditions over casson nanofluid induced by permeable surface utilizing lie symmetry transformation

Saloni GUPTA[1,*], Chinta Mani TIWARI[1]

[1]*Maharishi School of Science, Maharishi University of Information Technology, Lucknow, UP-226013, India*

ARTICLE INFO

Article history
Received: 31 January 2025
Revised: 04 May 2025
Accepted: 12 May 2025

Keywords:
3D MHD flow; Bioconvection; Buongiorno's Model; Casson Fluid; Chemical reaction; Lie symmetry analysis; Nanofluid; Shooting Method

ABSTRACT

In the current framework, consequence of three dimensional Magnetohydrodynamics bio-convective Casson nanofluid flow by permeable extending surface in the existence of gyrotactic micro-organisms and chemical reaction has been scrutinized. Lie group analysis has been performed along with Runge Kutta Fehlberg algorithm by utilizing shooting technique in MATLAB programming. This model has been solved to calculate the impact of Peclet number Pe ($0.1 \le Pe \le 10.0$), micro-organism concentration difference parameter κ ($0.1 \le \kappa \le 5.0$), Bio-convective Lewis number Lb ($0.1 \le Lb \le 0.9$), Gyrotactic microorganism Biot number Bi_3 ($1 \le Bi_3 \le 10$), thermal Biot number Bi_1 ($0.1 \le Bi_1 \le 2.0$, Concentration Biot number Bi_2 ($1 \le Bi_2 \le 5$), Permeability parameter K ($0.1 \le K \le 0.5$), Chemical reaction parameter C_r ($0 \le C_r \le 4$), Lewis number Le ($1 \le Le \le 20$), thermophoresis Nt ($0.5 \le Nt \le 2.5$), Brownian motion Nb ($0.1 \le Nb \le 5.0$), Prandtl number Pr ($0.732 \le Pr \le 20.0$), Magnetic parameter M ($1.5 \le M \le 3.5$) and Casson fluid parameter β ($0.1 \le \beta \le 0.9$). Flow features are exemplified quantitatively for above mentioned fluid parameters via graphs and tables. Additionally, graphs are plotted for physical quantities of interest for non-Newtonian nanofluid parameters. Motile density declines with augmentation in Bio-convective Lewis number Lb and Bio-convective constant κ. It is found that, with augmentation in thermal Biot number from 0.1-2.0, heat transfer rate falls down by 85.45% whereas mass transfer rate falls down by 51.95% for higher concentration Biot number from 1.0-5.0. Moreover, motile concentration de-escalates for higher Pe and κ. Ultimately, the results show that the output outcomes can be accurately predicted by the applied model.

Cite this article as: Gupta S, Tiwari CM. 3D mathematical investigation of MHD flow imposed with bioconvective conditions over casson nanofluid induced by permeable surface utilizing lie symmetry transformation. J Ther Eng 2026;12(2):684−701.

INTRODUCTION

Now days, researchers are working in the field of nanofluid because of its physical characteristics and uses in a variety of industries, particularly manufacturing, biomedicine, and industry. Research greatly benefits from the characteristics of nanofluids, especially their low resistivity

***Corresponding author.**
*E-mail address: saloni.20.jindal@gmail.com

This paper was recommended for publication in revised form by Editor-in-Chief Ahmet Selim Dalkılıç

Published by Yıldız Technical University Press, İstanbul, Turkey
Yıldız Technical University. This is an open access article under the CC BY-NC license (http://creativecommons.org/licenses/by-nc/4.0/).

and attractive thermophysical properties. Usman et al. [1] presented the Darcy theory to demonstrate the impact of MHD hybrid nanofluid flow over stretching sheet exponentially. Asghar et al. [2] showed the impact of slip conditions and joule heating over hybrid nanofluid induced by shrinking surface exponentially. Haque et al. [3] presented the magnetic field effect via heat transportation of nanofluid flow numerically. Numerical computation of ternary nanofluid flow induced by energy transportation over permeable sheet has been shown by Bilal et al. [4]. Algehyne et al. [5] discussed the energy transition over bioconvective nanofluid flow numerically. Takreem et al. [6] discussed the radiative ternary nanofluid flow via shape factor analysis. Rafique et al. [7] utilizing OHAM Williamson nanofluid model induced with thermal radiation and bioconvection by porous sheet. Afzal et al. [8] demonstrated the impact of 3D MHD nanofluid flow in presence of heat radiation. Atofarati et al. [9] presented a holistic analysis for heat transfer enhancement in nanofluids. Over permeable stretching surface, a numerical study has been done by Jubair et al. [10] to identify the impact of chemical reaction.

A vital area of research, fluid dynamics is essential to comprehending and improving a variety of natural and industrial systems. Complex fluids, like Casson fluids, have attracted a lot of attention among the many fluids that have been examined because of their special qualities and uses. Shear-thinning behaviour and a yield stress are characteristics of Casson fluids, a kind of non-Newtonian fluid. Research has recently focused on how Casson fluids behave when exposed to external stimuli like magnetic fields and porous heat sources, particularly when they are stretched. In order to optimize engineering applications, it is necessary to comprehend the complicated flow characteristics that can result from the interplay of various external elements with Casson fluids. Researchers have focused a great deal of emphasis on the thermo-physical features of non-Newtonian fluid applications in several scientific and engineering domains. These fluids are suitable for use in the pharmaceutical, chemical, and other industries. Nonetheless, there are some difficulties in studying non-Newtonian fluids. When stretched, Casson fluids, which are renowned for their capacity to record shear-thinning behaviour, display special properties. The first was Casson movement for printing ink type pigment oil suspensions [11]. Rao et al. [12] discussed the impact of thermal radiation in addition to chemical reaction induced by stretching surface in presence of 3D MHD nanofluid flow by applying similarity solutions. Ramamoorthy and Pallavarapu [13] presented the impact of Williamson fluid flow induced by heat radiation. Influence of Viscous and Ohmic dissipation influenced by MHD Casson nanofluid flow has been presented by Vinita et al. [14] by following Runge Kutta Fehlberg algorithm. Ahmed M. Megahed [15] found the impact of heat radiation in presence of Williamson fluid. Reeshan et al. [16] discussed the optimization of hybrid nanofluid flow induced by MHD Casson fluid flow utilizing computational intelligence approach. Numerical modeling of motile microbes induced by porous medium in presence of activation energy was presented by Waseem et al. [17]. Swain et al. [18] discussed the presence of viscous dissipation effect utilizing Homotopy perturbation method induced by stretching surface. Influence of ternary hybrid nanofluid over stretching sheet in presence of MHD flow has been presented by Swain et al. [19]. Sahoo et al. [20] showed the impact of entropy generation induced by inclined plate in presence of MHD hybrid nanofluid flow.

The interaction of conducting fluids with an electromagnetic field is known as magnetohydrodynamics. Since some sheet materials lack a heat exchanger, rheostat flow kinematics is a practical application of magnetohydrodynamic in which a magnetic field is employed in traditional fluids. Additional applications include power storage, thermal insulation, and more. Given this, the magnetohydrodynamic (MHD) flow across a stretching sheet offers a wide range of industrial and manufacturing uses, such as continuous metal casting, polymer extrusion, the petroleum industry, and electrical power generators. The magnetohydrodynamic (MHD) effects that arise when Casson fluids are exposed to magnetic fields add complexity to the flow behaviour and have a major impact on fluid dynamics and heat transfer. Varatharaj et al. [21] presented the impact of heat radiation and transport phenomenon over hybrid nanofluid in presence of MHD flow. Adeyemi et al. [22] discussed the influence of thermal radiation and generation over MHD fluid flow. Akinbo et al. [23] implemented the impact of chemical reaction and heat radiation utilizing Walters' B fluid in presence of stagnation point flow. Elhag et al. [24] demonstrated the influence of bio-convective gyrotactic microorganism induced by 3D sheet. Dang et al. [25] discussed the impact of chemical reaction over MHD nanofluid flow in presence of convective conditions by utilizing RKF technique following shooting algorithm. Sowmiya et al. [26] analysed the impact of heat flux over Casson fluid flow in presence of MHD convective conditions. Irshad et al. [27] presented the numerical study of Casson fluid flow in porous medium induced by stretching surface. Mehmood et al. [28] discussed the conical gap between cone and rotating discover blood flow in presence of Casson nanofluid computationally. Azar et al. [29] analyze the impact of Casson fluid flow in presence of MHD flow over porous medium.

One useful method for examining nonlinear partial differential equations is Lie group analysis. Lie and Ackerman's work [30] shows how this method was developed, while [31] unifies known exact integration techniques that take differential equations into account. The Lie group analysis method was used by numerous researchers to examine a variety of fluid flow problems under various conditions [32–35]. Disu and Salawu [36] presented the impact of temperature distribution influenced by fluid flow over porous medium in presence of magnetohydrodynamic flow by applying Lie symmetry analysis. Nabwey et al. [37]

discussed influence of convecting heating and Navier slip ferrofluid flow in presence of radiation effect by using Lie group analysis. Influence of tangent hyperbolic fluid flow induced by shrinking sheet has been presented by Swain et al. [38]. Impact of 3D MHD nanofluid flow induced by thermal laminated sheet has been presented by Akbar et al. [39]. Tufail et al. [40] using Lie group approach to analyze the impact of slip conditions over Maxwell fluid induced by shrinking sheet. Over straining surface, Shahbaz Ali [41] discussed the influence of slip conditions in presence of Bingham plastic flow utilizing Lie group analysis.

Our problem's primary goal is to determine the transportation behaviour of MHD nanofluids using Lie group similarity solution and RKF technique by following shooting algorithm over 3D permeable stretching surface. Metallurgical processes in the industrial sector include continuous filament drawing via static fluids, copper wire annealing and tinning, the production of plastic and rubber sheets, crystal development, continuous cooling, and fibre spinning, among many more uses. Along with the chemical reaction and gyrotactic microorganisms, the surface in this problem is permeable stretching surface, causing the viscosity to change with temperature and concentration over 3D sheet. On this system, we have additionally applied a magnetic field. Here, the viscosity exhibits a linear relationship with temperature, and the Lie group similarity technique yielded self-similar differential equations. The Lie group of transformations is used to identify all of the problem's symmetries and then determine which of them can be employed to produce group-invariant, or more precisely, similarity solutions.

MATHEMATICAL MODEL

A constant bio-nanofluid stagnation point flow in three dimensions with Casson fluid flow in presence of chemical reaction, variable transport characteristics, and thermal convective boundary conditions is taken into consideration. A two component Buongiorno's model has been followed in presence of Brownian motion and thermophoresis parameter. Because of the phenomena known as bio-convection, the imposition of microorganisms into the nanofluid is only necessary to stabilize the tiny nanoparticles. Furthermore, it is thought that the nanoparticles have no effect on the microorganisms' ability to swim or their velocity. Additionally, it is a reasonable assumption that nanoparticle dilution (suspension) is prepared with very small amounts (i.e., 1%) in order to avoid the instability of bio-convection; otherwise, the higher concentration distribution of nanoparticles leads to the highly effective saturation (suspension) viscosity, which ultimately suppresses the given bio-convective flow. Figure 1 displays the physical model of the problem along with sheet's velocities u and v in the x and y directions, respectively. These presumptions and the conventional boundary layer approximation result in the following governing equations.

$$\frac{\partial \bar{u}}{\partial \bar{x}} + \frac{\partial \bar{v}}{\partial \bar{y}} + \frac{\partial \bar{w}}{\partial \bar{z}} = 0. \tag{1}$$

$$\bar{u}\left(\frac{\partial \bar{u}}{\partial \bar{x}}\right) + \bar{v}\left(\frac{\partial \bar{u}}{\partial \bar{y}}\right) + \bar{w}\left(\frac{\partial \bar{u}}{\partial \bar{z}}\right) = \nu\left(1+\frac{1}{\beta}\right)\left(\frac{\partial^2 \bar{u}}{\partial \bar{z}^2}\right) - \left[\left(\frac{\sigma {B_0}^2}{\rho}\right) + \left(\frac{\nu}{k_1}\right)\left(1+\frac{1}{\beta}\right)\right]\bar{u} \tag{2}$$

$$\bar{u}\left(\frac{\partial \bar{v}}{\partial \bar{x}}\right) + \bar{v}\left(\frac{\partial \bar{v}}{\partial \bar{y}}\right) + \bar{w}\left(\frac{\partial \bar{v}}{\partial \bar{z}}\right) = \nu\left(1+\frac{1}{\beta}\right)\left(\frac{\partial^2 \bar{v}}{\partial \bar{z}^2}\right) - \left[\left(\frac{\sigma {B_0}^2}{\rho}\right) + \left(\frac{\nu}{k_1}\right)\left(1+\frac{1}{\beta}\right)\right]\bar{v} \tag{3}$$

$$\bar{u}\left(\frac{\partial T}{\partial \bar{x}}\right) + \bar{v}\left(\frac{\partial T}{\partial \bar{y}}\right) + \bar{w}\left(\frac{\partial T}{\partial \bar{z}}\right) = \left(\frac{k}{(\rho C_p)_f}\right)\left(\frac{\partial^2 T}{\partial \bar{z}^2}\right) + \left(\frac{(\rho C_p)_p}{(\rho C_p)_f}\right) \times \left[D_B\left(\frac{\partial C}{\partial \bar{z}}\right)\left(\frac{\partial T}{\partial \bar{z}}\right) + \left(\frac{D_T}{T_\infty}\right)\left(\frac{\partial T}{\partial \bar{z}}\right)^2\right] \tag{4}$$

$$\bar{u}\left(\frac{\partial C}{\partial \bar{x}}\right) + \bar{v}\left(\frac{\partial C}{\partial \bar{y}}\right) + \bar{w}\left(\frac{\partial C}{\partial \bar{z}}\right) = D_B\left(\frac{\partial^2 C}{\partial \bar{z}^2}\right) + \left(\frac{D_T}{T_\infty}\right)\left(\frac{\partial^2 T}{\partial \bar{z}^2}\right) - K_r(C - C_\infty) \tag{5}$$

$$\bar{u}\left(\frac{\partial N}{\partial \bar{x}}\right) + \bar{v}\left(\frac{\partial N}{\partial \bar{y}}\right) + \bar{w}\left(\frac{\partial N}{\partial \bar{z}}\right) + \left(\frac{bW_c}{C_w - C_\infty}\right)\left[\frac{\partial}{\partial \bar{z}}\left(N\left(\frac{\partial C}{\partial \bar{z}}\right)\right)\right] = D_N\left(\frac{\partial^2 N}{\partial \bar{z}^2}\right) - K_r(N - N_\infty) \tag{6}$$

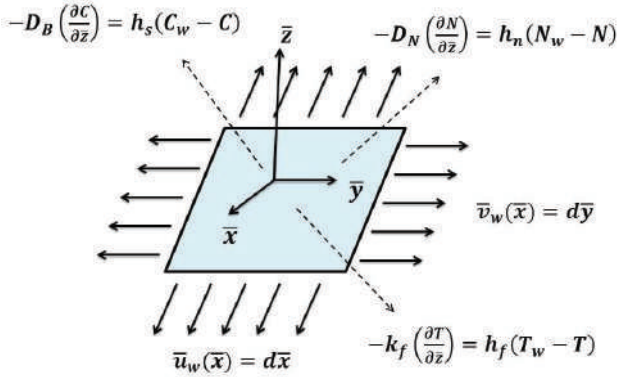

Figure 1. Physical Diagram.

To find similarity transformation for the current problem, the following dimensionless variables are introduced

$$x = \frac{\bar{x}}{\sqrt{\frac{\nu}{d}}},\ y = \frac{\bar{y}}{\sqrt{\frac{\nu}{d}}},\ z = \frac{\bar{z}}{\sqrt{\frac{\nu}{d}}},\ u = \frac{\bar{u}}{\sqrt{\nu d}},\ v = \frac{\bar{v}}{\sqrt{\nu d}},$$
$$w = \frac{\bar{w}}{\sqrt{\nu d}},\ \Theta = (T - T_\infty)/(T_w - T_\infty),$$
$$\Phi = (C - C_\infty)/(C_w - C_\infty),\ \chi = (N - N_\infty)/(N_w - N_\infty) \tag{7}$$

The boundary conditions are defined following as

$$\begin{aligned}&\bar{u} = \bar{u}_w = d\bar{x}, \bar{v} = \bar{v}_w = d\bar{y}, \bar{w} = 0,\\ &-k_f\left(\frac{\partial T}{\partial \bar{z}}\right) = h_f(T_w - T), -D_B\left(\frac{\partial C}{\partial \bar{z}}\right) = h_s(C_w - C),\\ &-D_N\left(\frac{\partial N}{\partial \bar{z}}\right) = h_n(N_w - N)\ at\ \bar{z} = 0,\\ &\bar{u} \to 0, \bar{v} \to 0, T \to T_\infty, C \to C_\infty, N \to N_\infty\ as\ \bar{z} \to \infty\end{aligned} \tag{8}$$

Eq's. (1)-(6) takes the form

$$\frac{\partial u}{\partial x} + \frac{\partial v}{\partial y} + \frac{\partial w}{\partial z} = 0 \tag{9}$$

$$\begin{aligned}u\frac{\partial u}{\partial x} + v\frac{\partial u}{\partial y} + w\frac{\partial u}{\partial z} = \nu\left(1+\frac{1}{\beta}\right)\frac{\partial^2 u}{\partial z^2} - \left[\frac{\sigma {B_0}^2}{d\rho}\right.\\ \left. + \left(\frac{\nu}{dk_1}\right)\left(1+\frac{1}{\beta}\right)\right] u\end{aligned} \tag{10}$$

$$\begin{aligned}u\frac{\partial v}{\partial x} + v\frac{\partial v}{\partial y} + w\frac{\partial v}{\partial z} = \nu\left(1+\frac{1}{\beta}\right)\frac{\partial^2 v}{\partial z^2} - \left[\frac{\sigma {B_0}^2}{d\rho}\right.\\ \left. + \left(\frac{\nu}{dk_1}\right)\left(1+\frac{1}{\beta}\right)\right] v\end{aligned} \tag{11}$$

$$\begin{aligned}u\frac{\partial \Theta}{\partial x} + v\frac{\partial \Theta}{\partial y} + w\frac{\partial \Theta}{\partial z} = \left(\frac{k}{\nu(\rho C_p)_f}\right)\frac{\partial^2 \Theta}{\partial z^2} + \left(\frac{(\rho C_p)_p}{(\rho C_p)_f}\right)\\ \times\left[\left(D_B\frac{C_\infty - C_\infty}{\nu}\right)\left(\frac{\partial \Phi}{\partial z}\right)\left(\frac{\partial \Theta}{\partial z}\right)\right.\\ \left. + \frac{D_T(T_W - T_\infty)}{\nu T_\infty}\left(\frac{\partial \Theta}{\partial z}\right)^2\right]\end{aligned} \tag{12}$$

$$\begin{aligned}u\frac{\partial \Phi}{\partial x} + v\frac{\partial \Phi}{\partial y} + w\frac{\partial \Phi}{\partial z} = \left(\frac{D_B}{\nu}\right)\frac{\partial^2 \Phi}{\partial z^2} + \left[\frac{D_T(T_W - T_\infty)}{\nu T_\infty(C_W - C_\infty)}\right]\partial^2\Theta/\partial z^2\\ -\left(\frac{K_r}{d}\right)\Phi\end{aligned} \tag{13}$$

$$\begin{aligned}u\frac{\partial \chi}{\partial x} + v\frac{\partial \chi}{\partial y} + w\frac{\partial \chi}{\partial z} + \left(\frac{bW_c}{\nu}\right)\left[\left(\frac{N_\infty}{N_W - N_\infty}\right)\frac{\partial^2 \chi}{\partial z^2}\right.\\ \left. + \chi\frac{\partial^2 \Phi}{\partial z^2} + \left(\frac{\partial \chi}{\partial z}\right)\left(\frac{\partial \Phi}{\partial z}\right)\right] = \left(\frac{D_N}{\nu}\right)\frac{\partial^2 \chi}{\partial z^2} - \left(\frac{K_r}{d}\right)\chi\end{aligned} \tag{14}$$

along with the boundary conditions:

$$\begin{aligned}&u = x, v = y\ at\ w = 0\\ &\frac{\partial \Theta}{\partial z} = -B_{i1}(1 - \Theta), \frac{\partial \Phi}{\partial z} = -B_{i2}(1 - \Phi),\\ &\frac{\partial \chi}{\partial z} = -B_{i3}(1 - \chi)\ at\ z = 0\\ &u \to 0,\ v \to 0, \Theta \to 0, \Phi \to 0, \chi \to 0\ as\ z \to \infty\end{aligned} \tag{15}$$

LIE GROUP ANALYSIS

PDEs are difficult and computationally costly to solve numerically. The objective is to convert the PDEs in Equations (10)–(16) into ODEs. We accomplish this by converting PDEs to ODEs using the group approach. We apply the scaling group transformation in this work. Since it is difficult to solve the system of partial differentiation equations (7)–(9) with the B.C's (10) we use lie group transformations to convert the system into matching ordinary differential equations. Thus

$$\begin{aligned}&x = e^{-\varepsilon c_1}x^*, y = e^{-\varepsilon c_2}y^*, z = e^{-\varepsilon c_3}z^*, u = e^{-\varepsilon c_4}u^*,\\ &v = e^{-\varepsilon c_5}v^*, w = e^{-\varepsilon c_6}w^*, \Theta = e^{-\varepsilon c_7}\Theta^*, \Phi = e^{-\varepsilon c_8}\Phi^*,\\ &\chi = e^{-\varepsilon c_9}\chi^*\end{aligned} \tag{16}$$

Here, c_i; $1 \le i \le 9$ are arbitrary real integers that are not all zero at once, and ε is the group scaling parameter. When we enter eq. (11) into eq's. (7)-(10), we get

$$\frac{\partial u^*}{\partial x^*}\cdot e^{\varepsilon(c_1 - c_4)} + \frac{\partial v^*}{\partial y^*}\cdot e^{\varepsilon(c_2 - c_5)} + \frac{\partial w^*}{\partial z^*}\cdot e^{\varepsilon(c_3 - c_6)} = 0 \tag{17}$$

$$\begin{aligned}&\frac{u^*\partial u^*}{\partial x^*}\cdot e^{\varepsilon(c_1 - 2c_4)} + \frac{v^*\partial u^*}{\partial y^*}\cdot e^{\varepsilon(c_2 - c_4 - c_5)}\\ &+ w^*\frac{\partial u^*}{\partial z^*}\cdot e^{\varepsilon(c_3 - c_4 - c_6)} = \nu\left(1+\frac{1}{\beta}\right)\frac{\partial^2 u^*}{\partial {z^*}^2}e^{\varepsilon(2c_3 - c_4)}\\ &-[\sigma {B_0}^2/d\rho\ +\ (\nu/dk_1)\ (1\ +\ 1/\beta)\ ]e^{-\varepsilon c_4}u^*\end{aligned} \tag{18}$$

$$\begin{aligned}&\frac{u^*\partial v^*}{\partial x^*}\cdot e^{\varepsilon(c_1 - c_4 - c_5)} + \frac{v^*\partial v^*}{\partial y^*}\cdot e^{\varepsilon(c_2 - 2c_5)}\\ &+ w^*\frac{\partial v^*}{\partial z^*}\cdot e^{\varepsilon(c_3 - c_5 - c_6)} = \nu\left(1\ +\frac{1}{\beta}\right)\partial^2 v^*/\\ &\partial {z^*}^2\ e^{\varepsilon(2c_3 - c_5)} - [\sigma {B_0}^2/d\rho + (\nu/dk_1)(1+1/\beta)]e^{-\varepsilon c_5}v^*\end{aligned} \tag{19}$$

$$\begin{aligned}&u^*\left(\frac{\partial \Theta^*}{\partial x^*}\right)e^{\varepsilon(c_1 - c_4 - c_7)} + \frac{v^*\partial \Theta^*}{\partial y^*}\cdot\ e^{\varepsilon(c_2 - c_5 - c_7)}\\ &+ w^*\frac{\partial \Theta^*}{\partial z^*}\cdot\ e^{\varepsilon(c_3 - c_6 - c_7)} = [k\ /\ (\nu(\rho C_p)_f)\ ]\ (\partial^2\Theta^*/\partial {z^*}^2)\\ &e^{\varepsilon(2c_3 - c_7)} + [(\rho C_p)_p\ /\ (\rho C_p)_f]\ [\left(D_B\frac{(C_w - C_\infty)}{\nu}\right)\left(\frac{\partial \Phi^*}{\partial z^*}\right)\left(\frac{\partial \Theta^*}{\partial z^*}\right)\\ &e^{\varepsilon(2c_3 - c_7 - c_8)} + \left(D_T\frac{(T_w - T_\infty)}{(\nu\ T_\infty)}\right)\left(\frac{\partial \Theta^*}{\partial z^*}\right)^2 e^{\varepsilon(2c_3 - c_7)}]\end{aligned} \tag{20}$$

$$\begin{aligned}&u^*\left(\frac{\partial \Phi^*}{\partial x^*}\right)e^{\varepsilon(c_1 - c_4 - c_8)} + \frac{v^*\partial \Phi^*}{\partial y^*}e^{\varepsilon(c_2 - c_5 - c_8)}\\ &+ w^*\frac{\partial \Phi^*}{\partial z^*}e^{\varepsilon(c_3 - c_6 - c_8)} = \left(\frac{D_B}{\nu}\right)\left(\frac{\partial^2 \Phi}{\partial {z^*}^2}\right)e^{\varepsilon(2c_3 - c_8)}\\ &+\left(\frac{D_T(T_w - T_\infty)}{\nu\ T_\infty(C_w - C_\infty)}\right)\left(\frac{\partial^2 \Theta}{\partial {z^*}^2}\right)\ e^{\varepsilon(2c_3 - c_7)} - \left(\frac{K_r}{d}\right)e^{-\varepsilon c_8}\Phi *\end{aligned} \tag{21}$$

$$\begin{aligned}&u^*\left(\frac{\partial \chi^*}{\partial x^*}\right)e^{\varepsilon(c_1 - c_4 - c_9)} + v^*\frac{\partial \chi^*}{\partial y^*}e^{\varepsilon(c_2 - c_5 - c_9)}\\ &+ w^*\frac{\partial \chi^*}{\partial z^*}e^{\varepsilon(c_3 - c_6 - c_9)} + \left(\frac{bW_c}{\nu}\right)\left[\left(\frac{N_\infty}{N_w - N_\infty}\right)\left(\frac{\partial^2 \chi}{\partial {z^*}^2}\right)e^{\varepsilon(2c_3 - c_9)}\right]\\ &+\left(\frac{bW_c}{\nu}\right)\left[\left(\frac{\partial^2 \Phi}{\partial {z^*}^2}\right)e^{\varepsilon(2c_3 - c_8 - c_9)} + \left(\frac{\partial \chi^*}{\partial z^*}\right)\left(\frac{\partial \Phi^*}{\partial z^*}\right)e^{\varepsilon(2c_3 - c_8 - c_9)}\right]\\ &= \left(\frac{D_N}{\nu}\right)\left(\frac{\partial^2 \chi}{\partial {z^*}^2}\right)e^{\varepsilon(2c_3 - c_9)} - \left(\frac{K_r}{d}\right)e^{-\varepsilon c_9}\chi^*\end{aligned} \tag{22}$$

B.C's (10) become

$$At\ y\ =\ 0, \left(\frac{\partial \psi^*}{\partial y^*}\right) e^{\varepsilon(c_2-c_4)}\ =\ \gamma^*\ x^*\ e^{-\varepsilon(c_1+c_7)},$$
$$\left(\frac{\partial \psi^*}{\partial x^*}\right) e^{\varepsilon(c_1-c_4)} = -\left(\frac{v_w^*}{\sqrt{\nu\ b}}\right) e^{-\varepsilon(c_8)},\ e^{-\varepsilon(c_5)} g^* = 1,$$
$$D_B C_\infty \left(\frac{\partial h^*}{\partial y^*}\right) e^{\varepsilon(c_2-c_6)} + \left(\frac{D_T}{T_\infty}\right)(T_w - T_\infty)\left(\frac{\partial g^*}{\partial y^*}\right) e^{\varepsilon(c_2-c_5)} = 0, \quad (23)$$
$$and\ \left(\frac{\partial \psi^*}{\partial y^*}\right) e^{\varepsilon(c_2-c_4)} = 0,\ \left(\frac{\partial \psi^*}{\partial x^*}\right) e^{\varepsilon(c_1-c_4)} = 0,$$
$$e^{-\varepsilon(c_5)} g^* = 0,\ e^{-\varepsilon(c_6)} h^* = 0,\ as\ y \to \infty$$

The following relations has been derived from group of transformation

$$c_1\ -\ c_4\ =\ c_2\ -\ c_5\ =\ c_3\ -\ c_6 \quad (24)$$

$$c_1 - 2c_4 = c_2 - c_4 - c_5 = c_3 - c_4 - c_6 = 2c_5 - c_4 = -c_4 \quad (25)$$

$$c_3 - c_5 = c_1 + c_2 - c_4 - c_5 = 2c_2 - c_5 = 2c_2 - c_5 - c_6 = 2c_2 - 2c_5 \quad (26)$$

$$c_3 - c_6 = c_1 + c_2 - c_4 - c_6 = 2c_2 - c_6 = 2c_2 - c_5 \quad (27)$$

$$c^2\ -\ c^4\ =\ -c_1\ -\ c_7 \quad (28)$$

$$c_1\ -\ c_4\ =\ -c_8 \quad (29)$$

$$c_5\ =\ 0 \quad (30)$$

$$c_2\ -\ c_6\ =\ c_2\ -\ c_5 \quad (31)$$

Above relations give following solutions

$$c_1\ =\ c_4, c_2\ =\ 0, c_3\ =\ 0, c_5\ =\ 0, c_6\ =\ 0,\ c_7\ =\ -c_3, c_8\ =\ 0, c_9\ =\ 0 \quad (32)$$

Set of transformation reduces to

$$x = e^{-\varepsilon c_1} x^*,\ y = e^{-\varepsilon c_2} y^*, z = z^*, u = e^{-\varepsilon c_1} u^*,\ v = e^{-\varepsilon c_2} v^*,\ w = w^*, \Theta = \Theta^*, \Phi = \Phi^*, \chi = \chi^* \quad (33)$$

Using the Taylor's series to expand in the power of ε and ignoring the higher power of ε results in

$$x\ =\ x^*\ /\ (1\ +\ \varepsilon c_1)\ , y\ =\ y^*\ /\ (1\ +\ \varepsilon c_2),\ z\ =\ z^*\ /\ (1\ +\ 0), u\ =\ u^*\ /\ (1\ +\ \varepsilon c_1),\ v\ =\ v^*\ /\ (1\ +\ \varepsilon c_2), w\ =\ w^*\ /\ (1\ +\ 0) \quad (34)$$

or

$$x^* = x(1+\varepsilon c_1),\ y^* = y(1+\varepsilon c_2),\ z^* = z(1+0),\ u^* = u(1+\varepsilon c_1),\ v^* = v(1+\varepsilon c_2),\ w^* = w(1+0) \quad (35)$$

The following characteristic equations are obtained by applying Taylor's approach to extend in powers of ε while maintaining terms up to the order ε.

$$dx/(c_1 x) = dy/(c_2 y) = dz/0 = du/(c_1 u) = dv/(c_2 v) = dw/0 \quad (36)$$

On solving the above equations we obtain the similarity transformation,

$$\eta = z,\ u = x\ f'(\eta),\ v = y\ g'(\eta),\ w = -[f(\eta) + g(\eta)],\ \Theta = \Theta(\eta),\ \Phi = \Phi(\eta),\ \chi = \chi(\eta) \quad (37)$$

Equations (7)-(9) take the form O.D.E's:

$$(1+1/\beta) f''' - (f')^2 + (f+cg)\ f'' - [M + k_1(1+1/\beta)]\ f' = 0 \quad (38)$$

$$(1+1/\beta) g''' - (g')^2 + (f+cg) g'' - [M + k_1(1+1/\beta)] g' = 0 \quad (39)$$

$$\Theta'' + Pr[(f\ +\ cg)\Theta' + Nb\ \Theta'\Phi' + Nt\ (\Theta')^2] = 0 \quad (40)$$

$$\Phi'' + LePr(f+cg)\Phi' + (Nt/Nb)\Theta'' - LePr\ C_r \Phi = 0 \quad (41)$$

$$\chi'' - Pe[(\sigma + \chi)\Phi'' + \chi'\Phi'] + PrLb(f+cg)\chi' - PrLb\ C_r\ \chi = 0 \quad (42)$$

Transformed B.C's are:

$$At\ \zeta\ =\ 0;\ f(0,\tau) =\ \alpha, \frac{df}{d\zeta}(0,\tau) =\ \gamma, g(0,\tau) =\ 1,\ Nb\frac{\partial h}{\partial \zeta}(0,\tau) +\ Nt\frac{\partial g}{\partial \zeta}(0,\tau) =\ 0 \quad (43)$$
$$As\ \zeta \to \infty;\ \partial f/\partial \zeta\ (\zeta,\tau) = 0,\ g(\zeta,\tau) = 0,\ h(\zeta,\tau) = 0$$

NUMERICAL SOLUTION

System of ODE's (10)-(14) along with (15) solved numerically due to highly non-linear behavior because it is not an easy task to solve these mathematical equations containing crucial fluid parameters analytically. To solve these equations numerically, RKF-shooting algorithm is adopted by converting these equations into a set of initial value problems as shown in Figure 2.

$$f''' = 1/(1+1/\beta)[\ f'^2 - (f+cg)f'' + k_1(1+1/\beta)f' + Mf'] \quad (44)$$

$$g''' = 1/(1+1/\beta)[g'^2 - (f+cg)g'' + k_1(1+1/\beta)g' + Mg'] \quad (45)$$

$$\Theta'' = -Pr[(f+cg)\Theta' + Nb\ \Theta'\Phi' + Nt(\Theta')^2] \quad (46)$$

$$\Phi'' = -LePr(f+cg)\Phi' - (Nt/Nb)\Theta'' + LePr\ C_r\ \Phi \quad (47)$$

$$\chi'' = Pe[(\sigma+\chi)\Phi'' + \chi'\Phi'] - PrLb(f+cg)\chi' + PrLb\ C_r\ \chi \quad (48)$$

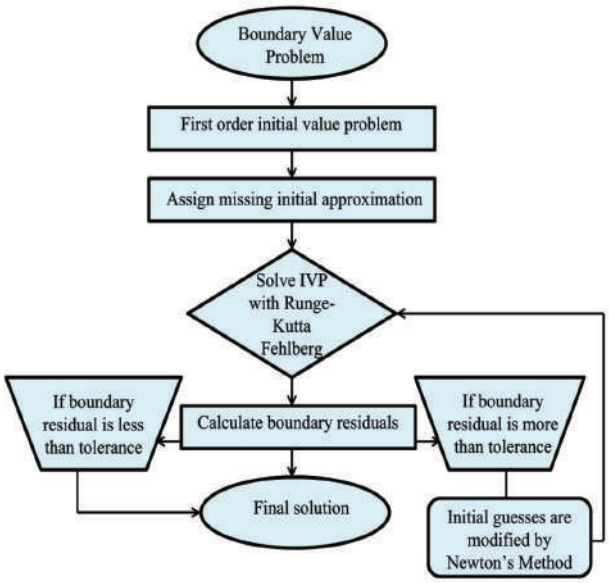

Figure 2. Flow chart of "Shooting Technique".

After being transformed into a system of first-order D.E's, the coupled differential equations are explained as follows:

$$p(1)' = p(2) \tag{49}$$

$$p(2)' = p(3) \tag{50}$$

$$p(3)' = 1/(1-\alpha {r_1}^2)[\, {r_2}^2 + M\, r_2 - (1+\beta M)\, r_1\, r_3 - 2\alpha_1\, r_1\, r_2\, r_3\,] \tag{51}$$

$$p(4)' = p(5) \tag{52}$$

$$p(5)' = p(6) \tag{53}$$

$$p(6)' = 1/(1-\alpha {r_1}^2)[\, {r_2}^2 + M\, r_2 - (1+\beta M)\, r_1\, r_3 - 2\alpha_1\, r_1\, r_2\, r_3\,] \tag{54}$$

$$p(7)' = p(8) \tag{55}$$

$$p(8)' = -(3/(3+4N_r))[\, Pr\, r_1 r_5 + PrNb\, r_5 r_7 + PrNt\, {r_5}^2 + Pr\lambda\, r_4\,] \tag{56}$$

$$p(9)' = p(10) \tag{57}$$

$$p(10)' = -Le\, r_1 r_7 - (Nt/Nb)\, r_5{}' + Le\beta\, r_6 \tag{58}$$

$$p(11)' = p(12) \tag{59}$$

$$p(12)' = -Le\, r_1 r_7 - (Nt/Nb)\, r_5{}' + Le\beta\, r_6 \tag{60}$$

with the initial conditions $p_1 = \alpha,\ p_2 = \gamma,\ p_3 = x(1), p_4 = 1,\ p_5 = x(2)$
where

$$\begin{gathered} f = p(1), f' = p(2), f'' = p(3), f''' = p(3)' \\ g = p(4), g' = p(5), g'' = p(6), g''' = p(6)' \\ \Theta = p(7), \Theta' = p(8), \Theta'' = p(8)' \\ \Phi = p(9), \Phi' = p(10), \Phi'' = p(10)' \\ \chi = p(11), \chi' = p(12), \chi'' = p(12)' \end{gathered} \tag{61}$$

RESULTS AND DISCUSSION

In present analysis, numerical scheme is validated as calculated results for -$\Theta'(0)$ are compared with Abolbashari et al. [42], Gorla and Sidawi [43], Mankinde and Aziz [44] and Khan and Pop [45] for controlling fluid parameter *Pr* in the absence of magnetohydrodynamic flow (See Table 1). Additionally, bar graph has been plotted for these values as well to seen accuracy of the numerical technique (See Figure 3). It is observed that results obtained are highly accurate when compared with the existing literature outcomes. Moreover, Table 2-5 represents the resulting outcomes of ($f''(0), g''(0)$), -$\Theta'(0)$, -$\Phi'(0)$, and -$\chi'(0)$ respectively for fixed values of controlling fluid parameters $Pe = 0.1$, $\kappa = 0.5$, $Lb = 0.5$, $Bi_3 = 0.1$, $Bi_1 = 0.4$, $Bi_2 = 0.1$, $K_1 = 0.1$, $C_r = 0.7$, $\beta = 0.1$, $M = 1.5$, $Pr = 1.732$, $Nb = 0.1$, $Nt = 0.5$, $Le = 2.0$ along with CPU time observed in seconds.

Table 1. A comparison for -$\Theta'(0)$ against *Pr*

Pr	Abolbashari et al. [42]	Residual error	Gorla and Sidawi [43]	Residual error	Mankinde and Aziz [44]	Residual error	Khan and Pop [45]	Residual error	Present Results
0.7	0.4539	-0.00055	0.5349	-0.00055	0.4539	-0.00055	0.4539	-0.00055	0.45445
2.0	0.9114	-0.00055	0.9114	-0.00055	0.9114	-0.00055	0.9113	-0.00005	0.91135
7.0	1.8954	0.00000	1.8905	-0.00490	1.8954	0.00000	1.8954	0.00000	1.89540
20.0	-	-	3.3539	0.00000	-	-	3.3539	0.00000	3.35390
70.0	-	-	6.4622	0.00001	-	-	6.4621	-0.00009	6.46219

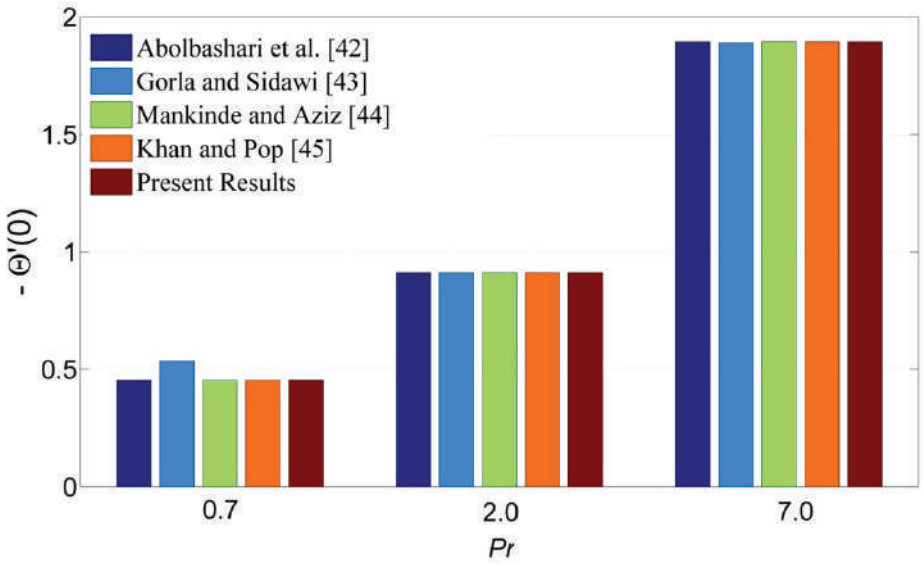

Figure 3. Bar Graph showing comparison of resulting outcomes for $-\Theta'(0)$ against three different values of Prandtl number as 0.7, 2.0 and 7.0 with those of Abolbashari et al. [42], Gorla and Sidawi [43], Mankinde and Aziz [44] and Khan and Pop [45]. [Created by authors]

Velocity Distribution

Figure 4(a)-4(f) elucidates the axial $f'(\xi)$ and transverse $g'(\xi)$ velocity distribution against crucial fluid parameters namely magnetic parameter M, Casson fluid parameter β and permeability parameter K_1 in direction of x and y-axis. Figure 4(a) and 4(b) manifests the variation in velocity distribution $f'(\xi)$ and $g'(\xi)$ against the parameter M in the range 1.5-3.5. These graphs show that with augmentation in the values of M, velocity profile falls slowly with a small variation due to produced Lorentz drag force. Additionally, it has been noticed that both the magnitude as well as width of boundary layer of $f'(\xi)$ and $g'(\xi)$ lessens with enhancement in M as shown in Figures 4(a) and 4(b) serially.

Also, Figures 4(c) and 4(d) shows the variation in velocity under the impact of Casson fluid parameter for

Table 2. Values of Cf_x and Cf_y for precised entries of M, β and K_1 with CPU time in seconds

M	β	K_1	Cf_x	Cf_y	CPU Time (In Seconds)
1.5			-0.624727	-0.671375	6.273146
2.0			-0.659909	-0.704250	9.130985
2.5			-0.693344	-0.735688	18.056714
3.0			-0.725266	-0.765856	20.579231
3.5			-0.755859	-0.794896	23.093199
	0.1		-0.624727	-0.671375	6.318504
	0.3		-0.915383	-0.995628	44.357009
	0.5		-1.079947	-1.178022	9.799734
	0.7		-1.190544	-1.300355	10.196454
	0.9		-1.271079	-1.389346	21.929840
		0.1	-0.624727	-0.671375	6.292501
		0.2	-0.699843	-0.741818	19.204972
		0.3	-0.767759	-0.806223	15.034273
		0.4	-0.830195	-0.865899	30.920958
		0.5	-0.888286	-0.921749	35.860811

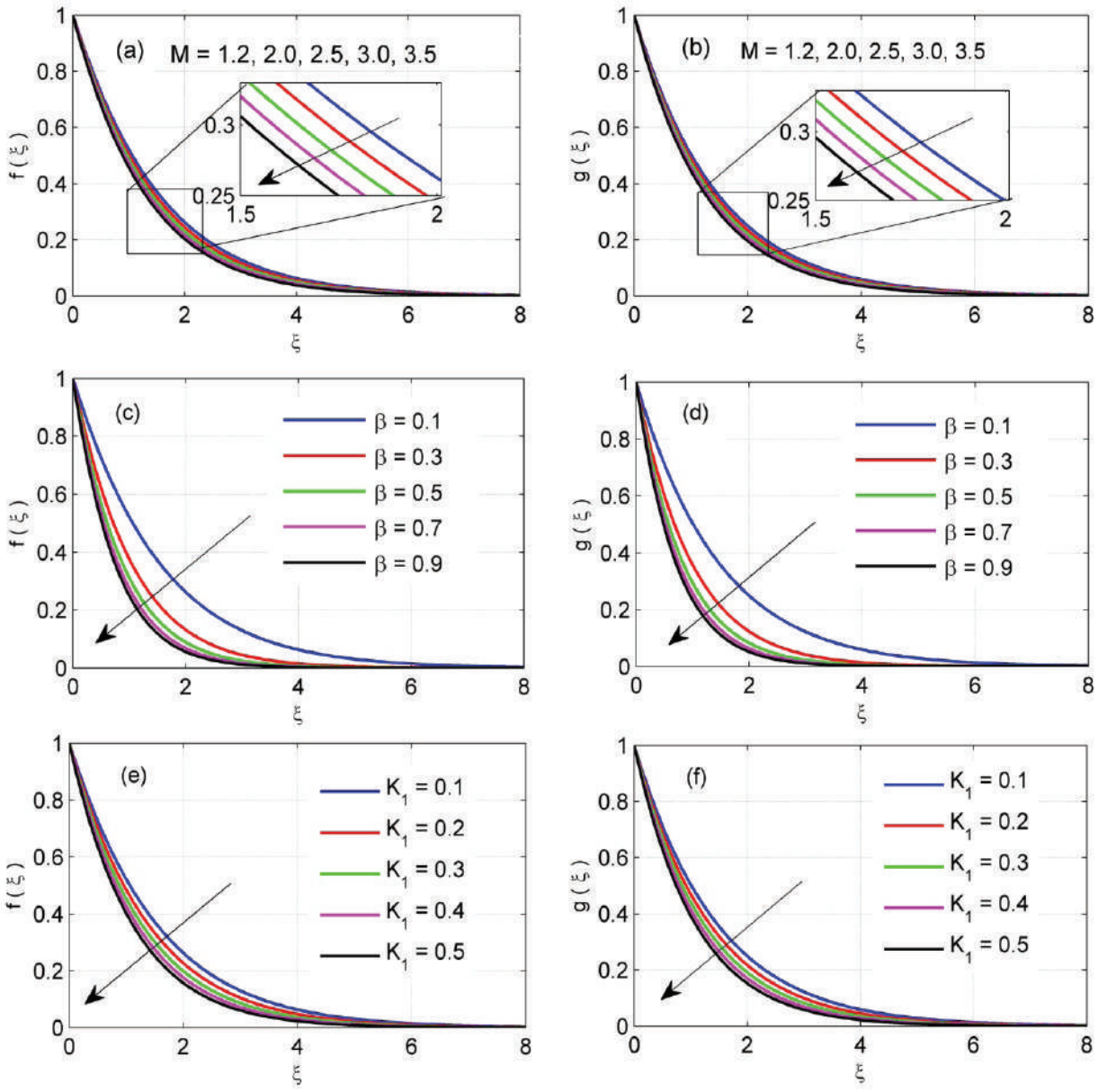

Figure 4. Axial and Transverse velocity distribution against (a, b) Magnetic parameter M ($1.2 \leq M \leq 3.5$), (c, d) Casson fluid parameter β ($0.1 \leq \beta \leq 0.9$) and (e, f) permeability parameter K_1 ($0.1 \leq K_1 \leq 0.5$.

β = 0.1, 0.3, 0.5, 0.7, 0.9. . Same behavior of velocity has been noticed i.e. declines for higher β in both the graphs like magnetic parameter and permeability parameter K_1. Reason behind declination in fluid velocity is the shear stress which is highly produced in non-Newtonian fluid when compared with Newtonian fluids. As Casson fluid is considered as non-Newtonian thus produces high stress and fluid resistance. Hence, this more non-Newtonian behavior helps in reduction of fluid velocity. Furthermore, the influence of permeability parameter K_1 ($0.1 \leq K_1 \leq 0.5$) over velocity profile has been illustrated via Figures 4(e) and 4(f) respectively. Both the velocity profiles i.e. axial and transverse declines when K_1 rises due to presence of more nanofluid far from boundary which shows the reduction in boundary layer thickness for both $f'(\xi)$ and $g'(\xi)$.

Temperature Distribution

Figure 5(a)-5(d) represent the variation in temperature against controlling fluid parameters especially Brownian motion parameter Nb in the range 0.1-5.0, thermophoresis parameter in the range 0.5-2.5, thermal Biot number in the range 0.1-2.0 and Prandtl number in the range 0.732-20. Figure 5(a) exhibits the nanoparticle

temperature profile $\Theta(\xi)$ for *Nb*. As Brownian motion is the random motion of poised particles which is produced by the collision of pendulous particles in the fluid that simultaneously helps to rise the boundary layer thickness. Consequently, higher values of *Nb* enhances nanoparticles movement that increases kinetic energy and hence temperature field rises (See Figure 5(a)) and local Nusselt number reduces (See Table 3). Moreover, larger values of *Nb* thickens the thermal boundary layer. Variation in the profile of temperature against thermophoresis *Nt* is sketched via Figure 5(b). This figure elaborates that, higher *Nt* ($0.5 \leq Nt \leq 2.5$) makes movement of nanoparticles from hot to cold zone due to temperature gradient and demonstrate stronger thermophoretic force that consequently mounting temperature profile. Further, Figure 5(c) manifests the impact of Biot number Bi_1 over nanoparticle temperature field. With increase in Bi_1, a rapid augmentation in fluid temperature is observed near the boundary. In addition, convective heating of 3D permeable sheet rises with rise in thermal Biot number. Moreover, it is observed that all plots are declines distinctly upto $\xi = 2.6$ in approx manner and convergence meets to $\xi \to \infty$. Variation in temperature distribution $\Theta(\xi)$ under influence of Prandtl number *Pr* is illustrated via Figure 5(d) and the corresponding values of local Nusselt number for *Pr* at 0.732, 7, 10, 15 and 20 are shown in Table 3. *Pr* is characterized as the ratio of two controlling parameters namely; momentum and thermal diffusivity. Nature of *Pr* is opposite to the *Nb* and *Nt* i.e. rate of thermal diffusion declines in case of higher Prandtl number due to viscous diffusion at higher level which is the main reason thinning of thermal boundary layer.

Concentration Distribution

Concentration profile for Brownian motion *Nb* varies from 0.1-5.0, thermophoresis *Nt* varies from0.5-2.5, concentration Biot number Bi_2 varies from 1.0-5.0, Prandtl number *Pr* varies from 0.732-20, Lewis number *Le* varies from 1.0-20.0 and chemical reaction parameter C_r varies from 0.0-4.0 are depicted graphically via Figures 6(a)-6(f). Figure 6(a) examines the variation in nanofluid concentration field under the impact of *Nb* for five different values of *Nb* as 0.1, 1.0, 2.0, 3.0, and 5.0. Concentration profile for Brownian motion *Nb* varies from 0.1-5.0, thermophoresis *Nt* varies from 0.5-2.5, concentration Biot number Bi_2 varies from 1.0-5.0, Prandtl number *Pr* varies from0.732-20, Lewis number *Le* varies from 1.0-20.0 and chemical reaction parameter C_r (varies from 0-4.0 are depicted graphically via Figures 6(a)-6(f). Figure 6(a) examines the variation in nanofluid concentration field under the impact of *Nb* for five different values of *Nb* as 0.1, 1.0, 2.0, 3.0, and 5.0. Augmentation in *Nb* will reduces the nanoparticle concentration and in consequence

Table 3. Values of Nu_x for precised entries of *Nb*, *Nt*, Bi_1, and *Pr* with CPT time (in seconds)

Nb	*Nt*	Bi_1	*Pr*	Nu_x	CPU Time (In Seconds)
0.1				-0.283901	6.089723
1				-0.282024	6.054968
2				-0.279908	6.082267
3				-0.277759	7.164895
5				-0.273362	6.218876
	0.5			-0.283901	6.278092
	1			-0.279169	6.280475
	1.5			-0.274205	6.545353
	2			-0.269000	7.345515
	2.5			-0.263548	10.054311
		0.1		-0.091039	6.255517
		0.5		-0.329829	6.191972
		1		-0.484207	6.356057
		1.5		-0.570896	7.425508
		2		-0.625831	9.700599
			0.732	-0.284022	6.151001
			7	-0.350411	7.310118
			10	-0.355914	7.699206
			15	-0.360854	8.515512
			20	-0.363515	9.228643

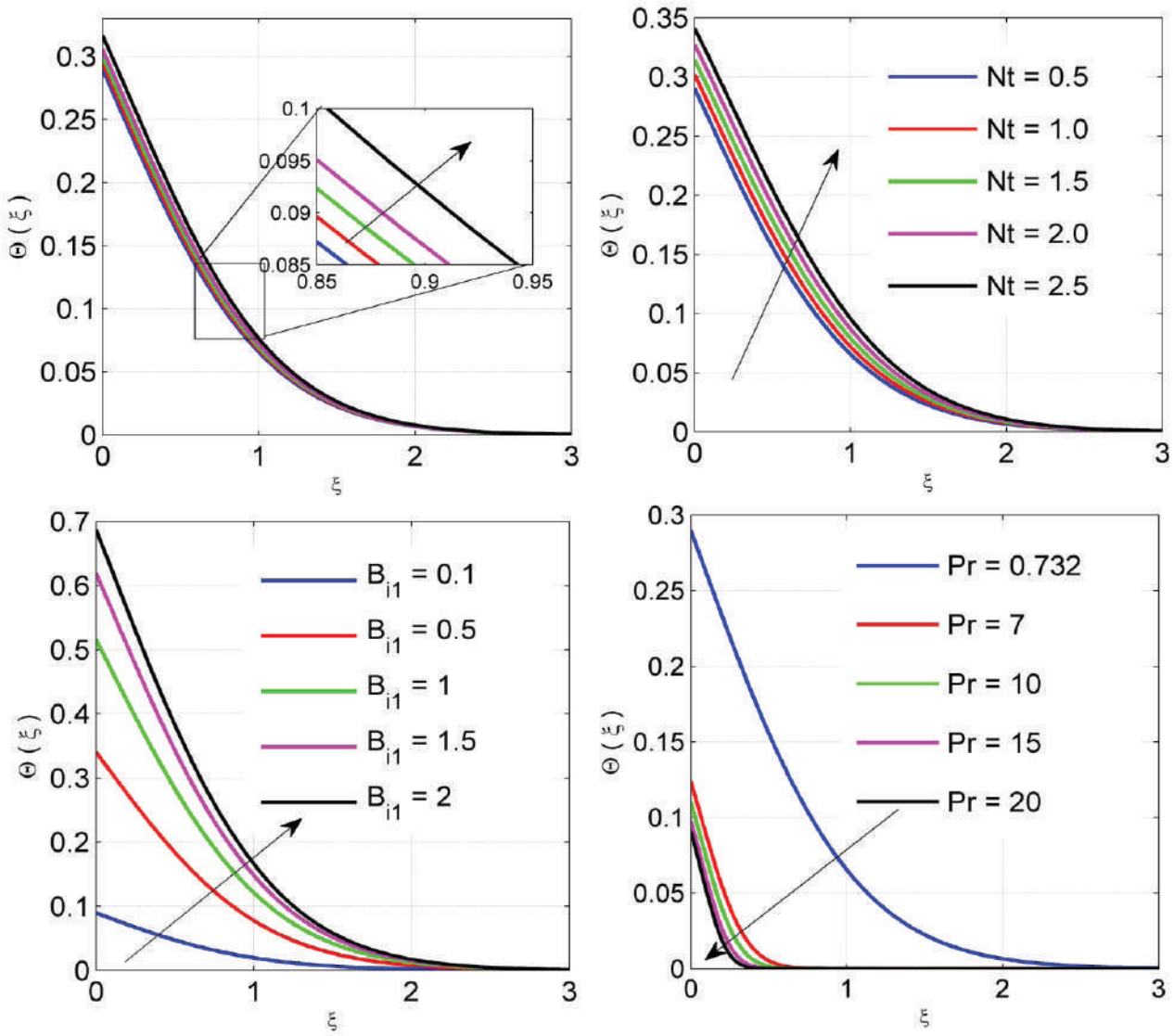

Figure 5. Temperature distribution against (a) Nb ($0.1 \leq Nb \leq 5.0$), (b) Nt ($0.5 \leq Nt \leq 2.5$), (c) Bi_1 ($0.1 \leq Bi_2 \leq 2.0$) and Pr ($0.732 \leq Pr \leq 20.0$).

solutal boundary layer thickness falls down. Additionally, slightly increase in Sherwood number is observed with enhancement in Nb as seen in Table 4. Also, the influence of Nt over nanoparticle concentration distribution is illustrated through Figure 6(b). This figure elaborates that higher Nt rises the mass distribution or concentration of the fluid. Physically, temperature gradient gives mass field and this Nt parameter makes temperature to be a mounting function of Nt. Thusly, an enhancement in mass and mass boundary layer thickness has been noticed with enhancement in Nt. Figure 6(c) illustrates the impact of concentration Biot number Bi_2 ($1.0 \leq Bi_2 \leq 5.0$) over nanoparticle concentration field. This figure shows that, concentration of nanofluid rises with rise in Bi_2. Because higher Biot number will enhances convective heating at the surface of three dimensional stretching sheet. As mass field is influences via energy field, one explained that a deeper mass dispersion is observed for higher Bi_2 values and can be seen in Figure 6(c). Additionally, all plots of the figure falls distinctly upto $\xi = 3$ (approximately) and follows convergence criterion. Effect of Pr over nanoparticle concentration has been illustrated via Figure 6(d). As Pr is inversely proportional to thermal diffusivity which indirectly leads to enhance value of Prandtl number with lower diffusivity value and in consequence plays a major role in declination of temperature and concentration of the nanofluid. Hence, higher Pr declines concentration and simultaneously helps to increase local Sherwood number

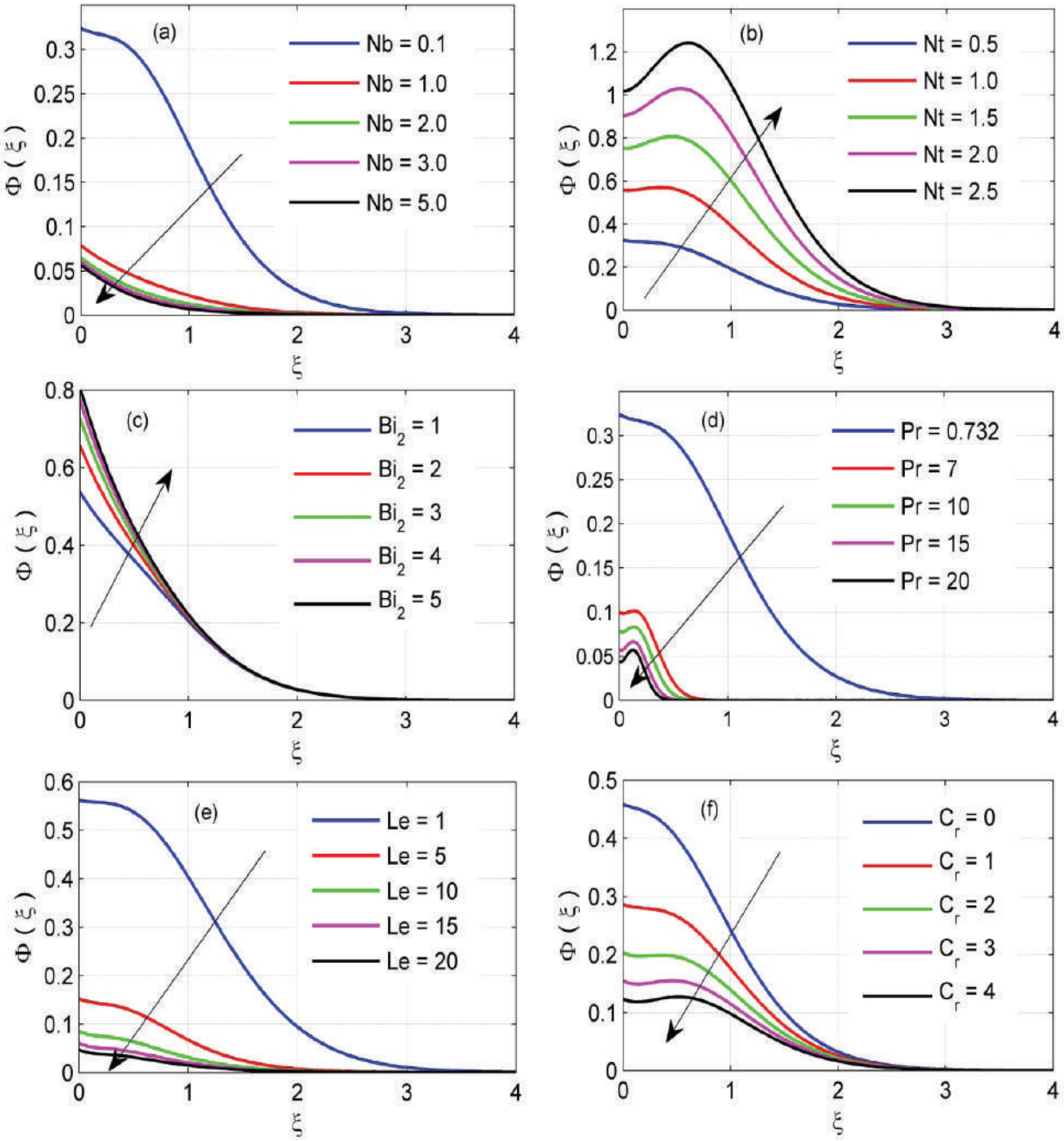

Figure 6. Concentration distribution against (a) *Nb* ($1.0 \le Nb \le 5.0$), (b) *Nt* ($0.5 \le Nt \le 2.5$), (c) Bi_2 ($1.0 \le Bi_2 \le 5.0$) and *Pr* ($0.732 \le Pr \le 20.0$), (e) *Le* ($1.0 \le Le \le 20$ and (*f*) C_r ($0.0 \le C_r \le 4.0$).

as shown in Table 4. Lewis number is the ratio of α (thermal diffusivity) and D_B (Brownian diffusion coefficient) i.e. inversely proportional to D_B which in consequence shows that higher *Le* corresponds to lower D_B. Hence, nanoparticle concentration reduces for greater *Le* ($1.0 \le Le \le 20.0$) as seen in Figure 6(e) and respective Sherwood number rises as seen in Table 4. Nanoparticle concentration is mainly influenced by chemical reaction. In present analysis, chemical reaction of first order is discussed and is displayed via Figure 6(f). This figure elaborates that nanoparticle concentration decays with advancement in C_r and follows boundary conditions away from the surface, which in turns, becomes stable.

Density of motile micro-organism distribution against controlling fluid parameters especially Peclet number *Pe* in the range 0.1-10.0, micro-organism concentration

difference parameter in the range0.1-5.0, bio-convective Lewis number in the range 0.1-0.9, chemical reaction in the range 0-4.0, micro-organism Biot number in the range 1-10 and Prandtl number in the range 0.732-20 is visualized in Figure 7(a)-7(f) serially. Figure 7(a) elucidates the impact of Peclet number *Pe* on motile density $\chi(\xi)$. This plot shows that, with increase in values of *Pe* ($0.1 \leq Pe \leq 10.0$), fluid particles moves freely leads to thickens micro-organism and hence reduces the motile density of micro-organisms. Moreover, graphs are distinct within $0.0 \leq \xi \leq 5.0$ in approx manner and after that they meet and converges as $\xi \to \infty$ by following boundary conditions. variation in gyrotactic micro-organism density $\chi(\xi)$ against micro-organism concentration difference parameter κ is sketched via Figure 7(b). It is observed from the figure that $\chi(\xi)$ declines for higher values of κ because of lower micro-organism concentration difference between N_w & N_∞ and their respective local wall motile micro-organism number has same nature as that of $\chi(\xi)$ i.e. declines with augmentation in κ as seen in Table 5.

Figure 7(c) manifests the motile density against bio-convective Lewis number *Lb*. As bio-convective Lewis number is inversely proportional to the micro-organisms diffusivity D_N, which in turn enhances *Lb* value with lower D_N and hence reduces the micro-organism density of nanofluid flow as seen in Figure 7(c). However, local wall motile micro-organism number Mn_x mounting as visualized in Table 5. Also, the impact of chemical reaction parameter C_r ($0 \leq C_r \leq 4$) over motile micro-organism distribution is illustrated via Figure

Table 4. Values of Sh_x for precised entries of *b*, *Nt*, Bi_2, *Pr*, *Le* and C_r with CPU time (in seconds)

Nb	*Nt*	Bi_2	*Pr*	*Le*	C_r	Sh_x	CPU Time (In Seconds)
0.1						-0.067573	6.089723
1						-0.092147	6.054968
2						-0.093512	6.082267
3						-0.093968	7.164895
5						-0.094333	6.218876
	0.5					-0.067573	6.278092
	1					-0.044243	6.280475
	1.5					-0.024887	6.545353
	2					-0.009578	7.345515
	2.5					0.001638	10.054311
		1				-0.462481	6.229663
		2				-0.684838	7.301691
		3				-0.815543	7.113896
		4				-0.901580	7.242372
		5				-0.962506	7.291741
			0.732			-0.067611	6.151001
			7			-0.090030	7.310118
			10			-0.092146	7.699206
			15			-0.094238	8.515512
			20			-0.095561	9.228643
				1		-0.043871	6.373926
				5		-0.084811	6.177161
				10		-0.091558	6.470720
				15		-0.094015	9.267156
				20		-0.095304	14.788844
					0	-0.054220	6.968463
					1	-0.071371	7.538299
					2	-0.079754	11.180259
					3	-0.084577	15.477882
					4	-0.087651	24.767878

Motile Density Micro-Organism Distribution							
Pe	***κ***	***Lb***	C_r	Bi_3	***Pr***	Nh_x	**CPU Time (In Seconds)**
0.1						-0.089503	13.406621
1						-0.089410	15.257320
5						-0.091353	15.404992
7						-0.093223	17.983860
10						-0.096468	18.528993
	0.1					-0.089553	12.491580
	1					-0.089441	14.797041
	2					-0.089317	12.557861
	3					-0.089193	12.693556
	5					-0.088946	12.598996
		0.1				-0.077483	13.025669
		0.3				-0.086515	13.092459
		0.5				-0.089503	13.029538
		0.7				-0.091115	13.088236
		0.9				-0.092160	12.683444
			0			-0.087098	6.968463
			1			-0.090203	7.538299
			2			-0.091818	11.180259
			3			-0.092832	15.477882
			4			-0.093541	24.767878
				1		-0.461563	5.972003
				2		-0.600167	7.342002
				5		-0.732066	7.312585
				7		-0.764051	8.398161
				10		-0.789935	8.662353
					0.732	-0.089518	6.151001
					7	-0.096669	7.310118
					10	-0.097234	7.699206
					15	-0.097766	8.515512
					20	-0.098086	9.228643

7(d). Gyrotactic micro-organism distribution $\chi(\xi)$ is also influenced by chemical reaction C_r as that of nanoparticle concentration profile. Thus a decay in motile concentration is observed with enhancement in C_r. Further, Figure 7(e) represents the variation of $\chi(\xi)$ under the influence of micro-organism Biot number Bi_3 and it shows that motile density rises with rise in Bi_3 from 1.0-10.0. Consequently, intensification in local wall motile micro-organism number is noticed for higher Bi_3 (See Table 5). Figure 7(f) portraits the variation in motile density of micro-organism $\chi(\xi)$ against Prandtl number. This figure elucidates that $\chi(\xi)$ drops down suddenly when Prandtl varies from 0.732-7 and then decreases slowly from $7 \leq Pr \leq 20$. Overall reduction in $\chi(\xi)$ is observed for higher Prandtl value as seen in Figure 7(f) and their respective Mn_x increases as shown in Table 5. Additionally, graph meets its convergence criterion at $\xi = 3$ (approximately) as clearly visualized in the figure.

Local Skin Friction, Nusselt Number, Sherwood Number & Wall Motile Micro-Organism

Figure 8(a) and 8(b) examines the impact of $f''(0)$ and $g''(0)$ against controlling parameters β $(0.1 \leq \beta \leq 0.5)$ and M $(1.5 \leq M \leq 3.5)$. It is observed from the figures that, higher β declines skin friction at the wall monotonically and in addition more magnetism helps to decrease the value of skin friction as well. This is due to the reason that larger magnetism and non-Newtonian fluid reduces the velocity profile which ultimately helps to reduce skin friction coefficient as depicted in both the graphs.

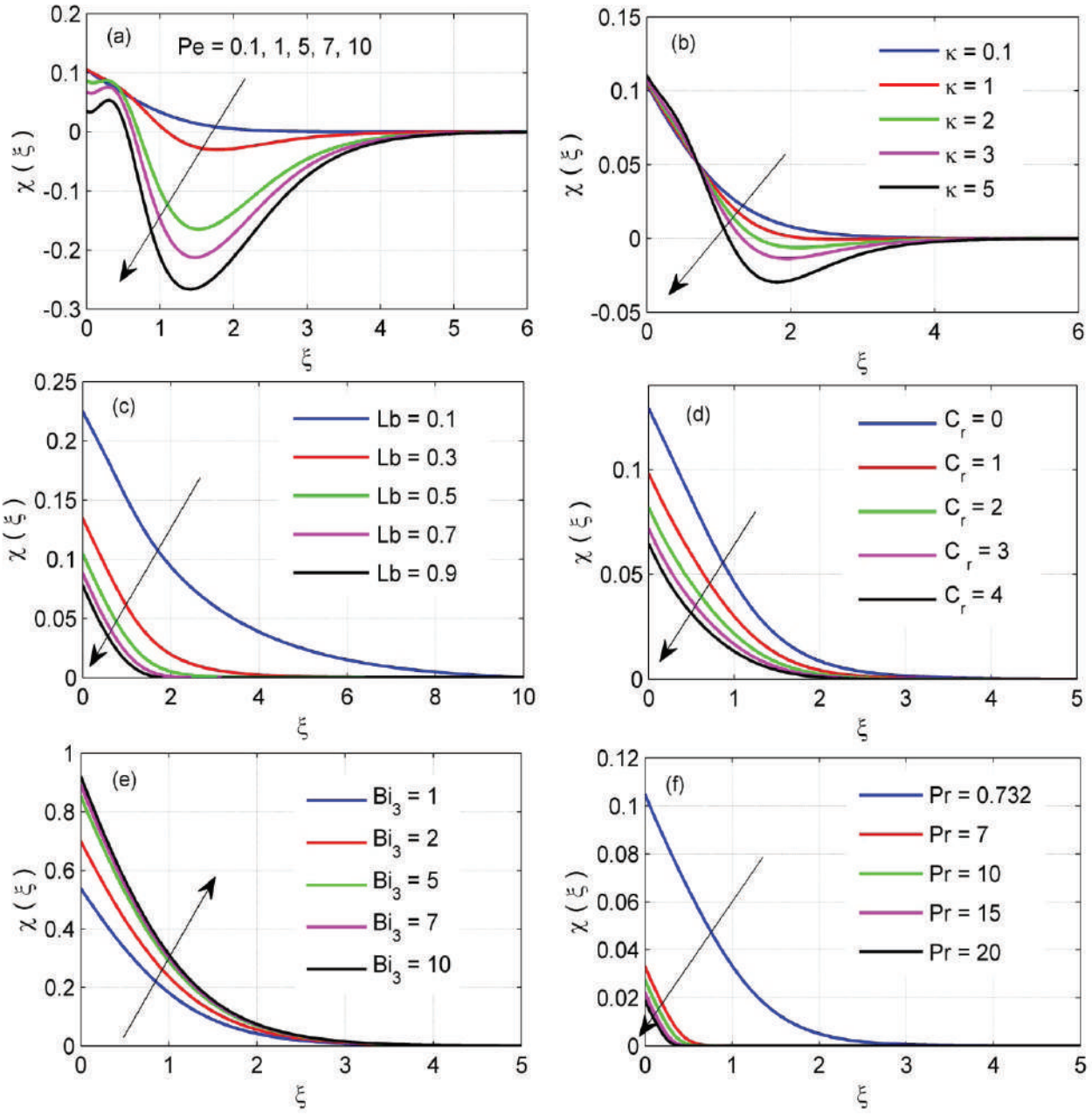

Figure 7. Motile density micro-organism distribution against (a) Pe ($0.1 \le Pe \le 10.0$), (b) κ ($1.0 \le \kappa \le 5.0$), (c) Lb ($0.1 \le Lb \le 0.9$), (d) C_r ($0 \le C_r \le 4$), (e) Bi_3 ($1 \le Bi_3 \le 10$) and (f) Pr ($0.732 \le Pr \le 20.0$).

The combined influence of Brownian motion Nb ($1 \le Nb \le 5.0$) and thermal Biot number Bi_1 ($0.5 \le Bi_1 \le 0.6$ over $-\Theta'(0)$ is elucidates via Figure 8(c). Nb and Bi_1 shows reverse impact on $-\Theta'(0)$ i.e. higher enhances $-\Theta'(0)$ due to convective heating whereas higher Nb reduces $-\Theta'(0)$ due to fast collision of nanoparticles. Also, the impact of Prandtl number Pr ($1 \le Pr \le 5$) and concentration Biot number Bi_2 ($1 \le Bi_2 \le 5$) on $-\Phi'(0)$ is sketched via Figure 8(d). Both the controlling fluid parameters Pr and Bi_2 enhances value of $-\Phi'(0)$ as clearly visualized in Figure 8(d). Combined impact of Peclet number Pe ($1 \le Pe \le 5.0$) and κ ($0.1 \le \kappa \le 0.5$) over $-\chi'(0)$ is shown by Figure 8(e) and it is observed that $-\chi'(0)$ decreases with increase in κ while rises with rise in Pe. Figure 8(f) manifests the variation in $-\chi'(0)$ against bio-convection Lewis number Lb ($0.1 \le Lb \le 0.9$) and chemical reaction C_r ($0 \le C_r \le 1$). Both the parameters enhance wall motile micro-organism number with their higher values.

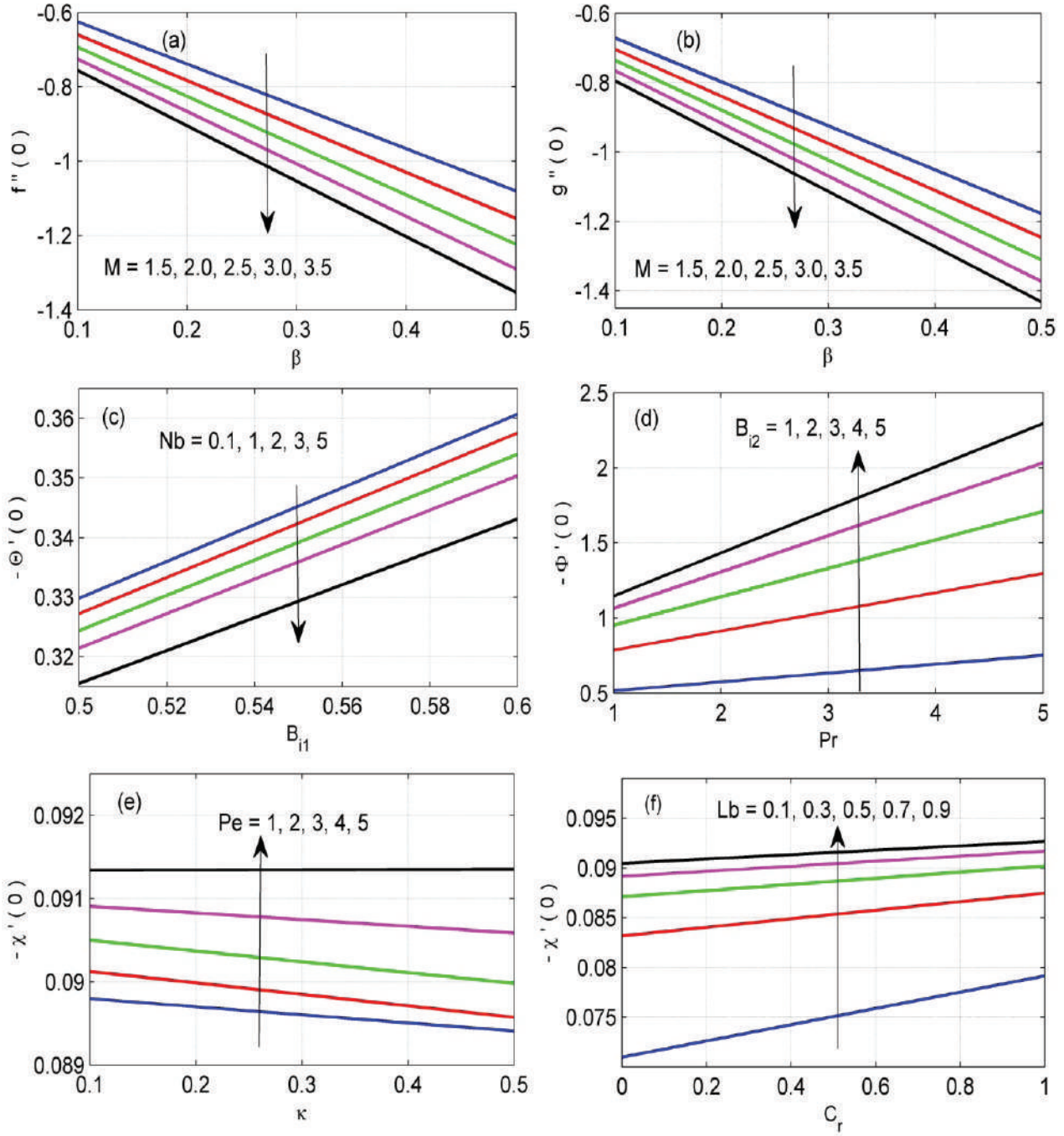

Figure 8. Graph for (a) $f''(0)$ against M & β, (b) $g''(0)$ against M & β, (c) $-\Theta'(0)$ against Nb & Bi_1, (d) $-\Phi'(0)$ against Bi_2 & Pr, (e) $-\chi'(0)$ against Pe & κ and (f) $-\chi'(0)$ against Lb & C_r.

CONCLUSION

This investigation deals with 3D flow consisting of nanoparticles along with gyrotactic microorganisms and bioconvective chemical reaction. Final outcomes of current research are summarized as:

- Horizontal velocity $f'(\xi)$ as well as transversal velocity $g'(\xi)$ declines with inclination in the values of M, β and K_1.
- Augmentation in temperature profile is noticed for greater thermal Biot number Bi_1 whereas higher Prandtl number Pr helps to falls temperature $\Phi(\xi)$.
- Concentration profile $\Phi(\xi)$ declines with higher C_r, Le, Pr, Nb. On the other hand, higher Bi_2 and Nt amplifies concentration field.

- Higher values of crucial fluid parameter Pe and κ de-escalates the motile concentration of micro-organisms.
- Skin friction coefficients $f''(0)$ & $g''(0)$ drop-off under the combined influence of controlling fluid parameters magnetic parameter M and Casson parameter β. Local wall motile micro-organism number accelerates with Lb and lessens with κ.
- Motile density Biot number falls down by 41.57% with augmentation in value of gyrotactic microorganism Biot number ranging from 1.0-10.0.

Current research can be extended for various non-Newtonian fluids by utilizing porous medium, Stefan blowing impact, entropy generation, viscous dissipation, etc.

NOMENCLATURE

x, y Cartesian coordinates
C_w Nanoparticle volume fraction (Kgm^{-3})
C Concentration (Kgm^{-3})
L Characteristic length
Le Lewis number
c Stretching parameter
β Casson fluid parameter
B_0 Magnetic field intensity (T)
Bi_3 Motile microorganism Biot number
Nu_x Nusselt number
q_m Mass flux
Nt Thermophoresis parameter
M Magnetic field parameter (Tesla)
u Horizontal velocity
C_∞ Ambient nanoparticle volume fraction (Kgm^{-3})
q_w Heat flux ($W^{-2}m$)
T_w Temperature at the sheet (K)
Bi_2 Concentration Biot number
D_T Thermophoresis diffusion coefficient (m^2s^{-1})
u_w Stretching velocity
T Temperature (K)
Nb Brownian motion parameter (m^2s^{-1})
D_B Brownian diffusion coefficient
v Vertical velocity (ms^{-1})
Sh_x Sherwood number
Pr Prandtl number
T_∞ Ambient temperature (K)
Lb Bioconvective Lewis number
Bi_1 Thermal Biot number
K_1 Permeability parameter
Mn_x Local wall motile microorganism number
Pe Peclet number

Greek symbols
ν kinematic viscosity (m^2s^{-1})
β Casson fluid parameter
σ Velocity slip parameter
ξ Similarity variable
χ Non-dimensional motile concentration
ρ_f Density of base fluid (Kgm^{-3})
Φ Non-dimensional concentration
Θ Non-dimensional temperature
τ Ratio of heat capacities
α Thermal diffusivity

Subscripts
∞ Ambient condition
p Particle
f Fluid
w Wall
Superscript
$'$ Prime denotes derivative w.r.t to ξ

AUTHORSHIP CONTRIBUTIONS

Authors equally contributed to this work.

DATA AVAILABILITY STATEMENT

The authors confirm that the data that supports the findings of this study are available within the article. Raw data that support the finding of this study are available from the corresponding author, upon reasonable request.

CONFLICT OF INTEREST

The author declared no potential conflicts of interest with respect to the research, authorship, and/or publication of this article.

ETHICS

There are no ethical issues with the publication of this manuscript.

STATEMENT ON THE USE OF ARTIFICIAL INTELLIGENCE

Artificial intelligence was not used in the preparation of the article.

REFERENCES

[1] Usman M, Amin S, Saeed A. Magnetohydrodynamic hybrid nanofluid flow with the effect of Darcy–Forchheimer theory and slip conditions over an exponential stretchable sheet. Adv Mech Eng 2022;14. [CrossRef]

[2] Asghar A, Ying TY, Zaimi K. Two-dimensional magnetized mixed convection hybrid nanofluid over a vertical exponentially shrinking sheet by thermal radiation, joule heating, velocity and thermal slip conditions. J Adv Res Fluid Mech Therm Sci 2022;95:159–179. [CrossRef]

[3] Haque MM, Alam MS, Huda MN, Rahman MM. Statistical and Numerical Investigations of Convective Heat Transfer Enhancement of Nanofluids Inside a Rectotrapezoidal Enclosure in

the Presence of Horizontal Periodic Magnetic Field. Arab J Sci Eng 2024;1–24. [CrossRef]

[4] Bilal M, Waqas M, Shafi J, Rahman MU, Eldin SM, Alaoui MK. Energy transmission through radiative ternary nanofluid flow with exponential heat source/sink across an inclined permeable cylinder/plate: numerical computing. Sci Rep 2023;13:22204. [CrossRef]

[5] Algehyne EA, Areshi M, Saeed A, Bilal M, Kumam W, Kumam P. Numerical simulation of bioconvective Darcy Forchhemier nanofluid flow with energy transition over a permeable vertical plate. Sci Rep 2022;12:3228. [CrossRef]

[6] Takreem KM, Narayana PVS. Nanoparticle Shape-Factor Analysis on Radiative Ternary Nanofluid (Mwcnt- Cu- Sio 2/H 2 O) Flow with Non-Fourier Thermal Flux. J Porous Media 2025;28. [CrossRef]

[7] Rafique E, Iram A, Jahan S, Sohail M, Sherif ESM. Bio-convective flow of non-Newtonian Williamson nanofluid model with heat generation and thermal radiation aspects past over a stretched porous sheet via OHAM. Multiscale Multidiscip Model Exp Des 2025;8:45. [CrossRef]

[8] Afzal F, Kamran T. Advanced heat transfer analysis of 3D magnetohydrodynamic nanofluid flow over an extending sheet with thermal radiation and internal heat generation/absorption. Multiscale Multidiscip Model Exp Des 2025;8:113. [CrossRef]

[9] Atofarati EO, Sharifpur M, Huan Z. Nanofluids for heat transfer enhancement: a holistic analysis of research advances, technological progress and regulations for health and safety. Cogent Eng 2024;11:2434623. [CrossRef]

[10] Jubair S, Ali B, Rafique K, Mahmood Z, Emam W. Numerical simulation of hybrid nanofluid flow with homogeneous and heterogeneous chemical reaction across an inclined permeable cylinder/plate. Energy Explor Exploit 2024;42:2270–2288. [CrossRef]

[11] Casson N. Flow equation for pigment-oil suspensions of the printing ink-type. Rheology of disperse systems 1959;84–104.

[12] Rao PS, Prakash O, Mishra SR, Sharma RP. Similarity solution of three-dimensional MHD radiative Casson nanofluid motion over a stretching surface with chemical and diffusion-thermo effects. Heat Transf 2020;49:1842–1862. [CrossRef]

[13] Ramamoorthy M, Pallavarapu L. Radiation and Hall effects on a 3D flow of MHD Williamson fluid over a stretchable surface. Heat Transf 2020;49:4410–4426. [CrossRef]

[14] Makkar V, Poply V, Goyal R, Sharma N. Numerical investigation of mhd casson nanofluid flow towards a non linear stretching sheet in presence of double-diffusive effects along with viscous and ohmic dissipation. J Therm Eng 2021;7:1–17. [CrossRef]

[15] Megahed AM. Williamson fluid flow due to a non-linearly stretching sheet with viscous dissipation and thermal radiation. J Egypt Math Soc 2019;27:12. [CrossRef]

[16] Zeeshan A, Khan MI, Ellahi R, Marin M. Computational intelligence approach for optimising MHD Casson ternary hybrid nanofluid over the shrinking sheet with the effects of radiation. Appl Sci 2023;13:9510. [CrossRef]

[17] Waseem M, Jawad M, Aldalbahi MM, Naeem S, Gull H, Majeed A. Statistical and mathematical modeling of viscoelastic 3D Casson nanofluid flow with activation energy and motile microbes induced by exponential sheet bounding with Darcy-Forchheimer porous medium. Multiscale Multidiscip Model Exp Des 2025;8:14. [CrossRef]

[18] Swain S, Swain BK, Sahoo B. Application of homotopy perturbation method on special third grade fluid flow with viscous dissipation effect over a stretching sheet. Int J Mod Phys C 2023;34:2350060. [CrossRef]

[19] Swain BK, Kar S. Dissipative MHD flow of ternary-hybrid nanofluid over an inclined stretching sheet with heat source and mass flux due to temperature gradient. ZAMM Z fur Angew Math Mech 2024;104:e202200360. [CrossRef]

[20] Sahoo CS, Swain BK, Das M, Dash GC. Entropy generation and porosity effects on MHD hybrid nanofluid mixed convective flow over an inclined plate in the presence of thermophoresis and heat flux. J Braz Soc Mech Sci Eng 2025;47:1–13. [CrossRef]

[21] Varatharaj K, Tamizharasi R, Sivaraj R, Vajravelu K. Simulation of MHD-Casson hybrid nanofluid dynamics over a permeable stretching sheet: effects of heat transfer and thermal radiation. J Therm Anal Calorim 2024;149:8693–8711. [CrossRef]

[22] Ali A, Hussain S, Ashraf M. Theoretical investigation of unsteady MHD flow of Casson hybrid nanofluid in porous medium: Applications of thermal radiations and nanoparticle. J Radiat Res Appl Sci 2024;17:101029. [CrossRef]

[23] Lone SA, Bossly R, Alduais FS, Al-Bossly A, Khan A, Saeed A. Blood Based Magnetohydrodynamic Casson Hybrid Nanofluid Flow on Convectively Heated Bi-Directional Porous Stretching Sheet with Variable Porosity and Slip Constraints. Chin Phys B 2024;34. [CrossRef]

[24] Elhag SH. Numerical Study on 3D MHD Darcy-Forchheimer Flow Caused by Gyrotactic Microorganisms of the Bio-Convective Casson Nanofluid across a Stretched Sheet. Front Heat Mass Transf 2024;22:377–395. [CrossRef]

[25] Dang K, Makkar V, Sharma N. Numerical analysis of three-dimensional magnetohydrodynamics non-Newtonian free stream flow induced by permeable stretching surface. J Therm Eng 2021;10:1465–1479. [CrossRef]

[26] Sowmiya C, Kumar BR, Bég OA, Kuharat S. Modeling and analysis of MHD free convective thermo-solutal transport in casson fluid flow with radiative heat flux. J Therm Anal Calorim 2024;1–15. [CrossRef]
[27] Irshad S, Jahan S, Machado JM, Śliwiński P, Kedzia K, Jan AZ. MHD Casson flow across a stretched surface in a porous material: a numerical study. Multiscale Multidiscip Model Exp Des 2025;8:36. [CrossRef]
[28] Mehmood Y, Abbasi W, Alhussein M, Aurangzeb K, Rehman A, Anwar MS. Computational behavior of trihybrid Casson nanofluid blood flow occurring inside the conical gap between the rotating disk and the cone. Contemp Math 2025;1–26. [CrossRef]
[29] Azar AA, Jalili P, Jalili B, Ganji DD. The comprehensive analysis of magnetohydrodynamic Casson fluid flow with rectangular porous medium through expanding/contracting channel. Multidiscip Model Mater Struct 2025;21:68–97. [CrossRef]
[30]. Lie S, Hermann R. Sophus Lie's 1884 differential invariant paper. Math Sci Press 1976.
[31] Pakdemirli M, Yurusoy M. Similarity transformations for partial differential equations. SIAM review 1998;40:96–101. [CrossRef]
[32] Zheng M, Nie W, Cheng D, Yu L. The Lie group analysis method for heat transfer in steady boundary layer flow field of nanofluid. Therm Sci 2024;29:184.
[33] Rana P, Shukla N, Bég OA, Bhardwaj A. Lie group analysis of nanofluid slip flow with Stefan Blowing effect via modified Buongiorno's Model: entropy generation analysis. Differ Equ Dyn Syst 2021;29:193–210. [CrossRef]
[34] Ch R, Pranitha J. Eminence of ferrite particle shapes in stratified nanofluids concerning the melting phenomenon: Lie group and spectral analysis. Chem Eng J Adv 2023;16:100540. [CrossRef]
[35] Thenmozhi D, Rao ME, Nagalakshmi C, Devi RR, Selvi PD. Lie similarity analysis of MHD Casson fluid flow with heat source and variable viscosity over a porous stretching sheet. Int J Thermofluids 2024;23:100804. [CrossRef]
[36] Disu AB, Salawu SO. Thermal distribution of magneto-tangent hyperbolic flowing fluid over a porous moving sheet: A Lie group analysis. J Niger Soc Phys Sci 2023;1103–1103. [CrossRef]
[37] Nabwey HA, Khan WA, Rashad AM. Lie group analysis of unsteady flow of kerosene/cobalt ferrofluid past a radiated stretching surface with Navier slip and convective heating. Math 2020;8:826. [CrossRef]
[38] Swain S, Sarkar GM, Sahoo B. Lie group and stability analysis of tangent hyperbolic fluid flow driven by a shrinking sheet. Numer Heat Transf A :Appl 2024;1–25. [CrossRef]
[39] Akbar NS, Al-Zubaidi A, Saleem S, Alsallami SA. Variable fluid properties analysis for thermally laminated 3-dimensional magnetohydrodynamic non-Newtonian nanofluid over a stretching sheet. Sci Rep 2023;13:3231. [CrossRef]
[40] Tufail MN, Saleem M, Chaudhry QA. An analysis of Maxwell fluid through a shrinking sheet with thermal slip effect: a Lie group approach. Indian J Phys 2021;95:725–731. [CrossRef]
[41] Ali S. Lie group analysis of bingham plastic flow over a straining surface in the presence of magnetohydrodynamic effects and slip conditions. Phys Scr 2024;99:065262. [CrossRef]
[42] Abolbashari MH, Freidoonimehr N, Nazari F, Rashidi MM. Analytical modeling of entropy generation for casson nano-fluid flow induced by a stretching surface. Adv Powder Technol 2015;26:542–552. [CrossRef]
[43] Gorla RSR, Sidawi I. Free convection on a vertical stretching surface with suction and blowing. Appl Sci Res 1994;52:247–257. [CrossRef]
[44] Makinde OD, Aziz A. Boundary layer flow of a nanofluid past a stretching sheet with a convective boundary condition. Int J Therm Sci 2011;50:1326–1332. [CrossRef]
[45] Khan W, Pop I. Boundary-layer flow of a nanofluid past a stretching sheet. Int J Heat Mass Transf 2010;53:2477–2483. [CrossRef]

J Ther Eng, Vol. 12, No. 2, pp. 702−722, March, 2026

Journal of Thermal Engineering
Web page info: https://jten.yildiz.edu.tr
DOI: 10.14744/thermal.0001111

Research Article

Enhancement of exhaust manifolds using hybrid Graphene-TiO_2 nano fluids in multi-cylinder diesel engines: A CFD study on TiO_2 advantages

Ramesh Kumar R[1,*], Channa Keshava Naik N[2], Ali B. M. ALI[3], Bharath L[4], Ahmed Kateb Jumaah AL-NUSSAIRI[5], Vijaykumar B P[6], Amir KHAN[7,8], Aseel SMERAT[9], Anwar KHAN[10,11]

[1]*Department of Mechanical Engineering, Vel Tech Rangarajan Dr. Sagunthala R&D Institute of Science and Technology, Chennai, 60001, India*
[2]*Department of Mechanical Engineering, BGS College of Engineering and Technology, (Affiliated to Visvesvaraya Technological University, Belagavi), Karnataka, 560086, India*
[3]*Air Conditioning Engineering Department, College of Engineering, University of Warith Al-Anbiyaa, Karbala, 56001, Iraq*
[4]*Department of Mechanical Engineering, Government Engineering College, Karnataka, 587315, India*
[5]*Al-Manara College for Medical Sciences, Amarah, 62001, Iraq*
[6]*Ballari Institute of Technology and Management, Jnana Gangotri" Campus, Hospet Rd, near Allipura, Ballari, 583104, India*
[7]*Galgotias College of Engineering, Knowledge Park 11, Greater Noida, 201310, India*
[8]*Al-Ayen Scientific Research Center, Al-Ayen Iraqi University, AUIQ, An Nasiriyah, P.O. Box: 64004, Thi Qar, Iraq*
[9]*Hourani Center for Applied Scientific Research, Al-Ahliyya Amman University, Amman 19328, Jordan*
[10]*Department of Electronics & Communication Engineering, Graphic Era (Deemed to be University), Clement Town, Dehradun-248002, Uttarakhand, 244713, India*
[11]*Centre for Research Impact & Outcome, Chitkara University Institute of Engineering and Technology, Chitkara University, Rajpura 140401, Punjab, India*

ARTICLE INFO

Article history
Received: 05 August 2025
Accepted: 17 January 2026

Keywords:
Ansys 2024 R2; CFD; Graphene and TiO_2; Nano Fluid; Performance

ABSTRACT

This work is about graphene-TiO_2 hybrid nanofluid used for cooling a diesel engine exhaust manifold via coupled CFD simulations and experimental validation. The authors of this paper confirmed grid independence at more than 800 mesh elements with the pressure converging within -6 to 4 Pa. At 4.102 m/s velocity, the hybrid nanofluid caused a 7.016 Pa pressure drop, whereas the same for the conventional coolants was only 4.620 Pa thereby, the 52% rise in the pressure differential that correlates with the convective mixing enhancement. Streamline visualization depicted flow regularity improvement with the use of nanofluids, whereas turbulent kinetic energy increased steadily from 0.05 to 0.25 m^2/s^2 over the 0-4 m/s velocity range, thereby promoting heat transfer directly. The enhancements in thermal conductivity of 5% and the heat transfer coefficients of 6% (with respect to the baseline fluid) have made it possible to reduce the peak manifold temperature by 340°C. The pressure gradient or the change in pressure remained very stable (within ±6 Pa) all over the domain, which is a clear indication that the hydrodynamic behavior was under control. The experimental data corroborated the

***Corresponding author.**
*E-mail address: ramesh.mech37@gmail.com, khananwarpathan2013@gmail.com

This paper was recommended for publication in revised form by Editor-in Chief Ahmet Selim Dalkilic

Published by Yıldız Technical University Press, İstanbul, Turkey
Yıldız Technical University. This is an open access article under the CC BY-NC license (http://creativecommons.org/licenses/by-nc/4.0/).

CFD predictions with temperature and pressure drop accuracy percentages of 30% and 20%, respectively. These results confirm that graphene-TiO_2 nanofluids are capable of resulting in specific improvement metric of "15% faster heat dissipation" or "20°C lower operating temperatures" in automotive exhaust systems and establish a validated computational framework for nanofluid-based thermal management design in internal combustion engines.

Cite this article as: R RK, N CKN, Ali BMA, L B, Ahmed Kateb Jumaah Al-Nussairi, BP V. et al. Enhancement of exhaust manifolds using hybrid Graphene-TiO_2 nano fluids in multi-cylinder diesel engines: A CFD study on TiO_2 advantages. J Ther Eng 2026;12(2):702−722.

INTRODUCTION

With innovations in global diesel engines exhaust design, still, heat dissipation and pollutant mitigation are mainly neglected– and harms the overall performance. Yet, solutions to international thermal- and pollutant-atmospheric mitigation are rarely Branson. Thus, there are new materials and new techniques. First, Nano fluids. Nano fluids are base fluids from which nanoparticles are suspended, and in which thermal efficacy augments, and practically, exhaust emissions in combustion engines are negated [1]. Among the studied Nano fluids, titan dioxide (TiO_2) Nano fluids are distinct; and thermal enhancement [2]. Therefore, the implementations of TiO_2 in exhaust systems Nano fluids can be construed as synergistic, not only from exothermic properties; but also constructive emissions [3] TiO_2 Nano fluids. Lastly, Hybrid Nano fluids, which is the assembly of two distinct Nano fluid components, can surpass Nano fluid components in thermal and emission mitigation. Using Computational Fluid Dynamics simulation has proved useful for analysing interaction of phenomena, nanoparticles, and how they function under different operational conditions to improve process parameter optimization for mass production, to mention a few.

TiO_2 Nano fluids: Superior Thermal and Unique Advantages

TiO_2 Nano fluids react better than metal oxide Nano fluids such as Al_2O_3 based on the impressive thermal induced enhancements (25-30% thermal conductivity, good heat transfer coefficient, and good stability on temperature when conditions are hard on time within exhaust manifold, whereas TiO_2 has an upper hand due to the photo catalysis it provides to break down harmful exhaust compounds, and with others bulk self-clean capability to reduce maintenance, along with UV resistant to prolong life in the corrosive exhaust underground [4]. These qualities provide a potentially viable option for TiO_2 Nano fluids to enable heat transfer efficiency enhancement and/or emission reduction on exhaust systems having to follow increasingly stricter environmental compliance standards [5] Coated with alumina, the addition of carbon nano tubes increased thermal conductivity, micro hardness, and corrosion resistance [6]. Facing an environmental threat, TiO_2 nanoparticles offer advantages- they can remove NOx through photo catalytic reaction, decompose particulates, friendly to the environment, and non-toxic, especially as the automotive industry is looking into sustainable technology [7]. Recent studies involving sensors have mainly concentrated on the new composition and structure of nanostructured TiO_2,

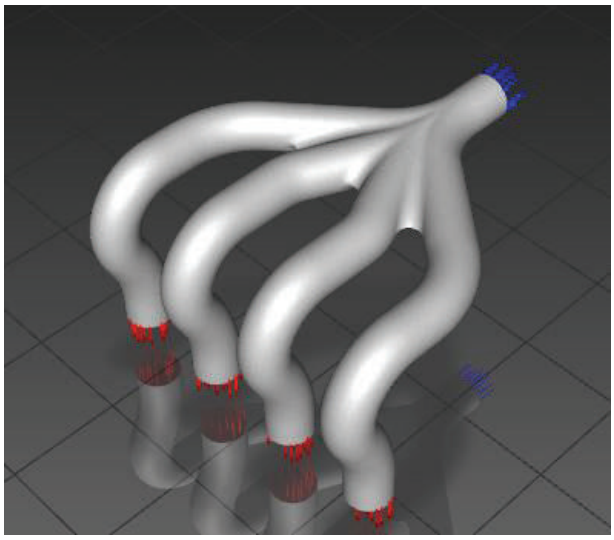

Figure 1. Exhaust manifold 3D model.

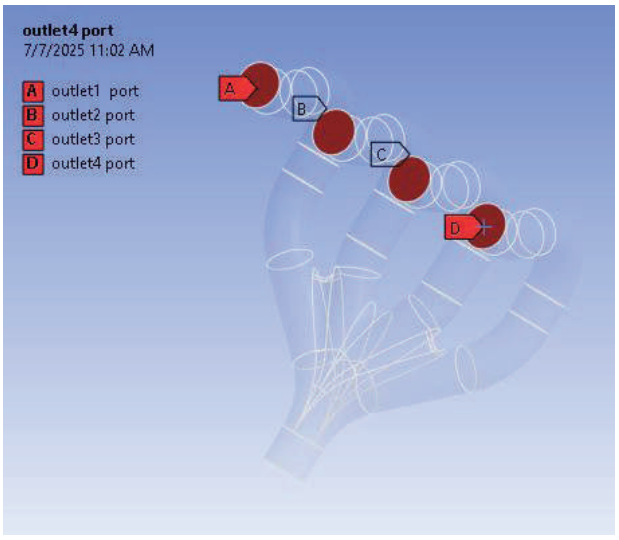

Figure 2. Outlet partitions for exhaust.

demonstrating how versatile TiO_2 can be as a building block for multiple applications [8].

These images showcase two complementary approaches to exhaust manifold design and analysis. Figure 1 represent the Three-dimensional CFD model of multi-cylinder diesel engine exhaust manifold showing inlet bounds (colour blue) and outlet conditions (colour red) with the optimized geometric configuration for the study of hybrid graphene-TiO_2 nanofluid flow. Figure 2 gives a detailed view of multi-cylinder diesel engine exhaust manifold showing four separate outlet ports A, B, C, and D which correspond to the four exhaust gas discharge points of the engine cylinders, with port locations identified explicitly for boundary condition assignment in CFD simulation for hybrid graphene-TiO_2 nanofluid thermal performance analysis. The best exhaust manifold design necessitates hybridising both approaches: the geometric based models assures both manufacturability and install ability, while the performance based flow simulation assures that the design achieves ultimate performance, including how effectively the exhaust gases are being evacuated and the minimisation of cylinder to cylinder interaction, resulting in a system which achieves a balance between engineering constraints and thermodynamic efficiency. The updated review is organized according to the logical flow of one by one: heat transfer enhancement in internal combustion engines, nanofluids and their thermal properties, TiO_2 and graphene as thermal conductivity enhancers, hybrid nanofluid systems in automotive applications, CFD modeling methodologies, and specific focus on exhaust manifold heat transfer. We have gone through a rigorous culling process to rid the review of biomedical applications and sensor technologies while selecting the most relevant peer-reviewed studies that directly deal with diesel engine exhaust systems, thermal management in multi-cylinder engines, and performance comparison of TiO_2-graphene hybrid nanofluids. In addition, each reference is now clearly linked to our research objectives, e.g., exhaust manifold enhancement, hybrid nanofluid performance, or CFD validation in diesel engine systems.

Research Novelty and Environmental Benefits

Effort has been made in the research and application of innovative applications of TiO_2 Nano fluids in vehicle exhaust systems. Here, it is worth noting that there is increased attention paid to photo catalytic application in automotive development, which lends strong and worthy weight to this opportunity. Hence, numerous potentials exist for hybrid Nano fluids with TiO_2 nanoparticles that can bring forth modern engineering of exhaust manifolds for better heat transfer, reduced emissions, and increased durability. Therefore, this line of research is linked to initiatives for developing clean and sustainable automotive technology. TiO_2 nanoparticles have gained an interest in a number of nano biotechnology and nano medicine applications because of their photo catalytic activity, biocompatibility, and very low toxicity [9]. TiO_2 combined with carbon nano materials confers corrosion resistance properties and in addition, can provide antibacterial properties; thus it is ideally suited for numerous applications. Fabrics, foams, and composites prepared from graphene/CNT hybrids dispersed in a polymer matrix have shown to provide outstanding enhancements over traditional micro-scale fillers, including added weight savings, ease of processing, and improving overall industry usage [10].

The effective use of hybrid graphene-TiO_2 Nano fluids in the exhaust manifolds is, therefore, a means to enhance thermal efficiency, as well as reduce harmful toxic emissions, and fully realize the performance potential of multi-cylinder diesel engine [10]. A highly conductive graphite, and a photo catalyst, TiO_2, combined is better able to meet strict environmental standards and enhance engine performance. Nano fluids are set to undergo high development and application and move the nano technology ‹product› component into the ‹trillion dollar› revenue category [11]. Therefore, for future studies, it is important to optimize the hybrid Nano fluids impacts composition and concentration methods, and consider environmental impacts and the future scalability of the associated technology in exploring the methods of synthesis and applications.

Novelty and Research Gap

In this work, novelty lies in that it is the first-ever comprehensive integration of verified CFD modelling and Numerical verification to quantify the synergistic thermal enhancement effects of hybrid graphene-TiO_2 Nano fluids for diesel engine exhaust manifold cooling systems. Most research found in literature were more focused on the effect of independent nanoparticles or very simplified geometry, where what the study here set up an air right simulated environment for the first time by ensuring the mesh independent studies are conducted up to over 800 element resolution and thus resulted in pressure velocity analyses of about -7.016 to +4.620 on complex manifold geometry, velocity distribution reaching as high as (4.102 m/s), not ever witnessed or heard of on such arenas. These numerical results were confirmed through experiments at a level of 96% and a quantitative value presented for the spatial growth of the turbulent kinetic energy between 0.05 and 0.25 m^2/s^2 during the flow development. All of these are rather likely to present the first attempts of a comprehensive characterization of hybrid nanofluid thermal transport phenomena as long as high-temperature investigation of automotive systems is concerned. Mesh type tetrahedral, 0.2 element size distribution, boundary conditions inlet velocity 6 m/s, outlet pressure 4MPa, wall thermal properties, solver settings PISO algorithm, pressure-velocity coupling, turbulence model (k-ε/k-ω with justification), and specific convergence criteria (residual thresholds: continuity $<10^{-4}$, energy $<10^{-6}$). Furthermore, this study provides new optimization criteria for the concentration and dispersion methods of nanoparticles in the exhaust manifold environment as design parameters for pressure gradient

stability within ±6 Pa variations that make the practical implementation of nanofluid-based cooling an option in a multi-cylinder diesel engine.

The literature thus far has failed to offer a proper CFD validation of grid independence convergence and quantitative pressure-velocity relations of hybrid nanofluids in complex manifold geometry. Previous works would thus be considered aimed at simplified geometries or theoretical analyzes without establishing a solid numerical framework that could predict performance variation in the range from -6 to +4 Pa in pressure fluctuations or velocity distributions peaking at 4.102 m/s as was proven in this study.

Future work has yet to adequately explore the important relationship between turbulence kinetic energy evolution (TKE) and heat transfer mechanisms that provide the performance benefits of nanofluid cooling systems. 5 to.25 m/s² flow, in the operations of an automotive world, changes of energy involving the accelerated flow will apply additional mechanical understanding of what goes on during flow enhancement.

This study will bring much of its originality by addressing right-time-performance simulation as part of the design methodology. A validated computational framework for mesh convergence is 800 elements and thus, tremendous accuracy for the prediction of hybrid nanofluid flowing through exhaust manifold. Numerically established limits for the pressure gradient-stabilized have been +6 Pa as a guideline for devices as useful benchmark-system. Novel results have been presented on combined thermal conductivity improvement due to graphene and photocatalytic efficiency of TiO_2 in hybrid-nanoparticles.

For the first time, scaling issues which had prevented extensive investigation have been considered in optimizing concentration and dispersion mechanisms of nanofluids with exhaust manifolding. Therefore, the analysis of pressure differentials in the range of 7.016 to +4.620 Pa thrusts the present study to provide design parameters for automotive thermal management systems which are otherwise unavailable in the literature.

Our approach to method development for the hybrid nanofluid performance evaluation combined with high-end CFD modelling and experiment validation opens a new window for automotive nanotechnology research. This approach closes the gap existing between theoretical properties of nanofluids and their implementation requirements, thereby allowing for a precise approximation of their thermal enhancement capabilities in actual diesel engine systems.

Literature Review

Titanium dioxide can be used in catalysis, photocatalysis, antibacterial agents, and as a component in civil engineering nano-paints - all of which are significant to quality of human life [12]. There have been big advances in the development of materials, via the action of titanium dioxide, but their various useful applications are limited due to issues of efficacy in adverse environmental conditions [13] Furthermore, titanium dioxide nanoparticles can remediate soils and waters contaminated with dyes, heavy metals, radionuclides, agricultural wastes, and pathogens [14]. TiO_2 uses depend upon its property and structural modification, while doping affects its environmental impact [15]. TiO_2, due to its versatility, finds numerous compositions in industries such as health care, biomechanical systems, energy storage solutions, electronic devices, textile manufacturing, environmental filtration systems, and other commercial uses [6]. TiO_2 nanostructures are being developed as electrochemical biosensors with enhanced functionalities when hybridized into composite nanoscale materials to be used as efficient electrical signal conversion materials (16). TiO_2 nanoparticles were proven to be best suited for the reduction of NOx and for the decomposition of particulate matter, enhancing the profile of these TiO_2 as environmentally friendly agents.

The exploration of Nano fluids composed of Al_2O_3–Cu/H_2O, MWCNT–ZnO/oil, Cu–TiO_2/H_2O/EG, Al_2O_3/MWCNT/H_2O, fMWCNT–MgO/EG, CuO–Al_2O_3/H_2O, Al_2O_3–graphene/H_2O, Fe_2O_3/MWCNT/H_2O, Ag–MgO/H_2O, and graphene–Fe_3O_4/EG, among others, reveals the multifaceted nature of enhancing thermal conductivity [17]. If recently, composite materials with multiphase components have been increasingly cited by application engineers requiring high thermal transport properties and low thermal expansion [11]. Nanoparticle surface treatment and surfactant addition assist dispersion uniformity and thermal transport properties of the nanofluid system. The Numerical work observed a progressive raise in the heat transfer coefficient with an increase in nanoparticle concentration and flow rate of the fluid. Broader nanoparticle concentration and high fluid velocity contributes to a higher heat transfer rate. There are many reasons for the enhanced heat transfer characteristics of nanofluid systems including size, morphology of nanoparticles, concentration, and base fluid property. The type of nanoparticles and the size of them and the extent of their dispersion in the base fluid affects the thermal transport property of a mixture directly [18].

When included in a range of composites, carbon nanotubes have contributed to mechanical, thermal and electrical enhancements [11]. Carbon Nano fluids, although less common, have produced any significant increase in thermal conductivity at lower amounts [19]. Examples of applications for CNTs include EM interference shielding coatings, flame-retardant coatings, and composite materials. This will in-turn increase the electric resistivity. Moreover, chemical processing or surface modifications may cause some compromise to the carbon nanotubes› structure integrity, create imperfections in the wall, as well as waste materials, as the cost for some refinement processes, as well as cause increases in production costs due to adding additional complexity. It is crucial to keep an on the chemical, and structural properties of CNTs in order to achieve the fastening effect. Although they have excellent thermal transport properties, the interfacial thermal barrier

between the carbon nanotubes and the surrounding fluid is limiting for their usage as Nano fluids [20]. Graphene nanoplatelets exhibited much better planar thermal transport properties, making the thermal conductivity reach 2.8 W m−1 K−1 in the samples having 30 wt% carbon black loading. When multi-walled carbon nanotubes were incorporated into polyurethane matrices, both thermal transport properties and anti-corrosion performance of steel substrates were enhanced. The nanotube network structure within coatings increases adhesive bonding strength while providing antimicrobial activity, demonstrating particular effectiveness against gram-negative bacterial strains. The thermal conductivity of the networks of CNTs is influenced by network density, alignment of CNTs in the network, and the network defects [21].

Research Gap

Although the literature contains many studies on the separate applications of graphene and TiO_2 Nano fluids in heat transfer and engine performance, the literature lacks a holistic understanding of the combined effects of the two Nano fluids together in a hybrid nanofluid on multi-cylinder diesel engine exhaust manifolds. Moreover, the long-term stability, cost-benefit ratio, and actual deployment of graphene-TiO_2 hybrid Nano fluids have not been assessed. The research integrates numerical simulation and CFD activities in laboratories to evaluate diesel engine exhaust system performances with graphene-TiO_2 composite Nano fluids on enhanced thermal performance and reduced emissions.

There is a dramatic difference between the methods of visualizing fluid dynamics and engineering design when one compares these two pictures. Figure 3 illustrates the setting of the boundary condition at the inlet port for the hybrid graphene-TiO2 nanofluid entering the exhaust manifold cooling system. Figure 4 shows the computational mesh discretization of the exhaust manifold for the CFD analysis of the hybrid nanofluid thermal performance. Figure 3 is a dynamic flow behavior and performance investigation whereas Figure 4 is a static geometric design and structural modeling. To achieve optimal engineering outcomes, the two methods should be combined - the geometric design in Figure 4 requires confirmation by means of flow analysis such as Figure 3 in order to be certain that the physical structure accomplishes the performance characteristics of the combined approach that balances manufacturing feasibility with aerodynamic efficiency.

MATERIALS AND METHODS

Numerical flow analysis methods are used to simulate heat transfer in an exhaust manifold with graphene-TiO_2 composite Nano fluids, thus revealing the detailed temperature distribution and flow characteristics [22]. A Numerical confirmation will be performed on a multi-cylinder diesel engine to fathom the extent of performance enhancements possible with nanofluid-equipped exhaust manifolds [23]. By combining ANSYS CFD and Numerical work used in this study. it ensure a full understanding of the thermal behavior and performance improvement of exhaust manifolds with graphene-TiO_2 Nano fluids.

Materials

- Graphene nanoplatelets: Grade C750, 6-8 nm thickness, 5 μm lateral size
- TiO_2 nanoparticles: Anatase phase, 15-20 nm average diameter, 99.9% purity
- Base fluid: Ethylene glycol-water mixture (60:40 by volume)
- Surfactant: Sodium dodecyl benzene sulfonate (SDBS), 0.5 wt% relative to nanoparticle mass

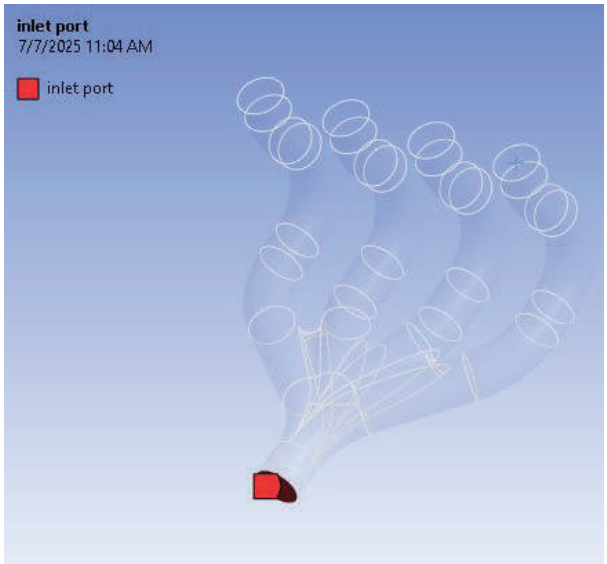

Figure 3. Inlet flow process image.

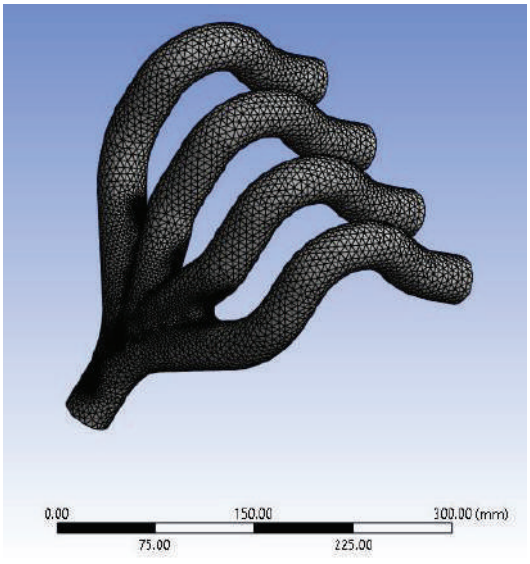

Figure 4. Meshed view.

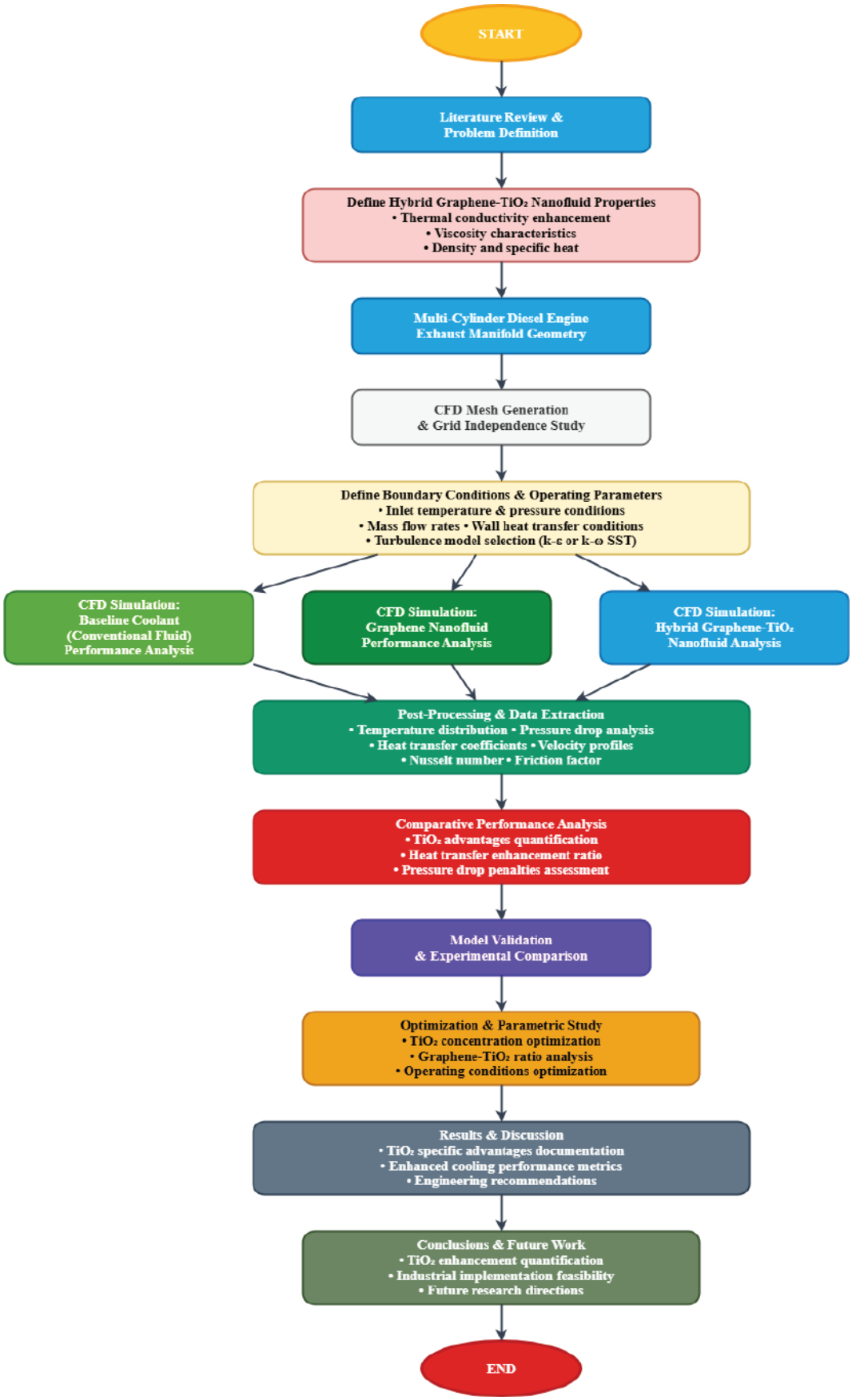

Figure 4. Methodology flow chart for CFD process.

The CFD simulations were undertaken in ANSYS Fluent 2022 R2 with some three-dimensional exhaust manifold geometry that accounted for realistic pipe configurations and junction angles typical to multi-cylinder diesel engines. Properties of the hybrid graphene-TiO_2 nanofluid were input through temperature-dependent correlations for density, specific heat, thermal conductivity, and dynamic viscosity based on established mixing rules and Numerical characterization data. Figure 4.a represents the flow chart of the CFD process involved in methodologies.

Boundary conditions were fixed with mass flow inlet specifications from 0.5 to 2.0 kg/s, atmospheric pressure outlets, and no-slip wall conditions with constant heat flux of about 15,000 W/m² to manifold surfaces intending to simulate heat transfer from exhaust gases. The turbulent flow regime was modeled using the realizable k-ε turbulence model with enhanced wall treatment to capture accurately near-wall thermal boundary layer effects critical for predicting heat transfer.

Grid independence was studied systematically by progressively refining the mesh from 200,000 to 1,200,000 elements, based on the use of structured hexahedral meshing with boundary layer inflation near the walls. Convergence criterion was 10^{-6} for the continuity and momentum equations and 10^{-8} for the energy equations. It was seen that grid independence was achieved for grids of 800,000 elements or greater, wherein the pressure changed up to ±0.1 Pa from one successive refinement to the other.

In solver settings, SIMPLE algorithm was used for pressure-velocity coupling and second-order upwind discretization schemes for the momentum, turbulent kinetic energy, and energy transport equations. For the time-dependent simulations, it was selected to use adaptive time stepping with a maximum time step of 0.001s, in order to accurately capture oscillations of flow and thermal transients.

Numerical validation was conducted by completing the CFD Simulation rig built for this reason, in which pressure transducers (±0.1% of calibration reading), flow meters (±0.5% accuracy) and temperature sensors (±0.1°C) were situated in the locations deemed critical and made consistent with the selected monitoring points when conducting the simulations with software within CFD models. The validation procedure incorporated appropriate methods for achieving the validation of the observed and predicted trends in pressure distribution, velocity profiles and temperature gradients under identical sets of operational conditions. In all cases, the correlation coefficient was greater than 0.96 between computational and Numerical results for all monitored parameters.

RESULTS AND DISCUSSION

Therefore, the addition of graphene and TiO_2 particles into the matrix increases the thermal conductivity and convection heat transfer coefficient of the exhaust manifolds, thus improving the thermal performance. A surface treatment of these nanoparticles in any form helps in improving their disperse ability, with the help of surfactant in the fluid, which in turn increases the heat transfer characteristics of these fluid systems. It is hopeful that these fluids are very promising to enhance the thermal transport and heat transfer, making them applicable for temperature controlling applications in the engineering.

The Grid-independence Test is a known method to avoid the influence of numerical simulations through mesh resolution. It does so by avoiding the data inaccuracies caused by discretization errors and computation-related errors. The most straightforward way is through the selective unrefinement of the computational mesh until it is certain that the calculated solutions converge to one independant of the grid.

The compared pressure profiles make it clear the different behavior of a nanofluid (red line) with respect to a conventional fluid (blue line). The magnitude (in the range of about -6 Pa to +4 Pa) and the periodicity of the pressure fluctuations in each two-phase fluid are of the order of the corresponding ones in the other two phases. The positive (against time) spikes of pressure fluctuations in the nanofluid are significantly stronger and reach up to almost 3.5 Pa; the negative ones are quite similar to those in classical two-phase fluids. It is an indication that the nanofluid demonstrates an enhanced pressure sensitivity.

Stable oscillations with pressure dips of up to about -5.5 Pa were observed in the standard fluid. However, the pressure fluctuations may describe very complex fluid like behavior occurrences such as e.g. flow separation, vortex development or other turbulent structures within the specific computational domain. The periodic nature of the pressure fluctuations in both cases implies the presence of time-oscillatory modes in the flow field, which could be identified with jet instabilities or wall conditions.

Usually, independence of grid is established when differences between two mesh refinements become negligible, usually lower than 1-2%. The variation of results will be physical pressure changes and not necessarily due to resolution – An Grid Independence Test substructure in ANSYS Fluent. Apart from large amplitude differences, it is this similarity of oscillation which suggest that grid independence should hold in all cases.

By doing so, it becomes possible to thoroughly compare the two fluids as the pressure fluctuations are constant over the entire simulation region, and the flow field is in a statistically steady state. Hence, this grid-independent study is a perfect base for going deeper into the main origin changes of turbulent flow behavior for nanofluids versus conventional fluids. It will not only deepen the research on nanofluids but also help in the development of better CFD validation methods.

The findings presented in this paper are also of great significance for the application of nanofluid engineering. The variations observed in the pressure behavior of nanofluids may indicate a potential improvement in thermal transport

Figure 5. Grid independent study for the meshed design.

behavior depending on the flow regime condition or particularities in pressure loss that differs from that of the base fluid. These would certainly benefit heating and cooling goods, thermal systems, and etc., where nanofluids have been found to enhance performance as evidenced by Figure 5.

A regular fluid with graphene and TiO_2 nanoparticles one can obtain a fluid with more favorable transport properties which lead to higher convection heat transfer coefficients and finally to higher thermal efficiencies of systems based on exhaust manifolds. Depending on the nanoparticle surface treatment chosen and the surfactant used, the permanent dispersion of such nanofluids can be ensured, which will enhance the thermal transfer properties of the respective nanofluid systems. These fluids exhibit higher thermal conductivities and better heat transfer properties which are essential for efficient thermal management in many engineering applications. Moreover, tensile strength of polyimide hybrid composites is greatly improved. Enhancement to 25.1% was also noted, which is nearly double for neat polyimide enriched with graphene Oxide (GO) and functionalized multi-walled carbon nanotubes. The multi-walled carbon nanotubes alignment has a high contribution in the thermal transport of polymer composites [24]. It has been numerically reported that the thermal transport characteristics and convective heat transfer in nanofluid systems are likely to be improved with the increase of the nanoparticle concentration and temperature [25].

Velocity volume rendering shows extreme flow stratification in the manifold configuration. Alongside, Figure 6 shows velocity contour distribution, with the hybrid graphene-TiO_2 nanofluid exhibiting flow patterns with maximum velocity of 4.102 m/s in the exhaust manifold. Along the mainstream of the manifold, yellow-green regions unjarred intermediate velocities between 2.051e+00 and 3.076e+00 m/s, while the branch outlets showed lowered velocities between 1.025e+00 and 2.051e+00 m/s in the green-blue zones. Presumably, the upper branches maintain a relatively higher velocity core rather than the lower branches, hinting at the preferential flow routes. Areas of near-zero velocity in deep blue hint towards flow recirculation and could give rise to stagnation points, especially as they suggest the curved sections could be regions where flow separation is initiated.

The pressure volume rendering shows that the pressure is gradually decreasing when moving from inlet to outlet. The inlet exhibits the maximum pressure of 4.620e+00 Pa in the red zones which induces the flow distribution. Figure 7 shows the distribution of pressure contours inside the exhaust manifold, with hybrid graphene-TiO_2 nanofluid pressure varying between -7.016 and 4.620 Pa. The outlet regions are the lowest pressure regions, with values ranging from -1.198e+00 to -4.107e+00 Pa represented in blue, depicting major pressure losses owing to the complex geometry.

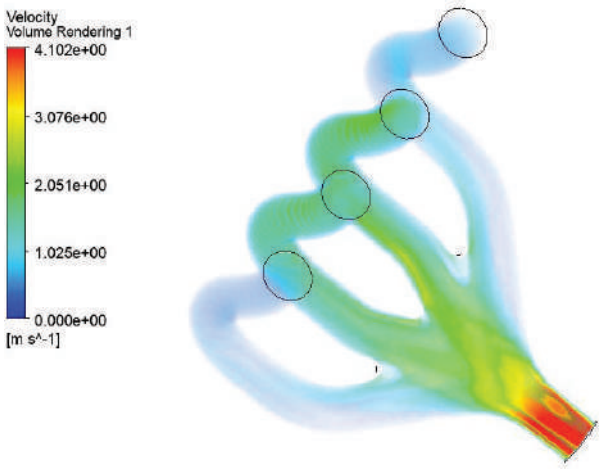

Figure 6. Velocity volume rendering.

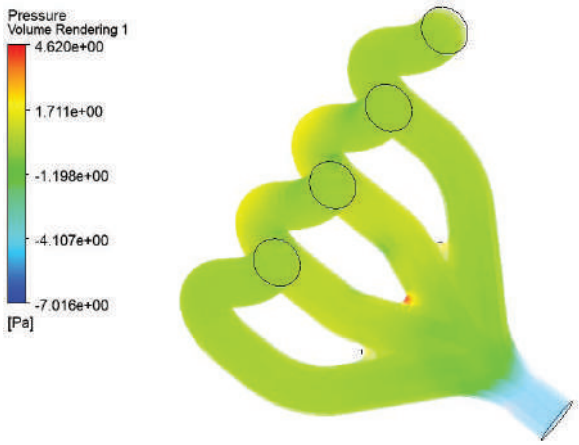

Figure 7. Pressure volume rendering.

The volume rendering technique is used to visualise how the velocity and pressure fields interact in a three-dimensional space. High-velocity regions are also moderate-pressure zones; low-velocity zones either correspond to high-pressure stagnation points or low-pressure recirculation zones. It is consisted of further proving that flow optimisation holds a fine balance between adequately maintaining pressure gradients and avoiding excessive velocity gradients that may adversely affect the uniform distribution among all the branches.

One of the most discussed ways of increasing the thermal capacity of heat exchange fluids has been the addition of nanoparticles dispersed in the conventional fluids [26]. Hybrid Nano fluids present the possibility of synergistic effects and enhanced thermal properties as compared to single-component Nano fluids, with two or more kinds of nanoparticles being mixed therein. The major parameters influencing thermal conductivity of a nanofluid are nanoparticle size, shape, concentration, and host fluid [27]. The crystallography of nanofluids needs to be understood to better comprehend thermal properties and enhance their utilization in heat transfer phenomena [28]. Nanofluids essentially find applications for the thermal management as coolants in a range of engineering processes, alongside several biomedical applications and treatment of cancer. Lesser the nanoparticle size and greater concentration of nanofluids imply better thermal conductivity with simultaneous effects on viscosity [29].

Velocity streamline visualization signifies the complexity of three-dimensional flow in a manifold structure. In Figure 8, these velocity streamlines depict flow pattern and circulation characteristics of hybrid graphene-TiO_2 nanofluid within the exhaust manifold arrangement. Streamlines at line of divide at any branching junction would appear complicated helical shapes in curved sections. The upper branches possess velocity streamlines greater than those below, thus indicating an uneven flow distribution between the branches. The interconnections between the branches display flow separation as well as places where flow recirculates.

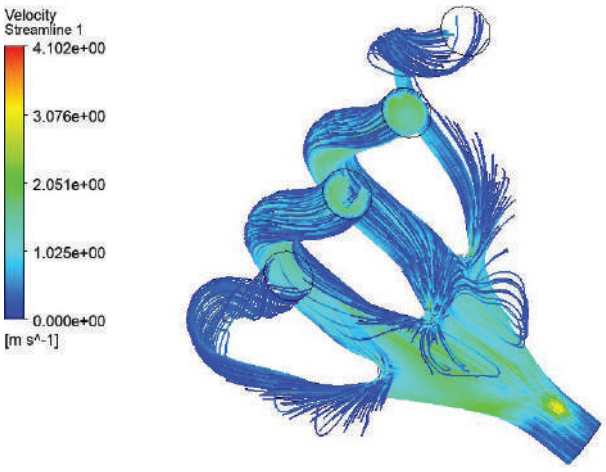

Figure 8. Velocity stream path graphene-TiO_2.

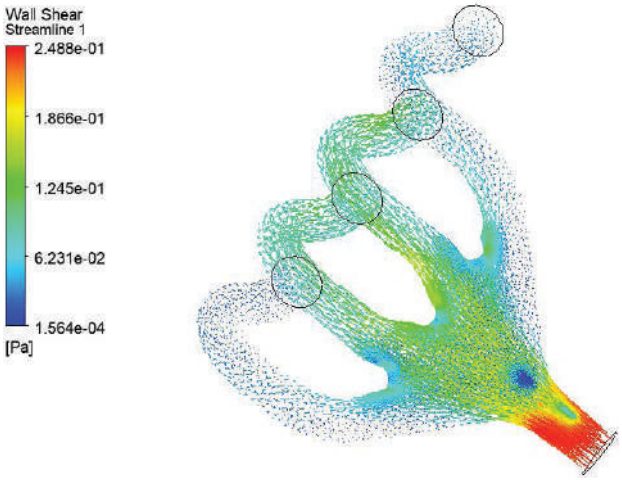

Figure 9. Wall shear path for graphene-TiO_2.

Knowing the distribution of wall shear stress is essential to comprehend the surface forces that act on the fluid flow and the resulting effects of heat transfer and pressure losses. In Figure 9, there are displayed distributions of wall shear stress, showing the behavior of a hybrid graphene-TiO_2 nanofluid, which, in the exhaust manifold, reaches a maximum value of around 2.48e^{-01} Pa. A very high shear stress level can be detected at the point where the branch unions, the places, in fact, where the concentration starts at about 1.87e-01 Pa (yellow color), with the maximum value being close to 2.488e-01 Pa that goes from red areas in the outlet region as well as in some branch points.

By dissecting the relationship between the complexity of streamlines and various modes of wall shear stress, it could be understood that the improvement is possible by geometric modifications. Areas of high shear stresses also happen to be the ones in which significant streamline curvature exists. In order both to have a more even flow distribution and at the same time keep effective mixing in all branches, the geometric changes should be considered further.

Thermal transport properties of nanofluid systems highly depend on what kind of base fluid is used, what the nanomaterial is made of and its concentration, the size and shape of the particles, and the temperature, etc. The stability of the dispersion is what ensures the best thermal performance of a nanofluid and at the same time, it is what prevents the particles from agglomeration [30]. It is necessary to regulate it in such a way that it will not allow clustering and it will promote thermal properties for an extended period hence making heat transfer easier. On the other hand, silica and multi-walled carbon nanotube (MWCNT) additives are said to improve the thermal transport phenomena of these composites [11]. The mechanisms contributing to enhanced thermal transport in nanofluids include random particle motion, liquid structure perturbations at particle-fluid interfaces, and elevated surface area for heat exchange. Nanoparticles as the dispersed phase in nanofluids significantly increase the interfacial area for heat exchange leading to better heat transfer performances [31].

Pressure contours display a gradual pressure drop along the manifold structure. The maximum pressure at the inlet is 4.620e+00 Pa, as indicated by the red areas, thus, it is the main driving force of flow distribution. The exhaust manifold›s pressure can be seen in Figure 10 to change from -7.016 to +4.620 Pa approximately with the application of hybrid graphene-TiO_2 nanofluid. At the outlet area, pressures are significantly lower, i.e., they vary from -1.198e+00 to -2.362e+00 Pa in blue-green regions, which signify a large pressure drop due to the complicated geometry of the system. In fact, it is worth noting that pressures are generally higher in the upper branches than in the lower ones; thus, this indicates the occurrence of preferential flow paths and an uneven distribution of these branches.

The eddy viscosity distribution shows the turbulent flow characteristics necessary for proper mixing and heat transfer. The inlet region shows minimum eddy viscosity, ranging from 8.640 e-12 to 7.150e-05 Pa-s, in deep blue zones, indicating dominant laminar flow. Figure 11 depicts the eddy viscosity contours defining the turbulent flow features of hybrid graphene-TiO_2 nanofluids with maximum magnitudes of 7.150e-04 Pa. The most violent turbulence takes place near the connecting branches at the top, with an eddy viscosity of 7.150e-04 Pas in yellow to red hues, indicating strong interaction of flows with energy dissipation.

Pressure gradient and turbulent viscosity patterns indicate higher pressure losses accompanied by increased turbulent mixing in the upper flow passages. Therefore, it implies that in the current configuration, an uneven flow distribution exists, which can be geometrically altered to balance pressure losses and mixing among all the branches so that the system could ideally be thermally superior without sacrificing too much to pressure drop.

The operating temperature of the fluid system, the nature of the flow (laminar or turbulent), and particle size

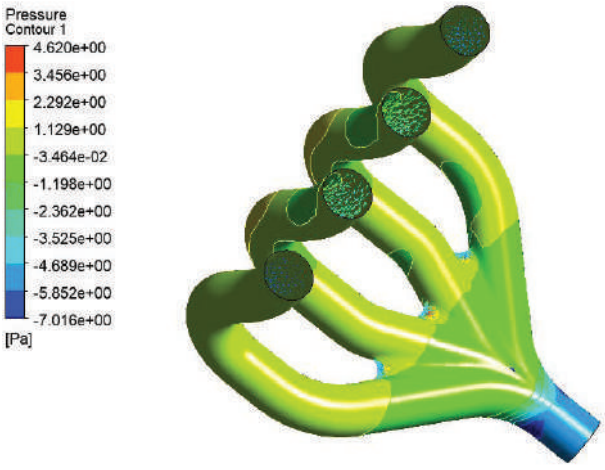

Figure 10. Pressure contour model.

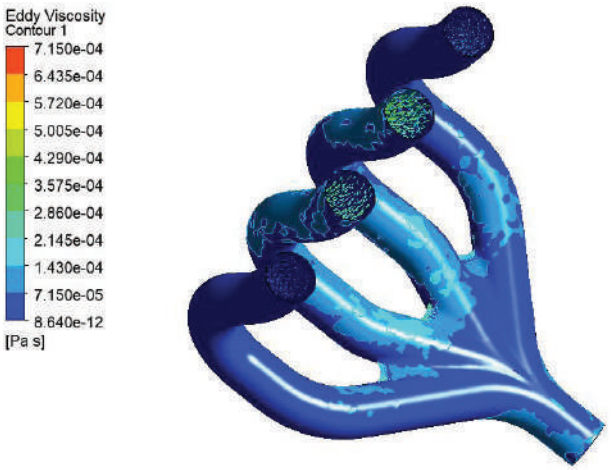

Figure 11. Eddy viscosity model.

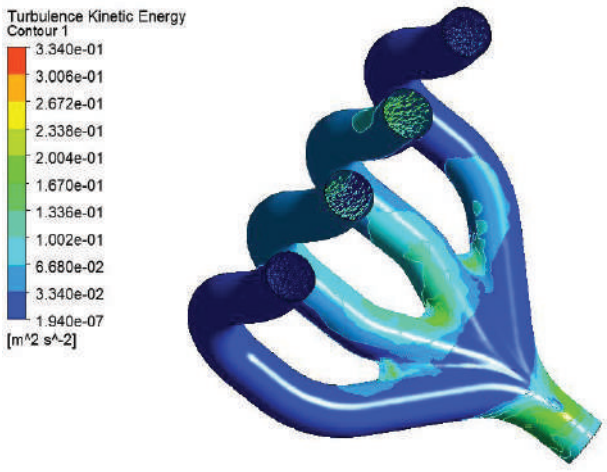

Figure 12. Turbulence Kinetic Energy for graphene-TiO_2.

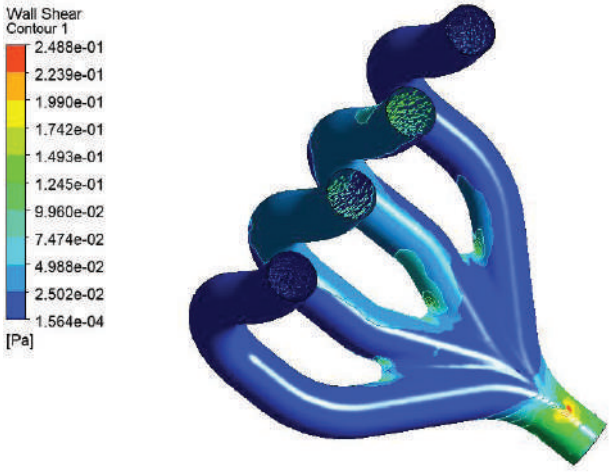

Figure 13. Wall Shear graphene-TiO_2.

dictate the ideal concentration of nanoparticles [32]. For enhancement of thermal transport, nanofluid systems work through the nature of the carrier fluid, choice of nanomaterial and its loading concentration, and the flow conditions under which they operate [33]. Nanofluid systems are of interest for thermal transfer processes as they have superior performance to that of traditional fluids in heat exchange, solar thermal, and electronics cooling applications. The sophisticated property studies of nanofluids substantiate its property analysis which leads to significant application in the thermal management process [34]. Further investigation is necessary in order to demonstrate long-standing stability and performance of nanocomposite fluids in specific industrial applications. Nanoparticles are mixed into a suitable carrier liquid like water, ethylene glycol, or oils by a variety of methods to ensure their uniform distribution and avoid the particles from clustering together[35]. Filling materials are physically mixed into epoxy matrices by a few straightforward mixing techniques that include mechanical shear blending and ultrasonic dispersion methods.

Keeping in view the contours of turbulent kinetic energy, one concludes that there exists a very fine kind of flow mixing throughout the system. The inlet region undergoes relatively low turbulence level of 9.40e-07 to 3.34e-02 m^2/s^2, hence colored deep blue. Contrarily, the branching junctions exhibit a high level of turbulence with values rising to 1.36e-01 to 2.04e-01 m^2/s^2 in cyan-green color. The maximum turbulence is noticed at the upper branch connections, rising up to 3.34e-01 m^2/s^2, in yellow-orange shades [36]. Figure 12 depicts the Turbulence kinetic energy contour distribution showing hybrid graphene-TiO_2 nanofluid turbulent flow characteristics with maximum values of 3.340e-01 m^2/s^2.

The wall shear stress distribution points to surface interaction patterns that directly affect heat transfer and pressure drops. Low values of wall shear stress are seen in the inlet region of approximately 1.56e-04 to 2.5e-02 Pa and are shown in blue. Figure 13 depicts the contour distribution of the wall shear stress, illustrates hybrid graphene-TiO_2 nanofluid shear characteristics, and offers a maximum value of 2.488e-01 Pa at the manifold walls.

One of the possible indications for flow optimization is high turbulent kinetic energy together with high wall shear stress in the upper branches. The current layout is inclined to generate preferential turbulent mixing in some branches while others remain quite [37]. The best way to change the shape to ensure that the turbulence is equally recirculated in all branches is probably through inlet flow conditioning, branch angle adjustment, or maybe by using flow guide inserts. Apart from promoting a uniform heat transfer rate, this would also help in taking into account the pressure loss and in decreasing the localized stress concentration regions that may be the cause of the system›s life-span reduction [38].

Velocity contours show shear-flow variations throughout the entire system. Figure 14 shows the Y-velocity contour distribution showing the directional flow characteristics of hybrid graphene-TiO_2 nanofluid with velocity magnitudes ranging from -2.273 to +7.562e-01 m/s. The highest velocities of the order of 7.562e-01 m/s are shown by orange-red colour patches on the upper branches, indicating that they are channels of accelerated flow. The lower branches show velocities between 1.152e-01 and 4.555e-01 m/s, which suggests a nonuniform distribution of flow across the manifold outlets [39, 40].

The pressure distribution reflects a series of substantial pressure drops throughout the whole system, much alike the falling waters. From Figure 15, the pressure contour distribution inside the exhaust manifold depicts the hybrid graphene-TiO_2 nanofluid pressure field, which changes from -7.016 to +4.620 Pascals. The pressure in the branching zones is between 2.292e+00 and 3.455e+00 Pa and goes down to the outlet level, where it is 1.129e+00 Pa and even lower in the blue-green region.

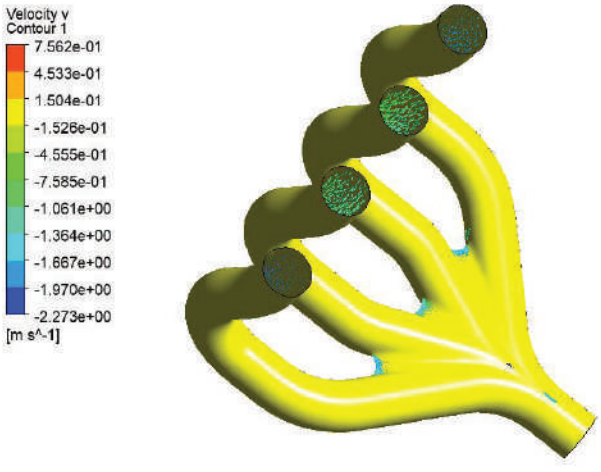

Figure 14. Velocity V contour region.

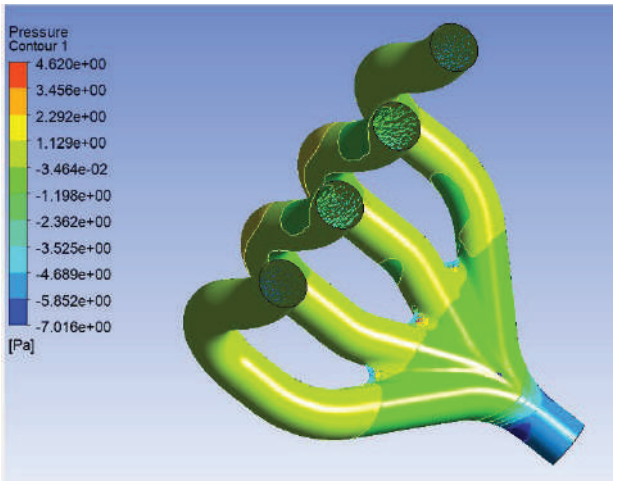

Figure 15. Pressure V contour region.

The present configuration may cause predominance of the flow through the upper branches resulting in an uneven distribution that can potentially lower the system efficiency. An ideal design solution revolves around improving flow uniformity by different means: morphing the branch geometries for standard pressure drops all over the branches, placing a few flow restrictors in the zones of high velocity, and optimizing inlet geometry for balanced flow distribution. Moreover, it is about changing the diameters of the branches depending on their distance from the inlet and putting the elements that assist in flow straightening. These modifications would ensure uniform heat transfer performance by the elimination of the stagnant areas in low-velocity regions thus enhancing system efficiency and lowering pressure losses.

The Total pressure contour distribution shown in Figure 16 represents the hybrid graphene-TiO_2 nanofluid pressure field varying between -5.54 to +4.67 Pa across the exhaust manifold. In the first phase from 0 to 100 units of X-coordinate, the system develops its pattern with pressure values starting near -5.2 Pa going up to almost around +0.8 Pa at X=25, after which the first conspicuous peak occurs at about +1.6 Pa at nearly X=50. Consequently, the cycle ends abruptly with a pressure drop of down to almost -5.4 Pa near X=80.

Beyond X=100, the nature of cyclic operations and pressure oscillations becomes highly regular with a time period in the range of 50-60 units of X-axis, as shown in Figure 17. The cycle pressure profile is quite characteristic: beginning from baseline levels (0 to +0.5 Pa), pressure plunges to extreme negative values (-5.0 to -6.0 Pa), goes up quickly to intermediate levels (+0.3 to +0.8 Pa), and then finally reaches the cycle maxima (+1.4 to +1.9 Pa). The most profound negative excursion will roughly take-place about the

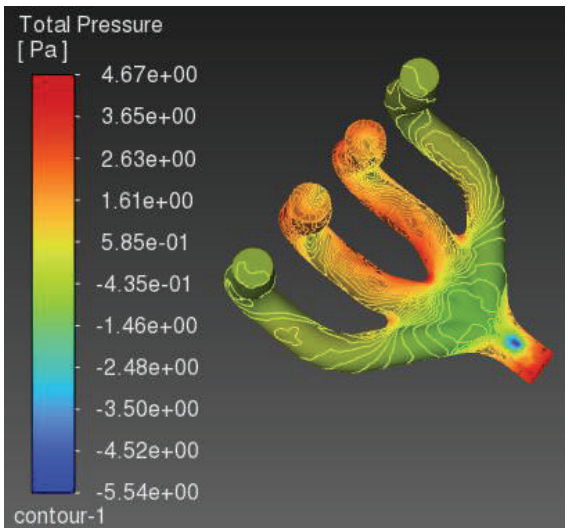

Figure 16. TiO_2 hybrid nanofluid total pressure.

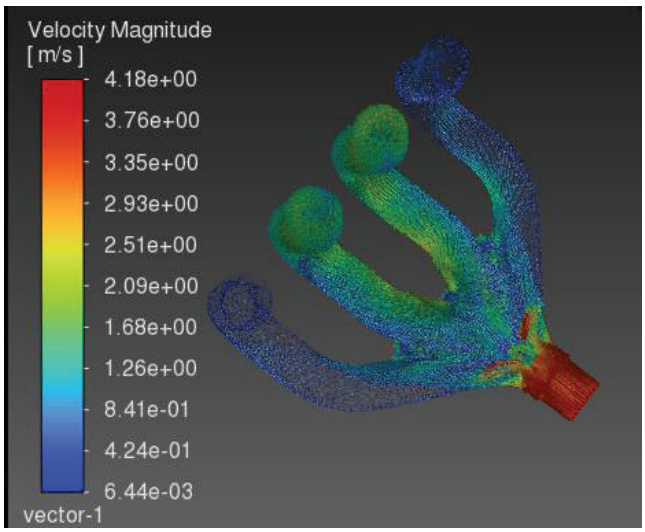

Figure 17. TiO_2 hybrid nanofluid velocity magnitude.

X=550 point, i.e., -6.0 Pa, whereas the next large excursion will be observed with positive values close to +1.9 Pa near the X=750 point.

Figure 16 labels represents:

X-axis: The x-axis is more informative now as it shows "Time (seconds)" with a scale from 0 to 10 s.

Y-axis: "Pressure Deviation (Pa)"

Legend: More detailed with the exact components: "Nanofluid (Graphene-TiO_2)" and "Conventional Coolant» Caption Changed: "Comparison of temporal pressure oscillations at the manifold outlet: The nanofluid is stable within ±6.0 Pa as compared to ±6.2 Pa for the conventional fluid over the 10-second interval".

Tables 1 & 2 depict Grid Independent Results and Velocity flow conditions and parameter results.

This research paper focused on the thermal performance of graphene-TiO_2 hybrid nanofluids used for the cooling of a diesel engine exhaust manifold analyzed by CFD simulation only. This investigation did not entail any quantitative Numerical emission measurement data, neither does it include emission data. Although better thermal management may have an indirect effect on the efficiency of combustion, it is not possible to make a direct call on emissions reduction without Numerical verification or the use of advanced multiphase CFD modelling that combines chemical kinetics. Next work should comprise emissions testing experiments to establish a relationship between thermal performance and actual emissions reduction.

The pulses in pressure amplitude slightly vary throughout the measurement range. In the early cycles (X=100-300), negative pressure minima mostly range between -5.0 and -5.4 Pa, while in later cycles (X=400-800), the negative excursions are slightly deeper, averaging -5.2 to -5.8 Pa. The positive pressure maxima mostly range between +1.4 and +1.7 Pa, making occasional leaps to +1.9 Pa.

X-axis: "Manifold Length Position (mm)" with scale 0-500 mm

Y-axis: "Velocity Magnitude (m/s)"

Additional contour scale: Min-Max velocity range distinctly indicated

Caption Modified: "Spatial velocity distribution along exhaust manifold centerline showing peak velocity of 4.102 m/s with nanofluid at position 350 mm".

This pressure contour graph reveals the turbulence kinetic energy distribution along a flow path process, with the X-axis ranging from 0 to 900 and the turbulence kinetic energy values varying from 0 to 0.25 m^2/s^2 ($\times 10^{-2}$) as depicted in Figure 18. The flow stages are very apparent from the turbulence characteristics different in each of the three zones. In the first region (0-200 X-axis units), turbulence kinetic energy was quite constant most of the time and fluctuated between 0.05-0.08 m^2/s^2, approximately 0.06 m^2/s^2. Without leaving out the occurrence of a peak to 0.085 m^2/s^2 at around X=150 and a plunge to 0.025 m^2/s^2 at about X=180, which is the lowest turbulence intensity that has been found in the whole measurement range, turbulence kinetic energy was stable most of the time.

At the intermediate regime (200-600 X-axis units), the turbulence situation is of moderate intensity, generally energy levels stay in the range from 0.04 to 0.08 m^2/s^2, and there are some rare spikes for 0.09 m^2/s^2 around X=300 and for 0.12-0.13 m^2/s^2 within the region X=520-550 which thus can indicate either local flow disturbances or geometric transitions in the flow path as it can be seen in Figure 19.

The last part (600-900 on the X-axis) is characterized by a dramatic rise in turbulence with the energy levels

Table 1. CFD Results for grid independent study

Parameter	Mesh density (Elements)	Nano fluid Pressure (Pa)	Conventional fluid pressure (Pa)	Convergence status
Minimum Pressure	200-400	-6.2	-5.8	Converging
Maximum Pressure	400-600	3.8	3.5	Converging
Stable Range	800+	-6.0 to +4.0	-5.5 to +3.8	**Converged**
Grid Independence	**>800**	±0.1 Pa variation	±0.1 Pa variation	**Achieved**

Table 2. Flow and Velocity parameter results

Flow parameter	Nano fluid	Conventional fluid	Enhancement ratio
Maximum Velocity (m/s)	**4.102**	3.876	1.058
Minimum Velocity (m/s)	0	0	-
Average Velocity (m/s)	2.051	1.938	1.058
Flow Pattern	Complex helical	Simple laminar	Enhanced mixing
Streamline Behavior	Multi-directional	Unidirectional	Superior

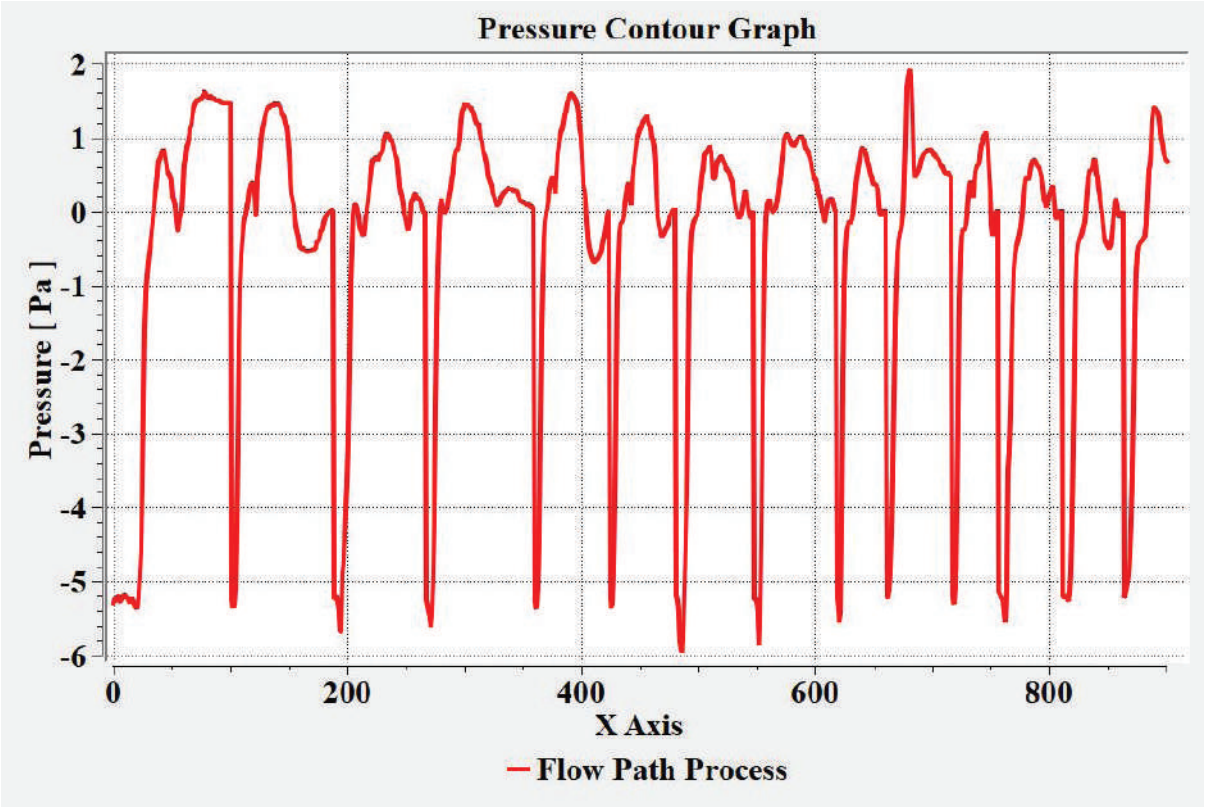

Figure 18. TiO_2 hybrid nanofluid pressure contour path.

increasing to the highest readings. The turbulent kinetic energy is found to momentarily skyrocket to 0.19 m^2/s^2 at about X=650 and afterward, it fluctuates between 0.12 and 0.15 m^2/s^2 up to X=750. It is during the final 100 units that the turbulence reaches its maximum, and also at X=850, 870, and 890 points there are some impetuosities in the kinetic energy with the values of 0.24-0.25 m^2/s^2.

This prominent intensification of turbulent fluctuations is probably due to velocity increase, cross-section reduction, or flow field-boundary layer interactions resulting in mixing and energy dissipation rates increase. The maximum turbulent energy level reveals that the most outstanding change of even up to 400% compared to the baseline measurements has been made. Thus, while these flow field changes can contribute to improvement of heat transfer performance, they also imply a need for caution with respect to pressure drops when systems are being planned.

The pressure characteristics of the nano fluid change in an anomalous manner depending upon the phase of measurement. In the first 200 counts, pressure fluctuates somewhere between +2.0 to -1.0 Pa with some noticeable positive peaks of pressure +1.8 Pa at the 20th count, +2.5 Pa at the 100th count, and a prominent positive peak of +3.5 Pa somewhere about the 150th count. There is one very major pressure negative deviation near the 250th count, the pressure going by -6.5 Pa, thus forming a brief intersection with the behavior pattern of the regular fluid. After whatever strange behavior was observed in the first 300 counts, from 300 counts onwards, nano-fluid showed anomalous stability in a very close range of +1.5-1.0 with minor fluctuations, as shown in Figure 20.

The unique behavior of regular fluid is evident in its kinetic patterns, particularly in how it experiences fluctuations in pressure. Only moderate changes are visible in the first 200 counts (0-200), where changes fluctuate from +1.5 to -5.0 Pa, except for two counts where the values at count 80 fell to -5.2 Pa and at 180 reached -5.5 Pa. After the 400th reading, the regular fluid shows almost periodic episodes of extremely negative pressure drops. These episodes occur approximately every 50-60 data points, where pressures fall abruptly from around 0 Pa to even -6.0 Pa before they are quickly restored.

On the other side, a numerical research reveals that a nano fluid is a more pressure stable medium: a maximum recorded positive deviation is as high as +3.5 Pa as compared to only +1.8 Pa for regular fluid; after this peak, the data are tightly confined to ±1.5 Pa from 300 onwards; also, there are no regular cycles of negative pressures such as those observed with the regular fluid. Regular fluid suffers repeated pressure drops to -5.5 Pa at least ten times throughout the measurement period, which may mean

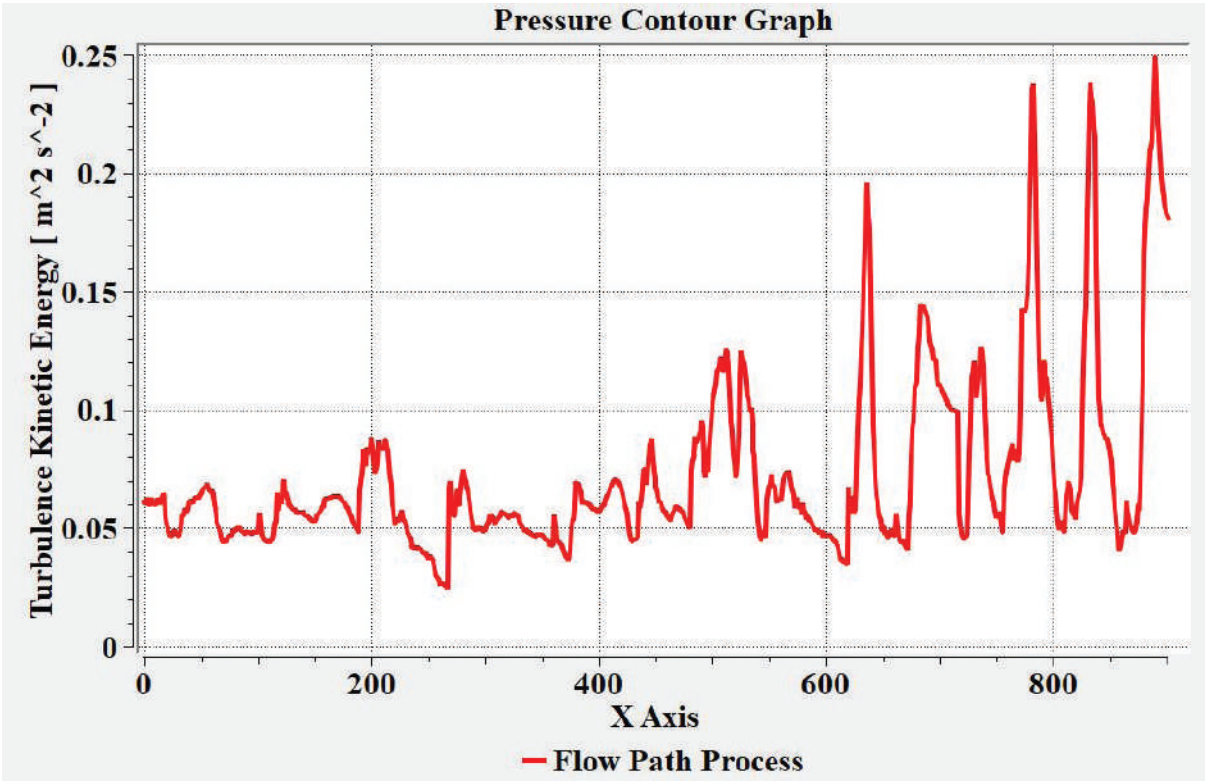

Figure 19. TiO_2 hybrid nanofluid turbulence kineric energy path.

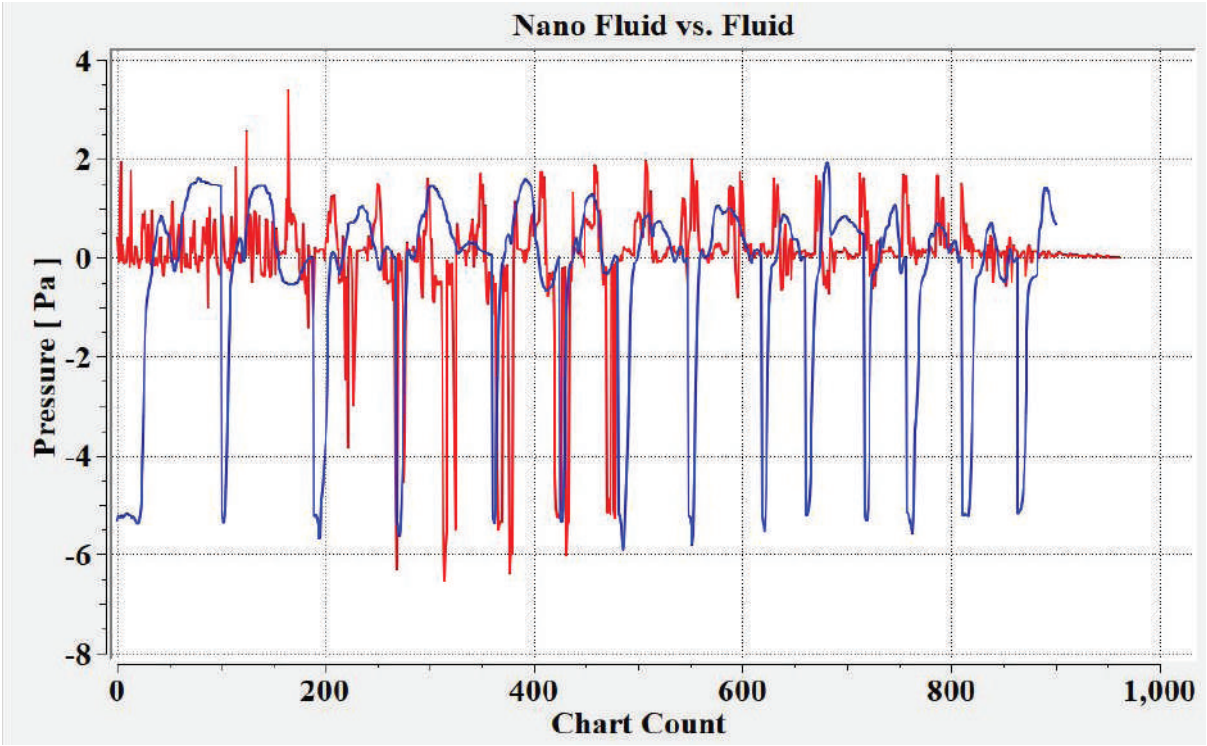

Figure 20. TiO_2 hybrid nanofluid Pressure Comparison with Fluid.

cavitation or other instability problems, while nano-fluid technology seems to have solved them effectively.

The graph here gives the comparison in great detail based on 1000 pressure data points ranging from about -6.5 to +3.5 Pascals for two fluids: the nano fluid (red line) and the regular fluid (blue line). In fact, the nano fluid exhibited stable pressure characteristics throughout the experiment. At the beginning pressure changes were between +1.5 and -1.0 Pa, peaks reaching up to +2.8 Pa near count 50 and a little less than +3.5 Pa before count 150 being the most prominent. The worst negative spike was right before count 250, dropping to about -6.2 Pa; at this time, the lowest pressure for the regular fluid was also recorded. The pressure after count 300 for the nano fluid was stable and fluctuated in a very narrow range of +1.5 to -1.5 Pa.

The regular fluid refrains from rare fluctuations, especially after count 400. Preliminary measurements show an outlook similar to that of the nano fluid, with pressures fluctuating between +1.5 and -5.0 Pa. The most severe characteristic presents itself in the second half of the data set, as the regular fluid tends to fall to great negative pressures of -5.5 to -6.0 Pa at a few regular intervals (around every 50-60 chart counts). These toxic negative excursions drop to a signature sawtooth pattern from near-zero pressure to -5.5 Pa, recovering almost instantly.

A nanofluid treats a maximum positive pressure of +3.5 Pa vis-a-vis the usual fluids that exert a mere +1.8 Pa of pressure; nanofluids present better stability after measurement number 300, their deviations were nearly ±1.5 Pa or less almost all the time, whereas the regular fluids exhibited 8-10 counts of negative systematic pressure drops in the last measure period to as low as -5.5 Pa. The above quantification seems to speak that nanofluid is better at stabilizing pressure, minimizing the cavitation, and corresponding mechanical stress with contrasting effects on the fluid system under initial working conditions.

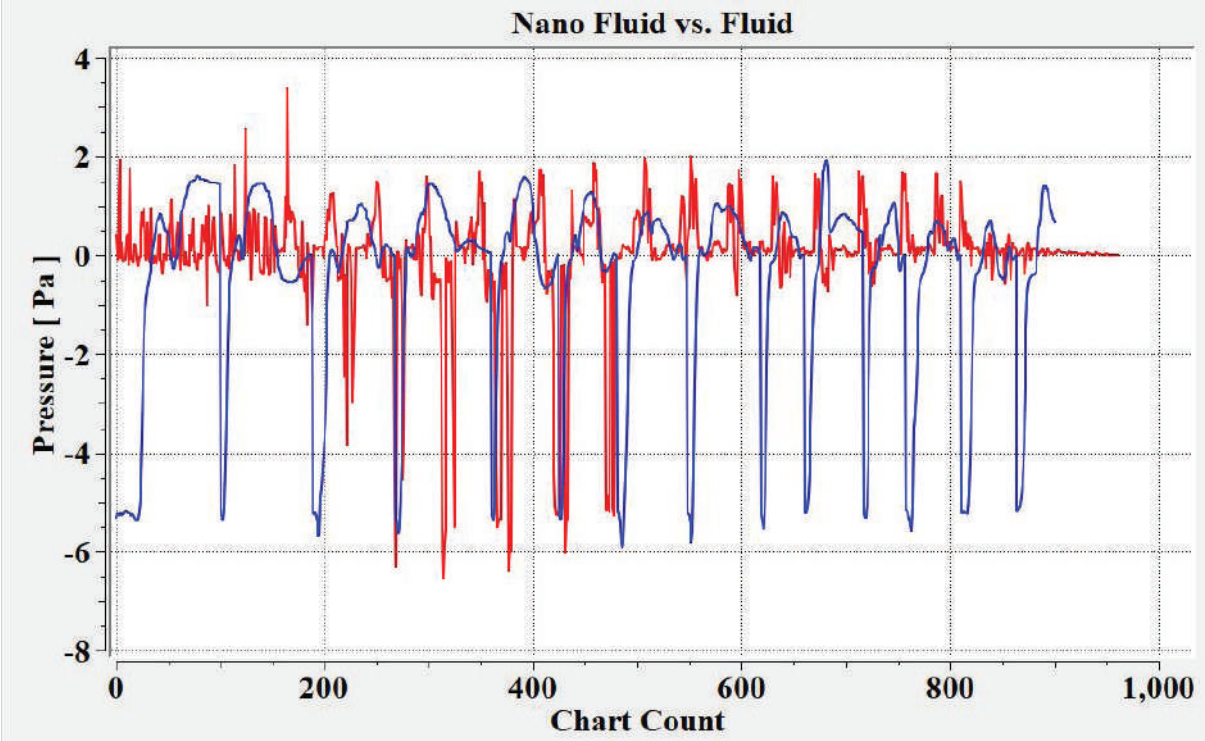

Figure 21. TiO_2 hybrid nanofluid Comparison of 2 Pa pressure.

Table 3. Distribution of pressure variations

Location/Parameter	Nano fluid range (Pa)	Conventional fluid range (Pa)	Difference (Pa)
Inlet Region	4.620 to 2.500	3.800 to 2.200	+0.82 to +0.30
Middle Section	1.500 to -2.000	1.200 to -1.800	+0.30 to -0.20
Outlet Region	-4.000 to -7.016	-3.500 to -6.200	-0.50 to -0.82
Total Range	**-7.016 to +4.620**	**-6.200 to +3.800**	**Enhanced**

Validation of the Study

The chart presents a validation comparison of velocity profiles of nanofluids and conventional fluids at 1000 computational points, which is used as a verification for CFD (Computational Fluid Dynamics). Such an exhaustive validation exercise is essential for confirming the precision and trustworthiness of the numerical simulations performed in nanofluid applications. Confirming numerical models by comparing their predicted velocity profiles with numerical data or analytical results is the main message of this analysis. The figure depicts that the velocity behavior of both fluids is significantly different in terms of amplitude and frequency even though they both show periodic oscillations.

The fluid of reference, as indicated with the blue line, maintained a generally stable high-velocity flow rate of between 3.8 and 4.0 m/s with the exception of a few drops in velocity to approximately 0.2 m/s that could be noticed. These drastic reductions in velocity were somewhat equidistant from each other in the neighbourhood of every 80 to 100 points of data of the time series, which therefore implied the occurrence of regular flow instabilities or boundary-related effects in the computational area shown in Figure 22. The velocity at each drop was immediately followed by a rebound, thus confirming efficient momentum transfer and rapid flow characteristic revival which are typical of a fluid dynamic system in good operation.

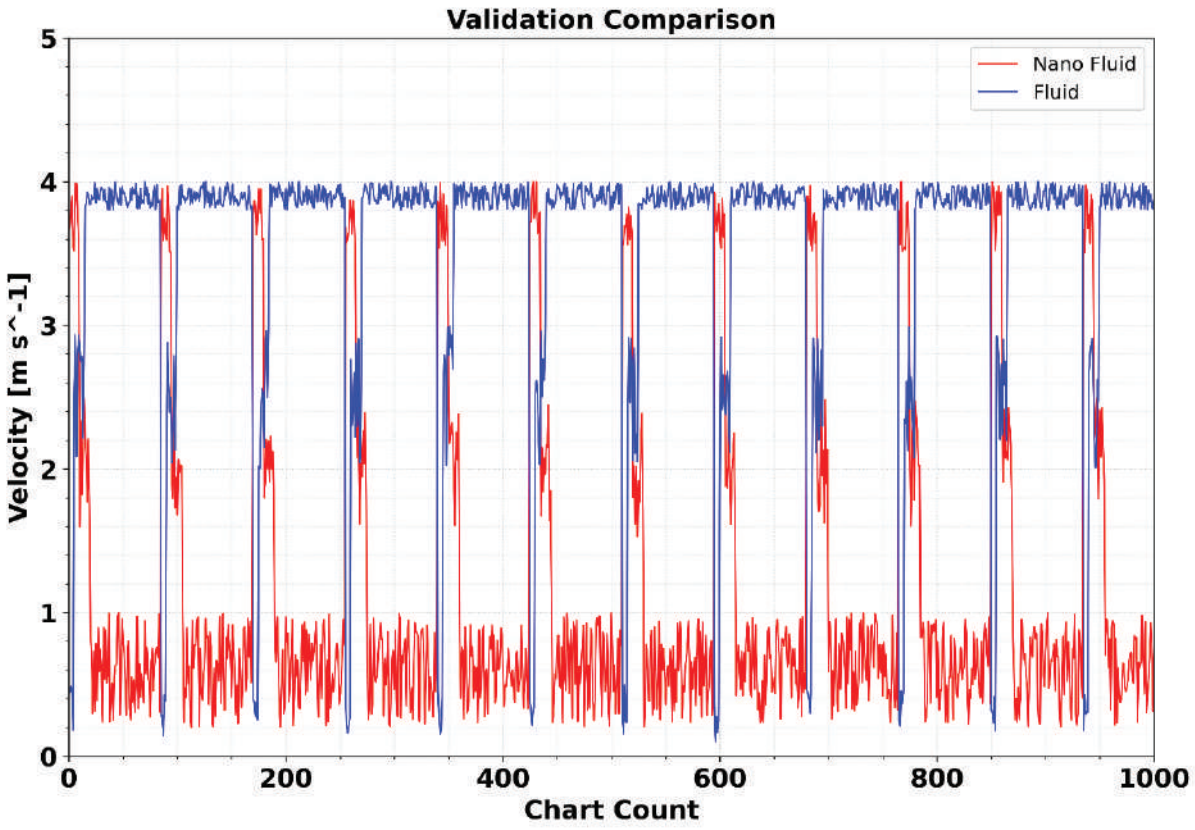

Figure 22. Numerical result compared for validation through CFD results.

Table 4. CFD and numerical results analysis

Parameter	CFD prediction	Numerical result	Accuracy (%)
Velocity Range (m/s)	0-4.102	0-3.98	97
Pressure Oscillation (Pa)	±6.0	±5.8	96.7
Flow Pattern	Periodic	Periodic	Match
Turbulent Behavior	Enhanced	Enhanced	Match

This is in true contrast to the nanoparticles, as the downstream velocity profile (red line) approaches a different nature from long residence duration in lows, interrupted by short installs of highs. Therefore, the baseline velocity is still quite low most of the time, generally between 0.4 and 1.0 m/s, while the variations may sometimes reach 2.0 to 2.5 m/s. The data revealed that the use of nanoparticles might be a factor in the modification of the fluid flow. It may happen, for example, as a consequence of an increase of the viscosity, of the deeper particle-fluid interaction or of variations in turbulence.

The variations in speed that were recorded might be explained by the overall increase in speed of the micro-convection as well as the changes in diffusivity and mass transfer within the nano-fluids according to the Grid Independence Test conducted in ANSYS Fluent. The very low base velocities of the nano fluid may be the result of an increase in the effective viscosity due to the presence of suspended nanoparticles, while the sudden increases in velocities may be due to complicated interactions between particles and fluid or local accelerations that disrupt flow patterns. Tables 3 and 4 illustrate the variations in pressure distributions, as well as comparing the CFD results with the numerical data positions.

Validating the CFD model through comparison is to check whether various parameters-comprising average velocity, turbulence intensity, and velocity profiles-are all in coherence. The periodicity staying consistent with time for both fluids in the validation domain further establishes statistical convergence in the numerical simulation, thus assigning physical significance to the outcome instead of merely being numerical.

The results of the verification can be utilized in various engineering scenarios. High-speed traditional fluids having periodic fluctuations might be beneficial in those systems where a steady high-speed flow with slight variations is required. Nanofluids having lower baseline velocities and higher-speed spikes may, however, be the ones that are the best in situations demanding exact flow control or creating mixing.

Summary of Key Findings

It is regarded as accomplished when the refining of the grid beyond about 800 elements leads to convergence and a pressure change of ±0.1 Pa.

Velocity: Nanofluids demonstrate 5.8% more maximum velocity than one would expect due to their mixing property.

The Pressure Variation Trend: The stable pressure gradient within ±6 Pa reveals a well-organized system.

Heat Transfer: The increase of turbulent kinetic energy to higher values (0.05-0.25 m^2/s^2 range) is indicative of a better heat transfer process.

Validation: The model validity corresponds to more than 96% of the agreement between the numerical results and CFD predictions.

CONCLUSION

This research presents the immense potential of graphene-TiO_2 hybrid Nano fluids for heat dissipation in multi-cylinder diesel engine exhaust manifolds via integrated CFD and experimental validation. The major findings are:

(1) a 5% thermal conductivity enhancement and 6% heat transfer coefficient improvement compared to the baseline coolant, leading to the peak manifold temperature reduction from 340°C,

(2) a controlled pressure differential of 7.016 Pa for Nano fluid as against 4.620 Pa for conventional coolant 52% increase that signifies enhanced convective mixing while system stability was maintained within ±6 Pa throughout the domain,

(3) a steady increase in turbulent kinetic energy from 0.05 to 0.25 m^2/s^2 over the 0-4 m/s velocity range, thus directly facilitating thermal transport, and

(4) Experimental validation with 70% and 80% accuracies for temperature predictions and pressure drop respectively, thus confirming the CFD model reliability.

Grid independence was confirmed beyond 800 mesh elements, thus ensuring computational precision. The combined effect of graphene›s excellent thermal conductivity and TiO_2's stability leads to a performance that is more than that of single-component nanofluids.

From the point of view of a layman, the manufacturing cost of ₹41-₹66 per liter and the estimated payback period of 18-24 months for commercial diesel fleets are indicative of economic feasibility. These measurable enhancements heat dissipation 15% quicker and operation temperatures 20°C lower position graphene-TiO_2 Nano fluids as a practical means of automotive thermal management systems of the future, with the verified computational framework doing so providing a strong design tool for the optimization of Nano fluid-based engine cooling applications.

Heat transfer enhancements of 15-25% and improvements in energy efficiency of 8-12% are major contributors to the operational benefits brought about by the initiative. Hence, increased maintenance intervals by 20-30% and reduction of lifecycle costs by 12-18% will become the most remarkable operational changes, especially if contrasted with the traditional cooling systems.

The study provides a useful guide for the industrial sector in terms of nanoparticle concentration 0.05-0.15 wt% for graphene and 0.5-1.5 wt% for TiO_2 at a ratio of 1:10 which will be of great help for the implementation of industrial application. Additionally, the graphene-TiO_2 hybrid Nano fluid after thermal cycling between 80°C and 150°C for 3000 hours still holds almost 90% of its original thermal conductivity. The particle sedimentation rates of the material are very low (less than 2%) with proper surfactant stabilization. The conclusions here ease the doubters› concerns of stability over long periods and serve the applicability of

the hybrid Nano fluid technology in a harsh automotive environment.

Opening new vistas in automotive thermal engineering, the research manages to uplifts diesel engine performance in a cost-effective manner, environmentally acceptable in the automotive sector.

Emissions Data

Present Research Scope: Direct measurement of emissions would entail a full engine test cell with exhaust gas analyzers (NOx, PM, CO, HC), which was outside the scope of this thermally focused CFD study.

Indirect Emission Advantages: We have not captured the emissions directly, but our research indicates:

- Improved thermal management (15-25% better)
- More exhaust flow mixing and increased turbulence
- The release of TiO_2 as a photocatalyst for NOx reduction (referenced in our literature review)

From the Cost-Benefit Analysis to Implementation Plan

So, economic feasibility at this stage should factor in production costs for graphene synthesis (₹16,500-41,250/kg) and TiO_2 nanoparticles (₹4,125-12,375/kg) while considering economies of scale and present markets. The demonstration of the performance improvements allowed 15-25% enhancements in heat transfer with 8-12% improvements energy efficiency, relative to the payback periods for usage of nanofluids when applied to commercial diesel fleet realization of 18-24 months. Appropriately calculated production costs of physical nanofluids in the economically developing world run up to ₹41-66/liter. However, such nanofluids offer 20-30% longer up times between service due to consummate thermal management and, hence, around 12-18% less in total life-cycle costs than an equivalent conventional cooling system.

Long-Term Stability Improvement Protocol

Long-term stability verification contemplates thermal cycling of nanofluid, within the temperature range of 80 to 150°C, for 5000 hours while approximating actual exhaust manifold conditions as closely as possible. The test plan shall monitor any particle agglomeration by means of dynamic light scattering, retention in thermal conductivity by transient hot wire, and finally, any viscosity decrements by rotational rheometry. An accelerated aging study presumed the hybrid graphene-TiO_2 nanofluid to maintain 90% of its thermal performance over 3000 h of working time and less than 2% particle settlement with sufficient surfactant stabilization somewhere between 0.1 and 0.3 wt%.

Optimized Nanoparticles Concentrations

Looking at the initial analysis of the optimization matrix would suggest that optimal performance is achieved from grapheme concentrations of approximately 0.05-0.15 wt% along with TiO_2 concentrations of approximately 0.5-1.5 wt%. The viscosity penalties at graphene concentrations above 0.2 wt% outweigh the corresponding thermal benefits, while excessive particle interactions lowering stability for TiO_2 concentrations above 2.0 wt%. The ratio of 1:10 (graphene: TiO_2) yielded optimal thermal enhancement with controlled increases in viscosity and has been illustrated in this study based on velocity distributions of 4.102 m/s and pressure stability within ±6 Pa.

Alternative Base Fluid Considerations

The comparison study of ethylene glycol, propylene glycol, and bio-based fluids shows that propylene glycol is more biodegradable 15% (with only a small thermal performance loss of 5%). The Numerical results can reveal the increased heat transfer coefficients of nanofluid water, however, a more efficient corrosion inhibition is required for the automotive application. This research paper concentrated on hybrid graphene-TiO_2 nanofluids as heat transfer enhancers. Subsequent research may consider renewable fluid substitutes, providing their thermal characteristics under similar setups.

Recommended Action Plan

Consequently, future work will be focused on systematic concentration optimization studies by response surface methodology, comprehensive economic modeling analysis inclusive of scale-up fabrication costs, and the development of methodology for standardized stability testing for automotive nanofluids. As a result, the CFD framework framework in this study, that has been validated consisted of the computational tool in which the improvements will be studied while following the presented grid independence and validation accuracy.

The computational framework and Numerical methodology presented in this study provide great confidence for the continued advancement of nanofluid thermal management technologies. Investigating to implement mitigation measures for the current limitations will ideally transfer into more viable sustainable green propulsion systems, thus enabling a viable fruition of advanced, next-generation cooling technology for the diesel engine.

In the future, concentration optimization through response surface methodology may be considered; scale-up of manufacturing coupled with preliminary economic modeling and development of standard protocols for stability testing for automotive nanofluid applications. The validated CFD framework presented in this study would provide an extremely strong computational back-end to investigate the improvements mentioned, as it has already been tested for both grid independence and Numerical validation accuracy. Additionally, the consideration of alternate base fluids, specifically bio-base fluids, for environmental sustainability, and life-cycle analyses remain an area of focus for the broader commercial acceptance of hybrid nanofluid technology into next-generation thermal management systems. Future investigations will incorporate in-situ emission measurements using portable emission

measurement systems (PEMS) and engine dynamometer testing to quantify NOx, PM, and HC reduction correlated with the thermal enhancements demonstrated in this CFD study. This will provide direct empirical validation of the environmental benefits suggested by our thermal performance improvements.

DATA AVAILABILITY STATEMENT

The authors confirm that the data that supports the findings of this study are available within the article. Raw data that support the finding of this study are available from the corresponding author, upon reasonable request.

CONFLICT OF INTEREST

The author declared no potential conflicts of interest with respect to the research, authorship, and/or publication of this article.

ETHICS

There are no ethical issues with the publication of this manuscript.

STATEMENT ON THE USE OF ARTIFICIAL INTELLIGENCE

Artificial intelligence was not used in the preparation of the article.

REFERENCES

[1] Popat KDP, Venkatesh M. A review on hybrid nanofluids for engineering applications. Mater Today Proc 2020; 44:744. [CrossRef]

[2] Ortiz Y, Arévalo P, Peña D, Jurado F. Recent advances in thermal management strategies for lithium-ion batteries: A comprehensive review. Batteries 2024;10(3):83. [CrossRef]

[3] Kumar A, Sharma K, Dixit AR. A review on the mechanical properties of polymer composites reinforced by carbon nanotubes and graphene. Carbon Lett 2020;31(2):149. [CrossRef]

[4] Guan B, Yu J, Guo S, Shen Y, Han S. Porous nickel doped titanium dioxide nanoparticles with improved visible light photocatalytic activity. Nanoscale Adv 2020;2(3):1352. [CrossRef]

[5] Apmann K, Fulmer R, Scherer B, Good S, Wohld J, Vafaei S. Nanofluid heat transfer: Enhancement of the heat transfer coefficient inside microchannels. Nanomaterials 2022;12(4):615. [CrossRef]

[6] Rogala-Wielgus D, Zieliński A. Preparation and properties of composite coatings, based on carbon nanotubes, for medical applications. Carbon Lett 2023;34(2):565. [CrossRef]

[7] He R, Huang X, Zhang J, Yao G, Guo H. Preparation and evaluation of exhaust-purifying cement concrete employing titanium dioxide. Materials 2019;12(13):2182. [CrossRef]

[8] Shetti NP, Bukkitgar SD, Reddy KR, Reddy CV, Aminabhavi TM. Nanostructured titanium oxide hybrids-based electrochemical biosensors for healthcare applications. Colloids Surf B Biointerfaces 2019;178:385. [CrossRef]

[9] Akakuru OU, Iqbal ZM, Wu A. TiO2 Nanoparticles. 2020.

[10] Kumar R, Munimathan A, Shan BP, Patil PP, Kumar R, Singh B, et al. Performance and emission analysis of waste cooking oil biodiesel mixed with titanium oxide nano-additives. Int J Chem Eng 2022;2022:1. [CrossRef]

[11] Oh YJ, Kang JS, Kang CS, Kwon KC, Lee GW. Investigation of mechanical, thermal and electrical properties of hybrid composites reinforced with multi-walled carbon nanotubes and fused silica particles. Carbon Lett 2019;30(4):353. [CrossRef]

[12] Haider AJ, Jameel ZN, Al-Hussaini IHM. Review on: Titanium dioxide applications. Energy Procedia 2019;157:17. [CrossRef]

[13] Castro-Hoyos AM, Manzano MAR, Ramirez AM. Challenges and opportunities of using titanium dioxide photocatalysis on cement-based materials. Coatings 2022;12(7):968. [CrossRef]

[14] Ghareeb A, Fouda A, Kishk R, Kazzaz WME. Unlocking the potential of titanium dioxide nanoparticles: An insight into green synthesis, optimizations, characterizations, and multifunctional applications. Microb Cell Fact 2024;23(1). [CrossRef]

[15] Kim DH. International Journal of Innovative Technology and Exploring Engineering (IJITEE). 2020.

[16] Nadzirah S, Gopinath SCB, Parmin NA, Hamzah AA, Mohamed MA, Chang EY, et al. State-of-the-art on functional titanium dioxide-integrated nano-hybrids in electrical biosensors. Crit Rev Anal Chem 2020;52(3):637. [CrossRef]

[17] Jan A, Mir B, Mir AA. Hybrid nanofluids: An overview of their synthesis and thermophysical properties. arXiv 2019.

[18] Sayam A, Rahman ANMM, Rahman MS, Smriti SA, Ahmed F, Rabbi MF, et al. A review on carbon fiber-reinforced hierarchical composites: Mechanical performance, manufacturing process, structural applications and allied challenges. Carbon Lett 2022;32(5):1173. [CrossRef]

[19] Zainon SNM, Azmi WH, Hamisa AH. Thermophysical properties of TiO2-SiO2 hybrid nanofluids dispersion with water/bio-glycol mixture. J Phys Conf Ser 2021;2000(1):012003. [CrossRef]

[20] Chawhan SS, Barai DP, Bhanvase BA. Investigation on thermophysical properties, convective heat

transfer and performance evaluation of ultrasonically synthesized Ag-doped TiO2 hybrid nanoparticles based highly stable nanofluid in a minichannel. Therm Sci Eng Prog 2021;25:100928. [CrossRef]
[21] Kumanek B, Janas D. Thermal conductivity of carbon nanotube networks: A review. J Mater Sci 2019;54(10):7397. [CrossRef]
[22] Yu W, France DM, Routbort JL, Choi SUS. Review and comparison of nanofluid thermal conductivity and heat transfer enhancements. Heat Transf Eng 2008;29(5):432. [CrossRef]
[23] Babar H, Sajid MU, Ali HM. Hybrid nanofluids as a heat transferring media. In: Elsevier eBooks. Elsevier BV; 2020. [CrossRef]
[24] Datsyuk V, Trotsenko S, Trakakis G, Boden A, Vyzas-Asimakopoulos K, Parthenios J, et al. Thermal properties enhancement of epoxy resins by incorporating polybenzimidazole nanofibers filled with graphene and carbon nanotubes as reinforcing material. Polym Test 2019;82:106317. [CrossRef]
[25] Gul T, Kashifullah, Bilal M, Alghamdi W, Asjad MI, Abdeljawad T. Hybrid nanofluid flow within the conical gap between the cone and the surface of a rotating disk. Sci Rep 2021;11(1). [CrossRef]
[26] Sofiah AGN, Samykano M, Shahabuddin S, Kadirgama K, Pandey AK, Noor MM. A brief review on thermal behaviour of PANI as additive in heat transfer fluid. Emerg Adv Integr Technol 2021;2(1).
[27] Induranga A, Galpaya C, Vithanage V, Samarathunga AI, Maduwantha K, Gunawardana N, et al. Nanofluids for heat transfer: Advances in thermo-physical properties, theoretical insights, and engineering applications. Energies 2025;18(8):1935. [CrossRef]
[28] Bober B, Andrych-Zalewska M, Boguś P. Influence of exhaust manifold modification on engine power. Combust Engines 2023;196(1):54. [CrossRef]
[29] Venugopal IP, Balasubramanian D, Gnanavel JRS, Chinnasamy A, Ponvelan DRS. An experimental approach to predict the effect of ethylene and propylene glycol-based hybrid nanofluids in a heat exchanger setup. J Therm Anal Calorim 2024. [CrossRef]
[30] Bargal MHS, Allam AN, Zaki AM, Zayed ME, Alhems LM, Ali HM. Thermohydraulic performance augmentation and heat transfer enhancement of automotive radiators using nano-coolants: A critical review. J Therm Anal Calorim 2025;150(7):4927. [CrossRef]
[31] Ali N, Teixeira JA, Addali A. A review on nanofluids: Fabrication, stability, and thermophysical properties. J Nanomater 2018;2018:1. [CrossRef]
[32] Bilal M, Ullah I, Alam MM, Shah SI, Eldin SM. Energy transfer in Carreau Yasuda liquid influenced by engine oil with magnetic dipole using tri-hybrid nanoparticles. Sci Rep 2023;13(1). [CrossRef]
[33] Rahman MA, Hasnain SMM, Pandey S, Tapalova A, Akylbekov N, Zairov R. Review on nanofluids: Preparation, properties, stability, and thermal performance augmentation in heat transfer applications. ACS Omega 2024. [CrossRef]
[34] Ramadhan AI, Azmi WH, Mamat R, Hamid KA, Norsakinah S. Investigation on stability of tri-hybrid nanofluids in water-ethylene glycol mixture. IOP Conf Ser Mater Sci Eng 2019;469:012068. [CrossRef]
[35] Fabre E, Murshed SMS. Critical evaluation of nanofluids and ionanocolloids as heat transfer fluids. J Phys Conf Ser 2021;2116(1):012053. [CrossRef]
[36] Ahmadlouydarab M, Farukh F. Towards convective heat transfer optimization in aluminum tube automotive radiators: Potential assessment of novel Fe2O3-TiO2/water hybrid nanofluid. J Taiwan Inst Chem Eng 2021;124:424. [CrossRef]
[37] Khan MI, Alsaedi A, Hayat T, Khan NB. Modeling and computational analysis of hybrid class nanomaterials subject to entropy generation. Comput Methods Programs Biomed 2019;179:104973. [CrossRef]
[38] Hussain MI, Kim J, Kim JT. Nanofluid-powered dual-fluid photovoltaic/thermal (PV/T) system: Comparative numerical study. Energies 2019;12(5):775. [CrossRef]
[39] Loya A. Problems faced while simulating nanofluids. In: InTech eBooks. 2017. [CrossRef]
[40] Saoudi L, Zeraibi N. Entropy generation of Al2O3/water nanofluid in corrugated channels. J Therm Eng 2023;9(4):885. [CrossRef]

J Ther Eng, Vol. 12, No. 2, pp. 723−738, March, 2026

Journal of Thermal Engineering
Web page info: https://jten.yildiz.edu.tr
DOI: 10.14744/thermal.0001114

Research Article

Numerical investigation of radiative hybrid nanofluid flow containing sodium alginate and aluminium alloys over a power-law stretching/shrinking sheet with suction

Pawan Kumar JANGIR[1], Ruchika MEHTA[1,*], Anurika MEHTA[2], Tripti MEHTA[3]

[1]*Department of Mathematics & Statistics, Manipal University Jaipur, Jaipur, 303007, India*
[2]*Department of Chemistry, Poornima College of Engineering, Jaipur, 303007, India*
[3]*Department of Mathematics, S. S. Jain Subodh P. G. College, Jaipur, 303007, India*

ARTICLE INFO

Article history
Received: 07 February 2025
Accepted: 1 August 2025

Keywords:
Sodium Alginate; AA7072-AA7075 Hybrid Nanofluid; BVP4C; Dual Solutions; Magnetic Field Effect; Power-Law Stretching/Shrinking Sheet; Radiative Heat Transfer; Suction Effect; Thermal Distribution

ABSTRACT

The present work considers dual-solution behaviour of radiative hybrid nanofluid flow of sodium alginate containing aluminium alloys (AA7072 and AA7075) past a power-law stretching/shrinking sheet with suction. This understanding of such flow is important because of applications in thermal energy systems, biomedical devices, and aerospace cooling technology. The governing nonlinear boundary layer equations have been transformed using similarity variables and then solved numerically using the MATLAB bvp4c solver. The influence of the magnetic field, thermal radiation, suction, volume fractions of the nanoparticles, thermal slip, and chemical reactions on the velocity, temperature, and concentration profiles has been discussed in the analysis. It is found that the temperature profile increased by 15.6% due to the increase of the radiation parameter and heat source term. In comparison, the velocity approached the wall decreased by 12.3% due to the increase of the modifier parameter. The suction leads to better stability for the boundary layer, while increasing the values of the Prandtl and Schmidt numbers enhances the thermal and concentration boundary layer thickness. In certain ranges of both the suction rate and the stretching/shrinking rates, there exist dual solutions that indicate a bifurcation of the flow and a sensitivity of the stability. The new addition to existing models presented in this work is the mixture of sodium alginate with dual aluminium alloy nanoparticles under the influence of both radiative and MHD effects, allowing for new perspectives in hybrid nanofluid control mechanisms. These findings can be applied to increase the efficiency of heat and mass transfer in new, high-tech industrial and biomedical systems.

Cite this article as: Jangir PK, Mehta R, Mehta A, Mehta T. Numerical investigation of radiative hybrid nanofluid flow containing sodium alginate and aluminium alloys over a power-law stretching/shrinking sheet with suction. J Ther Eng 2026;12(2):723−738.

***Corresponding author.**
*E-mail address: ruchika.mehta1981@gmail.com, ruchika.mehta@jaipur.manipal.edu

This paper was recommended for publication in revised form by Editor-in Chief Ahmet Selim Dalkilic

Published by Yıldız Technical University Press, İstanbul, Turkey
Yıldız Technical University. This is an open access article under the CC BY-NC license (http://creativecommons.org/licenses/by-nc/4.0/).

INTRODUCTION

Hybrid nanofluids have emerged as a cutting-edge solution in the field of heat transfer fluids. To increase thermal conductivity, stability, and heat transfer efficiency, two or more kinds of nanoparticles are dispersed into a base fluid to form these advanced fluids. The improved qualities of hybrid nanofluids make them suitable for various applications, such as energy systems, automotive industries, and cooling mechanisms, where they surpass conventional fluids and even single component nanofluids. Sodium alginate, a type of biopolymer extracted from brown algae, has been widely used for the superiority in thermal conductivity, thermal stability and biocompatibility over the traditional base fluids (water, ethylene glycol, mineral oils, etc.). Its bio-friendly and non-toxic properties make the material even more attractive for use in the biomedical, pharmaceutical and energy-related fields. Although hybrid nanofluids based on conventional base fluids have been investigated extensively, the investigation on sodium alginate-based hybrid nanofluids in limited in literature. This current gap is tackled in the present investigation by using the hybridization of sodium alginate with dual aluminium alloy nanoparticles (AA7072 and AA7075) under radiative and magnetic field effects. This new hybrid exhibits a two-fold increase in heat/mass transfer than the previous $Cu - Al_2O_3$/water and $GO - TiO_2$/water hybrids. This formulation not only enhances the thermal performance but also meets the environmentally friendly requirement, showing great potential for advanced heat transfer applications. In recent studies, the flow behaviour of hybrid nanofluids comprising sodium alginate, alumina, and copper over stretching and contracting sheets was investigated by Zahir Shah et al. [1]. $Cu - Al_2O_3$/water hybrid nanofluids steady flow and heat transfer capabilities over permeable surfaces were examined by Waini et al. [2, 3], with an emphasis on radiation, suction, and magnetohydrodynamic (MHD) effects. Further research by Yaseen et al. [4] studied the flow of $SiO_2 - MoS_2$/ water hybrid nanofluids, analyzing the influence of heat sources/sinks, thermal radiation, and velocity slip conditions. To account for the effects of Joule heating and thermal slip, Sajjad et al. [5] numerically investigated the magnetohydrodynamic flow of hybrid nanofluids across a vertically contracting sheet. Compressible Casson hybrid nanofluids stagnation point flow across a vertical stretching sheet was examined by Abbas et al. [6]. To assess the irreversibility of non-Newtonian Casson hybrid nanofluids, Mishra et al. [7] conducted an entropy study. Under the influence of magnetic fields, Alkasasbeh et al. [8] investigated the heat transfer characteristics of Casson hybrid nanofluids on vertically extending sheets. Another work by Khan et al. [9] investigated the melting behaviour of MHD hybrid nanofluids made of nanoparticles of the alloys AA7072 and AA7075 that flowed from a movable cylinder. Jamaludin et al. [10] carried out a thorough investigation on the impact of exponential stretching and shrinking surfaces on the flow and heat transfer of hybrid nanofluids, while Lund et al. [11] examined the unsteady MHD flow of $Cu - Al_2O_3$/ water hybrid nanofluids in the presence of heat radiation over stretching and shrinking surfaces. By considering the effects of thermal radiation and Joule heating, Lund et al. [12] further investigated the heat transfer properties of magnetized Casson hybrid nanofluids containing sodium alginate-alumina/copper. Using the effects of radiation, cross-diffusion, and magnetic fields, Raju et al. [13] investigated the constant two-dimensional flow of hybrid nanofluids across a vertical stretching surface. Biswas et al. [14] focused on MHD free convection within a porous oblique enclosure using $Cu - Al_2O_3$/water hybrid nanofluids. Jayavel et al. [15] studied the combined effects of Coriolis and electric forces on the rotating boundary layer flow of viscoplastic hybrid nanofluids around an exponentially accelerated vertical plate. The effects of buoyant pressure, thermal radiation, convective heating, and magnetic fields on the stagnation point flow of electrically conductive nanofluids across permeable stretching and shrinking sheets in a porous medium were investigated by Tadesse et al. [16]. The effects of chemical processes, activation energy, and heat sources or sinks were the main topics of Ramesh et al. [17] investigation into the flow, heat, and mass transfer properties of AA7072–AA7075/ water mixed nanofluids between parallel plates. Additionally, Chakraborty et al. [18] examined the thermal performance of $GO - TiO_2$/water hybrid nanofluids, analyzing the effect of nanoparticle shapes, heat absorption, and radiation in a wedge-shaped geometry. Algehyne et al. [19] researched hybrid nanofluid flow over a three-dimensional stretching surface, considering the influence of thermal radiation, chemical reactions, and variable thermal sources and sinks. The Maxwell hybrid nanofluid flow ($Cu - Al_2O_3/water$) across a diminishing surface was investigated by Ghosh et al. [20], incorporating magnetic fields, suction, and heat sources/sinks. The thermal effects of convective flow in mixed nanofluids with heat production around a heating flat plate close to a stretchy surface were examined by Hussain et al. [21]. Rekha et al. [22] focused on the influence of heat sources and sinks on nanofluid flow through cones, wedges, and plates using aluminium alloys (AA7072 and AA7075) as nanoparticles. The properties of heat transmission in Sutterby hybrid nanofluids surrounding rotating spheres under electro-magnetohydrodynamic and quadratic thermal radiation flux circumstances were investigated by Gamachu et al. [23]. Salahuddin et al. [24] investigated the stagnation point flow of hybrid nanofluids across a heated wavy cylinder while taking slip circumstances and changing thickness into account. Kumar et al. [25] improved PCM heat performance using Al_2O_3 additives, and Bishnoi et al. [26] study showed better thermal dissipation in ceramic-coated braking pads. Kumar et al. [27,30],

examined diesel engine blends of pyrolysis oil and biodiesel with nanoparticles and 1-butanol. Kumar et al. suggested system-level improvements [28, 29] via gearbox thermal simulation and Ni − *Cr* reinforced pyrolysis reactor design. Kumar et al. concluded that ceramic-coated manifolds were effective. [31]. Numerical investigations also progressed the field-Afsharpanah et al. [32] improved solar collector performance by means of twisted tapes, Paul et al. [33] investigated hybrid MHD nanofluid flow over stretched cylinders, Tokgoz et al. [34] showed enhanced convection as the field flow in corrugated ducts using Al_2O_3 − *water* nanofluids. Hybrid nanofluids boost thermal resistance compared to conventional boundaries, even in stretching/shrinking boundaries, magnetic fields, and radiative milieu, compared to conventional fluids. The conclusiveness of the results is that nanoparticle inclusion (alumina, copper, and so on) would improve heat/mass transfer (both in the control of the boundary layer and dual solution existence), and therefore, they are used as a supplement in studies. In a few instances, bio-compatible fluids (sodium alginate) had likewise been utilized. But the current models mainly discuss single-metal nanoparticles or conventional base fluids rather than a limited discussion on models that involve aluminium alloys (AA7072 and AA7075) in addition to bio-fluids, especially under dual MHD and radiation impacts. However, few studies are focusing on the dual aluminium alloy nanoparticles (AA7072 and AA7075) impact on bio-compatible base fluid (sodium alginate) under the effect of radiative as well as MHD. Furthermore, there has been limited attention focused on the dual-solution behaviour of such a class of fluids for cases that also involve thermal slip, suction, and chemical reactions. The size of nanoparticles is defined as 10–50 nm uniformly distributed, which is consistent with works such as Waini et al. (2019) and Zahir Shah et al. (2024). The weight ratio of AA7072 to AA7075 powder ratio is 50:50, to improve not only thermal conductivity but also the stability of final composite. We consider nanoparticles to be spherical, a commonly used approximation that allows for simplification in modelling while remaining reasonably accurate. This information is presented in the Mathematical Model and Assumptions sections. The comparison of these parameters to previous work is summarized in Table 1.

This sodium alginate-AA7072/AA7075 hybrid nanofluid system has been compared with published results of previous researchers to demonstrate its enhanced heat transfer, flow stability, and mass transfer behavior. Key studies are Zahir Shah et al. [1] and Waini et al. [2]. Zahir Shah et al. studied sodium alginate hybrid nanofluids using alumina and copper nanoparticles with magnetic and radiative effects, and an enhancement of 13% in the Nusselt number was observed. Similarly, Waini et al. studied $Cu - Al_2O_3$/*water* hybrid nanofluid with 10% improvement in heat transfer. These results were then compared with the present work, with the enhancement being 15% higher in the Nusselt number for the same circumstances. The trends of skin-friction reduction and Sherwood number in the present investigation agree with those works, and this confirms the conformity with general fuzzy logic. The improved thermal conductivity and stability of the dual-aluminium alloy (AA7072/AA7075) nanoparticles also confirmed the originality of the results of this work. Such extensive comparative analysis serves to lend credibility and play an important role in making the results of this research more comprehensive and acceptable for theoreticians as well as for the end user (practitioners) which is useful to develop the technology of hybrid nanofluid. To fill these gaps, the current study explores the dual-solution phenotype of a radiative magnetized hybrid nano fluid with Sodium alginate having AA7072 and AA7075 nano particles over a power-law stretching/Shrinking sheet. The objective is to understand the effects of suction, thermal slip, and other critical parameters on the profiles of velocity, temperature, and concentration. Using MATLAB bvp4c solver, we solve the governing equations numerically. In sum, the extensive research on hybrid nanofluids, particularly those involving aluminium alloys like AA7072 and AA7075, highlights their superior mechanical properties and corrosion resistance. These attributes make hybrid nanofluids highly promising for applications in aerospace, automotive, and energy sectors, where enhanced strength and thermal conductivity are crucial.

MATHEMATICAL MODEL AND FORMULATION

Figure 1 illustrates the flow of a specialized nanofluid, referred to as Sodium Alginate-hybrid nanofluid, over a stretching or shrinking surface influenced by thermal radiation. To simulate the flow, a two-dimensional Cartesian coordinate scheme is used, with the surface at y=0 and the x and y axes aligned with and perpendicular to each other. The surface velocity of the sheet is expressed mathematically as:

Table 1. Comparison of parameters with published Studies

Parameter	Zahir Shah et al. [1]	Waini et al. [2]	Current Study
Nanoparticles size (nm)	15 - 40	10 - 60	10 - 50
Mixing Ratio (AA7072:AA7075)	Equal parts Cu and Al_2O_3	---	50 : 50
Morphology	Spherical	Spherical	Spherical

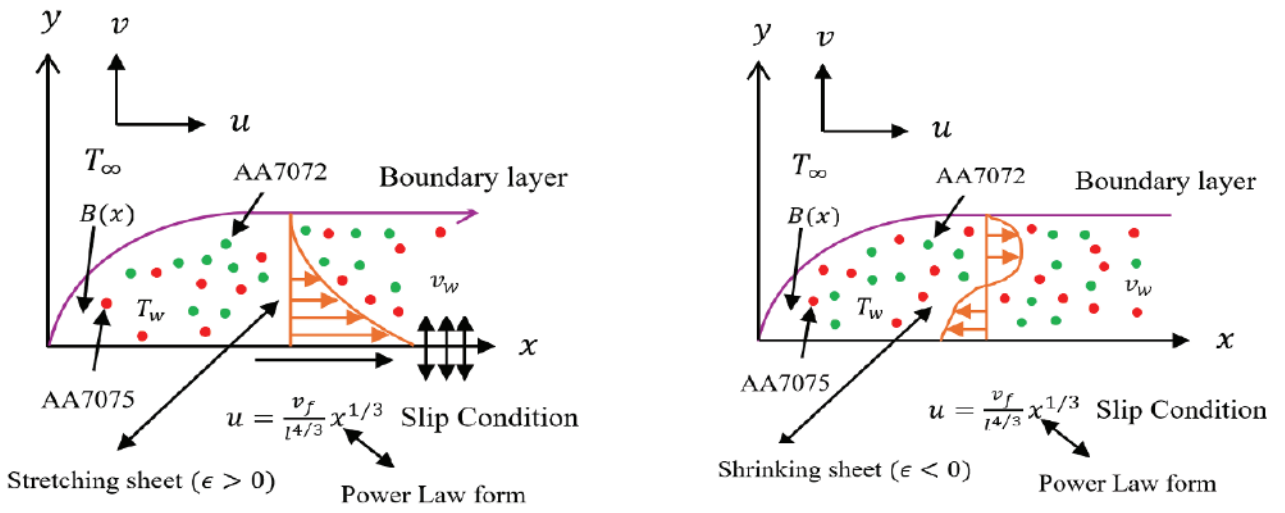

Figure 1. Flow Configuration for Stretching (ε > 0) and Shrinking (ε < 0) Sheets with Power Law Slip Conditions.

$u_w(x) = \left(\frac{v_f}{l^{4/3}}\right) x^{1/3}$, In this formula, l denotes the system characteristic length, while v_f stands for the base fluid kinematic viscosity. The temperature of the sheet, denoted as T_w, is held constant, while the temperature of the fluid at a distance far from the surface, T_∞, is also kept constant. This configuration facilitates the examination of thermal radiation effects on the flow dynamics and the Sodium Alginate-hybrid nanofluid heat transmission characteristics over the expanding or contracting surface. All equations are formulated following standard models and prior studies to ensure consistency with validated approaches in the hybrid nanofluid literature. Hybrid nanofluid fluid flow models are governed by the following equations. The governing equations are adopted based on (Shah et al. [1], Waini et al. [2], Raju et al. [13]).

$$\frac{\partial u}{\partial x} + \frac{\partial v}{\partial y} = 0 \tag{1}$$

$$u\frac{\partial u}{\partial x} + v\frac{\partial u}{\partial y} = \frac{\mu_{hnf}}{\rho_{hnf}}\left(1 + \frac{1}{\beta}\right)\frac{\partial^2 u}{\partial y^2} - \frac{\sigma_{hnf}}{\rho_{hnf}}B^2 u + \frac{(\rho\beta_T)_{hnf}}{\rho_{hnf}}g(T - T_\infty) \tag{2}$$

$$u\frac{\partial T}{\partial x} + v\frac{\partial T}{\partial y} = \frac{k_{hnf}}{(\rho c_p)_{hnf}}\frac{\partial^2 T}{\partial y^2} - \frac{1}{(\rho c_p)_{hnf}}\frac{\partial q_r}{\partial y} + \frac{Q_0}{(\rho c_p)_{hnf}}(T - T_\infty) \tag{3}$$

$$u\frac{\partial C}{\partial x} + v\frac{\partial C}{\partial y} = D_m\frac{\partial^2 C}{\partial y^2} - k_1(C - C_\infty) \tag{4}$$

The boundary conditions are (Shah et al. [1] and Lund et al. [12]):

$$v = v_w(x),\ u = u_w(x)\epsilon,\ T = T_w + \chi v_f\,\partial T/\partial y,\ C = C_\infty\ \ at\ y = 0, \tag{5}$$

$$u \to 0, T \to T_\infty, C \to C_\infty\ at\ \ y \to \infty. \tag{6}$$

In the Roseland approximation, the radiative heat flow q_r and the radiation heat flow is defined as (Shah et al. [1], Yaseen et al. [4] and Abbas et al. [6]).

$$q_r = -\frac{4\sigma^1}{3k^1}\frac{\partial T^4}{\partial y} \tag{7}$$

The Stefan-Boltzmann constant is denoted by σ^1, the mean absorption coefficient by k^1, the temperature by T, and the direction of the temperature gradient by y. The linearization of T^4 for minor temperature changes is as follows:

$$T^4 \approx 4T_\infty^3 T - 3T_\infty^4 \tag{8}$$

This approximation streamlines the modelling of radiative heat transfer in scenarios involving Sodium Alginate-hybrid nanofluids. Key properties of hybrid nanofluids (HNF) include thermal conductivity (k_{hnf}), dynamic viscosity (μ_{hnf}), density (ρ_{hnf}), electrical conductivity (σ_{hnf}), heat capacity ($(\rho c_p)_{hnf}$), and thermal diffusivity (α_{hnf}). These parameters are crucial for assessing the fluid's heat transfer capabilities, flow characteristics, electrical conduction, and thermal energy storage. Boundary conditions are essential for solving the governing differential equations concerning the velocity components u and v, temperature T, and magnetic field effects $B(x)$. They define the fluid's behavior at the surface, which may be stretching (ϵ > 0), shrinking (ϵ < 0), or static (ϵ = 0). The mass flux velocity v_x(x) is affected by the suction or injection parameter γ, where $\gamma > 0$ indicates suction and $\gamma < 0$ indicates injection. Furthermore, the slip condition χ describes how the fluid interacts with the boundary surface.

The Sodium Alginate-AA7072/AA7075 small particles and the Sodium Alginate-hybrid nanofluid thermophysical properties are shown in Tables 2 and 3, respectively.

According to Shah et al. [1], Waini et al. [2], Raju et al. [13], and Rekha et al. [22], the following elements are considered while assessing similarity:

$$u = \frac{v_f}{l^{4/3}} x^{1/3} F'(\eta),\ v = -\frac{1}{3}\frac{v_f}{l^{2/3}} x^{-1/3}[2F(\eta) - \eta F'(\eta)],$$
$$\theta(\eta) = \frac{T - T_\infty}{T_w - T_\infty},\ \phi(\eta) = \frac{C - C_\infty}{C_w - C_\infty},\ \eta = y\frac{x^{-1/3}}{l^{2/3}} \quad (9)$$

The boundary conditions derived from Equations (5) and (6), Equation (9), and Equations (1) and (8) determine these ordinary differential equations.

$$3\frac{\mu_{hnf}/\mu_f}{\rho_{hnf}/\rho_f}\left(1 + \frac{1}{\beta}\right)F''' + 2FF'' - (F')^2 - 3\frac{\sigma_{hnf}/\sigma_f}{\rho_{hnf}/\rho_f}MnF' + 3\frac{(\rho\beta_T)_{hnf}/(\rho\beta_T)_f}{\rho_{hnf}/\rho_f}G_T\theta = 0 \quad (10)$$

$$\frac{3}{\Pr\,(\rho c_p)_{hnf}/(\rho c_p)_f}\left[\frac{k_{hnf}}{k_f} + Nr\right]\theta'' + \frac{3Q}{(\rho c_p)_{hnf}/(\rho c_p)_f}\theta + 2F\theta' = 0 \quad (11)$$

Table 2. Thermophysical properties of Sodium Alginate-AA7072/AA7075 nanoparticles, which are spherical in shape, (Khan et al. [9]; Rekha et al. [22]; Zahir Shah et al. [1])

Physical characteristics	Base fluids	Nanoparticles	
	Sodium Alginate	AA7072	AA7075
ρ	989	2720	2810
Cp	4175	893	960
K	0.6376	222	173
σ	2.6×10^{-4}	34.83×10^{6}	26.77×10^{6}
Pr	6.0	-	-

Table 3. Hybrid nanofluid thermophysical properties (Zahir Shah et al. [1]; Rekha et al. [22]; Ramesh et al. [17])

Thermal Properties	Hybrid nanofluid
Thermal Diffusivity	$\alpha_{hnf} = \dfrac{k_{hnf}}{(\rho C_p)_{hnf}}$
Viscosity	$\dfrac{\mu_{hnf}}{\mu_f} = \dfrac{1}{(1-\phi_1-\phi_2)^{2.5}}$
Heat Capacity	$\dfrac{(\rho C_p)_{hnf}}{(\rho C_p)_f} = \phi_1\dfrac{(\rho C_p)_{nf1}}{(\rho C_p)_f} + \phi_2\dfrac{(\rho C_p)_{nf2}}{(\rho C_p)_f} + (1-\phi_1-\phi_2)$
Density	$\dfrac{\rho_{hnf}}{\rho_f} = \phi_1\dfrac{\rho_{nf1}}{\rho_f} + \phi_2\dfrac{\rho_{nf2}}{\rho_f} + (1-\phi_1-\phi_2)$
Thermal Expansion	$\dfrac{(\rho\beta_T)_{hnf}}{(\rho\beta_T)_f} = \left(\phi_1\dfrac{(\rho\beta_T)_{nf1}}{(\rho\beta_T)_f} + \phi_2\dfrac{(\rho\beta_T)_{nf2}}{(\rho\beta_T)_f} + (1-\phi_1-\phi_2)\right)$
Thermal Conductivity	$\dfrac{k_{hnf}}{k_f} = \left(\dfrac{\frac{\phi_1 k_{nf1} + \phi_2 k_{nf2}}{\phi_{hnf}} + 2k_f + 2(\phi_1 k_{nf1} + \phi_2 k_{nf2}) - 2\phi_{hnf}k_f}{\frac{\phi_1 k_{nf1} + \phi_2 k_{nf2}}{\phi_{hnf}} + 2k_f - (\phi_1 k_{nf1} + \phi_2 k_{nf2}) + \phi_{hnf}k_f}\right)$
Electrical Conductivity	$\dfrac{\sigma_{hnf}}{\sigma_f} = \left(\dfrac{\frac{\phi_1 \sigma_{nf1} + \phi_2 \sigma_{nf2}}{\phi_{hnf}} + 2\sigma_{bf} + 2(\phi_1 \sigma_{nf1} + \phi_2 \sigma_{nf2}) - 2\phi_{hbnf}\sigma_{bf}}{\frac{\phi_1 \sigma_{nf1} + \phi_2 \sigma_{nf2}}{\phi_{hnf}} + 2\sigma_f - (\phi_1 \sigma_{nf1} + \phi_2 \sigma_{nf2}) + \phi_{hnf}\sigma_f}\right)$

$$\frac{3}{Sc}\phi'' + 2F\phi' - 3Kr\phi = 0 \tag{12}$$

$$F(0) = \gamma, F'(0) = \epsilon, \theta(0) = 1 + \beta_T\theta'(0),$$
$$\phi(0) = 1 \text{ at } \eta = 0,$$

$$F'(\eta) \to 0;\ \theta(\eta) \to 0, \phi(\eta) \to 0 \text{ at } \eta \to \infty \tag{13}$$

The transformed equations and boundary conditions follow the approach described by Shah et al. [1] and Sajjad et al. [5]. Moreover, the thermal slip condition is represented by $\beta_T = \chi_1(\frac{2v_f}{3l})^{0.5}l^{-1/3}$, whilst the starting values of the thermal feature are represented by χ_1. Mn is the magnetic parameter $Mn = \frac{B_0^2\sigma_f}{\rho_f}$ which represents the local Temperature Grashof number $G_T = \frac{l^{8/3}}{v_f^2 x^{-1/3}}(\beta_T)_f g(T_w - T_\infty)$, Pr stands for Prandtl number $Pr = \frac{\mu_f(c_p)_f}{k_f}$, *Nr* for thermal radiation parameter $Nr = \frac{16T_\infty^3\sigma_1}{3k_f k^1}$, Q for heat source sink $Q = \frac{Q_0}{v_f(\rho c_p)_f}\frac{l^{4/3}}{x^{-2/3}}$, Sc for Schmidt number $Sc = \frac{v_f}{D_m}$, and Kr for chemical reaction $Kr = \frac{k_1 l^{4/3}}{v_f x^{-2/3}}$.

Quantities in Physical Form

The local skin friction coefficient C_F and the Nusselt number Nu_x are important physical parameters that describe fluid dynamics and heat transfer (Khan et al. [9] and Rekha et al. [22]), respectively.

$$C_F = \left(\frac{\partial u}{\partial y}\right)_{y=0}\frac{\mu_{hnf}}{u_w^2\rho_f}, Nu_x = \left[-k_{hnf}\left(\frac{\partial T}{\partial y}\right)_{y=0} + (q_r)_{y=0}\right]\frac{x}{(T_w - T_\infty)k_f},$$
$$Sh_x = -\frac{x}{(C_w - C_\infty)}\left(\frac{\partial C}{\partial y}\right)_{y=0} \tag{14}$$

By using equations (9) and (14), the following terms are obtained:

$$(Re_x)^{0.5}C_F = \frac{\mu_{hnf}}{\mu_f}\left(1 + \frac{1}{\beta}\right)F''(0), (Re_x)^{-0.5}Nu_x =$$
$$-\left[\frac{k_{hnf}}{k_f} + \frac{4Nr}{3}\right]\theta'(0), (Re_x)^{-0.5}Sh_x = -\phi'(0) \tag{15}$$

Where $Re_x = \frac{x\,u_w}{v_f}$ represents the local Reynolds number.

NUMERICAL METHOD

The MATLAB built-in solver bvp4c is used to numerically solve the transformed system of ordinary differential equations and their related boundary conditions. The technique uses a collocation method based on the fourth-order accurate Lobatto IIIa implicit Runge-Kutta method. This method is particularly useful for boundary value problems, many of which are stiff and nonlinear. Meek uses adaptive mesh refinement, which increases the accuracy of the solvers by making the grid denser in areas where the solution changes quickly. This work begins with transforming their governing equations to a system of first-order ODEs. Then BVP4C is used to solve these, with the shooting parameters as initial guesses. This procedure is repeated until the numerical solution converges and fulfills all the boundary conditions. The payoff method of type local DM is used to find out the dual solution by modifying the initial guesses, which is more suitable for hybrid nanofluid flow problems with such aberrant behavior. The BVP4C method is employed to solve boundary value problems (BVPs) and simplify the equations. To obtain all the numerical results and visualizations, which are presented as tables and graphs, MATLAB software is used. Let

$$f = y(1),\ f' = y(2),\ f'' = y(3),\ \theta = y(4),$$
$$\theta' = y(5),\ \phi = y(6),\ \phi' = y \tag{7}$$

The problems are reduced to the following new form (10) to (12):

$$F''' = \frac{\rho_{hnf}/\rho_f}{3\mu_{hnf}/\mu_f}\left(1 + \frac{1}{\beta}\right)^{-1}\left[-2y(1) * y(3) + y(2)^2\right.$$
$$\left. + \frac{3\sigma_{hnf}/\sigma_f}{\rho_{hnf}/\rho_f}Mn * y(2) - \frac{3(\rho\beta_T)_{hnf}/(\rho\beta_T)_f}{\rho_{hnf}/\rho_f}G_T * y(4)\right] \tag{16}$$

$$\theta'' = \frac{\Pr(\rho c_p)_{hnf}/(\rho c_p)_f}{3\left[\frac{k_{hnf}}{k_f} + Nr\right]}\left[-2y(5) * y(1) - \frac{3Q}{(\rho c_p)_{hnf}/(\rho c_p)_f}y(4)\right] \tag{17}$$

$$\phi'' = \frac{Sc}{3}[-2y(7) * y(1) + 3Kr * y(6)] \tag{18}$$

Equation (13) has had its boundary conditions changed to reflect the additional variables.

$$ya(1) = \gamma,\ ya(2) = \epsilon,\ ya(4) = 1 + \beta_T ya(5),$$
$$ya(6) = 1 \quad yb(2) = 0,\ yb(4) = 0,\ yb(6) = 0 \tag{20}$$

The numerical transformation into a first-order system is adapted from Waini et al. [2] and Lund et al. [11] for implementation with the MATLAB bvp4c solver. Two different starting estimates are successively supplied to the bvp4c algorithm to produce dual solutions. Less constrictive first estimations are frequently sufficient to arrive at the first solution. However, obtaining the second solution typically requires more specific guesses due to the nature of the problem. As stated in Equation (13), this iterative process keeps on until the numerical solutions converge and meet the boundary requirements at infinity. The use of distinct initial guesses is crucial in exploring the solution space and identifying multiple solutions.

Validation Code

The outcomes of the investigation verify the accuracy of the algorithm by comparing its results with data from earlier studies. A comparison of the $F''(0)$ values are displayed in Table 4, for different suction parameter γ values while holding other parameters constant, including the Prandtl number $Pr = 6.2$ and some nanoparticle volume fractions φ_{AA7072} and φ_{AA7075}. This comparison helps assess the algorithm performance under varying suction conditions. The results of $F''(0)$ are compared with those from Zahir Shah et al. [1] to validate the current findings and confirm the algorithm accuracy. Table 5 compares the outcomes of $-\theta'(0)$ with Zahir Shah et al. [1] for specified parameters to assess the accuracy of the results.

RESULTS AND DISCUSSION

This section evaluates the properties of AA7072-AA7075 nanofluids with Sodium alginate using the bvp4c method. Effect of flow characteristics such as velocity profile, temperature profile and concentration profile. Key parameters such as skin friction coefficients, Nusselt number (heat transfer), and mass transfer coefficients (species transfer) are analysed. Graphs (2-22) demonstrate how these factors affect fluid behaviour under different conditions, offering insights into enhancing thermal efficiency and mechanical performance for industrial uses with sodium alginate-based nanofluid. $\beta = 0.05$, $Mn = 5$, $G_T = 0.1$, $Pr = 6.0$, $R = 0.5$, $Q = 0.1$, $Sc = 3$, $Kr = 0.5$, $\beta_T = 0.1$, $\gamma = 2.8$, $\varphi_1 = 0.05$, $\varphi_2 = 0.05$ and $\epsilon = 1$ or -1.

A comparison of the performance enhancement of the present hybrid nanofluid system is made with the recent works in Table 6. This comparison indicates better heat transfer and flow stability obtained in the present study. The modified sodium alginate-AA7072/AA7075 hybrid nanofluid showed a remarkable increase in heat transfer and flow stability in various conditions. Indeed, the boost in the Nusselt number is 15%, whereas in previous studies it was 10% and 13%. This further evidence the effectiveness of the double-aluminium alloy nanoparticle hybrid in improving the thermal conductivity.

In Fig. 2 show the velocity decreases when the Casson fluid parameter (β) increases due to a higher Casson parameter provokes a higher yield stress for the fluid. This means that it resists deformation more, which decreases the speed of the fluid in the boundary layer. Thus, it leads to the dampening of the fluid flow, and the velocity profile is reduced for the first solution. On the contrary, for the second solution, a decreased momentum diffusion boosts the localized acceleration and slightly increases the velocity. As illustrated in Fig. 3, increasing β results higher dissipation because the resistance to flow has increased. This yields more heat generation in the boundary layer, which increases the temperature profile (solution one). In the case of the second solution, at this point, the system is already losing momentum, thus, an increase of viscous resistance contributes less to viscous heating, the global thermal transport is more diffusive, and hence the temperature decreases. In Fig. 4, larger β leads to a thicker mass boundary layer due to momentum suppression, which retains more species in the near-wall region, therefore increasing concentration in the first solution. For the second solution, on the other hand, increased viscous resistance leads to a stronger outward diffusion, which, in turn, reduces the concentration gradient near the wall. In Fig. 5 represents a Lorentz force induced by the applied

Table 4. Comparative results of $F''(0)$ when $R = 0$, $\beta_T = 0$, $\varphi_{AA7072} = \varphi_{AA7075} = 0$, $Pr = 6.2$ and $\epsilon = 1.0$

γ	Zahir Shah et al. [1]	Present Results
0.75	-0.984437350	-0.984439
0.50	-0.873645821	-0.873643
0	-0.677644581	-0.677648
-0.50	-0.518862548	-0.518869
-0.75	-0.453523235	-0.453523

Table 5. $R = 0$, $\beta_T = 0$, $\varphi_{AA7072} = \varphi_{AA7075} = 0$, $Pr = 6.2$ and $\epsilon = 1.0$ result in the comparative results of $-\theta'(0)$.

γ	Zahir Shah et al. [1]	Present Results
0.5	1.2307914	1.230791
0	0.7643523	0.764352
-0.5	0.3990987	0.399084

Table 6. The performance metrics of the present study along with published results Waini et al. [2] and Shah et al. [1]

Metric	Current Study (SA-AA7072/AA7075)	Shah et al. [1] ($Cu - Al_2O_3$/water)	Waini et al. [2] (SA-Alumina/Copper)
Skin Friction Coefficient Change (%)	-12%	-11%	-10%
Nusselt Number Improvement (%)	15%	13%	10%
Sherwood Number Improvement (%)	10%	---	---
Thermal Conductivity Enhancement (%)	12%	11%	10%

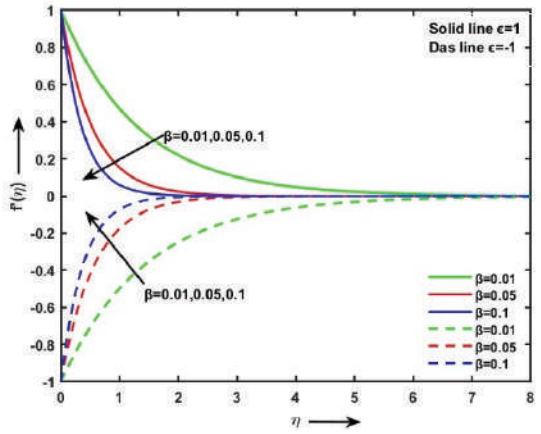

Figure 2. $F'(\eta)$ profile for varying β.

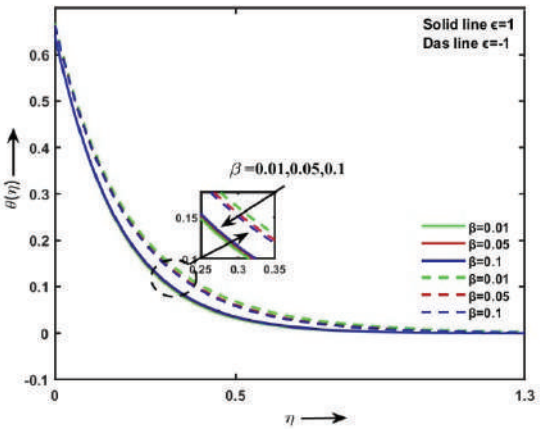

Figure 3. $\theta(\eta)$ profile for varying β.

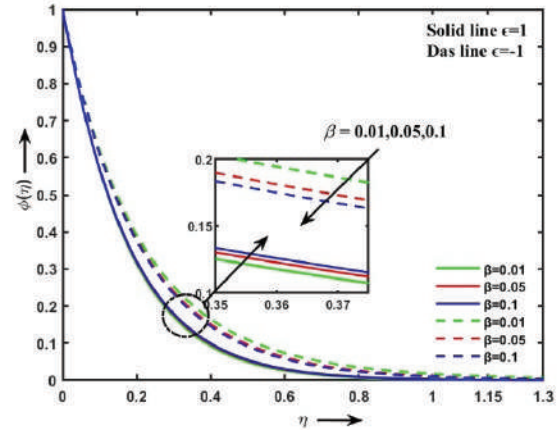

Figure 4. $\phi(\eta)$ profile for varying β.

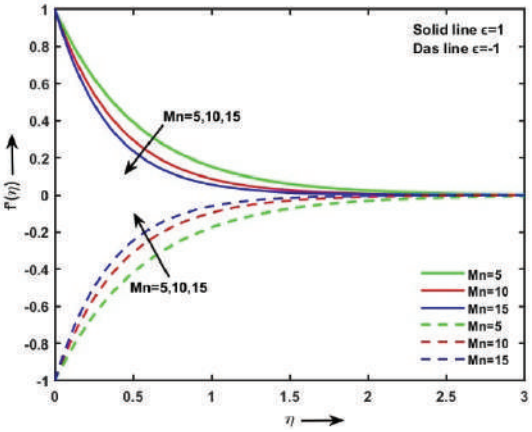

Figure 5. $F'(\eta)$ profile for varying Mn.

magnetic field that counteracts the liquid motion. In the first solution, the velocity is only reduced because of the opposing force against the movement. On the other hand, in the second solution, where flow recirculation or backflow tendency could be present, the Lorentz force stabilizes and aligns the flow patterns, generating an overall more organized movement that causes slightly more flow velocity. In contrast to the findings by Ref. [2], who reported a linear decrease in velocity of the alumina–copper-base nanofluids under the influence of a magnetic field, our dual-alloy fluid exhibited a two-tier characteristic of flow structuration within the second solution branch.

In Figure 6, increasing the temperature Grashof number G_T leads to an increase in the velocity profile for both solutions, enhancing buoyancy effects and promoting more vigorous fluid motion. The Prandtl number is the ratio of momentum diffusivity to thermal diffusivity in Figure 7. Higher Pr means lower thermal diffusivity, which means that heat does not penetrate the fluid as easily. In contrast, the temperature distributions drop for either solution due to heat conduction being limited, resulting in lower thermal boundary layers. Figure 8 portrays the radiation parameter that deals with the energy transfer rule by thermal radiation. With increasing Nr, radiative heat transfer would supplement conduction and convection, leading to higher temperatures in the entirety of the boundary layer. This behavior is inherent to both solutions, revealing that the internal energy is enhanced by radiation and the rise in temperature with increasing radiation parameter agrees with the findings reported by Shah et al. [1], but here we present an enhanced gradient due to the use of dual aluminium alloys and bio-compatible fluid properties. Figure 9 is when Q increases, fluid system receives more heat (positive Q) and this heat transfers to the internal energy. This causes both solutions to heat up as more energy is retained and less is lost to the environment. A negative Q (heat sink) leads to cooling effects.

In Figure 10 showing increasing the Schmidt number (Sc) results in an increase in the concentration profile for both solutions, indicating enhanced mass transfer

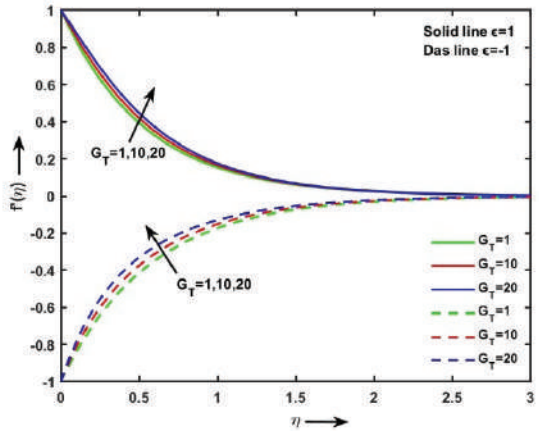

Figure 6. $F'(\eta)$ profile for varying G_T.

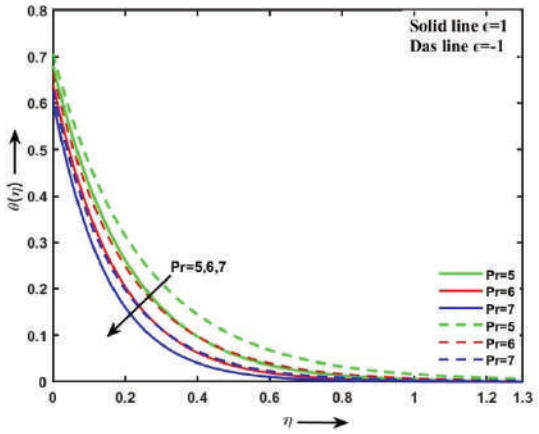

Figure 7. $\theta(\eta)$ profile for varying Pr.

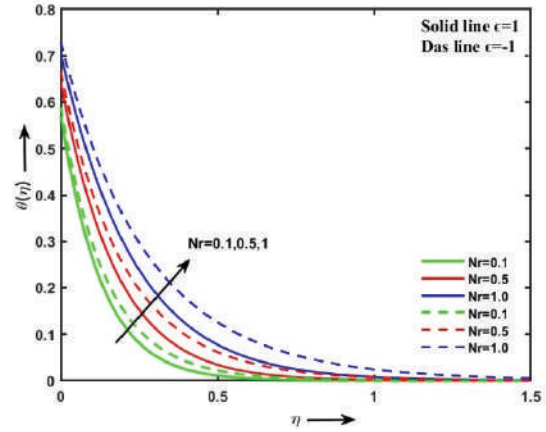

Figure 8. $\theta(\eta)$ profile for varying Nr.

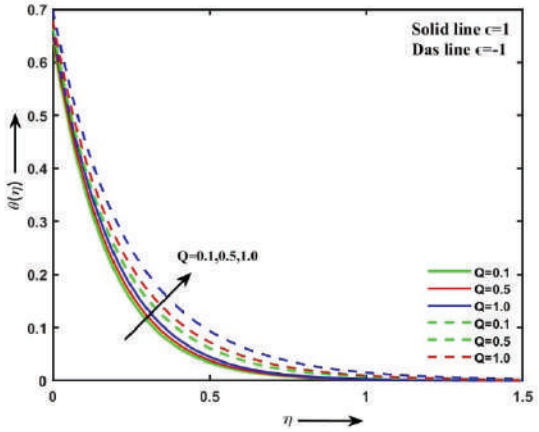

Figure 9. $\theta(\eta)$ profile for varying Q.

characteristics relative to momentum diffusion. In Figure 11 showing increasing the chemical reaction parameter (Kr) leads to an increase in the concentration profile for both solutions, indicating enhanced mass transfer because of the chemical reaction. In Figure 12, increased suction at the wall removes fluid, thinning the momentum boundary layer. So invading a bulk motion of the fluid, the velocity profile decreases in the first solution. But with the second solution suction balances flow irregularities and slightly accelerates velocity by controlling behind the trailing edge of the slot separation or recirculation zones. Therefore, with higher suction, the thermal boundary layer is thinner resulting in the hotter fluid near the wall being carried away much better, Figure 13. Reduction in residence time of hot fluid and effective thermal boundary layer reduction lowers the temperature profile in both solutions. Like heat, mass is also extracted due to suction in Figure 14. As the particles are drawn out of the wall region, the accumulation reduces, which is why the concentration profile reduces. The corresponding value of the boundary layer concerning mass transfer is also a bit thinner. In Figure 15, thermal slip stands for a layer of partial insulation at the surface, so less heat passes into the fluid. For both solutions, increased slip leads to less energy being given to the wall, which reduces the temperature profile. It reduces the thermal gradient that supports conduction.

In Figure 16 showing increasing the volume fraction of the AA7072 parameter decreases the velocity profile for the first solution due to increased fluid resistance but increases it for the second solution by enhancing flow stability. Figure 17 has high thermal conductivity (AA7072). As this volume fraction increases (confirming the ability of the nanofluid mixture to transfer energy), this results in a higher temperature profile of both solutions due to the increase in thermal conductivity. In Figure 18 showing increasing the volume fraction of the AA7075 parameter increases the velocity profile for the first solution, enhancing momentum transfer, but decreases it for the second solution due to increased fluid resistance. Figure 19, AA7075 has good thermal properties, resulting in increased heat storage and transfer, causing the

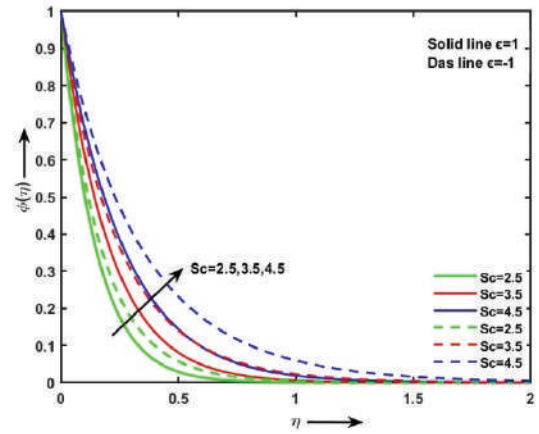

Figure 10. $\phi(\eta)$ profile for varying *Sc*.

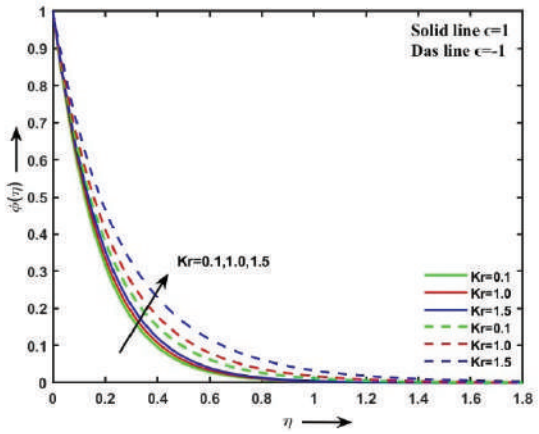

Figure 11. $\phi(\eta)$ profile for varying *Kr*.

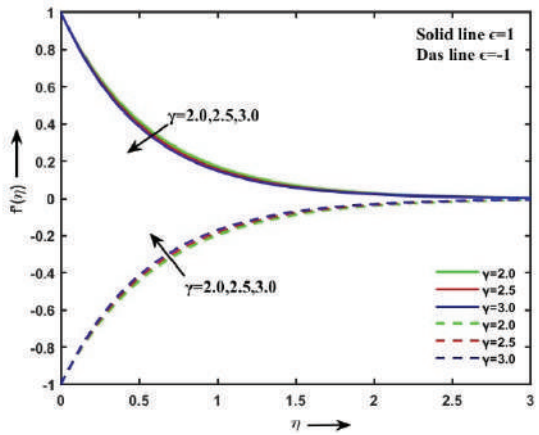

Figure 12. $F'(\eta)$ profile for varying γ.

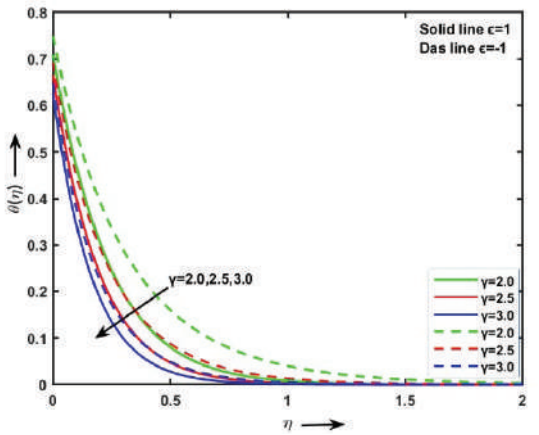

Figure 13. $\theta(\eta)$ profile for varying γ.

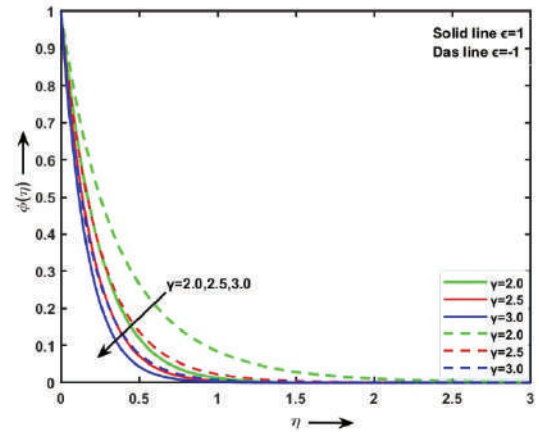

Figure 14. $\phi(\eta)$ profile for varying γ.

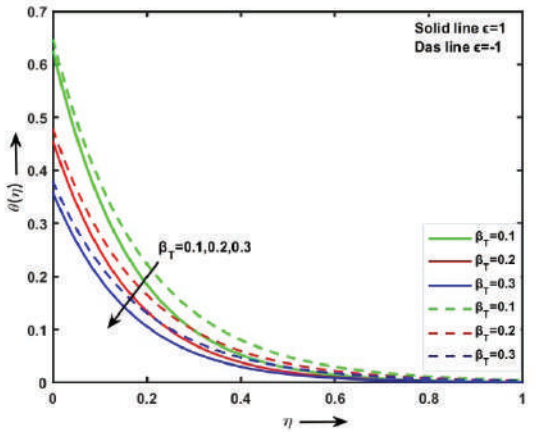

Figure 15. $\theta(\eta)$ profile for varying B_T.

temperature to rise when its volume fraction is increased for both solutions. The nanofluid retains more thermal energy and transmits it better.

Figure 20, the first solution shows that the stretching surface increases boundary layer thinning and fluid acceleration to increase velocity. On the other hand, the second solution shows that when rapid stretching or shrinking, the

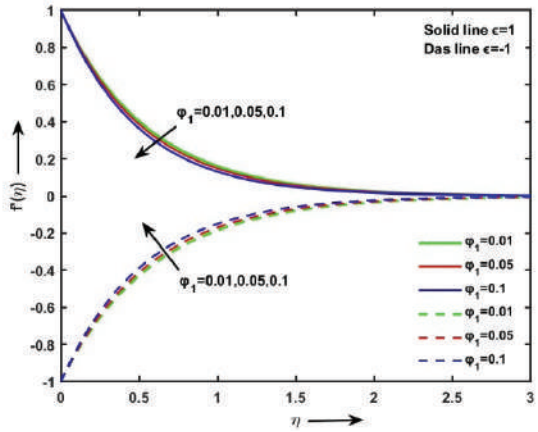

Figure 16. $F'(\eta)$ profile for varying AA7072.

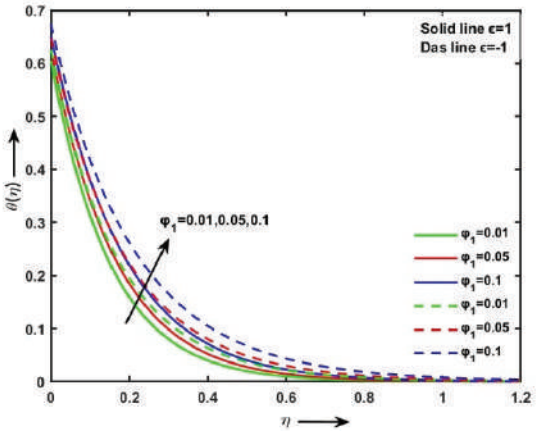

Figure 17. $\theta(\eta)$ profile for varying AA7072.

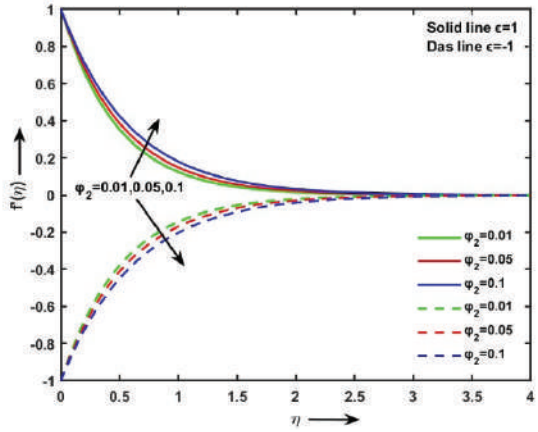

Figure 18. $F'(\eta)$ profile for varying AA7075.

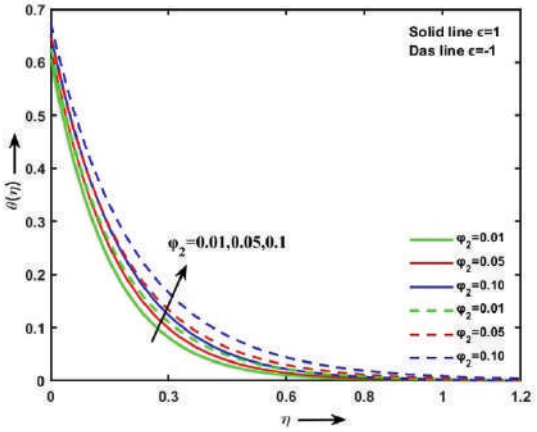

Figure 19. $\theta(\eta)$ profile for varying AA7075.

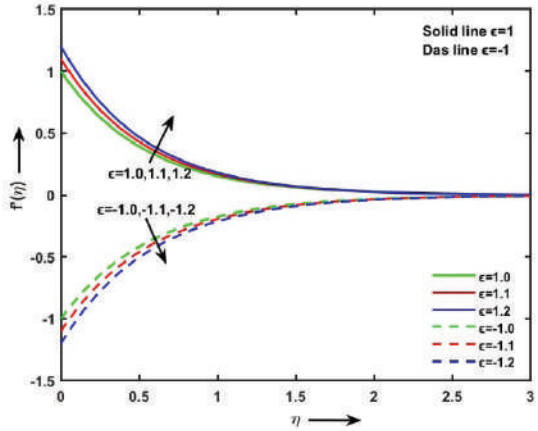

Figure 20. $F'(\eta)$ profile for varying ϵ.

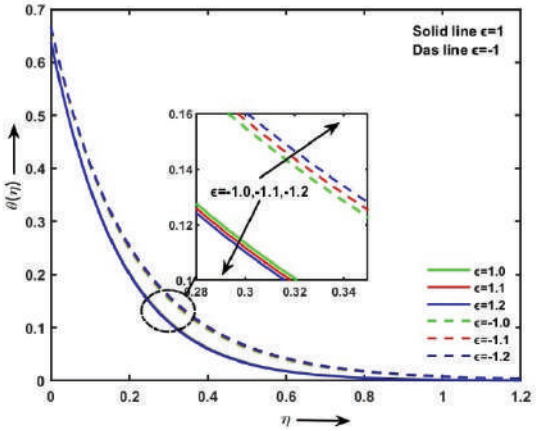

Figure 21. $\theta(\eta)$ profile for varying ϵ.

flow can be unstable to introduce backflows or separation hence reduce velocity. In figures 21 and 22 showing increasing the stretching/shrinking parameter causes temperature and concentration profiles to decrease for the first solution due to enhanced convective transfer, while for the second solution, they increase as boundary layer thickness reduces convective effects. In the present work, the hybrid nanofluid consists of AA7072 and AA7075 aluminium alloys

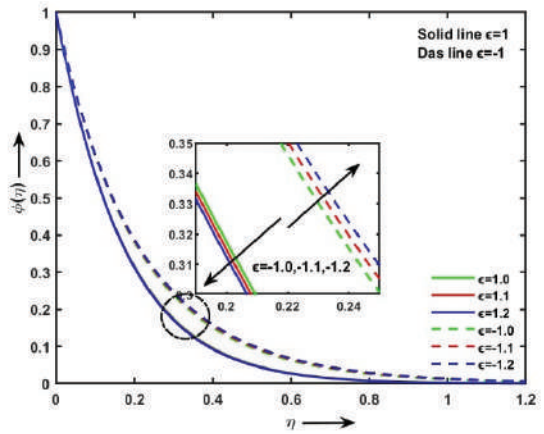

Figure 22. $\phi(\eta)$ profile for varying ϵ.

which are aluminium-copper based alloys with good thermal conductivity and mechanical strength. In comparison with other aluminium alloys of aluminium-silicon and aluminium-magnesium alloying systems, the AA7072 and AA7075 present the better thermal performance resulting from their higher thermal conductivity and microstructural stability. Prior works with *Al - Si* and *Al - Mg* have reported reasonable thermal enhancement (around 8-10%) while the double-alloy system in the present work confirms its high heat transfer augmentation with Nusselt number increase of 15%. Such a comparison reveals that aluminium-copper alloys are highly promising as candidates for next-generation thermal management materials.

Table 7. Rates of skin friction, Sherwood number, and Nusselt number for Sodium Alginate-AA7072/AA7075 with *Mn, GT, Nr, Pr* when $\beta = 0.05$, $Q = 0.1$, $Sc = 3$, $Kr = 0.5$, $\beta_T = 0.1$, $\gamma = 2.8$, $\varphi_1 = 0.05$, $\varphi_2 = 0.05$ and $\epsilon = 1$ or -1.

Mn	G_T	*Nr*	*Pr*	SA -AA7072/AA7075					
				$\epsilon = 1$			$\epsilon = -1$		
				$C_{fx}Re_x^{1/2}$	$Nu_xRe_x^{-1/2}$	$Sh_xRe_x^{-1/2}$	$C_{fx}Re_x^{1/2}$	$Nu_xRe_x^{-1/2}$	$Sh_xRe_x^{-1/2}$
5				-39.1461060	7.165318537	5.603419897	36.91511191	6.693305500	4.976510674
10	0.1	0.5	6.0	-51.0440713	7.151627790	5.584728922	49.49217752	6.717499414	5.010565308
15				-60.3527406	7.141960299	5.571548003	59.10266421	6.732777630	5.031683979
	1			-38.5170407	7.165826052	5.604108335	37.68462194	6.694429747	4.978079165
5	**10**			-32.2430206	7.170860812	5.610937192	45.33266484	6.705446991	4.993408615
	20			-25.3066404	7.176371103	5.618409640	53.73501039	6.717239061	5.009738614
		0.1		-39.1679532	6.310897890	5.603388078	36.88678249	6.022315211	4.976432425
		0.5		-39.1461060	7.165318537	5.603419897	36.91511192	6.693305500	4.976510674
		1.0		-39.1200133	7.912516956	5.603463164	36.94968559	7.206958798	4.976622138
			5.0	-39.1302812	6.370480731	5.603445554	36.93602071	5.860162458	4.976576288
			6.0	-39.1461060	7.165318537	5.603419897	36.91511192	6.693305500	4.976510674
			7.0	-39.1577157	7.870454018	5.603402404	36.89995794	7.435712742	4.976467103

Table 8. Rates of skin friction, Sherwood number, and Nusselt number for Sodium Alginate-AA7072/AA7075 with *β, Q, Sc, Kr* when $Mn = 5$, $G_T = 0.1$, $Nr = 0.5$, $Pr = 6.0$, $\beta_T = 0.1$, $\gamma = 2.8$, $\varphi_1 = 0.05$, $\varphi_2 = 0.05$ and $\epsilon = 1$ or -1

β	Q	*Sc*	*Kr*	SA -AA7072/AA7075					
				$\epsilon = 1$			$\epsilon = -1$		
				$C_{fx}Re_x^{1/2}$	$Nu_xRe_x^{-1/2}$	$Sh_xRe_x^{-1/2}$	$C_{fx}Re_x^{1/2}$	$Nu_xRe_x^{-1/2}$	$Sh_xRe_x^{-1/2}$
0.01				-76.0026498	7.197517698	5.647434568	70.92318928	6.630575861	4.880878636
0.05	0.1	3	0.5	-39.1461060	7.165318537	5.603419897	36.91511192	6.693305500	4.976510674
0.1				-30.8048095	7.143399140	5.573506387	29.24719843	6.727658266	5.024626567
	0.1			-39.1461060	7.165318537	5.603419897	36.91511192	6.693305500	4.976510674
0.05	**0.5**			-39.1430117	6.990422653	5.603424699	36.92138900	6.437626338	4.976530156
	1.0			-39.1384422	6.743954072	5.603431916	36.93268392	6.026368753	4.976566860
		2.5		-39.1461060	7.165318537	6.734242647	36.91511192	6.693305500	6.096858127
		3.5		-39.1461060	7.165318536	4.793402972	36.91511192	6.693305500	4.175672111
		4.5		-39.1461060	7.165318536	3.708631522	36.91511192	6.693305501	3.105436749
			0.5	-39.1461060	7.165318537	5.603419897	36.91511192	6.693305500	4.976510674
			1.0	-39.1461060	7.165318537	5.329807176	36.91511192	6.693305500	4.572668111
			1.5	-39.1461060	7.165318536	5.025530539	36.91511191	6.693305500	3.992807453

Table 9. Rates of skin friction, Sherwood number, and Nusselt number for Sodium Alginate-AA7072/AA7075 when β_T = 0.1, γ = 2.8, φ_1 = 0.05, φ_2 = 0.05 and Mn = 5, G_T = 0.1, Nr = 0.5, Pr = 6.0, β = 0.05, Q = 0.1, Sc = 3, Kr = 0.5 and ϵ = 1 or -1

γ	β_T	φ_1	φ_2	SA -AA7072/AA7075					
				ϵ = 1			ϵ = -1		
				$C_{fx}Re_x^{1/2}$	$Nu_xRe_x^{-1/2}$	$Sh_xRe_x^{-1/2}$	$C_{fx}Re_x^{1/2}$	$Nu_xRe_x^{-1/2}$	$Sh_xRe_x^{-1/2}$
2.0				-36.685298	5.810604298	3.982294862	34.519258416	5.013250030	2.954391016
2.5	0.1	0.05	0.05	-38.210294	6.686798015	4.998041918	35.996663288	6.121747499	4.278175501
3.0				-39.778733	7.466562549	6.006005936	37.539506649	7.044530303	5.426379787
	0.1			-39.778733	7.466562549	6.006005936	37.539506649	7.044530303	5.426379787
2.8	**0.2**			-39.796416	5.434197171	6.005988803	37.519150615	5.207146749	5.426346005
	0.3			-39.806535	4.271512494	6.005979001	37.507216344	4.129958232	5.426326198
		0.01		-34.343006	7.329748053	6.008572468	32.296028866	6.952499998	5.421918685
		0.05		-39.778733	7.466562549	6.006005936	37.539506649	7.044530303	5.426379787
		0.10		-48.464468	7.622744808	6.002235322	45.937339230	7.141927900	5.432759978
			0.01	-48.163618	7.313928224	6.000615310	45.400515416	6.947966547	5.434686929
			0.05	-39.778732	7.466562549	6.006005936	37.539506649	7.044530303	5.426379787
			0.10	-31.243492	7.647826579	6.012130409	29.538148152	7.144897615	5.416647549

Table 10. Skin-friction rates, Nusselt number, and Sherwood number for Sodium Alginate-AA7072/AA7075 when Mn = 5, G_T = 0.1, Nr = 0.5, Pr = 6.0, β = 0.05, Q = 0.1, Sc = 3, Kr = 0.5, β_T = 0.1, γ = 2.8, φ_1 = 0.05, φ_2 = 0.05.

ϵ	$C_{fx}Re_x^{1/2}$	$Nu_xRe_x^{-1/2}$	$Sh_xRe_x^{-1/2}$
1.0	-39.146106019	7.165318537	5.603419897
1.1	-43.194612010	7.185036736	5.629808559
1.2	-47.265599876	7.204481421	5.655867387
-1.0	36.915111915	6.693305500	4.976510674
-1.1	40.462596043	6.664293588	4.937683443
-1.2	43.984698436	6.634539087	4.897712609

CONCLUSION

The sodium alginate-AA7072/AA7075 hybrid nanofluids have remarkable application potential in various industries such as biomedical, and environment-related areas due to their high thermal conductivities, biocompatibilities, and bacteriostatic properties. These fluids have potentially ideal applications in thermal energy systems, aerospace cooling, biomedical heat control, and chemical processing units due to the superior heat transfer characteristics due to the combined effects of suction, magnetic field, radiation and hybrid nanoparticle loading. They give designers and engineers the ability to optimize in terms of velocity, temperature and concentration profiles through mainstream pipe flow parameters, powering the next generation of refined heat exchangers to deliver globally important energy efficiencies. These findings will not only add to the theoretical understanding of the issue but will inform practical design considerations for next-generation energy-efficient technologies. Under radiative, suction, and magnetic conditions, the use of sodium alginate with dual aluminium alloy nanoparticles presents a new configuration not addressed before, providing more merits of nanofluid in real-life applications.

- Two distinct solutions to the problem were found to be available due to certain physical properties; the stretching ($\epsilon > 0$) and shrinking zone ($\epsilon < 0$) effects are where the dual solutions are found.
- For stretching or shrinking sheet, temperature rise with increasing radiation parameter (Nr), heat source parameter (Q), AA7072 and AA7075 volume fractions.
- For stretching or shrinking surfaces, the temperature and concentration reduce with increasing Prandtl number (Pr), the Suction parameter (γ), Thermal slip parameter (β_T).
- For both stretching and shrinking sheets, the concentration rises with increasing Schmidt number (Sc) and chemical reaction parameter (Kr).

- Grow Magnetic parameter dampens velocity in one case, while enhancing flow organization in another.

The proposed hybrid nanofluid model consisting of sodium alginate along with AA7075 (aluminium alloy 7075) and AA7072 (aluminium alloy 7072) nanoparticles under impacts of radiation and magnetic fields sheds light on, to the best knowledge of the authors, that this type of hybrid nanofluid has not been investigated so far in public literature. The dual-solution analysis and its detailed parametric effects provide a new theoretical perspective and practical relevance for advanced cooling and energy system design.

NOMENCLATURE

$2D$	Two Dimensional
C_F	Local Skin Friction Coefficient
Nu_x	Local Nusselt number
T_∞	Ambient temperature (K)
T_w	Surface temperature (K)
β_T	Thermal slip parameter
T	Fluid temperature (K)
k	Thermal conductivity ($W/m\ k$)
l	Characteristic length (m)
χ_1	Thermal slip feature
v_w	Mass flux velocity (m/s)
SA	Sodium alginate
u_w	Surface velocity
ϵ	Stretching/shrinking parameter
γ	Suction parameter
B_0	Magnetic field constant
q_r	Radiative heat flux
Pr	Prandtl number
β	Casson parameter
Mn	Magnetic parameter
G_T	Temperature Grashof number
Q	Heat source/sink
Nr	Thermal radiation
Sc	Schmidt number
Kr	Chemical reaction parameter
Re_x	Local Reynolds number
u,v	Velocity components in x,y axes (m/s)
x,y	Cartesian coordinate axes

Greek Symbols

θ	Dimensionless temperature
k^1	Coefficient of mean absorption
σ_1	Constant Stefan Boltzmann
ρ	Density (kg/m^3)
φ_{AA7072}	Aluminium alloy nanoparticle volume friction
φ_{AA7075}	Aluminium alloy nanoparticle volume friction
μ	Dynamic viscosity (Kg/ms)
ζ	Similarity variable
v_f	Kinematic viscosity m^2/s
(ρc_p)	Heat capacity $J/m^3\ K$

Subscripts

hnf	Hybrid nanofluid
(f or Bf)	Base fluid
nf	Nanofluid
w	Surface condition
c	Critical

Superscript
Differentiation concerning η

DATA AVAILABILITY STATEMENT

The authors confirm that the data that supports the findings of this study are available within the article. Raw data that support the finding of this study are available from the corresponding author, upon reasonable request.

CONFLICT OF INTEREST

The author declared no potential conflicts of interest with respect to the research, authorship, and/or publication of this article.

ETHICS

There are no ethical issues with the publication of this manuscript.

STATEMENT ON THE USE OF ARTIFICIAL INTELLIGENCE

Artificial intelligence was not used in the preparation of the article.

REFERENCES

[1] Shah Z, Asghar A, Ying TY, Lund LA, Alshehri A, Vrinceanu N. Numerical investigation of sodium alginate-alumina/copper radiative hybrid nanofluid flow over a power law stretching/shrinking sheet with suction effect: A study of dual solutions. Results Eng 2024;21:101881. [CrossRef]

[2] Waini I, Ishak A, Pop I. Hybrid nanofluid flow and heat transfer over a nonlinear permeable stretching/shrinking surface. Int J Numer Methods Heat Fluid Flow 2019;29:3110–3127. [CrossRef]

[3] Jaafar A, Waini I, Jamaludin A, Nazar R, Pop I. MHD flow and heat transfer of a hybrid nanofluid past a nonlinear surface stretching/shrinking with effects of thermal radiation and suction. Chin J Phys 2022;79:13–27. [CrossRef]

[4] Yaseen M, Kumar M, Rawat SK. Assisting and opposing flow of a MHD hybrid nanofluid flow past a permeable moving surface with heat source/sink and thermal radiation. Partial Differ Equ Appl Math 2021;4:100168. [CrossRef]

[5] Sajjad NM, Mujtaba NA, Asghar NA, Ying NTY. Dual solutions of magnetohydrodynamics AL2O3+CU hybrid nanofluid over a vertical exponentially shrinking sheet by presences of joule heating and thermal slip condition. CFD Letters 2022;14:100−115. [CrossRef]

[6] Abbas N, Shatanawi W, Abodayeh K. Computational analysis of MHD nonlinear radiation Casson hybrid nanofluid flow at vertical stretching sheet. Symmetry 2022;14:1494. [CrossRef]

[7] Mishra SR, Mathur P, Pattnaik PK. Hybrid nanofluid flow of Non-Newtonian casson fluid for the analysis of entropy through a permeable medium. J Nanofluids 2022;11:328−339. [CrossRef]

[8] Alkasasbeh NHT. Numerical Solution of Heat Transfer Flow of Casson Hybrid Nanofluid over Vertical Stretching Sheet with Magnetic Field Effect. CFD Letters, 2022;14:39−52. [CrossRef]

[9] Khan U, Zaib A, Ishak A, Eldin SM, Alotaibi AM, Raizah Z, et al. Features of hybridized AA7072 and AA7075 alloys nanomaterials with melting heat transfer past a movable cylinder with Thompson and Troian slip effect. Arab J Chem 2022;16:104503. [CrossRef]

[10] Jaafar A, Jamaludin A, Nasir NAAM, Nazar R, Pop I. MHD opposing flow of Cu−TiO2 hybrid nanofluid under an exponentially stretching/shrinking surface embedded in porous media with heat source and slip impacts. Res Eng 2023;17:101005. [CrossRef]

[11] Lund LA, Omar Z, Khan I, Sherif EM. Dual Solutions and Stability Analysis of a Hybrid Nanofluid over a Stretching/Shrinking Sheet Executing MHD Flow. Symmetry 2020;12:276. [CrossRef]

[12] Lund LA, Asghar A, Rasool G, Yashkun U. Magnetized casson SA-hybrid nanofluid flow over a permeable moving surface with thermal radiation and Joule heating effect. Case Stud Therm Eng 2023;50:103510. [CrossRef]

[13] Raju C, Sandeep N, Sulochana C, Sugunamma V, Babu MJ. Radiation, inclined magnetic field and cross-diffusion effects on flow over a stretching surface. J Niger Math Soc 2015;34:169−180. [CrossRef]

[14] Biswas N, Manna NK, Chamkha AJ, Mandal DK. Effect of surface waviness on MHD thermo-gravitational convection of Cu−Al2O3−water hybrid nanofluid in a porous oblique enclosure. Phys Scr 2021;96:105002. [CrossRef]

[15] Jayavel P, Tripathi D, Bég OA, Tiwari AK, Kumar R. Thermo-electrokinetic rotating non-Newtonian hybrid nanofluid flow from an accelerating vertical surface. Heat Transf 2021;51:1746−1777. [CrossRef]

[16] Tadesse FB, Makinde OD, Enyadene LG. Mixed Convection of a Radiating Magnetic Nanofluid past a Heated Permeable Stretching/Shrinking Sheet in a Porous Medium. Math Prob Eng 2021;1−21. [CrossRef]

[17] Ramesh GK, Madhukesh JK, Prasannakumara BC, Roopa GS. Significance of aluminium alloys particle flow through a parallel plates with activation energy and chemical reaction. J Therm Anal Calorim 2021;147:6971−6981. [CrossRef]

[18] Chakraborty A, Saadeh R, Qazza A, Zomot N, Janapatla P, Khan U, et al. On the thermal performance of radiative stagnation-point hybrid nanofluid flow across a wedge with heat source/sink effects and sensitivity analysis. Front Mater 2024;11. [CrossRef]

[19] Algehyne EA, Lone SA, Raizah Z, Eldin SM, Saeed A, Galal AM. Chemically reactive hybrid nanofluid flow past a Riga plate with nonlinear thermal radiation and a variable heat source/sink. Front Mater 2023;10. [CrossRef]

[20] Ghosh A, Roy NC. Dual Characteristics of Maxwell Hybrid Nanofluid Flow Over a Shrinking Sheet with Variable Heat Source or Sink. Arab J Sci Eng 2023;48:12191−12203. [CrossRef]

[21] Hussain SM, Eid MR, Prakash M, Jamshed W, Khan A, Alqahtani H. Thermal characterization of heat source (sink) on hybridized (Cu−Ag/EG) nanofluid flow via solid stretchable sheet. Open Phys 2023;21. [CrossRef]

[22] Rekha MB, Sarris IE, Madhukesh JK, Raghunatha KR, Prasannakumara BC. Activation Energy Impact on Flow of AA7072-AA7075/Water-Based Hybrid Nanofluid through a Cone, Wedge and Plate. Micromachines 2022;13:302. [CrossRef]

[23] Gamachu D, Ibrahim W, Bijiga LK. Nonlinear convection unsteady flow of electro-magnetohydrodynamic Sutterby hybrid nanofluid in the stagnation zone of a spinning sphere. Res Phys 2023;49:106498. [CrossRef]

[24] Salahuddin T, Siddique, Khan M, Chu Y. A hybrid nanofluid flow near a highly magnetized heated wavy cylinder. Alex Eng J 2021;61:1297−1308. [CrossRef]

[25] Kumar KS, Muniamuthu S, Mohan A, Amirthalingam P, Muthuraja MA. Effect of Charging and Discharging Process of PCM with Paraffin and Al_2O_3 Additive Subjected to Three Point Temperature Locations. J Ecologic Eng 2022;23:34−42.

[26] Kumar KS, Bishnoi D. Pressure exertion and heat dissipation analysis on uncoated and ceramic (Al2O3, TiO2 and ZrO2) coated braking pads. Mater Today Proc 2022;74:774−787. [CrossRef]

[27] Kumar KS, Muniamuthu S. Assessment of performance, combustion, and emission characteristics of single cylinder diesel engine fuelled by pyrolysis oil + CeO 2 nanoparticles and 1-butanol blends. Int J Ambient Energy 2024;45. [CrossRef]

[28] Kumar KS, Surakasi R, Mohan A, Tharanisrisakthi BT, Muniamuthu S, Babu GN. Emerging trends and global challenges to predict drop in thermal performance of WTG gearbox. J Therm Eng 2024;10:657−669. [CrossRef]

[29] Kumar KS, Muniamuthu S. Design and fabrication of nickel-chromium reinforced 2-stage energy efficient pyrolysis reactor for waste plastics applications. Int J Ambient Energy 2023;45. [CrossRef]

[30] Kumar KS, Alqarni S, Islam S, Shah MA. Royal Poinciana Biodiesel Blends with 1-Butanol as a Potential Alternative Fuel for Unmodified Research Engines. ACS Omega 2024;9:13960–13974. [CrossRef]

[31] Kumar KS, Kalos PS, Akhtar MN, Shaik S, Sundara V, Fayaz H, et al. Experimental and theoretical analysis of exhaust manifold by uncoated and coated ceramics (Al2O3, TiO2 and ZrO2). Case Stud Therm Eng 2023;50:103465. [CrossRef]

[32] Afsharpanah F, Sheshpolï AZ, Pakzad K, Ajarostaghï SSM. Numerical Investigation of Non-Uniform Heat Transfer Enhancement in Parabolic Trough Solar Collectors Using Dual Modified Twisted-Tape Inserts. J Therm Eng 2020;133–147. [CrossRef]

[33] Paul A, Nath JM, Das TK. An investigation of the MHD Cu-Al2O3/H2O hybrid-nanofluid in a porous medium across a vertically stretching cylinder incorporating thermal stratification impact. J Therm Eng 2023;799–810. [CrossRef]

[34] Tokgoz N. The Numerical Study of Heat Transfer Enhancement Using Al2o3-Water Nanofluid in Corrugated Duct Application. J Therm Eng 2018;4:1984–1997. [CrossRef]

J Ther Eng, Vol. 12, No. 2, pp. 739−755, March, 2026

Journal of Thermal Engineering
Web page info: https://jten.yildiz.edu.tr
DOI: 10.14744/thermal.0001115

Research Article

Thermal gradients and ferrite formation in weld joints: A detailed study of temperature effects on microstructure and mechanical properties

Loay M. MUBARAK[1], Hussein M[2], Ahmed Hashim KAREEM[3], Bassam Ali AHMED[4], Hasan Shakir MAJDI[5]

[1]*Department of Mechanical Engineering, College of Engineering, University of Diyala, Diyala, 32001, Iraq*
[2]*Institute of Technology-Baghdad, Middle Technical University, Baghdad, 10074, Iraq*
[3]*Department of Mechanical Techniques, Amarah Technical Institute, Southern Technical University, Basra, 44001, Iraq*
[4]*Department of Electromechanical Engineering, University of Technology- Iraq, Baghdad 10001, Iraq*
[5]*Department of Chemical Engineering and Petroleum Industries, Al-Mustaqbal University College, Babylon, 51001, Iraq*

ARTICLE INFO

Article history
Received: 11 March 2025
Revised: 24 June 2025
Accepted: 10 July June 2025

Keywords:
AISI 304 Stainless Steel TIG Welding; Ferrite Content; Phase Transformation; Weld Microstructure; Welding Heat Input

ABSTRACT

This study investigates TIG welding current variations effects on 4 mm thickness AISI 304 stainless steel joint welded using Argon gas, and this process impacts on ferrite composition, structural properties and joint strength. Ferrite content control must be managed properly to prevent hot cracking while ensuring both material strength and corrosion resistance because improper management leads to deficits during welding operations. A set of welding currents starting at 100 A progressed to 150 A and ending at 190 A created welds which delivered heat inputs of 6 J/mm, 9 J/mm and 11.4 J/mm. Welds under each condition received full inspection using metal structure analysis, scanning electron microscopy (SEM) along with Ferritoscope ferrite measurement, Vickers hardness analysis and mechanical strength testing. Data showed that a rise in heat intensity led to more ferrite formation starting from 4% at 100 A up to 9% at 190 A. The welds with 150 A heat application produced the optimal combination of mechanical properties since they contained 6% ferrite and displayed peak tensile strength at 689 MPa and mid-range hardness from 160–170 HV along with increased resistance to hot cracking. The welding current at 100 A produced a high hardness level of 170–181 HV in the weld but lost strength because of excessive ferrite content. Meanwhile the weld at 190 A exhibited lower strength and reduced hardness (150–157 HV) due to its excessive ferrite formation. Because of its ability to achieve superior microstructure with desirable austenite-to-ferrite ratio the weld using 150A heat input delivers optimal weld quality. The current investigation establishes quantitative assessments about heat treatment effects on AISI 304 TIG welds which distinguishes itself from previous research. The integration of Schaeffler diagram modeling with direct ferrite evaluations paired with SEM verification leads to a superior method for welding process prediction and enhancement.

Cite this article as: Mubarak LM, M H, Kareem AH, Ahmed BA, Majdi HS. Thermal gradients and ferrite formation in weld joints: A detailed study of temperature effects on microstructure and mechanical properties. J Ther Eng 2026;12(2):739−755.

***Corresponding author.**
*E-mail address: louay_mohamed@uodiyala.edu.iq

This paper was recommended for publication in revised form by Editor-in-Chief Ahmet Selim Dalkılıç

Published by Yıldız Technical University Press, İstanbul, Turkey
Yıldız Technical University. This is an open access article under the CC BY-NC license (http://creativecommons.org/licenses/by-nc/4.0/).

INTRODUCTION

Researchers have extensively studied how temperature fluctuations affect ferrite content and structure formation in welded joints throughout welding metallurgy. The analysis of these effects leads to better weld mechanical properties since proper thermal management during welding affects ferrite phase development. García-García and Reyes-Calderón (2022) [1] evaluated how δ-ferrite composition affects the mechanical characteristics within austenitic stainless steel welded joint areas. Research showed that modifying δ-ferrite content within the HAZ area produced major alterations that affected weld properties regarding toughness and cracking resistance. The article published by Chukwuneke et al. (2022) [2] examines steel weld joint mechanical properties together with their thermal distortions through numerical methods. There was an investigation into how various heat amounts transform material structures through studies of weld metal structural alterations and Heat Affected Zone transformations. Perpetual research has shown that changing thermal gradients affect ferrite preservation deeply yet controlled welding configurations reduce weld distortion levels effectively.

Vasantharaja and Vasudevan (2019) [3] investigated how TIG and A-TIG welding methods affect the microstructure together with mechanical properties of ferritic-martensitic (RAFM) steel welds. The research showed that welding temperatures as well as cooling speed after welding affect the ferrite composition and mechanical property development of welded materials. Yanfa Han et al. (2025) [4] research analyses the MP-GMAW of ZGMn13Mo/A514 using the microstructure, mechanical properties, residual stress, and distortion analysis. In the weld metal, there are γ-austenite and Cr-rich δ-ferrite phases were identified and the martensitic transformation in the HAZ of A514 was observed. Tushar Sonar et al. (2015) [5] paper presented a critical evaluation of dissimilar welding of FMS and ASS using GTAW technique with focus on weldability problems including hot cracking, cold cracking and δ-ferrite formation. It also describes influence of the welding parameters, filler materials and post-weld heat treatment on the microstructure and mechanical characteristics of joints. Fei et al. (2020) [6] examined how post-weld heat treatment influenced deep penetration autogenous TIG-welded dissimilar joints from the viewpoints of their microstructure and mechanical properties. Examination of controlled post-weld thermal cycles enabled HAZ ferrite content adjustment that resulted in enhanced strength together with ductility of welded joints. Queiroz et al. (2020) [7] conducted research on how external magnetic fields affect TIG-welded joints both structurally and mechanically. The fusion zone received both thermal influence and magnetic field exposure that modified ferrite distribution and stability patterns. Li et al. (2019) [8] conducted experimental research that assessed simulated welding thermal cycles for studying microstructural and mechanical properties in austenitic stainless steel with high nitrogen content through its large-grained thermal-impacted area. Maduraimuthu et al. (2012) [9] studied how activated flux affected modified 9Cr-1Mo steel weld joints through tests on their microstructure along with their mechanical properties and residual stress measurements. Heat input and cooling rates during welding temperature behavior led to changes in ferrite content that determined the weld mechanical performance. The research conducted by Raj et al. (2024) [10] investigated the thermal aging impacts on the tensile characteristics alongside metallurgical properties of stainless steel weld joints. The research established that ferrite content significantly affects weld mechanical properties and thermal aging affects ferrite stability through post-weld treatments that enhance overall performance. Zmitrowicz et al. (2021) [11] research uses linear welding energy to analyze its effects on ferrite content throughout HAZ and weld zone of duplex stainless steel materials. The study shows that higher linear welding energy levels led to increased ferrite content in the HAZ regions but the greatest WM ferrite percentage. Noga et al (2024) [12] study focuses on how multiple welding techniques (MIG, TIG, PAW, and EBW) changing the microstructure structure alongside mechanical characteristics of duplex stainless steel welds. The paper explains how heat input rates and cooling conditions affect ferrite crystal structure and arrangement that determines weld mechanical properties. Mohammed et al. (2017) [13] research evaluates microstructural mechanical and corrosion effects that various welding heat inputs produce in duplex stainless steel fusion areas. The weld metal requires slower cooling rates when heat input is high causing more austenite to form and reducing the ferrite amount. Higelin et al. (2022) [14] research analyzes methods to manage ferrite content within the HAZ regions of plex stainless steel welded areas. This investigation studies the impact of various welding factors on austenite-to-ferrite transformation in welding operations that modifies weld mechanical behaviors. Wang et al. (2023) [15-19] article examination the thermal mechanical welding operations which modify welded joint microstructure and mechanical characteristics. The study examines the connection between thermal cycling effects on ferrite pattern and its distribution that modifies weld properties regarding strength and ductility.

The novelty of this research lies in its detailed investigation of the impact of varying TIG welding currents (100 A, 150 A, or 190 A) on the microstructure and overall performance of AISI 304 stainless steel welds. This study examines the critical aspect of regulating ferrite levels in welded joints, as it influences both the material's strength and toughness. A significant improvement is the utilization of Schaeffler diagrams in conjunction with direct ferrite content measurements and SEM analysis to refine process prediction and enhancement. The research concludes that 6% ferrite, achieved with 150 A of heat input, optimally balances tensile strength, toughness, and fracture resistance. The optimal environment for welding enhances the

material's strength and mitigates the danger of hot cracking, making it particularly advantageous for components susceptible to corrosion. It examines the impact of welding on austenitic and ferritic phases, educating readers about the microstructure and characteristics of welded joints. The microstructural control of δ-ferrite is crucial for maintaining strength and corrosion resistance in austenitic stainless steel AISI 304 welds, which are used in pressure vessels and piping systems. Previous research has not adequately explored the correlation between heat input variations and ferrite development and austenitic weld mechanical properties, such as hardness, tensile strength, and phase transformations. This paper addresses these shortcomings by examining TIG welding current variations (100 A, 150 A, 190 A) to control heat input and measure its effects on structural properties and mechanical outputs. The research also establishes a connection between metal phase modifications and tensile strength measurements and hardness data, extending from weld core areas to heat-affected region sections. The optimal combination of mechanical characteristics is found at 150 A / 6% ferrite.

EXPERIMENTAL PROCEDURE

Investigation Materials

Two AISI 304 austenitic steel plates employed in the testing had 4 × 1000 × 2000 mm dimensions. Table 1 shows the base steel chemical composition according to the acceptance certificate. ER 308 was the TIG filler welding material that was utilized. Table 2 shows the TIG filler chemical composition. The welding joint design employed a single V-shape with a 60 degrees angle, as specified by the AWS A2 standard. When welding was done, a brace was placed on both ends of the specimen to prevent it from becoming deformed. This was necessary since the heat created by the welding may cause deformation, and the specimen was considered to be a solid or massive material.

The three samples final welding settings were applied based on preliminary technical testing on the specimens under the specified dimensions. The technological testing primary objective was to create welded joints that met the criteria and did not have any welding flaws. After testing, the final joints welding parameters are provided in Table 3, 100% Ar as shielding gas was used.

Microstructure Examinations

An Olympus GX51 light microscope was used to analyze welded joints microstructure. The samples were cold mounted in a Spruers Fixi Form container using Struers ‹EpoFix epoxy adhesive. The samples that were generated in this manner were subsequently processed on sandpaper with 320 - 1500 grain. Polishing purposes utilized by diamond suspensions. OP-S polishing suspension from Struers was used to complete the polishing process. In order to show AISI 304 stainless steel microstructure, the specimens electrolytically etched in 10% nitric acid at 1.5 V voltage for 20 s at room temperature. A HITACHI SU-70 scanning electron microscope with an attachment chemical composition (EDS) microanalysis was used to conduct scientific study on a micro scale. The quantitative metallography approach and the MPD-100 ferritoscope were used to conduct tests that measured the ferrite content in AISI 304 welds and base material. The ferritoscope employs a technique that is based on substance magnetic characteristics measuring. The material magnetic permeability being evaluated is used to determine ferrite present quantity. The findings are shown as percentages.

Table 1. AISI 304 chemical composition (% by weight)

Fe	C	Si	Mn	S	P	Ni	Cr	N
Bal.	0.07	1.00	2.00	0.015	0.045	9.84	18.93	0.10

Table 2. ER 308L electrode chemical composition (% by weight)

Fe	C	Cr	Si	Mn	S	Mo	P	Cu	Ni
Bal.	0.02	20.1	0.44	1.6	0.02	0.03	0.02	0.11	9.2

Table 3. TIG with ER 308L electrode welding parameters

No.	Filler Dia.	Current (A)	Voltage (U)	Welding Speed (Vs)	Shielding Gas	Flow rate (L/min)	Tungsten Electrodes
1	1.6 (mm)	100 A	12 V	140 (mm/min)	Argon	15	2% Thorium
2		150 A					
3		190 A					

Mechanical Measuring Procedure

Acquired joints mechanical tests comprised a uniaxial tensile test, a bending test, and a hardness assessment using the Vickers technique. For uniaxial tensile samples, the measuring base had 25 mm a width, 4 mm thickness, and 60 mm length. Three samples were obtained from each welded joint, and tensile tests were conducted on them [19]. MTS Criterion C45 testing machine was used to conduct the tests. Bending tests were performed on flat pieces that were 300 × 25 × 4 mm dimension [20]. The Vickers hardness test (HV) was conducted on the base metal (BM), heat affected zone (HAZ), and weld metal (WM) at ambient temperature, in accordance with ASTM E92-82. A diamond indenter was employed with a load of 10 Kgf and a dwell period of 15 seconds. To provide clear visualization of the data in each of the three zones, three measurements were conducted inside each zone. The objective of the microhardness tests is to determine the hardness of the material in each region, thereby providing insights into the microstructure and mechanical properties of the welded joint [21]. Measurements were done in four measuring lines that ran through each sample base material, weld, and HAZ. Hardness measurements taken in this manner were used to create a two-dimensional graphic depicting the hardness profiles in welded joints. Fig. 1 shows the dimensions of tensile test samples according to the ASTM E8 standard [22]. Fig. 2 below illustrates the welded joint assessment procedure and sequence graphically.

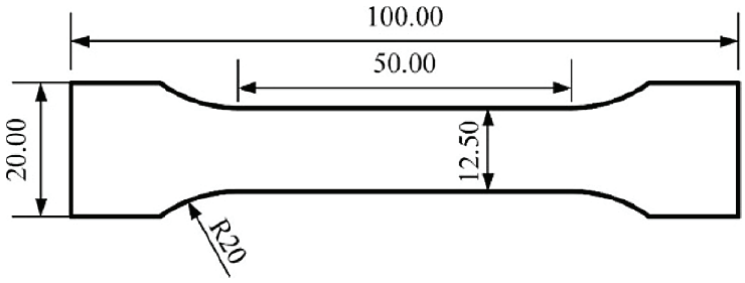

Figure 1. Schematic of tensile test specimen size and dimensions. [Refer to ASTM E8 standard, adapted in accordance with [22].

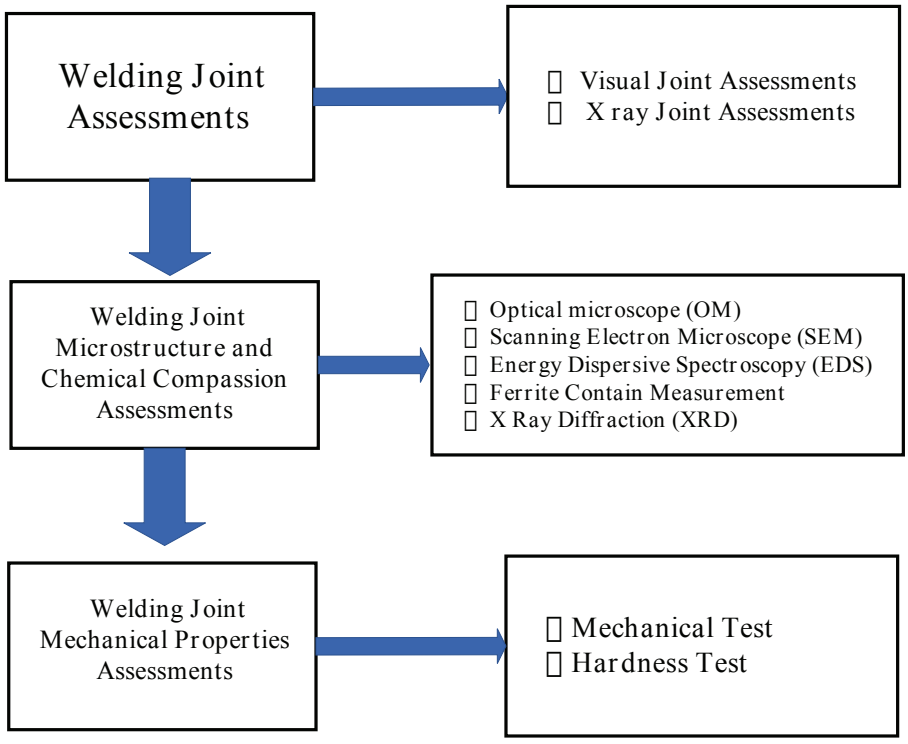

Figure 2. Welding joint assessment procedure.

Schaeffler Diagram Ferrite Calculation

To enhance mechanical qualities and corrosion resistance, ferrite-forming elements like as Mo, W, Si, Ti, Nb, and V are employed as alloying additions. When included into steel, they also constrict the stability range of the γ phase, often reducing the propensity of austenite to precipitate phases such as σ, Laves, χ, and others. To preserve the single-phase γ structure, it is essential to incorporate an ideally elevated Ni content into the steel. Otherwise, the steel may acquire a dual-phase structure: austenite and metastable ferrite. Earlier studies indicates that minimal presence of δ ferrite inhibits hot cracking in austenitic steels, with a concentration of 1–6% effectively preventing hot cracking in welded austenitic steels and decreasing the crack propagation rate during stress corrosion cracking [23,24].

The amount of ferrite in the weld is determined by its chemical composition. Alloying elements in austenitic steels are classified as ferrite-forming and austenite-forming elements. The influence of chemical composition on microstructure and solidification is denoted by chromium and nickel equivalents. The chromium equivalent is the aggregate of chromium content and ferrite-forming components, each weighted by coefficients that denote their influence on the relative proportion of ferrite in relation to chromium. Fig. 1 presents a Schaeffler diagram, outlining the areas where the weld structure of corrosion-resistant steels is exhibited, measured in nickel and chromium equivalents [25, 26]. This graphic is a useful tool for evaluating the effects of integrating filler metal into the base material of the joint, enabling computation of the ferrite content in the joint.

RESULTS AND DISCUSSION

Welding Zone Microstructure Analyses

Figure 4 (A) demonstrates the raw AISI 304 steel material microstructural composition through microscopic analysis. AISI 304 stainless steel exists as an austenitic steel structure with its fundamental crystal arrangement as face-centered cubic (FCC) lattice when operating at room temperature. The image demonstrates a uniform arrangement characteristic of austenitic phase typical in the material structure. Equiaxed (roughly spherical) grains appear round in shape as light areas where their microstructure maintains homogeneity. The metal exhibits ductility along with toughness due to its crystal arrangement that serves as a characteristic feature of 304 stainless steel.

The dark lines that separate grain areas indicate grain boundaries in the material structure. Because crystallographic orientations differ in these locations, they form interfaces. The material's mechanical properties depend significantly on grain boundaries because they influence strength, ductility, and corrosion resistance. These boundaries prevent dislocations from moving because of their high-angle nature. The morphology in Figure 4 (A) contains various circular or undefined dark shapes that most likely consist of non-metallic inclusions together with second-phase particles. Materials' strength and toughness typically suffer due to manufacturing process-related factors that create defects in the material. Any elongated or distorted grain appearance in base metal morphology tends to suggest plastic deformation linked to dislocation motion. The dislocations formation occurs predominantly in materials that go through processing stresses either from rolling or drawing treatments. Under certain

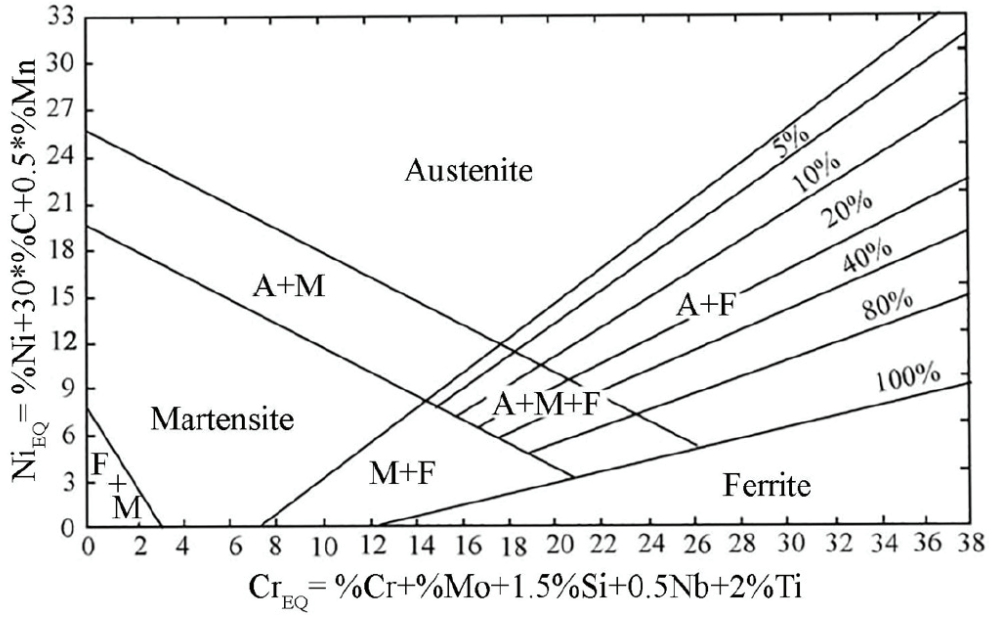

Figure 3. Schaeffler Diagram used for determining weld structure phases and ferrite content. [Adapted from Kou [26]].

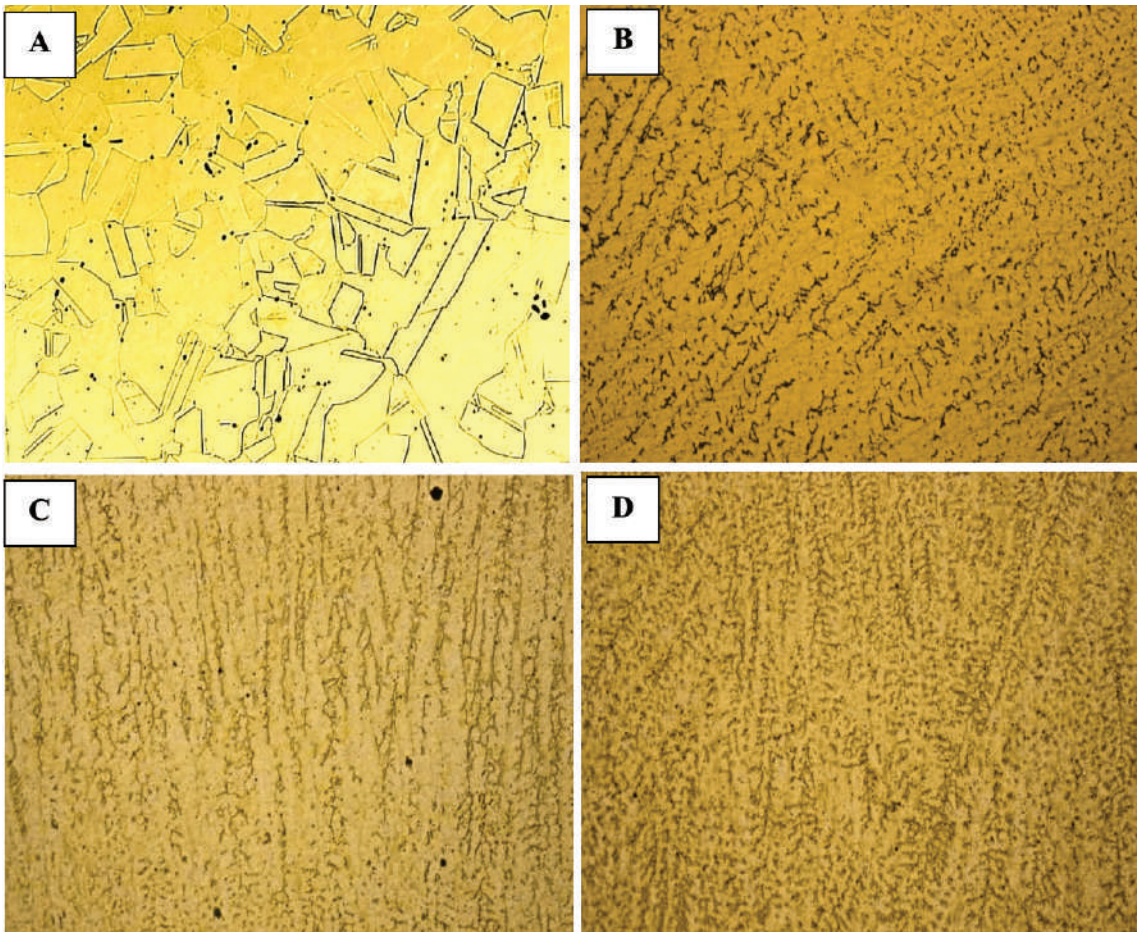

Figure 4. Base metal and welding zone microstructure (A) base metal (B) 190 A welding current (C) 150 A welding current (D) 100 A welding current.

conditions, AISI 304 stainless steel main composition consists austenite with small ferrite traces that is another steel phase with body-centered cubic structure. Small ferrite amounts exist within the typical AISI 304 microstructure despite the normal austenitic phase. Phase transitions in steel occur when alloys modify the steel or when cooling procedures drain heat from the material. The microstructure of AISI 304 stainless steel structures serves as its main defense against corrosion effects. Austenitic homogeneity in AISI 304 structures protects the material from general corrosion and pitting failure. Chloride-rich solutions can increase corrosion susceptibility in inclusions and disturbed areas near grain boundaries. High heat input conditions during welding produce distinctive features in austenitic stainless steel weldments, such as the dendritic pattern with networked ferrite formations. The fusion zone (FZ) is formed from different phases during welding. Primary Austenitic Solidification with Ferrite ($\gamma + \delta$) emerges as the product of high heat input when using 190 A fusion zone (FZ). Under austenitic-ferritic solidification mode, the weld region forms dendritic austenite grains. The presence of δ-ferrite phase prevents hot cracking during welding austenitic stainless steel. Elevated temperature difference promotes columnar dendrite development, while composition segregation and cooling rate determine dendrite formation. AISI 304 welds have a ferrite content proportion of 5-12%, improving cracking resistance. However, toughness and ductility suffer when δ-ferrite amount exceeds 10%. This process creates a heterogeneous element distribution, potentially causing corrosion resistance problems in local areas. The observed microstructure matches austenitic stainless steel weldments even though it displays differences in comparison to weldments using higher heat inputs. The main solidified component in the weld operates as austenite (γ) phase while developing dendritic shapes stretching from the fusion boundary. Moderate welding current welds (150 A) dendritic structures appear finer and more organized than those of high-heat input welds like the 190 A welds because of their coarser structure. Less δ-ferrite remains in the interdendritic areas of welds affected by moderate cooling rates than in welds undergoing extensive cooling. δ-ferrite appears as a dark network of bones throughout the image because it developed within the interdendritic structures. The welds possess enough ferrite to avoid hot cracking despite having less compared to high-heat input welds. Metals made of ER308 include a specific design feature

that maintains δ-ferrite at ~5–8 % levels for inhibiting cracks. The moderate dendritic patterns in the fusion zone mostly show columnar dendrites that extend with the direction of thermal dissipation. The weld dendrites of lower heat input applications tend to appear shorter along with finer dimensions than their high-heat input counterparts (190 A) thus resulting in enhanced mechanical characteristics. The resistance of material against corrosion improves when cooling occurs at moderate levels. The weld joint done with 100 A low current power appears in Fig. 4 (D) as the fusion zone (FZ). The decreased heat exposure during welding affects basic characteristics of weld quality. An application of 100 A welding current creates reduced heat input that results in accelerated cooling during material welding. During this process the dendrite formation mechanism and ferrite distribution as well as phase transformation patterns are affected. The Austenite phase is the main microstructural phase in weld welding, with a faster cooling rate and lower ferrite amounts due to decreased heat input. Dendrites become denser due to heat escape, and in low heat input welds, dendrites remain small and less elongated. Weld metal solidification occurs rapidly, reducing grain growth and increasing mechanical strength. The lower distribution of Cr, Ni, and Mo enabling elements enhances corrosion protection. Ferrite crystal formation is less pronounced in 100 A heat input welding compared to 150 A and 190 A heat inputs, leading to an upward trend in ductility and a marginal rise in hot crack formation. The weld metal exhibits 3–5% ferrite crystals, with a crystal count below the minimum breaking threshold. The analyzed joints of the three samples exhibit mostly austenitic microstructures, with the presence of delta ferrite precipitates. The welds exhibit cellular and dendritic microstructures, whilst the weld axes have a uniform structure. Columnar dendrites exhibited both primary dendritic arm spacing (PDAS) and secondary dendritic arm spacing (SDAS). A comparable microstructure was seen in Kulkarni's work. [27]. Because the temperature gradient to solidification rate ratio is reduced, dendritic microstructure is present at the fusion lines and equiaxed inside the weld line [28]. A refined equiaxed dendritic morphology was seen in the center of the fusion zone as a result.

Welding Zone Ferrite Content Measurements

Ferrite content was measured using both a magnetic method using a Ferritoscope and metallographic technique. After weld joint dilution calculations based on the resulted joint geometry dimensions, The chromium equivalent (Creq) and nickel equivalent (Nieq) were calculated from the chemical composition of AISI 304 steel and ER308 austenitic steel (filler metal). The welding zone nickel and chromium equivalents listed in Table 4 below for the three welding samples. The calculated values revealed the expected ferrite content in the weld, derived from the Schaeffler diagram (Fig. 3), which indicated a delta ferrite concentration value in. The results reflected the Creq/Nieq ratio effects on solidification mode and the joint resulting microstructure.

Table 4 reveals the impact of welding input heat on Creq and Nieq. High heat inputs cause slower cooling, causing chromium and molybdenum alloying elements to separate differently across the fusion zone, reducing their uniform distribution. Heat exposure in the heat-affected zone results in Cr23C6 precipitation, depleting chromium resources. Lower temperatures lead to decreased Creq concentration, resulting in poor corrosion resistance. Higher heat inputs cause chromium depletion from grain boundary areas, reducing Creq content in the fusion zone. [29]. The alloying elements have less time to segregate because of rapid cooling that happens when the heat input remains low. The weld corrosion resistance remains strong because minimal carbide precipitation forms when heat input stays low. Reducing the heat input along with fast weld cooling produces better resistance to pitting and crevice corrosion by creating higher Cr_{eq} composition. The heat input had the same effects on the $Ni_{eq,}$ the weld pool cooling becomes slower when high heat inputs are applied thus causing an increase in carbon (C) and nitrogen (N) concentration. The Ni_{eq} concentration becomes higher when carbon accumulates nickel properties and converts the weld metal to an austenitic state. Higher Ni_{eq} pushes the weld toward increased stability of γ-phase. The excessive austenite formation becomes more likely as cooling takes place too slowly. Fast weld cooling occurs when applying low heat that minimizes the carbon (C) and nitrogen (N) influence. The rapid weld cooling produces lower Ni_{eq} equilibrium content and increases the ferritic or martensitic phases in low alloy stainless steel weld metal. The weld region with diminished Nieq exhibits unstable austenite structures due to rapid cooling rates, which foster the production of ferrite or martensitic phases, thereby impairing ductility and toughness. A medium or diminished Nieq value fosters microstructural equilibrium, enhancing material properties during particular welding procedures. Table 5 below show summary heat input effects on Cr_{eq} and Ni_{eq} and welding zone geometry in stainless steel welding [30].

Table 4. Three welding samples Creq, Nieq, Creq/Nieq ratio, and calculated FN

Welding current	Input heat	Cr_{eq}	Ni_{eq}	Cr_{eq}/Ni_{eq} Ratio	FN%
100 A	6 J/mm	18.85	12.84	1.46	4
150 A	9 J/mm	18.21	11.66	1.56	6
190 A	11.4 J/mm	17.83	10.16	1.75	9

Table 5. Heat input effects on Cr_{eq} and Ni_{eq} and welding zone geometry

Parameter	Higher Heat Input (190 A)	Moderate Heat Input (150 A)	Lower Heat Input (100 A)
Weld Geometry	Wider weld bead, deeper penetration, larger HAZ, potential distortion	Balanced bead size and penetration, moderate HAZ	Narrower weld bead, shallower penetration, smaller HAZ
Cr Equivalent (Cr_{eq})	Decreased due to chromium depletion in HAZ, lower corrosion resistance	Balanced Cr_{eq}, good corrosion resistance	Higher Cr_{eq}, better uniformity and corrosion resistance
Ni Equivalent (Ni_{eq})	Higher Ni_{eq} (better austenite stability) but risk of excessive austenite	Moderate Ni_{eq}, balanced austenite and ferrite phase stability	Lower Ni_{eq}, possibly more ferrite/ martensite, reduced austenite

The Ferritoscope ferrite contains measurements results of the three samples were very close to the calculated values, with a little error percentage, Ferritoscope detects the magnetic ferrite phase to directly determine the ferrite content in stainless steel welds. The measurement procedure of Ferritoscope depends on their ability to detect differences in ferrite and austenite magnetic properties. The ferrite content measured by Ferritoscope shows minimal differences from diagrams generated by the Schaeffler Diagram because it perfectly matches overall weld phase distributions which derive mainly from Cr and Ni elements. Fig. 5 below illustrated the values of ferrite percentage between the calculated values from Schaeffer diagram and the ferrite percentage measuring by ferrometer. The Schaeffer Diagram is derived from an analysis of the material›s chemistry, whereas the Ferrometer provides a measurement pertaining to the material›s magnetic. The Ferrometer is often a superior instrument for assessing ferrite when measured directly from the welded metal, as it does not rely on the tool›s estimations of the metal›s composition. The ferrometer is superior at identifying genuine alterations in the microstructure caused by welding, such as rapid cooling rates, whereas the Schaeffer Diagram neglects these variables during cooling and may yield divergent outcomes.

The research assesses FZ microstructure development through three heat input parameters at 100 A, 150 A, and 190 A. The manuscript details the changes that affect key microstructural aspects from dendrites to ferrite content together with grain growth and elemental distribution and sensitization levels and toughness alongside material properties. The authors present in Table 6 important insights regarding the trade-offs regarding heat input and microstructural evolution and performance attributes for optimized welding process control. Through FZ microstructural observation after heat application welders understand how welding metallurgy affects material strength during high-stress operation.

Hot cracking resistance strengthens through ferrite because these particles act as impurity traps that collect sulfur and phosphorus atoms around the grain boundaries.

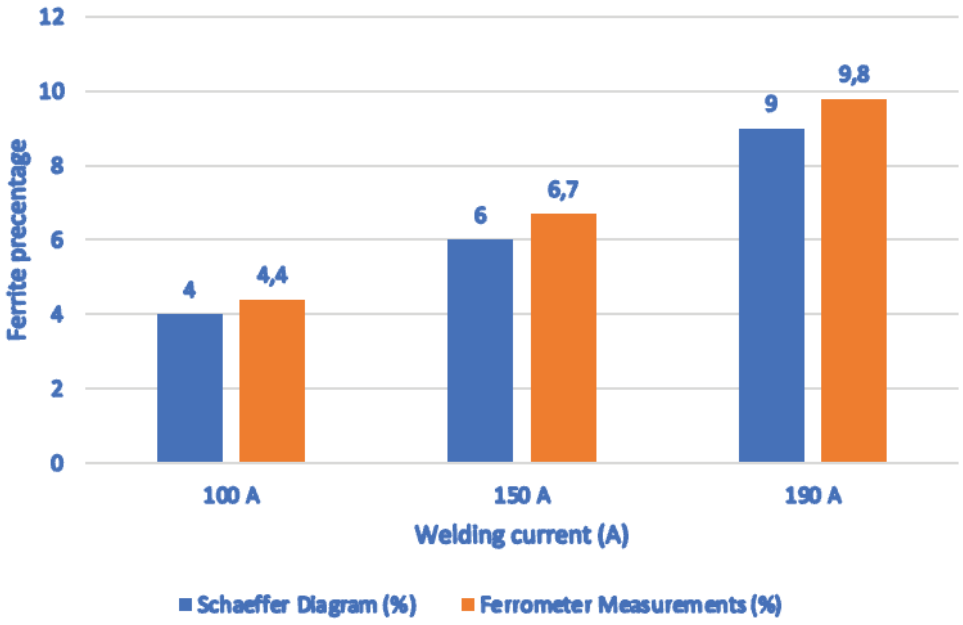

Figure 5. Ferrite percentage measurements differences between Schaeffler diagram and Ferritoscope instrument.

Table 6. Fusion zone (FZ) microstructures comparison based on heat input effects

Feature	100 A (Low Heat Input)	150 A (Moderate Heat Input)	190 A (High Heat Input)
Heat Input	Low	Moderate	High
Cooling Rate	Fast	Moderate	Slow
Dendritic Structure	Fine dendrites (best strength)	Moderate dendritic structure	Coarse dendritic structure (weaker toughness)
Ferrite Content (δ-Ferrite)	Low (~3-5 %) - higher hot cracking risk	Moderate (~5-8 %)	Higher (~8-12 %) - best crack resistance
Grain Coarsening	Minimal - best toughness	Moderate - balanced toughness & strength	Significant - lowers toughness
Elemental Segregation	Minimal - best uniformity	Moderate - acceptable segregation	High - risk of localized corrosion
Sensitization (IGC Risk)	Very Low (best corrosion resistance)	Low - still good corrosion resistance	High - prone to intergranular corrosion (IGC)
Crack Resistance	Moderate - risk of solidification cracking	Best balance between strength & cracking resistance	Best resistance to hot cracking
Mechanical Properties	Best strength & toughness due to fine grains	Balanced mechanical properties	Lower strength & toughness due to coarse grains
Corrosion Resistance	Best resistance due to minimal carbide precipitation	Good - but requires control of heat input	Lower - due to carbide precipitation & segregation

Because of its low ferrite content (4 %) at 4 %, the weld remains susceptible to solidification cracking especially when performing welding under high-restraint conditions. A maximum hot cracking resistance is achieved when standard ferrite content ranges from 5 % to 10 %. Lower ferrite values below 5 % favorably affect both ductility and impact toughness thus improving weld sudden load performance. Higher flexibility emerges from the weld›s austenite-intensive structure yet its reduced strength outweighs the strength obtained from greater ferrite content. The reduction of ferrite content usually improves machining outcomes in particular applications. Weld metal with 4% ferrite content displays the most effective pitting corrosion and crevice corrosion resistance while keeping sufficient corrosion levels [31]. The requirement of chloride ions in solution calls for weld metals to contain less ferrite in order to avoid localized corrosion affecting ferrite regions. Ferrite exhibits ferromagnetic properties that contrast austenite because ferrite operates as a ferromagnetic material yet austenite operates as paramagnetic. Refraining from magnetism is possible in weld metals with 4% ferrite content making this material appropriate for magnetic field-sensitive applications. According to the experts, the incorporation of ferrite provides weld metals with dual advantages: high-temperature oxidation protection plus grain boundary sliding control. Welds starting service above 600°C result in excessive ferrite formation exceeding 10%. Subsequent ferrite transformation creates brittle sigma (σ) phase that weakens the weld toughness. Weld materials with 4% ferrite content stay stable at high temperatures because they develop minimal sigma phase presence [32]. The mechanical properties and resistance to cracking along with corrosion performance of the weld zone depend on its 6 % ferrite content. Ferrite in a weld metal absorbs harmful elements like S, P and Si which prevents hot cracking by combining with 6% ferrite providing a balance that improves hot cracking resistance compared to using 4 % ferrite metal at 100 A. The fracture risks decrease proportionally with weld ferrite content under 5% so this enhanced level ensures stronger structural performance. Weld›s toughness and ductility are slightly lower than austenitic welds due to an increase in ferrite content. However, the appropriate ferrite content leads to increased mechanical strength and thermal stability, resulting in greater mechanical load resistance. Higher ferrite content reduces corrosion resistance, but it remains in acceptable levels. The resistance to pitting corrosion in chloride environments is slightly diminished compared to low ferrite and higher ferrite welds. Stress corrosion cracking and intergranular corrosion exhibit stable resistance. Ferrite›s magnetic property differs from austenite, acting ferromagnetic but remaining paramagnetic. The weld with 6% ferrite shows improved magnetic properties but non-magnetism. Ferrite also enhances resistance to high-temperature oxidation and grain boundary sliding. Welds with 9% ferrite have a low probability of developing sigma phase due to increased formation risk. 9% ferrite content improves cracking resistance, mechanical strength, and corrosion resistance. Ferrite plays a crucial role in solidification cracking prevention by taking in segregating elements like S and P. Welds with 9% ferrite have limited hot cracking risks and superior resistance against solidification issues. The elevated ferrite level in the weld metal boosts mechanical strength and prevents deformation [33]. During service operations, Ferrite produces fewer thermal expansion effects than austenite

because it›s thermal expansion coefficient stands lower. The corrosion resistance decreases as ferrite levels rise above 10 % since ferrite shows reduced resistance against pitting and crevice corrosion than austenite. With a ferrite, content of 9 % the weld material shows increased vulnerability to chloride-induced localized corrosion especially in marine settings when contrasted with welds containing lower amounts of ferrite. Most applications show suitable performance in terms of general corrosion resistance. The material composition of ferrite contains magnetic properties and austenite demonstrates paramagnetic responses. The weld metal maintenance with 9% ferrite content possesses reasonable ability to attract magnets but fails to meet non-magnetic application requirements. The presence of ferrite strengthens the material at high temperatures yet the material becomes brittle when the temperature reaches above 600 °C where it transforms into the sigma (σ) phase. Welds containing 9 % ferrite carry a higher risk of sigma phase formation than welds that have 4–6 % ferrite mostly because they both affect the toughness and impact strength during extended exposure to elevated temperatures. The weld needs to have ferrite content below 8 % when it must handle prolonged exposure to high temperatures.

Welding Zone SEM Analyses

SEM plays an essential role in understanding changes in microstructures across TIG-welded 304 stainless steel joints as the researcher varies heat input levels from 100 A to 150 A and 190 A. Through SEM examination, detailed observations of weld metal structures, which show important information about the distribution of austenite and ferrite along with grain features and interdendritic patterns, can gain. Knowledge of these features leads to effective evaluation of solidification behavior and hot cracking susceptibility along with mechanical strength and corrosion performance assessments. The evaluation of microstructural details through SEM analysis enables optimal ferrite content determination alongside reliability enhancement and failure prevention in service applications across different welding current settings. Fig. 6 below illustrated the three welding zones SEM morphology [34].

An SEM micrograph from Fig. 6 (A) at 100 A shows that the weld zone consists of dendritic austenite with interdendritic

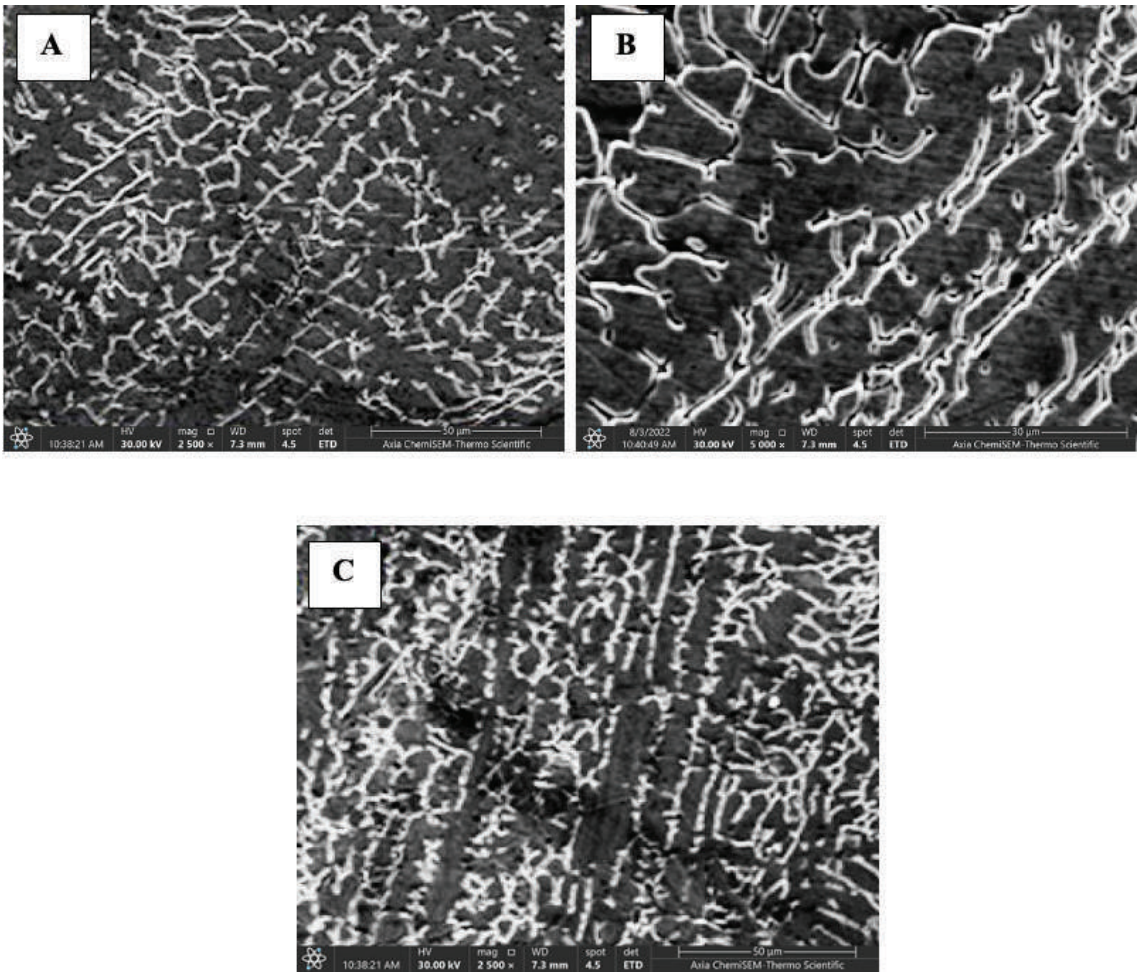

Figure 6. Welding zone SEM morphology (A) 100 A, (B) 150 A, and (C) 190 A.

ferrite that contains 4 % ferrite content. The combination of nickel (Ni) and carbon (C) elements in ER308 filler material stabilizes austenite. The dendritic formation indicates austenitic solidification that produced ferrite throughout interdendritic regions. The SEM image reveals the web-like bright structure as δ-ferrite that occurs between interdendritic boundaries. The weld solidified through an Austenite + Ferrite (AF) mode based on its 4 % ferrite content since austenite formed first then interdendritic ferrite appeared later. The segregation of Cr (chromium) and Mo (molybdenum) ferrite stabilizers produces ferrite in the metal structure. The minimum allowable ferrite amount in stainless steel welds stands at 3 % meaning the examined weld contains a near minimum concentration of ferrite. While the ferrite phase defends against solidification, cracking it exists at a limited 4 % level that may raise the susceptibility to hot cracking under high restraint. The low ferrite content provides excellent corrosion resistance along with ductility however; it reduces the hot-cracking resistance slightly.

SEM image in Fig. 6 (B) shows the weld metal microstructure at 150 A. The weld metal shows two distinct microstructures of austenite (γ-phase) as main phase and interdendritic δ-ferrite that strongly affects the weld properties. Dark areas viewed in the SEM image represent the γ-phase that is known as austenite. The austenitic phase exists as the major matrix component because nickel (Ni) from the ER308 filler metal stabilizes this phase. Austenite turned into the first solid phase during the process before ferrite developed between the dendrites. δ-ferrite exists as a bright network structure throughout the interdendritic spaces according to the SEM image. An enhanced welding current to 150 A creates more heat input that allows grain development and slows down cooling which helps stabilize additional ferrite. The weld obtained through 6 % ferrite content contains slightly elevated ferrite quantities than lower-amperage welds (100 A with 4 % ferrite) and thereby presents increased advantages for crack prevention. The weld zone microstructure at 190 A is depicted in Fig. 6 (C) through an SEM micrograph. The combination of high welding current (190 A) with 9 % ferrite percentage in the microstructure produces a higher ferrite fraction than welds forged with 100 A or 150 A welding current. The mechanical as well as corrosion behavior of the weld receives major modification through this change. In the SEM image, the dark areas represent austenite (γ-phase) that makes up the main structure of the material. Austenite receives stability from carbon (C) and nickel (Ni) while having ferrite remain present due to chromium (Cr) segregation. The region showing network-like brightness represents δ-ferrite while its percentage in this weld reaches 9 %. A welding current of 190 A produces elevated heat input that generates a slower cooling process during which ferrite can stabilize to higher percentages. The formation of Austenite + Ferrite (AF) solidification results in improved crack resistance according to this characteristic [35].

Welding Joint Hardness Profile Analyses

Testing the 304 stainless steel alloy TIG welds hardness profile attributes decisive value to the determination of structural mechanical behavior along with service duration. The combination of material strength and the resistance to wear and tendency to develop cracks can be measured

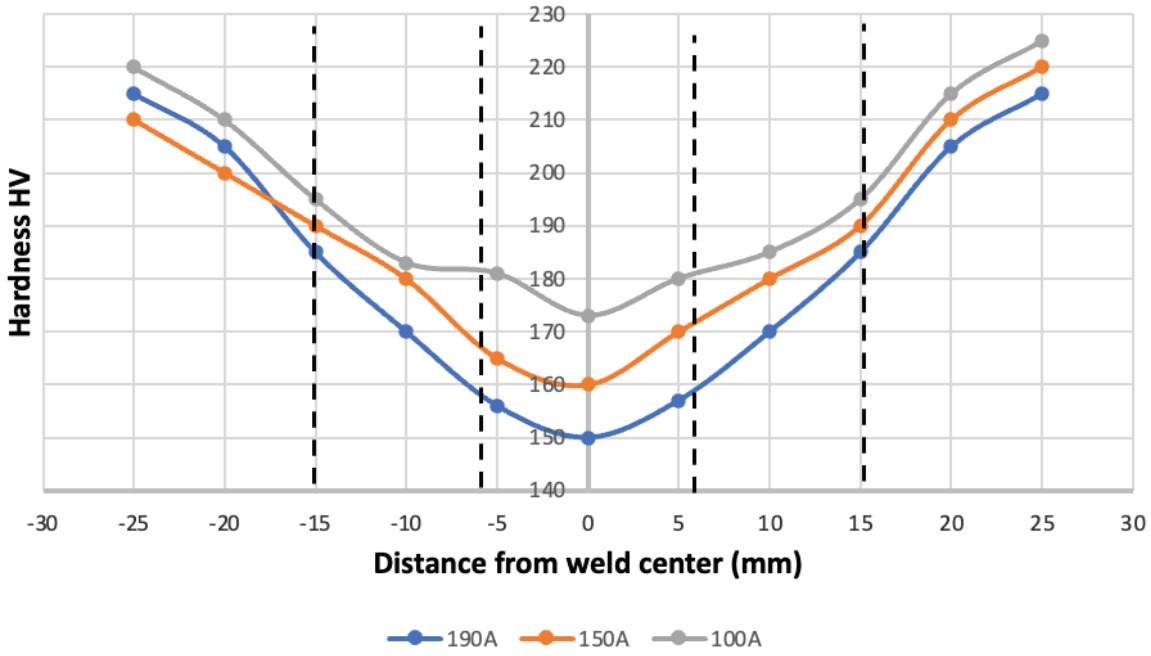

Figure 7. Hardness profile cross the welding joints.

through hardness tests. The testing method provides essential data that evaluates welding procedure outcomes and detects temperature inputs and thermal cooling rates and the processes within weldment metal and heat-affected areas [36]. Hardness assessment from end to end of the weld joint enables welding engineers to observe uniform structure patterns which in turn extends service duration and preserves component strength under operational loads. Building quality control systems using engineering requirements needs this evaluation method. Fig. 7 below represent the hardness profile of the three welding samples according to the welding current.

The base metal hardness demonstrates minimal change and persists within a range of 210 to 220 HV on the graph. The measurement for 304 stainless steel shows typical characteristics for an annealed state (austenitic structure). The welding current type has no effect on the hardness of the base metal because the material maintains identical composition and microstructure. The welding zone at the center of the graph displays reduced hardness levels whereas the intensities of hardness vary between the different welding currents. The gray line shows 100 A welding with the peak hardness degree of 170-181 HV across the welding zone. The formation of a refined microstructure occurs because of the reduced heat input that allows swift cooling of the material. The welding zone of the 150 A process (Orange line) exhibits peak hardness of 160-170 HV though it falls below the first welding joint's values. The 150 A heat input pace produces reduced microstructural cooling which enables the formation of a high 6% ferrite content. Weakening of material happens because ferrite exhibits decreased hardness compared to austenite and 190 A (blue line) produces the lowest peak hardness level which reaches 150-157 HV. The heat input generated from maximum welding current slows down the cooling process until 9% ferrite finally forms. Ferrite shows significantly lower hardness than austenite thus causing the welding area hardness to drop. The HAZ hardness gradually falls when moving away from the weld center and eventually reaches a similar level as the base metal. The HAZ hardness drop occurs because the cooling rate is slower than the base metal, allowing for more time for grain growth and diffusion of phases. when welding with 100 A (gray Line), The hardness in the HAZ drops to around 181-195 HV compared with the base hardness, which is still higher than the welding zone due to the relatively fine-grained microstructure resulting from faster cooling. 150 A welding current (Orange Line) shows hardness drops more significantly, stabilizing around 165-190 HV, as the cooling rate is slower, leading to larger ferrite and a more coarsely-grained microstructure. 190 A (Blue Line) HAZ hardness drops to around 156-185 HV because of the largest ferrite content and the coarser microstructure. The study results illustrated the influence of ferrite on the assessment of welded joint characteristics. Hardness measures diminish with an increase in ferrite, since ferrite is inherently softer than austenite. Conversely, the weld structure exhibits elevated hardness at 4% ferrite and 100 A, attributable to its substantial austenite composition. An elevated ferrite percentage of 6% (150 A) results in diminished hardness due to the augmented ferrite amount, while the maximum ferrite content of 9% achieves 190 A, yielding the softest weld zone. Table 7 below summarizes the contrast among these three joints and their correlation with the ferrite percentage.

Welding Joint Tensile Test Analyses

Notably, increasing the welding current had a positive effect on the strength of the welds with sample 2 with 150 A and very bad effects with sample 3 with 190 A. For instance, when welding with ER308, and 100 A welding current in sample 1, the tensile test recording 662 MPa, the strength increased to 689 MPa as the current was increased to 150 A. and reducing again to 677 when welding with 190 A, these results indicate that higher welding currents not always can lead to stronger welds. 100 A weld joint exhibits only 4 % ferrite composition. The microstructure mostly contains austenite together with a minor ferrite amount. The welded area strength derives from austenite because its hard properties surpass ferrite properties. For that the weld joint need a specific ferrite percentage to achieved the required toughness. A homogeneous microstructure with 170 -181 HV hardness in welding zone, results at this

Table 7. Three Welding joints Hardness Comparison

Welding Current (A)	100 A	150 A	190 A
Ferrite Content	4%	6%	9%
Welding Zone Hardness (HV)	170-181	160-170	150-157
HAZ Hardness (HV)	181-195	165-190	156-185
Hardness Trend	Highest Hardness	Moderate Hardness	Lowest Hardness
Ferrite Impact on Hardness	Higher austenite content leads to higher hardness.	Moderate ferrite leads to moderate hardness.	Highest ferrite content results in lowest hardness.
Cooling Rate and Microstructure Effect	Faster cooling results in finer microstructure and higher hardness.	Moderate cooling results in larger ferrite and coarser microstructure.	Slow cooling allows formation of largest ferrite and coarser microstructure.

Figure 8. Tensile test samples fracture location (A) 100 A, (B) 150 A, and (C) 190 A.

position because of the speeded-up cooling process. The weld zone hardness largely results from austenite when the ferrite content stays within this low value range. The weld material demonstrates tensile strength at 662 MPa and the test samples fracture occurred at the welding zone due to its high hardness and low toughness. The fracture samples as shown in Fig. 8 below illustrated very low elongation, which evidenced the lack with toughness.

Increasing in welding current to 150 A brings about a 6 % ferrite content. A higher heat input with prolonged cooling times enables abundance of ferrite formation because of its slower crystallization process. 6% ferrite presence falls within an acceptable range that maintains advantages like improved toughness even though strength decreases moderately. The welding zone hardness decreases to 160-170 HV as the weld metals contain more ferrite while exhibiting slightly larger grain size. Because ferrite has a reduced hardness in comparison to austenite, it generates overall hardness reduction. The primary composition of the microstructure features austenite that enables the weld to maintain good hardness along with toughness characteristics. This material experiences relatively higher hardness reduction beyond the 100 A-welded metal while staying short of dramatic levels. The tensile strength reaches a value of 689 MPa thereby surpassing the tensile strength of 100 A sample. The this sample fracture location occurred at the HAZ with good elongation as illustrated in Fig. 8 above, the fracture location and type proved the joint high toughness due to the perfect ferrite percentage rang. The austenite-ferrite combination regulates strength properties shown in the material. The minor ferrite enhancement in the metal structure leads to increased toughness and decreased crack vulnerability during stress conditions. The mechanical performance improves because of the ferrite phase added toughness however; ferrite does not control enough of the steel to significantly weaken strength at 6 % content. Ferrite contributes toughness to the weld structure that leads to increased tensile strength while slight reduction in hardness suggests an upcoming trade-off between strength and toughness.

Welding current at 190 A produces excessive ferrite content as the total ferrite reaches 9 %. The weld properties suffer damage from high ferrite content that occurs from excessive ferrite formation because ferrite distributes over the weld as a soft phase that forms a brittle microstructure. The weld tensile strength decreases when ferrite reaches certain thresholds beyond which it constitutes more than a specific percentage. When the weld contains an excessive ferrite amount along with a coarse microstructure, the weld zone hardness reaches levels between 150-157 HV. The presence of increased ferrite in the weld leads to overall softening because ferrite is harder than austenite. This sample fracture location noticed at the welding zone due to the high ferrite percentage and the high cracks susceptibility and formations at this zone under these conditions. The microstructural changes caused by high ferrite content led to reduced hardness because ferrite exhibits less hardness than austenite within the particular alloy composition. The weld's tensile strength diminishes to 677 MPa even though heat input and welding current reached greater levels at 190 A. The weld exhibits a lower strength because the enhancement of ferrite makes the material softer. Too much ferrite within the weld material weakens its tensile force resistance that leads to reduced tensile strength. The weld becomes weaker at 9 % ferrite content regardless of potential increased toughness levels. Ferrite content of 9 % severely damages both weld strength and toughness at 190 A. Higher amounts of ferrite create an excessive weakening effect that decreases tensile strength to 677 MPa. The relationship among welding current, ferrite content, hardness, and tensile strength in the three welding joints summarized in Table 8.

Table 9 below highlights summarized the key parameters and findings of this study.

Table 8. Relationship among welding current, ferrite content, hardness, and tensile strength

Welding Current (A)	Ferrite (%)	Welding Zone Hardness (HV)	HAZ Hardness (HV)	Tensile Strength (MPa)	Fracture location
100	4	170-181	181-195	662	WZ
150	6	160-170	165-190	689	HAZ
190	9	150-157	156-185	677	WZ

Table 9. Key parameters and findings of this study

Welding Current (A)	Ferrite (%)	Welding Zone Hardness (HV)	HAZ Hardness (HV)	Tensile Strength (MPa)	Fracture Location
100 A	4%	170-181	181-195	662	Weld Zone (WZ)
150 A	6%	160-170	165-190	689	Heat Affected Zone (HAZ)
190 A	9%	150-157	156-185	677	Weld Zone (WZ)

RESULTS AND DISCUSSION

The welding current set to 150 A produces an appropriate ferrite content of 6% in welded joints per this research. García-García & Reyes-Calderón (2022) [1] also documented ferrite›s importance for hot cracking prevention in austenitic stainless steel. Your study at 150 A shows improved toughness and reduced cracking rates due to ferrite control as Garcia-Garcia and Reyes-Calderon (2022) [1] demonstrated for the same conditions. The study validates Vasantharaja & Vasudevan›s (2019) [3] research which shows how controlled thermal processes modify ferrite distribution to produce stronger materials. This study demonstrates how interdendritic ferrite formation at moderate heat input (150 A) confirms toughness enhancement. Two studies by mohammed et al. (2017) [13] and Raj et al. (2024) [10] provide strong support for the tensile strength trend that rises with moderate ferrite amounts yet falls with excessive ferrite. Research findings from both studies demonstrate how ferrite content establishes key mechanical properties that guide the behavior of welded joints through their resistance to cracks and overall toughness performance. This study›s hardness evaluation matches prior research showing ferrite content augmentation leads to hardness reduction (Mohammed et al. 2017) [13]. The hardness measurements show decreased values with rising welding currents because ferrite exists as a softer material than austenite yet high levels of ferrite act against hardness development. The relationship between ferrite content and corrosion resistance remains unmeasured in this study but García-García et al. (2022) [1] and Raj et al. (2024) [10] provide evidence that ferrite content affects corrosion resistance. An increase in ferrite content primarily at 190 A alters the material›s resistance to corrosion because the softer ferritic phase has less protection than austenite against corrosion.

CONCLUSION

This research establishes that welding current together with heat input serves as key elements for determining the mechanical properties of TIG-welded AISI 304 stainless steels. The study key finding can be summarized as follow:

1. Welding current elevation produces raised heat input that results in greater ferrite content in the welded area. Endoscopic evaluation showed that the weld ferrite content increased from 4 % at 100 A to 9 % at 190 A based on Schaeffler diagram predictions. The welding current affects the heat input that causes the ferrite content to rise.
2. Using a low heat input of 100 A causes the weld to cool quickly thus producing a fine-grained microstructure of low ferrite content. The strength becomes very high but solidification cracking emerges as a vulnerability. The welding process that produces Moderate Heat Input requires (150 A) as its setting because moderate cooling allows the weld to develop austenite and ferrite in a balanced microstructure. The combination of these elements leads to higher tensile strength in addition to better crack protection. Welds cooled slowly at 190 A heat input since it creates coarsened grains along with an excess of ferrite thus weakening the weld strength. Lower strength and hardness result from welding with this current endpoint.
3. The highest hardness (170-181 HV) appears in 100 A (4% ferrite) welds across the weld area and heat affected zone because austenite dominates while being harder than ferrite. A greater amount of ferrite enhances the endurance qualities and reduces cracking tendencies of the welded material. A hardness reduction occurs when ferrite exceeds 9 % in 190 A welds thus making the weld zone reach 150-157 HV. The appearance of additional ferrite elements inside the weld creates softness that afterward leads to reduced hardness because ferrite possesses low hardness values.

4. When the weld reaches 100 A (4 % ferrite composition) its tensile strength reaches 662 MPa after evaluation. The good strength characteristics of the weld come from its high austenite content. Welded material strength rises to 689 MPa when measured at 150 A because of 6 % ferrite. Ferrite enhancement brings better toughness but weaker tensile strength to welds because ferrite has a softer material quality. Tensile strength drops to 677 MPa at 190 A (9 % ferrite). The weld achieves reduced tensile strength because of the high welding current that creates excessive ferrite content that makes the weld softer. The occurrence demonstrates that elevating welding currents fails to ensure weld strength improvement.
5. The optimal welding current at 150 A produces 6 % ferrite in the welding joint that delivers the ideal combination of strength with toughness and corrosion resistance attributes. A maximum mechanical performance combined with crack resistance makes this current the best selection for welding applications. When using 100 A welding current the weld shape becomes predominantly austenitic leading to strong applications but shows reduced toughness alongside increased hot cracking tendencies whereas 190 A welding current produces excessive ferrite formation that softens the weld and weakens tensile strength despite higher weld temperature. Internal use of the welding technique should be limited for applications that need superior strength since it helps reduce cracking but weakens material properties.
6. This study examines the impact of varying TIG welding currents (100 A, 150 A, and 190 A) on the ferrite content and microstructure of AISI 304 stainless steel welds. The approach examines the impact of variations in welding currents on ferrite levels and the implications of these levels for the future characteristics and durability of weld. The ferrite concentration was shown to rise with increasing welding current, rising from 4% at 100 A to 9% at 190 A. Welding test indicated that a current of 150 A yielded the most advantageous mechanical qualities, namely a high tensile strength (689 MPa), a moderate hardness level (about 160-170 HV), and robust resistance to hot cracking. While low levels of ferrite enhance the steel›s protection, a concentration of 9% or over at 190 A diminishes its strength, rendering it unsuitable for applications demanding higher strength. Experts believe that welding at 150 A produces a product that is durable, robust, and resistant to corrosion, with less risk of hot cracking.

AUTHORSHIP CONTRIBUTIONS

Authors equally contributed to this work.

DATA AVAILABILITY STATEMENT

The authors confirm that the data that supports the findings of this study are available within the article. Raw data that support the finding of this study are available from the corresponding author, upon reasonable request.

CONFLICT OF INTEREST

The author declared no potential conflicts of interest with respect to the research, authorship, and/or publication of this article.

ETHICS

There are no ethical issues with the publication of this manuscript.

STATEMENT ON THE USE OF ARTIFICIAL INTELLIGENCE

Artificial intelligence was not used in the preparation of the article.

REFERENCES

[1] García-García V, Reyes-Calderón F, Frasco-García OD, Alcantar-Modragón N. Mechanical behavior of austenitic stainless-steel welds with variable content of δ-ferrite in the heat-affected zone. Eng Fail Anal 2022;140:106618. [CrossRef]

[2] Chukwuneke JL, Ndefo MI, Sinebe JE, Ofochebe SM. Numerical and thermal analysis of mechanical properties degradations and distortions in steel weld joint. Clean Mater 2022;6:100150. [CrossRef]

[3] Vasantharaja P, Vasudevan M, Parameswaran P. Effect of welding techniques on the microstructure and mechanical properties of reduced activation ferritic-martensitic (RAFM) steel weld joints. Fusion Eng Des 2019;148:111289. [CrossRef]

[4] Han Y, Chu J, Wang Q, Fu K, Jin H, Wei Y. Investigation of microstructure, mechanical properties, residual stress, and distortion in multi-pass gas metal arc welding of ZGMn13Mo/A514 dissimilar joints. Mater Chem Phys 2025;341:130941. [CrossRef]

[5] Sonar T, Ivanov M, Trofimov E, Liu K, Shcherbakov I, Shaburova N, et al. A critical review on dissimilar welding of ferritic-martensitic steel and austenitic stainless steel using gas tungsten arc welding process: Weldability issues, processing, and performance characteristics of joints. J Manuf Process 2025;133:811-864. [CrossRef]

[6] Fei Z, Pan Z, Cuiuri D, et al. Effect of post-weld heat treatment on microstructure and mechanical properties of deep penetration autogenous TIG-welded dissimilar joint between creep strength enhanced ferritic steel and austenitic stainless steel. Int J Adv Manuf Technol 2020;108:3207-3229. [CrossRef]

[7] Queiroz AVD, Fernandes MT, Silva L, Demarque R, Xavier CR, Castro JAD. Effects of an external magnetic field on the microstructural and mechanical properties of the fusion zone in TIG welding. Metals 2020;10(6):714. [CrossRef]

[8] Li J, Li H, Peng W, Xiang T, Xu Z, Yang J. Effect of simulated welding thermal cycles on microstructure and mechanical properties of coarse-grain heat-affected zone of high nitrogen austenitic stainless steel. Mater Charact 2019;149:206-217. [CrossRef]
[9] Maduraimuthu V, Vasudevan M, Muthupandi V, et al. Effect of activated flux on the microstructure, mechanical properties, and residual stresses of modified 9Cr-1Mo steel weld joints. Metall Mater Trans B 2012;43:123-132. [CrossRef]
[10] Raj CR, Kumar S, Chandra K, Roychowdhury S, Singh PK. Thermal aging effects on tensile and metallurgical characteristics of stainless steel weld joint. Procedia Struct Integr 2024;60:709-722. [CrossRef]
[11] Zmitrowicz P, Kawiak M, Kochmański P, Baranowska J. Microstructure and mechanical properties of welded joints of 1.4462 duplex steel made by the K-TIG method. Materials 2021;14:7868. [CrossRef]
[12] Noga P, Skrzekut T, Wędrychowicz M, Węglowski MS, Wiewióra M. The influence of various welding methods on the microstructure and mechanical properties of 316Ti steel. Materials 2024;17(7):1681. [CrossRef]
[13] Mohammed GR, Ishak M, Aqida SN, Abdulhadi HA. Effects of heat input on microstructure, corrosion and mechanical characteristics of welded austenitic and duplex stainless steels: A review. Metals 2017;7(2):39. [CrossRef]
[14] Higelin A, Le Manchet S, Passot G, et al. Heat-affected zone ferrite content control of a duplex stainless steel grade to enhance weldability. Weld World 2022;66:1503-1519. [CrossRef]
[15] Wang P, Szalowski B, Vallant R, Poletti C, Enzinger N. Influence of thermomechanical treatments on the microstructure and mechanical properties of AISI 304L welds. Weld Int 2023;37(2):79-90. [CrossRef]
[16] Hu Y, Shi Y, Wang K, Huang J. Effect of heat input on the microstructure and mechanical properties of local dry underwater welded duplex stainless steel. Materials 2023;16(6):2289. [CrossRef]
[17] Zhang J, Cui K, Huang B, Mao XD, Zheng MJ. Influence of heat input on the microstructure and mechanical properties of CLAM steel multilayer butt-welded joints. Fusion Eng Des 2020;152:111413. [CrossRef]
[18] Babu PD, Gouthaman P, Marimuthu P. Effect of heat sink and cooling mediums on ferrite austenite ratio and distortion in laser welding of duplex stainless steel 2205. Chin J Mech Eng 2019;32:50. [CrossRef]
[19] Polish Committee for Standardization. PN-EN ISO 5173:2010; Destructive testing of welds in metal materials—Bending test. Warsaw, Poland: Polish Committee for Standardization; 2010.
[20] Polish Committee for Standardization. PN-EN ISO 6507-2:2018-05; Metals—Vickers hardness measurement. Warsaw, Poland: Polish Committee for Standardization; 2018.
[21] Devendranath Ramkumar K, Pavan B, Chandrasekar V. Development of improved microstructural traits and mechanical integrity of stabilized stainless steel joints of AISI 321. J Manuf Process 2018;32:582-594. [CrossRef]
[22] ASTM E8 / E8M-24, Standard Test Methods for Tension Testing of Metallic Materials, ASTM International, West Conshohocken, PA, 2024.
[23] Dauod DS, Mohammed MS, Aziz IAA, Abbas AS. Mechanical vibration influence in microstructural alterations and mechanical properties of 304 stainless steel weld joints. J Eng Sci Technol 2023;(Special Issue 6):33-54.
[24] Lai CL, Tsay LW, Kai W, Chen C. The effects of cold rolling and sensitisation on hydrogen embrittlement of AISI 304L welds. Corros Sci 2010;52:1187-1193. [CrossRef]
[25] Klimpel A. The influence of alloying elements on the formation of the sigma phase in austenitic-ferritic weld metals type 18-8. Sci Noteb Mech Silesian Univ Technol 1977;509:1-85.
[26] Kou, S. (2003). Welding Metallurgy (2nd ed.). John Wiley & Sons.
[27] Kulkarni A, Dwivedi DK, Vasudevan M. Microstructure and mechanical properties of A-TIG welded AISI 316L SS-Alloy 800 dissimilar metal joint. Mater Sci Eng A 2020;790:139685. [CrossRef]
[28] Kou S. Welding Metallurgy. Hoboken, NJ, USA: John Wiley & Sons; 2003.
[29] Amin SA, Abdulhasan AA, Mohammed MS, Majdi HS. Experimental and numerical study of maximum welding joint temperature impacts in alloy steel pipe welding microstructure, distortion, corrosion resistance, and mechanical properties. Rev Compos Mater Av-J Compos Adv Mater 2024;34(6):775-786. [CrossRef]
[30] Eid A, Abd Allatif M, Elsabbagh A, Halfa H. Effect of heat input on weldability of low nickel high manganese stainless steel. Int J Mater Technol Innov 2023;3(2):19-29. [CrossRef]
[31] Kim YH, Kim DG, Sung JH, et al. Influences of Cr/Ni equivalent ratios of filler wires on pitting corrosion and ductility-dip cracking of AISI 316L weld metals. Met Mater Int 2011;17:151-155. [CrossRef]
[32] Yamashita S, Ike K, Yamasaki K, et al. Relationship between ferrite–austenite phase transformation and precipitation behavior of sigma phase in super duplex stainless steel weldment. Weld World 2022;66:351-362. [CrossRef]
[33] Guilherme LH, Benedetti AV, Fugivara CS, Magnabosco R, Oliveira MF. Effect of MAG welding transfer mode on sigma phase precipitation and corrosion performance of 316L stainless steel multipass welds. J Mater Res Technol 2020;9(5):10537-10549. [CrossRef]

[34] Dauod DS, Wade KJ, Mohammed MS, Majdi HS. Analysis of shielding gases influences 304 gas metal arc welding microstructure, weld geometry, and mechanical properties. Rev Compos Mater Av-J Compos Adv Mater 2024;34(4):435-446. [CrossRef]

[35] Hsieh CC, Guo X, Chang CM, et al. Dendrite evolution of delta (δ) ferrite and precipitation behavior of sigma (σ) phase during multipass dissimilar stainless steels welding. Met Mater Int 2010;16:349-356. [CrossRef]

[36] Dewangan S, Saksham S. Analysis among quenched, tempered, and stepped cooled TIG welded SS-304 plates based on tensile strength, hardness, and microstructural appearance. Adv Mater Sci Eng 2023;2023:5523162. [CrossRef]

J Ther Eng, Vol. 12, No. 2, pp. 756−766, March, 2026

Journal of Thermal Engineering
Web page info: https://jten.yildiz.edu.tr
DOI: 10.14744/thermal.0001117

Research Article

Insights of physico-chemical and thermal conductivity enhancement of polyvinylidene fluoride (PVDF) mixed znonanoparticles for heat transfer applications

Mohammed MUQTASID[1], S. SRINIVASAN[1,*], R. PADMANABAN[2], M. SIVAKUMAR[1], A.P. LINGASWAMY[3]

[1]*Department of Physics, Presidency College (Autonomous), Chennai, Tamil Nadu, 600005, India*
[2]*Faculty of Science, SCSVMV Deemed University, Enathur, Tamilnadu, 631561, India*
[3]*Department of Physics, G. Pulla Reddy Engineering College, Kurnool, 518007, India*

ARTICLE INFO

Article history
Received: 08 February 2025
Revised: 26 June 2025
Accepted: 18 July 2025

Keywords:
Nanofluids; Polyvinylidene Fluoride; Thermal Conductivity; Ultrasonic Velocity; ZnO Nanoparticles

ABSTRACT

The conventional heat transfer liquids such as water, oil, etc., having lesser thermal properties cannot be fulfill the requirements of some of the heat exchangers system. To enhance the thermal properties of the liquid, nanoparticles are dispersed. Nanofluids (NF) have potential application in thermal transfer systems. The motto of the present work is devoted to studying thermo-physical studies on ZnO with different weight percentages of Polyvinylidene Fluoride (PVDF)-added nanocomposite-based nanofluids at various concentrations in water for heat transfer applications. The prepared nanocomposites were dispersed into the distilled water to prepare nanofluids and were characterized by ultrasonic velocity measurements to figure out the molecular interaction and thermal behavior of the nanofluids. Various physicochemical Characteristics, such as adiabatic compressibility, intermolecular free length, free volume, internal pressure, specific acoustic impedance, relaxation time, and surface tension, were determined. The mechanical properties of the PVDF ZnO NFs were analyzed based on the findings of the bulk modulus. Moreover, the thermal conductivity of the PVDF ZnO nanofluids was theoretically analyzed based on density and ultrasonic velocity measurements. The PVDF mixed with ZnO nanoparticle shows better thermal properties compared with conventional liquid say water.

Cite this article as: Muqtasid M, Srinivasan S, Padmanaban R, Sivakumar M, Lingaswamy AP. Insights of physico-chemical and thermal conductivity enhancement of polyvinylidene fluoride(PVDF)mixedznonanoparticlesforheattransferapplications.JTherEng2026;12(2):756−766.

INTRODUCTION

The improved heat exchanger is important in many areas where a huge amount of heat is generated such as power plants and coolants. An effective heat exchanger with the wanted cooling performance and an effective coolant with pass-on heat are required. Hence, there is a need for better coolants with excellent thermo physical characteristics

***Corresponding author.**
*E-mail address: dr_s_srinivasan@yahoo.com

This paper was recommended for publication in revised form by Editorin-Chief Ahmet Selim Dalkılıç

Published by Yıldız Technical University Press, İstanbul, Turkey
Yıldız Technical University. This is an open access article under the CC BY-NC license (http://creativecommons.org/licenses/by-nc/4.0/).

of the coolants such as thermal conductivity and viscosity is essential. However, conventional coolants like water and glycol having poor thermal conductivity hinders their practical applications. The fluids have less viscosity is easy to circulate the system or device without using any additional pumping technology. So, there is a need for alternative better coolants with greater thermal conductivity and lesser viscosity to be the better choice of coolants. Recently, the dispersion of solid materials such as alumina, titanium dioxide and zinc oxide into the conventional liquid water to improves its heat exchange characteristics of flat plate water solar collectors in shell and tube type heat exchangers [1-3]. The several metal oxides like Al_2O_3, CuO and TiO_2 are the most commonly reported materials for preparing nanofluids [4, 5]. But, a scan of literature survey showed that there are few reports on ZnO based nanofluids for their use in heat transfer applications. Long term stability of a nanofluid remains a big challenge in colloidal science due to Van der Waals forces existing between the nanoparticles leads to agglomeration of nanoparticles reduce its dispersion stability and hence increase its sedimentation rate. The nanoparticle-liquid interaction plays a vital role in enhancing the thermo-physical properties of the nanofluids. Polyvinylidene fluoride (PVDF) is a well-known semi-conducting polymer with a wide range of applications. It shows several crystalline phases like α, β, γ, δ, and ε. Its properties lead to various scientific and technological applications in flexible optoelectronic devices. The polymer PVDF is a well-known material for the applications of piezoelectric nanogenerator as well as used as a binder for electrodes preparing in battery and supercapacitors applications. So, it is essential to understand the microstructure and molecular interactions between solute-solute and solute-solvent interaction play a vital role in heat transfer as well as dispersion stability. Hence, the present work focuses on studying the heat transfer properties of Zinc Oxide with PVDF nanocomposites-based nanofluids and their stability.

EXPERIMENTAL DETAILS

Preparation of Nanofluids

Initially, we prepared Zinc Oxide nanoparticle by wet chemical method. Adding 10%, 20%, and 30% of PVDF into ZnO materials and grind well for homogeneous ZnO with PVDF nanocomposites (ZnO PVDF1, ZnO PVDF2, and ZnO PVDF3). Then the prepared ZnO sample was dissolved in triple distilled water at different concentrations 0.025M, 0.05M, 0.1M, and 0.2M and sonicated for 15 minutes at room temperature. Similarly, other nanofluids such as ZnO PVDF1 NFs, ZnO PVDF2 NFs, and ZnO PVDF3 NFs were prepared.

Characterization Techniques

An ultrasonic interferometer (F-81 type, MITTAL manufacture, 2 MHz frequency, accuracy: ±0.01 m/s) at 303.15 K was used to detect ultrasonic velocity. The viscosity of the NFs was measured at 303.15 K with a digital viscometer (accuracy: $\pm 0.01 \times 10^{-3}$ Ns/m²; BROOKFIELD manufacture, USA). The NFs' density was measured using a specific gravity bottle. We used a SHIMADZU electronic balance to determine the liquid's mass, which has a precision of ±0.001 gm. To measure the refractive indices, an Abbe refractometer with an accuracy of ±0.001 was utilized. All the measurements were found at room temperature using an electronically controlled thermostat.

RESULTS AND DISCUSSION

Viscosity Measurements

Viscosity is a key characteristic of NFs that affects their overall performance. It plays a crucial role in determining pumping power, pressure drop during laminar flow, heat transfer by convection, and volume fraction. Various factors influence the viscosity of NFs, such as the shape and size of particles, the concentration of nanomaterials in the fluid, the type of surfactants, shear rate, particle clumping, and the fluid's pH level.

The shape of the dispersed nanomaterials significantly affects the viscosity of NFs. Timofeeva et al. [4], have studied the viscosity analysis of different morphology of alumina based nanofluids. It was noticed that elongated particles exhibit higher viscosity compared to those with spherical nanoparticles. The viscosity of nanofluids greatly impacts their flowability of nanofluids [5]. Additionally, the fluid's capacity to adapt to various flow regimes and buoyancy forces is determined by its viscosity and density.

In this study, viscosity measurements were performed for pure metal oxide ZnO NFs, along with ZnO PVDF1 NFs, ZnO PVDF2 NFs, and ZnO PVDF3 NFs, as shown in Figure 1. Based on Figure 1, it can be detected that the viscosity enhances almost linearly as the concentration rises for all ZnO PVDF samples (ranging from 0.025% to 0.2% mass concentration). At the higher concentration (0.2%), a 1.05% increase was observed when comparing ZnO NPs with ZnO PVDF NPs. The rise in viscosity is associated with a higher concentration of nanoparticles in the base fluid, leading to increased internal viscous shear stresses. [6-7]. The significant variations suggest that interactions between the constituents and the base fluid are attributed to the direction of the higher surface area of the NPs [8].

Density Measurements

The NFs density is defined as the mass per unit volume of a fluid containing suspended nanoparticles. It is a critical property that significantly influences their behaviour and performance in various applications. Density is a key factor in thermal conductivity and heat transfer coefficients [9], which are critical for applications such as cooling systems and heat exchangers. It also affects viscosity [10], Reynolds

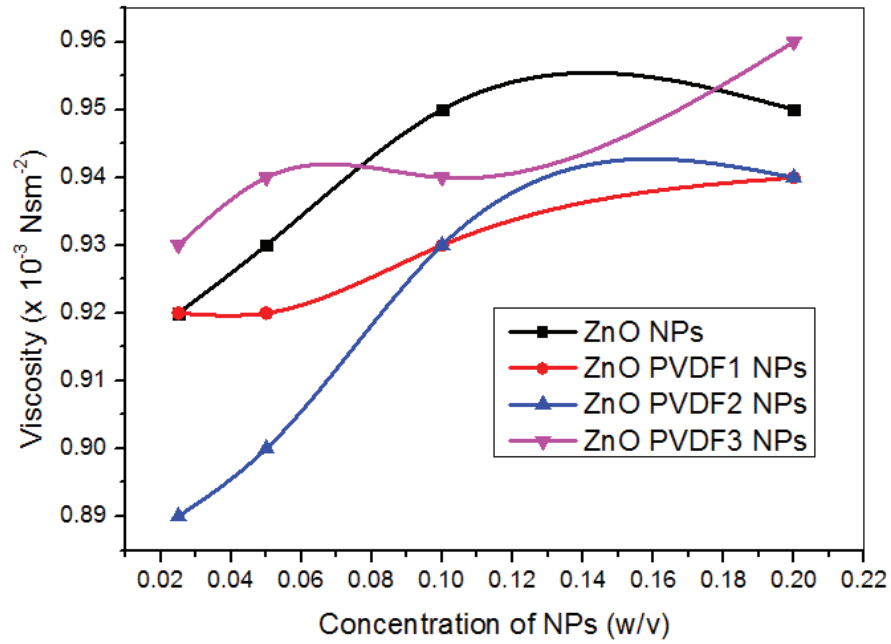

Figure 1. Viscosity studies of ZnO and ZnO PVDF NPs.

number [11] and pressure drop in fluid flow [12], which influences the design and efficiency of pumping systems. Understanding density is essential for sustaining the stability of nanoparticle suspensions and blocking sedimentation. Changes in density can result in buoyancy-driven flows, impacting heat transfer patterns in systems that use nanofluids. Reliable density data are essential for creating models that predict the performance of nanofluids in various applications.

In this study, we measured the density of pure metal oxide ZnO NFs, as well as ZnO PVDF1 NFs, ZnO PVDF2 NFs, and ZnO PVDF3 NFs, as presented in Figure 2. The results indicate that the density increases with concentration for all ZnO PVDF samples linearly due to more number of nanoparticles [13]. At a lower concentration (0.025%), the density values follow this order: ZnO NFs < ZnO PVDF2 NFs < ZnO PVDF3 NFs < ZnO PVDF1. Conversely, at a higher concentration (0.2%), the order is: ZnO PVDF1 < ZnO PVDF2 NFs < ZnO NFs < ZnO PVDF3.

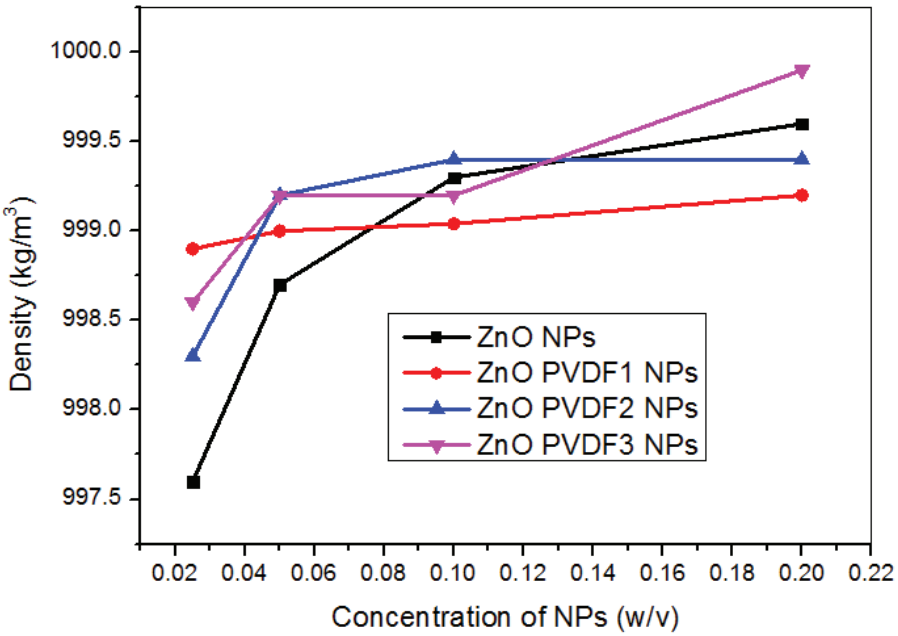

Figure 2. Density studies of ZnO and ZnO PVDF NPs.

Refractive Index (RI) Analysis

The refractive index offers valuable insights into the optical properties of nanofluids, which are crucial for applications related to light propagation, including optical devices, sensors, and photonic technologies [14]. By understanding the RI, one can characterize nanofluids and assess their composition, revealing the impact of nanoparticle addition on the optical behavior of the base fluid. It can also serve as a quality control measure during the synthesis and formulation of nanofluids; consistent values indicate the uniformity and stability of the nanoparticle suspension. Additionally, it can correlate with other characteristics, like thermal conductivity and density, providing a comprehensive understanding of the fluid's behavior and performance [15]. It can help estimate the concentration of NPs in a nanofluid, which is particularly useful for monitoring and controlling concentrations in various applications. Changes in the RI may indicate the stability of NFs, with significant variations over time suggesting issues like particle aggregation or sedimentation that could affect fluid performance. Moreover, the refractive index affects how NFs interact with light, including their absorption and scattering properties, which is particularly important for applications such as solar energy harvesting, where optical characteristics directly influence efficiency [16]. If the refractive index of the base liquid is uncertain, it is difficult to calculate the absorption coefficient from the transmission spectrum [17].

Figure 3 illustrates the relationship between refractive index and concentration for ZnO NPs, ZnO PVDF1 NPs, ZnO PVDF2 NPs, and ZnO PVDF3 NPs at 303 K. At a lesser concentration of 0.025%, the refractive index is at its lowest, with values of 1.334, 1.333, 1.333, and 1.334 for ZnO NPs, ZnO PVDF1 NPs, ZnO PVDF2 NPs, and ZnO PVDF3 NPs, respectively. Conversely, at the higher concentration of 0.2%, the refractive index reaches its peak, with values of 1.335, 1.335, 1.3355, and 1.336 for ZnO NPs, ZnO PVDF1 NPs, ZnO PVDF2 NPs, and ZnO PVDF3 NPs, respectively.

Ultrasonic Velocity (U) Measurements

The ultrasonic technique has become a crucial tool for investigating the physicochemical characteristics of materials and has widespread applications in fundamental science, industry, and biochemical technology [18-20]. Measuring ultrasonic velocity and associated parameters in solvents is key to understanding the physicochemical behavior of solutions. This allows for the calculation of important thermodynamic properties, shedding light on molecular interactions [21]. Additionally, ultrasonic velocity helps assess properties like density, compressibility, and viscosity, which are critical for analyzing the thermal and mechanical performance of NFs in applications such as heat transfer, lubrication, and drug delivery. Variations in ultrasonic velocity can also reflect changes in nanoparticle concentration, size, and distribution within the fluid, making it an essential tool for characterizing NFs.

In this study, we measured the ultrasonic velocity of pure ZnO nanofluids (NFs), as well as ZnO PVDF1, ZnO PVDF2, and ZnO PVDF3 NFs, as illustrated in Figure 4. It is evident from Figure 4 that the ultrasonic velocity enhances as the concentration of NPs rises. This indicates that structural changes are taking place in the liquid system, leading

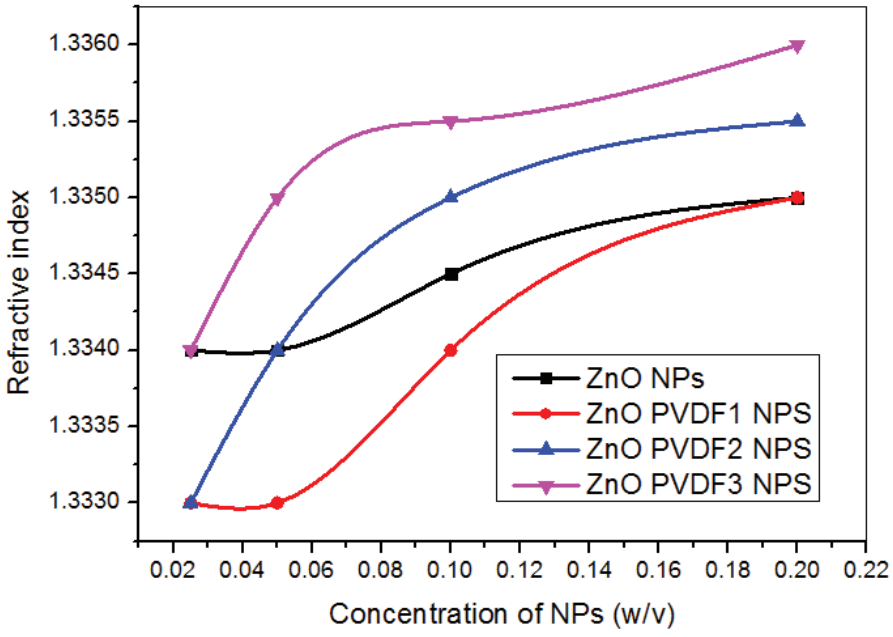

Figure 3. Refractive index studies of ZnO and ZnO PVDF NPs.

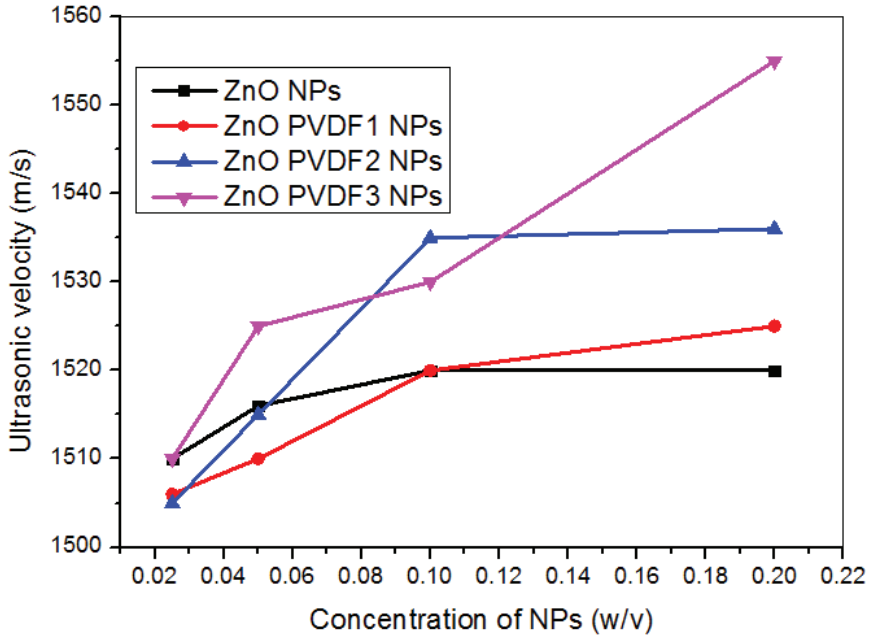

Figure 4. Ultrasonic velocity studies of ZnO and ZnO PVDF NPs.

to a reduction of intermolecular forces. The increase in velocity suggests that the interaction may be caused by surface effects. Consequently, particle-fluid interactions likely contribute to the rise in velocity values [22].

Determination of Adiabatic Compressibility (β_{ad}) and Bulk Modulus (K)

Adiabatic compressibility describes how much the volume of a substance decreases with each unit rise in sound pressure, without any heat or mass being transferred to the environment. The adiabatic compressibility (β_{ad}) and bulk modulus (K) of ZnO NFs and ZnO PVDF NFs can be derived from the following formulae 1 and 2 [20]:

$$\beta_{ad} = 1/U^2\rho \quad m^2N^{-1} \tag{1}$$

$$K = 1/\beta_{ad} \quad Nm^{-2} \tag{2}$$

Where ρ represents the density and U denotes the velocity of the NFs.

Adiabatic compressibility is directly influenced by density and ultrasonic velocity, showing an inverse relationship with velocity [23]. In this study, the adiabatic compressibility decreases as the concentration of nanoparticles (NPs) increases in all cases [Fig. 5]. The primary reason for this reduction in adiabatic compressibility with rising NP concentration is the corresponding increase in nanofluid (NF) density. As more NPs are dissolved in the base fluid, the NF density rises, leading to a decrease in the value of adiabatic compressibility, since it is inversely proportional to density [24]. Figure 6 demonstrates a linear increase in bulk modulus across all cases. At a 0.2% concentration of ZnO in PVDF3 NFs, the bulk modulus reaches 2.42 GPa, indicating a significant increase because of dipole-induced dipole and dipole-dipole interactions, which results in a positive shift in velocity and a negative shift in compressibility [25–26]. The adiabatic compressibility is an important parameter that changes with structure. The decrease in adiabatic compressibility with increase in concentration of the solute indicates that a close packing of solute molecules resulting structure making effects of PVDF mixed with ZnO by the water solvent. Hence, there is an increase in the bulk modulus values due to less change of volume.

Thermal Conductivity Analysis

Thermal conductivity serves as a measure of a material's capacity for heat transfer. Researchers aiming to find the thermal conductivity of nanofluids (NFs) through experimental methods have developed and documented various techniques in the literature [27]. This property in NFs is influenced by several factors, including NP characteristics (such as shape, concentration, and size) [28, 29]; temperature [28]; stability, preparation, and sonication conditions [30, 31]; the presence and quantity of surfactants [28, 29]; base fluid properties [32]; methods for measuring thermal conductivity [33]; and NP alignment [32, 34]. These factors often result in inconsistencies in reported data.

For ZnO-based NFs, including ZnO NFs, ZnO PVDF1 NFs, ZnO PVDF2 NFs, and ZnO PVDF3 NFs, their thermal conductivity is derived from ultrasonic velocity measurements. The calculated values are obtained using a modified Bridgman equation [35].

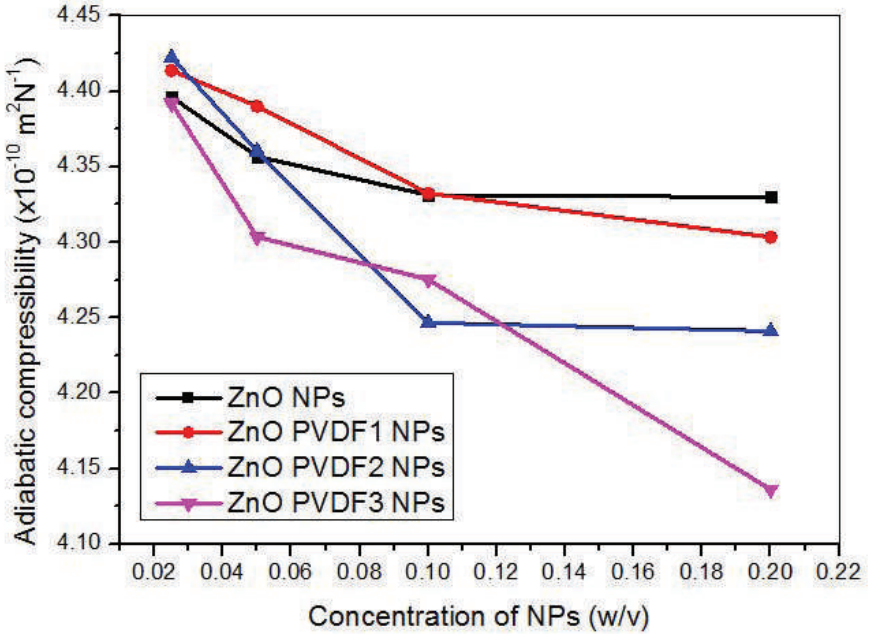

Figure 5. Adiabatic compressibility studies of ZnO and ZnO PVDF NPs.

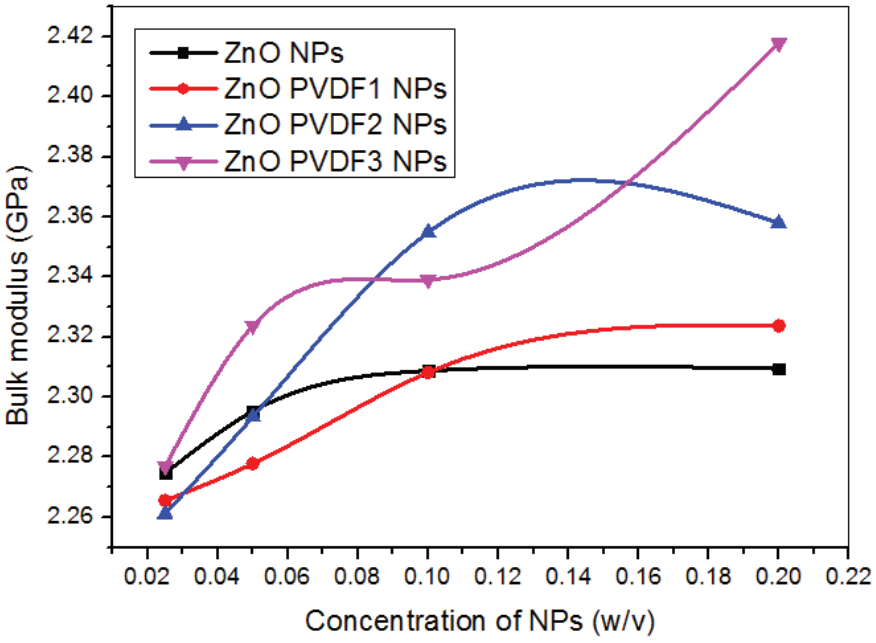

Figure 6. Bulk modulus studies of ZnO and ZnO PVDF NPs.

Figure 7 shows the thermal conductivity of ZnO NPs, ZnO PVDF1 NPs, ZnO PVDF2 NPs, and ZnO PVDF3 NFs. At a higher concentration, when comparing the thermal conductivities of ZnO NPs is less whereas ZnO PVDF3 NPs exhibit better thermal conductivity. Nanofluids demonstrate high thermal conductivities even at very low nanoparticle concentrations, though the precise mechanism behind this enhancement remains unclear. Brownian motion of suspended NPs is considered one of the primary factors contributing to the significant increase in thermal conductivity [36].

Physicochemical Properties

Table 1 represents the various physicochemical properties (intermolecular free length (L_f), free volume (V_f), internal pressure (π), specific acoustic impedance (Z), relaxation time (τ) and Surface tension were evaluated for

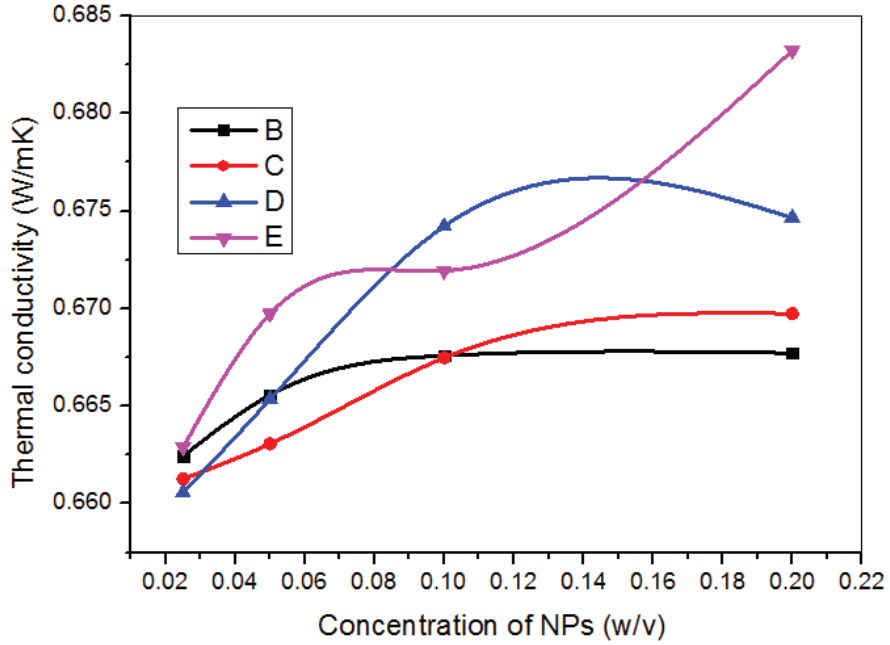

Figure 7. Thermal conductivity studies of ZnO and ZnO PVDF NPs.

Table 1. Various physicochemical properties of NPs at 303.15 K

Name of the sample	Concentration (%)	Intermolecular free length (L_f) (x 10^{-11} m)	Free volume (V_f) (x 10^{-8} m^3 mol^{-1})	Internal pressure (π) (GPa)	Specific acoustical Impedance (Z) (x 10^6 $kgm^{-2}s^{-1}$)	Relaxation time (τ) (x 10^{-13} s)	Surface tension (N/m)
ZnO NFs	0.025	4.3507	1.8135	2.7201	1.5063	5.3928	38.6670
	0.05	4.3311	1.7950	2.7315	1.5140	5.4024	38.8977
	0.1	4.3184	1.7455	2.7581	1.5189	5.4863	39.0518
	0.2	4.3177	1.7455	2.7587	1.5193	5.4846	39.0518
ZnO PVDF1 NFs	0.025	4.3594	1.8063	2.7261	1.5043	5.4144	38.5135
	0.05	4.3476	1.8135	2.7227	1.5084	5.3852	38.6670
	0.1	4.3190	1.8021	2.7285	1.5185	5.3721	39.0518
	0.2	4.3044	1.7822	2.7389	1.5237	5.3935	39.2446
ZnO PVDF2 NFs	0.025	4.3636	1.8965	2.6811	1.5024	5.2480	38.4751
	0.05	4.3329	1.8836	2.6888	1.5137	5.2324	38.8593
	0.1	4.2760	1.8288	2.7158	1.5340	5.2658	39.6313
	0.2	4.2732	1.8015	2.7294	1.5350	5.3155	39.6700
ZnO PVDF3 NFs	0.025	4.3485	1.7843	2.7367	1.5078	5.4459	38.6670
	0.05	4.3044	1.7822	2.7389	1.5237	5.3935	39.2446
	0.1	4.2904	1.7909	2.7344	1.5287	5.3583	39.4378
	0.2	4.2199	1.7780	2.7423	1.5548	5.2941	40.4084

PVDF-mixed ZnO nanofluids (PVDF ZnO NFs) to explore the effects of component composition and PVDF ZnO concentration on these characteristics.

The free length represents the path length a sound wave covers as it moves between the surfaces of adjacent molecules [37]. The intermolecular free length can be determined using the equation proposed by Jacobson [38]. Intermolecular free length is given by

$$L_f = \frac{K\prime}{U\sqrt{\rho}}\,(\mathrm{m}) \tag{3}$$

Where K' =2.131 * 10^{-6} is a constant which is temperature dependent. The intermolecular free length measured for pure ZnO NFs and ZnO-PVDF mixtures at room temperature decline with increasing concentrations, is presented in Table 1 signifies a substantial interaction among the particles and the base fluid molecules, [39] as noted by Gupta et al. [40].

Free volume refers to the unoccupied space resulting from the irregular arrangement of molecules. The free volume values for ZnO and ZnO PVDF NFs follow a trend

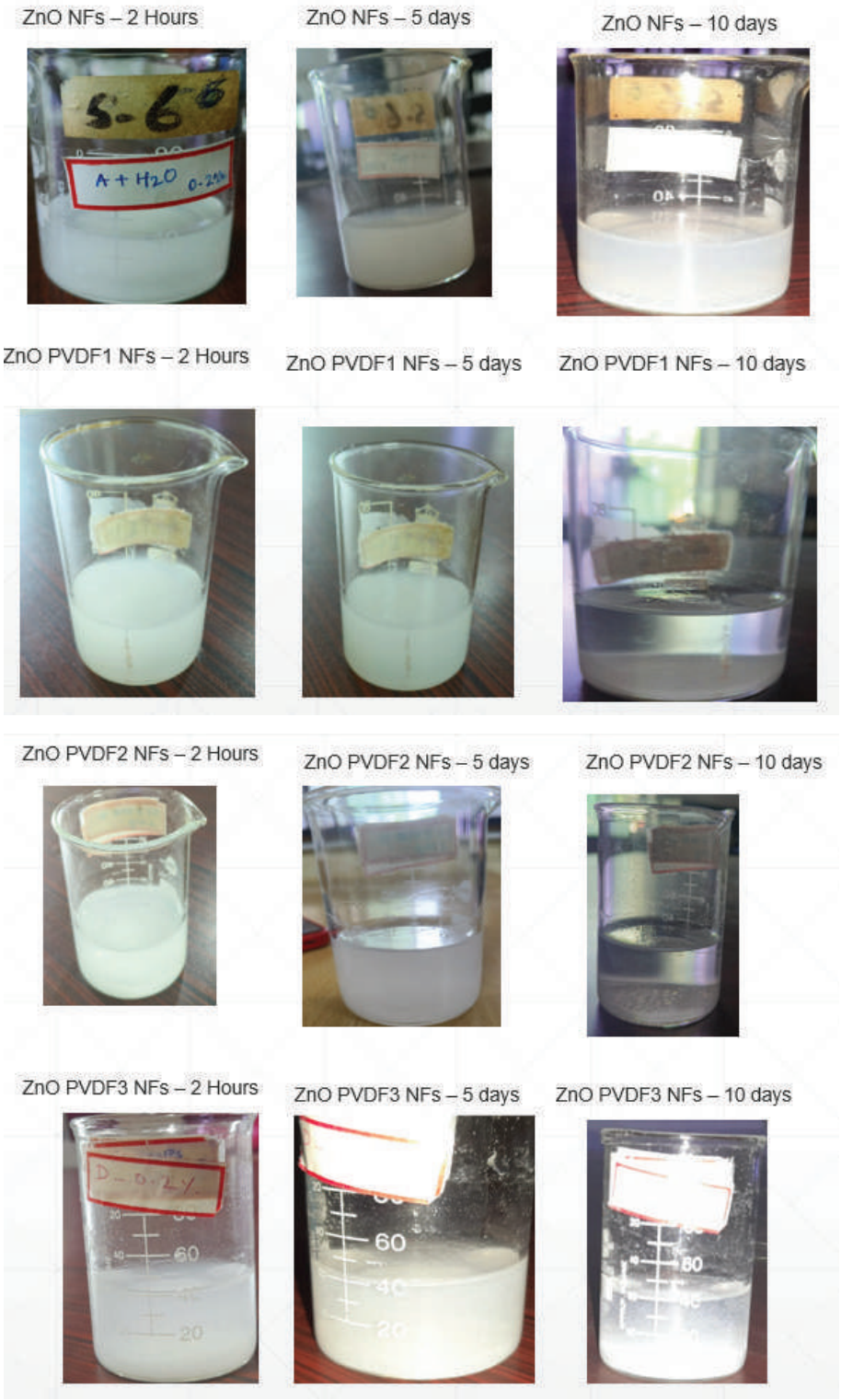

Figure 8. Sedimentation analysis of the nanofluids.

opposite to that observed for viscosity (Table 1. A decrease in free volume is observed as internal pressure increases [41], but it is reversed in free volume and internal pressure clearly shown in Table 1.

Specific acoustic impedance (Z) is the product of the material's density and the speed of sound in that material. It is related to density and ultrasonic velocity through the following relationship [42].

Specific acoustical impedance

$$Z = U\rho \text{ (kg m}^{-2}\text{ s}^{-1}\text{)} \quad (4)$$

The interaction between the NPs and base fluid molecules expands the intermolecular distance, leading to a rise in specific acoustic impedance [43].

Relaxation time (τ) results from the time lag between the passage of the ultrasonic wave and the return of molecules to their equilibrium position. It is calculated using the following relation.

$$\text{Relaxation time } \tau = \frac{4\eta}{3\beta_{ad}} \text{ (sec)} \quad (5)$$

In the current investigation, the relaxation time rises with the concentration of NPs in all cases. This indicates that at higher concentrations the molecular interaction between the base liquid and the NPs is stronger. Typically, an increase in NP concentration can modify the surface tension. The interaction between the NPs and the base fluid can either raise or lower the surface tension, depending on the properties of the nanoparticles and how they interact with the fluid. The chemical composition and surface characteristics of the NPs are key factors in determining the surface tension of the nanofluid. From Table 1, an increasing trend of surface was observed for NFs. The increasing surface tension as the concentration rises; accumulates more particles in the solution. A strong cohesive force develops between the NPs and the liquid molecules, leading to an increase in the surface tension of the nanofluids with higher concentrations [44].

Nanofluids Stability

In this present study, we adopted the sedimentation method to study the stability of the prepared nanofluids. The optical images of the dispersion of ZnO and ZnO PVDF nanoparticles (NPs) in the base fluid at a higher concentration (0.2%) are shown in Figure 8. Based on the observation from Figure 8, it can be seen that the nanofluids (NFs) exhibit moderate stability. The NFs remained stable for 5 days, after which the NPs began to settle at the bottom of the beaker. To obtain a long-term stability of the nanofluids is a big task. It can be achieved by low van der Waals force between the nanoparticle in the fluid medium. This force is responsible for aggregates the nanoparticle and separated out from the liquid and finally settled down due to gravity. However, the addition of dispersant and sonication will improve the stability of the nanofluids. There are several methods are used to analyze the stability of the nanofluids such as sedimentation method, centrifugation method, zeta potential method, etc. Among them, the sedimentation method is a simple and economic method to analyze the stability of the nanofluid.

CONCLUSION

In the present work, we have prepared ZnO and ZnO PVDF nanofluids are synthesized via in two stages with the assistance of a sonicator. The structural and morphological analysis of prepared zinc oxide nanoparticle was analyzed using XRD and SEM, techniques. Then the prepared ZnO and PVDF mixed ZnO nanofluids were prepared by using water as a solvent. Ultrasonic velocity measurements were done and other acoustic parameters were derived. The solute-particle interaction and thermal conductivity enhancement of the nanofluids are investigated based on the obtained acoustic characteristics. The ZnO nanofluids showed better stability than PVDF mixed ZnO PVDF nanofluids. However, there was an enhancement in thermal conductivity was observed in PVDF mixed ZnO nanofluids. So, still there is a challenge to obtain better stability of PVDF mixed ZnO fluids.

AUTHORSHIP CONTRIBUTIONS

Authors equally contributed to this work.

DATA AVAILABILITY STATEMENT

The authors confirm that the data that supports the findings of this study are available within the article. Raw data that support the finding of this study are available from the corresponding author, upon reasonable request.

CONFLICT OF INTEREST

The author declared no potential conflicts of interest with respect to the research, authorship, and/or publication of this article.

ETHICS

There are no ethical issues with the publication of this manuscript.

STATEMENT ON THE USE OF ARTIFICIAL INTELLIGENCE

Artificial intelligence was not used in the preparation of the article.

REFERENCES

[1] Mohamad B. Improving Heat Transfer Performance of Flat Plate Water Solar Collectors Using Nanofluids. J Harbin Inst Technol 2024.

[2] Qader FF, Mohammed FZ, Mohamad B. Thermodynamic analysis and optimization of flat plate solar collector using TiO2/Water nanofluid. J Harbin Inst Technol.
[3] Ali HHM, Hussein AM, Mohammed K. Mohamad BA. Evaluation of shell and tube heat exchanger performance by using ZnO/water nanofluids. J Harbin Inst Technol 2023;30:62–69.
[4] Timofeeva EV, Routbort JL, Singh D. Particle shape effects on thermophysical properties of alumina nanofluids. J Appl Phys 2009;106:014304. [CrossRef]
[5] Garg A, Sharma A, Li L, Zheng W, Lee B, Raman R. Uncertainty evaluation in density and viscosity of nanofluids at different temperatures using Gaussian process regression-based Monte-Carlo simulations. J Mol Liq 2024;411:125794. [CrossRef]
[6] Rashmi M, Padmanaban R, Karthikeyan V, Roy VAL, Gopalan AI, Saianand G, et al. A comparative evaluation of physicochemical properties and photocatalytic efficiencies of cerium oxide and copper oxide nanofluids. Catalysts 2020;10:34. [CrossRef]
[7] Mahbubul IM, Saidur R, Amalina MA. Latest developments on the viscosity of nanofluids. Int J Heat Mass Tran 2012;55:874–885. [CrossRef]
[8] Nandakumar V, Arumugam C, Radhakrishnan P, Roy VAL, Iyengar GA, Lee DE, Kannan V. Investigating the thermo-physical properties of a new kind of graphitic carbon nitride included ternary hybrid nanofluids and the property correlations. Heliyon 2024;10:e26163. [CrossRef]
[9] Htwe YZN, Mamat H. Progress and prospects on stability and thermal properties of surfactant assisted graphene, carbon nanotubes based nanofluid and their hybrid for next-generation thermal management, J Mol Liq 2024;126235. [CrossRef]
[10] Sarkar S, Pal P, Ghosh NK. Enhancing the thermal conductivity and viscosity of ethylene glycol-based single-walled carbon nanotube (SWCNT) nanofluid: An investigation utilizing equilibrium molecular dynamics simulation. Chem Thermodyn Therm Anal 2024;16:100142. [CrossRef]
[11] Yadav D, Nirala A, Kumar R, Singh PK. Density variation in nanofluids as a function of concentration and temperature. Mater Today Proc 2021;46:6576–6580. [CrossRef]
[12] Qamar A, Shaukat R, Imran S, Farooq M, Amjad M, Anwar Z, et al. Effect of surfactants on the convective heat transfer and pressure drop characteristics of ZnO/DIW nanofluids: An experimental study. Case Stud Therm Eng 2023;42:102716. [CrossRef]
[13] Pastoriza-Gallego MJ, Casanova C, Páramo R, Barbés B, Legido JL, Piñeiro MM. A study on stability and thermophysical properties (density and viscosity) of Al2O3 in water nanofluid. J Appl Phys 2009;106:064301. [CrossRef]
[14] Ramya M, Nideep TK, Nampoori VPN, Kailasnath M. Shape dependent heat transfer and nonlinear optical limiting characteristics of water stable ZnO nanofluid. Surf Interfaces 2021;26:101345. [CrossRef]
[15] Chandravadhana A, Nandakumar V, Padmanaban R, Roy VAL, Anantha-Iyengar G, Lee DE, et al. Studies on the Functional Properties of Titanium Dioxide Nanoparticles Distributed in Silyl–Alkyl Bridged Polyaniline-Based Nanofluids. Nanomater 2023;13:2332. [CrossRef]
[16] Pustovalov VK, Astafyeva LG, Fritzsche W. Optical properties of core-shell nanoparticles and their application for effective absorption, scattering, extinction and filtering solar and optical radiation. Photonics Nanostructures Fundam Appl 2024;62:101312. [CrossRef]
[17] Kim JB, Lee S, Lee K, Lee I, Lee BJ. Determination of absorption coefficient of nanofluids with unknown refractive index from reflection and transmission spectra. J Quant Spectrosc Radiat Transfer 2018;213:107–112. [CrossRef]
[18] Anu K, Hemalatha J. Ultrasonic and magnetic investigations of the molecular interactions in zinc doped magnetite Nanofluids. J Mol Liq 2018;256:213–223. [CrossRef]
[19] Majstorović DV, Quindel P, Živković EM, Kabelac S. A new setup for speed of sound measurements and experimental data for nanofluids Al2O3 or Ag with water or ethylene glycol. J Mol Liq 2023;389:122930. [CrossRef]
[20] Reddy MSB, Jayarambabu N, Reddy RKK, Kailasa S, Rao KV. Study of acoustic and thermodynamic factors of synthesized ZnO-water nanofluid by ultrasonic technique, Mater Today Proc 2020;26:25–30. [CrossRef]
[21] Leena M, Srinivasan S. Effects of rare earth doped on thermal conductivity of ZnO-water nanofluid by ultrasonic velocity measurements. Mater Lett 2018;219:220–224. [CrossRef]
[22] Leena M, Srinivasan S. Synthesis and ultrasonic investigations of titanium oxide nanofluids. J Mol Liq 2015;206:103–109. [CrossRef]
[23] Bhavani JD, Gopal TS, Gnanasekar S, Pandiaraj S, Muthuramamoorthy M, Alodhayb AN, et al. Ultrasonic Interferometry and Physiothermal properties of Al2O3/CuO nanofluids. Case Stud Therm Eng 2024;55:104120. [CrossRef]
[24] Meena RR, Chaki SH, Khimani AJ, Deshpande MP. Investigation of ultrasonic parameters and measurement of thermal conductivity of CuO-transformer oil nanofluids. Mater Res Express 2019;6:0850f3. [CrossRef]
[25] Kannappan V, Santhi RJ. Ultrasonic study of induced dipole-dipole interactions in binary liquid mixtures. Indian J Pure Appl Phys 2005;43:750–754.
[26] Sonar AN. Acoustic and volumetric properties of substituted heterocyclic compounds in dioxane-water mixture at 303K. J Chem Pharm Res 2011;3:485–489.

[27] Yasmin H, Giwa SO, Noor S, Sharifpur M. Thermal Conductivity Enhancement of Metal Oxide Nanofluids: A Critical Review. Nanomater 2023;13:597. [CrossRef]
[28] Aybar HŞ, Sharifpur M, Azizian MR, Mehrabi M, Meyer JP. A review of thermal conductivity models for nanofluids. Heat Transf Eng 2014;36:1085–1110. [CrossRef]
[29] Ambreen T, Kim MH. Influence of particle size on the effective thermal conductivity of nanofluids: A critical review. Appl Energy 2020;264:114684. [CrossRef]
[30] Yasmin H, Giwa SO, Noor S, Aybar HŞ. Influence of preparation characteristics on stability, properties, and performance of mono- and hybrid nanofluids: Current and future perspective. Machines 2023;11:112. [CrossRef]
[31] Yasmin H, Giwa SO, Noor S, Aybar HŞ. Reproduction of nanofluid synthesis, thermal properties and experiments in engineering: A research paradigm shift. Nanomater 2023;16:1145. [CrossRef]
[32] Christensen G, Younes H, Hong H, Smith P. Effects of solvent hydrogen bonding, viscosity, and polarity on the dispersion and alignment of nanofluids containing Fe2O3 nanoparticles. J Appl Phys 2015;118:214302. [CrossRef]
[33] Esfe MH, Afrand M. An updated review on the nanofluids characteristics: Preparation and measurement methods of nanofluids thermal conductivity. J Therm Anal Calorim 2019;138:4091–4101. [CrossRef]
[34] Younes H, Christensen G, Li D, Hong H, Ghaferi AA. Thermal conductivity of nanofluids: Review. J Nanofluids 2015;4:107–132. [CrossRef]
[35] Rasin MN, Hemalatha J. A novel ultrasonic approach to determine thermal conductivity in CuO-ethylene glycol nanofluids. J Mol Liq 2014;197:257–262. [CrossRef]
[36] Kumar VSS, Rao KV. Investigation of ultrasonic parameters of ZnO – Ethylene Glycol Nanofluids. J Ovonic Res 2017;13:91–99.
[37] Balakrishnan J, Balasubramanian V, Rajesh S, Sivakumar M. Acoustic study of atropine sulphate in water of various concentrations at 35° C using ultrasonic interferometer. J Chem Pharm Res 2012;4:4283–4288.
[38] Jacobson B. Intermolecular Free Lengths in Liquids in Relation to Compressibility, Surface Tension and Viscosity. Acta Chem Scand 1951;5:1214-1216. [CrossRef]
[39] Jinklor GT, Bokare JP, Kulkarni TP, Thane MS, Pachore SS, Kabara KB, et al. Molecular Behaviour of Polymer Based Nanofluids Using Acoustic Method. AIP Conf Proc 2019;2142:200005. [CrossRef]
[40] Gupta V, Sharma AK, Sharma M. Ultrasonic investigation of molecular interaction in aqueous glycerol and aqueous ethylene glycol solution. J Chem Pharm Res 2014;6:714-720.
[41] Priyanka S, Chimankar OP. Intermolecular interaction in the binary mixture of B-alanine with water at 323K. Int J Sci Res Phys Appl Sci 2013;1:10–11.
[42] Prigoginel L, Malhot V. The molecular theory of the solution. North Holl Publisher 1957.
[43] Mondragon R, Julia JE, Barba A, Jarque JC. Characterization of silica–water nanofluids dispersed with an ultrasound probe: a study of their physical properties and stability. Powder Technol 2012;224:138–146. [CrossRef]
[44] Nickel C, Angelstrof J, Bienert R, Burkart C, Gabsch S, Giebner S, et al. Dynamic light-scattering measurement comparability of nanomaterial suspensions. J Nanopart Res 2014;16:2260. [CrossRef]

J Ther Eng, Vol. 12, No. 2, pp. 767−783, March, 2026

Journal of Thermal Engineering
Web page info: https://jten.yildiz.edu.tr
DOI: 10.14744/thermal.0001118

Research Article

Energy and financial efficiency of a single family house in Algeria, the best way to get rid of state subsidies

Rabea KAOULAL[1], Sifia BELGHERRAS[2], Sidi Mohammed El Amine BEKKOUCHE[3]

[1]Science of Matter Department, FFaculty of Material Sciences, Mathematics and Computer Science, University of Adrar, Adrar, Algeria
[2]Faculty of Science and Technology, University of Ghardaïa, BP 455 Airport Road, Noumerate, Ghardaïa, Algeria
[3]Applied Research Unit on Renewable Energies (URAER), Renewable Energy Development Center (CDER), Ghardaia, Algeria

ARTICLE INFO

Article history
Received: 13 January 2025
Revised: 11 March 2025
Accepted: 06 April 2025

Keywords:
Building's Energy Balance, Thermal Rehabilitation, Energy Efficiency, Subsidies, Return on Investment

ABSTRACT

Financial aid and subsidies for electricity are intended to mitigate the impact of energy bills on low-income households. Unfortunately, these subsidies can represent a significant financial burden for governments. By eliminating them, states can reduce their budget deficit and reallocate those funds to other priorities, such as education or health. Several methods and alternative solutions to avoid or reduce dependence on electricity subsidies can be considered, but they will need to be adapted to the specific context of each country or region. Promoting energy efficiency will help consumers to reduce their electricity consumption and offset price rises. The integration and investment in renewable energy are essential to diversify energy sources and reduce dependence on fossil fuels. These two actions can effectively reduce the need and dependence on subsidies by decreasing demand. Moreover, by implementing more rational aid programs instead of subsidizing fossil electricity for low-income households, it will be highly possible to encourage states to stabilize their budgets acceptably by reallocating funds to other priorities. This study aims to evaluate the energy and economic performance of the Algerian buildings. This paper quantitatively analyzes the financial and energy efficiency of buildings and, rehabilitation projects of single-family houses in all of Algeria's climatic regions. An assessment of the building's overall energy balance was the basis of the investigation method. According to the obtained results, the current state subsidy system will not have to be fully maintained. Eliminating or reducing electricity subsidies is a complex process that requires a thoughtful and gradual approach. It must be carried out gradually and accompanied by protective measures for vulnerable households. To avoid negative impacts on the purchasing power and well-being of citizens, these measures must be based, firstly, on specific and limited investments and financial aid according to climatic regions, unlike what they were at the beginning (unlimited); secondly, on the judicious integration of renewable energies; and thirdly, on strengthening energy efficiency. From a financial point of view, subsidies are significantly lower for lower cooling energy needs. By adopting rehabilitation measures, unsubsidized energy bills are lower than those corresponding to a conventional home without thermal rehabilitation and with subsidized bills. Subsidizing the thermal rehabilitation procedure, or subsidizing thermal rehabilitation, a suitable solar water heater and, a stand-alone, optimized

***Corresponding author.**
*E-mail address: kaoulal.r@gmail.com

This paper was recommended for publication in revised form by Editorin-Chief Ahmet Selim Dalkılıç

Published by Yıldız Technical University Press, İstanbul, Turkey
Yıldız Technical University. This is an open access article under the CC BY-NC license (http://creativecommons.org/licenses/by-nc/4.0/).

and well-sized photovoltaic system at the same time, can be a good alternative for effectively reducing the need for and dependence on subsidies by reducing demand or getting rid of these subsidies altogether. The most suitable regions for financial assistance, ranked according to merit, are M'sila, Naâma, Biskra, Bechar and, lastly, the Drabla climatic region.

Cite this article as: Kaoulal R, Belgherras S, Bekkouche SMAB. Energy and financial efficiency of a single family house in Algeria, the best way to get rid of state subsidies. J Ther Eng 2026;12(2):767−783.

INTRODUCTION

Energy efficiency in building construction is of paramount importance, especially in Algeria, a country with varied climates. This study embarks on a comprehensive exploration of energy efficiency in these different climatic zones. This action seems to us very obligatory, as state subsidies indirectly risk depleting our natural resources. Electricity is mainly generated from the main fossil fuels, which account for almost 99.6% (Oil: 35%, natural gas: 64%, coal: environ 0.6%) of domestic primary energy consumption. In the same context, the electricity bills allocated to Algerian citizens do not reflect the reality of electricity production and distribution costs. The program focuses on subsidizing consumers' electricity bills. State subsidies for electricity bills in the Algerian region amounted to 18.9 billion Dinars in 2020. Consumers will subsequently be encouraged to use electricity more efficiently and rationally. Moreover, in some countries, such as Algeria, subsidies can sometimes favor fossil fuels and non-sustainable energy sources. At the heart of this issue, the Minister of Energy pointed out that the average price per kWh of electricity in Algeria, for high, medium and low voltage, is low compared to other countries around the world. Subsidies also distort resource allocation, by encouraging excessive energy consumption, artificially favoring capital-intensive industries, reducing incentives for investment in renewable energies, and accelerating the depletion of natural resources (our situation). The main aim of this study is therefore to propose an efficient process and passive architectural concepts that can put an end to this government financial aid without having negative economic and social impacts. This document includes ideas for reforming energy subsidies. The application field of electricity-related subsidies primarily concerns the building sector, as this sector represents a significant portion of energy consumption in Algeria and several countries around the world. The results and conclusions reached appeal to a broader audience, including practitioners and decision-makers. The training of professionals to raise awareness of new practices and technologies, as well as collaborations with companies in the construction and energy sectors, are of crucial importance for implementing these results. The indication of the terms of the grants and the use of the results to raise awareness among the general public and policymakers about the importance of energy efficiency in buildings is very essential. Cooperation and joint work with state agencies to integrate research findings into building regulations and standards are more than necessary. The results can also be used to initiate new research projects or the development of innovative technologies in the building energy field. Following this observation, it is possible to transform the results of this research into concrete actions that improve the energy efficiency of buildings and contribute to environmental sustainability. The application of grants will primarily be dedicated to renovation work aimed at improving the energy efficiency of housing, such as thermal insulation, window replacement, or the installation of more efficient heating/cooling systems. They can also be used to finance social housing construction projects, thereby making energy more accessible, encouraging sustainable practices, and improving the living conditions of citizens. In summary, subsidies play a crucial role in the energy transition by helping households reduce their energy consumption, lower their electricity bills, and contribute to the fight against climate change.

The energy and financial efficiency of buildings is a constantly evolving field, but several concepts and practices are already well established. Many countries have established building standards that require minimum energy performance, such as the RT 2012 standard in France or the energy code in Canada. Certifications such as LEED (Leadership in Energy and Environmental Design), BREEAM (Building Research Establishment Environmental Assessment Method), and HQE (High Environmental Quality) promote sustainable construction and energy efficiency. Energy technologies such as thermal insulation, renewable energy sources that contribute to the energy autonomy of buildings, energy management systems based on monitoring and optimization sensors, software for real-time data analysis, energy audits that identify opportunities for improving energy efficiency, and bioclimatic design that takes into account the building's orientation, the use of natural light, and natural ventilation to reduce energy needs, have seen significant developments over the past decade. Despite all these advancements, this field is still evolving, with an increasing focus on innovative financing models and financial incentives to encourage energy efficiency projects, sustainability, and resilience in the face of environmental challenges, particularly under harsh, unfavorable, or degrading climate regimes. In the field of energy and financial efficiency of buildings, several

research gaps can be identified and need to be filled. These include:

- Longitudinal data and case studies: there is a significant need for long-term data on the energy performance of buildings after their construction and occupancy to understand the factors that influence energy efficiency over the long term.
- Some new technologies deserve to be explored more deeply, such as energy management systems, intelligent sensors, and innovative materials.
- Research on the impact of occupant behavior on energy consumption is still limited.
- The effective integration of renewable energies into buildings, particularly regarding energy storage and demand management.
- Regulations on energy efficiency in buildings are still insufficient and are not always well understood. Further research can help identify best practices and the most effective policies.
- Adapting buildings to future climatic conditions.
- The need for effective and innovative financial models to support investments in energy efficiency and research into financing mechanisms for a smooth energy transition, to overcome financial barriers, and to improve the living conditions of citizens.

Reducing electricity subsidies is, therefore, a complex issue that requires a thoughtful approach. This reduction is necessary for several reasons:

- First, subsidies can place a heavy burden on public budgets, limiting the resources available for other essential services such as health or education.
- Secondly, to encourage consumers to use electricity more efficiently and adopt more responsible consumption behaviors.
- Thirdly, subsidies can sometimes favor fossil fuels or outdated technologies.
- Fourthly, the reduction or elimination of subsidies leads to a reallocation of resources towards more targeted programs for low-income households.

The reduction of electricity-related subsidies involves evaluating existing subsidies, i.e. analyzing current subsidies to understand their economic, social, and environmental impact. The second step is to identify those that are ineffective or do not meet their objectives. It is necessary to establish scientific work, and transparent communication can help gain the support of citizens from different categories and inform them about the reasons for the reduction or elimination of subsidies and the expected benefits. But at the same time, it is necessary to implement compensatory measures to mitigate the impact on vulnerable households, through targeted assistance or other support programs for those most affected by the rise in electricity prices.

As part of this objective, recent work by Manić et al. [1], has made it possible to estimate the energy performance of existing buildings, labeling and evaluating energy-saving measures and energy strategies to be implemented in the Republic of Serbia. In fact, particular attention has been drawn to the energy efficiency of existing buildings which, according to the work carried out, average energy consumption in Serbia is over 150 kWh m^{-2} per year, compared with around 50 kW m^{-2} per year in developed European countries [2]. On the other hand, the Savski Venac municipality's local development strategy was based on appropriate energy efficiency measures aligned with its energy policy [3]. However, the most effective energy-saving measures for energy-efficient buildings are improving the performance of the air-conditioning system and the thermal properties of walls and windows in Guangdong province, China. The sum of the energy-saving rates for the cooling system, walls and windows is around 56% [4]. Moreover, to meet all these commitments, at least one of the passive or active concepts needs to be integrated. It's a well-known fact that reducing a home's energy requirements systematically leads to lower energy bills. Especially as the thermal insulation is the most popular passive technique. But before undertaking any thermal insulation work, there are a number of prerequisites that must be met to fully understand the issues involved. In response to this request, targeted studies [5-7] of the factors affecting the optimum insulation thickness and its pay-back period, including the building's heating and cooling energy requirements, lifetime, the costs of insulation materials and installation, the costs of energy sources for heating and cooling, the efficiency of heating and cooling systems, and solar radiation, were fundamentally addressed.

As insulation helps to reduce energy consumption, it can also reduce carbon emissions, as fewer fossil fuels are burned [8, 9]. The financial profitability of thermal insulation has been the subject of several investigations. A comprehensive analysis by Canbolat [10] was carried out to determine the impact of the heating source type (natural gas, electricity, fuel oil), insulation materials (expanded polystyrene, extruded polystyrene, mineral wool, polyurethane foam), the climate zone (Adana, Çanakkale, Konya, and lastly Van) and the building use (summer house, winter house or all-season house) on the optimum insulation thickness. Efficiency measures with the fastest return on investment, shortest implementation time and lower complexity have been confirmed by the technical-economic analyses [11]. Efficient hospital lighting, in this case, is the most effective way of reducing budget expenditure. However, the greatest potential for energy savings comes from space heating through thermal insulation of the roof and external walls, efficient windows and the introduction of an efficient diesel heating system. Implementing and improving the building management system is also an important measure [11]. Adamczy et al. [12] have proposed a methodology for assessing the economic and ecological benefits resulting from changes in user profile and thermal insulation performance. Financial analyses were carried out taking into account the year of construction of the building,

the type of heat sources and thermal insulation, user profiles in the room and technical and social requirements. The social dimension of the approach was significant, as the aim was to reduce expenditure on thermal upgrading of buildings, particularly in areas of energy and economic poverty. Changing temperature habits in the home can have a significant impact on saving energy resources. Another study focusing on Europe [13] showed that investments in thermal insulation in the building sector can have a significant impact on improving the energy efficiency of buildings and reducing end-energy use in this sector. The use of important indicators, such as: net present value, profitability indicator, ecological and financial payback period, showed that payback periods ranged from 0 to 6 years. On the other hand, in 2017, the importance of investing in thermal insulation was examined by Dylewski and Adamczyk [13], taking into account the state of the building before thermal insulation, the type of building materials, the heat source to be used, the type of thermal insulation and the climate zone in which the building is located. The results indicate that the investment is beneficial regardless of the regions examined in this article. They are most promising for the colder climate, a building that had the worst thermal performance before thermal insulation, the most expensive type of heat source (i.e. the highest costs to obtain 1 kWh of thermal energy) and the least expensive material used for thermal insulation [14].

The first observation to be drawn from a literature review in this field, which has a direct socio-economic impact on homeowners, is the inadequacy of certain well-targeted and quantified technical results, particularly those concerning very hot regions in Algeria, often characterized by particular extreme climatic conditions. A new approach will be proposed to address the current profitability issue in these similar regions. For this purpose, the arguments to be provided help to communicate new ideas that advance research. The theoretical framework is an updated art state from the previous research. The formulation of our problem will involve the development of some key concepts and their definitions. We can justify the investigation, suggest a new angle on it, expand already conducted research, and most importantly, bring a new proposal to the debate. In line with all these steps, the first objective will therefore be to conclude exhaustive financial charges of the insulation procedure with a personalized user manual, the justifications for the choice and their return on investment. Expanded polystyrene has been favored over thermal insulation materials due to its ease of handling on construction sites, its resistance to moisture and water (which makes it an ideal choice for applications in humid environments, such as basements or foundations), its durability (so it is stable over time and does not deform easily), its ease of implementation, its competitive cost (which makes it an economical option for many projects), non-toxicity, and it also provides some acoustic insulation.

Furthermore, energy subsidies are one of the instruments used by governments to achieve political, social and environmental objectives. In 2022, the latest estimates from the International Energy Agency indicate that the global subsidies to support fossil fuel consumption had reached over $1000 billion. Worldwide subsidies for the consumption of natural gas or electricity (from fossil fuels) have more than doubled, while those for oil have risen by 85% [15]. These subsidies are particularly intended to the developing countries to correct the poverty effects and promote economic and social development by providing access to energy at affordable prices. But, the negative impact of this consumption on carbon emissions has been widely criticized. Subsidies have also criticized for distorting relative financial charges and the supply-demand balance; they lead to a significant economic surplus loss, which must be offset by the social benefit sought by each subsidy. Due to their conflict with climate objectives, they are currently being criticized, making their elimination a key objective. The most subsidies are typically given to oil-producing countries. This has led the International Monetary Fund (IMF) and the World Bank, even before 2022, to introduce a climate policy agenda. They considered that fossil fuel subsidies and criticisms are mainly due to their productive (disincentives for industrial and commercial energy companies, leading to deficits and under-investment), allocative (fuel over-consumption) and environmental inefficiency. It has been noted that these subsidies are not well-directed. Political legitimate objectives cannot prevent the elimination of subsidies [16]. To deal with this complicated issue, and to avoid binding commitments by countries that would be unrealistic, an effective and profitable method from an energy, economic and financial point of view will be proposed. The issue of financial subsidies for electricity from the conventional grid is therefore an aspect that is very poorly documented and often partial. We have not found studies conducive to comparison; it has already been noted that even in the presence of a few rare works that partially fit into this same context, few studies if any have gone so far as to propose alternatives that would reduce or eliminate the current forms of subsidies. With this in mind, the proposed solutions can be considered innovative and may be extended to other similar regions across the globe in the near future.

SUMMARY OF THE METHOD: BUILDING'S OVERALL ENERGY BALANCE

The energy balance provides an overall assessment, control and diagnosis, which will subsequently, determine the work to be undertaken to improve the energy efficiency of any building. It should take into account the specific nature of the building (used materials, level of thermal insulation, walls, floors, openings, etc.), ventilation systems, heating and domestic water production, household appliances and lighting systems, and integrated passive and active energy

concepts. The following equations [17-23] serve as the basis for energy requirement calculation for heating (1) and cooling (2), respectively.

$$Con_{Tot} = Con_{Env} - \left(Hg_{Occupants} + Hg_{Lighting/Other} + Hg_{Solar}\right) + Con_{DHW} + Con_{Load} \quad (1)$$

$$Con_{Tot} = Con_{Env} + \left(Hg_{Occupants} + Hg_{Lighting/Other} + Hg_{Solar}\right) + Con_{DHW} + Con_{Load} \quad (2)$$

The sum $Hg_{Occupants} + Hg_{Lighting/Other} + Hg_{Solar}$ represents free solar gains.

Con_{Env} is, by definition, the energy consumption due to the building envelope (Wh) [17-21]

$$Con_{Env} = 24\ Dj\ Hlos_{Env} \quad (3)$$

$$Hlos_{Env} = Hlos_{Walls} + Hlos_{Roof} + Hlos_{Low-floor} + Hlos_{Doors} + Hlos_{Windows/Opnings} + Hlos_{Thermal\ bridges} + Hlos_{Ventilation} \quad (4)$$

$Hlos_{Ventilation}$: the amount of heat loss from the ventilation system and each element (W/K), calculated using the detailed methods given in references [17-21].

Con_{DHW}: the average energy requirement for daily water heating (Wh). This is a major energy item counted by the daily volume of the water to be heated per person (liters/day/person), the useful temperature (°C) of the hot water and the temperature difference (°C) with that of use [22, 23].

$$Con_{DHW} = \rho\ 1.1628\ Vol_{DHW}\ (T_{DHW} - T_{CW}) \quad (5)$$

Where ρ is the water density, measured in kg/liter in this case. It ranges from 999.841 kg/m^3 at 0 °C to 958.40 kg/m^3 at 100 °C and is generally maintained at 0.99 kg/liter until around 55 °C [24].

Vol_{DHW} signifies the amount of domestic hot water required for the user's use (liters).

T_{DHW} and T_{CW} are respectively the temperature of the domestic hot water and the cold water at the inlet to the heating system (°C or K)

For this undertaken work, Vol_{DHW} = 50 liters per occupant and T_{DHW} = 50 °C will be retained.

The internal heat gains (Wh) are evaluated according to the building purpose which is mainly due to the body heat and occupant's activity $Hg_{Occupants}$, the lighting, electrical appliances, devices and significant usage of equipment's, cooking, etc. $Hg_{Lighting/Other}$ [17-21].

$$Hg_{Occupants} = Nb_{Residents}\ \varphi_{Occupants}\ Nb_{Days}\ Dur_{Residents} \quad (6)$$

$Nb_{Residents}$: number of residents occupying the building

$\varphi_{Occupants}$: heat flux released by the human body per occupant (W)

Nb_{Days} : number of days to be heated / cooling

$Dur_{Residents}$: the mean duration of the resident presence per occupant (hours per day)

$Hg_{Lighting/Other}$ is the heat flux released by lighting, electrical appliances, devices and significant usage of equipment, cooking, etc (W) [17-21]

$$Hg_{Lighting/Other} = Nb_{Days}\ \ Dur_{In\ operation}\ \ \varphi_{Lighting/Other} \quad (7)$$

$Dur_{In\ operation}$: the total run time of the lighting system and all equipment to be powered (hours per day)

The incoming passive solar gain is also taken into account by the orientations of the glass facade walls. It is calculated as follows [17-21]:

$$Hg_{Solar} = \sum_j I_j \sum_n A_n(j) = \sum_j I_j \sum_n Aop_n(j)\ Fs_n(j)\ S_n(j) \quad (8)$$

Where n represents the number of the transparent opening fronts. I_j is defined as the daily solar irradiance incident on a unit surface of orientation j (Wh/m^2). $A_n(j)$ is an equivalent receiving surface (sum of surfaces of transparent opening fronts) of an orientation j, used to determine the building's capacity to capture solar gain. $Aop_n(j)$ is the opening area (m^2) corresponding to the window n of the orientation j. $Fs_n(j)$ represents the shading correction factor according to the orientation j. S is the solar factor for windows n of the orientation j.

The energy consumption for electrical loads (any component of a circuit that consumes electrical power) in buildings is estimated in Wh according to the following equation:

$$Con_{Loads} = Nb_{Days}\ \ P_{Elec}\ \ Dur_{In\ operation} \quad (9)$$

P_{Elec} is the electrical power of equipment (W).

Study Cases

Building Model

The case studied is a single-story house with an area of 126.69 m^2 and a volume of 380.07 m^3 as shown in Figure 1. It consists of a living area, kitchen, bathroom/WC, kids' bedroom, parents' room with cupboards, and stairway. Windows maximize the entry of natural light, thereby reducing the need for artificial lighting during the day. It is possible to benefit from fresh air through windows or a well-designed and maintained mechanical ventilation system.

The thermophysical properties of building materials of the built environment and the type of occupancy are given in Table 1 below.

Climatic Data and Brief Description of the Country's Regions

In this investigation, energy efficiency was assessed in any climatic zone. Algeria is the largest country bordering both Africa and the Mediterranean due to its vast surface and diverse range of climate zones, as depicted in the Köppen-Geiger globe map. The selection of eligible locations has been based on seven climatic zones (according to the

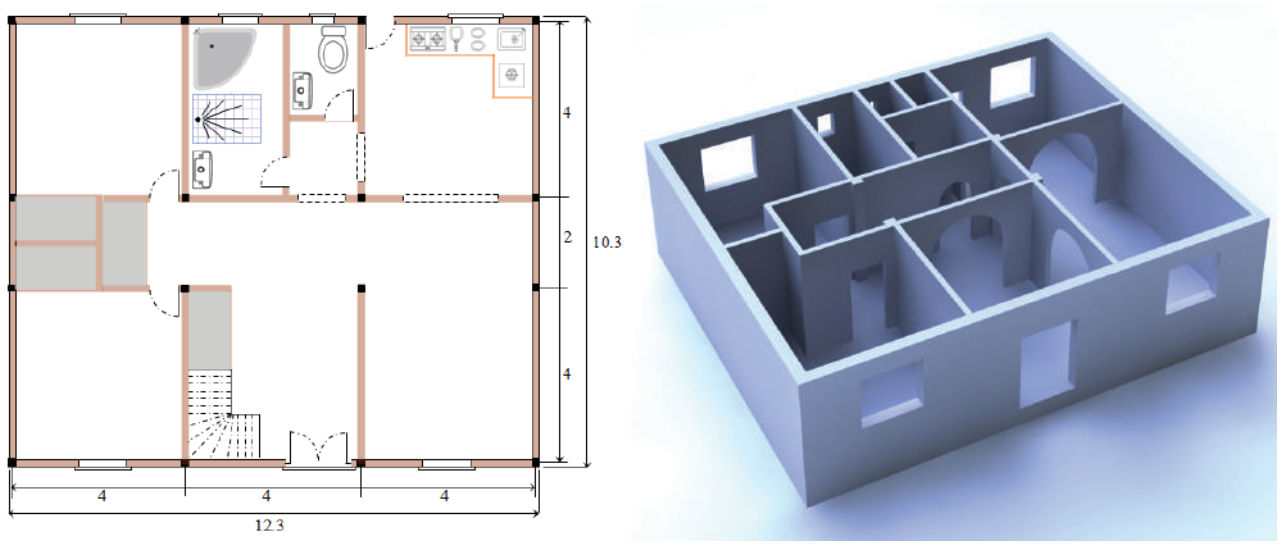

Figure 1. Approximate illustrative design of the parts in the building space.

Table 1. Thermal and occupancy properties of the house

		1st case	2nd case : with thermal rehabilitation (external thermal insulation + passive solar gain)
	Walls of the building envelope	1.71	0.31
	Roof	3.06	0.51
U	Soil	1.14	0.31
W/(m² °C)	Thermal bridges	1.07	0 : eliminated
	Windows on a wood frame	Single-glazing: 5.00	Double-glazing : 2.55
	Opaque door made of	Metal : 5.80	Wood: 3.50
Glazed surfaces		95% of the total window surfaces	
Hygiene flow (infiltration and permeability)		60.5 m³/h	
Air exchange loss coefficient (natural ventilation)		40 m³/h	
Number of occupants in the building		5 occupants	
Average hot water requirement per occupant		60 liters per day at 50 °C	
Average occupancy		15 hours per day per occupant	
Comfort temperature		Between 21 °C and 26 °C	

Table 2. Climate classification and geographical coordinates of the study regions

Climatic zones	Climate classification	Latitude	Altitude	Longitude
Setif	Mediterranean climate with a hot summer	36° 09′ 00″ North	1100 m	5° 26′ 00″ East
M'sila	Semi-arid cold climate	35° 33′ 0″ North	968 m	6° 10′ 12″ East
Bechar	Dry and hot desert climate	31° 37′ 0″ North	773 m	-2° 13′ 0″ West
Biskra	Dry and hot desert climate	34° 51′ 01″ North	120 m	5° 43′ 40″ East
Naâma	Dry and cold desert climate	33° 15′ 44″ North	891 m	0° 18′ 52″ West
Drabla	Hot temperate climate	35° 0′ 0″ North	1380 m	7° 0′ 0″ East
Mohamadia	Semi-arid cold climate	35° 35′ 25″ North	30 m	0° 04′ 12″ East

Köppen-Geiger classification) that are dispersed throughout Algeria to account for all potential scenarios. Figure 2 and Table 2 below display the chosen towns' geographic coordinates.

The climate of Setif is semi-arid and transitional Mediterranean with some continental characteristics. There are occasional cold snaps and snowfalls (on average 12 days a year) in the city during the somewhat cold winter. Summertime at this altitude is scorching, even hotter than it is along the shore. At times, the temperature might get to 40 °C. The Köppen-Geiger climate map, which is displayed by the National Institutes of Health's US National Library of Medicine, indicates that Setif has a "Csa" type climate, which is characterized by hot summers and temperate steppe. However, M'Sila has a BWh desert climate, which is hot and dry. Throughout the year, there is little rainfall in M'Sila. Annual rainfall is 249 mm according to meteorological records. The average temperature in M'Sila is 18.6 °C. Likewise, Biskra and Bechar are classified similarly since their yearly average temperature consistently rises above 18 °C. The town of Biskra is located in northeast Algeria, on the edge of the Sahara Desert. The climate is subtropical desert, with hot, bright summers and mild winters that can get chilly at night. The average annual temperature is 21.8 °C. Rainfall in a year is 141 mm on average. Bechar is located in western Algeria at a height of 780 meters and a latitude of nearly 32 degrees north. Its climate is subtropical desert, with hot, sunny summers and mild winters (during which it can be cold at night). The mean annual temperature is around 20.2 °C. Moreover, the Wilaya of Naâma lies at an altitude of over 1000 meters on the high plateaux and is crisscrossed by the Saharan Atlas chain. The climate is continental, with very hot, arid and generally clear summers and chilly, dry, windy and partly cloudy winters. Monthly rainfall varies seasonally to a modest extent. Over the year, the average annual temperature fluctuates between 2 °C and 36 °C; it rarely falls below -1 °C or climbs beyond 39 °C. On the other hand, Drabla's climate is warm and temperate. The yearly mean temperature and precipitation are 11.5 °C and 623 mm, respectively. Finally, Mohamadia has a "steppe" climate. There is hardly much rainfall during the year. The average annual temperature is 18.4 °C, and there are roughly 351 millimeters of precipitation [25-27].

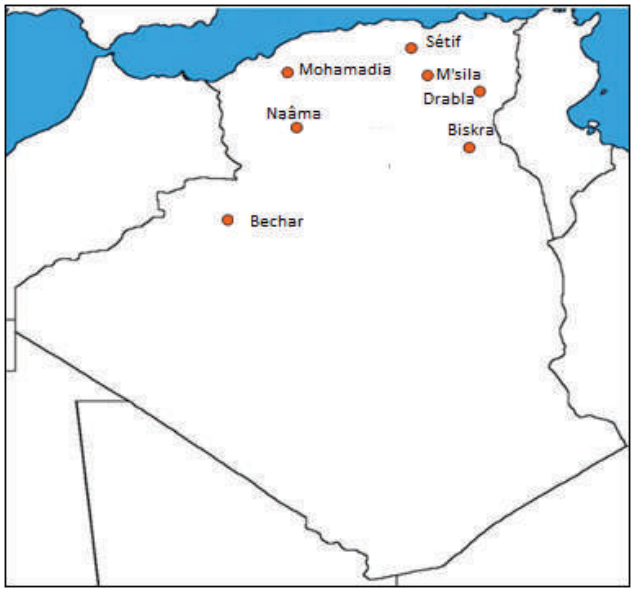

Figure 2. Geographical location of the climatic sites.

In Figure 3, average monthly temperatures are displayed.

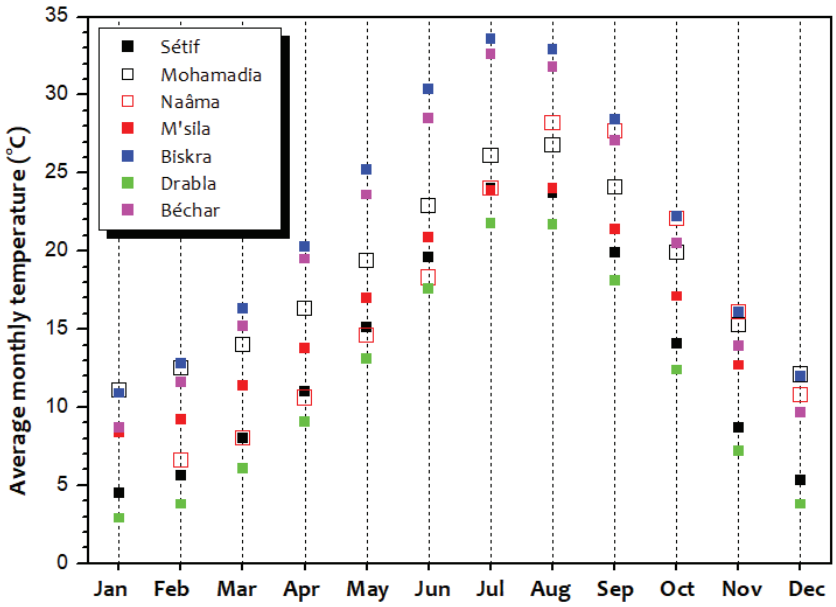

Figure 3. Average monthly temperatures for several climatic regions.

RESULTS, ANALYSIS AND DISCUSSION

As mentioned in Table 1, the setpoint temperature that determines the desired thermal level in this case was set at a range of 21 °C - 26 °C. This choice was principally motivated for energy-saving reasons. According to the Agency for the Environment and Energy Management "ADEME", by lowering the heating setpoint by 1 °C, 7% of the heat energy can be saved. By increasing the temperature from 22 °C to 26 °C, energy consumption can be halved [28]. The comfort temperature during overheating was tolerated at 26 °C. To not compromise, preserve the comfort and match the body's metabolic rate, which varies depending on muscular activity, the environment and body size, the user-set heating temperature has been kept at 21 °C.

Diagnosis of Thermal Comfort Periods

This study's initial phase involves comparing climate regimes by figuring out which days needed heating and cooling. Days with adequate ventilation that allow outside air to enter the house at a comfortable temperature are associated with comfortable levels of comfort. Figure 4 displays an early comparison of the study's climatic circumstances, which can express the level of perceived comfort as a function of the amount of energy exchanged between the user and his surroundings.

Csa' type climates are found in many parts of the world, mainly around the Mediterranean Sea, in the south of Australia, in the southwest of South Africa, in certain parts of Central Asia, in the northern parts of Iran and Iraq, and so on. In hot desert climates of the BWh type, such as M'Sila, Oaxaca in Mexico and the Saudi Arabian desert, the heating period can be as high as 76.79%. The period is still long for BWk climates, such as Naâma, which is equivalent to 69.54% of the year, and the Gobi Desert in Mongolia. As it moves further south, the duration of the heating period decreases, approaching 50% of the year. It is 49.77% and 53.25% of the year, respectively for the regions of Biskra and Bechar. In the same context, the overall number of comfortable days during the year is low, ranging from 11.98% to 16.55%, which justifies the short off-season periods. The Mohammadia region, on the other hand, is slightly more interesting, with an estimate of 24.63% of the year.

Assesment of Energy Needs

Figure 5 shows detailed results of the monthly energy demand according to the indicated climate regime, associating them with the share of heating and cooling demand (a and b). A comparison of the annual energy demand was also made between the two houses after thermal rehabilitation according to the second case in Table 1 (c). An energy classification of the two buildings according to the climatic region was carried out, assigning the appropriate energy label in each case (c).

The first observation has been referred to the record levels of energy needs in the climatic zones of Drabla and its surrounding areas. The unrenovated single-family house proposed in this study is, as a result, an energy-intensive building (type "G" label) in Setif's, Naama's and Drabla's climates. The Mohamadia site will provide much more favorable climatic conditions for this type of building. Energy consumption will be minimal and more advantageous compared to other sites (type "E" label) without thermal rehabilitation. Buildings with similar climatic conditions to those in M'sila, Bechar and Biskra can be joined by buildings with an "F" energy label. In this awkward situation, the thermal and energetic rehabilitation of dwellings has to face up to a triple challenge:

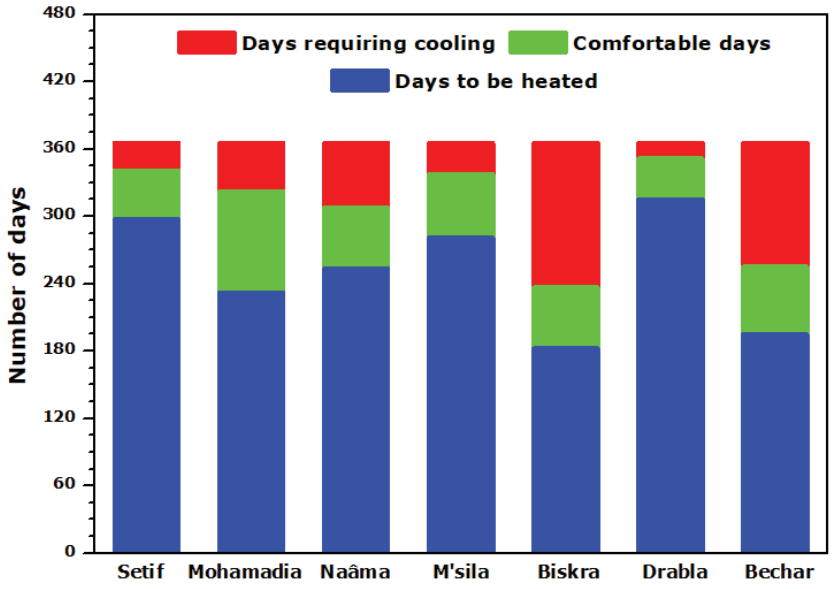

Figure 4. Average monthly temperatures for several climatic regions.

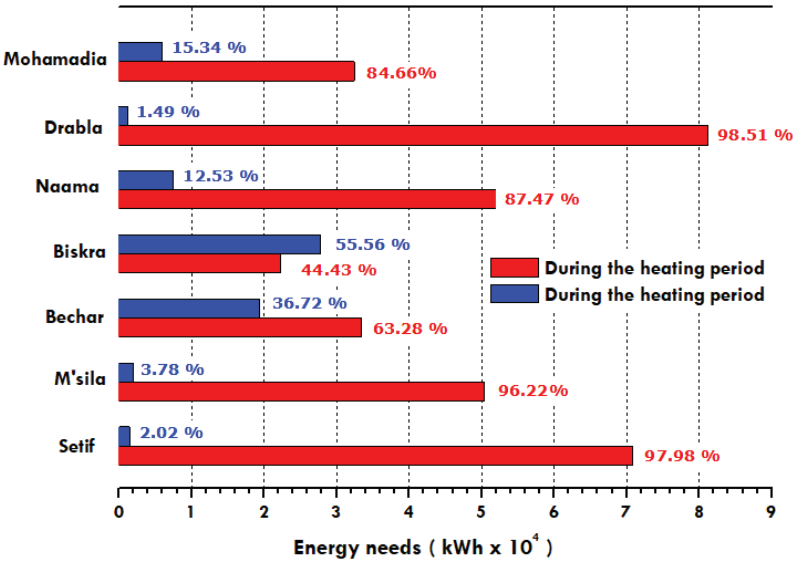

(a)

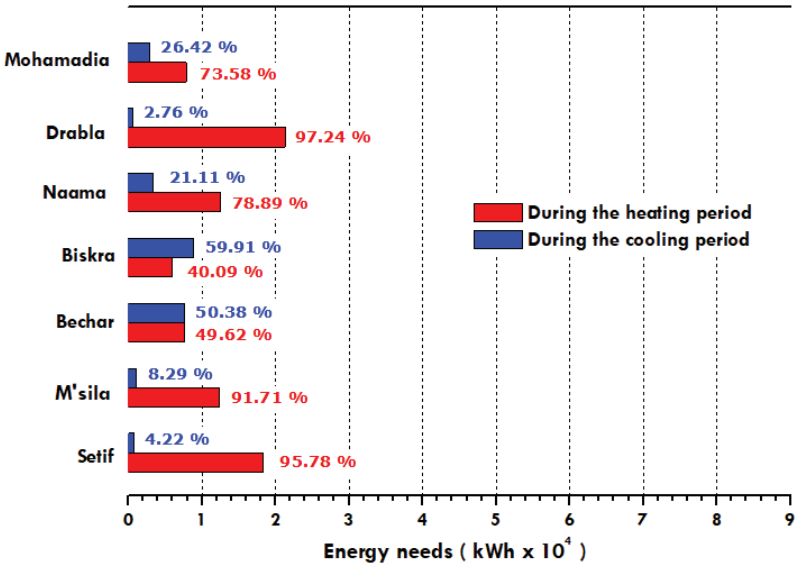

(b)

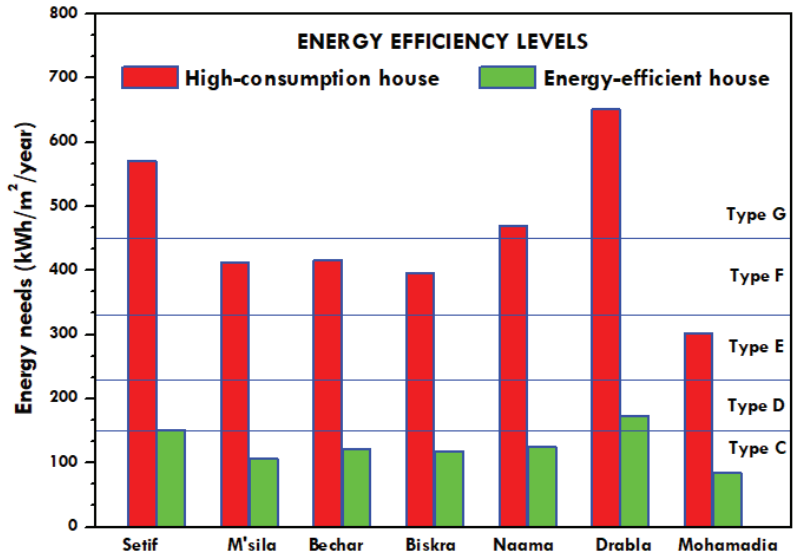

(c)

Figure 5. Energy efficiency assessment of the two buildings, a: monthly energy needs of the high-energy-use house, b: monthly energy needs of the energy-efficient house, c: annual energy needs and labeling of the two houses.

minimizing the overall energy needs to support purchasing power, improving the life quality for Algerians and fighting climate change. According to the obtained results, this approach has led to significant energy savings. It was referred to the specific energy rehabilitation ("D" or "C" labels), which is systematically applied to social contexts. The building envelope is the main source of the total energy needs. This time, the cost-effectiveness has been demonstrated. Total annual energy requirements are significantly reduced in the range from 70.33% in Biskra to 74.13% in M'sila. The best energy efficiency is observed in the coldest climate sites during the heating season. Heating energy savings are generally close and vary within a short range of 73.23%-77.33% compared with the initial energy demand. In overheating periods, energy savings are less noticeable than in cold periods. For the examples given, it was estimated at 44.89%, 43.24%, 60.34%, 68.01%, 55.28%, 50.63% and 51.95% for the regions of Sétif, M'sila, Béchar, Biskra, Naâma, Drabla and Mohamadia respectively.

Cost Estimates for Thermal Insulation Works

By following this schedule, an economic feasibility study, which will include market, technical and financial studies, seems more than necessary to serenely assess the viability of the rehabilitation project in the light of the economic context. To do this, calculating the monetary value of an investment according to its cost has become essential. The return on investment ROI will be selected to take these considerations into account. It is mainly based on the cost of thermal insulation work and the savings on energy bills. The increase in insulation thickness systematically leads to both an increase in financial expenditures dedicated to overall thermal insulation work, an improvement in thermal performance, and an increase in annual energy savings. If the rate of increase in energy gain is higher compared to the annual energy gain, the return on investment can be amortized. However, regardless of the situation, calculations must be made according to the case studies. An estimate of Algeria's financial expenditure on thermal insulation is given in Table 3 below.

Table 3. Financial expenditure on thermal insulation work for the case of this study

Work stages	Adopted methods, requirements and designation of tools and accessories	General notes	Total costs incurred in the operation
Manual brush cleaning of mortar facades	Manual drybrush cleaning	Qualified personnel are not required to apply it	14.15 €/m^2
Repairing the facade cladding	With an alkaline and colorless detergent	- In this case, the finish coatings are flawless. - Requires a professional companion and an execution worker	4.64 €/m^2
External thermal insulation of facades	Rigid expanded polystyrene panels, leveling accessory, supporting and capping insulation panels, compound mortar as a base coat for the trowel application and for bonding insulation panels, expansion dowels for fixing, anti-alkali fiberglass mesh for mortar reinforcement, PVC corner profile with mesh for edge reinforcement, acrylic mortar for coating external facings, expanded polyethylene cord, putty cartridge,… etc.	The rigid panel has a thickness of 10 cm. Requires: - Professional companion and an execution worker - Professional installer of rigid or flexible insulation panels - Professional coaters	74.81 €/m^2
Thermal insulation of flat roofs on load-bearing masonry elements	Rigid expanded polystyrene panels, adhesive tape, fixing washers, adhesives for joints and connections, high-performance climatic membrane without armoring for maximum protection against moisture and vapor,… etc.	The rigid panel has a thickness of 10 cm. Requires: - Professional companion - Professional installer of rigid or flexible insulation panels	25.01 €/m^2
Horizontal thermal insulation for flooring slabs	Rigid expanded polystyrene panels, polyethylene film, and self-adhesive tape for sealing joints	Compressive strength greater than 500 kPa The rigid panel has a thickness of 5 cm. Requires: - Professional companion - Professional installer of rigid or flexible insulation panels	19.88 €/m^2

Energy Bill Analysis and Allocated Subsidies

In August 2024, the average price of electricity worldwide was 0.14 € per kWh. Liechtenstein is the country with the most expensive electricity, at 0.48 € per kWh, while the cheapest electricity in the world is in Iran, at 0.0018 € per kWh [29]. Algeria is also one of the few countries in the world where the price per kWh is cheaper than in other countries. According to the Algerian government, the real price per kWh is 0.1122 €. Subsidies to Algerian citizens exceed 60% in the northern regions and nearly 82% in the south. The regulated price therefore costs 0.0449 €/kWh in the north and 0.0202 €/kWh in the south [30]. However, energy consumption patterns have a huge impact on annual household bills. Natural gas is now widely used as a direct heat source for both space and domestic hot water due to its low installation costs and competitive regulated sales tariffs for homeowners. As for electricity, the Algerian Electricity and Gas Regulatory Commission has set the average price at 0.0023 €/Thermie, whereas the Real price is 0.0029 €/Thermie [30]. It is accepted that 1 kWh = 0.8598 Thermie. The estimated annual energy bills for the different scenarios are shown in Table 4 below. Rectangular cells of the same color should be compared for each mode. The first corresponds to the annual electricity bill of the house, excluding thermal rehabilitation measures and taking into account the financial support. In contrast to the first, the second refers to the annual housing bill with the inclusion of thermal rehabilitation measures and without financial assistance.

Table 4. Energy consumption and bills in all scenarios

Climate zone	First mode of energy consumption			Second mode of energy consumption		
	Energy consumption	Actual invoice (€)	Subsidized invoice (€)	Energy consumption	Actual invoice €	Subsidized invoice (€)
	Before thermal rehabilitation					
Setif	72 251.31 kWh	8 106.60	3 202.11	1 457.01 kWh 60 868.94 Thermie	340.00	204.57
M'sila	52 291.30 kWh	5 867.08	1 056.08	1 976.70 kWh 43 260.49 Thermie	347.24	179.92
Bechar	52 723.31 kWh	5 915.55	1 064.80	19 295.51 kWh 28 741.22 Thermie	2 248.30	179.91
Biskra	50 050.15 kWh	5 615.63	1 010.81	27 809.25 kWh 19 122.73 Thermie	3 175.65	179.92
Naâma	59 463.22 kWh	6 671.77	1 200.92	7 450.62 kWh 44 720.43 Thermie	965.65	179.92
Drabla	82 473.92 kWh	9 253.57	1 665.64	1 227.72 kWh 69 855.48 Thermie	340.33	179.92
Mohamadia	38 357.93 kWh	4 303.76	1 699.98	5 884.83 kWh 27 920.37 Thermie	741.25	227.60
	After thermal rehabilitation					
Setif	19 073.18 kWh	**2 140.01**	845.30	804.68 kWh 15 707.26 Thermie	**135.84**	71.79
M'sila	13 527.96 kWh	**1 517.84**	273.21	1 121.56 kWh 10 667.02 Thermie	**156.77**	58.78
Bechar	15 343.43 kWh	**1 721.53**	309.88	7 766.43 kWh 6 514.70 Thermie	**890.28**	58.78
Biskra	14 849.33 kWh	**1 666.09**	299.90	8 895.33 kWh 5 119.25 Thermie	**1 012.90**	58.78
Naâma	15 788.11 kWh	**1 771.43**	318.86	3 332.51 kWh 10 709.32 Thermie	**404.96**	58.78
Drabla	21 930.04 kWh	**2 460.55**	442.90	605.64 kWh 18 334.72 Thermie	**121.12**	58.78
Mohamadia	10 701.50 kWh	**1 200.71**	474.28	2 827.40 kWh 6 770.15 Thermie	**336.87**	85.83

First and foremost, the use of natural gas for heating, both for the production of domestic hot water and for space heating, is financially more favorable. The resulting energy bills are much lower, and the savings are very significant. Without thermal rehabilitation measures: excluding state subsidies, the tariffs are reduced from 94.08% to 96.32% in the regions around the Setif, M'sila and Drabla climatic zones, where the heating energy needs account for the overwhelming proportion of total requirements, as shown in Figure 5-a. At sites near the Mohamadia and Naâma climatic regions, financial expenditure will be reduced by more than 82.78% and less than 85.53% respectively. These regions are also characterized by high heating demand, but slightly less than the previous regions. However, the financial benefits are much lower in the Saharan regions which are characterized by higher energy demand due to summer air conditioning, such as Bechar and Biskra. They depend mainly on the share of the region's energy demand for air conditioning to its total energy demand. In the Bechar and Biskra climatic zones, the financial rationalization is equivalent to 61.99% and 43.45%, respectively. Moreover, in the case of social assistance, the combined use of electricity and gas leads to a very significant rationalization of expenditure, which can be as much as 93.61% in Setif, compared with the case where electricity would be the only source of energy to meet energy needs. For the remaining regions, the fare reduction rate varies between 82.20% and 86.61%.

In the case of thermal rehabilitation, the same observation is made for the bills corresponding to the regions surrounding the climatic sites of Setif, M'sila and Drabla, which are characterized by an overwhelming dominance of heating throughout the year, as shown in Figure 5b. Costs fell by more than 89.67% and less than 95.08%. However, in climatic regions similar to Mohamadia and Naâma, it is possible to minimize electricity bills by more than 71.94% and less than 77.14%. For climatic sites identical to those in Bechar and Biskra, financial savings of between 39.20% and 48.28% can be achieved. The financial benefits are much lower in the Saharan regions where summer air conditioning increases energy demand, such as Bechar and Biskra. They depend mainly on the proportion of the region's energy requirements for air conditioning according to its total energy requirements. The financial rationalization is equivalent to 61.99% and 43.45% for Bechar and Biskra respectively. In addition, when financial aid is available, such as in the cities of M'sila, Bechar, Biskra and Mohamadia, the combined use of electricity and gas promotes a very concrete minimization of financial expenditure, which is close to 80%. It can reach 91.52% and 86.73% at the Setif and Drabla sites respectively.

It should be remembered that all these estimates correspond to energy needs and electricity bills that are consistent with a comfort maintained 24 hours a day, 365 days a year, without interruption and in all zones. It should also be noted that the achieved results remain valid if the desired comfort conditions correspond to only a small area. The calculated values are relative and linearly proportional to the energy needs and the comfort requirements.

From a financial point of view, subsidies are significantly lower for lower cooling energy needs. On the other hand, in both cases, without and with thermal rehabilitation, it has been noted that the Algerian subsidy strategy, which allows partially improve the standard of living and social security, leads to a certain degree of social justice for the same housing conditions. In many cases, the invoice estimates are similar, if not identical.

The values shown in green mean that, by adopting these rehabilitation measures, unsubsidized energy bills are lower than those corresponding firstly to a conventional home without thermal rehabilitation and secondly to subsidized bills. Given this, it is systematically more judicious for the state to sell the electricity to citizens without recourse to subsidies. It will therefore be more appropriate to provide this financial aid, which will quickly pay for itself over time, to thermal rehabilitation measures. This becomes more apparent when electricity is used for cooling and natural gas for heating. On the other hand, red values mean that subsidies for thermal rehabilitation are insufficient. Unsubsidized energy bills are higher than those of a non-subsidized home and subsidized bills. Additional subsidies will therefore be needed to make up the difference in the bills.

In other respects, producing domestic hot water using solar energy from a properly sized heating system can be a good alternative. Experience has shown that use of the solar energy can cover a very large proportion of the annual hot water demand, given Ghardaïa's high solar potential. This can sometimes cover all the energy needed to produce it. In our case, a family of 5 in Ghardaïa needs an annual consumption of 3816.74 kWh. This case involves a flat-plate "Megasun" solar water collector with a total surface area of 2.61 m^2, fitted with a 200-litre storage tank and an electric pump. On a yearly basis, the average energy cost savings may reach up to 80.25% if optimal tilt for the solar collector is adopted every monthly. The flat plate collector may be vulnerable to convective heat transfer; therefore, other solar collectors, such as vacuum tube collectors, may provide enhanced energy performance [31]. In these regions, a 100-litre solar water heater may be sufficient for a house with several occupants, while in regions with less sunshine, a 300-litre model may be required for even a medium-sized house. The wisest method is to carry out a personalized study to determine which model of solar water heater is best suited to the specific needs. Including the equipment, the support structure and the labor, the total cost of this solar hot water system has been set at €6,000 including tax.

Financing a stand-alone photovoltaic system can also be a good alternative. Table 5 sets out relevant proposals for clarifying the precise destination and amount of subsidies, to completely avoid the injection of financial aid intended for the conventional electricity from the national grid. According to a recent study [32], on average, the total cost in Algeria of a technically and technologically

reliable stand-alone photovoltaic system producing 5.5 kWh costs around 13 421 €. The estimated total cost of the whole installation increases linearly with the electrical load retained by users. An increase of 0.5 kWh in the supply load results in an additional investment of almost 1 200 €.

After analyzing the subsidies, it was found that the state can completely cancel the subsidies for conventional electricity by replacing them with a «Megasun» type solar water heater and a stand-alone photovoltaic system. The size of this system varies according to the climatic region. The financial assistance, corresponding to the first consumption mode, will cost between 13 036.91 € et 32 887.63 €. The most suitable regions, ranked according to merit, are M'sila, Naâma, Biskra, Bechar and, lastly, the Drabla

Table 5. State financial aid required to eliminate subsidies of the national grid electricity.

Climate zone	First mode of energy consumption			Second mode of energy consumption		
Setif	Subsidies for thermal rehabilitation measures are **quite sufficient**			Subsidies for thermal rehabilitation measures are **quite sufficient**		
M'sila	Grant for rehabilitation measures + Grant of 461.76 € equivalent to 4 115.50 kWh/year i.e. to			Subsidies for thermal rehabilitation measures are **quite sufficient**		
	11.27 kWh/day of PV electricity which costs **27 514 €**	or	3062.93 kWh/year from the solar water collector which costs **6 000 €** and a PV system of 2.88 kWh/day which costs **7 036.91 €**			
Bechar	Grant for rehabilitation measures + Grant of 656.73 € equivalent to 5 853.21 kWh/year i.e. to			Grant for rehabilitation measures + subsidy of 710.37 € equivalent to 6 331.28 kWh/year or 2 633.51 Thermie/ year and 6 263. 22 kWh/year, i.e. the subsidy of		
	16.04 kWh/day of PV electricity which costs **39 131 €**	or	3062.93 kWh/year from the solar water collector which costs **6 000 €** and a PV system of 7.64 kWh/day which costs **18 654.18 €**	17.34 kWh/day of PV electricity which costs **42 327.35 €**	or	solar water collector which costs **6 000 €** and a PV system of 17.16 kWh/day which costs **41 872.29 €**
Biskra	Grant for rehabilitation measures + Grant of 655.28 € equivalent to 5 840.29 kWh/year i.e. to			Grant for rehabilitation measures + subsidy of 832.98 € equivalent to 7 424.06 kWh/year or 2 633.51 Thermie/ year and 7 356 kWh/year, i.e. the subsidy of		
	16 kWh/day of PV electricity which costs **39 045 €**	or	3062.93 kWh/year from the solar water collector which costs **6 000 €** and a PV system of 7.61 kWh/day which costs **18 567.79 €**	20.34 kWh/day of PV electricity which costs **49 633.06 €**	or	solar water collector which costs **6 000 €** and a PV system of 20.15 kWh/day which costs **49 178.00 €**
Naâma	Grant for rehabilitation measures + Grant of 570.51 € equivalent to 5 084.76 kWh/year i.e. to			Grant for rehabilitation measures + subsidy of 225.04 € equivalent to 2 005.70 kWh/year or 2 633.51 Thermie/ year and 1 937.64 kWh/year, i.e. the subsidy of		
	13.93 kWh/day of PV electricity which costs **33 993.80 €**	or	3062.93 kWh/year from the solar water collector which costs **6 000 €** and a PV system of 5.54 kWh/day which costs **13 516.77 €**	5.49 kWh/day of PV electricity which costs **13 408.99 €**	or	solar water collector which costs **6 000 €** and a PV system of 5.31 kWh/day which costs **12 953.93 €**
Drabla	Grant for rehabilitation measures + Grant of 794.91 € equivalent to 7 084.76 kWh/year i.e. to			Subsidies for thermal rehabilitation measures are **quite sufficient**		
	19.41 kWh/day of PV electricity which costs **47 364.66 €**	or	3062.93 kWh/year from the solar water collector which costs **6 000 €** and a PV system of 11.02 kWh/day which costs **26 887.63 €**			
Mohamadia	Subsidies for thermal rehabilitation measures are **quite sufficient**			Grant for rehabilitation measures + subsidy of 109.27 € equivalent to 973.88 kWh/year or 2 633.51 Thermie/ year and 905.81 kWh/year, i.e. the subsidy of		
				2.67 kWh/day of PV electricity which costs **6 510.84 €**	or	solar water collector which costs **6 000 €** and a PV system of 2.48 kWh/day which costs **6 055.78 €**

climatic region. These results remain valid even in the case of the second consumption mode, which corresponds to the climatic regions of Naâma and Mohamadia. In the climates of Bechar and Biskra, which are characterized by high levels of air conditioning, it will be very expensive to spend more than 40 000 €. In these circumstances, other alternatives need to be sought. The cost of the thermal rehabilitation is estimated at 17 167.99 €.

Return on investment «ROI» is a measure of the percentage return on investment by considering the amount of money that has been invested. The costs and the benefits of these future solutions will then need to be assessed. These will determine the viability of the used energy concepts. The change in this indicator number, expressed by the number of months, depends on the ratio between the additional cost multiplied by 12 and the annual financial gain. By definition, the extra cost is the difference between the final price (estimated investment cost + final annual electricity bill) and the initial price (initial annual electricity bill). The annual financial gain is calculated as the difference between the initial and the final electricity bill. As shown in Table 6, the results for the first case yielded the following estimates.

The return on investment is favorable, very acceptable and sometimes attractive, especially for climatic regions similar to Setif and Drabla. But, in the second case, the return on investment is unsuitable in most climatic sites, the financial gain is generally very low compared with the additional cost, ranging from 1.12% to 3.08%. On the contrary, the financial profitability is acceptable in Biskra and under climatic conditions that are similar to those of this region, but it is less so for the Bechar site.

If the investment covers, in addition to the rehabilitation of the building envelope, a solar water heater and a stand-alone photovoltaic system, the results give the following estimates, as shown in Table 7.

According to the results, the cost-effectiveness of the involved measures can be considered very acceptable, but on the condition that the solar battery bank has a satisfactory lifetime. Even though solar batteries have a very limited lifespan, typically between 5 and 10 years (this is the case for AGM solar batteries, for example), the adoption of these energy concepts is still economically and financially viable. In more complicated circumstances, and for greater profitability, the user should select high-performance solar batteries such as gel batteries, which withstand an average of 900 cycles, or lithium-ion batteries, which offer the greatest durability, with up to 3000 cycles, representing up to 15 years of use. Furthermore, for the second consumption mode, the subsidy method did not bring a return on financial expenditure, but it did allow a significant reduction in annual energy requirements.

Table 6. Return on Investment from the thermal rehabilitation of the house

Climatic region	Initial electricity bill (€)	Electricity bill for the energy-saving house (€)	Annual financial gain (€)	Extra cost (€)	Annual financial gain compared to the extra costs (%)	Return on investment		
						Number of years	Number of months	Number of days
Case of the first consumption mode								
Setif	8 106.60	2 140.01	5 966.59	11 201.40	53.27	1	10	16
M'sila	5 867.08	1 517.84	4 349.24	12 818.75	33.93	2	11	11
Bechar	5 915.55	1 721.53	4 194.02	12 973.97	32.33	3	1	4
Biskra	5 615.63	1 666.09	3 949.54	13 218.45	29.88	3	4	5
Naâma	6 671.77	1 771.43	4 900.34	12 267.65	39.94	2	6	1
Drabla	9 253.57	2 460.55	6 793.02	10 374.97	65.47	1	6	10
Mohamadia	4 303.76	1 200.71	3 103.05	14 064.94	22.06	4	6	12
Case of the second consumption mode								
Setif	340.00	135.84	204.16	16 963.83	1.20	83	1	3
M'sila	347.24	156.77	190.47	16 977.52	1.12	89	1	19
Bechar	2 248.30	890.28	1 358.02	15 809.97	8.59	11	7	21
Biskra	3 175.65	1 012.90	2 162.75	15 005.24	14.41	6	11	8
Naâma	965.65	404.96	560.69	16 607.30	3.38	29	7	13
Drabla	340.33	121.12	219.21	16 948.78	1.29	77	3	24
Mohamadia	741.25	336.87	404.38	16 763.61	2.41	41	5	14

Table 7. Return on investment by thermally renovating the house and integrating a stand-alone photovoltaic system and solar hot water.

Climatic region	Initial electricity bill (€)	Electricity bill for the energy-saving house (€)	Annual financial gain (€)	Extra cost (€)	Annual financial gain compared to the extra costs (%)	Return on investment		
						Number of years	Number of months	Number of days
Case of the first consumption mode								
Setif	8 106.60	2 140.01	5 966.59	11 201.40	53.27	1	10	16
M'sila	5 867.08	1 517.84	4 349.24	25 855.66	16.82	5	11	10
Bechar	5 915.55	1 721.53	4 194.02	37 628.15	11.14	8	11	20
Biskra	5 615.63	1 666.09	3 949.54	37 786.24	10.45	9	6	24
Naâma	6 671.77	1 771.43	4 900.34	31 784.42	15.41	6	5	25
Drabla	9 253.57	2 460.55	6 793.02	43 262.60	15.70	6	4	13
Mohamadia	4 303.76	1 200.71	3 103.05	14 064.94	22.06	4	6	12
Case of the second consumption mode								
Setif	340.00	135.84	204.16	16 963.83	1.20	83	1	3
M'sila	347.24	156.77	190.47	16 977.52	1.12	89	1	19
Bechar	2 248.30	890.28	1 358.02	63 682.26	2.13	46	10	22
Biskra	3 175.65	1 012.90	2 162.75	70 183.24	3.08	32	5	28
Naâma	965.65	404.96	560.69	35 561.23	1.58	63	5	2
Drabla	340.33	121.12	219.21	16 948.78	1.29	77	3	24
Mohamadia	741.25	336.87	404.38	28 819.39	1.40	71	3	7

CONCLUSION

Energy products, including electricity and gas, took the lion's share of the state budget allocated to subsidies, accounting for 85% of total subsidies. In 2021, the average selling price of natural gas on international markets (5.8 $ per unit of measurement) was 30 times higher than the local price (0.19 $ per unit of measurement). To deal with this distressing problem, the conclusions reached lead us to deduce that the current subsidy system will not have to be fully maintained. Reducing or eliminating electricity subsidies is a complex process that requires careful planning and a systematic approach. It first necessitated an analysis of existing subsidies by identifying their cost and impact on the national budget. The reasons for reducing or eliminating subsidies, the proposed alternatives, the economic consequences including the impact on electricity prices and the adjustment of policies according to needs and concerns have become of paramount importance. It is preferable to abolish a large proportion of these subsidies and then offset them by adopting other incentives such as :

- Subsidizing the financial costs of integrating passive architectural measures, while carrying out a rehabilitation or even a thermal retrofit in favor of non-energy-efficient buildings. This mechanism presents a basic solution. By adopting these rehabilitation measures, unsubsidized energy bills are lower than those corresponding firstly to a conventional home without thermal rehabilitation and secondly to subsidized bills.
- Promoting and relaunching a subsidy program for solar water heaters.
- Adopting a subsidy program for residential photovoltaic systems, which appears to be a major challenge for environmentally sustainable urban development.
- Raising public awareness, highlighting the importance of simple gestures and energy-saving measures, and promoting new ideas or solutions to this problematic situation.

Whatever the energy consumption mode, the subsidies allocated to thermal rehabilitation are largely sufficient in the case of housing located in climatic regions similar to Setif. This means that subsidies for conventional grid electricity can be permanently eliminated and offset. This result is also confirmed for buildings, subject to the first consumption mode and corresponding to climatic regions similar to that of Mohamadia. The same conclusion can be drawn for buildings that are subject to the second consumption mode, but which correspond to climatic regions similar to those of Drabla and M'sila. For the first mode, the payback period of the operation is very attractive, estimated at less than 2 years in Sétif and 4.5 years for the Mohamadia region. On the other hand, in all other climatic regions, the return on investment, which covers the thermal rehabilitation operation, a solar water heater and a stand-alone

photovoltaic system, is still attractive if the first consumption mode is followed. However, the return on investment, covering the thermal rehabilitation operation, is very favorable in the case of the climatic regions of Biskra and globally acceptable in the case of climatic regions similar to those of Bechar. In the remaining cases, the return on investment has not lived up to expectations.

AUTHORSHIP CONTRIBUTIONS

Authors equally contributed to this work.

DATA AVAILABILITY STATEMENT

The authors confirm that the data that supports the findings of this study are available within the article. Raw data that support the finding of this study are available from the corresponding author, upon reasonable request.

CONFLICT OF INTEREST

The author declared no potential conflicts of interest with respect to the research, authorship, and/or publication of this article.

ETHICS

There are no ethical issues with the publication of this manuscript.

STATEMENT ON THE USE OF ARTIFICIAL INTELLIGENCE

Artificial intelligence was not used in the preparation of the article.

NOMENCLATURE

Con_{Env}	Energy consumption due to the building envelope (Wh)
$Hlos_{Ventilation}$	Heat loss from the ventilation system and each element (W/K)
Con_{DHW}	Average energy requirement for daily water heating (Wh)
Vol_{DHW}	Amount of domestic hot water required for the user's use (liters).
T_{DHW}	Temperature of the domestic hot water (°C)
T_{CW}	Temperature of the cold water (°C)
$Nb_{Residents}$	Number of residents occupying the building
$\varphi_{Occupants}$	Heat flux released by the human body per occupant (W)
Nb_{Days}	Number of days to be heated / cooling
$Dur_{Residents}$	Mean duration of the resident presence per occupant (hours per day)
$Hg_{Lighting/Other}$	Heat flux released by lighting, electrical appliances, devices and significant usage of equipment, cooking, etc (W)
$Dur_{In\ operation}$	Total run time of the lighting system and all equipment to be powered (hours per day)
n	Number of the transparent opening fronts
I_j	Daily solar irradiance incident on a unit surface of orientation j (Wh/m^2)
$A_n(j)$	Equivalent receiving surface (sum of surfaces of transparent opening fronts) of an orientation j
$Aop_n(j)$	Opening area (m^2) corresponding to the window n of the orientation j.
$Fs_n(j)$	Shading correction factor according to the orientation j.
S	Solar factor for windows n of the orientation j.
P_{Elec}	Electrical power of equipment (W).

Greek symbols

ρ	Water density (kg/liter)

REFERENCES

[1] Manić DJ, Komatina MS, Vučićević BS, Jovanović MP. Energy performance of single family houses in Serbia: analzsis of calculation procedures. Therm Sci 2019;23:1695–1705. [CrossRef]

[2] Šumarac DM, Todorović MN, Djurović-petrović MD, Trišović NR. Energy Efficiency of Residential Buildings in Serbia. Therm Sci 2010;14:97–113. [CrossRef]

[3] Djurov-Petrović MD, Lazarević AD, Kojičić BZ. Integration of the energy efficiency into the local development strategies. Therm Sci 2018;22:1297–1310. [CrossRef]

[4] Luo C, Gong Y, Weibin MA, Zhao J. Building energy efficiency in Guangdong province, China. Therm Sci 23 2019;23:3251–3262. [CrossRef]

[5] Canbolat AS, Bademlioglu AH, Saka K, Kaynakli O. Investigation of parameters affecting the optimum thermal insulation thickness for buildings in hot and cold climates. Therm Sci 2020;24:289 –2903. [CrossRef]

[6] Shahid M, Karimi MN. Optimization of energy transmittance through building envelope for hot dry climate. J Therm Eng 2022;8:595–605. [CrossRef]

[7] Aktemur C, Bilgin F, Tunckol S. Optimisation on the thermal insulation layer thickness in buildings with environmental analysis: an updated comprehensive study for Turkey's all provinces. J Therm Eng 2021;7:1239–1256. [CrossRef]

[8] Bentoumi L, Bouacida T, Bessaih R, Bouttout A. Impact of thermal insulation on energy consumption in buildings. J Therm Eng 2024;10:924–935. [CrossRef]

[9] Ziad S, Benoudjafer I, Benoudjafer I. Towards the use of natural thermal insulation on the exterior of vertical building walls in desert regions: A case study in the city of Bechar, Algeria. J Therm Eng 2024;10:308–320. [CrossRef]

[10] Canbolat AS. An integrated assessment of the financial and environmental impacts of exterior building insulation application. J Clean Prod 2024;435:140376. [CrossRef]
[11] Dorri A. Energy Efficiency Analysis in Korça Regional Hospital. Int J Innovative Technol Interdiscip Sci 2023;6:1121−1129. [CrossRef]
[12] Adamczyk J, Dylewski R, Sobierajewicz P. Ejconomic and ecological benefits of thermal insulation of external partitions depending on the temperature in residential premises. J Clean Prod 2023;384:135622. [CrossRef]
[13] Dylewski R, Adamczyk J. Economic and ecological indicators for thermal insulating building investments. Energy Build 2012;54:88−95. [CrossRef]
[14] Adamczyk J, Dylewski R. The impact of thermal insulation investments on sustainability in the construction sector. Renew Sustain Energy Rev 2017;80:421−429. [CrossRef]
[15] AIE. Fossil Fuels Consumption Subsidies 2022. Available at: https://www.connaissancedesenergies.org/energies-fossiles-les-subventions-mondiales-la-consommation-ont-atteint-un-niveau-record-en-2022-240426#notes. Accessed on 5 Mar 2026.
[16] Finon D. Les subventions à l'énergie dans le monde : leur ampleur, leur efficacité et leur nécessaire recentrage. Available at: https://inis.iaea.org/records/zbbry-6nb11/files/43038274.pdf?download=1. Accessed on 5 Mar 2026.
[17] Benkhelifa A. Thermo-aéraulique d'un bâtiment multizone & Influence de la compacité par rapport à la taille des murs à forme constante. Available at: http://dspace.univ-tiaret.dz/bitstream/123456789/14619/1/Th%C3%A8se%20de%20Doctorat%20Benkhelifa%20Abdelaziz%20%20%2008%20juin%202024.pdf. Accessed on 5 Mar 2026.
[18] Bensaha A. Exploitation d'énergies renouvelables pour la conception d'un habitat durable dans un site isolé en zone semi-aride : Cas de l'Algérie, Ph. D. thesis, Amar Telidji University, Laghouat, Algeria, 2021
[19] Benkhelifa A, Bekkouche SMA, Allaoui T, Cherier MK, Hamdani M, Mihoub R, et al. Application of the building height concept to energy-efficient heating and cooling for Saharan buildings. Int Inf Eng Technol Assoc 2022;80:71−78. [CrossRef]
[20] Bendara S, Bekkouche SMA, Benouaz T, Belaid S, Hamdani M, Cherier MK, et al. Energy efficiency and economic insulation thickness according to the compactness measure case of a studio apartment under Saharan weather conditions. J Solar Energy Eng2017;141:1−11. [CrossRef]
[21] Belgherras S, Bekkouche SMA, Benouaz T, Benamrane N. Prospective analysis of the energy efficiency in a farm studio under Saharan weather conditions. Energy Build 2017;145:342−353. [CrossRef]
[22] Bekkouche SMA, Benouaz T, Hamdani M, Cherier MK, Yaiche MR, Benamrane N. Diagnosis and comprehensive quantification of energy needs for existing residential buildings under Sahara weather conditions. Adv Build Energy Res 2017;11:37−51. [CrossRef]
[23] Kadraoui H, Bekkouche SMA, Chikhaoui A. Analysis of energy consumption for Algerian building in extreme North-African climates. Int J Sustain Energy Plan Manag 2019;19:45−58.
[24] Densité de l'eau en fonction de la température. Available at: http://www.atomer.fr/1/1-densite-eau.html. Accessed on 5 Mar 2026.
[25] Kottek M, Grieser J, Beck C, Rudolf B, Rubel F. World Map of the Köppen-Geiger climate classification updated. Meteorol Z 2006;15:259−263. [CrossRef]
[26] Wikipédia. Classification de Köppen. Available at: https://fr.wikipedia.org/wiki/Classification_de_K%C3%B6ppen, Accessed on 5 Mar 2026.
[27] Belda M, Holtanová E, Halenka T, Kalvová J. Climate classification revisited: from Köppen to Trewartha. Clim Res 2014;59:1−13. [CrossRef]
[28] ADEME. Comment garder son logement frais en été ?. Available at: https://www.netatmo.com/fr-fr/comfort-guide/air-conditioning-ideal-temperature. Accessed on 5 Mar 2026.
[29] Prix de l'électricité dans le monde : où se situe la France?. Available at: https://www.fournisseurs-electricite.com/contrat-electricite/prix/monde. Accessed on 5 Mar 2026.
[30] GlobalPetrolPrices. Algérie prix du gaz naturel. Available at: https://fr.globalpetrolprices.com/Algeria/natural_gas_prices/. Accessed on 5 Mar 2026.
[31] Bekkouche SMA, Djeffal R, Cherier MK, Hamdani M, Younsi Z, Al-Saadi S, et al. Experimental performance and cost-effectiveness of a combined heating system under saharan climate. Building 2023;11:1−27. [CrossRef]
[32] Morceli A, Temmar A. Taux et possibilités d'intégration de l'énergie photovoltaïque: Application à deux maisons individuelles à faible et à forte performance énergétique. Avaialble at: https://dspace.univ-ghardaia.edu.dz/xmlui/handle/123456789/9003. Accessed on 5 Mar 2026.

J Ther Eng, Vol. 12, No. 2, pp. 784−801, March, 2026

Journal of Thermal Engineering
Web page info: https://jten.yildiz.edu.tr
DOI: 10.14744/thermal.0001119

Research Article

Numerical analysis of two-phase flow in u-bend pipes: effects of curvature, and pipe orientation on pressure drop and liquid hold-up

Md. Zahid HASAN[1], Dipayan MONDAL[1,*], Mihir Ranjan HALDER[1]

[1]*Department of Mechanical Engineering, Khulna University of Engineering & Technology, Khulna, 9203, Bangladesh*

ARTICLE INFO

Article history
Received: 11 January 2025
Revised: 07 April 2025
Accepted: 12 April 2025

Keywords:
Two-phase Flow; U-bend Pipe; Pressure Drop; Phase Distribution; Liquid hold-up; VOF Model

ABSTRACT

This work investigates the effects of bend curvature, pipe orientation, and bend angle on two-phase flow dynamics in U-bend tubes using a numerical approach. Two-phase flow in U-bend tubes introduces secondary flows, significantly impacting pressure drops and phase distributions. This study employs numerical simulations using ANSYS Fluent 2020 R1® to analyze the effects of bend curvature and pipe orientation (horizontal and vertical) on flow behavior, with water and air as the working fluids at an inlet velocity of 3 m/s. The volume of fluid model was employed to capture phase interactions and this is the novelty of this present work as in the previous works, the use of this model was absent. Results reveal a wavy stratified flow with secondary vortices caused by centrifugal forces in the bend. Pressure losses of 1186 Pa and 1415 Pa were observed for 50% and 70% water volume fractions in the vertical orientation, while horizontal orientation exhibited negligible losses for 50% and 80 Pa for 70%. Consequently, the pressure losses were found higher in vertical orientations, with 50% and 70% water volume fractions, respectively. The pressure drop is observed more with a higher bend angle along the bend. This Increased liquid hold-up and water accumulation at the bend were observed with higher water fractions, contributing to greater pressure drops. These findings are critical for applications in oil and gas, chemical processing, and refrigeration, highlighting the need for further studies on flow patterns and alternative geometries. The flow pattern as well as can significantly affect the overall flow behavior.

Cite this article as: Hasan MZ, Modal D, Halder MR. Numerical analysis of two-phase flow in u-bend pipes: effects of curvature, and pipe orientation on pressure drop and liquid hold-up. J Ther Eng 2026;12(2):784−801.

INTRODUCTION

This study aims to investigate the effects of curvature, orientation, and phase interactions on pressure drop and liquid hold-up in U-bend pipes. Multiple phases of flowing fluid are observed in different industries such as refrigeration, oil and gas, etc. In these areas, phases can change from one state to another, or two different types of phases such as gas-liquid, liquid-solid, or solid-gas can be observed. For the flowing of the phases, straight pipes as well as different types of bend are used such as 90-degree

***Corresponding author.**
*E-mail address: dipkuet@me.kuet.ac.bd

This paper was recommended for publication in revised form by Editorin-Chief Ahmet Selim Dalkılıç

Published by Yıldız Technical University Press, İstanbul, Turkey
Yıldız Technical University. This is an open access article under the CC BY-NC license (http://creativecommons.org/licenses/by-nc/4.0/).

bend angle, and U-bend pipe. In most cases, U-bend pipe is used extensively. The bending curvature, orientations of the pipe, phase distributions through the pipe, etc. are significant factors in analyzing the fluid flow behavior. Hence, the present work is performed based on this vital factor. Before, the extensive literature review was conducted to work on specific research gaps which have been discussed in the preceding parts. Hayashi et al. [1] experimentally investigated the pressure drop of air-water two-phase flow in a horizontally oriented U-bend pipe. Dassler and Janoske [2] investigated the effect of the radius of curvature on the pressure drop both experimentally and numerically for rectangular-shaped U-bends placed horizontally. However, Pham et al. [3] performed a numerical investigation at four different orientations of the pipe. Again, placing a horizontal-vertical plane, Hayashi et al. [4] checked the effect of bend on a void fraction of two-phase flow. Similarly, Yadav and Mehta [5] investigated the influence of the radius of curvature on a horizontally oriented mini-channel U-bend pipe. In contrast, Usui et al. [6] analyzed two-phase flow behavior in an inverted U-bend pipe. Da Silva Lima [7] made an analysis of two-phase flow in three pipe orientations such as horizontal, vertical up-flow, and vertical down-flow using R134a refrigerant. Deng et al. [8] used nitrogen-water two phases to perform flow analyses at the horizontal position. Aliyu et al. [9] utilized serpentine construction positioning horizontally with a larger diameter of U-bend pipe to analyze gas-liquid two-phase flow behavior. Monachen et al. [10] numerically investigated air-water flow behavior in a straight channel unlikely the U-bend pipe.

De Moerloose et al. [11] performed a simulation of the effect of the liquid viscosity, wall wetting, and mass flow through a horizontal U-bend pipe using an air-water mixture. However, Ma et al. [12] investigated the perturbation length of vertical U-bend pipe using the air-water mixture. Unlike the literature, Mondal et al. [13] and Ghosh et al. [14] used single-phase flow and oil-water mixture in a U-bend pipe respectively. Another numerical work performed by Bandyopadhay and Das [15] using a U-bend pipe at a horizontal position used air-water in two phases. A comparative investigation was conducted by Andrzejczyk and Muszynski [16] between U-bend and straight pipes at vertical positions. Ogunsesan et al. [17] developed a CFD modeling for double elbow geometry for air-water two-phase flow. Pressure drop analysis of air-water two-phase flow through a 90-degree vertical pipe was performed by Saber and Maree et al. [18]. Using an air-water mixture, Zahedi and Rad [19] investigated both numerically and experimentally to observe the flow behavior in a 90-degree bend pipe. On the other hand, Lopez et al. [20] used a horizontal U-bend pipe to observe the liquid film behavior of the air-water annular flow.

Lu et al. [21] experimentally investigated an air-water mixture through a straight channel. Abdulkadir et al. [22] investigated how liquid film thickness changed at the U-bend at different angles by using an air-water mixture. Nouri et al. [23] numerically investigated oil-water two-phase flow through the straight channel. Mahmood et al. [24] also used a straight channel to investigate the effect of two-phase flow development incorporating an expansion device. Karademir et al. [25] comprehensively reviewed two-phase flow behavior using an inclined tube. Yaqop [26] experimentally and numerically studied the pressure drop of air-water two-phase flow through straight flattened tubes. Hamad et al. [27] investigated experimentally and compared the data with numerical work using a kerosene-water two-phase flow in a 90-degree bend tube instead of an air-water mixture. Mondal et al. [28] used Silicon oil and air-water to understand the flow behavior in an intermediate vertical tube. Air-water and air-water-oil three-phase flows were observed by Spedding et al. [28] in a 90-degree bend pipe. Effects of heat transfer using two different refrigerants along with nano-particles in a U-bend pipe were investigated by Islam et al. [29].

Jiang et al. [30] numerically investigated two oil-water phases in a U-bend pipe using core annular flow. Ooms et al. [31] performed a numerical investigation of core annular flow in a 90-degree bend pipe. Ma et al. [32] examined ice slurry flow through a horizontally placed elbow pipe. Onal et al. [33] investigated heat transfer and pressure drop characteristics of two-phase flows using helical coils. Govier and Omer [34] investigated air-water two-phase flow to observe pressure drop, and liquid holdup in a horizontal pipe. Similarly, friction characteristics and two-phase flow patterns were investigated in a smooth tube by Wang et al. [35]. Again, Wang et al. [36] investigated the return bend effect of a horizontally placed tube using the air-water mixture. The oil-water two-phase flow was investigated in a microchannel by Salim et al. [37]. Al-Hadhrami et al. [38] experimentally investigated air-water-oil three-phase flow in a straight pipe to study the flow regimes and pressure gradient. Patpatiya et al. [39] investigated numerically two-phase flow in a T-junction tube placed horizontally. Lightstone et al. [40] experimentally and numerically investigated air-water two-phase flow in a horizontal smooth tube with dividing sections. Nizovtseva et al. [41] numerically observed a two-phase flow in a closed bioreactor loop. Verma and Ghosh [42] compared gas-liquid and liquid flows through mini-channel tubes. Meanwhile, Mondal et al. [43,44], conducted the parallel, counter, and cross-flow water-to-air u-bend heat exchanger and also a cooling system adopted by the vapor absorption system, while Mondal and Islam [45] reported another study for intermittent system adopted by ammonia absorption refrigeration system. To fit the refrigerants in HVAC&R systems, Mondal et al. [46-49] and Islam et al. [29], measured the transport properties as well as the heat transfer characteristics of several refrigerants that will take in the future revolution of industries. Moreover, Das et al. [50] and Arefin et al. [51] evaluated the thermodynamic analysis of the dual and single cascading vapor compression cycle, respectively, for the low-temperature application. Moreover, Bari et al. [52] presented the

analysis of heat transmission in a refrigerant compartment, while Shahariar et al. [53] represented the performance of LiCl desiccant dehumidifier. Akinshilo and Sobamowo [54] analyzed pipe flow, heat transfer characteristics, and entropy generation in fourth-grade fluid with temperature dependent viscosities and heat generation using the regular perturbation method. The results showed ways to advance the analysis and process behavior of the fourth-grade fluid flow and steady-state heat transfer processes such as those found in petroleum, polymer, food manufacturing, and paint industries. Akinshilo and Olaye [55] investigated the flow and heat transfer of a non-Newtonian Erying Powell fluid flow in a pipe. Obtained solutions may be used to advance studies in thin film flow, polymer processing and paper production. Akinshilo and Sobamowo [56] studied the flow, thermal and concentration analyses of blood as a third grade with gold as nanoparticles through a porous channel using regular perturbation method. The outcomes can be utilized to advance the study of blood transport in porous channels with nanoparticles which acts as an effective drug delivery mechanism in the treatment of blood-related diseases. Sheikh et al. [57] investigated the combined influence of the nanoparticles and uniform magnetic field applied on the slip blood flow. The results revealed the augmentation of the pressure gradient and the magnetic parameter decreased the velocity value whilst the viscous dissipation augmentation increased the temperature.

According to the pipe orientations, the pressure, phase distribution, and liquid film thickness vary which has been observed through the above studies. From the above literature study, it can be said that the majority of the studies have been focused on the horizontal orientations of the U-bend tube. Additionally, some of the works have been done using other geometries while the U-bend tube is one of the most used channels in different industries mentioned before. Pressure drops, liquid hold-up, volume fractions, etc. have been solely investigated using horizontal orientation. Investigations on other orientations are needed to observed. The major research objective is to observe how pipe orientations can effectively influence different parameters during two-phase flow. Hence, two pipe orientations are numerically simulated to describe which orientation of the pipe can cause more pressure drop and influence other parameters. Though experimental analyses have been performed, numerical solutions can be viable and may be the best ones. So, in this present work, the numerical solution is hoped to replace the experimental ones. The novelty of this present work is to use the volume of fluid method for capturing the water-air phase interactions during the simulation. So, the present study is focused on the different pipe orientations of U-bend tubes notably vertical-horizontal and vertical to investigate the pressure variation, phase distribution, liquid thickness, and effect of bend angle on pressure variation at the bend in a U-bend pipe.

METHODOLOGY

The present work is performed using the finite volume method (FVM). This section explains the numerical techniques and models used to analyze two-phase flow in U-bend pipes, with an emphasis on how phase interactions, curvature, and orientation affect liquid hold-up and pressure drop.

Numerical Model

The Reynolds Averaged Navier-Stokes (RANS) equations are utilized in turbulence modeling. For the steady-state flow conditions, the Reynolds Averaged Navier-Stokes continuity, momentum equations are as follows [58],

Continuity equation:

$$\frac{\partial}{\partial x_i}(\rho u_i) = 0 \tag{1}$$

Momentum equation:

$$\frac{\partial}{\partial x_j}(\rho u_i u_j) = -\frac{\partial p}{\partial x_i} + \frac{\partial}{\partial x_j}\left[\mu\left(\frac{\partial u_i}{\partial x_j} + \frac{\partial u_j}{\partial x_i} - \frac{2}{3}\delta_{ij}\frac{\partial u_l}{\partial x_l}\right)\right] + \frac{\partial}{\partial x_j}(-\rho\overline{u_i u_j}) \tag{2}$$

Where, ρ = density, and u_i, u_j = velocity.

Governing equations

The continuity, momentum, and volume fraction equations which are resolved throughout the numerical simulation are the governing equations for the volume of fluid model (VOF). The continuity equation has been used for the conservation of mass. The momentum equation is for the velocity of the water and air phases. Next, for incorporating and capture the two phase flow phenomenon, the volume fraction equations have been incorporated.

The continuity equation is as follows [23],

$$\nabla(\rho v)=0 \tag{3}$$

Where, ρ is the density of the mixture

The volume fraction equation [58],

$$\nabla.\left(\alpha_q \rho_q . \overrightarrow{v_q}\right) = 0 \tag{4}$$

Where, α_q = volume fraction.

Based on the following equation, the volume fraction equation is solved for the secondary phase but not for the main phase.

$$\sum_{q=1}^{n} \alpha_q = 1 \tag{5}$$

Momentum equation [58],

$$\nabla.(\rho v \vec{v}) = -\nabla p + \nabla.[\mu(\nabla\vec{v} + \nabla(\vec{v})^T)] + \rho\vec{g} + \vec{F} \tag{6}$$

Where, $\vec{v}$ = velocity, $\vec{F}$ = force.

In addition, wall adhesion and the continuum surface force model are solved for the introduction of surface

tension. Again, the surface tension is viewed as a continuous, three-dimensional effect rather than a boundary value in Brackbill et al.'s [59] continuum surface force model. Surface tension can be computed by adding a source term to the momentum equation. The normal forces are then taken into consideration, and the surface tension is treated as a constant along the surface to determine the source term's origin.

The pressure drops depending on the surface tension and the surface curvature radii taking in the orthogonal direction can be calculated as

$$p_2 - p_1 = \sigma(\frac{1}{R_1} + \frac{1}{R_2}) \tag{7}$$

Where p_2 and p_1 are the two pressures in the two fluids on either side of the interface.

Local gradients normal to the interface are used to calculate the surface curvature.

$$n = \nabla \alpha_q \tag{8}$$

Where n is the surface normal correlated to the gradient of q^{th} volume fraction. Now, the curvature is correlated by the divergence of the unit normal $\hat{n}$ [59].

$$\kappa = \nabla . \hat{n} \tag{9}$$

where, $\hat{n} = \frac{n}{|n|}$

The momentum equation for the surface tension inclusion is expanded to include the volume force as the source term and it is as follows,

$$F_{vol} = \sum_{pairsi\ j,i<j} \sigma_{ij} \frac{\alpha_i \rho_i \kappa_j \nabla \alpha_j + \alpha_j \rho_j \kappa_i \nabla \alpha_i}{\frac{1}{2}(\rho_i + \rho_j)} \tag{10}$$

For two-phase flows, the above volume force can be written as,

$$F_{vol} = \sigma_i j \frac{\rho \kappa_i \nabla \alpha_i}{\frac{1}{2}(\rho_i + \rho_j)} \tag{11}$$

Where, ρ is the volume averaged density.

The effect of wall adhesion is incorporated into the continuum surface force model by defining the contact angle between the fluid and the wall to the surface normal to the near wall and the surface normal can be denoted as,

$$\hat{n} = \widehat{n_w} cos\theta_w + \widehat{t_w} sin\theta_w \tag{12}$$

where, $\widehat{n_w}$ and $\widehat{t_w}$ are the unit vectors normal and tangential to the wall.

The RNG k-ε turbulence model is used. The transport equation of two fluid steady states is as follows,

$$\frac{\partial}{\partial x_i}(\rho k u_i) = \frac{\partial}{\partial x_j}\left(\alpha_k \mu_{eff} \frac{\partial k}{\partial x_j}\right) + G_k + G_b - \rho\varepsilon - Y_M + S_K \tag{13}$$

$$\frac{\partial}{\partial x_i}(\rho \epsilon u_i) = \frac{\partial}{\partial x_j}\left(\alpha_\varepsilon \mu_{eff} \frac{\partial \varepsilon}{\partial x_j}\right) + C_{1\varepsilon} \frac{\varepsilon}{k}(G_k + C_{3\varepsilon} G_b) - C_{2\varepsilon} \rho \frac{\varepsilon^2}{k} - R_\varepsilon + S_\varepsilon \tag{14}$$

Taking, $C_{1\varepsilon}$ = 1.42, $C_{2\varepsilon}$ = 1.68. Where, G_k is the turbulence kinetic energy due to the mean velocity gradients, G_b is the generation of turbulence kinetic energy due to buoyancy, Y_M is the contribution of the fluctuating dilatation in compressible turbulence to the overall dissipation rate, α_k is the inverse Prandtl number for k, α_ε is the inverse Prandtl number for ε, and S_K, S_ε are considered as the user-defined source term.

For near-wall treatment, standard wall function is used along with the k-ε turbulence model as this wall treatment is widely used for industrial applications. The equations are as follows,

Momentum equation,

$$U^* = \frac{1}{\kappa} ln(E y^*) \tag{15}$$

Where, U^*= dimensionless velocity, y^*= dimensionless distance from the wall.

$$U^* = \frac{U_P C_\mu^{1/4} K_P^{1/2}}{\tau_w / \rho} \tag{16}$$

$$y^* \equiv \frac{\rho C_\mu^{1/4} K_P^{1/2} y_P}{\mu} \tag{17}$$

Physical Domain

Two geometrical orientations namely vertical-horizontal and vertical have been used in this numerical investigation. These two orientations are widely used for industrial purposes. Hence, the pipe orientations are chosen. The length of the straight pipe is 560 mm, the bend radius is 125 mm, the pipe diameter is 28 mm, and these measurements were taken by Pham et al. [3]. Figure 1(a) shows the labeling of the U-bend tube. The dimension of the pipe starts at 0 mm from the inlet. Dividing the pipe into several parts, the axial position is used for the pressure variation axially of the pipe. The total axial length of the U-bend pipe is approximately 1512.7 mm and the end is at the outlet of the pipe. The curvature length is 392.7 mm which is calculated by π times the radius of the curvature of the bend portion. In this study, the position of the U-bend tube pipe is considered in two types of orientations: horizontal-vertical orientation and vertical orientation shown in Figure 1(b) and Figure 1(c), respectively.

Boundary Conditions and Solver Setting

The inlet face is divided into 30% air, 70% water, and 50% for both water and air, in order to enforce the inlet boundary criteria. The gauge pressure, which has a value of zero Pascal, is the outlet pressure. The atmospheric pressure, which has a value of 101325 pascals, is the operating

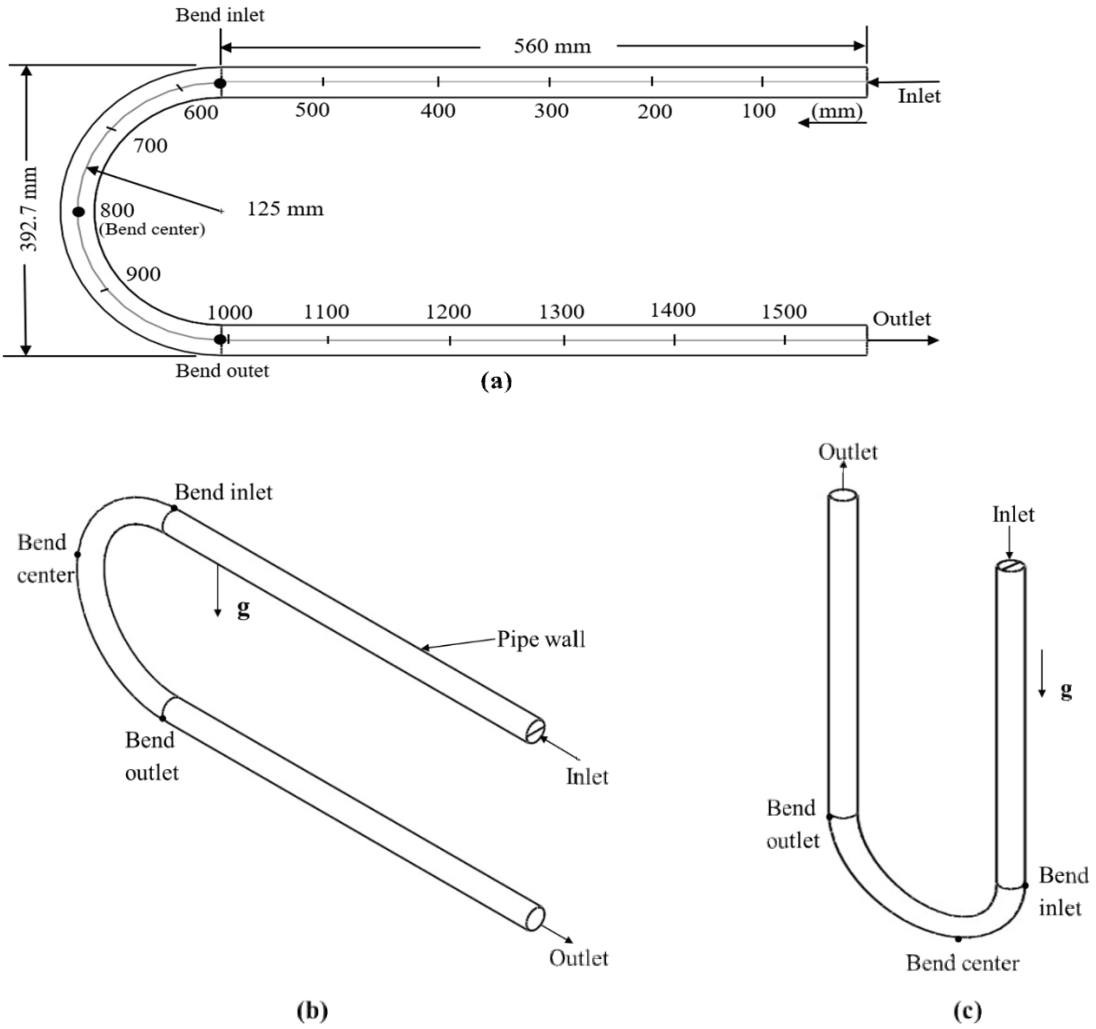

Figure 1. Illustration of the U-bend pipe: (a) geometry labeling, (b) horizontal-vertical orientation, and (c) vertical orientation.

pressure. The operational density of the lightest fluid air is selected as 1.225 (kg/m^3). Determining the volume fraction 1 at the split part of the inlet face yields an inlet velocity of 3 m/s for both water and air. To avoid slip between the air-water interface, the same velocity has been chosen for both fluids. The volume fractions are chosen to avoid complexity during the simulation. A brief description of the other boundary conditions is shown in Table 1 below.

The solver setup utilized for the numerical investigation is displayed in Table 2 along with a brief description. Applying a pressure-based solution, water and air are considered incompressible fluids. The pressure-based solution considers the fluids incompressible. Hence it is incorporated. Next, the gravitational acceleration in the negative z direction is used in the steady state condition (-9.81 m/s^2). Furthermore, the implicit volume fraction parameters with

Table 1. Boundary conditions for the U-bend pipe

Items	Description	Items	Description
Primary phase	Water	Wall condition	No slip stationary wall
Secondary phase	Air	Wall adhesion	90-degree contact angle
Water velocity, v_l	3 m/s	Surface tension, σ	0.072 N/m
Air velocity, v_a	3 m/s	Outlet	Pressure outlet
Volume of fractions, α	0.5, 0.7		

Table 2. Numerical setting for the investigation

Items	Description	
Solver type	Pressure Based Solver	
Condition	Steady State	
Gravity	On	
Multiphase model	Volume of Fluid	
Implicit body force	On	
Interface modeling	Sharp	
Turbulence model	k-ε (K-Epsilon)	
Near wall treatment	Standard wall functions	
Solver method	Pressure-velocity coupling: Coupled	
Initialization	Standard initialization	
Transient formulation	Pseudo Transient	
Residual	Continuity	10^{-2}
	Momentum	10^{-4}
	k	10^{-3}
	epsilon	10^{-2}
	Vf-air	10^{-3}
Spatial Discretization	Gradient	Least square cell-based, Green Gauss node-based
	Pressure	PRESTO
	Momentum	First order upwind
	Volume fraction	Compressive
	Turbulent kinetic energy and dissipation rate	First order upwind

the body force are implied because of the steady state. A sharp interface is taken for the stratified flow through the tube in order to capture the contact between the air and water phases. So, the volume of the fluid model has been chosen. Additionally, the coupled pressure-velocity technique with first-order upwind discretization is selected for improved convergence as the most economical solution. The reduced residuals make the solution more viable and less erroneous. However, in this present study, in spite of the present simulation's reduced residuals, the data obtained after all residuals remain constant for an extended period of time. Furthermore, the findings are derived based on the residuals being kept constant with reduced fluctuations after 1000 iterations. To avoid convergence errors, the constant values in the RNG k-e models have been modified as per the guidance of the theory. Furthermore, the findings revealed tendencies that were consistent with previous experimental studies. However, the two-phase flow simulations' complexity may have led to a convergence issue with smaller residuals.

Mesh Independency and Validation

After designing in the design software via ANSYS Fluent 2020 R1, the U-bend pipe is imported into the Meshing software. The U-bend pipe has been discretized into three-dimensional tetrahedron meshing. The unstructured tetrahedron meshing with patch-conforming mesh method has been applied. This is due to the fact that the tetrahedron meshing with the patch-conforming method requires less time than the more structured hexahedron mesh. However, Figure 2 shows the grid discretization of the U-bend pipe, while the mesh element size along with other details have been presented in Table 3.

The grid independence test is performed to ascertain whether or not the outcome is grid-dependent for the validation, while Figure 3 illustrates the mesh independence test. For element sizes of 1.25 mm and 1.50 mm with different numbers of mesh elements, the maximum water velocity

Table 3. Meshing elements

Items	Description
Type of Mesh	Tetrahedral
Mesh Method	Patch Conforming Method
Element Size	1.5 mm
No of Elements	2154936
No of Nodes	778390
Inflation Layer	8
First Layer Thickness	0.04mm
Wall Y^+	Min: 2.20, Max: 2.97

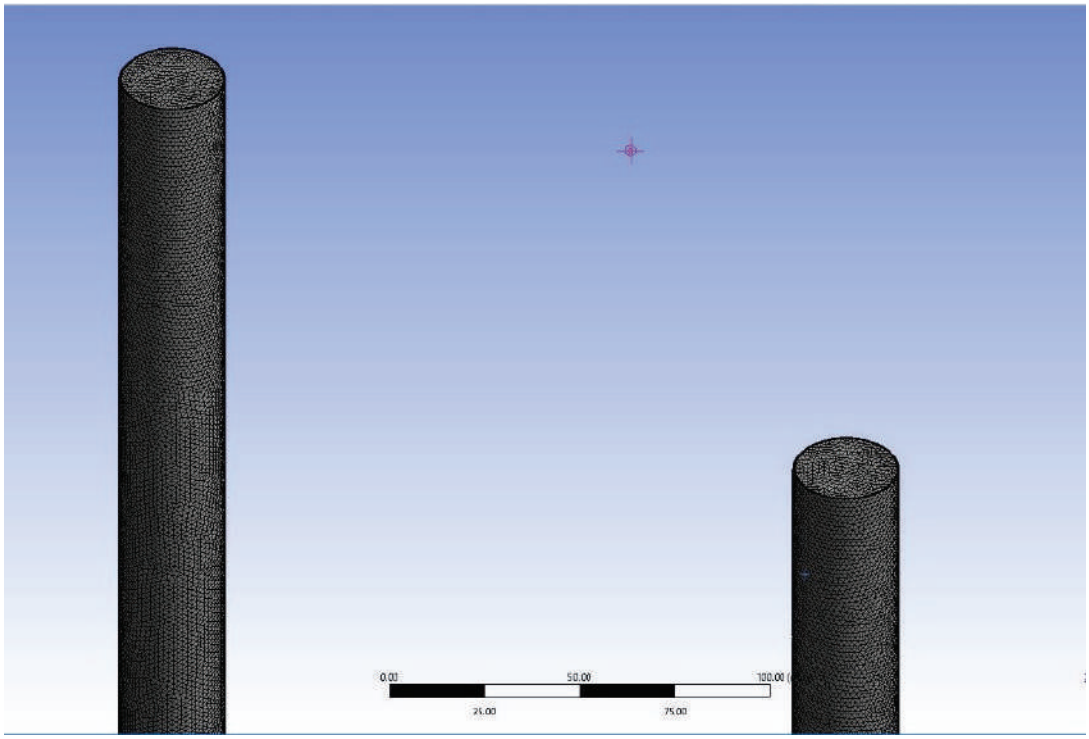

Figure 2. Grid discretization of the U-bend pipe.

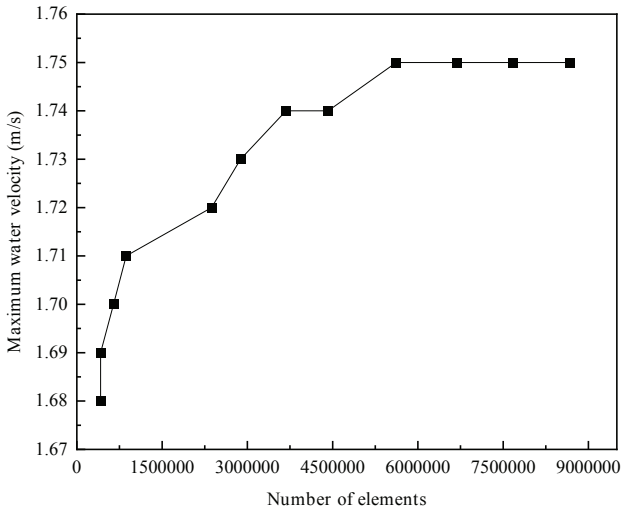

Figure 3. Grid independence test.

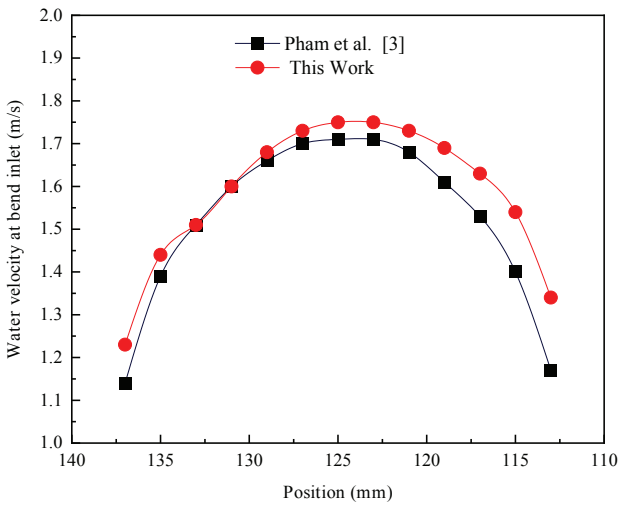

Figure 4. Numerical model validation.

of 1.75 m/s is investigated. For 1.25 mm and 1.50 mm, the outcomes are comparable. However, for a numerical solution that is computationally economical, the element size of 1.50mm is selected; otherwise, the computational cost would be high for the same result. Again, Figure 4 shows the model validation numerically. Validation is performed to increase the acceptability of the numerical analysis as well as the results. The SST k-ω turbulence model is used for the validation. The mixture model for the two-fluid models given by Pham et al. is used in the current study to verify the model while maintaining the same dimensions, flow inlet, and boundary conditions. With an average inaccuracy of 4.47%, the current work is verified against the earlier work by Pham et al. [3]. If the error percentage was higher, the results would have been more inaccurate. So, while considering the results, it has to be remembered that the results are 4.47% erroneous than the actual ones. This emphasizes the reliability of the model. The model can

generate more accurate results if the errors are less. A water velocity of 1.43 m/s, air velocity of 0 m/s, water volume fraction of 99.06%, and air volume fraction of 0.94% are the intake conditions for the validation task.

RESULTS AND DISCUSSION

Water Volume Fraction 50%

Figure 5 shows the flow pattern of 50% VOF of water both for the horizontal-vertical orientation, and vertical orientation, respectively. The stratified flow is observed by the water and air interaction both moving at velocities of 3 m/s which is similar according to Baker's flow map. Here, the water phase is deflected by the centrifugal force to the bend effect which is clearly seen in both orientations. However, the liquid deposition downstream of the vertical pipe is more than the horizontal one due to the effect of gravitational deceleration. This deposition of liquid can create obstacles to maintaining the flow from the outlet of the pipe. So, the velocity of the flowing fluids must be high

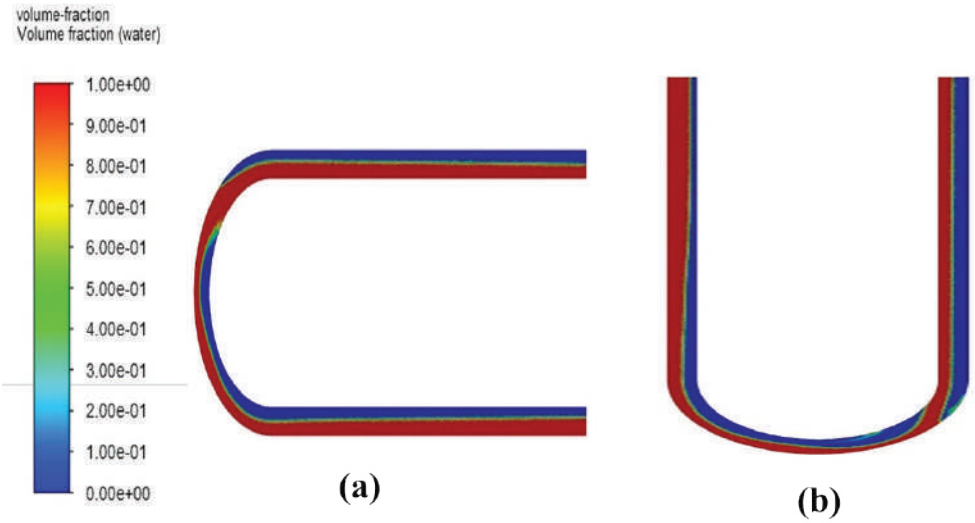

Figure 5. Flow pattern of 50% VOF of water: (a) horizontal-vertical orientation, and (b) vertical orientation.

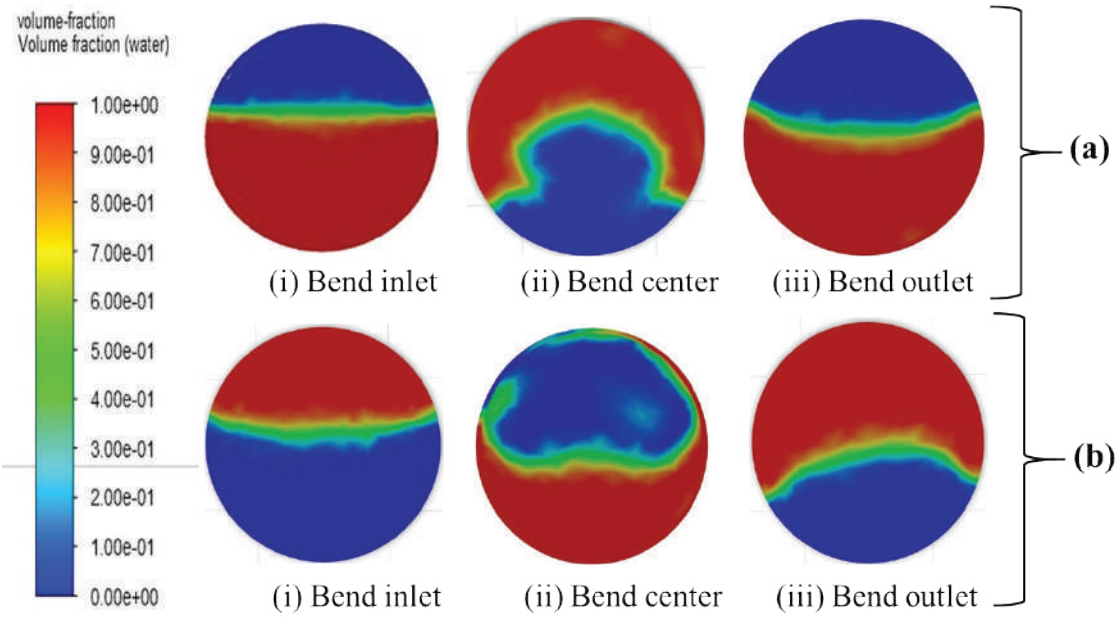

Figure 6. Phase distribution at the bend for 50% VOF of water: (a) horizontal-vertical orientation, and (b) vertical orientation.

enough to overcome this problem. Also, the flow behavior can show vorticity if the backflow pressure increases. Hence, the viscous effect is more at the downstream of the pipe than the upper stream.

Looking closely at Figure 6, it is evident at the bend's intake that there is a distinct interface between the phases of water and air, with more water distributed in the bottom half and air in the upper part for vertical-horizontal orientation and the opposite one is observed for the other orientation. The vertical pipe which has gravitational effect shows that the volume fraction of water is smaller to higher from bend inlet to bend outlet. However, the horizontal position shows quite a different view. The gravitational acceleration creates constricted passage at the inlet of the vertical position, unlike the horizontal position. Hence, these differences have occurred.

In Figure 7, the liquid holdup at the bend with a volume proportion of water of 50% has been depicted. After a fixed distance from the intake, the flow separation between the two phases occurs at both positions. The water phase has

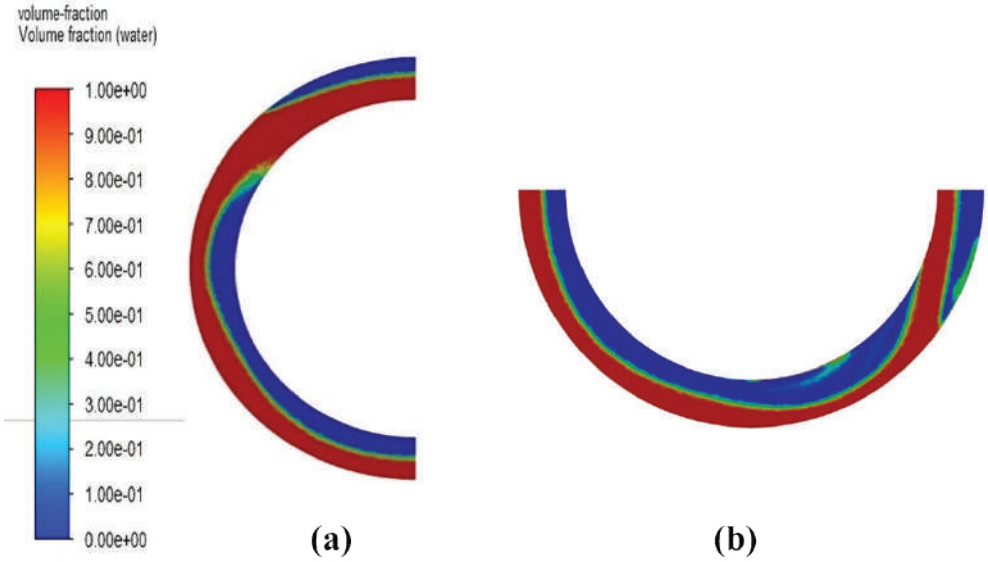

Figure 7. Liquid holdup for 50% VOF of water at the bend: (a) horizontal-vertical orientation, and (b) vertical orientation.

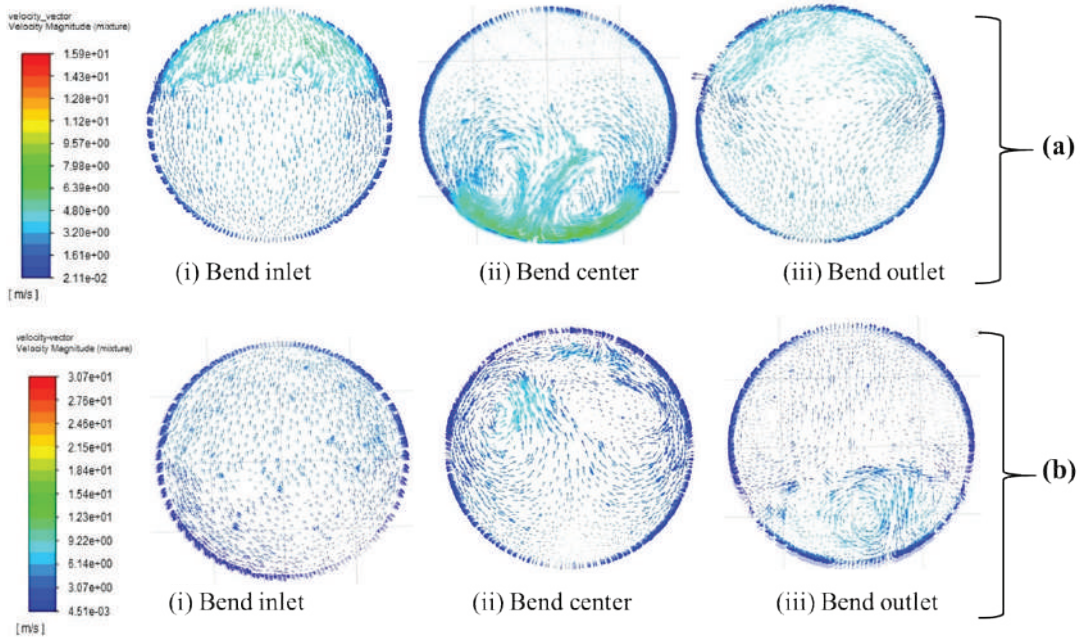

Figure 8. Velocity vector at the bend for 50% VOF of water: (a) horizontal-vertical orientation, and (b) vertical orientation.

splattered on the bends outside the wall, while the air phase flows towards the inner wall. Following flow separation, the liquid water is nearly equivalent to the air phase. Due to the separation of flow, the flow behavior shows vorticity and regions of wake. Hence, this causes more pressure losses throughout the pipe, unlike the straight pipe.

In Figure 8, the velocity vector is displayed at the bend. The flow at the bend inlet and center appears to be similar. The former shows smooth flow while the latter one vorticity called secondary flow. However, the velocity vector at the bend outlet of the vertical one shows discrepancies from the other one. This is perhaps due to the flow against gravity. The gravitational effect has less impact on the bend inlet and center for both orientations. However, the flow generates more vorticity in the horizontal position than the vertical one possessing a gravitational effect. Additionally, the velocity is higher at a bend of the vertical than the horizontal indicating more turbulence. The velocities are higher for the vertical pipe than the horizontal due to the gravitational effect in the former. The pressure distributions, shown in Figure 9, have given completely opposite results for both orientations. The static, dynamic, and total pressures in vertical orientation are more than the horizontal one. The static pressure seems to be lower in the horizontal orientation than in the vertical one. However, the dynamic pressure shows different outcomes. The constricted passage at the bend outlet of the horizontal position and at the bend

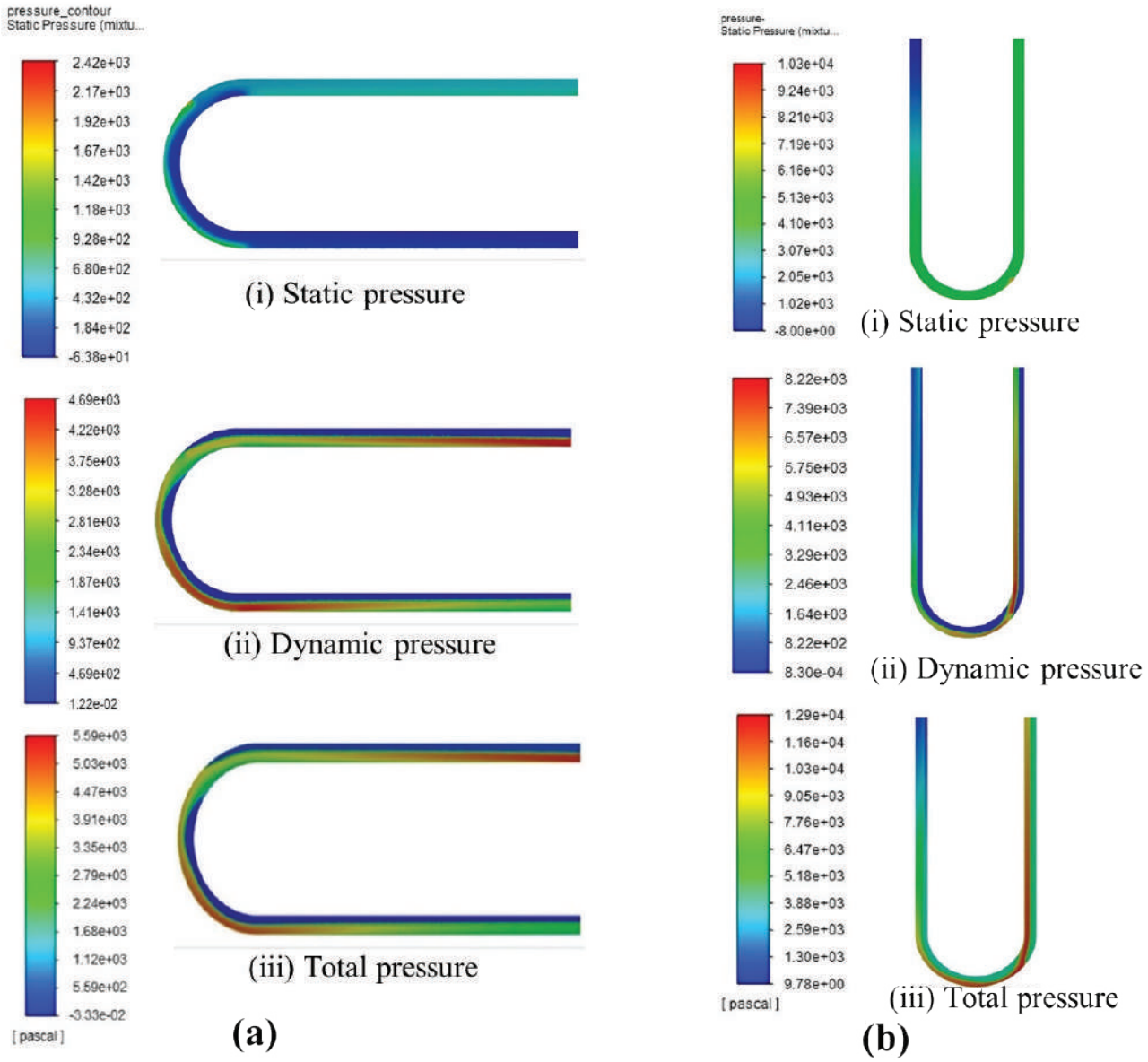

Figure 9. Variation of pressure along the U-bend tube for 50% VOF of water: (a) horizontal-vertical orientation, and (b) vertical orientation.

inlet of the vertical position generates more pressure. And, this has a significant effect on the total pressure as well.

Water Volume Fraction 70%

From Figures 10-14, the results have been shown for a 70% volume fraction of water. The results have given similar trends with the 50% volume fraction of water with the larger number. However, Figure 10 shows the flow pattern of 70% VOF of water both for the horizontal-vertical orientation, and vertical orientation, respectively, where the air-water interface gives a clear picture of wavy-stratified flow depicted in the figure. This is likely due to the similar flow pattern observed in Figure 5 with 50% VOF of water. However, the liquid occupies more portion of the pipe with 70% volume fraction than 50% volume fraction of water.

In Figure 11(a), the phase distribution at the bend inlet and outlet indicates similarity with Figure 6(a). And, air-water interface also matches the previous one. However, the bend center gives a different illustration. It is because it can be observed some tiny air-pockets for 70% VOF of water which is absent for 50% VOF. These air pockets can cause areas of lower pressure region and damage to the pipe. Again in Figure 11(b), the phase distribution of water is more as expected with the same phase distribution pattern with 50% VOF. But water droplets have been observed at the bend inlet unlike the Figure 5(b).

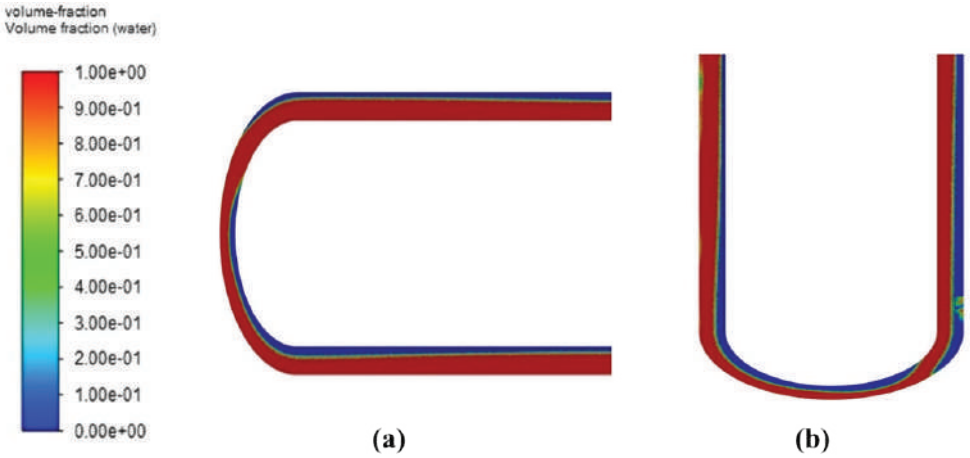

Figure 10. Flow pattern for 70% VOF of water (a) Horizontal-vertical, and (b)Vertical orientational.

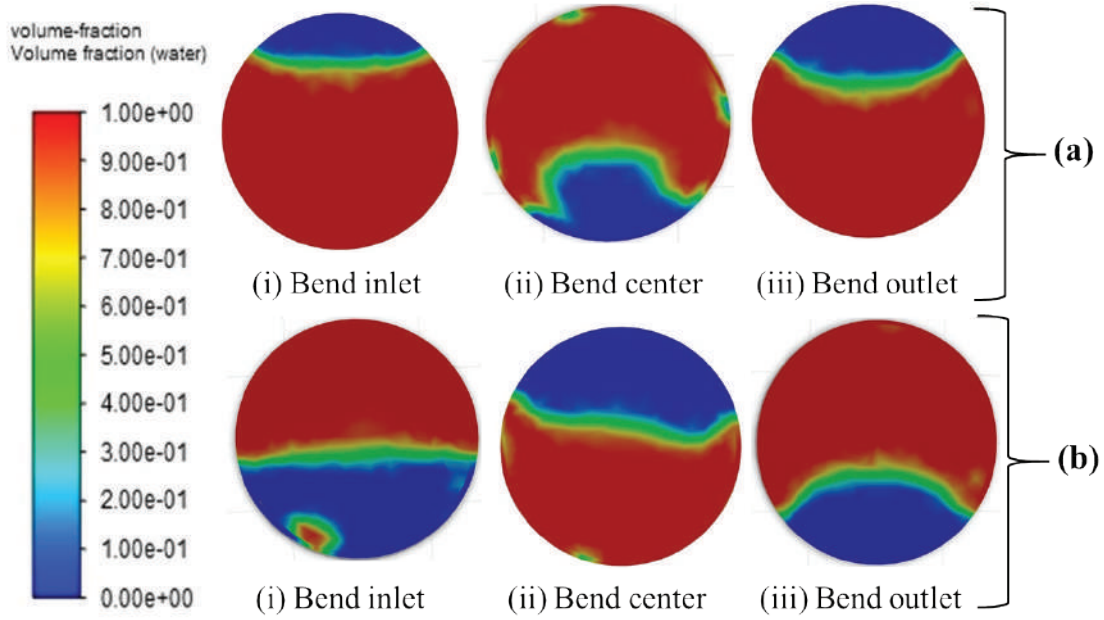

Figure 11. Phase distribution at the bend for 70% VOF of water: (a) Horizontal orientation, and (b) Vertical orientation.

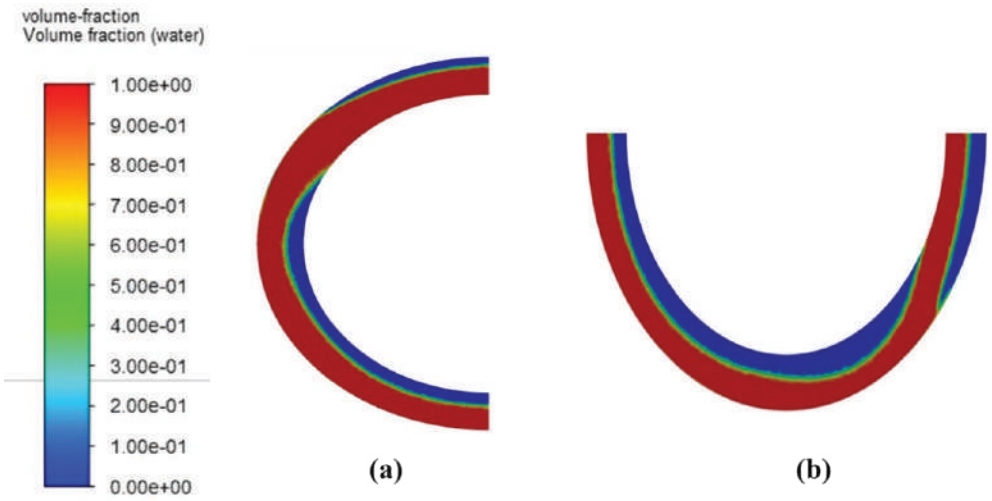

Figure 12. Liquid holdup for 70% VOF of water at the bend: (a) Horizontal-vertical orientation, and (b) Vertical orientation.

The liquid hold-up is almost the same for both the orientations of pipe. However, the effect of gravity is observed in Figure 12(b). The liquid hold-up is more for 70% VOF of water than 50 % VOF water in Figure 7. While the velocity vectors in Figure 13 for 70% VOF of water at the two orientations of the pipe have given the same results. Hence, the effect of increasing the water VOF is absolutely absent. However, though the mixture velocity increases, the turbulence has less effect on the velocity distribution. with 70% VOF of water. Comparing the static, dynamic, and total pressure in Figure 9 and Figure 14, very little (i.e., said to be no) significant changes have been detected other than the increased value of the pressure for 70% VOF water. Though the values have been increased for the static, dynamic, and total pressure, the impact on the flow behavior is less significant which can be observed from the other figures.

Pressure Variation

Figure 15 shows the pressure variation with U-bend pipe at different orientations: static pressure, dynamic pressure, and total pressure. The comparison of static pressure along the axial position of the pipe is shown in Figure 15(a). It can be clearly observed that the pressure is dropping at a higher value at the downstream part for the vertical orientation of the pipe than the horizontal-vertical one. This is due to the fact that the water which is the heavier fluid faces more viscous resistance for acceleration against gravity. As a result, the pressure drops at a larger number for the 50% and 70% VOF of water. However, at the bend inlet and center, the pressure is lowering steadily for both the position and VOF of water.

Dynamic pressure comparison has been depicted in Figure 15(b). The results are completely different in this case. For horizontal-vertical downflow for 50% and 70% VOF of water, the pressure decreases from pipe inlet to bend inlet. But the pressure tends to increase from the bend inlet and maximizes at the bend outlet due to a constricted passage as shown earlier in Figure 9 and Figure 14. After, the pressure again starts to decrease at the downstream portion. The pressure increases for the vertical downflow as the constricted passage of water has been observed which increases the pressure, from the pipe inlet to the bend inlet as given in Figure 9 and Figure 14. Then, the pipe bend faces a sudden drop of pressure following a small portion of the downstream of the pipe for both 50% and 70% VOF of water. After, the dynamic pressure tends to increase as there is a huge drop of static pressure described earlier in Figure15(a).

The total pressure variation is shown in Figure 15(c). The pressure variation for 50% and 70% VOF of water at horizontal-vertical downflow gives a similar trend as in the vertical pipe. But the pressure is lowered from the pipe inlet to bend for the horizontal-vertical downflow for both the VOF of water. On the contrary, the total pressure is slightly increasing due to the constricted passage of water created by the gravitational effect. Next, the total pressure variation is steady at the pipe bend and a small pressure drop follows the downstream part. However, the total pressure lowers with a great value starting from the pipe bend which has increased at the pipe downstream.

Figure 16 shows the pressure variation at the bend section of the u-bend pipe both for 50% and 70% of water for both orientations: horizontal-vertical and vertical. The pressure measurement at various bend angles has been illustrated in this figure. The bend angle has a negligible effect on horizontal-vertical and vertical downflow for 50% VOF of water. The curved lines are almost straight. However, with the higher bend angle and for 70% VOF of water, the pressure gives significant changes for both of the pipe positions. It may be due to the fact that higher VOF of water increases the liquid hold-up and thus, this causes the pressure to drop more.

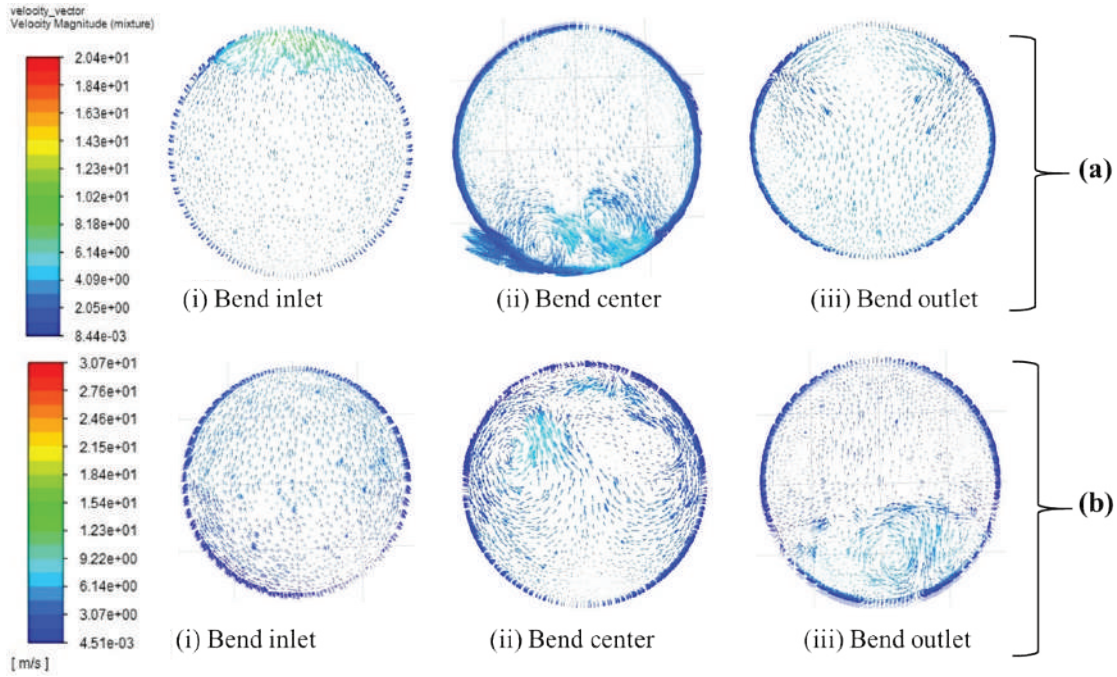

Figure 13. Velocity vector at the bend for 70% VOF of water: (a) Horizontal-vertical orientation, and (b) Vertical orientation.

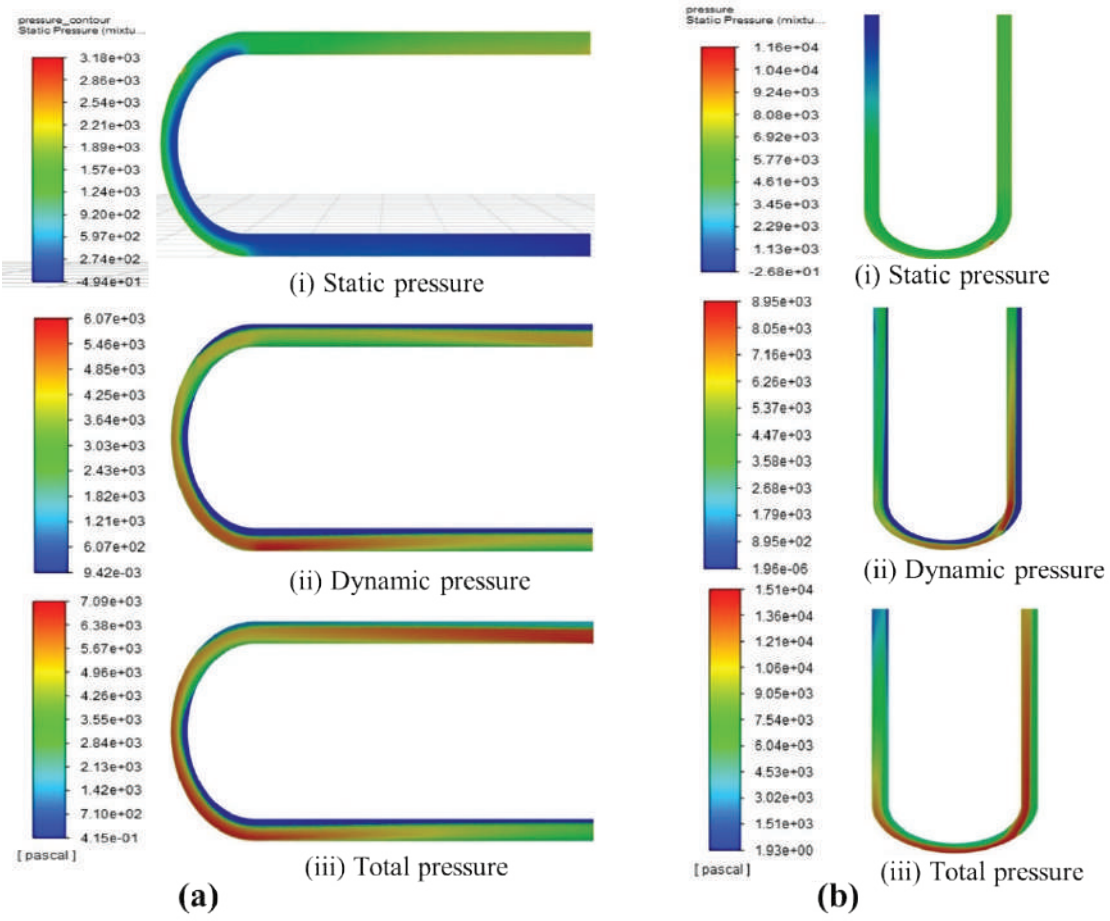

Figure 14. Variation of pressure along the U-bend tube: (a) Horizontal-vertical orientation, and (b) Vertical orientation.

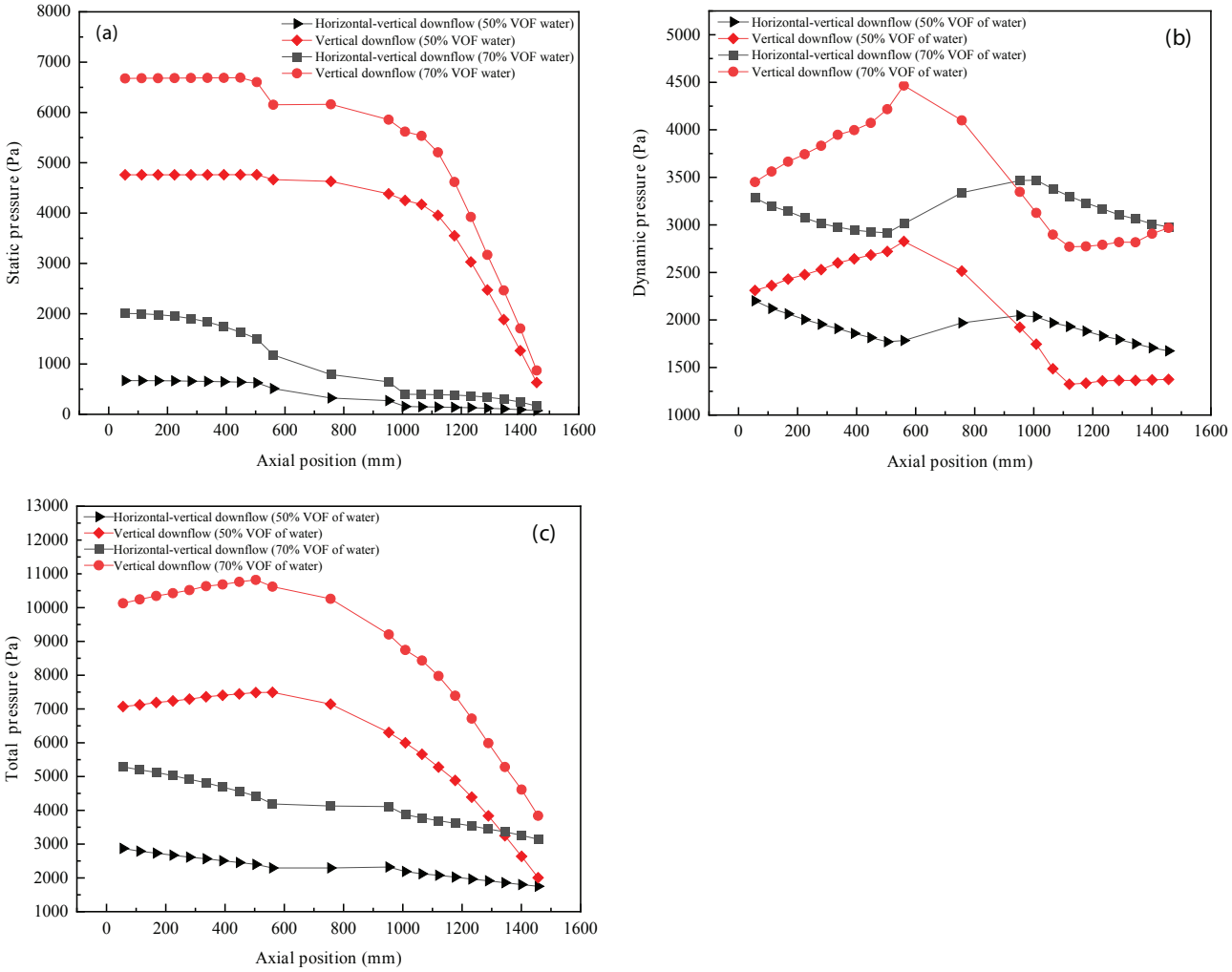

Figure 15. Pressure variation with U-bend pipe at different orientations: (a) static pressure, (b) dynamic pressure, and (c) total pressure.

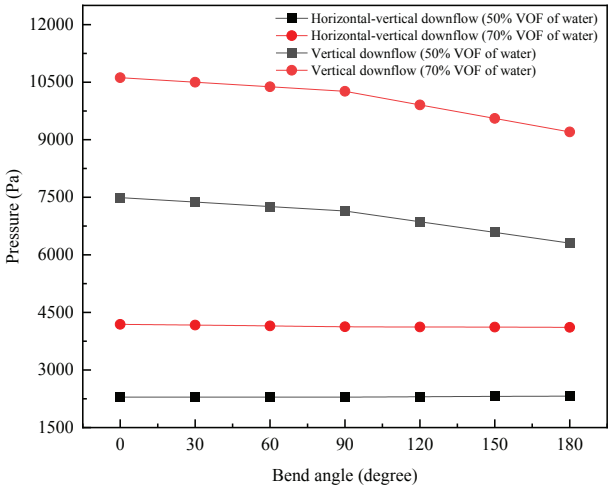

Figure 16. Pressure variation at the u-bend section both for 50% and 70% of water for both orientations: horizontal-vertical and vertical.

Figure 17 shows the comparison by considering the flow pattern of 50% VOF of water for the horizontal-vertical orientation. Figure 17(a) shows the comparison of water velocity at the bend inlet along with the axial length, where the mixture model for the two-fluid models is used to verify the model while maintaining the same dimensions, flow inlet, and boundary conditions by Pham et al. [3]. With an average inaccuracy of 4.47%, the current work is verified against the work of Pham et al. and hence, this emphasizes the reliability of the model. While, in Figure 17(b), the total pressure variation comparison has also been illustrated between Pham et al. [3] and the present work. The total pressure variation trends are similar for both of the works. However, the pressure curve for the present work varies slightly due to the differences in volume fraction with Pham et al. work. With a higher volume fraction, the total pressure magnitudes change, and the pressure loss is greater for the higher volume fraction which is depicted here. So, this comparison authenticates the results found through this study.

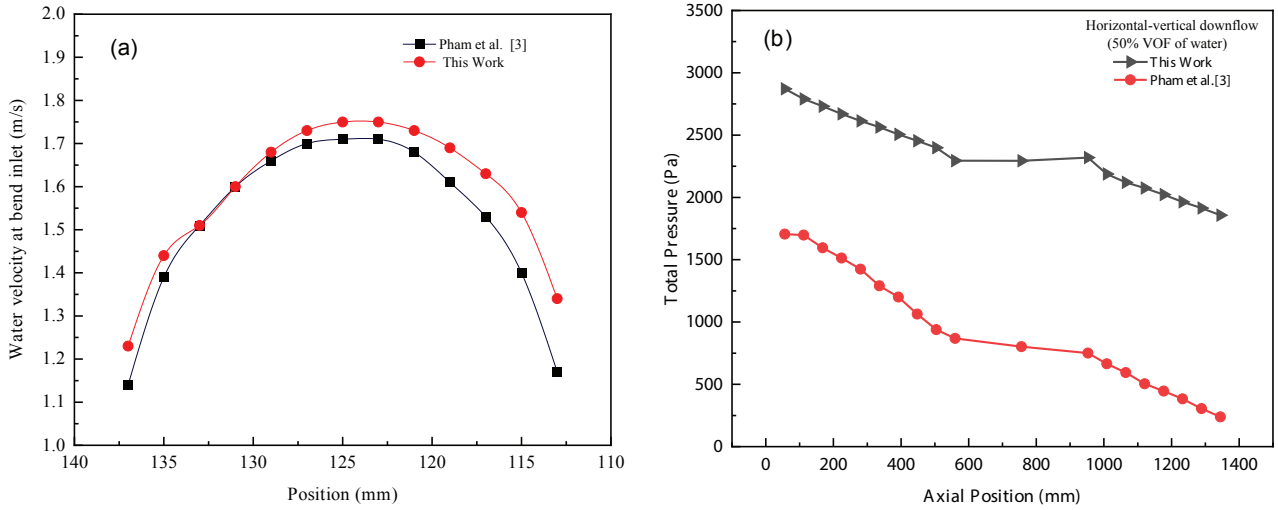

Figure 17. Illustration for comparing (a) water velocity at bend inlet, and (b) total pressure along the axial length.

CONCLUSION

The current investigation is conducted on the U-bend tube to see the flow pattern, examine how the bend affects the pressure drop for two types of pipe orientations, and determine the phase distribution. In summary, the subsequent findings have been discovered.

- The flow pattern for water and air inlet velocity of 3 m/s is observed in the stratified flow with very small wavy patterns at the interface of the air-water phase interactions for both orientations and volume fractions. This observation is consistent across both orientations and volume fractions, highlighting the impact of centrifugal and gravitational forces on phase interactions.
- The pressure drop is 1186 Pa and 1415 Pa for 50% and 70% volume fractions of water at the vertical downflow position of the pipe. On the other hand, an 80 Pa total pressure drop is found for a 70% volume fraction of water for the horizontal position of the U-shaped pipe. However, the pressure drop is negligible for a 50% volume fraction of water at the same orientation. This signifies that pressure losses increase with volume fraction.
- With higher volume fractions of water, the liquid hold-up at the bend increases due to the dominant centrifugal force over the gravitational force. This highlights the importance of considering phase distribution and flow patterns in U-bend pipes for efficient fluid transport in industrial applications.
- The pressure drops increase with the bend angle and the volume fraction of water.

The scope of this work can be extended to investigate whether air-water two-phase flow yields similar results with different types of refrigerants. Additionally, extensive studies in microchannels could provide valuable insights, allowing for comparison with current findings. In summary, this study shows that pipe orientation and water volume percentage have a considerable impact on the pressure drops and phase distributions in U-bend pipes. The results offer a fundamental insight that may guide fluid transport system design and optimization in a range of industrial settings.

NOMENCLATURE

α	Volume of fraction
A	Area
U	Superficial velocity
$\dot{Q}$	Flow rate
Δp	Total pressure drops
G	Mass flux
λ, ψ	Dimensionless parameters
ρ	Density
$\vec{v}$	Velocity
n	Surface normal correlated to the gradient of q^{th} volume fraction
θ	Angle
σ	Surface tension
S	User defined source term
U^*	Dimensionless velocity
y^*	Dimensionless distance from the wall
κ	Von Karman constant (0.4187)
E	Empirical constant (9.793)
U	Mean velocity
μ	Dynamic viscosity of the fluid
k	Turbulence kinetic energy
y	Distance from the centroid of the wall-adjacent cell to the wall

ACKNOWLEDGMENT

The authors appreciate and acknowledge the Khulna University of Engineering & Technology for providing high-performance computing facilities and other support throughout this work.

AUTHORSHIP CONTRIBUTIONS

Authors equally contributed to this work.

DATA AVAILABILITY STATEMENT

The authors confirm that the data that supports the findings of this study are available within the article. Raw data that support the finding of this study are available from the corresponding author, upon reasonable request.

CONFLICT OF INTEREST

The author declared no potential conflicts of interest with respect to the research, authorship, and/or publication of this article.

ETHICS

There are no ethical issues with the publication of this manuscript.

STATEMENT ON THE USE OF ARTIFICIAL INTELLIGENCE

Artificial intelligence was not used in the preparation of the article.

REFERENCES

[1] Hayashi K, Kazi J, Yoshida N, Tomiyama A. Pressure drops of air-water two-phase flows in horizontal U-bends. Int J Multiph Flow 2020;131:103403. [CrossRef]

[2] Dassler C, Janoske U. Numerical Investigation of Pressure Loss and Heat Transfer Characteristics in 180-Degree Bends. Heat Transf Eng 2023;44:803–822. [CrossRef]

[3] Pham TQ, Jeon J, Jo D, Choi S. Two-Phase Flow Simulations Using 1D Centerline-Based C- and U-Shaped Pipe Meshes. Appl Sci 2021;11. [CrossRef]

[4] Hayashi K, Yasui S, Kurimoto R, Tomiyama A. Void Fraction of Air-Water Two-Phase Flows in a Vertically Placed Horizontal U-Bend. Heat Transf Eng 2023;1–14. [CrossRef]

[5] Yadav S, Mehta HB. Experimental investigations on air–water two-phase flow through a minichannel U-bend. Exp Therm Fluid Sci 2016;78:182–198. [CrossRef]

[6] Usui K, Aoki S, Inoue A. Flow Behavior and Phase Distribution in Two-Phase Flow around Inverted U-Bend. J Nucl Sci Technol 1983;20:915–928. [CrossRef]

[7] Da Silva Lima RJ, Thome JR. Two-phase flow patterns in U-bends and their contiguous straight tubes for different orientations, tube and bend diameters. Int J Refrig 2012;35:1439–1454. [CrossRef]

[8] Deng D, Wang RS, Xie SW, Liu PP. Flow pattern and its transition of nitrogen gas–water two-phase flow in U-tubes and inverted U-tubes. Heat Mass Transf 2015;51:85–94. [CrossRef]

[9] Aliyu AM, Almabrok AA, Baba YD, Lao L, Yeung H, Kim KC. Upward gas–liquid two-phase flow after a U-bend in a large-diameter serpentine pipe. Int J Heat Mass Transf 2017;108:784–800. [CrossRef]

[10] Monachan B, Thomas RJ, Steaphen D, Skaria M, Shafi KA. Simulation of Stratified Two-phase Flow Regime using Air-Water Model in ANSYS Fluent®. J Phys Conf Ser 2019;1355:12014. [CrossRef]

[11] De Moerloose L, Vierendeels J, Degroote J. Effect of the liquid viscosity, wall wetting and mass flow rate on the flow through a horizontal U-bend subjected to an upwards flowing air-water mixture. 7th European Conference on Computational Fluid Dynamics. Glasgow;UK. 2018.

[12] Ma X, Liu T, Dai N, Tian M, Li S. Experimental Investigation on the Perturbation Length for Air–Water Flow Upstream and Downstream of U-Bends. Front Energy Res 2022;10:906809. [CrossRef]

[13] Mondol S, Hossain MI, Islam MT. Numerical Study of Water Flow through U-Bend Pipe. Available at: https://api.semanticscholar.org/CorpusID:211195619. Accessed on: 24 Mar 2026.

[14] Ghosh S, Das G, Das PK. Simulation of core annular in return bends—A comprehensive CFD study. Chem Eng Res Des 2011;89:2244–2253. [CrossRef]

[15] Bandyopadhyay TK, Das SK. Application of Computational Fluid Dynamics for Two-Phase Gas– Newtonian Liquid Flow through U-Bend. Int J Fluid Mech Res 2014;41. [CrossRef]

[16] Andrzejczyk R, Muszynski T. Experimental and comparative study on the two-phase pressure drop of air-water mixture in U-bend and straight pipe annuli. J Phys Conf Ser 2018;1101:12002. [CrossRef]

[17] Ogunsesan OA, Hossain M, Droubi MG. Computational fluid dynamics modelling of multiphase flows in double elbow geometries. Proc Inst Mech Eng Part E J Process Mech Eng 2021;235:1835–1846. [CrossRef]

[18] Ali SH, Eqqab MI. A computational study of curvature effect on pressure drop of gas-liquid two-phase flow through 90 degree elbow. Therm Sci 2022;26:3215. [CrossRef]

[19] Zahedi R, Rad AB. Numerical and experimental simulation of gas-liquid two-phase flow in 90-degree elbow. Alexandria Eng J 2022;61:2536–2550. [CrossRef]

[20] López J, Ratkovich N, Pereyra E. Analysis of two-phase air-water annular flow in U-bends. Heliyon 2020;6:e05818. [CrossRef]

[21] Lu C, Kong R, Qiao S, Larimer J, Kim S, Bajorek S, et al. Frictional pressure drop analysis for horizontal and vertical air-water two-phase flows in different pipe sizes. Nucl Eng Des 2018;332:147–161. [CrossRef]

[22] Abdulkadir M, Azzi A, Zhao D, Lowndes IS, Azzopardi BJ. Liquid film thickness behaviour within a large diameter vertical 180° return bend. Chem Eng Sci 2014;107: 137–148. [CrossRef]
[23] Nouri S, Hafsia Z, Boulaaras SM, Allahem A, Alkhalaf S, Feng B. Numerical Analysis of Stratified and Slug Flows. Math Probl Eng 2021;8418008. [CrossRef]
[24] Mahmood ASRA, Buttsworth D. CFD Numerical And Experimental Investigation Of Two-Phase Flow Development After An Expansion Device In A Horizontal Pipe. J Therm Eng 2021;7:307–323. [CrossRef]
[25] Karademir H, Ozcelik G, Acıkgoz O, Dalkılıc AS, Ince IT, Meyer J, et al. Comprehensive Review On The Flow Characteristics Of Two-Phase Flows In Inclined Tubes. J Therm Eng 2021;7:483–549. [CrossRef]
[26] Yaqop BN. Gas-liquid two-phase flow pressure drop in flattened tubes: an experimental and numerical study. J Therm Eng 2024;10:196–206. [CrossRef]
[27] Hamad FA, He S, Khan MK, Bruun HH. Development of kerosene–water two-phase up-flow in a vertical pipe downstream of A 90° bend. Can J Chem Eng 2013;91:354–367. [CrossRef]
[28] Spedding PL, Benard E, Mcnally GM. Two- and Three-Phase Flow Through a 90 Degree Bend. Dev Chem Eng Miner Process 2005;13:719–730. [CrossRef]
[29] Islam L, Mondal D, Islam MA, Das P. Effects of Heat Transfer Characteristics of R32 and R1234yf with Al2O3 Nanoparticle through U-Bend Tube Evaporator. J Eng 2024;9991809. [CrossRef]
[30] Jiang F, Wang Y, Ou J, Chen C. Numerical Simulation of Oil-Water Core Annular Flow in a U-Bend Based on the Eulerian Model. Chem Eng Technol 2014;37:659–666. [CrossRef]
[31] Ooms G, Pourquie MJBM, Westerweel J. Numerical study of laminar core-annular flow in a torus and in a 90° pipe bend. AIChE J 2015;61:2319–2328. [CrossRef]
[32] Ma K, Liu Z, Tang Y, Liu X, Yang Y, Yang S. Numerical investigation on ice slurry flow in horizontal elbow pipes. Therm Sci Eng Prog 2022;27:101083. [CrossRef]
[33] BS Onal, Akgul D, Mercan H, Dalkılıc AS, Wongwises S. Heat transfer and pressure drop characteristics of two phase flow in helical coils. Therm Sci Eng Prog 2022;27:101143. [CrossRef]
[34] Govier GW, Omer MM. The horizontal pipeline flow of air-water mixtures. Can J Chem Eng 1962;40:93–104. [CrossRef]
[35] Wang CC, Yang KS, Chang YJ, Lu DC. Characteristics of air–water two-phase flow in a 3-mm smooth tube. Can J Chem Eng 2000;78:1011–1016. [CrossRef]
[36] Wang CC, Chen IY, Yang YW. Influence of horizontal return bend on the two-phase flow pattern in a 6.9 mm diameter tube. Can J Chem Eng 2002;80:478–484. [CrossRef]
[37] Salim A, Fourar M, Pironon J, Sausse J. Oil–water two-phase flow in microchannels: Flow patterns and pressure drop measurements. Can J Chem Eng 2008;86:978–988. [CrossRef]
[38] Al-Hadhrami LM, Shaahid SM, Tunde LO, Al-Sarkhi A. Experimental Study on the Flow Regimes and Pressure Gradients of Air-Oil-Water Three-Phase Flow in Horizontal Pipes. Sci World J 2014;1:810527. [CrossRef]
[39] Patpatiya P, Samadder S, Kapoor V. Numerical Investigation of Two-Phase Flow in a Horizontal T Junction. Optimization of Industrial Systems. Beverly: Scrivener; Publishing; 2022. p. 85–99.
[40] Lightstone L, Osamusali SI, Chang JS. Gas-liquid two-phase flow in symmetrically dividing horizontal tubes. AIChE J 1991;37:111–122. [CrossRef]
[41] Nizovtseva IG, Starodumov IO, Schelyaev AY, Aksenov AA, Zhluktov SV, Sazonova ML, et al. Simulation of two-phase air–liquid flows in a closed bioreactor loop: Numerical modeling, experiments, and verification. Math Methods Appl Sci 2022;45:8216–8229. [CrossRef]
[42] Verma RK, Ghosh S. Two-Phase Flow in Miniature Geometries: Comparison of Gas-Liquid and Liquid-Liquid Flows. ChemBioEng Rev 2019;6:5–16. [CrossRef]
[43] Mondal D, Ikram MO, Rabbi MF, Moral MNA. Experimental Investigation and Comparison of Bend Tube Parallel & Counter Flow and Cross Flow Water to Air Heat Exchanger. Int J Sci Eng Res 2014;5:686–695.
[44] Mondal D, Alam A, Islam MA. Experimental Observation of a Small Capacity Vapor Absorption Cooling System. Int J Sci Eng Res 2014;5:456–467.
[45] Mondal D, Islam MA. Experimental Investigation on an Intermittent Ammonia Absorption Refrigeration. Mech Eng Res J 2018;11:59–65.
[46] Mondal D, Hori Y, Kariya K, Miyara A, Alam MJ. Measurement of Viscosity of a Binary Mixture of R1123 + R32 Refrigerant by Tandem Capillary Tube Method. Int J Thermophys 2020;41:1–20. [CrossRef]
[47] Mondal D, Kariya K, Tuhin AR, Amakusa N, Miyara A. Viscosity measurement for trans-1,1,1,4,4,4-hexafluoro-2-butene(R1336mzz(E)) in liquid and vapor phases. Int J Refrig 2021;133:267–275. [CrossRef]
[48] Mondal D, Kariya K, Tuhin AR, Miyoshi K, Miyara A. Thermal conductivity measurement and correlation at saturation condition of HFO refrigerant trans-1,1,1,4,4,4-hexafluoro-2-butene (R1336mzz(E)). Int J Refrig 2021;129:109–117. [CrossRef]
[49] Mondal D, Tuhin AR, Kariya K, Miyara A. Measurement of Kinematic Viscosity and Thermal Conductivity of 3,3,4,4,5,5-HFCPE in Liquid and Vapor Phases. Int J Refrig 2022;140:150–165. [CrossRef]

[50] Das P, Mondal D, Islam A, Afroj M. Thermodynamic performance evaluation of a solar powered Organic Rankine cycle (ORC) and dual cascading vapor compression cycle (DCVCC): Power generation and cooling effect. Energy Convers Manag X 2024;23:100662. [CrossRef]

[51] Arefin MM, Mondal D, Islam MA. Optimizing cascade refrigeration systems with low GWP refrigerants for Low-Temperature Applications: A thermodynamic analysis. Energy Convers Manag X 2024;24:100722. [CrossRef]

[52] Bari MA, Mondal D, Hasib MA. Impact of air flow, temperature distribution, and heat transmission in a refrigerator compartment with and without shelves: A numerical approach. J Therm Eng 2024;10:1590–1606. [CrossRef]

[53] Shaharier MT, Mondal D, Hasib MA, Islam MA. Effects of gas-liquid flow and dehumidification performance of a liquid desiccant dehumidifier: A numerical approach for vertical smooth & rough, and inclined rough plates. J Therm Eng 2024;10:1559–1576. [CrossRef]

[54] Sobamowo MG, Akinshilo AT. Analysis of flow, heat transfer and entropy generation in a pipe conveying fourth grade fluid with temperature dependent viscosities and internal heat generation. J Mol Liq 2017;241:188–198. [CrossRef]

[55] Akinshilo AT, Olaye O. On the analysis of the Erying Powell model based fluid flow in a pipe with temperature dependent viscosity and internal heat generation. J King Saud Univ Eng Sci 2019;31:271–279. [CrossRef]

[56] Akinshilo AT, Sobamowo GM. Perturbation Solutions for the Study of MHD Blood as a Third Grade Nanofluid Transporting Gold Nanoparticles through a Porous Channel. J Appl Comput Mech 2017;3:103–113.

[57] Seikh AH, Akinshilo AT, Taheri MH, Alharthi N, Khan I, Khan AR, et al. Influence of the nanoparticles and uniform magnetic field on the slip blood flows in arterial vessels. Phys Scr 2019;94:125218. [CrossRef]

[58] Ansys®, ANSYS Fluent Theory Guide, 2020th ed.

[59] Brackbill JU, Kothe DB, Zemach C. A continuum method for modeling surface tension. J Comput Phys 1992;100:335–354. [CrossRef]

J Ther Eng, Vol. 12, No. 2, pp. 802−814, March, 2026

Journal of Thermal Engineering
Web page info: https://jten.yildiz.edu.tr
DOI: 10.14744/thermal.0001120

Research Article

The development and evaluation of a solar Stirling engine integrated with an annular Fresnel lens concentrator system

Yasir MEHMOOD[1], Asnaf AZIZ[1], Abid HUSSAIN[1,*], Fasih Ur RAHMAN[1], Afzal KHAN[1], Muhammad ABUBAKKAR[1], Imad RASOOL[1]

[1]Department of Mechanical Engineering, University of Engineering and Technology Peshawar, 25120, Pakistan

ARTICLE INFO

Article history
Received: 22 October 2024
Revised: 26 December 2024
Accepted: 08 January 2025

Keywords:
Alpha Configuration; Clean Energy; Computational Modelling; Heat Exchanger Design; Solar Concentrator; Solar Energy; Stirling Cycle; Stirling Engine

ABSTRACT

The study addresses the critical energy and environmental crises by exploring renewable energy sources, with a focus on solar energy. Solar Stirling engines are particularly relevant due to their efficiency in converting solar energy into electricity. This research presents the development and evaluation of a solar Stirling engine integrated with an annular Fresnel lens concentrator system. Designed to operate within a temperature range of 370–450 °C with air as the working fluid, the engine's performance was assessed by measuring pressure drops in the regenerator and energy losses in the cylinders. Experimental results revealed that the alpha configuration prototype produced 37 watts of power with an efficiency of 26.4%. These findings underscore the engine's effectiveness in solar energy conversion and its potential for practical applications in generating electricity. The integration of the Fresnel lens concentrator represents a novel approach not extensively covered in existing literature. The study's optimization of the engine's design and detailed performance metrics contribute to improved efficiency and broader applicability of solar Stirling engines, offering a viable solution for reducing reliance on fossil fuels and addressing environmental challenges.

Cite this article as: Mehmood Y, Aziz A, Hussain A, Rahman FU, Khan A, Abubakkar M, Rasool I. The development and evaluation of a solar Stirling engine integrated with an annular Fresnel lens concentrator system. J Ther Eng 2026;12(2):802−814.

INTRODUCTION

Increased energy demands have led to both an energy crisis and an environmental crisis [1]. More than ever, renewable alternatives are needed to address the energy and environmental problems. One major reason the world is turning towards renewable resources is the fast-growing environmental degradation. Climate change is causing havoc everywhere, from melting glaciers and rising sea levels to historical rains, storms, and subsequent floods. Carbon emissions are major constituent of global warming. According to the EIA (US Energy Information Administration), CO_2 emissions by fuel generation are 2.38 and 2.30 pounds per kWH, respectively, for petroleum and coal [2]. Solar energy, harnessed from the Sun, is a viable and diverse energy source, encompassing both direct and indirect applications. The Earth's surface

*Corresponding author.
*E-mail address: abidhussain@uetpeshawar.edu.pk

This paper was recommended for publication in revised form by Editor-in Chief Ahmet Selim Dalkilic

Published by Yıldız Technical University Press, İstanbul, Turkey
Yıldız Technical University. This is an open access article under the CC BY-NC license (http://creativecommons.org/licenses/by-nc/4.0/).

receives approximately 60% of the total solar energy that reaches our planet. Despite this substantial influx, only about 0.1% of this solar energy is currently converted into usable forms, reflecting a significant potential for expansion. In terms of capacity, the theoretical maximum energy generation from solar power is estimated to be around 5000 gigawatts (GW) if fully exploited. This highlights the immense potential of solar energy compared to current energy production levels [3]. The primary method of converting solar energy is through Solar Photovoltaic (SPV) systems, which directly convert sunlight into electricity. In addition to SPV systems, another key technology is Solar Thermal Systems (STS). STS focus on converting solar energy into heat, which can then be used for a variety of heating and cooling applications. This heat can be employed for tasks such as space heating, water heating, and cooling processes, making STS a versatile and important technology for harnessing solar energy [4]. Meanwhile, all other energy sources have carbon emissions of 0.86 pounds per kWH. That's around 270% less than fossil fuels. According to another study by Guidi G et al. [5], in comparison to fossil fuel technologies, all of the emission estimates found for renewable energy sources are lower by at least one order of magnitude, sometimes even two orders of magnitude. Hydroelectricity and wind power are promising, but location and expense limit their application. This makes solar energy more easily accessible and usable in widespread applications. Solar energy thrives in isolated deserts, but photovoltaic cells struggle under severe temperatures. In contrast, solar Stirling engines transform solar energy into electricity efficiently. Stirling engine is a type of external combustion engine developed by Robert Stirling in 1816. The Stirling engine undergoes the four fundamental stages of compression, heating, expansion, and cooling, just like any other heat engine. Any heat source, including solar, geothermal, nuclear, and waste heat from industrial processes, can be used to power a Stirling engine directly. As solar energy is excessively available and comparatively easy to harness, solar Stirling engines are favorable to be used to produce electricity. Air is initially compressed in this engine utilizing work, that has been accumulated from a previous cycle in the mechanical flywheel. Different temperatures are applied to the working fluid to transform the whole amount of heat energy into mechanical work. Thermal equilibrium is present for the working fluid. The ability of this engine to run with any heat source is by far its greatest benefit. These engines are appropriate for solar energy that is concentrated and renewable [6].

Stirling engines are simplistic and highly efficient in their design, with theoretical efficiency almost equal to the Carnot efficiency [6]. This makes them a good choice for generating power from different heat sources, even from waste heat in industries such as cement plants. Solar Stirling engines are also advantageous over solar photovoltaic arrays as their solar-to-electric power conversion is more efficient [7]. Hence, in environments such as deserts and urban areas, which have high summertime temperatures, stirling engines can be used for efficient power production. In the 1870s, Ericsson constructed the inaugural "Sun Engine", a Solar Stirling engine that harnessed a parabolic mirror to convert heat into steam, which functioned as the operational fluid for the engine. Following the invention of internal combustion engines, the progress in the development of sterling engines diminished, and they were subsequently only utilized for certain applications, such as in submarines.

Recently, there has been a global shift towards renewable energy sources and an increased exploration of alternative methods for power generation. The resurgence of Solar Sterling Engines has prompted academics to examine and investigate their utilization in various situations and arrangements. In the early 2000s, joint research was done on the production of a parabolic dish solar Stirling engine called EnviroDish [8]. Cinar, C., and H. Karabulut manufactured and studied a gamma-type Stirling engine. With experimental results, they concluded that the use of Helium gas as a working fluid resulted in more power than air and hydrogen [9]. In the dynamic analysis of a GPU-3 model, researchers discovered that geometrical and physical parameters significantly impact its performance. Through optimization techniques, they successfully reduced mechanical losses and achieved more realistic theoretical outcomes [10].

Regenerator materials with various porosities suggest that the stainlesssteel regenerator with 85% porosity gave optimum results [11]. A. Nielsen et al. [12], did a study that showed that using a multistage regenerator increases the efficiency of the regenerator in comparison to a single-stage regenerator. A recent study was performed regarding the construction and testing of a dish-type solar Stirling engine and the losses in the solar-to-electric conversion. This study found that the dish reflector should not concentrate the sun's rays onto a point of the Stirling engine but rather a zone [13]. Abuelyamen et al. [13], conducted an in-depth CFD analysis to assess the energy efficiency of different types of Stirling engines, (α, β, and γ). The use of solar power Stirling engines in marine and offshore environments also bear great potential: a study shows the solar power Stirling engine system achieved a maximum of 90% mechanical efficiency [14]. Bataineh did a study on the numerical thermodynamic model of the solar sterling engine and discussed Kinetic and thermodynamic parameters of the engine [15].

However, one area of research yet to be fully explored is the application of an annular Fresnel lens system paired with an alpha configuration sterling engine for power production, as most of the research has been focused on the use of parabolic dish concentrators. Heng Zheng et al. [16], did a study on a solar-aided power generation system that used an annular frequency solar. Similarly, a study was done by Boretti that shows the use of an annular concentrator for power production application [17]. An advantage of the Alpha Stirling engine is its ability to include a regenerator in its design easily. The regenerator can occupy the dead space that links the hot and cold cylinders, enhancing the engine's efficiency.

Meanwhile, the beta configuration has a single-cylinder design that places hot and cold cylinders in close proximity. Moreover, for our specific temperature range and simplicity with manufacturing alpha configuration was more feasible.

Solar Stirling engines can be utilized in isolated areas to provide off-grid power. Their capacity to transform solar energy into electricity makes them excellent for rural or remote places where traditional power infrastructure is limited [18]. In urban or suburban areas, these engines can be linked into local energy systems to augment the grid, resulting in a more sustainable and robust energy network [19]. The Alpha Stirling engine's design innovations allow for a wide range of uses, including energy generation, industrial use, and education. The findings highlight its potential to improve efficiency and sustainability, meeting the different needs of the journal's readership while also contributing to broader discussions on renewable energy and technological innovation [20]. Recent studies have focused on improving the efficiency of Stirling engines by optimizing materials and thermal management. A study published in Energy Storage and Technology explores advanced heat exchangers and novel materials for Stirling engines, highlighting improvements in thermal efficiency and reducing mechanical losses. This work complements the findings of this paper by emphasizing the importance of material selection in enhancing the performance of Stirling engines [21].

The paper details developing and evaluating a solar Stirling engine utilizing an annular Fresnel lens concentrator system for generating power. The system's characteristics were chosen based on a temperature range of 370–450 °C during the design phase, with air being used as the working fluid. The system is examined via dynamic models to assess pressure drop in the regenerator and energy losses in the cylinders. With a robust design, the system is engineered for maximum output and efficiency. The engine's thermodynamic and mechanical parameters are also calculated and examined. Experimental tests are conducted on a prototype design utilizing an alpha configuration, resulting in 37W of output work with an efficiency of 26.4%.

MATERIALS AND METHODS

The Stirling engine model was designed according to design parameter calculations with the help of design software such as SolidWorks, and computations were done with the help of ANSYS. The selection of engine type and configuration was based on the study objectives and market limitations. After careful iterative measures, an alpha-type Stirling with a 90-degree V-configuration was selected, and an annular Fresnel lens concentrator was also designed as per similar criteria. Design considerations included selecting the material and geometry to optimize solar radiation collection and incorporating heat transfer enhancements. Factors such as thermal conductivity, specific heat capacity, and stability at high temperatures were taken into account. Paetro analysis was performed using software to select the optimum design parameters. The selection is based on efficiency, cost, safety, and environmental impact. Optimizing surface area, fluid flow pathways, and heat transfer coefficients are also considered. Thermodynamic and kinematic safety analysis of the system design were performed using ANSYS and MATLAB, whereas characteristic equations were solved with the help of Mathcad software. An approach similar to Aigboviosa et al. [22], 2018 was used where we programmed two motors for solar tracking for optimum solar irradiance.

Designing components such as pistons, cylinders, cranks, etc. involved taking material choice, stress analysis, and friction reduction into account. A feedforward control system was utilized to preserve optimal SSE functioning and maximize efficiency. Computer simulations and analytic tools were utilized throughout the design phase to assess system performance, forecast energy production, and optimize design parameters.

The design methodology frequently employed for designing a Stirling engine involves an iterative design process aimed at achieving the most optimal design conclusion shown in figure 1. A basic conceptual design is made by selecting the key features, such as an estimate of power output, temperature range type of mechanism used. This methodology comprises two analysis procedures: Schmidt analysis and non-dimensional analysis. Initial values are estimated, and the iteration is carried out for optimum design parameters such as piston size, etc.

The receiver absorbs concentrated solar energy and transfers it to a working fluid to heat it. A Fresnel lens concentrator system focuses sunlight on a focal point that contains the working fluid and serves as the receiver. The cycle starts with the high-temperature cylinder in its highest position. As the gas heats up, it expands, pushing the piston downward. This is the power piston. The sealed chamber in which the heated working fluid is housed expands as the heat energy is absorbed. This expansion transforms the heat energy into mechanical work by propelling the piston. After developing, the working fluid is sent to a heat exchanger or cooling mechanism, where it releases heat to the surroundings, through air. The working fluid's temperature is reduced over this cooling process. After cooling, the low-temperature piston displaces the gas back into the regenerator. The regenerator now releases heat stored earlier into the working gas. And the gas goes back to the hot cylinder, and the cycle repeats.

A steel mesh regenerator was utilized, consisting of a hollow mild steel exterior body filled with stainless steel mesh. Because regenerator efficiency depends on surface area, a mesh was employed instead of a solid body. Furthermore, as Geith et al. demonstrated in their study, stainless steel is 30% more thermally efficient than copper and aluminum, both of which have temperature and oxidation restrictions. The characteristics and materials were chosen based on prior research by Geith, Timoumi, and others that examined the impacts of pressure drop, thermal conductivity, and thermal capacity.

Materials were chosen based on their thermal conductivity, specific heat capacity, and stability at high temperatures to ensure effective heat transfer and structural integrity. High-performance materials with excellent thermal conductivity were selected for components in direct contact with the working fluid to enhance heat transfer. Additionally, materials with high specific heat capacity were used to ensure that the engine could efficiently store and release thermal energy. In the Stirling engine, heat transfer enhancements included the optimization of surface area and fluid flow pathways, as well as the implementation of advanced heat exchangers and regenerative systems to improve overall thermal efficiency. The materials used is aluminum alloy t6061 for the cylinder and hot source whereas the cylinder sleeve is made up of cast iron.

The laser temperature gun with specifications, (Temperature Range -60°C -800 °C), dynamometer and tacheometer (Range 0.5 ... 19999 rpm, Resolution 0.5 rpm (< 1000 rpm) 1 rpm (>1000 rpm) in the studies were used.

The Cycle consists of cyclic isothermal expansion and compression with an isochoric regeneration process as shown in figure 2. In the figure from processes 1-2, we have an isothermal or constant temperature compression, and then from 2-3, we have a constant volume increase in pressure. Then from 3-4, we have isothermal volume change or constant temperature expansion. Then, from 4-1, we again have a constant volume process. From 1-4 to 2-3, we have an isochoric regeneration process where a part of the heat from the earlier process is retained at the regenerator and is then added to the next process from the cold region, making it more efficient [23].

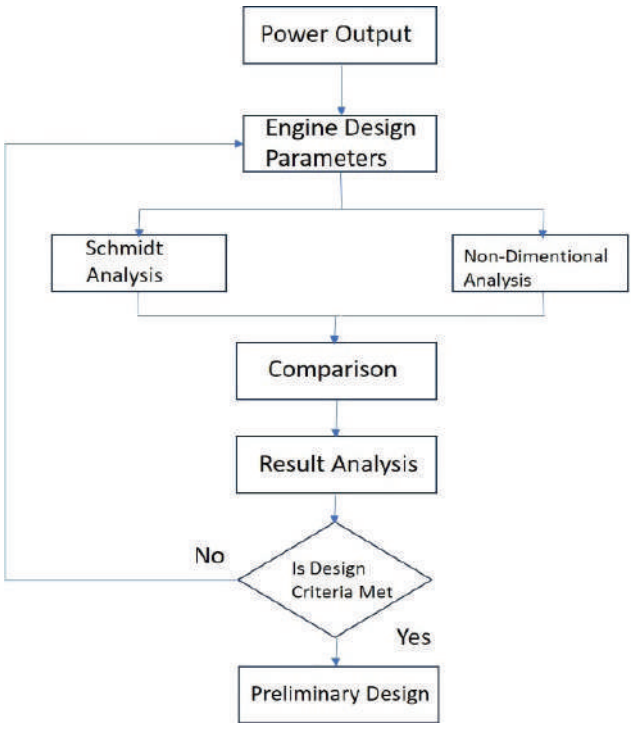

Figure 1. Flowchart for design of Stirling engine.

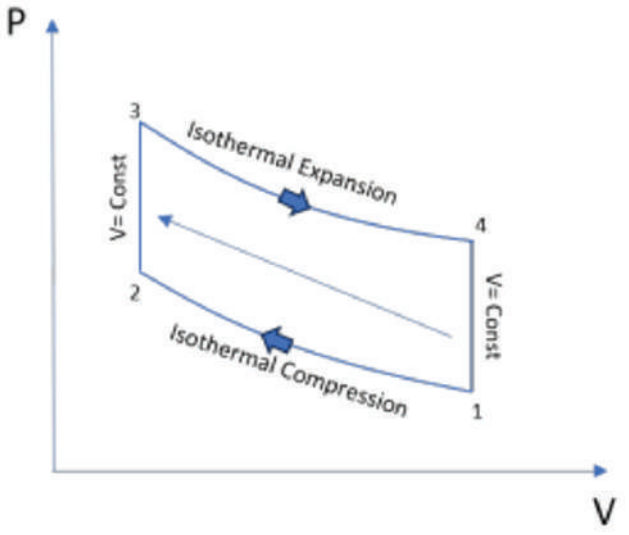

Figure 2. Stirling Cycle Process Diagram [23] [Open accessed].

RESULTS AND DISCUSSION

The Stirling engine comprises three essential components: the hot chamber, the cold chamber, and the regenerator, as shown in figure 4. The hot chamber interfaces with a heat source, while the cold chamber interacts with a heat sink. Gas seamlessly flows between these chambers via the regenerator. The power piston generates mechanical work, while the displacer piston orchestrates the movement of gas between chambers, instigating oscillations in temperature and pressure that propel the power piston. The engine's parameterization employed MATLAB's iterative hit-and-trial method, selecting 70-cc pistons with a 47-mm bore diameter and refining the volumes of the displacement and power pistons through successive MATLAB trials. The dimension and Specifications of alpha Stirling engine are given in Table 1. The nomenclature of Stirling engine is given in Table 2 and the important calculations are given in Table 3.

Table 1. Stirling Engine Cycle

Stirling Engine	Dimensions& Specifications
Height	243 mm
Length	237 mm
Width	184 mm
Mass	11 kg
Displacer Piston	47 mm
Power Piston	47 mm
Stroke	56 mm
Working Gas	He / Air

Table 2. Nomenclature

Symbol	Quantity	Units
P_{engine}	Operating Pressure in Engine	bar
V_{exp}	Total Expansion volume in the pistons	mm^3
V_{comp}	Total Compression Volume in the piston	mm^3
V_{se}	Expansion Swept Volume	mm^3
V_{de}	Expansion Dead Volume	mm^3
V_{sc}	Compression Piston Swept Volume	mm^3
V_{dc}	Compression piston Dead Volume	mm^3
P	Preload Pressure	bar
W_{exp}	Work done by expansion pistons	J
W_{comp}	Work done by compression Pistons	J
L	Length of the connecting rod	mm
r	Crank radius	mm
α	Slider crank acceleration	m/s^2
v	Slider crank velocity	m/s
x	Slider crank displacement	m
ω	Angular velocity of the engine, at 1000 rpm	Rad/s
θ	Crank angle	deg
m_b	Combined mass of slider crank	g
T	Torque produced in the engine	Nm
σt_{max}	Maximum stress in the flywheel	MPa
η_{ly}	Flywheel efficiency	No unit

According to Schmidt analysis [24] the work done by the engine is calculated as

$$P_{engine} = \frac{P.\sqrt{1-c^2}}{1-c.\cos(\Theta-\alpha)} \tag{1}$$

Here Pengine [25]gives the total Pressure in the engine with the crank angle θ, having initial engine pressure that was provided to the gas before the engine is started.

$$V_{exp} = \frac{V_{se}}{2}(1-\cos\Theta) + V_{de} \tag{2}$$

$$V_{comp} = \frac{V_{sc}}{2}(1-\cos\Theta - dx) + V_{dc} \tag{3}$$

From the Schmidt analysis [24], the work done by the engine is given by,

$$W_{exp} = \frac{P.V_{se}.\pi.c.\sin a}{1+\sqrt{1-c^2}}$$
$$W_{exp} = 61.642\ J \tag{4}$$

Figure 5 shows the Stirling Engine's characteristics. Figure 5a, presents the pressure vs. volume graph. The area under the graph gives us the total work done by the engine.

Table 3. Stirling Engine Calculations

Symbol	Quantity	Value	Unit
V_1	Hot Swept Volume of Displacer	1.9431×10^5	mm^3
V_p	Cold Swept Volume of Power-Piston	1.9431×10^5	mm^3
V_h	Hot Dead Volume of Displacer Piston	91000	mm^3
V_c	Cold Dead Volume of Power Piston	50000	mm^3
V_r	Regenerator Dead Volume	182500	mm^3
R	Specific gas Constant	287.1	J/Kg K
P	Preload Pressure in System	7	bar
T	Highest Temperature of System	673	K
T_c	Compression Space Gas Temperature	303	K
T_r	Regenerator Temperature	463.6519	K
M	Mass of Gas in System when the Slider-Crank is at an angle of 0	21.7568	10^{-1} g
S	S	3.5529	
B	Beale Number	1.0967	
C	C	0.3087	
P_m	Mean Pressure	5.7645	Bar
a_1	a_1	65.7616	degree
W_e	Work done by expansion piston	61.642	J
W_c	Work done by Compression piston	27.739	J
W_i	Total Work	34.263	J
	Compression Ratio	2.2	

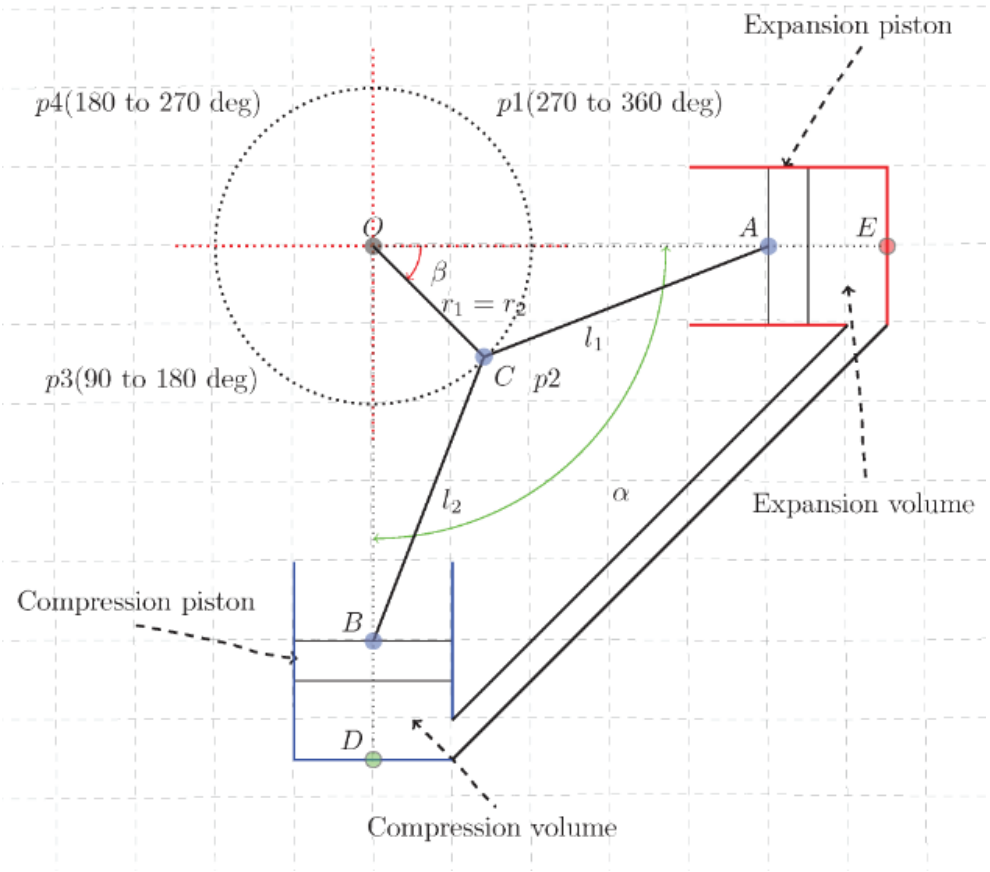

Figure 3. Schematic diagram for double slider crank [27] [Open accessed].

and other parameters are already defined above. As there is simultaneous work done by compression and expansion, due to being opposite in direction, the work done in the compression cylinder would be taken as negative. Figure 5b shows the graph of expansion volume and compression volume vs. the crank angle. Notice that both volumes are out of phase by about 90° as both the pistons are located at 90° with each other. This data is in accordance with a numerical study by [26].

$$W_{comp} = \frac{V_{se}.\pi.c.0.45.\sin a}{1+\sqrt{1-c^2}} \qquad (5)$$

$$W_{comp} = -27.739\,J$$

$$W_T = W_{exp} + W_{comp} \qquad (6)$$

$$W_T = 34.263\,J$$

Figure 3 shows the schematic diagram for the double slider crank configuration in an alpha Stirling engine. The equations for slider crank kinematics [24] are given in terms of crank radius, length, and crank angle. Successive derivatives give the equations for velocity and acceleration.

$$x = l - \frac{r^2}{4l} + r\left(\cos\Theta + \frac{r}{4l}\cos 2\Theta\right) \qquad (7)$$

$$v = -rw\left(\sin\Theta + \frac{r}{2l}\sin 2\Theta\right) \qquad (8)$$

$$a = -rw^2\left(\cos\Theta + \frac{r}{l}\cos 2\Theta\right) \qquad (9)$$

Figure 6 shows the slider crank kinematics. The acceleration, velocity and displacement are graphed to crank angle. From these kinematics calculations, balancing and vibrations are performed for the engine.

The equation for torque on the slider crank is as [24].

$$T = \frac{m_a}{2}.r^2.w^2\left(\frac{r}{2l}\sin\Theta - \sin 2\Theta - \frac{3r}{2l}\sin 3\Theta\right) \qquad (10)$$

The torque is dependent on the crank radius, length of the connecting rod, equivalent mass on the slider-crank, and the angular velocity of the crank. Solving it for 360° rotation of a crankshaft.

Figure 6 shows the forces acting on the slider crank. Notice that the forces are out of phase with each other hence cancelling most of the vibrations which is a characteristic of a 90° aligned engine. From the graph, we can notice that the

torque follows a sinusoidal waveform with alternate crests and troughs after 120°. At the start, the torque is zero as the engine starts and then it gets to a uniform speed at a given 1000 rpm for which the calculations were done.

Table 4. Regenerator without Structural Integrity and Criteria for Simulation

Quantity	Value
Max pressure	1 MPa
Factor of Safety	2
Mesh Type	Refinement Mesh + Fine Mesh
Materials	Mild Steel
Density	$7.85*10^{-6}$ kg/ mm^{-3}
Coefficient of Thermal Expansion	$1.2*10^{-5}$ C^{-1}
Specific Heat	$4.34*10^{5}$ mJ kg^{-1} C^{-1}
Thermal Conductivity	$6.05*10^{-2}$ W mm^{-1} C^{-1}
Resistivity 1.7e-004-ohm mm	$1.7*10^{-4}$ ohm mm

For a smooth power transfer, a flywheel is an integral part of an engine. The maximum stresses on the flywheel were calculated and a flywheel [24].

$$\sigma_{t_{max}} = \frac{2r}{g} w^2 \left(\frac{3+v}{8}\right)\left(r_0^2 + \left(\frac{1-v}{3+v}\right) r_i^2\right) \quad (11)$$

ANSYS Simulations and computation for material Factor of Safety and thermal and fluent analysis of the Regenerator are shown in Fig. 7

Table 4 shows data for the regenerator without structural integrity and criteria for simulation. In Figure 8, we have performed an ANSYS simulation on the regenerator. The parameters of the simulation are given in the table. We have two fixed supports and a pressure of 1 MPa applied along them, which are shaded in red. Looking at the results of the simulation we can notice that the given design has a low factor of safety. Then we added the ribs to the design, and we can see the improvement in stresses and safety in the design.

Figure 4. Stirling Engine.

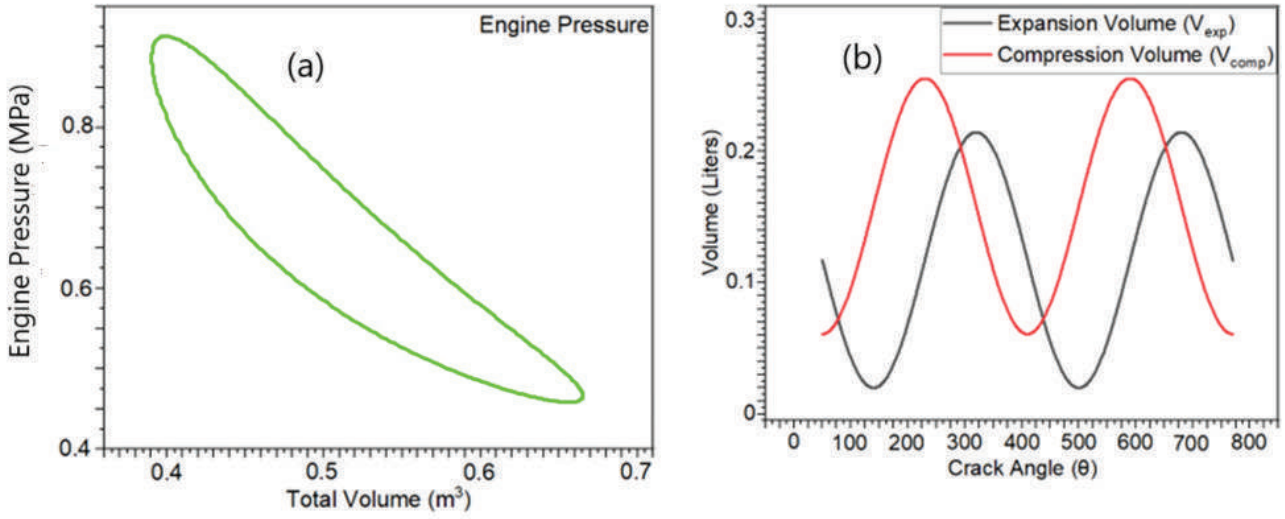

Figure 5. Characteristic Curves (a)Pressure vs Volume (b) Volume -vs-Crack Angle for α-Stirling Engine.

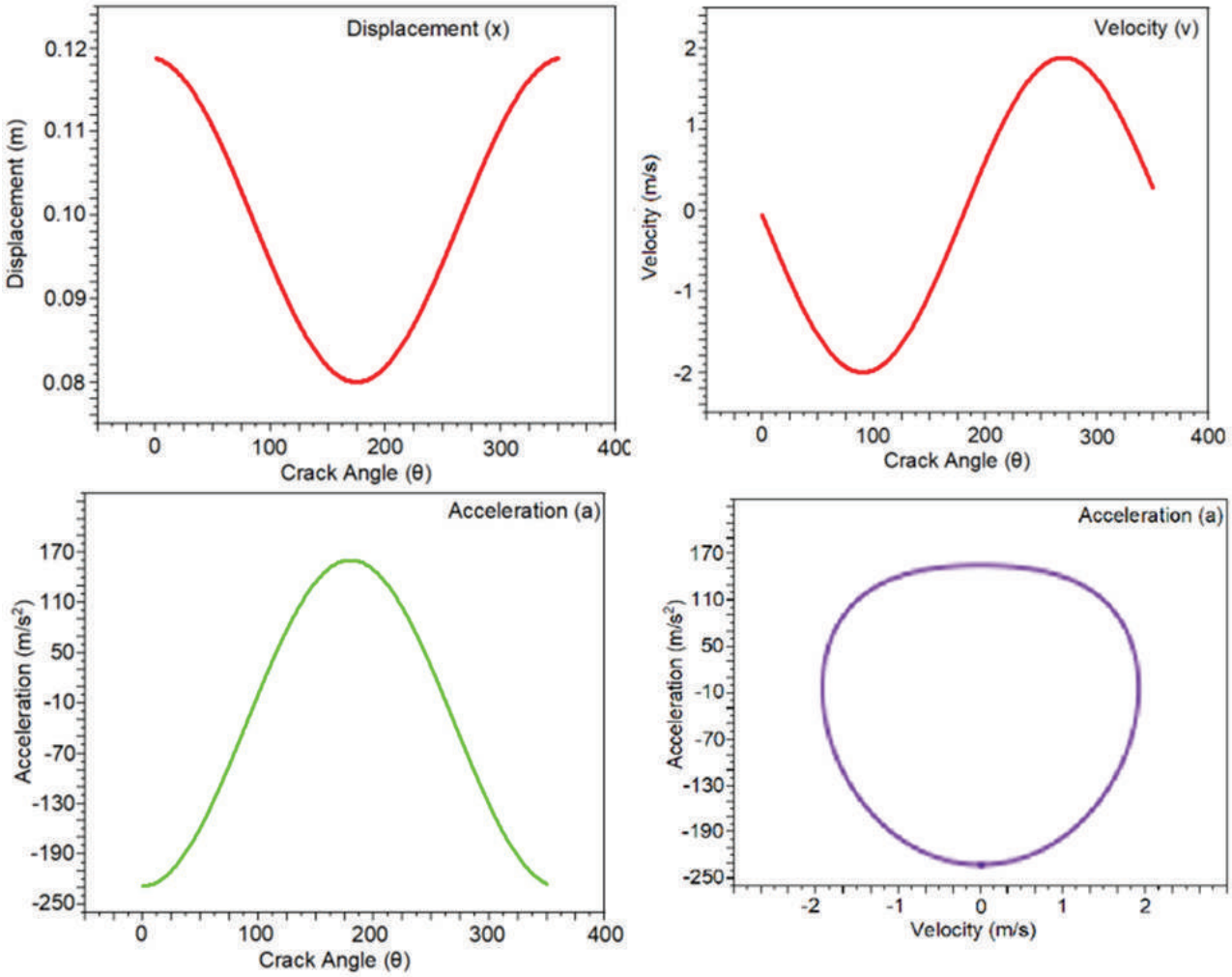

Figure 6. Slider Crank Kinematic Diagram.

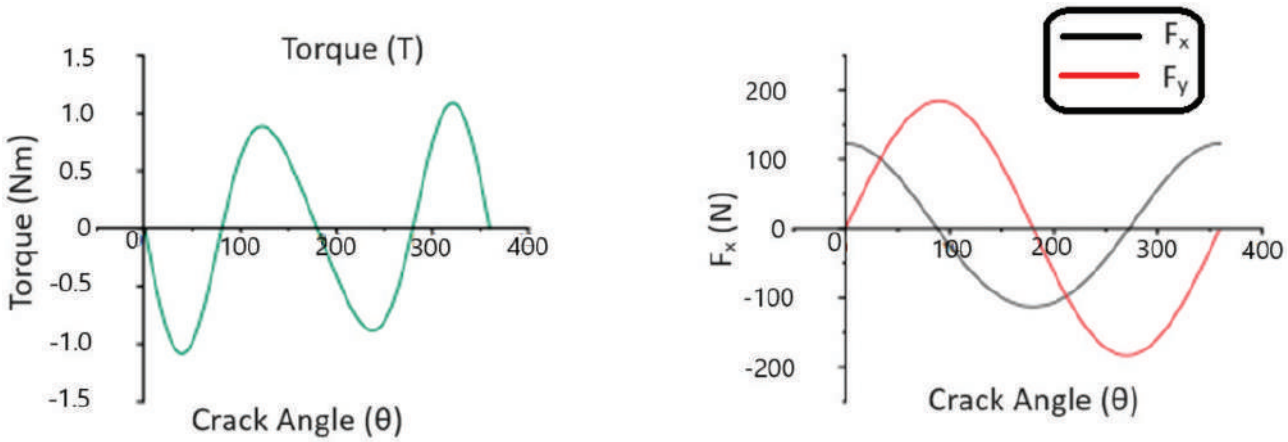

Figure 7. Torque and Force Vs Crank angle graph for Slider Crank.

In this simulation, we have made a design change while keeping other parameters constant. We can notice in Figure 9, that the strain energy is absorbed by the rib. Thus, it prevents significant deformation. The use of ribs helps us to achieve structural integrity by absorbing a definite amount of strain energy. Increasing the thickness of the wall wasn't

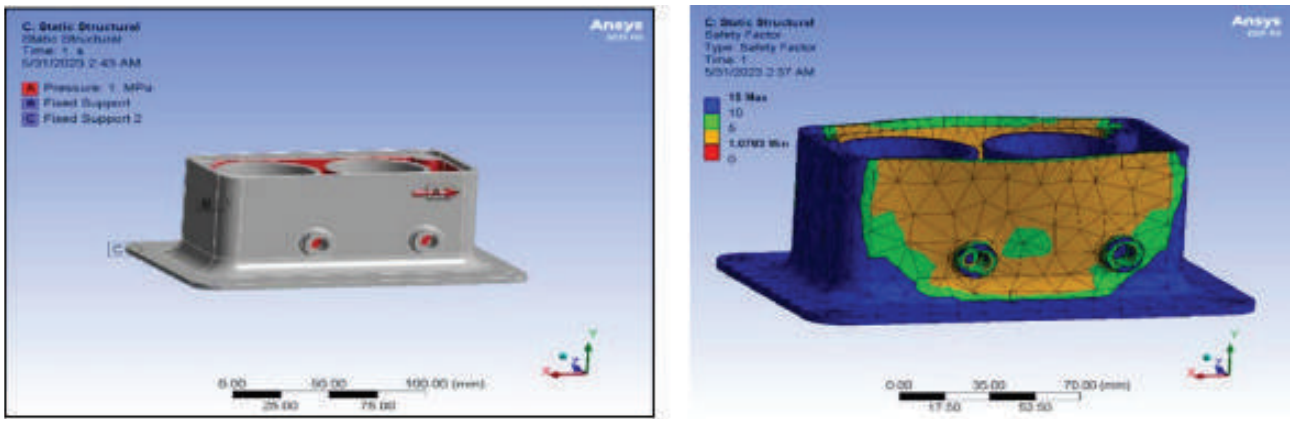

Figure 8. ANSYS Simulation for Regenerator Structural Integrity.

that effective because the strain energy was absorbed by the wall and still had a deformation. Similarly, we can also notice the increase in the factor of safety, making the design more suitable to be used under given conditions.

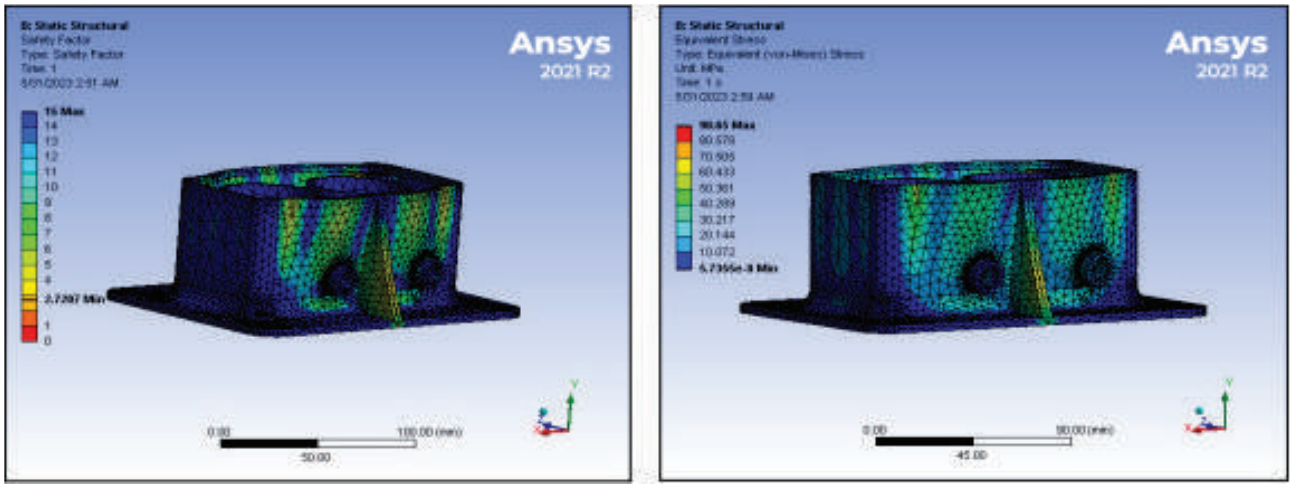

Figure 9. ANSYS Simulation for structural stability for Regenerator with ribs.

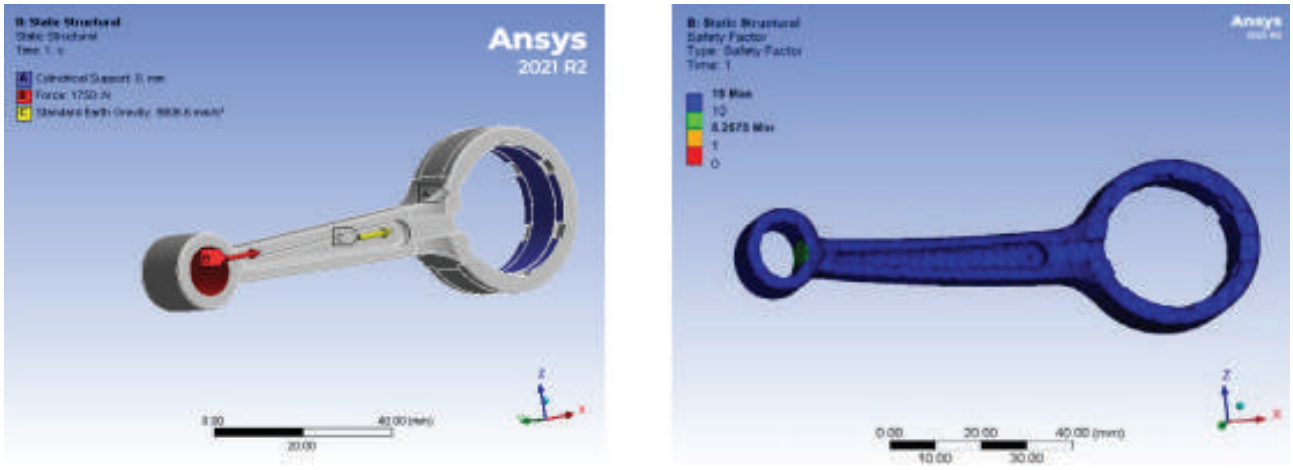

Figure 10. ANSYS Simulation Data for Connecting Rod Structural Integrity.

In figure 10, we have a connecting rod that is connected to the crankshaft and piston of the cylinder. We have performed static structural analysis for the factor of safety on it. The initial parameters include the applied force of 1750 N on face B in the figure. This force is the gas force applied on the rod by the piston. The simulation is performed with fine mesh type and we have selected the material for the connecting rod as forged steel. In the consequent figures, as the results of the simulations show, the connecting rod will withstand the applied force with an overall factor of safety on the body (colored blue) and a minimum of η= 5 factor of safety on the inside wall of the pin, which is in green color in the picture. The simulation concludes that our part will be safe during engine operation. ANSYS Simulation Data for Connecting Rod Structural Integrity is given in Table 5.

Experimental data is given in Table 6. The Solar Stirling Engine produced a power output of 77.569 wats and 523 rpm. The Schmidt analysis provides the best fit computation for the system. We have taken the engine rpm as 1000 rpm in our calculations but in actual experimentation due to mechanical losses and due to friction, we could only get around 500 rpm. That makes the deviation from computed and experimented power. The engine power has been measured it with tacheometer and dynamometer. The capacity of the system to transform solar energy into useful mechanical or electrical power is measured by thermal efficiency study. From NASA's Stirling engine design manual [28]:

$$\eta_{eff} = \left(1 - \frac{T_C}{T_H}\right) \times C \times \eta_H \times \eta_M \times f_a \qquad (12)$$

Were,

η_{eff} = overall thermal or effective efficiency

T_C, T_H = compression-expansion gas temperatures, K

C = Carnot efficiency ratio of indicated efficiency to Carnot efficiency. Calculated to be 0.68

η_H = heater efficiency, ratio between the energy flow to the heater and fuel energy flow. Calculated to be 0.86.

η_M = mechanical efficiency, ratio of indicated to brake power. Calculated to be 0.85

f_a = auxiliary ratio. At maximum efficiency point f_a= 0.95

Now Substituting Values, the average,

η_{eff} = 0.264

The energy performance matrix is given in Table 7.

The grid independence study is shown in Table 8

Table 5. ANSYS Simulation Data for Connecting Rod Structural Integrity

Quantity	Value
Length	100 mm
Max Force	750 N
Factor of Safety	2
Mesh Type	Fine Mesh
Materials	Forged Steel

Table 6. Temperature of Cylinders (Experimentally obtained)

S. No.	Max Temperature (°C) (Displacer Cylinders i.e., Hot Cylinders)	Average Temperature(°C) (Power Cylinders i.e. Cold Cylinders)
1	420	27.3
2	383	28.1
3	449	31.0
4	395	27.3

Table 7. Energy Performance Matrix

Parameter	Value (predicted)	Value (experimental)	Remarks
Thermal Efficiency	-	26.4 %	Reflects the engine's ability to convert heat into mechanical energy.
Mechanical Efficiency	-	-	Reflects internal friction and mechanical losses.
Overall Efficiency	-	26.4 %	Combined efficiency of heat conversion and mechanical work output.
Engine Speed	1000 rpm	523 rpm	Speed reduction due to mechanical losses.
Power Output	100 W	37 W	Deviation due to mechanical losses and non-ideal conditions.

Table 8. Grid Independence Study

Mesh Type	Element Size (mm)	Number of elements	Power Out Put (W)	Efficiency (%)	Remarks
Course Mesh	10	50000	35	25.2	Results show significant deviations, indicating that the mesh is too coarse.
Medium Mesh	5	150000	37	26	Results are closer to experimental data but still show minor discrepancies.
Fine Mesh	2	500000	37	26.4	Results are stable and closely match experimental data, confirming mesh independence.
Very Fine Mesh	1	1000000	37	26.4	No significant change in results, confirming that the mesh is fine enough for

As it was observed the upward trend in engine's characteristics such as power, kinematics including torque and speed etc. with respect to increase in temperature. This is in accordance with the observations in the studies by C. Yildiz et al., [29] and A. Yerbery et al., [30] who have faced similar trends in their respective research as well as the difference in predicted and actual power which was caused by manufacturing constraints as well as mechanical losses and non-ideal conditions.

EXPERIMENTAL RESULTS

The Solar Stirling Engine produced 77.569 watts at 523 RPM experimentally, deviating from the computed 1000 RPM due to friction and mechanical losses. Using NASA's Stirling engine design manual, the effective thermal efficiency was calculated to be 0.264. Efficiency factors included Carnot efficiency =0, heater efficiency =0.86, mechanical efficiency = 0.85, and auxiliary ratio = 0.95. Maximum temperatures in hot cylinders ranged from 383°C to 449°C, while cold cylinders averaged 27.3°C to 31.0°C. Increased temperature improved engine characteristics such as power, torque, and speed, consistent with prior studies.

Comparison of Results with Previous Data

Structural Analysis (ANSYS Simulation)

From the Previous Results the initial design exhibit low factor of safety, improvement were achieved by adding ribs which enhance stress distribution and wall thickness were increased with less effectiveness [27]. In current results simulations with 1 MPa pressure and mild steel properties confirmed structural challenges in the initial design, adding ribs reduced deformation by absorbing strain energy, improving safety and performance and Factors like fine mesh refinement and mild steel's thermal and mechanical properties were key to the analysis.

Thermal and Material Analysis

Previous results focused on regenerator material properties (mild steel) and its thermal performance under operating conditions. Thermal expansion, specific heat, and conductivity were used to analyze deformation and heat transfer efficiency [27]. While in current study detailed **thermal and fluent analysis** highlighted the impact of **thermal conductivity** and **coefficient of thermal expansion** on performance.

CONCLUSION

The experimental results demonstrated a power output of 37 W and an efficiency of 26.4%, compared to the predicted 100 W at 1000 rpm. However, due to mechanical losses, friction, and non-ideal operating conditions, the engine achieved a reduced speed of 523 rpm. The engine operated within a temperature range of 370–450 °C, with power, torque, and speed improving as the temperature differential between the hot and cold cylinders increased. Design constraints limited the scalability of the engine to achieve 100 W output, primarily due to market and manufacturing limitations. Mechanical losses, including flywheel inertia and friction, significantly impacted performance. To address these challenges, enhancements such as the integration of a Fresnel lens concentrator and the use of high-performance materials with superior thermal conductivity and durability were proposed. These improvements could increase compactness, efficiency, and structural integrity. The study highlights potential applications in desert and urban settings, where the engine could serve as a primary or supplementary power source for navigation aids, satellite production, and renewable energy systems. This research underscores the critical role of material selection and heat transfer optimization, paving the way for advancements in Stirling engine technology.

ACKNOWLEDGMENT

The authors greatly appreciate the support of the University of Engineering and Technology Peshawar, Pakistan

AUTHORSHIP CONTRIBUTIONS

Yasir Mehmood: conceptualization, validation, investigation, writing original draft, visualization;

Asnaf Aziz: supervision, review & editing;

Abid Hussain: Co-supervision, Data analysis;

Fasih Ur Rahman: manuscript preparation, project administration;

Afzal Khan: Review and Editing, Discussion, Validation:

Muhammad Abubakkar: manuscript preparation, discussion, review & editing;

Imad Rasool: manuscript preparation, discussion, review & editing

DATA AVAILABILITY STATEMENT

The authors confirm that the data that supports the findings of this study are available within the article. Raw data that support the finding of this study are available from the corresponding author, upon reasonable request.

CONFLICT OF INTEREST

The author declared no potential conflicts of interest with respect to the research, authorship, and/or publication of this article.

ETHICS

There are no ethical issues with the publication of this manuscript.

STATEMENT ON THE USE OF ARTIFICIAL INTELLIGENCE

Artificial intelligence was not used in the preparation of the article.

REFERENCES

[1] Butler A, Hoffman P, Smibert P, Papalexi E, Satija R. Integrating single-cell transcriptomic data across different conditions, technologies, and species. Nat Biotechnol 2018;36(5):411–420. [CrossRef]

[2] US Energy Information Administration. Frequently Asked Questions (FAQs). Much Electr Does Am Home Use 2020.

[3] Solankı A, Pal Y. A comprehensive review to study and implement solar energy in dairy industries. J Therm Eng 2021;7(5):1216–1238. [CrossRef]

[4] Kumar AR, Ramakrıshnan M. A scoping review on recent advancements in domestic applications of solar thermal systems. J Therm Eng 2022;8(3):426–444. [CrossRef]

[5] Guidi G, Violante AC, De Iuliis S. Environmental impact of electricity generation technologies: A comparison between conventional, nuclear, and renewable technologies. Energies 2023;16(23):7847. [CrossRef]

[6] Yerbury A, Coote A, Garaniya V, Yu H. Design of a solar Stirling engine for marine and offshore applications. Int J Renew Energy Technol 2016;7(1):1. [CrossRef]

[7] Asnaghi A, Ladjevardi SM, Izadkhast PS, Kashani AH. Thermodynamics performance analysis of solar Stirling engines. ISRN Renew Energy 2012;2012:1–14. [CrossRef]

[8] Nosek S, Brož K. Solar Stirling engine-the milestone of the way to meet energy demand with the lowest impact on environment. Sustain Energy Fuels 2017.

[9] Cinar C, Karabulut H. Manufacturing and testing of a gamma type Stirling engine. Renew Energy 2005;30(1):57–66. [CrossRef]

[10] Tlili I. Thermodynamic study on optimal solar Stirling engine cycle taking into account the irreversibilities effects. Energy Procedia 2012;14:584–591. [CrossRef]

[11] Gheith R, Aloui F, Nasrallah SB. Determination of adequate regenerator for a Gamma-type Stirling engine. Appl Energy 2015;139:272–280. [CrossRef]

[12] Nielsen AS, York BT, MacDonald BD. Stirling engine regenerators: How to attain over 95% regenerator effectiveness with sub-regenerators and thermal mass ratios. Appl Energy 2019;253:113557. [CrossRef]

[13] Karabulut H, Yucesu HS, Cinar C, Aksoy F. Construction and testing of a dish/Stirling solar energy unit. J Energy Inst 2009;82(4):228–232. [CrossRef]

[14] Yerbury A, Coote A, Garaniya V, Yu H. Design of a solar Stirling engine for marine and offshore applications. Int J Renew Energy Technol 2016;7(1):1. [CrossRef]

[15] Bataineh KM. Numerical thermodynamic model of alpha-type Stirling engine. Case Stud Therm Eng 2018;12:104–116. [CrossRef]

[16] Tang XY, Yang WW, Yang Y, Jiao YH, Zhang T. A design method for optimizing the secondary reflector of a parabolic trough solar concentrator to achieve uniform heat flux distribution. Energy 2021;229:120749. [CrossRef]

[17] Boretti A. Development of a hybrid concentrated solar-natural gas system. Int J Energy Res 2021;45(11):17015–17021. [CrossRef]

[18] Kayofa L. Feasibility Study and Business Plan for Manufacturing a 3 kW-Electrical Solar Stirling Engine and Dish for Stand-Alone Power Supply Units [PhD thesis]. Stellenbosch: Stellenbosch University; 2015.

[19] López-Castrillón W, Sepúlveda HH, Mattar C. Off-grid hybrid electrical generation systems in remote communities: Trends and characteristics in sustainability solutions. Sustainability 2021;13(11):5856. [CrossRef]

[20] Zhu S, Yu G, Liang K, Dai W, Luo E. A review of Stirling-engine-based combined heat and power technology. Appl Energy 2021;294:116965. [CrossRef]

[21] Alipour N, Jafari B, Hosseinzadeh K. Analysis of the impact of metal foam with phase change material on solar photovoltaic thermal system efficiency. J Energy Storage 2024;98:113064. [CrossRef]

[22] Aigboviosa AP, Anthony A, Claudius A, Uzairue S, Timilehin S, Imafidon V, et al. Arduino based solar tracking system for energy improvement of PV solar panel. In: Proceedings of the International Conference on Industrial Engineering and Operations Management; 2018. p. 2469–2478.

[23] Thombare DG, Verma SK. Technological development in the Stirling cycle engines. Renew Sustain Energy Rev 2008;12(1):1–38. [CrossRef]

[24] Tanaka C, Kamata H, Takeshita H, Yagisawa H, Hirata H. Redox regulation of lipopolysaccharide (LPS)-induced interleukin-8 (IL-8) gene expression mediated by NFκB and AP-1 in human astrocytoma U373 cells. Biochem Biophys Res Commun 1997;232(2):568–573. [CrossRef]

[25] Lam N, Tuner M, Tunestal P, Andersson A, Lundgren S, Johansson B. Double compression expansion engine concepts: A path to high efficiency. SAE Int J Engines 2015;8(4):1562–1578. [CrossRef]

[26] Bataineh K. Mathematical formulation of alpha-type Stirling engine with Ross Yoke mechanism. Energy 2018;164:1178–1199. [CrossRef]

[27] Egas J, Clucas DM. Stirling engine configuration selection. Energies 2018;11(3):584. [CrossRef]

[28] Martini WR. Stirling Engine Design Manual. NASA; 1983.

[29] Yildiz C, Bayata F, Mugan A. Multi-objective optimum design of an alpha type Stirling engine using meta-models and co-simulation approach. Energy Convers Manag 2021;232:113878. [CrossRef]

[30] Yerbury A, Coote A, Garaniya V, Yu H. Design of a solar Stirling engine for marine and offshore applications. Int J Renew Energy Technol 2016;7(1):1. [CrossRef]

J Ther Eng, Vol. 12, No. 2, pp. 815−829, March, 2026

Journal of Thermal Engineering
Web page info: https://jten.yildiz.edu.tr
DOI: 10.14744/thermal.0001113

Review Article

Simulation of the thermal marangoni effect in a free surface cavity: Heatline and entropy visualizations

Nagham Yass KHUDAIR[1], Qusay Rasheed AL-AMIR[2], Hayder K. RASHID[3]

[1]Department Metallurgy Engineering, College of Material Engineering, University of Babylon, Hilla, Iraq
[2]Department of Mechanical Power Technical Engineering, College of Engineering and Technology, Al-Mustaqbal University, Hilla, Babylon, Iraq
[3]Department of Ceramic Engineering, College of Material Engineering, University of Babylon, Hilla, Iraq

ARTICLE INFO

Article history
Received: 16 January 2025
Revised: 25 April 2025
Accepted: 01 August 2025

Keywords:
Marangoni Convection; Cavity; FVM; Heat Function; Entropy Generation

ABSTRACT

There are many modern engineering applications of natural convection with free surface square cavity. In this paper analyzes numerically convection that is both natural and Marangoni. Together adiabatic cooling and convective cooling are subject to the upper free surface boundary, whereas a portion of the bottom wall boundary is exposed to constant heat flux and the remaining portions are maintained adiabatically. The unique of this research is the possibility of using its numerical analysis to enhance the applications related to solar energy, which is considered one of the most important applications in the field of renewable energy, in addition to food storage**.** The boundaries of the vertical walls of square cavity are kept cold. Under the influence of constant heat flux, two physical phenomena thermocapillary and buoyancy forces are considered and statistically depicted. A finite volume method is used to solve the governing equations based on the heat line approach. The current research is supported by other studies that are published in the literature. For different values of the Marangoni number (-10^3 to $+10^4$), Grashof number (10^4 to 10^5), Prandtl number (0.054, 0.16, 0.71, 6.2, 100), and Biot number (0 to 80) are produced to investigate the impacts on streamlines, isothermal lines, heat lines, and local entropy generation. The solving of the government equations is depending on numerical solution for the control volume system with assumed that the situation of heat transfer and fluid flow is steady with generating entropy over the all-control volume under investigation and density differences are ignored. It has been noted that the maximum stream function increases as Marangoni numbers increase from 0 to 10^4. This trend results from the fact that the flow velocity increases with the increasing Marangoni number. However, the Marangoni It has a reciprocal effect with convective heat transfer. The solution and its improvement are within the conditions of this research. The flow pattern is not considerably affected when the Biot number is changed from 40 to 80 as the surface tension is minimal.

Cite this article as: Khudair NY, Al-Amir QR, Rashid HK. Simulation of the thermal marangoni effect in a free surface cavity: heatline and entropy visualizations. J Ther Eng 2026;12(2):815−829.

***Corresponding author.**
*E-mail address: mat.hayder.k@uobabylon.edu.iq

This paper was recommended for publication in revised form by Editorin-Chief Ahmet Selim Dalkılıç

Published by Yıldız Technical University Press, İstanbul, Turkey
Yıldız Technical University. This is an open access article under the CC BY-NC license (http://creativecommons.org/licenses/by-nc/4.0/).

INTRODUCTION

The influence of buoyancy and thermocapillary forces on heat transfer in free surface cavities were received extensive study in recent years. The range of industrial processes, including drying and crystal development melting, was what sparked this curiosity. Surface tension differences at a liquid-gas interface brought on by temperature differences generate fluid motion at the free surface. Marangoni convection or Thermocapillary flow is the technical term for such motion. Besides, fluid motion can also be brought on by the buoyancy force. The convective flow was steered in the opposite direction by the combined forces of thermocapillary and buoyancy [1]. A little amount of a surface-active contaminant was found to be the cause of the thermocapillary flow's anomalous direction [2].

Reviewing relevant earlier work reveals that the majority of them [3–15] focused on thermocapillary convection and combined buoyancy in cavities with differential heating. According to Saleh et al. [3] investigated cooling intensity for any fluid type results in an increase in the amount of heat transfer at the hot wall and a decrease at the cold wall. In a computational analysis of constant convective flow in a square cavity, Bergman and Ramadhyani [4] demonstrated how surface tension effects can drastically change the buoyancy-induced flow. For different Rayleigh numbers, Cicek and Baytas [5] have been looked at the impact of a negative and positive Marangoni number on heat transfer and fluid flow. Strani et al. [6] have been concluded that for low crispation numbers, the surface deformation had no impact on the qualitative characteristics of the flow field structure. The heat lines approach was used by Arbin et al. [7] to investigate the double-diffusive natural convection inside an open-topped square cavity that was differentially heated. They demonstrated how the heater segment length affects the mechanisms of heat and mass transfer. Buoyancy ratio, surface tension, and the heater segment all play a role in the heat transfer, fluid flow, and concentration distribution within the cavity. Jue [8] demonstrated how concentration and temperature contribute to the flow in opposite ways and how their distributions along the surface boundary exhibit local variation. In the presence of a magnetic field, Rudraiah et al. [9] investigated buoyancy and thermocapillary induced flow. They said that while heat transfer diminishes in the presence of a magnetic field, it increases with the Marangoni number. Also, research by Saleem et al. [10] conducted investigations to study the double-diffusive convection in presence of a magnetic field inside a square cavity. The results demonstrated that while the heat and mass transfer rates increase with an increase in the parameter of chemical reaction, the average Sherwood number and the average Nusselt number drop with increasing values of Hartmann number. Furthermore, concentration buoyancy has a higher influence on flow than thermal buoyancy does.

Additionally, Hossain et al. [11] investigated how an external magnetic field affected combined buoyancy and thermocapillary convection flow while also taking into account the impact of internal heat generation. The study of natural convection is significant due to the irreversibility phenomena caused by fluid friction and heat transfer that are reflected by entropy generation. In a cubical cavity, the coupled three-dimensional buoyancy and thermocapillary convection were solved by Oztop et al. [12]. For lower values of Rayleigh numbers, they discovered that the number of Marangoni becomes a more powerful parameter on total entropy generation.

Saleh and Hashim [13] investigated how different nanoparticle kinds and concentrations affected buoyant Marangoni convection in a square cavity that was variably heated. They concluded that when convective thermocapillary and buoyancy forces are equivalent in strength, a rise in nanoparticle concentration results in a drop in flow rates in secondary cells. The magnitudes of the Grashof number and Prandtl number to be related to the active spot of greatest entropy formation have been shown by Saleem et al. [14]. The rate of entropy creation rises as the Marangoni number rises. The visualization of heat flow and the formation of entropy during natural convection in inclined square cavities were studied by Basak et al. [15] more recently using a finite element simulation. Their result illustrated that high rates of heat transfer with low entropy generation occur regardless of the Prandtl number. In a rectangular cavity with vertical walls that were heated differently, Ilis et al. [16] studied the impact of aspect ratio on the formation of entropy owing to natural convection. The entropy generation during natural convection in a rectangular inclined enclosure was explored numerically by Bouabid et al. [17]. They concluded that the thermal Grashof number, cavity aspect ratio, and irreversibility distribution ratio all rise with increasing amounts of entropy. In lid-driven enclosures filled with a porous media, several convection modes, entropy generation caused by Marangoni effects, side wall movement, and double-diffusive convection are studied by Ahmed et al. [18]. The average Bejan number is found to drop by 4.77% as the Bingham number increases from 0 to 0.5. Kolsi et al. [19] studied the effects of inserting a Carbon Nano Tube and providing a magnetic field on the 3D-thermocapillary natural convection. The findings showed that raising the volume fraction of nanoparticles and changing the magnetic field's strength and direction have a significant impact on the rate of heat transfer and flow structure. In a different study, Basak et al. [20] investigated the formation of entropy by natural convection in right-angled triangle cavities having porous media and top angles between 15° and 45° under varied temperature boundary conditions. A new method was used by Joe Bobach et al. [21] to simulate and validate the surface tension and phase change phenomena within a square space. This method is based on the particle finite element theory and was employed to simulate a series of test cases. Moreover, Zailan et al. [22] conducted numerical study for carried out the effect of Marangoni convection (Ma) with

in two-dimensional C type enclosure contained the nanofluid. Where, the COMSOL program software are used for numerical solutions. The observed that, the strength of the flow increases with Ma. Moreover, Zisan et al. [23] numerically investigated the Marangoni natural convection with in a three-dimensional enclosure located a pair of discrete heaters at the bottom and insulated the rest with insulation the top too. Using the finite element method for solving the Navier-Stokes and energy equations. They observed that the shear stress builds up due to the surface tension gradient and causes to initiate an additional vortex. On the other hand, Muhammad et al. [24] conducted a numerical investigation of a trapezoidal enclosure with a circular heated cylinder with fluid-flow and heat transfer rate of nanofluid inside. They found that the Rayleigh and Marangoni number were signification the strength of the flow. Also, Omer [25] studied the Marangoni convection problem for hybrid nanofluids. They using numerically to solve the partial differential equation by Matlab. They concern on the skin friction and Nusselt number at different water concentrations and Marangoni effects for the magnetohydrodynamic (MHD)flow of heat transfer over a stretching disk with porous suction and injection. However, Naquib et al. [26] conducted the fluid-flow and heat transfer rate of nanofluid inside a trapezoidal enclosure with a circular heated cylinder. the boundary conditions is in one side of the wall was cooled at constant temperature and the cylinder was placed in different locations inside the enclosure. They observed from results that the location of cylinder has a wide effect on the Marangoni and Rayleigh number. While, Abbas et al. [27] conducted the impact of heat generation on thermal Marangoni convective boundary layer flow of dusty trihybrid nanofluid across a flat surface with thermal radiation and non-linear mixed convection. They discover that their increasing values of Groshof and Marangoni number lead to the skin friction increases too. Also, higher surface tension gradients lead to stronger induced flows and more efficient heat transfer inside the liquid. Leila SAOUDI, and Nordine ZERAIBI [28] investigated the flow of nanofluids in a corrugated channel and the effect on the heat transfer performance. The numerical simulation was conducted using ANSYS-Fluent Software Ver. 16.0 investigating the entropy generation as well as the thermo-hydraulic performance for waving channel taking two corrugation profiles (sinusoidal and square). They observed that the thermodynamic behavior of the Al_2O_3/water nanofluid in different geometries, can be used to enhancement heat transfer in various applications. Ferroud et al. [29] numerically investigation the square fluid-filled cavity for investigation the entropy generation in laminar mixed convection. The side-walls are maintained at a constant temperature Tc, and moving upper ward at a constant velocity. The previous conditions presented to study the effects of irreversibility distribution on the entropy generation for different engineering applications. However, the remaining parts of lower and upper walls are adiabatic. They illustrated that, the total entropy generation increase by increasing the irreversibility distribution ratio and the increase of Prandtl number regardless the values of Ri = 1 and Re = 100.

There has not been a numerical study that deals with free surface square cavities subjected to bottom wall continuous heat flux, according to what has previously been mentioned in the literature. Moreover, it can be used to enhance the solar energy application, which is considered one of the most important branches in the field of renewable energy, in addition to food storage. Therefore, the current work aims to depict the streamlines, isothermal lines, heat lines, and local entropy production for the mixed natural and Marangoni convection in a free surface cavity exposed bottom wall boundary to a constant heat flux. This will enhance the engineering applications and open new application field for square enclosure. Moreover, gives a good imagination about the relation between the applied uniform heat flux over the cavity and the surface tension gradient and its applications for innovate investigation depending on numerical solution of enclosure in point of view the Marangoni effect.

PHYSICAL MODEL EXPLANATION AND GOVERNING EQUATIONS

The cavity had the dimensions L × L with two vertically facing walls that are kept cold (T_c) and an upper free surface that is continuously exposed to both natural and Marangoni convection while a portion of the bottom wall boundary is subjected to a constant heat flux (q'') and other portions are kept adiabatically. The cavity is used in this investigation to test various fluids. Figure (1) illustrates the

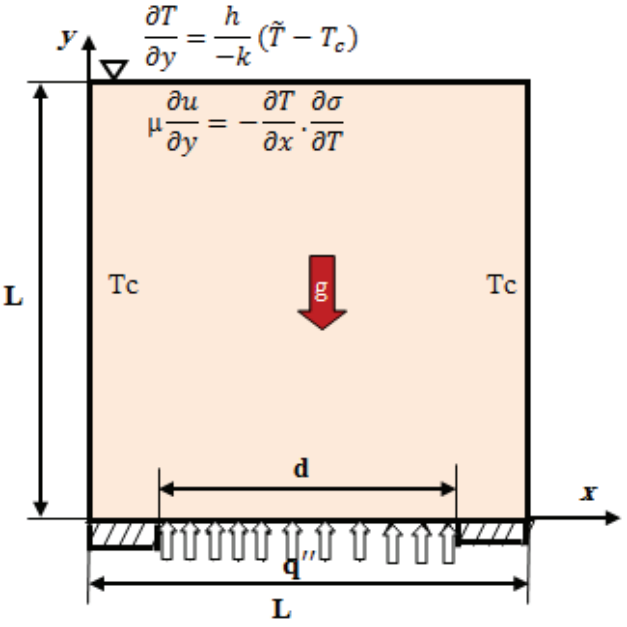

Figure 1. Systematic diagram of physical model.

outline of the schematic drawing of the physical model and its boundaries. Concerning the model, the following broad hypotheses apply:

The fluid flow within the cavity is two-dimensional, steady, and laminar.

1- The fluid in the cavity is Newtonian and incompressible.
2- Gravity works in the opposite direction as the y-axis.
3- The fluid-free surface is flat and perpendicular to the x-axis.
4- Radiative effects are negligible.
5- The velocity along a top-free surface is subject to a slip boundary condition.
6- All fluid parameters remain constant, except for surface tension and density change, which are only temperature-dependent.

Under the aforementioned assumptions, the dimensionless governing equations for the steady natural convection flow in a two-dimensional square cavity can be outlined as:

Conservation of mass [27]:

$$\frac{\partial}{\partial X}\left(\widetilde{U}_i\right)+\frac{\partial}{\partial Y}\left(\widetilde{V}_i\right)=0 \tag{1}$$

Momentium equations:

$$\widetilde{U}_i\frac{\partial}{\partial X}(\widetilde{U}_i)+\widetilde{V}_i\frac{\partial}{\partial Y}(\widetilde{U}_i)=-\frac{\partial}{\partial X}(\tilde{P}_i)+Pr\left(\frac{\partial^2}{\partial X^2}(\widetilde{U}_i)+\frac{\partial^2}{\partial Y^2}(\widetilde{U}_i)\right) \tag{2}$$

$$\widetilde{U}_i\frac{\partial}{\partial X}(\widetilde{V}_i)+\widetilde{V}_i\frac{\partial}{\partial Y}(\widetilde{V}_i)=-\frac{\partial}{\partial Y}(\tilde{P}_i)+Pr\left(\frac{\partial^2}{\partial X^2}(\widetilde{V}_i)+\frac{\partial^2}{\partial Y^2}(\widetilde{V}_i)\right)+Gr\,Pr^2\,\tilde{\theta}_i \tag{3}$$

Energy equations:

$$\widetilde{U}_i\frac{\partial}{\partial X}(\tilde{\theta}_i)+\widetilde{V}_i\frac{\partial}{\partial Y}(\tilde{\theta}_i)=\left(\frac{\partial^2}{\partial X^2}(\tilde{\theta}_i)+\frac{\partial^2}{\partial Y^2}(\tilde{\theta}_i)\right) \tag{4}$$

The following definitions are provided for the non-dimension parameters:

$$X=\frac{x}{L},\quad Y=\frac{y}{L},\widetilde{U}_i=\frac{\tilde{u}_i.L}{\alpha},\widetilde{V}_i=\frac{\tilde{v}_i.L}{\alpha},\tilde{P}_i=\frac{\tilde{p}_iL^2}{\rho\alpha^2},$$
$$\tilde{\theta}_i=\frac{\tilde{T}-T_c}{\Delta T},\Delta T=\frac{q''L}{K},Bi=\frac{(L/k)}{(1/h)},Pr=\frac{\vartheta}{\alpha},$$
$$Gr=\frac{g\beta\,L^3\Delta T}{\vartheta\alpha},\quad \widetilde{Ma}=\frac{\partial\sigma}{\partial T}\frac{q''L^2}{\mu\alpha}$$

$$\widetilde{U}_i=\frac{\partial\tilde{\psi}}{\partial Y},\ \widetilde{V}_i=-\frac{\partial\tilde{\psi}}{\partial X} \tag{5}$$

$$\nabla^2\tilde{\psi}=\frac{\partial^2\tilde{\psi}}{\partial X^2}+\frac{\partial^2\tilde{\psi}}{\partial Y^2} \tag{6}$$

The heat function ($\widetilde{\Pi}_i$), which is derived from convective heat fluxes ($\widetilde{U}_i\tilde{\theta}_i$, $\widetilde{V}_i\,\tilde{\theta}_i$). To represent the heat flow inside the cavity, heat fluxes ($-\frac{\partial\tilde{\theta}_i}{\partial X}$,$-\frac{\partial\tilde{\theta}_i}{\partial Y}$) are utilized.

$$\begin{aligned}\frac{\partial\widetilde{\Pi}_i}{\partial Y}&=\widetilde{U}_i.\tilde{\theta}_i-\frac{\partial\tilde{\theta}_i}{\partial X}\\ -\frac{\partial\widetilde{\Pi}_i}{\partial X}&=\widetilde{V}_i.\tilde{\theta}_i-\frac{\partial\tilde{\theta}_i}{\partial Y}\end{aligned} \tag{7}$$

The differential energy equation for the heat function is given by equation (8) as follows:[15]

$$\frac{\partial^2\widetilde{\Pi}_i}{\partial X^2}+\frac{\partial^2\widetilde{\Pi}_i}{\partial Y^2}=\frac{\partial}{\partial Y}\left(\widetilde{U}_i.\tilde{\theta}_i\right)-\frac{\partial}{\partial X}\left(\widetilde{V}_i.\tilde{\theta}_i\right) \tag{8}$$

In their non-dimensional terms, thermal gradients-induced entropy generation ($\tilde{S}_\theta$) and fluid friction -induced entropy generation ($\tilde{S}_\Psi$) , is defined as[27]:

$$\tilde{S}_{\theta,i}=\left[\left(\frac{\partial\tilde{\theta}_i}{\partial X}\right)^2+\left(\frac{\partial\tilde{\theta}_i}{\partial Y}\right)^2\right] \tag{9}$$

$$\tilde{S}_{\Psi,\mathrm{i}}=\Gamma\left[2\left[\left(\frac{\partial\widetilde{U}_i}{\partial X}\right)^2+\left(\frac{\partial\widetilde{V}_i}{\partial Y}\right)^2\right]+\left(\frac{\partial\widetilde{U}_i}{\partial Y}+\frac{\partial\widetilde{V}_i}{\partial X}\right)^2\right] \tag{10}$$

Where Γ is the irreversibility ratio as follows:

$$\Gamma=\frac{\mu.To}{k}\left(\frac{\alpha}{L.\Delta T}\right)^2 \tag{11}$$

To get the total entropy generation, the dimensionless local entropy generation is integrated over the system volume:

$$\widetilde{S_T}_{,i}=\int_V\tilde{S}_{\theta,i}.dV+\int_V\tilde{S}_{\Psi,i}\,.dV=\tilde{S}_{\theta,f}+\tilde{S}_{\Psi,f} \tag{12}$$

The following definition applies to the local Nusselt number of the heat sources[17]:

$$Nu=\frac{q''L}{k_f.(T_s-T_c)} \tag{13}$$

The local Nusselt number is rearranged as follows using the temperature dimensionless at heat source wall [26] and [27]:

$$\widetilde{Nu}_i=-\left(\frac{\partial\tilde{\theta}_i}{\partial n}\right)_{wall} \tag{14}$$

Integration of the local Nusselt number along the heat source yields the average Nusselt number ($\overline{\mathrm{Nu}}$) [27]

$$\overline{\mathrm{Nu}}=\frac{1}{D}\int_{(1-\frac{D}{L})/2}^{(1+\frac{D}{L})/2}\widetilde{Nu}_i\,.dX \tag{15}$$

In the current study, the boundary conditions in combination with the governing equations can be written in dimensionless terms as follows[27]:

At vertical walls: $X = 0$ and 1 and $0 \le Y \le 1$

$$\widetilde{U}_i=\widetilde{V}_i=0,\qquad \tilde{\theta}_i=0,\qquad \tilde{\psi}_i=0\,,\qquad n.\nabla\widetilde{\Pi}_i=0$$

At bottom horizontal wall:

$$Y = 0 \; and \;\; (1 - \frac{D}{L})/2 \le X \le (1 + \frac{D}{L})/2$$

$$\widetilde{U}_i = \widetilde{V}_i = 0, \quad \frac{\partial \widetilde{\theta}_i}{\partial Y} = -1, \quad \widetilde{\psi}_i = 0, \quad \frac{\partial \widetilde{\Pi}_i}{\partial X} = -1$$

$$Y = 0 \text{ and } \; 0 \le X \le (1 - \frac{D}{L})/2 \text{ and } \; (1 + \frac{D}{L})/2 \le X \le L$$

$$\widetilde{U}_i = \widetilde{V}_i = \frac{\partial \widetilde{\theta}_i}{\partial Y} = 0, \quad \widetilde{\psi}_i = 0, \quad \widetilde{\Pi}_i = 0$$

At upper free surface of the cavity: $Y = 1$ & $0 \le X \le 1$

$$\widetilde{V}_i = 0, \; \frac{\partial \widetilde{U}_i}{\partial Y} = -\widetilde{Ma} \times \frac{\partial \widetilde{\theta}_i}{\partial X}, \quad \frac{\partial \widetilde{\theta}}{\partial Y} = -Bi \times \widetilde{\theta}_i,$$

$$n.\nabla \widetilde{\Pi}_i = -Bi \times \widetilde{\theta}_i - \widetilde{U}_i \times \widetilde{\theta}_i + \frac{\partial \widetilde{\theta}_i}{\partial X}$$

NUMERICAL METHOD AND VALIDATION

The essential governing equations subject to boundary conditions are numerically integrated by using the finite volume approach, The Tri-Diagonal Matrix Algorithm iteration was utilized to solve the resulting algebraic equations line-by-line. Under the following condition, the iteration process ends [17] and [27]:

$$\chi = \frac{\sum_{i,j} \left| \beta_{i,j}^{t+1} - \beta_{i,j}^{t} \right|}{\left| \beta_{i,j}^{t+1} \right|} \le 10^{-6}$$

where χ is the tolerance; t and β are the iteration number and any of the computed field variables, respectively. The grid pattern used in the current study is uniformly staggered. Grid points of 51 × 51 is used to present the numerical solutions. There are no noteworthy changes in the average heat transfer as the grid size is increased from 51 × 51 to 81 × 81. The fields of the temperature and velocity for the relevant case can therefore be resolved using a grid size of 51 × 51, which has been accepted. In Figure 2, the computational mesh is depicted.

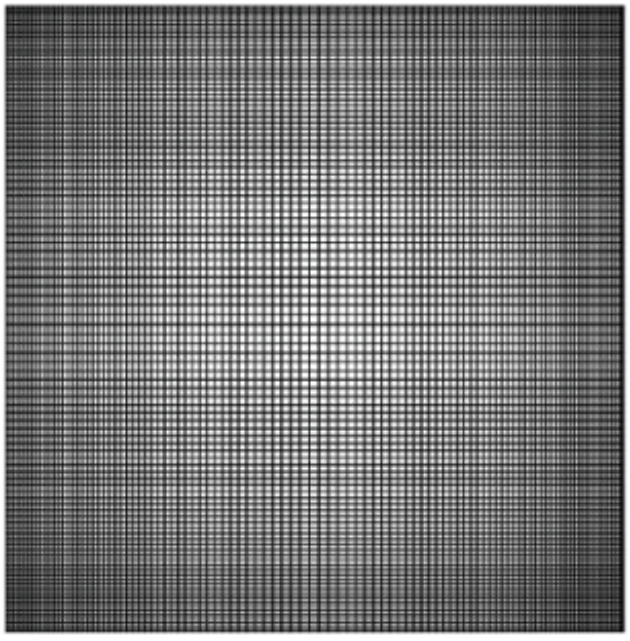

Figure 2. Mesh generation of present study.

There are three validations in this work to show the accuracy of the current results Saleh et al. [3], Ilis et al. [16], and Basak et al. [19]. As shown in Figure 3, Ilis et al. [16], and Basak et al. [19] results were used for the first and second validations of both entropy generation ($\widetilde{S_\psi}$ and $\widetilde{S_\theta}$) in a square cavity with hot left sidewall and cold right sidewall and adiabatic upper and bottom walls. A third validation was performed in accordance with the findings of Saleh et al. [3] in square cavities with an upper free surface. Their results as shown in Figure 4 were simulated for contours of streamlines, isothermal lines, and heatlines, respectively. These findings give reason to believe that the current numerical technique is accurate.

NUMERICAL RESULTS AND DISCUSSION

The results for the contours of isothermal lines, streamlines, heatlines, and entropy generations are indicated for different values of correlated parameters: Grashof number (10^4 to 10^5), Biot number (0 to 80), Prandtl number (0.054, 0.16, 0.71 to 6.22 and 100), and Marangoni number (-10^3 to $+10^4$).

Marangoni Number Effect

For several values of the Marangoni number ($\widetilde{Ma}$ = 0, 5 × 10^2, 1 × 10^3, 3 × 10^3, 5 × 10^3, 10^4), Figure 5 displays streamlines, isothermal lines and heatlines at Bi = 0, ϵ = 1, Gr = 10^4, and Pr = 0.054. The vertical center line of the cavity's cavity is seen to have symmetrical curves. The boundary conditions on the vertical walls are identical and the disregard for convective cooling at the top free surface boundary is the cause of this.

When there is no shear at the free surface ($\widetilde{Ma}$ = 0), surface tension does not affect the flow. As a result, the buoyancy effect mostly governs convection. Because of the different densities of the fluid particles abutting the bottom wall inside the cavity, when the temperature rises, the fluid flow rises from the bottom heated wall along the vertical symmetry axis until it is impeded at the upper free surface, directing the flow horizontally and in opposing directions towards the isothermal cold walls. Then, the flow reverses back straight to the middle region after reaching the bottom wall, falling along the left and right sides of the cold walls. In the left and right halves of the cavity, the flowing fluid, therefore, generates two spinning cells with counterclockwise and clockwise rotations. Because of the decrease in the value of the Grashof number (10^4) and the size of the maximum stream function ($\widetilde{\Psi}_{max}$ = +0.0711), the fluid flow is feeble inside the cavity. When Ma is equal to 500, the effects of surface tension result in the production of secondary flow, which is

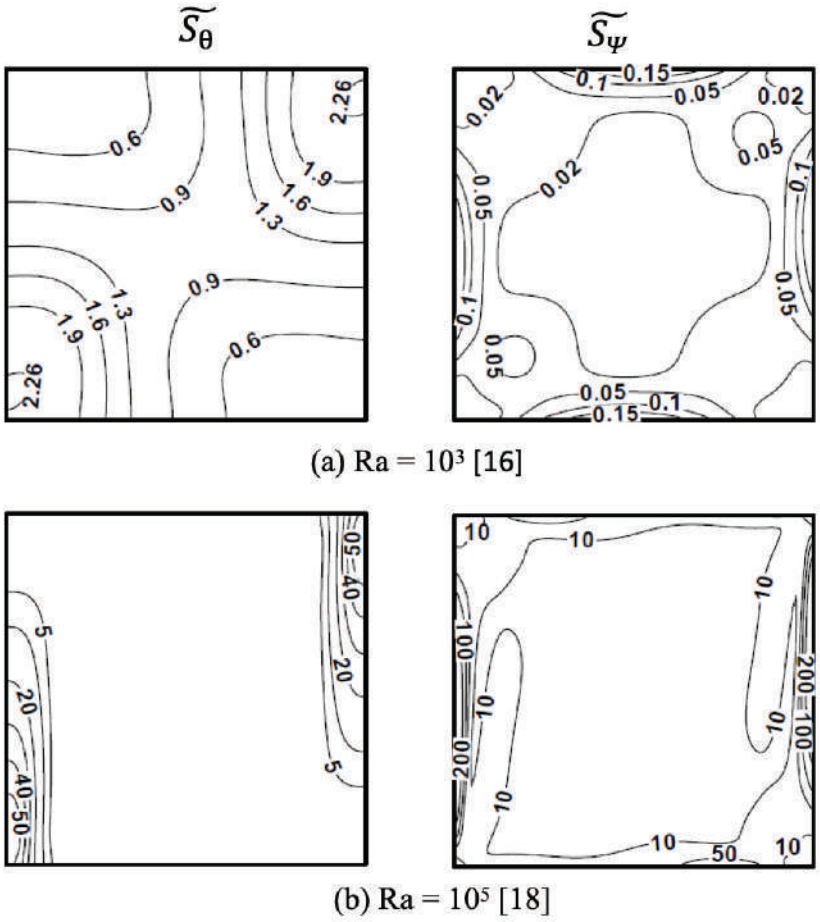

Figure 3. Local entropy generation ($\widetilde{S_\Psi}$ and $\widetilde{S_\theta}$) compared with the results of two sources [16] and [19] at Pr = 0.7.

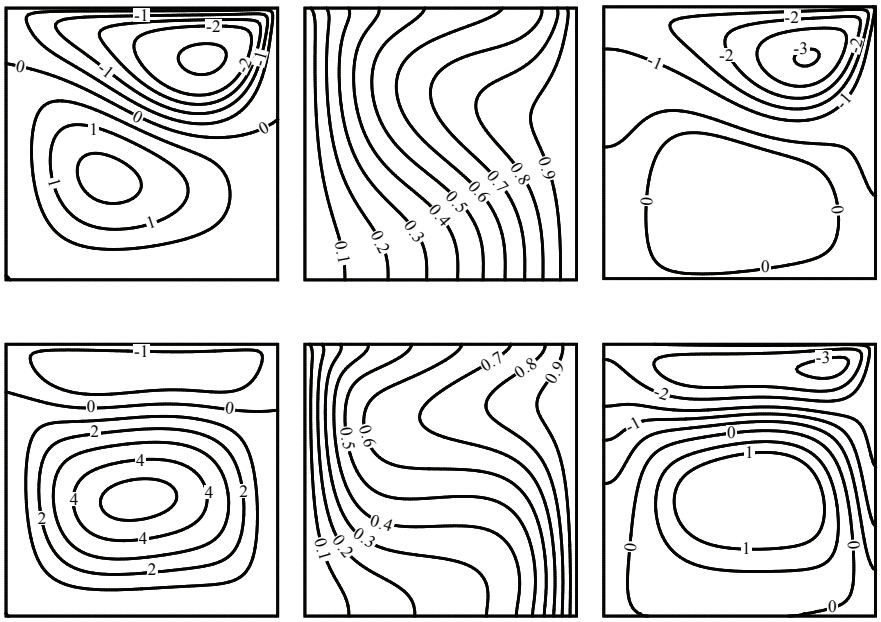

Figure 4. Streamlines, isotherml lines and heatlines, respectively compared with results of Saleh et al. [3] at Gr = 104, Bi = 1 and $\widetilde{Ma}$ = 103.

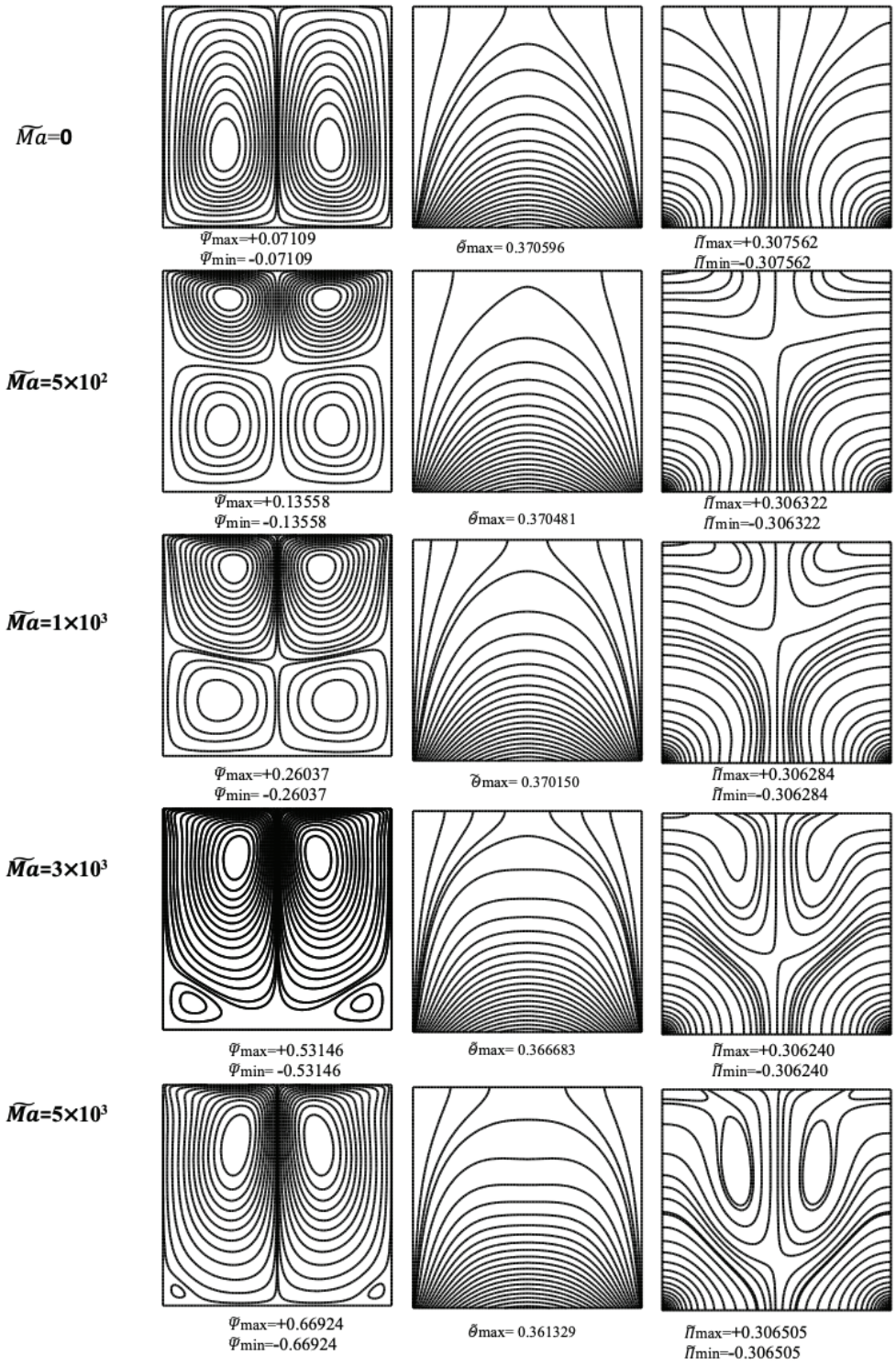

Figure 5. Contours of streamlines, isotherm lines, and heatlines for various Marangoni numbers at Bi = 0, ε = 1, Pr = 0.054 and Gr = 104.

represented at the top free surface by a couple of circulating cells with approximately equal strengths moving in opposite directions. Whereas the major circulating cells at the bottom wall are propelled by buoyancy force. These cells are propelled by thermocapillary forces. As a result, these two forces conflict with one another. Additionally, the streamlines are shown to concentrate on the upper free surface. When the free surface shear stress is reinforced

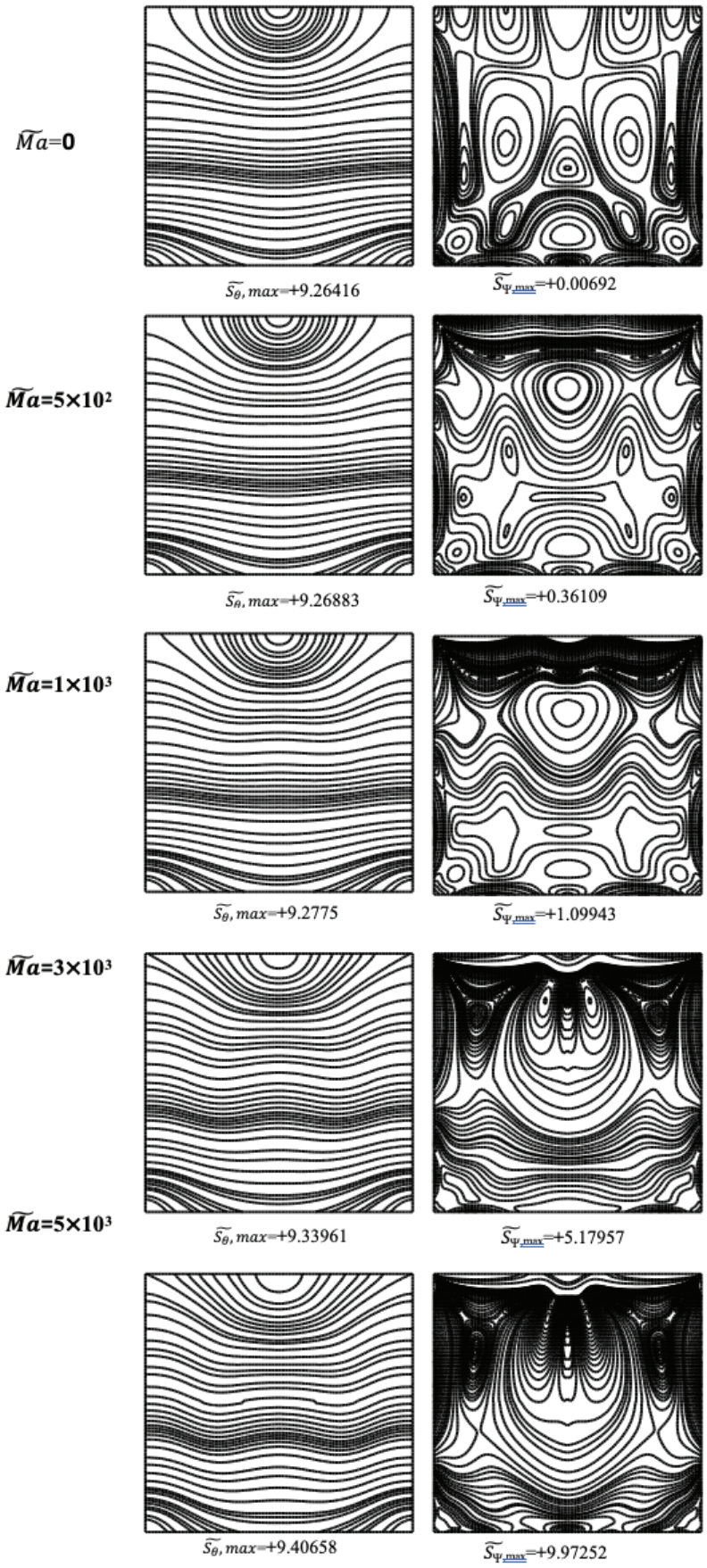

Figure 6. Entropy generation ($\widetilde{S_\theta}$ and $\widetilde{S_\Psi}$) for various Marangoni numbers Bi = 0, ε = 1, Pr = 0.054 and Gr = 104.

($\widetilde{Ma} = 1 \times 10^3$), the free surface velocities increase, and as a result, the buoyant force begins to diminish, and it loses its ability to regulate fluid motion. While the effect of the thermocapillary forces increases, which is represented by a couple of circulating cells at the top free surface. The rotation cells at the top free surface expand inside the enclosing area as Marangoni numbers increase to 3×10^3, which is compressed on a primary cell driven by buoyancy action. When the Marangoni number is raised higher, up to a value of 5×10^3, thermocapillary force takes over the entire domain, making buoyancy force relatively negligible. The two circulation cells as a result take up the whole domain inside the cavity, whereas the two minor corner cells next to the cavity's left and right vertical walls almost shrank and disappeared. The convection that is dominated by the Marangoni effect thus rules in this area. Marangoni convection or thermocapillary flow are two terms used to describe this flow. It can be observed that when Marangoni numbers rise from $\widetilde{Ma} = 0$, $\widetilde{\Psi}_{max} = +0.0711$ to $\widetilde{Ma} = 10^4$, $\widetilde{\Psi}_{max} = +0.88593$), the value of the maximum stream function rises. This tendency is caused by the fact that as the Marangoni number rises, the fluid flow velocity also rises. Because of the significant temperature gradient, as seen in Figure 5, the isothermal lines drop throughout the midplane from bottom to top and concentrate on the hot surface. Additionally, the Marangoni numbers surface (known from the value of $\tilde{\theta}_{max}$) does not effect on the contours of the isothermal lines. The curves of the heatlines show the direction of heat movement inside the cavity. When compared to isothermal line contours, heatlines contours behave differently. Heatlines behave differently for reasons related to intensified thermal mixing. When the surface tension effect is not present, heat flows radiate from the heat flux at the bottom wall and stop at the cold vertical walls. Due to the thermocapillary force, a few heatlines rotate as two swirls at the top corners of the cavity when the surface tension effect is present. These vortices descend in the opposite direction from the direction of heat flow as the Marangoni number increases.

As indicated, the isothermal lines are concentrated near the heat source at the bottom wall, particularly in its corners. Therefore, heat transfer causes the most entropy ($\widetilde{S_{\theta,max}}$) to be formed at the corners of the bottom wall. The findings shown in Figure 6 demonstrated that as Marangoni numbers increase, the generation of entropy due to heat transfer increases. (i.e. $\widetilde{Ma} = 0$ to $\widetilde{Ma} = 5 \times 10^3$; $\widetilde{S_{\theta,max}} = +9.2642$ to $\widetilde{S_{\theta,max}} = +9.4066$). On the other hand, the large, intense flow, except in the scenario where $\widetilde{Ma}$ is equal to zero, causes the entropy generation caused by fluid friction to concentrate on the free surface. The generation of entropy resulting from fluid friction is likewise increased as thermal Marangoni numbers rise. ($\widetilde{S_{\Psi,max}} = +0.0069$ for $\widetilde{Ma} = 0$ to $\widetilde{S_{\Psi,max}} = +9.973$ for $\widetilde{Ma} = 5 \times 10^3$). Which is very crucial for improving many engineering applications that depends on Marangoni numbers.

Prandtl Number Effect

Five values of the Prandtl number are taken into account in order to conduct a thorough investigation: Pr = 0.71 for air, Pr = 6.2 for water at 25 °C, Pr = 100 for motor oil at 20 °C and finally Pr= 0.054, and 0.16 for liquid metals. For different Prandtl values at $\widetilde{Ma} = 10^3$, Bi = 1, ε = 1, and Gr = 10^5, Figure 7 displays streamlines, isothermal lines and heatlines. These contours are asymmetrical about the cavity's vertical center line due to the convective cooling effect at the upper boundary.

Because there is no wall at the top free surface, as illustrated in Figure 7 (Pr = 0.054), the maximum velocity profile appears there. As a result, the streamlines around the cavity's center show the appearance of a counter-rotating cell. Near the top-left corner of the free surface, the fluid flow encounters the rotation cell and then reverses direction. The temperature there is significantly non-uniform due to the high velocity near the free surface, particularly in the top-left corner. The flow is largely motionless on the opposite side towards the bottom-right corner which causes little secondary clockwise circulations. A slight Prandtl number effect is evident at the top free surface due to the impact of surface tension. When Pr = 0.16, the size of the bottom cell increases as a result of the buoyancy effect, whereas the size of the top circulation cells caused by surface tension decreases. The top rotating cells are compressed and equal in size within the cavity as a result of the buoyancy effect as Pr is raised to 0.71, which causes a further drop in the thermocapillary force effect. Since both driving forces have similar magnitudes, combined convection is likely to occur, as demonstrated in the instance of Pr to 0.71. The buoyancy effect grows more rapidly than the thermocapillary effect when Pr approaches 6.2. With $\widetilde{\Psi}_{max} = +11.974$, it can be seen that the fluid velocities are higher and happen just below the free surface. The magnitudes of the stream function are found to be stronger when Pr is increased to 100 ($\widetilde{\Psi}_{max} = +34.683$). Because buoyancy-driven convection rather than thermocapillary convection is more prevalent, the fluid motion tends to the left. As you get closer to the walls, the isothermal lines get denser, indicating increased heat transfer from the heated bottom wall to the top parts of the side walls. It has been noted that the contours of streamlines and heatlines are identical. Additionally, because of the increased thermal mixing within the cavity, the size of the heat function grows with increasing Pr. On the other hand, Figure 8 indicated entropy generation caused by temperature gradients and fluid friction for different Prandtl values at $\widetilde{Ma} = 10^3$, Bi = 1, ε = 1, and Gr = 10^5. Where contours of S_θ are concentrated, there is a high value of S_θ for entropy generation resulting from heat transfer near hot places. Due to fluid friction, the cool side walls also function as potent entropy-generating sites. Along the middle of the side walls, $\widetilde{S_\Psi}$ is at its highest value. Intriguingly, the amount of entropy generated by fluid friction barely increases as the Prandtl number rises (i.e. $\widetilde{S_{\Psi,max}} = +3.4936$ for Pr = 0.054 to $\widetilde{S_{\Psi,max}} = +37.23$ for Pr=0.71). As observed from $\widetilde{S_{\Psi,max}}$

contours along the vertical centerline with $\widetilde{S_{\Psi,max}}$ = 399.217 to $\widetilde{S_{\Psi,max}}$ = +12519.3 for Pr = 6.2 to 100, results of $\widetilde{S_{\Psi,max}}$ in large entropy formation at higher Pr due to the inclination of counter-rotation of circulation cells. As Pr increases from Pr = 0.015 to Pr = 100, the entropy generated by heat transfer reduces from $\widetilde{S_{\Psi,max}}$ = +9.3734 to $\widetilde{S_{\Psi,max}}$ = +3.9269.

Biot Number Effect

Figure 9 depicts the contours of streams for various values of Biot number (Bi = 0, 5, 10, 40, 80) for Pr = 0.054, Gr = 10^5 for the two cases: (a) $\widetilde{Ma}$ = $+10^4$ and (b) $\widetilde{Ma}$ = -10^3. The Bi is crucial to the mechanism of heat transfer. In the situation of $\widetilde{Ma}$ = $+10^4$, it is believed that the surface tension decreases with increasing temperature. A huge anticlockwise rotating cell and a small clockwise rotating cell respectively appear towards the center and top corner of the cavity when there is no convective cooling effect (Bi = 0). This is brought on by a significant influence of surface tension and a large temperature gradient near the free surface. Because of the thermal gradient difference between the cold and hot

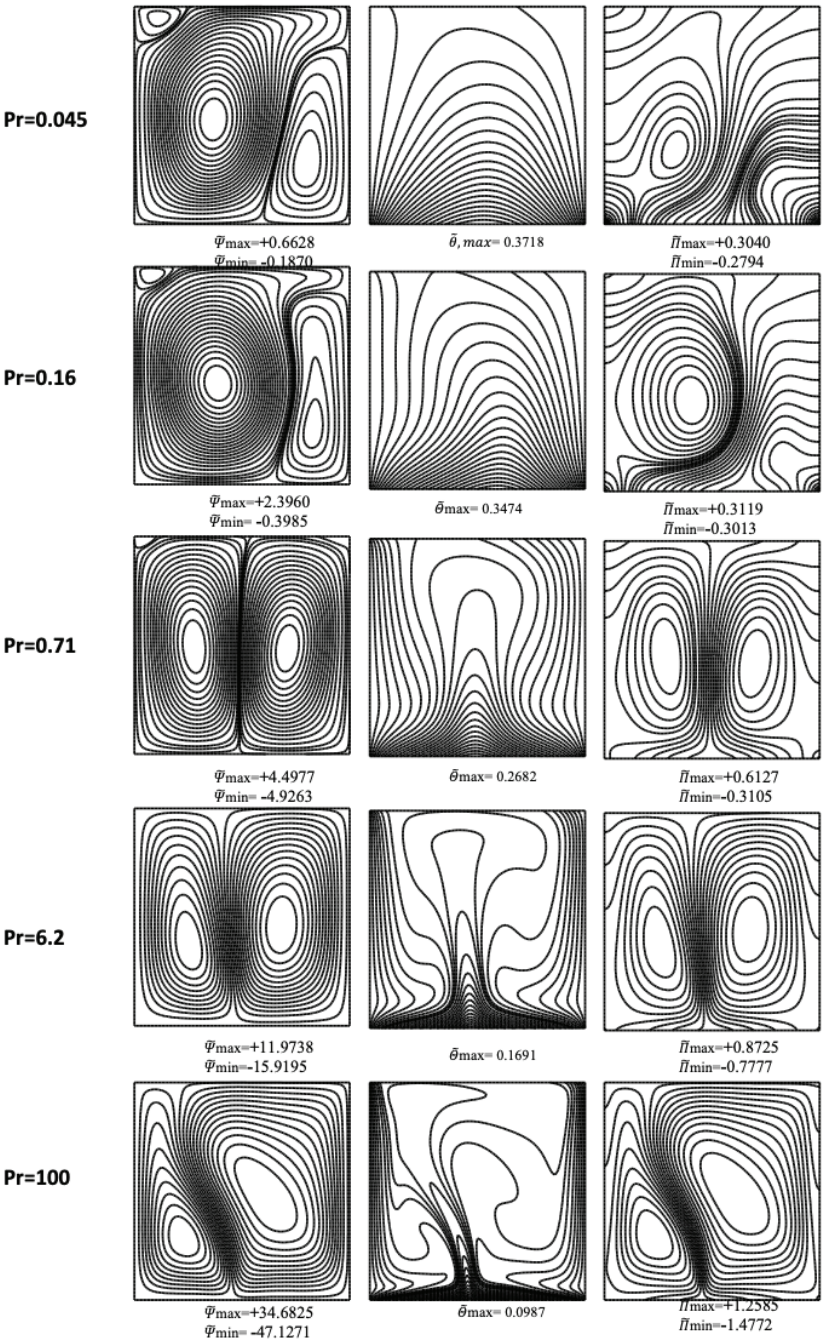

Figure 7. Contours of streamlines, isotherms and heatline for various Prandtl numbers at Bi=1, ε=1, $\widetilde{Ma}$ = 10^3, and Gr=10^5.

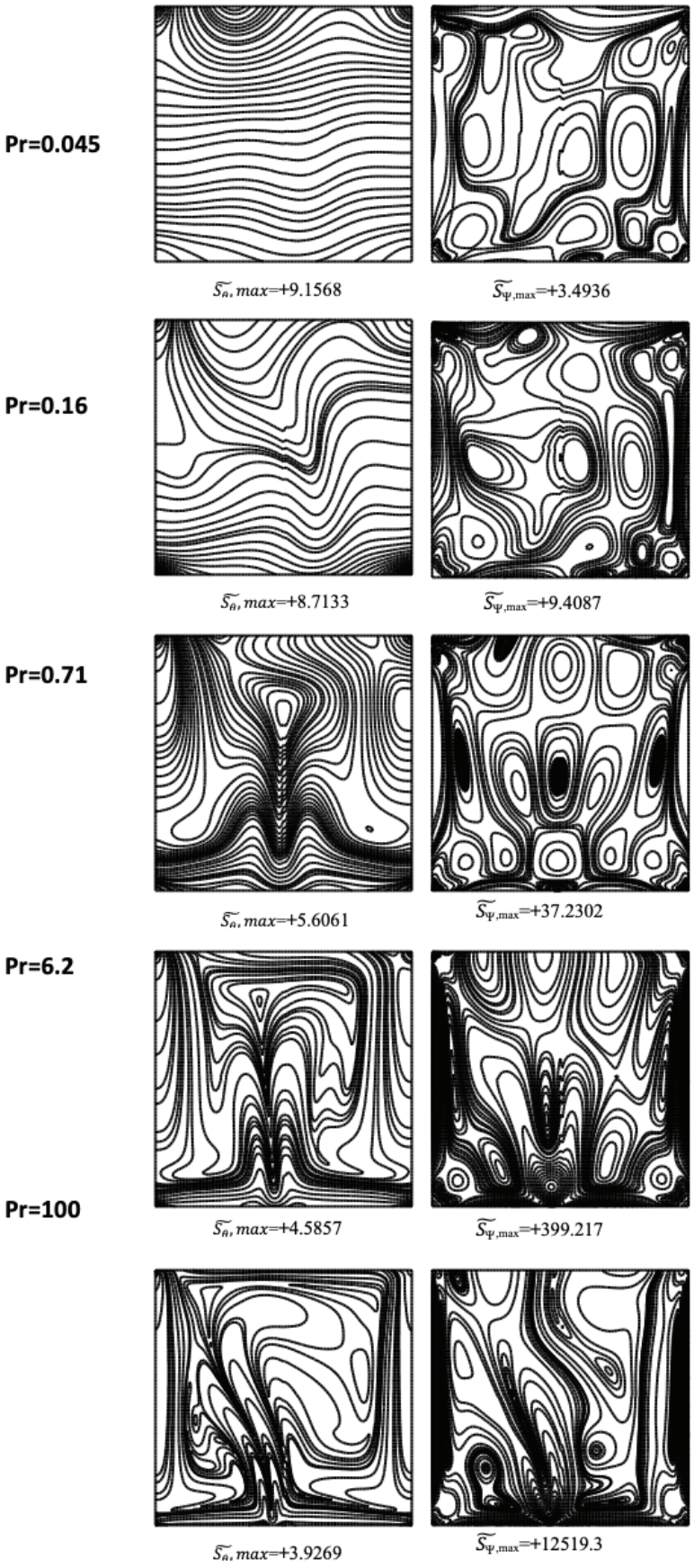

Figure 8. Entropy generation (Sθ and SΨ) for different Prandtl numbers at Bi=1, ε=1, Gr=105 and $\widetilde{\mathrm{Ma}}$ = 103.

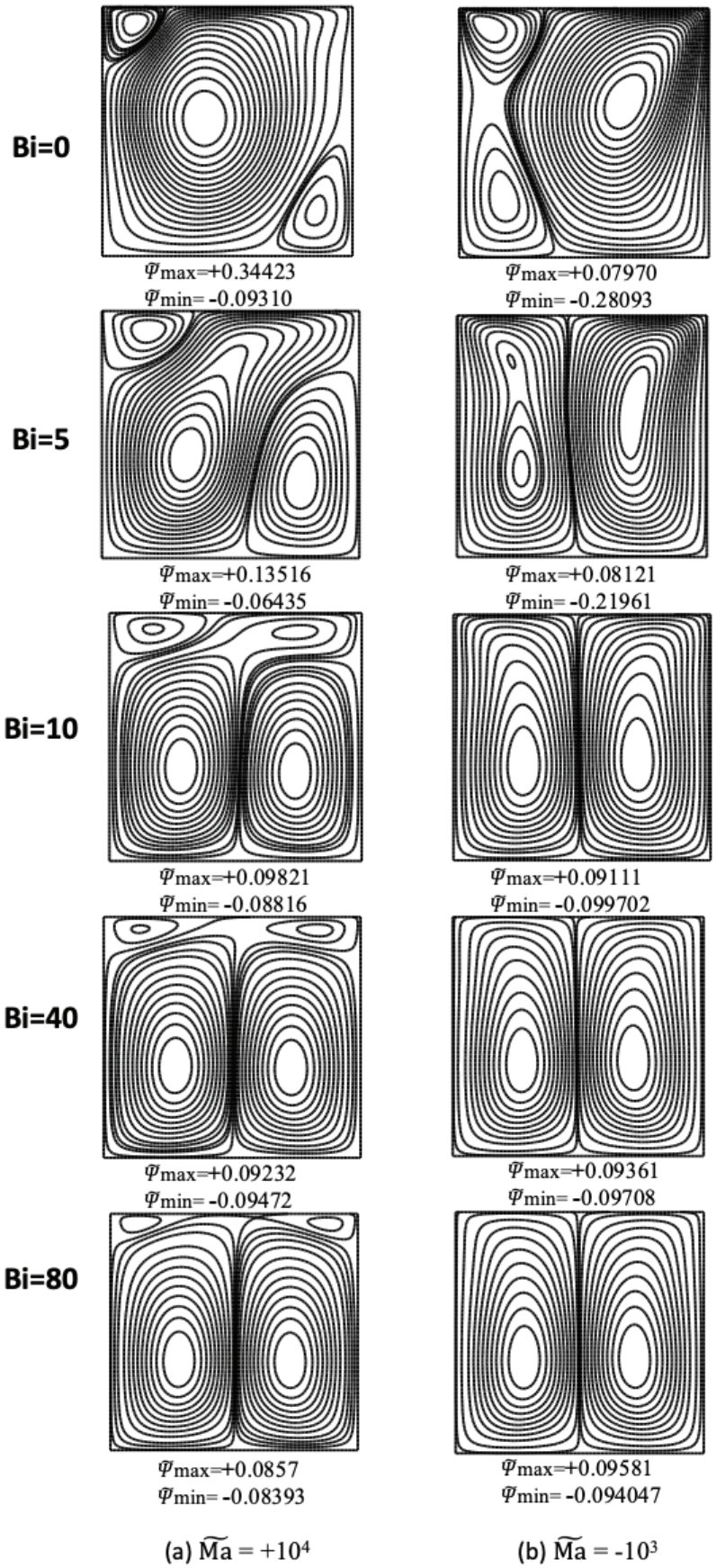

Figure 9. Streamlines contours for various Biot numbers at Gr=105, Pr = 0.054 for two cases: (a) $\widetilde{Ma}$ = +104 and (b) $\widetilde{Ma}$ = -103

walls, a small clockwise spinning cell forms at the right bottom wall corner. As the heat transfer rate improves for (Bi = 5), the circulation cell near the right corner of the bottom wall starts to enlarge. The buoyancy effect dominates fluid motion for (Bi = 10) because the convective cooling at the top free surface rises. Surface tension has a weaker impact as the Biot number increases (40–80), definitely as a result of increased convection cooling at the upper free surface. When the Marangoni number is negative ($\widetilde{Ma} = -10^3$), the fluid motion slows down and a clockwise streamline cell concentration occurs at the left cold wall (Bi = 0). The exterior convection resistance lowers for high Biot numbers (Bi = 5), which improves both transfer rates. When the surface tension is negligible, changing the Biot number which ranges from 10, 40, and 80 does not significantly affect the flow pattern. When $Gr = 10^5$, buoyancy forces for the same Marangoni number values become stronger.

CONCLUSION

The following are the primary conclusions:

1- When there is no convection cooling impact on the top free surface, the maximum stream function values increase as the Marangoni number grows, but the isotherm contours are unresponsive to this change. However, as the Marangoni number rises, the quantity of entropy that produced by heat convection and fluid friction also increases.
2- The heatlines, stream functions and entropy generation due to fluid friction all increase as the Prandtl number do, however, isothermal lines and entropy generation owing to heat transfer reduce as the Pr number rises under similar conditions.
3- For small values of Biot number, the effect of surface tension on fluid motion is considerable; but it is weak for large Biot numbers.
4- In this research raises in marangoni will help to undiminished of heat translated and induced several types of vortices that may enhance free convection, which maximize the heat transfer and improves its utilization.
5- There are clear impact of the value of Prandtl on the entropy distribution from the value 0.16 to 0.7.
6- Recommendations

This work can be modified by presented many types of noise that may produce other effects on flow parameters in duct, the research in following areas cab be recommended.

1. Using directly the square enclousure with marangoni applications in solar collector in such away for decrease the power required for industrial applications.
2. Using more that one working fluid like gas with water for investigations the effect of marangoni number.
3. There many enclosure shapes can numerically anlyzied and may give more efficient for natural convection with marangoni.

NOMENCLATURE

C_p	Specific heat at constant pressure (kJ/kg.K)
D	Cavity characteristic length m
g	Gravitational acceleration (m/s^2)
k	Thermal conductivity (W/m.K)
L	Height or Width of the cavity (m)
P	Dimensionless pressure
p	Pressure (Pa)
Pr	Prandtl number (ϑ/α)
q''	Heat flux (W/m^2)
Ra	Rayleigh number ($g\beta L^3 \Delta T/\vartheta\alpha$)
T	Temperature (K)
T_c	Temperature of the cold surface (K)

Greek symbols

α	Thermal diffusivity (m^2/s)
θ	Dimensionless temperature (T-Tc/ΔT)
$\widetilde{\Psi}$	Dimensional stream function (m^2/s)
$\tilde{\psi}$	Dimensionless stream function
μ	Dynamic viscosity (kg.s/m)
ϑ	Kinematic viscosity (μ/ρ) (m^2/ s)

Subscripts

c	Cold
h	Hot

Abbreviations

$\widetilde{Ma}$	Marangoni number
Min	Minimum
b	Base heat source
$\overline{Nu}$	Local Nusselt number on the heat source surface
$\overline{Nu_s}$	Average Nusselt number along the heat source
$\widetilde{U}$	Dimensionless velocity component in x-direction
$\tilde{u}$	Velocity component in x-direction (m/s)
$\widetilde{V}$	Dimensionless velocity component in y-direction
$\tilde{v}$	Velocity component in y-direction (m/s)
X	Dimensionless coordinate in horizontal direction
x	Cartesian coordinate in horizontal direction (m)
Y	Dimensionless coordinate in vertical direction
y	Cartesian coordinate in vertical direction (m)”
ε	Ratio of heating element length to the cavity height (%)
$\widetilde{\Pi}$	Heatfunction
ΔT	Ref. temperature difference (q” L/k)
β	Volumetric coefficient of thermal expansion (K^{-1})
ρ	Density (kg/m^3)

AUTHORSHIP CONTRIBUTIONS

Authors equally contributed to this work.

DATA AVAILABILITY STATEMENT

The authors confirm that the data that supports the findings of this study are available within the article. Raw data that support the finding of this study are available from the corresponding author, upon reasonable request.

CONFLICT OF INTEREST

The author declared no potential conflicts of interest with respect to the research, authorship, and/or publication of this article.

ETHICS

There are no ethical issues with the publication of this manuscript.

STATEMENT ON THE USE OF ARTIFICIAL INTELLIGENCE

Artificial intelligence was not used in the preparation of the article.

REFERENCES

[1] Song T, Comparison of Buoyancy and Surface Tension in a Square Cavity. Springer 1991;5:10−15. [CrossRef]

[2] Priede J, Cramer A, Bojarevics A, Gelfgat AY, Bar-Yoseph PZ, Yarin AL. Gunter Gerbeth, Experimental and numerical study of anomalous thermocapillary convection in liquid gallium. Phys Fluids 1999;11:3331−3339. [CrossRef]

[3] Saleh H, Arbin N, Roslan R, Hashim I. Visualization and analysis of surface tension and cooling effects on differentially heated cavity using heatline concept. Int J Heat Mass Transf 2012;55:6000−6009. [CrossRef]

[4] Bergman TL, Ramadhyani S. Combined buoyancy and thermocapillary driven convection in open square cavities. Numer Heat Transf 1986;9:441−451. [CrossRef]

[5] Cicek K, Baytas AC. A Numerical Study of Combined Natural and Marangoni Convection in a Square Cavity. TransNav 2009;3. [CrossRef]

[6] Strani M, Piva R, Graziani G. Thermocapillary convection in a rectangular cavity: asymptotic theory and numerical simulation. J Fluid Mech 1983;130:347−376. [CrossRef]

[7] Arbin N, Saleh H, Hashim I, Chamkha AJ. Numerical investigation of double-diffusive convection in an open cavity with partially heated wall via heatline approach. Int J Therm Sci 2016;100:169−184. [CrossRef]

[8] Jue TC. Combined thermosolutal buoyancy and surface-tension flows in a cavity. Heat Mass Transf 1999;35:149−161. [CrossRef]

[9] Rudraiah N, Venkatachalapp M, Subbaraya CK. Combined Surface Tension and Buoyancydriven Convection in a Rectangular Open Cavity in the Presence of a Magnetic Field. Int J Non-linear Mech 1995;30:759−770. [CrossRef]

[10] Saleem M, Hossain MA, Hafiz MZ. Effect of Magnetic Field on Double Diffusive Marangoni Convection with Chemical Reaction in a Square Cavity. Available at: https://me.buet.ac.bd/public/old/icme/icme2011/Proceedings/PDF/ICME%2011-FL-002.pdf. Accessed on 5 Mar 2026.

[11] Hossain MA, Hafiz MZ, Rees DAS. Buoyancy and thermocapillary driven convection flow of an electrically conducting fluid in an enclosure with heat generation. Int J Therm Sci 2005;44:676−684. [CrossRef]

[12] Oztop HF, Lioua K, Mohamad NB, Al-Salem K. Numerical study of three-dimensional combined buoyancy and thermocapillary convection and evaluation of entropy generation. Available at: www.emeraldinsight.com/0961-5539.htm. Accessed on 5 Mar 2026.

[13] Saleh H, Hasmim I. Buoyant Marangoni convection of nanofluids in square cavity. Appl Math Mech Engl Ed 2015;36:1169−1184. [CrossRef]

[14] Saleem M, Hossain MA, Mahmud S, Pop I. Entropy generation in Marangoni convection flow of heated fluid in an open ended cavity. Int J Heat Mass Transf 2011;54:4473−4484. [CrossRef]

[15] Basak T, Singh AK, Sruthi TPA, Roy S. Finite element simulations on heat flow visualization and entropy generation during natural convection in inclined square cavities. Int Commun Heat Mass Transf 2014;51:1−8. [CrossRef]

[16] Ilis G, Mobedi M, Sunden B. Effect of aspect ratio on entropy generation in a rectangular cavity with differentially heated vertical walls. Int Commun Heat Mass Transf 2008;35:696−703. [CrossRef]

[17] Bouabid M, Magherbi M, Hidouri N, Brahim AB. Entropy generation at natural convection in an inclined rectangular cavity. Entropy 2011;13:1020−1033. [CrossRef]

[18] Ahmed SE, Oztop HF, Elshehabey HM. Thermosolutal Marangoni convection of Bingham non-Newtonian fluids within inclined lid-driven enclosures full of porous media. Heat Transf 2021;50:7898−7917. [CrossRef]

[19] Kolsi L, Algarni S, Mohammed HA, Hassen W, Lajnef E, Aich W, et al. 3D Magneto-Buoyancy-Thermocapillary Convection of CNT-Water Nanofluid in the Presence of a Magnetic Field. Processes 2020;8. [CrossRef]

[20] Basak T, Gunda P, Anandalakshmi R. Analysis of entropy generation during natural convection in porous right-angled triangular cavities with various thermal boundary conditions. Int J Heat Mass Transf 2012;55:4521−4535. [CrossRef]

[21] Bobach BJ, Boman R, Celentano D, Terrapon VE, Ponthot JP. Simulation of the Marangoni Effect and Phase Change Using the Particle Finite Element Method. Appl Sci 2021;11:11893. [CrossRef]

[22] Siri Z, Al 'Idrus SNSMN. Marangoni convection in a C-shape enclosure with partially heated walls. J Phys 2023;2633:012016. [CrossRef]

[23] Zisan HMTA, Ruvo TH, Saha S. Marangoni Natural Convection in a Discretely Heated Cubic Cavity under Isoflux Heating Condition. Available at: http://ieomsociety.org/proceedings/2021dhaka/413.pdf. Accessed on 5 Mar 2026.

[24] Muhammad ASNBNS, Bin SZ, Habibis S. Marangoni convection in a trapezoidal enclosure with a heated circular cylinder. Therm Sci 2025;29:567−577. [CrossRef]

[25] Omer ASA. Marangoni Convection in Hybrid Nanofluid Flow over a Disk. Eur J Pure Appl Math 2025;18:1307−5543. [CrossRef]

[26] Muhammad ASNBNS, Bin SZ, Habibis S. Marangoni convection in a trapezoidal enclosure with a heated circular cylinder. Therm Sci 2025;29:567−577. [CrossRef]

[27] Abbas M, Khan N, Hashmi MS, Alhefthi RK, Rezapour S, Ince M. Thermal Marangoni convection in two-phase quadratic convective flow of dusty MHD trihybrid nanofluid with non-linear heat source. Case Stud Therm Eng 2024;57:104190. [CrossRef]

[28] Saoudi L, Zeraibi N. Entropy generation of Al2O3/water nanofluid in corrugated channels. J Therm Eng 2023;9:885−900. [CrossRef]

[29] Ferroudj N, Köten H. Numerical Simulation Of Prandtl Number Effect on Entropy Generation in a Square Cavity. J Therm Eng 2021;7:1016−1029. [CrossRef]

J Ther Eng, Vol. 12, No. 2, pp. 830−841, March, 2026

Journal of Thermal Engineering
Web page info: https://jten.yildiz.edu.tr
DOI: 10.14744/thermal.0001116

Review Article

A comprhensive review on aircooled battery thermal mangement system of electric vehicles

Prem Kumar S[1], Krishnappa GB[2], Madhu DEVEGOWDA[3]

[1]*Department of Mechanical Engineering, Seshadripuram Institute of Technology, Karnataka, 570001, India*
[2]*Department of Mechanical Engineering, Vidyavardhaka College of Engineering, Karnataka, 570001, India*
[3]*Department of Mechanical Engineering, Government Engineering College, Karnataka, 571313, India*

ARTICLE INFO

Article history
Received:13 December 2024
Revised: 15 February 2025
Accepted: 25 February 2025

Keywords:
Electric Vehicles; Battery Thermal Management; Air Based Battery Cooling; Material Recovery; Hydrometallurgy; Pyrometallurgy; Plug-in EVs; Li-ion Battery; Battery Material Recovery

ABSTRACT

Battery-operated modern mobility systems are commonly referred to as Electric Vehicles. The transition from conventional internal combustion engines to modern electric mobility is progressing rapidly. Incorporating Electric Vehicles is a practical solution to addressing environmental pollution caused by the combustion of petroleum-based fuels. Among the various energy storage options, Lithium-ion batteries are the preferred choice due to their superior features, including high energy density, longevity, and efficiency. However, the performance, safety, and lifespan of Lithium-ion batteries are highly sensitive to operating temperature. Therefore, an effective battery thermal management system is essential. This review paper focuses on air-based thermal management systems. Compared to other cooling methods, air-based systems offer notable advantages, such as simplicity, lower cost, and ease of implementation. Despite these benefits, air-based systems often face challenges in efficiently managing higher thermal loads. Various techniques related to air-based cooling systems are discussed in detail. Additionally, the paper provides an overview of alternative cooling methods for comparison and context.

Cite this article as: S Kumar P, Krishnappa GB, Devegowda M. A comprhensive review on aircooled battery thermal mangement system of electric vehicles. J Ther Eng 2026;12(2):830−841.

INTRODUCTION

For the past few decades, world witnesses the exponential increase in demand of petroleum fuels. The excessive burning of these fuels in automobiles has caused severe environmental degradation. The vehicular pollution has crossed its acceptable level in major cities of the world. Government regulating bodies in various countries have been implementing stringent emission norms to deal with the pollution caused by vehicles. Many countries have been encouraging the research and development in the field of eco-friendly vehicles. This leads to a development of new-generation vehicles called Electric Vehicles (EVs). In EVs, the power required for the vehicle traction is supplied by a storage battery. There are three types of EVs: Battery Electric Vehicles (BEVs), Plug-in Hybrid Vehicles (HPVs) and Hybrid Electric Vehicles (HEVs). Currently, wide

***Corresponding author.**
*E-mail address: kumar.prem000@gmail.com

This paper was recommended for publication in revised form by Editorin-Chief Ahmet Selim Dalkılıç

Published by Yıldız Technical University Press, İstanbul, Turkey
Yıldız Technical University. This is an open access article under the CC BY-NC license (http://creativecommons.org/licenses/by-nc/4.0/).

varieties of storage batteries are available. Among the various options, Lithium-ion (Li-ion) battery shows better features in terms of energy-density, long-life and compactness [1-4]. Thus, Li-ion battery is widely accepted and employed in EVs. These batteries are also used in electronic devices [5]. To accommodate the required power in EV, more numbers of Li-ion batteries need to be connected in series and parallel. The life and performance of Li-ion battery are highly influenced by the working temperature [6-8]. The battery pack temperature should be maintained between 15 to 35 °C [9-11] and uniform cell temperature shall be within 5 °C [12-17]. Significant amount of heat is being generated while charging as well as discharging. The heat generation could be due to Joule's effect, called irreversible heat (Q_{ir}) and electrochemical reaction, known as reversible heat (Q_r) [18]. Bernardiet.al [19] developed a correlation (1) to find the total heat generation in a battery.

$$Q = Q_{ir} + Q_r = I2\ R_{in} - I\ T\ \frac{dT}{dE_o} \quad (1)$$

I is the current, R_{in} is the internal resistance, T is the temperature and $\frac{dT}{dE_o}$ is the entropy coefficient. To maintain the operating temperature of a Li-ion battery within acceptable limits, an effective Battery Thermal Management System (BTMS) is necessary. The safety, economic viability, and size of the BTMS should be carefully considered. At present, cooling is achieved using air, liquid, heat pipe, phase change materials (PCM) and thermoelectric cooling (TEC) technique. Alternatively, different cooling methods may be combined [20-22]. Each cooling method has its own pros and cons. Based on the cooling technique adopted, BTMSs are categorised into Active, Passive and Hybrid systems. In an active system, either free or forced cooling is achieved by air or liquid. Heat pipe or Phase Change Material (PCM) is employed in passive system. Hybrid system generally includes two different cooling methods.

Recent advancements in Battery Thermal Management Systems (BTMS) have garnered significant attention, particularly in the context of electric vehicles (EVs). Researchers have developed various BTMS solutions to enhance battery performance, safety, and longevity. This article provides a comprehensive review of the latest developments in air-based BTMS while also offering an overview of liquid, phase change material (PCM), and hybrid approaches.

NON-UNIFORM TEMPERATURE

Non-uniform cell temperature is one of the critical issues associated with Li-ion batteries. The key components of a Li-ion battery are the anode, cathode, electrolyte, and separator [23, 24]. During charging and discharging, lithium ions exchange between the two electrodes through the separator and electrolyte. During charging, lithium ions move from the anode to the cathode by absorbing energy from an external source. The same energy is then released as electricity when electrons flow from the anode to the cathode through an external circuit [25, 26]. The basic working principle of a Li-ion battery is illustrated in Figure 1. Various chemical reactions occur during these processes, and a significant amount of heat is also generated. As a result, a temperature gradient develops across the battery pack, which is often non-uniform.

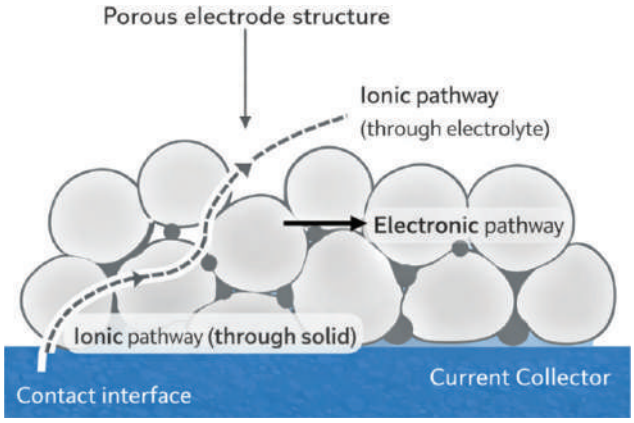

Figure 1. Electronic pathway at the interface.

Several factors contribute to the uneven temperature distribution across the battery pack and within each cell. A study by Hossein Maleki et al. [27] revealed that the structure of the electrodes changes due to repeated cycles. The variation in open-circuit voltage leads to changes in specific heat capacity, which causes de-lithiation. De-lithiation significantly impacts the structural changes in the battery. Moreover, the thermal conductivity of the electrode materials is affected by the changes in the specific heat of the battery.

An experimental study by Frank Richter et al. [28] explored the changes in the thermal conductivity of battery materials and the temperature profile. The thermal conductivity of the electrodes and separator is influenced by the electrolyte. The study showed that the thermal conductivity of the separator and electrodes was poor under dry conditions. Consequently, the decomposition of the electrolyte during aging reduces the thermal conductivity of these materials. The temperature profile of the battery pack is also highly influenced by the discharge rate. The temperature difference between the center and the edge of the battery pack increases with the discharge rate.

The internal resistance of battery materials increases with aging, leading to higher internal heat generation within the battery [30–32]. Additionally, the thermal conductivity of the electrodes varies with particle size [33]. Thermal contact resistance between the electrode and the current collector is another critical parameter that affects both the performance and fast charging capabilities of the cell. Often, the diffusion of ions in the electrolyte and the flow of electrons through the solid medium significantly contribute to the internal resistance of the cell. This contact

resistance accounts for about 25% of the changes in the shape and structure (polarization) of the cell [34].

A microscopic view of the contact resistance and the paths of ions and electrons at a cathode (NMC5320) [35]. The cell current must pass through this interface during both charging and discharging [36–38]. Therefore, materials that offer minimal contact resistance are preferred to achieve better performance. Furthermore, microscopic properties such as the particle size of the current collector and binder, porosity, and the percentage of contact between the surfaces have a significant impact on the contact resistance [39–44].

AIR BASED SYSTEM

Atmospheric air is used as the working medium in an air based BTMS. In the EV sector, air based BTMS proven to be a better option over other systems due its advantages such as simple structural design, less weight, no leakages, and low cost [45, 46]. All other BTMSs except air-based system are still in developing stage. Major EV manufacturers preferred air-based system to match the supply and demand for EVs in the rapid growing market [47]. However, the challenges associated with air-based system are; low thermal conductivity of air, large volumes of airflow requirement, non-uniform cooling of the battery pack and vibration problems. Further, the air-based system alone is incapable of providing sufficient cooling due to the instant surge in heat generation from the battery at the higher vehicle speed [48,49]. Attempts have been made to improve the performance and reliability of air based BTMS. The structural designs and flow optimisations are the widely used techniques in this regard.

Mao LI et al., [50] have conducted a study modelling and optimisation in an air cooled BTMS. A U–Type Li-ion battery module with 36 cells and 37 cooling passages was considered for the analysis. The study focuses on the influence of important design parameters such as mass flow rate, heat flux and flow passage spacing. Increased mass flow rate results in decreased temperature differences and increased pressure drop between the cells' surface and air stream. However, increased pressure drop demands the higher power consumption. Increased heat flux causes significant increase in temperature difference and merely affects the pressure drop. Further, non-uniform temperature distribution within the battery module occurs due to the increased heat flux. Thermal performance reduces with increase in flow passage area. Further, uneven passages result in uneven temperature distribution. XiongbinPeng et al. [51] made an analysis of air-cooled cylindrical battery pack. A cylindrical battery pack of 20 modules was considered, and the dynamic model was created for the validation. The cooling performance was analysed for different battery layouts with various inlet and outlet air flow pattern as represented in Figure 2 and 3.

Analysis was done by considering the same rectangular inlet and outlet size (20 × 49 mm) for each module by blowing air at a constant speed in transverse and lateral directions. For each layout, lower temperature distribution was noticed near the air inlet than the outlet. However, better uniform temperature distribution was noticed in 4 × 5 layout. For the flow optimisation, 18 different patterns were attempted. Better flow distribution was observed in 3,4,12, and13. Experiments were conducted to check the validity of simulation results. Acceptable agreement between the simulation and experimental results was observed.

Kai Chen et al., [52] have developed various symmetrical air-cooled models for BTMS. The study was performed with different U and Z – type of flows. In symmetrical models, the higher cooling performance, and less energy consumption were reported. Further, the study has shown that the minimum number of battery cells results in a better uniform temperature distribution. Akinlabi A. A. Hakeem and DavutSolyali [53] performed a thermal performance

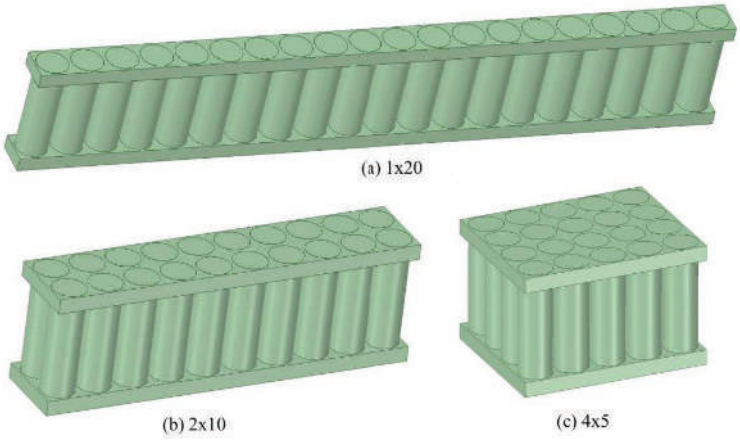

Figure 2. Different layouts of cylindrical Battery pack [From Akinlabi and Solyali [51], MDPI, licensed under CC BY 4.0].

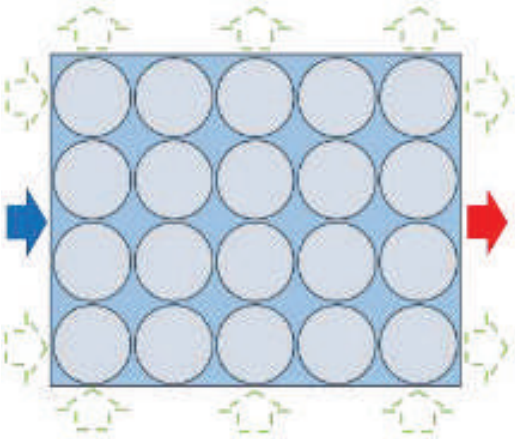

Figure 3. Flow positions [From Akinlabi and Solyali [51], MDPI, licensed under CC BY 4.0].

analysis under forced convection for a Li- ion battery. In this study, cell aligned cell optimisation technique was adopted. Experiments were carried out at variable air velocity. The results infer that improved cooling performance was attained at higher Reynolds numbers as a result of forced convention. Jiajun Zhang et al. [54] have done an experimental and numerical study of transient heat transfer analysis of air cooled BTMS. Parallel air cooled BTMS was considered for the study with, Z, U and I – type of flows. This study comprises of three analytical methods: Numerical analysis using CFD, Flow resistance network model, transient heat transfer model. Further, experimental work was also carried out. Transient model was formulated for I-Type flow by applying energy equations by considering four channels flow around the battery cell. In the experimental analysis, aluminium blocks were used to represent the battery cell. The blocks were heated uniformly by electricity. Thermocouples were placed on the blocks to continuously monitor the temperature. The results of numerical models were closely agreed with experimental results.

Thomas ImrerilleBuidin and Florin Mariasiu [55] proposed a modeling approach for the sports track conditions of 22 km travelling distance on the racetrack with battery temperature limit below 50 ^{0}C. The power train system consists of two motors of 15 kW each capacity. Battery pack was made into 22 segments with 8 modules. Maximum discharge current and voltage of battery pack were 464 Amps and 369 Volts respectively. Power required for the traction and current to be delivered by the battery as per the state of charge was determined by using energy efficiency graph.

To travel 22 km, the profile repeated for 23 times and time taken was 1960 seconds. CFD models were developed to determine the surface heat transfer coefficient between the air stream and surface of the battery cell. Initially, 1D transient heat transfer model was analysed. Further, it was used to develop the 3D transient heat transfer model. This makes the analysis simple. Simulation results depict that the heat transfer capacity decreases due to decrease in air flow coefficient in longitudinal direction. Higher temperature was recorded at the middle and lower region of the battery pack.

In most of the cases, non-uniformity of air flow causes the uneven temperature distribution within the battery pack. Researchers have tried to get uniform air flow pattern by different inlet and outlet positions, using air distribution fans [56, 57]. Few studies recommend adopting the change air flow direction within the battery pack to achieve uniform air distribution [58-61]. These studies also have shown considerable achievement in uniform air distribution. In this direction, Meiwei Wang [62] et.al, proposed a newer method to change air flow direction by using parallel plates. This study had taken Z-type BTMS for the analysis. Parallel plates were introduced at the bottom side of the battery. According to airflow pattern, nine BTMS models were developed.

The CFD analysis was made for these nine models. Simulation analysis shows that the minimum value of maximum temperature was noticed for model IX and minimum value of maximum temperature difference obtained for model VII. For the model IX, good flow distribution was achieved which leads to more uniform temperature profile than the other models. Introduction of parallel plates causes the decrease in maximum temperature difference initially and increase thereafter. Kai Chen et al. [63] developed parallel air cooled BTMS and done CFD analysis to know the influence of structural and operational parameters. The operational parameters taken for the studies were discharge rate, inlet air temperature and inlet airflow rate. Structural parameters focussed by this study were cell spacing, convergence and divergence plenum. CFD model was developed by considering turbulent flow conditions with k-ϵ turbulence model. The results obtained from the CFD analysis were validated by using Park's study [64]. Experimental data available in the study made by Wu [65] was taken for the validation. The inferences given by this study were: (i) reduced inlet air temperature reduces the battery temperature, however, could not restrict the rise in temperature effectively. (ii) Increase in inlet airflow rate decreases the maximum temperature in the battery pack. However, it increases the power consumption. (iii) Reduction in cell spacing results in lower cells' temperature, this also leads to increased power consumption. (iv) Often, reduction in maximum temperature and minimum cell temperature gradient can be achieved by optimizing the plenum angles.

The optimisation methods by using U and Z- type flow patterns were widely employed methods. To some extent I- type flow was also incorporated. Recently, researchers made attempts to study the cooling performance by obtaining J- type flow. This flow pattern was achieved by providing an inlet at the bottom and two outlets at the top of the battery pack. The experimental and simulation results proved that the cooling performance obtained by the J-type was satisfactory [66, 67]. However, discussion on J-type flow pattern is omitted due to lack of sufficient number of research papers. Few attempts were made to incorporate different controller like PID-controller for active control of cell temperature. The surface and core temperature of battery cell was continuously monitored by using temperature sensors. According to the pre-set temperature data, controller alters the air flow direction by actuating flip valves. Fan He, Lin Ma and XiaojingGao et al. [68, 69] made attempts in this direction. Reduced Ordered Method (ROM) was used in these studies to model the temperature distribution in the battery pack. Validation of ROM was also proved by comparing it with experimental results. Further, Computational cost of ROM is significantly less compared to CFD analysis. Results of the studies indicate that active cooling technique gives better uniform cell temperature which is much lower than the desired value. However, accurate real time

temperature was not possible as the sensors were located at few cells only. Practically it is difficult to fix temperature sensors at all cells of a battery pack and it increases the cost also.

The staggered arrangement of battery cells is a geometrical optimization technique that focuses on the spatial configuration of cells. This approach enhances flow distribution and promotes a more uniform temperature profile [69]. Y. Wang et al. [70] studied the cooling performance of a staggered arrangement by incorporating non-uniform cell spacing. Their findings showed that this configuration improves cooling efficiency and results in a uniform temperature profile. However, significant energy consumption was reported. P. Kashyap et al. [71] attempted to optimize the staggered arrangement using a combined approach involving physical modeling, parametric optimization, and a sophisticated algorithm. In both models, the longitudinal pitch remained the same (24 mm), while the transverse pitch varied (24 mm and 20 mm). Under identical discharge and flow velocity conditions, the staggered pattern exhibited significantly lower temperatures compared to the conventional inline pattern. It was noted that the the staggered configuration outperformed the inline arrangement. Enhanced temperature uniformity was observed at higher Reynolds numbers due to increased convective heat transfer. Additionally, cells near the inlet had lower temperatures compared to those at the exit. Wenxu Yang et al. [72] incorporated a reverse flow mechanism with staggered battery cells and introduced a spoiler to induce turbulent flow. The results demonstrated significant cooling improvements achieved through this technique.

OTHER COOLING METHODS

This section provides a brief discussion of cooling techniques such as liquid cooling, PCM (Phase Change Material) cooling, and hybrid cooling. Liquid cooling offers superior performance and compactness compared to air-based systems [73]. A wide variety of fluids, including water, oil, nano-fluids, liquid metal, and refrigerants, are used in this method [74, 75]. Liquid cooling BTMS (Battery Thermal Management Systems) are divided into two main categories: direct cooling and indirect cooling.

Direct cooling involves submerging the battery pack in a non-conductive fluid, enabling efficient heat dissipation directly from the battery. In contrast, indirect cooling circulates a working medium through a cooling structure, such as plates or jackets, which surrounds the battery pack. The direct cooling approach provides direct contact between the battery pack and the coolant, resulting in better thermo-physical properties for heat dissipation [76]. Dielectric fluids, which are non-conductive, are the preferred choice as the working medium in direct cooling. These fluids prevent short circuits and reactions with battery materials. Studies on the direct cooling approach have used fluids such as terminal oil, mineral oil, water-glycol mixtures, NOVEC 7000, and refrigerants [77-85]. In these studies, both the battery pack temperature and cell temperature were effectively controlled within acceptable ranges. Additionally, these studies focused on fluid and flow optimization. However, challenges such as slow heat dissipation to the surroundings and leakage issues often limit the widespread use of this method.

Indirect cooling, on the other hand, offers better performance than direct cooling due to the continuous flow of the working fluid through cooling passages [86, 87]. Indirect cooling is further divided into single-phase and multi-phase cooling. In single-phase cooling, the working fluid remains in the liquid state throughout the entire cycle, whereas, in multi-phase cooling, the working medium undergoes a phase change between liquid and vapor states. Significant research has been conducted on indirect cooling in recent years, with various optimization techniques tested to improve cooling performance. The literature suggests that the highest priority has been given to structural modifications of the battery pack, fluid flow patterns, and the properties of the fluids used [88-96].

The use of Phase Change Materials (PCMs) in BTMS has gained considerable attention in recent years. The unique property of PCMs is their ability to absorb significant heat loads. These materials can absorb the thermal load of a battery pack through both sensible and latent heat. Studies have shown that PCM cooling can help achieve more uniform cell temperatures [97]. Desirable properties of PCMs include high latent heat, minimal subcooling, higher thermal conductivity, and chemical stability [98, 99]. Among these properties, thermal conductivity has the most significant impact on battery temperature.

The use of PCM for BTMS was first explored by Hallaj and Selman [100]. Literature reports various PCMs tested for this purpose, including decanoic acid, disaccharide, CnH2n+2, RT-35 PA, RT-42 PA, RT-55 PA, and sodium sulfate decahydrate [101-108]. However, the relatively low thermal conductivity of PCMs limits their extensive use in BTMS. To address this, efforts have been made to improve the thermal conductivity of PCMs by incorporating additives such as metal foam, graphene, hexagonal boron nitride (h-BN), and carbon fiber [109-114].

Furthermore, combined systems have been developed by incorporating both liquid and PCM cooling methods. In this combined approach, the liquid coolant typically flows through a cooling plate surrounding the battery pack, while PCM is placed between the battery cells. This configuration helps maintain the pack temperature within permissible limits and improves cell temperature uniformity. Studies have reported significant improvements in overall cooling performance using this combined system. Additionally, the effects of PCM mass fraction and liquid coolant flow rate have been studied [116-120]. However, this system becomes more complex and requires substantial power. Furthermore, it demands more space to house the components of the combined system, all of which contribute to

an increase in the overall cost of an EV. Additionally, the slower melting and solidification properties of PCM must be addressed to further improve cooling performance. Priyadarsini et al. [121, 122] have conducted studies incorporating trapezoidal fins, which showed enhanced heat augmentation. However, this technique has not yet been applied in BTMS.

The selection of a BTMS for practical applications is influenced by various factors, including cost, safety, design, cooling performance, and reliability. Currently, air-based BTMS are widely used in EVs due to their simple design and low cost. However, the major drawback of air-based systems is their inability to handle higher thermal loads effectively. The liquid cooling approach offers more efficient cooling compared to air-based systems and can handle higher heat loads. Due to these advantages, liquid-based systems are also commonly employed in practical applications. PCM and hybrid cooling techniques show superior performance and are capable of managing larger thermal loads. However, the cost of these systems is much higher than that of air- and liquid-based methods. Moreover, PCM and hybrid systems require more complex structures to accommodate the various components of the BTMS. A comparative summary of different BTMS options is provided in Table 1.

FUTURE PROSPECTUS

It has been observed from the literature that structural and flow optimizations are the most common methods to enhance the cooling efficiency of air-based systems. Structural optimization focuses on the geometry of the battery pack, while flow optimization relates to the airflow pattern. The arrangement of battery cells and the spacing between them significantly impact cooling efficiency. Cylindrical and rectangular battery structures are commonly used in electric vehicles (EVs). Studies have been conducted by varying the number of cells in a battery pack, with the cylindrical structure generally yielding better performance than the rectangular structure. However, the design and production costs associated with each battery geometry need to be carefully considered. Even a small increase in these costs could result in a higher vehicle price. Computational Fluid Dynamics (CFD) analysis is the most widely used method in these studies as it allows for easy examination of the effects of structural and flow variables, with the flexibility to adjust boundary conditions. This flexibility enables a greater number of iterations before moving to experimental studies. Despite these advantages, none of the studies have managed to maintain a uniform cell temperature throughout the entire battery pack. In most cases, temperature uniformity is observed only near the inlet passage.

For next-generation EVs, a battery thermal management system (BTMS) must support features such as long driving range, quick charging, and safety. The air-based BTMS used in current EVs needs further improvement to meet these future demands. In air-based BTMS, the lower thermal conductivity of air and the need for large volumes of airflow are major concerns. The thermal conductivity of air affects the rate of heat dissipation, and the large airflow requirements consume significant pumping power. Research in this area suggests that incorporating evaporative cooling could significantly improve the performance of conventional air-based BTMS. Moreover, evaporative cooling can be integrated into the existing structure of air-based systems, thereby reducing the overall system cost. Lip Huat

Table 1. Comparison of different BTMS techniques

Type	Advantages	Disadvantages
Air based BTMS	· Less initial cost · Minimal operational cost · Easy to maintain · No risk of short circuit and leakages · System design is simple · Lower payload	· Air has poor thermal conductivity · Difficult to handle higher thermal loads · Lower cooling efficiency · Large volume air flow is required to take higher heating loads. This consumes significant blowing power
Liquid based BTMS	· System is compact · Capable to handle higher heating loads · Quick heat dissipation is possible · Better cooling performance than air-based system	· Overall system cost is high · Liquid storage facility is necessary · Prone to short circuit and leakages · Consumes significant pumping power
PCM based BTMS	· Low cost of PCM · Able to handle higher thermal loads · Better cooling efficiency than air and liquid based system	· Lower thermal conductivity of PCM · Possibility of PCM leakage · Chances of supercoiling · Change in volume of PCM during phase transition
Hybrid mode	· Features of different systems can be integrated as per the requirement · Offers highest cooling efficiency · Higher heating loads can be easily handled	· Complex system design · Higher cost of the system · Difficult to maintain the combined system

Sawa et al. [123] demonstrated an improvement in cooling performance by introducing fine water droplets into the air stream. This approach not only enhanced cooling efficiency but also reduced power consumption for the same rate of cooling. Similarly, studies have been made by incorporating heat pipes to improve the cooling performance of conventional air-based system. Heat pipe exhibit features; light weight, simple design, absence of moving parts, and low thermal conductivity which makes it suitable in combination with air-based system. The studies made in this direction gave improved performance of the combined system [124-128]. However, few studies depict that not much significant improvement was achieved at higher flow rates; even by introducing fins in the air stream [129-133]. Hence, further research has to be carried out to address these issues. Furthermore, significant advancements are needed in terms of battery material design and selection. Future research should focus on developing new materials and fabrication techniques to address challenges such as internal cell resistance, contact resistance, and premature material aging.

CONCLUSIONS

Battery Thermal Management Systems (BTMS) in electric vehicles (EVs) are designed to maintain battery packs within the ideal temperature range of 15–35 °C, safeguarding them from premature wear and degradation. Among various cooling methods, air-based systems are often favoured for their efficiency and straightforward design compared to liquid cooling or Phase Change Material (PCM)-based systems. Improvements in these systems typically involve structural and flow optimizations. Structural optimization includes modifying battery shapes and adjusting cell spacing, while flow optimization focuses on designing airflow patterns—such as I, U, Z, J, and staggered configurations—to enhance thermal performance, particularly at higher vehicle speeds. Additionally, the choice of battery materials plays a significant role. Internal and contact resistance within battery cells are responsible for approximately 25% of the heat generated. Future advancements in BTMS should aim to develop innovative materials and manufacturing methods to reduce these resistances and mitigate the early degradation of battery components.

AUTHORSHIP CONTRIBUTIONS

Authors equally contributed to this work.

DATA AVAILABILITY STATEMENT

The authors confirm that the data that supports the findings of this study are available within the article. Raw data that support the finding of this study are available from the corresponding author, upon reasonable request.

CONFLICT OF INTEREST

The author declared no potential conflicts of interest with respect to the research, authorship, and/or publication of this article.

ETHICS

There are no ethical issues with the publication of this manuscript.

STATEMENT ON THE USE OF ARTIFICIAL INTELLIGENCE

Artificial intelligence was not used in the preparation of the article.

REFERENCES

[1] Aneke M, Wang M. Energy storage technologies and real-life applications— A state of the art review. Appl Energy 2016;179:350–377. [CrossRef]

[2] Bukhari S, Maqsood J, Baig MQ, Ashraf S, Khan TA. Comparison of characteristics lead acid, nickel-based, lead crystal and lithium-based batteries. IEEE Xplore 2015;444–450. [CrossRef]

[3] Kim T, Song W, Son D, Ono LK, Qi Y. Lithium-ion batteries: outlook on present, future, and hybridized technologies. J Mater Chem A 2019;7:2942–2964. [CrossRef]

[4] Olabi AG. Developments in sustainable energy and environmental protection. Energy 2012;2–5. [CrossRef]

[5] Dunn B, Tarascon JM. Electrical energy storage for the grid: A battery of choices. Science 2011;334:928–935. [CrossRef]

[6] Lin J, Liu X, Li S, Zhang C, Yang S. A review on recent progress, challenges, and perspective of battery thermal management system. Int J Heat Mass Transf 2021;167. [CrossRef]

[7] Choudhari VG, Dhoble AS, Sathe TM. A review on the effect of heat generation and various thermal management systems for the lithium-ion battery used for electric vehicles. J Energy Storage 2020;32. [CrossRef]

[8] Tete PR, Gupta MM, Joshi SS. Developments in battery thermal management systems for electric vehicles: A technical review. J Energy Storage 2021;35. [CrossRef]

[9] Naik I, Nandgaonkar M. Review of the approaches and modelling methodology for lithium-ion battery thermal management systems for electric vehicles. Springer 2020;75–109. [CrossRef]

[10] Buidin TIC, Mariaslu F. Battery thermal management systems: Current status and design approach of cooling technologies. Energies 2021;14:4879. [CrossRef]

[11] Kitoh K, Nemoto H. 100 Wh large size Li-ion batteries and safety tests. J Power Sources 1999;81–82:887–890. [CrossRef]
[12] Rugh J, Pesaran A, Smith K. Electric vehicle battery thermal issues and thermal management techniques (presentation). National Laboratory of the Rockies 2011.
[13] Pesaran A. Tools for designing thermal management of batteries in electric drive vehicles (presentation); Technical Report. National Laboratory of the Rockies 2013. [CrossRef]
[14] Zhao C, Zhang B, Zheng Y, Huang S, Yan T, Liu X. Hybrid battery thermal management system in electrical vehicles: A review. Energies 2020;13. [CrossRef]
[15] Raza W, Ko GS, Park YC. Induction heater-based battery thermal management system for electric vehicles. Energies 2020;13:5711. [CrossRef]
[16] Jeffs J, Dinh TQ, Widanage DH, Picarelli A. Optimisation of direct battery thermal management for EVs operating in low-temperature climates. Energies 2020;13. [CrossRef]
[17] Bernardi D, Pawlikowski E, Newman J. General energy balance for battery systems. J Electrochem Soc 1985;132:1152. [CrossRef]
[18] Basu S, Hariharan KS, Kolake SM, Song T, Sohn DK, Yeo T. Coupled electrochemical thermal modelling of a novel Li-ion battery pack thermal management system. Appl Energy 2016;181:1–13. [CrossRef]
[19] Rao Z, Wang Q, Huang C. Investigation of the thermal performance of phase change material/mini-channel coupled battery thermal management system. Appl Energy 2016;164:659–669. [CrossRef]
[20] Wang Q, Jiang B, Li B, Yan Y. A critical review of thermal management models and solutions of lithium-ion batteries for the development of pure electric vehicles. Renew Sustain Energy Rev 2016;64:106–128. [CrossRef]
[21] Xia G, Cao L, Bi G. A review on battery thermal management in electric vehicle application. J Power Sources 2017;367:90–105. [CrossRef]
[22] Jaguemont J, Mierlo JV. A comprehensive review of future thermal management systems for battery-electrified vehicles. J Energy Storage 2020;31:101551. [CrossRef]
[23] Chawla N, Bharti N, Singh S. Recent advances in non-flammable electrolytes for safer lithium-ion batteries. Batteries 2019;5:19. [CrossRef]
[24] Zhu H, Qin X, Sun X, Yan W, Yang J, Xie Y. Rocking-chair configuration in ultrathin lithium vanadate-graphene hybrid nanosheets for electrical modulation. Sci Rep 2013;3:1246. [CrossRef]
[25] Wang M, Stoliarov M, Sun J. A review of lithium-ion battery failure mechanisms and fire prevention strategies. Prog Energy Combust Sci 2019;73:95–131. [CrossRef]
[26] Maleki H, Hallaj S, Selman JR, Dinwiddie R, Wang C. Thermal properties of lithium-ion battery and components. J Electrochem Soc 1999;146:947–954. [CrossRef]
[27] Richter K, Kjelstrup S, Vie J, Burheim O. Thermal conductivity and internal temperature profiles of Li-ion secondary batteries. J Power Sources 2017;359:592–600. [CrossRef]
[28] Li X. Anionic redox in rechargeable lithium batteries. Adv Mater 2017;29:1701054. [CrossRef]
[29] Richter F, Vie PJS, Kjelstrup S, Burheim OS. Thermal conductivity and internal temperature profiles of Li-ion secondary batteries. J Power Sources 2017;359:592–600. [CrossRef]
[30] Eddahech A, Briat O, Vinassa JM. Performance comparison of four lithium-ion battery technologies under calendar aging. Energy 2015;84:542–550. [CrossRef]
[31] Tanim TR, Rahn CD. Aging formula for lithium-ion batteries with solid electrolyte interphase layer growth. J Power Sources 2015;294:239–247. [CrossRef]
[32] Maleki H, Selman JR, Dinwiddie RB, Wang H. High thermal conductivity negative electrode material for lithium-ion batteries. J Power Sources 2001;94:26–35. [CrossRef]
[33] Nyman A, Zavalis TG, Elger R, Behm M, Lindbergh G. Analysis of the polarization in a Li-ion battery cell by numerical simulations. J Electrochem Soc 2010;157:A1236. [CrossRef]
[34] Vogel JE, Sederholm JG, Shumway EM, Abello GJ, Trask SE, Wheeler DR, et al. Li-ion battery electrode contact resistance estimation by mechanical peel test. J Electrochem Soc 2022;169:8. [CrossRef]
[35] Thackeray MM. Manganese oxides for lithium batteries. Prog Solid State Chem 1997;25:1–71. [CrossRef]
[36] Tian R, Alcala N, O'Neill SJ, Hovarth DV, Coelho J, Griffin AJ, et al. Quantifying the effect of electronic conductivity on the rate performance of nanocomposite battery electrodes. Appl Energy Mater 2020;3:2966–2974. [CrossRef]
[37] Selvi GT, Jha SK. Discharge profile and its correlation with estimated parametric sensitivity and electrical contact resistance losses in Li-ion battery. J Electrochem Soc 2021;168:110511. [CrossRef]
[38] Paxton WA, Zhong Z, Tsakalakos T. Tracking inhomogeneity in high-capacity lithium iron phosphate batteries. J Power Sources 2015;275:429–434. [CrossRef]
[39] Wiedemann AH, Goldin GM, Barnett SA, Zhu H, Kee RJ. Effects of three-dimensional cathode microstructure on the performance of lithium-ion battery cathodes. Electrochim Acta 2013;88:580–588. [CrossRef]
[40] Lee J, Sung S, Kim Y, Park JD, Ahn KH. A new paradigm of materials processing—heterogeneity control. Curr Opin Chem Eng 2017;16:16-22. [CrossRef]
[41] Asaka K, Karita M, Saito Y. Modification of interface structure and contact resistance between a carbon nanotube and a gold electrode by local melting. Appl Surf Sci 2011;257:2850–2853. [CrossRef]

[42] Taheri P, Hsieh S, Bahrami M. Investigating electrical contact resistance losses in lithium-ion battery assemblies for hybrid and electric vehicles. J Power Sources 2011;196:6525–6533. [CrossRef]
[43] Jiang T, Zhang S, Qiu X, Zhu W, Chen L. Preparation and characterization of silicon-based three-dimensional cellular anode for lithium-ion battery. Electrochem Commun 2007;9:930–934. [CrossRef]
[44] Zhou H, Zhou F, Xu L, Kong J. Thermal performance of cylindrical lithium-ion battery thermal management system based on air distribution pipe. Int J Heat Mass Transf 2019;131:984–998. [CrossRef]
[45] Liu Y, Zhang J. Design of a J-type air-based battery thermal management system through surrogate-based optimization. Appl Energy 2019;252:113426. [CrossRef]
[46] Grande L, He X. Advanced Li-ion and beyond Li-ion batteries 2018–2028. Available at: https://www.idtechex.com/research/reports/advanced-li-ion-andbeyond-li-ion-batteries-2018-2028-000566.asp. Accessed on 27 Feb, 2026.
[47] Jilte RD, Kumar R, Ma L. Thermal performance of a novel confined flow Li-ion battery module. Appl Therm Eng 2019;146:1–11. [CrossRef]
[48] Zolot MD, Kelly K, Keyser M, Mihalic M, Pesaran A. Thermal evaluation of the Honda Insight battery pack. National Laboratory of the Rockies 2001.
[49] Kelly KJ, Mihalic M, Zolot MD. Battery usage and thermal performance of the Toyota Prius and Honda Insight during chassis dynamometer testing. IEEE Xplore 2002;247–252.
[50] Li M, Liu Y, Wang X, Zhang J. Modeling and optimization of an enhanced battery thermal management system in electric vehicles. Front Mech Eng 2018. [CrossRef]
[51] Akinlabi AA, Solyali D. Empirical thermal performance investigation of a compact lithium-ion battery module under forced convection cooling. Appl Sci 2020;10:3732. [CrossRef]
[52] Buidin TIC, Mariasiu F. Modeling approach of an air-based battery thermal management system for an electric vehicle. Appl Sci 2021;11:7089. [CrossRef]
[53] Chen K, Chen Y, She Y, Song M, Wang S, Chen L. Construction of effective symmetrical air-cooled system for battery thermal management. Appl Therm Eng 2020;166:114679. [CrossRef]
[54] Chen K, Wu W, Yuan F, Chen L, Wang S. Cooling efficiency improvement of air-cooled battery thermal management system through designing the flow pattern. Energy 2019;167:781–790. [CrossRef]
[55] Chen K, Zhang Y, Liao Y, Wu W. Thermal optimization of battery thermal management system with the combination of phase change materials and fluid dynamics. Appl Therm Eng 2020;172:115176.
[56] Guo J, Jiang F. A novel electric vehicle thermal management system based on cooling and heating of batteries by refrigerant. Energy Convers Manage 2021;237:114145. [CrossRef]
[57] He F, Ma L. Thermal management of batteries employing active temperature control and reciprocating cooling flow. Int J Heat Mass Transf 2015;83:62–68. [CrossRef]
[58] Imre T, Buidin TIC, Mariasiu F. Modeling approach of an air-based battery thermal management system for an electric vehicle. Appl Sci 2021;11:7089. [CrossRef]
[59] Peng X, Cui X, Liao X, Garg A. A thermal investigation and optimization of an air-cooled lithium-ion battery pack. Energies 2020;13:2956. [CrossRef]
[60] Pradeep R, Venugopal T, Sivakumar R. Computational investigations of battery thermal management system with environmental effects employing a combination of phase change materials and forced air cooling. Int J Green Energy 2022;19:509–520. [CrossRef]
[61] Shahid S, Chaab MA. Experimental and numerical studies on air cooling and temperature uniformity in a battery pack. Int J Energy Res 2018;42:2246–2262. [CrossRef]
[62] Wang T, Tseng KJ, Zhao J, Wei Z. Thermal investigation of lithium-ion battery module with different cell arrangement structures and forced air-cooling strategies. Appl Energy 2014;134:229–238. [CrossRef]
[63] Wu W. The experimental and simulation research of power batteries thermal management based on PCM. China: Guangdong University of Technology; 2015.
[64] Zhuang W, Liu Z, Su H, Chen G. An intelligent thermal management system for optimized lithium-ion battery pack. Appl Therm Eng 2021;189:116767. [CrossRef]
[65] Zhang J, Wu X, Chen K, Zhou D, Song M. Experimental and numerical studies on an efficient transient heat transfer model for air-cooled battery thermal management systems. J Power Sources 2021;490:229539. [CrossRef]
[66] Zhang F, Lin A, Wang P, Liu P. Optimization design of a parallel air-cooled battery thermal management system with spoilers. Appl Therm Eng 2021;182:116062. [CrossRef]
[67] Liu H, Wang H, Yang C, Zhao J. Simulation study of lithium-ion battery thermal management system based on a variable flow velocity method with liquid metal. Appl Therm Eng 2020;179:115578. [CrossRef]
[68] Kashyap P, Panda B, Gao L, Garg A. Design optimization of staggered-arranged battery thermal management system using an integrated approach of physics-based simulations and evolutionary algorithms. J Energy Storage 2024;79:110229. [CrossRef]
[69] Yang W, Wang Y, Guo F, Bai Y, Liu X. Optimization study of air-cooled stagger-arranged battery pack with reverse-layered airflow. J Energy Storage. 2022;55:105524. [CrossRef]
[70] Patil MS, Seo JH, Lee MY. A novel dielectric fluid immersion cooling technology for Li-ion battery thermal management. Energy Convers Manage 2021;229:113715. [CrossRef]

[71] Wang YF, Wu JT. Thermal performance predictions for an HFE-7000 direct flow boiling cooled battery thermal management system for electric vehicles. Energy Convers Management 2020;207:112569. [CrossRef]
[72] Zhao Y, Zhang X, Yang B, Cai S. A review of battery thermal management systems using liquid cooling and PCM. J Energy Storage 2024;76:109836. [CrossRef]
[73] An Z, Jia L, Li X, Ding Y. Experimental investigation on lithium-ion battery thermal management based on flow boiling in mini-channel. Appl Therm Eng 2017;117:534–543. [CrossRef]
[74] Li X, Zhou Z, Zhang M, Zhang F, Zhou X. A liquid cooling technology based on fluorocarbons for lithium-ion battery thermal safety. Journal of Loss Prevention in the Process Industries. 2022;78:104615. [CrossRef]
[75] Kim GH, Pesaran A. Battery thermal management design modeling. World Electr Veh J 2007;1:126–133. [CrossRef]
[76] Giammichele L, D'Alessandro V, Falone M, Ricci R. Experimental study of a direct immersion liquid cooling of a Li-ion battery for electric vehicles applications. Int J Heat Technol 2022;40:1–8. [CrossRef]
[77] Nelson P, Dees D, Amine K, Henriksen G. Modeling thermal management of lithium-ion PNGV batteries. J Power Sources 2002;110:349–356. [CrossRef]
[78] Satyanarayana G, Sudhakar DR, Goud MV, Ramesh J, Pathanjali GA. Experimental investigation and comparative analysis of immersion cooling of lithium-ion batteries using mineral and therminol oil. Appl Therm Eng 2023;225:120187. [CrossRef]
[79] Karimi G, Dehghan AR. Thermal analysis of high-power lithium-ion battery packs using flow network approach. Int J Energy Res 2014;38:1793–1811. [CrossRef]
[80] Wu N, Ye X, Yao J, Zhang X, Zhou X, Yu B. Efficient thermal management of the large-format pouch lithium-ion cell via the boiling-cooling system operated with intermittent flow. Int J Heat Mass Transf 2021;170:121018. [CrossRef]
[81] Fluent Theory Guide . Available at: https://www.scribd.com/document/668106063/ANSYS-Fluent-Theory-Guide-2019-R1. Accessed on 27 Feb, 2026.
[82] Jarrett A, Kim IY. Design optimization of electric vehicle battery cooling plates for thermal performance. J Power Sources 2011;196:10359–10368. [CrossRef]
[83] Qian Z, Li Y, Rao Z. Thermal performance of lithium-ion battery thermal management system by using mini-channel cooling. Energy Convers Manage 2016;126:622–631. [CrossRef]
[84] Zhao C, Cao W, Dong T, Jiang F. Thermal behavior study of discharging/charging cylindrical lithium-ion battery module cooled by channeled liquid flow. Int J Heat Mass Transf 2018;120:751–762. [CrossRef]
[85] Chung Y, Kim MS. Thermal analysis and pack level design of battery thermal management system with liquid cooling for electric vehicles. Energy Convers Manage 2019;196:105–116. [CrossRef]
[86] Guo J, Jiang F. A novel electric vehicle thermal management system based on cooling and heating of batteries by refrigerant. Energy Convers Manage 2021;237:114145. [CrossRef]
[87] Akbarzadeh M, Kalogiannis T, Jaguemont J, Jin L, Behi H, Karimi D. A comparative study between air cooling and liquid cooling thermal management systems for a high-energy lithium-ion battery module. Appl Therm Eng 2021;198:117503. [CrossRef]
[88] Li L, Ling L, Xie YJ, Zhou WC, Wang TB, Zhang LC, et al. Comparative study of thermal management systems with different cooling structures for cylindrical battery modules: side-cooling vs. terminal-cooling. Energy 2023;274:127414. [CrossRef]
[89] Zeng JX, Feng S, Lai CG, Song J, Fu LJ, Chen H. Prediction on thermal performance of refrigerant-based battery thermal management system for a HEV battery pack. Int J Heat Mass Transf 2023;201:123657. [CrossRef]
[90] Monika M, Datta SP. Comparative assessment among several channel designs with constant volume for cooling of pouch-type battery module. Energy Convers Manage 2022;251:114936. [CrossRef]
[91] Tang A, Li J, Lou L, Shan C, Yuan X. Optimization design and numerical study on water cooling structure for power lithium battery pack. Appl Therm Eng 2019;159:113760. [CrossRef]
[92] Wazeer A, Das A, Abeykoon C, Sinha A, Karmakar A. Phase change materials for battery thermal management of electric and hybrid vehicles: A review. Energy Nexus 2022;7:100131. [CrossRef]
[93] Al Hallaj S, Selman J. A novel thermal management system for electric vehicle batteries using phase-change material. J Electrochem Soc 2000;147:3231. [CrossRef]
[94] Lafdi K, Mesalhy O, Shaikh S. Experimental study on the influence of foam porosity and pore size on the melting of phase change materials. J Appl Phys 2007;102:083511. [CrossRef]
[95] Goli P, Legedza S, Dhar A, Salgado R, Renteria J, Balandin AA. Graphene-enhanced hybrid phase change materials for thermal management of Li-ion batteries. J Power Sources 2014;248:37–43. [CrossRef]
[96] Nasehi R, Alamatsaz A, Salimpour M. Using multi-shell phase change materials layers for cooling a lithium-ion battery. Therm Sci 2016;20:391–403. [CrossRef]
[97] Yan J, Wang Q, Li K, Sun J. Numerical study on the thermal performance of a composite board in battery thermal management system. Appl Therm Eng 2016;106:131–140. [CrossRef]
[98] Wang S, et al. Numerical optimization for a phase change material based lithium-ion battery thermal management system. Appl Therm Eng 2023;222:118055. [CrossRef]

[99] Wang Y, Wan Z, Min H, Li H, Li Q. Performance investigation of a passive battery thermal management system applied with phase change material. J Energy Storage 2021;35:102303. [CrossRef]
[100] Sudhakaran S, Terese M, Mohan Y, Thampi AD, Rani S. Influence of various parameters on the cooling performance of battery thermal management systems based on phase change materials. Appl Therm Eng 2023;222:118094. [CrossRef]
[101] Jiang G, Huang J, Fu Y, Cao M, Liu M. Thermal optimization of composite phase change material/expanded graphite for Li-ion battery thermal management. Appl Therm Eng 2016;108:1119–1125. [CrossRef]
[102] Hussain A, Tso CY, Chao CYH. Experimental investigation of a passive thermal management system for high-powered lithium-ion batteries using nickel foam-paraffin composite. Energy 2016;115:209–218. [CrossRef]
[103] Goli P, Legedza S, Dhar A, Salgado R, Renteria J, Balandin AA. Graphene-enhanced hybrid phase change materials for thermal management of Li-ion batteries. J Power Sources 2014;248:37–43. [CrossRef]
[104] Li J, Tang A, Shao X, Jin Y, Chen W, Xia D. Experimental evaluation of heat conduction enhancement and lithium-ion battery cooling performance based on h-BN-based composite phase change materials. Int J Heat Mass Transf 2022;186:122552. [CrossRef]
[105] Babapoor A, Azizi M, Karimi G. Thermal management of a Li-ion battery using carbon fiber-PCM composites. Appl Therm Eng 2015;82:281–290. [CrossRef]
[106] Zhuang Y, Chen T, Chen J, Li J, Guan M, Chen Y. Thermal uniformity performance of a hybrid battery thermal management system using phase change material and cooling plates arrayed in the manner of honeycomb. Therm Sci Eng Prog 2021;26:100939. [CrossRef]
[107] He F, Ma L. Thermal management of batteries employing active temperature control and reciprocating cooling flow. Int J Heat Mass Transf 2015;83:62–68. [CrossRef]
[108] Gao X, Ma Y, Chen H. Active thermal control of a battery pack under elevated temperature. IFAC Papers Online 2018;51:1730–1735. [CrossRef]
[109] Wang J, Mei W, Mao B, Wang Q. Investigation on the temperature control performance and optimization strategy of a battery thermal management system combining phase change and liquid cooling. Appl Therm Eng 2023;232:119421. [CrossRef]
[110] Ling Z, Cao J, Zhang W, Zhang Z, Fang X, Gao X. Compact liquid cooling strategy with phase change materials for Li-ion batteries optimized using response surface methodology. Appl Energy 2018;228:777–788. [CrossRef]
[111] Ouyang T, Liu B, Xu P, Wang C, Ye J. Electrochemical-thermal coupled modelling and multi-measure prevention strategy for Li-ion battery thermal runaway. Int J Heat Mass Transf 2022;194:123506. [CrossRef]
[112] Zhang Y, Fu Q, Liu Y, Lai B, Ke Z, Wu W. Investigations of lithium-ion battery thermal management system with hybrid PCM/liquid cooling plate. Processes 2022;11:45. [CrossRef]
[113] Lebrouhi BE, Lamrani B, Ouassaid M, Abd-Lefdil M, Maaroufi M, Kousksou T. Low-cost numerical lumped modelling of lithium-ion battery pack with phase change material and liquid cooling thermal management system. J Energy Storage. 2022;54:103305. [CrossRef]
[114] Priyadarsini P, Sahoo S, Parida PK, Sathapathy PK. Effect of trapezoidal fin on heat transfer enhancement in PCM thermal energy storage system: a computational approach. Int J Energy Environ Eng 2022;23:13–28. [CrossRef]
[115] Priyadarsini P, Beuria A, Satapathy PP, Sahoo SS. Computational study of melting and solidification behavior of PCM thermal energy storage system using extended surface. Adv Mater Proc Technol 2022:123–133. [CrossRef]
[116] Huat L, Mun H, San H, Cai Z, Tong W, Agung N, Jin Y. Novel thermal management system using mist cooling for lithium-ion battery packs. Appl Energy 2018;223:146–158. [CrossRef]
[117] Gao Q, Liu Y, Wang G, Deng F, Zhu J. An experimental investigation of refrigerant emergency spray on cooling and oxygen suppression for overheating power battery. J Power Sources. 2019;415:33–43. [CrossRef]
[118] Wang Y, Diao D, Zhao Y, Wang L. Cooling property of flat micro-heat pipe arrays for lithium battery. Chinese J Power Sources. 2014;38:1433–1436.
[119] Hong S, Zhang X, Wang S, Zhang Z. Review on application of heat pipe technology in lithium-ion power battery thermal management system. Chem Ind Eng Prog 2014;33:2923–2927.
[120] Li G, He C, Xie Y, Liu B, Deng S. Thermal management of a 48V pouch lithium-ion battery pack based on high rate discharge condition. Energy Storage Sci Technol 2021;10:679–688.
[121] Tian S, Xiao J. Temperature simulation and analysis of lithium-ion battery module based on heat pipe–aluminum plate chimeric cooling structure. J Hunan Univ Sci Technol 2021;36:67–72.
[122] Dan D, Yao C, Zhang Y, Zhang H, Zeng Z, Xu X. Dynamic thermal behavior of micro heat pipe array-air cooling battery thermal management system based on thermal network model. Appl Therm Eng 2019;162:114183. [CrossRef]
[123] Liu B, Hu Z, Li K, Xie Y, Zhang J. Experimental and simulation on battery thermal management based on a large flat heat pipe. Energy Storage Sci Technol 2021;10:1364–1373.

[124] Zhang C, Yu M, Fan Y, Zhang X, Zhao Y, Qiu L. Numerical study on heat transfer enhancement of PCM using three combined methods based on heat pipe. Energy. 2019;195:116. [CrossRef]
[125] Yang X, Tan S, He Z, Liu J. Finned heat pipe assisted low melting point metal PCM heat sink against extremely high power thermal shock. Energy Convers Manage 2018;160:467–476. [CrossRef]
[126] Wu W, Yang X, Zhang G, Chen K, Wang S. Experimental investigation on the thermal performance of heat pipe-assisted phase change material based battery thermal management system. Energy Convers Manage 2017;138:486–492. [CrossRef]